

Replaceable Unbonded Tendons for Post-Tensioned Bridges

This report is separated into four parts:

Page 2: Extended Summary

Page 64: Part I Mockup for Flexible Filler Injection

Page 202: Part II Structural Testing

Page 415: Part III Wire Break Detection

Final Report

December 2017

Principal investigator:

H. R. Hamilton

Co-Principal investigator:

J. A. Rice

Research assistants:

A.B.M. Abdullah

Rahul Bhatia

Natassia Brenkus

Devon Skelton

Sponsor:

Florida Department of Transportation (FDOT)

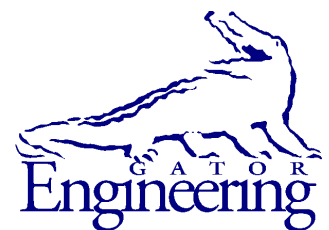
William Potter, P.E. – Project Manager

Rick W. Vallier, P.E. –Project Manager

Contract:

UF Project No. 000112216 & 000112218

FDOT Contract No. BDV31-977-15



University of Florida

Engineering School of Sustainable Infrastructure and Environment

Department of Civil and Coastal Engineering

University of Florida

P.O. Box 116580

Gainesville, Florida 32611

Replaceable Unbonded Tendons for Post-Tensioned Bridges

Extended Summary

This report is one of a four-part compilation published under separate covers as follows:

Extended Summary

Part I Mockup for Flexible Filler Injection

Part II Structural Testing

Part III Wire Break Detection

Final Report

December 2017

Principal investigator:

H. R. Hamilton

Co-Principal investigator:

J. A. Rice

Research assistants:

A.B.M. Abdullah

Rahul Bhatia

Natassia Brenkus

Devon Skelton

Sponsor:

Florida Department of Transportation (FDOT)

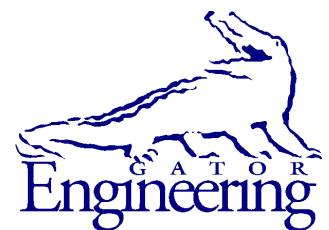
William Potter, P.E. – Project Manager

Rick W. Vallier, P.E. –Project Manager

Contract:

UF Project No. 000112216 & 000112218

FDOT Contract No. BDV31-977-15



University of Florida

Engineering School of Sustainable Infrastructure and Environment

Department of Civil and Coastal Engineering

University of Florida

P.O. Box 116580

Gainesville, Florida 32611

Disclaimer

The opinions, findings, and conclusions expressed in this publication are those of the authors and not necessarily those of the State of Florida Department of Transportation.

Unit of Measurement Conversions

SI* (MODERN METRIC) CONVERSION FACTORS

APPROXIMATE CONVERSIONS TO SI UNITS

SYMBOL	WHEN YOU KNOW	MULTIPLY BY	TO FIND	SYMBOL
LENGTH				
in	inches	25.4	millimeters	mm
ft	feet	0.305	meters	m
yd	yards	0.914	meters	m
mi	miles	1.61	kilometers	km
AREA				
in²	square inches	645.2	square millimeters	mm ²
ft²	square feet	0.093	square meters	m ²
yd²	square yard	0.836	square meters	m ²
ac	acres	0.405	hectares	ha
mi²	square miles	2.59	square kilometers	km ²
VOLUME				
fl oz	fluid ounces	29.57	milliliters	mL
gal	gallons	3.785	liters	L
ft³	cubic feet	0.028	cubic meters	m ³
yd³	cubic yards	0.765	cubic meters	m ³
NOTE: volumes greater than 1000 L shall be shown in m ³				
MASS				
oz	ounces	28.35	grams	g
lb	pounds	0.454	kilograms	kg
T	short tons (2000 lb)	0.907	megagrams	Mg (or "t")
TEMPERATURE (exact degrees)				
°F	Fahrenheit	5(F-32)/9 or (F-32)/1.8	Celsius	°C
ILLUMINATION				
fc	foot-candles	10.76	lux	lx
fl	foot-Lamberts	3.426	candela/m ²	cd/m ²
FORCE and PRESSURE or STRESS				
kip	1000 pound force	4.45	kilonewtons	kN
lbf	pound force	4.45	newtons	N
lbf/in²	pound force per square	6.89	kilopascals	kPa

*SI is the symbol for the International System of Units. Appropriate rounding should be made to comply with Section 4 of ASTM E380.

SI* (MODERN METRIC) CONVERSION FACTORS
APPROXIMATE CONVERSIONS FROM SI UNITS

SYMBOL	WHEN YOU KNOW	MULTIPLY BY	TO FIND	SYMBOL
LENGTH				
mm	millimeters	0.039	inches	in
m	meters	3.28	feet	ft
m	meters	1.09	yards	yd
km	kilometers	0.621	miles	mi
AREA				
mm²	square millimeters	0.0016	square inches	in ²
m²	square meters	10.764	square feet	ft ²
m²	square meters	1.195	square yards	yd ²
ha	hectares	2.47	acres	ac
km²	square kilometers	0.386	square miles	mi ²
VOLUME				
mL	milliliters	0.034	fluid ounces	fl oz
L	liters	0.264	gallons	gal
m³	cubic meters	35.314	cubic feet	ft ³
m³	cubic meters	1.307	cubic yards	yd ³
MASS				
g	grams	0.035	ounces	oz
kg	kilograms	2.202	pounds	lb
Mg (or "t")	megagrams (or "metric ton")	1.103	short tons (2000 lb)	T
TEMPERATURE (exact degrees)				
°C	Celsius	1.8C+32	Fahrenheit	°F
ILLUMINATION				
lx	lux	0.0929	foot-candles	fc
cd/m²	candela/m ²	0.2919	foot-Lamberts	fl
FORCE and PRESSURE or STRESS				
kN	kilonewtons	0.225	1000 pound force	kip
N	newtons	0.225	pound force	lbf
kPa	kilopascals	0.145	pound force per square inch	lbf/in ²

*SI is the symbol for the International System of Units. Appropriate rounding should be made to comply with Section 4 of ASTM E380.

Technical Report Documentation Page

1. Report No.		2. Government Accession No.		3. Recipient's Catalog No.	
4. Title and Subtitle Replaceable Unbonded Tendons for Post-Tensioned Bridges				5. Report Date December 2017	
				6. Performing Organization Code	
7. Author(s) Brenkus, N. R., Abdullah, A. B. M., Bhatia, R., Skelton, D., Rice, J. A., and Hamilton, H. R.				8. Performing Organization Report No.	
9. Performing Organization Name and Address University of Florida Department of Civil & Coastal Engineering P.O. Box 116580 Gainesville, FL 32611-6580				10. Work Unit No. (TRAIS)	
				11. Contract or Grant No. BDV31-977-15	
12. Sponsoring Agency Name and Address Florida Department of Transportation 605 Suwannee Street, MS 30 Tallahassee, FL 32399				13. Type of Report and Period Covered Final Report Feb. 2014-Dec. 2017	
				14. Sponsoring Agency Code	
15. Supplementary Notes					
16. Abstract <p>Prestressed concrete is widely used as a cost-effective and efficient method of bridge construction and offers a number of unique advantages over other systems. Florida Department of Transportation (FDOT) is implementing the use of flexible fillers in lieu of cementitious grout in certain post-tensioning tendon profiles. This research was divided into three areas of focus. The first area of work involved the design, construction, and injection of full-scale post-tensioning tendon mockups. Five 200-ft long specimens were fabricated with a profile that simulated both internal and external tendons. HDPE duct of 4-in. diameter with nineteen 0.6-in. prestressing strands formed the tendon. Injection rates and venting procedures were varied among the five mockups, primarily in an effort to determine the most suitable approach. Based on constructability tests conducted, no cause to restrict use of any of the PT systems or filler products was found. The second area of research was on the structural implications of the change to flexible fillers. This part of the research project focused on the flexural strength behavior of specimens with internal and external tendons using AASHTO Type IV sections. It was found that the AASHTO-LRFD design specifications adequately predicted the flexural strength of members with external unbonded tendons with flexible fillers. In addition, fatigue specimens were constructed to test the fatigue performance of the unbonded tendons with diablo deviators. Duct damage was noted at one of the deviator exit locations that was the result of the strands pinching the HDPE wall against the concrete. Providing sufficient flare curvature in the deviator was critical for good performance. The third area of research focused on developing a robust and cost-effective monitoring system for unbonded post-tensioning tendons. The change from bonded to unbonded tendons allows a unique opportunity to develop an efficient system for tendon damage detection with the ultimate goal of providing maintenance decision support. Analytical and experimental investigations were performed to develop an algorithm that can be used to detect, locate, and quantify tendon damage by monitoring the strain distribution in the wedge plates of the anchors.</p>					
post-tensioned concrete, grout, wax flexible filler, health monitoring, fatigue, flexure				18. Distribution Statement No restrictions	
19. Security Classif. (of this report) Unclassified		20. Security Classif. (of this page) Unclassified		21. No. of Pages 62	22. Price

Acknowledgments

The authors would like to thank the Florida Department of Transportation (FDOT), the Marcus H. Ansley Structures Research Center and the FDOT State Materials Office for their technical advice and structural and materials testing support.

The authors would like to express sincere gratitude to Dr. Gary Gan at Construction Technologies Laboratories for testing of prestressing strand specimens.

Executive Summary

Prestressed concrete is widely used as a cost-effective and efficient method of bridge construction and offers a number of unique advantages over other systems. Bonded multi-strand post-tensioning tendons have typically been the primary method of prestressing long-span spliced-girder and box-girder bridges in Florida. To attain bonded tendons, however, a cementitious grout must be injected into the tendon and allowed to harden. Recent years have seen durability issues arise from poor grouting practice or poor material performance. To address this issue, Florida Department of Transportation (FDOT) is implementing the use of flexible fillers (petroleum wax or grease) in lieu of cementitious grout as the primary choice for corrosion protection of post-tensioning tendons.

The use of flexible fillers is not a wholly new idea; they have been in regular use in the nuclear industry for many years and have more recently been used in post-tensioning tendons for bridges in France and elsewhere. Nevertheless, the decision has constructability and structural implications. The objective of the research covered in this report is to address some of the potential issues that come with the use of flexible fillers.

The research project was divided into three broad areas. The first area of work involved the design, construction, and injection of full-scale post-tensioning tendon mockups. Five 200-ft long specimens were fabricated with a profile that simulated both internal and external tendons. HDPE duct of 4 in. diameter with nineteen 0.6-in. prestressing strands formed the tendon. In addition, the tendons were lightly stressed to ensure that the strand bundle was oriented in the duct in a similar manner to a fully stressed tendon in the field.

Injection rates and venting procedures were varied among the five mockups, primarily in an effort to determine the most suitable approach. In spite of the variation of procedures, all of the strands in each of the specimens were well-coated with filler material even though the first two tendons injected contained a void at the top of the duct cross-section in the parabolic portion of the mockup. In one case, venting was intentionally omitted. In the other case, the void was thought to be the result of inadequate venting procedures and not the PT system or individual filler products used. At the completion of these mockup tests, no cause to restrict use of any of the PT systems or filler products was found.

In addition, a simplified heat transfer model has been developed that computes the decrease in temperature of the moving filler front during injection as it cools while interacting with the surrounding strands and duct. The proposed model has been subsequently validated by multiple mockup experiments conducted with different filler materials and injection rates. The detailed results of this work are covered separately in *Part I—Mockup for Flexible Filler Injection*.

The second area of research was on the structural implications of the change to flexible fillers. This part of the research project focused on the flexural strength behavior of specimens with internal and external tendons using AASHTO Type IV sections. The use of flexible fillers instead of grout in both internal and external tendons will result in a change in the contribution that the unbonded tendons will make to the flexural strength of the section. Depending on the situations in which flexible fillers are used, prestressed members could have bonded and unbonded tendons or mixed tendons. It was found that the AASHTO-LRFD design specifications adequately predicted the flexural strength of members with external unbonded tendons with flexible fillers. The hinge length in mixed tendon specimens (with internal tendons), as estimated from inspection of the final cracking patterns, was found to be less than

that assumed in the formulation of the unbonded tendon stress prediction equation given in AASHTO-LRFD (Section 5.7.3.1.2).

In addition, fatigue specimens were constructed to test the fatigue performance of the unbonded tendons in conjunction with the diabolo deviator configuration, which is a necessary component when considering the replaceability of fully unbonded external tendons. The focus was on wedge and anchor fatigue; fretting at the diabolo; and wear and damage of the duct at the diabolo. Duct damage was noted at one of the deviator exit locations that was the result of the strands pinching the HDPE wall against the concrete. Because the other deviator exit locations did not exhibit this behavior, it is concluded that the geometry selected for the diabolo was adequate and that the damage may have been caused by diabolo misalignment. Providing additional flare curvature beyond that provided for this design would allow more tolerance for misalignment during construction. Furthermore, inspection of the deviator would be prudent prior to tendon installation to ensure that pinching does not occur. Up to 20% reduction in ultimate tensile strength of prestressing strands was noted in the fatigue specimen with a tendon deviation angle of 11 degrees. Brittle fracture patterns were noted that appear to have been induced by strand-to-strand fretting. The tensile strength of the prestressing strands in the fatigue specimen with the 18 degree deviation angle exceeded the minimum ultimate tensile strength requirement. The detailed results of this work are covered separately in *Part II – Structural Testing*.

The third area of research focused on developing a robust and cost-effective monitoring system for unbonded post-tensioning tendons. The change from bonded to unbonded tendons allows a unique opportunity to develop an efficient system for tendon damage detection with the ultimate goal of providing maintenance decision support. Specifically, the aim was to detect wire or strand breaks and identify the broken strand at the earliest possible stage; ideally this would be as early as a single wire break. Analytical and experimental investigations were performed to develop an algorithm that can be used to detect, locate, and quantify tendon damage by monitoring the strain distribution in the wedge plates of the anchors. The detailed results of this work are covered separately in *Part III – Wire Break Detection*.

Table of Contents

Disclaimer	ii
Unit of Measurement Conversions	iii
Technical Report Documentation Page	v
Acknowledgments.....	vi
Executive Summary	vii
List of Figures	xi
List of Tables	xiii
1 Introduction.....	1
2 Post-Tensioning Tendons.....	2
2.1 Bonded Tendons	3
2.2 External Tendons	3
2.3 Unbonded Tendons	4
2.3.1 Monostrand Systems	4
2.3.2 Multi-strand systems	6
2.3.3 Wire Systems.....	9
2.3.4 Unbonded Tendon Systems.....	11
3 Multi-strand Unbonded Tendon Applications	12
3.1 Itztal Bridge	13
3.2 Weidatal Bridge	14
3.3 Nibelungenbrücke	14
3.4 Kleine-Laber-Viaduct	15
3.5 Rossriether Graben.....	16
3.6 Muhlenberg Viaduct	17
3.7 Nuclear Containment	19
4 Replaceability of Post-Tensioning Tendons	20
4.1 Precast Segmental Balanced Cantilever.....	20
4.2 Cast-in-place Segmental Balanced Cantilever.....	22
4.3 Precast Segmental Span-by-span	23
4.4 Post-tensioned AASHTO Bulb-T and Splice Girder	23
4.5 Substructures.....	24
4.6 In-Service Inspection Requirements (NRC)	25
4.7 Implications.....	27
5 Part I—Mockup for Flexible Filler	29
5.1 Test Set-up Design and Construction	29
5.2 Results.....	31
5.3 Temperature	32
5.4 Summary and Conclusions	34
6 Part II—Structural Testing.....	36
6.1 Specimen Design and Construction	36
6.2 Construction.....	39
6.3 Testing.....	40
6.4 Summary and Conclusions	41
7 Part III—Wire Break Detection	44
7.1 Wedge Plate Test Setup	44
7.2 Wedge Plate Results	44

7.3	Finite Element Analysis	45
7.4	Experimental Evaluation of Tendon Behavior	46
7.5	Tendon Monitoring Framework.....	46
7.6	Summary and Conclusions	49

List of Figures

Figure 2-1 Components of a typical post-tensioning tendon.....	2
Figure 2-2 Segmental and I-girder bridge construction (FDOT 2002).....	3
Figure 2-3 Components of a bonded tendon.....	3
Figure 2-4 External tendons with cementitious grout.....	4
Figure 2-5 Components of unbonded monostrand (PTI 2006).....	5
Figure 2-6 Unbonded monostrand anchor (PTI 2006).....	5
Figure 2-7 Unbonded multi-strand tendons: (a) bare and (b) bundled monostrand (c) monostrand in duct (d) bundled epoxy-coated strand.....	7
Figure 2-8 Unbonded multi-strand stacked system (BBR 2013).....	7
Figure 2-9 Multi-strand anchor for bare strand (Parsons Brinkerhoff 2012).....	8
Figure 2-10 Multi-strand anchor for unbonded monostrand (Parsons Brinkerhoff 2012).....	8
Figure 2-11- Wedges and epoxy strand	9
Figure 2-12 Wire strand tendon	9
Figure 2-13 Button headed wire anchorage and tendon systems (a) DSI (Traute and Weiher 2011) (b) BBR (BBR 2013).....	10
Figure 3-1 Strand replacement: (a) strands coupled (b) introducing the new strand (Thonier 2009).....	12
Figure 3-2 Itztal bridge (Zilch et al. 2007)	14
Figure 3-3 Weidatal bridge under construction (Zilch et al. 2007)	14
Figure 3-4 Rhine bridge (Zilch et al. 2007)	15
Figure 3-5 Ariel view of Kleine-Laber-Viaduct (Traute and Weiher 2011)	15
Figure 3-6 Tendon being replaced (Traute and Weiher 2011)	16
Figure 3-7 Cross-section of bridge with the tendon being replaced in red (Traute and Weiher 2011).....	16
Figure 3-8 Rossriether Graben (Weiher and Zilch 2008)	16
Figure 3-9 Concrete deviator (Weiher and Zilch 2008).....	17
Figure 3-10 External and internal tendon path (Weiher and Zilch 2008).....	18
Figure 3-11 Tendon location at the diaphragm (Weiher and Zilch 2008)	18
Figure 3-12 Greased and sheathed detailing scheme (NEA 2015).....	19
Figure 4-1 Construction methods for precast segmental balanced cantilever (FDOT 2002-1)...	21
Figure 4-2 Precast segmental box girder with cantilever tendons (FDOT 2002-1).....	22
Figure 4-3 Continuity tendons in precast segmental construction (FDOT 2002-1)	22
Figure 4-4 Form travelers (Corven J. and Moreton A 2004).....	23
Figure 4-5 Typical tendon detail for precast segmental span-by-span bridges (FDOT 2002-1). 23	
Figure 4-6 Splice construction for AASHTO Bulb-T and Splice girders (FDOT 2002-1)	24
Figure 4-7 Options for using post-tensioning in substructure construction (a) hammer head piers (b) straddle bent (c) cantilever pier (FDOT 2002-1) (d) segmental pier (Garcia P. and Theryo T. 2006)	25
Figure 4-8 Schedule of lift-off test for two containments at one site (NRC Regulatory Guide 1.35 1990).....	26
Figure 5-1 Tendon profile for the mockup testing on unbonded tendons.....	30
Figure 5-2 Window locations on tendon.....	30
Figure 5-3 Viking pump used for filler injection (left) and vacuum pump and reservoirs (right)	31

Figure 5-4 (a) Barrel heater position on barrel (b) heaters covered with insulation blanket	31
Figure 5-5 Inspection port (IP) locations on Cirinject, Visconorust, and VZ Inject mockup specimens.....	32
Figure 5-6 Inspection port (IP) locations on Trenton 1 and Trenton 2 mockup specimens	32
Figure 5-7 Typical results at HDPE inspection port.....	32
Figure 5-8 Filler temperature in duct during injection with vacuum assist	33
Figure 5-9 Pressure loss from thermal model.....	34
Figure 6-1 Internal tendon specimen cross-section	37
Figure 6-2 Internal tendon specimen	37
Figure 6-3 External tendon specimens.....	38
Figure 6-4 External tendon specimen profile.....	38
Figure 6-5 Elevation View of Fatigue Specimen.....	39
Figure 6-6 Segments in prestressing bed	39
Figure 6-7 Segments arranged for casting of deviation block (EWS and EWC)	39
Figure 6-8 Flexible filler injection.....	40
Figure 6-9 Completed fatigue specimen	40
Figure 6-10 Three-point flexural test set-up for IGS and IWS	41
Figure 6-11 Fatigue test set-up schematic	41
Figure 7-1 Experimental setup.....	45
Figure 7-2 Axial strain variations due to wire breaks.....	45
Figure 7-3 Discretization and boundary conditions of FE model for calibration	46
Figure 7-4 Cutting the strands.....	47
Figure 7-5 Wedge movement after strand cuts	47
Figure 7-6 Wire breakage identification flowchart.....	48

List of Tables

Table 2-1 Vendors with ETA approvals for unbonded tendon systems in Europe (ETA website).....	11
Table 4-1 Unbonded tendon anchor accessibility.....	28
Table 6-1 Fatigue beam specimen abbreviations.....	39

1 Introduction

Prestressed concrete is widely used as a cost-effective and efficient method of bridge construction and offers a number of unique advantages over other systems. Bonded multi-strand post-tensioning tendons have typically been the primary method of prestressing long-span spliced-girder and box-girder bridges in Florida. To attain bonded tendons, however, a cementitious grout must be injected into the tendon and allowed to harden. Recent years have seen durability issues arise from poor grouting practice or poor material performance. To address this issue, Florida Department of Transportation (FDOT) is implementing the use of flexible fillers in lieu of cementitious grout as the primary choice for corrosion protection of post-tensioning tendons.

The use of flexible fillers is not a wholly new idea; they have been in regular use in the nuclear industry for many years and have more recently been used in post-tensioning tendons for bridges in France. Nevertheless, the decision has constructability and structural implications, which this research addresses.

Report organization

This research project was divided into three broad areas. The first area of work involved the design, construction, and injection of full-scale post-tensioning tendon mockups. Five 200-ft long specimens were fabricated with a profile that simulated both internal and external tendons. HDPE duct of 4 in. diameter with nineteen 0.6-in. prestressing strands formed the tendon. In addition, the tendons were lightly stressed to ensure that the strand bundle was oriented in the duct in a similar manner to a fully stressed tendon in the field. The detailed results of this work are covered separately in *Part I—Mockup for Flexible Filler Injection*.

The second area of research was on the structural implications of the change to flexible fillers. This part of the research project focused on the flexural strength behavior of specimens with internal and external tendons using AASHTO Type IV sections. The use of flexible fillers instead of grout in both internal and external tendons will result in a change in the contribution that the unbonded tendons will make to the flexural strength of the section. Depending on the situations in which flexible fillers are used, prestressed members could have bonded and unbonded tendons or mixed tendons. In addition, fatigue specimens were constructed to test the fatigue performance of the unbonded tendons in conjunction with the diablo deviator configuration, which is a necessary component when considering the replaceability of fully unbonded external tendons. The focus was on wedge and anchor fatigue; possible fretting at the diablo; and wear and damage of the duct at the diablo. The detailed results of this work are covered separately in *Part II – Structural Testing*.

The third area of research focused on developing a robust and cost-effective monitoring system for unbonded post-tensioning tendons. The change from bonded to unbonded tendons allows a unique opportunity to develop an efficient system for tendon damage detection with the ultimate goal of providing maintenance decision support. Specifically, the aim is to detect wire or strand breaks and identify the broken strand at the earliest possible stage, as early as the occurrence of a single wire break. The detailed results of this work are covered separately in *Part III – Wire Break Detection*

The following *Extended Summary* provides background information on post-tensioning tendons in Chapters 2, 3, and 4, and a concise overview of Parts I, II, and III in Chapters 5, 6, and 7, respectively.

2 Post-Tensioning Tendons

Post-tensioning tendons typically consist of single or bundled seven-wire prestressing strands (Figure 2-1). Less commonly, tendons may be composed of bars or bundled wire. Post-tensioning tendons are used extensively in segmental and I-girder bridge construction (Figure 2-2).

To house the post-tensioning tendons, ducts are placed in the concrete during section fabrication. When the concrete surrounding the duct has reached the specified strength, prestressing strands are pushed or pulled through these ducts and are anchored to the concrete at each end of the tendon.

Post-tensioning tendons can be either bonded or unbonded, categorized based on the tendon's contact with the surrounding concrete. After installation and stressing of the tendon, the space in the duct is typically filled with cementitious grout (referred to as grout in the remainder of the report). Grout provides both bond and corrosion protection to the prestressing steel; tendons surrounded by grout are referred to as bonded tendons. Alternatively -though much less common in the U.S. than in Europe- the duct space can be filled with a non-cementitious material which provides protection without bond; tendons using these filler materials are referred to as unbonded tendons.

Three non-cementitious pliable filler materials can be used for the corrosion protection: petroleum wax, grease, and gel. For the remainder of the document, the term "unbonded tendon" will refer to this type of tendon.

This chapter describes the various types of post-tensioning tendons currently available and used in U.S. bridges, including bonded tendons, external tendons, and unbonded tendons.

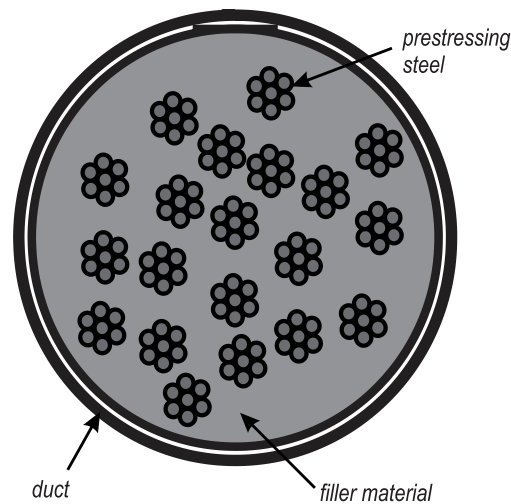


Figure 2-1 Components of a typical post-tensioning tendon



Figure 2-2 Segmental and I-girder bridge construction (FDOT 2002)

2.1 Bonded Tendons

Bonded tendons are the most common tendon used in bridge construction in the U.S (Figure 2-3). To be considered a bonded tendon, two conditions must be satisfied. First, the tendon duct must be cast into the cross-section. This type of tendon is also known as an internal tendon. The second condition is that the filler material must be a cementitious grout. These two conditions ensure that bond transfer occurs between the prestressing steel and the surrounding concrete section. Cementitious grout also provides two forms of protection for the prestressing strands. One is the physical barrier between the exterior elements and the prestressing strand. The second is the high alkaline environment provided by cementitious grout that chemically passivates the prestressing steel, which, when properly formulated and injected, reduces the steel corrosion rate to negligible levels.

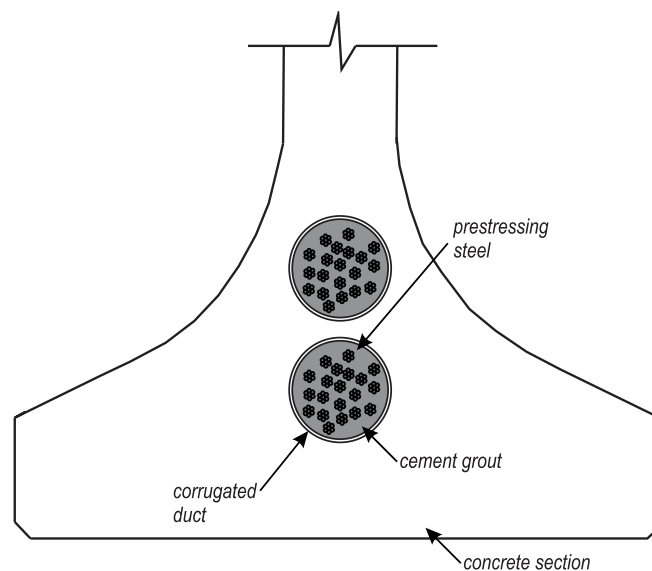


Figure 2-3 Components of a bonded tendon

2.2 External Tendons

Tendons placed outside of the concrete section are known as external tendons. External tendons impart prestressing to the concrete section at anchor points and deviators. They are most commonly used in segmental bridge construction. External tendons combine characteristics of

both bonded and unbonded tendons. In the U.S., external tendons are typically enclosed in a high-density polyethylene (HDPE) duct and injected with high-performance cementitious grout (Figure 2-4). At the anchors and deviation points, a steel pipe is used to protect the strand from the lateral pressure imparted at these locations that would otherwise damage the HDPE.



Figure 2-4 External tendons with cementitious grout

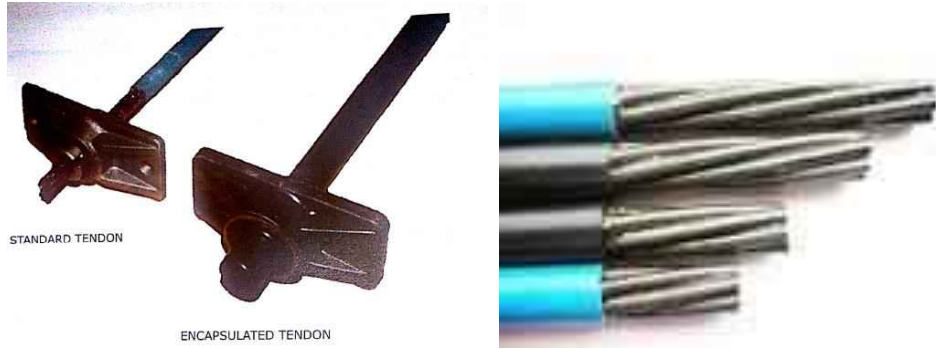
2.3 *Unbonded Tendons*

In the U.S., unbonded tendons are found primarily in building construction, though their use in bridge repair and maintenance has increased in recent years. The prestressing strand is placed inside a duct and the duct is filled with a non-cementitious material (such as petroleum wax or grease), which provides corrosion protection for the enclosed tendon. An unbonded tendon is not bonded with the concrete cross-section at any location, but instead imparts prestressing force to the concrete at deviations and anchorages. Unbonded tendons can be either internal or external to the concrete cross-section; because the tendon is not in contact with the concrete, however, strain compatibility is not applicable. The various commercially-available unbonded systems are described in the following sections.

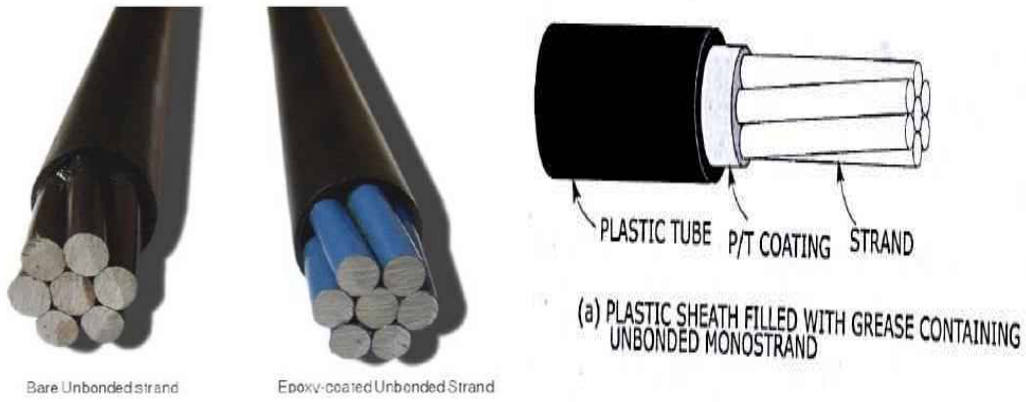
2.3.1 Monostrand Systems

While the majority of bridge construction in the U.S. uses bonded multi-strand tendons, the building construction industry commonly uses single-strand unbonded tendons - also referred to as monostrand tendons. Figure 2-5 illustrates the latest single-strand technology: a protective coating is placed over the strand to inhibit corrosion and the coating is then surrounded by a plastic sheathing, which provides further physical and chemical protection of the prestressing strand. The sheathing is typically extruded over the coated strand and allows the individual strand to be embedded in concrete before stressing. The coating over the strand lubricates the strand so that it moves easily relative to the concrete during stressing, thus reducing friction losses.

Monostrand tendons are commonly used in parking-garage deck construction. Parking garages in cold climates are subject to a rather harsh environment due to the deicing salts tracked into the garage and deposited on the slab. The resistance of monostrand tendons to this harsh environment has been improved over the years through advances in both the coating and sheathing materials. An additional level of protection is provided by a fully-encapsulated monostrand tendon, which provides a continuous barrier over the tendons and anchorage. Monostrand systems include the strand, anchor, and wedge (Figure 2-6).



(a) Mono and encapsulated unbonded tendon (b) Unbonded strand



(c) Bare and epoxy coated strand (d) unbonded monostrand

Figure 2-5 Components of unbonded monostrand (PTI 2006)

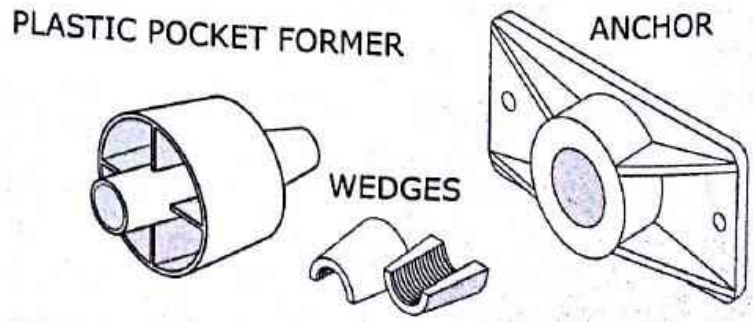


Figure 2-6 Unbonded monostrand anchor (PTI 2006)

2.3.2 Multi-strand systems

Multi-strand tendons are composed of single strands bundled together to form a single tendon. Multi-strand unbonded tendon systems are not commonly used in the U.S. bridge industry, but have been used occasionally in the repair of segmental bridges (VSL International Ltd. 2008). Figure 2-7 shows the multi-strand unbonded tendon technology that is generally commercially available, but is not common in the U.S. As shown in Figure 2-7 the strand may be bundled together bare and placed inside the duct. The duct is then filled with a PT coating such as grease or petroleum wax.

Monostrands can be bundled (Figure 2-7b) or bundled and placed in a duct (Figure 2-7c), depending on the application. If left bare, care must be taken at deviation points to avoid strand movement and sheathing damage (VSL International Ltd. 2008). One option, though more costly, is to provide individual deviation to each strand. Another option is to place the bundle in a duct and inject with cementitious grout (Figure 2-7c). The grout fixes the strand in place and provides uniform force transfer between the strand and deviator. Testing (VSL report 498 (2005)) of monostrand bundles has shown that the best approach is to apply a small prestressing force to the tendon prior to grouting. The full prestress force can then be applied after the grout has gained sufficient strength to resist the lateral force of the individual strands during prestressing. The same testing indicated that when the monostrand bundle was fully tensioned prior to grouting, the sheathing was damaged.

Another multi-strand system—even more uncommon—is bundled epoxy-coated strand (Figure 2-7d).

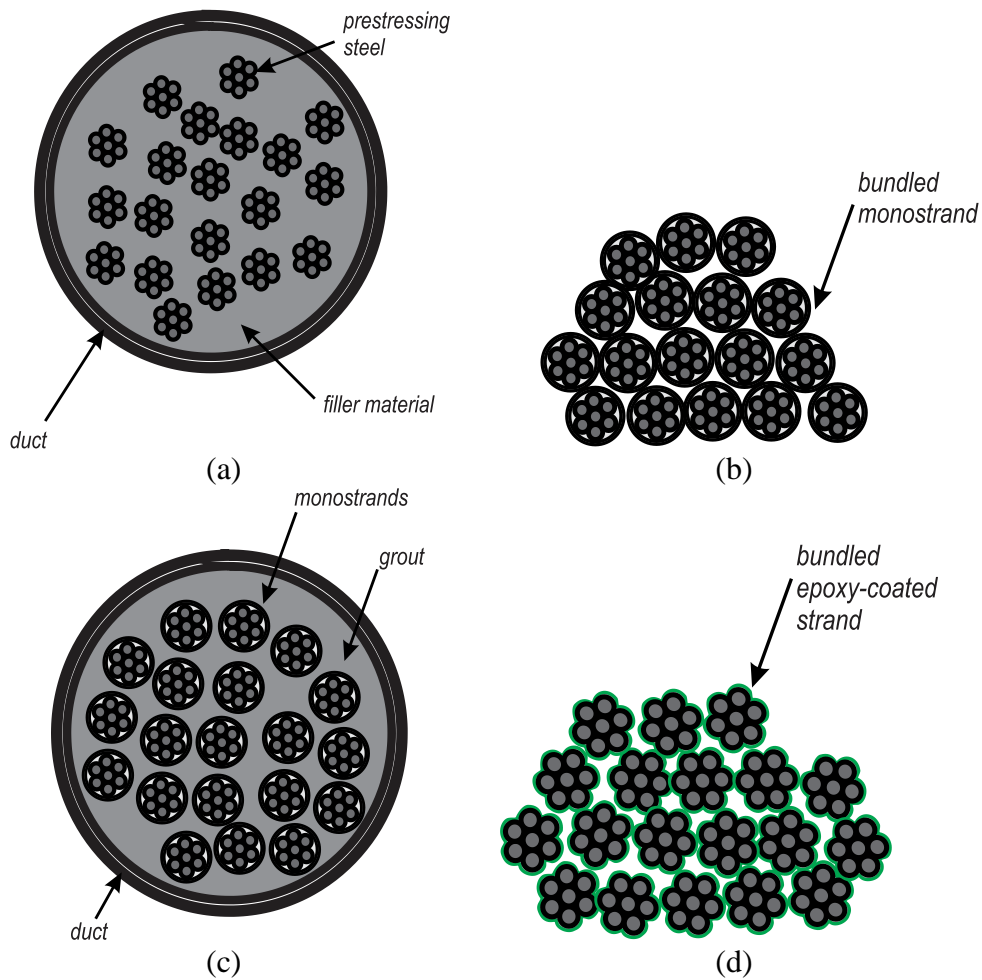


Figure 2-7 Unbonded multi-strand tendons: (a) bare and (b) bundled monostrand (c) monostrand in duct (d) bundled epoxy-coated strand

Figure 2-8 shows an alternative to bundling. Monostrands are placed in rectangular HDPE sheathing in groups of four. These groups can then be stacked to form a uniform stack of strands.

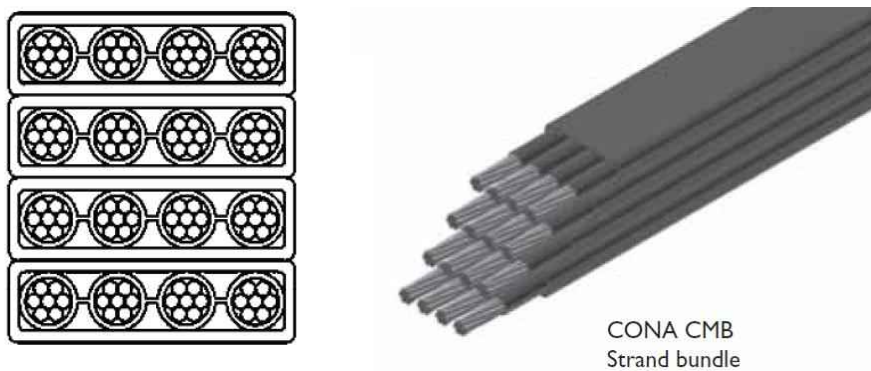


Figure 2-8 Unbonded multi-strand stacked system (BBR 2013)

Anchorage assemblies for these various tendon systems can vary depending on the details needed to inject and accommodate the corrosion protection systems. In general, the anchorages can be classified into three categories. The first type is designed to house bare strand tendons and allow the injection of either grout or pliable filler (Figure 2-9). Subtle differences may be necessary in the anchorage systems depending on the material being injected.

The second anchorage type is for housing monostrand bundles must be detailed to accommodate the larger bundle size caused by the individual sheathing. Furthermore, the anchorage system must accommodate the termination of the individual sheathing and provide corrosion protection for the areas of the strand where the sheathing has been removed. Figure 2-10 shows one such example of an anchor designed to house monostrand bundles.

The third anchorage type is designed to anchor epoxy-coated strand. Wedges with deep serrations are needed to cut through the epoxy and grip the strand to transfer the prestressing force to the anchor plate (Figure 2-11). Special anchor plates with increased spacing between strands are required to accommodate these larger diameter wedge sets.

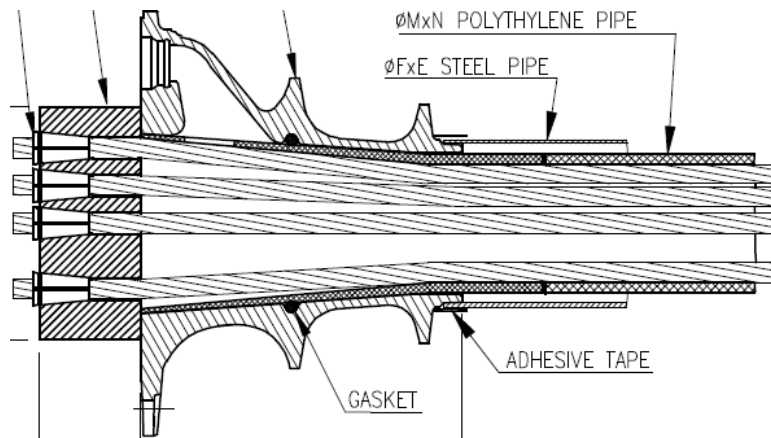


Figure 2-9 Multi-strand anchor for bare strand (Parsons Brinkerhoff 2012)

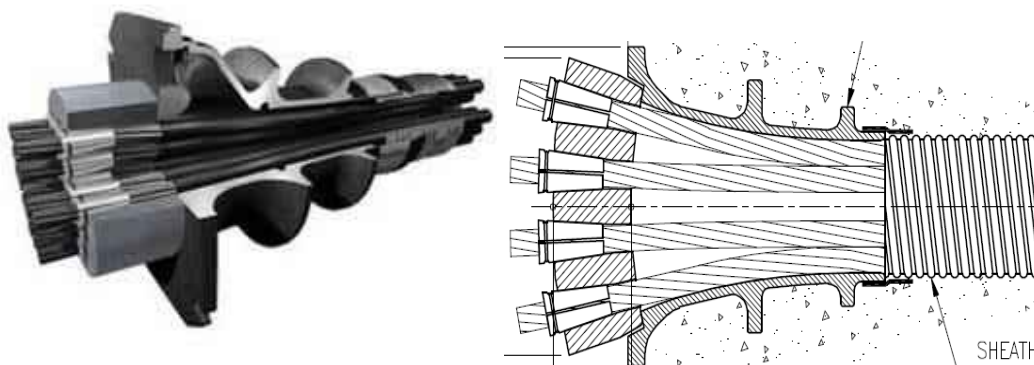


Figure 2-10 Multi-strand anchor for unbonded monostrand (Parsons Brinkerhoff 2012)



Figure 2-11- Wedges and epoxy strand

2.3.3 Wire Systems

Tendons made of high-strength prestressing wires are also commercially available. In these systems, wires are bundled to form the tendon; the wire group is cold-welded or button-headed at the anchor-head. PT coating is injected into the duct to protect against corrosion (Figure 2-12).

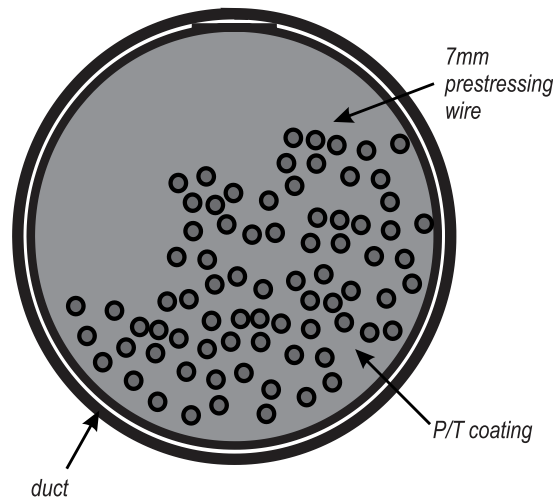


Figure 2-12 Wire strand tendon

While this system is used in Europe, it is not typically used in U.S. bridge construction. One advantage of this system is that the entire tendon, including the corrosion protection system and anchorages, is factory-assembled and shipped to the site for installation. This advantage is offset somewhat by the need to provide duct and anchorage openings of sufficient size to allow the passage of the anchorage assembly during installation. The anchorage then requires special stressing equipment to stress the tendons. (Figure 2-13) shows the anchorage system used by DSI for their wire-bundled tendons.



Figure 2-13 Button headed wire anchorage and tendon systems (a) DSI (Traute and Weiher 2011) (b) BBR (BBR 2013)

2.3.4 Unbonded Tendon Systems

The technical approval from ETAG for each of these suppliers is shown in Table 2-1.

Table 2-1 Vendors with ETA approvals for unbonded tendon systems in Europe (EOTA website)

Vendor	ETA Approval Number	Unbonded tendon system
TECPRESSA Madrid, Spain	ETA 07/0003	Approval Expired in July 12.
TENSACCAI Milano, Italy	ETA 08/0012	
SPIE BATIGNOLLES- Boulogne, France	ETA 08/0124	
VBT-BI Austria	NONE	Affiliated to National Technical Approval (Z-13.2.87)
TESIT- Monostrand Milano, Italy	ETA 11/0007	
BBR Zurich, Switzerland	ETA 06/0165	Unbonded PT up to 4 strands
	ETA 10/0065	Unbonded PT up to 16 strands
VSL Berne, Switzerland	ETA 06/0006	Unbonded PT up to 55 strands
FREYSSINET Velzy, France	ETA 06/0226	Unbonded PT 3 to 55 strands
DSI Aschhaim, Germany	ETA 09/0068	Unbonded PT up to 66 strands
BBV Bobenheim-Roxheim, Gemany	ETA 12/0150	Unbonded PT 7 to 15 strands
CCL Stressing Int. Ltd. Leeds UK	ETA 10/0107	Unbonded PT 3 to 55 strands.

3 Multi-strand Unbonded Tendon Applications

In the U.S., unbonded post-tensioning tendons are most commonly found in office, residential, parking, and nuclear containment structures. In Europe, however, unbonded tendons are also utilized in pedestrian bridges, silos, and major highway bridges. This chapter presents current information on the application of multi-strand tendons that are unbonded by virtue of the material used to fill the tendon duct.

European use of unbonded tendons in bridges initially began in the late 1970s with the design of the Exe and Exminster Viaducts Bridge in England (VSL International Ltd. 2008). During the 1980s, France and Germany expanded unbonded tendon technology, primarily using unbonded tendons as an economical repair method to rehabilitate old bridges (VSL International Ltd. 2008). During this time, unbonded tendons were generally installed outside the concrete section, but inside the box of existing concrete bridges, hence the term “external” tendon. When tensioned, these tendons actually reduced problematic deflections found in these old bridges (Ganz H. R. 1996). These projects led to the idea of making unbonded tendons replaceable in case of partial tendon damage.

Starting in the mid-1990s, European engineers (particularly those from Germany and France) began designing bridges with external unbonded tendons as well as internal unbonded tendons, with the intention of making these tendons replaceable (Zilch et al. 2007). Replaceable tendons allow repair without affecting the entire tendon or structural system.

Thonier describes strand replacement in a nuclear containment structure (Thonier 2009). The strand selected for replacement was de-tensioned and left in place. A new replacement strand was then fastened to the end of the strand being replaced. The opposite end of the existing strand was then pulled out of the tendon, in turn, pulling the new strand into the space evacuated by the existing strand (Figure 3-1). To complete the replacement process, the new strand was stressed using a single-strand jack.



Figure 3-1 Strand replacement: (a) strands coupled (b) introducing the new strand (Thonier 2009)

One item of concern with unbonded tendons is how to run them through deviator saddles. Saddles change the tendon’s path as needed to accommodate the structural needs of the design. External tendons are typically deviated at member supports and at the third-points within a span. Because the tendons bear against the saddles, the corrosion protection system (sheathing) is vulnerable to damage, which may eventually lead to tendon corrosion. Through research

conducted in France and Germany, engineers have decided thicker sheathing is the best way to protect the tendon system from damage at the saddle points (VSL Construction Systems 2008).

Notably, both countries still rely on visual observation to monitor for tendon damage. Damage is detected by inspection for the presence of cracks in the concrete near a support or tendon anchorages. The presence of cracks indicates that the tendons are not taking the entire design load and may require replacement (Weiher and Zilch 2008). Little to no research has been conducted using electrically or acoustically monitored tendon systems in Europe.

A recent report to FDOT describes the current practices adopted in Europe (primarily in France and Germany) for the unbonded tendons for bridge structures (Parsons Brinkerhoff 2012). France and Germany are the biggest contributors to tendon technology, but their practices are not always similar. France and Germany allow both internal bonded and unbonded tendons, but Germany requires metal duct for internal tendons; France installs either metal or plastic ducting. Tendons in the web of box sections are not used in Germany, but are in France (Weiher and Zilch 2008). Both countries also allow external unbonded tendons, but in Germany these tendons must be replaceable. Another significant difference is that Germany does not use segmental bridge construction (Parsons Brinkerhoff 2012).

It is also reported in the technical report on the unbonded tendons (Parsons Brinckerhoff 2012) that both countries, France and Germany suggest to use petroleum wax over grease. This suggestion is supported by the fact that the wax is more suitable at the higher service temperatures. However, grease is preferable at lower temperatures as it is more homogeneous than the petroleum wax. The same recommendations are given in the report published on external tendons by the Service d'Etudes Techniques des Routes et Autoroutes (SETRA) regarding flexible filler products such as grease and petroleum wax. Wax is preferred at the higher service temperatures because of stability due to its crystalline structures.

Unbonded tendon technology has historically and continues to be used for structural restorations and repairs, while its use in new construction has remained limited. This is because unbonded tendons have not been implemented as widely as bonded tendons and majority of practicing engineers still know little about the technology, especially in the U.S.

The following sections provide some examples of unbonded tendon use.

3.1 Itztal Bridge

The Itzal Bridge is part of the Autobahn highway near Coburg, Germany. A 2800 ft (852-m) long bridge composed of two superstructures; it is prestressed with both external unbonded tendons and internal bonded tendons (Figure 3-2). The maximum span length is 190 ft (58 meters).



Figure 3-2 Itztal bridge (Zilch et al. 2007)

3.2 Weidatal Bridge

The Weidatal Bridge also composes a portion of the Autobahn and is located between the German cities of Kassel and Halle (Figure 3-3). Completed in 2007, it is 1430 ft (435-m) long and includes a 550 ft (169-m) main span. This bridge incorporates both external unbonded tendons and internal bonded tendons (Zilch et al. 2007).



Figure 3-3 Weidatal bridge under construction (Zilch et al. 2007)

3.3 Nibelungenbrücke

The Nibelungenbrücke was constructed in 2004 and crosses the Rhine River in Germany. It combines external unbonded tendons and internal bonded tendons (Figure 3-4). Twelve spans create a total length of 2440 ft (745 m), including a maximum span of 380 ft (115 m) (Zilch et al. 2007).



Figure 3-4 Rhine bridge (Zilch et al. 2007)

3.4 *Kleine-Laber-Viaduct*

Spanning 900 ft (273 m), the Kleine-Laber-Viaduct in Germany is constructed with internal unbonded tendons. The bridge provides six traffic lanes over four concrete T-beams (Figure 3-5), and includes a 280 ft (84-m) tendon which extends over two spans. Replaceable tendons cannot be coupled so the span-by-span is made continuous by overlapping the tendons at the supports (Traute and Weiher 2011).



Figure 3-5 Ariel view of Kleine-Laber-Viaduct (Traute and Weiher 2011)

Each side of the bridge has eight tendons, including one designed as a reserve tendon. During construction, tendon replaceability was tested on one of the 280 ft (84-m) long reserve tendons as show in Figure 3-6 and Figure 3-7.

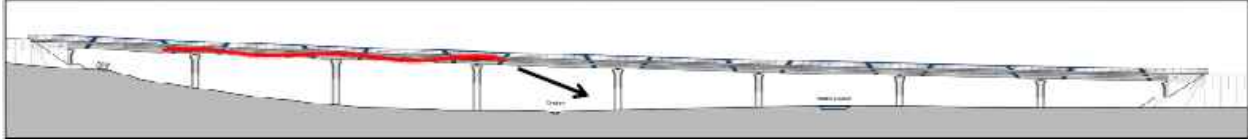


Figure 3-6 Tendon being replaced (Traute and Weiher 2011)

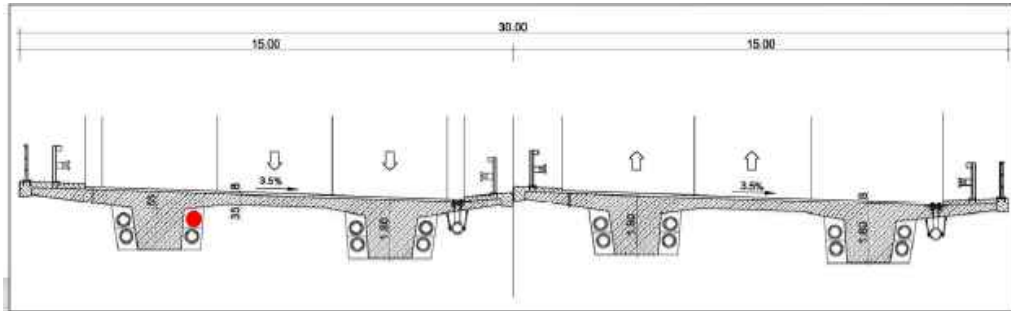


Figure 3-7 Cross-section of bridge with the tendon being replaced in red (Traute and Weiher 2011)

3.5 *Rossriether Graben*

Located in Mellrichstadt, Germany, the Rossriether Graben bridge is a 430 ft (130-m) three-span bridge. The Rossriether Graben was one of two pilot projects to test the practicality of using both external and internal unbonded tendons (Figure 3-8).



Figure 3-8 Rossriether Graben (Weiher and Zilch 2008)

The internal tendons of the Rossriether Graben were arranged in the slabs with one concrete deviator per slab. During construction, a strand within an internal tendon was replaced to check the feasibility of removal. The strand was successfully replaced, but required a high force to remove it due to friction and clamping between wires (Weiher and Zilch 2008).

3.6 Muhlenberg Viaduct

Located in Arnsberg, Germany, the Muhlenberg Viaduct was another pilot project to test the practicality of using both external and internal unbonded tendons. With a 840-ft (255-m) span, the internal tendons were located in the bottom slab of pier regions as well as in the deck slab of the center span. The external tendons were deviated at each diaphragm (Figure 3-9). Figure 3-10 illustrates the tendon path along the length of the bridge; the blue lines represent the internal tendons and the red lines represent the external tendons. Figure 3-11 shows the location of internal and external tendons at the diaphragm (Weiher and Zilch 2008).

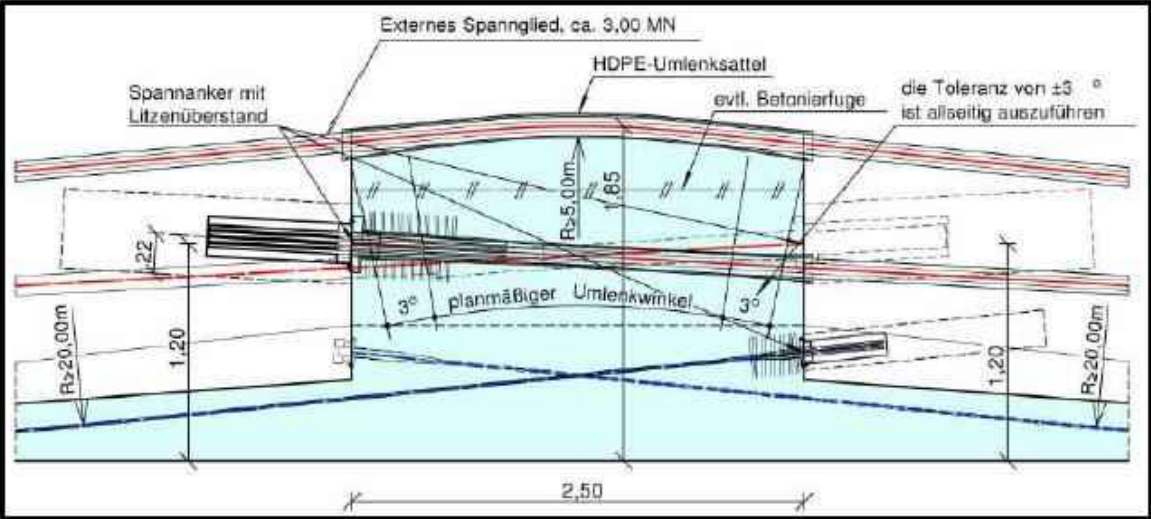


Figure 3-9 Concrete deviator (Weiher and Zilch 2008)

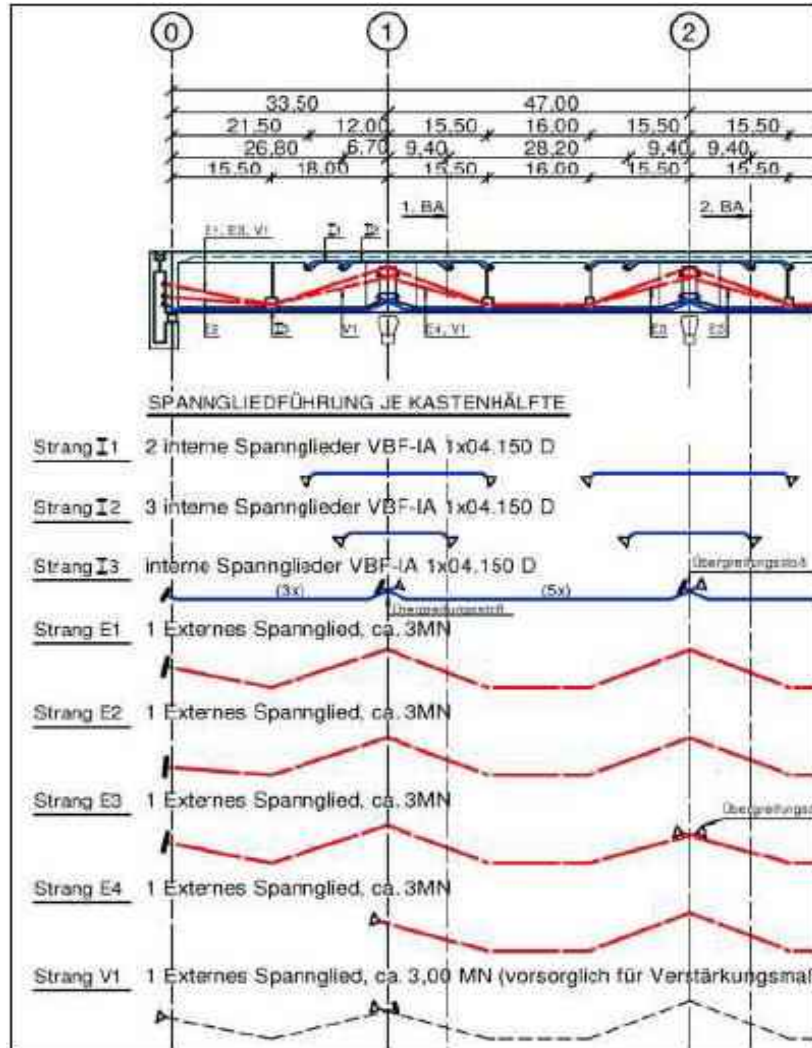


Figure 3-10 External and internal tendon path (Weiher and Zilch 2008)

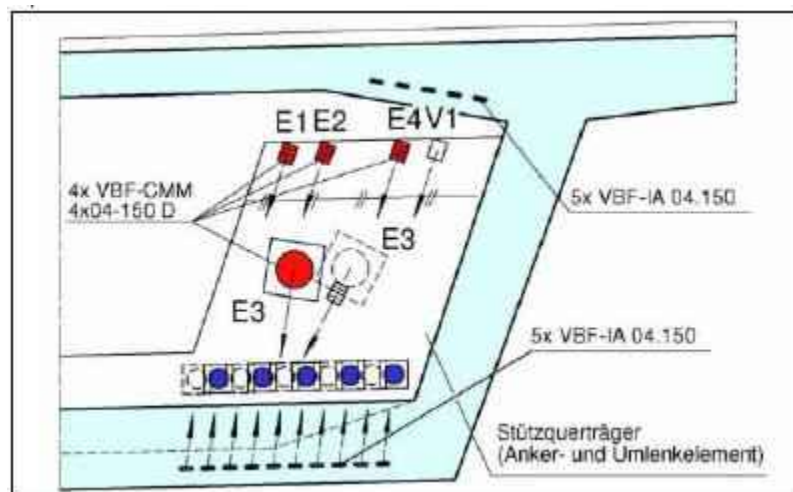


Figure 3-11 Tendon location at the diaphragm (Weiher and Zilch 2008)

3.7 Nuclear Containment

Nuclear containment structures have utilized the two bond-types discussed herein – bonded and unbonded – extensively; half of the existing inventory of prestressed containment structures utilize unbonded tendons in their construction (Nuclear Energy Agency [NEA] 2015). Given the inherent safety considerations of these structures, durability requirements are stringent, with particular attention paid to maintaining integrity of the prestressing components through the service life (40-60 years) and beyond – past the decommissioning of the nuclear plant itself for an additional storage time of 100 years.

In a 2015 review of current nuclear industry practice concerning prestressed containment structures, the Nuclear Energy Agency summarized the industry’s experience with either grease/wax filler materials – or “soft products” – and with grout filler material with the intent of “tendon preservation.” The nuclear industry has utilized unbonded tendons in several forms. Some systems, for example, have included the grease in the tendon duct during production, as opposed to injecting on-site, with later filling of the anchor caps to protect the tendon ends.

One type of detailing used is shown in Figure 3-12, in which the prestressing strand is in housed in a greased sheathing inside a grouted duct. This detailing scheme provides “optimal anti corrosion protection” with reduced individual strand interaction (twisting and additional friction loss) during post-tensioning (NEA 2015).

Various injection/application techniques have been used to install these filler materials, through application of the material prior to installation, or injection of the filler after strand placement, or a combination of both.

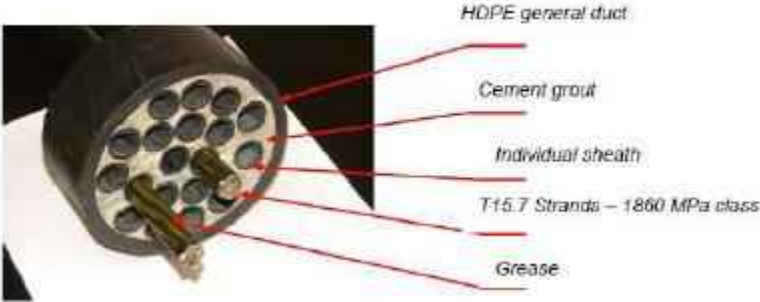


Figure 3-12 Greased and sheathed detailing scheme (NEA 2015)

Corrosion of unbonded tendons has been documented (NEA 2015). Initial soft product injections in Europe utilized grease, though the observed instability (oil separation) and issues with leakage of grease has led to their abandonment, in favor of more stable wax products. The strengthening of the Bayonne Bridge by additional prestressing is a documented example of grease use. Wax – a more stable product in the long-term – is now used instead. The few inspections made to date (opening of anchorage caps and sheathing) have not uncovered any durability concerns (NEA 2015).

4 Replaceability of Post-Tensioning Tendons

Grouted post-tensioned tendons are typically used in both superstructures and substructure components. The types of bridges superstructures include, but are not limited to:

- Precast segmental balanced cantilever
- Precast segmental span-by-span
- Precast spliced I-girder continuous
- Precast spliced I-girder simply supported
- Cast-in-place segmental balanced cantilever

Bridge substructure components using grouted tendons include, but are not limited to:

- Hammerhead piers
- Straddle bents
- Cantilever piers
- Segmental or cast-in-place piers

Each bridge superstructure type is distinguished, not only by its form, but also by the method of construction. The standard practice in Florida has been to use prestressing strand with cementitious grout for both internal and external tendons. The alternative corrosion protection methods discussed in the previous chapter are pliable and their use will result in unbonded tendons. The use of unbonded tendons to replace bonded tendons, either fully or selectively, will have some effect on the ultimate strength and serviceability, as well as the fabrication and erection of the structure itself. Furthermore, if tendon replaceability is required, then the detensioning, replacement, and tensioning of new tendons must be accommodated. The following sections present the current methods of construction using tendons that contain grout. In addition, the implications of replacing grout with pliable filler or strand coating are discussed.

4.1 *Precast Segmental Balanced Cantilever*

Balanced segmental cantilever construction was introduced in Florida in 1984 with the construction of a new ramp over I-75 (FDOT/FTBA Construction Conference 2010). A number of Florida bridges/ramps have since been constructed using this method.

In this type of construction, precast segments are erected symmetrically about the pier, keeping an unbalance of only one segment at any given time. Two methods are typically used to erect the precast segments (Figure 4-1). The first method uses a crane for the erection of segments while the second method uses overhead gantry for the erection.

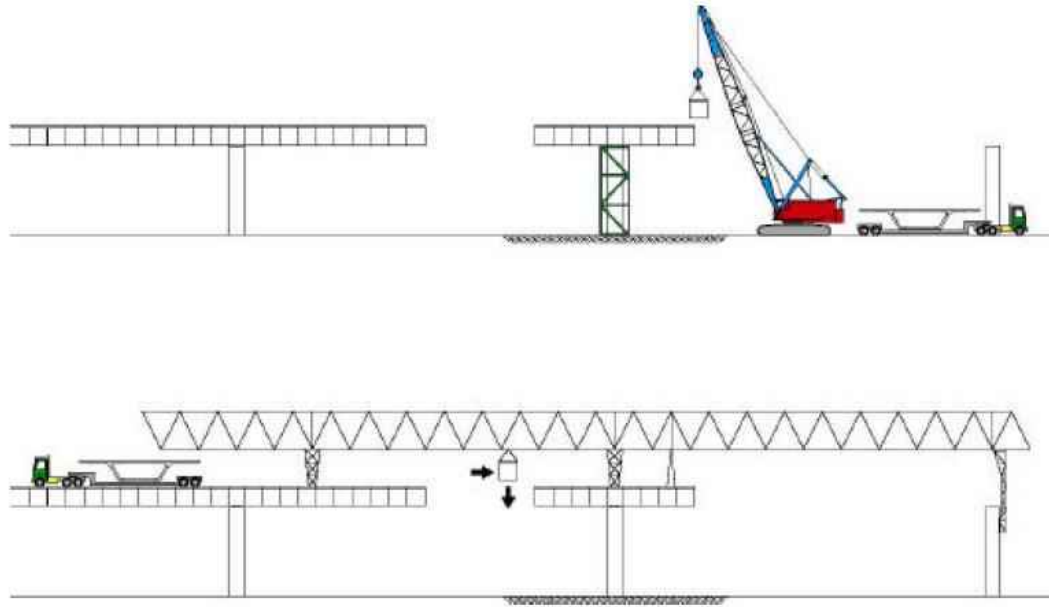


Figure 4-1 Construction methods for precast segmental balanced cantilever (FDOT 2002-1)

Post-tensioning tendons are generally classified as either cantilever tendons or continuity tendons. Cantilever tendons are generally placed in the top slab of the section in a single layer to counter the dead load and are stressed once the segment is in place. Temporary PT may be used to hold the segment in place until the cantilever tendon is stressed. As additional segments are added, more cantilever tendons are added to the system. The number of tendons is greatest at the pier, and decreases toward the midspan. Cantilevered tendons are placed in ducts and anchored either within the section (face anchored) or in a blister near to the junction of the top slab and web (Figure 4-2).

The second type of post-tensioning tendon provides continuity to the bridge superstructure through the closure pours between the individual cantilevers. Continuity tendons are stressed after all cantilevered segments are erected and closure joint is poured. This type of tendon is typically straight, internal, and bonded; these tendons are placed at the bottom of the section to resist the dead and live load actions resulting from the continuity following closure placement (Figure 4-3). A small quantity of continuity tendons are also provided at the top of the section to counteract the tensile stresses produced by the bottom continuity tendons and by live load actions from adjacent joints.

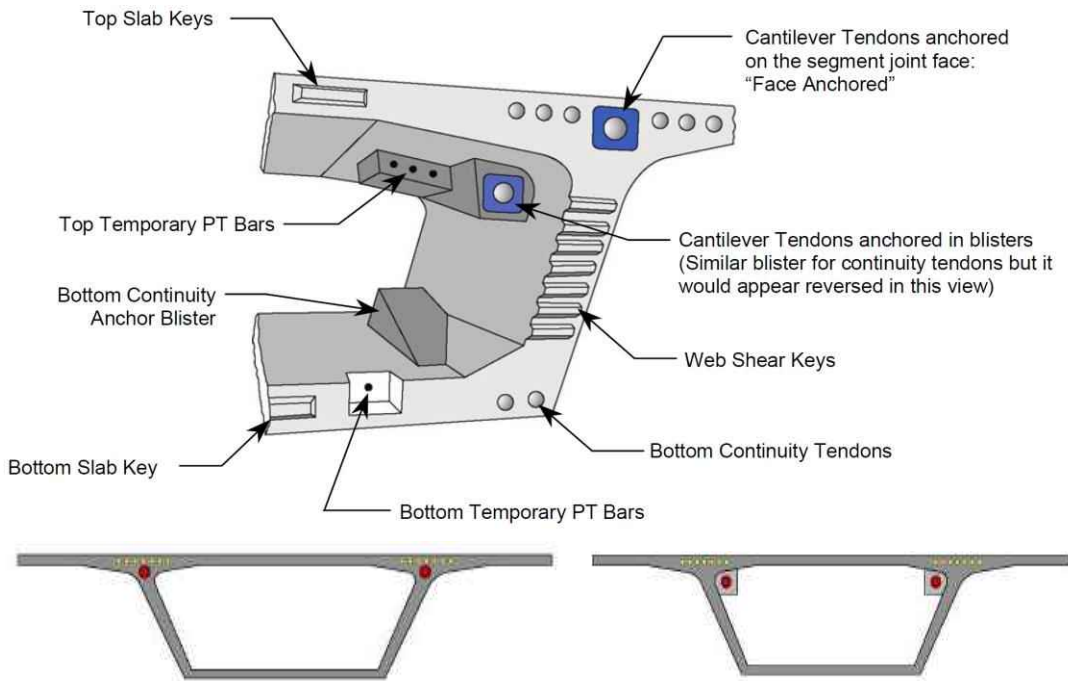


Figure 4-2 Precast segmental box girder with cantilever tendons (FDOT 2002-1)

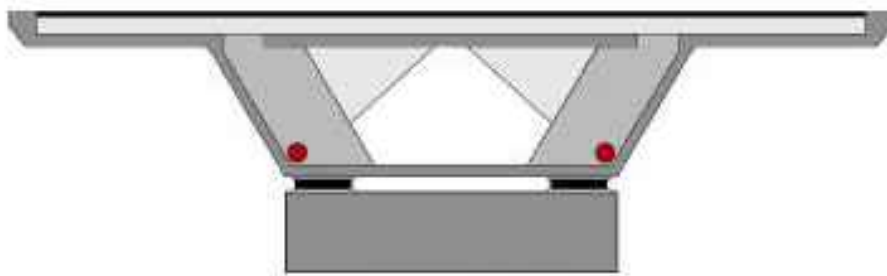


Figure 4-3 Continuity tendons in precast segmental construction (FDOT 2002-1)

4.2 Cast-in-place Segmental Balanced Cantilever

This type of construction includes the same post-tensioning philosophy as used in precast segmental balanced cantilever bridges. The primary difference is that cast-in-place construction does not require temporary longitudinal PT. Traveling formwork supports the concrete poured for the cast-in-place segments until the concrete has reached specified strength (Figure 4-4).

In some cases, to keep the segment casting cycle duration short, segments are stressed soon after casting (sometimes only two days after), prior to the development of the full specified 28-day concrete compressive strength. The longitudinal prestressing tendons within the newly-cast segment will be post-tensioned, rigidly connecting it with the existing cantilever arm. The form traveler is then advanced to the next casting position and whole casting cycle is repeated.



Figure 4-4 Form travelers (Corven J. and Moreton A 2004)

4.3 Precast Segmental Span-by-span

Florida's first segmental span-by-span bridge, Long Key Bridge, was constructed in 1981. Three more bridges (Channel 5, Seven Mile Bridge and Niles Channel Bridge) were constructed in the following two years.

Span-by-span construction uses either internal or external tendons (Figure 4-5). The tendon profile is harped to counter the moment demand; the tendon is above the centroid at the pier section and at the bottom of the section at the midspan. Prestressing continuity in the negative moment region is provided by overlapping tendons at pier supports. Tendons are stressed after span construction is completed. The use of external tendons makes the section more efficient by maximizing the eccentricity at midspan to counter the moments produced by loads.

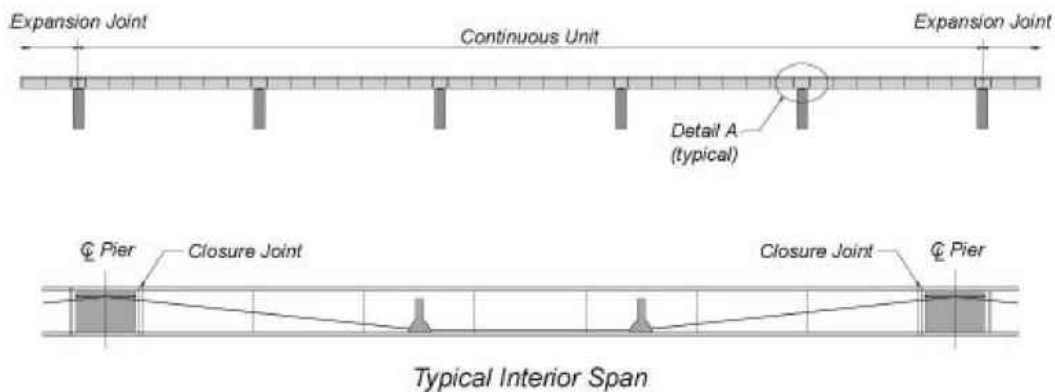


Figure 4-5 Typical tendon detail for precast segmental span-by-span bridges (FDOT 2002-1)

4.4 Post-tensioned AASHTO Bulb-T and Splice Girder

Florida's first drop-in span structure, Dupont Bridge in Panama City, was built in 1965. This type of construction utilizes precast, pretensioned I-girders fabricated in transportable segments, which are then assembled in place and post-tensioned. The girders are pretensioned to

resist stresses encountered during the transport and erection; live and other loads are resisted by internal post-tensioning tendons extending through the entire span length. Tendon profiles are typically parabolic to form a smooth curved drape profile.

In this construction method, girder segments are erected at the pier and supported by falsework. A drop-in girder is placed between two pier segments and supported by hangers; tendon ducts are spliced and the closure joint is cast (Figure 4-6). After the closure has reached specified strength, the tendons are stressed to provide continuity for the system. The bridge deck is then placed and tendons are stressed again to complete the composite construction.



Figure 4-6 Splice construction for AASHTO Bulb-T and Splice girders (FDOT 2002-1)

4.5 Substructures

In most cases, a bridge substructure is composed of reinforced concrete; however, for particular cases (such as where space is limited), post-tensioning is used. Post tensioning is used in hammerhead piers when the cantilever portion is sufficiently large, or where there is limited vertical clearance; internal bonded tendons are typically used (Figure 4-7).

Post tensioning in straddle bents is used when the vertical clearance restricts the overall depth of the bent. Straddle bent tendons are typically internal bonded tendons placed in a parabolic drape (Figure 4-7b). Occasionally, external tendons are used (with the same drape profile) to repair or strengthen existing bents.

Cantilever piers may have vertical and transverse post-tensioning. The tendons are usually internal straight bonded tendons and may be used in the pier, column, and footing (Figure 4-7c). In some cases, if space permits, a single tendon is curved to serve as both vertical and horizontal post-tensioning. External tendons may also be used in place of internal tendons to repair and strengthen girders.

Piers can also be constructed using precast segments such as the Sunshine Skyway Bridge (Figure 4-7d). The segments are precast off site, shipped to the site and stacked vertically on the foundation. Vertical external tendons are then post-tensioned to tie the segments together.

In the case of the Skyway, the tendon anchorage was placed in the top of the pier and the tendon was externally post tensioned to complete erection of the segmental columns.

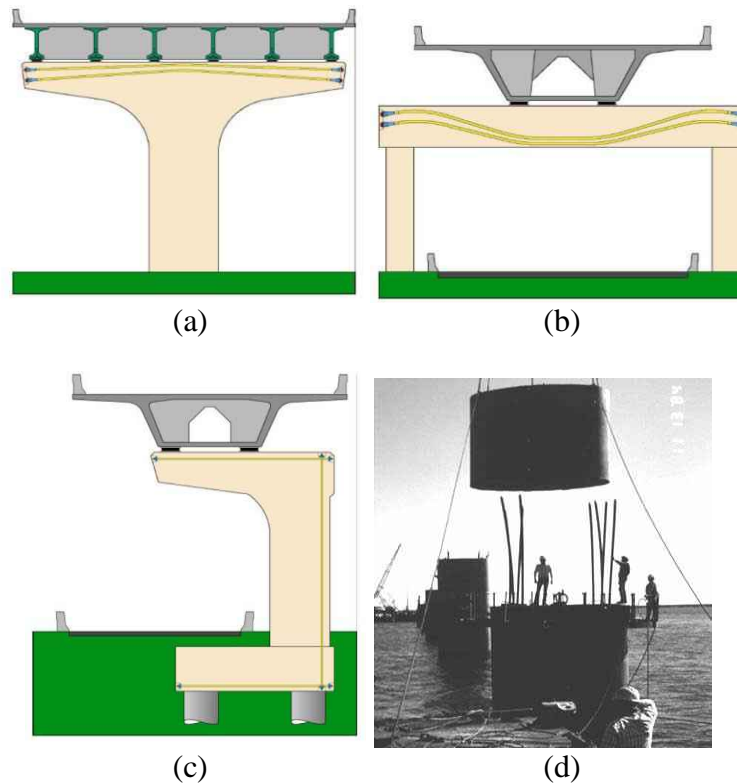


Figure 4-7 Options for using post-tensioning in substructure construction (a) hammer head piers (b) straddle bent (c) cantilever pier (FDOT 2002-1) (d) segmental pier (Garcia P. and Theryo T. 2006)

4.6 In-Service Inspection Requirements (NRC)

The Nuclear Regulatory Commission (NRC) has prepared regulatory guidelines for various construction and inspection requirements for post-tensioning bonded and unbonded tendons. Although inspection and testing procedures for containment structures are quite stringent, inspection of unbonded bridge tendons using a condensed version of the NRC requirements might be desirable.

NRC Regulatory Guide 1.35 provides guidance for in-service inspection procedures and acceptability criteria for ungrouted tendons in nuclear containment structures. The guide requires in-service performance tests at one, three, and five years after the Initial Service Integrity Test, and every five years thereafter. Anchors should be accessible for the inspection. Frequency of lift-off force comparison for two containments may be done as shown in Figure 4-8, if the following conditions are met:

- Both the containments should be identical in size, shape, material and number of tendons.
- Initial Service Integrity test should have been completed within last two years.

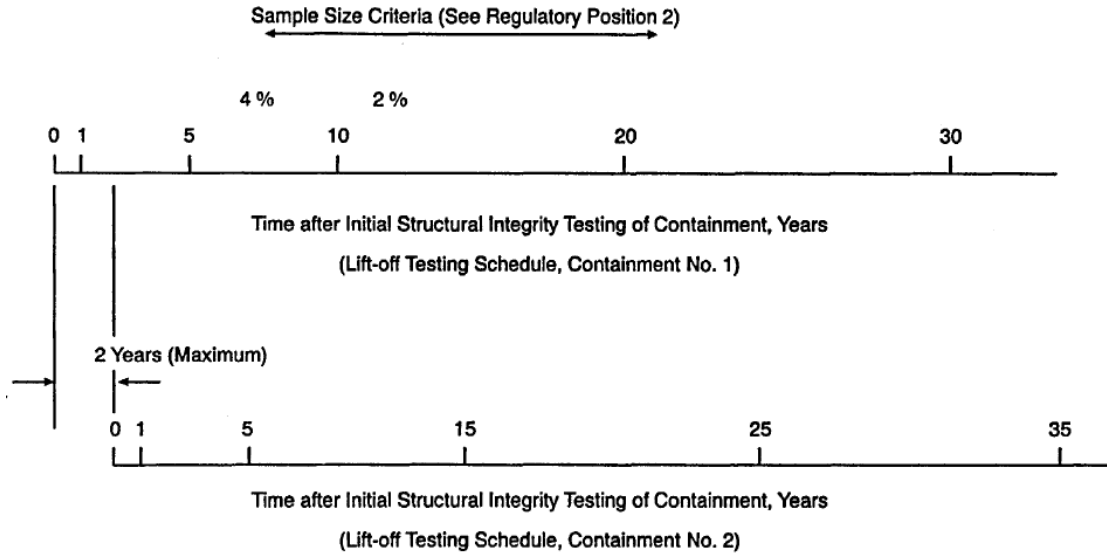


Figure 4-8 Schedule of lift-off test for two containments at one site (NRC Regulatory Guide 1.35 1990)

The sample size for the in-service performance should have 4% of tendon population from each group, with a minimum of 4 tendons in each group (vertical, hoop, inverted U tendon groups). Tendon selection should be random; one tendon from each group, however, should be unchanged after the initial selection, and the unchanged tendon should be identified as the control tendon. Tendons that are accepted in the previous inspection should not be selected in the next inspection cycle.

Acceptance criteria for prestress force include:

- 95% of the predicted force in two out of the three tendons when measured, or
- The average of measured forces against the minimum required force in an average (hypothetical) tendon in a group

Visual inspection consists of examining for areas of concrete spalling and tendon anchorage assembly hardware of all tendons. All tendon grease caps should be visually inspected. Concrete surrounding the duct should also be inspected for signs of problems.

Another criterion was set for the anchor heads. One incident reported about the tendon anchor head failures at Farley demonstrated (NRC Regulatory Guide 1.35 1990) that the free water in grease was the main source of hydrogen for hydrogen stress-cracking of high-hardness anchor heads.

A wire or a strand previously stressed should be removed and examined thoroughly over its entire length for corrosion or other deleterious effects. Tensile tests should be conducted on three samples cut from each wire or strands; samples should be taken at each end and in the middle. Tests should provide the information about the yield strength, ultimate tensile strength and elongation at the ultimate tensile strength.

Liftoff tests are required by NRC during regular periodic evaluations. The tendon is considered acceptable if the measured prestressing force is 95% or above the prescribed limits (0.93 of initial prestressing force at the start of 1st year). If the measured tendon force is between 90% and 95% of the prescribed limit, then adjacent tendons should be checked for measured

prestress force using a liftoff test. If the elongation measured during a liftoff test differs by 10% or more from the elongation recorded during installation, then that tendon should be investigated for potential wire failures.

4.7 Implications

The focus of this literature review is on two main issues. One is the use of an alternative corrosion protection system to cementitious grout. The systems considered are pliable and their use will result in internal tendons that are unbonded. The second issue - and one that is related to bond - is that of replaceability. Although grouted tendons are, in theory, replaceable, the actual practice of removal is extremely difficult, expensive, and potentially dangerous. This section explores unbonded tendon replaceability in the context of typical post-tensioned construction in Florida.

Anchorage access is the key component of a replaceable tendon. Sufficient space must be provided in the final structural configuration to allow the hydraulic jack to be transported to and fit into the jacking configuration. Externally anchored tendons (tendons anchored at the end of a segment for which the anchorage is accessible) or tendons anchored at an accessible blister are replaceable. When face anchored, the anchorage is not accessible for inspection or replacement. Table 4-1 summarizes the accessibility of the PT tendons for each type of construction.

In general, for each type of construction, the use of a pliable corrosion protection system can be substituted for grout, which limits the corrosion of the steel. Though unbonded tendons provide reduced moment capacity to the section (since the pliable filler does not add to the section moment of inertia), the replaceability of tendon is an advantage. Additional reinforcement may be required to compensate for the reduced strength.

Some current construction methods provide easy access to the tendon anchor heads. In span-by-span construction, for example, the external tendons would be a prime candidate for the use of pliable filler. Tendon replacement would be easier; a tendon could be easily removed by detensioning from one end. Other construction types, with modification, could also allow for tendon replaceability. For example, tendons used in drop-in construction can be made external by providing blisters. The tendons can also be made external and replaceable by using side blisters in hammerhead piers, straddle bents and cantilever piers. The ease with which tendons can be replaced is enhanced when the anchorage is exposed and sufficient space is available for placement of the prestressing jack.

In addition to anchorage access, several replacement methods are possible:

1. Strand-by-strand replacement: Detension an individual strand with monostrand jack and pull strand through using the strand to be replaced. In an unbonded tendon with pliable filler, the difficulty is the friction between strands. Depending on a strand location in the group, it could be difficult to remove.
2. Strand-by-strand detensioning: Detension entire tendon strand-by-strand with single strand jack. Requires that strand tails be left in place with special elongated grout caps.
3. Multi-strand detensioning: Detension entire tendon with multi-strand jack. This method requires that strand tails be left in place with special elongated caps.
4. Torch individual strands to remove tendon. This is possible on external tendons where tendon is exposed. Grouted tendons will maintain some of the prestressing

- strand stress, but tendons with pliable fillers will not, making this procedure a less dangerous operation. Install new tendon strand-by-strand or as a complete tendon.
5. Torch strands individually in anchor plate to individually remove strands. This is effective only for pliable fillers.
 6. Strand-by-strand with wedge remote unseating: By this method, a fabricated device is used to unseat an individual wedge from a remote distance.

Table 4-1 Unbonded tendon anchor accessibility

Construction Type	Anchor accessibility			Tendon Profile
	External	Blister	Face-anchored	
PC segmental cantilever	Yes	n/a	n/a	draped
CIP segmental cantilever	Yes	n/a	n/a	draped
PC segmental span-by-span	No	n/a	n/a	draped
Drop-in I-girders	n/a	Yes	Yes	draped
Hammerhead piers	n/a	Yes	Yes	draped
Straddle bents	n/a	Yes	Yes	draped
Cantilever piers	n/a	Yes	n/a	straight

5 Part I—Mockup for Flexible Filler

Five mockup PT tendons were injected with four different heated, flexible fillers. Preliminary testing was also conducted on a small-scale setup to evaluate individual components to be used in the full-scale mockup to ensure the safety of the laboratory staff during the full-scale mockup injections, and acclimate the staff to the new procedures and equipment in a smaller, more controlled setup.

This part of the research project was intended to help develop heating and injection procedures for flexible fillers. Four different commercially available microcrystalline wax filler materials were selected for use, not with the intent to test the material, but rather to use different materials to test the heating and injection procedures. Consequently, the differences in behavior among the five tests are likely due to the injection procedures rather than the material properties.

Temperature and pressure of the filler material was monitored along the length of the tendon during and immediately following injection. Transparent pipe windows were placed along the length to allow visual observation of the injection process. Short sections of duct were removed one day after injection at critical locations to investigate whether voids formed, and if so, determine their extent.

In addition to the experimental testing, a simplified analytical model was developed to compute the change in flexible filler temperature during injection, which can be useful in determining tendon constructability. After validating the model with multiple experiments, a sensitivity analysis was performed to obtain useful relationships between filler front temperature and effective strand surface area, tendon length, injection rate, ambient temperature, injection temperature, and strand pattern. Moreover, pressure losses for different flow velocities and tendon lengths were estimated.

The objective of this research was to investigate the constructability of unbonded multi-strand, post-tensioned bridge tendons injected with flexible filler. The testing focused on tendon and duct detailing, filler material preparation, injection process and equipment, and venting procedures. The results are intended to provide background information on this process and to assist in the preparation of material and construction specifications.

5.1 Test Setup Design and Construction

Five 200-ft long specimens were fabricated with a profile that simulated both internal and external tendons. In addition, the tendons were lightly stressed to ensure that the strand bundle was oriented in the duct in a similar manner to a fully stressed tendon in the field (Figure 5-1). HDPE duct of 4 in. diameter with nineteen 0.6-in. prestressing strands formed the tendon. Anchors from FDOT approved post-tensioning equipment suppliers were used at each end of the tendon. Three locations were selected along the length of each tendon at which transparent polycarbonate tubes were installed to allow the injection process to be visible. Figure 5-2 shows an example of one of the locations.

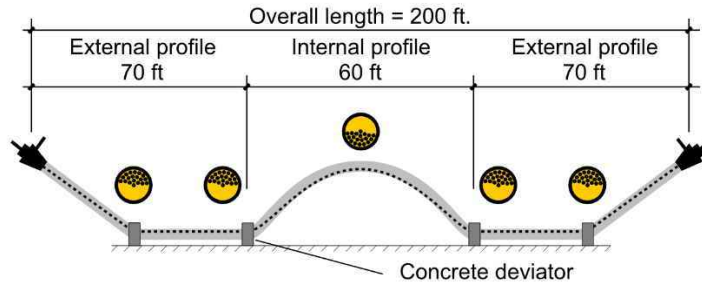


Figure 5-1 Tendon profile for the mockup testing on unbonded tendons



Figure 5-2 Window locations on tendon

Tendon construction began with fabrication of the HDPE duct, which was composed of fusion welding, placement on the frames, and connecting to the anchors. Clear windows were then installed, and strands were pushed and stressed to obtain the desired tendon profile. Instrumentation was installed followed by an air test to check for leaks before injection.

The pump used for most of the mockup injections was a Viking centrifugal pump with a variable frequency electric drive (Baldor VFD controller) (Figure 5-3). An in-house assembled vacuum pump was used in the vacuum assist filler injection.

Flexible fillers were delivered in 55 gallon barrels and were solid at room temperature. To liquefy the filler, the barrels were heated to about 220° F, which was achieved by using barrel heaters on the outer surface of the barrel (Figure 5-4). Insulation blankets were used to improve the efficiency of the barrel heaters.



Figure 5-3 Viking pump used for filler injection (left) and vacuum pump and reservoirs (right)

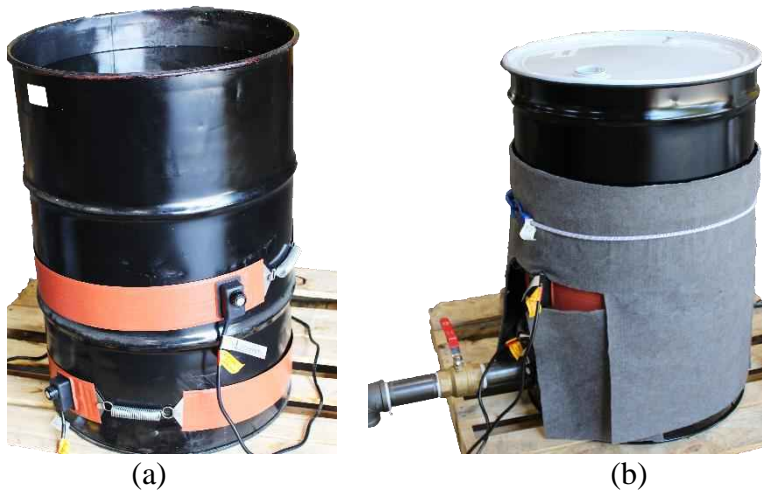


Figure 5-4 (a) Barrel heater position on barrel (b) heaters covered with insulation blanket

5.2 Results

The tendon was inspected at approximately 24 hours after injection. Eleven to fifteen inspection ports (IP) were prepared, at which the duct was opened to inspect the relative fill of the flexible fillers, filler cover of the strands, and void presence, if any. Each inspection port opening was formed by cutting and removing the top half of the HDPE duct over a length of approximately one or two feet; IP09, however, was located on the bottom half of the duct. Duct windows, vents, and caps were also inspected for the relative fill. Figure 5-5 shows the location of the inspection ports and windows along the length of the tendon for first three injections while Figure 5-6 shows the location of inspection ports and windows for the final two injections. These inspection ports were carefully opened and the filler coverage was visually inspected and documented with photographs (Figure 5-7).

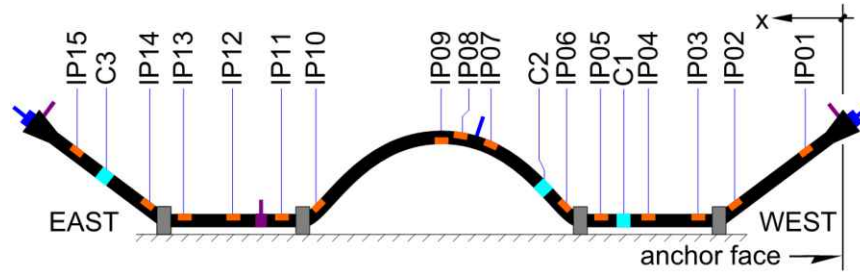


Figure 5-5 Inspection port (IP) locations on Cirinject, Visconorust, and VZ Inject mockup specimens

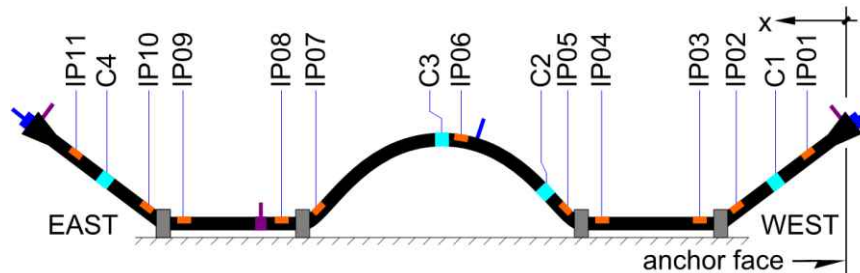


Figure 5-6 Inspection port (IP) locations on Trenton 1 and Trenton 2 mockup specimens

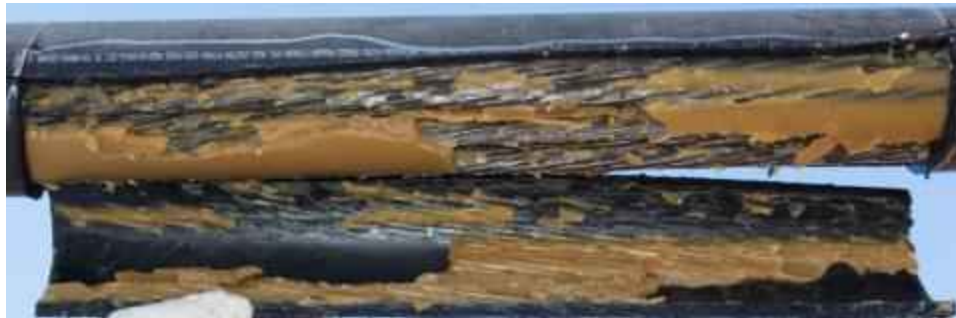


Figure 5-7 Typical results at HDPE inspection port

5.3 Temperature

Figure 5-8 shows the variation of temperature with time in the specimen where vacuum assist injection was used. In general, the sudden increase in temperature indicates the time at which the front of the filler had reached that position. The filler arrived at the temperature sensors in this order: T1, T2, T3, T4, T5, T6, and T7. This specimen was injected from the east anchorage, so sequential arrival times would be expected. In the specimens where filler was injected directly into the duct (e.g., Cirinject CP), however, the filler was flowing in opposite directions away from the injection point, which explains the non-sequential arrival times.

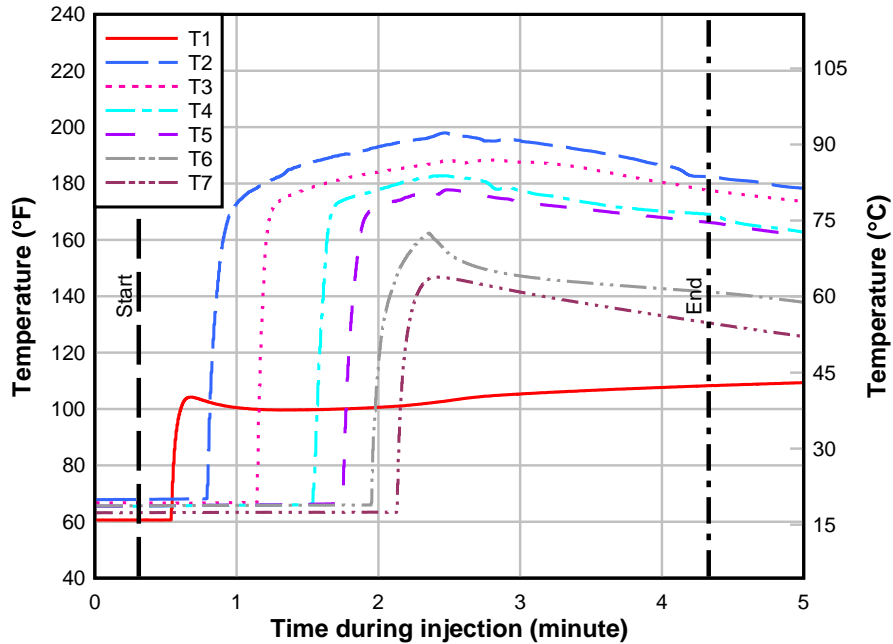


Figure 5-8 Filler temperature in duct during injection with vacuum assist

A thermal model was developed to compute the decrease in filler temperature as it moves away from the injection port. Based on conservation of energy, the model aims to estimate the difference in bulk temperature, which represents energy average conditions (Holman 1990) between two locations along the tendon length. The model primarily considers forced-convection heat transfer between filler, strands, and duct, and does not take into account the portion of energy transfer through conduction or radiation.

To obtain an estimate of the required minimum injection pressure for different tendon lengths, filler front temperatures were determined first using the model. Figure 5-9 illustrates that the pressure loss for shorter tendon lengths (up to ~150 ft or ~46 m) does not significantly vary with flow velocity, but becomes increasingly sensitive to it for longer lengths. If vacuum assisted injection is used, then the pressure loss would be reduced by the magnitude of the vacuum pulled on the specimen.

This simplified approach in estimating the minimum injection pressure assumes laminar flow in a straight horizontal tendon. In reality, the strand bundle is expected to cause some turbulence, and the tendons often have deviated segments rather than a straight profile. Therefore, this approach should be viewed as an attempt to obtain a basic understanding of evaluating the pumping pressure; more detailed analysis is required for a better estimation. Mockup trials to confirm the efficacy of the injection should also be conducted.

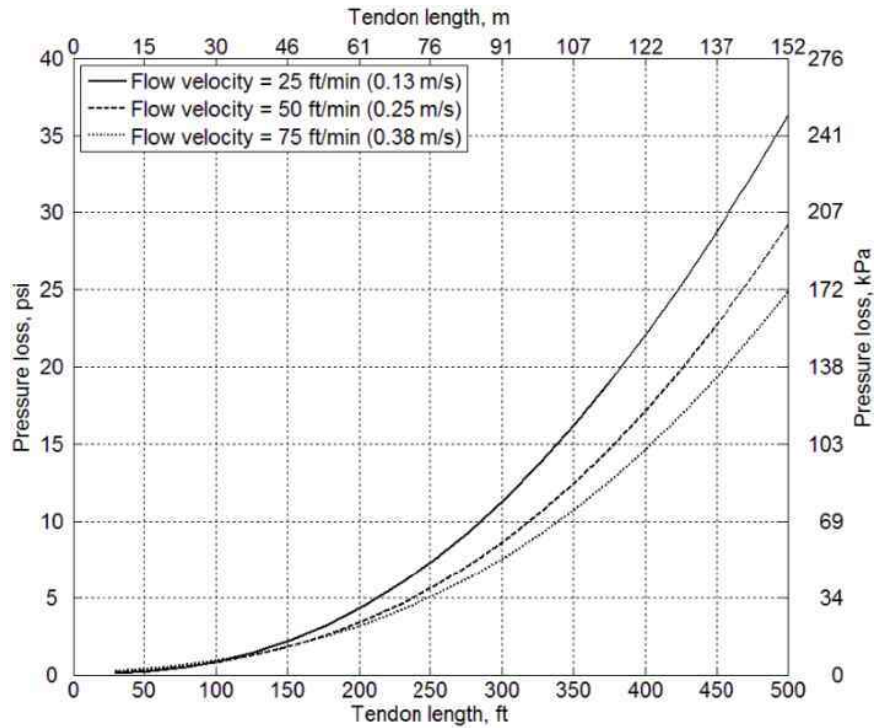


Figure 5-9 Pressure loss from thermal model

5.4 Summary and Conclusions

Four alternative flexible filler materials were selected and tested in a 200-ft mockup of a post-tensioning tendon to test for constructability and to understand the nuances of handling and injecting flexible fillers. The tendons were composed of nineteen 0.6-in. diameter prestressing strands that were lightly prestressed to ensure that the strands and duct were positioned as they would be in a fully stressed PT tendon. Temperature and pressure were measured during and after injection to track the behavior of the materials. The following are preliminary observations:

The target injection rate range was 40-70 ft/min. The average injection rate for Visconorust, VZ inject and Cirinject CP was 49 ft/min, 75 ft/min, and 62 ft/min, respectively. Injection rates for Visconorust and Cirinject CP were close to the target injection rate, while the VZ inject rate was higher. The average injection rate for Trenton 1 and Trenton 2 was 100 ft/min and 21.5 ft/min, respectively.

Injection rates and venting procedures were varied among the five mockups, primarily in an effort to determine the most suitable approach. In spite of the variation of procedures, all of the strands in each of the specimens were well-coated with filler material even though the first two tendons injected contained a void at the top of the duct cross-section in the parabolic portion of the mockup. In one case, venting was intentionally omitted. In the other case, the void was thought to be the result of inadequate venting procedures and not the PT system or individual filler products used. At the completion of these mockup tests, no cause to restrict use of any of the PT systems or filler products was found.

To better understand the heat transfer process and obtain an estimation on heat loss of filler front, a closed-form heat transfer model was developed and compared to the data gathered during the mockup injections. The experimental data confirmed the applicability of the thermal model to a wide range of tendon lengths, and material and injection parameters. After validating

with experiments, the model was then used to determine the sensitivity of filler temperature to various field parameters (e.g., tendon length, ambient temperature, injection rate) that can provide critical guidance on constructability of unbonded tendons with flexible fillers. The pressure loss for different flow velocities and tendon lengths has also been estimated to help decide injection pressure. Knowing the tendon geometry, hydraulic injection conditions, and filler material properties, this model can be used to compute the rate of cooling of filler front during injection, which can then be used to determine the maximum length of continuous injection. In addition, a method for determining the effective strand surface area, which is important to the heat transfer mechanism, was developed for use in the thermal model.

6 Part II—Structural Testing

Five 40-ft long I-girder beams – three beams with an internal parabolic 12-strand tendon and two beams with a pair of externally deviated 6-strand tendons – were post-tensioned, injected with filler material, and load tested. Two fatigue specimens were constructed and utilized to conduct a series of fatigue tests. This report covers the specimen design and construction, laboratory testing, and post-mortem inspection. Tendon replacement was also performed on one internal tendon specimen and is described herein.

This part of the research project focused on the flexural strength behavior of specimens with internal and external tendons using AASHTO Type IV sections. The use of flexible fillers in place of grout in both internal and external tendons will result in a change in the contribution that the unbonded tendons will make to the flexural strength of the section. Depending on the situations in which flexible fillers are used, prestressed members could have bonded and unbonded tendons or mixed tendons.

Two types of beam specimens were designed. One was precast with an internal parabolically draped unbonded tendon along with bonded pretensioned strands in the bottom flange. This was intended to simulate the spliced girder arrangement with post-tensioning duct placed in the web in a parabolic drape. The second specimen type was also precast, but was assembled segmentally and was prestressed externally with unbonded tendons. The tendons were deviated at cast-in-place deviator blocks, which also acted as closure pours for the assembly of the beam segments. This configuration was intended to simulate external tendons on box-girder sections.

In addition, fatigue specimens were constructed to test the fatigue performance of the unbonded tendons in conjunction with the diabolo deviator configuration, which is a necessary component when considering the replaceability of fully unbonded external tendons. The specimen was fitted with a mechanical hinge that allowed fatigue testing without causing damage to the remainder of the specimen. The focus was on wedge and anchor fatigue; fretting at the diabolo and wear; and damage of the duct at the diabolo.

6.1 Specimen Design and Construction

Three (IGS, IWS and IWC) 40-ft long simple-span precast concrete I-girders with an 8-in. by 34-in. concrete deck were constructed, each with three bonded 0.6-in. dia. pretensioned strands and a parabolic, internal multi-strand post-tensioned tendon composed of (12) 0.6-in. dia. prestressing strands. IGS was injected with post-tensioning grout and IWS and IWC were injected with flexible filler. Two 0.375-in. dia. prestressing strands were included to simplify installation of shear reinforcement stirrups. The chosen cross-section was a modified AASHTO shape; by using the side forms of an AASHTO Type IV with the bottom form of an AASHTO Type V, the resulting 10-in. wide web accommodated an internal tendon with the minimum concrete cover. Specimens are shown in Figure 6-1 and Figure 6-2.

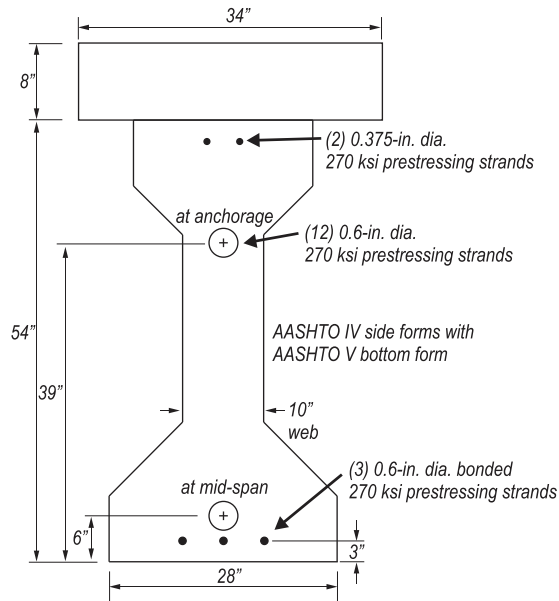


Figure 6-1 Internal tendon specimen cross-section

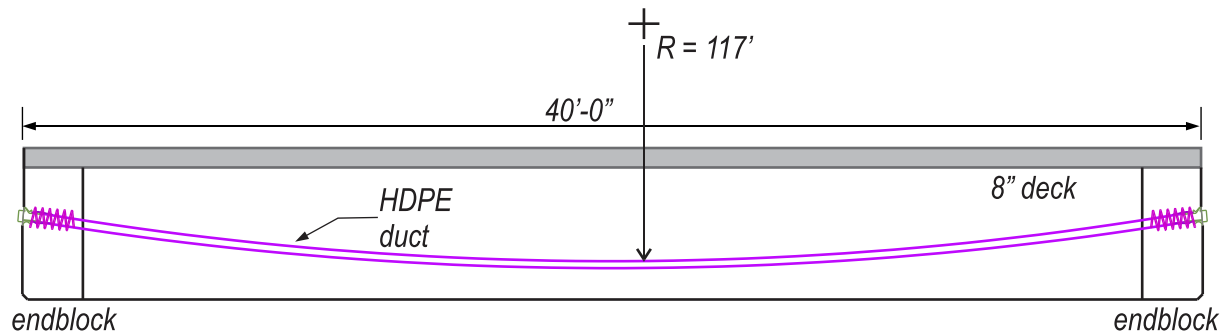


Figure 6-2 Internal tendon specimen

Two (EWS and EWC) 40-ft long simple-span precast concrete I-girders were constructed, each with two external tendons composed of (6) 0.6-in. dia. prestressing strands (Figure 6-3 and Figure 6-4).

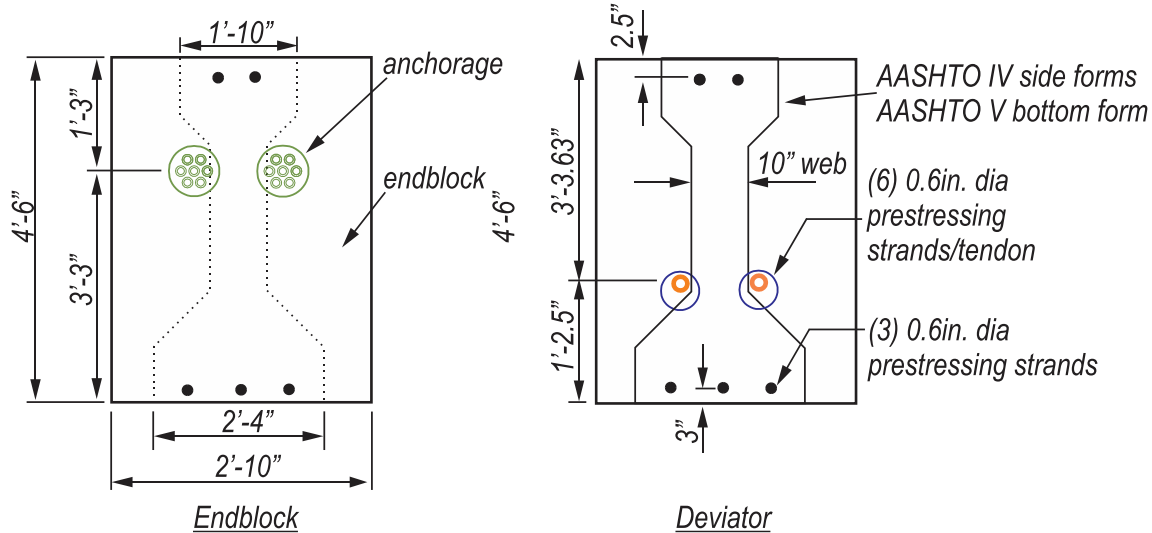


Figure 6-3 External tendon specimens

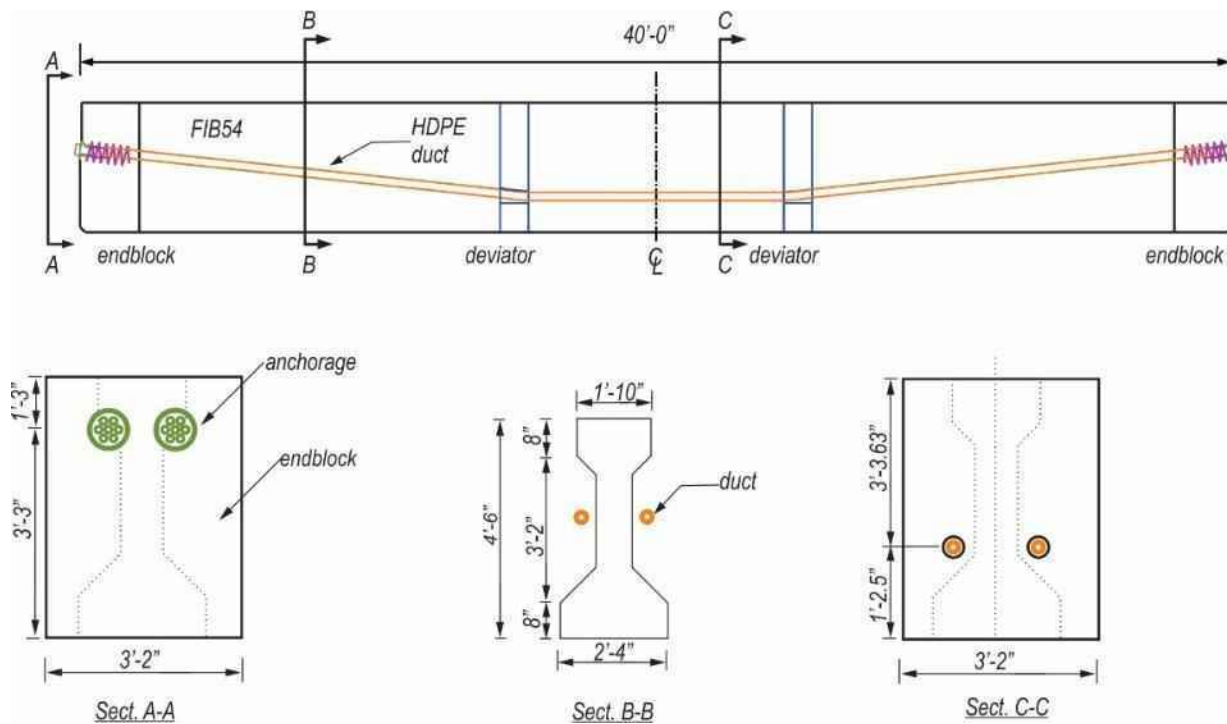


Figure 6-4 External tendon specimen profile

Two (F1, F2) fatigue specimens were designed to test the fatigue resistance of an unbonded PT tendon with diabolo deviators. The specimens were designed (Figure 6-5) to allow fatigue cycling of the tendon without accumulating undue stresses and potential damage on the remainder of the specimen. This required that the specimen be constructed in two segments and joined with a mechanical hinge. The two fatigue beam specimens differed only in the deviation angle of the six-strand post-tensioning tendons (Table 6-1).

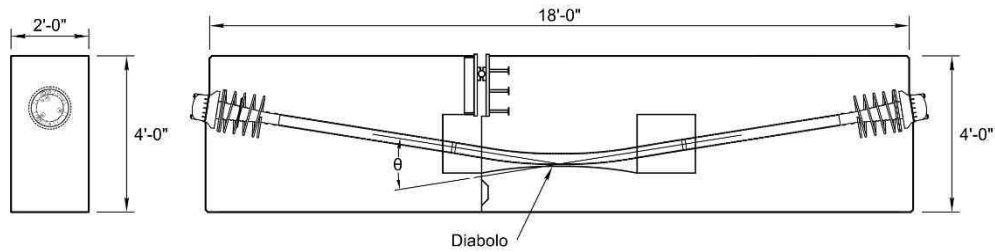


Figure 6-5 Elevation View of Fatigue Specimen

Table 6-1 Fatigue beam specimen abbreviations

Specimen	Tendon angle	Filler material	Loading configuration
F1	18°	Flexible filler	Single point
F2	11°	Flexible filler	Single point

6.2 Construction

Portions of the specimens were precast and pretensioned (Figure 6-6) and then shipped to FDOT Structures Laboratory to complete fabrication. Specimens with internal tendons (IGS, IWS and IWC) were precast in single lengths and shipped to the FDOT Structures Laboratory. The end blocks containing the post-tensioning anchorages were then cast. Specimens with external tendons (EWS and EWC) were constructed using three precast segments (Figure 6-7) with closure pours located at the deviators for the external tendons. The specimens were injected with post-tensioning grout or flexible filler (Figure 6-8) after the tendons were post-tensioned. The fatigue specimens were constructed in two segments with the mechanical hinge placed near midspan (Figure 6-9).



Figure 6-6 Segments in prestressing bed



Figure 6-7 Segments arranged for casting of deviation block (EWS and EWC)

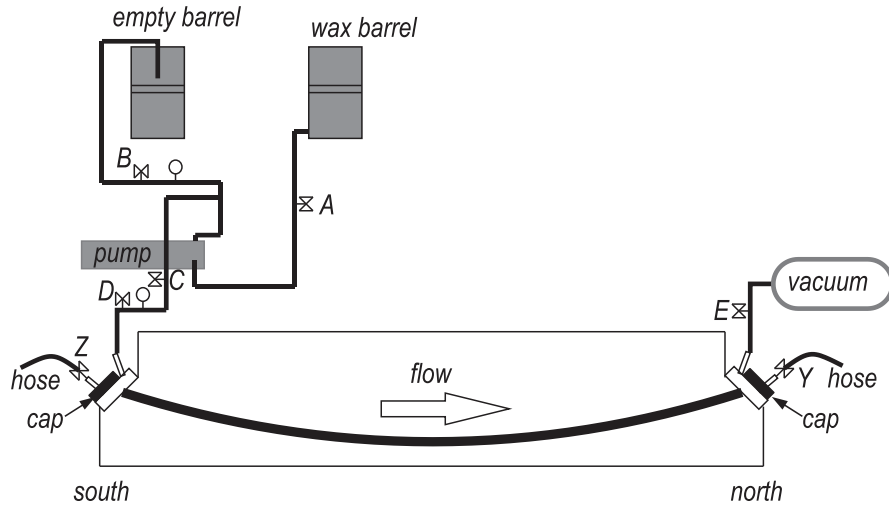


Figure 6-8 Flexible filler injection



Figure 6-9 Completed fatigue specimen

6.3 Testing

Three-point (Figure 6-10) static bending tests were conducted on IGS, IWS, and EWS; a four-point static bending test was conducted on IWC; and a three-point cyclic loading test was conducted on EWC. Strain, load, and prestressing force were recorded during load testing.

Fatigue specimens were tested for 2 million cycles at a stress range of 11.6 ksi. Tendon force and strain were monitored during the cycling. After completion of the load cycling, the specimen was examined to determine if fatigue damage could be detected. Wedges, prestressing strands, and HDPE duct near the diabolo deviator were examined.

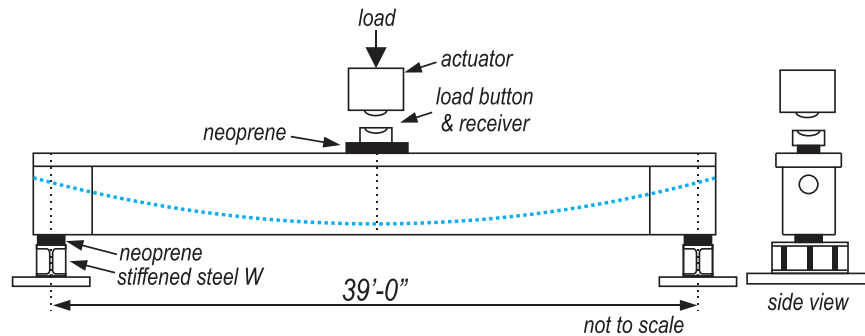


Figure 6-10 Three-point flexural test setup for IGS and IWS

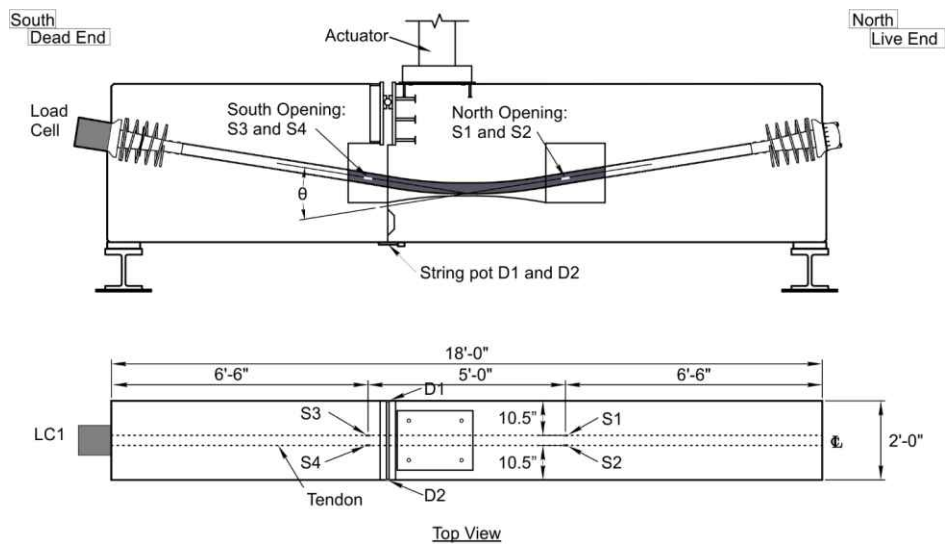


Figure 6-11 Fatigue test setup schematic

6.4 Summary and Conclusions

Five 40-ft long I-girder beams – three beams with an internal parabolic twelve-strand tendon and two beams with a pair of externally deviated six-strand tendons – were post-tensioned, injected with filler material, and load tested. Two fatigue specimens were constructed and utilized to conduct a series of fatigue tests. Tendon replacement was performed on one internal tendon specimen.

Conclusions:

- The flexural strength of members with external unbonded tendons and flexible fillers was adequately predicted by the AASHTO-LRFD provisions for unbonded tendons.
- The hinge length in mixed tendon specimens (with internal tendons), as estimated from inspection of the final cracking patterns, was found to be less than that assumed in the formulation of the unbonded tendon stress prediction equation given in AASHTO-LRFD (Section 5.7.3.1.2).
- Unbonded tendon stress at ultimate flexural strength is dependent on the effective prestress. A reasonable estimation of effective prestress is required to ensure an accurate prediction of ultimate flexural strength.

- Unbonded tendon stress at ultimate flexural strength is dependent on the global deformation patterns and geometry of the entire member.
- In components with mixed tendons (bonded and unbonded), the ductility and ultimate strength are governed by the rotational capacity of the hinge region.
- Ultimate flexural strength in specimen IWC was controlled by bonded strand rupture. This phenomenon limited the available increase in unbonded tendon stress for mixed tendons and the ultimate flexural strength.
- For single point loading, concentrated loads in mixed tendon members with low quantities of bonded steel, the observed hinge length was approximately d , the depth of the section, and did not match AASHTO-LRFD assumption ($2Z_s$). It is likely that the hinge length will vary as the ratio of bonded and unbonded tendons vary.
- The simplified approach given in AASHTO-LRFD was insufficient to predict flexural strength for in one tested specimen with mixed bonded and unbonded reinforcement. Particular care should be taken with low quantities of bonded reinforcement.
- Up to 20% reduction in ultimate tensile strength of prestressing strands was noted in the fatigue specimen with a tendon deviation angle of 11 degrees. Brittle fracture patterns were noted that appear to have been induced by strand-to-strand fretting. The tensile strength of the prestressing strands in the fatigue specimen with the 18 degree deviation angle exceeded the minimum ultimate tensile strength requirement.
- Threshold friction curvature coefficients were determined for the deviators and were compared to an analysis of a prototype bridge. The analysis indicated that the differential force across the deviators were well below those required to cause slip in the fatigue specimens.
- Duct damage was noted at one of the deviator exit locations that was the result of the strands pinching the HDPE wall against the concrete. Because the other deviator exit locations did not exhibit this behavior, it is concluded that the geometry selected for the diabolo was adequate and that the damage may have been caused by diabolo misalignment. Providing additional flare curvature beyond that provided for this design would allow more tolerance for misalignment during construction. Furthermore, inspection of the deviator would be prudent prior to tendon installation to ensure that pinching does not occur.
- Strands were installed parallel in both fatigue specimens, which provides the ideal case that is practically unattainable in the field. Future work should examine the effect of twisted strand on the fatigue resistance of the tendons.

Based on the performed testing and the available literature, it is recommended that design of members with mixed bonded and unbonded reinforcement include a detailed analysis considering global deformation behavior and strain compatibility between the concrete section and the bonded reinforcement; in lieu of a detailed analysis, a modification to the simplified approach given in AASHTO-LRFD is warranted, based on testing conducted in this project.

As of the completion of this research, little code guidance is available to address the use of mixed tendons. The existing AASHTO-LRFD provisions considering mixed tendons were evaluated using the simplified approach. Comparison of the current AASHTO-LRFD provision for members with mixed bonded and unbonded components versus experimentally and analytically determined ultimate strength and unbonded tendon stress reveals an overestimation by the code, leading to moderately unconservative predictions of ultimate strength and the

unbonded tendon stress in one test specimen. Members with mixed reinforcement were found to exhibit behavior different from fully bonded and fully unbonded systems. Further investigation of the parameters influencing the ultimate strength of mixed tendon members is warranted, as is more expansive guidance within the structural codes.

7 Part III—Wire Break Detection

Several small-scale test setups were constructed to evaluate the breaking behavior of single prestressing strands. Following testing of the full-scale specimens in Part II, wires were cut while monitoring to gather data to validate the wire break location algorithm. Finally, finite element analyses were conducted in support of the development of the algorithm.

This part of the research project focused on developing a robust and cost-effective monitoring system for unbonded post-tensioning tendons containing flexible filler. Although corrosion detection is considered a critical aspect of tendon monitoring, many of the monitoring approaches are insensitive to small defects or corrosion at an early stage, making them challenging to implement in a full-scale setting. By virtue of safety factors, the breakage of an individual wire in a multi-strand tendon system can serve as a warning, and an early detection of the breakage can enable proactive maintenance. Thus, the primary objective of this work is to develop an efficient system for tendon damage detection with the ultimate goal of providing maintenance decision support. Specifically, the aim is to detect a breakage event and identify the broken strand at the earliest possible stage, as early as a single wire break.

In developing the monitoring system, this research considers: (1) a comprehensive investigation of existing monitoring approaches to determine their limitations, (2) the development of an efficient method particularly suitable for unbonded tendons, (3) the creation of detailed analytical models to investigate strand failure mechanisms and assess the feasibility of the proposed monitoring method, (4) validation experiments to confirm its effectiveness and practicality, (5) an extensive parametric study to achieve an optimized sensor arrangement, (6) the development of an efficient data processing algorithm to detect, locate, and quantify the tendon damage programmatically, (7) a sensitivity study with measurement errors to examine the robustness of the model, (8) the characterization of static and dynamic strand response to loading and wire breakage, (9) a behavioral investigation of wire breaks with various confinement conditions, (10) the investigation on stress recovery and load distribution among wires to determine the effectiveness of the method, and (11) full-scale laboratory experiments with both internal and external tendons to investigate the effectiveness of the proposed monitoring approach. Completion of these tasks have resulted in an efficient breakage detection framework that enables an automated tendon monitoring strategy suitable for in-field implementation.

7.1 *Wedge Plate Test Setup*

An approximately 5-ft long steel reaction fixture (Figure 7-1) was used to react against the strands. A stiffened anchor plate was placed at the stressing end of the fixture to bear an anchor head, whereas a load cell was positioned between the end bearing plate and the anchor plate at dead end. In each of the three sets of tests, two strands were stressed during the experiment (Figure 7-1).

7.2 *Wedge Plate Results*

Under the loading and boundary conditions, the resulting strain in an anchor head is expected to develop primarily in three directions: axial (because of tension in strands), circumferential, and radial (because of wedge seating in anchor head). The strain response in all these three directions was captured to assess the sensitivity of measured strains to wire breaks (Figure 7-2).

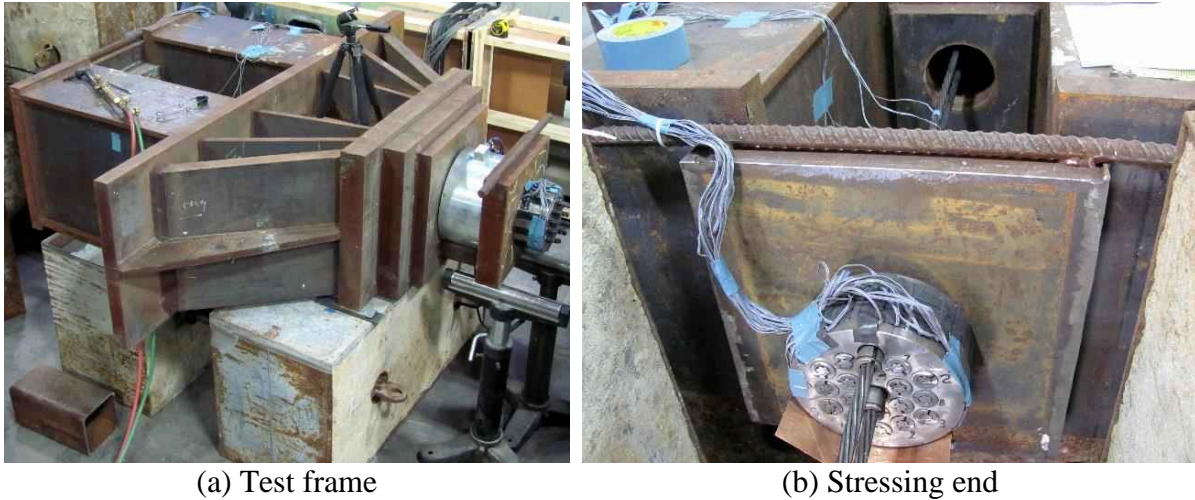


Figure 7-1 Experimental setup

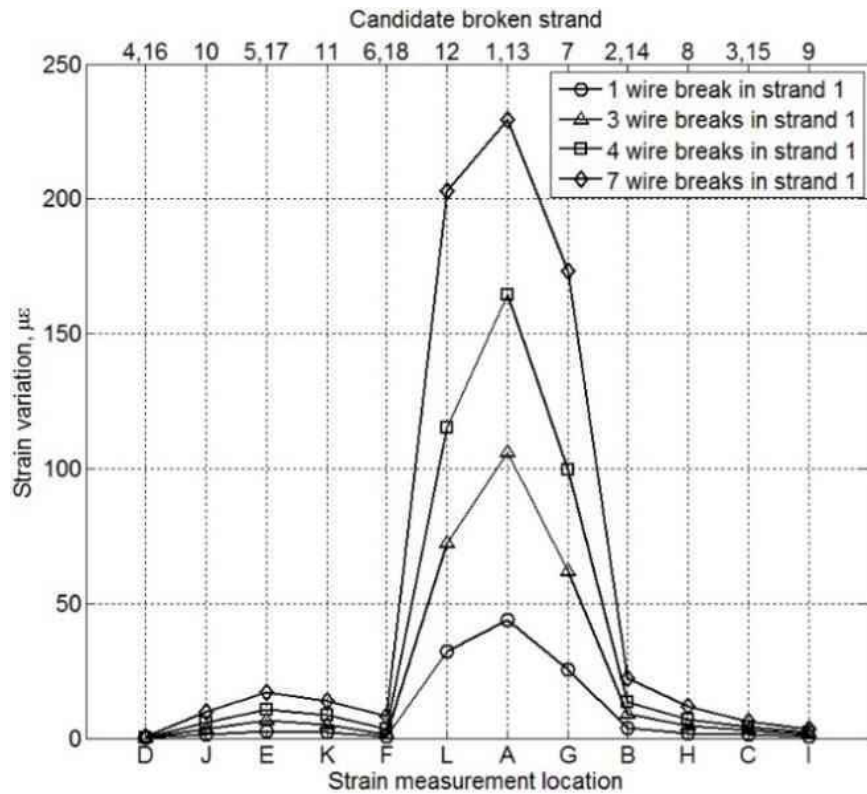


Figure 7-2 Axial strain variations due to wire breaks

7.3 Finite Element Analysis

FEA was focused on understanding the behavior of the wedge plate when loaded by wedges that are holding prestressing strands in place. The model was discretized with quadratic hexahedral and quadratic tetrahedral elements. A mesh convergence study was performed to confirm the adequacy of discretization. The compressive load was applied to the wedge with a

displacement-controlled method using variable incremental steps. Idealized pinned boundary conditions were enforced at four bolt locations as shown in Figure 7-3.

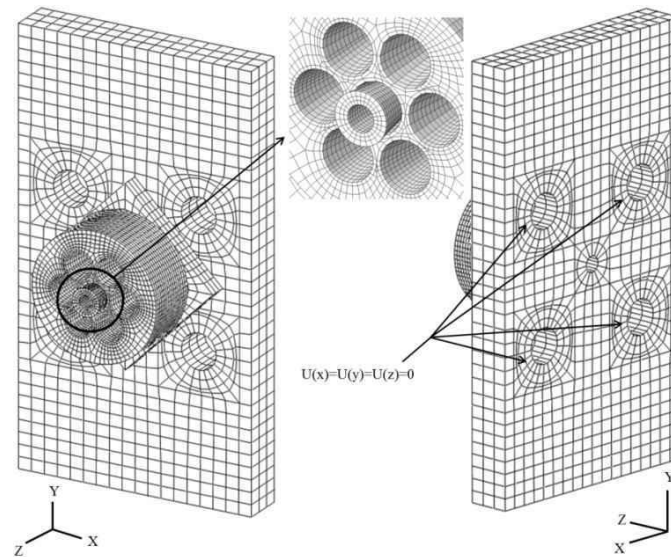


Figure 7-3 Discretization and boundary conditions of FE model for calibration

7.4 Experimental Evaluation of Tendon Behavior

Evaluation of the wire-break detection scheme was implemented on the full-scale specimens reported in Part II of this report. Tests were conducted with both external and internal unbonded tendons in I-girder specimens having deviated tendon profiles. After post-tensioning, the beams were loaded under three-point bending (simply supported beam with a concentrated load at the midspan) to investigate their ultimate capacity (presented in Part II) and then unloaded. Finally, the strands were detensioned (Figure 7-4 and Figure 7-5), and the changes in anchor strain distribution were captured. The broken strand identification model for a 12-strand wedge plate was applied to the experimental results.

7.5 Tendon Monitoring Framework

Figure 7-6 shows a monitoring framework for the strain-based approach developed. The purpose of the framework is to provide alerts when strand breakage is detected and to identify the strand that has sustained the damage. The data collection and processing is expected to be fully automated, requiring very little user input. The framework assumes that at least one wedge plate for the strand(s) of interest is instrumented with a number of strain gages capturing axial strains on a predetermined schedule (e.g., daily or weekly), such as at night when traffic loads and temperature loads are expected to be at their lowest. The anchor strain data is collected for an amount of time adequate to capture mean strain levels each day. Then the captured data may be pre-processed to exclude the effects of live load, temperature differentials, and other non-breakage events. The preprocessed data is compared with the data collected during the previous monitoring event to determine if any significant strain change has occurred, indicating a wire break. After detecting a break event, the next step is to identify the broken strand. Finally, an assessment of the damage level, relative to previous monitoring events, is carried out. The

damage level assessment may then be used by the maintenance office to decide whether to continue monitoring the strains or to perform a maintenance operation.



(a) exposing the duct to access the strands



(b) wire cuts with Dremel tool

Figure 7-4 Cutting prestressing strands



(a) before strand cuts



(b) after strand cuts

Figure 7-5 Wedge movement after strand cuts



Figure 7-6 Wire breakage identification flowchart

7.6 Summary and Conclusions

Analytical and experimental investigations were performed to develop an algorithm that can be used to detect, locate, and quantify tendon damage by monitoring the strain distribution in the wedge plates of the anchors. Because unbonded tendons are connected to the structure only through deviators and end anchorages, the anchor heads are normally under high prestressing load. A wire break in the strand results in prestress loss, and consequently, the strain distribution in the wedge plate varies from the unbroken state. This variation of strain field has been used to detect the wire breakage.

The algorithm was first investigated using a finite-element model calibrated with experimental data from a seven-strand anchor head. The model accounted for plasticity, large displacement, and other contact non-linearity. To account for the contact problem originating from the interactions of wedge-anchor head and anchor head-anchor plate interfaces, the FE model has been calibrated with friction coefficients of 0.015 and 0.1, respectively.

FE analysis results of a nineteen-strand wedge plate were used to demonstrate use of the algorithm. To locate the broken strand, damage indices were calculated for the candidate strands by considering the combined effect of the strain variations at monitoring points and their true distances from the respective wedge locations. The candidate strand group was selected by identifying the strand layer where the damage had occurred, and finally, the strand associated with the maximum index is identified as the broken strand. Monte Carlo simulations were used in a sensitivity study of measurement errors caused by gauge misalignment; transverse sensitivity of gauges, fabrication fault, and differential temperature at monitoring locations on wedge plates were considered in the simulations. The proposed model allows an efficient data processing algorithm and the adoption of an automated monitoring package for breakage detection. In addition, it overcomes many of the challenges faced by the available approaches through the use of low-cost sensors and conventional data acquisition, minimal accessibility requirement, easy instrumentation, sensor installation, and replacement. The following specific conclusions are noted:

- The anchorage region near the broken strand is more affected by a wire break compared to other regions, which results in differential strain variation among the monitoring points (strain gauge locations) around the wedge plate perimeter.
- Because of proximity to the monitoring points, a larger strain drop occurs for breakages on the outer layer strands in contrast to the inner layers.
- The magnitude of strain-change increases with the number of wire breaks, indicating the severity of damage.
- Axial strain in the wedge plate was found to be the most sensitive strain to wire breakage.
- In experimental work on the unraveling of a single wire from a strand, confined strands lost less force due to a wire break than a bare strand even under minimal radial pressure.
- Wire breaks in strands on the outer layers were found to be detectable with the presence of higher measurement errors compared to the inner layers
- The AE system successfully captured wire breakage events in controlled laboratory conditions on relatively small bridge girders. Field tests should be conducted, however, on full-scale bridge elements to confirm its performance in practical conditions in the presence of environmental and traffic noise.

Replaceable Unbonded Tendons for Post-Tensioned Bridges

Part I Mockup for Flexible Filler Injection

This report is one of a four-part compilation published under separate covers as follows:

Extended Summary

Part I Mockup for Flexible Filler Injection

Part II Structural Testing

Part III Wire Break Detection

Final Report

December 2017

Principal investigator:

H. R. Hamilton

Co-Principal investigator:

J. A. Rice

Research assistants:

A.B.M. Abdullah

Rahul Bhatia

Natassia Brenkus

Devon Skelton

Sponsor:

Florida Department of Transportation (FDOT)

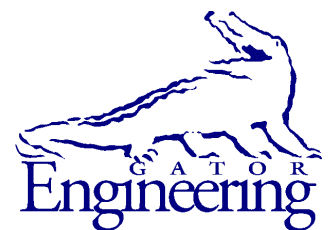
William Potter, P.E.–Project Manager

Rick W. Vallier, P.E.–Project Manager

Contract:

UF Project No. 000112216 & 000112218

FDOT Contract No. BDV31-977-15



University of Florida

Engineering School of Sustainable Infrastructure and Environment

Department of Civil and Coastal Engineering

University of Florida

P.O. Box 116580

Gainesville, Florida 32611

Disclaimer

The opinions, findings, and conclusions expressed in this publication are those of the authors and not necessarily those of the State of Florida Department of Transportation.

Units of Measurement Conversion

SI* (MODERN METRIC) CONVERSION FACTORS

APPROXIMATE CONVERSIONS TO SI UNITS

SYMBOL	WHEN YOU KNOW	MULTIPLY BY	TO FIND	SYMBOL
LENGTH				
in	inches	25.4	millimeters	mm
ft	feet	0.305	meters	m
yd	yards	0.914	meters	m
mi	miles	1.61	kilometers	km
AREA				
in²	square inches	645.2	square millimeters	mm ²
ft²	square feet	0.093	square meters	m ²
yd²	square yard	0.836	square meters	m ²
ac	acres	0.405	hectares	ha
mi²	square miles	2.59	square kilometers	km ²
VOLUME				
fl oz	fluid ounces	29.57	milliliters	mL
gal	gallons	3.785	liters	L
ft³	cubic feet	0.028	cubic meters	m ³
yd³	cubic yards	0.765	cubic meters	m ³
NOTE: volumes greater than 1000 L shall be shown in m ³				
MASS				
oz	ounces	28.35	grams	g
lb	pounds	0.454	kilograms	kg
T	short tons (2000 lb)	0.907	megagrams	Mg (or "t")
TEMPERATURE (exact degrees)				
°F	Fahrenheit	5(F-32)/9 or (F-32)/1.8	Celsius	°C
ILLUMINATION				
fc	foot-candles	10.76	lux	lx
fl	foot-Lamberts	3.426	candela/m ²	cd/m ²
FORCE and PRESSURE or STRESS				
kip	1000 pound force	4.45	kilonewtons	kN
lbf	pound force	4.45	newtons	N
lbf/in²	pound force per square	6.89	kilopascals	kPa

*SI is the symbol for the International System of Units. Appropriate rounding should be made to comply with Section 4 of ASTM E380.

SI* (MODERN METRIC) CONVERSION FACTORS
APPROXIMATE CONVERSIONS FROM SI UNITS

SYMBOL	WHEN YOU KNOW	MULTIPLY BY	TO FIND	SYMBOL
LENGTH				
mm	millimeters	0.039	inches	in
m	meters	3.28	feet	ft
m	meters	1.09	yards	yd
km	kilometers	0.621	miles	mi
AREA				
mm²	square millimeters	0.0016	square inches	in ²
m²	square meters	10.764	square feet	ft ²
m²	square meters	1.195	square yards	yd ²
ha	hectares	2.47	acres	ac
km²	square kilometers	0.386	square miles	mi ²
VOLUME				
mL	milliliters	0.034	fluid ounces	fl oz
L	liters	0.264	gallons	gal
m³	cubic meters	35.314	cubic feet	ft ³
m³	cubic meters	1.307	cubic yards	yd ³
MASS				
g	grams	0.035	ounces	oz
kg	kilograms	2.202	pounds	lb
Mg (or "t")	megagrams (or "metric ton")	1.103	short tons (2000 lb)	T
TEMPERATURE (exact degrees)				
°C	Celsius	1.8C+32	Fahrenheit	°F
ILLUMINATION				
lx	lux	0.0929	foot-candles	fc
cd/m²	candela/m ²	0.2919	foot-Lamberts	fl
FORCE and PRESSURE or STRESS				
kN	kilonewtons	0.225	1000 pound force	kip
N	newtons	0.225	pound force	lbf
kPa	kilopascals	0.145	pound force per square inch	lbf/in ²

*SI is the symbol for the International System of Units. Appropriate rounding should be made to comply with Section 4 of ASTM E380.

Table of Contents

Disclaimer	ii
Units of Measurement Conversion	iii
List of Figures	vii
List of Tables	ix
1 Introduction.....	1
2 Research Approach	2
3 Corrosion Protection Materials for Unbonded Tendons	3
3.1 Suppliers	3
3.2 Material Specifications	3
3.3 Installation.....	6
3.4 Implications.....	7
4 Flexible Filler Material Selection	9
5 Test Setup Design and Construction.....	12
5.1 Tendon Design	12
5.2 Tendon Details	13
5.2.1 Anchorage	13
5.2.2 Duct	14
5.2.3 Injection Ports.....	17
5.3 Tendon Support Frame and Deviators	18
5.4 Tendon Fabrication and Stressing.....	20
5.5 Injection Equipment.....	26
5.6 Flexible Filler Preparation	27
6 Instrumentation and Data Acquisition	29
6.1 Instrumentation Plan	29
6.1.1 Pressure Transducers	31
6.1.2 Thermocouples	31
6.1.3 Volume Calculation.....	33
6.1.4 Gravity Deviator Displacement.....	33
6.2 Data Acquisition	33
7 Small Specimen Component Tests	34
8 Injections.....	38
8.1 Cirinject CP.....	38
8.1.1 Injection Process.....	38
8.1.2 Observations	39
8.2 Visconorust	40
8.2.1 Injection Process.....	41
8.2.2 Observations	41
8.3 VZ Inject	42
8.3.1 Injection Process.....	42
8.3.2 Observations	43
8.4 Trenton-1.....	43
8.4.1 Injection Procedure.....	44
8.4.2 Observations	45
8.5 Trenton 2.....	45
8.5.1 Injection Procedure.....	45

8.5.2	Observations	47
9	Results and Discussion	48
9.1	Post-Injection Inspection	48
9.1.1	Cirinject CP	50
9.1.2	Visconorust.....	57
9.1.3	VZ Inject.....	63
9.1.4	Trenton 1	70
9.1.5	Trenton 2	77
9.2	Injection pressure	84
9.3	Temperature	87
9.4	Injection Rate	92
9.5	Relative Fill.....	94
10	Heat Transfer Analysis	95
10.1	Model Development.....	95
10.2	Model Validation	96
10.3	Sensitivity of filler front temperature to injection parameters.....	98
10.4	Estimation of effective strand surface area.....	101
10.5	Injection Pressure.....	101
11	Summary and Conclusions	104
	References.....	105
	Appendix A—Filler Rheology Testing.....	106
A.1	Test Procedures	106
A.2	Test Results	107
	Appendix B—Mockup Frame Construction Drawings	110

List of Figures

Figure 5-1 Tendon profile for the mockup testing on unbonded tendons.....	12
Figure 5-2 Anchor block placed on the frame	13
Figure 5-3 Window locations on tendon.....	16
Figure 5-4 Typical mechanical coupler	17
Figure 5-5 Injection ports (a) DSI (b) VSL (c) Freyssinet.....	17
Figure 5-6 Injection into saddle	18
Figure 5-7 Plan and elevation of the foundation plan.....	18
Figure 5-8 Mockup support system including (a) anchorage frame (b) middle frame (c) supports between frames, and (d) gravity deviators.....	19
Figure 5-9 (a) McElroy HDPE fusion machine (b) Duct fusion in progress	21
Figure 5-10 HDPE duct on the support frame after welding	22
Figure 5-11 HDPE duct connected to the anchor block at the east end.....	22
Figure 5-12 Clear windows in duct.....	22
Figure 5-13 West end connected to the anchor block.....	23
Figure 5-14 Strand installation using Model 00143604/2 strand pusher from PAUL Maschinenfabrik GmbH & Co.....	23
Figure 5-15 Bullet on the head of the strand during pushing	24
Figure 5-16 Wedge plate installation.....	24
Figure 5-17 Wedge plate installed on anchor	24
Figure 5-18 Monostrand hydraulic jack and pump used to stress strands	25
Figure 5-19 Deviators suspended by tendon after stressing	25
Figure 5-20 Strand tails cutting in operation	26
Figure 5-21 Grout pump (Schwager Davis Inc.)	26
Figure 5-22 Viking pump used for filler injection.....	27
Figure 5-23 Vacuum pump and reservoirs.....	27
Figure 5-24 (a) Barrel heater position on barrel (b) heaters covered with insulation blanket	28
Figure 5-25 Filler heating logistics (a) transfer of filler between barrels and (b) filler agitation.....	28
Figure 6-1 Schematic of sensor location and orientation of temperature probes relative to duct and strand.....	30
Figure 6-2 Instrumentation orientation on the tendon	30
Figure 6-3 Typical pipe saddle (Ford Meter Box).....	31
Figure 6-4 Typical transducer installed on the tendon.....	31
Figure 6-5 Thermocouple probe to measure filler temperature (a) with both thermocouple and surface probe installed on the duct (b) top internal orientation (c) bottom orientation and (d) inclined orientation (e) side orientation	32
Figure 7-1 Typical small scale test setup.....	34
Figure 7-2 Typical small scale test specimen	35
Figure 7-3 Deformation in the duct due to high pressure	37
Figure 8-1 Schematic of set up for Cirinject CP and VZ Inject specimens.....	38
Figure 8-2 Schematic of set up for Visconorust injection	40
Figure 8-3 Schematic of test setup for Trenton wax injection with vacuum assist	44
Figure 9-1 Inspection port (IP) locations on Cirinject, Visconorust, and VZ Inject mockup specimens.....	48
Figure 9-2 Inspection port (IP) locations on Trenton 1 and Trenton 2 mockup specimens	48
Figure 9-3 Duct internal pressure during Cirinject CP injection	84

Figure 9-4	Variation in duct internal pressure during Visconorust injection	85
Figure 9-5	Duct internal pressure during VZ-inject injection	85
Figure 9-6	Duct internal pressure during Trenton 1 filler injection.....	86
Figure 9-7	Duct internal pressure during Trenton 2 filler injection.....	86
Figure 9-8	Filler temperature in duct during Cirinject injection.....	87
Figure 9-9	Filler temperature in duct during Visconorust injection	88
Figure 9-10	Filler temperature in duct during VZ-inject injection	88
Figure 9-11	Filler temperature in duct during injection with vacuum assist (Trenton 1).....	89
Figure 9-12	Filler temperature in duct during Trenton filler injection (Trenton 2).....	89
Figure 9-13	Surface temperature of the duct during Cirinject CP injection	90
Figure 9-14	Surface temperature of the duct during Visconorust injection.....	91
Figure 9-15	Surface temperature of the duct during VZ-inject injection	91
Figure 9-16	Surface temperature of duct during injection with vacuum assist (Trenton 1)	92
Figure 9-17	Surface temperature of duct during Trenton filler injection (Trenton 2)	92
Figure 9-18	Injection rate during Visconorust injection.....	93
Figure 9-19	Injection rate during VZ inject injection	93
Figure 9-20	Injection rate during Cirinject CP injection	93
Figure 9-21	Injection rate during Trenton filler injection with vacuum assist (Trenton 1).....	94
Figure 9-22	Injection rate during Trenton filler injection (Trenton 2)	94
Figure 10-1	Filler flow through a tendon system.....	95
Figure 10-2	Duct filling sequence during mockup injection	97
Figure 10-3	Sensitivity study	100
Figure 10-4	Effective strand surface.....	102
Figure 10-5	Experimentally obtained viscosity for Cirinject CP.....	103
Figure 10-6	Pressure loss	103
Figure A-1	Cirinject filler results.....	107
Figure A-2	Visconorust filler results	107
Figure A-3	VZ Inject filler results	108
Figure A-4	Trenton filler results	108
Figure A-5	Sanchem filler results	109

List of Tables

Table 3-1	Acceptance criteria for PT coatings	4
Table 3-2	EOTA acceptance criteria for filling grease (ETAG 013).....	5
Table 3-3	EOTA acceptance criteria for petroleum wax (ETAG 013).....	6
Table 3-4	NRC acceptance criteria for PT coating	6
Table 4-1	Physical and chemical properties of different injection material for mockup test	11
Table 5-1	ETA table for HDPE smooth pipe selection (ETA 06/226 2012).....	14
Table 5-2	Size of HDPE duct based on various specifications.....	15
Table 5-3	Cell classification for HDPE duct (ASTM 3350, 2012).....	15
Table 6-1	Distance from the face of the east anchor to the sensor. See Figure 6-1	30
Table 7-1	Small scale test specimens and components tested	35
Table 9-1	Distance from the face of the west anchor to inspection ports. See Figure 9-1 and Figure 9-2.....	49
Table 9-2	Distance from the face of the west anchor to duct windows. See Figure 9-1 and Figure 9-2	49
Table 9-3	Post-injection inspection of Cirinject CP	50
Table 9-4	Post-injection inspection of Visconorust.....	57
Table 9-5	Post-injection inspection of VZ inject.....	63
Table 9-6	Post-injection inspection of Trenton 1	70
Table 9-7	Post-injection inspection of Trenton 2	77
Table 9-8	Comparison of theoretical and injected volume for the mockup	94
Table 10-1	Comparison of mockup test results with proposed thermal model	97
Table 10-2	Sensitivity study matrix.....	99

1 Introduction

This is Part I of the research report covering Task 1 of the FDOT Project BDV31-977-15 “Replaceable Unbonded Tendons for Post-Tensioned Bridges”. Five mockup PT tendons were injected with four different heated, flexible fillers. This report documents the process and results of the testing. Preliminary testing was also conducted on a small-scale setup to evaluate individual components to be used in the full-scale mockup to ensure the safety of the laboratory staff during the full-scale mockup injections and acclimate the staff to the new procedures and equipment in a smaller, more controlled setup.

Chapter 2 provides a brief overview of the approach taken in this portion of the research project. Chapter 3 provides the background on the selection of the flexible filler materials. Chapter 4 presents the design and details of the mockup specimen and support systems. Chapter 5 describes the instrumentation to be monitored during injection. Chapter 6 describes the construction of small trial specimens that were used to gain familiarity in working with the filler material. Chapter 7 describes each injection in detail including dissection following injection. Chapter 8 provides results and discussion of injection and dissection. Chapter 9 covers the thermal model developed and its validation with experimental results followed by summary and conclusions in Chapter 10.

2 Research Approach

The objective of this part of the research project was to investigate the constructability of unbonded multi-strand, post-tensioned bridge tendons injected with flexible filler. The testing focused on tendon and duct detailing, filler material preparation, injection process and equipment, and vacuum and venting procedures. The results are intended to provide background information on this process and to assist in the preparation of material and construction specifications.

Flexible filler materials are solid at ambient temperatures and liquefy to a pumpable viscosity at elevated temperatures. To test the behavior of the flexible filler material in the expected environment, five mockup specimens of full-scale post-tensioning tendons were constructed and injected. Four different commercially available materials were selected for use, not with the intent to test the material, but rather to use different materials to test the heating and injection procedures. Consequently, the differences in behavior among the five tests are likely due to the injection procedures rather than the material properties.

Temperature and pressure of the filler material was monitored along the length of the tendon during and immediately following injection to determine the change in each during the injection process. Clear pipe windows were placed along the length to allow visual observation of the injection process. Short sections of duct were removed one day after injection at critical locations to investigate whether voids formed, and if so, determine their extent. While different fillers were used in the first three mockups, the same filler was used in the remaining two specimens; vacuum-assisted injection was conducted in one of tests, with the filler injected through anchor cap, while the other test was not equipped with a vacuum pump and the filler was directly injected into the duct.

In addition to the experimental testing, a simplified analytical model was developed to compute the change in flexible filler temperature during injection, which can be useful in determining tendon constructability. After validating the model with multiple experiments, an extensive sensitivity analysis was performed to obtain practically useful relationships between filler front temperature and effective strand surface area, tendon length, injection rate, ambient temperature, injection temperature, and strand pattern. Moreover, pressure losses for different flow velocities and tendon lengths were estimated.

3 Corrosion Protection Materials for Unbonded Tendons

Similar to bonded PT tendons, corrosion protection of unbonded tendons can be provided in multiple layers such as concrete cover, enclosing duct, PT coating, and protection for the individual strand. Some or all of these protection methods may be employed in a given design. Ducts used for unbonded tendons are typically high-density polyethylene (HDPE) or corrugated steel. PT coatings that can be used to fill the space between the prestressing strand and the enclosing duct and provide corrosion protection are typically in grease, wax, or gel form. Also prestressing strands can be protected individually using PT coating with an extruded sheath. Yet another method of individual protection is epoxy coated and filled strand. This chapter describes the available materials used for PT coating and filling along with relevant material specifications. In addition, injection procedures and equipment are discussed.

3.1 Suppliers

The materials used for coating prestressing strand or wire are typically petroleum based. While this list is not intended to be exhaustive, the following indicated some of the products available for corrosion protection:

Grease:

- For monostrand tendons: Mobil Greasrex K-218
- Nuclear grease: NO-OX-ID.

Petroleum-based wax:

- Cirinject CP (ETA 10/0209)
- Nontribos VZ-inject (August-Gähringer 2013)

Petroleum Jelly:

- Visconorust 2090P

Gel: Uni-gel: A polymer blend with a refined base oil and additives. Manufactured by UNIGEL USA Inc.

Epoxy coated strand: Sumiden Wire products corporation

3.2 Material Specifications

In the U.S., the Post-Tensioning Institute (PTI) and American Concrete Institute publish guide material specifications for post-tensioning coatings and individual strand sheathing. ACI 423.7-07 recommends specific acceptance criteria for PT coating to be used to protect unbonded tendons. It also recommends that all coatings be tested every five years, even if no changes have been made. Table 3-1 outlines the test methods and acceptance criterion for coating material.

ACI 423.7-07 requires that individual strand sheathing be manufactured from polyethylene or polypropylene. If any other material is used then it should satisfy the durability criteria. Sheathing plays an important role in the durability of the post tensioning system as it provides a layer of protection, particularly in aggressive environments where water is contaminated with alkali, chlorides. This layer being the protection layer to the post tensioning system, if damaged allows water and chemicals to seep into the system which affects the durability. The sheathing material should also satisfy the following durability criteria such as

Abrasion resistance; UV resistance ; Impact resistance; Chemical resistance; Chloride ion permeability; Tear resistance; Cold weather exposure; Thermal cracking; Tensile strength; Compressive strength; Brittleness; and Functionality within a temperature range of –20 to +120 °F (–30 to 49 °C).

Table 3-1 Acceptance criteria for PT coatings

Characteristics	Test Methods	Acceptance Criterion
Dropping Test	ASTM D566 or D2265	Minimum 300 °F [149 °C]
Oil separation at 160 °F [71 °C]	FTMS 791 B Method 321.2	0.5 % maximum by mass
Water Content	ASTM D95	0.1 % maximum
Flash Point	ASTM D92	Minimum 300 °F [149 °C]
Soak test (5% salt fog at 100 °F [38 °C] 0.005 in.[0.127 mm] coating, Q Panel Type S. Immerse panels 50% in a 5% salt solution and expose to salt fog)	ASTM B117	No emulsification of the coating after 720 hours of exposure.
Compatibility with sheathing: a. Hardness and volume change of polymer after exposure to grease, 40 days at 150 °F (66 °C) b. Tensile strength change of polymer after exposure to grease, 40 days at 150 °F (66 °C)	ASTM D4289 (ASTM D792 for density) ASTM D638	Permissible change in hardness: 15%; volume: 10% Permissible strength in tensile strength: 30%
Corrosion test (5% salt fog at 100 °F [38 °C] 0.005 in. [0.127 mm], minimum hours, Q Panel Type S)	ASTM B117	Rust Grade 7 or better after 1000 hours of exposure according to ASTM D610
Water-soluble ions:*		
a. Chlorides	ASTM D512	10 ppm maximum
b. Nitrates	ASTM D3867	10 ppm maximum
c. Sulfides	ASTM D4500-S2E	10 ppm maximum

The minimum thickness of polyethylene or polypropylene should be 0.050 in and minimum density of 0.034 lb/in³ with an internal diameter of the sheathing 0.030 in more than the maximum strand diameter. Sheathing should cover the strand completely and should provide a smooth circular surface. (ACI 423.7 2007). In addition, sheathing should be continuous and provide a water-tightness to the tendons when manufactured through the extrusion process.

The European Organization for Technical Approval (EOTA) presents guidelines for bridges, buildings, and other structures using unbonded tendons. ETAG-013 covers the EOTA technical specifications for products to be used in post-tensioning systems. The general EOTA acceptance criteria for grease or petroleum wax are based on the tests shown in Table 3-2 and Table 3-3, respectively. Table 3-2 is intended for mineral oil-based grease to be used as a coating in unbonded external tendons or in monostrand. Other properties such as flash point,

water content and soak test results should be declared by the supplier. Table 3-3 is intended for bitumastic petroleum-based wax to be used as filling material in ducts of external tendons.

The Nuclear Regulatory Committee (NRC) provides specifications for PT coating material in unbonded tendons used in nuclear containments. Table 3-4 outlines the acceptance criteria for the PT coating.

Table 3-2 EOTA acceptance criteria for filling grease (ETAG-013)

Characteristics	Test Methods	Acceptance Criterion
Cone Penetration, 60 strokes (1/10 mm)	ISO 2137	250-300
Dropping Point	ISO 2176	> 302 °F (150 °C)
Oil Separation at 104 °F (40 °C)	DIN* 51 817	At 72 hours <0.5 % At 7 days <4.5 %
Oxidation Stability	DIN 51 808	100 hours at 212 °F (100 °C) <0.06 MPa 1000 hours at 212 °F (100 °C) <0.2 MPa
Corrosion Protection 168 hours at 95 °F (35 °C) 168 hours at 95 °F (35 °C)	NF** X 41-002 (salt spray) NF** X 41-002 (distilled water spray)	Pass No Corrosion
Corrosion Test	DIN 51 802	Grade: 0
Content of Aggressive Elements Cl ⁻ , S ⁻² , NO ₃ ⁻ , SO ₄ ⁻²	NF** M 07-023 NF** M 07-023	< 50 ppm <100 ppm

*DIN- Deutsches Institut für Normung

**NF- Francaise de Normalisation

Table 3-3 EOTA acceptance criteria for petroleum wax (ETAG-013)

Characteristics	Test Methods	Acceptance Criterion
Congealing point	NF** T 60-128	> 149 °F (65 °C)
Penetration at -4 °F (-20 °C) (1/10 mm)	NF** T 60-119	No cracking
Bleeding at 104 °F (40 °C)	BS*** 2000: PT 121 (1982)	<0.5 %
Resistance to oxidation	ASTM D942.70	100 hours at 212 °F (100 °C) <0.03 MPa
Corrosion Protection 168 hours at 95 °F (35 °C) 168 hours at 95 °F (35 °C)	NF** X 41-002 (salt spray) NF** X 41-002 (distilled water spray)	Pass No Corrosion
Copper strip corrosion at 100 hours at 212 °F (100 °C)	ISO 2160	Class 1a
Content of Aggressive Elements Cl ⁻ , S ⁻² , NO ₃ ⁻ , SO ₄ ⁻²	NF** M 07-023 NF** M 07-023	< 50 ppm <100 ppm

*DIN- Deutsches Institut für Normung

**NF- Francaise de Normalisation

***BS- British Standards Institute

Table 3-4 NRC acceptance criteria for PT coating

Characteristics	Test Methods	Acceptance Criterion
Water content	ASTM D 95	Exceeding 10% by wt.
Reserve alkalinity	ASTM D 974	Less than 50% of the installed value or less than zero when the installed value was less than 5
Water-soluble ions:*		
a. Chlorides	ASTM D512	Exceeding 10 ppm
b. Nitrates	ASTM D3867	Exceeding 10 ppm
c. Sulfides	APHA 428	Exceeding 10 ppm

3.3 Installation

This section describes construction aspects of injecting filler material into unbonded post-tensioning tendons. Implications of using non-cementitious grout are described. Construction specifications are covered by a number of agencies, including the EOTA and the NRC. Additionally, and the main focus of the section, guidance on the construction of unbonded

tendons is provided by post-tensioning manufacturers. Several PT companies were contacted to obtain the information included in this section.

For cement-based grout, pumps and mixers are generally located on the same skid, which facilitates continuous mixing and injection operations. For the injection of wax and grease –due to the lower solidification temperatures of these two materials –heating and stirring equipment is required, in addition to a pump, to insert the filler material. These components can be combined together or used individually to pump the product into the duct. Heaters are used to ensure the filler material maintains a sufficiently low viscosity to ensure pumpability. Stirrers are generally used to place the grease and wax completely in the duct. Pumps are used to continuously inject the liquefied grease or wax. Gel filling equipment comprises of a discharge pump, filling head and a metering unit for stable dosing.

For grout-filled bonded multi-strand tendons, the main concern during injection is verification of complete filling of the duct. This is usually done by mechanically checking the grout level with rods and by visual inspection of vents and outlets for bleed. Similar verification should be done with non-cementitious filler material: discharge of product (grease or wax) from vents and outlets should be checked to ensure complete filling of the duct.

The properties of the grout discharged through the bleed points are quality-inspected, checked to ensure that the properties match those of the injected product. This is done because cement grout is a non-homogeneous mixture whose property might change during the filling. The same criterion may not be applicable for the unbonded tendon filled with grease or wax, since both are homogeneous. NRC, however, instructs to check the leakage during filling and presence of free water in the grease.

3.4 Implications

Several material implications exist in making the switch from a grout to pliable filler and must be investigated. Potential issues so far identified include:

- Prevent microbial growth in filler material
- Chemical compatibility of filler material with duct and tendon accessories
- Incompatible volume change of filler with temperature change
- Cold weather injection of heated materials
- Adjustment in port locations and frequency requirements for injecting heated materials
- Safety implications of working with heated materials
- Potential for damage to epoxy coating or monostrands during handling/installation
- Environmental implications of material leakage
- Increased cost of material
- Lack of expertise in the U.S.
- Anchorage and wedge details differ for epoxy coated strand

The compatibility of pliable fillers must be checked against typically utilized tendon components and materials, including: seals, elastomeric boots at deviators, and duct material. Cement grout provides a chemically passive, high pH environment for prestressing strand (FDOT 2002); pliable materials must, at least, provide a non-aggressive environment. Neither grease nor wax provides a passive environment, though both materials provide corrosion protection: grease incorporates a cathodic and anodic chemical inhibitor system that forms a stronger polar bond to steel than water and wax is made up of chemically inert components with anti-corrosion additives. Additionally, pliable materials must be checked that they allow proper sealing at anchor heads (inadequately sealed tendons can allow moisture ingress).

Cement grout has nearly the same coefficient of thermal expansion as that of concrete and steel, making for compatible movements during temperature changes. Thermal stability of filler materials must be quantified for each filler material to ensure that seals and ducts are not pressurized due to temperature changes.

Grease and wax filler material may need to be heated in order to flow, requiring the use of heaters during the injection process. The additional equipment, while required, is not anticipated to have a significant impact of the construction as a whole. Working with the heated material, however, will present a potential safety hazard that was not an issue with grout. Furthermore, the environmental impact of leakage during and after injection must be evaluated.

Monostrand or epoxy coated strand require special care during handling and installation. The ruggedness of sheathed strands should be examined to ensure no damage occurs to the sheath during construction.

4 Flexible Filler Material Selection

Both grease and microcrystalline wax were considered for filler material when selecting materials for mockup testing. Grease is a semisolid lubricant that is composed of three components: Liquid base oil, solid thickener, and solid or liquid additives or both. The liquid base oil is a long hydrocarbon chain or cyclic aliphatic compounds that are usually produced from refining of crude petroleum oil. It can also be produced from synthesis of mineral oil or from vegetables. The solid thickeners that are used in manufacturing of greases are mostly soap based (alkali); in some cases, however, non-soap based thickeners are used. Solid thickener reacts with the base oil to generate saponification reaction. The most common is Lithium (Li) based grease. It is produced from Lithium soap thickener. Further, in order to improve the properties and performance of the grease for a particular application, additives, such as corrosion inhibitors are added to grease for improving the corrosion protection of the surfaces, and lubricating function of grease in engine oils or transmission oil.

Unlike grease, which is a mixture of base oil, thickener and additives, petroleum (or microcrystalline) waxes are produced by de-oiling of petrolatum. Petrolatum is a semisolid petroleum product generally having a carbon number more than 25; it is commonly used as a petroleum jelly or ointment. Microcrystalline waxes are mostly branched isoparaffinic or naphthenic hydrocarbons and differ from paraffin waxes, which have unbranched straight hydrocarbon chains. Due to their small and thin crystal structure, microcrystalline waxes are more flexible than the paraffin waxes. The elastic nature of these waxes is governed by their branched chain components. These waxes are darker, more viscous when in the liquid state and have a higher melting point than paraffin wax.

In the U.S., unbonded post-tensioning tendons are most commonly found in office, residential, parking, and nuclear containment structures. In Europe, however, unbonded tendons are also utilized in pedestrian bridges, silos, and major highway bridges. European use of unbonded tendons in bridges initially began in the late 1970 with the design of the Exe and Exminster Viaducts Bridge in England. Europeans started using grease as the filler material for their external tendons, but soon switched to microcrystalline wax, as they faced issues with the grease; particularly issues of oil separation from grease. Since 1990, Europeans (Particularly Germany and France) have been using microcrystalline wax for external tendons.

A search for commercially available filler materials was conducted to aid in the selection of the materials to be used in mockup testing. Alternatives were evaluated based on their conformance to either PTI-ACI specification (PTI 2006) or EOTA (European Organization for Technical Approvals) specifications (ETAG-013 2002). Samples of each of the filler materials were collected, along with their MSDS (material safety data sheet). Although the primary aim of the mockup testing was to evaluate constructability, the use of multiple specimens provided the opportunity to test several different materials. While the selection of a single material would have eliminated the variation in results due to the use of several products, it was decided that the knowledge gained by using several different materials outweighed the need to control variables.

Visconrust-2090-P (Sonneborn), Cirinject CP (Civetea), and Nontribos VZ Inject (Gähringer) were chosen for the first three mockup. Sanchem NO-OX-ID-NG was selected for use in small specimen component testing. Visconrust-2090-P and Sanchem NO-OX-ID-NG are currently used in PT tendons in the construction of nuclear containment structures in the U.S. and abroad. Both Cirinject CP and Nontribos VZ Inject have been used in post-tensioned tendons in Europe for more than 30 years. Moreover, two additional mockups were conducted

with Trenton Fill-Flex 100. Table 4-1 outlines the physical and chemical properties of each of the selected fillers as provided by the manufacturer.

Properties that are important to the injection of these materials are drop melting point, congealing point, density, and viscosity. EOTA associates congealing point only with wax and not with grease. This property is particularly important since it signifies the temperature at which the wax stiffens, forming a plug and interrupting the injection. Density and viscosity of these materials at elevated temperature were used in selection of the pump and preparing the heat transfer model.

Table 4-1 Physical and chemical properties of different injection material for mockup test

	Sanchem	Cirinject CP	Visconorust	VZ Inject	Trenton
Density (g/cm ³)	—	880	750-870	—	
Specific Gravity @ 60° F	0.88-0.95	—	0.88-0.94	—	0.83 - 0.9
Drop melting point °F (°C)	135 (58) — 155 (68)	149 (65) — 167 (75)	95 (35) — 176 (80)	176 (80)	100 (37.7) — 120 (48.8)
Congeeing Point °F (°C)	—	—	135 (57)	154 (68)	—
Cone Penetration @ 77° F (1/10 mm)	160-250	65-115	170-200	85	—
Flash Point °F (°C)	420 (215)	>392 (200)	420 (215)	>536 (280)	>400 (205)
Viscosity @ 210° F (mm ² /sec)	—	17-22	5-30	20-25	
Solubility in water	Insoluble	Insoluble	Insoluble	Insoluble	Insoluble
Salt spray test (168 hours @ 95° F)	No corrosion	No corrosion	—	—	—
Copper corrosion	—	No corrosion	—	No corrosion	—
Water soluble chlorides	<5 ppm	—	2 ppm	40 ppm	—
Water soluble Nitrates	—	—	4 ppm	10 ppm	—
Water soluble Sulfides	<2 ppm	—	2 ppm	10 ppm	—

5 Test Setup Design and Construction

This chapter summarizes the design and construction of the mockup post-tensioning tendon specimens. Five 200-ft long specimens were fabricated with a profile that simulated both internal and external tendons. The specimens were constructed in phases because the frame was capable of holding a maximum of three specimens. In addition, the tendons were lightly stressed to ensure that the strand bundle was oriented in the duct in a similar manner to a fully stressed tendon in the field. Duct, strand, filler material, and anchorage details are also discussed. Finally, design and detailing of the mockup support frame is summarized.

5.1 Tendon Design

Figure 5-1 illustrates the profile of the mockup tendon, which was designed to simulate the geometry of a post-tensioned tendon in a bridge. The overall length of the tendon was 200 ft with the profile symmetrical about the mid-length of the tendon. Two profile forms were incorporated into the tendon. The external tendon profile included a draped tendon at ends (~30 ft) and straight tendon (~40 ft) in the middle. The parabolic profile (~60 ft) at mid-length mimicked the internal tendon profile in a girder bridge with drop-in spans. Deviators were placed at four locations to hold the tendon geometry. HDPE duct of 4 in. diameter with 19-0.6 in. prestressing strands formed the tendon. Anchors from FDOT approved post-tensioning equipment suppliers were used at each end of the tendon.

The tendon was designed to follow the profile shown in Figure 5-1 by inducing sufficient prestressing force on the anchors. The weight of each “gravity” deviator was 0.6 kips, while the collective weight of the tendon (including weight of strands, duct, and flexible filler) was approximately 19 plf. This approach was intended to draw the strand bundle toward the top of the duct in the external profile and the bottom of the duct in the internal profile.

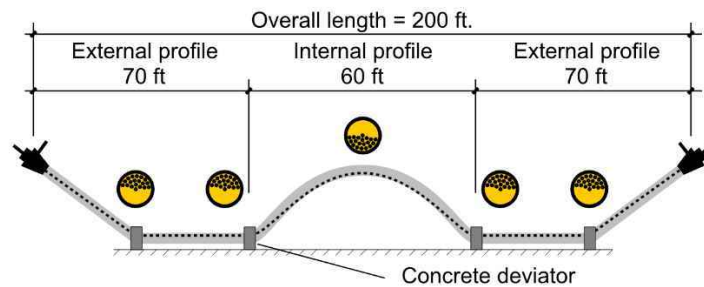


Figure 5-1 Tendon profile for the mockup testing on unbonded tendons

5.2 Tendon Details

5.2.1 Anchorage

The mockup tests were conducted with three different anchorages from the Florida Department of Transportation's list of approved devices:

1. Freyssinet USA, model no. 19C15
2. V Structural LLC (VSL), model no. ECI 6-19
3. DYWIDAG System International (DSI), model no. 68 19 248

Each anchorage was modified by welding an outer steel pipe to its anchor casting, which was subsequently filled with grout to provide confinement to the inner steel pipe/plastic trumpet seam of the anchors. The length of this outer steel pipe was such that it covered the trumpet and a part of the inner steel pipe, which coupled the trumpet to the HDPE duct. Anchor blocks were then cast around the anchorages. The inner steel pipe was connected to HDPE duct using a ductile iron pipe coupling. See Appendix A for fabrication and construction details.

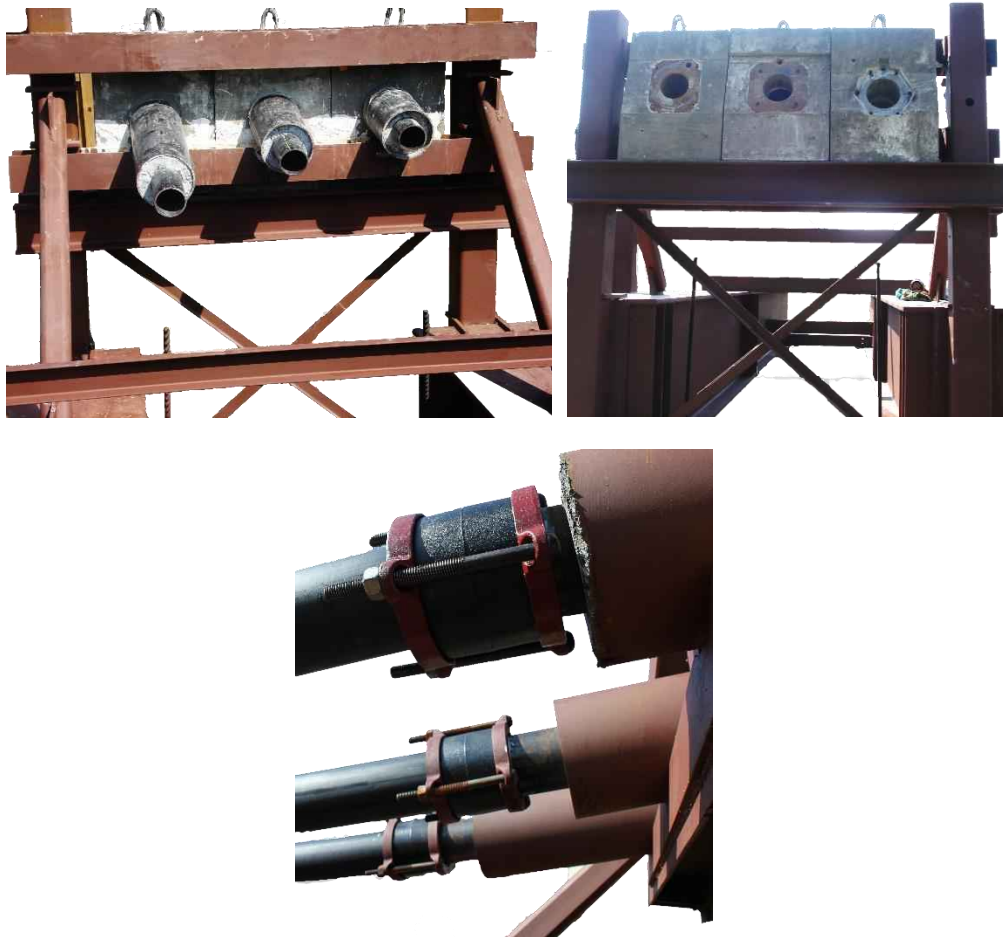


Figure 5-2 Anchor block placed on the frame

5.2.2 Duct

The minimum internal area of duct required by FDOT specifications is 2.5 times the cross-sectional area of the prestressing steel (FDOT Specification 2013: 960-2.2.1.4 (c)). This also meets PTI Specification (2006) requirements for either pulling or pushing strands into the duct. For the mockup specimen, the cross-sectional area of nineteen 0.6-in. diameter strands is 4.12 in² which requires a minimum theoretical duct diameter of 3.62 in. The smallest available diameter of HDPE pipe that provides sufficient cross-sectional area was 4 in. (specified outer diameter of 4.5 in.), which was chosen for use in the mockup. The wall thickness for DR17 pipe is 0.264 in., which meets the minimum wall thickness of 0.12 in. specified in the FDOT standard.

Because flexible fillers are not widely used in U.S. bridges, specifications for selection of HDPE to accommodate higher temperatures were not available. According to European standards (EN), however, the wall thickness of the duct is governed by the material rating (PE), dimensional ratio (DR), nominal class of the duct (PN), and the size of the duct (Table 5-1). EN does not specify the maximum SDR value, but rather specifies minimum nominal class of the duct for injection of filler with temperatures above 60° C. Experience over the past 15 years by European post-tensioning companies has indicated that the SDR17 HDPE is adequate for wax injection at temperatures up to 220° F. Available HDPE specifications are compared in Table 5-2.

Table 5-1 ETA table for HDPE smooth pipe selection (ETA 06/226 2012)

EN 12201-2	PE 80		PE 100
Series	Low pressure	Pressure	Pressure
PN**	6.3	10	10
SDR	21	13.6	17
Nominal external diameter	Thickness	Thickness	Thickness
(mm)	(mm)	(mm)	(mm)
50	3.7*	3.7	
63	4.7*	4.7	
75	5.5*	5.5	
90	6.6*	6.6	
110	5.3	8.1	
125	6.0	9.2	
140	6.7	10.3	
160	7.7	11.8	
180	8.6		10.7
200	9.6		
SDR: ratio of external diameter to nominal wall thickness			
* these pipes have not standardised dimensions			
** PN values are based on a global service factor C = 1.25			

Table 5-2 Size of HDPE duct based on various specifications

Specification	Internal Diameter (in.)	Thickness (in.)	Outer Diameter (in.)
FDOT	3.62	0.24	3.86
PTI	3.62	0.24	3.86
EN	3.97	0.265	4.5

HDPE duct material is characterized in ASTM 3350 by cell classification (Table 5-3). The cell classification has six numbers followed by a letter; the number signifies the value of the particular property (density, melt index, flexural modulus, tensile strength, crack growth and hydrostatic strength) from 1 to 6 while the letter signifies color and UV stabilization of the material. FDOT specifies a minimum cell classification of 445574C (FDOT 2017, 960-2.4.5). The specified pressure rating of the duct material is 125 psi (FDOT 2017, 960-2.2.1.2). HDPE duct used in the mockup testing met these requirements.

Table 5-3 Cell classification for HDPE duct (ASTM 3350, 2012)

Property	Test Method	0	1	2	3	4	5	6	7	8
1. Density, gm/cm ³	D1505	a	0.925 or lower	>0.925-0.940	>0.940-0.947	>0.947-0.955	>0.955	--	b	
2. Melt Index	D1238	a	>1.0	1.0 to 0.4	<0.4 to 0.15	<0.15	c	--	b	
3. Flexural Modulus, psi	D790	a	<20,000	20,000 to <40,000	40,000 to <80,000	80,000 to <110,000	110,000 to <160,000	>160,000	b	
4. Tensile Strength at Yield, psi	D638	a	<2200	2200 to <2600	2600 to <3000	3000 to <3500	3500 to <4000	>4000	b	
5. Slow Crack Growth Resistance I. ESCR a. Test condition (100% Igepal) b. Test duration, h c. Failure, max, % II. PENT (hours) Molded Plaque. 80°C, 2.4 MPa Notch depth. F1473. Table 1	D1693 F1473	a a a	A 48 50	B 24 50	C 192 20	C 600 20 10	30	100	500	b b
6. Hydrostatic Strength Classification I. Hydrostatic design basis, psi (23°C) II. Minimum required strength, MPa (psi) (20°C)	D2837 ISO 12162	d	800	1000	1250	1600	8 (1160)	10 (1450)		

Three locations along the tendon profile were selected at which the HDPE duct was replaced with transparent polycarbonate tubes to allow the injection process to be visible. These tubes were rated to withstand temperatures up to 280° F. The tube size was selected to match the outer diameter of the HDPE duct (4.5 in.). The wall thickness of the polycarbonate tube was 1/8 in., which made the inner diameter slightly larger than that of the HDPE. Figure 5-3 shows the location of transparent windows on each tendon.

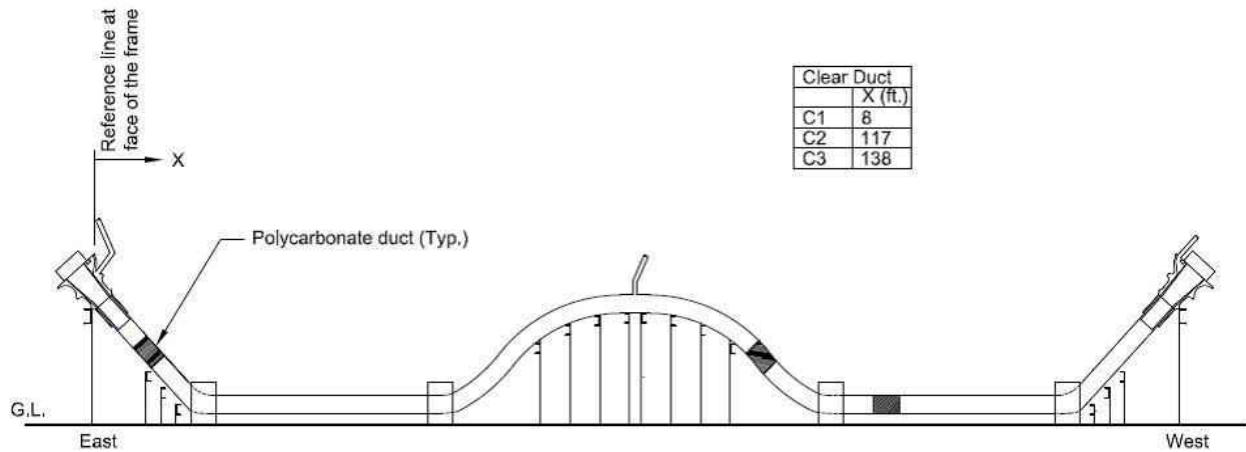


Figure 5-3 Window locations on tendon

To connect HDPE duct and polycarbonate tube, a mechanical ductile iron coupler was used (Figure 5-4). The polycarbonate tube and couplers were used to facilitate testing. They did not meet FDOT Specifications and are not intended to be used in field installations. Couplers had an inner diameter of 4.5 in. and a length of 6 in. These couplers were also used to transition from the steel pipe at the anchorages to HDPE duct.

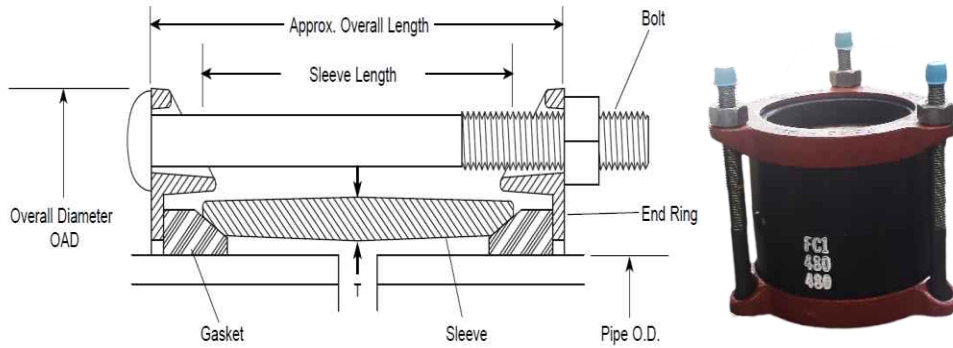


Figure 5-4 Typical mechanical coupler

5.2.3 Injection Ports

The anchorages used in this study were fitted with injection ports intended for use with cementitious grout (Figure 5-5). Filler was introduced into the tendon through either the anchorage injection port or a saddle connected directly to the duct (Figure 5-6). A pipe saddle with an opening diameter of 1½ in. was mounted on the duct; the duct was also lifted slightly in the vicinity of the injection point to ensure that the strands did not block the injection. The material was injected by connecting the discharge hose of the pump to the saddle fitting. After injection was completed, the valve was closed to prevent filler from escaping when the injection hose was removed.

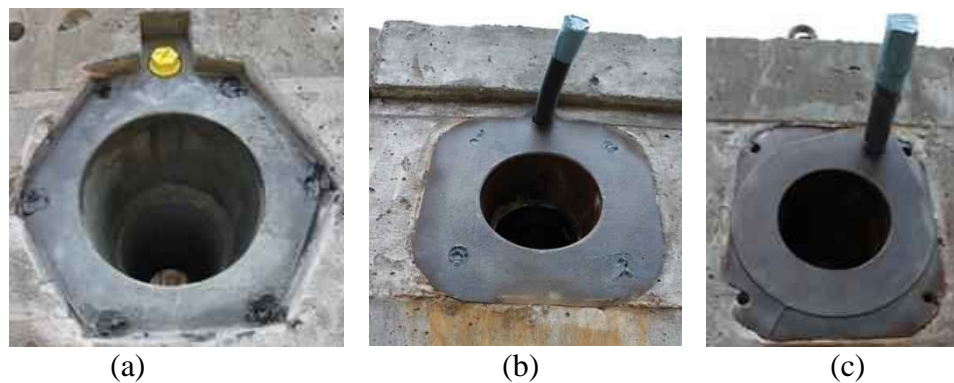


Figure 5-5 Injection ports in (a) DSI, (b) VSL, and (c) Freyssinet anchors



Figure 5-6 Injection into saddle

5.3 Tendon Support Frame and Deviators

To support the tendons, structural steel frames were placed at each end (anchorage) and at mid-length (Figure 5-7 and Figure 5-8). These frames were then supported by salvaged pile segments and footings. Cast-in-place footings (10 ft x 6 ft x 2 ft) were placed under the anchorages at each end frame. Square pile segments were placed prone at the other end of the end frames and evenly distributed under the middle frame. The foundation was constructed such that the three support frames were at the same elevation. This ensured a uniform and symmetric tendon profile.

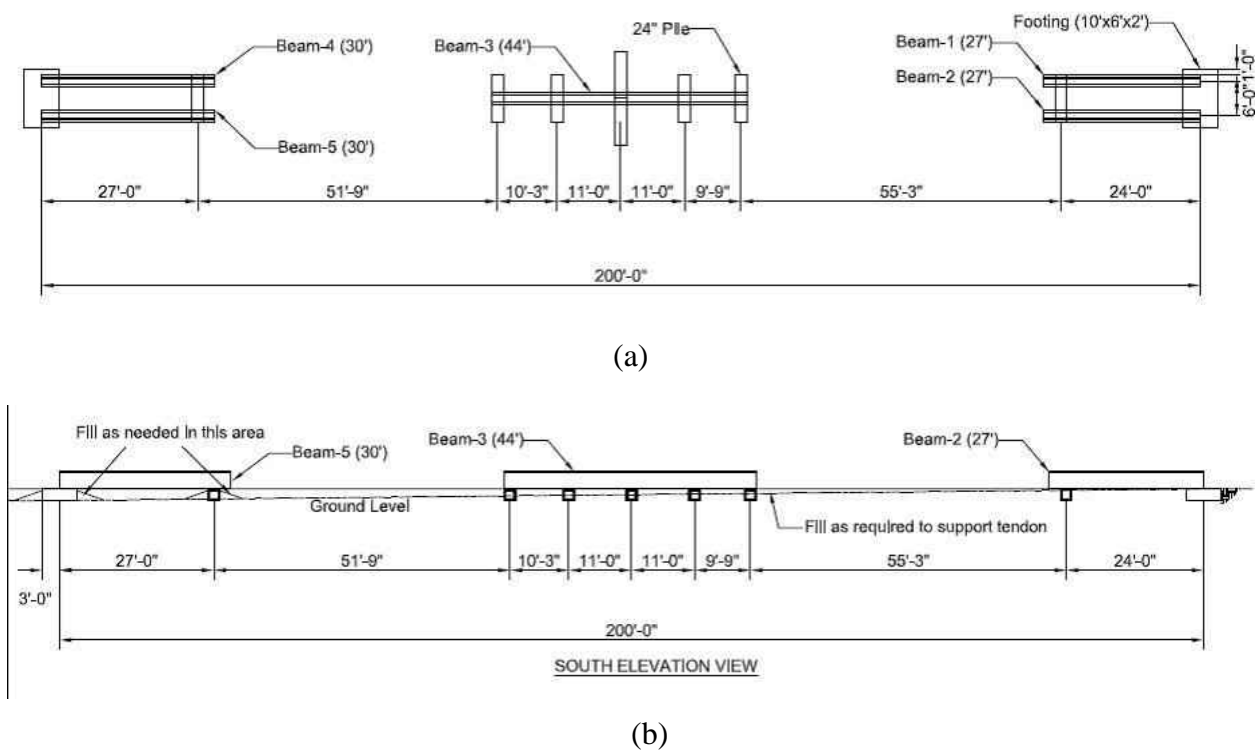


Figure 5-7 Plan and elevation of the foundation plan

The support at the end frame was designed to carry the loads from the prestressing force applied at the anchors and dead loads from the strand and duct. Prestressing force was transferred to the steel beams through the cross beams and the vertical members on the frame. Epoxy anchors were used to connect the steel beams to the footings and transfer force from steel beams to the footing. A friction coefficient of 0.45 between steel and concrete was assumed. Details of the end frame are shown in Appendix A.



(a)



(b)



(c)



(d)

Figure 5-8 Mockup support system, including (a) anchorage frame, (b) middle frame, (c) supports between frames, and (d) gravity deviators

The middle support was designed to carry the tendon self-weight and to shape the tendon into a parabolic profile. Bracing was provided to each vertical member in the longitudinal and transverse directions. Bracing in the longitudinal direction was connected from the vertical members to the top of the steel beams and in the transverse direction to the concrete pile through the anchor plate. Tendons were placed on top of the channel, which spanned between the main vertical members.

Intermediate supports were designed to carry tendon dead load and were provided every 5 ft in both the straight and parabolic profile of the tendon. Intermediate supports in the draped profile were supported by temporary wood blocking when unstressed. Wood blocking was used to shim the duct into the final tendon profile. The straight portion of the tendon was also supported by wood blocking spaced 4 ft between the gravity deviators.

Gravity deviators were used to obtain the desired tendon profile. These were used in conjunction with the support frame to balance the nominal prestress force on the tendon. Four deviators were used on each tendon (Figure 5-8).

Deviators were designed to accommodate the profile change of 11.3° in the tendon and to ensure a bend radius of approximately 20 times the diameter of the duct (90 in.), which results in an arc length of contact of approximately 19 in. The deviator dimensions were selected to give a total weight of 600 lb.

5.4 Tendon Fabrication and Stressing

Tendon construction began with fabrication of the HDPE duct, which included assembling pieces by fusion welding, placing assembled duct on frames, and connecting to anchors. Clear windows were then installed and strands were pushed and stressed to obtain the desired tendon profile. Instrumentation was installed followed by an air test to check for leaks before injection. The following sections describe the assembly in detail.

1. Duct Fusion

HDPE pipe was delivered in 20 ft and 40 ft lengths. A McElroy 14.0 HDPE duct fusion machine (Figure 5-9a) was used to fusion weld HDPE ducts. The following procedure was used to weld HDPE ducts.

- Inside and outside surfaces of the ducts were cleaned.
- Upper jaws of the machine were opened and ducts were inserted in each pair of jaws with applicable inserts installed. The ends of the ducts protruded at least 1 in. beyond the face of jaws.
- The cut end the HDPE was squared using the facing tool. Pipe ends were visually checked for square.
- Pipe ends were brought together and visually checked. Ducts were trimmed if gaps were detected.
- Heaters, which were kept in the heating machines, were periodically checked for the optimum temperature for butt weld fusion (425° F).
- Heaters were placed in position between the pipe ends, the pipe or fitting ends were brought into full contact with the heater to ensure proper seating. The locking cam was raised into the engaged position during the heating cycle. Proper contact was maintained without force, while a bead of molten polyethylene developed between the heater and the pipe or fitting ends. Heating was continued until the minimum melt bead size ($3/16$ in. for 4 in. duct) had developed.

- The ends of the ducts were pushed together to join the beads. The force was maintained for about 3 min. and then removed. The optimal interfacial pressure to join beads is 75 psi. The required torque reading corresponding to this pressure for 4 in. duct size was 25 ft-lb.
- The cam was unlocked and unscrewed to open the clamps. Pipe was pulled through machine, and prepared for fusing the next joint. The joint was inspected and checked for any high or low locations or misalignment. The process was repeated if the joint was not properly fused.



Figure 5-9 (a) McElroy HDPE fusion machine; (b) Duct fusion in progress

2. Duct placement

The total length of the welded duct for a single mockup tendon was approximately 230 ft. Ducts were placed on the support frame using a fork lift (Figure 5-10).

3. Deviator block installation

Each deviator block was placed at the specified locations. Each tendon had 4 deviator blocks; a total of 12 blocks were installed.

4. Duct connection to anchors at east end

The east end of the HDPE duct was connected to the anchorage pipe using the coupler (Figure 5-11).

5. Duct window installation

Clear window locations were marked and HDPE duct was cut and removed at these locations (Figure 5-12). Clear windows were precut in 2-ft lengths and installed with couplers.



Figure 5-10 HDPE duct on the support frame after welding



Figure 5-11 HDPE duct connected to the anchor block at the east end



Figure 5-12 Clear windows in duct

6. Duct connection at west end

Excess HDPE duct was cut at the west end and HDPE duct was connected to the anchor pipe using a coupler (Figure 5-13).



Figure 5-13 West end connected to the anchor block

7. Strand pushing

A hydraulic strand pushing machine was used to push individual strands into the duct (Figure 5-14). The machine had the capacity to push strand up to 500 ft. This machine consisted of three parts: strand pusher that pushed the strand into the duct, a hydraulic controller that controlled the speed of the machine, and a diesel-hydraulic power unit.



Figure 5-14 Strand installation using Model 00143604/2 strand pusher from PAUL Maschinenfabrik GmbH & Co

The strand coil was loaded onto the reel, which was placed behind the strand pusher. The strand pusher was connected to the diesel generator and controller. The diesel generator was started. A strand bullet was placed on the end of the strand and the strand number was marked on tape (Figure 5-15). Machine speed was adjusted and strand was pushed at about 20 ft/sec. The tail of the strand at east end was cut and a new bullet was placed on the end and the strand was pushed again. This process was repeated until all 19 strands were pushed into the duct.



Figure 5-15 Bullet on the head of the strand during pushing

8. Wedge plate installation

The last three strands pushed were marked and then placed at the top of anchor wedge plate. The other strands were placed at random in the wedge plate (Figure 5-16). Wedges were placed on the strands. Strand tails of about 5 feet were left beyond wedge plate for stressing (Figure 5-17).



Figure 5-16 Wedge plate installation



Figure 5-17 Wedge plate installed on anchor

9. Tendon Stressing

Strands were stressed individually with a monostrand jack (Figure 5-18). The first strand was pulled until the concrete deviator lifted slightly off of the ground (Figure 5-19). Subsequent strands were stressed until slight movement was noticed in the deviator. No strand was stressed more than 1 kip. This approach ensured that the tendon formed the correct tendon shape without developing undue prestressing force.



Figure 5-18 Monostrand hydraulic jack and pump used to stress strands



Figure 5-19 Deviators suspended by tendon after stressing

10. Tendon air testing

Following assembly, tendons were left undisturbed for at least 24-hours to ensure that they had been subjected to the temperature fluctuation caused by a full diurnal cycle. A preliminary air pressure test to 30 psi was conducted on each tendon before installing instrumentation to detect any leaks that may have formed during assembly.

11. Cut tendon tails

Strand tails were cut and caps were installed (Figure 5-20).



Figure 5-20 Strand tails cutting in operation

12. Instrumentation

Instrumentation was installed on each tendon as per instrumentation plan.

13. Pre injection test

Each tendon was air tested by pressurizing to 50 psi and then checked for potential leaks. Generally, the pressure decrease was approximately 1 to 2 psi per minute.

5.5 Injection Equipment

A positive displacement grout pump was used in the small-scale tests and the first mockup injection (Visconorust). It was a 20 gallons per minute (gpm) air driven pump with a hopper intake and required 185 cfm at 100 psi air supply. The discharge line of the pump had a 1 in. diameter opening and thus 1 in. hose was used to supply filler from pump to injection port. Figure 5-21 shows the pump used in the mockup and small-scale tests.



Figure 5-21 Grout pump (Schwager Davis Inc.)

The pump used for the remainder of the mockup injections was a Viking centrifugal pump with a variable frequency electric drive (Baldor VFD controller) (Figure 5-22). The maximum running speed of the pump was 780 rpm. The pump housing was heated (up to 250° F). The pump had 2-in. diameter NPT suction and discharge cast iron ports. At maximum speed, the discharge rate was 100 gpm @ 75psi for a liquid with a viscosity of 20 cP.

A vacuum pump was used in the vacuum assist filler injection for the Trenton 1 specimen (Figure 5-23). The vacuum pump was a high capacity HVAC vacuum pump with a capacity to pull a nearly complete vacuum. The pump was connected to two chambers. One of the chambers was fitted with a filter to protect the pump from debris.



Figure 5-22 Viking pump used for filler injection



Figure 5-23 Vacuum pump and reservoirs

5.6 Flexible Filler Preparation

Flexible fillers were delivered in 55 gallon barrels and were solid at room temperature. To liquefy the filler, the barrels were heated to about 220° F, which was achieved by using barrel heaters on the outer surface of the barrel (Figure 5-24). These were 4-in. wide with a variable range of 50 to 425° F. Two or more heaters were required to obtain and maintain the required temperature; one was placed near the base and other near the mid-height of the barrel. This ensured that the material at the bottom of barrel was liquefied and did not clog the outlet when injection is started. Insulation blankets were used to improve the efficiency of the barrel heaters.

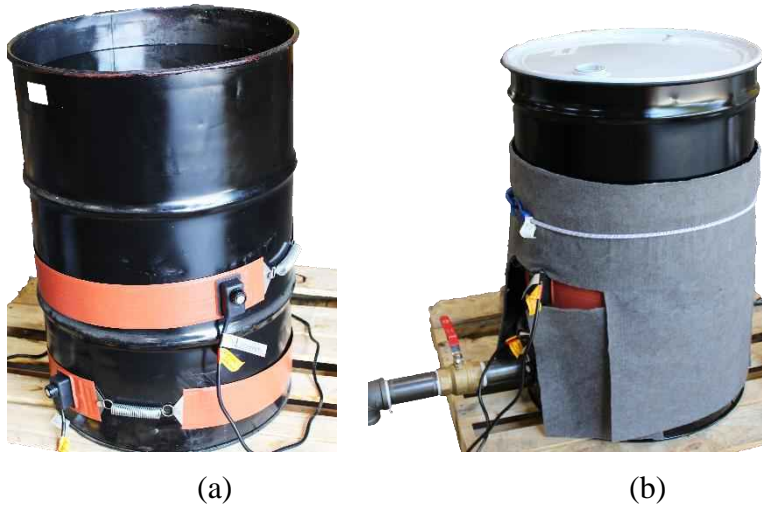


Figure 5-24 (a) Barrel heater position on barrel; (b) Heaters covered with insulation blanket

Once the filler was heated sufficiently, it was transferred to the injection barrels using an air driven transfer pump (Figure 5-25 (a)). Barrel heaters and insulation blankets were also moved to the injection barrels to maintain temperature for injection. The filler was stirred regularly to ensure even distribution of heat in the barrel (Figure 5-25 (b)).



Figure 5-25 Filler heating logistics: (a) transfer of filler between barrels and (b) filler agitation.

6 Instrumentation and Data Acquisition

Mockup instrumentation was used to measure filler pressure and temperature inside the duct; additional thermocouples measured surface temperature of the duct along the length of the tendon. In addition, rate of injection of flexible fillers was monitored to confirm the volume input and compare it with the theoretical volume of the duct. The following section details the instrumentation plan and type of instruments used in the full-scale mockup on flexible fillers.

6.1 Instrumentation Plan

Figure 6-1 shows the schematic locations of pressure transducers (P), internal temperature probes (T), and surface temperature gages (ST) along the length of the tendon; also shown is the gage orientation on the cross-section. Specific instrument locations were measured from the face of the anchor where the grout cap was fixed (Table 6-1). Seven pressure transducers and seven internal temperature probes were installed on each specimen. Additionally, seven surface temperature gages were installed adjacent to the thermocouples. The probes were used to measure the temperature of the filler inside the duct while surface gages were used to measure the outside temperature of the duct.

Temperature probes and pressure transducers were oriented to avoid contact with the strand bundle to minimize the effect of the strands on their measurements (Figure 6-1). For the Visconrust test, instruments in the draped profile (P1, T1, ST1, P7, T7 and ST7) were installed at the bottom; in the straight profile (P2, P5, P6, T2, T5, T6, ST2, ST5 and ST6), they were installed on the side (90 degrees); and in the parabolic profile (P3, P4, T3, T4, ST3 and ST4), they were installed at the top. For subsequent tests, instrument orientations of T2, ST2, T5, and T5 were adjusted to the top of the section, while T6 and ST6 were adjusted to. Note that the orientation of the strand bundle at location 2 and 5 was intended to be in the top of the duct. The effect of the close proximity of the temperature probe to the strand bundle on the temperature readings in the Visconrust test and the difficulty installing the probe so close to the ground led to a change in the tendon profile. In future tests, the duct was raised relative to the strand bundle so that the temperature probe could be installed on the top of the duct as illustrated. This provided provide clearance between the probe and actual location of the strand bundle.

Pipe saddles were used to mount pressure transducers and thermocouples on the duct (Figure 6-3). The following section describes the type of instrumentation used in the mockup tests.

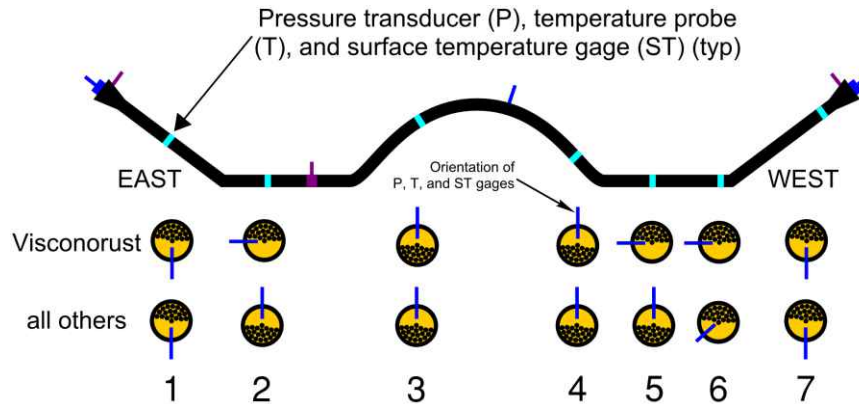


Figure 6-1 Schematic of sensor location and orientation of temperature probes relative to duct and strand.

Table 6-1 Distance from the face of the east anchor to the sensor. See Figure 6-1

Sensor	Pressure (ft)	Temperature (ft)
1	14	16
2	44	46
3	80	82
4	122	124
5	144	146
6	164	166
7	182	184



Figure 6-2 Instrumentation orientation on the tendon

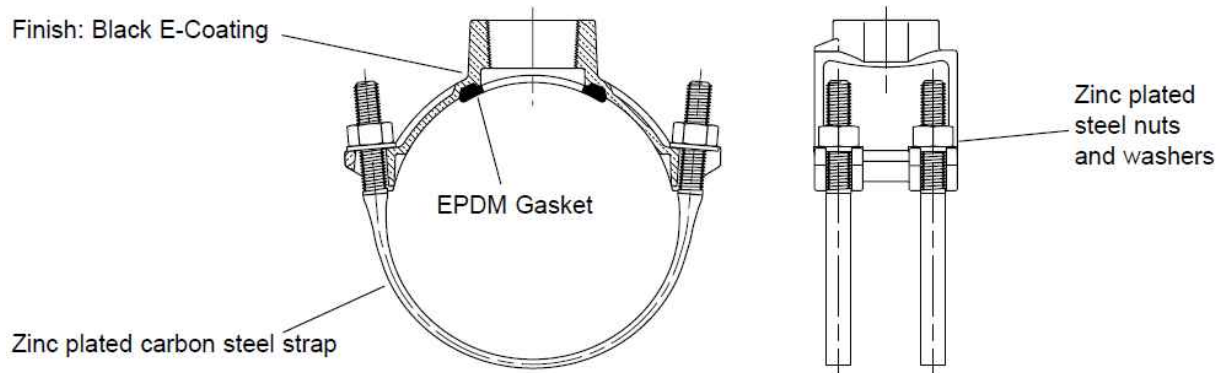


Figure 6-3 Typical pipe saddle (Ford meter box)

6.1.1 Pressure Transducers

Pressure transducers were used to measure the pressure inside the duct during and after injection of flexible fillers. They were selected based on a maximum pressure of 75 psi and a maximum temperature of 220° F (105° C). Omega PX209-015G5V pressure transducers were used, which had operating temperature from -65°F (-54°C) to 250°F (121° C) and operating pressure up to 300 psi. The transducer's response time of 2 ms allowed quick measurement of the pressure. Transducers were installed on the duct using a pipe saddle (Figure 6-3) with ¾ in. NPT opening. A ¾ in. male to ¼ in. female adapter was used to connect transducer and saddle. Figure 6-4 shows a typical pressure transducer.



Figure 6-4 Typical transducer installed on the tendon

6.1.2 Thermocouples

Thermocouples were used internally to measure filler temperature while surface-mounted thermocouples were used to measure the surface temperature of the duct; both types were monitored during and after injection. Type K thermocouples were selected based on the anticipated injection temperature of 220° F (105° C). Omega thermocouple part no. TJ36-

CASS-116G-6-SMPW-M was chosen to measure the filler temperature. A compression fitting was needed to obtain a pressure-tight seal around the probe.

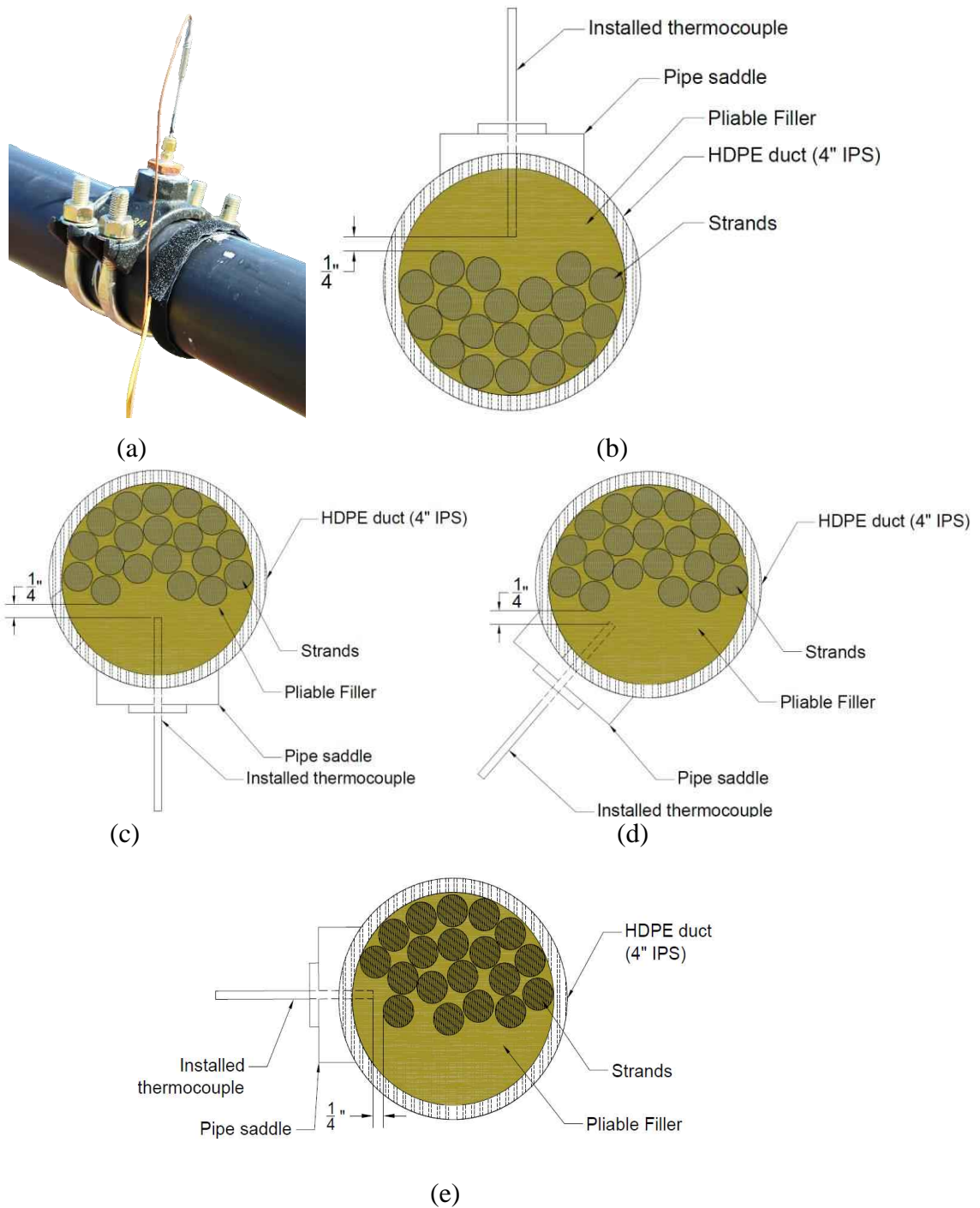


Figure 6-5 Thermocouple probe to measure filler temperature (a) with both thermocouple and surface probe installed on the duct, (b) top internal orientation, (c) bottom orientation, (d) inclined orientation, and (e) side orientation

Fluke 80-pk-11 flexible cuff type K thermo probes were used to measure the duct surface temperature. Thermocouples and surface probes were connected to the data acquisition station with type K thermocouple wires. Thermocouples and surface probes were set for a temperature range of 0° to 320° F while the ambient temperature range was set to 0° to 150° F.

6.1.3 Volume Calculation

Volume of injected material for each test was determined by measuring the depth of flexible filler in the barrels before and after the test. Flexible filler depths collected in the buckets through vent during the mockup were also measured. The volume of flexible filler collected in buckets was then deducted from the volume of flexible filler in the barrels to give the net volume of filler in the mockup. This volume was then compared to the theoretically computed flexible filler volume and percent gain/loss was calculated.

6.1.4 Gravity Deviator Displacement

Gravity deviators displaced upwards when the tendon was stressed. To ensure that the tendon did not elongate or shorten excessively due to diurnal temperature variations, the vertical position of the deviators was monitored over a period of 24 hours. No significant movement was noted visually in any of the deviators during this period.

6.2 *Data Acquisition*

The data acquisition system (DAQ) was located approximately at the mid-length of the mockup to ensure the best access and visibility during injection. Data were recorded at a frequency of 10 Hz during injection. After injection, data were recorded for 24 hours at 15 minute intervals.

7 Small Specimen Component Tests

Several small specimens were injected prior to the full length mockups. These tests were conducted to proof test the individual components of the tendon including the HDPE duct, polycarbonate tube, mechanical couplers, pipe saddles for instrumentation, and vent ports. The effect of strand on heat transfer and the feasibility of injection through a pipe saddle were also investigated. In addition, the injection of small specimens provided an opportunity to improve familiarity with the equipment; to develop procedures for injection operations; and to refine injection protocols.

Figure 7-2 shows a representative illustration of the small specimen test setup; several variations in equipment and procedures, however, were executed. The small-scale specimen consisted of two end plates with steel pipes that were coupled to a short piece of HDPE pipe. Each end plate was fitted with a pipe that served as an inlet and outlet during injection. Rather than wasting the material, it was recycled back to the heated barrel and re-injected forming a closed-loop system.

Table 7-1 outlines the details of each of the small specimen tests conducted along with a summary of the findings.

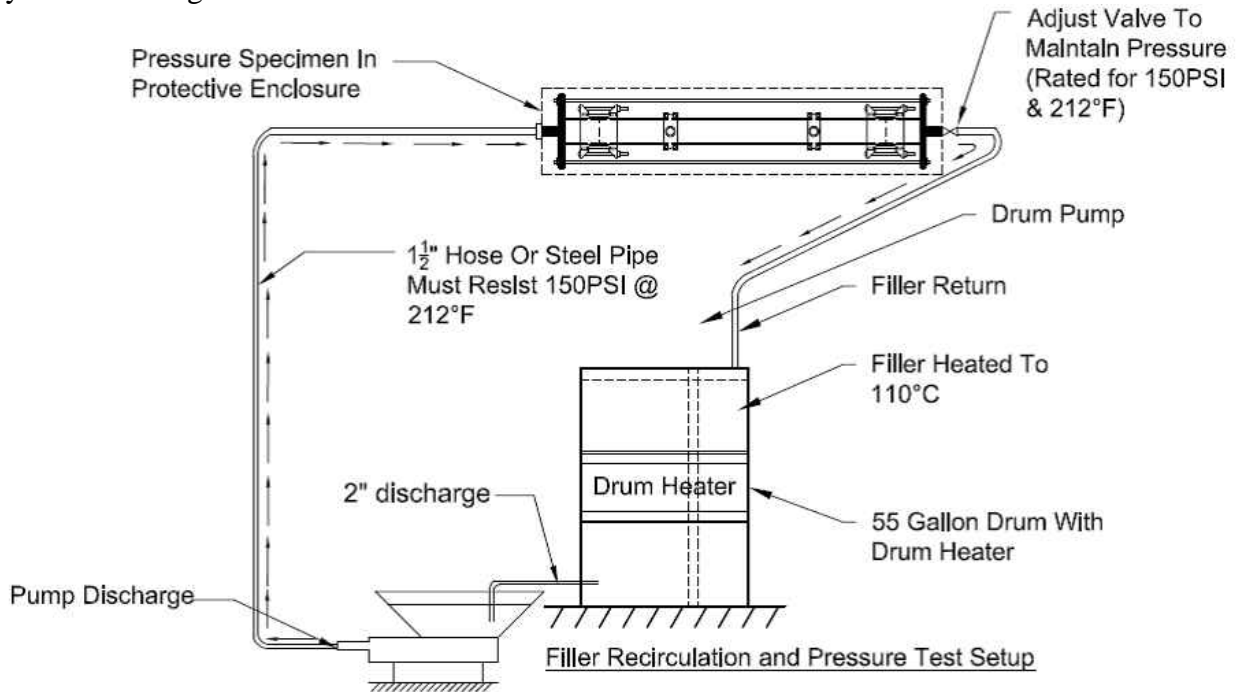


Figure 7-1 Typical small-scale test setup

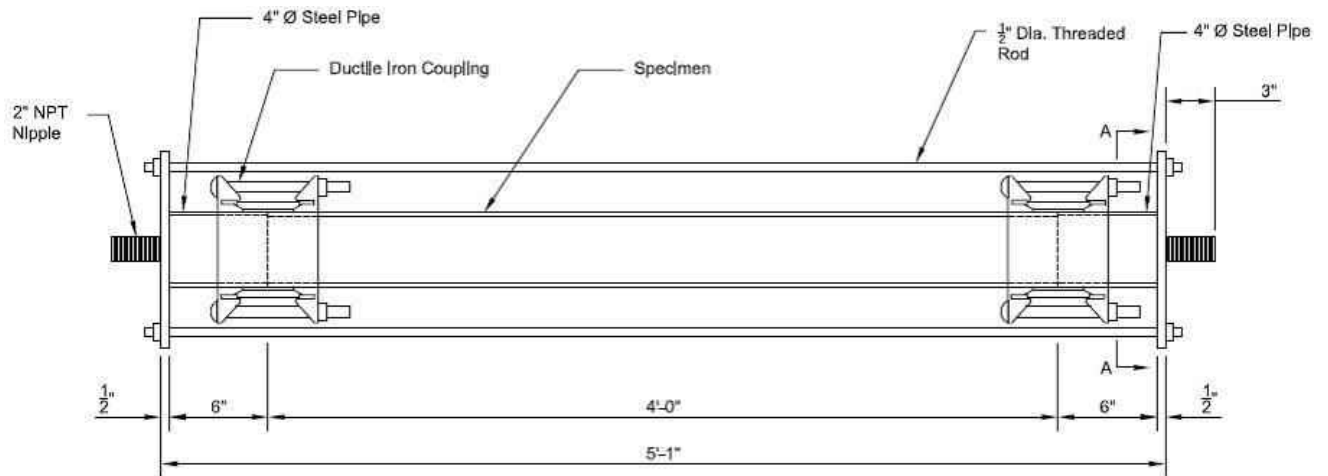










Figure 7-2 Typical small-scale test specimen

Table 7-1 Small scale test specimens and components tested

Test number	Component(s) tested	Findings	Specimen
1	HDPE duct	Injection went smoothly with no leaks	
2	HDPE duct, thermocouple, pressure transducer	Pressure transducers worked well but not thermocouples. No leaks.	
3	Clear window, thermocouple, pressure transducer	Pressure transducers worked well but not thermocouples. No leaks.	
4	HDPE duct, PVC pipe, heat shrink wrap and vent pipe	Leaks through heat shrink wrap.	

5	HDPE duct, clear window, vent pipe and thermocouple	Vent pipe worked well (with small hole near it). Thermocouple did not read correct reading.	
6	HDPE duct with beaded wire thermo probe at gradient	Beaded wire thermocouple worked well with correct temperature readings.	
7	HDPE duct, clear window, strands, side vent tube and thermocouple with compression fitting	Vent tube vented almost all air from specimen. Thermocouple with compression fittings read correct temperature reading. Significant drop in temperature due to presence of strands.	
8	HDPE duct with injection through the saddle and Viking pump.	Injection through saddles worked well. Pump control was better with respect to varying flow rate.	

In one of the tests conducted, the HDPE duct deformed due to heat accumulation during the prolonged circulation of filler (more than 8 minutes) and high injection pressure (above 100 psi) (Figure 7-3). No leaks occurred, however, in any part of the specimen (duct and coupling). Hence the injection pressure was limited to 75 psi for full-scale mockup tests.

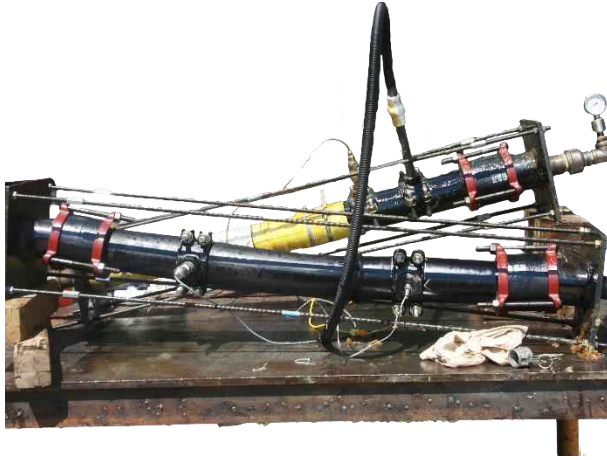


Figure 7-3 Deformation in the duct due to high pressure

8 Injections

Five tendons were injected using four different materials. This chapter describes the process used to perform the injection and observations made during injection.

8.1 *Cirinject CP*

Cirinject CP was injected into the tendon with Freyssinet anchors using the Viking pump through a pipe saddle mounted to the duct (Figure 8-1). Injection was carried out on the morning of October 15, 2014 at FDOT Structures Lab at Tallahassee. A double-bend pipe saddle that had an opening of 1½ in. was installed on the duct; the pump discharge line was connected to the saddle through a 1½ in. line and valve. Three barrels were plumbed in parallel to provide filler supply for injection.

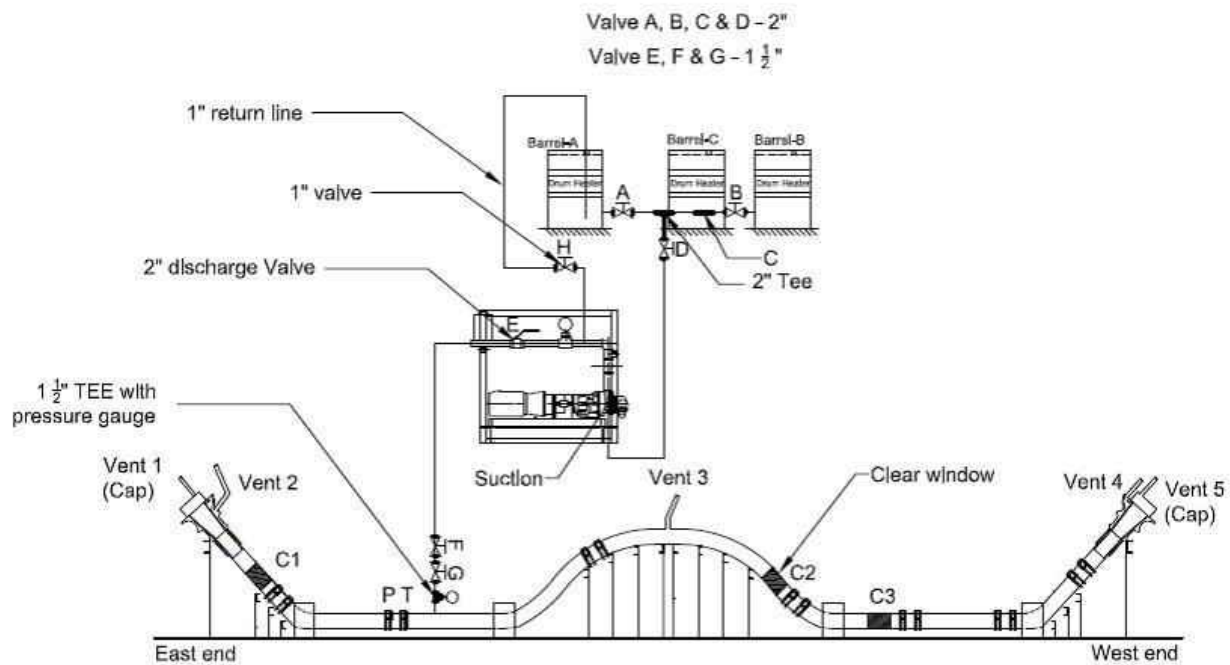


Figure 8-1 Schematic of setup for *Cirinject CP* and VZ Inject specimens

8.1.1 Injection Process

Pre-injection:

1. Air test of the tendon was conducted at 50 psi. The test was accepted if pressure drop was less than 15 psi in 1 minute.
2. The filter was heated to 220° F. Sufficient time was allowed to ensure all three barrels are at the proper temperature. The filler was stirred occasionally to ensure uniform temperature.
3. All hoses were clear and preheated.
4. Personnel outfitted with full personal protective equipment (PPE) were positioned at all vents with buckets and wet towels. Personnel were made visible to the pump operator.

5. Video cameras and LED lights were positioned at each of the windows to record injection.

Injection:

1. Drums were position on a pallet and placed adjacent to the suction line of pump.
2. The 1 in. return line was connected to the barrel and the 1.5 in. discharge line was connected to the pump. The outlet end of the discharge line was left open. Injection occurred at the location shown in Figure 8-1.
3. The pump was preheated to 250° F.
4. Vents at the east anchor (vent 1 and 2), middle frame (vent 3) and at the west anchor (vent 4 and 5) were opened.
5. Valves A, B, C, D, and F were opened. Before connecting the discharge line to the inlet valve G, the pump was started and discharged two gallons into a clean container. Valve F was closed after discharge.
6. Data acquisition system was started and video recording was begun. IR measurements of filler in barrel and at discharge locations were recorded periodically. Small samples of filler was gathered from the inlet and outlet locations for testing.
7. Discharge line was connected to inlet valve (valve G).
8. Discharge line valve E and F and throttle pump were opened to keep injection pressure less than 75 psi. The filler was injected continuously at approximately 40 gpm. The filler was allowed to discharge from vents (vents 1, 2, 3, 4, and 5) during injection. The filler was observed during discharge and the valve was closed when all free air was discharged and consistent filler was exiting. Approximately 3 gallons were discharged at each vent to get the consistent filler without any air. At anchorages, the anchorage vent was closed first and then the anchor cap vent was closed to ensure proper filling of anchor cap. Once vents at the east anchorage were closed, the filler injection was slowed to 30 gpm. Once vents at west end were closed, valve F was closed. Thirty seconds was allowed to pass to check if any entrapped air was present in the tendon. If air was present, valve F and vent 3 (possibly vent 1 and 2 as well) were opened and the filler was injected at approximately 20 gpm. Vents were closed when consistent filler was exiting from the vent.
9. The pressure in the tendon was increased for 1 minute at very low flow rate (about 5 gpm) and was stopped at pressure 30 psi above the injection pressure. Inlet valve (valve G) was closed and the pump was stopped.
10. The discharge line was disconnected at valve G and the pump was reversed to pull filler from injection hose and deliver back into drum. The hoses were disconnected and cleaned.

8.1.2 Observations

- Pressure drop in pre-injection air test was 2 psi in 1 minute.
- The overall injection process went smoothly with no leaks observed in the tendon.
- Duration of injection (from the pump start to pump stop including hold time during injection) was 5 minutes 17 seconds.
- The pump was running at varying flow rates (20-40 gpm).

- Injection pressure was held less than 75 psi.
- Temperature of the filler at the start of the test was 225° F in all the barrels.
- Ambient temperature at the start of the test was 67° F.
- Filler from vent 1 exited first with very small quantity of air. Vent 1 was closed but vent 2 remained open until filler was discharged. Both vents were closed when good flow was observed.
- Vent 3 subsequently started discharging filler. At this same time, Barrel A was observed to have a blockage. Pumping was paused while blockage was removed from discharge line of barrel.
- Pumping was resumed. Vent 3 was closed as filler started discharging.
- Vent 4 and 5 were closed following filler discharge that was clear of air. Valve F was also closed to stop injecting filler in the tendon. Air bubbles were observed at window 2 travelling towards the middle vent.
- Injection was resumed to remove the air from the tendon. Flow was slowed to 20 gpm and the middle vent was opened simultaneously to remove the air. When vent 3 started discharging filler (no air), vent 3 was closed. Injection continued for approximately one minute at 4 gpm to increase the pressure. Pumping was stopped at 45 psi.
- No air was observed at window 1 traveling towards the east end.

8.2 Visconorust

Visconorust-2090-P was injected into the tendon with VSL anchors using the hopper-fed pump with injection at the east anchor (Figure 8-2). Injection was carried out on September 3, 2014 at FDOT Structures Research Center at Tallahassee. Injection progressed from one end to the other. To create the injection port, 3/4 in. NPT steel nipples were epoxy welded onto the anchor head. The VSL plastic grout port and hose (typically used in cement grouting operations) were not used in the test setup.

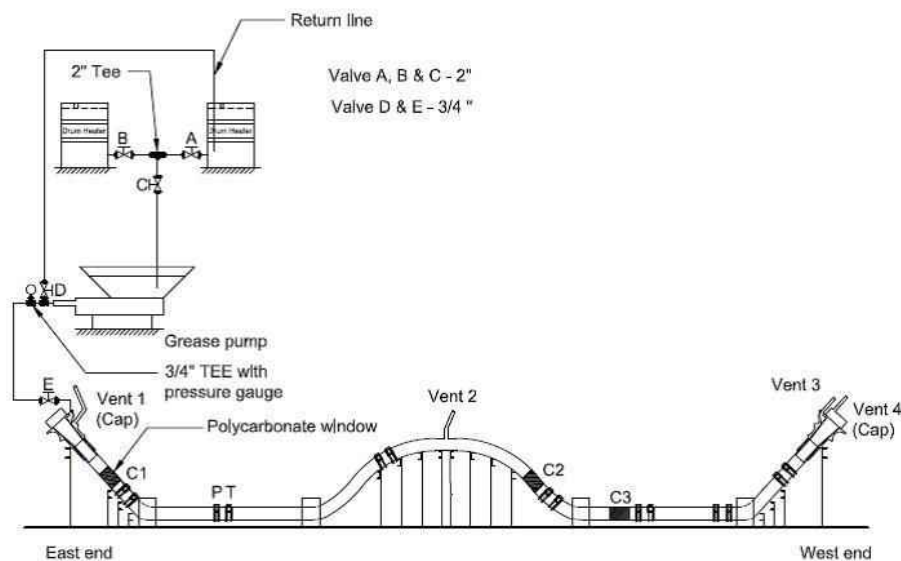


Figure 8-2 Schematic of setup for Visconorust injection

8.2.1 Injection Process

Pre-injection:

1. Air test of the tendon was conducted at 50 psi. The test was accepted if pressure drop was less than 15 psi in 1 minute.
2. The filter was heated to 220° F. Sufficient time was allowed to ensure all three barrels were at the proper temperature. The filler was stirred occasionally to ensure uniform temperature.
3. All hoses were clear and preheated.
4. Position personnel at all vents with buckets and wet towels. Personnel were visible to the pump operator.
5. Position video cameras at each of the windows to record injection.

Injection:

1. The barrels were positioned to discharge directly into the pump hopper. Discharge port was positioned to discharge below the surface of the filler to reduce splashing and foaming.
2. The hoses from pump were connected to injection port on the anchor and a return line from pump to the barrel. Injection occurred at the east end of the test setup.
3. Vents at the inlet anchor (vent 1), middle frame (vent 2), and at the opposite anchor (vent 3 and 4) were opened.
4. Valves A, C, and D were opened. Valves B and E were closed and the filler was allowed to circulate through one barrel. Valve A was closed and valve B was opened to ensure the flow from second barrel. Once filler started flowing from second barrel, valve C was closed and valve A was opened.
5. Data acquisition system was started for recording data.
6. Valves C and E were opened. Injection pressure was controlled by throttling flow with valve D. Pressure remained less than 75 psi.
7. The filler was continuously injected. The filler was discharged until clear of air at vent 2, 3, and 4. Outlets were closed in sequential order as they discharged. At outlet anchorage, the anchorage outlet was closed first and then anchor cap outlet was closed to ensure proper filling of anchor cap. Inlet anchor cap outlet (vent 1) followed the same procedure; however, if it discharged early due to location, then the vent was closed and reopened (burp) near the end of the injection process. Once all outlets were closed, the pressure was increased within duct to 30 psi and valve E was closed.
8. All pressure and temperature measurements were recorded electronically during filler injection. IR measurements of filler in barrel and at discharge locations were recorded periodically. Small samples of filler were gathered from the inlet and outlet locations for review.
9. Clean up: The transfer of filler from drum to hopper was stopped. The pump was restarted and run until the pump was empty. The hoses were disconnected and made those empty into barrel if the filler was still liquid.

8.2.2 Observations

- Pressure drop in pre-injection air test was 1-2 psi in 1 minute.

- The overall injection process went smoothly with no leaks observed
- Duration of the injection (from the pump start to pump stop including hold time during injection) was 5 minutes 10 seconds. The process was slower than expected as the pump was not running at its full flow rate (20 gpm).
- Temperature of the filler in the hopper during the circulation was 230° F.
- Ambient temperature at the start of the injection was 81° F.
- Filler from vent 1 discharged initially with excessive air, followed by vent 2, 3, and 4. Discharged filler was collected in buckets for later volume measurement.
- Air was seen travelling through window 2. Air bubbles were due to incomplete venting at vent 2 location.
- A line of foam could be seen through the window 1. Some foam was injected as the hopper was near empty, which was likely due to drawing air into the intake at the hopper.

8.3 VZ Inject

NONTRIBOS VZ Inject was injected into the tendon with DSI anchors using the Viking pump through a pipe saddle mounted to the duct in a similar manner as for Cirinject CP specimen (Figure 8-1). Injection was carried out on the morning of October 8, 2014 at FDOT Structures Research Center at Tallahassee.

8.3.1 Injection Process

Pre-injection:

1. Air test of the tendon was conducted at 50 psi. The test was accepted if pressure drop was less than 15 psi in 1 minute.
2. The filter was heated to 220° F. Sufficient time was allowed to ensure all three barrels are at the proper temperature. The filler was stirred occasionally to ensure uniform temperature.
3. All hoses were clear and preheated.
4. Personnel were positioned at all vents with buckets and wet towels. Personnel were visible to the pump operator.
5. Video cameras and LED lights were positioned at each of the windows to record injection.

Injection:

1. Drums were position on a pallet and placed adjacent to suction line of pump.
2. The 1in. return line was connected to the barrel and the 1.5 in. discharge line was connected to the pump. The outlet end of the discharge line was left open. Injection occurred at the location shown in Figure 8-1.
3. Vents 1, 2, 4, and 5 were opened. Vent 3 was closed.
4. The pump was preheated to 250° F.
5. Valves A, B, C, and E were opened. Before connecting the discharge line to valve F, the pump was started and discharged 2 gallons into a clean container. Valve E was closed after discharge.
6. Data acquisition system was started and video recording was begun. IR measurements of filler in barrel and at discharge locations were recorded periodically. Small samples of filler were collected from the inlet and outlet locations for testing.

7. The hose was connected to valve F. Discharge line valve E and F and throttle pump were opened to control pressure. The pressure of 75 psi was not exceeded. The transfer pump was operated as needed to move filler from Barrel C to Barrel B.
8. The filler was injected continuously at approximately 60 gpm. The filler was allowed to discharge from vents 1, 2, 4, and 5. The filler was observed during discharge and valve was closed when all free air was discharged and consistent filler was exiting. At anchorages, the anchorage vent was closed first and then the anchor cap vent was closed to ensure proper filling of anchor cap. Once anchorage vents were closed, vent 3 was opened and discharged until consistent filler was exiting. Vent 3 was closed.
9. Once all valves were closed, the pressure was increased to 30 psi. Valve F was closed and the pump was stopped.
10. Discharge line at valve F was disconnected and the pump was reversed to pull filler from injection hose and deliver back into drum. The hoses were disconnected and cleaned.

8.3.2 Observations

- Pressure drop in pre-injection air test was 3-4 psi in 1 minute.
- The overall injection process went smoothly with no leaks in the tendon.
- Duration of injection (From the pump start to pump stop including hold time during injection) was 3 minutes 29 seconds.
- The filler pump was run at varying flow rates (40-60 gpm) keeping injection pressure less than 75 psi.
- Temperature of the filler at the start of the test was 230° F in all the barrels.
- Ambient temperature at the start of the injection was 72° F.
- Temperature of the discharge line of the pump through infra-red gun was 118° F.
- Filler from vent 1 and 2 exited first with considerable amounts of air. Both vents were closed when good flow was noticed visually. Vent 4 and 5 started discharging filler subsequently.
- Vent 3 was then opened, which discharged filler with considerable amounts of air. Vent 3 was closed when air was cleared. At this time, pumping was stopped and window 1 and 2 were checked for potential air bubbles.
- Window 1 showed air travelling towards the east anchor. Pumping was started again to burp the air at the East end. Vent 2 was reopened and burped until good flow of filler was discharged. Pumping was then terminated.

8.4 *Trenton-1*

Trenton wax was injected into the tendon with Freyssinet anchors using the Viking pump through the east anchor cap with vacuum pump connected to the west anchor cap (Figure 8-3). Injection was carried out on the morning of March 10, 2015 at FDOT Structures Research Center in Tallahassee. Piping was installed on the three barrels to provide sufficient filler supply for uninterrupted injection of the entire mockup specimen.

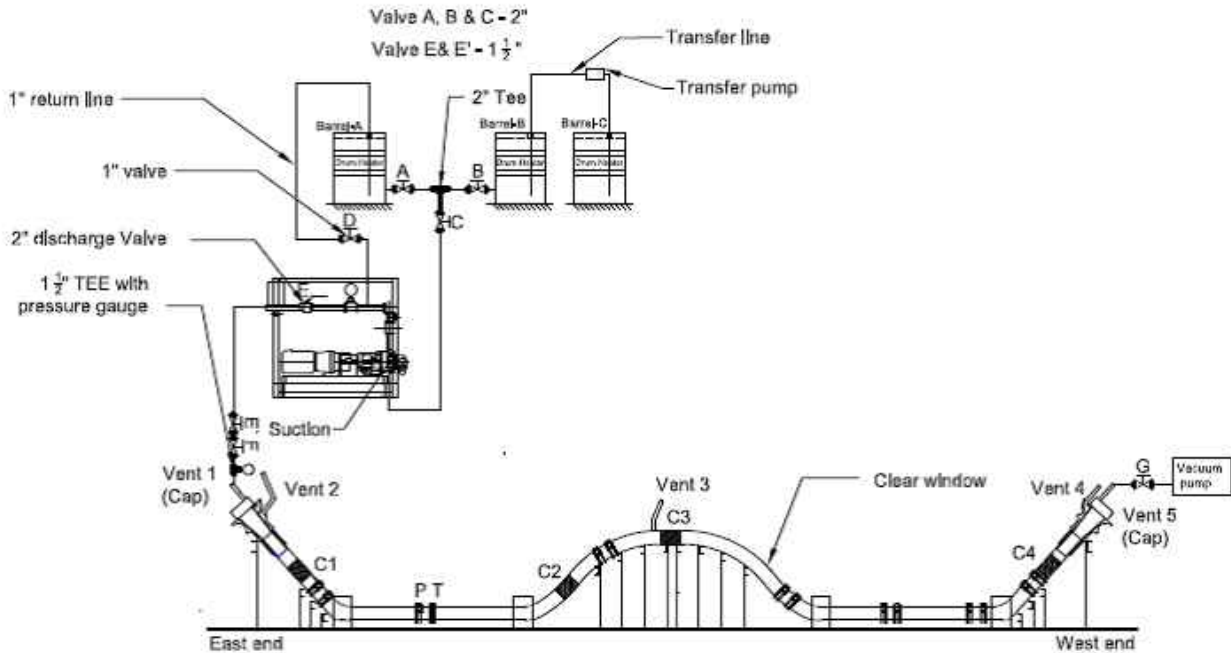


Figure 8-3 Schematic of test setup for Trenton wax injection with vacuum assist

8.4.1 Injection Procedure

Preinjection:

1. Air test of the tendon was conducted at 50 psi. The test was accepted if pressure drop was less than 15 psi in 1 minute.
2. Vacuum test was done with all valves closed including F and G. The vacuum pump was started and was pumped to -650 millibar pressure, the pump was then stopped for five minutes to assure sealed tendon. If not sealed, leaks were repaired and the test was repeated.
3. The filler was heated to 220° F. Sufficient time was allowed to ensure all three barrels were at the proper temperature. The filler was stirred occasionally to ensure uniform temperature.
4. All hoses were cleared and preheated.
5. Personnel were positioned at all vents with buckets and wet towels. Personnel were made visible to the pump operator.
6. Video cameras and LED lights were positioned at each of the windows to record injection.

Injection:

1. Drums were positioned on a shipping pallet and were placed adjacent to the suction line of pump.
2. The 1 in. return line was connected to the barrel and the 1.5 in. discharge line was connected to the pump. The outlet end of the discharge line was left open. Injection occurred at the location shown in Figure 8-3.
3. The pump was preheated to 250° F.

4. Valves A, B, C, D and E were opened. Before connecting the discharge line to the inlet valve F, the pump was started and discharged 2 gallons into a clean container. Valve E was closed after discharge.
5. The data acquisition system was started and video recording was initiated. IR measurements of filler in barrel and at discharge locations were recorded periodically. Small samples of filler were gathered from the inlet and outlet locations for testing.
6. Discharge line was connected to inlet valve (valve F).
7. Discharge line valve E and F and throttle pump were opened to keep injection pressure less than 75 psi. The filler was injected continuously at approximately 30 gpm. As the filler was pumped in, and the vacuum decreased in the tendon, the vacuum pump was started periodically to increase the vacuum to -650 millibar in intervals. The vacuum pump was not kept running the entire time.
8. When the filler was noticed in the discharge line, valve G was closed before the filler entered into the vacuum pump.
9. The pressure in the tendon was increased for 1 minute at very low flow rate (about 5 gpm) and the injection was stopped at pressure 30 psi above the injection pressure. Inlet valve (valve F) was then closed and the pump was stopped.
10. Discharge line at valve G was disconnected and the pump was reversed to pull filler from injection hose and deliver back into drum. Finally, the hoses were disconnected and cleaned.

8.4.2 Observations

- Pressure drop in preinjection air test was 1 psi in 1 minute.
- No pressure drop was observed during the vacuum pull before injection.
- The overall injection process went smoothly with no leaks observed.
- Duration of the injection (from the pump start to pump stop including hold time during injection) was 4 minutes 1 second.
- Average temperature of the filler in the barrels before injection was 230° F.
- Ambient temperature at the start of the injection was 69° F.
- Vacuum pump was started at 26.5 in of Hg and stopped at 28 in of Hg (13.5 psi) at the far end.
- Temperature of the wax at the west end exiting from the vent was 138° F.

8.5 *Trenton 2*

Trenton was injected into the tendon with DSI anchors using the Viking pump through a pipe saddle mounted to the duct (Figure 8-1). Injection was carried out on the morning of March 12, 2015 at FDOT Structures Research Center at Tallahassee. A double-bend pipe saddle, which had an opening of 1½ in., was installed on the duct; the pump discharge line was connected to the saddle through a 1½ in. line and valve. Piping was installed on the three barrels to provide sufficient filler supply for uninterrupted injection of the entire mockup specimen

8.5.1 Injection Procedure

Preinjection:

1. Air test of the tendon was conducted at 50 psi. The test was accepted if pressure drop was less than 15 psi in 1 minute.
2. The filler was heated to 220° F. Sufficient time was allowed to ensure all three barrels were at the proper temperature. The filler was stirred occasionally to ensure uniform temperature.
3. All hoses were cleared and preheated.
4. Personnel were positioned at all vents with buckets and wet towels. Personnel were made visible to the pump operator.
5. Video cameras and LED lights were positioned at each of the windows to record injection.

Injection:

1. Drums were positioned on pallets and placed adjacent to suction line of pump.
2. The 1 in. return line was connected to the barrel and the 1.5 in. discharge line was connected to the pump. The outlet end of the discharge line was left open. Injection occurred at the location shown in Figure 8-3.
3. Pump was preheated to 250° F.
4. Vents at the east anchor (vent 1 and 2), middle frame (vent 3) and at the west anchor (vent 4 and 5) were opened.
5. Valves A, B, C, D, and F were opened. Before connecting the discharge line to the inlet valve G, the pump was started and discharged 2 gallons into a clean container. Valve F was closed after discharge.
6. The data acquisition system was started and video recording was begun. IR measurements of filler in barrel and at discharge locations were recorded periodically. Small samples of filler was gathered from the inlet and outlet locations for testing.
7. Discharge line was connected to inlet valve (valve G).
8. Discharge line valve E and F and throttle pump were opened to keep injection pressure less than 75 psi. The filler was injected continuously at approximately 10 gpm. The filler was allowed to discharge from vents (vents 1, 2, 3, 4, and 5). The filler was observed during discharge and the valve was closed when all free air is discharged and consistent filler was exiting. Approximately 3 gallons at each vent was discharged to get the consistent filler without any air. The anchorage vent was closed first, followed by anchor cap vent to ensure proper filling of anchor cap. Once vents at west end were closed, valve F was closed for 30 seconds to check if any entrapped air was present in the tendon. If air was present, valve F and vent 3 were opened and filler was injected at approximately 20 gpm. Vents were closed when consistent filler was exiting from the vent.
9. The pressure in the tendon was increased for 1 minute at very low flow rate (about 5 gpm) and injection was stopped at pressure 30 psi above the injection pressure. Inlet valve (valve G) was closed and the pump was stopped.
10. Discharge line at valve G was disconnected and the pump was reversed to pull filler from injection hose and deliver back into drum. Finally, the hoses were disconnected and cleaned.

8.5.2 Observations

- Pressure drop in pre-injection air test was 1 psi in 1 minute.
- The overall injection process went smoothly with no leaks observed
- Duration of the injection (from the pump start to pump stop including hold time during injection) was 15 minutes 29 seconds.
- Average temperature of the filler in the barrels before injection was 236° F.
- Ambient temperature at the start of the injection was 72° F.
- Wax exited first from middle vent first followed by west and east vent.
- Temperature of the wax exited from the vents was 165° F at east end, 204° F at middle vent and 170° F at west end.
- Air gap was observed at the top of window 2 which was pushed through middle vent pumping wax at the higher rate.

9 Results and Discussion

9.1 Post-Injection Inspection

The tendons were inspected at approximately 24 hours after injection. Eleven to fifteen inspection ports (IP) were prepared, at which the duct was opened to inspect the relative fill of the flexible fillers, filler cover of the strands, and void presence, if any. Each inspection port opening was formed by cutting and removing the top half of the HDPE duct over a length of approximately one or two ft; IP15, however, was made on the bottom half of the duct. Duct windows, vents, and caps were also inspected for the relative fill. Figure 9-1 and Table 9-1 show the location of the inspection ports and windows along the length of the tendon for first three injections while Figure 9-2 and Table 9-2 show the location of inspection ports and windows for Trenton injections. Inspection observations for each tendon are summarized in the following sections.

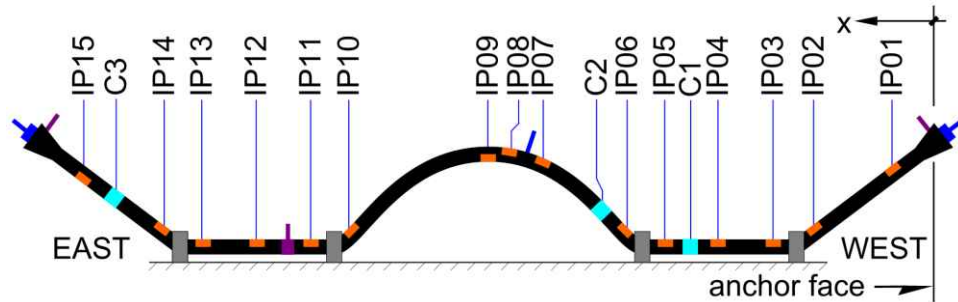


Figure 9-1 Inspection port (IP) locations on Cirinject, Visconorust, and VZ Inject mockup specimens

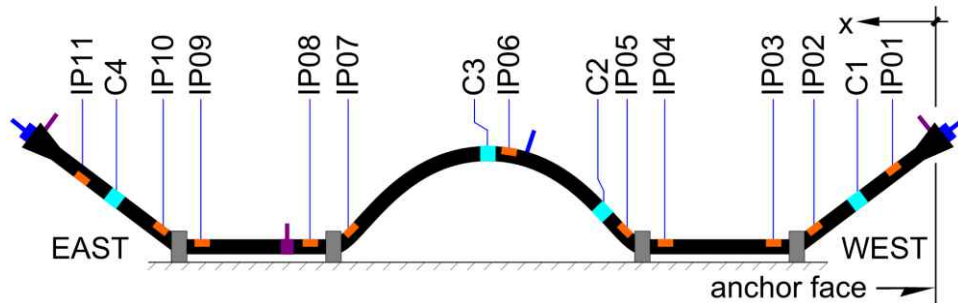


Figure 9-2 Inspection port (IP) locations on Trenton 1 and Trenton 2 mockup specimens

Table 9-1 Distance from the face of the west anchor to inspection ports.
See Figure 9-1 and Figure 9-2.




Inspection Port	Cirinject, Visconorust, and VZ Inject location(ft)	Trenton 1 and 2 location (ft)
1	1	1
2	27	28
3	31	31
4	55	68
5	67	71
6	71	97
7	92	126
8	97	129
9	100	168
10	125	171
11	129	198
12	145	n/a
13	167	n/a
14	171	n/a
15	197	n/a



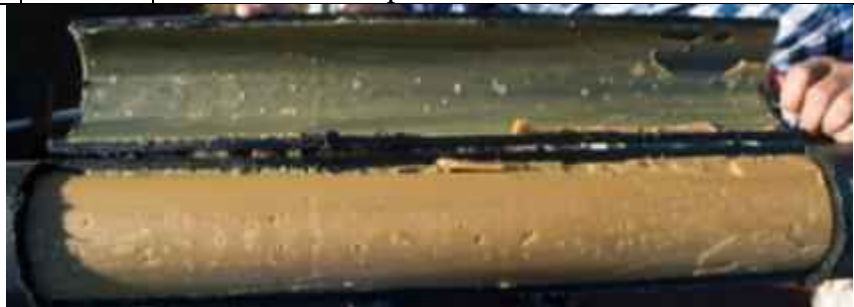

Table 9-2 Distance from the face of the west anchor to duct windows.
See Figure 9-1 and Figure 9-2





Window	Cirinject, Visconorust, and VZ Inject location(ft)	Trenton 1 and 2 location (ft)
1	60	8
2	81	81
3	190	99
4	n/a	190




9.1.1 Cirinject CP




Table 9-3 Post-injection inspection of Cirinject CP


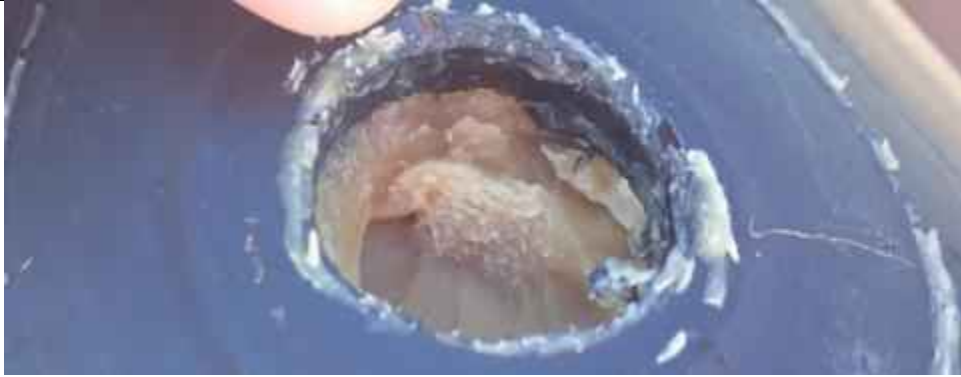

Inspection port	Distance from east end, ft	Strand location	Comments
IP01	1	Bottom	No voids visible. Strands completely coated with filler.
			
IP02	27	Top	No voids visible. Strands completely coated with filler.
			
IP03	31	No inspection due to instrumentation	
IP04	55	Top	No voids visible. Strands completely coated with filler.
			

IP05	67	Top	No voids visible. Strands coated with filler.
			
IP06	71	Top	No voids visible. Strands completely coated with filler.
			
IP07	92	Bottom	No voids visible. Strands completely coated with filler. Small bubbles on the top of the filler.
			
IP08	97	Bottom	No voids visible. Strands completely coated with filler.
			

IP09	100	Bottom	No voids visible. Strands completely coated with filler.
			
IP10	125	Top	No voids visible. Strands completely coated with filler.
			
IP11	129	Top	No voids visible. Strands completely coated with filler. Small bubbles on east side of the inspection port.
			
IP12	145	Top	No voids visible. Strands completely coated with filler. Bubbles on the top of the filler.
			

IP13	167	Top	No voids visible. Strands completely coated with filler.
			
IP14	171	Top	No voids visible. Strands completely coated with filler.
			
IP15	197	Middle	No voids visible. Strands completely coated with filler. Filler came off the strands.
			





Duct windows			
C1	60	Top	Elongated cracks on the top of the filler. Strands completely coated with filler.
			
C2	81	Middle	Small air bubbles on the top of the filler. Strands completely coated with filler.
			
C3	190	Middle	Cracks in the filler at the top and north side of the window. Strands completely coated with filler.
			




Vents and caps			
East anchor and cap vent	0	-	Anchor vent had a pin hole in the filler. Cap vent completely filled with filler.
			
Middle vent	97	Bottom	No void visible. Vent completely filled with filler.
			
Injection port	140	Bottom	Port completely filled with filler.
			





West anchor and cap vent	200	-	Anchor vent had a ¼ in. hole in the filler. Cap vent completely filled with filler.
			
West end Cap	0	Middle	Cap completely filled with filler.
			
East end Cap	200	Middle	Cap completely filled with filler.
			




9.1.2 Visconorust




Table 9-4 Post-injection inspection of Visconorust




Inspection port	Location (ft)	Strand location	Comments
IP01	1	Top	No voids visible. Visible strands completely coated with filler.
			
IP02	27	Top	No voids visible. Visible strands coated with filler.
			
IP03	31	No inspection due to instrumentation.	
IP04	55	Bottom	No voids visible. Visible strands completely coated with filler.
			
IP05	67	Top	No voids visible. Strands coated with filler.
			


IP06	71	Top	Dry stand at some locations and some voids. Strands mostly coated with filler.
			
IP07	92	Bottom	Void at the top on east side ¼ in. deep. Strands completely coated with filler.
			
IP08	97	Bottom	Void at the top. 1 ¼ in. on west side, 7/8 in. on east side. Void through to IP-7. Strands completely coated with filler.
			

IP09	100	Bottom	No voids visible. Strands completely coated with filler.
			
IP10	125	Top	No voids visible. Strands completely coated with filler.
			
IP11	129	Top	No voids visible. Strands completely coated with filler.
			
IP12	145	Middle	No voids visible. Strands completely coated with filler.
			

IP13	167	Top	No voids visible. Strands completely coated with filler.
			
IP14	171	Top	Foam/bubble at the top of the filler. Strands coated with filler.
			
IP15	197	Top	Foam/bubble at the top of the filler. Strands coated with filler.
			



Duct windows			
C1	60	Top	Elongated void at the top of the filler. Strands completely coated with filler.
			
C2	81	Middle	Discontinuous bubble at the top of the filler. Strands completely coated with filler.
			
C3	190	Middle	Foam/bubble at the top of the filler. Strands coated with filler.
			





Vents and Caps			
West end vent	0	-	Anchor vent had a pin hole about 1 in. deep. Cap vent was completely filled with filler. Cap was not opened at west anchor.
			
East end Cap	200	Middle	Cap was completely filled with filler.
			
East end vents	200	Middle	Anchor vent had a pin hole about 1 in. deep. Cap vent was completely filled with filler. Cap was not opened at west anchor.
			





Middle vent	97	Bottom	Void at the top of the filler about 1 in. deep.
			





9.1.3 VZ Inject




Table 9-5 Post-injection inspection of VZ Inject



Inspection port	Distance from east end, ft	Strand location	Comments
IP01	1	Bottom	A small pin hole on the east side of the port. Strands completely coated with filler.
			
IP02	27	Top	No voids visible. Strands completely coated with filler.
			



IP03	31	No inspection due to instrumentation	
IP04	55	Top	No voids visible, small air bubbles on the top of the filler. Strands completely coated with filler.
			
IP05	67	Top	No voids visible. Strands coated with filler.
			
IP06	71	Top	No voids visible. Strands completely coated with filler.
			
IP07	92	Bottom	Void at the top of filler 1 in. deep on east side and a small hole on west side. Strands completely coated with filler.
			

IP08	97	Bottom	Void on the top of filler about 1 ½ in. on east side and 1 in. on west side. Strands completely coated with filler.
			
IP09	100	Bottom	No voids visible. Strands completely coated with filler.
			
IP10	125	Top	No voids visible. Strands completely coated with filler.
			
IP11	129	Top	Line void at the top near east end of the inspection port. Strands coated with filler.
			

IP12	145	Top	No voids visible. Strands completely coated with filler.
			
IP13	167	Top	No voids visible. Strands completely coated with filler.
			
IP14	171	Top	No voids visible. Strands completely coated with filler.
			
IP15	197	Middle	No voids visible. Strands completely coated with filler.
			

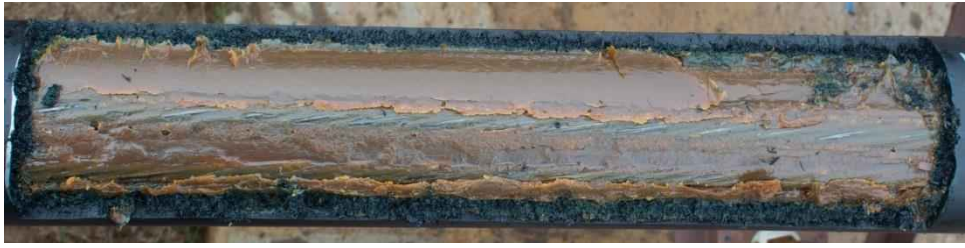
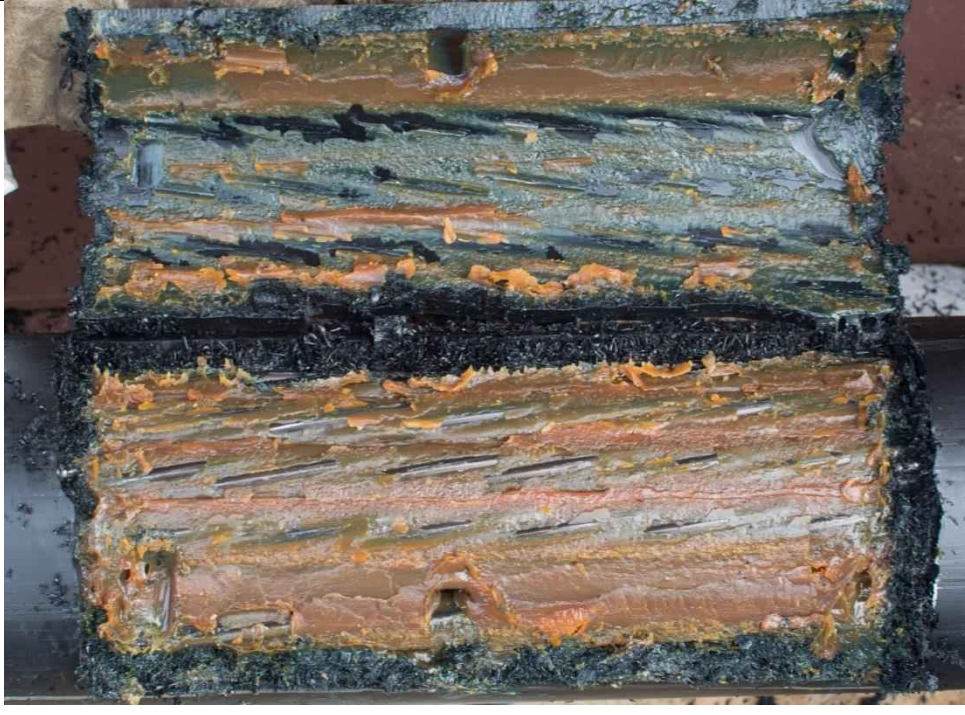
Duct windows			
C1	60	Top	Elongated cracks on the top of the filler. Strands completely coated with filler.
			
C2	81	Middle	Cracks on the south side of the window. Strands completely coated with filler.
			
C3	190	Middle	Cracks in the filler at the top of the window. Strands completely coated with filler.
			




Vents and caps			
East anchor and cap vent	0	-	Anchor vent had a pin hole in the filler. Cap vent completely filled with filler.
			
Middle vent	97	Bottom	Void at the top of the filler 1 in. deep.
			

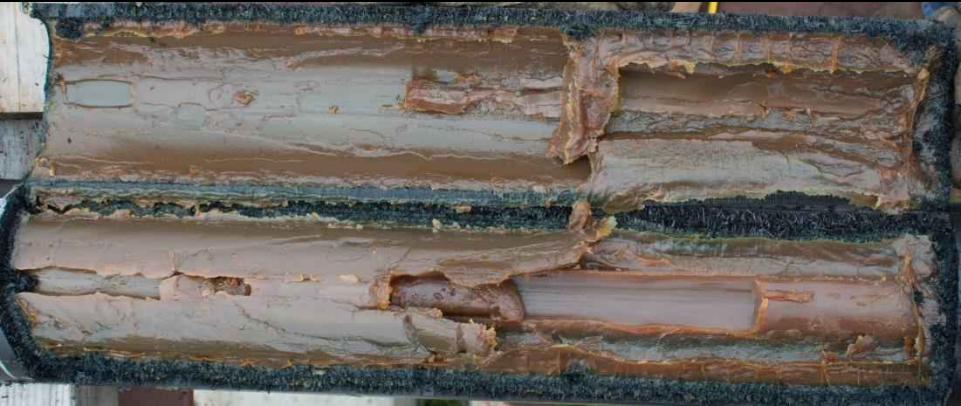

Injection port	140	Bottom	Port completely filled with filler.
			
West anchor and cap vent	200	-	Anchor vent had a pin hole in the filler. Cap vent completely filled with filler.
			
East and West Caps	0, 200	Middle	Caps completely filled with filler.
			



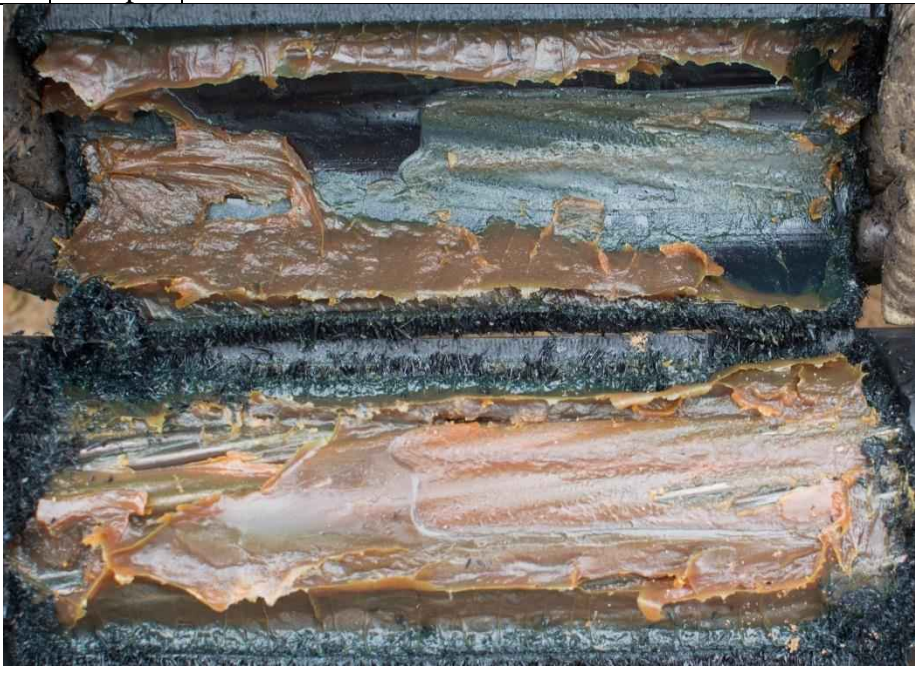
9.1.4 Trenton 1


Table 9-6 Post-injection inspection of Trenton 1





Inspection port	Distance from east end, ft	Strand location	Comments
IP01	1	Bottom	No voids visible. Strands completely coated with filler. 
IP02	28	Top	No voids visible. Strands completely coated with filler. 




IP03	31	Top	No voids visible. Strands coated with filler.
			
IP04	68	Top	No voids visible. Strands coated with filler.
			
IP05	71	Top	No voids visible. Strands coated with filler.
			

IP06	97	Bottom	Small air bubbles at top of filler. 1/8 in void at the top of the wax near east end of the port. Strands completely coated with filler.
			
IP07	126	Top	No voids visible. Strands coated with filler.
			

IP08	129	Top	No voids visible. Strands coated with filler.
			
IP09	168	Top	No voids visible. Strands coated with filler.
			
IP10	171	Top	No voids visible. Strands coated with filler.
			



IP11	198	Middle	Small air hole on the top of the filler. Strands coated with filler.
 The image contains two photographs stacked vertically. Both show a cross-section of a composite material. The top photograph shows a central horizontal layer of a light-colored, translucent filler material. This filler is surrounded by a dark, fibrous material, likely carbon or glass fibers. A small, circular air hole is visible on the top surface of the filler layer. The bottom photograph shows a similar cross-section, but the filler layer appears more irregular and possibly more saturated with a resin or coating, with some darker spots and a more textured appearance. The surrounding fibers are also visible.			

Duct windows			
C1	8	Middle	Elongated crack on the top of the filler. Strands completely coated with filler.
			
C2	81	Middle	Cracks in the wax at the top. Air pockets on north west end of the window. Strands completely coated with filler.
			
C3	99	Bottom	Elongated cracks in the filler at the top of the window. Air pockets on the north side of the window. Strands completely coated with filler.
			
C4	190	Middle	Elongated cracks in the filler at the top of the window. Strands completely coated with filler.
			




Vents and caps			
East and west anchor vents	0	-	Anchor vent had a pin hole in the filler. Cap vent completely filled with filler.
			
East anchor cap	0	-Middle	Anchor vent had a pin hole in the filler. Cap vent completely filled with filler.
			
West anchor caps	200	Middle	Caps completely filled with filler.
			



9.1.5 Trenton 2


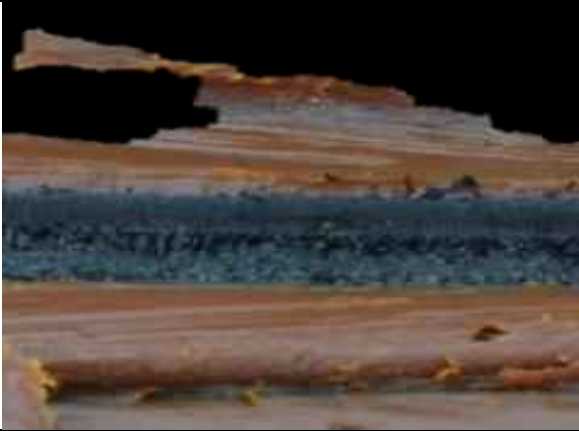
Table 9-7 Post-injection inspection of Trenton 2





Inspection port	Distance from east end, ft	Strand location	Comments
IP01	1	Bottom	<p>No voids visible. Strands completely coated with filler.</p> 
IP02	28	Top	<p>No voids visible. Strands completely coated with filler.</p> 





IP03	31	Top	No voids visible. Strands coated with filler.
IP04	68	Top	No voids visible. Strands coated with filler.

IP05	71	Top	No voids visible. Strands coated with filler.
			
IP06	97	Bottom	Small air bubbles at top of filler. 1/8 in void at the top of the filler. Strands completely coated with filler.
			
IP07	126	Top	No voids visible. Strands coated with filler.
			

IP08	129	Top	No voids visible. Strands coated with filler.
			
IP09	168	Top	No voids visible. Strands coated with filler.
			

IP10	171	Top	No voids visible. Strands coated with filler.
			
IP11	198	Middle	Small holes in the filler. Strands coated with filler.
			

Duct windows			
C1	8	Middle	Elongated cracks at top of the window. Strands coated with filler.
			
C2	81	Middle	Elongated crack at the top of the window. Strands coated with filler.
			
C3	99	Bottom	Air void on the top of the window. Strands coated with filler.
			
C4	190	Middle	Air void around top east side of the window. Strands completely coated.
			

Vents and caps			
East and west vents	0, 200	Middle	Vent ports with air voids at east and west anchors.
			
West cap	0	Middle	Small void in the middle of the anchor. Strands completely coated with filler.
			
East cap	200	Middle	Strands coated with filler. Cap completely filled.
			
Injection port	60	Bottom	Port full of filler.
			

9.2 Injection pressure

Figure 9-3, Figure 9-4, and Figure 9-5 show the variation of internal pressure during the injection and hold period for Cirinject CP, Visconorust, and VZ Inject, respectively. The plots indicate that there was little variation in the pressure readings among the individual pressure gages (P1 through P7 are approximately the same) along the length of the duct during the hold period after injection. The injection pressure was in the range of 10 to 20 psi for the Visconorust and 40 to 60 psi for VZ Inject and Cirinject CP, which was due to the differences in pumping equipment, injection point, and pumping and venting technique, and not the material selection. Similarly, the duct hold pressure was varied; the hold pressure was 34 psi for Visconorust and 45-60 psi for VZ Inject and Cirinject CP, again due to variation in technique and equipment. Gage P1 malfunctioned during VZ injection and Cirinject CP injection.

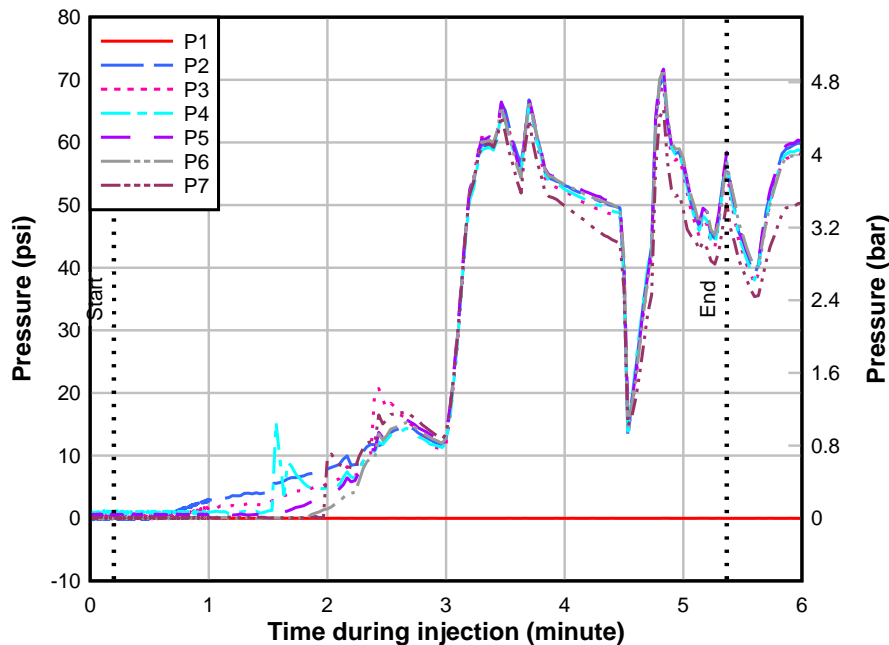


Figure 9-3 Duct internal pressure during Cirinject CP injection

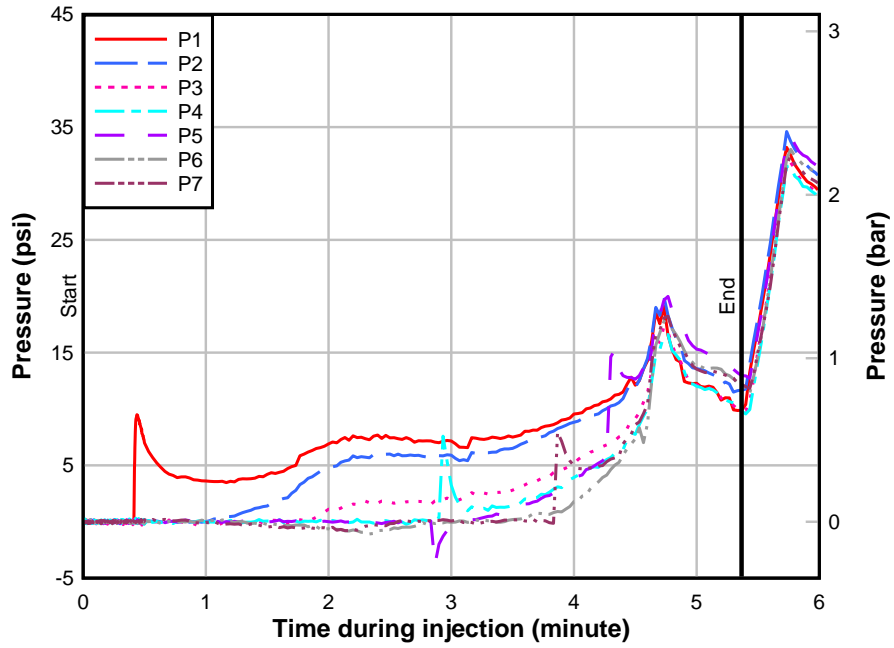


Figure 9-4 Variation in duct internal pressure during Visconorust injection

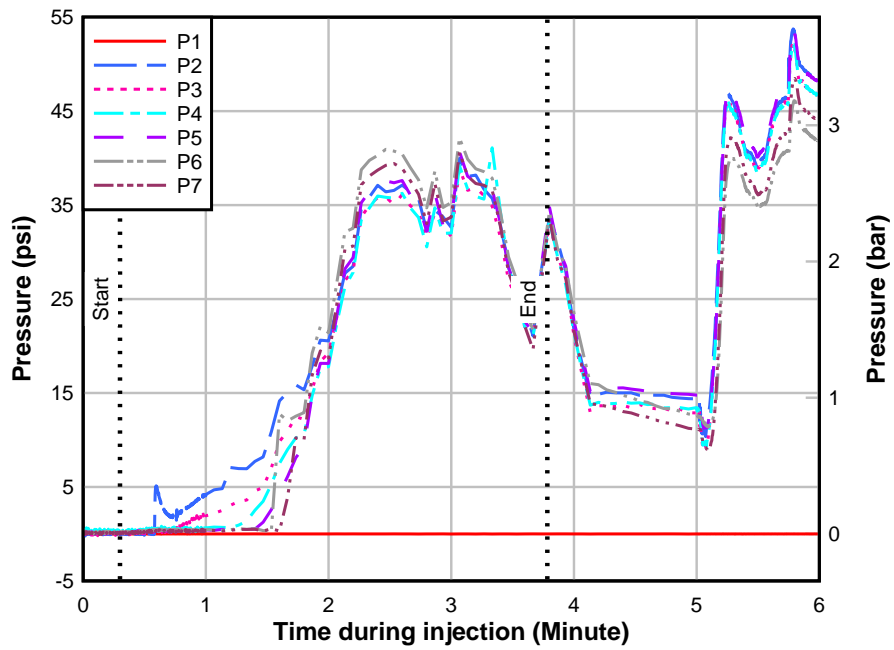


Figure 9-5 Duct internal pressure during VZ Inject injection

Figure 9-6 and Figure 9-7 illustrate the internal duct pressure during the injection of Trenton filler. Figure 9-6 shows the vacuum pulled on the tendon before injection. The plot also indicates that the pressure was built in the tendon once the filler crossed P7 location. The vacuum in the tendon was 13.5 psi while the hold pressure was about 45 psi. The duct internal pressure during the slow injection was about 10 psi which was raised to 40 psi for the hold period. The variation in the internal pressure was due to the different injection scheme.

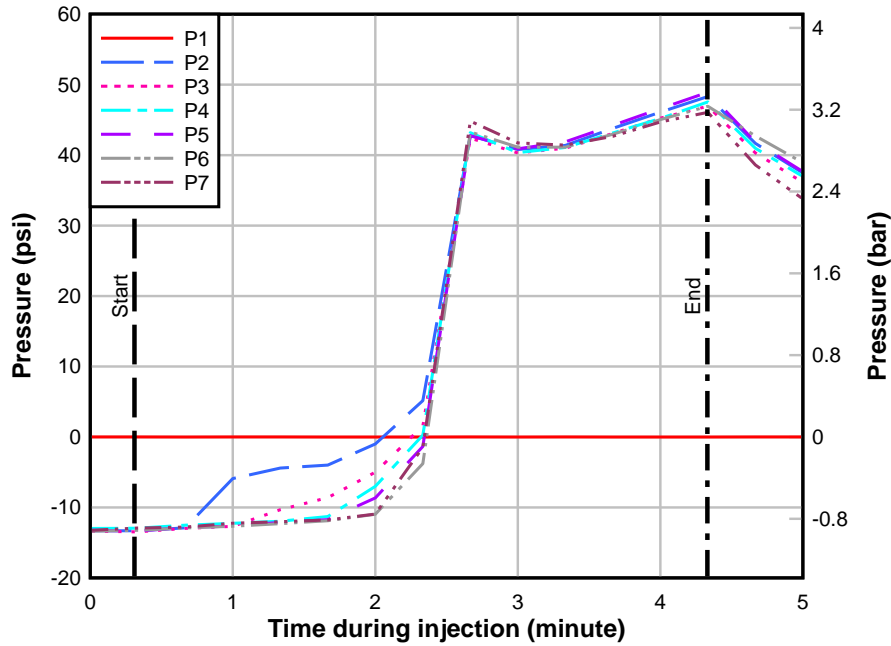


Figure 9-6 Duct internal pressure during Trenton 1 filler injection

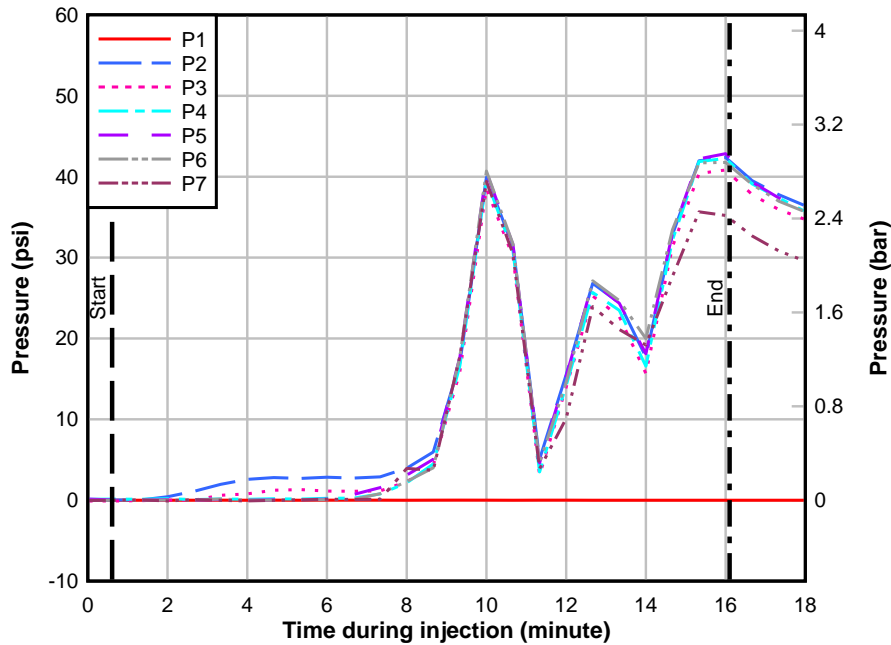


Figure 9-7 Duct internal pressure during Trenton 2 filler injection

9.3 Temperature

Figure 9-8 through Figure 9-12 show the variation of temperature with time in each of the five specimens. The temperature probe positions are noted in (Figure 6-1). In general, the sudden increase in temperature indicates the time at which the front of the filler had reached that position. For instance, in the Visconorust specimen, the filler arrived at the temperature sensors in this order: T1, T2, T3, T4, T5, T6, and T7. This specimen was injected from the east anchorage, so sequential arrival times would be expected. In the specimens where filler was injected directly into the duct (e.g., Cirinject CP), however, the filler was flowing in opposite directions away from the injection point, which explains the non-sequential arrival times. See Section 9.4 for further discussion of the filler flow.

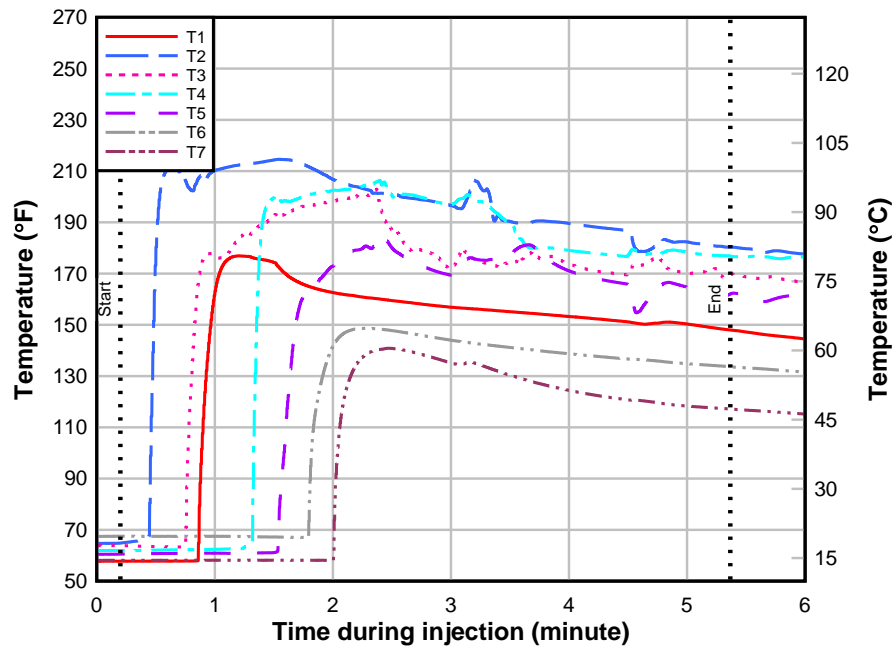


Figure 9-8 Filler temperature in duct during Cirinject injection

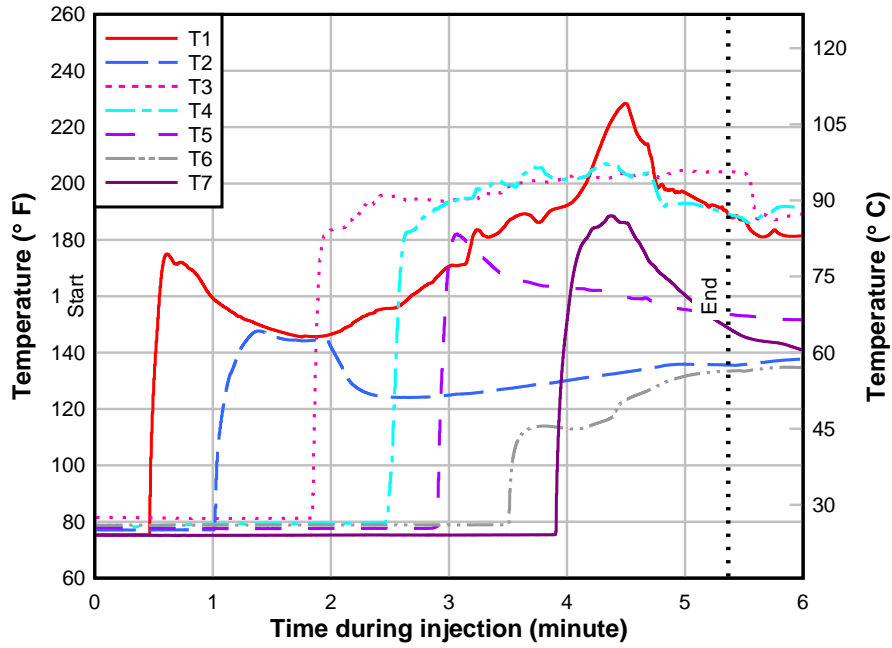


Figure 9-9 Filler temperature in duct during Visconorust injection

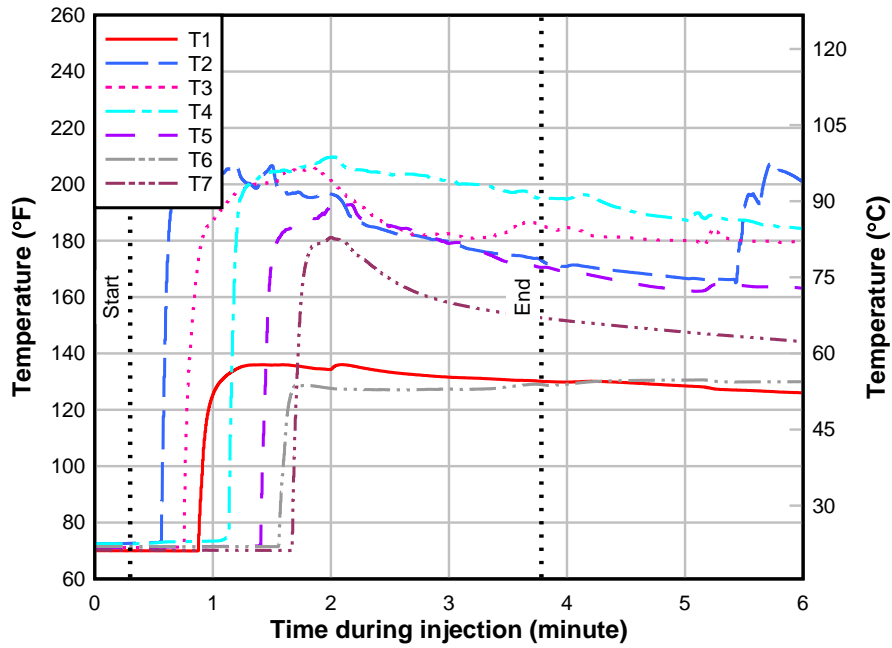


Figure 9-10 Filler temperature in duct during VZ-inject injection

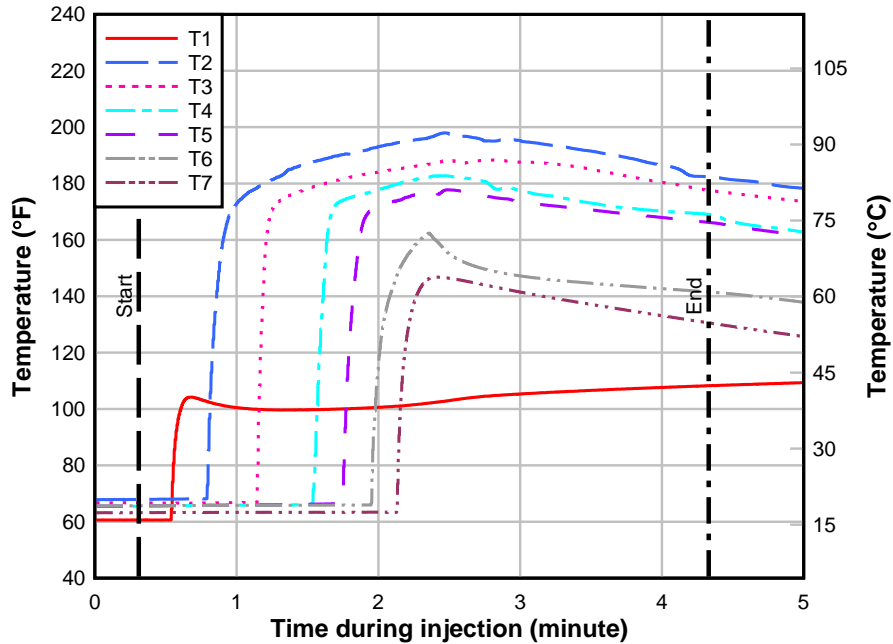


Figure 9-11 Filler temperature in duct during injection with vacuum assist (Trenton 1)

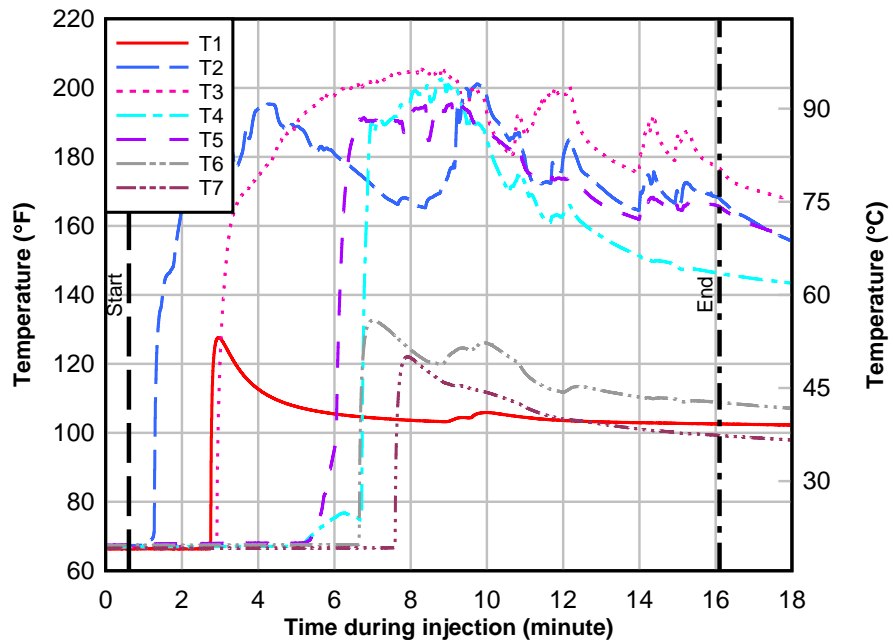


Figure 9-12 Filler temperature in duct during Trenton filler injection (Trenton 2)

Temperature generally decreased rapidly during the initial minutes after contact as the heat was transferred to strands. The rate of temperature decrease slowed once equilibrium was attained between the flexible filler and the strands. However, thermocouples in the parabolic profile (T3 and T4) had a slower rate of temperature decrease and typically settled at a higher temperature than the other thermocouples. This was due to their orientation in the top of the duct, which, in the high point of the profile, is open and clear of strands. Thermocouples in the straight profile were oriented at 90 degrees from vertical, which placed them in close proximity

to the strand bundle and likely had more effect on the rate of temperature decrease (Figure 9-9). In subsequent tests, the duct was raised to move the strand bundle to the bottom of the duct and the thermocouple was moved to the top of the duct (see Figure 6-1).

The difference between the temperature at the injection point and the far end (west end) of the tendon at the end of the injection duration for injection was 38° F, 25° F, and 62° F for Visconorust, VZ Inject, and Cirinject CP, respectively. This difference represents the rate of cooling of filler along the tendon length.

The trend of the surface temperature of HDPE duct (Figure 9-13-26) was similar at all locations and for all injections. Curves started near ambient temperature and immediately started rising as the filler passed the probe. Readings plateaued at varying temperatures depending on the orientation and location of the surface-mounted thermocouples. In general, surface temperatures on the bottom of the duct (ST1, ST6, and ST7) were lower than the surface temperatures at other locations, which was likely due to effects of being shaded from solar heating. Top temperatures were higher before the initiating injection. ST3 and ST4 showed the highest temperature as they were installed at the top of the duct and had the highest elevation among the surface-mounted thermocouples.

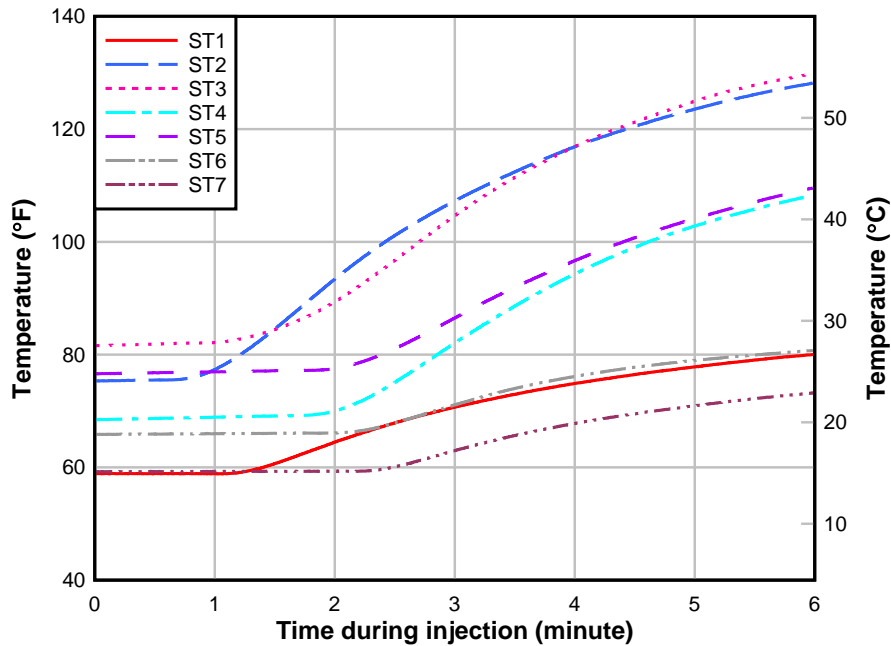


Figure 9-13 Surface temperature of the duct during Cirinject CP injection

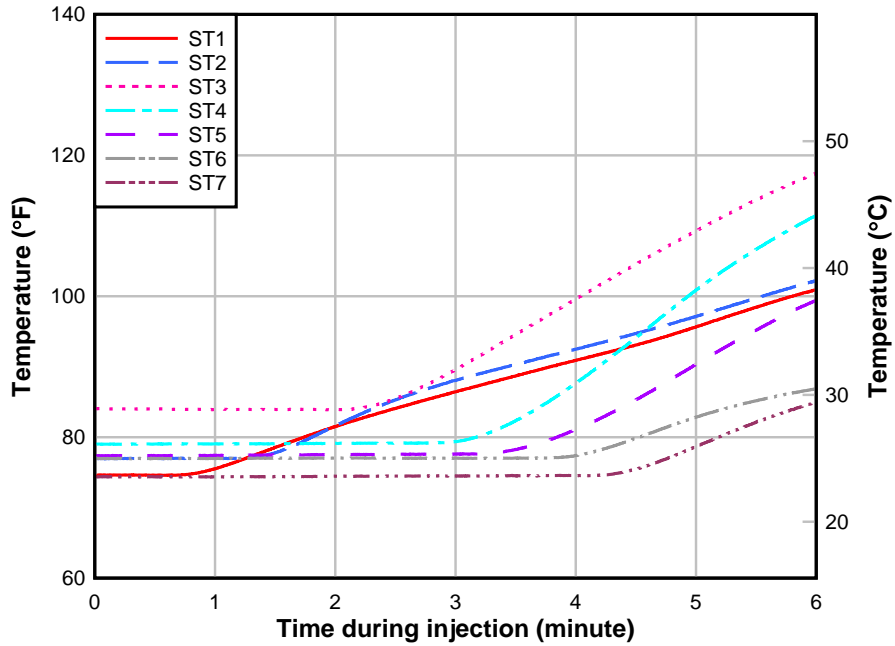


Figure 9-14 Surface temperature of the duct during Visconorust injection

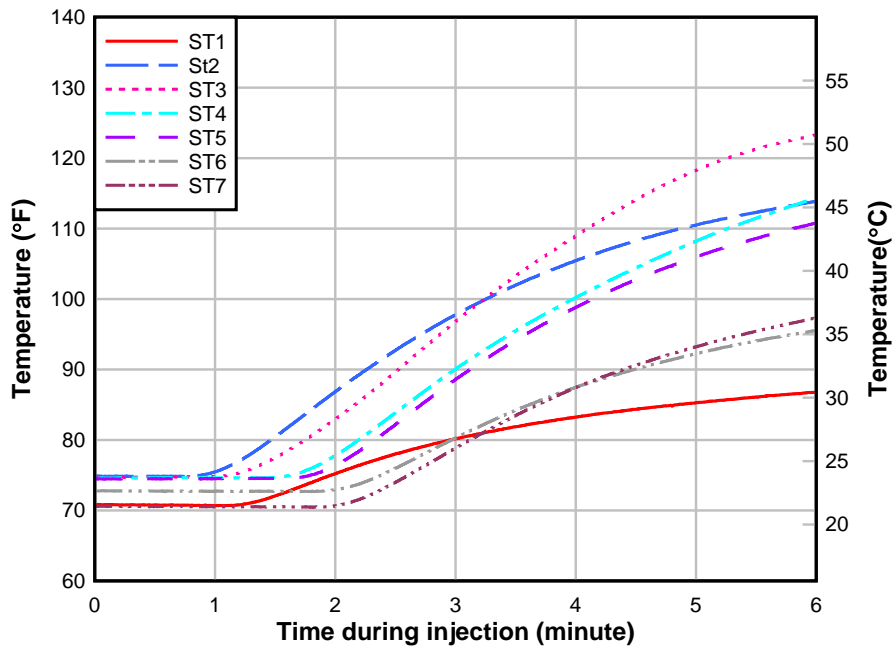


Figure 9-15 Surface temperature of the duct during VZ-inject injection

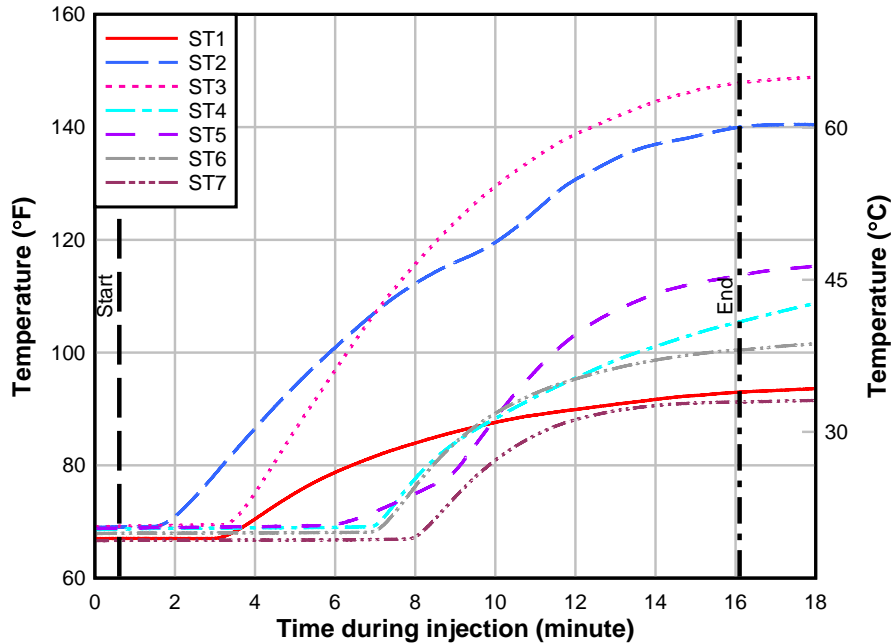


Figure 9-16 Surface temperature of duct during injection with vacuum assist (Trenton 1)

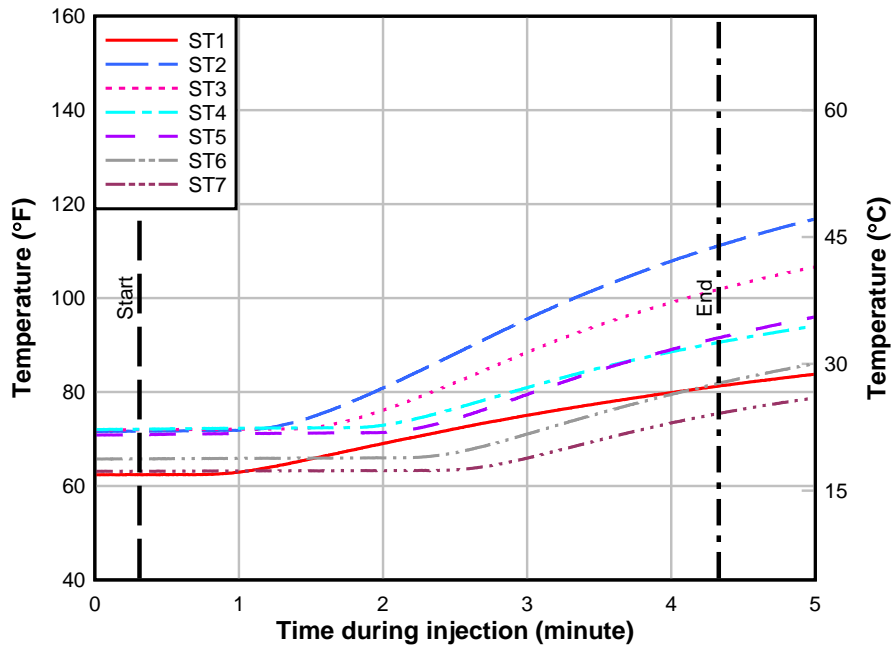


Figure 9-17 Surface temperature of duct during Trenton filler injection (Trenton 2)

9.4 Injection Rate

The target flow rate of the filler during the injection was 50 ft/min for injection at the anchorage and 80 ft/min for injection directly into the duct (or 40 ft/min in each direction). Actual flow rates can be obtained from the time-temperature plots based on the assumption that the sudden increase in temperature indicates the time of arrival for the filler. Figure 9-18-31 show the time of arrival and the resulting flow rate of filler between the temperature probes. For

Visconorust, which was injected through the anchor (one directional), the average rate of injection (From T1 to T7) was 49 ft/min. This was close to the target injection rate.

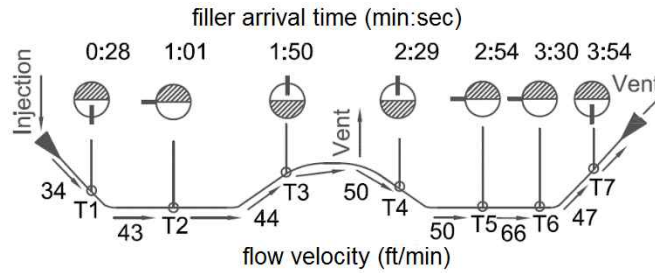


Figure 9-18 Injection rate during Visconorust injection

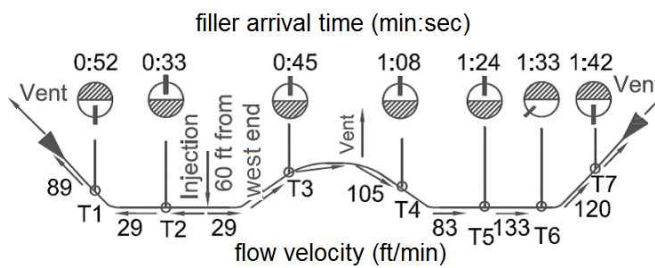


Figure 9-19 Injection rate during VZ Inject injection

VZ Inject and Cirinject were injected directly into the duct, which resulted in filler flowing in opposite directions away from the injection point and toward the opposing anchorages. The average rate for the VZ Inject was 53 ft/min (average rate from the injection point to T1) for filler flowing east and 75 ft/min (average rate from injection point to T7) for filler flowing west. The average rate for the Cirinject CP was 53 ft/min (average rate from the injection point to T1) for filler flowing east and 62 ft/min (average rate from injection point to T7) for filler flowing west.

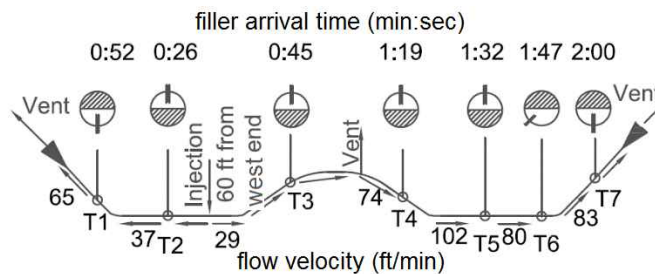


Figure 9-20 Injection rate during Cirinject CP injection

For Trenton 1, which was injected through the anchor (one directional), the average rate of injection (From T1 to T7) was 100 ft/min.

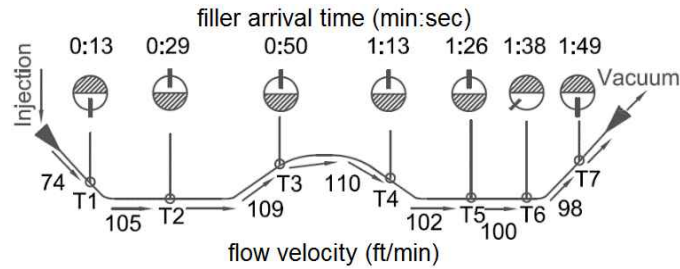


Figure 9-21 Injection rate during Trenton filler injection with vacuum assist (Trenton 1)

Trenton 2 was injected directly into the duct, which resulted in filler flowing in opposite directions away from the injection point and toward the opposing anchorages. The average rate for the filler was 21.5 ft/min (average rate from the injection point to T1) for filler flowing east and 21.6 ft/min (average rate from injection point to T7) for filler flowing west.

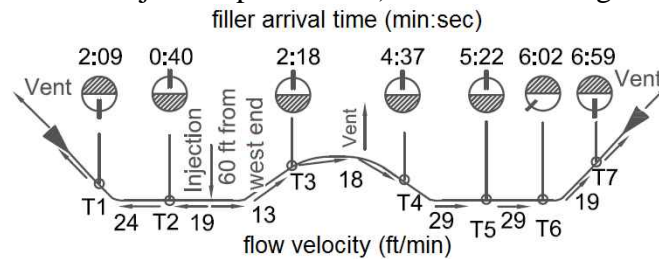


Figure 9-22 Injection rate during Trenton filler injection (Trenton 2)

9.5 Relative Fill

Filler volume was determined by deducting the volume of flexible fillers, collected in buckets through venting from the volume of the filler used from the barrels. The actual flexible filler volume pumped during the injection for all three tendons are shown in Table 9-8 below. The theoretical volume of the flexible filler in the tendon was 96.4 gallons considering 10% of the volume loss in pumping and change in volume due to temperature. Although small, it is not clear why the Cirinject CP injected volume appears to be greater than the calculated volume of the tendon. This may be due to an incorrect accounting of the excess filler material gathered from venting and discharge locations.

Table 9-8 Comparison of theoretical and injected volume for the mockup

Filler material	Theoretical volume (gallons)	Injected volume (Gallons)	Percent difference (%)
Visconrust-2090-P	96.4	91.38	(5.21)
VZ Inject	96.4	95.76	(0.66)
Cirinject CP	96.4	98.75	2.44
Trenton wax (vacuum assist)	96.4	93.46	(3.05)
Trenton wax	96.4	94.64	(1.82)

10 Heat Transfer Analysis

10.1 Model Development

A thermal model was developed to compute the decrease in filler temperature as it moves away from the injection port. Based on conservation of energy, the model aims to estimate the difference in bulk temperature, which represents energy average conditions (Holman 1990), between two locations along the tendon length (Figure 10-1). The model primarily considers forced-convection heat transfer between filler, strands, and duct, and does not take into account the portion of energy transfer through conduction or radiation. These assumptions have been considered reasonable for filler injection given the high-speed nature of injection process, which typically ranges 40-100 ft/min (12.2-20.5 m/min). In addition, the model assumes the filler flow to be laminar, although some flow turbulence is expected due to the presence of prestressing strand bundle inside the duct and the deviated profile of tendons commonly encountered in practice.

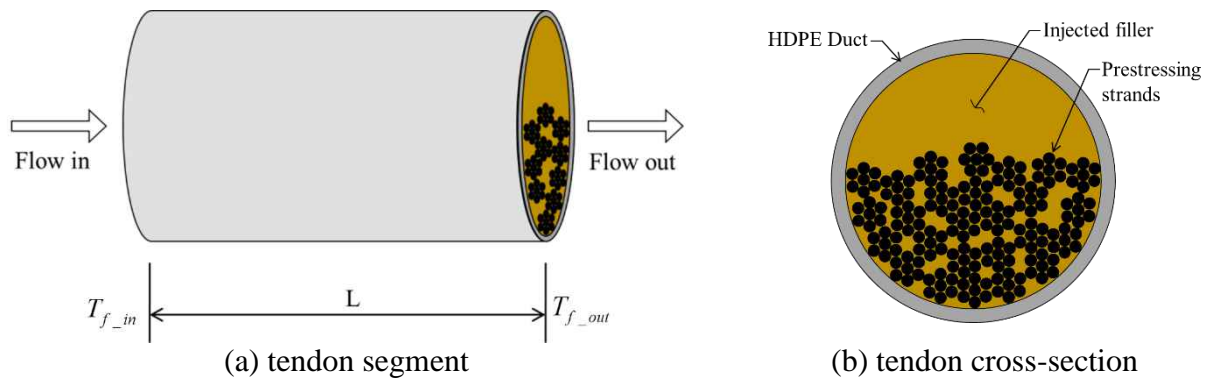


Figure 10-1 Filler flow through a tendon system

Considering a tendon segment of length L (Figure 10-1), the total energy added to the system (q_1) can be expressed in terms of bulk temperature difference (Holman 1990) as

$$q_1 = \dot{m}c(T_{f_in} - T_{f_out}) \quad (1)$$

where \dot{m} is mass flow rate, c is specific heat capacity of filler (assumed to be reasonably constant over the length L), and T_{f_in} and T_{f_out} are the temperatures of filler entering and exiting the duct segment, respectively.

The heat transfer from the filler to the duct (q_2) and the strands (q_3) can be expressed in terms of a heat transfer coefficient (h) as

$$q_2 = hA_d \left(\frac{T_{f_in} + T_{f_out}}{2} - T_d \right) \quad (2)$$

$$q_3 = hA_s \left(\frac{T_{f_in} + T_{f_out}}{2} - T_s \right) \quad (3)$$

where $h = \frac{N_u k}{d_h}$, Nusselt number, $N_u = 3.66 + \frac{0.0668 \left(\frac{d_i}{L} \right) R_e P_r}{1 + 0.04 \left[\left(\frac{d_i}{L} \right) R_e P_r \right]^{2/3}}$, Reynold's number,

$R_e = \frac{Q}{\nu} \times \frac{d_h}{A_i}$, Prandtl number, $P_r = \frac{\mu}{k} \times c$, k is thermal conductivity, d_h is hydraulic diameter, d_i is internal diameter of duct, Q is injection rate, ν and μ are kinematic and dynamic viscosity of filler, respectively, A_i is internal cross-sectional area of duct, A_d and T_d are inner surface area and initial temperature (ambient temperature) of duct, and A_s and T_s are those of strands, respectively.

Combining Eqns. 1, 2, and 3 for energy balance and solving for T_{f_out} yields

$$T_{f_out} = \frac{(2\dot{m}c - hA_d - hA_s)T_{f_in} + 2hA_d T_d + 2hA_s T_s}{2\dot{m}c + hA_d + hA_s} \quad (4)$$

Eqn. 4 provides an explicit expression for the filler temperature exiting the duct segment (T_{f_out}) in terms of flow rate, ambient and injection temperatures, and geometric and thermal properties of filler, strands, and duct.

10.2 Model Validation

The performance of the thermal model developed in the previous section was evaluated through the mockup injection experiments described earlier. Because the heat transfer model developed in the previous section estimates the temperature of filler front, the temperature readings only at the nearest and farthest thermocouples (except mockup VS) from the injection port have been considered (Table 10-1) and compared with the model estimates.

Table 10-1 Comparison of mockup test results with proposed thermal model

Mockup	Distance between reference and exit thermocouples, ft (m)	Average flow velocity between the locations of reference and exit thermocouples, ft/min (m/min)	Temperature, °F (°C) @ reference thermocouple	Temperature, °F (°C) @ exit		
				Thermocouple reading	Estimate by proposed model	% Error of model estimate
<i>CP</i>	102 (31.1)	84.8 (25.8)	177.8 (81.0) @ T3	140.6 (60.3) @ T7	149.2 (65.1)	+ 6.1%
<i>VS</i>	28 (8.5)	43.0 (13.1)	174.8 (79.3) @ T1	147.7 (64.3) @ T2	157.5 (69.7)	+ 6.7%
<i>VZ</i>	102 (31.1)	110.3 (33.6)	186.9 (86.1) @ T3	178.7 (81.5) @ T7	161.2 (71.8)	-9.8%
<i>TR1</i>	140 (42.7)	104.0 (31.7)	173.9 (78.8) @ T2	146.5 (63.6) @ T7	145.1 (62.8)	-1.0%
<i>TR2</i>	102 (31.1)	23.8 (7.3)	168.8 (76.0) @ T3	122.0 (50.0) @ T7	119.8 (48.8)	-1.8%

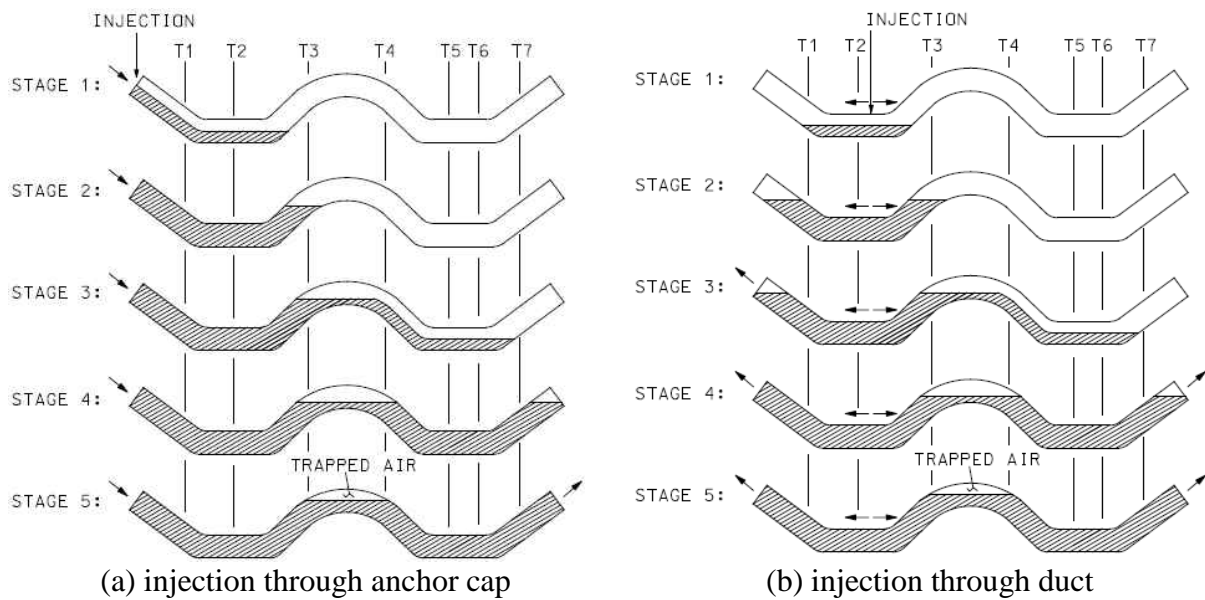


Figure 10-2 Duct filling sequence during mockup injection

As shown in Table 10-1, the proposed model closely matched the filler front temperatures in most of the experiments. Figure 9-8 shows that thermocouple T7 (located near the exit) in mockup VS read higher temperature than preceding thermocouple T6, indicating that either T7 was malfunctioning or the flow still might have been open channel due to complex tendon orientation and, thus, T7 might not read the filler front temperature. The temperature difference along a short segment of tendon (between T1 and T2), was, therefore, considered for mockup VS. The proposed model was found to perform well for a wide range of tendon lengths with different filler materials and injection rates. It is noted that the effective strand surface area used in the model was estimated by the surface area of a virtual cylinder tightly containing all the strands in the multi-strand tendon (surface area of the smallest enclosing circle containing the strand cross-section). More detailed discussion on effective strand surface area estimation has been provided later in this report.

10.3 Sensitivity of filler front temperature to injection parameters

After validating the proposed thermal model in the previous section with mockup test results, this section provides a sensitivity analysis for filler injection, which can be useful in selecting appropriate injection parameters. The explicit expression derived earlier to estimate filler front temperature (Eqn. 4) shows that the frontal temperature is a function of multiple injection parameters, namely, effective strand surface area, tendon length, injection rate, ambient temperature, injection temperature, and number of prestressing strands. The sensitivity of filler temperature to these parameters (Table 10-2) has been investigated using the proposed model. It is noteworthy that the filler front temperature estimated by the model is believed to be conservative because the model assumes full pipe flow; in reality, however, the deviators, piping bends, and elbows potentially make the flow open channel in certain segments of the tendon, allowing mixing of newly pumped filler with older fillers and, thereby, elevating the frontal temperature.

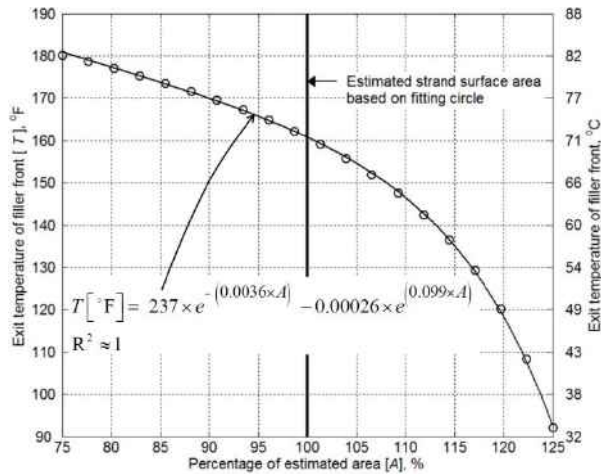
As mentioned earlier, the effective strand surface area in this report has been estimated based on the surface area of a virtual cylinder tightly containing the strands. Figure 10-3a illustrates how the filler front temperature exiting the tendon changes with the strand area, where the cylinder-based estimation has been considered as the baseline. For example, if the area is 10% less than the baseline, the exit temperature increases nearly 6%, whereas 10% more area decreases the temperature by 9%. Figure 10-3a also shows that the exit temperature can be considered to be exponentially related to the effective strand surface area. Thus, the filler temperature has been found quite sensitive to the strand surface area, indicating that tendon comprising fewer or more strands significantly affect the filler temperature. In addition, the high sensitivity suggests that a reasonable estimation of effective strand surface area is critical for accurately computing the filler front temperature. An investigation on the adequacy of this cylinder-based area estimation is reported in the following section.

Case II (Table 10-2) analyzes the sensitivity of exit filler temperature to tendon length. A 19-strand tendon has been considered with injection temperature of 220°F (104.4°C); other parameters are listed in Table 10-2. Figure 10-3b shows that the exit temperature exponentially decays with tendon length. Similarly, the sensitivity of filler temperature to injection rate (*Case III*) is shown in Figure 10-3c. As shown in the figure, the filler temperature rises exponentially with injection rate. The effects of ambient and injection temperatures (*Case IV* and *Case V*, respectively) have also been investigated and a linear relationship with frontal temperature has

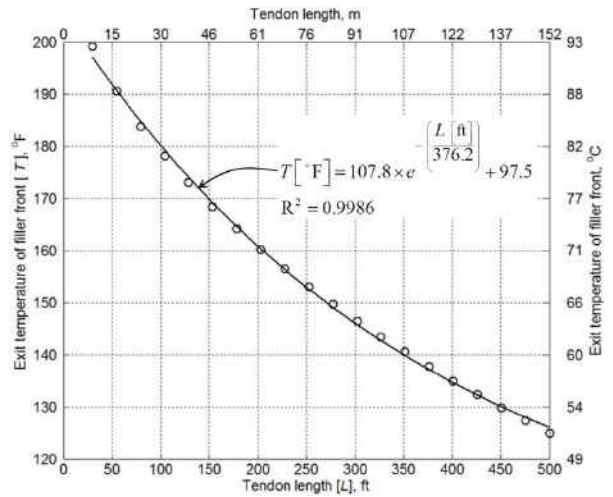
been found for both cases. Finally, as expected, Figure 10-3d shows lower filler temperature in case of higher number of strands for the same tendon length.

Table 10-2 Sensitivity study matrix

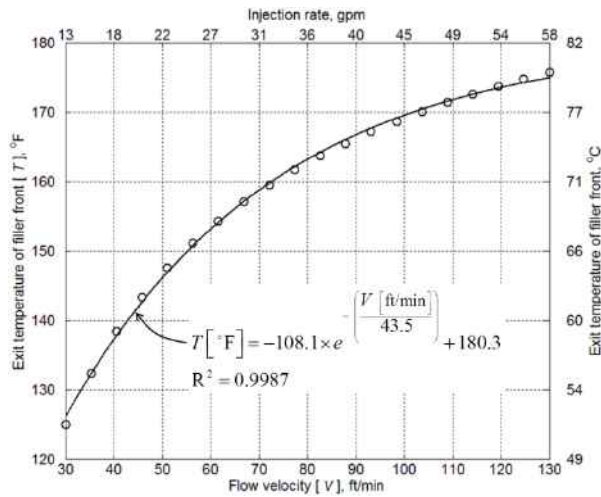
Case	Effective strand surface area	Tendon length, ft (m)	Injection rate, gpm	Ambient temperature, °F (°C)	Injection temperature, °F (°C)	Number of strands	Variable
<i>I</i>	-	200 (61)	33.5	70 (21.1)	220 (104.4)	19	Effective strand surface area
<i>II</i>	Based on smallest enclosing circle	-	33.5	70 (21.1)	220 (104.4)	19	Tendon length
<i>III</i>	Based on smallest enclosing circle	200 (61)	-	70 (21.1)	220 (104.4)	19	Injection rate
<i>IV</i>	Based on smallest enclosing circle	200 (61)	33.5	-	220 (104.4)	19	Ambient temperature
<i>V</i>	Based on smallest enclosing circle	200 (61)	33.5	70 (21.1)	-	19	Injection temperature
<i>VI</i>	Based on smallest enclosing circle	200 (61)	33.5	70 (21.1)	220 (104.4)	-	Number of strands



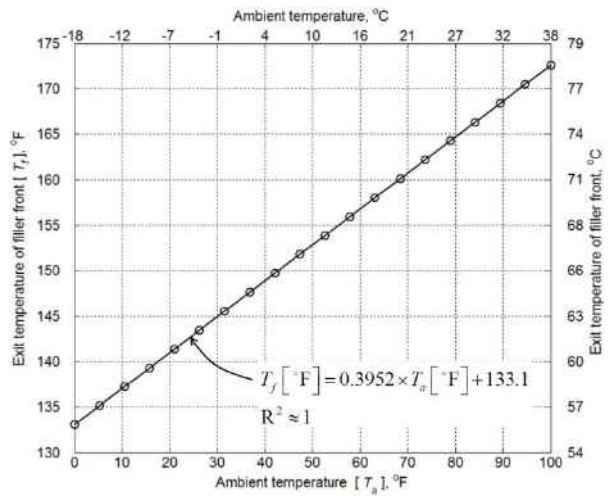
(a)



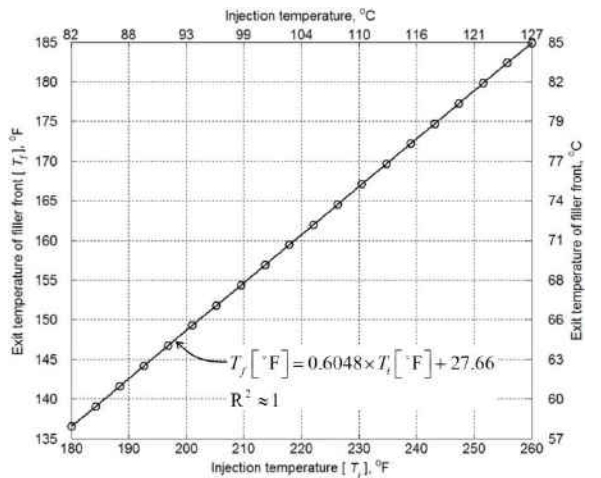
(b)



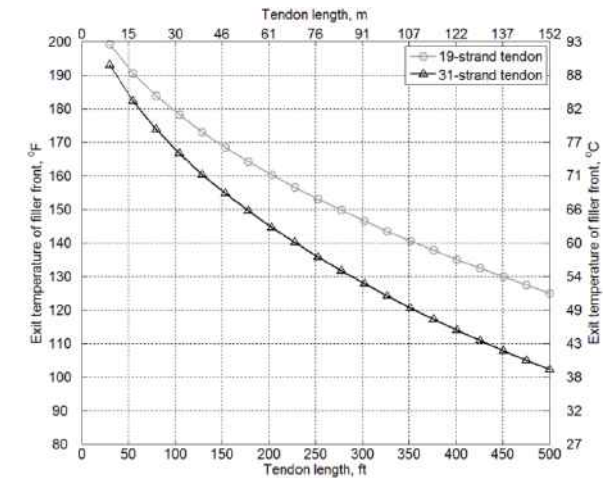
(c)



(d)



(e)



(f)

Figure 10-3 Sensitivity study

10.4 Estimation of effective strand surface area

Individual strands in a multi-strand tendon system are typically pushed through one end of the duct and are passed over multiple deviators. In addition, the current construction practice does not enforce that a strand is anchored at the same wedge locations at the two ends, which leads to twisted, non-parallel strands inside duct, some strands crossing each other. Thus, the practical strand arrangement inside a duct might be extremely complex, which poses challenges to accurate estimation of the effective surface area of strands that are in direct thermal contact with the flowing filler.

In an attempt to determine the effective strand surface area with reasonable accuracy, an estimation based on the smallest enclosing circle (Figure 10-4b, d, f) has been proposed in this report. In practice, the strands are expected to assemble as shown in Figure 10-4a, c, e due to the presence of deviators, suggesting that the total arc length of the curved frontal surface (highlighted in Figure 10-4) represents the effective strand surface directly interacting with filler. However, with the specified duct diameter (FDOT 2013), it can be observed from Figure 10-4 that the total arc length of the curved frontal surface is comparable to the perimeter of the smallest circle enclosing all the strands in the tendon. As shown in Figure 10-4, three different strand patterns—19-strand, 27-strand, and 31-strand—have been considered and the differences between estimates based on frontal surface and enclosing circle have been found minimal—0.97%, 4.9%, and 2.9%, respectively. Thus, a generalized and simple, yet reasonably accurate, measure of the effective strand surface area was obtained based on smallest enclosing circle. The performance of the thermal model developed in this report with this estimation of strand surface area has been tested with mockup experiments discussed in earlier section.

10.5 Injection Pressure

Individual strands in a multi-strand tendon system are typically pushed through one end of the duct and are passed over multiple deviators. In addition, the current construction practice Another critical injection parameter is the minimum pressure at which the filler must be pumped at the injection end to overcome frictional resistance over the duct length. The injection pressure is a function of filler temperature because the filler viscosity increases as its temperature decreases away from the injection point, requiring higher pumping pressure to avoid possible clogging. An accurate estimation of injection pressure is, therefore, necessary for successful injection. To determine the minimum injection pressure, a simplified approach has been adopted in this section and has been illustrated with experimentally obtained material properties of Cirinject CP filler.

To obtain an estimate of the required minimum injection pressure for different tendon lengths, filler front temperatures were determined first using Eqn. 4. These temperatures were then used to estimate the average viscosity within the duct length from experimentally determined viscosities of Cirinject CP filler with shear rate of $1/50 \text{ s}^{-1}$ for different temperatures (Figure 10-5). The pressure loss was then calculated using Darcy–Weisbach equation (Hunt 1995) for different tendon lengths and flow velocities. Figure 10-6 illustrates that the pressure loss for shorter tendon lengths (up to ~150 ft or ~46 m) does not significantly vary with flow velocity, but becomes increasingly sensitive to it for longer lengths. This simplified approach in estimating the minimum injection pressure assumes laminar flow in a straight horizontal tendon. Furthermore, if vacuum assisted injection is used, then the pressure loss would be reduced by the magnitude of the vacuum pulled on the specimen. In reality, the strand bundle is expected to cause some turbulence and the tendons often have piping bends, elbows, and deviated segments

rather than a straight profile. Therefore, this approach should be viewed as an attempt to obtain a basic understanding on evaluating the pumping pressure; more detailed analysis is required for a better estimation. Mockup trials to confirm the efficacy of the injection should also be conducted.

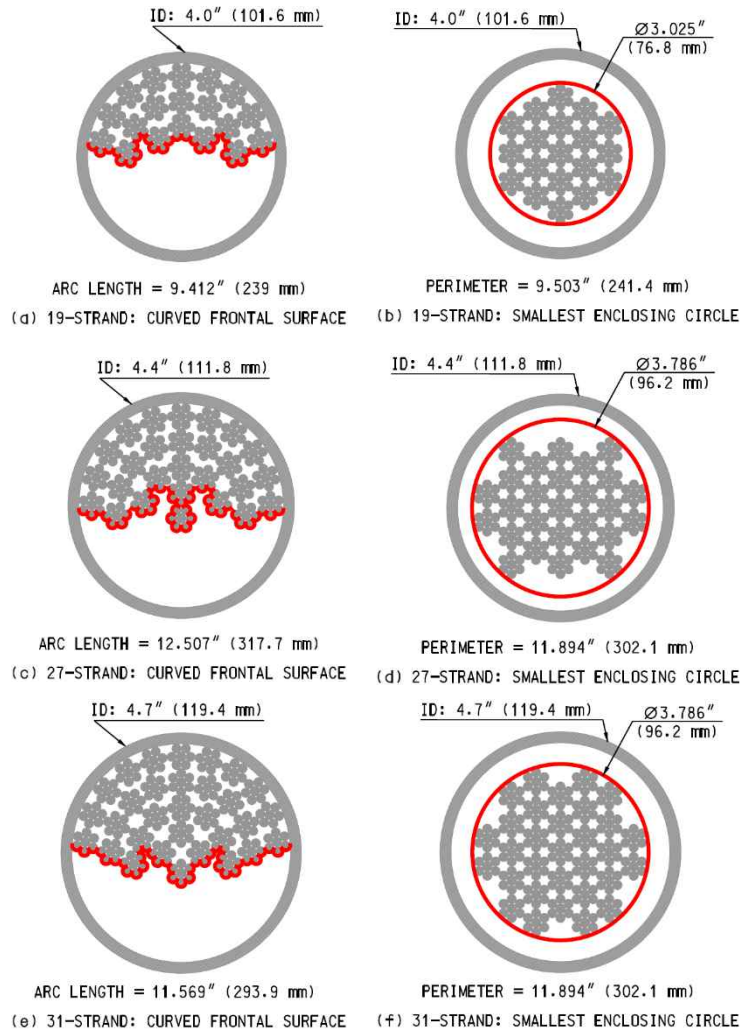


Figure 10-4 Effective strand surface

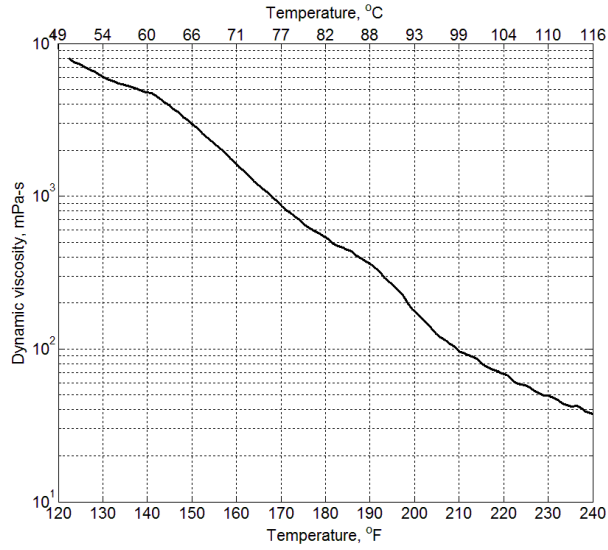


Figure 10-5 Experimentally obtained viscosity for Cirinject CP

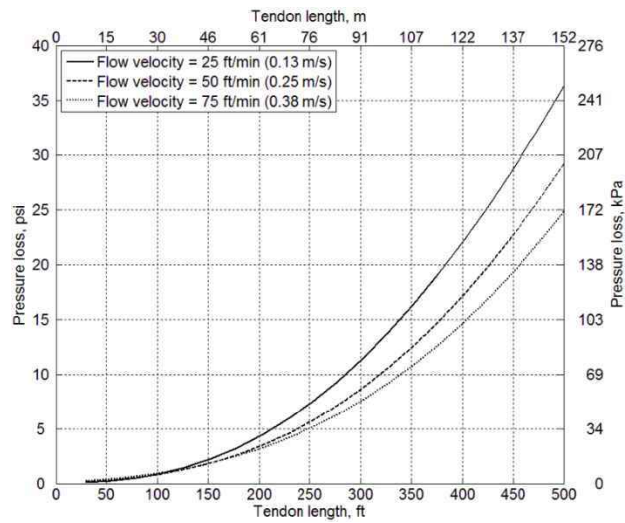


Figure 10-6 Pressure loss

11 Summary and Conclusions

Four alternative flexible filler materials were selected and tested in a 200-ft mockup of a post-tensioning tendon to test for constructability and to understand the nuances of handling and injecting flexible fillers. The tendons were composed of nineteen 0.6-in. diameter prestressing strands that were lightly prestressed to ensure that the strands and duct were positioned as they would be in a fully stressed PT tendon. Temperature and pressure were measured during and after injection to track the behavior of the materials. The following are preliminary observations.

The target injection rate range was 50-80 ft/min. The average injection rate for Visconorust, VZ Inject and Cirinject CP was 49 ft/min, 75 ft/min, and 62 ft/min respectively. Injection rate for Visconorust and Cirinject CP were close to the target injection rate, while the VZ Inject rate was higher. The average injection rate for Trenton 1 and Trenton 2 was 100 ft/min and 21.5 ft/min, respectively.

Injection rates and venting procedures were varied among the five mockups, primarily in an effort to determine the most suitable approach. In spite of the variation of procedures, all of the strands in each of the specimens were well-coated with filler material even though the first two tendons injected contained a void at the top of the duct cross-section in the parabolic portion of the mockup. These voids were thought to be the result of inadequate venting procedures and not the PT system or individual filler products used. At the completion of these mockup tests, no cause to restrict use of any of the PT systems or filler products was found.

To better understand the heat transfer process and obtain an estimation on heat loss of filler front, a closed-form heat transfer model was developed and compared to the data gathered during the mockup injections. The experimental data confirmed the applicability of the thermal model to a wide range of tendon lengths, material, and injection parameters. After validating with experiments, the model was then used to determine the sensitivity of filler temperature to various field parameters (e.g., tendon length, ambient temperature, injection rate) that can provide critical guidance on constructability of unbonded tendons with flexible fillers. The pressure loss for different flow velocities and tendon lengths has also been estimated to help decide injection pressure. Knowing the tendon geometry, hydraulic injection conditions, and filler material properties, this model can be used to compute the rate of cooling of filler front during injection, which can then be used to determine the maximum length of continuous injection. In addition, a method for determining the effective strand surface area, which is important to the heat transfer mechanism, was developed for use in the thermal model.

References

- American Society for Testing and Materials (ASTM) D 3350, (2012), “Standard specification for polyethylene plastics pipe and fittings materials”, Pg 2.
- Blanchard, B. (2010), “Segmental Bridges – It’s a Construction Technique with Design Implications: From the Florida Department of Transportation’s Perspective.” (Presentation)
- BS/EN 12201, (2003), “Plastics piping systems for water supply –Polyethylene (PE) – Part 1: General”.
- BS/EN 12201, (2003), “Plastics piping systems for water supply –Polyethylene (PE) – Part 2: Pipes”.
- DYWIDAG SYSTEM INTERNATIONAL (DSI), (2007), “External 19-0.6” MA system 100 assembly drawing”, Drawing: MA 68 19 013.
- ETA-06/0226 EOTA (2012), “Post-tensioning kit for prestressing of structures”, 37-38.
- ETAG-013 (2002), “Guideline for European Technical Approval of Post-tensioning Kits for Prestressing of Structures”. European Organisation for Technical Approvals.
- FDOT Standard Specification for Road and Bridge Construction, (2013), “Post-tensioning components”, Rev. 1-1-13.
- FHWA International Technology Exchange Program, (2001), “Performance of concrete segmental and cable-stayed bridges in Europe”.
- Freyssinet Prestressing, (2010), “The system of the inventor of prestressed concrete”, pp 8.
- Holman, J.P. (1990). “Heat Transfer”, McGraw-Hill, New York.
- Hunt, B.W. (1995). “Fluid mechanics for Civil Engineers”, Dept. of Civil Engineering, University of Canterbury, Christchurch, New Zealand.
- Institut français des sciences et technologies des transports, de l'aménagement et des réseaux (IFSTTAR), 2013, “Wax injection, from a process point of view”, Presentation.
- Post-Tensioning Institute (PTI) (2006). “Post-tensioning Manual 6th Edition” pp 59.
- V Structural LLC (VSL), (2004), “ECI 6-19 external tendon with bonded anchorage overall assembly”, Drawing: A153.
- VSL International Ltd. (2008), “External Post-tensioning - Design considerations and examples from the past”.

Appendix A—Filler Rheology Testing

Properties of flexible fillers are greatly dependent on the temperature at which they are pumped. Particularly, viscosity changes significantly between the solid (high viscosity) and liquid state (low viscosity) of these fillers. Viscosity of a material is defined by the resistance it offers against the motion. Viscosity of a material is a function of the temperature of the material and shear stress applied on it. Thus, a series of tests were conducted in the State Materials Office (SMO) at constant applied shear and generating plots of viscosity as a function of temperature for each flexible materials used in the mockup.

Tests were conducted on AR 2000 ex apparatus which is commonly used for the viscosity tests.

A.1 Test Procedures

1. Set the clean plates on the instrument.
2. Set the procedure including the ramp temperatures (start and end temperature of the wax), cooling temperature after test and sampling rate.
3. Calibrate the instrument by pushing the zero gap button. This will ensure that the gap between plates is zero. Increase the gap between plates by computer input.
4. Scoop out sample and place it on the lower plate. Smear it on the lower plate to make it even.
5. Set the gap to 1000 micro meters. This makes the upper plate move downwards and squeezes the sample between two plates.
6. Trim the extra wax outside the diameter of the plate.
7. Close the instrument and press start to start the shear test. The coil inside the instrument heats up and thus increases the temperature of the sample. Temperature of the sample increases to the start test temperature of the filler.
8. Data is recorded by the instrument at the sample rate fed in the procedure. Data recording stops when the temperature reaches to the end test temperature.
9. Allow instrument to cool down. Open instrument and increase the gap between plates. Clean both plates with solvent and repeat procedure for different shear rate.

A.2 Test Results

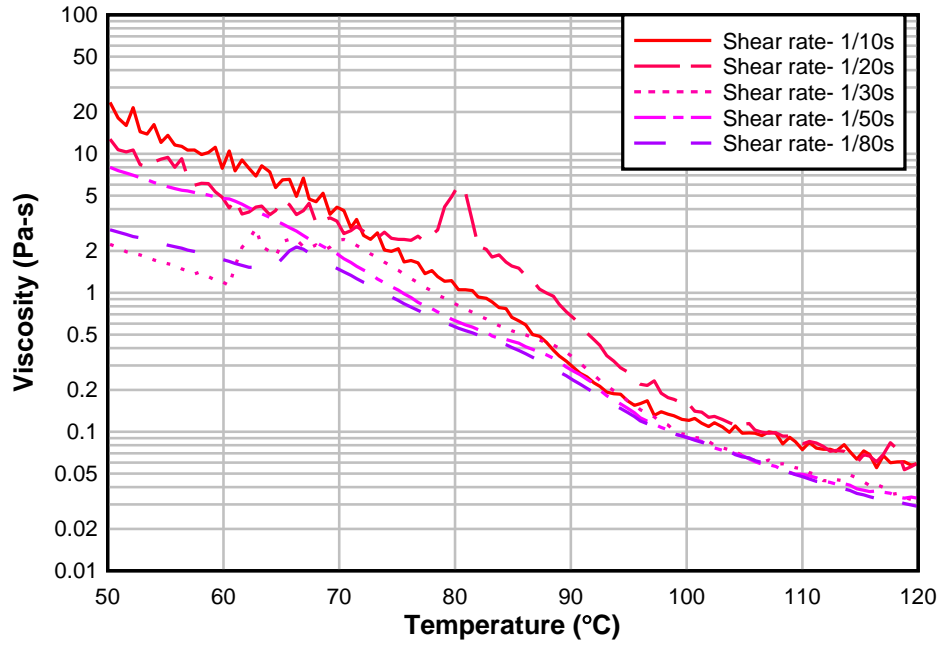


Figure A-1 Cirinject filler results

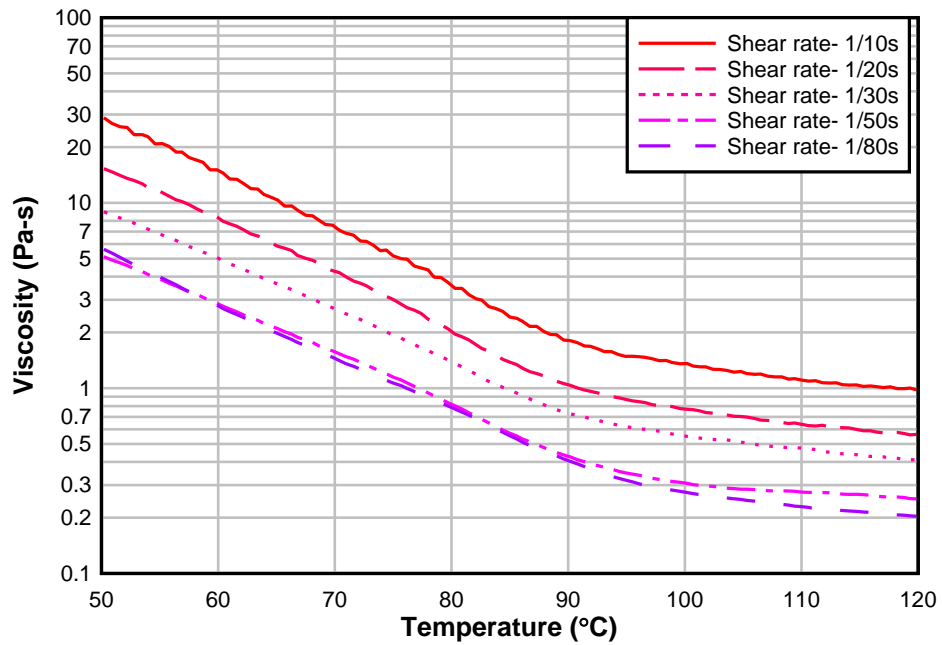


Figure A-2 Visconorust filler results

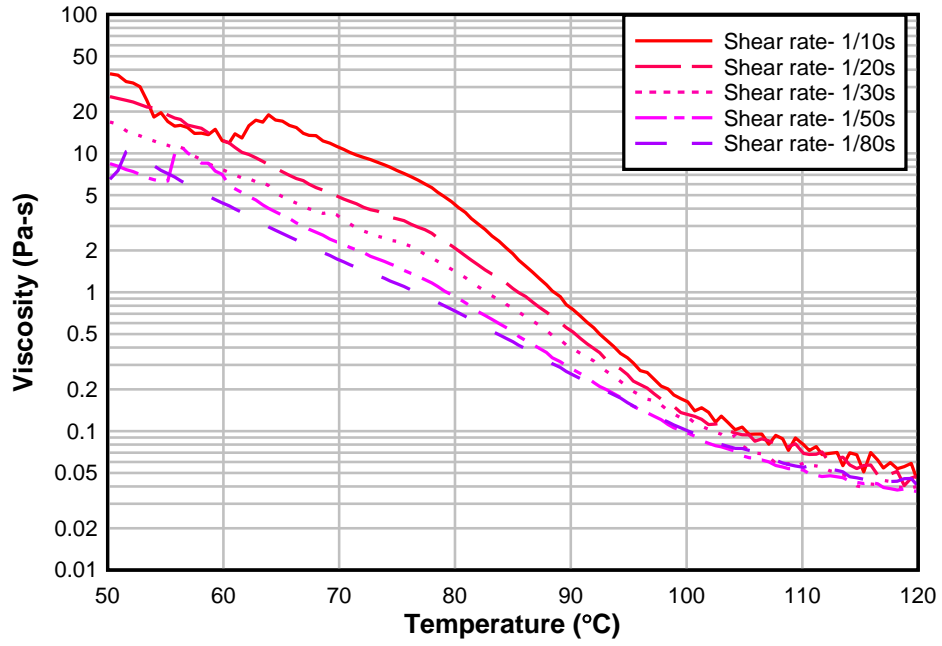


Figure A-3 VZ Inject filler results

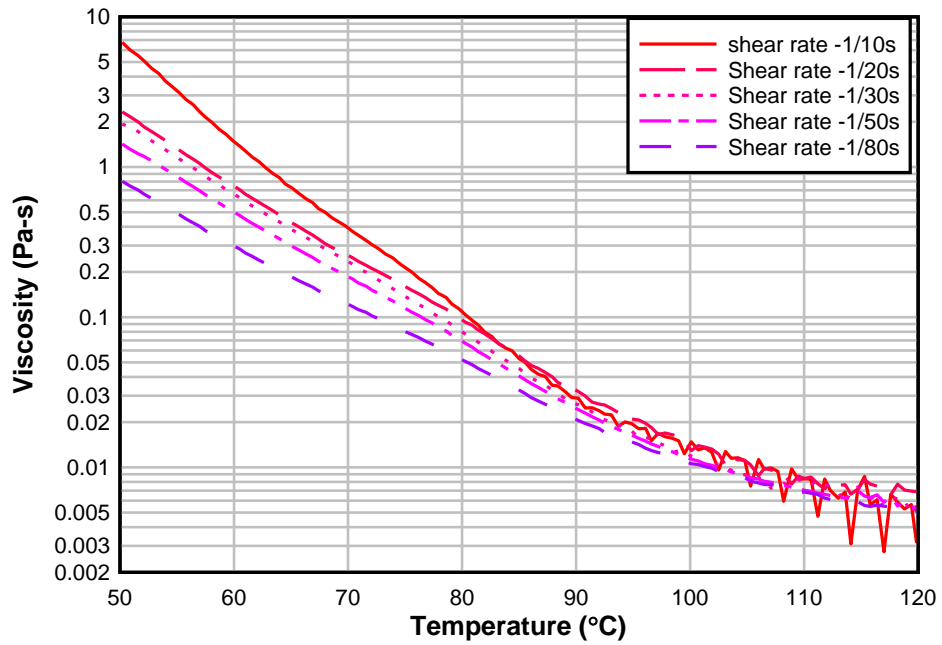


Figure A-4 Trenton filler results

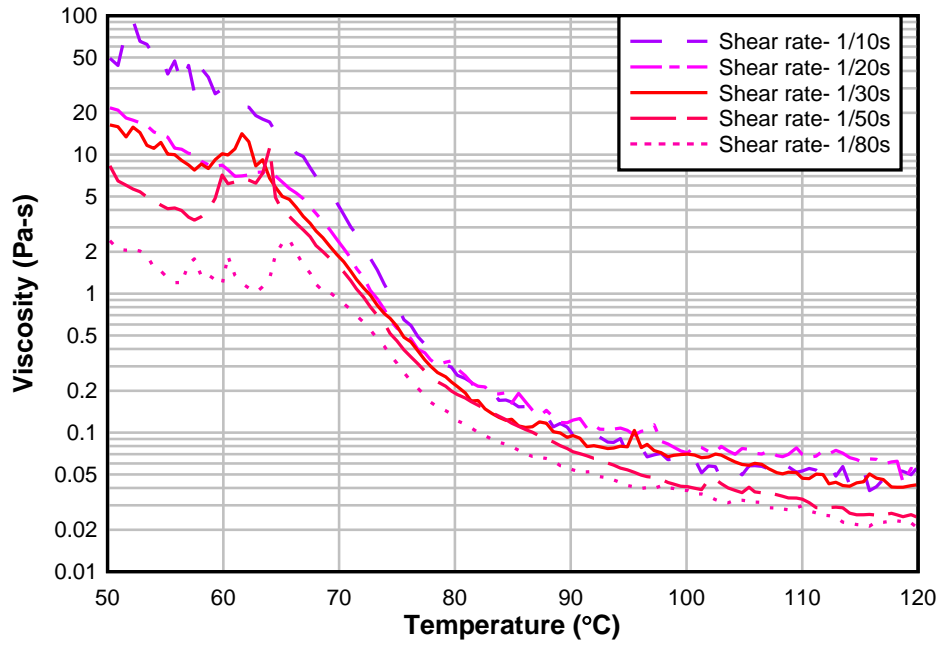
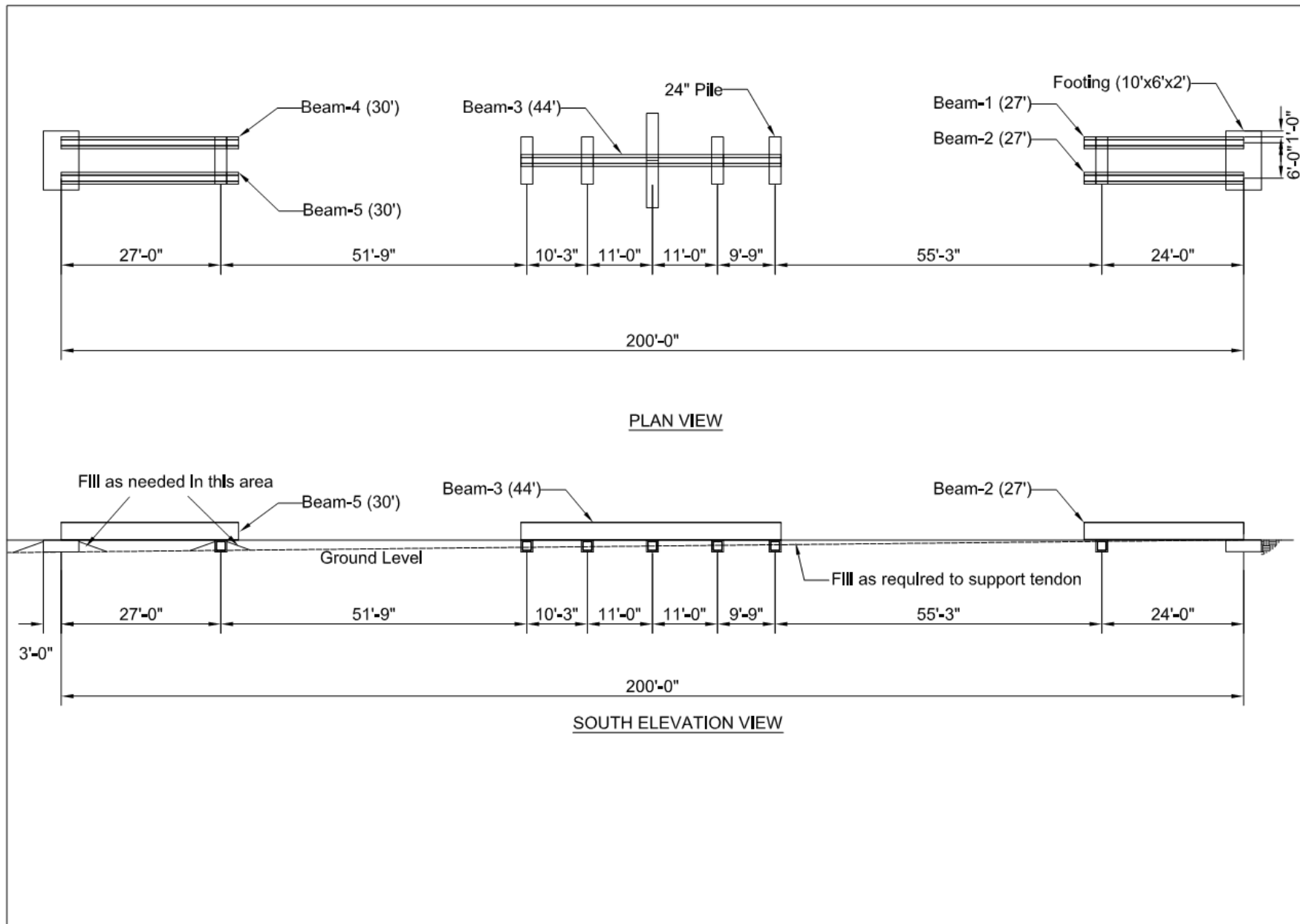

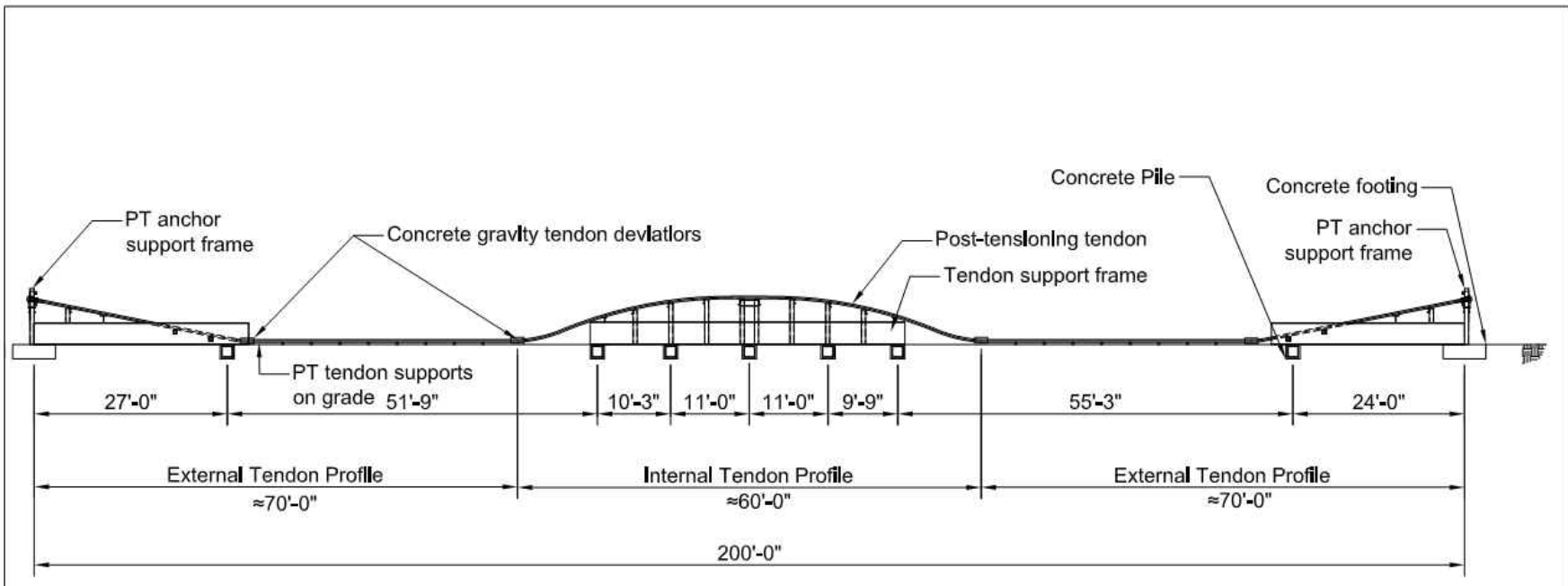


Figure A-5 Sanchem filler results


Appendix B—Mockup Frame Construction Drawings

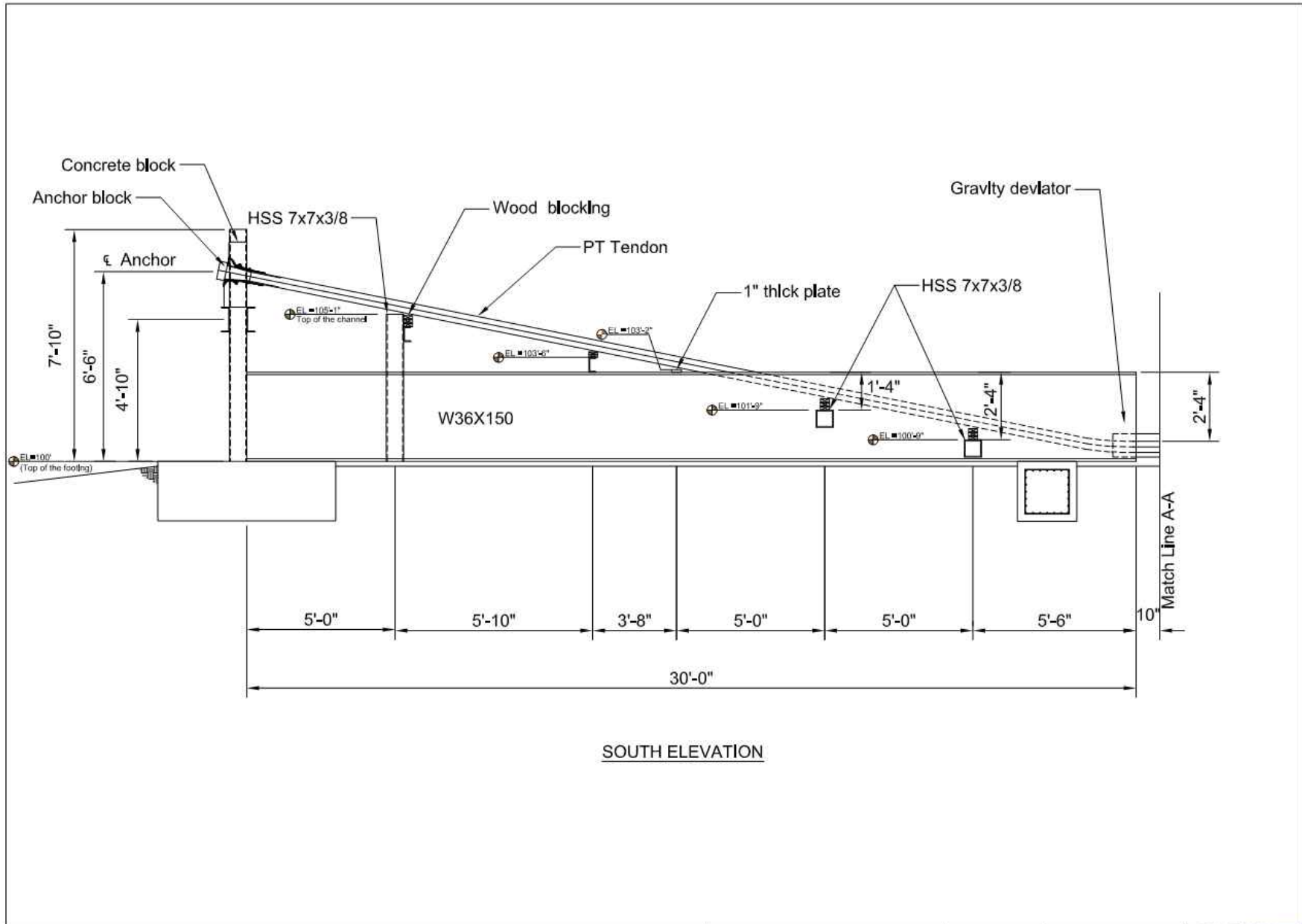


Prepared By: Rahul Bhatla		University of Florida	Rev:02	Page 1 of 20	
Project No: BDV31-977-15	Unbonded Tendon Mock-Up	Foundation Plan-Preliminary Design	05/19/2014	Scale: $\frac{3}{64}'' = 1'-0''$	




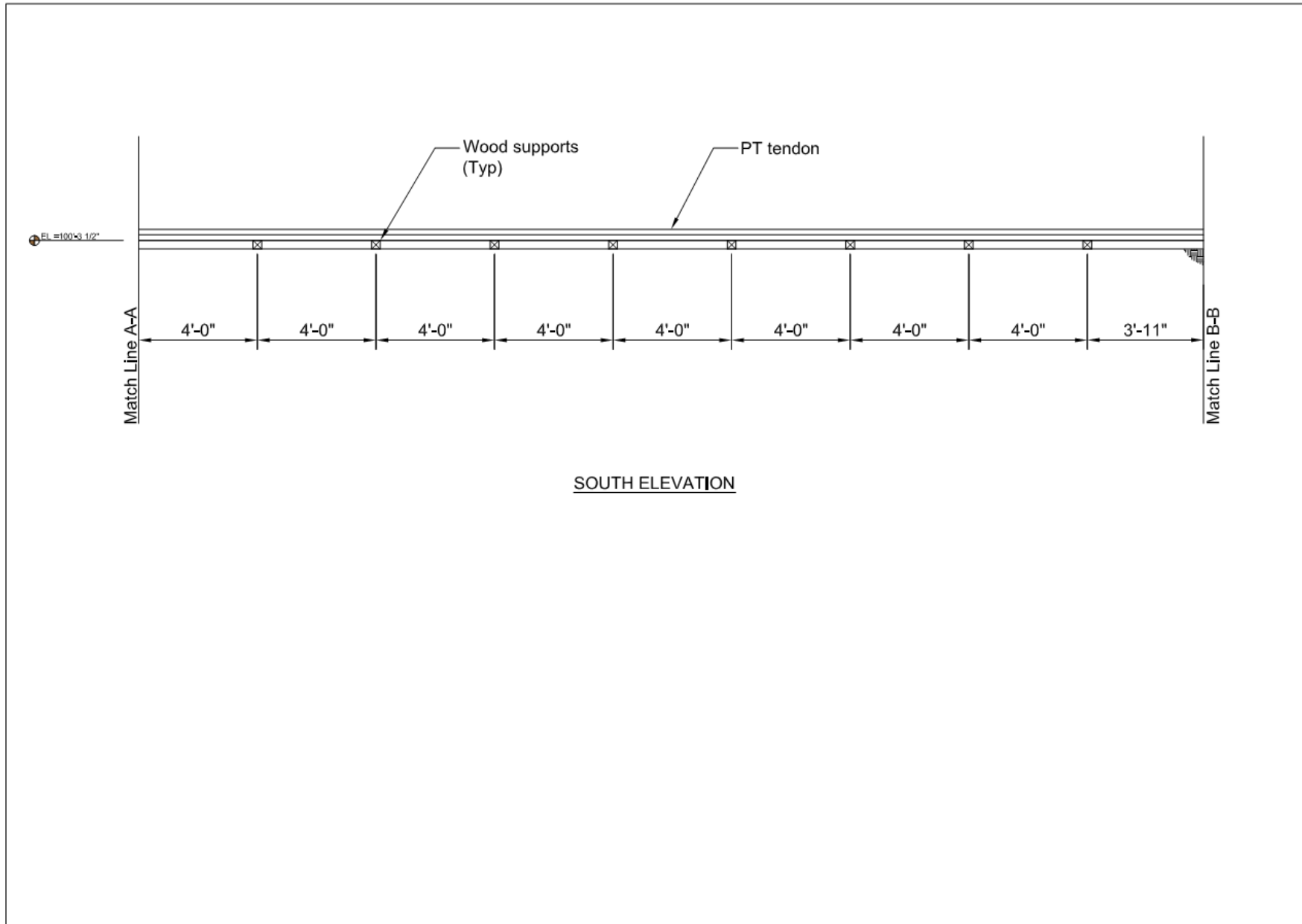
SOUTH ELEVATION

Prepared By: Rahul Bhatia	University of Florida	Rev:02	Page 2 of 20	
Project No: BDV31-977-15	Unbonded Tendon Mock-Up	Elevation With Tendon Profile	05/19/2014	




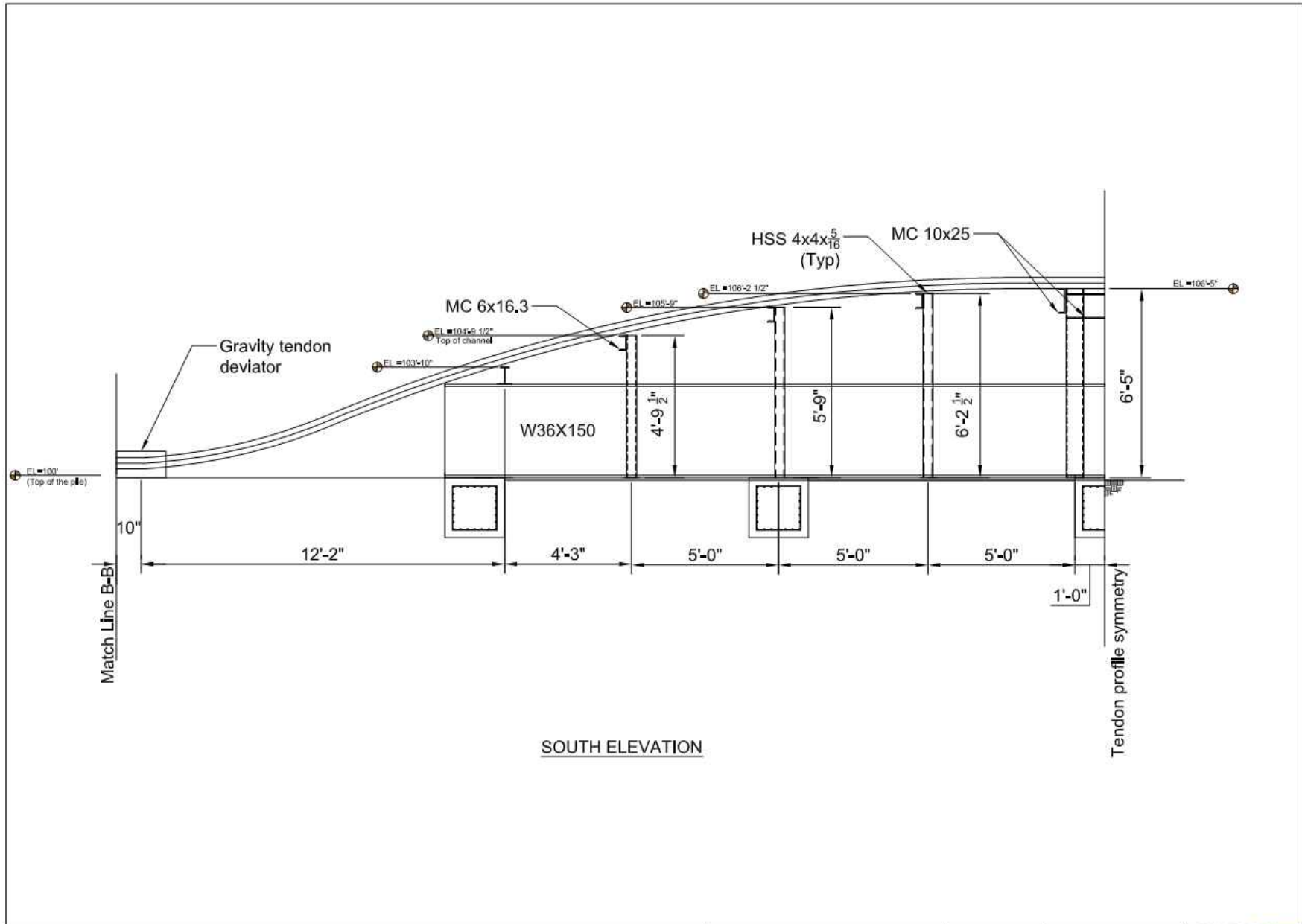
SOUTH ELEVATION


Prepared By: Rahul Bhatia		University of Florida	Rev:02	Page 3 of 20	
Project No: BDV31-977-15	Unbonded Tendon Mock-Up	Tendon Anchor Support	05/19/2014	Scale: 1/4"=1'-0"	

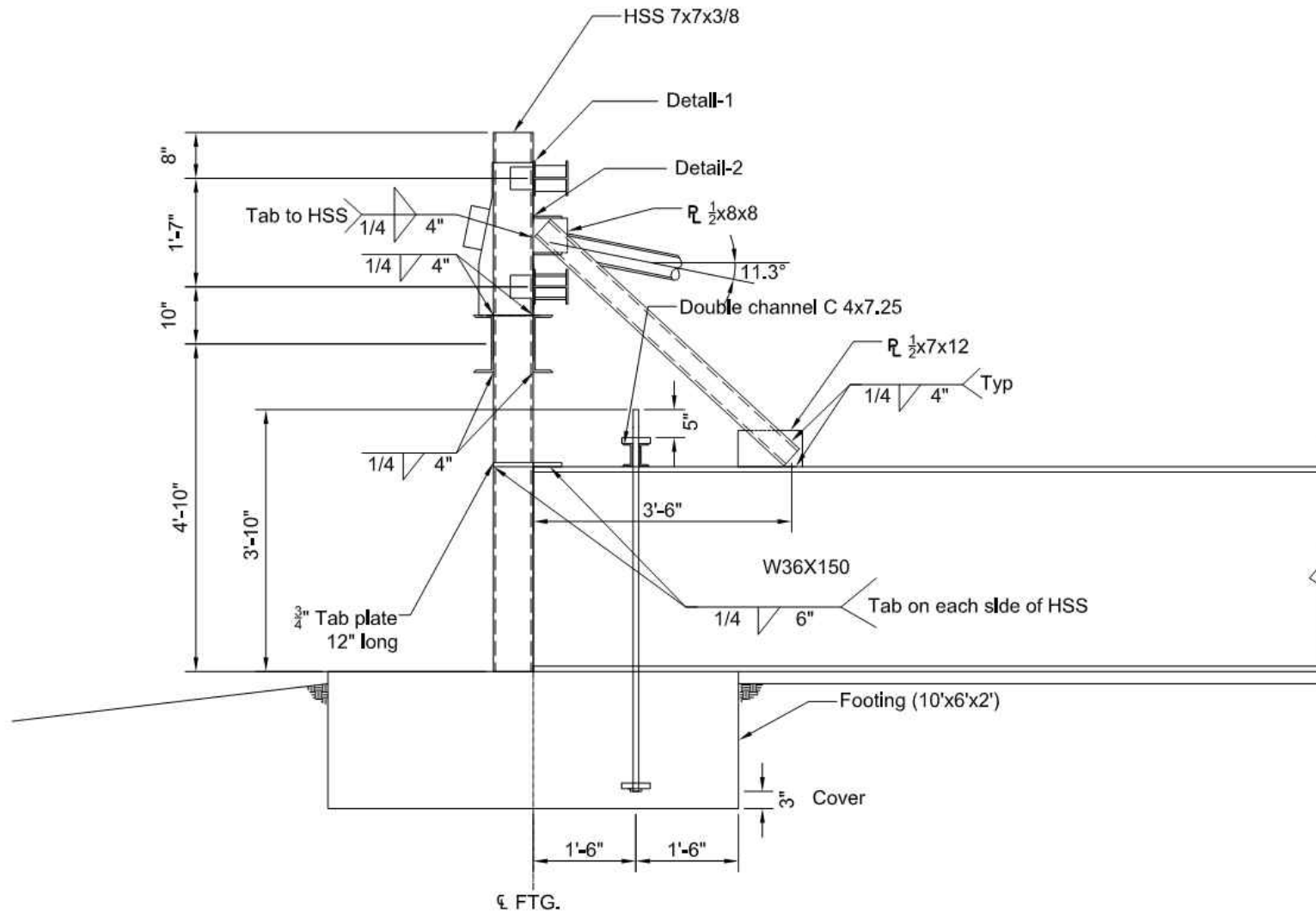


SOUTH ELEVATION

Prepared By: Rahul Bhatia			University of Florida	Rev:02	Page 4 of 20	
Project No: BDV31-977-15	Unbonded Tendon Mock-Up	Tendon Free Length	05/19/2014	Scale: 1/4"=1'-0"		

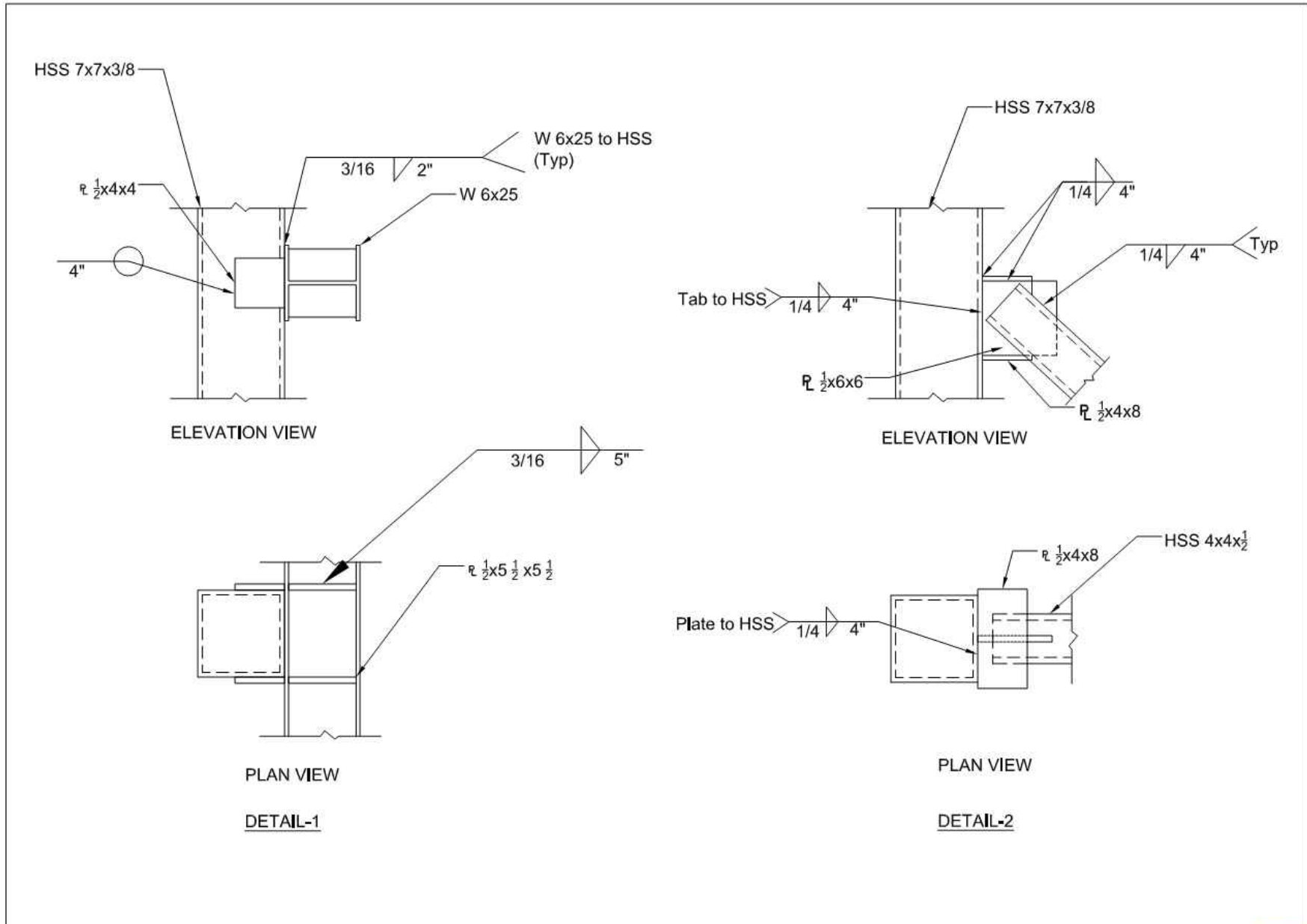


Prepared By: Rahul Bhatia		University of Florida		Rev:02	Page 5 of 20	
Project No: BDV31-977-15	Unbonded Tendon Mock-Up	Tendon Middle Support		05/19/2014	Scale: 1/4"=1'-0"	

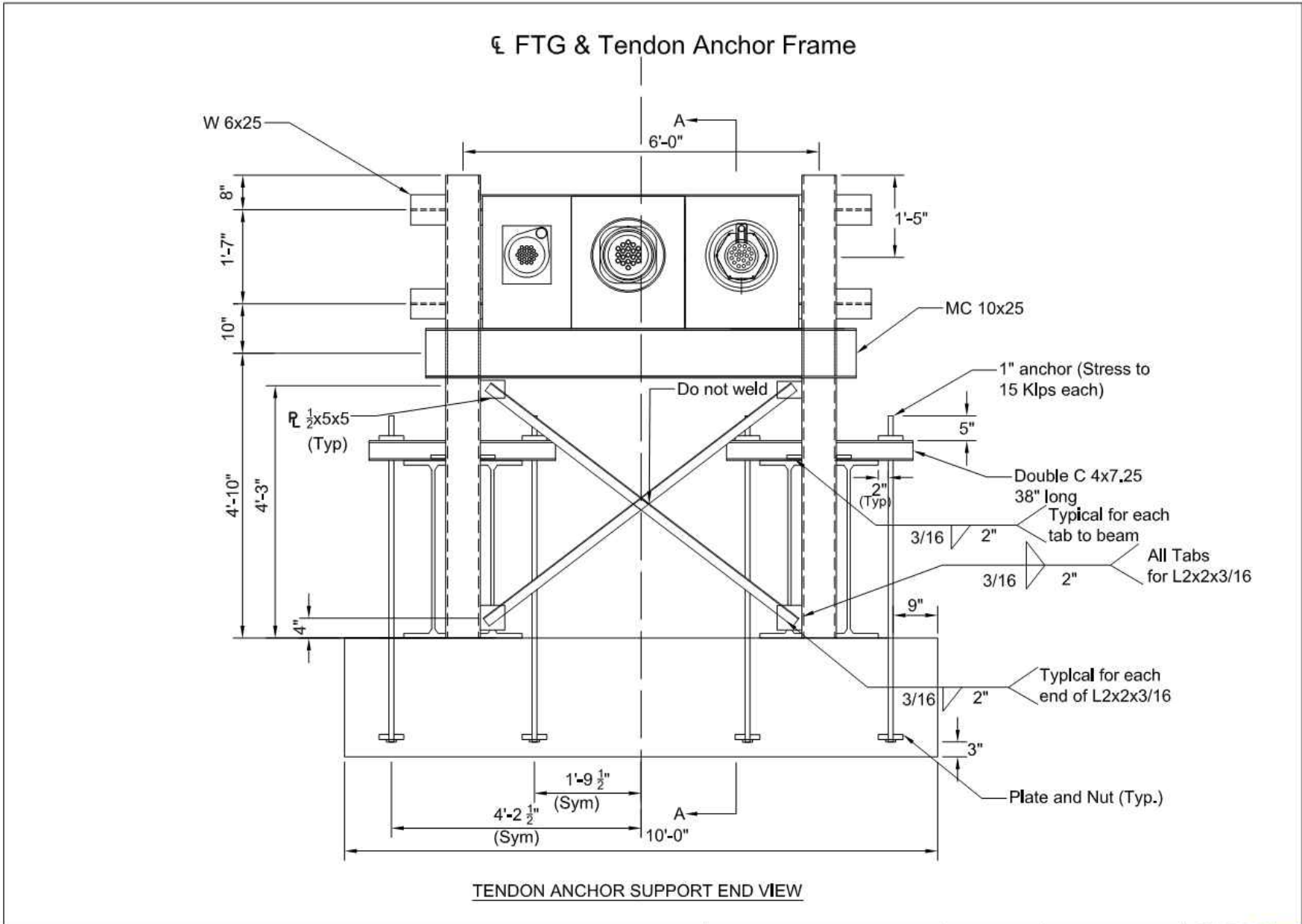



TENDON ANCHOR SUPPORT SIDE VIEW

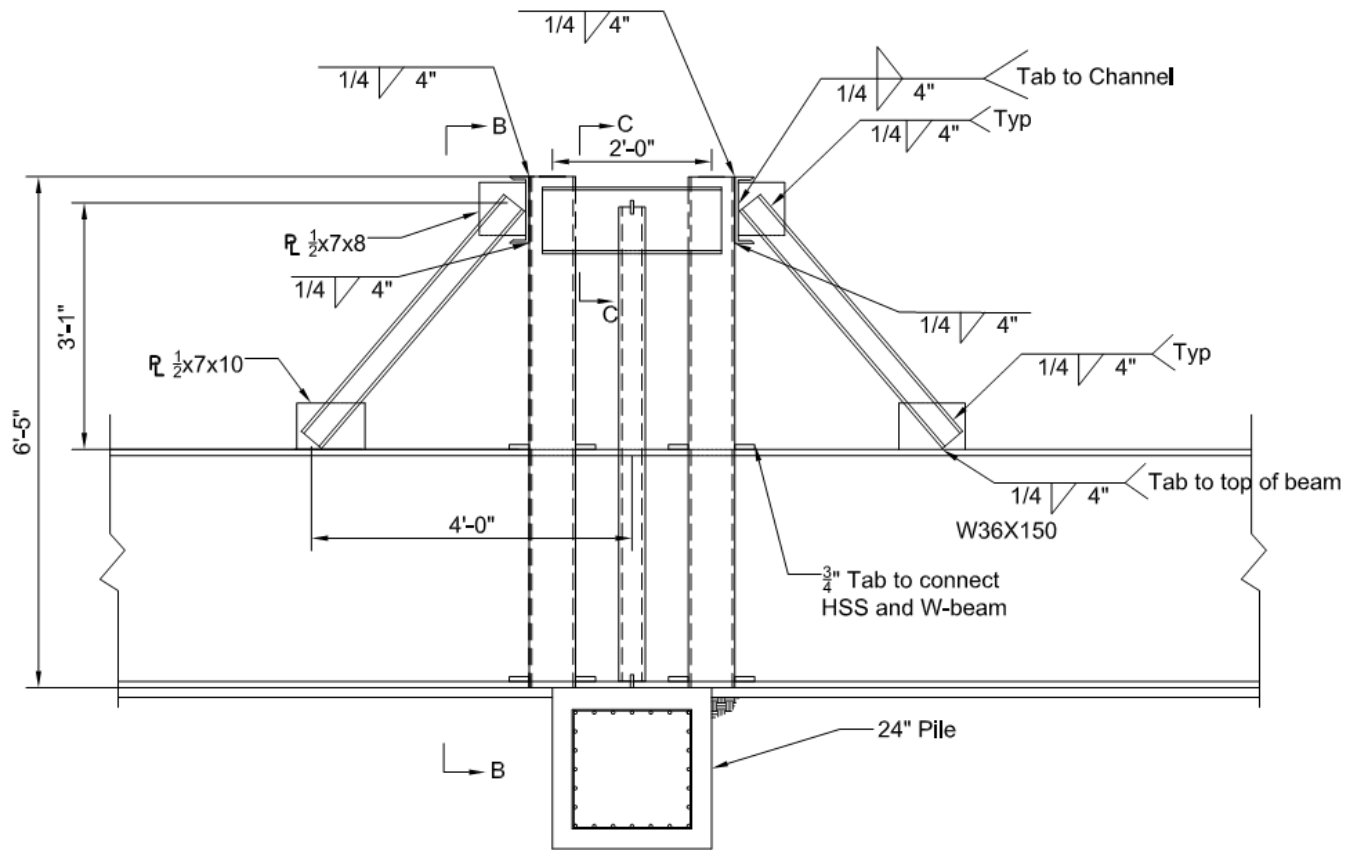
Prepared By: Rahul Bhatia	University of Florida	Rev:02	Page 6 of 20	
Project No: BDV31-977-15	Unbonded Tendon Mock-Up	Tendon Anchor Details	05/19/2014	




Prepared By: Rahul Bhatia	University of Florida	Rev:02	Page 7 of 20	
Project No: BDV31-977-15	Unbonded Tendon Mock-Up	Tendon Anchor Details-Connections	05/19/2014	Scale: 1"=1'-0"

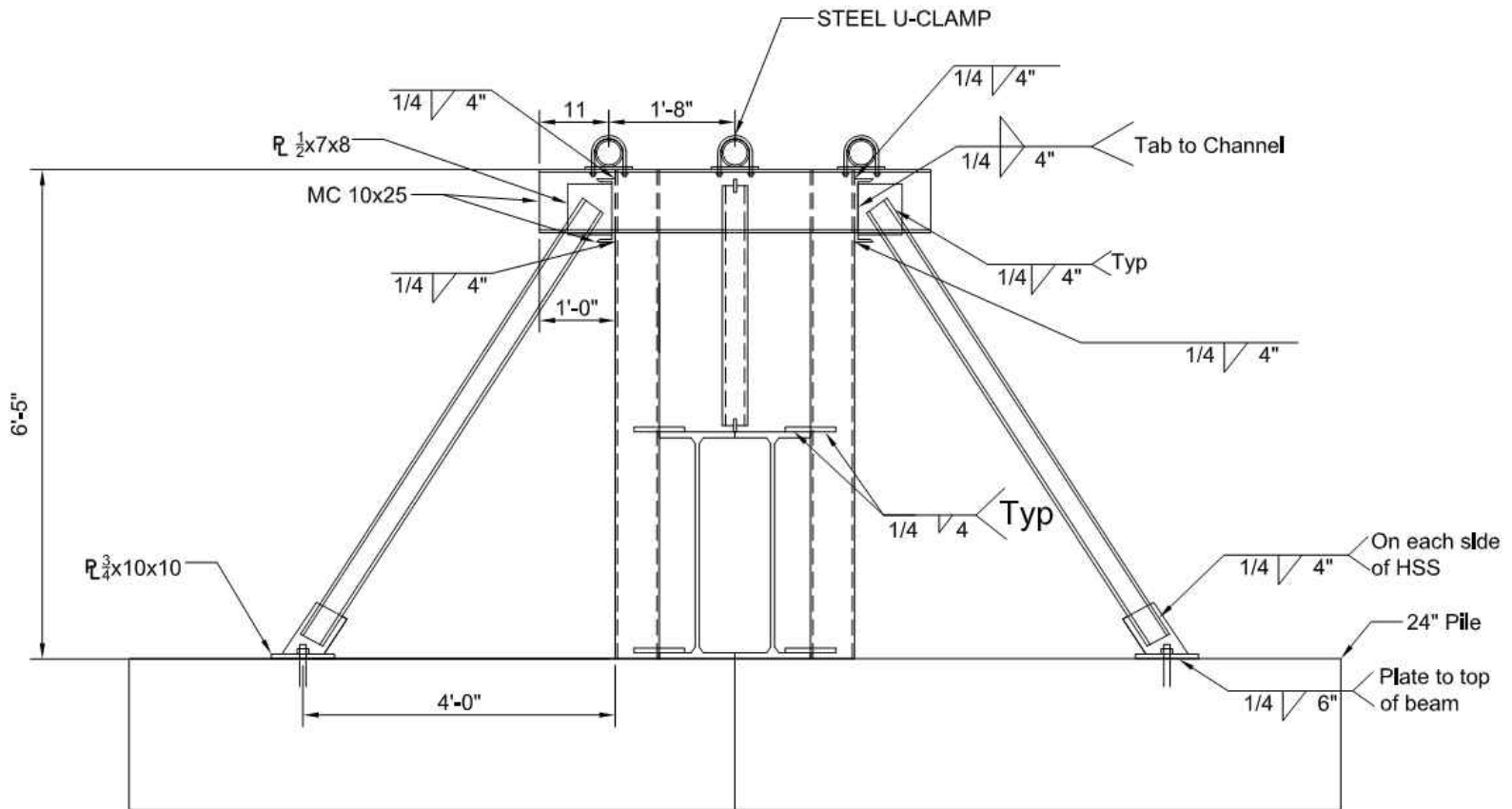


Prepared By: Rahul Bhatia		University of Florida	Rev:02	Page 8 of 20	
Project No: BDV31-977-15	Unbonded Tendon Mock-Up	Tendon Anchor Details	05/19/2014	Scale: $\frac{1}{2}"=1'-0"$	




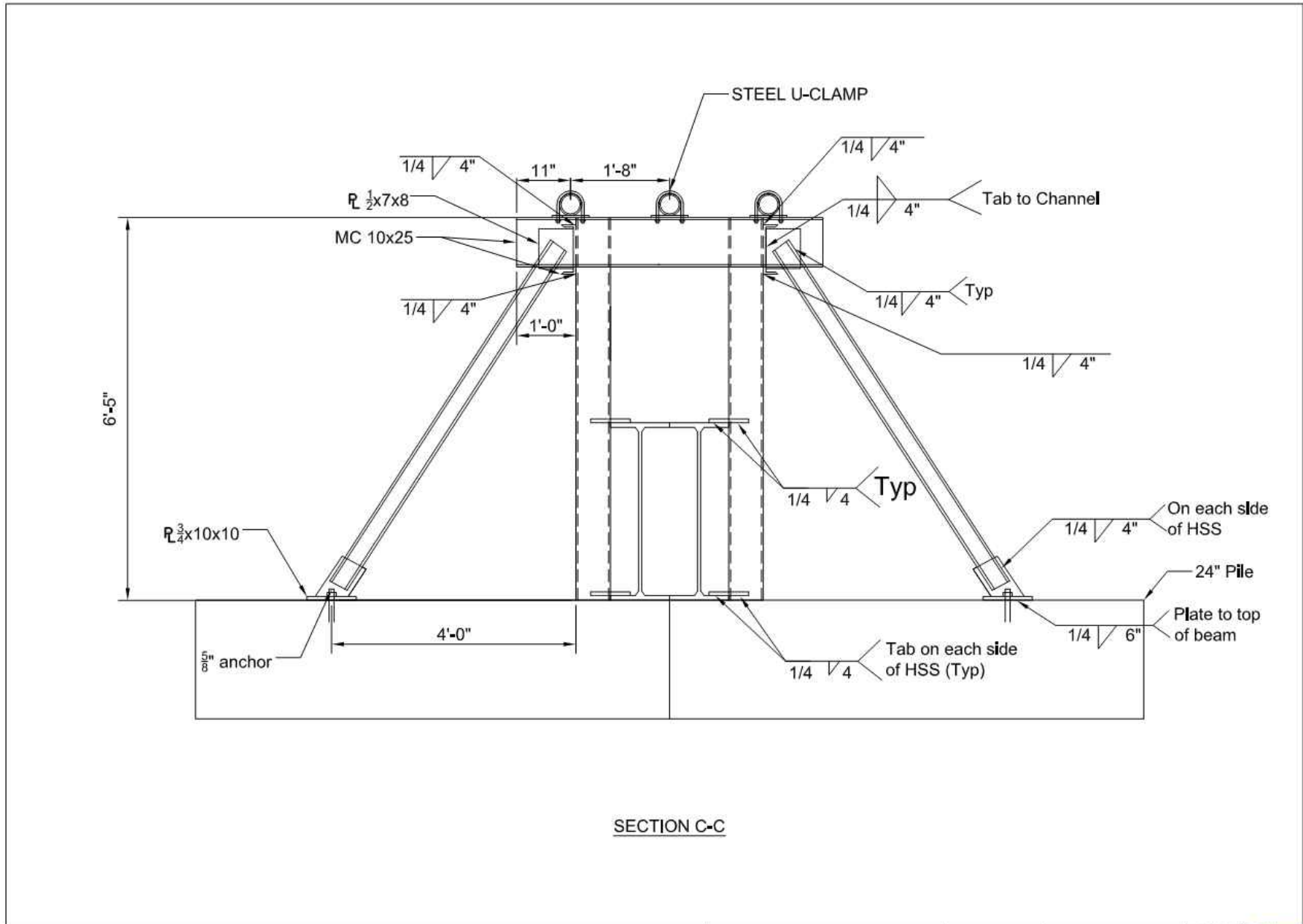
ELEVATION VIEW

Prepared By: Rahul Bhatia	University of Florida	Rev:02	Page 9 of 20
Project No: BDV31-977-15	Unbonded Tendon Mock-Up	05/19/2014	Scale: $\frac{1}{2}$ "=1'-0"
Middle Tendon Support			




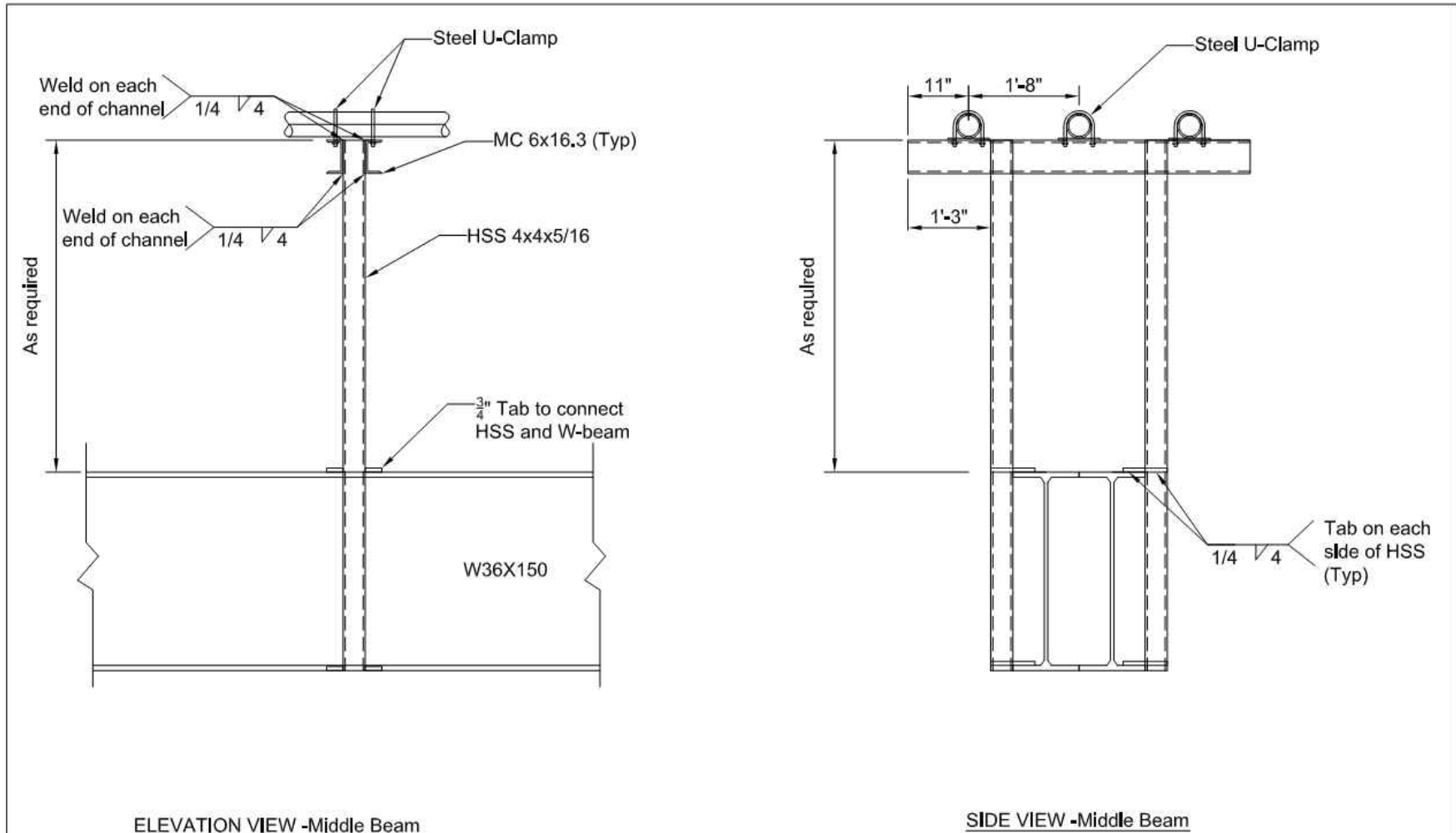
SECTION B-B

Prepared By: Rahul Bhatia	University of Florida	Rev:02	Page 10 of 20	
Project No: BDV31-977-15	Unbonded Tendon Mock-Up	Middle Tendon Support	05/19/2014	




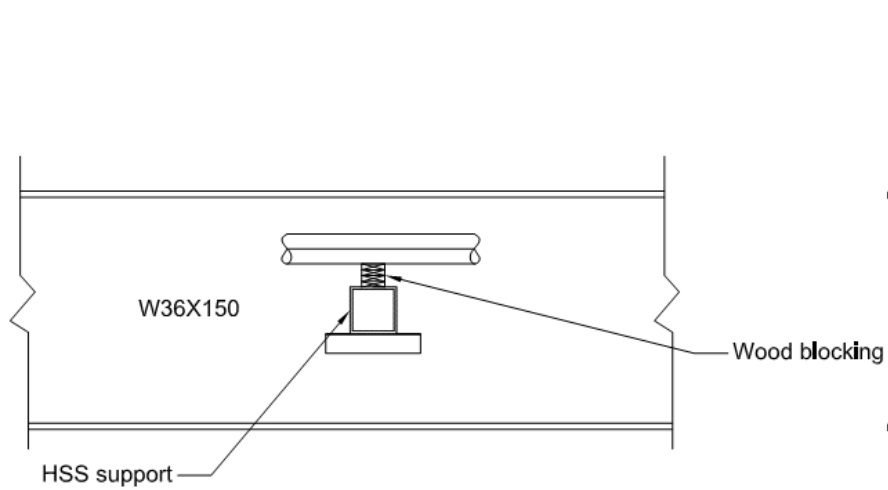
SECTION C-C

Prepared By: Rahul Bhatia	University of Florida	Rev:02	Page 11 of 20	
Project No: BDV31-977-15	Unbonded Tendon Mock-Up	Middle Tendon Support	05/19/2014	

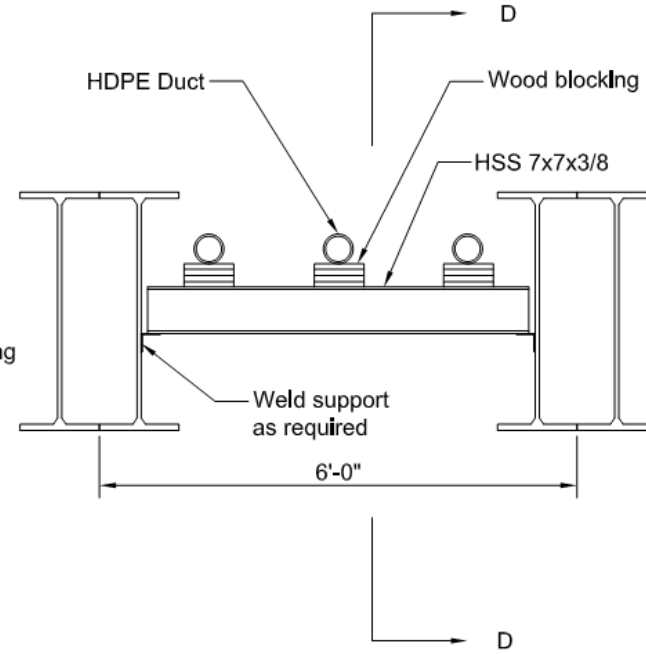


NOTE:
 1. Steel clamps shall be used only in parabolic profile of the tendon


Prepared By: Rahul Bhatia			University of Florida		Rev:02	Page 12 of 20	
Project No: BDV31-977-15	Unbonded Tendon Mock-Up	Intermediate Tendon Supports		05/19/2014	Scale: 1/2"=1'-0"		

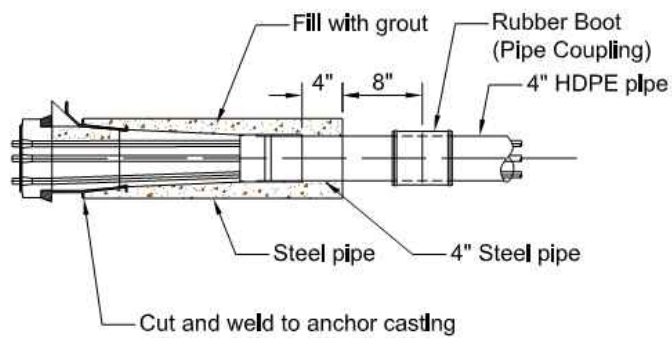


SECTION D-D

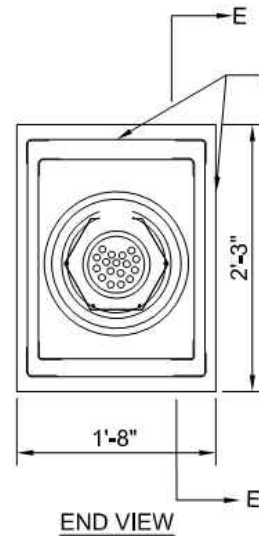


INTERMEDIATE TENDON SUPPORT

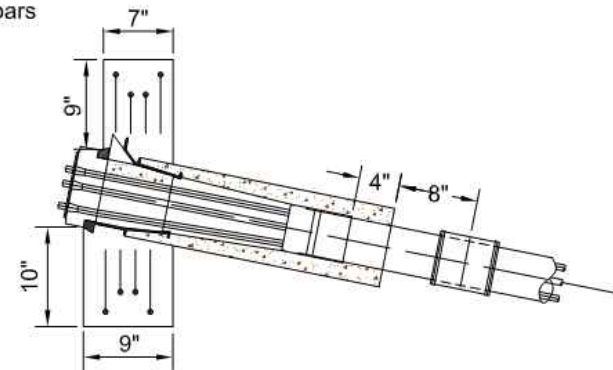
Prepared By: Rahul Bhatia	University of Florida	Rev:02	Page 13 of 20	
Project No: BDV31-977-15	Unbonded Tendon Mock-Up	Intermediate Tendon Supports	05/19/2014	



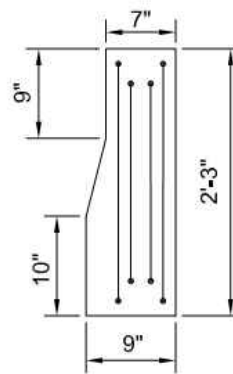
TRANSITION FROM CASTING TO HDPE




END VIEW

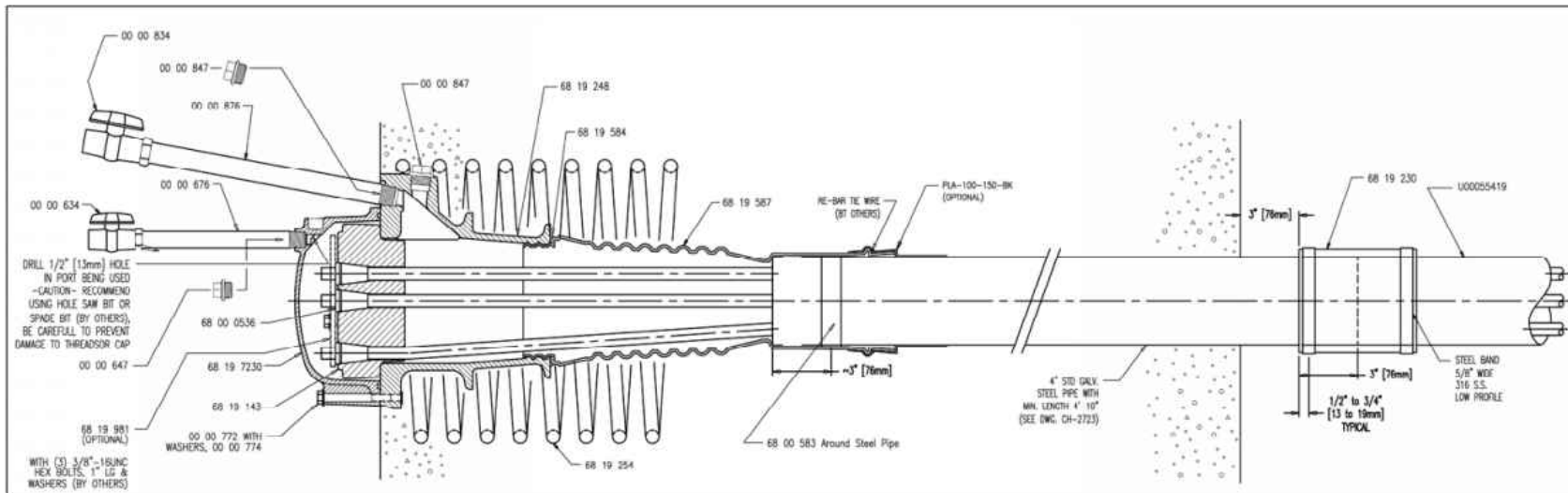
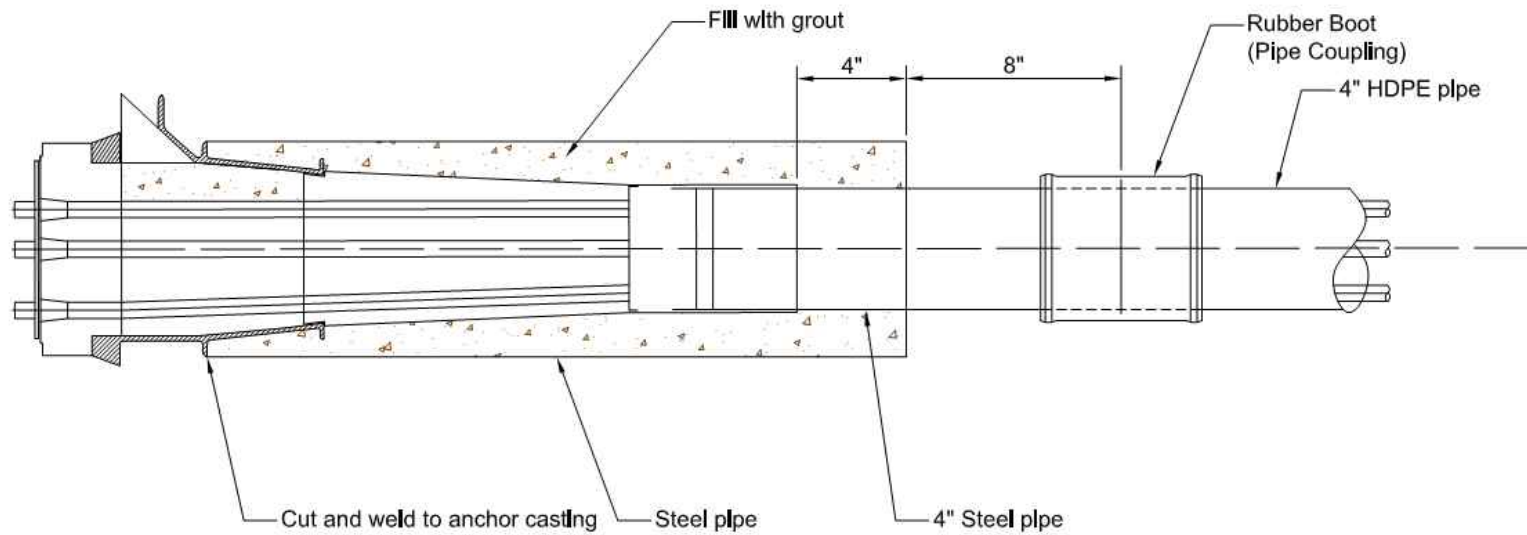



ELEVATION

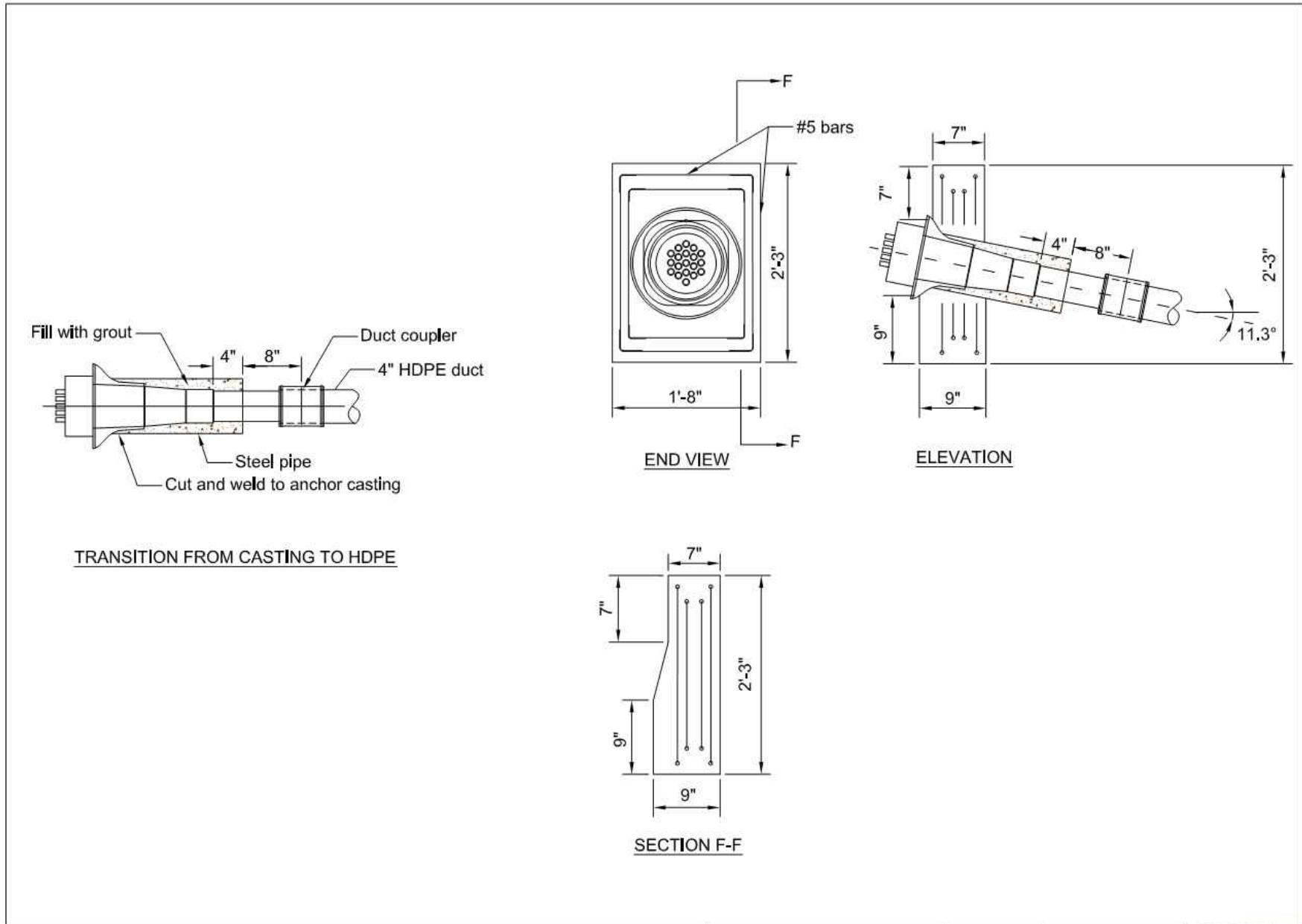



SECTION E-E

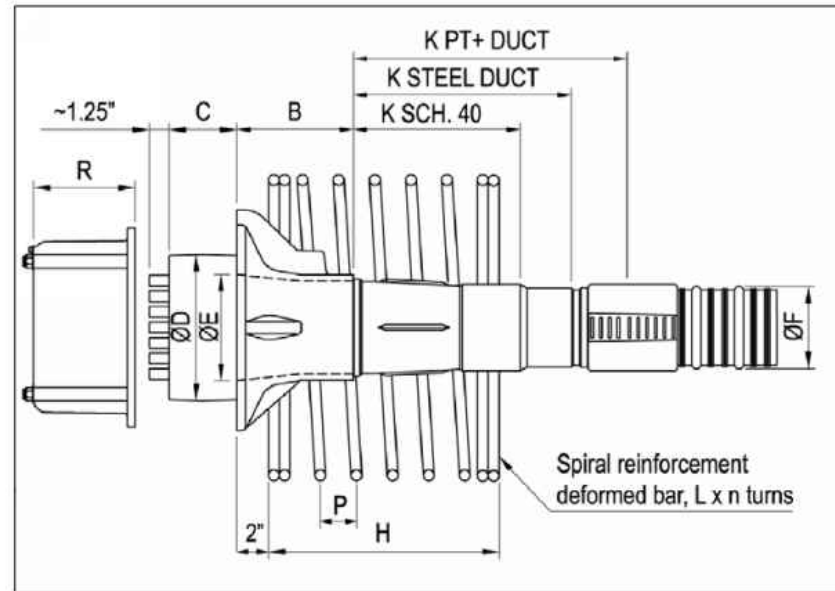
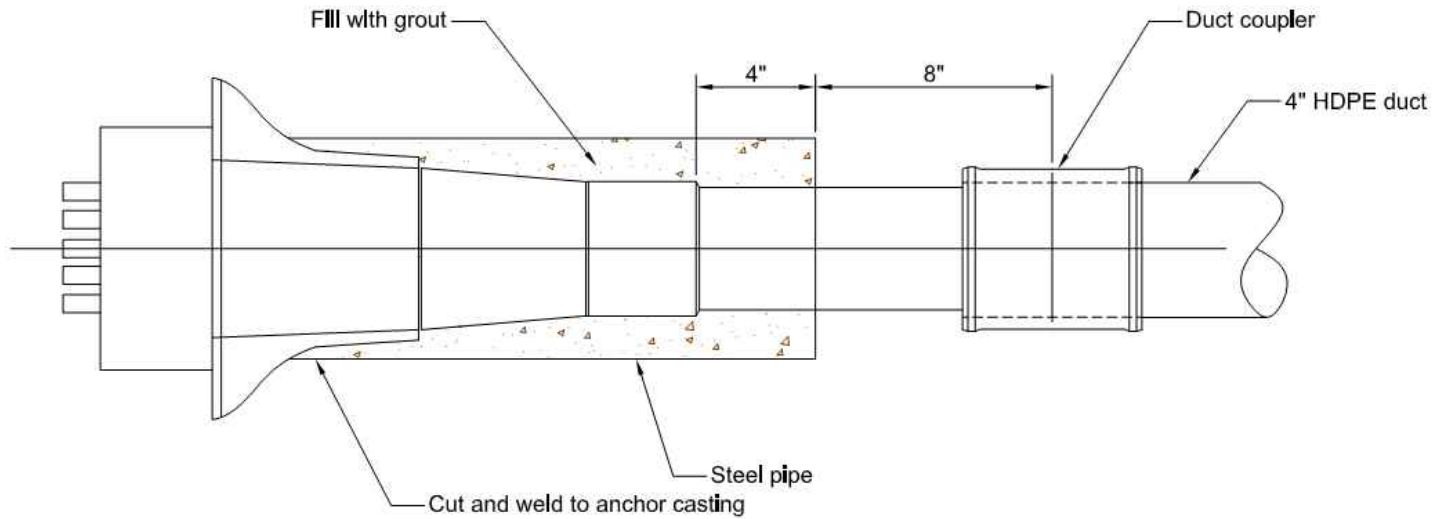
Prepared By: Rahul Bhatia	University of Florida	Rev:02	Page 14 of 20	
Project No: BDV31-977-15	Unbonded Tendon Mock-Up	DSI 19 Strand Tendon	05/19/2014	




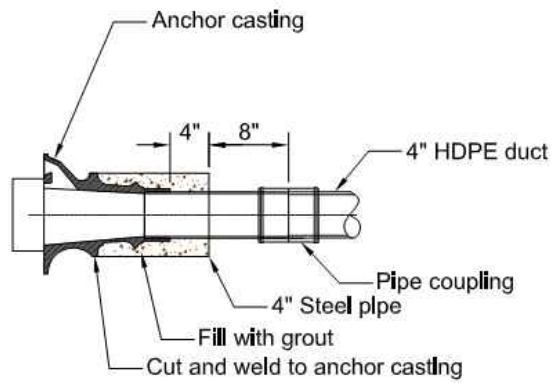
Prepared By: Rahul Bhatia	University of Florida	Rev:02	Page 15 of 20
Project No: BDV31-977-15	Unbonded Tendon Mock-Up	05/19/2014	Do not scale
DSI 19 Strand Tendon			



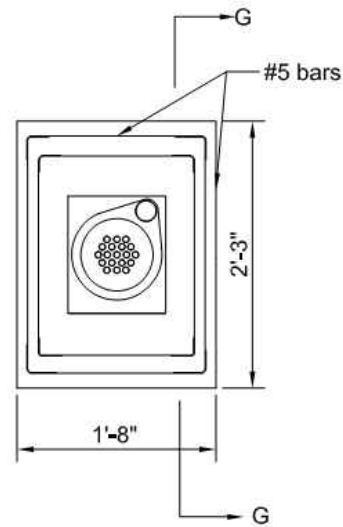
Prepared By: Rahul Bhatia	University of Florida	Rev:02	Page 16 of 20	
Project No: BDV31-977-15	Unbonded Tendon Mock-Up	VSL 19 Strand Tendon	05/19/2014	



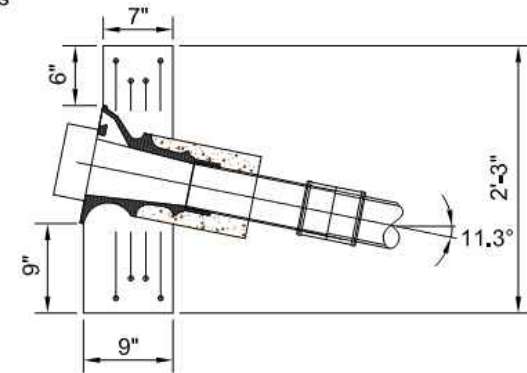
Prepared By: Rahul Bhatia	University of Florida	Rev:02	Page 17 of 20	
Project No: BDV31-977-15	Unbonded Tendon Mock-Up	VSL 19 Strand Tendon	05/19/2014	Do not scale



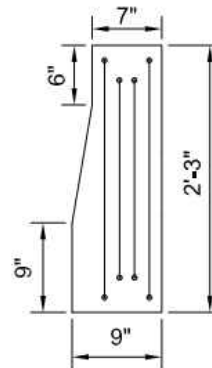
TRANSITION FROM CASTING TO HDPE



END VIEW

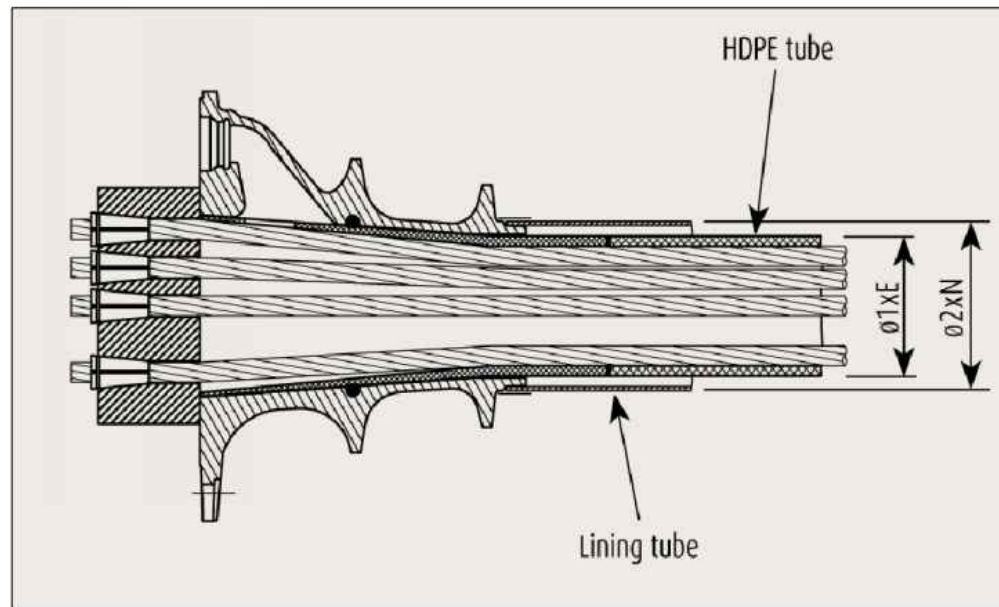
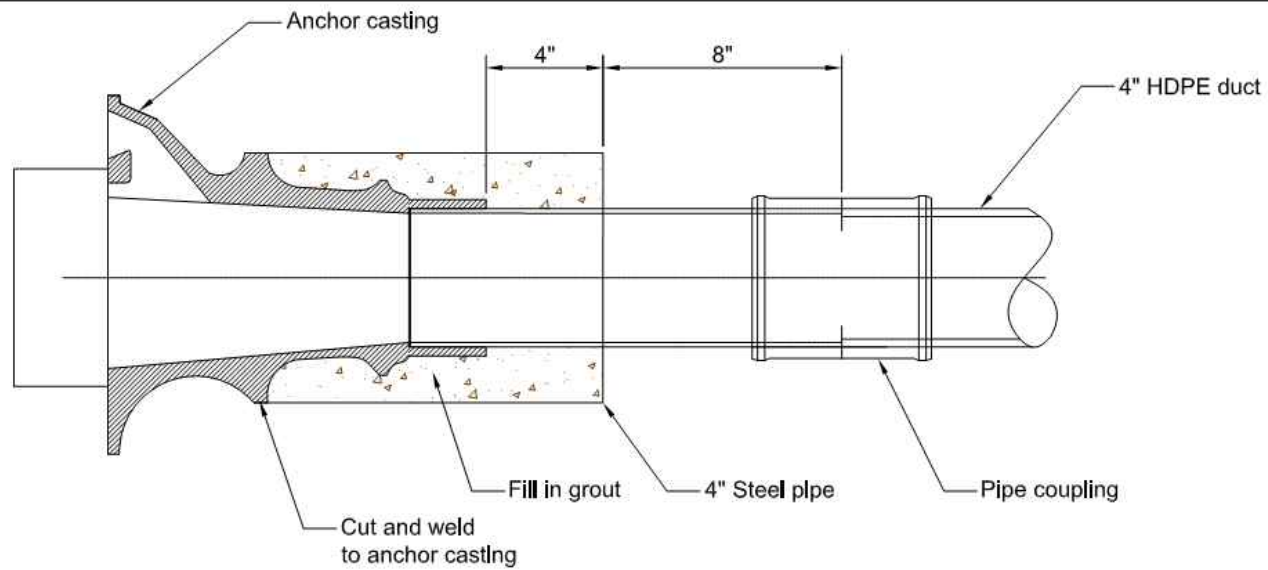


ELEVATION VIEW



SECTION G-G

Prepared By: Rahul Bhatia	University of Florida	Rev:02	Page 18 of 20	
Project No: BDV31-977-15	Unbonded Tendon Mock-Up	FREYSSINET 19 Strand Tendon	05/19/2014	Scale: $\frac{3}{4}''=1'-0''$

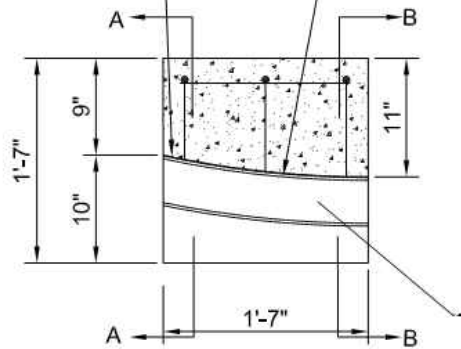


Prepared By: Rahul Bhatia	University of Florida	Rev:02	Page 19 of 20
Project No: BDV31-977-15	Unbonded Tendon Mock-Up	FREYSSINET 19 Strand Tendon	05/19/2014
			Do not scale

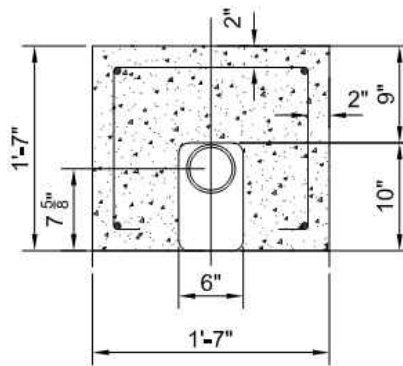


Opening to lay duct

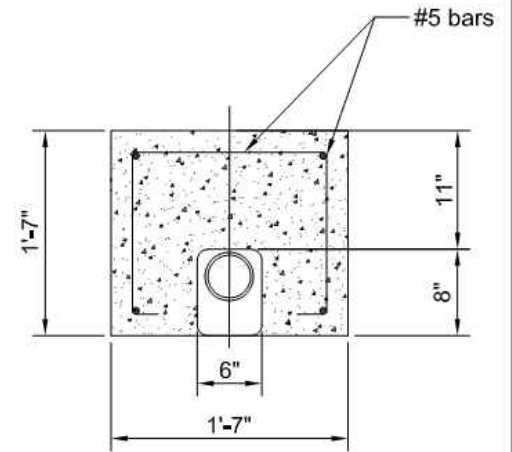
4" HDPE duct



ELEVATION VIEW DIABOLO



SECTION A-A



SECTION B-B

Prepared By: Rahul Bhatia

University of Florida

Rev:02

Page 20 of 20



Project No: BDV31-977-15

Unbonded Tendon Mock-Up

Concrete Gravity Tendon Deviator

05/19/2014

Scale: $\frac{3}{4}''=1'-0''$

Replaceable Unbonded Tendons for Post-Tensioned Bridges

Part II Structural Testing

This report is one of a four-part compilation published under separate covers as follows:

Extended Summary

Part I Mockup for Flexible Filler Injection

Part II Structural Testing

Part III Wire Break Detection

Final Report

December 2017

Principal investigator:

H. R. Hamilton

Co-Principal investigator:

J. A. Rice

Research assistants:

A.B.M. Abdullah

Rahul Bhatia

Natassia Brenkus

Devon Skelton

Sponsor:

Florida Department of Transportation (FDOT)

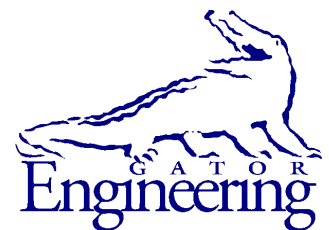
William Potter, P.E. – Project Manager

Rick W. Vallier, P.E. –Project Manager

Contract:

UF Project No. 000112216 & 000112218

FDOT Contract No. BDV31-977-15



University of Florida

Engineering School of Sustainable Infrastructure and Environment

Department of Civil and Coastal Engineering

University of Florida

P.O. Box 116580

Gainesville, Florida 32611

Disclaimer

The opinions, findings, and conclusions expressed in this publication are those of the authors and not necessarily those of the State of Florida Department of Transportation.

Units of Measurement Conversion

SI* (MODERN METRIC) CONVERSION FACTORS

APPROXIMATE CONVERSIONS TO SI UNITS

SYMBOL	WHEN YOU KNOW	MULTIPLY BY	TO FIND	SYMBOL
LENGTH				
in	inches	25.4	millimeters	mm
ft	feet	0.305	meters	m
yd	yards	0.914	meters	m
mi	miles	1.61	kilometers	km
AREA				
in²	square inches	645.2	square millimeters	mm ²
ft²	square feet	0.093	square meters	m ²
yd²	square yard	0.836	square meters	m ²
ac	acres	0.405	hectares	ha
mi²	square miles	2.59	square kilometers	km ²
VOLUME				
fl oz	fluid ounces	29.57	milliliters	mL
gal	gallons	3.785	liters	L
ft³	cubic feet	0.028	cubic meters	m ³
yd³	cubic yards	0.765	cubic meters	m ³
NOTE: volumes greater than 1000 L shall be shown in m ³				
MASS				
oz	ounces	28.35	grams	g
lb	pounds	0.454	kilograms	kg
T	short tons (2000 lb)	0.907	megagrams	Mg (or "t")
TEMPERATURE (exact degrees)				
°F	Fahrenheit	5(F-32)/9 or (F-32)/1.8	Celsius	°C
ILLUMINATION				
fc	foot-candles	10.76	lux	lx
fl	foot-Lamberts	3.426	candela/m ²	cd/m ²
FORCE and PRESSURE or STRESS				
kip	1000 pound force	4.45	kilonewtons	kN
lbf	pound force	4.45	newtons	N
lbf/in²	pound force per square	6.89	kilopascals	kPa

*SI is the symbol for the International System of Units. Appropriate rounding should be made to comply with Section 4 of ASTM E380.

SI* (MODERN METRIC) CONVERSION FACTORS
APPROXIMATE CONVERSIONS FROM SI UNITS

SYMBOL	WHEN YOU KNOW	MULTIPLY BY	TO FIND	SYMBOL
LENGTH				
mm	millimeters	0.039	inches	in
m	meters	3.28	feet	ft
m	meters	1.09	yards	yd
km	kilometers	0.621	miles	mi
AREA				
mm²	square millimeters	0.0016	square inches	in ²
m²	square meters	10.764	square feet	ft ²
m²	square meters	1.195	square yards	yd ²
ha	hectares	2.47	acres	ac
km²	square kilometers	0.386	square miles	mi ²
VOLUME				
mL	milliliters	0.034	fluid ounces	fl oz
L	liters	0.264	gallons	gal
m³	cubic meters	35.314	cubic feet	ft ³
m³	cubic meters	1.307	cubic yards	yd ³
MASS				
g	grams	0.035	ounces	oz
kg	kilograms	2.202	pounds	lb
Mg (or "t")	megagrams (or "metric ton")	1.103	short tons (2000 lb)	T
TEMPERATURE (exact degrees)				
°C	Celsius	1.8C+32	Fahrenheit	°F
ILLUMINATION				
lx	lux	0.0929	foot-candles	fc
cd/m²	candela/m ²	0.2919	foot-Lamberts	fl
FORCE and PRESSURE or STRESS				
kN	kilonewtons	0.225	1000 pound force	kip
N	newtons	0.225	pound force	lbf
kPa	kilopascals	0.145	pound force per square inch	lbf/in ²

*SI is the symbol for the International System of Units. Appropriate rounding should be made to comply with Section 4 of ASTM E380.

Table of Contents

Disclaimer	ii
Units of Measurement Conversion	iii
List of Figures	viii
List of Tables	xiv
1 Introduction.....	1
2 Research Approach	2
3 Structural Behavior of Unbonded Tendons	3
3.1 Redundancy.....	3
3.2 Section Properties	3
3.3 Flexural Cracking.....	4
3.4 Short and Long-Term Deflections	5
3.5 Flexural Strength.....	5
3.5.1 Design Guidance	6
3.5.2 Prestressed members with supplemental reinforcement	12
3.5.3 Components with Unbonded and Bonded Tendons.....	13
3.6 Fatigue.....	15
3.6.1 Design Guidance	18
3.6.2 Past Research.....	19
3.7 Implications.....	30
4 Specimen Design	31
4.1 Internal Tendon I-Girder.....	31
4.1.1 Detailing Considerations	33
4.1.2 Service and Cracking.....	34
4.1.3 Flexure and Shear Strength	35
4.2 External Tendon I-Girder.....	36
4.2.1 Detailing Considerations	38
4.2.2 Service and Cracking.....	42
4.2.3 Flexure and Shear Strength	43
4.3 Fatigue.....	44
4.3.1 Diabolo Tendon Deviators	45
4.3.2 Mechanical Hinge Design	47
4.3.3 Reinforcement Design.....	48
4.3.4 Shear Key Design.....	49
5 Instrumentation	52
5.1 I-Girder	52
5.1.1 Tendon force.....	52
5.1.2 Displacement	53
5.1.3 Strain	54
5.1.4 Temperature.....	56
5.2 Fatigue.....	61
5.2.1 Tendon Force.....	61
5.2.2 Strain	62
5.2.3 Gap Opening.....	63
6 Specimen Construction	65
6.1 Internal Tendon I-Girder.....	65

6.1.1	Laboratory Construction.....	68
6.1.2	Post-tensioning	69
6.1.3	Grout Injection	71
6.1.4	Flexible Filler Injection	73
6.2	External Tendon I-Girder.....	75
6.2.1	Laboratory Construction.....	76
6.2.2	Post-tensioning	80
6.2.3	Flexible Filler Injection	81
6.3	Fatigue.....	82
6.3.1	Formwork and Reinforcing Cage	82
6.3.2	Concrete Placement and Shear Key	84
6.3.3	Post-Tensioning.....	86
6.3.4	Flexible Filler Injection	90
7	Load Test Procedures.....	96
7.1	Static I-Girder	96
7.2	Cyclic I-Girder	96
7.3	Fatigue.....	99
8	Tendon Replacement	103
8.1	Procedure	103
8.2	Observations	106
9	Prestress Losses	107
9.1	Calculated Losses.....	107
9.2	Measured PT Losses	108
9.3	Cracking Moment	110
10	Internal Tendon Results and Discussion.....	114
10.1	Flexible Filler Injection.....	114
10.2	IGS: Static Three-Point Grouted.....	114
10.3	IWS: Static Three-Point Flexible Filler	116
10.4	IWC: Static Four-Point Flexible Filler	121
10.5	Service and Cracking Behavior	124
10.6	Strength.....	129
11	External Tendon Results and Discussion.....	132
11.1	Flexible filler injection.....	132
11.2	EWS: Static Three-Point Bending	133
11.3	EWC: Cyclic Three-Point Bending	137
11.4	Service and Cracking Behavior	140
11.5	Strength.....	143
11.6	Dissection.....	145
12	Analysis of Strength Results.....	150
12.1	Unbonded Tendon Stress and Ultimate Strength.....	151
12.2	Influence of Material Properties	155
12.3	Hinge Rotation and Hinge Length	157
13	Fatigue Results and Discussion	161
13.1	Initial Static Test.....	161
13.2	Cyclic Loading.....	161
13.2.1	Specimen F1	162

13.2.2 Specimen F2	164
13.3 Final Static Test	167
13.4 Specimen Dissection	167
13.4.1 Fatigue Specimen F1	167
13.4.2 Fatigue Specimen F2	175
13.4.3 Strand Tensile Strength Tests	177
13.4.4 Strand Slip	180
14 Summary and Conclusions	184
References	186
Appendix A—Assembly Drawings External I-Girder	190
Appendix B—Prestressing Strand and Post-Tensioning Hardware Information	194

List of Figures

Figure 3-1 Change in section properties for segmental construction	4
Figure 3-2 Change in section properties for I-girder construction	4
Figure 3-3 Joint mechanism for unbonded tendons.....	8
Figure 3-4 Tendon force versus curve length (MacGregor et al. 1989)	9
Figure 3-5 Unbonded diagram of (a) strain and force, and (b) joint opening.....	10
Figure 3-6 Moment-deflection of post-tensioning systems (MacGregor et al. 1989)	14
Figure 3-7 Typical S-N plot (Ryals et al., 1992)	15
Figure 3-8 Generation of slip due to friction stress and debonding in post-tensioned beam (Hall 1990)	16
Figure 3-9 Lateral pressure and frictional force on the deviator block (Hall 1990).....	17
Figure 3-10 Fatigue of plastic PT ducts with single and multi-strands (Paulson et al. 1984)	18
Figure 3-11 Fretting mechanism at deviated prestressing strand.....	20
Figure 3-12 Fatigue vs. fretting fatigue cracks (Waterhouse 1972)	21
Figure 3-13 Severity of fretting fatigue vs. slip amplitude (Yates 1987)	21
Figure 3-14 Cordes and Lapp-Emden (1984)	23
Figure 3-15 Oertle reduced-beam (a) force determination (b) test set-up	25
Figure 3-16 Oertle results (from Wollmann et al. 1988)	26
Figure 3-17 University of Texas at Austin reduced-beam tests (a) Yates single strand (Georgiou 1989) and (b) Wollmann multi-strand (Wollmann et al. 1988)	27
Figure 3-18 Influence of contact load (Wollmann et al. 1996).....	28
Figure 4-1 Internal tendon specimen cross-section	32
Figure 4-2 Internal tendon specimen	32
Figure 4-3 Continuous span	33
Figure 4-4 Tendon profiles from real bridge (FDOT 2008)	33
Figure 4-5 External tendon specimens.....	37
Figure 4-6 External tendon specimen profile.....	37
Figure 4-7 Shear keys and protruding reinforcement	39
Figure 4-8 Deviator STM.....	40
Figure 4-9 Diabolo geometry.....	40
Figure 4-10 Pre-assembled trumpet/duct	41
Figure 4-11 Duct exiting end block of external specimen	41
Figure 4-12 PT tendon (unstressed) (a) between deviator blocks and (b) clear polycarbonate window.....	42
Figure 4-13 Schematic illustration of fatigue specimen	44
Figure 4-14 Deviation of PT tendon in span-by-span construction.....	45
Figure 4-15 Removable diabolo formwork inserts for creating curved deviators.....	46
Figure 4-16 Tendons with point of contact located inside deviator. Note small gap between duct and concrete at tendon exit from deviator.....	46
Figure 4-17 PT duct theoretical point of contact to prevent pinching at deviator exit	47
Figure 4-18 Mechanical hinge details.....	47
Figure 4-19 Anchorage system (a) without local zone reinforcement (b) with local zone reinforcement	48
Figure 4-20 General and local zone anchorage reinforcement	48
Figure 4-21 General zone reinforcement at hollow section.....	49

Figure 4-22 Specimen F1 reinforced concrete shear key.....	50
Figure 4-23 Cracking in concrete surrounding shear key.....	50
Figure 4-24 Neoprene pad (a) before installation (b) after installation	51
Figure 5-1 Hollow-core load cell.....	52
Figure 5-2 IGS and IWS: displacement gage locations.....	53
Figure 5-3 IWC: deflection gage locations.....	53
Figure 5-4 EWS and EWC: deflection.....	54
Figure 5-5 Crack opening gage installation.....	54
Figure 5-6 Anchorage strain gages	55
Figure 5-7 IGS and IWS: strain gage locations	55
Figure 5-8 IWC: strain gage locations.....	56
Figure 5-9 EWS and EWC: strain gage locations.....	56
Figure 5-10 Probe (left) and surface strap (right) thermocouples.....	57
Figure 5-11 Installation of internal thermocouples.....	57
Figure 5-12 IWC and IWC: internal thermocouple layout	58
Figure 5-13 IWS and IWC: close-up of internal thermocouple layout.....	58
Figure 5-14 EWS: thermocouple layout	59
Figure 5-15 EWC: thermocouple layout.....	60
Figure 5-16 Instrumentation layout for fatigue specimens	61
Figure 5-17 Geokon hollow-core load cell	62
Figure 5-18 Removal of HDPE section to attach strain gage	62
Figure 5-19 Strand and strain gage locations for (a) F1 (b) F2	63
Figure 5-20 Gap displacement gages attached to specimen	64
Figure 6-1 Segments in prestressing bed	65
Figure 6-2 Construction staging of internal tendon specimens	66
Figure 6-3 Duct installation	67
Figure 6-4 Specimen construction: (a) main span, (b) endblocks	68
Figure 6-5 Deck casting on internal specimens	69
Figure 6-6 Strand pushing.....	69
Figure 6-7 Stressing plate	70
Figure 6-8 IWS tendon force history	70
Figure 6-9 Grout injection of IGS.....	71
Figure 6-10 Grouting operation: (a) feeding hopper, (b) uniform consistency, (c) at outlet.....	71
Figure 6-11 IGS Outlet (dead end) prior to and after cap removal.....	72
Figure 6-12 IGS inlet (live end) prior to and after cap removal (damaged).....	73
Figure 6-13 Flexible filler injection for internal tendons.....	73
Figure 6-14 Heating flexible filler for injection	74
Figure 6-15 Outlet (dead end) after cap removal (a) IWS and (b) IWC.....	74
Figure 6-16 Inlet (live end) after cap removal of IWS	75
Figure 6-17 Construction sequencing of external tendon specimens	76
Figure 6-18 Segments arranged for casting of deviation block	77
Figure 6-19 Grout pads for deviator blocks.....	78
Figure 6-20 Deviator block (a) formwork and (b) concrete placement.....	78
Figure 6-21 Epoxy application.....	79
Figure 6-22 EWS tendon force history	81
Figure 6-23 Flexible filler injection for external tendons.....	81

Figure 6-24 Reinforcement cage (a) schematic and (b) assembled	83
Figure 6-25 Reinforcing bar cage	83
Figure 6-26 Fatigue specimen formwork (a) during assembly (b) after insertion of reinforcing bar cage	84
Figure 6-27 Concrete placement of specimen F1	85
Figure 6-28 Concrete placement of specimen F2	85
Figure 6-29 Completed fatigue specimen without post-tensioning	85
Figure 6-30 Specimen F1 after formwork removal (a) concrete spalling and (b) concrete repair	86
Figure 6-31 Strand labeling and steel ties	86
Figure 6-32 Strand installation	87
Figure 6-33 Monostrand jack	87
Figure 6-34 Strand location in wedge plates at (a) live end and (b) dead end	88
Figure 6-35 Washers to reduce seating losses	89
Figure 6-36 F1 post-tensioning results	89
Figure 6-37 F2 post-tensioning results	90
Figure 6-38 Strand cutting after post-tensioning	90
Figure 6-39 Flexible filler injection specimen F1	91
Figure 6-40 Heating barrel containing flexible filler for injection	91
Figure 6-41 Pressure test for specimen	92
Figure 6-42 Vacuum for filler injection	92
Figure 6-43 Sealant placed on concrete around HDPE pipe	93
Figure 6-44 Positioning of filler barrels (a) transporting filler barrel and (b) centrifugal pump connection	93
Figure 6-45 F1 anchor after injection at (a) live end and (b) dead end	94
Figure 6-46 F2 vacuum hose attached to dead end cap (a) top of hose and (b) end of hose	94
Figure 6-47 F2 live end anchor after injection	95
Figure 6-48 F2 dead end anchor after injection	95
Figure 7-1 Flexural test set-up: (a) IGS, IWS; (b) EWS; and (c) IWC	97
Figure 7-2 EWC test set-up	98
Figure 7-3 Fatigue test set-up schematic	99
Figure 7-4 Specimen support (a) steel W section on top of 1-in. grout pad (b) neoprene pad ..	100
Figure 7-5 (a) Shore Western actuator (b) steel bearing pad for actuator	100
Figure 7-6 Testing frame	101
Figure 7-7 Fatigue test set-up	101
Figure 7-8 Actuator connected to fatigue specimen	102
Figure 8-1 IWC: (a) torched end and, (b) opposite end with protective plate	103
Figure 8-2 End of beam where wedges were torched	104
Figure 8-3 First tendon pull	104
Figure 8-4 Tendon pull-out: load vs. time	105
Figure 8-5 Tendon removal	105
Figure 9-1 Measured PT losses vs. AASHTO-LRFD refined method	110
Figure 9-2 Decompression: (a) IGS; (b) IWS; and (c) IWC	112
Figure 9-3 Variation in tendon stress	113
Figure 10-1 Internal concrete temperature measurements	114
Figure 10-2 IGS (a) elastic behavior and (b) ultimate strength behavior	115

Figure 10-3	IGS: deck strain at load point.....	116
Figure 10-4	IGS: strain along the top of deck.....	116
Figure 10-5	IWS (a) elastic behavior and (b) ultimate strength behavior	117
Figure 10-6	IWS: first crack	117
Figure 10-7	Cracking (a) after strand rupture, load held at 240 kip and (b) after load removed.....	119
Figure 10-8	IWS: applied load history.....	119
Figure 10-9	IWS: deck strain at load point.....	120
Figure 10-10	IWS: bonded strand rupture	120
Figure 10-11	IWS: strain along the top of deck.....	121
Figure 10-12	IWC (a) elastic behavior and (b) ultimate strength behavior	121
Figure 10-13	IWC: rupture of deck at load point	122
Figure 10-14	IWC: ruptured bonded strands	123
Figure 10-15	IWC: deck strain (a) at midspan and (b) along top of deck	123
Figure 10-16	IWC: tendon force.....	124
Figure 10-17	Internal tendon comparison: elastic behavior	125
Figure 10-18	Strain along profile at load point (a) IGS, (b) IWS, (c) IWC.....	126
Figure 10-19	Internal tendon specimens: first crack locations	127
Figure 10-20	Internal tendon specimens: final cracking patterns	127
Figure 10-21	Internal Specimens: applied load vs. tendon stress	128
Figure 10-22	IWS: string-pot measuring a primary crack	129
Figure 10-23	Flexural strength: internal tendon specimens.....	131
Figure 11-1	EWS: temperature	132
Figure 11-2	EWS tendon force during injection.....	133
Figure 11-3	EWS (a) elastic behavior and (b) ultimate strength behavior	133
Figure 11-4	EWS: south deviation block.....	134
Figure 11-5	EWS: string pots installed.....	134
Figure 11-6	EWS: load vs. displacement.....	135
Figure 11-7	Compression failure at north epoxy joint (beam shown under load).....	136
Figure 11-8	EWS: strain (a) along top, and (b) at load point	136
Figure 11-9	EWS: south joint opening	137
Figure 11-10	EWC: (a) cracking (b) load cycles and (c) ultimate.....	139
Figure 11-11	EWC near ultimate load	140
Figure 11-12	External tendon comparison: elastic behavior	141
Figure 11-13	External tendon specimens: first crack locations	142
Figure 11-14	Strain profiles for (a) EWS and (b) EWC	142
Figure 11-15	EWC flexural strength: external tendon specimens	143
Figure 11-16	External tendon specimens: ultimate tendon stress.....	144
Figure 11-17	EWC: tendon force.....	145
Figure 11-18	EWS: exterior of duct at diabolo.....	146
Figure 11-19	EWS: interior surface of duct in contact with strand at diabolo	146
Figure 11-20	Potential HDPE duct damage at deviator (a) effect of point of contact on HDPE damage in diabolo deviator (b) pinched HDPE at deviator exit in specimen EWS	147
Figure 11-21	EWC: exterior surface of duct at NE diabolo	147
Figure 11-22	EWC: strands at NE diabolo	148
Figure 11-23	EWC: strands at NW diabolo.....	148
Figure 11-24	EWC: dissection of tendon at SE diabolo	149

Figure 12-1 Behavior of members with bonded, unbonded, and mixed tendons	150
Figure 12-2 All specimens: ultimate tendon stress	151
Figure 12-3 External tendon specimens: ultimate tendon force	152
Figure 12-4 Internal tendon specimens: ultimate tendon stress.....	153
Figure 12-5 Ratio of observed to AASHTO-LRFD flexural strength and f_{ps}	155
Figure 12-6 Tendon stress and hinge length for varying reinforcement combinations	156
Figure 12-7 Tendon elongation at plastic hinge	157
Figure 12-8 Tendon force increase: bonded vs. unbonded (MacGregor et al. 1989)	158
Figure 12-9 Thirty degree zone of influence	160
Figure 13-1 Initial static ramp test for both fatigue specimens	161
Figure 13-2 Strand and duct contact during cyclic loading	162
Figure 13-3 Gap displacement and actuator force for F1	162
Figure 13-4 Stress range results during cyclic loading for F1	163
Figure 13-5 Stress range results for strain gage 1 and 2 for F1	163
Figure 13-6 Mean tendon force and ambient temperature for F1	164
Figure 13-7 Gap displacement and actuator force for F2	165
Figure 13-8 Stress range results during cyclic loading for F2	165
Figure 13-9 Stress range using readings from strain gages 1 and 2 for F2.....	166
Figure 13-10 Mean tendon force and ambient temperature for F2.....	166
Figure 13-11 Final static ramp test for both fatigue specimens.....	167
Figure 13-12 Tendon force during detensioning for F1.....	168
Figure 13-13 Dissection of F1 (a) detensioning and (b) tendon removal.....	168
Figure 13-14 Concrete repair for specimen F1 at the end of cyclic loading.....	169
Figure 13-15 Mechanical hinge post-dissection – dead end segment.....	169
Figure 13-16 Mechanical hinge post-dissection – live end segment	170
Figure 13-17 HDPE pipe section from F1 near south deviator exit (a) measurement of groove depth (b) pipe wear.	170
Figure 13-18 HDPE pipe thickness along length of deviator for F1	171
Figure 13-19 HDPE pipe at deviator corner (a) live end (b) dead end (c) pinched duct at dead end.....	172
Figure 13-20 Wedge inspection post-cyclic loading for specimen F1	173
Figure 13-21 Wedge serration impressions on strands following cyclic loading.....	174
Figure 13-22 Wedge “bite” marks specimen F1 (a) image of marks (b) schematic of marks...	175
Figure 13-23 Tendon force during detensioning for F2.....	175
Figure 13-24 Tendon removal from F2	176
Figure 13-25 HDPE Pipe Thickness along length of deviator for F2.....	176
Figure 13-26 F2 HDPE damage at (a) point of maximum groove depth and (b) at midpoint of deviator	177
Figure 13-27 Strand sampling location for tensile tests.....	177
Figure 13-28 Fracture surfaces of control specimens (a) c-2 (b) magnified fracture surface....	179
Figure 13-29 Specimen F1 strand ductile failures after tensile tests	179
Figure 13-30 Specimen F2 strand brittle failure (a) fretting fatigue (b) close-up of fracture due to fretting.....	180
Figure 13-31 Specimen F2 strand fracture locations	180
Figure 13-32 Forces on a short tendon segment at a deviator	181
Figure 13-33 Stress difference when tendon slip occurs (a) Specimen F1 (b) Specimen F2	182

Figure 13-34 Structural bridge model for strand slip investigation 182
Figure 13-35 Unit tendon friction variation with deviation angle 183

List of Tables

Table 3-1 Comparison of methods for calculating Δf_{ps} (Roberts-Wollmann et al. 2005)	7
Table 3-2 Testing of full-size bonded post-tensioned specimens	29
Table 4-1 Internal tendon specimen naming convention	32
Table 4-2 Summary of stress checks for precast AASHTO at release	34
Table 4-3 Summary of stress checks for loads associated with deck placement	35
Table 4-4 Summary of stress checks at post-tensioning release	35
Table 4-5 Internal tendon – bonded 3-point Strength	36
Table 4-6 Internal tendon – unbonded 3-point Strength	36
Table 4-7 Internal tendon – unbonded 4-point Strength	36
Table 4-8 External tendon specimens	39
Table 4-9 Summary of stress check for precast at release	42
Table 4-10 Summary of stress check at post-tensioning transfer	43
Table 4-11 External tendon – unbonded	43
Table 4-12 Fatigue beam specimen abbreviations	45
Table 5-1 Monitored instrumentation	52
Table 5-2 Monitored instrumentation	61
Table 6-1 Specimen life stages	66
Table 6-2 Post-tensioning force	80
Table 6-3 Important dates in the construction and testing of fatigue specimens	82
Table 7-1 EWC loading procedure	98
Table 7-2 Fatigue specimen loading procedure	102
Table 9-1 AASHTO-LRFD losses by refined method	107
Table 9-2 Predicted midspan decompression and cracking moment (compression is negative)	108
Table 9-3 Post-tensioning force	108
Table 9-4 Average PT anchorage set and elongation	109
Table 9-5 Measured PT losses	110
Table 9-6 Effective prestress force by decompression gages	112
Table 10-1 First crack of internal tendon specimens	126
Table 10-2 Crack widths at load holds (in.)	128
Table 10-3 Internal tendons - AASHTO-LRFD vs. observed flexural strength	130
Table 11-1 First cracks of external tendon specimens	141
Table 11-2 External tendons: AASHTO-LRFD vs. observed unbonded flexural strength	143
Table 12-1 Unbonded tendon stress at ultimate	152
Table 12-2 Ratio of observed to AASHTO-LRFD flexural strength and f_{ps}	154
Table 12-3 Hinge by measured strain and deflection	160
Table 13-1 Minimum 0.6-in. strand requirements for ASTM A416	178
Table 13-2 Steel certification results from manufacturer	178
Table 13-3 Summary of tensile test results for strands	178
Table 13-4 Strand slip results for both specimens	182

1 Introduction

This is Part II of the research report covering Tasks 2, 3 and 4 of the “Replaceable Unbonded Tendons for Post-Tensioned Bridges” FDOT Project BDV31-977-15. Five 40-ft long I-girder beams – three beams with an internal parabolic 12-strand tendon and two beams with a pair of externally deviated six-strand tendons – were post-tensioned at the lab, injected with filler material, and load tested. Two fatigue specimens were constructed and utilized to conduct a series of fatigue tests. This report covers the specimen design and construction, laboratory testing, and post-mortem inspection. Tendon replacement was also performed on one internal tendon specimen and is described herein.

Chapter 2 provides a brief overview of the approach taken in this portion of the research project. Chapter 3 provides a review of the relevant literature and design specifications. Chapter 4 covers the test specimen design, including both the full-scale beams and the fatigue specimens. Chapter 5 describes the instrumentation, considering the several stages of investigation during which the specimens were instrumented: stressing, injection, load testing and detensioning. Chapter 6 describes the specimen construction. Chapter 7 describes the load test procedures. Tendon replacement procedures and observations are discussed in Chapter 8. Chapter 9 reports the prestress losses. Test results and discussion related to internal tendons and external tendons are covered in Chapters 10 and 11, respectively. Further discussion and analysis of the static test results are provided in Chapter 12. Chapter 13 is devoted to the results of the fatigue testing followed by summary and conclusions in Chapter 14.

2 Research Approach

This part of the research project focused on the flexural strength behavior of specimens with internal and external tendons using AASHTO Type IV sections. The use of flexible fillers over grout in both internal and external tendons will result in a change in the contribution that the unbonded tendons will make to the flexural strength of the section. Depending on the situations in which flexible fillers are used, prestressed members could have bonded and unbonded tendons or mixed tendons.

Two types of full-size beam specimens were designed. One was precast with an internal parabolically draped unbonded tendon along with bonded pretensioned strands in the bottom flange. This specimen and its tendon profile were selected to simulate the negative moment region of a continuous spliced girder arrangement with post-tensioning duct placed in the web in a parabolic drape. Three specimens of this type were fabricated: 1) one specimen with a corrugated polypropylene duct filled with cementitious grout, intended to simulate recent construction practice for internal tendons in post-tensioned I-girders, and 2) two specimens with smooth HDPE duct filled with flexible filler material, intended to simulate the novel construction approach using flexible filler material. The choice of duct reflects recent construction practice with grout (corrugated polypropylene) and requirements to accommodate the heat and pressure experienced by the tendon during the injection process when using flexible filler material (smooth HDPE).

The second specimen type was also precast, but was assembled in segments and was prestressed externally with unbonded tendons. The tendons were deviated at cast-in-place deviator blocks, which also acted as match-cast closure pours for the assembly of the beam segments. This tendon configuration was intended to simulate external tendons on box-girder sections.

In addition, fatigue specimens were constructed to test the fatigue performance of the unbonded tendons in conjunction with the diablo deviator configuration, which is used to improve the replaceability of fully unbonded external tendons. The specimen was fitted with a mechanical hinge that allowed fatigue testing without causing damage to the remainder of the specimen. The focus was on wedge and anchor fatigue; fretting at the diablo and wear; and damage of the duct at the diablo.

3 Structural Behavior of Unbonded Tendons

Substituting unbonded PT tendons for bonded tendons will affect the structural strength and serviceability of the structure. The potential issues or concerns are discussed within this chapter.

3.1 Redundancy

Unbonded tendons provide less structural redundancy than bonded tendons. Bonded tendons transfer prestressing force at the anchorages and along the length of the tendon through bond. When a bonded tendon failure occurs – such as strand failure due to corrosion - no prestressing force remains at that particular location in the span, but the prestressing force is redeveloped and transferred again to the concrete at a development length on either side of the failed section (Kasan and Harries 2011). Mackie et al. (2011) investigated the effect of anchorage failure in external tendons. Tests were conducted on bridge models having tendons with 7, 12, and 19 strands. It was found that in the event of anchorage failure, secondary anchorage is provided by the grout in the deviators and in particular the pier anchors. The secondary anchorage was, however, dependent on the grout quality. For a 7-strand tendon system, a development length of 38 inches was sufficient to provide anchorage whereas a development length of 50 inches was found sufficient for 12 strand tendon. The results of the 19 strand tendon test shows that the pipe did not have sufficient strength in it to allow anchorage.

In an unbonded system, the prestressing force is only transferred to the concrete through the anchorages at the end of the member. A complete failure at any location along the tendon length, therefore, would result in a loss of prestress force along the entire length. In one-way unbonded beams, a secondary load path should be added with regular reinforcing steel, in case of a significant loss in the prestressing force (PTI 2006). The ACI 318-14 requires minimum amount of reinforcing steel to provide a secondary load path (PTI 2006).

Redundancy concerns are normally an issue in building construction, where one-way unbonded tendons are used. In bridge design, it is common for multiple strands to be used in one tendon, as well as multiple tendons to be used in one concrete section. Segmental construction bridges are typically post-tensioned with the multiple tendons. The tendons can be either internal, external, or a combination of both. Generally, multiple tendons pass through any given section; at any given section, therefore, multiple load paths are available. The overall effect of the multiple tendons is the sum of the individual effect of single tendons. However, failed internal tendons may not be apparent under service loads because redevelopment occurs. Although unlikely, this could potentially lead to a sudden collapse without sufficient warning if multiple internal bonded tendons failed over time in a given cross-section.

A system factor is incorporated into the bridge design system and is a function of structural determinacy, number of webs, and number of tendons per web. The system factor for a single tendon system per web is considered lower, because the system lacks a redundant load path (AASHTO-LRFR 2005). The failure of the tendon in this situation may result in the loss of overall capacity of the structure.

3.2 Section Properties

One implication of switching from bonded to unbonded tendons is reduction in section properties. The bonded tendons are filled with grout produce no gap in the cross-section while the unbonded tendons filled with filler material creates a hole in the section and, thus resulting a

reduced section. The reduced section properties can be seen in various constructions viz. reduced deck thickness in segmental construction (Figure 3-1) and reduced web thickness in I-girder construction (Figure 3-2). The reduced section properties are not significant relative to the entire section and might not affect significantly the various structural behaviors (flexure, shear, or deflection).

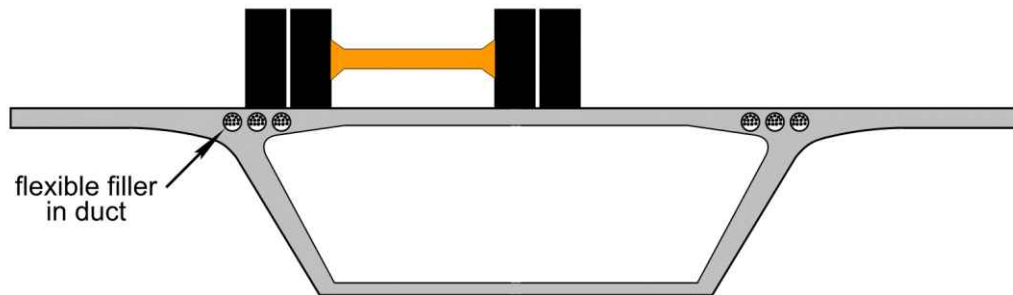


Figure 3-1 Change in section properties for segmental construction

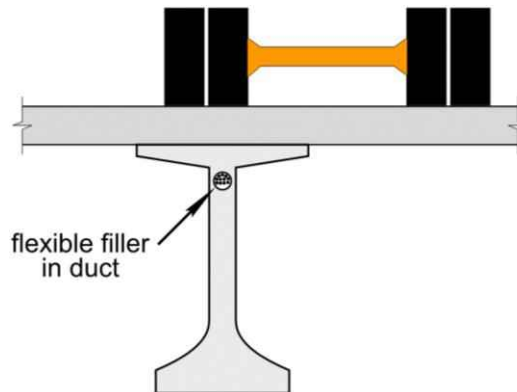


Figure 3-2 Change in section properties for I-girder construction

3.3 Flexural Cracking

Flexural cracking can result in both strength and serviceability problems. Minimum reinforcement requirements are imposed to prevent a sudden failure if the amount of reinforcement is not sufficient to support the cracking moment. This is addressed in both ACI 318-14 and AASHTO-LRFD (AASHTO 2014b) by requiring a minimum amount of reinforcement—either directly or indirectly—that will prevent a catastrophic failure should the applied moment exceed the cracking moment. Bonded tendons, unbonded tendons, mild steel, or a combination of the three can be used to satisfy this strength requirement.

Flexural cracking can also result in serviceability problems when the reinforcement size and placement is insufficient to produce well-distributed cracks that are of acceptably small widths. Members containing only unbonded tendons with no other bonded reinforcement are particularly prone to large flexural cracks. Crack distribution and crack widths, however, can be controlled through the inclusion of supplementary bonded reinforcement, as described and recommended by Mattock et al. (1971), Kosut et al. (1985), and Gerber and Burns (1985). ACI 318-14 requires a minimum amount of *bonded* reinforcement (either in the form of a bonded tendon or bonded mild steel) to ensure that cracking behavior is acceptable. AASHTO-LRFD,

however, does not have a comparable provision. Instead, it appears that they rely on prohibiting tensile stresses under Service III conditions (where the load factor for live load is 0.8) in concrete within sections that contain unbonded tendons. In cases where bonded reinforcement is provided, however, even though unbonded tendons are present, some tension is allowed at full service loads. Furthermore, for segmental construction made continuous by unbonded tendons, the section must be evaluated for the possibility of joint opening and its effect on the structural consequences of such joint opening.

3.4 Short and Long-Term Deflections

Theoretically, only the post-cracking behavior differs between sections with bonded tendons compared with those containing unbonded tendons assuming that the section properties are the same. Consequently, changing from bonded to unbonded tendons will not significantly affect the deflections in the service load range. The section loss due to duct remaining ungrouted will result in slightly lower section properties, but these differences can be accounted for directly when computing the section properties for a section with unbonded tendons.

Likewise, long-term deflections due to creep and shrinkage will not differ significantly between bonded and unbonded tendons.

3.5 Flexural Strength

When comparing flexural behavior of beams with bonded tendons to that of unbonded tendons, significant behavioral differences occur only when the beam is loaded beyond cracking. Once cracking occurs, strain compatibility of bonded tendons ensures that the accumulated tensile strain occurring at a crack is concentrated near the crack, resulting in large local stress increases in the tendon over the crack length. Conversely, in members with unbonded tendons, tensile strain associated with cracking is distributed over the full length of the tendon (or between deviation points); though cracks may be relatively wide (compared with those seen in bonded members), the resulting increase in overall tendon force is comparatively small. This difference results in higher ultimate flexural strengths at smaller deflections for bonded tendon members versus larger crack opening and lower ultimate strength for unbonded tendon members (Gerber and Burns 1971). To obtain the same flexural strength in the same size section of an unbonded tendon system, additional unbonded tendons or mild steel (or both) are necessary.

Though much research has been done on members with either bonded or unbonded tendons, members with *both* bonded and unbonded tendons have received little consideration in the literature or in experimental testing beyond providing a counterpoint to members with only one type of tendon. Components containing both bonded and unbonded tendons have not yet been rationally approached in code bodies, nor has a model for determining their ultimate strength been adopted.

An overview of the existing code treatment for determination of ultimate strength of unbonded and mixed tendons in concrete bridge construction is covered in the next section. To shed further light on the combination of bonded and unbonded reinforcement, literature that covers unbonded post-tensioned tendons used in conjunction with mild steel reinforcement is reviewed in Section 3.5.2.

Mixed tendons are covered briefly in AASHTO-LRFD (AASHTO 2014), without express justification for the provided guidance. A summary of the existing literature regarding mixed tendons is covered in Section 3.5.3.

3.5.1 Design Guidance

Determining the ultimate strength stress conditions in *bonded* prestressing steel can be accomplished through first principles. The fundamental assumption that the prestressing steel is perfectly bonded to the concrete is a prerequisite for this approach and allows the strength to be computed at a chosen section. Unbonded tendons, on the other hand, must be evaluated at the member level rather than the section level. Because unbonded tendons transfer stress only at anchorages and deviation points, consideration must be made for the tendon profile, load pattern, friction, and member geometry. The tendon stress, in other words, is dependent on the deformation of the entire member and assumptions concerning friction and tendon contact within the member.

This has led to numerous proposed models to estimate tendon stress at ultimate strength of varying levels of complexity for members with unbonded tendons, as reviewed by Naaman and Alkhairi (1991a), and Harajli (2006). Recommendations for the calculation of ultimate stresses in unbonded prestressing tendons came from ACI Subcommittee 423 in 2002 (Naaman et al. 2002) and was proposed as a modification for the ACI Code; a further modification/clarification to consider continuous members has been proposed by Harajli (2012). For an evaluative review of the numerous equations in use for the prediction of f_{ps} at nominal flexural strength for members with unbonded tendons, the reader is referred to Naaman and Alkhairi (1991b). Roberts-Wollmann et al. (2005) collected the various methods used by codes internationally as shown in Table 3-1.

Table 3-1 Comparison of methods for calculating Δf_{ps} (Roberts-Wollmann et al. 2005)

Source	Equation for Δf_{ps} (as presented)	Assumptions	Reduced equation
Canadian code	$\frac{5000}{L_e}(d_{ps} - c_y)$	—	$5000\left(\frac{d_{ps} - c_y}{L_e}\right)$
British code	$\frac{7030}{\left(\frac{L}{d_{ps}}\right)}\left(1 - \frac{1.7f_{pu}A_{ps}}{f_{cu}bd_{ps}}\right)$	$c_u = \frac{1.7f_{pu}A_{ps}}{f_{cu}b}$	$7030\left(\frac{d_{ps} - c_u}{L}\right)$
Swiss code (edge span)	$0.075E_{ps}\left(\frac{d_{ps}}{L}\right)$	$E_{ps} = 193 \text{ GPa}$	$14,000\left(\frac{d_{ps}}{L}\right)$
German code	$E_{ps}\left(\frac{\Delta L}{L}\right) \quad \Delta L = \frac{d_{ps}}{17}$	$E_{ps} = 193 \text{ GPa}$	$11,400\left(\frac{d_{ps}}{L}\right)$
Naaman and Alkhairi (1991) (uniform loading)	$\Omega_u E_{ps} \varepsilon_{cu} \left(\frac{d_{ps}}{c} - 1\right)$ $\Omega_u = \frac{3.0}{\left(\frac{L}{d_{ps}}\right)}$	$E_{ps} = 193 \text{ GPa}$ $\varepsilon_{cu} = 0.003$	$1740\left(\frac{d_{ps}}{c}\right)\left(\frac{d_{ps} - c}{L}\right)$
Tam and Pannell (1976)	$\psi \varepsilon_{cu} E_s \left(\frac{d(1-n)}{L}\right) \quad n = \frac{c}{d}$	$E_{ps} = 193 \text{ GPa}$ $\varepsilon_{cu} = 0.003$ $\psi = 10.5$	$6080\left(\frac{d_{ps} - c}{L}\right)$
Virlogeux (1985)	$\frac{E_{ps} \varepsilon_{cu} + \varepsilon_{su}}{L} \frac{d_s}{d_s} \left(d_{ps} - \frac{a}{2}\right) \left(d_s - \frac{a}{2}\right)$	$E_{ps} = 193 \text{ GPa}$ $\varepsilon_{cu} = 0.003$ $\varepsilon_{su} = 0.020$ $d_s \sim d_s - a/2$ $a = \beta_1 c_u$	$4440\left(\frac{d_{ps} - \frac{\beta_1 c_u}{2}}{L}\right)$
ACI 318-02 (span-to-depth ratio < 35)	$70 + \frac{f'_c}{100\rho_p} \quad (f'_c \text{ in MPa})$	—	—

AASHTO-LRFD 2014 AASHTO-LRFD (2014b) includes separate provisions for members with bonded prestressing, with unbonded tendons, or with mixed bonded and unbonded tendons.

For *bonded* members, tendon stress is estimated when the effective prestressing is at least $0.5f_{pu}$:

$$f_{ps} = f_{pu} \left[1 - k \left(\frac{c}{d_p} \right) \right] \quad \text{Equation 1}$$

$$k = 2 \left[1.04 - \frac{f_{py}}{f_{pu}} \right] \quad \text{Equation 2}$$

For members with *unbonded* tendons, AASHTO-LRFD guidance considers the global deformation of the flexural member, assuming the formation of a single hinge (Section 5.7.3.1.1; AASHTO 2014b). Equation 3 provides the tendon stress at ultimate strength for an unbonded tendon.

$$f_{ps} = f_{pe} + 900 \left(\frac{d_p - c}{l_e} \right) \quad \text{Equation 3}$$

where f_{pe} is the effective stress in the prestressing steel at section under consideration after all losses (ksi); d_p is the depth of the prestressing strand (in.); c is the distance from extreme compression fiber to the neutral axis assuming the tendon prestressing steel has yielded (in.); f_{py} is the yield strength of the prestressing steel (ksi) and l_e is the effective tendon length (in.), which is given by Equation 4

$$l_e = \frac{l_i}{1 + \frac{N_s}{2}} \quad \text{Equation 4}$$

where l_i is the length of tendon between anchorages and N_s is the number of support hinges crossed by a tendon.

MacGregor et al. (1989) developed an equation for determining the prestressing steel stress at ultimate based on experimental work is the basis of AASHTO-LRFD (AASHTO 2014b). MacGregor et al. (1989) recommended that the flexural strength design of members with unbonded tendons be based on the effective length of the tendons between deviators. The developed equation also included a factor developed by Tam and Pannell (1976) and incorporated the maximum allowable concrete strain allowed by ACI 318. Roberts-Wollmann et al. (2005) confirmed this approach and proposed equations with further verification using more current experimental data.

The derivation of the AASHTO-LRFD design equation of flexural strength for members with unbonded tendons considers the global displacement of the member and does not consider bonded reinforcement. Figure 3-3 shows the failure mechanism and geometry for unbonded tendons at ultimate.

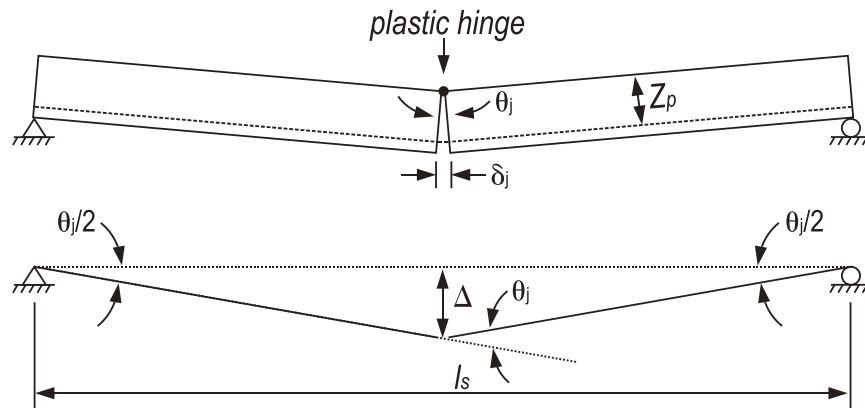


Figure 3-3 Joint mechanism for unbonded tendons

Maximum tendon elongation δ_j (and thereby tendons stress) is related to the ultimate curvature (related to the crushing strength of the concrete), length of plastic hinge, and plastic depth of the tendon in the system. A derivation of tendon stress follows.

From the rigid body displacement in Figure 3-3, tendon elongation δ_j is

$$\delta_j = \frac{4\Delta}{l_s} Z_p \quad \text{Equation 5}$$

where Z_p is the distance from the compressive force resultant to prestressing tendons; l_s is the length of the tendon segment, and Δ is the vertical displacement at the joint.

From mechanism geometry (Figure 3-3), the angular joint opening θ_j can be described:

$$\theta_j = \frac{4\Delta}{l_s} \quad \text{Equation 6}$$

Assuming the tendon behaves in elastic-plastic manner, the decompression moment M_d and the plastic moment capacity of the tendon M are defined:

$$M_d = A_{ps}f_{pe}Z_p \quad \text{Equation 7}$$

$$M = A_{ps}f_{pp}Z_p \quad \text{Equation 8}$$

where A_{ps} is the area of the prestressing steel, f_{pe} is the steel stress corresponding to decompression of the section, and f_{pp} is the steel stress corresponding to plastic deformation of tendon.

Incorporating plastic hinge behavior, the change in tendon force at a plastic hinge is shown in Figure 3-4. ΔT_j is the difference in the tendon force between decompression and plastic deformation. T_e is the force in the tendon at the decompression (also the effective tendon force due to prestressing of the tendon).

$$\Delta T_j = \frac{M - M_d}{Z_p} \quad \text{Equation 9}$$

$$T_e = A_{ps}f_{pe} \quad \text{Equation 10}$$

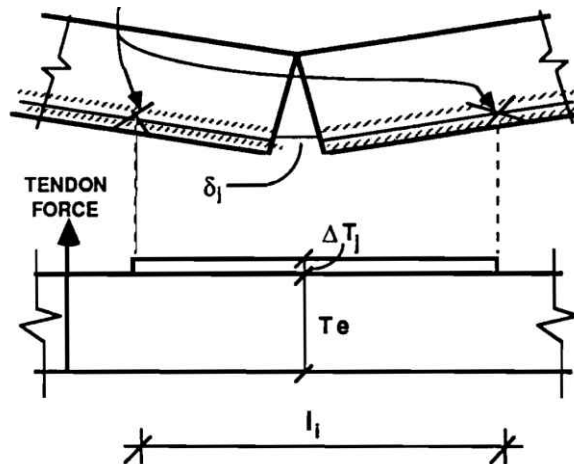


Figure 3-4 Tendon force versus curve length (MacGregor et al. 1989)

Assuming small deflection, the tendon elongation due to the tendon force beyond that required for decompression, can be written:

$$\delta_j = \frac{\Delta T_j l_i}{A_{ps} E_p} \quad \text{Equation 11}$$

Equating Equation 5 and Equation 11:

$$\frac{\Delta T_j l_i}{A_{ps} E_p} = \frac{4\Delta}{l_s} Z_p \quad \text{Equation 12}$$

Substituting ΔT_j from Equation 9 and rearranging:

$$\Delta = \frac{l_i l_s}{4 A_{ps} E_p Z_p^2} (M - M_d) \quad \text{Equation 13}$$

Incorporating Equation 7 and Equation 8, the vertical deflection is written:

$$\Delta = \frac{l_i l_s}{4 E_p Z_p} (f_{pp} - f_{pe}) \quad \text{Equation 14}$$

Virlogeux (1983) considered concentrated rotations to be distributed over a plastic hinge length equal to twice the distance from the resultant compressive force to the center of passive reinforcement in the tension side of the segment (Virlogeux 1983); this corresponds to a diffusion of the compressive force by 45-degree angles. The curvature is assumed to be constant over the hinge length. Ultimate curvature is determined by limiting the maximum concrete compressive strain to the concrete crushing strain (Figure 3-5). The elongation at the plastic hinge δ_h can be expressed in terms of maximum curvature ϕ_m , the distance between the compressive force resultant and prestressing tendons Z_p , and the distance to the passive segment reinforcement Z_s .

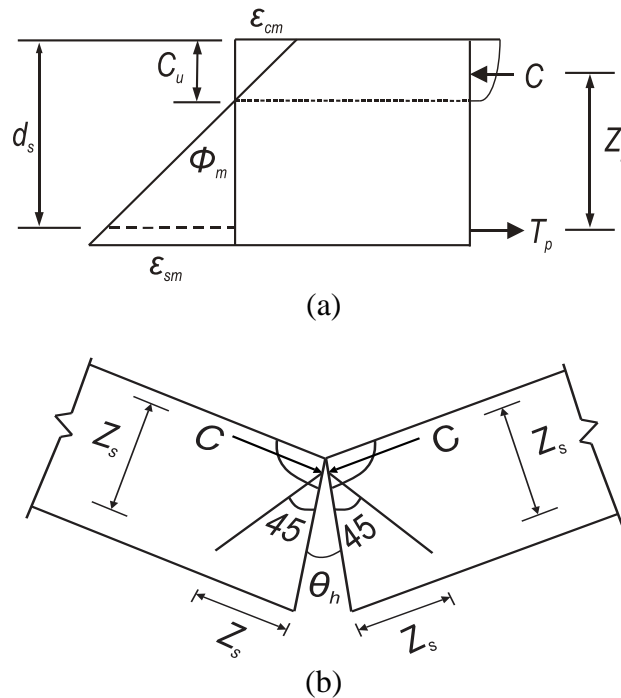


Figure 3-5 Unbonded diagram of (a) strain and force, and (b) joint opening

Calculating the tendon elongation along the hinge portion:

$$\delta_h = \int_{-Z_s}^{Z_s} \phi_m Z_p(x) \left(\frac{x}{Z_s} \right) dx \quad \text{Equation 15}$$

Assuming constant eccentricity of the tendon along the hinge length, therefore $Z_p(x) \rightarrow \text{constant}$.

$$\delta_h = \frac{2\phi_m Z_p}{Z_s} \int_0^{Z_s} (x) \partial x = \phi_m Z_p Z_s \quad \text{Equation 16}$$

From the rigid body plastic mechanism, the limiting mid-span deflection is

$$\Delta_m = \frac{\phi_m Z_s l_s}{4} \quad \text{Equation 17}$$

Combining Equation 14 and Equation 17:

$$\frac{\phi_m Z_s l_s}{4} = \frac{l_i l_s}{4 E_p Z_p} (f_{pp} - f_{pe}) \quad \text{Equation 18}$$

Therefore, the steel stress corresponding to plastic deformation of tendon:

$$f_{pp} = f_{pe} + \frac{\phi_m Z_s E_p Z_p}{l_s} \quad \text{Equation 19}$$

Where the maximum curvature:

$$\phi_m = \frac{\varepsilon_{cm} + \varepsilon_{sm}}{d_s} \quad \text{Equation 20}$$

Where ε_{cm} is the concrete strain and ε_{sm} is the strain in prestressing steel. The strain in the steel is much greater than the strain in the concrete and hence Equation 20 can be simplified:

$$\phi_m = \frac{\varepsilon_{sm}}{d_s} \quad \text{Equation 21}$$

Substituting Equation 21 into Equation 19, and assuming $d_s = Z_s$:

$$f_{pp} = f_{pe} + \frac{\varepsilon_{sm} E_p Z_p}{l_i} \quad \text{Equation 22}$$

From strain diagram Figure 3-5(a):

$$\varepsilon_{sm} = \frac{\varepsilon_{cm}}{C_u} (d_s - C_u) \quad \text{Equation 23}$$

The tendon stress equation then reduces to

$$f_{pp} = f_{pe} + \frac{Z_p \varepsilon_{cm} E_p (d_s - C_u)}{C_u l_i} \quad \text{Equation 24}$$

Tam and Pannell (1976) modified Equation 24 and presented their own equation based on maximum concrete compressive strain and the neutral axis depth, assuming the tendons have yielded. The equation is given by

$$f_{ps} = f_{pe} + \Psi \varepsilon_{cu} E_p \frac{d_p - c_y}{l_i} \quad \text{Equation 25}$$

where d_p is depth of prestressing steel, c_y is the neutral axis depth considering the tendons have yielded. Considering $\Psi = 10.5$ (found experimentally by Tam and Pannell 1976), $\varepsilon_{cu} = 0.003$ (limiting concrete compressive strain), E_p is the modulus of elasticity of prestressing steel (28,000 ksi):

$$f_{ps} = f_{pe} + 882 \frac{d_p - c_y}{l_i} \quad \text{Equation 26}$$

was modified into Equation 3 and presented by MacGregor et al. (1989).

Mixed bonded and unbonded tendons is covered briefly in AASHTO-LRFD (AASHTO 2014), without expressly described justification. The code states that either a “simplified” or a “detailed” approach be undertaken by the designer to assess the unbonded and bonded steel stress. The guidance given for the detailed analysis is a statement - that the designer is to “take into account the strain compatibility between the section and the bonded prestressing steel...[sic] the stress in the unbonded prestressing steel shall take into account the global displacement compatibility between the bonded sections of tendons located within the span.” Else, a second provision allows for a simplified approach with the following assumptions: 1) the ultimate stress in the unbonded tendon is estimated as the effective prestress after losses f_{pe} for determination of the bonded prestressing, 2) the stress in the bonded prestressing is determined by replacing the term $A_{ps}f_{pu}$ in Eqs. 5.7.3.1.1-3 and 5.7.3.1.1-4 with $A_{psb}f_{pu} + A_{psu}f_{pe}$, and 3) a weighted average of the bonded and unbonded steel stress is considered to act over the total area of prestressing steel.

ACI 318-14 ACI 318-14 (2014) provides two different equations for the tendon stress in members with unbonded tendons. These equations were developed with building members, not bridge members, in mind and are empirical. Equation 27 gives the prestressing steel stress for members with a span-to-depth ratio less than 35 and is based on experimental testing by Mattock et al. (1971). Equation 28 gives the prestressing steel stress for members with a span-to-depth ratio greater than 35 and is based on tests conducted by Mojtahedi and Gamble (1978).

$$f_{ps} = f_{se} + 10000 + \frac{f'_c}{100\rho_p} \quad \text{Equation 27}$$

$$f_{ps} = f_{se} + 10000 + \frac{f'_c}{300\rho_p} \quad \text{Equation 28}$$

where f'_c is the specified 28-day concrete strength and ρ_p is the steel reinforcement ratio (area of prestressing steel to the effective area of the concrete).

No specific requirements are given for mixed tendons.

Canadian Highway Bridge Design Code The Canadian Highway Bridge Design Code (CSA-S6-14 2014) states that the effective prestress (of the post-tensioning tendon) be conservatively used as the unbonded tendon stress at ultimate, unless a detailed analysis is used to determine tendon stress, considering global member deformation. No guidance is given for mixed tendons.

3.5.2 Prestressed members with supplemental reinforcement

Prestressed members with both unbonded prestressing and bonded *mild* reinforcement provide some insight into components with both bonded and unbonded prestressing strand, herein referred to as mixed tendons.

The use of mild reinforcement in members with unbonded sections has been observed by several researchers to improve both cracking behavior and reserve capacity. In 1971, Gerber and Burns observe that sections with bonded tendons have an increased maximum reserve capacity – defined as the ability to carry load after primary failure – when compared to sections with only unbonded tendons. They recommended the use of supplementary (mild steel) reinforcement to increase the maximum reserve capacity of unbonded systems, as well as to control cracking (Gerber and Burns 1971). Burns and Hemakom (1985) recommended a minimum percentage of mild steel reinforcement; this recommendation has since been incorporated into ACI 318 (2014).

Also in 1971, Mattock et al. conducted a comparative study of grouted and unbonded (ungROUTED) post-tensioned concrete beams, with the primary aim of investigating the effect of varying the amount of *non-prestressed* bonded reinforcement (in the form of prestressing steel). In addition to the presence, or lack, of bond, other variables in the study included span type (simple-span and continuous) and cross-section (rectangular and T-shape). It was found that unbonded post-tensioned (PT) beams with the minimum recommended non-prestressed bonded reinforcement had serviceability characteristics, strength and ductility equal to, or better than, those of comparable bonded PT beams. One of the intents of the study was to confirm the effectiveness of prestressing strand as auxiliary bonded reinforcement so they combined unbonded tendons with bonded strands that were not prestressed (Mattock et al. 1971).

Several recent investigations have provided models or inspection techniques for predicting tendon stress at ultimate for cases with non-prestressed reinforcing steel (mild) and unbonded tendons, a condition which is similar to the condition considered in this work.

Harajli (2006) provided an evaluation of database of existing test data against existing design equations for the prediction of tendon stress at ultimate. The assessment concluded two things: 1) ACI is conservative, but does not explicitly consider continuous members, and 2) AASHTO-LRFD is more rational but unconservative. Three alternative approaches to predict tendon stress were presented.

Ozkul et al. (2008) presented a rational approach for predicting unbonded tendon stress, considering cases with non-prestressed reinforcing steel (mild) with unbonded tendons. The described model can be used to calculate the stress in an unbonded tendon, including when bonded tendons are present.

Harajli (2012) built on the work presented in Harajli (2006) by specifically considering actual collapse mechanisms in continuous members (dependent on loading conditions). A revision to the existing ACI approach to unbonded tendon was proposed. Investigated examples, unlike the present case, were reinforced with non-prestressed reinforcing steel (mild) and unbonded tendons.

3.5.3 Components with Unbonded and Bonded Tendons: Mixed Tendons

Examination of mixed tendons has been limited, and usually conducted in experimental investigations as a counterpoint to the primary condition under investigation (unbonded or bonded members, depending).

MacGregor et al. conducted flexural testing of quarter-scale, precast segmental concrete box girder continuous span specimens to assess flexural capacity in specimens with external tendons and in specimens with combined internal and external tendons (MacGregor et al. 1989; Roberts-Wollmann et al. 2005). Based on this work, a prediction equation was developed for estimating tendon stresses at ultimate in members with only unbonded tendons; this prediction equation was later adopted into the AASHTO Guide Specification for the Design and Construction of Segmental Concrete Bridges (AASHTO 2014a) and into the AASHTO-LRFD Bridge Design Specifications (AASHTO 2014b, Roberts-Wollmann et al. 2005).

Figure 3-6 shows the moment-deflection comparison for the three tested girders versus the theoretical response of a girder with only internal tendons. Prior to cracking, the stiffness of each system was comparable; after cracking, the behavior differed as the stiffness changed. The differences in stiffness, however, were slight until the specimens neared the ultimate strength. The section with mixed tendons had marginally greater flexural capacity and increased ductility compared to the specimens with only external tendons. For sections with external tendons only,

the ultimate moment strength of the section with unbonded (greased) external tendons was slightly less than that of the section with bonded external tendons. MacGregor noted that members with mixed tendons did not offer significant improvements to either ultimate strength or deflection. MacGregor's work – unpublished due to his untimely death – was presented in a 2005 publication by colleagues (Roberts-Wollmann et al. 2005).

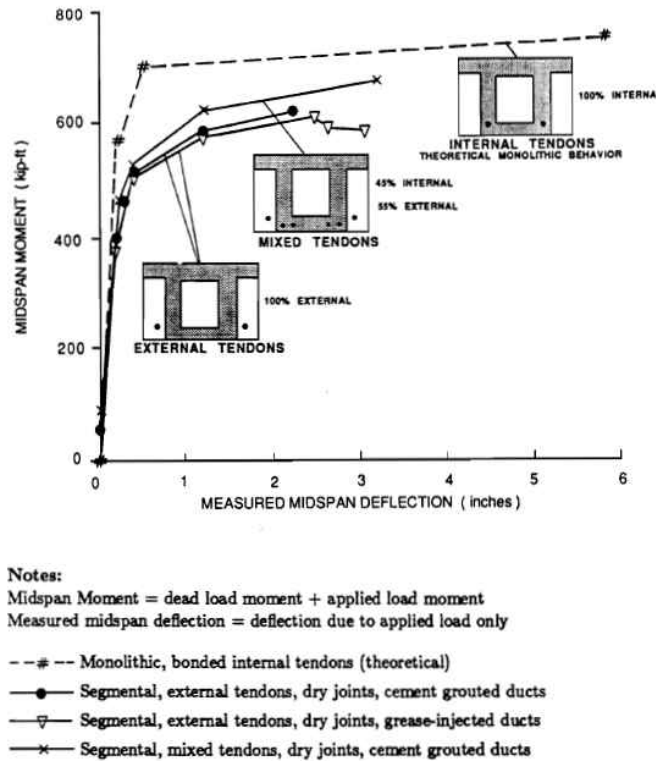


Figure 3-6 Moment-deflection of post-tensioning systems (MacGregor et al. 1989)

Gauvreau (1993) proposed a model for the rational calculation of tendon stress at ultimate for components with bonded reinforcement, unbonded tendons, or both, based on a truss model with explicit consideration of the angle of inclination of the internal concrete compression chords. The approach relates the global structural deformations (used to calculate the elongation of the unbonded prestressing steel) to the strain state corresponding to the internal forces in the truss at any given section. The proposed method was compared with experimental load tests of eight simply-supported concrete girders. Gauvreau's proposed rational approach has neither been acknowledged in subsequent research nor incorporated into code bodies.

Seismic tests by Megally et al. (2002) conducted on precast segmental bridge superstructures with different post-tensioning systems (internal, external, and both internal and external) also showed greater moment strength with internal bonded tendons versus those with either external tendons or versus those with a mix of external and internal tendons. Internal tendons were grouted, but external tendons were left ungrouted to observe behavior during testing to protect strain gages and to inspect for wire failures; the tested specimens could, consequently, be considered fully unbonded. The specimen with unbonded external tendons demonstrated increased ductility relative to the specimen with internal, fully bonded tendons. Megally et al. (2002) suggests that, for high seismic zones, external tendons instead of bonded

internal tendons should be used as they provide improved ductility. Further, they suggested a combination of combined internal bonded tendons and external tendons should not be used as the combination neither improves the strength, nor the ductility when compared to only bonded internal tendons.

3.6 Fatigue

Fatigue is the progressive and localized structural damage that occurs when a material is subjected to cyclic loading at stresses below the yield strength of the material. Fatigue failures can occur in structures subject to cyclic loads if the stress range is large enough. Generally, this mechanism starts with the development of a crack at a point under concentrated tensile stress. The crack continues to propagate until the cross-sectional area is reduced to the point where a brittle failure occurs. In prestressed concrete structures, the prestressing strand typically controls the fatigue strength of the member.

Prestressing strand's fatigue life is inversely related to the applied stress range; if the stress range is below a certain level, then the fatigue life is infinite. This point is called the endurance limit and is the maximum stress range for which the fatigue life is independent of the applied stress range (Figure 3-7). Paulson et al. (1984) studied the fatigue of individual strands in air and developed fatigue life recommendations for prestressing strand.

Prior to cracking the stress range of prestressing steel, whether in pretensioned or post-tensioned construction, is very small and is likely to be well below the endurance limit. If the fatigue loading takes the member beyond cracking, however, the stress range of the prestressing strand around the flexural crack can increase considerably. In pretensioned girders, the strands are typically only in contact with the surrounding concrete. Consequently, fatigue behavior of the strand in these conditions is very similar to that of strand-in-air (Ryals et al. 1992).

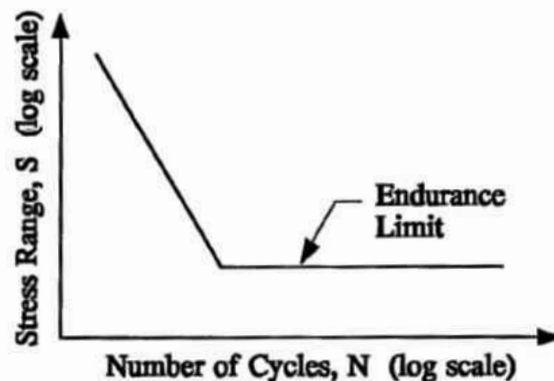


Figure 3-7 Typical S-N plot (Ryals et al., 1992)

In post-tensioned tendons, however, tests have shown that the fatigue strength can be significantly lower than would be predicted by strand-in-air tests. In pretensioned girders, when flexural cracks form, the individual strands are not generally in contact with surrounding strands or metal duct. But this is not true of post-tensioning tendons where they can be in contact with adjacent strands, duct, or anchorage assemblies. Consequently, the small strand deformations that occur at the flexural crack can produce metal-on-metal rubbing, which can lead to fretting fatigue.

Fretting is generally described as corrosion at the contact area between two materials subject to slippage under high pressure of repeated loads. Fretting leads to surface damage of the two materials (such as strand and post-tensioning duct), though there might not be any corrosion product. Wear, abrasion, and crack development are examples of damage caused by fretting; these may result in the reduction of the fatigue life. Fretting can create crack initiation points in post-tensioned strand, but crack development depends on the dynamic loading of the structure. If crack growth continues, then the crack depth may become critical resulting in strand rupture.

Factors that are influential to fretting fatigue include: tendon stress range, relative magnitude of slip between metals, duct curvature, and strand protective cover (sheathing or epoxy coating). A number of theories (Bill 1982; Waterhouse 1982) have been formulated to explain fretting fatigue. Some include:

- The protective oxide film is lost due to abrasion and wear, making the steel susceptible to the corrosion.
- Slip between the duct and strands leads to the surface damage.
- Cracks are caused by abrasion, wear, and stress induced by local pressure.
- Loose particles increase rubbing and slip action between two different materials.

In grouted internal tendons, the curved profile generates lateral contact pressure between the strands and between strands and duct (Figure 3-8). If the cyclic loads are sufficient to crack the grout, which is not prestressed, then strand deformations will occur near these cracks. The contact pressure combined with the strand deformation results in abrasion that can intensify fretting fatigue.

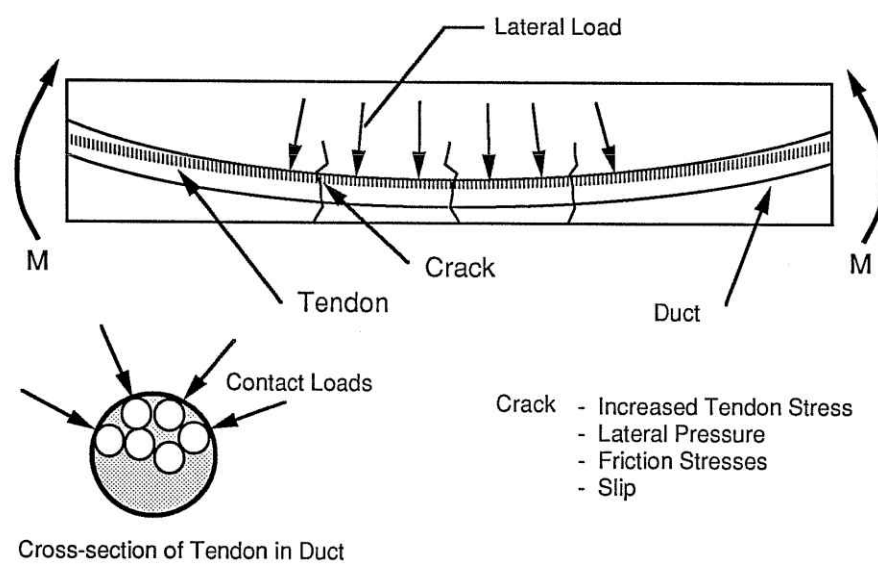


Figure 3-8 Generation of slip due to friction stress and debonding in post-tensioned beam (Hall 1990)

In external tendons, the acute angle change at deviators results in very large contact pressures between the strands and between the strands and steel pipe that lines the deviator (Figure 3-9). If the cyclic loads are sufficient to develop cracks in the grout, then the strand may slip relative to the grout resulting in abrasion that can intensify the fretting fatigue (Figure 3-9).

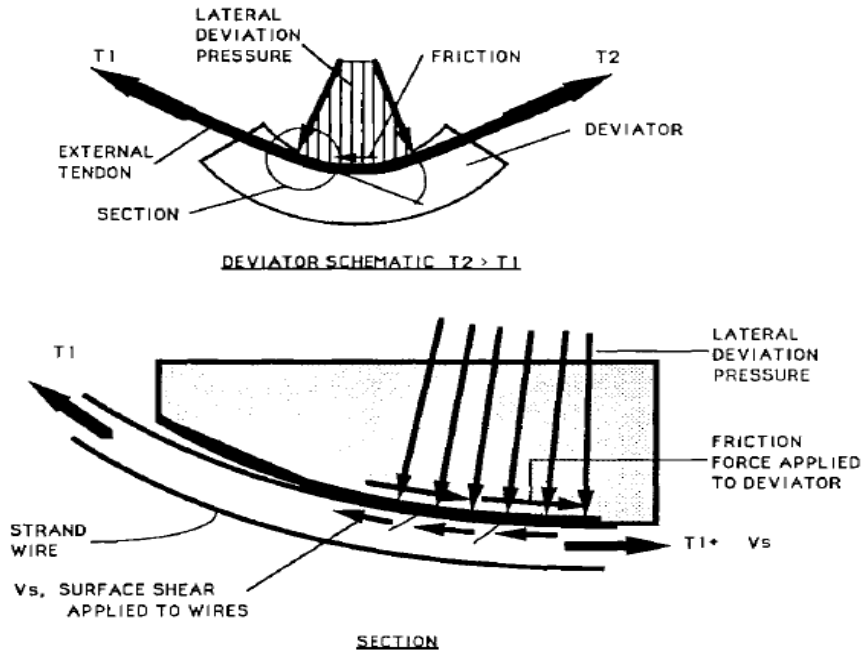


Figure 3-9 Lateral pressure and frictional force on the deviator block (Hall 1990)

Paulson et al. (1984) suggest that fretting fatigue with higher contact pressures can reduce the fatigue life for a given tendon stress range. As the contact pressure increases, the fatigue life decreases. Contact pressure is dependent on many variables, including the radius of curvature of the duct, the ratio of the duct area to the tendon area, and the strand arrangement in the duct.

The use of plastic ducts, and greased and/or sheathed tendons improve the fatigue life of the single strands, as there is less abrasion between materials. Abrasion is always present between strands in multi-strand systems. Figure 3-10 shows the comparison of the single and multi-strand systems (Paulson et al. 1984).

The previous discussion has focused on grouted internal and external tendons. The grout provides bond between the concrete section and prestressing strand, even in external tendons at anchorages and deviators. When the applied load causes the grout to crack, then the strain associated with the crack is concentrated in the strand at the location of the crack, resulting in a relative slip. In unbonded tendons, though, any excess strain developed at flexural cracks is distributed over the length of the tendon between anchorages. Consequently, unbonded tendons are thought to be subject to a small stress range (Traute and Weiher 2011). One possible exception would be where there are large frictional forces developed. In these cases, the strand may behave as if it is bonded.

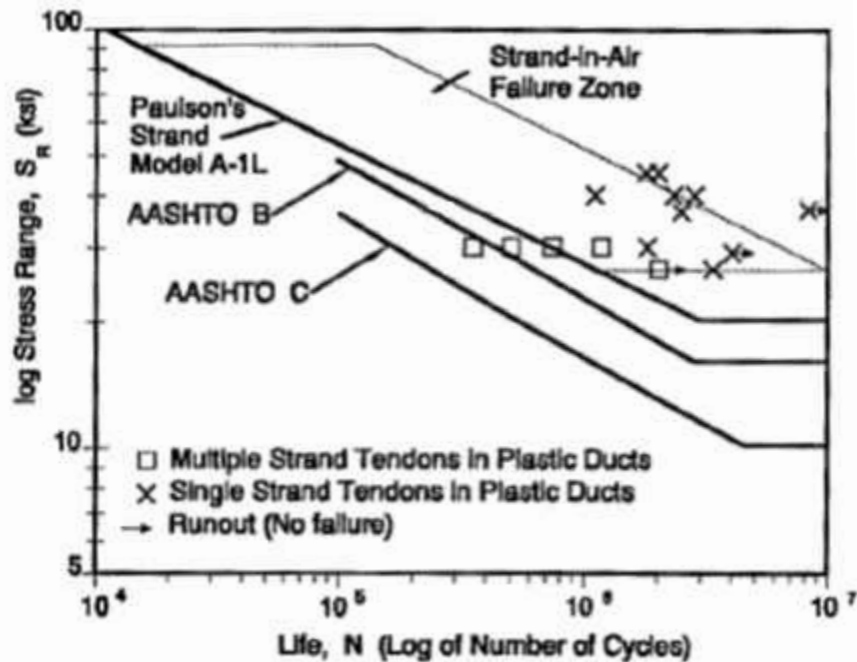


Figure 3-10 Fatigue of plastic PT ducts with single and multi-strands (Paulson et al. 1984)

3.6.1 Design Guidance

This section summarizes fatigue design requirements in U.S. codes for unbonded tendons. Code guidance regarding fatigue of unbonded post-tensioning tendon systems (including hardware) is limited.

AASHTO-LRFD Two AASHTO publications cover fatigue of prestressing tendons: the AASHTO-LRFD Bridge Design Specifications (AASHTO 2014b) and the AASHTO-LRFD Bridge Construction Specification (AASHTO 2014a).

For prestressing tendons, AASHTO-LRFD Bridge Design Specifications (AASHTO 2014b, Section 5.5.3.3) state that the design stress range shall not exceed 18 ksi for radii of curvature greater than 30 ft, or 10 ksi for radii of curvature less than 12 ft. For radii in between these two values, linear interpolation is permitted.

Fatigue performance acceptance criteria for unbonded anchorage systems are covered by the AASHTO-LRFD Bridge Construction Specifications (AASHTO 2014a), although, in general, the specification is focused on grouted tendons. For unbonded tendons, “representative anchorages” are to be dynamically tested in two different situations. Specimens are to be representative of the tendon system, composed of both the prestressing strand and anchorages; for multi-strand tendons, the number of strands in the test specimen may be reduced, but must provide at least 10% of the capacity of the full-size tendon. One specimen is required to withstand 60 to 66 % of its specified minimum ultimate tensile [strand] strength (MUTS) for at least 500,000 cycles. A second test specimen is required to withstand 50 cycles at 40 to 80% of the specified MUTS.

The AASHTO Bridge Construction Specifications also describe acceptance criteria and fatigue testing requirements for anchorage blocks. The reader is referred to the specifications for the required test procedure and criteria (AASHTO 2014a).

ACI 318-14 The ACI 318 Building Code Requirements for Structural Concrete is primarily focused on building members and systems, not bridges; within this document, “unbonded systems” primarily refer to monostrand (individually greased and sheathed prestressing strands) in post-tensioned slab applications. For unbonded prestressing tendons subject to repetitive loads, ACI states that the designer should consider the possibility of fatigue in anchorages and couplers (ACI 2014).

ACI Fatigue Committee Report 215 (1997) The commentary within ACI 318 guides the reader to ACI Committee Report 215 for discussion on fatigue design considerations. For prestressing tendons, a maximum stress range of $0.04 f_{pu}$ is recommended for strands, bars or wires prestressed between $0.4-0.6f_{pu}$.

ACI Guideway Committee 358 (1986) The ACI 358 (1986) Guideway Committee recommends the same stress range ($0.04 f_{pu}$ is recommended for strands, bars or wires prestressed between $0.4-0.6f_{pu}$) unless more severe conditions of curvature exist. In such cases, the maximum recommended stress range is $0.025f_{pu}$.

PTI Cable-Stayed Bridge Committee (PTI 2007) PTI Recommendations for Stay Cable Design, Testing and Installation cover grout-filled stay cable systems, which are similar enough in construction (typically, post-tensioned steel strand, housed in a duct, and anchored to the bridge) to warrant consideration for unbonded post-tensioning tendons, at least in the general idea that these systems are acceptance tested for fatigue prior to use. The PTI Recommendations (2007) state that for every project, the proposed stay cable system (the entire system), shall be tested for both static and fatigue strength to determine acceptance. For fatigue, a (minimum) 3.5 meter specimen with anchorages is to be tested to 2 million cycles. An upper stress limit and stress ranges are given by the PTI Recommendations. A cable-stay system is accepted if no more than 2% of the individual wires fail, and no bars fail, and no anchorage component fail. Additionally, after the cyclic loading is completed, the system must demonstrate either 92% of the actual, or 95% of the specified cable ultimate tensile strength.

3.6.2 Past Research

Reduced fatigue life of post-tensioned girders was first documented by Magura and Hognestad in 1966 (Hall 1990). Two pretensioned girders were compared to two post-tensioned girders: both post-tensioned specimens were observed to experience “serviceability distress and reduced flexural capacity from load repetitions,” while the pretensioned girders were described to perform adequately.

Subsequent research on post-tensioned concrete has found the same: the expected fatigue life of prestressing strand (as determined from strand-in-air tests) can be substantially reduced in post-tensioned concrete applications due to fretting fatigue of the prestressing tendon (Wollmann et al. 1988; Hall 1990). Commentary in the AASHTO-LRFD (2014b) Bridge Design Specifications encourages consideration of “metal-to-metal fretting caused by prestressing tendons rubbing on hold-downs or deviations,” in so far as such action causes an increase in bending stress at high curvature deviations, or in the development of reduced permissible fatigue stress ranges due to this action.

Fretting is defined as the action of two elements under high contact pressure subject to minute slippage due to repeated oscillations. Two elements subject to fretting develop fretting wear, or surface damage. Fretting over a long time period is described as fretting fatigue, which is also described as the process of surface damage (caused by cyclic load and relative slip between two surfaces, usually metal) initiating surface cracks which propagate until brittle

fracture occurs at a reduced fatigue life. Fretting corrosion refers to the chemical interaction between the environment and the fretting action; oxidation is the most common form of corrosion (Bill 1981).

The predominant mechanism of fretting fatigue in post-tensioning tendons is asperity contact initiation (Hall 1990). At asperities, or contact points, applied lateral pressure causes cold welding which joins the two elements (Figure 3-11). When the two elements are re-stressed (such as due to cyclic loading of a prestressing tendon), the two elements are torn apart at the cold weld and damage results. The forming and tearing of these cold welds results in abrasive wear, corrosion and accelerated initiation of surface cracks (Wollmann et al. 1996). A phenomena known as cold metal transfer occurs when the tearing of the two elements results in transfer of material from one element to the other. This transfer of material is known to accelerate fretting fatigue.

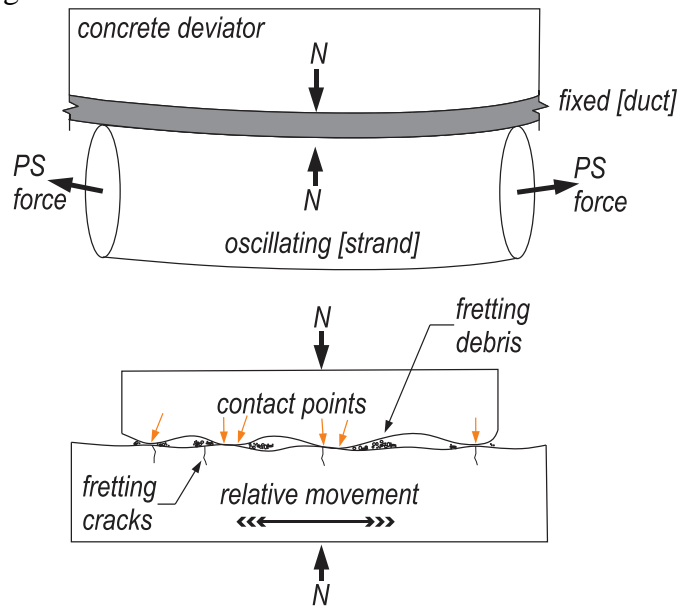


Figure 3-11 Fretting mechanism at deviated prestressing strand

Fretting Fatigue vs. Fatigue Crack Growth

Fretting crack initiation occurs differently than crack initiation in non-contact (such as strand-in-air) fatigue conditions (Figure 3-12). This is due to the stress state of the material when under fretting conditions, namely due to the influence of the normal (or contact or clamping) load. A fretting fatigue crack begins at an incline and develops at an angle such that the crack is parallel to the plane of principal tension (resulting from the lateral (contact) load and the prestressing force in the tendon). At a distance away from the surface, the direction of the crack changes such that it is perpendicular to the tensile force in the strand. (Hall 1990)

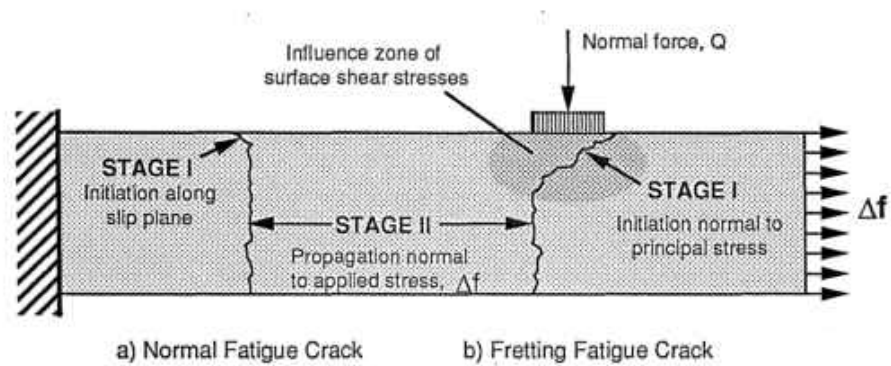


Figure 3-12 Fatigue vs. fretting fatigue cracks (Waterhouse 1972)

Factors Affecting Fretting Fatigue

Fretting fatigue is a function of contact conditions, environmental conditions, and material properties (Bill 1982). In the particular case of an external prestressing tendon at a deviation point, contact conditions include the lateral pressure acting on the tendon from the deviator, and the tendon stress range and related slip amplitude of the strand within the duct. Lateral pressure – or contact pressure between the strand/strand, or duct/strand, at a deviation point – has been shown to be positively correlated to the crack growth rate and a subsequent reduction of fatigue life (Hall 1990).

The severity of fretting fatigue is also dependent on slip amplitude (Bill 1981). At a large enough slip amplitude, fretting fatigue is not a problem; at small enough amplitudes, it is also not a problem (Figure 3-13). There exists, however, a range of slip amplitudes for which the potential for fretting fatigue is a concern.

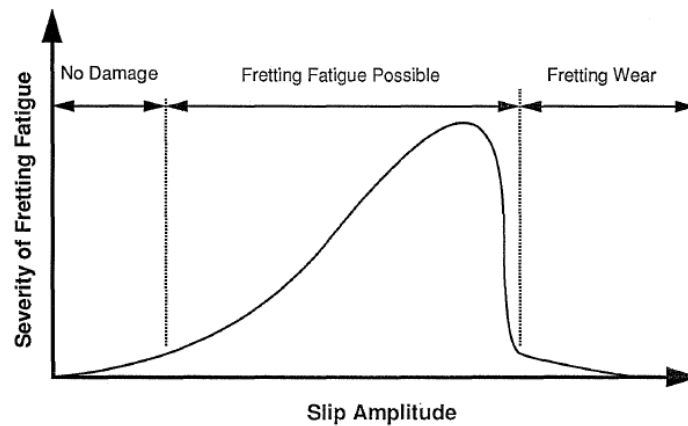


Figure 3-13 Severity of fretting fatigue vs. slip amplitude (Yates 1987)

Several environmental factors also influence the development of fretting wear in general conditions (not specifically post-tensioning tendons). These factors include temperature, humidity, and the presence of oxygen.

Fretting Mitigation

Lubricants have been shown to decrease fretting corrosion. The positive influence of lubricants on fretting corrosion is supposed to be due to three qualities: 1) oxygen restriction, 2)

friction reduction, and 3) removal of formed debris (“sweeping away of debris,” per Waterhouse 1972).

The use of lubricants in steel strand has been investigated to some degree. Waterhouse and Taylor (1971) evaluated the use of different lubricants used in locked coil 7-wire steel strand (the resulting 7-wire strand is of different geometry than the 7-wire strand typically used in most U.S. prestressing applications). The fretting fatigue strength of coated and uncoated strands were assessed after cyclic loading. In the tested application, the lubricants were applied during strand fabrication; the strands were not “encased” in a heavy application of lubricant, as would be true in unbonded post-tensioning tendons. Waterhouse found that the use of lubricants reduced fretting wear and increased the fretting fatigue strength of steel rope from 7-33% over that of uncoated strand (Waterhouse 1972).

Changing from cementitious grout filler to petroleum-based flexible filler will alter the humidity and oxygen presence inside the tendon. It is anticipated that the grease/wax substances will function, essentially, as lubricants much like bearing wheel greases, which have been shown to both reduce friction and prevent oxidation.

Several additives (both anti-oxidants and corrosion inhibitors) are used in lubricating greases to reduce corrosion effects; the more specific phenomena of fretting corrosion may also benefit from such additives. The use of different additives in lubricants has been shown to have some effect on the wear rate and fatigue strength of tested steel ropes.

Research on fretting fatigue in post-tensioning tendons has primarily been focused on grouted tendons. At least one study has been conducted to evaluate the fretting fatigue life of unbonded tendons with bare post-tensioned strand and no filler material (Hall 1990). To the best of the author’s knowledge, no research has been published on fretting fatigue evaluation of post-tensioning tendons filled with flexible material. Research on unbonded tendons – without any filler material – provides some insight into the potential behavior of post-tensioning tendons with flexible fillers.

This section covers the published research on fretting fatigue in both bonded and unbonded post-tensioning, as the implemented testing methods will be comparable to the proposed testing. Additionally, the behavior of bonded post-tensioning tendons (the currently employed practice) will serve as a comparison benchmark for assessment of unbonded, flexible material filled post-tensioning tendons.

Fretting Simulation

Cordes and Lapp-Emden (1984) conducted tests to simulate fretting fatigue in an isolated strand. In a set-up similar to strand-in-air tensile tests, single strands were subjected to localized contact pressure while the strand was tensioned cyclically. Lateral contact pressure was applied only to a short length of the test specimen. Figure 3-14 shows the test set-up.

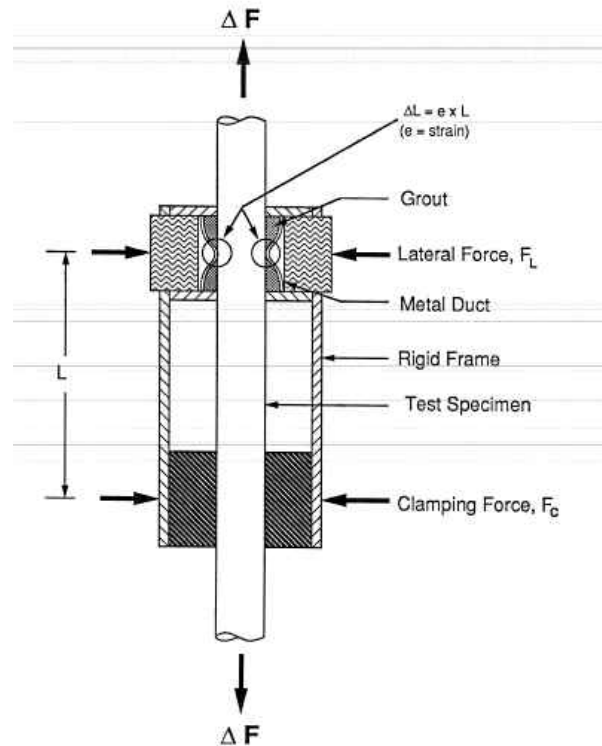


Figure 3-14 Cordes and Lapp-Emden (1984)

The Cordes-Lapp-Emden test set-up provided an opportunity to evaluate fretting fatigue as a function of easily isolated variables: contact pressure and applied stress range. Tests were conducted on four different specimen types: 0.6-in. dia. 7-wire prestressing strand, 7 mm dia. drawn wire and 12.2 mm dia. wire (both drawn and quenched). Two lateral loads were used (5.1 kip/ft and 6.8 kip/ft), while the slip amplitude was held constant at 0.15 mm. Metal duct was used in all cases.

Findings included:

- Large stress ranges did not induce fretting;
- Corrosion was observed at the duct contact points;
- Cracks at contact points initiated at an incline.

In some cases, failure occurred away from the applied lateral pressure, in the free length of the specimen and, therefore, fretting fatigue was not the failure mode. Recommendations were made to limit the allowable stress range to 25 ksi for 7-wire strand and 12.2 mm dia. wire (both quenched and drawn) and to 23 ksi for 7 mm dia. drawn wire. However, in comparison with other types of fretting fatigue testing (both full-size girder testing and reduced-beam testing), Wollmann et al. (1988) noted that the Cordes-Lapp-Emden fretting simulation tests tend to show a better fatigue performance than other test methods. Hall (1990) explained this improved performance by the absence of group effects (strand-to-strand fretting in multi-strand tendons, for example) and by the load path of the applied lateral force (tensioning of the prestressing strand rather than displacement of the lateral pressure point.) Because the real-life contact conditions are complex, their close approximation in the chosen test setup is important for accurate results, as is careful measurement of the slip amplitude and applied loads

(Waterhouse 1982). However, the main observation of the Cordes-Lapp Emden tests was that fretting can reduce fatigue life.

Reduced-beam

Because the effective prestress force affects the strand stress range at overload, and thereby the load range acting on the beam, its accurate determination is critical for assessing fretting fatigue. Oertle et al. (1987) developed a reduced-beam concept by which strand force can be accurately determined. Figure 3-15(a) illustrates the concept and Figure 3-15b shows the test set-up.

The specimen allowed for accurate determination of the tendon force and isolated observation of fretting behavior in a tendon at the deviator. Furthermore, the reduced size of the specimen permitted the completion of more tests by permitting higher frequency load cycling over shorter test duration. Given the usual spread in fatigue test results, trends determined from multiple tests become more valuable than any one test result (Figure 3-16).

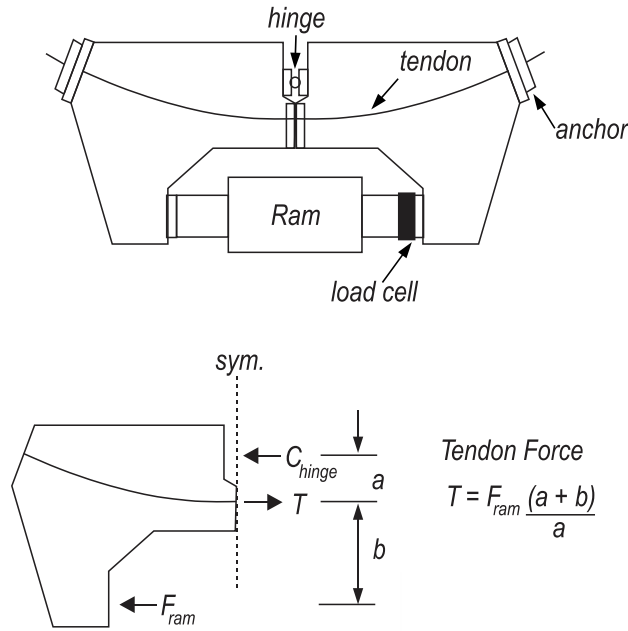
Oertle et al. (1987) investigated specimens with tendons composed of either (1) 7 mm wire, (5) 7 mm wires (held parallel), or (1) 0.6-in. dia. seven-wire prestressing strand. Metal and plastic ducts were tested, as well as grouted and ungrouted tendons.

Several observations/recommendations were reported:

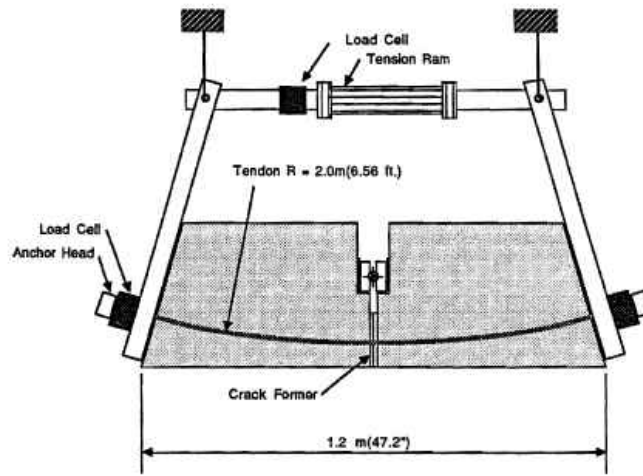
- Unbonded tendons performed better than bonded tendons;
- Plastic duct tendons had an increased fatigue life vs. metal duct tendons;
- Multiple wire tendons exhibited significantly reduced fatigue life;
- Increased stress range reduced the fatigue life of the tendon.

Several recommendations were made:

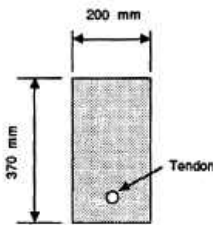
- Use of plastic duct in grouted tendons to reduce rubbing between duct and strand;
- Recommendation to limit the allowable stress range of 14.5 ksi for metal duct and 29 ksi for plastic duct (assuming a contact load at the duct corrugations of <0.45 kip).



(a)



a) Elevation



b) Section

Tendon	Duct	Grouted	Ungouted
1-7 mm dia Wire	Metal	●	●
	Plastic	●	
5-7 mm dia Parallel wires	Metal	●	
	Plastic	●	
1-0.6 in dia 7 wire strand	Metal	●	●
	Plastic	●	●

c) Test Program

(b)

Figure 3-15 Oertle reduced-beam (a) force determination (b) test set-up

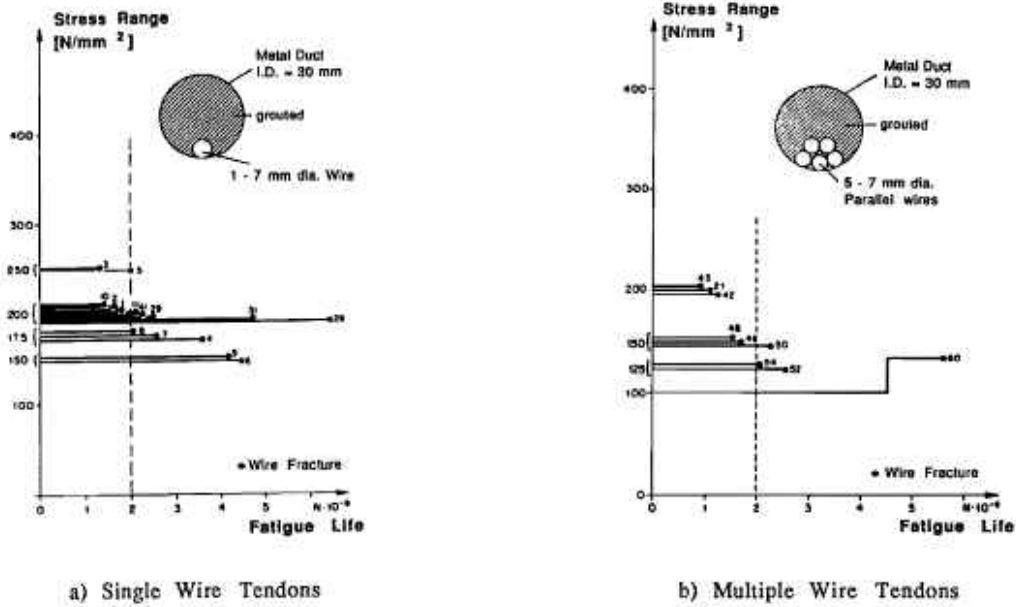
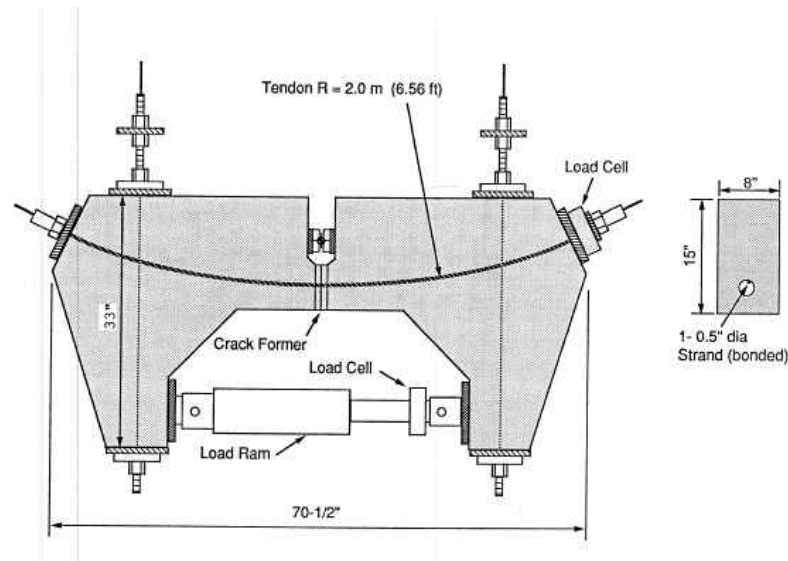


Figure 2.12 Comparison of Single Wire and Multiple Wire Tendons (from Oertle, et al. [19])

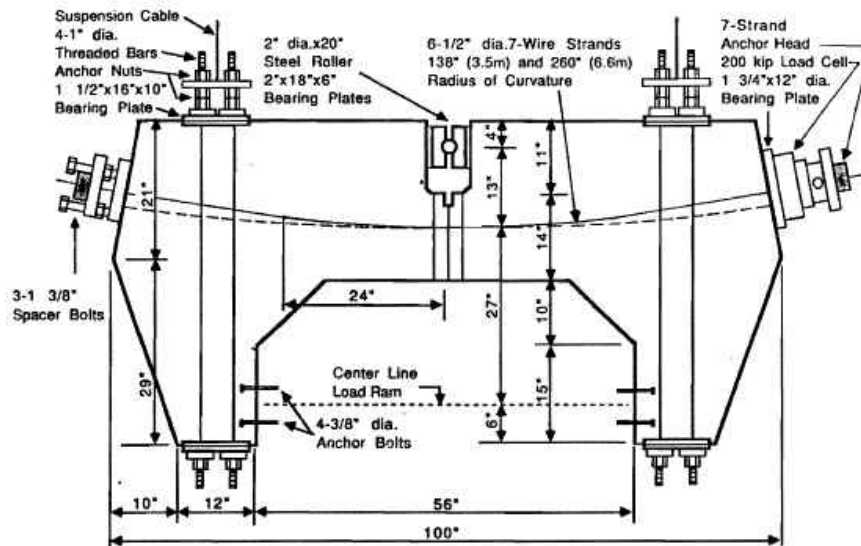
Figure 3-16 Oertle results (from Wollmann et al. 1988)

Several iterations of the reduced-beam concept have been used since Oertle et al. (1987). In tests at the University of Texas at Austin, Yates used a similar setup to investigate single-strand tendons (Yates 1987) and Wollmann developed a larger reduced-beam setup to investigate multi-strand tendons to investigate group effects (Wollmann 1988). Both Yates and Wollmann investigated grouted tendons.

The test results of both researchers' reduced-beam investigations were reported in a combined paper in the ACI Structural Journal in 1996 (Wollmann et al. 1996). In total, Wollmann et al. (1996) used twenty-two reduced-beam specimens – thirteen specimens with 1/2-in. diameter single strand tendons and nine with (6) 1/2-in. dia. strand multi-strand tendons. Wollmann and Yates reduced-beam test set-ups are shown in Figure 3-17.



(a)



(b)

Figure 3-17 University of Texas at Austin reduced-beam tests (a) Yates single strand (Georgiou 1989) and (b) Wollmann multi-strand (Wollmann et al. 1988)

Using a variation on Oertle's reduced-beam, the research team at the University of Texas was able to examine several parameters including different: radii of curvature, duct materials (plastic vs. metal), stress ranges (18-40 ksi) and standard strand vs. coated strand. In addition to experimentally determining the tendon fatigue life for these different parameters, Wollmann et al. (1996) were able to deduce the approximate deviation load on the tendon. A relationship between the contact load magnitude and the fatigue life was apparent; Wollmann et al. (1996) distinguished between contact loads less than and greater than 6 kip/ft (see Figure 3-18). Tendons with contact loads greater than 6 kip/ft appeared to exhibit a lower fatigue life, regardless of the applied tendon stress range.

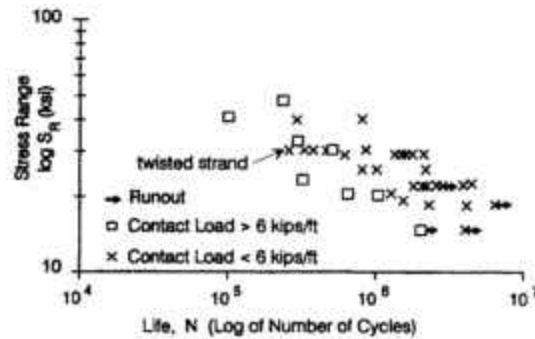


Figure 3-18 Influence of contact load (Wollmann et al. 1996)

Other important observations:

- All wire fractures occurred within 15 in. of cracks in regions of large tendon curvature.
- Most fractures occurred at contact points between duct and strand.
- Corrosion was observed to accelerate due to fretting.
- Some fatigue fractures were observed to occur at strand/strand contact points.
- Wire-to-wire contact fractures occurred in strands already diminished by wire fracture.
- Twisting of strands within a tendon resulted in a drastic reduction of fatigue life.

The propagation rate of fretting wear is mostly a function of the relative slip magnitude; Wollmann confirmed that extremely small slip amplitudes are sufficient to cause fretting fatigue (Wollmann et al. 1996). Though the researchers only noted that the twisted tendon resulted in a reduced fatigue life, this observation is important as twisted strands within tendons are common place.

Full-size Testing

Full-size testing of bonded (grouted) post-tensioned concrete girders has been reported by several research groups; one series of unbonded, ungrouted beam tests has demonstrated reduced fatigue strength (Brondum-Nielsen 1973). Table 3-2 is a summary of tests that have been conducted to evaluate fatigue and fretting behavior of post-tensioned full-size girders with bonded tendons. To the best of the authors' knowledge, no full-size testing has been performed on unbonded post-tensioned specimens with flexible filler material.

Table 3-2 Testing of full-size bonded post-tensioned specimens

Investigator	Type of specimen	Total # of specimens	Tendon type	Duct Material	Main Findings/Notes
Brondum-Nielsen (1973)	Bonded and unbonded (no filler) beams	6	(3) grouted and (3) ungrouted (12) 7-mm cable	Unspecified – presumed metal	Two stress ranges tested. Lower fatigue strength of unbonded tendons shown; points to “low fatigue strength of anchorages”. Recommends grouting.
Rigon and Thurlimann et al. (1985)	Bonded PT girders	8	(2) with parallel wire and (6) with 7-wire strands	Metal and plastic	Tendon stress by strain in passive reinforcement
Muller (1986)	Bonded PT girders		Parallel wire, strand and threaded bar	Metal only	Fretting observed at strand/duct, strand/strand and wire/wire contacts. No fretting with threaded bar. In wire and strand, fretting initiated at contact locations.
Oertle, Thurlimann and Esslinger (1987)	Bonded PT girders	4	Parallel wire and 7-wire strand	Metal and plastic	Tendon stress determined by analytical method. Better fatigue performance noted with parallel wire and plastic duct.
Diab (1988)	Bonded PT girders	3	(6) 0.5-in. dia. 7-wire strand	Metal	Primary variable was tendon stress range. Most fretting fractures due to strand-duct contact. Some due to wire-wire contact. Most located at drape points.
Georgiou (1989)	Parabolic and double draped bonded PT girders	5	(6) 0.5-in. dia. 7-wire strand	Metal and plastic	Three variables: duct layout, duct material and tendon stress range (25-40ksi).

3.7 Implications

The use of unbonded tendons in place of grouted tendons has several implications with regard to structural behavior. Unbonded tendon failures are observable, whether internal or external. Failed external tendons can be identified during inspection as they lay in the section. Failed unbonded internal tendons are likely to be observable at the anchor. Meanwhile, failure of bonded tendons can be hidden from observation under service loads due to redevelopment. Although highly unlikely, the failure of a sufficient number of tendons at a given section would result in a sudden collapse without sufficient warning.

With regard to redundancy, the effects of tendon failure are different for bonded and unbonded tendons. For bonded tendons, tendon failure at a point may not necessarily result in complete tendon loss, thus maintaining some redundancy. The same is not true for unbonded tendons, in which a complete loss is guaranteed if the tendon fails at any point. The consequences of tendon failure at a point are not the same for unbonded tendons as they are for bonded tendons.

AASHTO-LRFR does not appear to distinguish between bonded and unbonded tendons when considering redundancy. In addition, AASHTO-LRFD does require a minimum amount of bonded reinforcement systems that contain all unbonded tendons. ACI 318-14, however, guides the designer to provide minimum bonded reinforcement. This provision not only provides crack control, but also provides supplemental strength. Further, the required bonded reinforcement provides an alternate load path to the system, as this mild steel is in contact with the concrete and, in case of tendon failure, provides supplemental strength. On the other hand, if the system has more than one tendon, it allows a secondary load path in case of failure of one tendon.

AASHTO's ultimate strength provisions are based on testing of a segmental bridge scale model that was constructed with grouted tendons, both internal and external. While external tendons typically behave as nearly fully unbonded, it is not clear that completely unbonded tendons will behave in a similar manner.

Since most of the experimental testing reviewed has focused on grouted tendons, it is not clear how the use of unbonded tendons will affect flexural cracking behavior when used as internal tendons in I-girders or substructures, and as external tendons in segmental construction.

The use of unbonded tendons will result in reduced stress range for cyclic loads and may reduce the susceptible to fretting fatigue. No experimental work, however, was found to support this.

4 Specimen Design

This chapter describes the specimen design and detailing considerations of the three internal tendon girder specimens (IGS, IWS and IWC), two external tendon girder specimens (EWS and EWC) and the two fatigue beam specimens (R1, R2).

4.1 Internal Tendon I-Girder

Three 40-ft long simple-span precast concrete I-girders with an 8-in. by 34-in. concrete deck were constructed, each with three bonded 0.6-in. dia. pretensioned strands and a parabolic, internal multi-strand post-tensioned tendon composed of (12) 0.6-in. dia. prestressing strands. Two 0.375-in. dia. top prestressing strands were included to simplify installation of shear reinforcement stirrups. The chosen cross-section was a modified AASHTO shape; by using the side forms of an AASHTO Type IV with the bottom form of an AASHTO Type V, the resulting 10-in. wide web accommodated an internal tendon with the minimum concrete cover. Specimens are shown in Figure 4-1 and Figure 4-2. The naming convention and basics of the internal tendon specimens are given in Table 4-1.

The specified properties of the materials chosen for the internal tendon test specimen design were as follows:

Precast beams:	Dimensions and strand pattern (Figure 4-1): AASHTO Type IV-V Concrete strength at transfer, $f'_{ci} = 6$ ksi Concrete strength at 28 days, $f'_c = 8.5$ ksi
Cast-in-place slab:	Slab thickness = 8 in. Concrete strength at 28 days = 8.5 ksi Self-consolidating mix
Bottom pre-tensioned prestressing strands:	(3) 0.6-in. dia., seven wire lo-lax strand Area, per strand = 0.217 in. ² Ultimate strength, $f_{pu} = 270$ ksi Prestressing strand modulus of elasticity = 28,500 ksi Prestress level at jacking = $0.75f_{pu}$
Top pre-tensioned prestressing strands:	(2) 0.375-in. dia., seven wire lo-lax strand Area, per strand = 0.085 in. ² Ultimate strength, $f_{pu} = 270$ ksi Prestressing strand modulus of elasticity = 28,500 ksi Prestress level at jacking = 10 kip
Post-tensioned prestressing strands:	(12) 0.6-in. dia., seven wire lo-lax strand Area per strand = 0.217 in. ² Ultimate strength, $f_{pu} = 270$ ksi Prestressing strand modulus of elasticity = 28,500 ksi Prestress level at jacking = $0.8f_{pu}$ Radius of curvature = 117 ft.
Post-tensioning duct	HDPE 3-in. DR17 for flexible filler specimens 3-in. corrugated polypropylene for grouted specimens

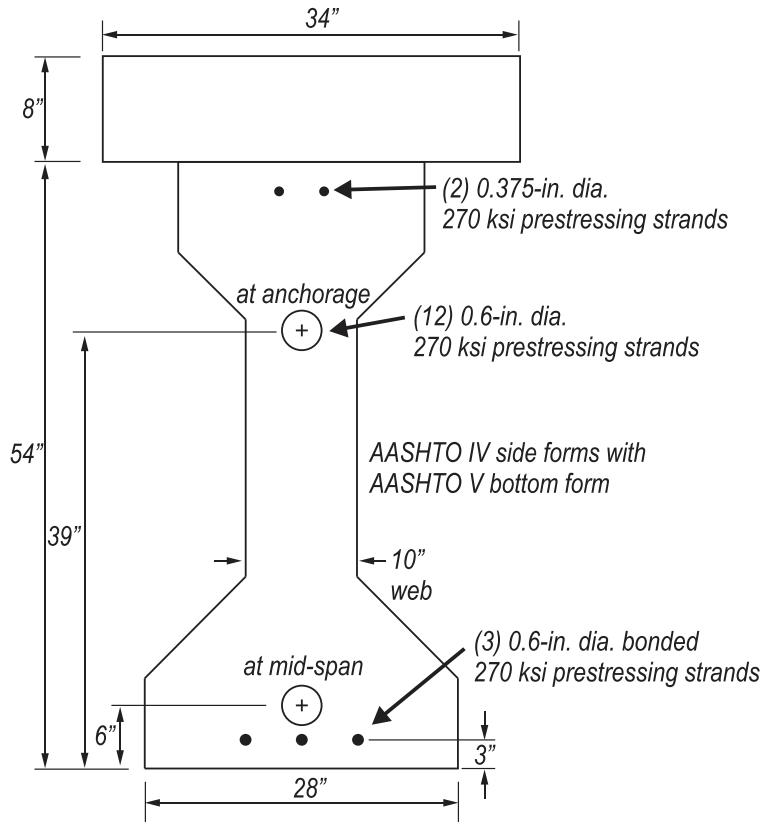


Figure 4-1 Internal tendon specimen cross-section

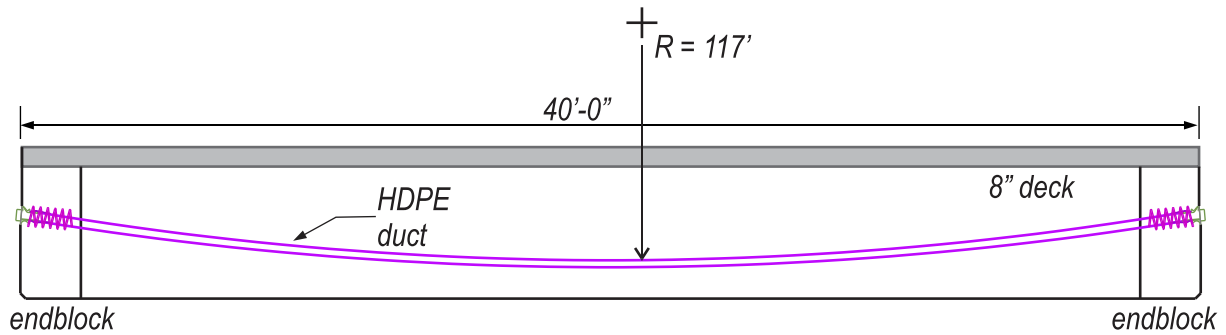


Figure 4-2 Internal tendon specimen

Table 4-1 Internal tendon specimen naming convention

Specimen	Tendon type	Filler material	Loading configuration
IWS	Internal	Flexible filler	Single point
IGS	Internal	Grout	Single point
IWC	Internal	Flexible filler	Constant moment

4.1.1 Detailing Considerations

Key details of the internal tendon specimens include:

- 40'-0" length;
- A tendon of parabolic shape, with the duct contained within the girder web at the ends and in the bottom flange towards the midspan;
- The tendon's radius of curvature is similar to that found in the example bridge;
- End-blocks to house anchorages and confinement reinforcement;
- Anchorage type: Schwager Davis anchorage for (12) 0.6-in dia. strand.

Tendon Profile

The radius of the parabolic profile was 117 ft, chosen to mimic the tight radii found in the negative bending regions of continuous spans (Figure 4-3). Design of the test specimens considered a haunched section from a real bridge (Figure 4-4) as an example of a typical internal tendon profile (FDOT 2008). The tightest radius of curvature in the bridge was selected for consideration/use in the internal tendon specimens. For testing purposes, the segment was inverted so that the reaction in the bridge was applied as a midpoint load on the laboratory specimen.

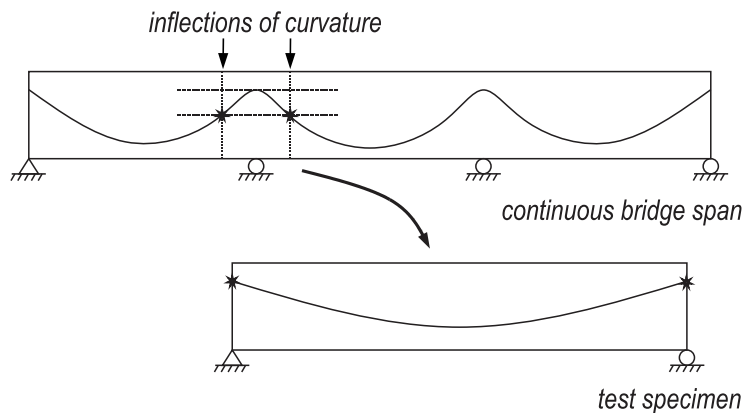


Figure 4-3 Continuous span

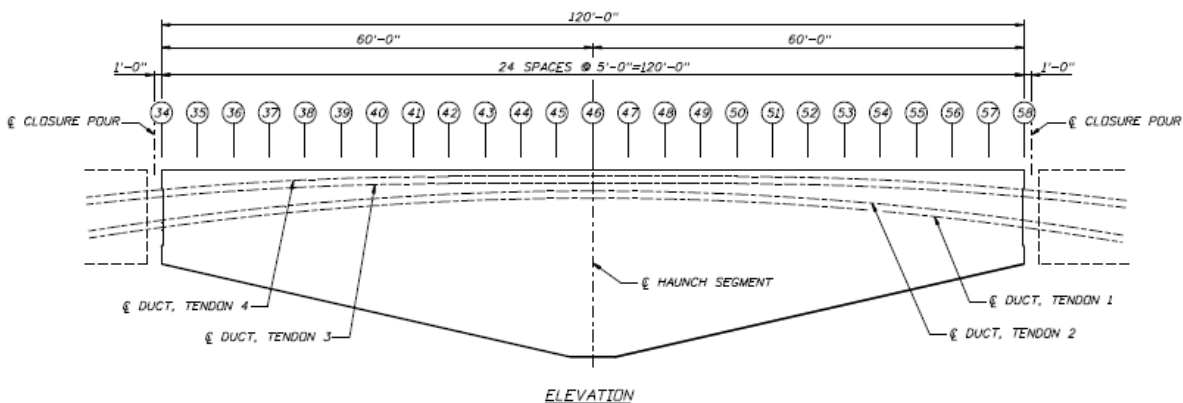


Figure 4-4 Tendon profiles from real bridge (FDOT 2008)

Deck Slab

All internal tendon specimens were topped with an 8-in. thick concrete slab to simulate the bridge deck. Deck steel was detailed in accordance with FDOT SDG 4.2.11, which states that all cast-in-place decks must have steel designed for temperature and shrinkage reinforcement per AASHTO-LRFD (AASHTO 2014b; provision 5.10.8) with additional requirements for spacing (may not exceed 12 in.) and bar size (minimum allowed No. 4).

Two specimens (IWS and IWC) had an unbonded internal tendon; a third specimen (IGS) had a grouted (bonded) tendon. The post-tensioning tendon was composed of a plastic duct, (12) 0.6-in. dia. 270-ksi prestressing strands, and a filler material. Two duct types were used: smooth HDPE 3-in. (nominal) DR17 was used in specimens injected with flexible filler material (IWS and IWC) and 3-in. dia. corrugated polypropylene was used in the grouted specimen (IGS). Unbonded tendons were filled using Civetex wax; the bonded tendon in IGS was filled using Euclid Cable Grout PTX – a product from the FDOT’s Approved Products List.

The specified beam concrete compressive strength at transfer was 6 ksi and at 28 days was 8.5 ksi; the concrete deck had a specified 28-day compressive strength of 8.5 ksi at 28 days. Three bonded 0.6-in. dia. 270 ksi prestressing strands had a specified prestress of $0.75f_{pu}$. The twelve 0.6-in. dia. 270 ksi lo-lax prestressing strands had a specified post-tensioning of $0.8f_{pu}$.

4.1.2 Service and Cracking

Concrete stresses were checked at key stages including: 1) prestress transfer, 2) deck placement, and 3) post-tensioning. Non-composite section properties were used for checks of bonded prestress release; composite section properties were used for checks after deck placement. For calculations related to the prestress release, the precast AASHTO shape segment (35 ft) was considered (vs. the finished beam length, with end-blocks in place). The effect of the duct was negligible and not considered.

The following allowable stresses were used to check the calculated stresses at bonded prestress release (Table 4-2). The specified concrete strength, f'_{ci} , for release was 6 ksi.

Compressive stress limit: $0.6f'_{ci} = -3600$ psi (AASHTO-LRFD 5.9.4.1.1 2014)

Tensile stress limit (outer 15% of segment): $7.5\sqrt{f'_{ci}}$ (psi) = 580 psi (SDG 2015)

Tensile stress limit (inner 70% of segment): $0.19\sqrt{f'_{ci}}$ (ksi) = 470 psi (AASHTO-LRFD 5.9.4.1.2 2014)

Table 4-2 Summary of stress checks for precast AASHTO at release

Position	Tensile Stress (psi)		Compressive Stress (psi)	
	Applied	Limit	Applied	Limit
0.15L	55	580	-325 (bottom of PC)	-3600
0.5L	n/a	470	-250 (bottom of PC)	-3600

Table 4-3 presents the stress checks using non-composite section properties for deck placement, which occurred prior to post-tensioning. The specified beam concrete strength for this stage was 8.5 ksi. Prestress losses in the bonded strand were (conservatively) assumed to be 30% of the specified jacking prestress.

The following limits were checked:

Compressive stress limit: $0.6f'_c = -5100$ psi

Tensile stress limit: $7.5\sqrt{f'_c}$ (psi) = 691 psi

Table 4-3 Summary of stress checks for loads associated with deck placement

Position	Tensile Stress (psi)		Compressive Stress (psi)	
	Applied	Limit	Applied	Limit
0.15L	n/a	580	-150 (bottom of PC)	-5100
0.5L	n/a	580	-200 (top of PC)	-5100

The allowable stress limits shown in Table 4-4 were used to check the calculated stresses during post-tensioning. The specified concrete strength (for beam and deck), f'_c , for post-tensioning release was 8.5 ksi.

Compressive stress limit: $0.6f'_c = -5100$ psi (AASHTO-LRFD 5.9.4.1.1 2014)

Tensile stress limit: $7.5\sqrt{f'_c}$ (psi) = 690 psi (SDG 2015)

Tensile stress limit (inner 70% of segment): $0.19\sqrt{f'_c}$ (ksi) = 553 psi (AASHTO-LRFD 5.9.4.1.2 2014)

Table 4-4 Summary of stress checks at post-tensioning release

Position (ft)*	Tensile Stress (psi)		Compressive Stress (psi)	
	Applied	Limit	Applied	Limit
0.15L	n/a	690	-305 (top of PC)	-5100
0.5L	343 (top of deck)	553	-1440 (bottom of PC)	-5100

The following represent the Service I and Service III limit states in accordance with AASHTO-LRFD Section 5.9.4.2.1 and 5.9.4.2.2:

Service I (1.0DL+1.0LL)

Compressive stress limit: $0.6f'_c = -5100$ psi

Service III (1.0DL+0.8LL)

Compressive stress limit: $0.4f'_c = -3400$ psi

Tensile stress limit: no tension (components with unbonded tendons)

4.1.3 Flexure and Shear Strength

Table 4-5, Table 4-6, and Table 4-7 present the calculated moment and shear strength for the bonded and unbonded internal specimens when loaded in either 3-point or 4-point bending. The applied shear (V_u) is that corresponding to the flexural strength. Flexure was calculated using AASHTO-LRFD's provisions. Shear was calculated using the ACI simplified approach. The specified beam and deck concrete compressive strength at 28 days of 8.5 ksi was assumed. Post-tensioning assumed 20% losses, acting over the composite section (performed after deck installation). Pretensioning strand were conservatively neglected. Phi for shear checks was assumed to be 0.75. Span length was 39 ft.

Table 4-5 Internal tendon – bonded 3-point Strength

Position	M _n (kip-ft)	V _n (kip)	V _u (kip)	$\phi V_n/V_u$
End	n/a	940	200	3.6
0.5L	3870	290	200	1.1

Table 4-6 Internal tendon – unbonded 3-point Strength

Position	M _n (kip-ft)	V _n (kip)	V _u (kip)	$\phi V_n/V_u$
End	n/a	940	190	3.7
0.5L	3680	290	190	1.1

Table 4-7 Internal tendon – unbonded 4-point Strength

Position	M _n (kip-ft)	V _n (kip)	V _u (kip)	$\phi V_n/V_u$
End	n/a	940	216	3.3
Spreader point	n/a	300	216	1.04
0.5L	3680	290	0	n/a

4.2 External Tendon I-Girder

Two 40-ft long simple-span precast concrete I-girders were constructed, each with two external tendons composed of (6) 0.6-in. dia. prestressing strands (Figure 4-5 and Figure 4-6).

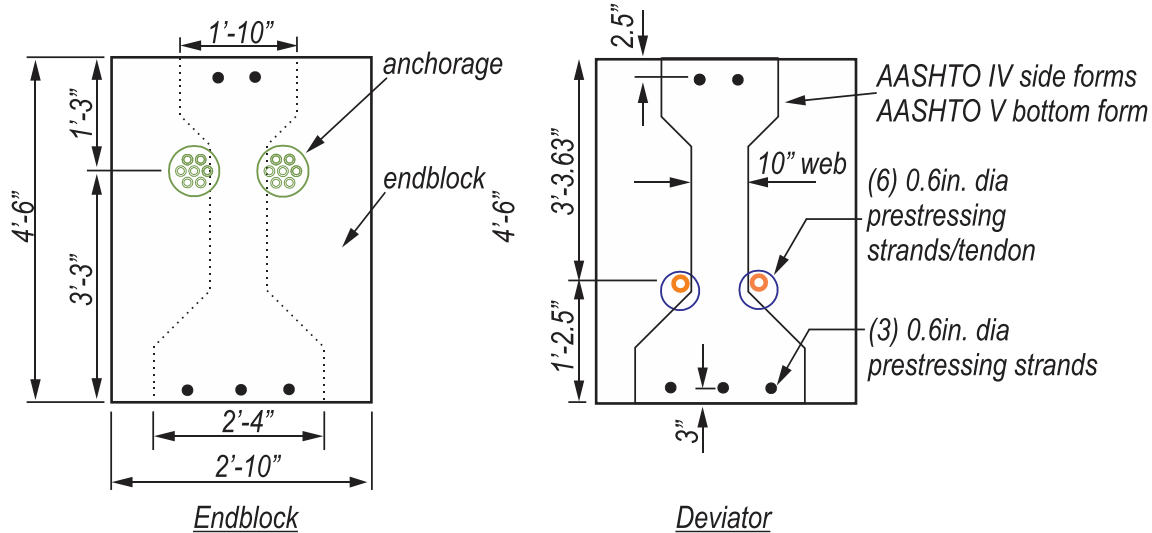


Figure 4-5 External tendon specimens

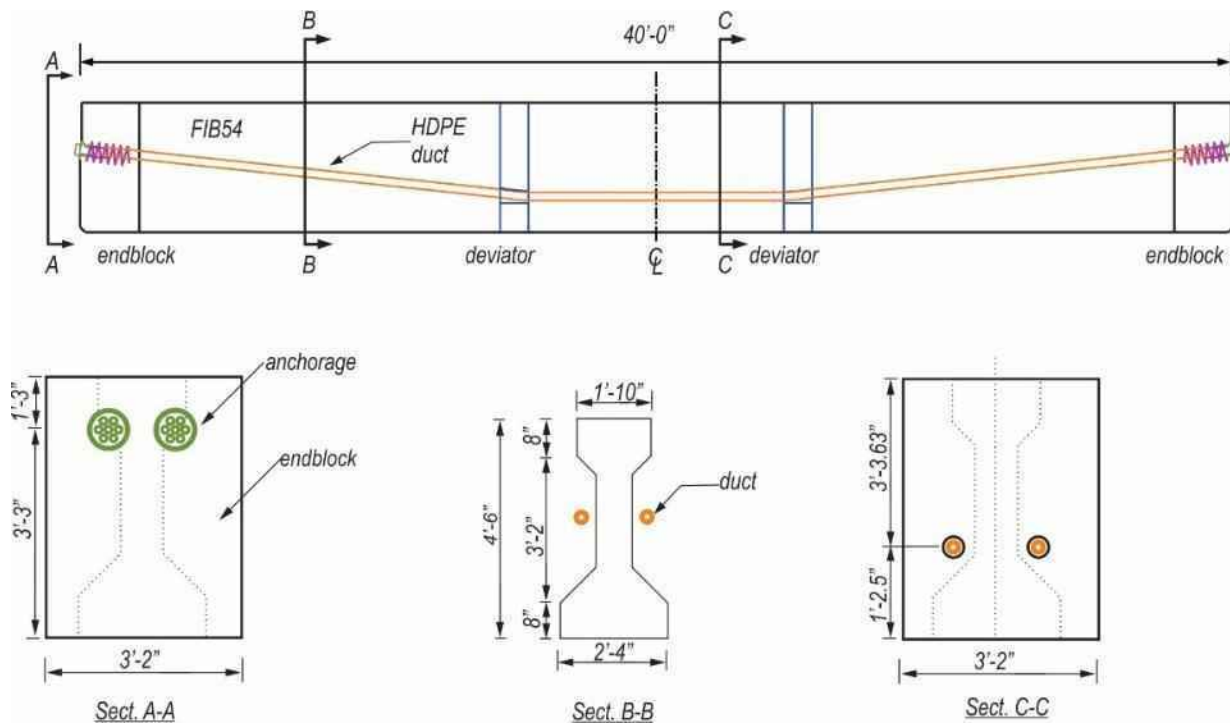


Figure 4-6 External tendon specimen profile

The specified properties of the materials chosen for the external tendon test specimen design were as follows:

- | | |
|-------------------|--|
| Precast beams: | Dimensions (Figure 4-5 and Figure 4-6): AASHTO Type IV-V
Concrete strength at transfer, f'_{ci} = 6 ksi
Concrete strength at 28 days, f'_c = 8.5 ksi
Self-consolidating mix |
| Deviation blocks: | Concrete strength at 28 days = 8.5 ksi
Self-consolidating mix |

Diabolo-type deviation voids (see below, Figure 4-9)

Bottom pre-tensioned prestressing strands:

(3) 0.6-in. dia., seven wire lo-lax strand

Area, per strand = 0.217 in.²

Ultimate strength, $f_{pu} = 270$ ksi

Prestressing strand modulus of elasticity = 28,500 ksi

Prestress level at jacking = $0.74f_{pu}$

Top pre-tensioned prestressing strands:

(2) 0.375-in. dia., seven wire lo-lax strand

Area, per strand = 0.085 in.²

Ultimate strength, $f_{pu} = 270$ ksi

Prestressing strand modulus of elasticity = 28,500 ksi

Prestress level at jacking = 10 kip

Post-tensioned prestressing strands:

(2) tendons of (6) 0.6-in. dia., seven wire lo-lax strand

Area, per strand = 0.217 in.²

Ultimate strength, $f_{pu} = 270$ ksi

Prestressing strand modulus of elasticity = 28,500 ksi

Prestress level at jacking = $0.8f_{pu}$

4.2.1 Detailing Considerations

Key details of the external tendon specimens include:

- 40'-0" length;
- Two end-blocks to house anchorages;
- Two deviation blocks, with diabolo-style voids;
- Deviation angle = approximately 0.09 radians;
- Flat profile near midspan;
- Anchorage type: Schwager Davis anchorage for (12) 0.6-in dia. strand.

Tendon Profile

The tendon profile of the external tendon specimens was chosen to simulate deviation angles from an example bridge in Florida. The naming convention and basics of the internal tendon specimens are given in Table 4-8.

Joints

Shear keys were detailed at the joint locations to provide mechanical interlock to increase the shear capacity of the interface between the precast concrete and the deviator block (Figure 4-7). Design recommendations are provided by AASHTO-LRFD regarding the geometry of shear keys; these recommendations are dependent on the size of the aggregate and the width of the web and were considered for the determination of the shear key dimensions. The bonded prestressing strand was detailed to protrude from the outside segments to extend into the deviator block (Figure 4-7).

Table 4-8 External tendon specimens

Specimen	Tendon Type	Filler	Test Procedure
EWS	External	Flexible filler	Static Flexural Service + Limit state
EWC	External	Flexible filler	Cyclic + Ultimate

A two-part epoxy, Pilgrim Permocoat CBC 6 Segmental Epoxy “slow set” (with an operating temperature of 70-115° F) was chosen from the FDOT Approved Products List for use at the simulated segmental joint. After mixing, the contact time of “slow set” epoxy is six hours (vs. 60 minutes for normal set), allowing additional time to adjust the alignment at the joint. Application of the segmental epoxy was performed in accordance with the FDOT Standard Specifications for Road and Bridge Construction (FDOT 2015) Section 453.



Figure 4-7 Shear keys and protruding reinforcement

Deviator Design

Deviator blocks were designed using strut-and-tie methodology (Figure 4-8). Diabolo-type void-formers were donated and had previously been used on a bridge construction project; the deviator block length was set based on the length of the diabolo form.

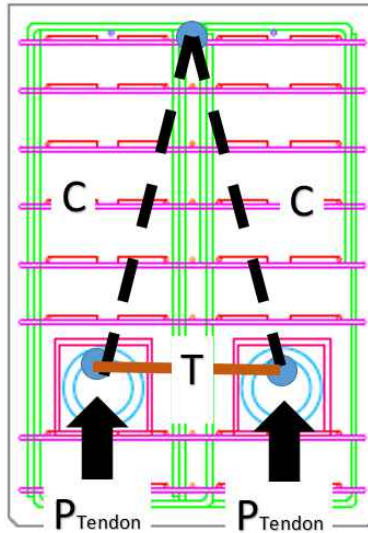


Figure 4-8 Deviator STM

Diabolos

At deviation points, as per the FDOT Structures Design Bulletin 14-06 (FDOT 2014), the HDPE duct was continuous through the deviation block without the use of a steel pipe; the deviator had a diabolo-style geometry. Diabolo-type voids were bell-shaped, allowing the smooth passage of the duct through the deviation. Details of the diabolo geometry used for the specimens are shown in Figure 4-9.

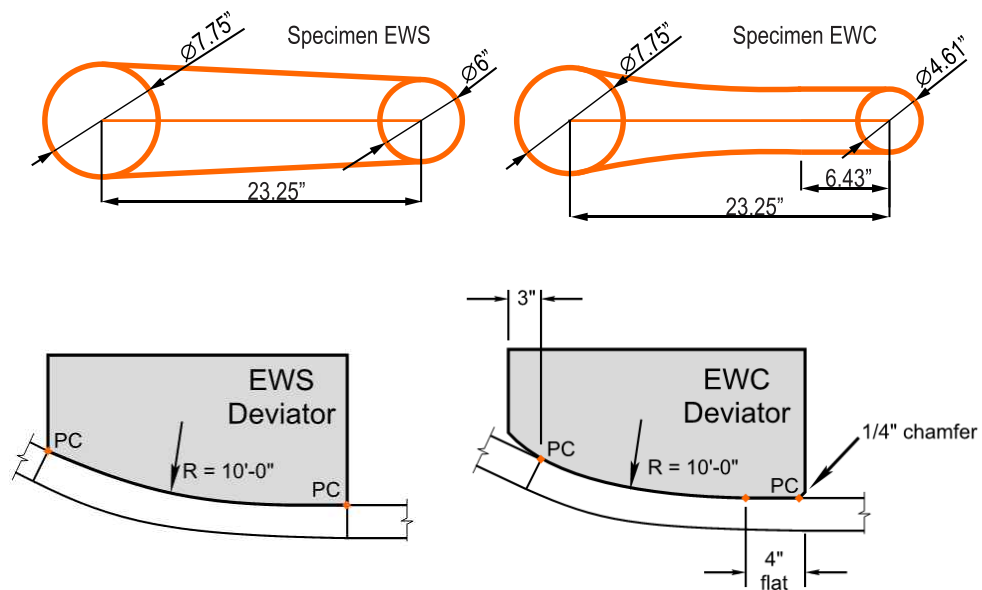


Figure 4-9 Diabolo geometry

Tendon

Each post-tensioning tendon was composed of smooth HDPE duct, (6) 0.6-in. dia. 270-ksi prestressing strands, a 12-strand anchorage and flexible filler material. Several detailing

considerations for the external tendon specimens had to be made to accommodate the post-tensioning anchorages.

Trumpet and exit from endblock

A 4-ft length of 3-in. DR-17 IPS (iron pipe size) HDPE duct was butt-welded to the plastic trumpet by the PT supplier prior to delivery to the precast yard because the trumpet-to-smooth-HDPE-duct connection is non-standard (the PT supplier's trumpet is designed to connect to corrugated duct); see Figure 4-10. The diameter of the HDPE duct (3-in.), however, was approximately the same as the corrugated 3-in. duct.



Figure 4-10 Pre-assembled trumpet/duct

Necking down duct diameter

The 3-in. DR17 IPS HDPE duct was necked down to 2-in. DR 17 IPS HDPE after exiting the end block. The transition piece and mechanical splice connections are shown in Figure 4-11. The smaller duct diameter was used for the critical section of the tendon length (between deviators and at mid-span) to simulate the strand congestion that would result from the specified ratio of duct area to strand area of 2.5.



Figure 4-11 Duct exiting end block of external specimen

Clear windows

A 30-in. length of clear 2-in. polycarbonate tube was spliced in-line with the 2-in. HDPE near midspan of both tendons to provide a clear observation window. Connection to the 3-in. HDPE was made through a commercially-available iron duct coupler. The clear window can be seen in Figure 4-12.



(a)



(b)

Figure 4-12 PT tendon (unstressed) (a) between deviator blocks and (b) clear polycarbonate window

4.2.2 Service and Cracking

Concrete stresses were checked at key stages, including: (1) prestress transfer and (2) post-tensioning. For calculations related to the prestress release, the precast segments were considered (vs. the finished segment length, with end blocks in place). For calculations related to the post-tensioning, the entire beam length was considered.

The allowable stresses at bonded prestress transfer used to check the calculated stresses are shown in Table 4-9. The specified concrete strength at release, f'_{ci} , was 6 ksi. The length of the end segment was 11.5 ft. The length of the middle segment was 8 ft.

Compressive stress limit: $0.6f'_{ci} = -3600$ psi (AASHTO-LRFD 5.9.4.1.1 2014)

Tensile stress limit (outer 15% of segment): $7.5\sqrt{f'_{ci}}$ (psi) = 580 psi (SDG 2015)

Tensile stress limit (inner 70% of segment): $0.19\sqrt{f'_{ci}}$ (ksi) = 470 psi (AASHTO-LRFD 5.9.4.1.2 2014)

Table 4-9 Summary of stress check for precast at release

Segment	Position	Tensile Stress (psi)		Compressive Stress (psi)	
		Applied	Limit	Applied	Limit
End (L=11.5ft)	0.15L	20 (top)	580	-7 (bottom)	-3600
	0.5L	n/a	470	-270 (bottom)	-3600
Middle (L=8ft)	0.15L	15	580	-80 (bottom)	-3600
	0.5L	5	470	-275 (bottom)	-3600

Following casting of the deviator block, the segments were assembled and post-tensioned. The following allowable stresses at post-tensioning were used to check the calculated stresses shown in Table 4-10. The specified concrete strength, f'_c , for post-tensioning transfer was 8.5 ksi. The finished beam length was 40 ft. The weight of the end blocks and deviators was considered.

Compressive stress limit: $0.6f'_c = -5100$ psi (AASHTO-LRFD 5.9.4.1.1 2014)
 Tensile stress limit (outer 15% of segment): $7.5\sqrt{f'_c}$ (psi) = 690 psi (SDG 2015)
 Tensile stress limit (inner 70% of segment): $0.19\sqrt{f'_c}$ (ksi) = 553 psi (AASHTO-LRFD 5.9.4.1.2 2014)

Table 4-10 Summary of stress check at post-tensioning transfer

Position	Tensile Stress (psi)		Compressive Stress (psi)	
	Applied	Limit	Applied	Limit
0.15L	n/a	690	-995 (top)	-5100
0.5L	n/a	553	-990 (bottom)	-5100

The following represent the Service I and Service III limit states in accordance with AASHTO-LRFD Section 5.9.4.2.1 and 5.9.4.2.2:

Service I (1.0DL+1.0LL)

Compressive stress limit: $0.6f'_c = -5100$ psi

Service III (1.0DL+0.8LL)

Compressive stress limit: $0.4f'_c = -3400$ psi

Tensile stress limit: no tension (components with unbonded tendons)

4.2.3 Flexure and Shear Strength

Table 4-11 presents the calculated moment and shear strength for the external tendon specimens. Flexure strength was calculated using strain compatibility. Shear strength was calculated using the ACI simplified approach. The specified beam and deviator concrete compressive strength at 28 days of 8.5 ksi was assumed. Post-tensioning assumed 20% losses. Pretensioning strand was conservatively neglected. Phi for shear checks was assumed to be 0.75. Span length was 39 ft.

Table 4-11 External tendon – unbonded

Position	M_n	V_n	V_u	$\phi V_n/V_u$
	(kip-ft)	(kip)	(kip)	
@ support	n/a	330	79	3.1
At outside of deviator (epoxy joint)	1790	197	79	1.9
0.5L	1790	189	79	1.8

4.3 Fatigue

The objective of the fatigue testing was to test the fatigue resistance of an unbonded PT tendon using diabolo deviators. Specifically, the resistance to fretting fatigue of the strands, anchor, wedges, and resistance of the HDPE to wear were explored. The fatigue beam specimen was designed to allow fatigue cycling of the tendon without accumulating undue stresses and potential damage on the remainder of the specimen (Figure 4-13). This required that the specimen be constructed in two segments and joined with a mechanical hinge similar to the specimens used by Oertle et al. 1987, Wollmann et al. 1988, and Georgiou 1989. The major difference, however, is that access (openings in the beam) was needed to the tendon near the deviator. This allowed the segments to be constructed with the diabolo form in place and then removed after casting. In addition, the openings provided access to the tendons to facilitate tendon fabrication and installation of instrumentation.

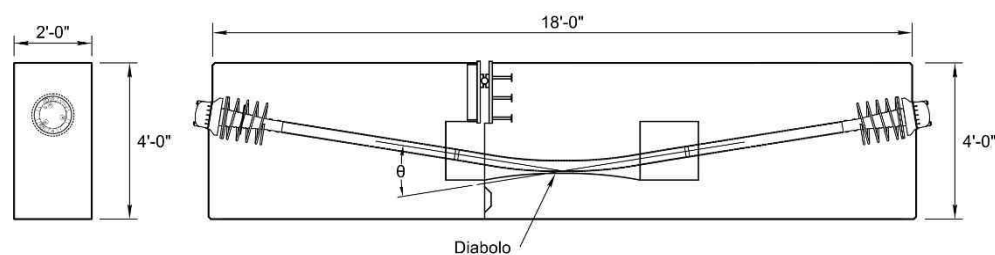


Figure 4-13 Schematic illustration of fatigue specimen

One of the goals of the fatigue testing was to determine the behavior of the tendon in the vicinity of the deviator. In steel pipe deviators used with grouted tendons, the tendon is essentially bonded to the deviator, which prevents movement relative to the deviator. In diabolo-formed deviator, however, the tendon is not fixed to the deviator. Rather, load is transferred by bearing between the HDPE duct and concrete of the deviator. In this situation, it is possible, with a sufficient stress differential across the deviator, for the tendon to slip relative to the deviator. This potential for slip is a function of the differential tendon force and friction coefficient. The other possibility is that no slip occurs. The fatigue stress differential is generated on both sides of the deviator, but the magnitude of the differential is insufficient to overcome the friction, which prevents relative slip.

To explore these two behaviors two different deviation angles were chosen (Table 4-12). External tendons are typically deviated at two locations (Figure 4-14). The 11-degree angle was chosen as a less extreme, but representative angle, where slip would occur. The 18-degree angle was chosen as an extreme angle, which would not be expected to slip.

Both beams were 18-ft long and had a 2-ft by 4-ft rectangular cross-section. Each beam contained a single unbonded post-tensioned tendon, composed of six 0.6-in. dia. prestressing strands, and injected with a flexible filler. The intent was to test a tendon in which the strands were installed parallel without twisting. This is the ideal case and is not required in the construction of actual tendons. Twisted strands in longer bridge girders will tend to have less of an effect than in this relatively short specimen.

The fatigue test was carried out in accordance with Section 960 of the FDOT Road and Bridge Specifications Manual, which requires fatigue testing to be done in accordance with ETAG-013 Section 6.1.2-I, with the exception that 6.5 ksi concrete was used in the construction of the beam. As specified by ETAG-013, the fatigue test was run for 2 million cycles while

maintaining a constant upper load limit of 65% of the tensile element characteristic strength and a load range of approximately 11.6 ksi.

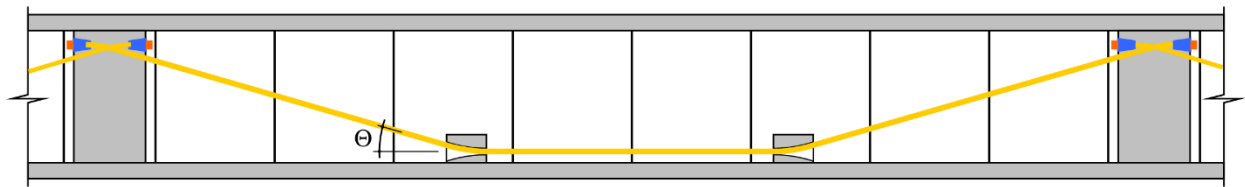


Figure 4-14 Deviation of PT tendon in span-by-span construction

Materials chosen for the fatigue beams were as follows:

Beam properties:

Dimensions: 4-ft high by 2-ft wide by 18-ft length

Concrete strength at 28 days, $f'_c = 6.5$ ksi

Duct properties:

3" smooth IPS HDPE

Pressure rating = DR 17

Post-tensioned prestressing strands properties:

six 0.6-in. dia., seven wire lo-lax strand

Area, per strand = 0.217 in^2

Ultimate strength, $f_{pu} = 270$ ksi

Prestressing strand modulus of elasticity = 28,500 ksi

Prestress level at jacking = $0.80f_{pu}$

Table 4-12 Fatigue beam specimen abbreviations

Specimen	Tendon angle	Filler material	Loading configuration
F1	18 degrees	Flexible filler	Single point
F2	11 degrees	Flexible filler	Single point

Key details of the fatigue beam specimen are as follows:

- 18 ft length;
- Two tendon angles of 18 degrees and 11 degrees;
- Diabolo deviators with radius of curvature of 10-ft;
- Mechanical steel hinge
- Anchorage type: Schwager Davis anchorage for (6) 0.6-in dia. strands.

4.3.1 Diabolo Tendon Deviators

Steel pipes have traditionally been used to deviate external tendon alignment. The difficulty in maintaining alignment of pipes during concrete placement for the deviator, however, has led to the use of removable forms to create a curved surface in the deviator against which the external tendon duct bears. These deviators are generally formed in the concrete using removable form inserts that are typically referred to as diabolo deviators (Figure 4-15). Diabolo inserts are generally composed of a two-part form insert. The parts are connected together at the

point of minimum diameter using a keyed connection to stabilize the insert during concrete placement. The insert is placed within the formwork prior to concrete placement and can be removed and reused multiple times.

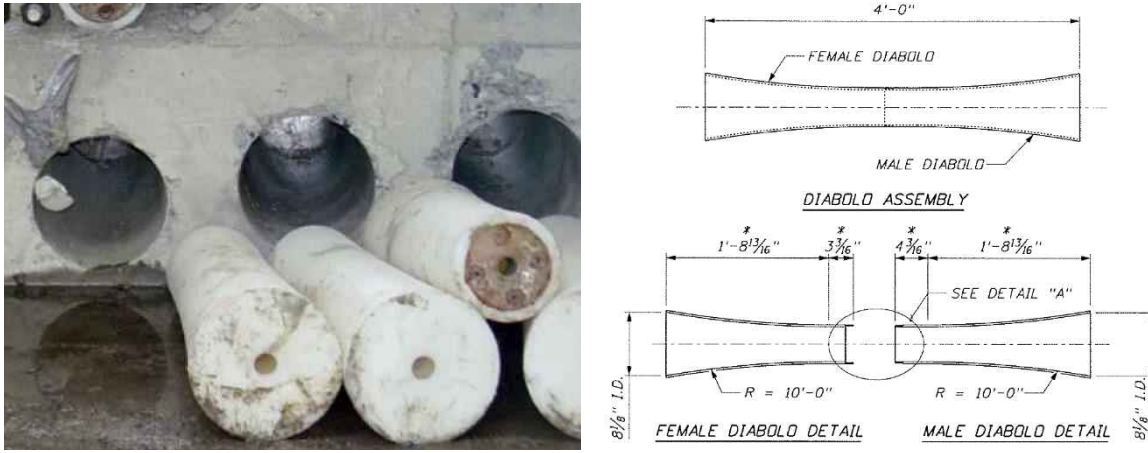


Figure 4-15 Removable diablo formwork inserts for creating curved deviators

The flare at the exit of the opening formed by the diablo inserts is an important design parameter. It is desirable for the curvature of the opening to continue beyond that of the tendon to ensure that a sharp angle change in the tendon does not occur at the exit. If it does, then the concentrated force at the corner of the concrete could cause spalling. Furthermore, the concentrated force at this location will cause high localized compressive stresses on the HDPE duct as it is pinched between the strand bundle and the corner of the concrete deviator. Another potential issue is the possibility of fretting fatigue caused by the high contact stresses between the prestressing strands at this point. Consequently, an appropriate duct lift off distance (Figure 4-16) is desirable to prevent stress concentrations at the deviator corner.



Figure 4-16 Tendons with point of contact located inside deviator. Note small gap between duct and concrete at tendon exit from deviator.

Reusable diablo inserts were chosen to create the concrete deviator inside each fatigue specimen to test their effect on fatigue and wear of the tendon. Bridge designers familiar with the use of diablo inserts were consulted and it was determined that a cover of 2 in. over the theoretical contact point inside of the deviator (Figure 4-17) would be used for both specimens. To accommodate the deviator angle change, the anchorage height was adjusted to achieve the

desired deviation angle and contact point inside the deviator. The selected deviator radius of 10 ft was slightly above the minimum radius of 9 ft as specified by FDOT SDG Table 1.11.4-2 for a six-strand tendon.

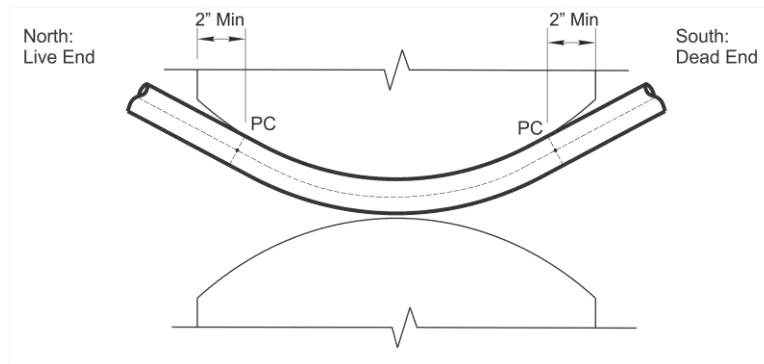


Figure 4-17 PT duct theoretical point of contact to prevent pinching at deviator exit

4.3.2 Mechanical Hinge Design

The mechanical hinge was formed in the beam adjacent to the deviator to ensure a smooth, relatively friction-free, action during load cycling. The top of the hinge was constructed from structural steel plates and a steel rod (Figure 4-18). Plates were fitted with welded headed studs and embedded in each of the segments. Two thicker steel plates were machined to fit the steel rod and were welded to the face of the embedded plates. These plates were intended to allow smooth rotation of the hinge and to evenly distribute the bearing stresses from the large compressive force routed through the steel rod.



Figure 4-18 Mechanical hinge details

The bottom of the hinge was formed by deliberately separating the concrete sections at that location, which formed the two separate specimen segments. During stressing of the PT tendon, compression occurred between the two segments at this location. During load cycling, however, a gap formed when load was applied to initiate cycling. The gap remained open even

at the low end of the load range, which ensured that the gap closing did not interfere with the fatigue cycling.

4.3.3 Reinforcement Design

Local zone reinforcement used to provide confinement for the SDI 12.6-PC anchorage system was specified by the anchorage manufacturer Schwager Davis (Figure 4-19). The local zone reinforcement specified by the manufacturer was #4 mild reinforcement steel spirals @ 13-in outside diameter with 6 turns @ 3 in. spiral pitch.



Figure 4-19 Anchorage system (a) without local zone reinforcement (b) with local zone reinforcement

General anchorage zone reinforcement was the same for specimens F1 and F2. Reinforcement was designed to resist the stress transfer from six 0.6-in dia. prestressing strands stressed to $0.8f_{pu}$ (216 ksi) and the permanent post-tensioning force applied to the specimen. A larger quantity of reinforcement was placed at the anchorage zone (Figure 4-20) to resist the expected higher stresses.

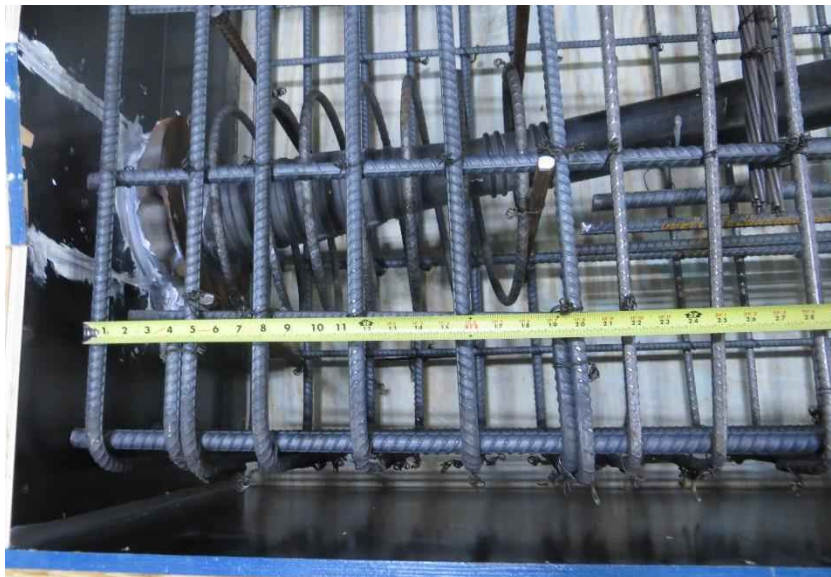


Figure 4-20 General and local zone anchorage reinforcement

The concrete section discontinuity created by the hollow rectangular section (Figure 4-21) was also reinforced heavier than other regions to prevent cracking.



Figure 4-21 General zone reinforcement at hollow section

General zone reinforcement was also designed to resist cracking during cyclic loading. A strut-and-tie model was developed to determine the transverse and longitudinal reinforcement required to resist these load cases.

4.3.4 Shear Key Design

Impact forces generated from the closing of the gap after unloading the specimen could potentially damage the small concrete section leading to overall structural degradation of the specimen. Specimen F1 included a reinforced concrete shear key (Figure 4-22) at the bottom of the specimen to resist these lateral forces. Plywood formwork was used to create the trapezoidal prism shape for the female portion of the shear key followed by match casting to form the male portion of the key.

During initial static loading of F1, concrete surrounding the shear key cracked as the specimen was unloaded (Figure 4-23). The intent of the shear key was to maintain alignment of the segments. What occurred, though, is that when the specimen was first loaded, the mechanical hinge seated, which caused a slight misalignment in the shear key joint. The specimen was then unloaded, and as the shear key re-seated during unloading, the misalignment caused cracking in the area around the key. Because the joint was open for the entirety of the static and fatigue cycling, the cracking had no effect on the test. To avoid this problem in F2, however, the joint was redesigned.



Figure 4-22 Specimen F1 reinforced concrete shear key

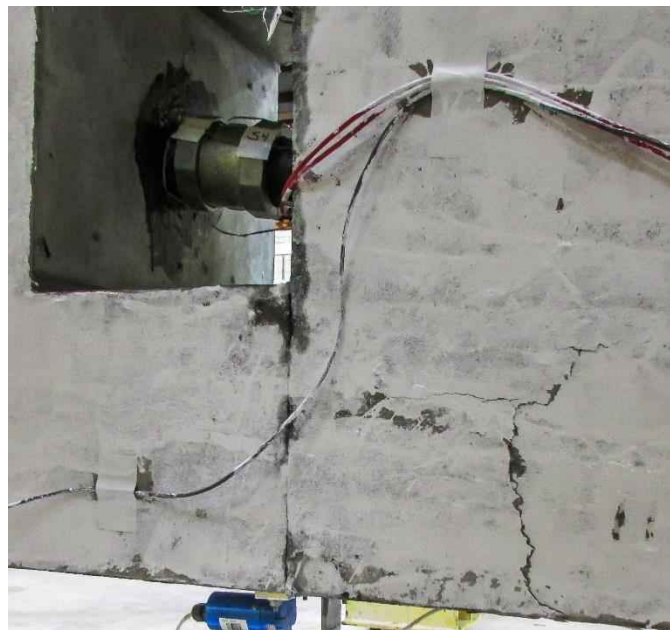


Figure 4-23 Cracking in concrete surrounding shear key

Specimen F2 used a 24-in. by 12-in. by 3/16-in. thick 70A durometer neoprene pad (Figure 4-24) instead of the concrete shear key used in specimen F1. The neoprene pad protected the structural integrity of the specimen by distributing stress concentrations caused by the slight mismatch of the two surfaces. Prior to concrete placement, a temporary steel plate was placed between both segments as a temporary placeholder for the neoprene pad. Once the concrete cured the steel plate was removed and the neoprene pad was adhered to the live end segment with epoxy.

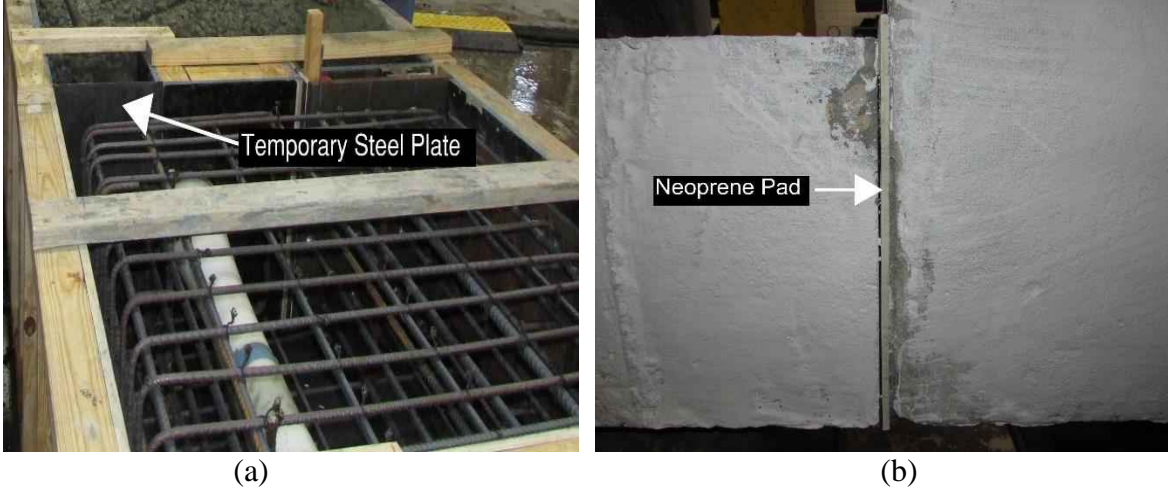


Figure 4-24 Neoprene pad (a) before installation (b) after installation

5 Instrumentation

This chapter describes the specimen instrumentation of three internal tendon specimens (IGS, IWS, and IWC), two external tendon specimens (EWS and EWC) and two fatigue beam specimens (F1, F2). Instrumentation included strategically placed displacement gages, load cells, thermocouples, and strain gages mounted to the concrete surface, anchorage, and prestressing strands.

5.1 I-Girder

Data were gathered from the instrumentation at four key events: stressing of the post-tensioning tendon, injection of the filler material, load-testing, and tendon cut-down. Different gages/instrumentation were monitored during each stage; Table 5-1 describes the general instrumentation plan for each stage. Instrumentation layouts specific to each specimen are given later.

Table 5-1 Monitored instrumentation

Stage	Tendon Force	Temperature	Displacement	Anchor Strain	Concrete Strain	Applied Load
Stressing	X		X	X	X	
Injection	X	X			X	
Load Test	X		X	X	X	X
Cut-down	X			X		

5.1.1 Tendon force

Tendon force was measured directly with hollow-core 850-kip Geokon load cells (Figure 5-1). The geometry of the load cell was specifically manufactured to ensure that a tendon of (12) 0.6-in. dia. 7-wire prestressing strands could pass through without obstruction, and to ensure that the face of the load cell would bear against only the face of the anchorage (in other words, such that the load cell would not bear on the concrete). Steel washers were machined at the laboratory and used to guide the alignment of the load cell and the wedge plate to ensure concentric application of the tendon force to the load cell (Figure 5-1). For specimen EWC, tendon force was also indirectly determined through strain measured by 5 mm foil type strain gages applied to individual wires of the prestressing strand after post-tensioning.



Figure 5-1 Hollow-core load cell

5.1.2 Displacement

Laser displacement transducers were used to monitor vertical displacement. The displacement gage layout for specimens IGS and IWS are shown in Figure 5-2. The layouts for IWC, EWS and EWC are shown in Figure 5-3 and Figure 5-4, respectively. In specimens IWS and EWS, a string-pot spanning the primary crack was installed during the test and subsequently monitored, measuring crack opening of a single primary crack.

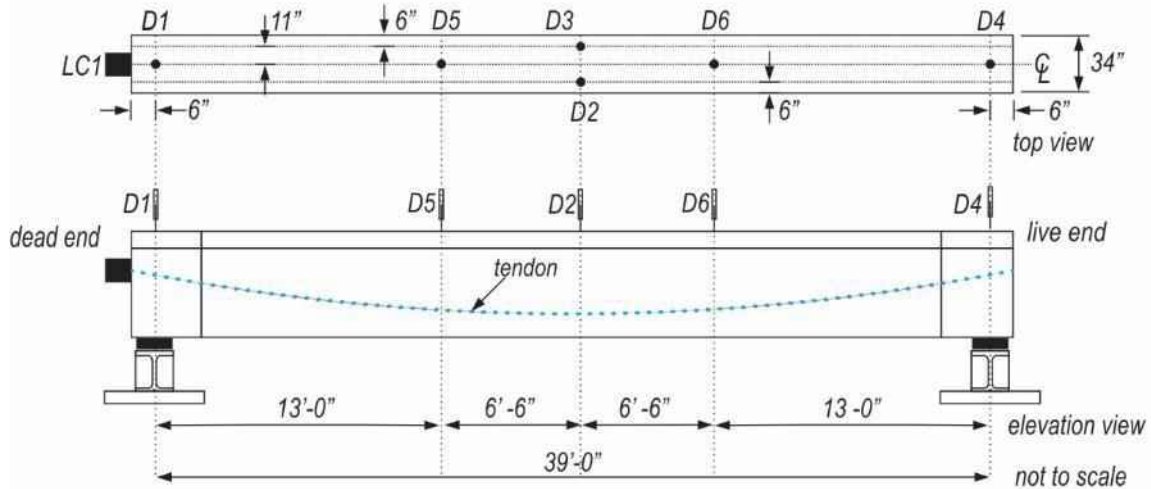


Figure 5-2 IGS and IWS: displacement gage locations

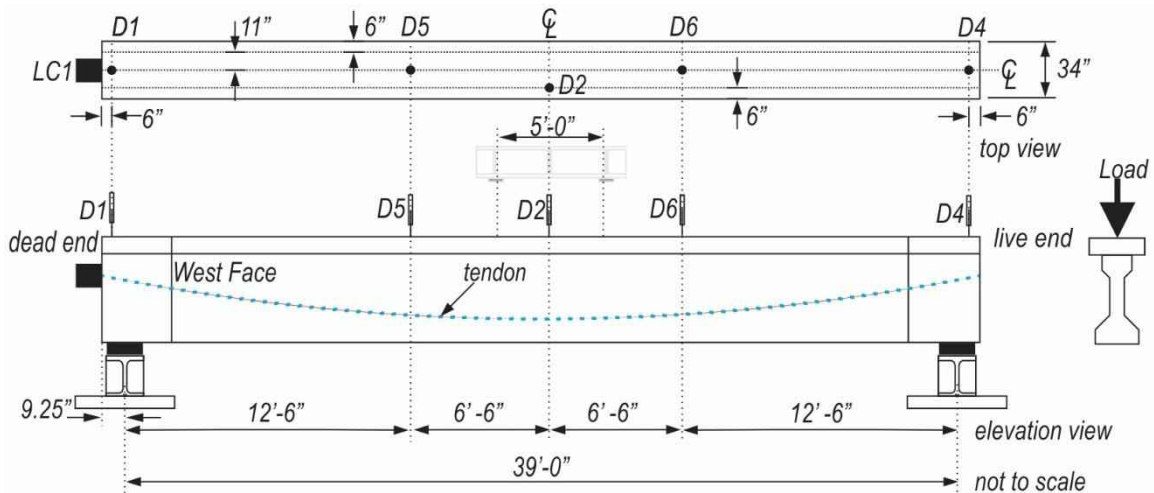


Figure 5-3 IWC: deflection gage locations

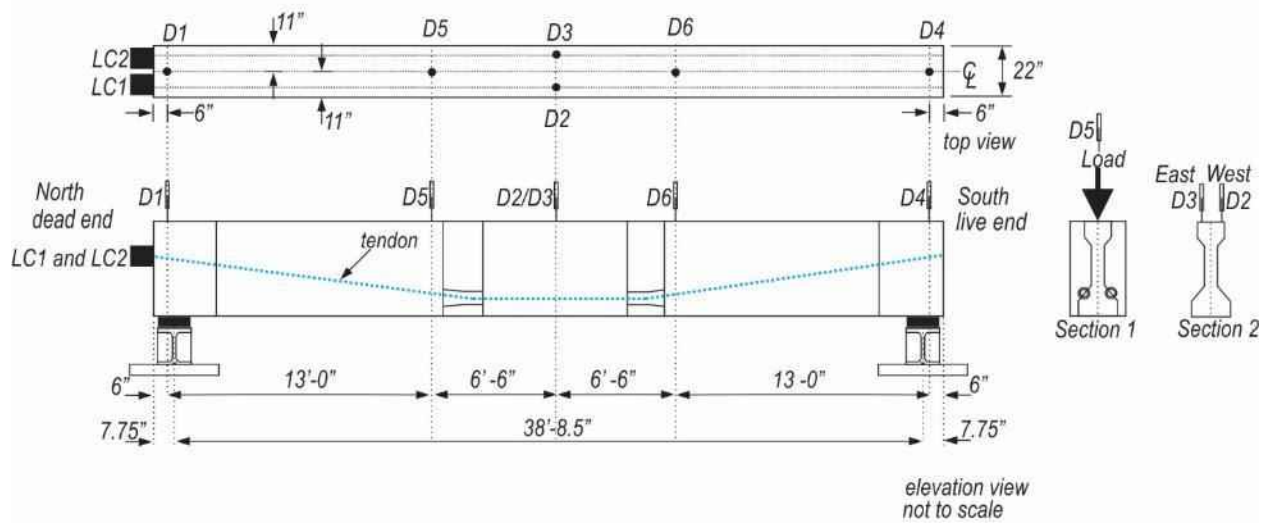


Figure 5-4 EWS and EWC: deflection

5.1.3 Strain

Concrete strain was measured with 60-mm foil-type strain gages. Post-tensioning tendon strain was measured during load application in one specimen – EWC – using 5-mm foil type strain gages. Strain gages used for crack opening determination were 5-mm foil-type; installation is shown in Figure 5-5. These gages were installed during testing to determine the load at which flexural cracks open upon reloading. These data were used to indirectly estimate the effective prestress force. Anchor strain was measured with 5-mm foil-type strain gages (Figure 5-6); description and discussion of the anchorage instrumentation is covered in Part III.

The same strain gage layout was used for specimens IGS and IWS (Figure 5-7). The strain gage layout for specimen IWC included additional strain gages and is shown in Figure 5-8. Strain gage placement for specimens EWS and EWC is shown in Figure 5-9.



Figure 5-5 Crack opening gage installation

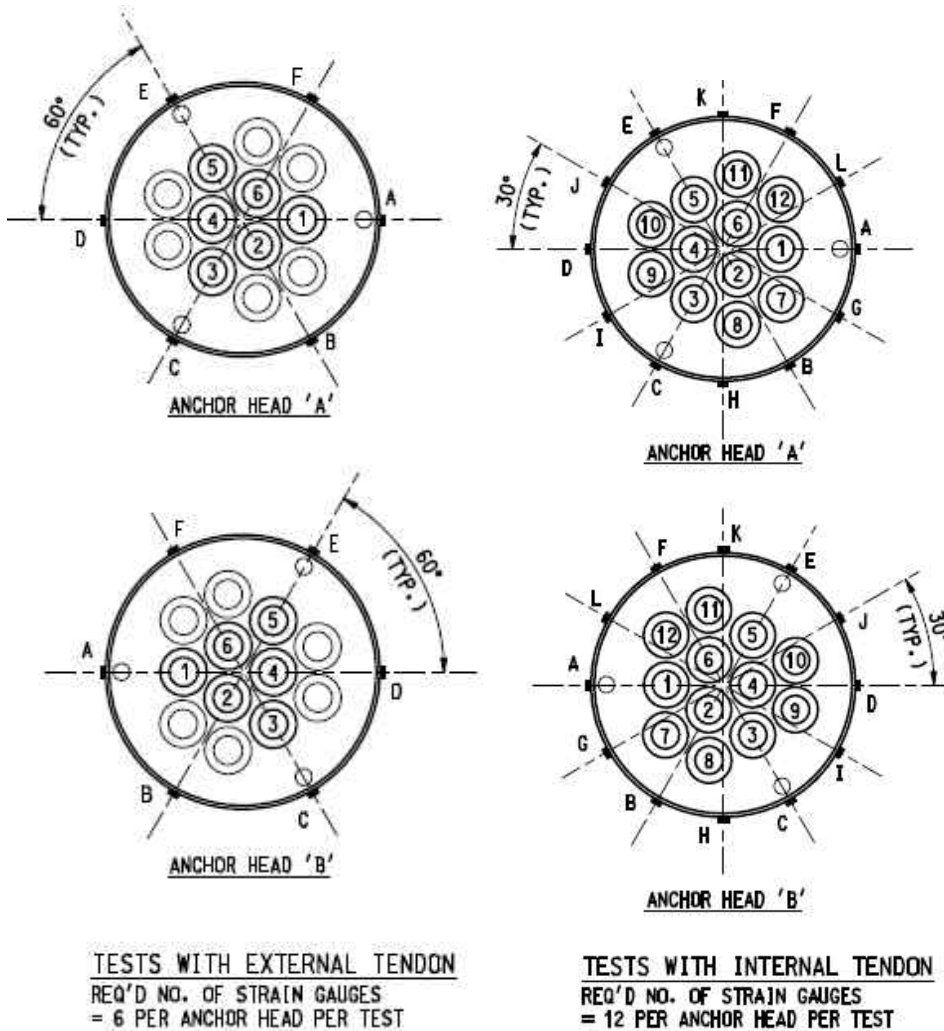


Figure 5-6 Anchorage strain gages

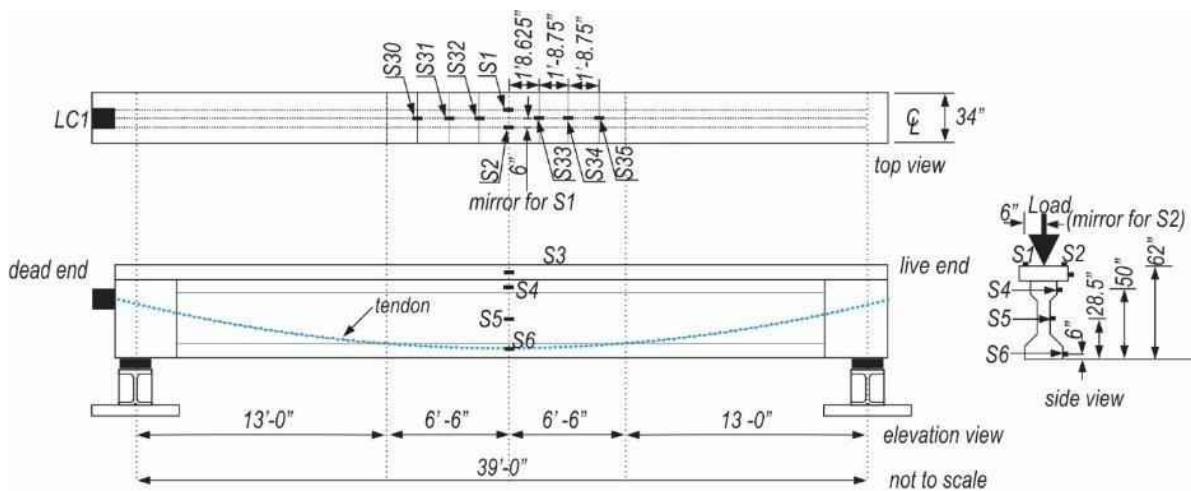


Figure 5-7 IGS and IWS: strain gage locations

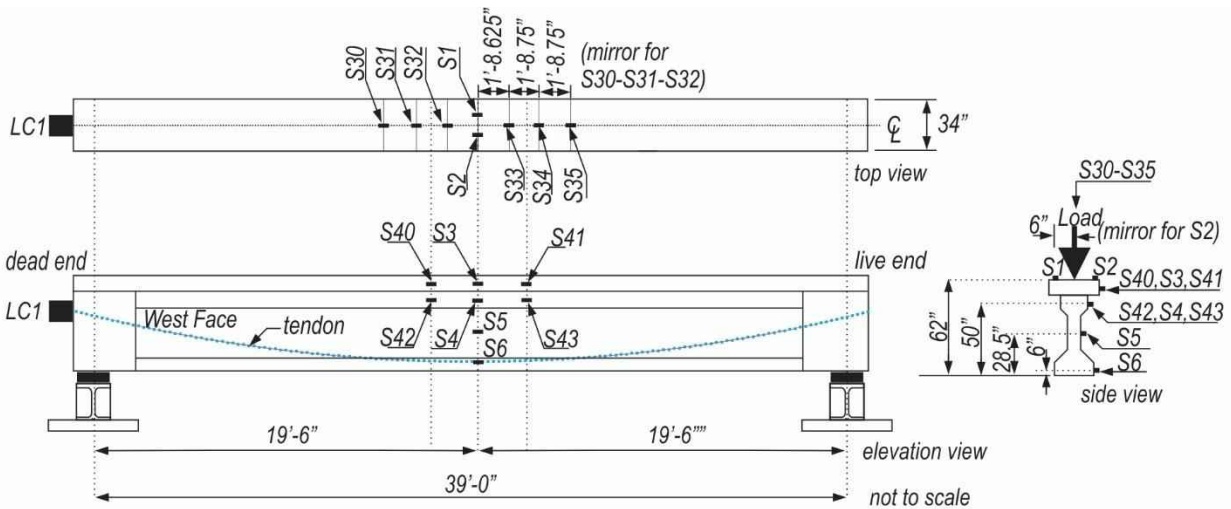


Figure 5-8 IWC: strain gage locations

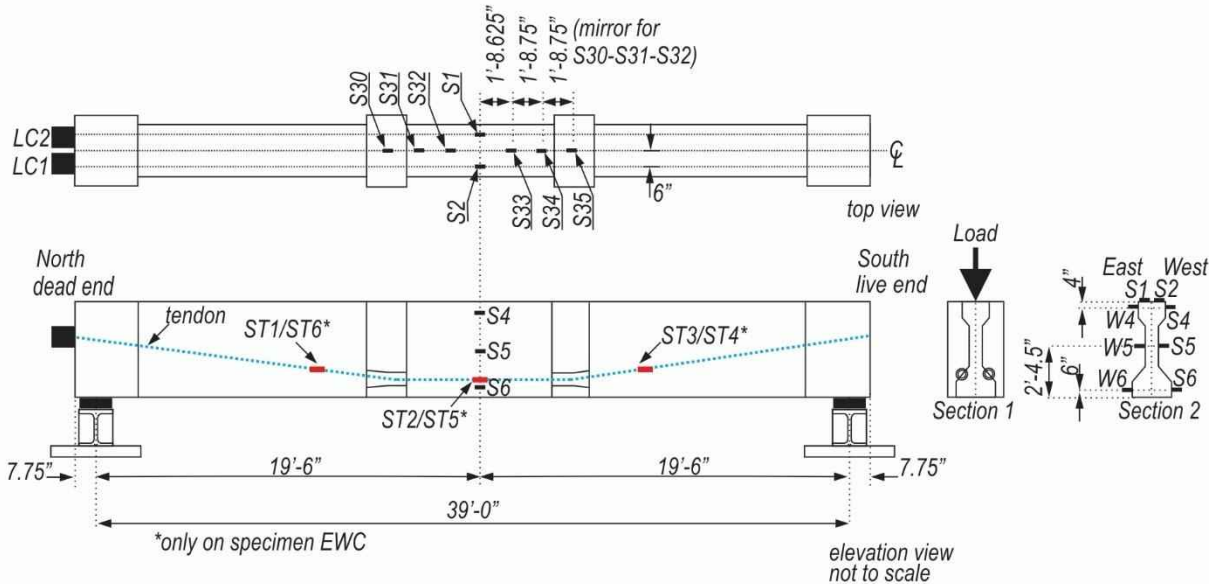


Figure 5-9 EWS and EWC: strain gage locations

5.1.4 Temperature

Specimens injected with flexible filler (all except specimen IGS) were instrumented with thermocouples to monitor thermal effects during injection. Temperature was measured along the length of the tendon. Thermocouples were used internally to measure filler temperature while surface mounted thermocouples were used to measure the surface temperature of the duct.

Several types of thermocouples were used:

- 1) Probe-type thermocouples were used to monitor filler temperature inside of the tendon duct. Type K thermocouples were selected based on the anticipated injection temperature of 220° F (105° C). Omega thermocouple part no. TJ36-CASS-116G-6-

- SMPW-M was chosen to measure the filler temperature. A compression fitting was needed to obtain a pressure-tight seal around the probe (Figure 5-10).
- 2) External tendon duct surface temperatures were monitored with Fluke 80-pk-11 flexible cuff type K surface strap instruments (Figure 5-10).
 - 3) Exposed wire type-K thermocouples were used to monitor internal concrete temperatures. Installation of the internal thermocouples is shown in Figure 5-11; a steel cage was used to set the locations of the internal thermocouples.



Figure 5-10 Probe (left) and surface strap (right) thermocouples

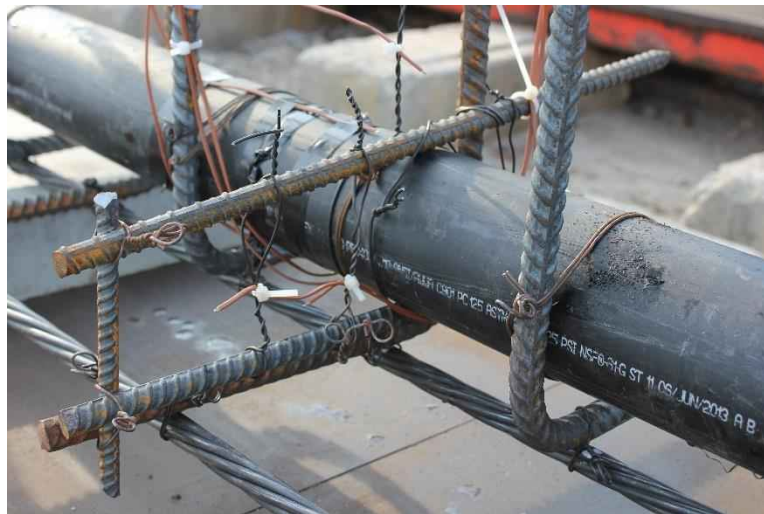


Figure 5-11 Installation of internal thermocouples

Thermocouple placement for specimens IWS and IWC is shown in Figure 5-12 and Figure 5-13; placement for EWS and EWC is shown in Figure 5-15.

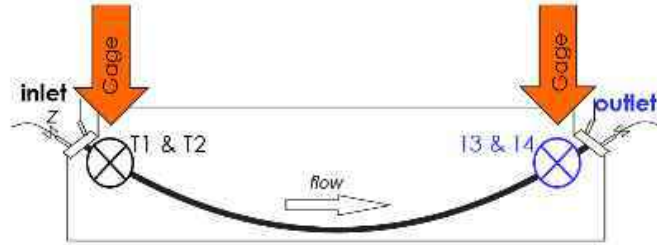


Figure 5-12 IWC and IWC: internal thermocouple layout

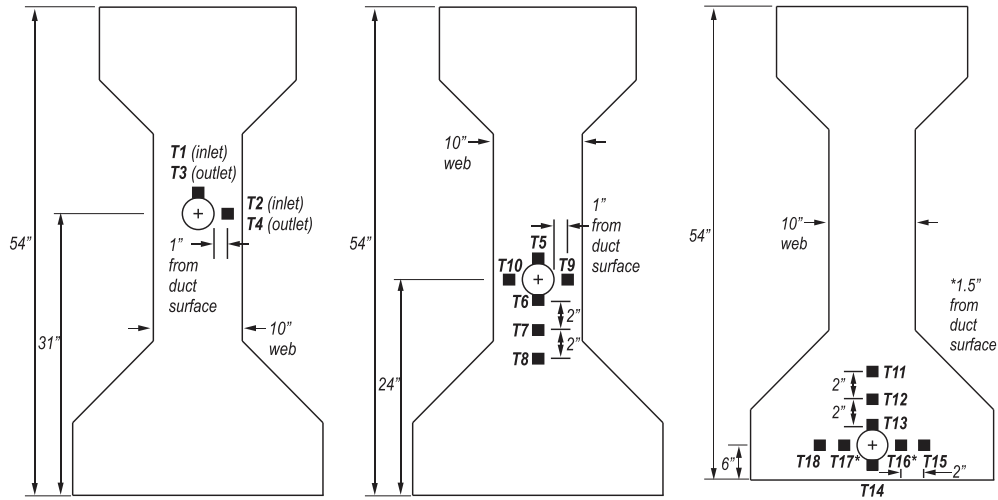


Figure 5-13 IWS and IWC: close-up of internal thermocouple layout

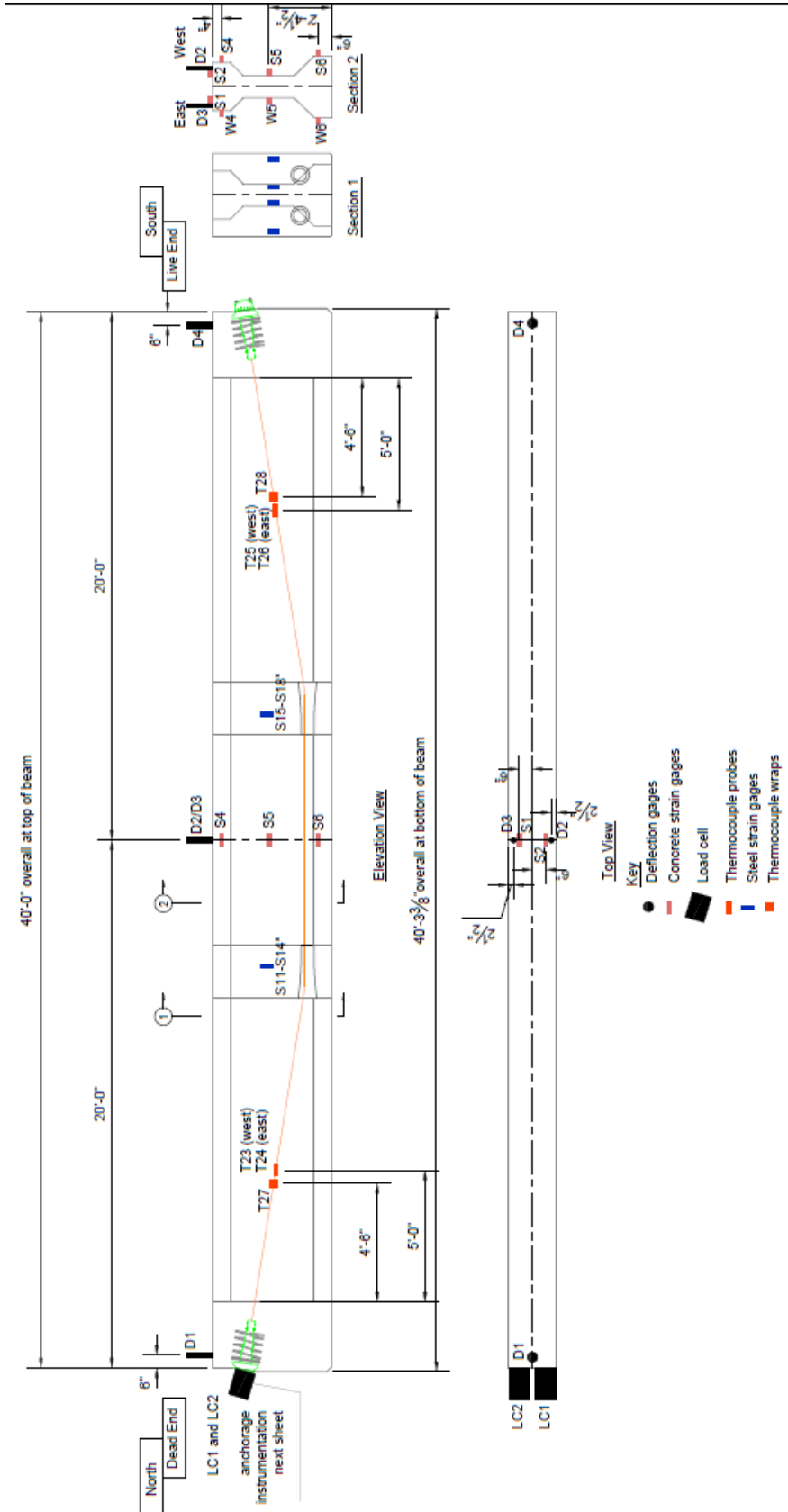


Figure 5-14 EWS: thermocouple layout

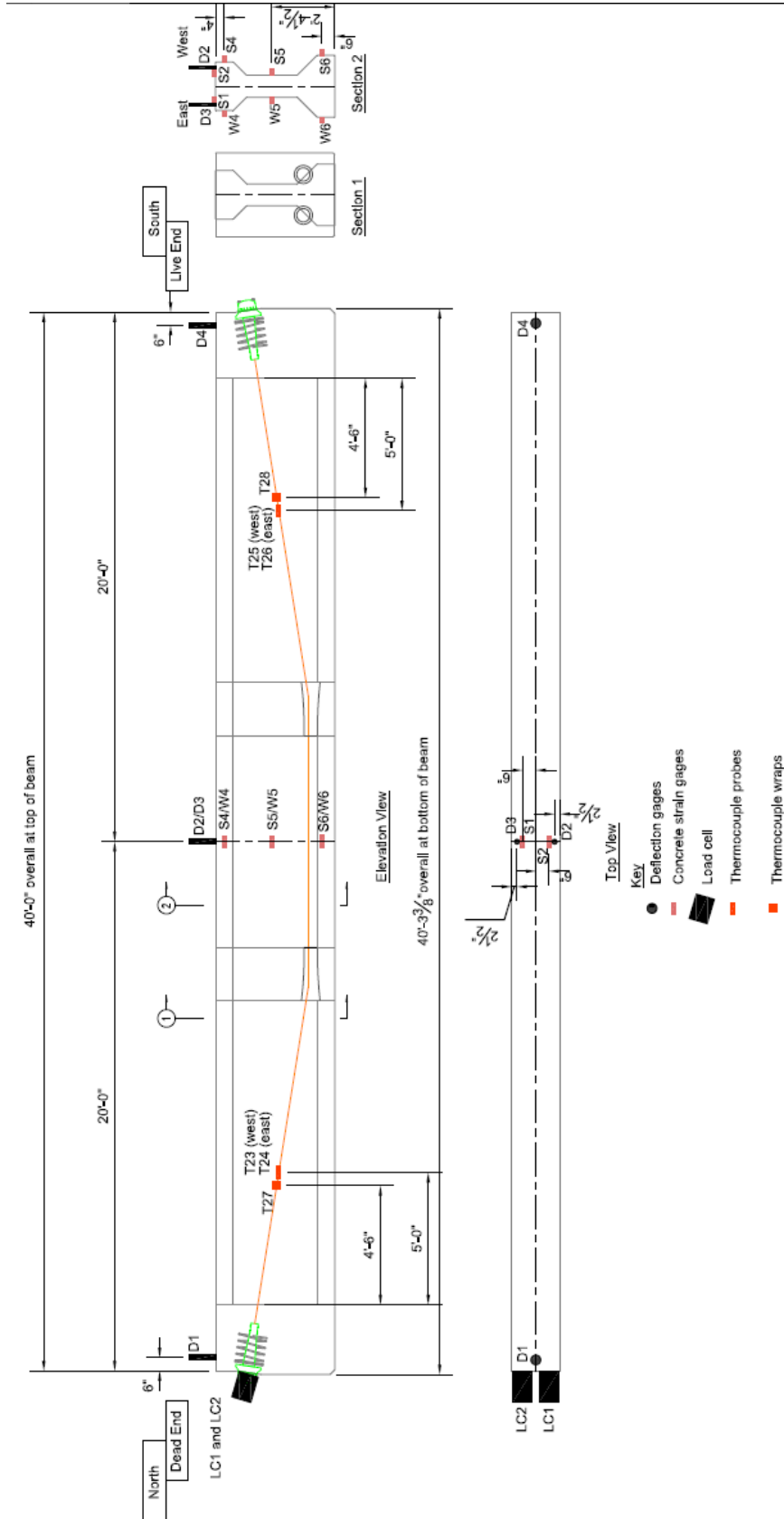


Figure 5-15 EWC: thermocouple layout

5.2 Fatigue

Instrumentation was installed to monitor each specimen during the following events: post-tensioning, filler injection, cyclic loading, and tendon detensioning (Figure 5-16 and Table 5-2). Monitoring for each event was tailored to ensure that the desired data were gathered for analysis.

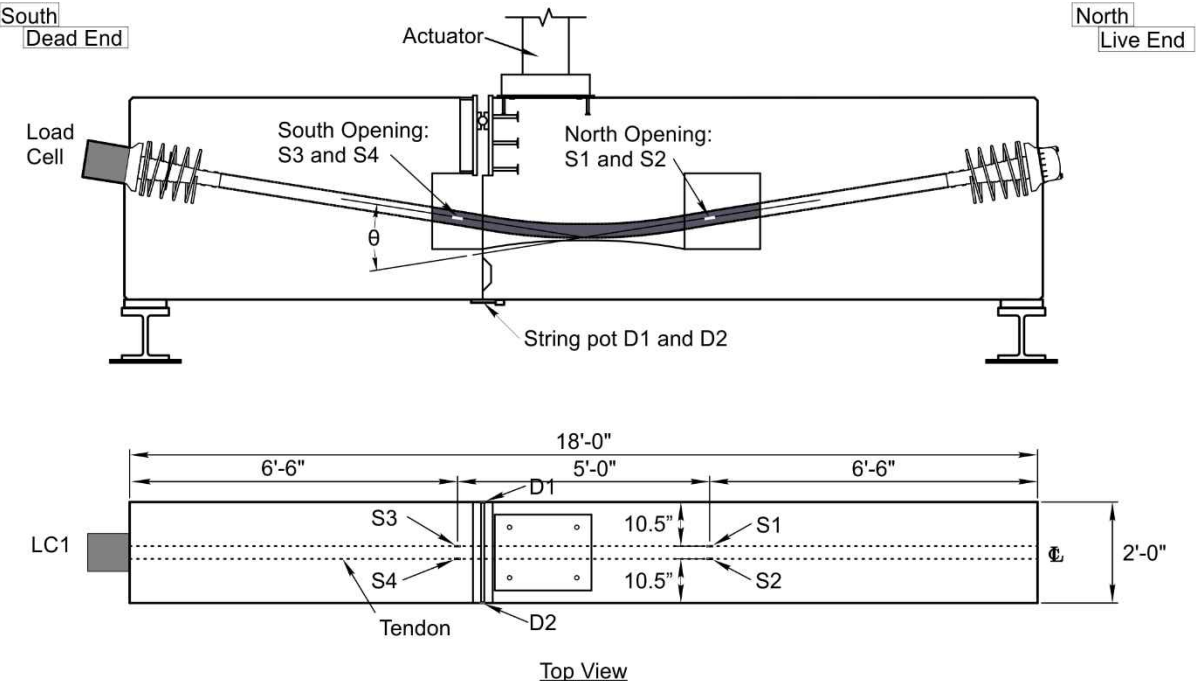


Figure 5-16 Instrumentation layout for fatigue specimens

Table 5-2 Monitored instrumentation

Stage	Tendon Force	Ambient Temperature	Tendon Strain	Gap Opening	Applied Load
Stressing	X				
Injection	X				
Cyclic Loading	X	X	X	X	X
Detensioning	X		X		

5.2.1 Tendon Force

Tendon force was measured directly with a hollow-core 850-kip Geokon 3000X-850-150MM load cell shown in Figure 5-17. The geometry of the load cell was the same as described in Section 5.1.1. The load cell was installed to ensure that six 0.6-in. dia. 7-wire prestressing strands passed through without obstruction and ensure that the tendon force was applied concentrically to the load cell.



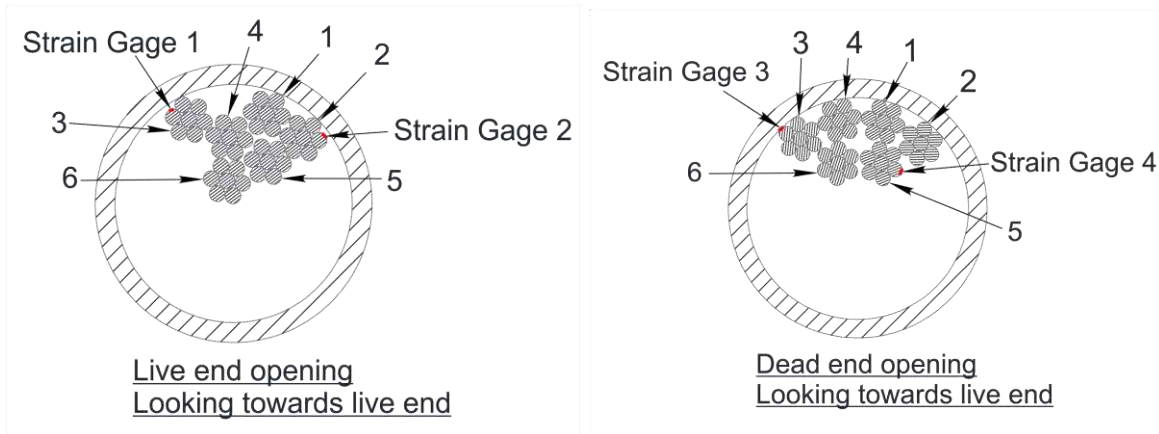
Figure 5-17 Geokon hollow-core load cell

5.2.2 Strain

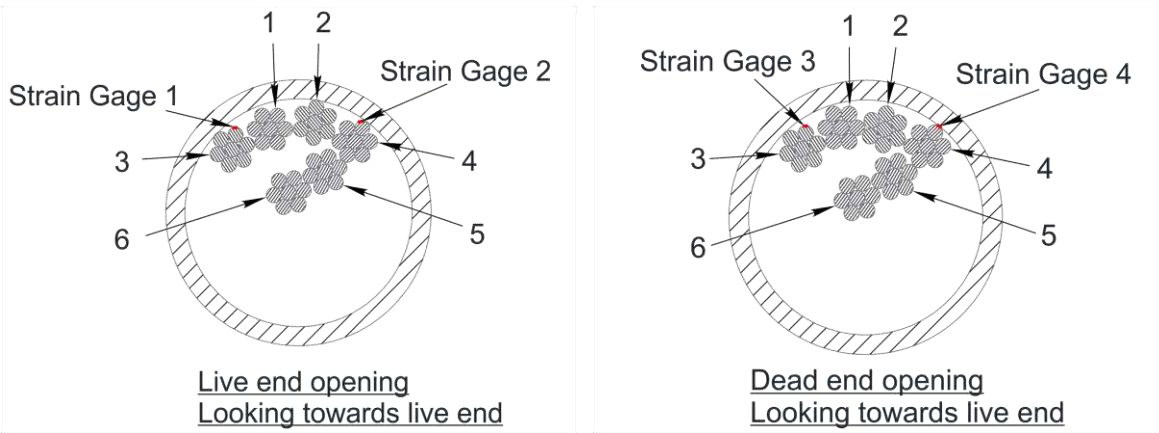
Prestressing strand strain was measured using TML FLA-05-11-1L 0.5-mm foil type strain gages during cyclic loading. After injection of the filler, the prestressing strands were accessed through a port cut into the HDPE sheathing (Figure 5-18) on each side of the deviator (Figure 5-16). Strain gages were placed on a single wire that was the most accessible in the areas where the HDPE was cut. Strain gages were placed on each side of the tendon (Figure 5-19) to provide redundant readings on both ends of the deviator. The strand numbers shown in the figure correspond with the strand arrangement in the wedge plate detailed in Section 6.1.2.



Figure 5-18 Removal of HDPE section to attach strain gage



(a)



(b)

Figure 5-19 Strand and strain gage locations for (a) F1 (b) F2

5.2.3 Gap Opening

Gap opening was measured using two Firstmark Controls 60-01-74C1-1 string potentiometer displacement gages (Figure 5-20). This measurement was used to evaluate the progression of the fatigue test and possible damage that might occur during the test. To maximize the displacement measurement, the gages were installed on the bottom face of the specimen mounted as close to the side face as practical. The potentiometer was bolted to the concrete face on one side (live-end segment) of the specimen. The reference attachment point was a steel angle mounted on the opposite side of the gap. This configuration caused a slight amplification of the readings due to the extension of the reference point by approximately 3.25 in. below the bottom of the beam. This amplification was corrected using the geometry of the mechanical hinge.



Figure 5-20 Gap displacement gages attached to specimen

6 Specimen Construction

This section describes the precasting and laboratory construction (including post-tensioning and injection with filler material) of the full-size and reduced-beam specimens.

6.1 Internal Tendon I-Girder

Nine precast beam segments with light pretensioning were constructed at a precast concrete prestressing yard. Three 40-ft long beams were constructed as internal tendon specimens (Specimens IGS, IWS and IWC).

To reduce the likelihood of strand recoil during detensioning, segments to be cast first were arranged in the bed such that segments were located close to one another, but away from the abutments (Figure 6-1).



Figure 6-1 Segments in prestressing bed

The modified AASHTO shape was cast first. After achieving the minimum specified transfer compressive strength (6 ksi), the bonded prestressing strands were torch-cut, and the beams were moved to another bed for casting the end-block. Full-size test specimens were precast at a prestressing yard in stages; the staging for the internal tendon specimens is shown in Figure 6-2.

A self-consolidating concrete mixture was used to ensure good flow. The same concrete mixture design was used for segments and end blocks. The concrete was further consolidated with internal hand-held vibrators. Care was taken near instrumentation to ensure gage integrity. The tops of the beams were roughened for future deck placement (internal tendon specimen segments only) or trowel-finished (external tendon specimen segments). The bed was covered with tarps for the curing period. The dates of strand stressing and cut-down are given in Table 6-1.

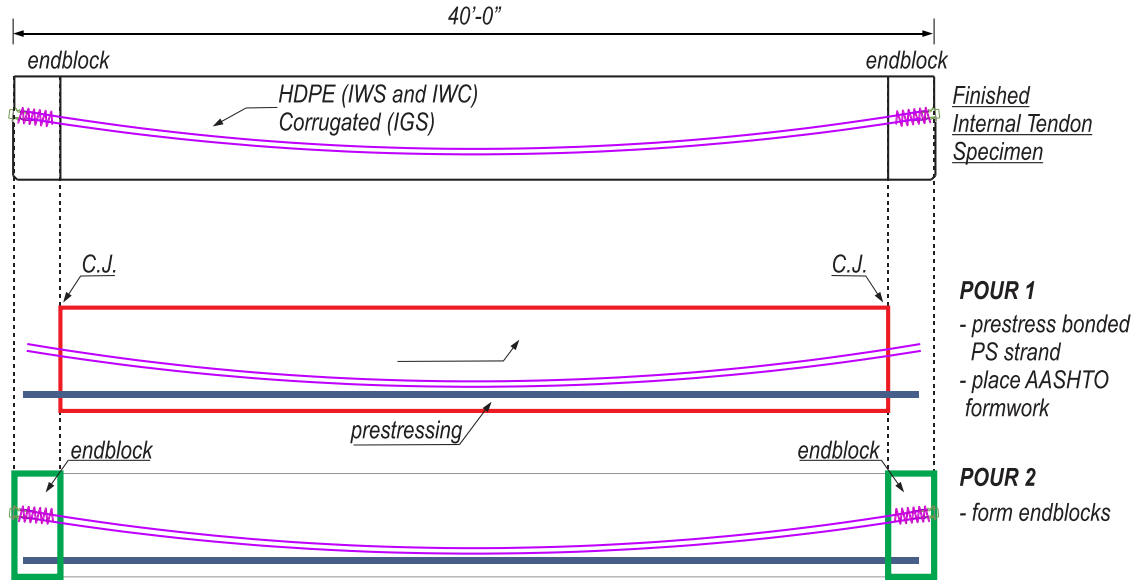


Figure 6-2 Construction staging of internal tendon specimens

Table 6-1 Specimen life stages

Specimen	Pre-tensioning	Casting date	Cut-down	Deck casting	Post-tensioning	Injection	Load Test
IGS	3-18-15	3-19-15	3-24-15	4-30-15	5-18-15	5-22-15	6-15-15
IWS	3-18-15	3-19-15	3-24-15	4-24-15	5-18-15	5-27-15	6-16-15
IWC	3-18-15	3-19-15	3-24-15	5-8-15	10-1-15	10-2-15	10-9-15
EWS	3-18-15	3-19-15	3-24-15	n/a	7-9-15	7-16-15	7-24-15
EWC	3-18-15	3-19-15	3-24-15	n/a	11-5-15	11-10-15	1-5-16

Stage #1 – AASHTO shape

The prestressing strands were stressed to $0.75f_{pu}$. Mild steel reinforcement (stirrups) were tied in and ducts for the internal tendon specimens (IGS, IWS, and IWC) were tied in between the stirrups (Figure 6-3). The ends of the ducts were covered with tape to prevent water/concrete from entering during casting. Thermocouple instrumentation for measurement of internal concrete temperature was installed prior to pulling up both side forms. Wire leads from the instrumentation were protected with plastic wrap. A self-consolidating mix with specified 28-day strength of 8.5 ksi was placed, taking care to not damage exposed instrumentation, to complete the AASHTO shape for all test specimens.



Figure 6-3 Duct installation

Stage #2 – End-blocks

End-blocks (housing the post-tensioning anchorage hardware and additional reinforcement) were constructed on a separate steel bed at the prestressing yard (Figure 6-4), reusing the plywood formwork for consistency. Alignment of the anchorages was controlled by bolting the anchorheads to the wooden forms.

In all internal tendon specimens, the plastic trumpet was mated to the duct using a 6-in. length of heat-shrink supplied by the PT supplier.

To connect the duct to the anchorage, the plastic trumpet was screwed directly into the anchorhead, as detailed by the PT supplier. Vent access holes in the anchorheads were covered with tape to prevent intrusion of concrete. Care was taken to avoid kinking the duct-trumpet connection.



Figure 6-4 Specimen construction: (a) main span, (b) endblocks

6.1.1 Laboratory Construction

Internal specimens were topped with an 8-in by 34-in. deck, which was cast in the lab prior to post-tensioning (Figure 6-5). Longitudinal and transverse deck reinforcement was detailed in consideration of FDOT temperature and shrinkage requirements. The deck concrete was a self-consolidating concrete (SCC) mix with a specified compressive strength of 8.5 ksi; vibrators were used, however, because of the steel reinforcement congestion. Concrete cylinders (6 in. × 12 in.) were cast to test for compressive strength and modulus of elasticity.



Figure 6-5 Deck casting on internal specimens

6.1.2 Post-tensioning

After the deck achieved the minimum specified compressive strength (8.5 ksi), the prestressing strands were hand-pushed into the specimen from the dead end, paying attention to install each strand in matching locations in the wedge plate; no effort was made to prevent strands from twisting around each other inside the specimen (Figure 6-6).



Figure 6-6 Strand pushing

The tendon was stressed with a monostrand jack incrementally to a target prestress of $0.8f_{pu}$, or 46.9 kip/strand. A stressing plate was utilized to protect adjacent wedges (from the nose of the monostrand jack) during stressing of individual strands (Figure 6-7). During the

prestressing procedure, the monostrand jack pressures were used to estimate the achieved prestress level for purposes of determining when to terminate the stressing procedure.

Stressing was completed in two passes. First, a single strand was stressed to 25% of the target prestress ($0.2f_{pu}$, or 11.7 kip) to align and fix the hardware in place (wedge plates and the load cell). Marks were then made on all strands at the dead and live ends to monitor prestress through elongation and wedge seat measurements. The remaining eleven strands were then stressed to 25% of the target. In a second pass, strands were stressed to the target prestress, $0.8f_{pu}$. Figure 6-8 shows the tendon force histories for IWS.



Figure 6-7 Stressing plate

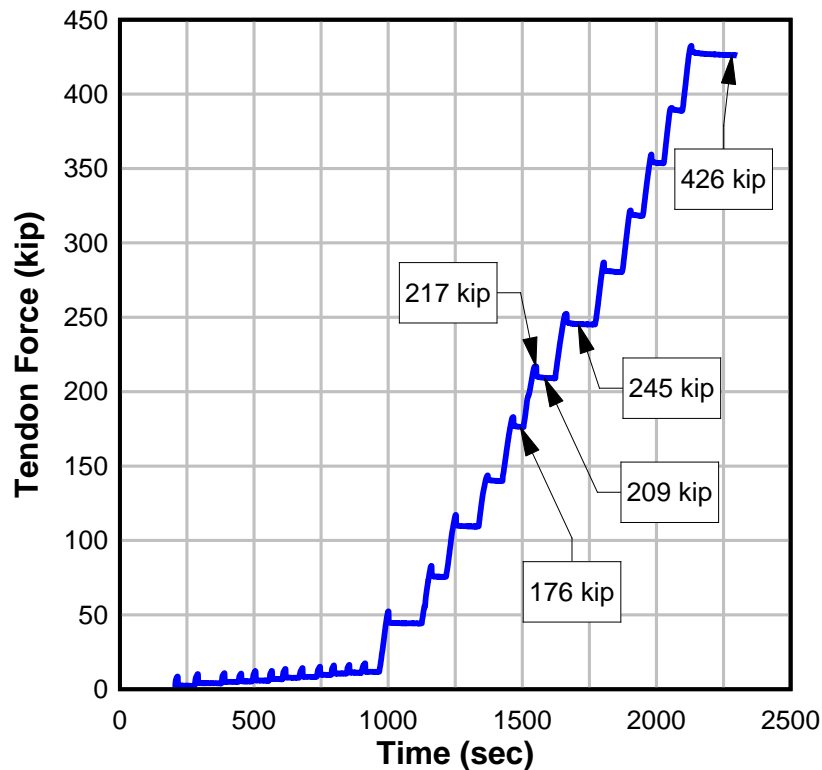


Figure 6-8 IWS tendon force history

6.1.3 Grout Injection

Post-tensioning tendons were injected with filler material after the stressing operation. Grout was used to inject one internal tendon specimen (IGS). All other specimens were injected with flexible filler.

Injection procedures were based on FDOT Road and Bridge Construction Specifications (2014), with safety modifications to accommodate the heated filler material (Figure 6-9). Prior to each injection, an air pressure test was performed to prove the tendon's air-tightness, in accordance with FDOT specifications and standard construction practice.

Specimen IGS was injected end-to-end with a commercially-available cementitious grout, Euclid Cable Grout PTX with a standard hopper-fed grout pump (Figure 6-10). The plastic grout tube typically supplied was not used. The inlet was a 3/4-in. dia. steel pipe in the top of the anchor; epoxy was used to secure the pipe. Vents were located at each nylon anchor cap and at the top of the anchor at the far end (3/4-in. dia. steel pipe).

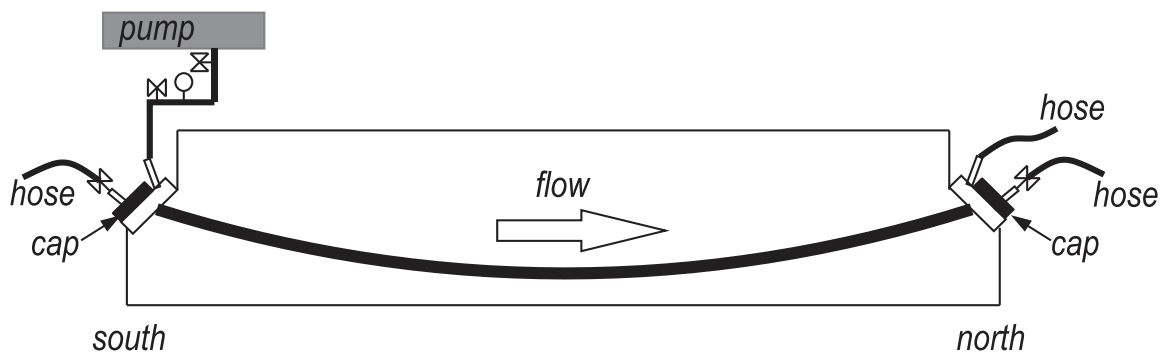


Figure 6-9 Grout injection of IGS



Figure 6-10 Grouting operation: (a) feeding hopper, (b) uniform consistency, (c) at outlet

Grout bags were weighed prior to mixing to ensure an accurate water-to-cement ratio during mixing. Grout was mixed according to manufacturer's instructions with a hand-held electric drill mixer.

Prior to connecting the injection hoses to the beam, grout was pumped continuously into a spare bucket to evacuate all water and air from the hoses and ensure good grout flow. The injection hose was then attached to the inlet and pumping commenced at a pressure of 10 psi to 50 psi; the two anchorage-vents and the outlet were open. When uniform consistency of the grout was observed at the outlet, the top outlet vent was closed. Pumping was continued until grout discharged from each cap; the cap-vents were then closed. The tendon was pressurized and the inlet valve was then sealed. The pressure was held for two minutes.

The system was then "burped" to allow trapped air to escape from the tendon. Pressure was relieved to 5 psi and held for ten minutes, to allow air to flow to high points. The pumping pressure was then increased not to exceed actual realized pumping pressure of tendon and grout was discharged at each high point outlet. To complete the process, the pump was held at a pressure of 30 psi while all valves were closed to lock this pressure into the tendon.

After 48 hours, the caps were removed for placement of anchor head instrumentation on the wedge plate. Grout caps were not greased prior to injection, making their removal difficult; some of the grout was damaged in the process.

Visual observations were noted during the cap removal (Figure 6-11 and Figure 6-12). At the outlet cap (dead end), grout started to fall away, but appeared to fill most of the cap. A small void was observed at the very top, with a thin layer of soft grout (1/8-in. thick) at this void. The void was approximately 1-in. deep from the top of the cap. At the inlet cap, most of the grout was damaged during the cap removal. From earlier sounding of the nylon cap, however, it is assumed the inlet cap was completely full.



Figure 6-11 IGS Outlet (dead end) prior to and after cap removal



Figure 6-12 IGS inlet (live end) prior to and after cap removal (damaged)

6.1.4 Flexible Filler Injection

Specimens injected with flexible filler were vacuum-injected end-to-end with Civetec Cirinject-CP using a heated centrifugal pump at the inlet and a vacuum at the outlet; Figure 6-13 shows the general injection set-up.

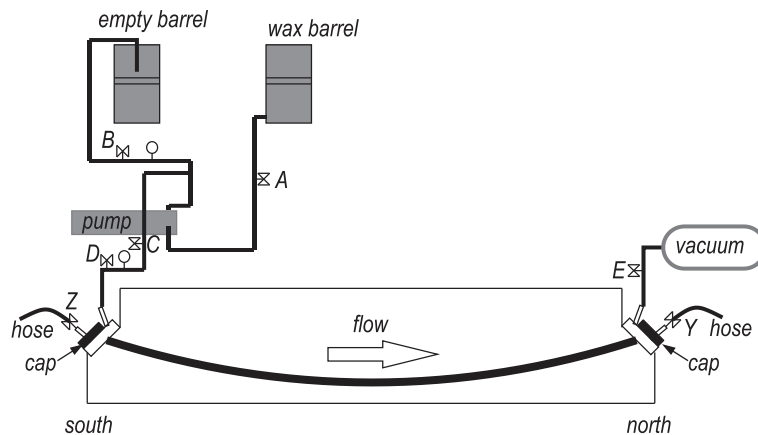


Figure 6-13 Flexible filler injection for internal tendons

The inlet line for the filler was attached to the injection port on the anchorage, which bypassed the grout cap and wedge plate. The vacuum line was attached to the inlet line at the discharge anchorage. Both the inlet and the outlet were 3/4-in. dia. steel pipes located at the top of the anchors, secured with epoxy. Valves and discharge lines were attached to the grout caps at each end of the specimen. These lines, however, were reserved for use if deemed necessary during injection, but ultimately were not used; no venting was conducted. Prior to injection, all valves were closed with the exception of the vacuum line and a vacuum was pulled on the

tendon. Strap barrel heaters were used to preheat the filler material (Figure 6-14Figure 6-40). The filler material was periodically stirred with a paddle mixer to ensure uniform temperature of the filler, and to prevent local overheating. Prior to connecting the injection hoses to the beam, filler material was pumped continuously into a spare bucket to evacuate air from the hoses and ensure good filler flow. Following heating of filler material and preparation of the pump, the pump line was opened to allow filler to flow into the tendon. Once the filler was observed to discharge from the vacuum line, that valve was closed. Pumping continued until the tendon was pressurized and the inlet valve was then closed. Pressure was monitored to ensure no pressure loss.



Figure 6-14 Heating flexible filler for injection

Visual observations were noted during the cap removal (Figure 6-15 and Figure 6-16). The voids at the top of the grout caps were thought to have formed from residual air trapped in the system after the valves had been closed. In addition, the filler will shrink as it cools, which may also have contributed. Subsequent testing of filler injection has shown that these voids can be nearly eliminated by installing a length of flexible tubing to the grout cap inlet. The tubing acts as a reservoir that allows the escape of incidental air without the need for active venting.

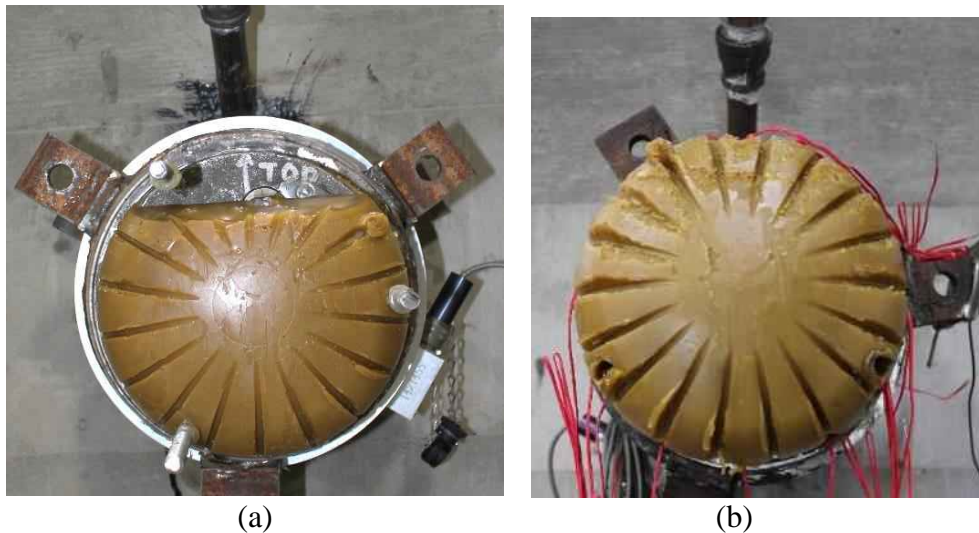


Figure 6-15 Outlet (dead end) after cap removal (a) IWS and (b) IWC



Figure 6-16 Inlet (live end) after cap removal of IWS

6.2 *External Tendon I-Girder*

The modified AASHTO shape was cast first. After achieving the minimum specified transfer compressive strength (6 ksi), the bonded prestressing strands were torch-cut and the beams were moved to another bed for casting the end-block. Full-size test specimens were precast at a prestressing yard in stages; the staging for the external tendon specimens is shown in Figure 6-17.

A self-consolidating concrete mixture was used to ensure good flow. The same concrete mixture design was used for segments and end blocks. The concrete was further consolidated with internal hand-held vibrators. Care was taken near instrumentation to ensure gage integrity. The tops of the beams were roughened for future deck placement (internal tendon specimen segments only) or trowel-finished (external tendon specimen segments). The bed was covered with tarps for the curing period. The dates of strand stressing and cut-down are given in Table 6-1.

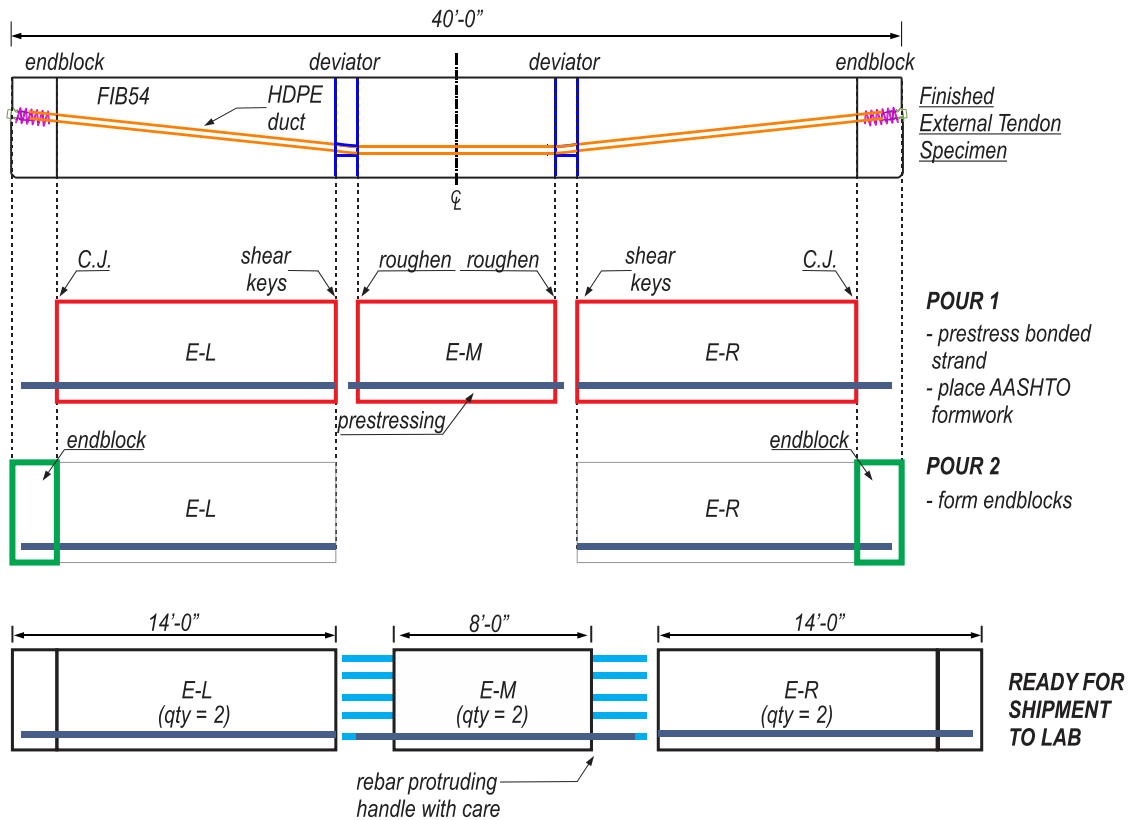


Figure 6-17 Construction sequencing of external tendon specimens

Stage #1 – AASHTO shape

The prestressing strands were stressed to $0.75f_{pu}$. Mild steel reinforcement (stirrups) were tied in. A self-consolidating mix with specified 28-day strength of 8.5 ksi was placed.

Stage #2 – End-blocks

End-blocks (housing the post-tensioning anchorage hardware and additional reinforcement) were constructed on a separate steel bed at the prestressing yard, reusing the plywood formwork for consistency. Alignment of the anchorages was controlled by bolting the anchorheads to the wooden forms.

For the external tendon specimens, a 4-ft length of 3-in. HDPE was butt-welded to the plastic trumpet by the PT supplier prior to delivery to the precaster to ensure straight alignment of the duct/anchorage.

To connect the duct to the anchorage, the plastic trumpet screwed directly into the anchorhead, as detailed by the PT supplier. Vent access holes in the anchorheads were covered with tape to prevent intrusion of concrete. Care was taken to not kink the duct-trumpet connection.

6.2.1 Laboratory Construction

This section describes laboratory construction specific to the external tendon specimens, including the deviation block casting and the joint preparation at the simulated segmental joints.

Deviation block

The external tendon specimens were delivered to the laboratory in segments, where the deviation blocks were match-cast to control shear key alignment at the joints. The general procedure is shown in Figure 6-18.

In preparation for casting the deviation blocks, a set of four level pads were placed in the lab; each pad was constructed with non-shrink cementitious grout (Lambert Corporation's Vibropruf #11) and 1-in thick steel plates (Figure 6-19). Precast segments were aligned and leveled on the grout pads, the reinforcement cage and diabolo void-former were installed, and the formwork constructed of plywood. Both deviators were cast from the same batch using a ready-mix self-consolidating concrete with 8.5 ksi specified compressive strength (Figure 6-20). Hand-held vibrators were used to consolidate the concrete. The top of the deviator block was trowel-finished and leveled to match the rest of the beam.

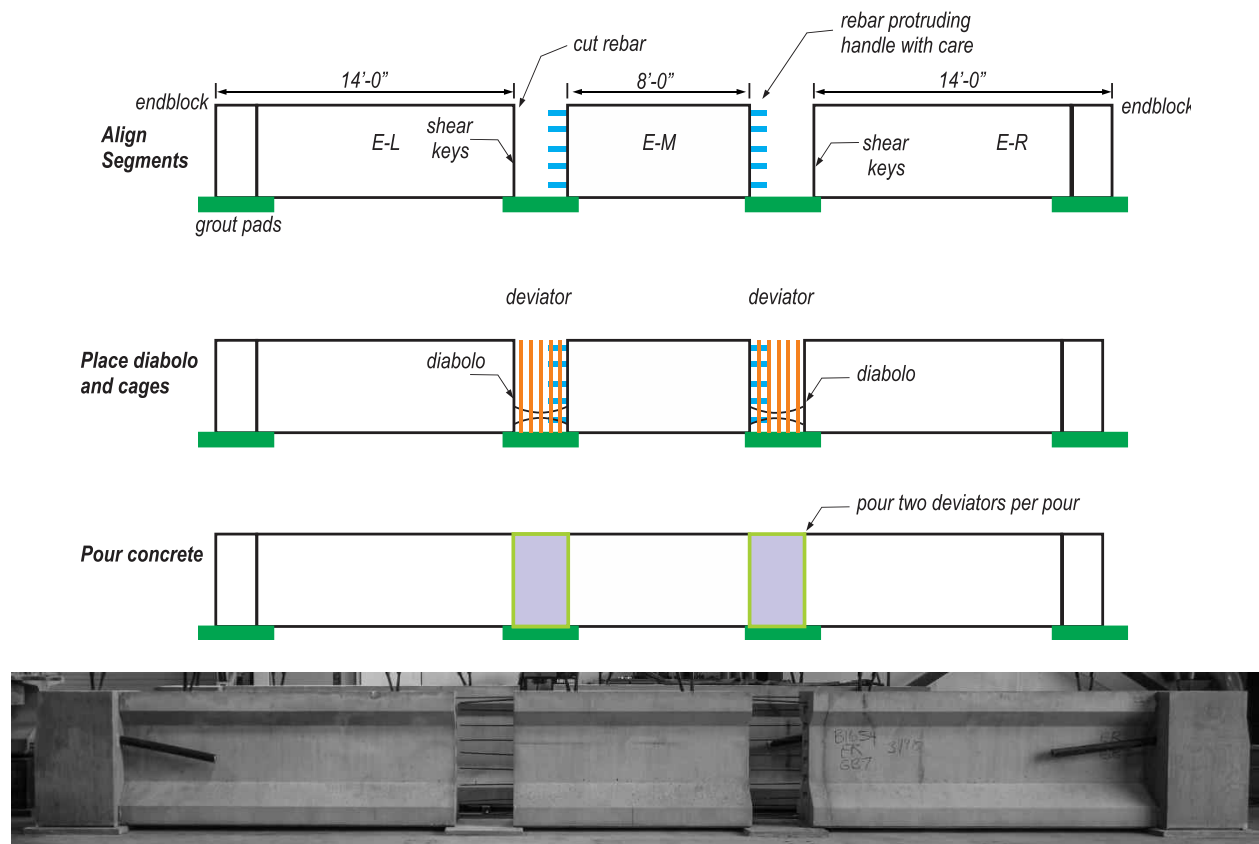


Figure 6-18 Segments arranged for casting of deviation block



Figure 6-19 Grout pads for deviator blocks



(a)



(b)

Figure 6-20 Deviator block (a) formwork and (b) concrete placement

Epoxy Joining and Stressing

After the deviation blocks achieved the minimum specified compressive strength (8.5 ksi), preparations were made to join the segments and stress the tendons in a combined procedure.

Prior to the epoxy application, the joints were prepared; each match-cast face was scrubbed with a wire brush and pressure washed. Segments were aligned, but set apart at each joint to provide working space. The prestressing strands were hand-pushed into each tendon, paying attention to install each strand in matching locations in the wedge plate; however, no effort was made to prevent strands from twisting around each other inside the specimen. The anchorages were loosely installed and wedges were left unset.

Segmental epoxy was applied to the match-cast joints of specimens EWS and EWC to simulate standard construction practice. Pilgrim CBC 6, slow-set segmental epoxy was selected from the FDOT Approved Products List.

The epoxy was prepared according to the manufacturer's instructions. The two-part epoxy was mixed in a bucket with a drill mixer until achieving a uniform color and consistency (approximately 3 minutes). The epoxy was then applied by hand to both faces of the joint.



Figure 6-21 Epoxy application

Following the epoxy application, the beam segments were adjusted with the crane to close the joints as much as possible (1/4 to 1/2 in.). Wedges were then hand-installed on each end and two strands per anchor were stressed using a monostrand jack to approximately 22 kip/strand, squeezing the joints closed. The specimen was left for 48 hours to allow the epoxy to set before completing the post-tensioning.

Each six-strand tendon was stressed with a monostrand jack incrementally to a target prestress of $0.8f_{pu}$, or 46.9 kip/strand, alternating between tendons to minimize eccentricity of the prestressing force about the weak axis. During the prestressing procedure, jack pressures were used to estimate the achieved prestress level. First, a single strand was stressed to 25% of the target ($0.2f_{pu}$, or 11.7 kip) to align and fix the hardware in place (wedge plates and the load cell). Marks were then made on all strands at the dead and live ends to quantify prestress through elongation and wedge seat measurements. The remaining eleven strands were then stressed to 25% of the target. In a second pass, strands were stressed to the target prestress, $0.8f_{pu}$. Elongation and wedge seat measurements were documented.

The post-tensioning tendon force was measured directly using hollow-core 850-kip load cells. Prestress transfer occurred incrementally as each strand was stressed with a monostrand

jack. Table 6-2 summarizes the measured tendon force at time of prestressing and at time of ultimate load test.

Table 6-2 Post-tensioning force

Specimen	Load Cell	Initial		At time of ultimate load test	
		PT Force by Load Cell (kip)	Average Tendon Stress (ksi)	PT Force by Load Cell (kip)	Average Tendon Stress (ksi)
EWS	LC1	253	0.67 f_{pu}	241	0.65 f_{pu}
	LC2	218		213	
EWC	LC1	227	0.69 f_{pu}	223	0.68 f_{pu}
	LC2	261		252	

Each specimen was post-tensioned with two 6-strand tendons

6.2.2 Post-tensioning

After the deck achieved the minimum specified compressive strength (8.5 ksi), the prestressing strands were hand-pushed into the specimen from the dead end, paying attention to install each strand in matching locations in the wedge plate; no effort was made to prevent strands from twisting around each other inside the specimen.

The tendon was stressed with a monostrand jack incrementally to a target prestress of 0.8 f_{pu} , or 46.9 kip/strand. A stressing plate was utilized to protect adjacent wedges (from the nose of the monostrand jack) during stressing of individual strands. During the prestressing procedure, the monostrand jack pressures (not the load cell measurements) were used to estimate the achieved prestress level for purposes of determining when to terminate the stressing procedure.

Stressing was completed in two passes. First, a single strand was stressed to 25% of the target prestress (0.2 f_{pu} , or 11.7 kip) to align and fix the hardware in place (wedge plates and the load cell). Marks were then made on all strands at the dead and live ends to monitor prestress through elongation and wedge seat measurements. The remaining eleven strands were then stressed to 25% of the target. In a second pass, strands were stressed to the target prestress, 0.8 f_{pu} . Figure 6-22 shows the tendon force histories for EWS.

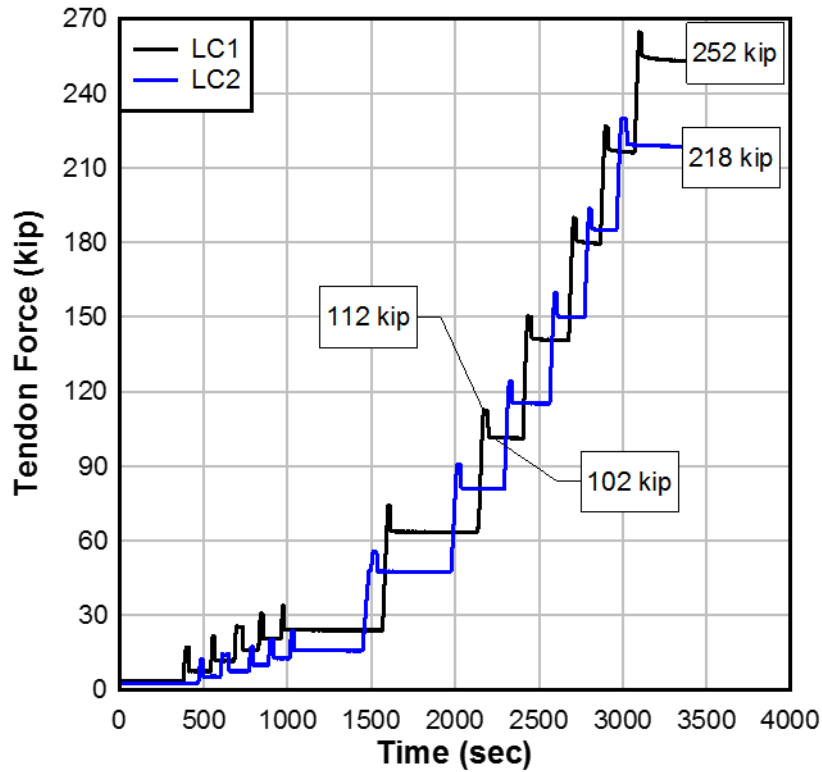


Figure 6-22 EWS tendon force history

6.2.3 Flexible Filler Injection

Specimens injected with flexible filler were vacuum-injected end-to-end with Civetec Cirinject-CP using a heated centrifugal pump at the inlet and a vacuum at the outlet; Figure 6-23 shows the general injection set-up. Tendon #1 was fully injected with flexible filler material prior to injecting Tendon #2.

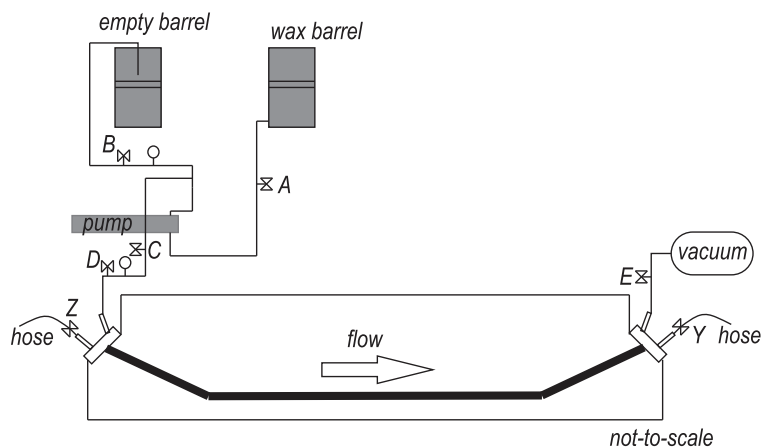


Figure 6-23 Flexible filler injection for external tendons

The inlet line for the filler was attached to the injection port on the anchorage, which bypasses the grout cap and wedge plate. The vacuum line was attached to the inlet line at the

discharge anchorage. Both the inlet and the outlet were 3/4-in. dia. steel pipes located at the top of the anchors, secured with epoxy. Valves and discharge lines were attached to the grout caps at each end of the specimen. These lines, however, were reserved for use if deemed necessary during injection, but ultimately were not used; no venting was conducted. Prior to injection, all valves were closed with the exception of the vacuum line and a vacuum was pulled on the tendon. Strap barrel heaters were used to preheat the filler material. The filler material was periodically stirred with a paddle mixer to ensure uniform temperature of the filler, and to prevent local overheating. Prior to connecting the injection hoses to the beam, filler material was pumped continuously into a spare bucket to evacuate air from the hoses and ensure good filler flow. Following heating of filler material and preparation of the pump, the pump line was opened to allow filler to flow into the tendon. Once the filler was observed to discharge from the vacuum line, that valve was closed. Pumping continued until the tendon was pressurized and the inlet valve was then closed. Pressure was monitored to ensure no pressure loss.

6.3 Fatigue

This section covers the construction of F1 and F2. Each specimen was constructed in two segments. Each specimen was a rectangular cross-section with dimensions 2-ft wide by 4-ft deep by 18-ft long. They both included a parabolic unbonded tendon which passed through a 4-ft deviator with a 10-ft radius. Specimen F1 had a tendon angle of 18 degrees while specimen F2 had a tendon angle of 11 degrees.

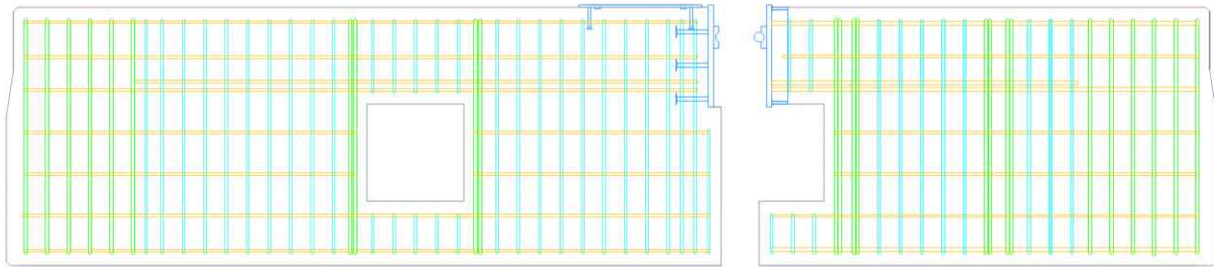
An FDOT class V concrete mixture with a specified compressive strength of 6500 psi was used for both specimens. The key periods showing the life cycle of the specimens are shown in Table 6-3.

Table 6-3 Important dates in the construction and testing of fatigue specimens

Specimen	Segment 1 casting date	Segment 2 casting date	Post-tensioning	Injection	Cyclic Loading Start	Cyclic Loading End	Detensioning
F1	11-18-17	12-06-17	01-03-17	01-06-17	01-19-17	02-13-17	02-17-17
F2	03-10-17	03-10-17	04-12-17	04-25-17	04-26-17	05-19-17	05-30-17

6.3.1 Formwork and Reinforcing Cage

Formwork and reinforcement cage, including portions of the mechanical hinge, were fabricated separately for each of the two segments (Figure 6-24). The reinforcing bar arrangement was the same for both specimens. Cages were assembled upright using 2x4 bracing and plywood sheets for stability (Figure 6-25). The plywood sheets were used to support the longitudinal steel in the arrangement indicated on the construction drawings.



(a)



(b)

Figure 6-24 Reinforcement cage (a) schematic and (b) assembled



Figure 6-25 Reinforcing bar cage

Formwork (Figure 6-26) was assembled separately from the reinforcement cage, consisting of 2×4 and plywood sections placed with the side face of the specimen on the floor. The reinforcement cage was placed inside of the formwork after assembly.



(a)



(b)

Figure 6-26 Fatigue specimen formwork (a) during assembly (b) after insertion of reinforcing bar cage

6.3.2 Concrete Placement and Shear Key

Each specimen was cast in separate segments. For F1, concrete was placed in the first segment and allowed to harden (Figure 6-27). The formwork for the second segment was then erected so that the concrete for the second placement was cast against that of the first segment. This was done to ensure a proper fit and alignment of the shear key. F2 (Figure 6-28) was also fabricated in two segments, but the concrete was placed for both segments at one time. Each segment was positioned flat on the floor to ensure proper alignment. Concrete in both specimens was consolidated with an internal vibrator. Slump tests were conducted before each concrete placement and concrete cylinders (4×8) were collected for 7-day, 14-day, 28-day and test-day compressive strength tests. Formwork was removed after 7 days of curing. Segments were then placed on steel supports in preparation for post tensioning (Figure 6-29).



Figure 6-27 Concrete placement of specimen F1



Figure 6-28 Concrete placement of specimen F2



Figure 6-29 Completed fatigue specimen without post-tensioning

During formwork removal of specimen F1, concrete spalled locally around the south (dead) end of the diabolo deviator. The damaged concrete was immediately repaired with mortar (Figure 6-30) to ensure sharp edges that could potentially damage the duct were removed.

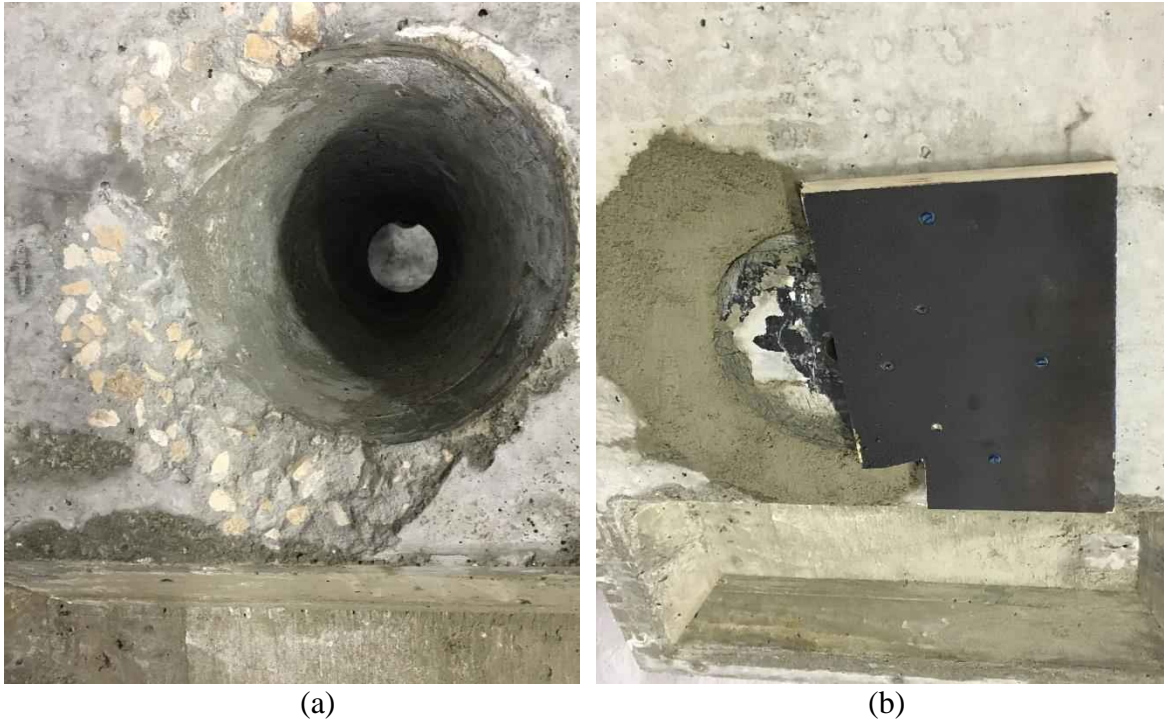


Figure 6-30 Specimen F1 after formwork removal (a) concrete spalling and (b) concrete repair

6.3.3 Post-Tensioning

Once the specimen attained the specified 28-day compressive strength (6.5 ksi) the post-tensioning tendon was installed and stressed. The installation process was controlled to ensure that the strands were installed parallel and that they occupied the same respective position in the wedge plates at each anchorage. Prior to insertion, each strand was labeled using duct tape at both ends to match their corresponding wedge plate position (Figure 6-31). The strands were also tied at both ends with steel tie wire to prevent twisting during installation. The strand bundle was pushed in by hand (Figure 6-32) and arranged to match their intended position in the wedge plate. Steel tie wires were removed from the strands after tendon was inserted. Post-tensioning of both specimens was done by individually stressing each strand with a monostrand jack (Figure 6-33).



Figure 6-31 Strand labeling and steel ties



Figure 6-32 Strand installation



Figure 6-33 Monostrand jack

The wedge plates were labeled to show the corresponding strand numbers (Figure 6-34). Strands were stressed in the order indicated by the numbering. As the stressing progressed, the strands pulled against the inside radius of the HDPE, which is deviated by the diabolo-shaped deviator formed in the concrete. Starting the stressing at the topmost strand in the bundle ensured that no unstressed strands would be bound or trapped against the deviator by stressing a strand lower in the bundle.

A stressing plate (Figure 6-35) was used to protect the adjacent wedges during stressing. To reduce seating losses, 1/8 in. thick washers were used inside the stressing plate. Specimen F1 used two washers to reduce seating losses, and specimen F2 used three washers. Monostrand jack pressure was used to estimate the prestress value of the strands; once the target pressure was attained, the jack pressure was relieved. Load cell readings were taken continuously during stressing, which allowed verification of the estimated prestress values.

Post-tensioning was completed in two rounds of sequential stressing of the individual strands. In the first round, the strand jacking force was 10% ($0.1f_{pu}$, or 5.9 kip) to align the

strands in the duct and provide enough force to align and hold the load cell and wedge plate in place. Hardware alignment was inspected during the process. Strands were marked after the initial stressing to facilitate strand elongation and wedge displacement measurements. In the final round, the strand jacking force was 80% ($0.8f_{pu}$, or 46.9 kip) for all strands in F1. In F2, strands 4 through 6 were instead stressed to 79% ($0.8f_{pu}$, or 46.3 kip) instead of 80%. This was done to ensure a more even stress distribution between strands at the end of the post-tensioning operation. The tendon force results during stressing for F1 and F2 are shown below in Figure 6-36 and Figure 6-37, respectively. The final prestress force in F2 was greater due to the addition of a washer between the wedges and retainer plate.

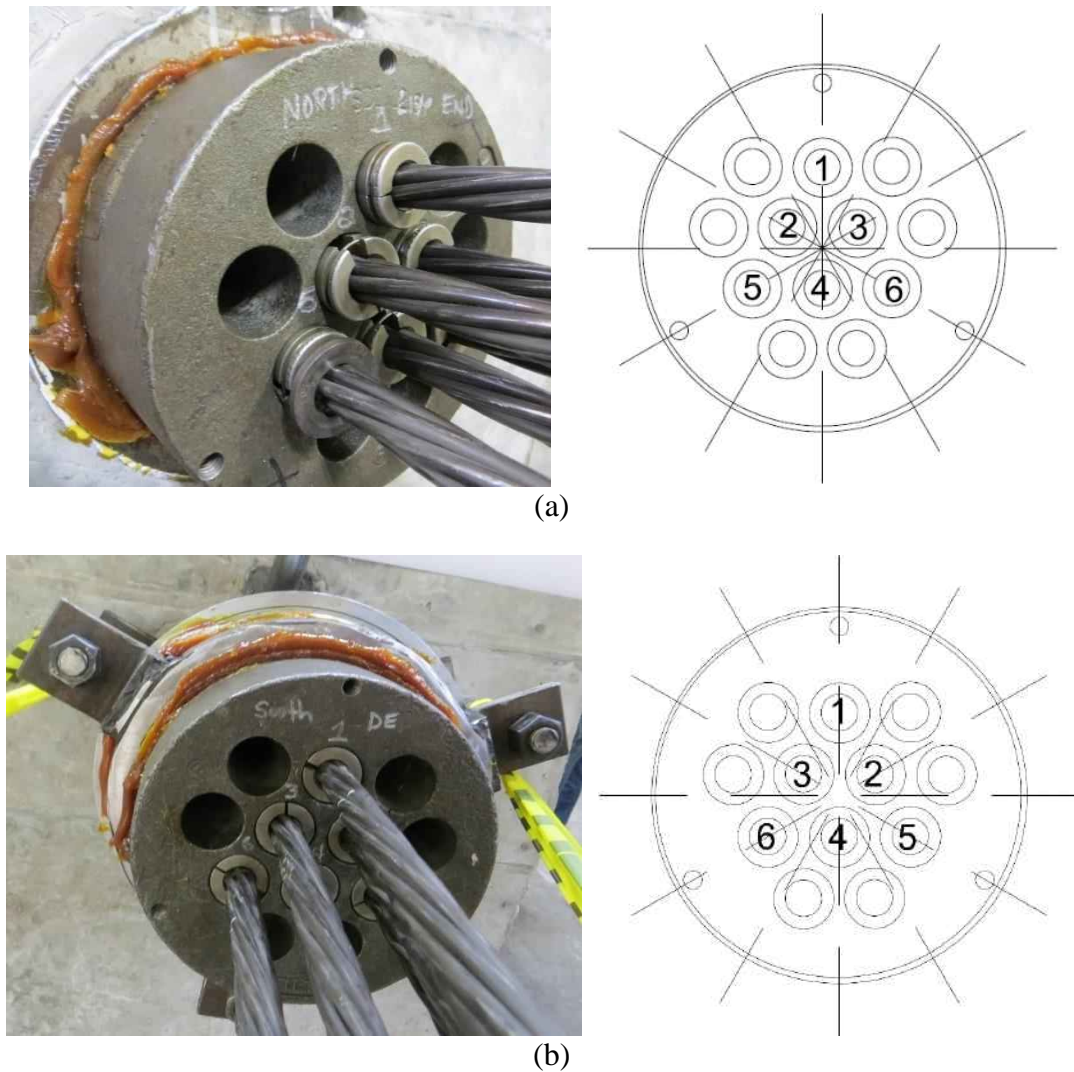


Figure 6-34 Strand location in wedge plates at (a) live end and (b) dead end



Figure 6-35 Washers to reduce seating losses

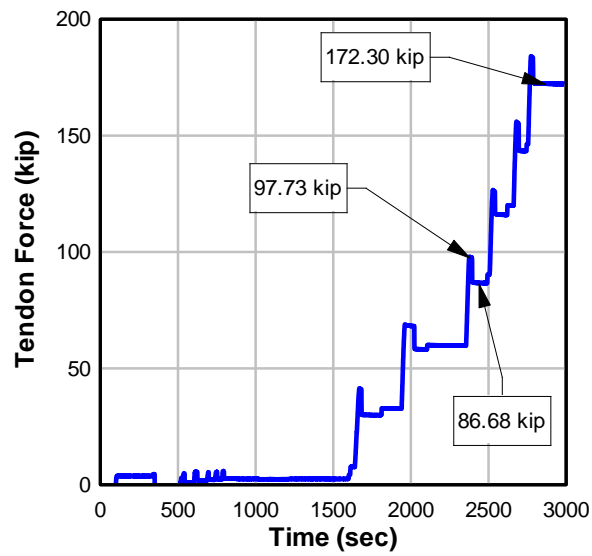


Figure 6-36 F1 post-tensioning results

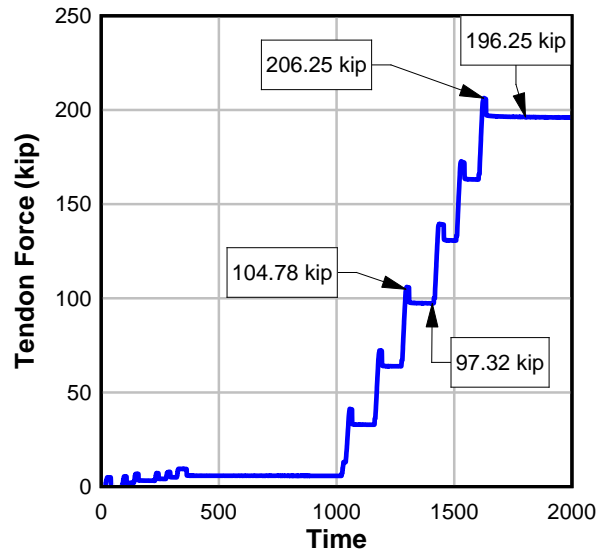


Figure 6-37 F2 post-tensioning results

At the end of the post-tensioning procedure the strands protruding at the live end and dead end were cut with a circular saw to 1.5 in. from the anchor head (Figure 6-38).



Figure 6-38 Strand cutting after post-tensioning

6.3.4 Flexible Filler Injection

Fatigue beam specimens were vacuum-injected end-to-end with flexible filler manufactured by Trenton using a centrifugal pump at the inlet and a vacuum at the outlet. Figure 6-39 shows the overall set-up for the injection of specimen F1.

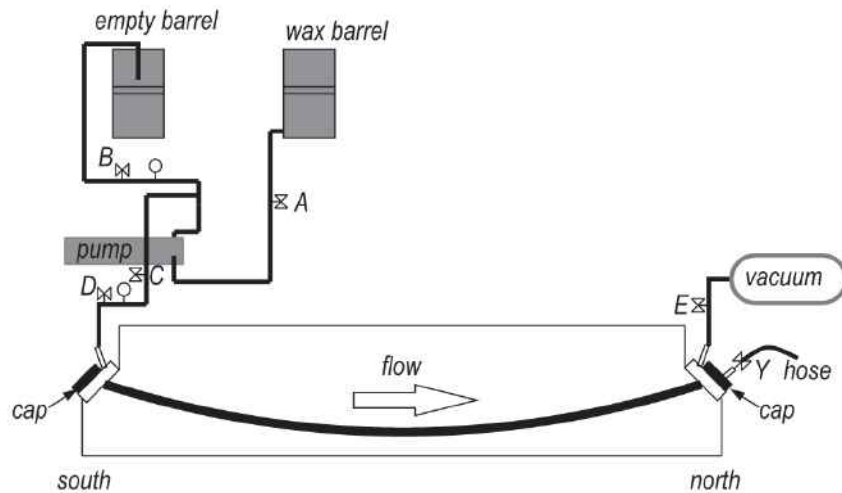


Figure 6-39 Flexible filler injection specimen F1

In preparation for injection, the filler was heated using strap barrel heaters (Figure 6-40) until the temperature was 220 degrees F. The filler material was periodically stirred to ensure uniform heating and prevent overheating.



Figure 6-40 Heating barrel containing flexible filler for injection

After the filler material had been sufficiently heated, pressure and vacuum tests were conducted on each specimen. The tendon was pressurized to 50 psi and the test was considered successful if the pressure drop after one minute was less than 25 psi (Figure 6-41).

The vacuum test was performed by creating a vacuum in the tendon of target gage pressure of -28 in. Hg. and was considered successful if the no more than 10% vacuum loss occurred after 1 minute (Figure 6-42). Leaks found during the test were repaired using generic methods (Figure 6-43).



Figure 6-41 Pressure test for specimen



Figure 6-42 Vacuum for filler injection



Figure 6-43 Sealant placed on concrete around HDPE pipe

Once all the tests associated with the pre-injection process were passed, the injection process began. The barrel containing the heated filler was placed adjacent to the centrifugal pump (Figure 6-44). The barrels were aligned and then connected to the centrifugal pump. A return line was also placed in an empty barrel to discharge filler if necessary.



Figure 6-44 Positioning of filler barrels (a) transporting filler barrel and (b) centrifugal pump connection

The discharge line connected to the pump was opened and the pump was started to allow filler to circulate through the pump. The heated filler was circulated until the pump was heated to about the same temperature as the filler. A vacuum was pulled to a target gage pressure of -28 in. Hg.

Before connecting the discharge line to the inlet valve, at least 2 gallons of filler were discharged to remove air and ensure a continuous flow of filler.

The discharge line was then connected to the inlet valve and filler was injected into the specimen. The flexible filler was injected continuously at a rate of 15 gpm until filler appeared

in the discharge line at the live end. Once the filler appeared in the discharge line the outlet valve was closed just before the filler material entered the vacuum pump. This ensured that the filler material had adequate time to fill the tendon. After closing the discharge valve, the pressure inside the tendon was increased to 40 psi and the inlet valve was closed followed by termination of pumping.

The filler was allowed to cool for 24 hours and then visual observations were noted after cap removal for each specimen. In F1, cap at the live end was full, but approximately half of the dead end cap was full (Figure 6-45).



Figure 6-45 F1 anchor after injection at (a) live end and (b) dead end

The injection process of specimen F2 was the same with one modification, which was the addition of a hose at the top of the dead end cap (Figure 6-46). This hose was introduced to create a vacuum at the dead end during injection wax, which would pull additional filler into the cap at the dead end.

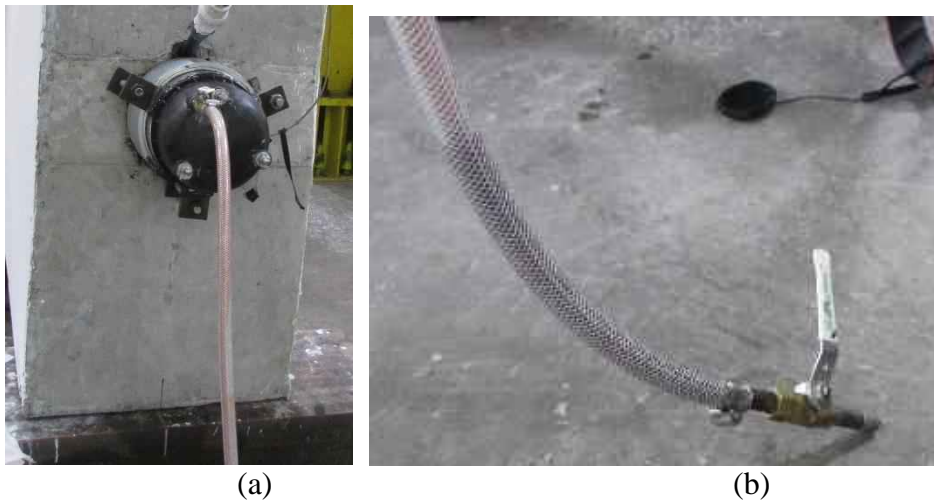


Figure 6-46 F2 vacuum hose attached to dead end cap (a) top of hose and (b) end of hose

The filler was allowed 24 hours to cool and the caps were removed for a visual inspection. Similar to specimen F1, the cap at the live end was full (Figure 6-47). More filler was under the dead end cap for F2 than for F1, where filler covered all the strands but was approximately 2 in. below the top of the cap (Figure 6-48).

The filler ejected into the vacuum hose from the dead end cap contained air. This may have been due to the positioning of the discharge hose below the cap outlet and the potential for

siphoning after injection. It is recommended to elevate the hose above the connection at all times during injection to better fill the cap.

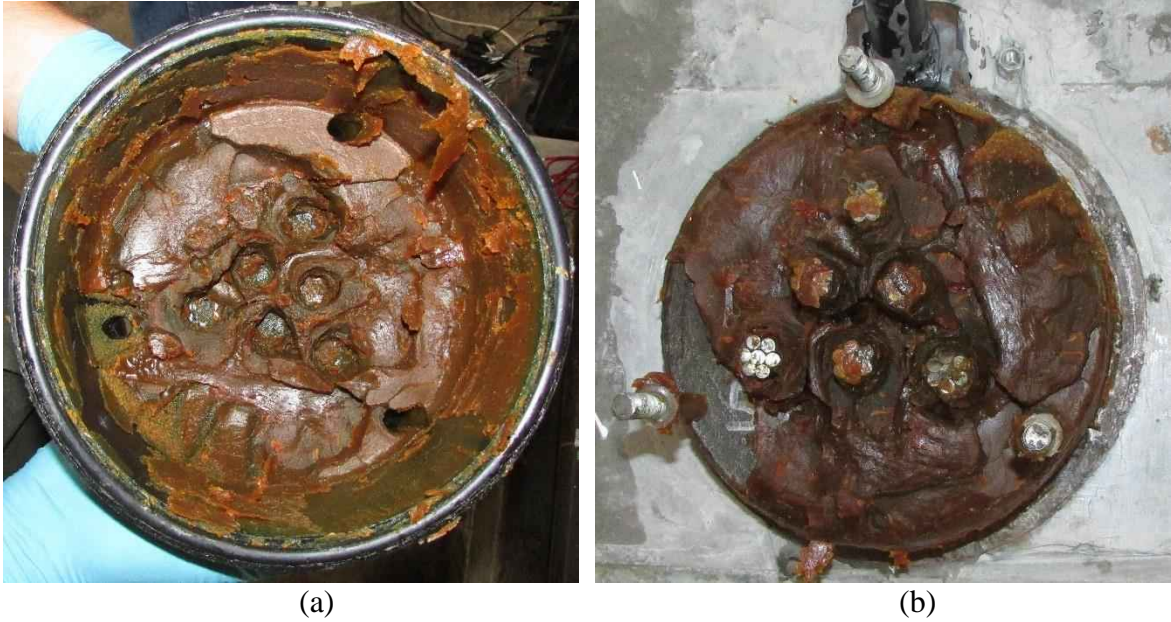


Figure 6-47 F2 live end anchor after injection

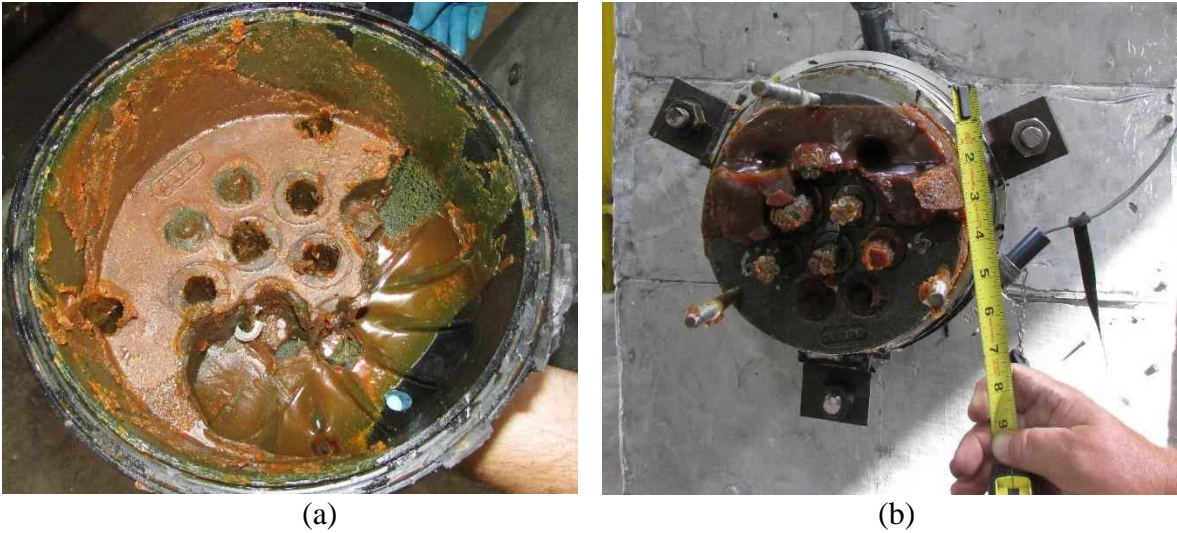


Figure 6-48 F2 dead end anchor after injection

7 Load Test Procedures

This section describes the load test procedures for all of the structural test specimens, including the full-size beams and the fatigue beam specimens. Instrumentation is covered in Chapter 4.3; the procedures for stressing and injection are covered in Chapter 5.2. Wire break detection is covered in Part III – Wire Break Detection.

7.1 Static I-Girder

Static flexure tests were performed on the three internal tendon specimens – one grouted specimen (IGS) and two with flexible filler (IWS and IWC) – and one external tendon specimen (EWS). Specimens IGS, IWS and EWS were tested in a three-point bending setup. Specimen IWC was tested in four-point bending; a spreader beam was used to create a 5-ft constant moment region. The specimens were arranged in the test set-ups shown in Figure 7-1.

In each test, load was applied at 0.2 kip/sec. When cracking was first visually observed, the load was held. The specimen was inspected, and cracks were marked. The beam was then completely unloaded to allow installation of additional instrumentation (crack opening gages and/or string pots).

Load application was then re-applied at 0.4 kip/sec until the approximate cracking load, when the load rate was reduced to 0.2 kip/sec until termination of the load test. Load application was periodically paused to mark and measure cracks. The test was terminated when either compressive failure occurred in the deck concrete or when peak load was reached. In all tests, the flexural capacity (maximum load) was reached prior to end of test.

7.2 Cyclic I-Girder

Specimen EWC was loaded in a series of stages: i) up to cracking, ii) load cycles, iii) high-stress cycles for target tendon stress range of 10 ksi, iv) load cycle to assess beam, v) low-stress cycles at service conditions, and vi) up to ultimate. The loading procedure for specimen EWC is given in Table 7-1.

The test set-up was the same for each stage and is shown in Table 7-2. To reduce the effects on the test set-up during the cyclic loading, several precautions were taken to reduce movement within the set-up and supports. To reduce movement of the supports during the test, the steel W-shapes were grouted to the laboratory floor. To prevent the spreader from walking off the beam, it was welded to a plate which was then bolted to the actuator foot. Measured deflections are, therefore, reflective of displacement of the test specimen and the neoprene pads.

For stage I, load was applied at approximately 0.2 kip/sec under load-control, with maximum load and displacement interlocks set. When cracking was first visually observed, the load was held. The specimen was inspected, and cracks were marked. The beam was then completely unloaded to allow installation of additional instrumentation.

Because steel reinforcement sees only low stress range under service conditions, assuming a span is designed to remain uncracked during its service life, it is typically not a considered vulnerable to fatigue. In the interest of investigating an overload event, the beam was first loaded up to cracking, exposing the strand/tendon to a higher stress range.

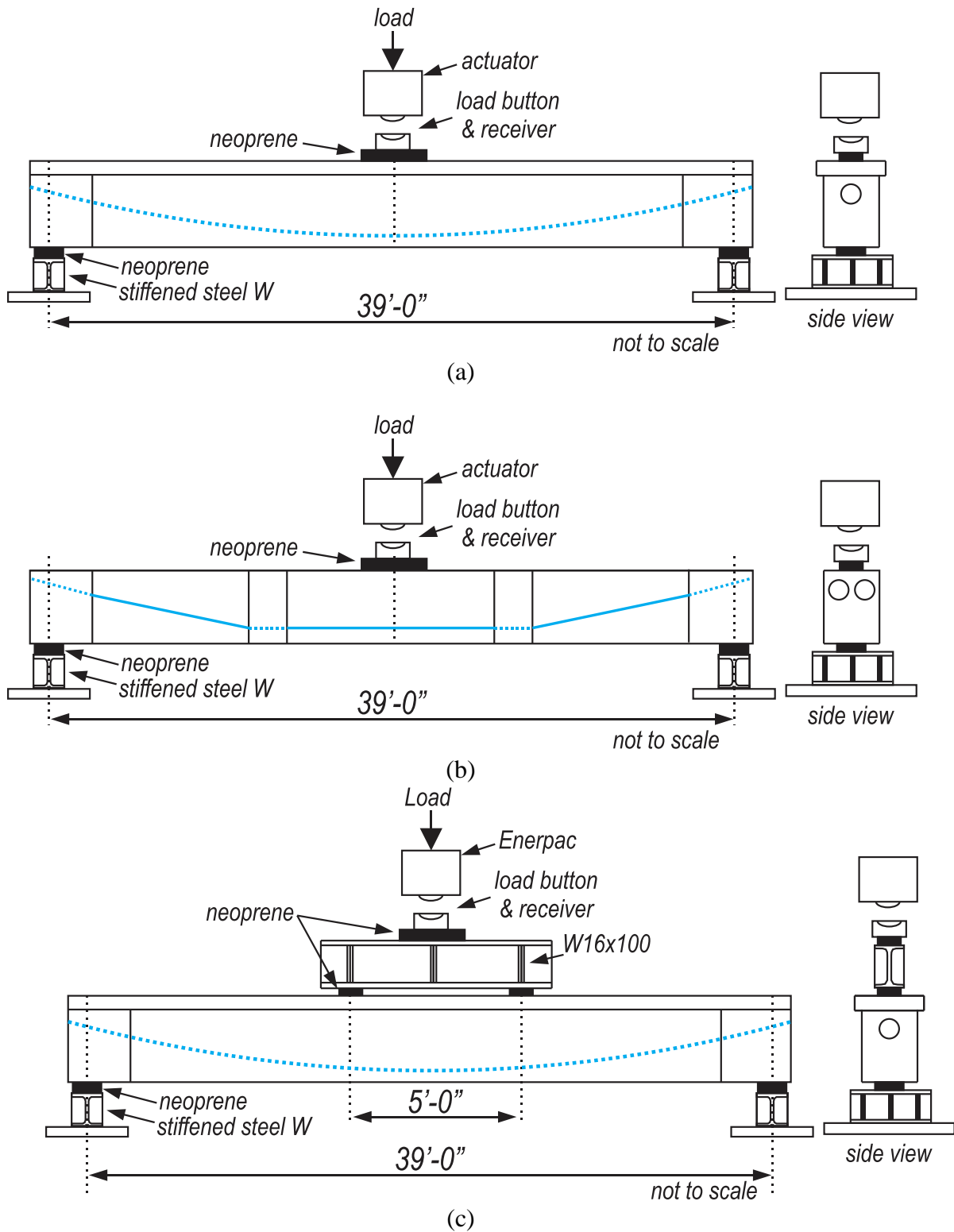


Figure 7-1 Flexural test set-up: (a) IGS, IWS; (b) EWS; and (c) IWC

Table 7-1 EWC loading procedure

Stage	Intent	Approximate # of cycles	Load Range (kip)	Tendon Stress Range (ksi)	Notes
I	Cracking	1	0-cracking	<1 ksi	Pre-crack specimen
II	Load Cycles	6	0-160	n/a	Crack measurement
III	High-stress	600	80-160	10 ksi	Fatigue the tendon
IV	Load Cycle	1	0-160	n/a	Crack development
V	Low-stress	2,000,000	80-112	1 ksi	Service
VI	Ultimate	1	0-max load	n/a	Ultimate load

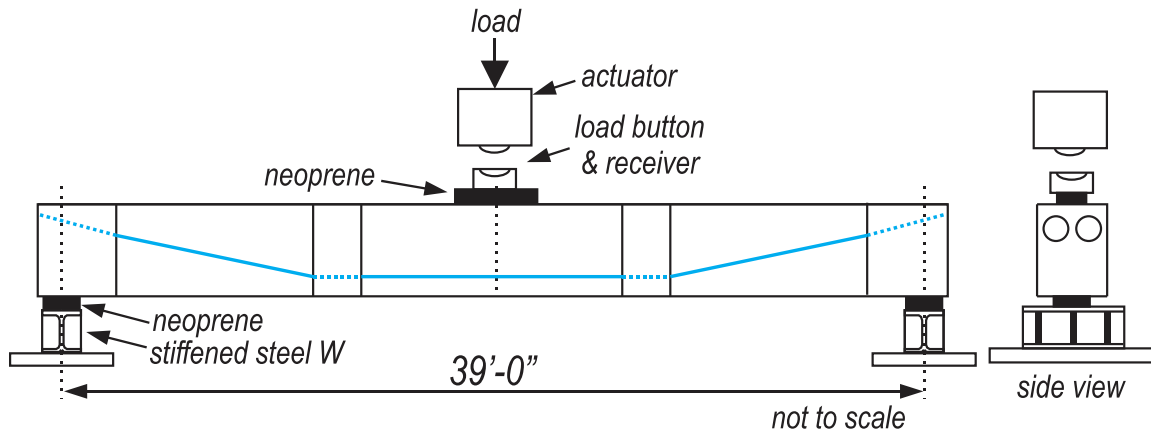


Figure 7-2 EWC test set-up

After initial cracking, specimen EWC was subjected to a series of load cycles, with the purpose of measuring the crack width development and determining the actuator set-points for displacement-control. During these load cycles, the epoxy joints opened, exposing the tendon to the applied load.

For stage III, the specimen was subjected to a high-stress range via displacement. Under displacement-control, the specimen was cycled through 0.38-in of vertical deflection. This corresponded to the displacement required to induce a tendon stress of 10 ksi, as determined using strain gages placed directly on strands of each external tendon. The actuator load at the start of this stage cycled between approximately 80-160 kip. Over the course of this loading stage, the beam experienced degradation and the tendon stress corresponding to the prescribed displacement decreased.

The tendon was considered the critical component in fatigue conditions. The high stress range was selected in consideration of the AASHTO-LRFD (AASHTO 2014b), fatigue acceptance criteria for post-tensioning systems (PTI 2007, ETAG-013 2002), and for comparison purposes with existing research on ungrouted tendon specimens (Brondum-Nielsen 1973, and Braihm et al. 2006). AASHTO-LRFD limits the design stress range to no more than 10 ksi for radii of curvature less than 12 ft – the radius of curvature created by the diabolo-type void.

After approximately 600 cycles, degradation of the beam concrete was observed; chunks of concrete were seen falling from the main crack and progressive crack elongation was noted. The cyclic loading was paused. A load cycle was performed to evaluate the crack development and beam's integrity.

For stage V, the stress range was reduced to simulate service-level conditions. For 2 million cycles, the beam was cycled using load-control between the decompression load (80 kip) and the cracking load (112 kip), simulating service level loads after an over-load occurrence.

Fatigue loading in service will be at a lower load than was used in the previous stage. This condition was chosen to determine if there are fatigue related issues with the PT tendons that might be discovered under this type of loading. The number of cycles is based on the typical number of cycles used in fatigue testing for highway bridge applications.

Following the 2 million cycles, the beam was loaded monotonically to ultimate strength in the same test set-up. Load was applied at approximately 0.2 kip/sec, until the maximum load.

7.3 Fatigue

This section describes the testing configuration and loading stages for the fatigue specimens. Each specimen was simply supported on neoprene bearing pads with the actuator placed near the hinge. Strand slip was monitored during cyclic loading by observing strain gage and load cell readings. The load and cycling test setup is shown in Figure 7-3.

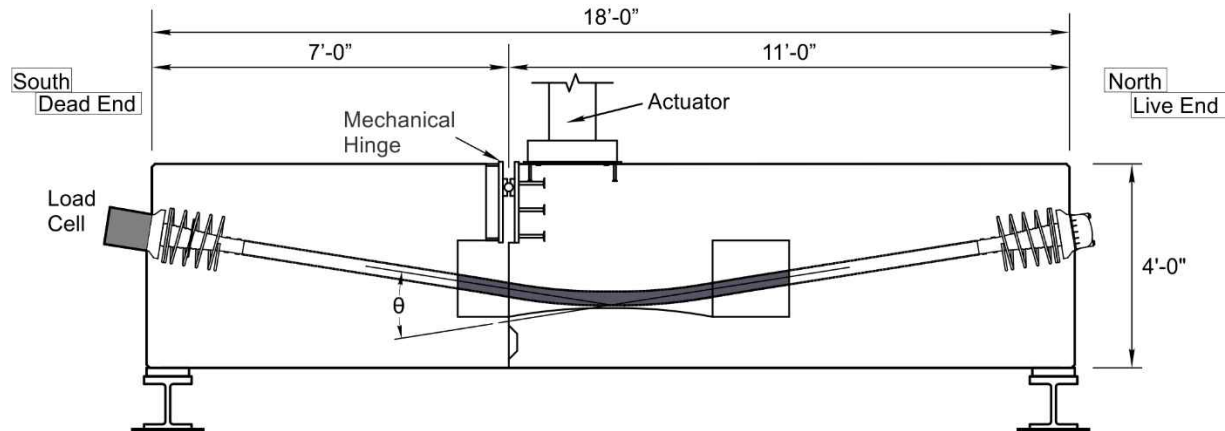


Figure 7-3 Fatigue test set-up schematic

A W-shape steel section (Figure 7-4) was grouted to the floor to ensure that the specimen would not move laterally or twist during the test. A 1 in. thick grout pad was placed to ensure each specimen was level. Two 10 in. \times 24 in. \times 2in. neoprene bearing pads were used to support the specimen on top of two W sections; pads were arranged so that the bearing length was 10 in. The bearing pad allowed for small rotations and small horizontal movements without generating significant reactions.



(a)

(b)

Figure 7-4 Specimen support (a) steel W section on top of 1-in. grout pad (b) neoprene pad

A Shore Western 926E-104/154-10(0)-5-2348 fatigue rated actuator (Figure 7-5) with a static capacity of 460 kip was attached to the specimen using 1 in. dia. steel bolts threaded into a steel plate embedded in each specimen.



(a)

(b)

Figure 7-5 (a) Shore Western actuator (b) steel bearing pad for actuator

The testing frame (Figure 7-6) was bolted to a reinforced concrete strong floor at the FDOT Structures Research Center. Columns of the testing frame were made up of four W14x90, double W21x73 spreader beams and a double W36x150 jacking beam.



Figure 7-6 Testing frame

The specimen was moved into the testing frame in preparation for loading as shown in Figure 7-7. Once in place, the actuator was bolted loosely (Figure 7-8) to the specimen in preparation for static and cyclic loadings.



Figure 7-7 Fatigue test set-up



Figure 7-8 Actuator connected to fatigue specimen

The cyclic loading stages for both fatigue specimens, shown in Table 7-2, were as follows:

- Three initial static ramp tests
- Fatigue test for 2 million cycles at a target stress range of 11.6 ksi
- Three final static ramp tests.

Table 7-2 Fatigue specimen loading procedure

Loading Stage	Number of cycles	Load Range (kip)	Tendon Stress Range (ksi)	Notes
Initial Beam Assessment	3	0-130	0 – 175.5	Actuator force and tendon force
Fatigue	2,090,000	114 - 126	163.9 – 175.5	Strain, gap opening, tendon force, actuator force
Final Beam Assessment	3	0-130	0 – 175.5	Actuator force and tendon force

The fatigue test consisted of loading the specimen to an upper tendon force of 228.5 kip and a lower tendon force of 213.4 kip for two million cycles. This was done to achieve a stress range of approximately 11.6 ksi for the tendon. The load was applied at a rate of 1 Hz for the entire fatigue cycle. These test criteria are based on ETAG-013 Section 6.1.2-I.

The final static ramp tests were done at the completion of the fatigue test. Both specimens were loaded from zero actuator force to the upper actuator force during which the specimens were assessed for undesirable out-of-plane movement.

8 Tendon Replacement

Tendon replacement was performed on internal tendon specimen IWC, which was filled with flexible filler material, prior to any structural load test. The effective prestress in the tendon, according to the load cell measurement, was 273 kip ($0.4f_{pu}$) at the time of detensioning.

Based on the successful tendon replacement conducted on internal tendon specimen IWC -- which was relatively straight-forward and completed with ease -- and a concern over the structural integrity of the beams post-ultimate test, tendon replacement was not attempted for specimens EWS and EWC.

8.1 Procedure

Tails were cut flush to the wedge plate using a rotary tool and wedges were burned out with a welding torch at one end (Figure 8-1). At the opposite end, a 0.5-in. steel plate was bolted into the wedge plate to prevent the strand from being propelled from the beam. Anchor strain and tendon force were monitored during detensioning. The torched end was inspected after detensioning (Figure 8-1). In-place hardware appeared to retain its integrity. Some melting of the plastic trumpet was observed, though the void provided by the trumpet remained open and passable.

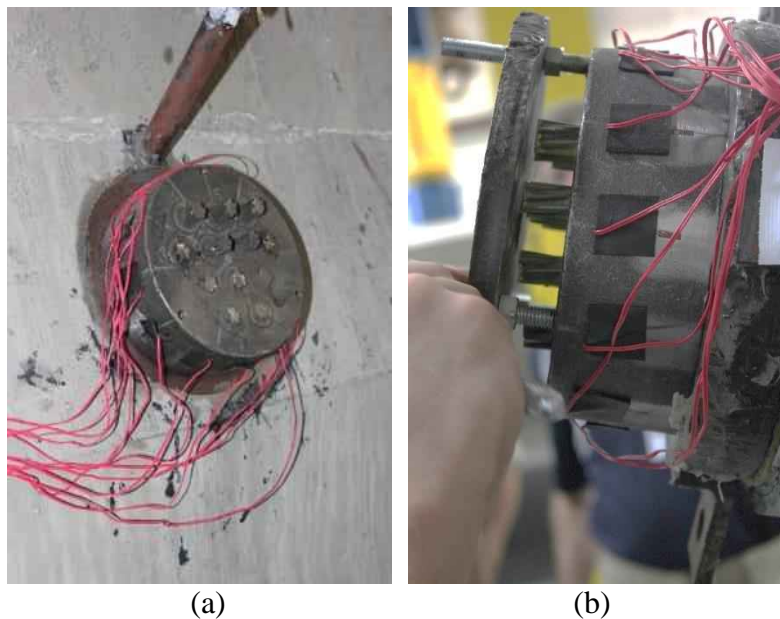


Figure 8-1 IWC: (a) torched end and, (b) opposite end with protective plate



Figure 8-2 End of beam where wedges were torched

To allow easier access to the anchorages, the beam was placed on the lab floor for the duration of the tendon replacement. After detensioning, the tendon was pulled from the non-torched anchorage in two stages: 1) with a hollow-core actuator and hand-pump and 2) with a chain attached to a forklift. During the initial pull, a tension ring was installed in-line with the tendon and care was taken to pull concentric to the tendon (Figure 8-3). The force required to break the tendon free (overcome friction) was monitored while pressure was applied with a hand-pump to the actuator (Figure 8-4); the maximum recorded load to overcome friction was 730 lbs.



Figure 8-3 First tendon pull

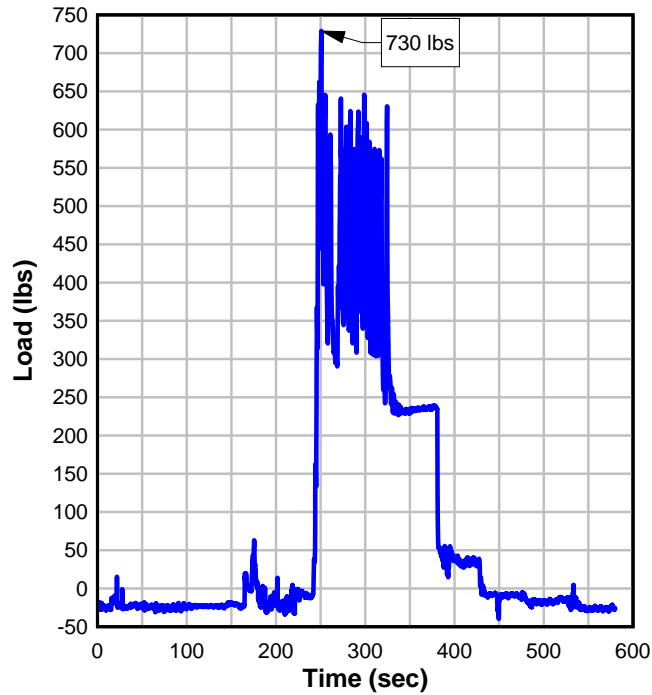


Figure 8-4 Tendon pull-out: load vs. time

To fully remove the tendon, an eye-hook and chain were attached to the wedge plate. The tendon was pulled via the chain with a forklift (Figure 8-5), removing the wedge plate, wedges, load cell and strand as a connected unit.



Figure 8-5 Tendon removal

Following the removal of the prestressing steel and anchorages, a cotton plug was pulled through the duct to remove the remaining filler from the internal tendon.

Replacement of the tendon proceeded similarly to the original tendon installation. Fresh strand was pushed in to the duct and new wedge plates and wedges were installed. The tendon was stressed in the same manner as the initial tendon installation.

8.2 *Observations*

Several observations were made during the tendon removal:

- Whenever a final wire of a strand was torch-cut, tension in the strand was suddenly relieved. This sudden release resulted in the strand and wedges ejecting from the opposite end and striking the retention plate confirmed by slight indentations in the plate caused by the strand impact.
- Tendon force was completely relieved after the last strand was cut.
- Wedge plates/wedges were unsalvageable, but the anchorheads appeared undamaged.
- Caps were re-useable.

9 Prestress Losses

Prestress losses affect structure serviceability; therefore, accurate prediction of the anticipated losses for systems utilizing flexible fillers is important. Prestress losses occur in both the pretensioned strand and the post-tensioning tendon; these were estimated using the refined method of loss determination presented in the AASHTO-LRFD (Section 5.9.5, AASHTO 2014b). Measurement of post-tensioning loss in the tendons with flexible filler was made using the hollow-core load cell, allowing for comparison with the predicted value.

9.1 Calculated Losses

To estimate the total prestress loss in each specimen, each stage of construction from pretensioning transfer to load testing was considered. Prestress losses occur as both immediate, or elastic losses, and time-dependent losses.

The initial prestress force is considered the jacking prestress force minus the elastic losses. For the bonded pretensioning strand, prestress transfer occurred when the strand was torch-cut free of the anchor in the prestressing bed. For the post-tensioning tendon, anchorage set and elastic shortening of previously stressed strands occurred incrementally as individual strands were stressed.

Predicted prestress losses (Table 9-1) were computed per AASHTO-LRFD. Calculations considered the tested concrete strength, and the girder age at key construction stages, i.e., time of deck installation, post-tensioning and load test. The effects of subsequent post-tensioning on additional elastic shortening of previously stressed prestressing strands (the bonded pretensioned strand, in this case) were considered, per AASHTO-LRFD (provision 5.9.5.2.3c, 2014). Anchorage set of the post-tensioning tendon was measured after jacking of all strands in the tendon; for a given tendon, the average measurement of anchorage set was used to estimate losses. Creep, shrinkage, and strand relaxation are time-dependent material effects which cause losses to occur over the structure's life. Estimates of their individual contributions to prestress loss are dependent on environmental conditions, materials and the amount of time under consideration.

Table 9-1 AASHTO-LRFD losses by refined method

Specimen	Pretensioning				Post-tensioning			
	Initial losses (combined) (ksi)	Long-term losses (ksi)	Total prestress loss (ksi)	Total prestress loss (%)	Initial losses (ksi)	Long-term losses (ksi)	Total prestress loss (ksi)	Total PT loss (%)
IGS	3	8	11	6	17	4	21	10
IWS	3	9	12	6	33	6	39	18
IWC	3	10	13	6	19	5	24	11
EWS	3	9	12	6	28	2	30	14
EWC	3	11	14	7	26	2	29	13

The total compressive stresses at the bottom fiber, considering both the pretensioning force and the post-tensioning force and the expected losses for each, as calculated per AASHTO-

LRFD for the pretensioning and as measured for the post-tensioning, are given in Table 9-2. Also shown is the decompression moment and cracking moment for midspan, considering average test-day material strengths.

Table 9-2 Predicted midspan decompression and cracking moment (compression is negative)

Specimen	Bottom fiber stress (psi)	Decompression		$7.5\sqrt{f'_c}$	
		Applied moment (kip-ft)	Applied load (kip)	Applied moment (kip-ft)	Applied load (kip)
IGS	-1090	1440	148	2520	259
IWS	-1060	1430	146	2490	255
IWC	-1100	1460	171*	2540	298*
EWS	-850	810	81	1630	163
EWC	-890	850	85	1760	167

* 4-pt bending

9.2 Measured PT Losses

Determinations of losses and strand force in the post-tensioning tendons utilize the measurements from the strand load cells. Through direct measurement using the load cell, all losses – elastic and long-term – were captured and used to determine the effective prestress force for each tendon. Table 9-3 summarizes the measured tendon force at time of post-tensioning and at time of the load test; f_{pu} is assumed to be 270ksi.

Table 9-3 Post-tensioning force

Specimen**	Initial		At time of load test	
	Average PT Tendon Force* (kip)	Average Tendon Stress (ksi)	Average PT Tendon Force* (kip)	Average Tendon Stress (ksi)
IGS	438	$0.62f_{pu}$	424	$0.60f_{pu}$
IWS	426	$0.61f_{pu}$	412	$0.58f_{pu}$
IWC	435	$0.62f_{pu}$	428	$0.61f_{pu}$
EWS	253	$0.72f_{pu}$	241	$0.69f_{pu}$
	218	$0.62f_{pu}$	213	$0.61f_{pu}$
EWC	227	$0.65f_{pu}$	223	$0.63f_{pu}$
	260	$0.74f_{pu}$	252	$0.72f_{pu}$

*per load cell

**Internal tendons: 12 strands. External tendons: 6 strands.

Anchorage set, or seating loss, is the prestress loss that occurs as each strand is released by the jack and is subsequently gripped by the wedges of the anchorage. As the wedge and strand seat, some prestress force is lost in the movement; the quantity of this loss is directly proportional to the tendon length. Power seating, which was not used for this research, can reduce the seating losses.

Post-tensioning of the test tendons was done with a monostrand jack so that the anchorage set occurred incrementally as each strand was stressed. Post-tensioning anchorage set

for wedge-type anchors is typically 0.125-0.375-in.; for simplicity of design calculations, it is usually assumed to be 0.25-in. (AASHTO 2014b). The average measured anchorage set of each wedge at the dead end was approximately 0.4-in. The measurement of the wedge movement that effects the prestressing force is difficult to measure and was only estimated for this research. Each strand's anchorage set (dead end) and elongation (live end) was visually determined following the post-tensioning procedure using a measuring tape. Two strands per anchor were initially stressed to a nominal 20% of the target prestress. These strands were ignored when determining the average anchorage set.

Measurement of elongation and wedge seat provided an additional estimation of the initial post-tensioning (Table 9-4). The tendon gauge length, from anchor-to-anchor, was 500 in.; the prestressing strand modulus of elasticity was 28,500 ksi. The average PT force per strand, based on this measured elongation, is given for comparison; due to the imprecision of the seating and elongation visual measurement, as well as the potential for strand slip influencing this measurement, this is reported for information only and is otherwise not used in future calculation.

Table 9-4 Average PT anchorage set and elongation

Specimen	Anchorage seating Dead end (in.)*	Live end (in.)*	Elongation (in.)	Average PT force/strand (kip)
IGS ^a	-0.24	4.66	4.42	54.7
IWS ^a	-0.54	5.02	4.49	55.5
IWC ^c	-0.29	4.14	3.84	48.3
EWS ^b	-0.46	3.41	2.94	37.1
EWCB ^b	-0.42	3.46	3.04	38.2

*average of strands *not* used to cinch up the anchorage hardware

^aPrecision-Hayes monostrand jack

^bEnerpac monostrand jack

^cchucks broke in Precision-Hayes jack during initial seat; most PT applied using Enerpac jack

Table 9-5 presents the measured post-tensioning losses, including initial and time-dependent losses, as captured by the hollow-core load cells. Losses due to anchorage set, friction, and elastic shortening are immediate. Losses due to anchorage set were calculated based on measurements given in Table 9-4 and not the estimates typically used in design. The girder concrete age at time of post-tensioning and at time of load test are given.

Figure 9-1 shows a comparison of the measured and calculated losses. The measured losses are significantly higher than that of the calculated, with the largest discrepancies found in the internal tendons. It is speculated that the differences are due to the relative shortness of the specimens when compared with the typical lengths found in post-tensioning tendons. This would contribute to large variations caused by seating loss, particularly when comparing the use of monostrand jack on the lab specimens to the multistrand jacks typically used in the field. The larger difference noted in the internal specimens may be due to the friction used to calculate the losses. Furthermore, because of the friction losses, the post-tensioning force will be larger at midspan than at the anchorage where the tendon force is being measure. Despite the necessity for accurate prestress loss prediction, the use of empirical methods to estimate creep and shrinkage losses cannot be expected to yield estimates with errors less than +/- 50% (AASHTO-LRFD commentary C5.4.2.3.1; AASHTO-LRFD 2014).

Table 9-5 Measured PT losses

Specimen	Initial losses (ksi)**	Seating losses (ksi)*	Concrete age at PT (days)	Final prestress loss (ksi)**	Concrete age at load test (days)
IGS	49	14	60	54	88
IWS	51	30	60	59	89
IWC	49	17	196	51	204
EWS	35	26	112	41	127
EWC	28	24	231	34	292

*determined by averaging measurements of individual strand elongation

**determined by load cell

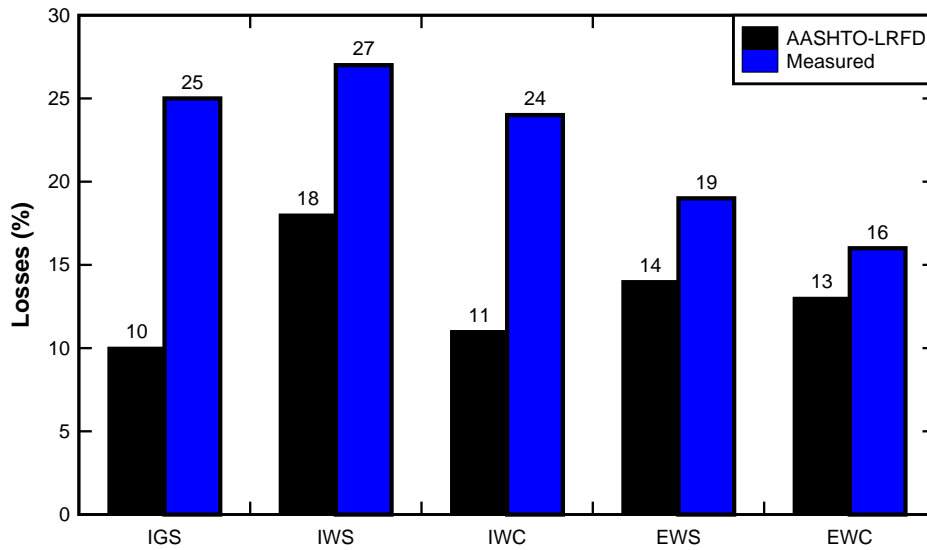


Figure 9-1 Measured PT losses vs. AASHTO-LRFD refined method

9.3 Cracking Moment

For comparison, a crack opening test was performed on the internal tendon (IGS, IWS, and IWC) specimens to determine the effective prestress level; the losses calculated using the decompression method were also determined (Crack opening tests were not performed on the external tendon specimens). Using “crack opening tests” to determine decompression are performed as follows. This method has been described by Pessiki et al. (1996).

1. During load application of a specimen, the load-deflection plot and the beam are monitored for cracking.
2. At first crack, the load is held and the crack location is identified and marked.
3. The load is then removed from the beam and two strain gages are placed on opposite sides of and perpendicular to the crack, longitudinal to the beam axis (Figure 5-5).
4. Load is then reapplied to the specimen.

5. When the crack re-opens, the slope of the load-strain plot changes, indicating that the pre-compression caused by the prestress force has been overcome.

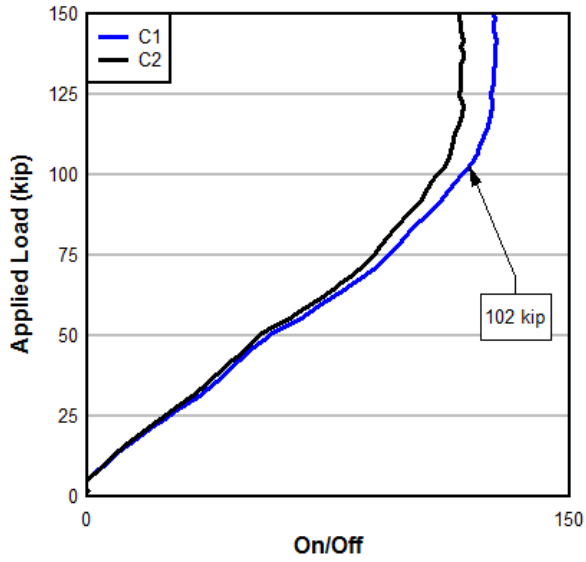
For purposes of comparison, the decompression load is defined as the average of the two loads at which the measured strain-load curve reaches a plateau. Figure 9-2 shows a plot of the applied load vs. strain (depicted as a switch, without units) from the gages applied adjacent to the first visible crack. Assuming the decompression load corresponds to zero stress at the bottom of the beam, the effective prestress can be calculated from the applied load required to reach decompression. To calculate the effective prestress, the compression caused by the prestress force and its eccentricity are equated to the tensile stress induced to reach the decompression load using gross section properties. The effective prestress values, as determined with this approach, are given in Table 9-6.

The tendon stress as determined from the decompression gages is less than that expected based on the readings of the hollow-core load cells, which indicates that for these mixed tendon conditions, the decompression approach for determining effective prestress may not be effective.

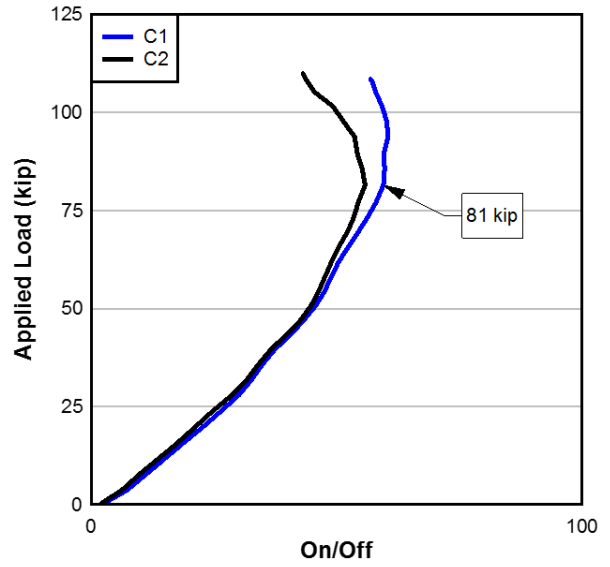
Figure 9-3 depicts the idealized variation in tendon stress along a post-tensioned tendon during jacking and after release. The tendon stress at both ends is expected to be less than that at mid-length of the tendon. Tendon stress at the live end is expected to be less than mid-tendon due to anchorage losses, which only affects a short distance near the anchor. Tendon stress at the dead end (load cell location) is also expected to be less than at mid-span due to friction loss along the tendon length. One would expect the tendon stress measured at the ends by the load cells to be (conservatively) low, if different at all.

No cause for the low cracking loads could be determined, although several possible explanations include:

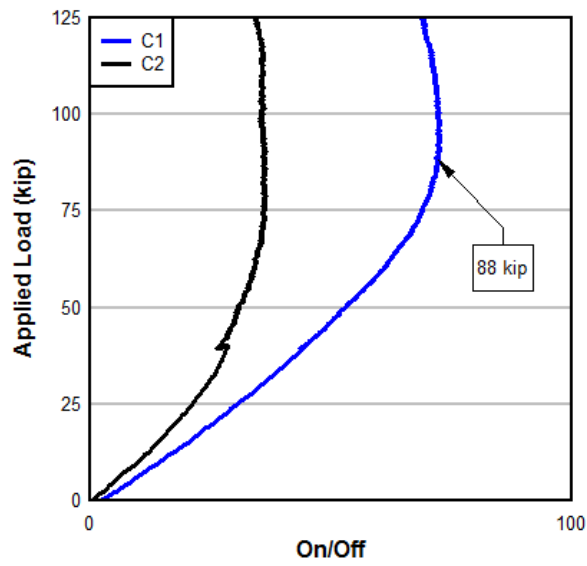
1. Concrete tensile strength is difficult to accurately predict; the assumption of $7.5 \sqrt{f_c}$ may be high.
2. Handling (during shipping, etc.) may have caused pre-cracking of the specimen.
3. The accuracy of the hollow-core load cells is limited. Per the manufacturer, the hollow-core load cells are accurate +/- 15 kip.



(a)



(b)



(c)

Figure 9-2 Decompression: (a) IGS; (b) IWS; and (c) IWC

Table 9-6 Effective prestress force by decompression gages

Specimen	Average Decompression Load (kip)	Total PS Force (kip)	Tendon Stress (ksi)	
			Decompression	Measured
IGS	102	285	108	163
IWS	81	200	76	159
IWC	88	215	83	165

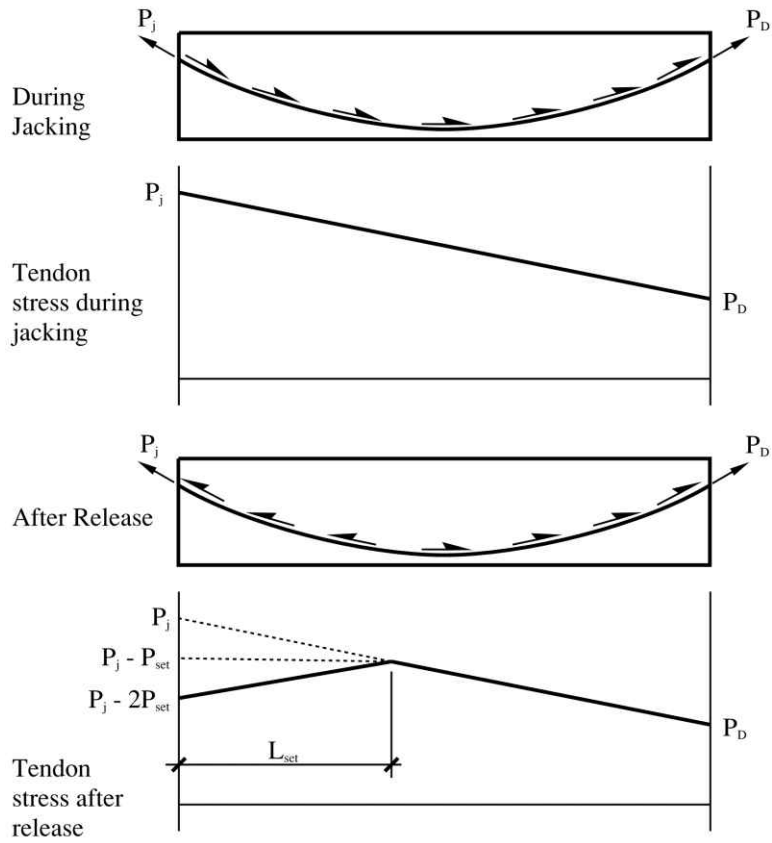


Figure 9-3 Variation in tendon stress

10 Internal Tendon Results and Discussion

This section describes the injection results and the static load tests of the three internal tendon specimens.

10.1 Flexible Filler Injection

Specimens IWS and IWC were injected with flexible filler after post-tensioning. Figure 10-1 shows the change in temperature of the concrete immediately surrounding the PT duct during and following the injection process. The plot shows the rise in temperature relative to the temperature measured at each sensor just prior to injection. The temperature of the concrete at the time of injection was 82 deg. F. Even though the injection lasted for approximately five minutes, the concrete temperature continued to rise until it peaked at around thirty minutes following injection. The maximum increase in temperature occurred at the sensor closest to the duct and inlet location and was relatively small.

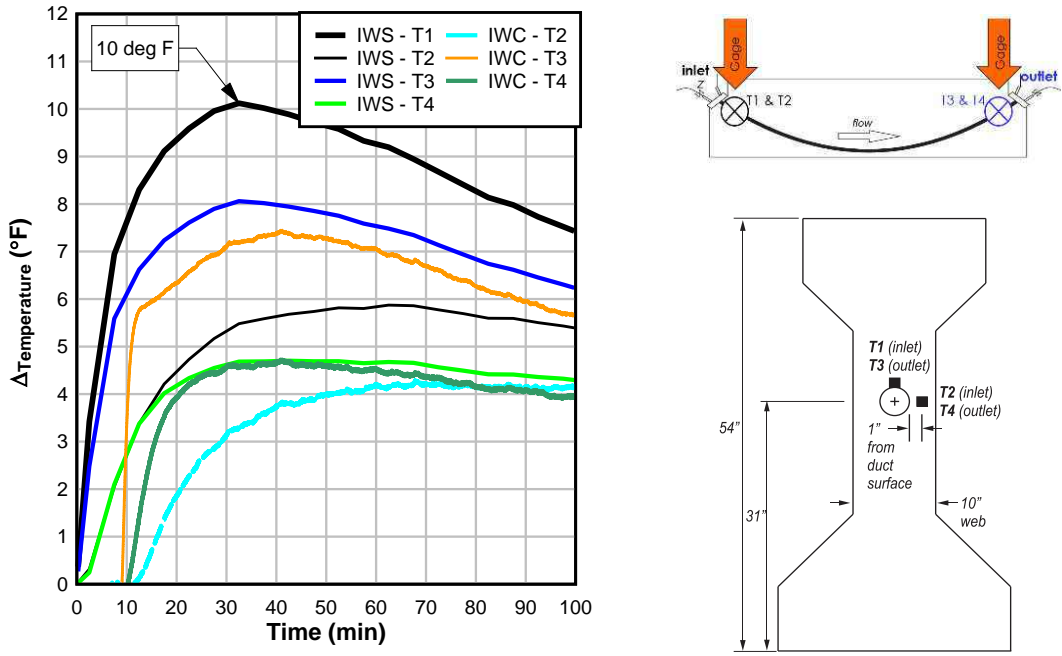


Figure 10-1 Internal concrete temperature measurements

10.2 IGS: Static Three-Point Grouted

A three-point bending flexure test was performed on specimen IGS (Figure 10-2). Load was applied at 0.2 kip/sec. As load was applied, IGS exhibited linear-elastic behavior up to the cracking load.

At approximately 188 kip, a single crack in the bottom flange was visually observed near midspan; the crack continued under the beam and was observable on both beam faces. Load was held and the crack was measured. The crack was 0.01 in. wide at approximately 3 in. from the bottom of the beam on the west face; the east face measurement was not taken but was observed

to be less prominent. The crack was marked and the beam was unloaded. Additional strain gages were added for decompression measurements to verify prestress.

Starting with the beam completely unloaded, load was applied at 0.4 kip/sec., until an applied load of 150 kip when load application was slowed to 0.2 kip/sec. Load application was paused at 200 kip and 300 kip for crack measurements.

As IGS was loaded beyond cracking, minor load losses occurred periodically until the midspan deflection was approximately 1.15 in. These decreases coincided with flexural crack formation confirmed with audible cracking sounds and visual observation. Cracks developed in a well-distributed fan pattern centered about midspan and progressed from the bottom flange towards the load point.

At 424 kip, the peak load was reached as IGS deflected 4.4 in. at midspan (Figure 10-2). Maximum load occurred when the deck at midspan crushed; deck crushing was accompanied with a sudden partial load loss. The specimen was unloaded and the test was terminated. Figure 10-3 and Figure 10-4 shows the strain measured at the load point and along the top of the deck; the maximum compressive strain measured in the deck strain at the load point reached approximately 0.005 (Figure 10-3)

At start and end of the load test, the measured effective tendon force in the 12-strand tendon was 424 kip, or $0.6f_{pu}$; this value – measured by the hollow-core load cell at the anchorage – remained constant during the test.

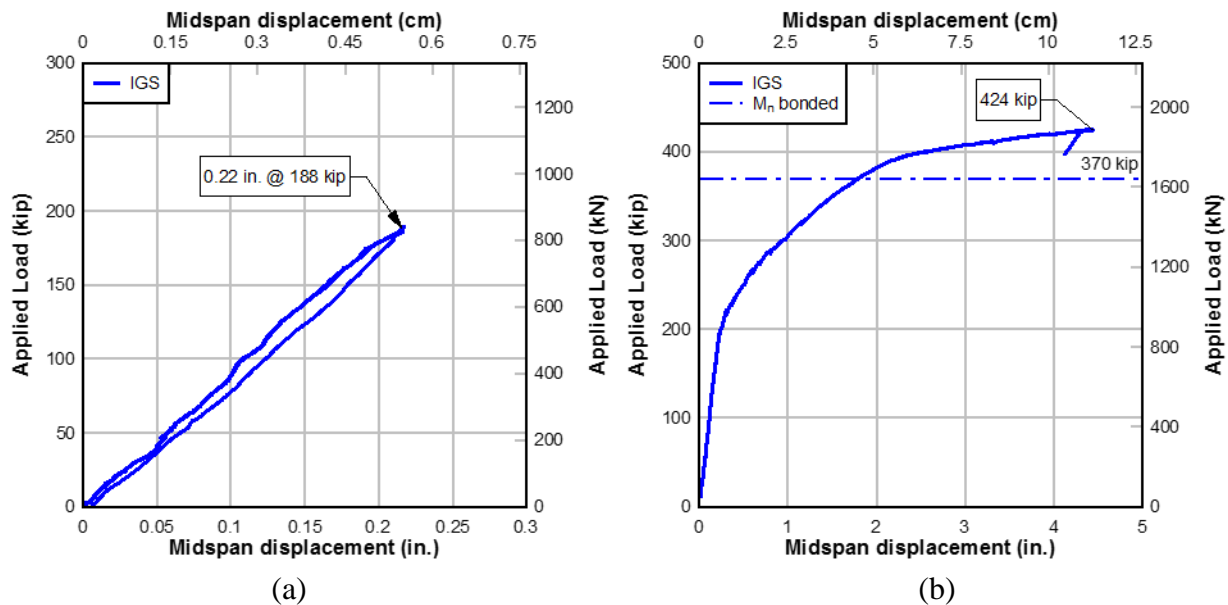


Figure 10-2 IGS (a) elastic behavior and (b) ultimate strength behavior

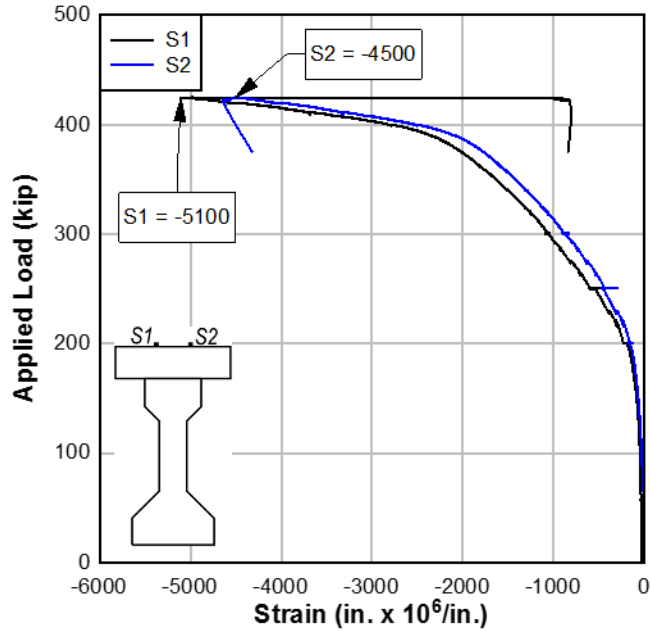


Figure 10-3 IGS: deck strain at load point

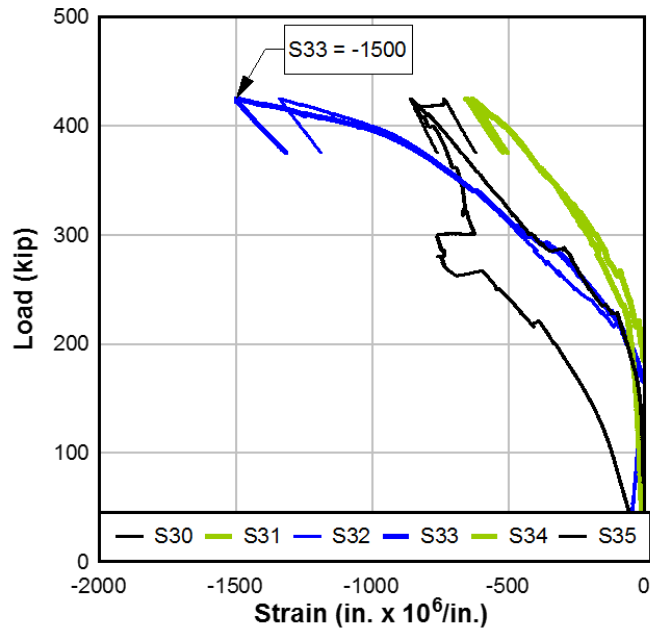


Figure 10-4 IGS: strain along the top of deck

10.3 IWS: Static Three-Point Flexible Filler

A three-point bending test was performed on specimen IWS. The load-deflection plots shown in Figure 10-5 show the (a) elastic and (b) ultimate behavior. The applied load indicated by the reference line labeled M_n is calculated using AASHTO-LRFD (AASHTO 2014b) Equation 5.7.3.1.3b, which provides a simplified approach for an approximation of the ultimate

tendon stress for members with mixed tendons; *specified material strengths and 20% PS losses* are assumed for this calculation.

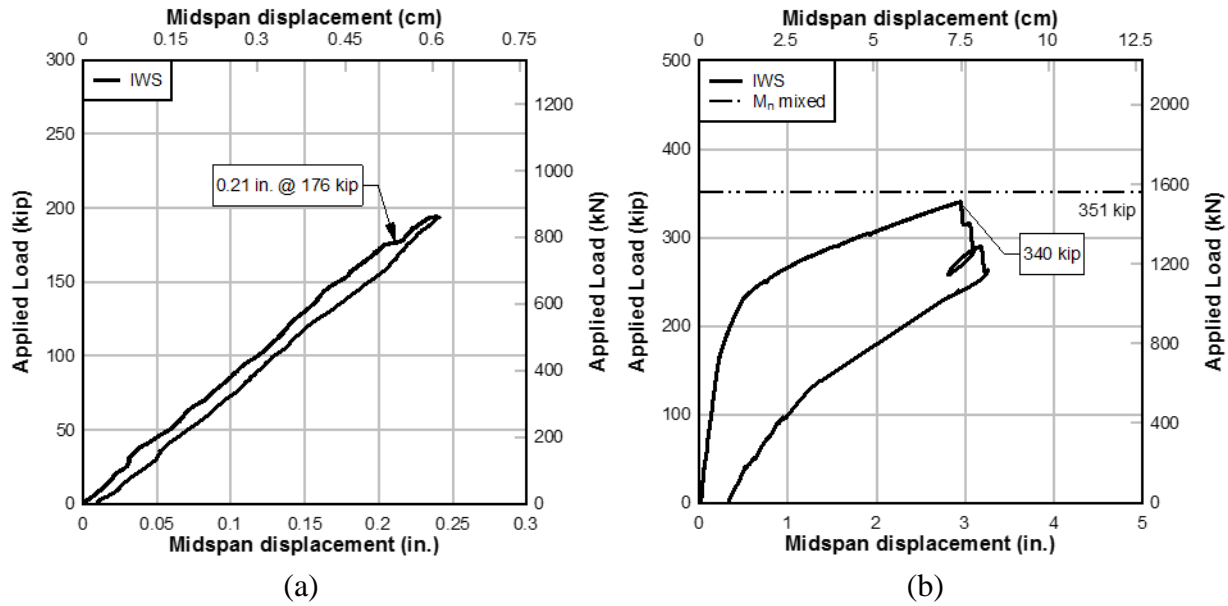


Figure 10-5 IWS (a) elastic behavior and (b) ultimate strength behavior

Load was applied at 0.2 kip/sec. As load was applied, IWS exhibited linear-elastic behavior up to cracking.

At approximately 176 kip, a single flexural crack in the bottom flange was visually observed near midspan, visible on the east face of the beam (Figure 10-6).

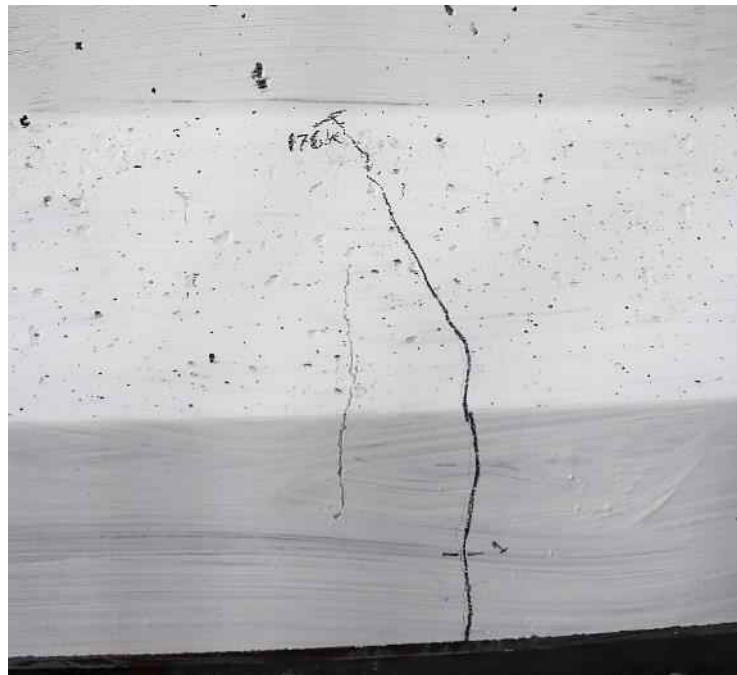


Figure 10-6 IWS: first crack

Load application was resumed at 0.2 kip/sec, with the intent of opening up the crack on both sides of the beam.

At 185 kip, load was held and cracks were marked. The original crack had propagated diagonally toward the load point by approximately 2 in. A second crack on the east face was identified: also located near the midspan, it initiated in the bottom flange. No cracks were located on the opposite beam face.

Load application was resumed at 0.2 kip/sec. At 193 kip, two cracks were observed to open on the opposite beam face. The load was held at 193 kip and all visible cracks were marked. After marking the cracks, the beam was unloaded and additional strain gages were added for decompression measurements to verify prestress; two gages were added to the bottom flange of the west face.

Starting with the beam completely unloaded, load was applied at 0.4 kip/sec., until an applied load of 150 kip when load application was slowed to 0.2 kip/sec. Load application was paused at 200 kip; no new cracks were observed, but existing cracks had elongated. Cracks were measured and load application resumed at 0.2 kip/sec.

As IWS was loaded beyond cracking, crack opening was observed to primarily occur at two crack locations – affording an opportunity to directly measure a wide crack opening. At 229 kip, the load application was paused and the two primary cracks were visually inspected. The north primary crack was marked on the east face at approximately 6 in. from the bottom of the beam. The beam was unloaded and a string pot was installed at this location (Figure 10-7). Two additional new cracks were observed to have initiated in the bottom flange; these were the last “new” cracks observed to form during the load test. Subsequent loading resulted in propagation of existing cracks with no new cracks forming.

At 250 kip, load was held and cracks measured. At 313 kip, spalling concrete was observed to fall from the bottom flange of the southernmost of the two primary crack locations.

At 340 kip, the peak load was reached as IWS deflected 2.9 in. at midspan. At peak load, loud popping sounds were heard, accompanied by a sudden load loss of approximately 25 kip.

Applied load was reduced to approximately 258 kip and held for approximately 1 minute. Load application was resumed and the specimen resisted load from 258 kip up to approximately 290 kip as IWS deflected 3.2 in. at midspan, when another loud pop was followed by another 50 kip load drop. Load application was not resumed and the test was terminated. For clarity, the load history is shown in Figure 10-8.

The deck was not observed to crush, but measured deck strain near the load point was greater than 0.003 (Figure 10-9) at ultimate load.

While unloading the beam, several horizontal cracks formed between the two primary flexural cracks and a portion of the bottom flange broke away. Otherwise, all flexural cracks formed during the load test completely closed and the hollow-core load cell measured a full return to the tendon force present at the start of the load test, suggesting that the PT tendon had not yielded. Post-mortem inspection revealed that all three bonded strands located in the bottom flange had ruptured (Figure 10-10).



Figure 10-7 Cracking (a) after strand rupture, load held at 240 kip and (b) after load removed

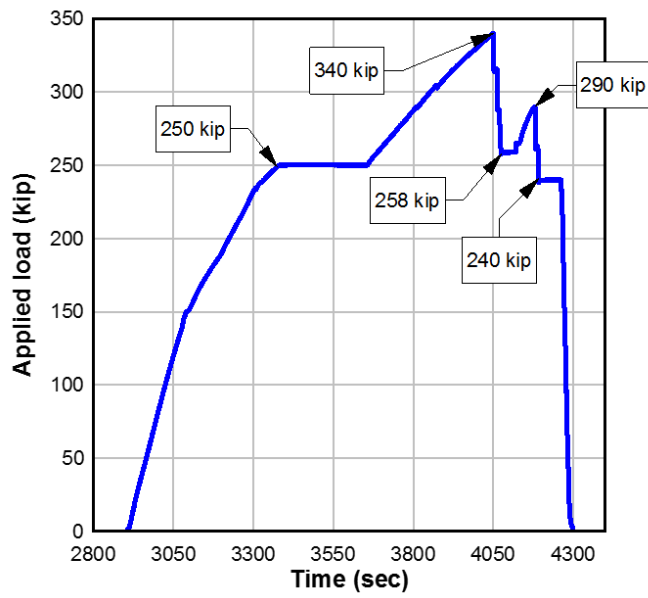


Figure 10-8 IWS: applied load history

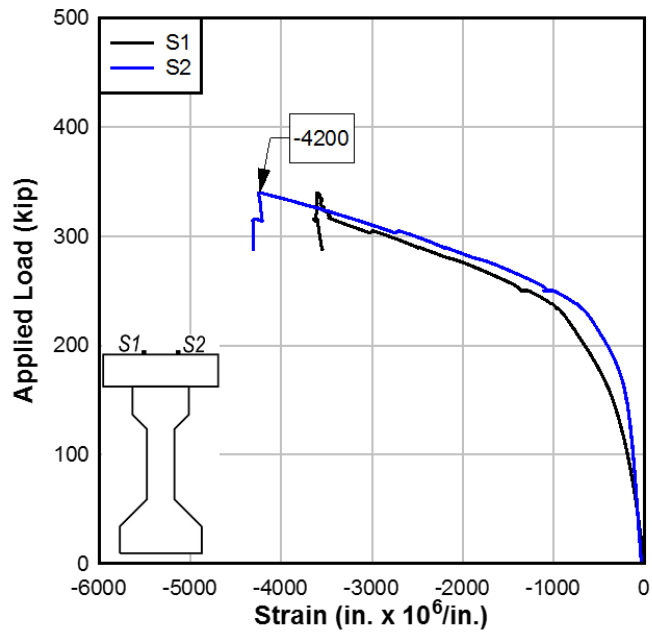


Figure 10-9 IWS: deck strain at load point

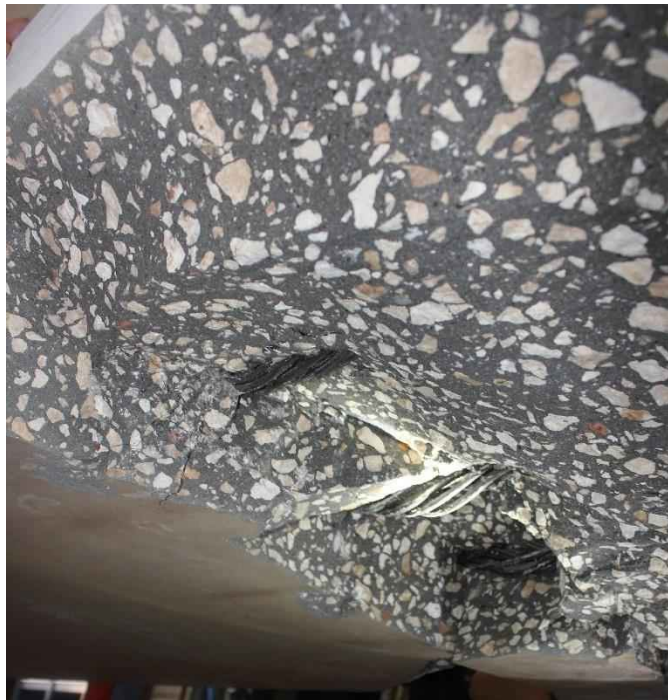


Figure 10-10 IWS: bonded strand rupture

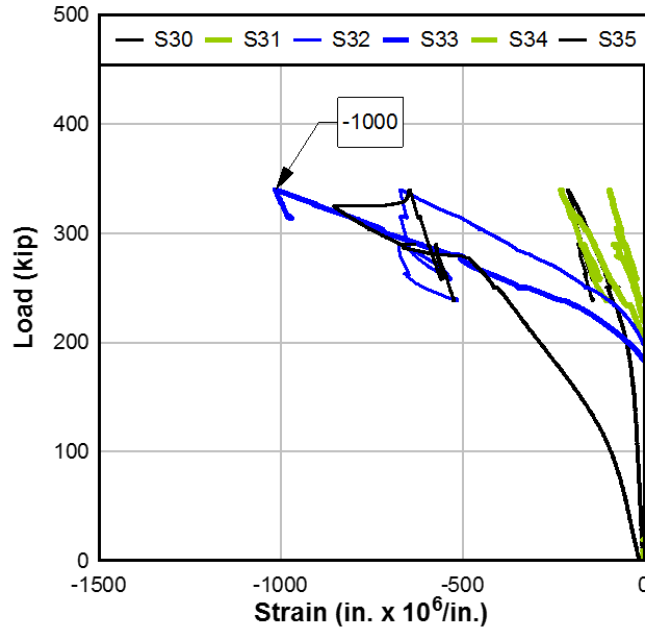


Figure 10-11 IWS: strain along the top of deck

10.4 IWC: Static Four-Point Flexible Filler

A four-point bending flexure test was performed on specimen IWC. The load-deflection plots shown in Figure 10-12 show the (a) elastic and (b) ultimate behavior. The applied load indicated by the reference line labeled M_n was calculated using AASHTO-LRFD Equation 5.7.3.1.3b, which provides a simplified approach for an approximation of the ultimate tendon stress for members with mixed tendons; *specified material strengths and 20% PS losses* are assumed for this calculation.

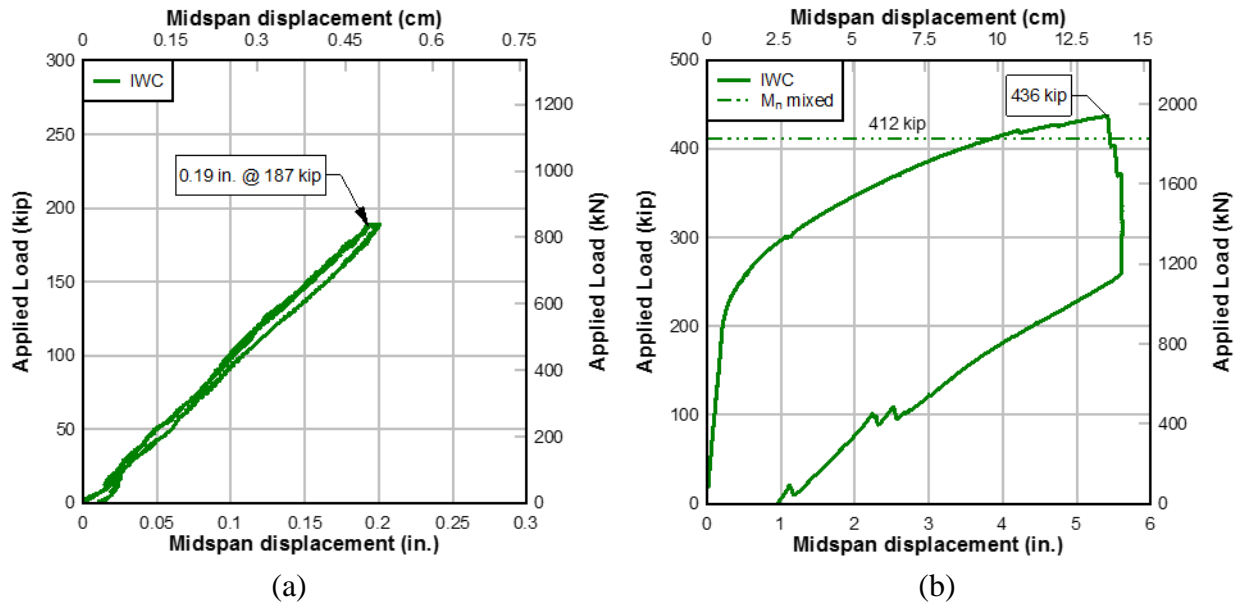


Figure 10-12 IWC (a) elastic behavior and (b) ultimate strength behavior

Load was applied at 0.2 kip/sec. As load was applied, IWC exhibited linear-elastic behavior up to cracking. At 188 kip, three cracks were visually observed to form near the midspan. Load application was paused and the cracks were marked. The beam was then unloaded for the application of additional strain gages for decompression measurements.

Starting with the beam completely unloaded, load was applied at 0.4 kip/sec., until an applied load of 150 kip when load application was slowed to 0.2 kip/sec. Load application was paused at 200 kip, 250 kip, and 300 kip to mark cracks and take crack width measurements.

At approximately 250 kip, an audible noise was accompanied by a slight load drop of 1 kip. Several new flexural cracks were visually observed to have developed near the specimen midspan. As load application continued, several additional cracks formed and existing cracks continued to lengthen toward the load point.

At approximately 436 kip, maximum load was reached at 5.5-in. of vertical displacement when a series of three loud pops occurred in succession indicating rupture of the bonded strand, accompanied by load drops of approximately 32.5 kip per event. Following the third strand rupture, the applied load was approximately 339 kip. Shortly after attempting to resume to load application, deck rupture occurred near a load point (Figure 10-13). Post-mortem inspection revealed that all three bonded strands located in the bottom flange had ruptured (Figure 10-14).



Figure 10-13 IWC: rupture of deck at load point



Figure 10-14 IWC: ruptured bonded strands

While unloading the beam, several horizontal cracks formed between the two primary flexural cracks and a portion of the bottom flange broke away. After completely unloading the beam, the tendon force (according to the load cell) was $0.6f_{pe}$ (the tendon stress at start of load test), indicating that the post-tensioned strand had yielded. Though the measured deck strain did not exceed -3000 microstrain (Figure 10-15), crushing of the deck was visually observed 12-in. from the midspan.

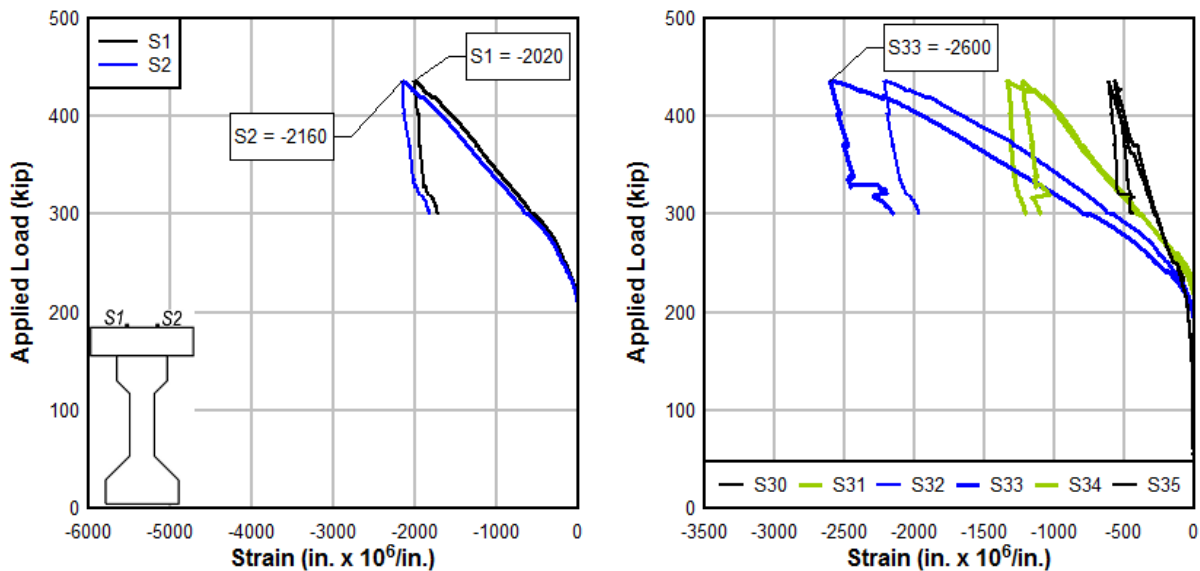


Figure 10-15 IWC: deck strain (a) at midspan and (b) along top of deck

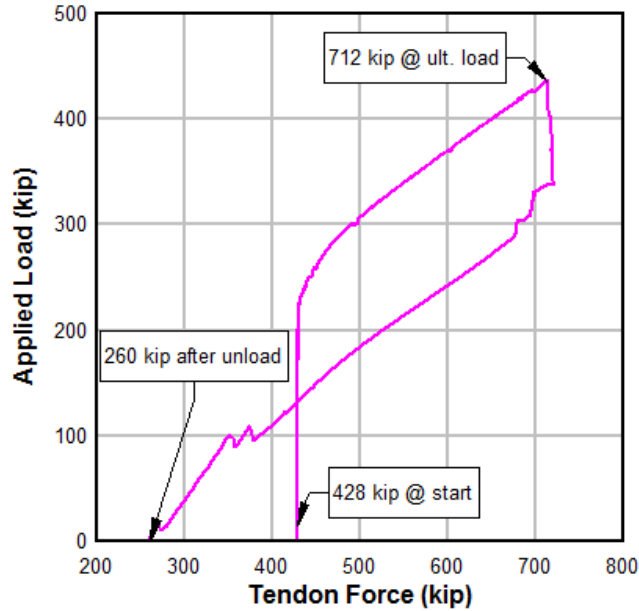


Figure 10-16 IWC: tendon force

10.5 Service and Cracking Behavior

To illustrate the elastic behavior of the internal tendon specimens, Figure 10-17 shows the moment-displacement plot up to cracking from the first load cycle (during which each beam was loaded until visible cracking); beam unloading is not shown. The secondary y-axis shows the ratio of the calculated bottom fiber stress to $\sqrt{f'_c}$ (psi). The bottom fiber stress is calculated with the following assumptions:

- 1) Bonded prestressing strand – f_{se} based on the initial prestress reported in the precaster's stressing records minus an assumed prestress loss of 20% and the area of the prestressing strand, as reported in the material certifications.
- 2) Post-tensioning tendon – f_{se} determined from the hollow-core load cell readings and area of the prestressing strand as reported in the material certifications.

The load level corresponding to the extreme fiber tensile stress for the Service III limit state ($0.19\sqrt{f'_c}$ (ksi), or 550 psi) and the cracking limit at ($7.5\sqrt{f'_c}$ (psi), or 690 psi) are shown for reference, assuming the specified concrete compressive strength (8.5 ksi). Each specimen behaved linear-elastically up until cracking, and all specimens exhibited approximately the same uncracked stiffness.

The cracking loads, determined from the data as the occurrence of a slope change in the plot of load versus midspan displacement (Figure 10-17), are given in Table 10-1. To confirm, the cracking load indicated in the applied load versus strain along the beam profile at the midspan was compared for each specimen (Figure 10-18). The predicted cracking load (applied jack load) was determined using transformed composite section properties, test-day material strengths, and the effective prestress based on the precaster's stressing records minus AASHTO-LRFD prestress loss estimates (for bonded steel) and the load cell readings for the unbonded post-tensioned tendon.

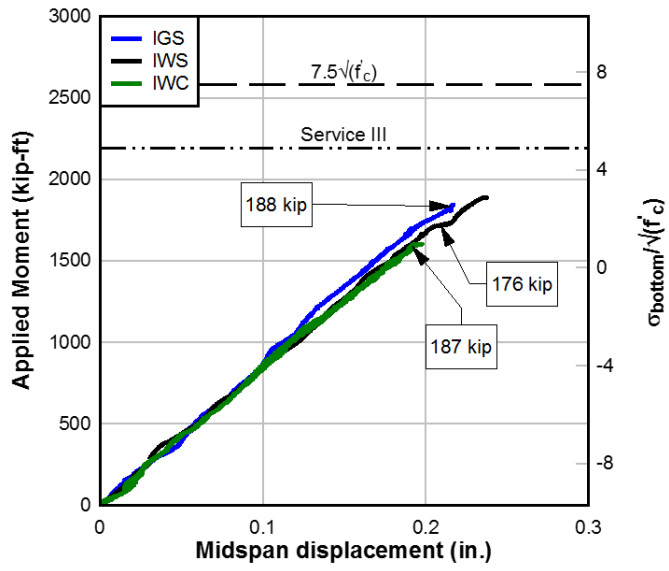


Figure 10-17 Internal tendon comparison: elastic behavior

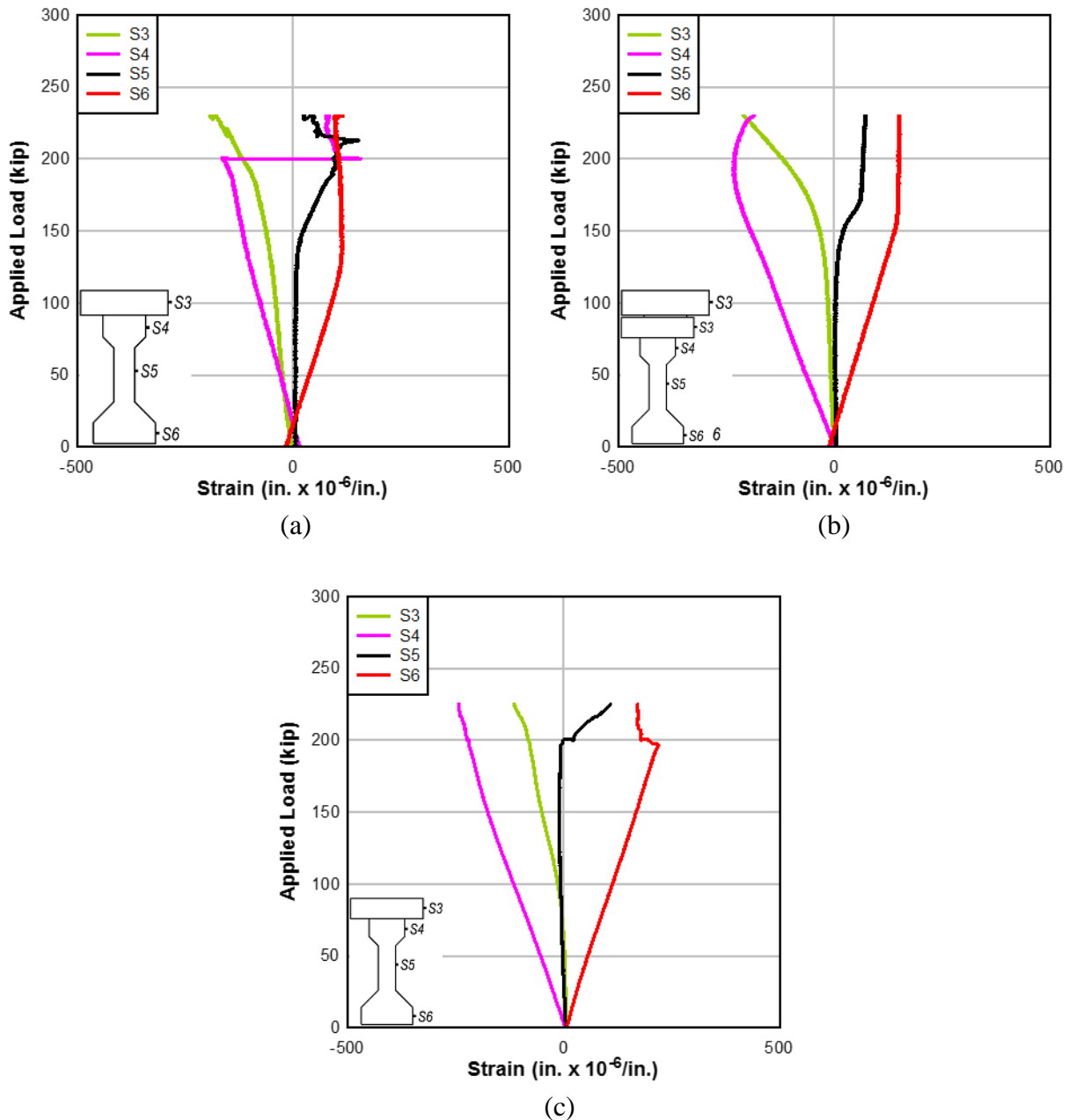


Figure 10-18 Strain along profile at load point (a) IGS, (b) IWS, (c) IWC

Table 10-1 First crack of internal tendon specimens

Specimen	Crack Type	Measured cracking load (kip)	Calculated cracking load (kip)
IGS	flexural	188	259
IWS	flexural	176	255
IWC	flexural	187	298*

*actuator load, 4-pt bending

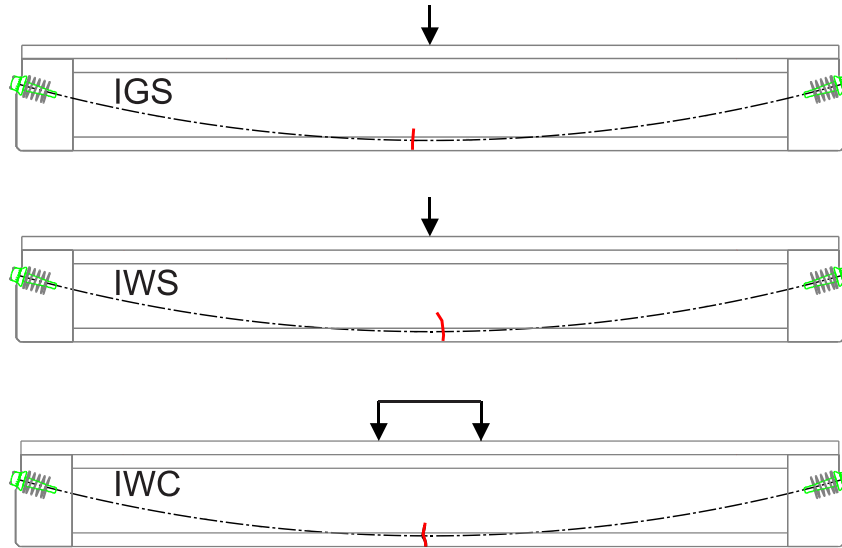


Figure 10-19 Internal tendon specimens: first crack locations

Figure 10-19 shows the first crack location of each specimen (thick red line). All specimens developed a flexural crack near the midspan. In all cases, the specimens exhibited first cracking prior to the calculated cracking load.

As loading progressed, cracks in specimen IGS were noted to be uniformly distributed beneath the load point, typical of bonded prestressed beam behavior. Conversely, both IWS and IWC exhibited behavior more typical of unbonded, prestressed beams: fewer cracks developed overall, and those cracks opened widely as the loading progressed (Figure 10-20). IWC developed a wider distribution of cracks compared to IWS due to the different loading configuration.

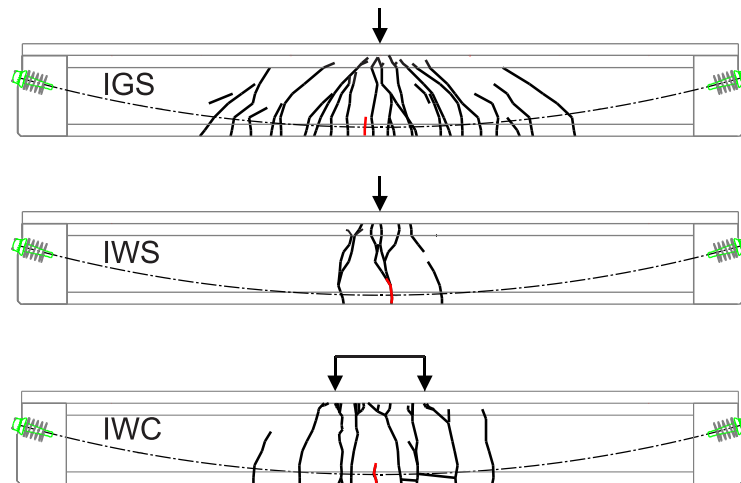


Figure 10-20 Internal tendon specimens: final cracking patterns

Crack widths of three selected cracks were measured for each specimen (Table 10-2) during load holds using a crack microscope. Specimen IWS was not inspected at the 300 kip load hold, to ensure the safety of the lab personnel. The cracks chosen for measurement were a

random selection of visible cracks near the specimen mid-span. Overall, typical crack width of specimen IGS was less than those in the unbonded specimens IWS and IWC. At lower loads, however, the crack widths of IWC were lower than that of IGS. This is likely due to the difference in loading condition as IGS and IWS were under three-point loading and IWC was under four-point loading.

Table 10-2 Crack widths at load holds (in.)

Specimen	Crack	P=200	P=250	P=300
IGS	1	0.017*	0.030	0.050
	2	-	-	0.035
	3	-	-	0.020
IWS	1	0.035	0.0125	Did not measure
	2	0.004	0.070	Did not measure
	3	0.018	0.0125	Did not measure
IWC	1	0.007	0.030	>0.06
	2	0.003	0.027	0.045
	3	0.007	0.030	>>0.06

Further, the crack measurements provide an estimate of the tendon stress increase in the unbonded specimens IWS and IWC. Figure 10-21 shows the tendon stress, measured directly using a hollow-core load cell on the tendon. Assuming the full tendon length carries the stress increase caused by the reduced moment of inertia at a crack, specimen IWS and IWC – based on crack measurements – experience a tendon stress increase as shown with symbols.

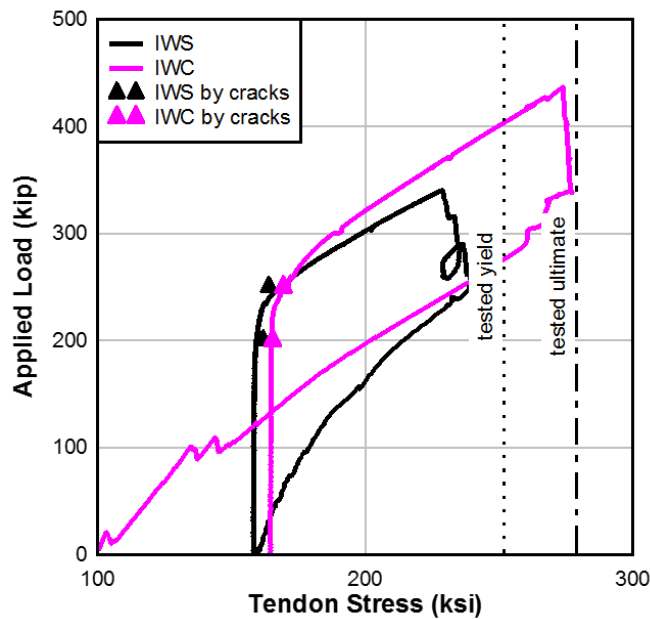


Figure 10-21 Internal Specimens: applied load vs. tendon stress

To quantify the crack opening in IWS, a string-pot was added after identifying an assumed primary crack (Figure 10-22). Figure 10-20 shows the applied load versus the instrumented crack; a second crack was visually observed to open a similar width during the test. At maximum load, the instrumented crack had opened 0.6 in.; rupture of the bonded strand at the bottom of the beam caused the crack to open to 0.8 in. Assuming that the other primary crack opened an equivalent amount, the total crack widths at ultimate can be estimated as 1.2 in. – or a stress increase (due to applied load) of approximately 70 ksi – the same tendon stress increase as measured by the hollow-core load cell (72 ksi; Figure 10-21). While this provides a validation method for determining the load cell’s accuracy at measuring a change in tendon force, it does not eliminate the possibility of initial offset or drift.

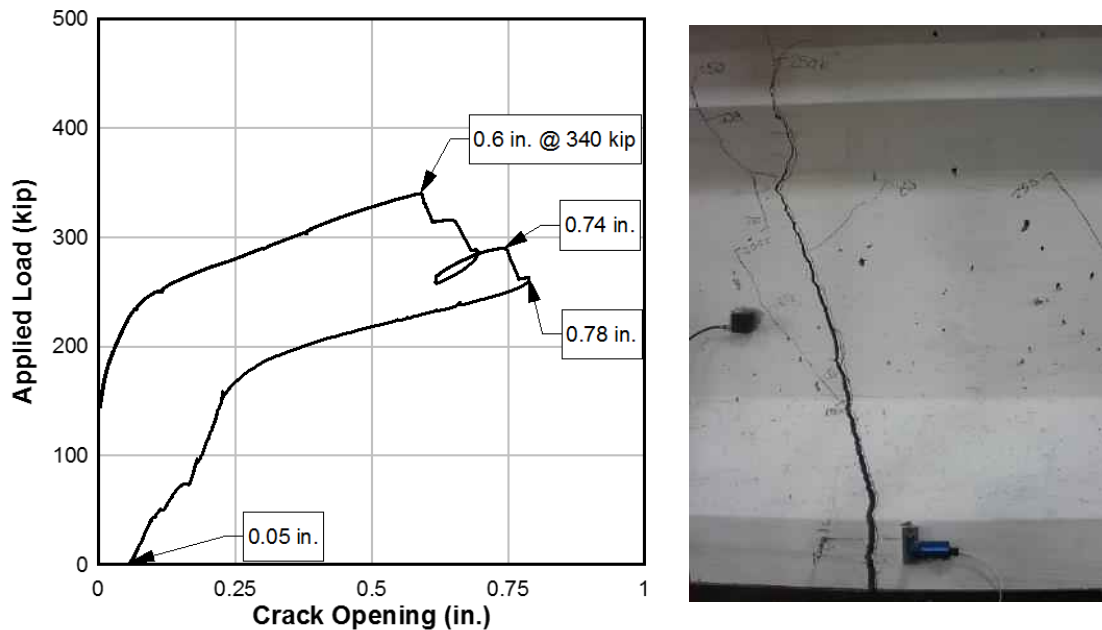


Figure 10-22 IWS: string-pot measuring a primary crack

10.6 Strength

The computed flexural strength of the internal tendon specimens is given in Table 10-3 and is compared to their respective load-displacement plots in Figure 10-23. The strength of IGS was computed in accordance with AASHTO-LRFD provisions for flexural strength of bonded members using test-day material strengths. The predicted bonded moment capacity at 0.003 concrete compressive strain was 4165 kip-ft., corresponding to an applied load of 402 kip. The peak load resisted by the grouted specimen, IGS, exceeded this predicted design strength of a bonded prestressed member.

For the unbonded specimens, IWS and IWC, the AASHTO-LRFD flexural strength was calculated using AASHTO-LRFD Equation 5.7.3.1.3b, which provides a simplified approach for an approximation of the ultimate tendon stress for members with mixed tendons. The calculated flexural strength (M_n), incorporating test-day material strengths, was 3830 kip-ft for IWS and 4030 kip-ft for IWC, corresponding to an applied (jack) load of 367 kip and 445 kip, respectively; the average applied moment (3680 kip-ft) is shown in Figure 10-23. Specimen IWC barely exhibited the calculated AASHTO-LRFD flexural strength, as calculated using the

simplified approach for members with both bonded and unbonded components, while specimen IWS did not.

The observed ultimate flexural strength of IWS and IWC was approximately 3320 kip-ft and 3710 kip-ft, respectively, compared with grouted control specimen IGS (4140 kip-ft); as expected, the calculated flexural strength of the bonded specimen is greater than that of the specimens with unbonded tendons. In laboratory testing, this expectation of greater flexural strength was confirmed: the bonded specimen resisted greater moment – by approximately 25% and 10%, compared to specimens IWS and IWC, respectively.

Specimen IWC underwent much greater displacement at a higher ultimate strength, compared to the specimen IWS, though the two specimens were detailed and constructed in the same manner. The differing behavior can be attributed to the loading scheme - IWS was loaded in a three-point bending setup and IWC was subjected to a four-point scheme – and the consequent development of the plastic region – or hinge length. The constant moment region creates a longer hinge length than a concentrated force. The hinge length – which affects the member’s rotational capacity - has apparent implications on the ultimate strength and deflection of the mixed-tendon members.

Estimates of each specimen’s hinge length at the strength limit state can be made through inspection of the final cracking pattern (Figure 10-20); the hinge length was assumed to be the length of the cracked portion of the bottom flange. Based on this assumption, bonded specimen IGS, with the well-distributed cracking pattern of a bonded prestressed beam, had an estimated hinge length of 248-in. Specimen IWS, with a single-point load and unbonded tendons, developed a hinge located under the load-point; the area is estimated to be approximately 47-in. encompassed by lines extending at approximately 22° from the load point. Specimen IWC had a longer hinge length over the constant moment region; it was estimated to be approximately 95 in., which is the length of the constant moment region plus the area encompassed by a line extending approximately 17° from the load points.

Table 10-3 Internal tendons - AASHTO-LRFD vs. observed flexural strength

Specimen	AASHTO-LRFD provision	Calculated		Observed			
		M _n	f _{ps} *	M _n	f _{ps}	Δ	Hinge length
		(kip-ft)	(ksi)	(kip-ft)	(ksi)	(in.)	(in.)
IGS	Bonded	4165	280	4384	n/a	4.4	248
IWS	Simplified Mixed Tendons	3830	259	3565	229	2.9	47
IWC	Simplified Mixed Tendons	4029	263	3956	274	5.5	95

*reflecting test-day material properties, per strand certifications

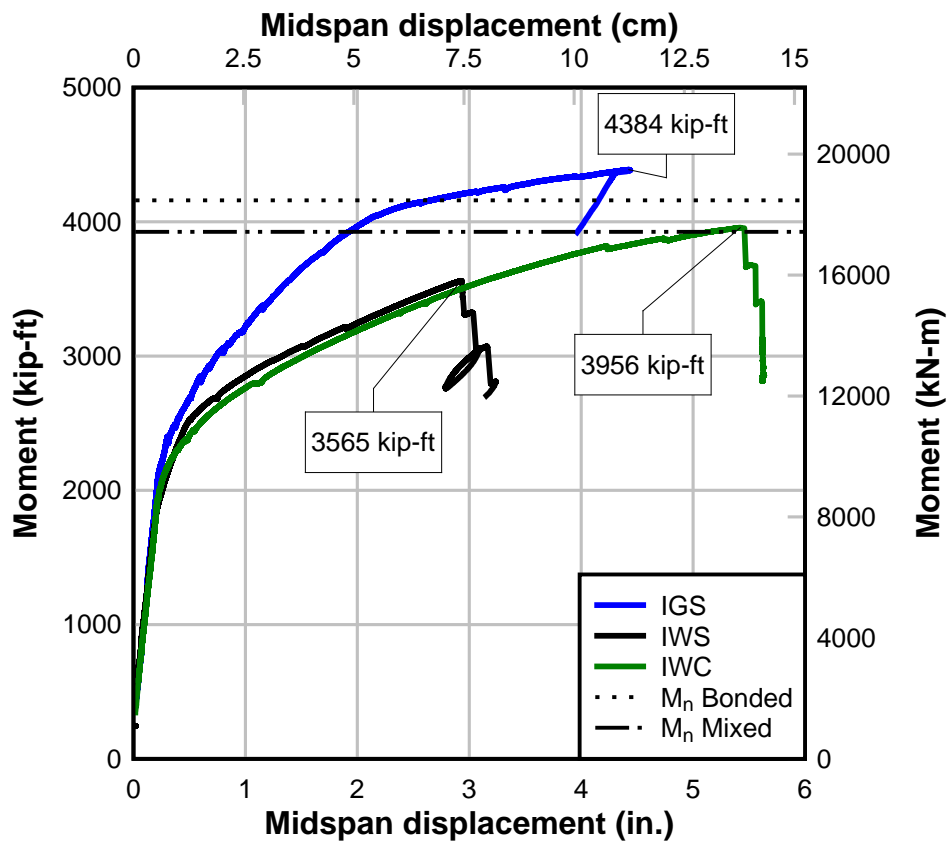


Figure 10-23 Flexural strength: internal tendon specimens

11 External Tendon Results and Discussion

This section describes the injection results and the load tests of the two external tendon specimens. Specimen EWS was subjected to a static load procedure; EWC was subjected to a series of load cycles, followed by a cyclic program and, finally, an ultimate load test.

11.1 Flexible filler injection

Specimens EWS and EWC were injected with flexible filler after post-tensioning. Two tendons were injected for each specimen; the two tendons were injected sequentially, on the same day. The same heated barrel was used to supply flexible filler to both tendons.

Figure 11-1 shows the temperatures measured inside the duct and on the surface of the duct during and following the injection process; the plot is intended to show a time history of the injection. The ambient temperature at the time of injection was approximately 84°F. Gages T27 and T28 measured the temperature of the duct surface of the west tendon; the maximum measured temperature on the duct surface was approximately 122°F. Gages T25 (towards inlet) and T23 (towards outlet) measured the internal tendon temperatures using a probe of the west tendon; Gages T26 (towards inlet) and T24 (towards outlet) measured the same of the east tendon (injected second). The peak measured temperature inside was 193°F. Following injection, the measured temperatures decreased quickly (within approximately 4 hours, not shown in plot) to the ambient lab conditions.

The tendon force was also measured during the injection process (Figure 11-2). The force in each tendon decreased by about 7% (14 kip) within 8 minutes of injection. Full tendon force was recovered in both tendons within 24 hours.

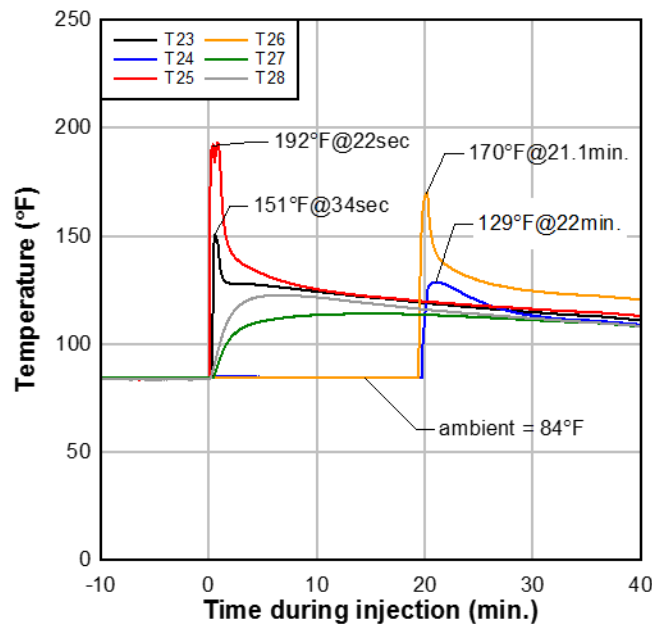


Figure 11-1 EWS: temperature

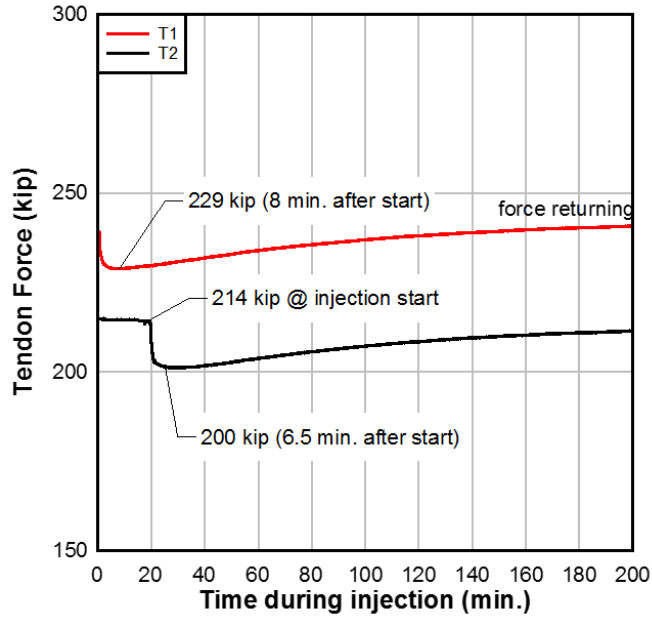


Figure 11-2 EWS tendon force during injection

11.2 EWS: Static Three-Point Bending

A three-point static flexure test was performed on specimen EWS (Figure 11-3). Although there was slight variations in the load displacement plot, the behavior was essentially linear up to cracking. The beam was visually inspected as load application was continued, but no significant out-of-alignment was observed.

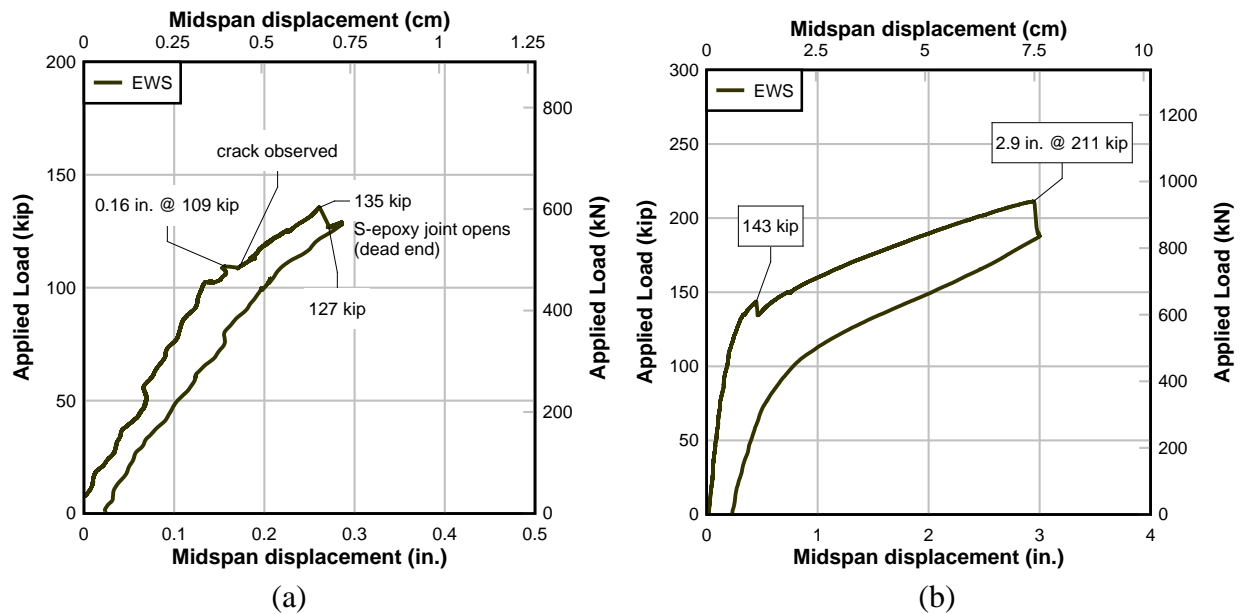


Figure 11-3 EWS (a) elastic behavior and (b) ultimate strength behavior

At 100 kip, minor noises were audible, though no cracks were identified (see Figure 11-4). At 112 kip, two cracks were visually located. The first extended from the precast dry joint of the north deviator block towards the load point. The second extended from the precast dry joint of the south deviator block towards the load point. Load application was continued to 125 kip and held. Cracks were marked and load application was resumed at 0.2 kip/sec.

At approximately 135 kip, a loud pop was heard, accompanied by a sudden load drop of approximately 8 kip. The south epoxy joint was observed to open on one side of the beam; the opposite beam face of the south epoxy joint appeared to remain closed (Figure 11-4). The north epoxy joint was inspected; it appeared intact. The specimen was unloaded to 100 kip, and the load was held. Cracks were again marked and the beam was completely unloaded to allow installation of string pots. Two string pots were installed on the south deviation block— one on each face of the beam –across the epoxy joint (Figure 11-5).



Figure 11-4 EWS: south deviation block

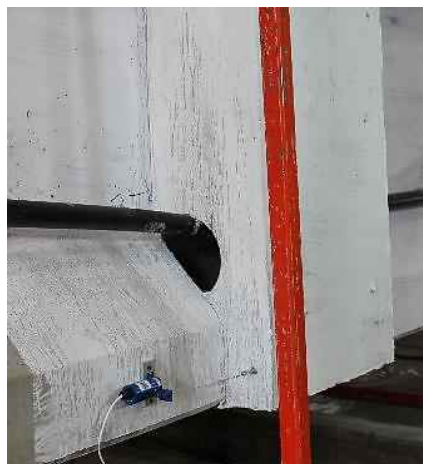


Figure 11-5 EWS: string pots installed

With the beam completely unloaded, load application was resumed at 0.2 kip/sec. At approximately 143 kip, the north epoxy joint was observed to open suddenly with an audible report. Subsequent to this event, the hollow-core tendon load cells were observed to measure an increase in the tendon force as load application continued. At 150 kip, the load was held and cracks marked. Cracks were observed at deviators running parallel to beam axis, near epoxy joints. Load application was resumed at 0.2 kip/sec until crushing of the concrete in the compression zone occurred approximately above the north epoxy joint at approximately 211 kip.

Figure 11-6 shows the applied jack load versus deflection (at midspan and at the north and south 1/3-points (labeled “N 1/3” and “S 1/3”, respectively) for the ultimate load test. The opening of the north epoxy joint is identifiable by the sudden load drop and subsequent stiffness change at 143 kip. The midspan exhibited the largest displacement as the specimen approaches the ultimate load of 211 kip. Measured displacements near the N1/3 point measure a jog in the data at 211 – reflecting, perhaps, the sudden upward displacement of the top portion of the beam as a section of concrete displaced upwards near the hinge (Figure 11-7). Measured concrete strain values at ultimate were greatest near this location (S30); measured strain was approximately -1575 microstrain (Figure 11-8). Much of the displacement that occurred after cracking is attributed to the joint opening (Figure 11-9).

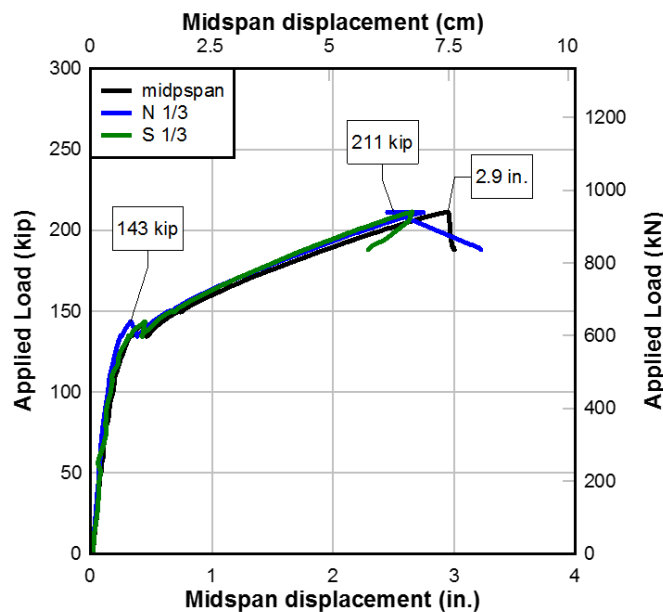


Figure 11-6 EWS: load vs. displacement

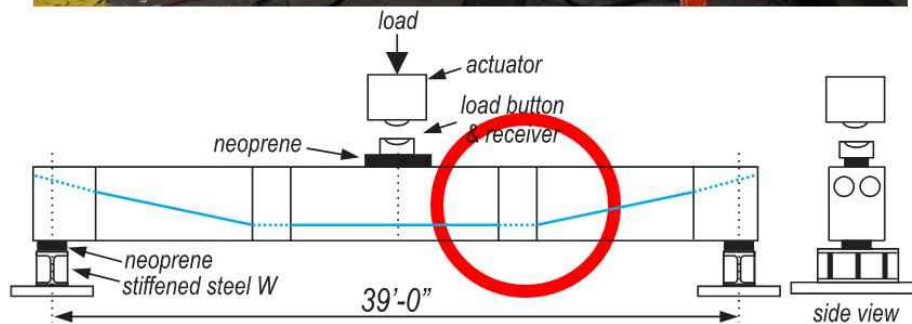
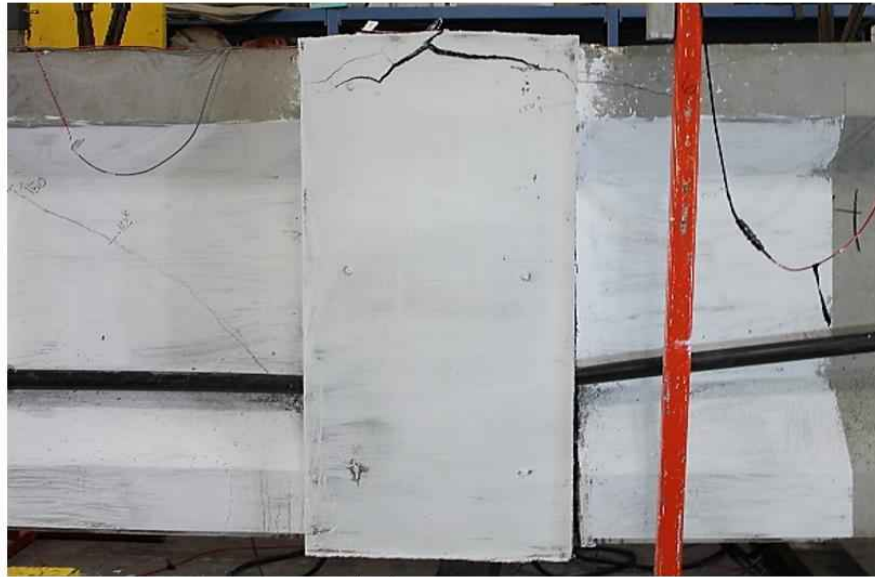


Figure 11-7 Compression failure at north epoxy joint (beam shown under load)

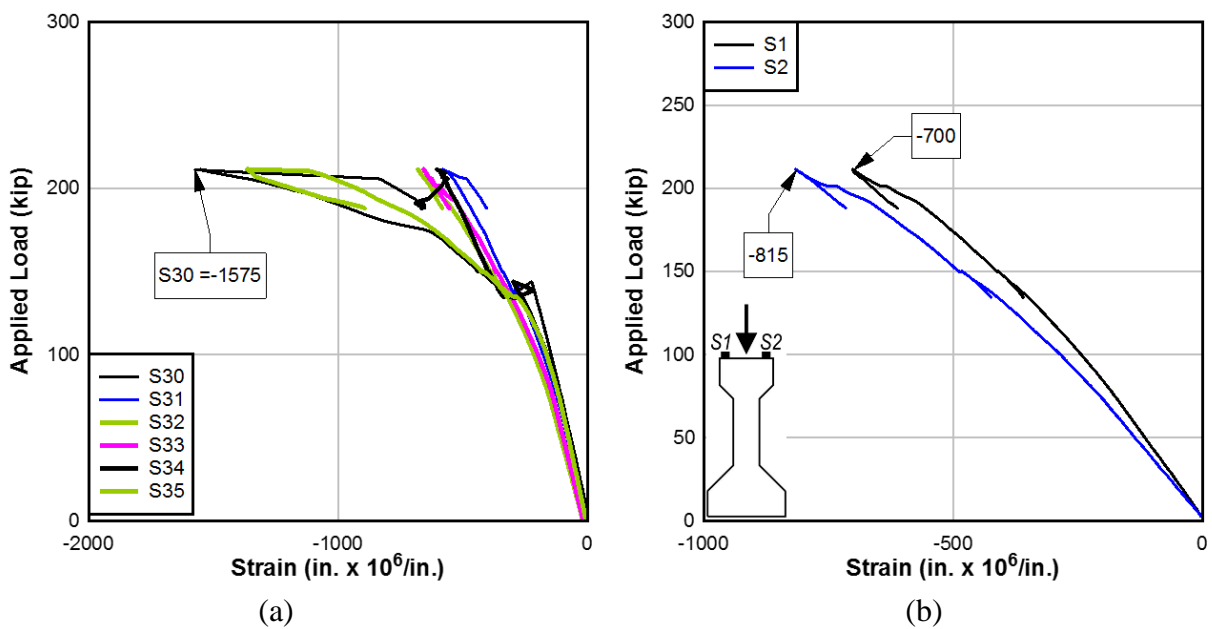


Figure 11-8 EWS: strain (a) along top, and (b) at load point

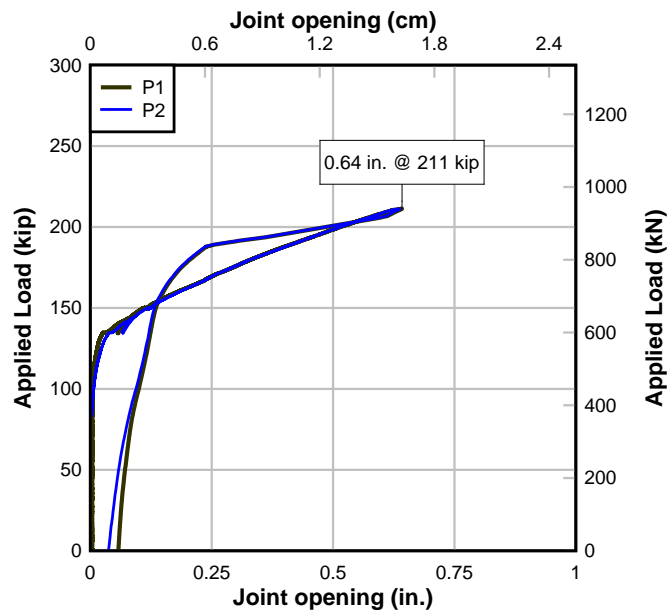


Figure 11-9 EWS: south joint opening

11.3 EWC: Cyclic Three-Point Bending

Specimen EWC was subjected to a series of load cycles for initial beam evaluation, followed by cyclic loading for 2 million cycles and, finally, an ultimate load test. All load tests were performed in the same three-point bending test set-up. Figure 11-10 shows the load-deflection plots for the key loading stages. The following describes the load test observations made during each load cycle:

Load Cycle 1 - Precracking

Load was applied at 0.2 kip/sec. As load was applied, EWC exhibited linear-elastic behavior up to cracking. At approximately 112 kip, a small change was observed in the load-deflection plot. The beam was inspected, but no visible cracks were located. At approximately 126 kip, a crack was visually observed at the north precast joint on one face. Load application was held at 128 kip. During the load hold, a loud pop occurred; a second crack was located at the south precast joint. These two cracks were observed to appear on both sides of the beam. The beam was unloaded for the installation of additional instrumentation.

Load Cycle 2

Load was applied at 0.2 kip/sec. At 135 kip, load was held and the beam inspected. During the load hold, a loud pop was heard, coinciding with the opening of the south epoxy joint. The beam was unloaded.

Load Cycle 3

Using displacement-control, displacement was applied at approximately 1E-04 in./sec. Displacement was held at approximately 150 kip and the width of the three cracks were measured with a crack microscope. No additional cracks developed -- only the existing three cracks were observed to open. The beam was completely unloaded.

Load Cycle 4

Using displacement-control, displacement was applied at approximately 1E-04 in./sec. Displacement was held at approximately 160 kip and the width of the three cracks were

measured. The beam was completely unloaded and additional strain gages were installed on the post-tensioning tendon.

Load Cycle 5-7

With the tendon strain gages in place, another three load cycles were conducted. Displacement was applied at approximately $1E-04$ in./sec. and held at applied loads of 120, 130, 140, 150 and 160 kip. During each load hold, cracks were measured. During the load hold at 160 kip of load cycle #5, a loud audible noise signaled the opening of the north epoxy joint. Crack measurements were taken after the joint opened, with load held at 160 kip. It was observed that the tendon strain gage measurements, previously disparate (east tendon vs. west tendon), equilibrated after the north joint opened. The beam was unloaded at the conclusion of each load cycle.

High Stress Cycles

The beam was then subjected to approximately 600 cycles of extreme loading to evaluate the post-tensioning tendon under fatigue cycling. The load range was set such that the tendon was subjected to a stress range of 10 ksi. The beam was loaded using displacement control.

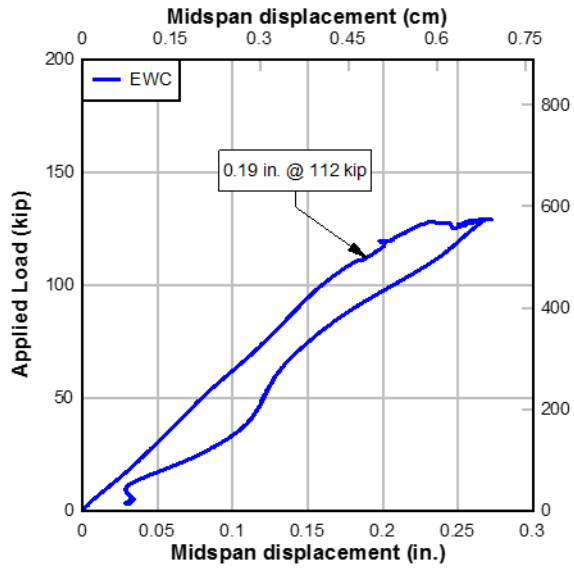
To determine the upper and lower ends of the displacement range, the tendon strain gages were used to note a strain change corresponding to 10 ksi in the tendon. At the start of loading, the beam was cycled between approximately 80-160 kip of actuator load, or an actuator load range of 80 kip.

Service – Low Stress Cycles

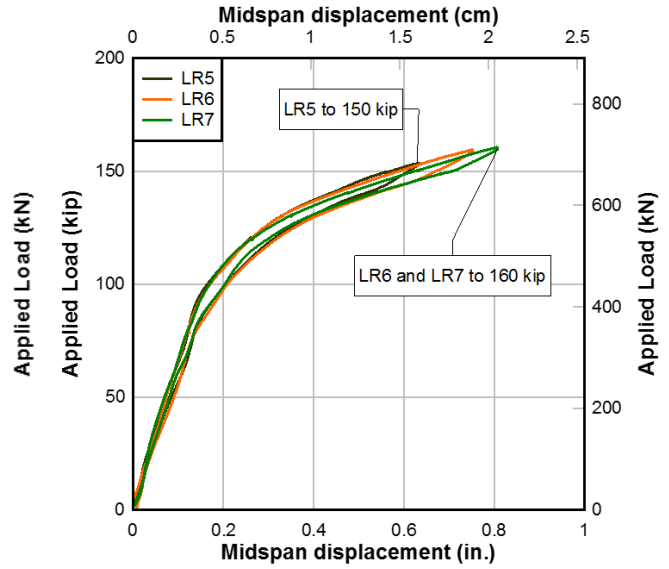
The beam was then subjected to approximately 2 million cycles of service level loading, assuming an initial overload had cracked the specimen. The beam was cycled using load control with interlocks, between an applied load of 80 kip (decompression load) and 112 kip (cracking load).

Ultimate Strength

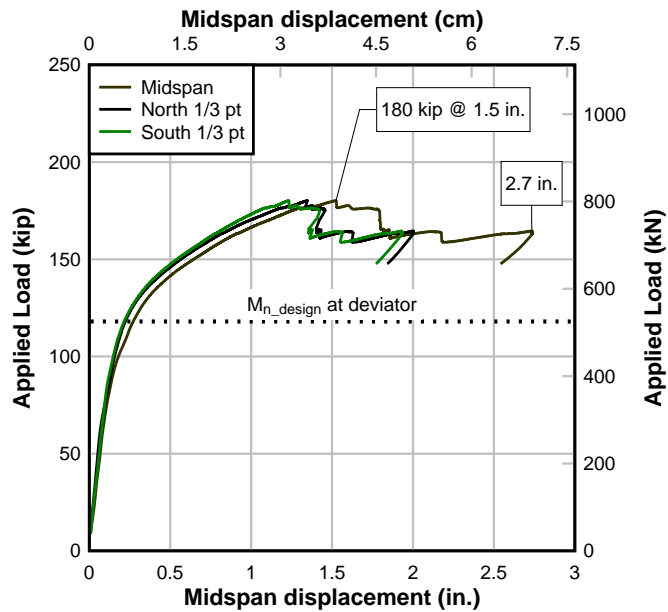
Following the cyclic loading, the specimen was subjected to a three-point bending test to ultimate. Load was applied at 0.2 kip/sec. As the beam was loaded, the south precast joint was observed to open widely, while the epoxy joints were observed to only open slightly (unlike the test of EWS). Shear cracking near the south precast joint developed and propagated toward the load point (Figure 11-11). At approximately 180 kip, several cracks emanating from the south precast joint widened significantly and the beam began to deflect without resisting additional load. The test was terminated to prevent a sudden shear failure. The maximum applied load was 180 kip at an approximate midspan displacement of 1.5 in.



(a)



(b)



(c)

Figure 11-10 EWC: (a) cracking (b) load cycles and (c) ultimate



Figure 11-11 EWC near ultimate load

11.4 Service and Cracking Behavior

To highlight the elastic behavior of the external tendon specimens, Figure 11-12 shows the moment-displacement plot up to cracking from the first load cycle (during which each beam was loaded until visible cracking); beam unloading is not shown. The secondary y-axis shows the ratio of the calculated bottom fiber stress to $\sqrt{f'_c}$ (psi). The bottom fiber stress is calculated with the following assumptions:

- 1) Bonded prestressing strand – f_{se} based on the initial prestress reported in the precaster's stressing records minus an assumed prestress loss of 20% and the area of the prestressing strand, as reported in the material certifications.
- 2) Post-tensioning tendon – f_{se} determined from the hollow-core load cell readings and area of the prestressing strand as reported in the material certifications.

The load level corresponding to the extreme fiber tensile stress for the Service III limit state (no tension for members with unbonded tendons) and the cracking limit at $(7.5\sqrt{f'_c}$ (psi), or 690 psi) are shown for reference, assuming the specified concrete compressive strength (8.5 ksi). Each specimen behaved linear-elastically (ignoring initial wobble of the specimen as it settled in the test set-up) until cracking, and both specimens exhibited approximately the same uncracked stiffness. Figure 11-14 shows the strain profiles through the beam depths at the load point for both specimens; measured strains on either face were nearly equivalent – indicating no torsional component was applied to either specimen.

The cracking loads, determined from the data as the occurrence of a slope change in the plot of load vs. midspan displacement (Figure 11-12), are given in Table 11-1. The predicted midspan cracking loads were determined using transformed composite section properties, test-day material strengths, and the effective prestress based on the precaster's stressing records minus AASHTO-LRFD (AASHTO 2014b) prestress loss estimates (for bonded steel) and the load cell readings for the unbonded post-tensioned tendon. The joint opening loads at the

deviator (in terms of applied jack load) is also given and were determined using transformed composite section properties, test-day material strengths, and the load cell readings for the unbonded post-tensioned tendon.

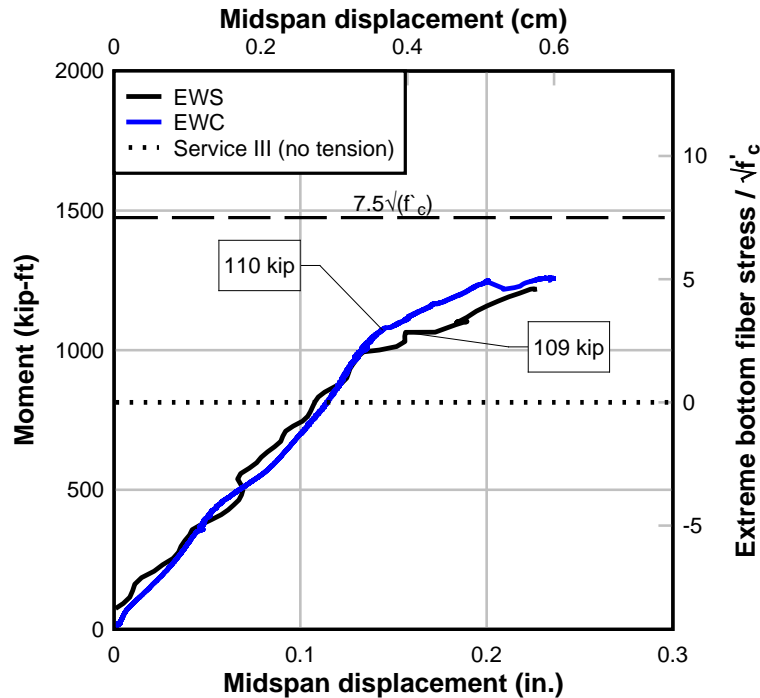


Figure 11-12 External tendon comparison: elastic behavior

Table 11-1 First cracks of external tendon specimens

Specimen	Cold joint opening (kip)	S-epoxy joint (kip)	N-epoxy joint (kip)	Calculated decompression load @ midspan (kip)	Calculated cracking load @ midspan (kip)
EWS	109	128	143	81	163
EWC	110	135	160	85	167

Figure 11-13 shows the first cracks to form during the initial loading of specimens EWS and EWC (shown as a red line), which were located at the dry (no epoxy) joints between the precast section and deviator block. Reinforcement and nonprestressed prestressing strand, however, did extend across this joint.

As loading progressed in both specimens beyond service level loads, the epoxy joints opened at each deviator block and primary crack opening occurred at the epoxy joints, which had no reinforcement across the joint (Figure 11-14). The cracks at the precast cold joints—across which ran mild steel reinforcement and nonprestressed prestressing strand—did not continue to elongate.

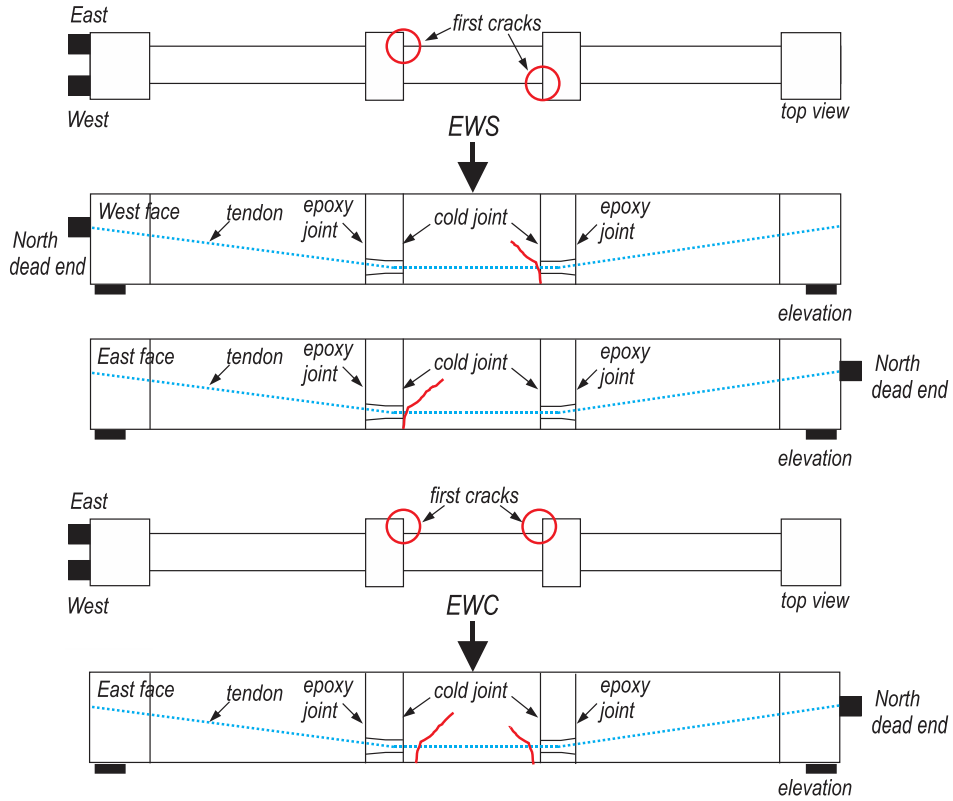


Figure 11-13 External tendon specimens: first crack locations

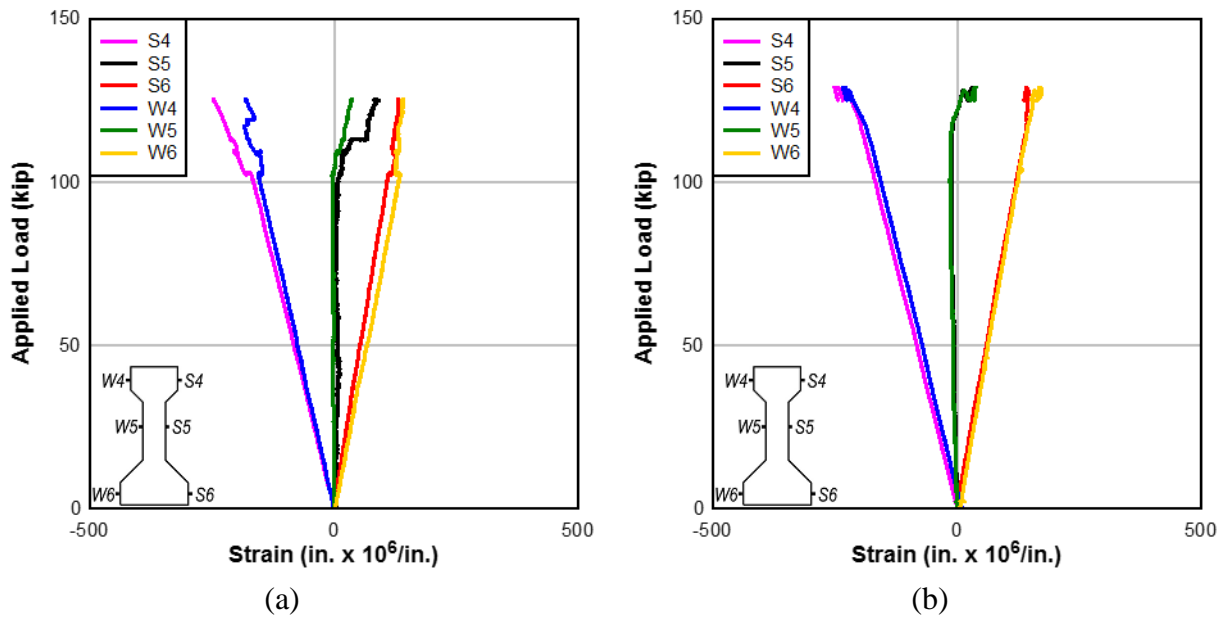


Figure 11-14 Strain profiles for (a) EWS and (b) EWC

11.5 Strength

Flexural strength of the external tendon specimens as calculated is given in Table 11-2 and is compared to the observed moment vs. displacement behavior exhibited during the ultimate load tests in Figure 11-15; the y-axis of Figure 11-15 reflects both the superimposed and self-weight moment. The calculated strength, M_n , was computed in accordance with AASHTO-LRFD provisions for flexural strength of unbonded members using test-day material strengths.

The predicted flexural strength was 1846 kip-ft and 1901 kip-ft for specimens EWS and EWC, respectively. The observed ultimate flexural strength of EWS and EWC was approximately 2320 kip-ft and 2015 kip-ft, respectively; self-weight is considered in these reported values. Both specimens exceeded the predicted flexural strength, as calculated per AASHTO-LRFD. The observed ultimate strength of specimen EWC, however, should not be considered representative of beam behavior under a normal loading condition, due to the loss in beam integrity/loss of concrete section observed during the high stress-range fatigue cycling. As to be expected, the displacements measured at the deviators of each of the specimens were less at a given load than the corresponding midspan displacement. In both EWS and EWC, the north deviator (located closer to the dead end of each specimen), exhibited greater displacement than the south deviator.

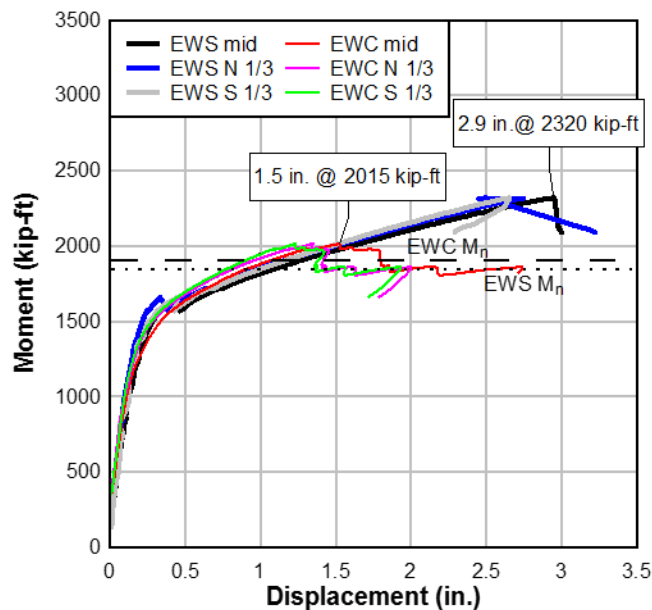


Figure 11-15 EWC flexural strength: external tendon specimens

Table 11-2 External tendons: AASHTO-LRFD vs. observed unbonded flexural strength

Specimen	AASHTO-LRFD Calculated		Observed	
	M_n	f_{ps}	M_n	f_{ps}
	(kip-ft)	(ksi)	(kip-ft)	(ksi)
EWS	1846	236	2320	229/256
EWC	1901	243	2015	195/223

Ultimate Tendon Stress

Comparison of the ultimate tendon stress calculated per AASHTO-LRFD and the observed tendon stress is given in Table 11-2. In all but one tendon, the measured tendon force by the hollow core load cell indicated that the tendon stress at ultimate strength was less than predicted by the AASHTO-LRFD equation (Equation 3).

Change in unbonded tendon stress is a function of the global displacement of the member. Based on this supposition, the ultimate strength of an unbonded member is determined from the tendon stress corresponding to the final displaced shape. For a given member geometry, such as that of EWS and EWC, both specimens should demonstrate the same change in tendon stress for a given displacement, if the structure is deforming the same way (same number of joint openings, cracking patterns). This expected behavior is confirmed: the change in tendon stress of EWC versus EWS is approximately equal during the pre-cracked and post-cracking stage, up until ultimate strength of EWC at 1.5-in. of displacement (Figure 11-16). Beyond ultimate strength, EWC exhibits slightly less tendon stress increase with increasing displacement, suggesting a lower stiffness than that of EWS.

Both tendons of EWC exhibited ultimate tendon stress versus the anticipated tendon stress (Table 11-2) as calculated per AASHTO-LRFD Equation 3.

Figure 11-17 compares the applied load versus tendon force of an early load cycle to the ultimate load test of specimen EWC; it can be seen that the measured tendon force at the start of load application appears to have reduced between the time of the early load cycles and the time of the final ultimate load test. This is likely due to the elastic losses occurring in the stressed tendon while the second tendon was being stressed. The reduction in tendon force is greater in load cell #2. Service level and post-cracking stiffness of the member appears unchanged between the early load cycles versus the ultimate load cycle.

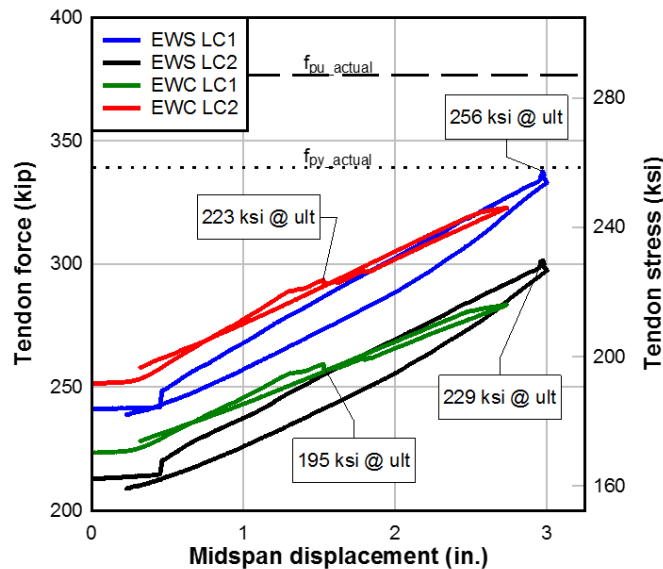


Figure 11-16 External tendon specimens: ultimate tendon stress

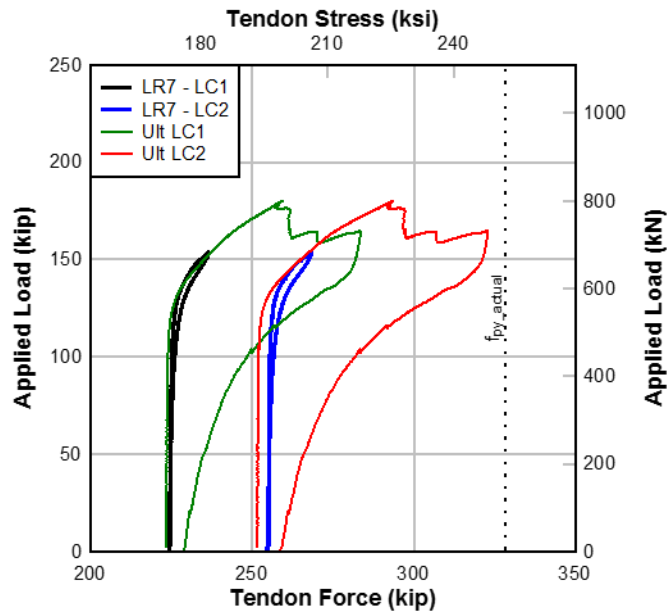


Figure 11-17 EWC: tendon force

11.6 Dissection

Following the structural load tests, each specimen was inspected to evaluate duct and strand wear at the diabolos.

Static wear

Figure 11-18 and Figure 11-19 show the approximately 5-ft sections of HDPE duct removed from the region near the diablo of specimen EWS. The blue box encloses the 4-ft. length of the diablo. The arrows indicate the direction to the anchorage – in other words, the side of the duct undergoing an angle change at the tendon deviated upon exiting the diablo.

Figure 11-18 shows the exterior surface of the duct in contact with the concrete surface of the diablo (the top of the duct). Figure 11-19 shows the same lengths cut open to reveal the interior surface of the duct, where the strand was in contact with the duct. Some scuffing of the exterior of the duct was observed, though it was minor. No gouging of the exterior surface duct was noted.

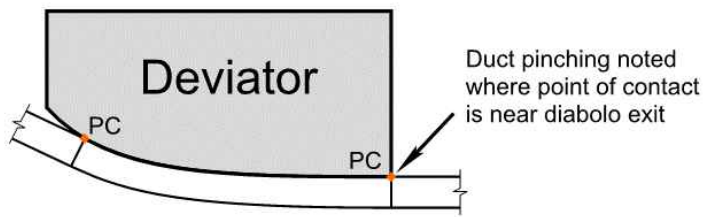
Figure 11-19 shows the interior surface of the duct in contact with the prestressing strand. While no noticeable wear of the prestressing strand was visually observed in the strands near the diablo, the interior surfaces of the ducts in these areas did exhibit imprinting/indenting along the length. A 1/8-in. deep indent, circled in Figure 11-19, was observed where the tendon exited the southeast diablo toward the midspan. The diablo geometry in this area was such that the theoretical point of contact aligned with the deviator exit location. This causes a pinch point that can be alleviated by flaring the diablo and moving the point of contact away from the exit point (Figure 11-20).



Figure 11-18 EWS: exterior of duct at diablo



Figure 11-19 EWS: interior surface of duct in contact with strand at diablo



(a)



(b)

Figure 11-20 Potential HDPE duct damage at deviator (a) effect of point of contact on HDPE damage in diabolo deviator (b) pinched HDPE at deviator exit in specimen EWS

Cyclic wear

Inspection of the duct and strand of specimen EWC was similarly conducted following an ultimate load test. Focus was paid to the length of tendon at each diabolo. Evidence of light exterior surface wear was found at the NE diabolo (Figure 11-21); no gouging or severe exterior wear was found. Evidence of red oxide was found during inspection of the strands at several locations, including at the NE, NW, and SE diabolo (Figure 11-22, Figure 11-23, and Figure 11-24). The presence of red oxide on the outside wires, where a strand would most likely be in contact with other strand, may be evidence of fretting fatigue; because close inspection of the strand prior to installation was not conducted, it cannot be definitively confirmed.

Also visible at the NW diabolo was clean/shiny steel wear on the exterior wires of several strands (Figure 11-23) – strand damage which may have occurred during the ultimate load test. It is noted that the north deviator block was the location of ultimate failure.



Figure 11-21 EWC: exterior surface of duct at NE diabolo



Figure 11-22 EWC: strands at NE diablo

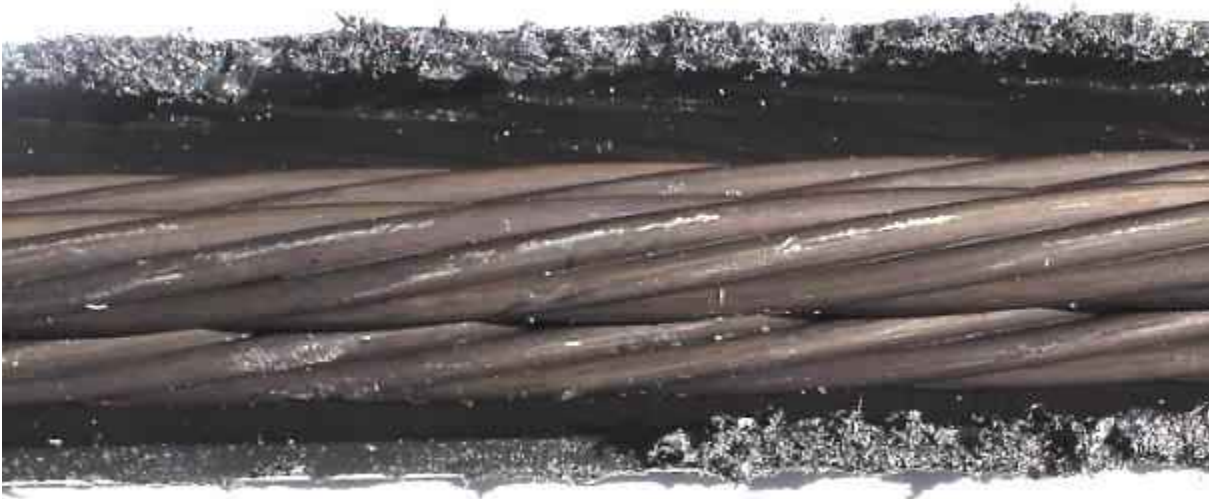


Figure 11-23 EWC: strands at NW diablo



Figure 11-24 EWC: dissection of tendon at SE diablo

12 Analysis of Strength Results

When loaded to ultimate flexural strength, as depicted in Figure 12-1, a post-tensioned beam with an unbonded tendon exhibits different behavior than an otherwise equivalent beam with a bonded tendon. An unbonded beam develops fewer cracks and those cracks are of larger widths than those of a bonded beam. Further, an unbonded beam also undergoes greater deflection as it approaches ultimate load compared to a bonded beam. While the deflection is higher, the unbonded tendon yield is generally delayed or never occurs. Consequently, the energy stored in the tendon is returned when unloaded. In contrast, the bonded tendon yields earlier in the loading and dissipates the energy as a result of the damage, thus providing a higher ductility than the unbonded tendon. In some cases, however, large displacements without tendon yielding may be desirable as the elastic energy stored in the tendon will result in a full recovery of deflection when unloaded, thus returning the member to its original configuration. Test specimens IWS and IWC – and the drop-in span construction the specimens mimic – have both unbonded post-tensioned tendons and bonded pretensioned steel (mixed tendons). The observed service and ultimate behavior of members with mixed tendons is between a bonded case and an unbonded case: the mixed tendon test specimens developed fewer cracks (versus a single theoretical crack in unbonded members, or versus many cracks, as in bonded test specimen), and exhibited a lower ultimate strength than the bonded test specimen, IGS.

The material change of post-tensioning filler material from cementitious grout to flexible fillers such as wax or grease results in a reduction of both ductility and ultimate strength (compared to fully bonded members) in favor of perceived better corrosion protection, structure durability, and maintenance access.

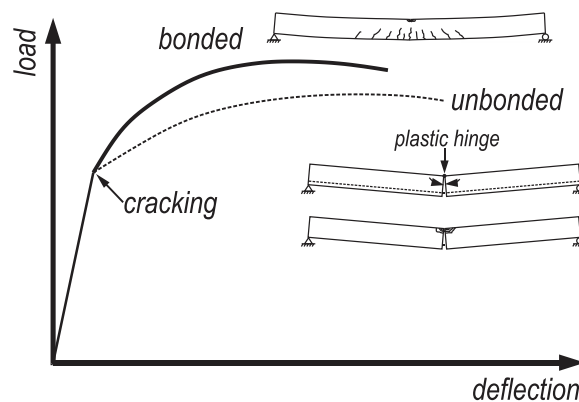


Figure 12-1 Behavior of members with bonded, unbonded, and mixed tendons

Determining the stress conditions in *bonded* prestressing steel at ultimate strength can be computed using strain compatibility. The fundamental assumption that the prestressing steel is perfectly bonded to the concrete is a prerequisite for this approach and allows the flexural strength to be computed at a chosen section. Unbonded tendons, on the other hand, must be evaluated at the global-level, rather than the section-level, because unbonded tendons transfer force only at anchorages, deviation points and other points of contact.

Ultimate strength of a member with unbonded tendons or mixed tendons is dependent on the unbonded tendon stress, which is, in turn, dependent on several parameters, including the reinforcement material properties, span-to-depth ratio, tendon profile, ratio of area of bonded-to-unbonded steel, loading, and the length of the equivalent plastic hinge.

12.1 Unbonded Tendon Stress and Ultimate Strength

An unbonded member's flexural strength is calculated from system equilibrium, with an estimated unbonded tendon stress. Without stress-strain compatibility between the tendon and the surrounding concrete, determination of unbonded tendon stress considers the global deformation of the system. The following discussion compares the observed (measured via hollow-core load cell) ultimate tendon stress to that predicted by AASHTO-LRFD (2014b). Predicted ultimate tendon stress for mixed-tendon members IWS and IWC was determined using the simplified approach; for the unbonded members EWC and EWS, the AASHTO-LRFD provisions for unbonded members were used.

The tendon stress calculations given by AASHTO-LRFD 5.7.3.1.2 (2014b) consider an assumed hinge length (equal to twice the depth from compressive force resultant to passive reinforcement) as a part of the derivation. The hinge length does not consider distributed loading, nor make an attempt to incorporate other factors in the hinge development (in other words, the presence of bonded reinforcement). This point is further discussed in 12.2.

Hollow-core load cells were used to directly measure the tendon force in the unbonded tendon during the load test. Figure 12-2 shows the tendon stress versus the applied moment for all specimens; the hollow-core load cell on specimen IGS did not measure a change in tendon stress during the load test and is not shown. Also shown is the actual tested strand yield and rupture stress, per the material certifications. Table 12-1 provides a comparison of observed tendon stress to calculated values, as well as actual strand material strengths (per material certifications).

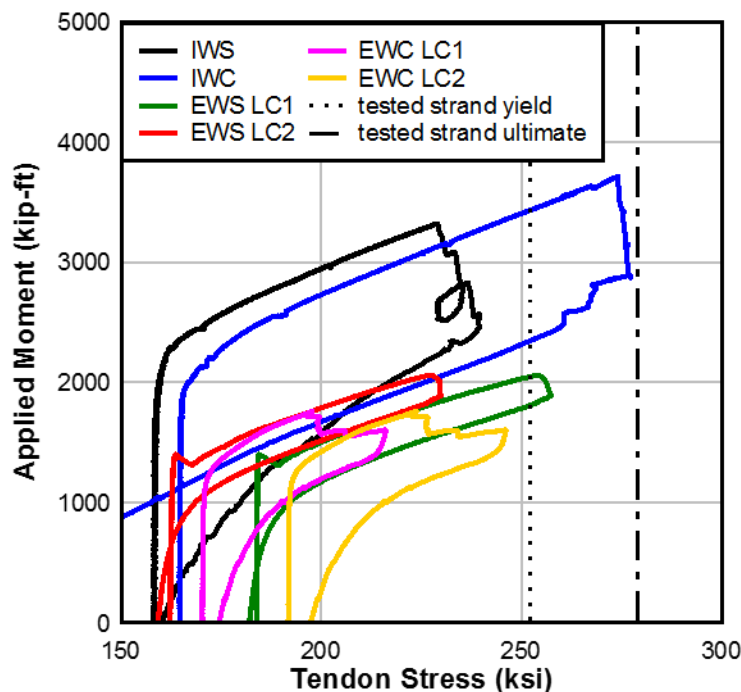


Figure 12-2 All specimens: ultimate tendon stress

In comparing the measured tendon force per the load cell of each external tendon specimen, there is a consistent 35 kip discrepancy between the left and right tendons (Figure

12-3); this discrepancy occurred in both tests. Causes for the discrepancy were investigated; causes considered included: 1) an inherent offset in the load cell, 2) uneven loading by the loading actuator during the load test, 3) immediate PS losses with each strand stressed in tendon #1 caused by the subsequent stressing of a strand in tendon #2. Errors in the load cell readings were investigated by checking each load cell periodically (between uses) in a Testmark compression testing machine to assess the calibration; both load cells exhibited the same response. Uneven loading during the load test was eliminated by noting that the measured change in tendon force as load is applied (the slopes of the lines) is nearly equal, indicating that each beam was loaded symmetrically. The cause of the 35 kip discrepancy was finally attributed to elastic losses caused by the performed stressing; the same stressing procedure was followed for both specimens.

Table 12-1 Unbonded tendon stress at ultimate

Specimen	Calc. per AASHTO-LRFD (ksi)	Obs. (ksi)	Obs./Calc.	Obs./ f_{py_actual}	Obs./ f_{pu_actual}
IWS	259*	229	0.88	0.91	0.82
IWC	263*	274	1.04	1.09	0.98
EWS - 1	236	229	0.97	0.91	0.82
EWS - 2	236	256	1.08	1.02	0.92
EWC - 1	243	195	0.80	0.77	0.70
EWC - 2	243	223	0.92	0.88	0.80

*Weighted, per simplified approach

Obs. = observed/measured during testing, Calc. = Calculated per AASHTO-LRFD (AASHTO 2014b)

f_{py_actual} = yield per strand material certifications, f_{pu_actual} = ultimate per strand material certifications

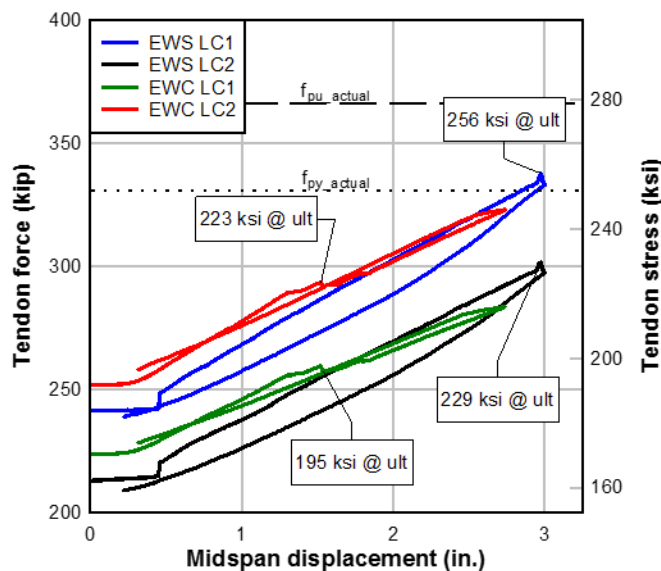


Figure 12-3 External tendon specimens: ultimate tendon force

In general, the statically tested specimens exhibited nearly the anticipated tendon stress at ultimate strength. Specimen EWC, however, did not exhibit the anticipated ultimate tendon stress in either tendon. It is hypothesized that the chosen loading regimen for EWC – which caused visually observable degradation of the concrete section at crack locations and may have contributed to the different failure mode observed vs. EWS – affected the ultimate tendon stress.

An unbonded beam, in general, typically reaches ultimate strength before the tendon stress reaches yield. This behavior was observed in specimens IWS, EWS, and EWC. In contrast with the expected behavior, and with specimen IWS, the tendon in specimen IWC did surpass the steel yield stress. The use of a constant moment region caused additional flexural cracking in IWC versus specimen IWS, which developed a single primary crack. The distributed cracking of IWC is indicative of distributed strain concentrations, with relatively lower peak strains per crack as the specimen deflected vs. IWS with one location of strain concentration, which limited IWS displacement at ultimate strength.

Closer inspection of the specimens with mixed tendons is warranted to understand the development of unbonded tendon stress under ultimate strength conditions (Figure 12-4). In both specimens IWS and IWC, the tendons exhibited similar behavior. Until each specimen overcame the precompression, the measured tendon stress remained at the effective tendon stress. At approximately an applied moment of 2515 kip-ft – corresponding to decompression of the specimen -- the tendons began to experience increasing tensile stress as the effective prestress was overcome. In both cases, the tendons experienced a similar rate of tendon stress increase. This behavior reflects the lack of strain compatibility between the concrete and the unbonded tendon. The change in tendon length due to the applied load is averaged over the entire tendon. At pre-cracking load levels, the change in tendon strain is low; post-cracking, significantly larger deformation occurs at the crack location and is transferred to the tendon, resulting in the change in slope seen in Figure 12-4.

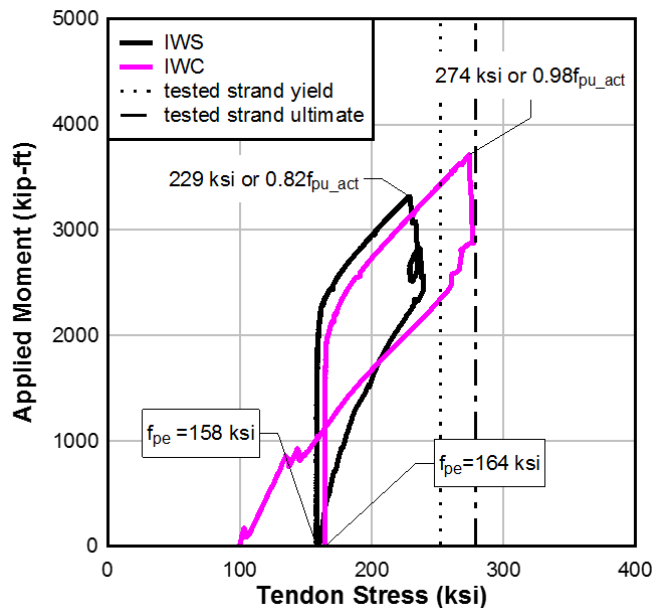


Figure 12-4 Internal tendon specimens: ultimate tendon stress

The ratio of measured-to-computed flexural strength of all specimens with flexible filler is given in Table 12-2; all calculations consider test-day material strengths. The strength of IGS was computed in accordance with AASHTO-LRFD provisions for flexural strength of bonded members using test-day material strengths. For the mixed tendon specimens, IWS and IWC, the AASHTO-LRFD flexural strength was calculated using AASHTO-LRFD provision 5.7.3.1.3, Equation 5.7.3.1.3b, which provides a simplified approach for an approximation of the ultimate tendon stress for members with mixed tendons. Flexural strength of unbonded specimens EWS and EWC was calculated with AASHTO-LRFD provisions for members with unbonded tendons (AASHTO-LRFD 5.7.3.1.2).

Table 12-2 Ratio of observed to AASHTO-LRFD flexural strength and f_{ps}

Specimen	Observed/AASHTO-LRFD	
	M_n	Unbonded f_{ps}
IGS	1.05	n/a
IWS	0.93*	0.88
IWC	0.98*	1.04
EWS - 1	1.26	0.97
EWS - 2		1.08
EWC - 1	1.06	0.80
EWC - 2		0.92

*per simplified approach for mixed tendons

Figure 12-5 presents a comparison of the ultimate tendon stress and ultimate flexural strength to that expected using the AASHTO-LRFD equations. A reference line at 1.0 indicates a perfect match between the predicted and observed behavior. The existing AASHTO-LRFD adequately predicted the flexural strength of the bonded specimen (IGS), mixed tendon specimen (IWC) and unbonded specimens (EWS and EWC); the AASHTO-LRFD simplified approach for members with mixed tendons, on the other hand, did not adequately predict the flexural strength of specimen IWS. While the AASHTO-LRFD also suggests a detailed analysis considering strain compatibility, the provision allowing for a weighted approach to determine the ultimate unbonded tendon stress and strength. In some cases, this weighted approach could lead to an overestimation of member strength. Further discussion of the behavior of members with mixed tendons is given in the following sections.

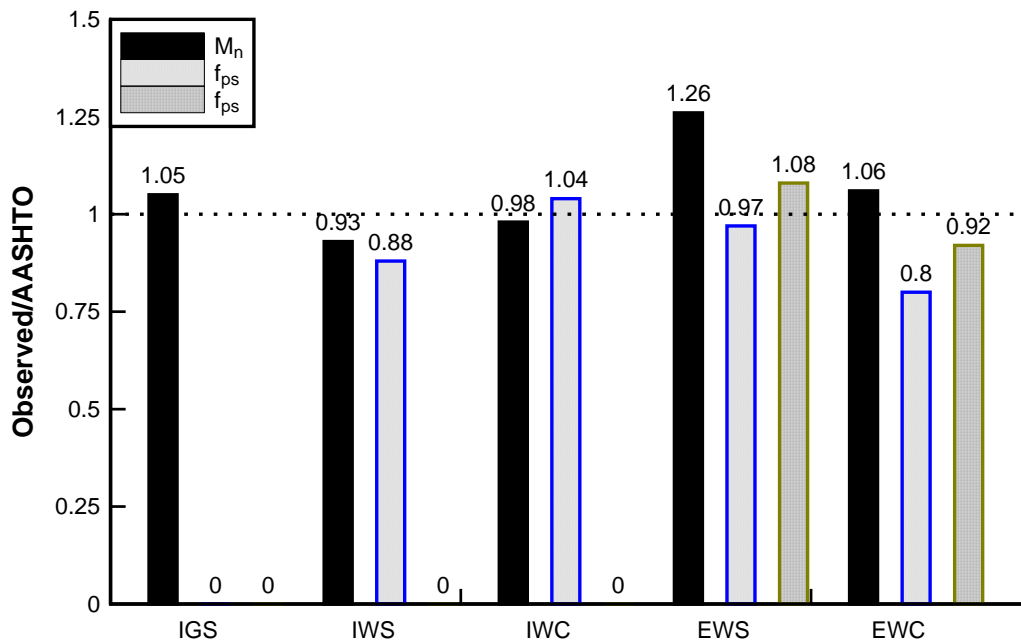


Figure 12-5 Ratio of observed to AASHTO-LRFD flexural strength and f_{ps}

12.2 Influence of Material Properties

Figure 12-6 presents three conceptual prestressing schemes. The first includes only bonded prestressed reinforcement, in which the prestressing is assumed to form a perfect bond with the concrete. The concentrated strain increases at crack locations result in localized yielding of the steel prior to reaching the limiting compressive strain of the concrete as illustrated by the stress plot below the beam. Although difficult to measure exactly, these localized points of yielded steel, taken together, are generally considered to define the hinge length. In contrast, members constructed entirely with unbonded reinforcement form a single crack at the point of maximum moment. The increase in strain caused by the crack opening would theoretically result in a uniform increase in strain over the entire length of the unbonded tendon. Since there is no localized yielding, the hinge length is concentrated at the single crack and is responsible for controlling the deformation of the member as loading increases; this is the least desirable behavior. If the two types of tendons are combined, however, cracking will be better distributed than the member with unbonded tendons alone, but perhaps have a shorter hinge length than the member with all bonded prestressing. Furthermore, the bonded prestressing and unbonded prestressing will almost certainly have different f_{ps} values at the ultimate flexural strength. The relative quantities of bonded and unbonded prestressing will dictate the size and influence of the hinge length.

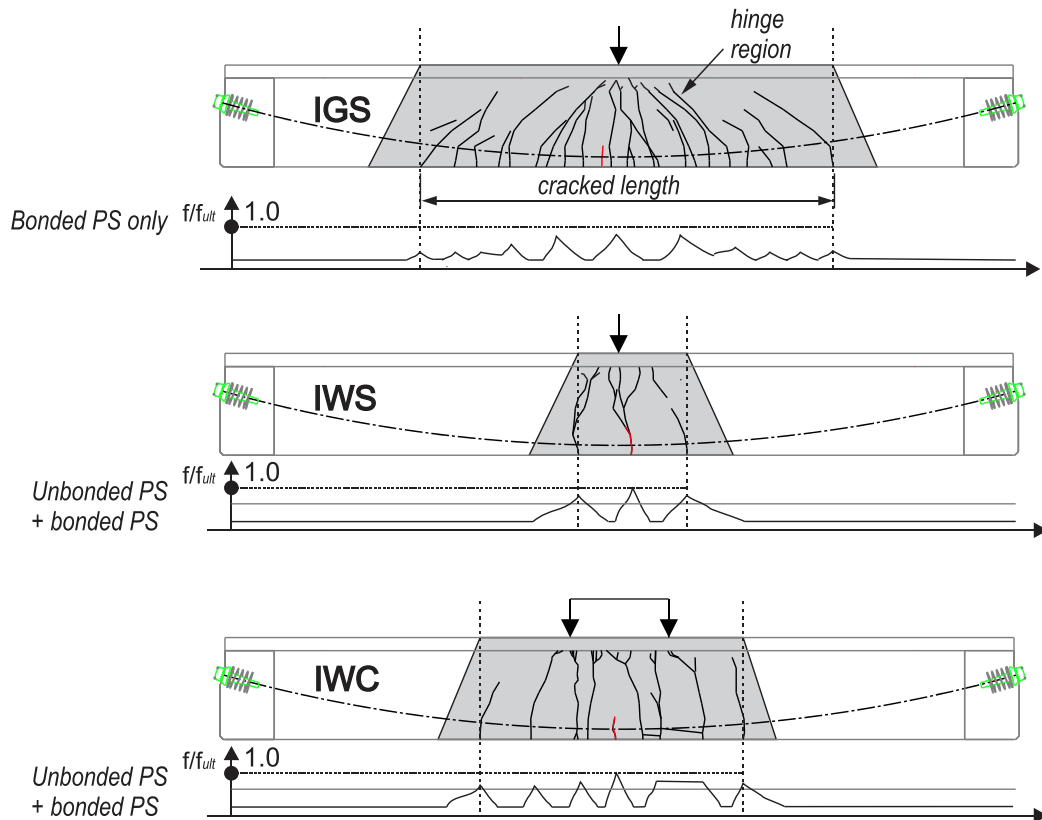


Figure 12-6 Tendon stress and hinge length for varying reinforcement combinations

For bonded prestressing steel in a precast girder combined with unbonded post-tensioning tendons, the bonded prestressing strands are subjected to concentrated strain increases at crack locations as would mild steel in combination with unbonded tendons. Two differences, however, impact the behavior: the steel grade and the prestrain due to prestressing. For the following discussion, commonly-used steel grades in bridge construction are considered: ASTM A615 Grade 60 for mild steel, and ASTM A416 Grade 270 prestressing strand.

The difference in rupture strain is significant to the ultimate strength behavior. Mild steel ruptures at strains greater than about 0.15 in./in., while prestressing steel ruptures at strains of approximately 0.06 in./in.—less than half. The implication is that mild steel rupture is unlikely to control the failure behavior; on the other hand, as observed in the testing of IWS and IWC, rupture of the prestressing steel is a possible failure mechanism and deserves consideration in members with both bonded and unbonded prestressed components.

While components with both unbonded prestressing and bonded mild (Gr. 60, typically) steel reinforcement provide some insight into members with mixed tendons, the use of bonded Grade 270 prestressing steel has several implications related to the characteristics of the material:

- Prestressing strand begins to yield (begins plastic hinge formation) at higher tendon stress versus mild steel, allowing greater overall beam displacement prior to steel nonlinearity;
- The rupture of prestressing strand occurs at a lower strain than the rupture of mild steel. As a result, members with mixed tendons have a lower rotational capacity compared to that expected of prestressed members with supplementary mild steel.

12.3 Hinge Rotation and Hinge Length

Hinge rotation limits the plastic behavior of all flexural members, whether they have only unbonded tendons, or if they have a combination of bonded and unbonded tendons. Ultimate strength is described through the maximum curvature, which was defined in Equation 20. Unlike an idealized hinge, which has unlimited rotation ability, the rotation of a hinge in a reinforced beam is controlled by the limiting strain of the constituent materials (Figure 12-7). Concrete compressive strains are limited to the crushing strain, while the tensile strain of the steel reinforcement is limited by the rupture strain. In previous investigations (by others) of unbonded tendons in which mild steel was considered, the rupture strain of the steel reinforcement was great enough that it was unlikely to control the hinge rotation.

In the examined cases of mixed tendons (internal PT tendons with bonded prestressing) – specimens IWS and IWC – the ultimate strength was controlled by the rupture strain of the bonded prestressing steel in the bottom flange, which predicated crushing of the deck concrete at midspan. In neither case did the unbonded tendon experience rupture, though specimen IWC did experience unbonded tendon yield.

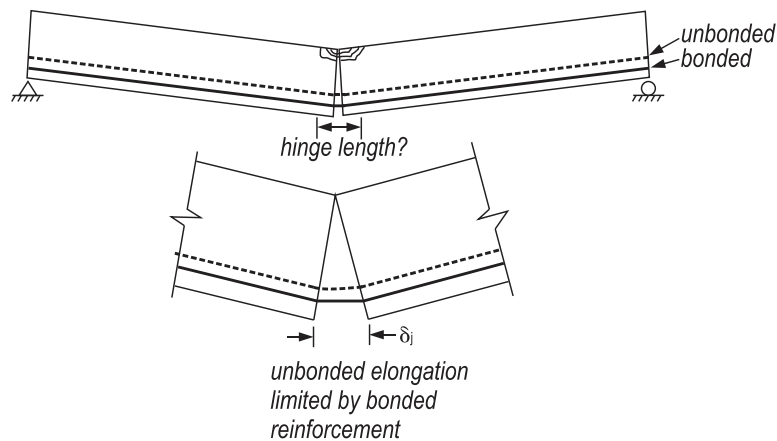


Figure 12-7 Tendon elongation at plastic hinge

Tendon elongation – and, by association, the ultimate tendon stress – at the hinge is a function of both the maximum curvature and the gage length, a.k.a. hinge length. The hinge length is defined as the length of the tensile steel undergoing elongation under the opening joint, and is dependent on the bond condition of the reinforcement. Figure 12-8 compares the hinge behavior for bonded members and unbonded members, respectively (MacGregor et al. 1989). The affected region – or gage length - of the bonded tendon is assumed to be limited to the joint opening plus twice the bond re-development length of the reinforcement. In contrast, an unbonded tendon experiences the stress increase along the length of tendon between attachment points (or anchors, in our case).

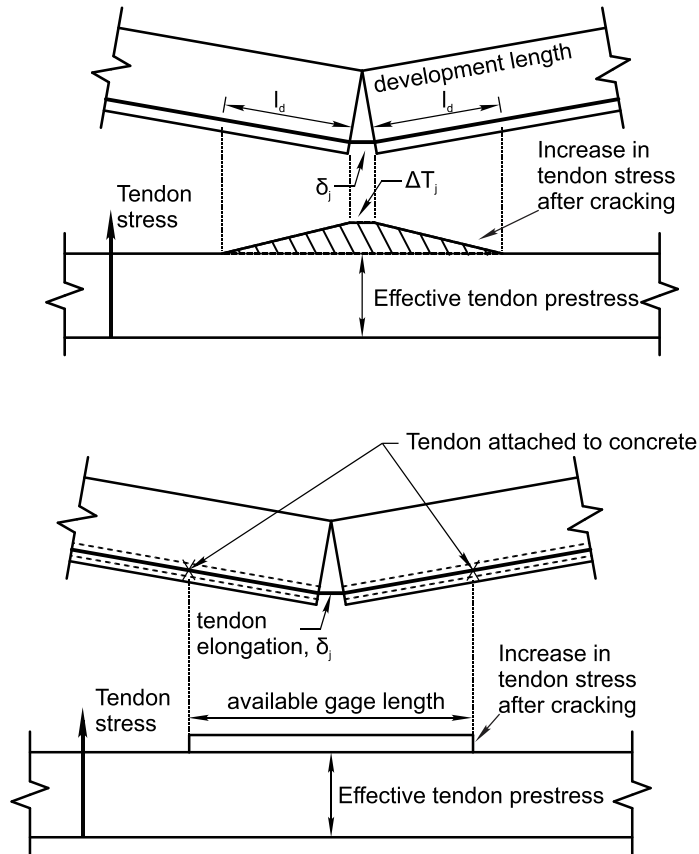


Figure 12-8 Tendon force increase: bonded vs. unbonded (MacGregor et al. 1989)

The length of the plastic hinge has been correlated to the depth of the neutral axis (Tam and Pannell 1976). From Equation 29, it can be seen that tendon elongation – and thereby development of unbonded tendon stress – is directly related to the hinge length. Assuming too long of a hinge would result in an overestimation of the tendon elongation, and an overestimation of the unbonded tendon stress and the member's ultimate flexural strength.

The increase in the unbonded tendon stress for lightly reinforced members with bonded mild steel or prestressing strands is effectively limited by the elongation of the bonded reinforcement over its hinge length.

Through examination of the experimental test specimens' behavior up to ultimate strength, the nuances of this theoretical behavior and the behavior of members with mixed tendons is further revealed. Displacement and ultimate strength of each tested specimen was controlled by the development of a hinge and locations of concentrated steel strain. Fully bonded specimen IGS exhibited well-distributed flexural cracking (typical of bonded prestressed beams); with further load application, the steel at each crack location was exposed to a concentrated strain increase. As the load on IGS increased, the cracking spread along the length of the beam, as the tensile strength of the concrete was overcome at multiple locations and new crack formation occurred until a stable cracked state (no new cracks formed, but existing cracks continued to lengthen) of the specimen was reached. Additional vertical displacement continued and at peak load, the deck crushed as specimen IGS experienced a ductile failure as the PS strand yielded prior to deck crushing. The spread distribution of cracks reduced the strain concentration

at any one crack, leading to a failure governed by the deck concrete's compressive strength, rather than by rupture of the prestressing strand.

In the ultimate load tests of mixed tendon specimens IWS and IWC, however, the opening of a primary crack under the load points – and exposure of the unbonded tendon - prevented additional flexural cracking, concentrating the strain of the bonded reinforcement to the primary crack location, which led to strand rupture prior to the compressive failure of the deck. Both specimens IWS and IWC experienced steel rupture of the bottom prestressing strand at the primary crack location (the crack observed to open widest) at ultimate strength (Figure 10-10; Figure 10-14).

The assumed hinge length – or the length of the reinforcement which undergoes plastic deformation – is key to the estimation of the ultimate unbonded tendon stress. Using Equation 5, the hinge length can be derived as a general term to be solved as a function of observed curvature and deflection:

$$\delta_h = \frac{4\Delta}{l_s} Z_p \quad \text{Equation 29}$$

Calculating the tendon elongation at the hinge:

$$\delta_h = \int_0^{l_{hinge}} \phi_m Z_p(x) \left(\frac{x}{Z_s} \right) dx \quad \text{Equation 30}$$

Assuming Z_p to be constant over the (assumed small) hinge length:

$$\delta_h = \phi_m \frac{Z_p}{Z_s} \int_0^{l_{hinge}} x dx \quad \text{Equation 31}$$

Solving the integral:

$$\delta_h = \phi_m \frac{Z_p}{2Z_s} l_{hinge}^2 \quad \text{Equation 32}$$

Combining and simplifying Equation 29 and Equation 33, the hinge length can be described as a function of the maximum curvature and ultimate deflection:

$$l_{hinge} = \sqrt{\frac{8\Delta}{l_s \phi_m}} Z_s \quad \text{Equation 33}$$

Based on the measured deck strain and measured tendon force during the ultimate load test, the maximum curvatures for the mixed tendon test specimens nearest the failure location were determined using Equation 33 and are given in Table 12-3; this estimate assumes the strain gage was positioned near the location of maximum concrete strain. The steel strain is determined as the rupture strain minus the prestrain (due to measured prestressing, considering losses); the rupture strain is assumed based on the observed failure mode of the test specimens. The hinge length at ultimate is calculated by Equation 33 using the measured deflection at ultimate. Z_s is approximated as the depth to the pretensioned bonded steel (59 in.); the tendon length, l_s , is 508 in. This estimation of hinge length is compared to that assumed for purely unbonded conditions ($2*Z_s$).

As in a fully unbonded case, the ductility and ultimate strength of members with mixed tendons (bonded and unbonded) are governed by the rotational capacity of the hinge region. The hinge length for the mixed specimens IWS and IWC was estimated two ways: 1) from inspection of the final cracking pattern and 2) from rigid body mechanics and measured strain and displacements. Both empirical estimations of the observed hinge length indicate AASHTO-LRFD overestimates the hinge length for the test specimens. While not explicit in AASHTO-LRFD equations, the derivation of the provided equations include an assumed hinge length of $2 \cdot Z_s$. A shorter hinge length assumption would better correspond to the observed behavior and predict a lower flexural strength. Figure 12-9 shows the final cracking patterns of IWS and IWC with an assumed compressive strut acting at 30° (instead of the currently assumed 45°).

Based on the test observations, ultimate strength determinations for mixed tendon members should be based on a hinge length less than $2 \cdot Z_s$, especially in cases with low quantities of bonded prestressing strand.

Table 12-3 Hinge by measured strain and deflection

Specimen	Measured concrete strain (in. ² /in.)	Steel strain (in./in.)	Measured Deflection (in.)	Calculated Curvature (rad·10 ⁻⁶ /in.)	Hinge length by Equation 33 (in.)	Equation 33/(2·Z _s)*
IWS	4200	0.06	2.9	1088	50	0.4
IWC	2600	0.06	5.5	1060	69	0.6

*AASHTO-LRFD assumed hinge length

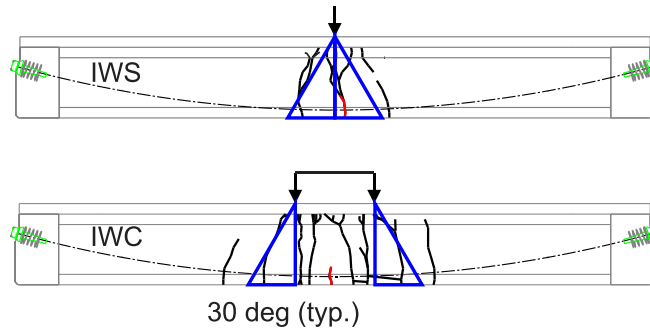


Figure 12-9 Thirty degree zone of influence

13 Fatigue Results and Discussion

This section describes the results of fatigue testing of specimens F1 and F2. The 6-strand PT tendon in F1 was constructed at an angle of 18 degree and F2 at an angle of 11 degree. Initial static loading results are described along with the details of the cyclic loading. Final static test results are also presented. Finally, details and results of deconstruction and individual strand testing are presented.

13.1 Initial Static Test

The results of the initial static test are shown in Figure 13-1. Both plots reveal bilinear relationships between the load applied to the specimen and the force recorded in the load cell under the PT tendon (Tendon Force). The bilinear plots reflect the change in specimen stiffness when the joint opens. The actuator force that corresponded to decompression for F1 was 81.5 kip and for F2 was 95.6 kip. The higher initial prestress force of F2 led to the specimen requiring more load for the gap to open. Some cracking occurred in the bottom of F1 due to the change in shear key alignment during loading. On F2, however, no cracks were observed following the gap closing. Loading and unloading plots created very small loops indicating that the hinge was generating very small resistance during cycling.

The static test results were used to determine the actuator force needed to achieve the upper (228.5 kip) and lower (213.4 kip) target tendon force. For F1, the initial actuator force range was determined to be 125 kip to 115 kip and for F2 the actuator force range was determined to be 120 kip to 109 kip.

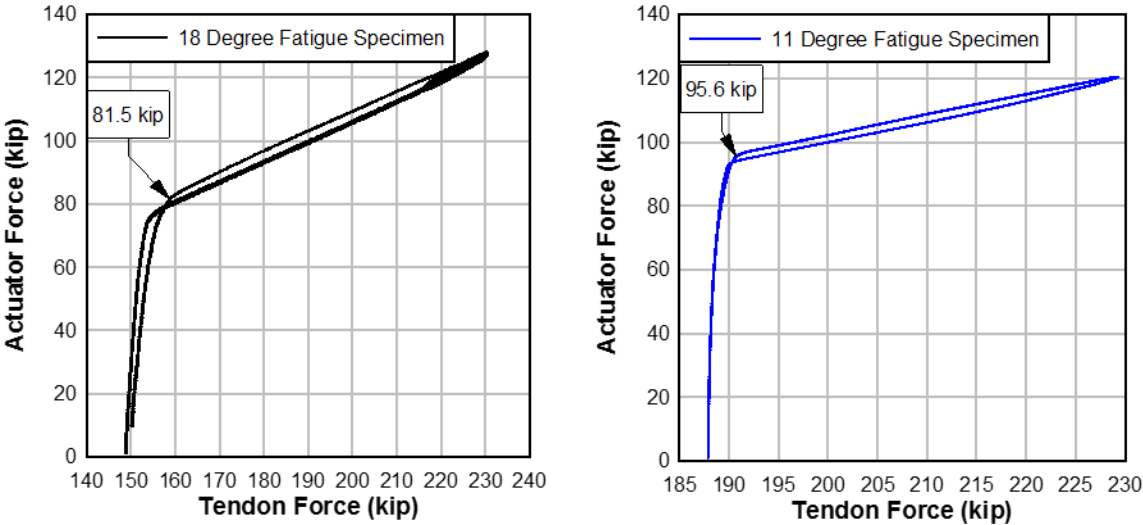


Figure 13-1 Initial static ramp test for both fatigue specimens

13.2 Cyclic Loading

F1 and F2 were tested for 2,090,000 cycles and 2,000,000 cycles, respectively. Of interest was the effect that tendon force cycling would have on fretting fatigue and duct wear, if any (Figure 13-2).

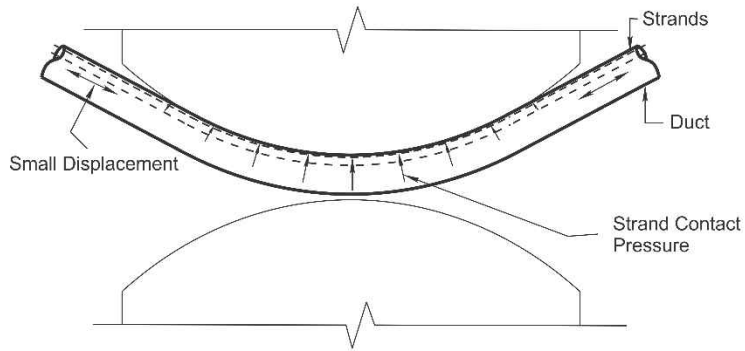


Figure 13-2 Strand and duct contact during cyclic loading

13.2.1 Specimen F1

Cyclic loading for F1 was done for 25 days continuously and stopped at 2,090,000 cycles. At approximately 1 million cycles displacement, gage D2 malfunctioned and the cyclic loading was paused to replace both displacement gages. At cycle 1,280,000 the experiment was paused to attach hydraulic hoses for an unrelated test.

Gap displacement was measured for the entirety of the cyclic loading process and is compared to the average actuator force in Figure 13-3. The average actuator force was calculated using the mean value between the maximum and minimum actuator forces during cyclic loading.

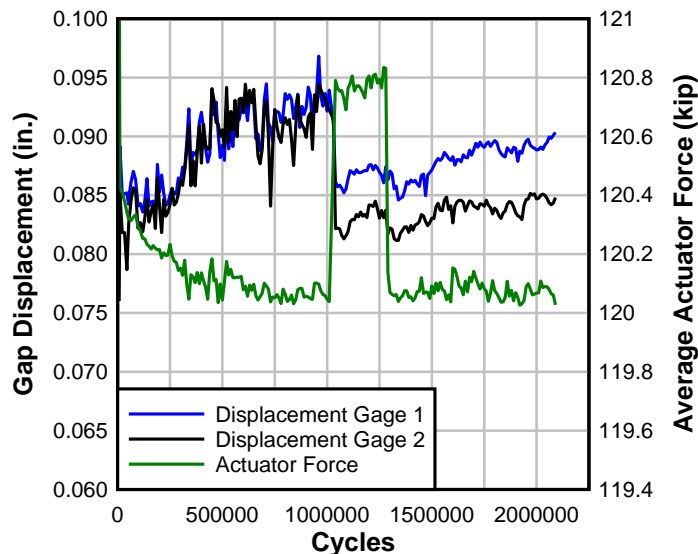


Figure 13-3 Gap displacement and actuator force for F1

A target tendon force range of 15.1 kip for the 6-strand tendon, corresponding to an 11.6 ksi stress range, was maintained during cyclic loading. Tendon force was read directly from the hollow-core load cell and the actuator force was adjusted to maintain the upper and lower tendon forces of 228.5 kip ($0.65f_{pu}$) and 213.4 kip ($0.607f_{pu}$) respectively. Average actuator force would be adjusted if the tendon force range fell below 14.5 kip but that was not necessary for this specimen. Stress range measured during cycling are shown in Figure 13-4 and Figure 13-5.

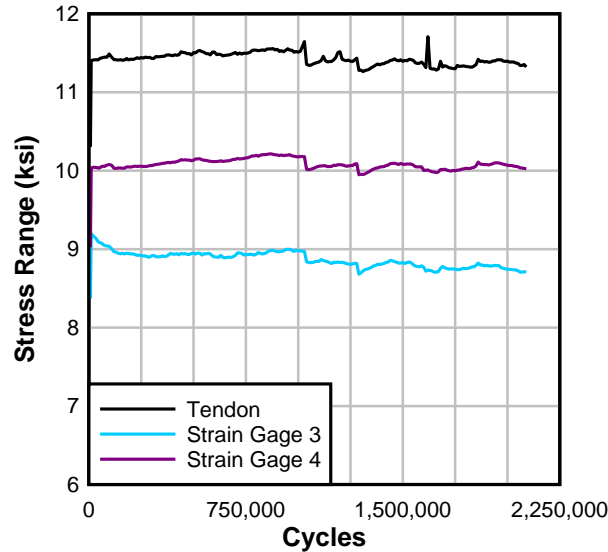


Figure 13-4 Stress range results during cyclic loading for F1

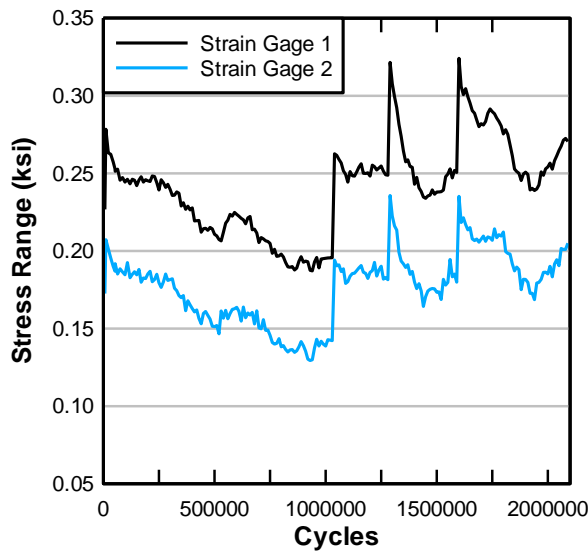


Figure 13-5 Stress range results for strain gage 1 and 2 for F1

Load ranges for strands at the dead end near the actuator was 13 kip and 11.5 kip for the duration of cyclic loading. The load range at the live end of the specimen, however, was much lower at around 0.25 kip and 0.35 kip. Fretting fatigue and HDPE pipe wear at the dead end is more likely in that region due to the expected higher contact pressure between strands and also between the HDPE pipe and the strands.

Mean tendon force was determined as the average tendon force during cycling. Mean tendon force varied closely with daily temperature change (Figure 13-6) as ambient temperature rose the tendon force increased and as temperature dropped it decreased. A rise in ambient temperature will heat both concrete and tendon, but the tendon would be expected to heat more quickly, causing an apparent tendon relaxation and a decrease in tendon force. It is suspected, however, that the filler and HDPE acted as an insulator for the strands causing less of a

temperature variation from ambient temperature conditions. As ambient temperature rose the concrete specimen expanded more quickly than the tendon, which caused tendon elongation, thus increasing tendon force. As ambient temperature dropped the concrete specimen contracted and caused tendon relaxation, thus lowering tendon force. The tendon experienced an overall drop in force by the end of cycling, which would be due to prestressing losses over time caused by further wedge seating and strand relaxation. Neither the diurnal heating, nor the time-dependent losses are considered to have affected the testing adversely.

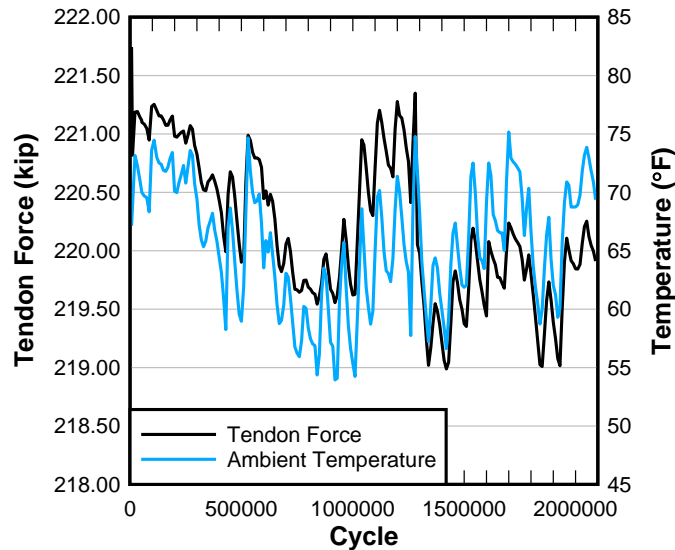


Figure 13-6 Mean tendon force and ambient temperature for F1

13.2.2 Specimen F2

Cycling of F2 was conducted for 23 days continuously. F2 had its actuator forces adjusted at cycles 678,000 and 1,272,000 due to the tendon force range dropping below 14.5 kip.

Gap displacement and actuator force (Figure 13-7) were measured continuously during cyclic loading. Displacement measurements were taken at 3.25 in. below the bottom of the beam, which amplified the gap opening readings. The gap opening of specimen F2 were adjusted using the specimen geometry to obtain the actual gap displacement.

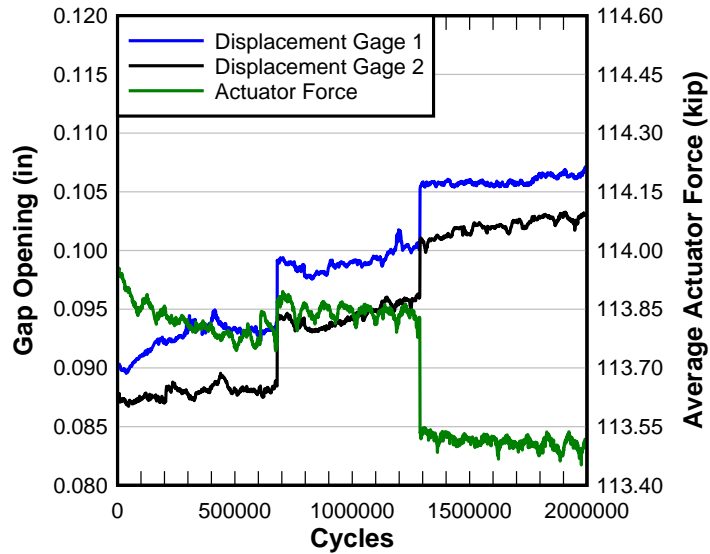


Figure 13-7 Gap displacement and actuator force for F2

Upper and lower tendon forces were maintained similarly to F1 in section 13.2.1. Unlike F1, however, stress range decreased with cycling (Figure 13-8). The average actuator force was adjusted once the tendon force range dropped below 14.5 kip. After the first adjustment at 678,000 cycles, the stress range decreased more gradually but continued for the entirety of cycling.

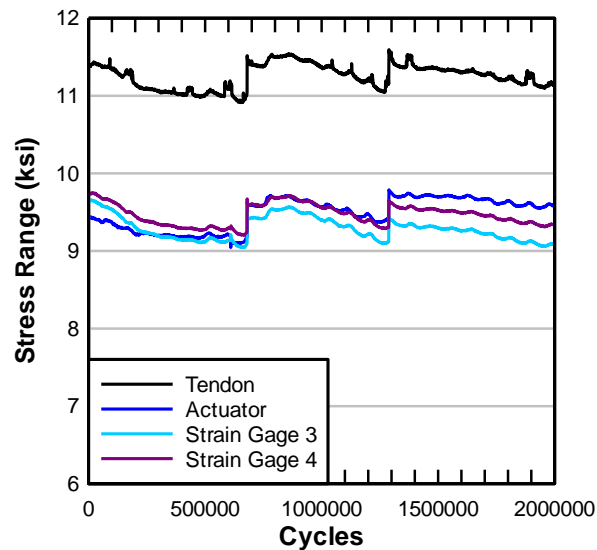


Figure 13-8 Stress range results during cyclic loading for F2

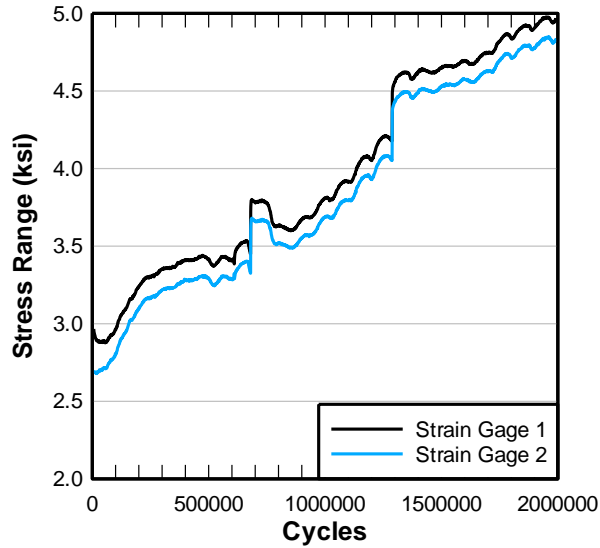


Figure 13-9 Stress range using readings from strain gages 1 and 2 for F2

Decreasing stress range on the dead-end side of the deviator (Figure 13-8) corresponded to an increase on the live-end side (Figure 13-9). It is apparent that the smaller deviation angle of F2 resulted in a reduction of friction force at the deviator, which allowed a commensurate incremental tendon slip to occur across the deviator during cycling. It is not clear why the stress range on the live-end side increased steadily over the entire fatigue test. One possibility is that the strand movement over the HDPE may have caused a slight reduction in friction coefficient, which increased the “leakage” of tendon force across the deviator. Mean tendon force for F2 was determined as it was for F1 in section 13.2.1. Mean tendon force varied with ambient temperature similar to that of F1 (Figure 13-10).

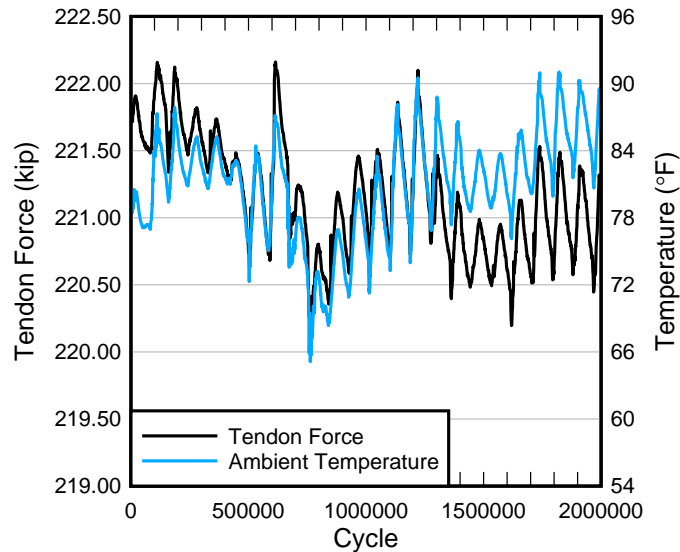


Figure 13-10 Mean tendon force and ambient temperature for F2

13.3 Final Static Test

Following cyclic loading a final static test with three load ramps were performed for both fatigue specimens (Figure 13-11). At the end of cyclic loading, F1 had a final prestress value of 144.7 kip with an overall prestress loss of 4 kip; F2 had a final prestress value of 185 kip with an overall prestress loss of 3 kip. The actuator force corresponding to decompression moment for F1 was 79 kip while F2 had an actuator force of 94.7 kip for its decompression moment. Following the final static tests each specimen was detensioned and prepared for tendon removal and specimen disassembly.

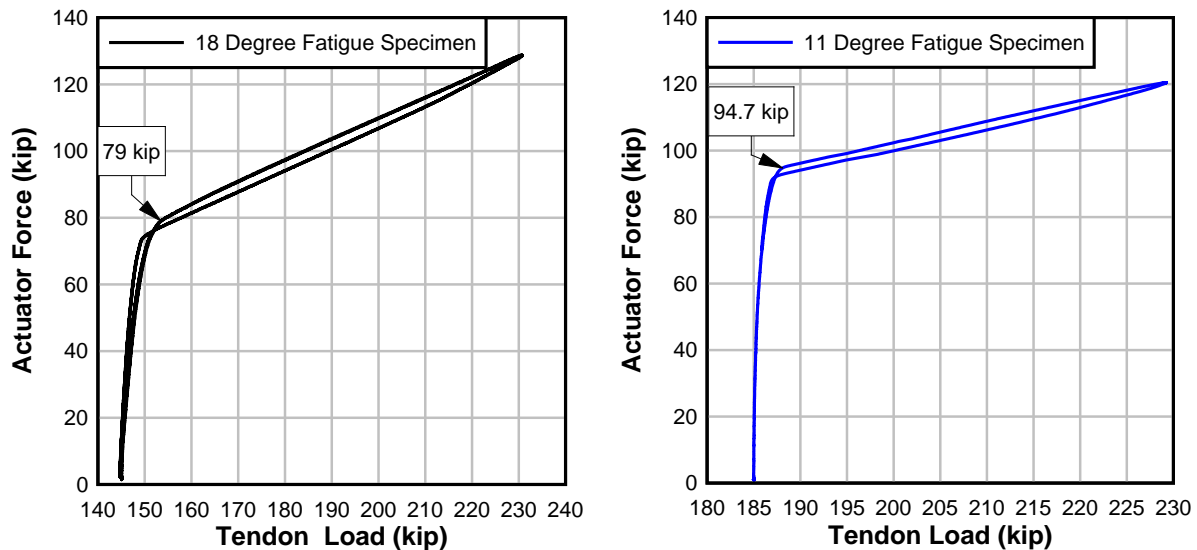


Figure 13-11 Final static ramp test for both fatigue specimens

13.4 Specimen Dissection

This section covers the inspection of and test results for the prestressing strands, wedges, and HDPE pipe recovered from the fatigue specimens, including tensile testing of the strands.

13.4.1 Fatigue Specimen F1

F1 tendon was detensioned at the live end in the opposite order it was stressed, starting with strand 6 and ending with strand 1. The tendon force readings (Figure 13-12) were taken during the entire detensioning procedure. The tendon was removed for inspection upon completion of detensioning (Figure 13-13).

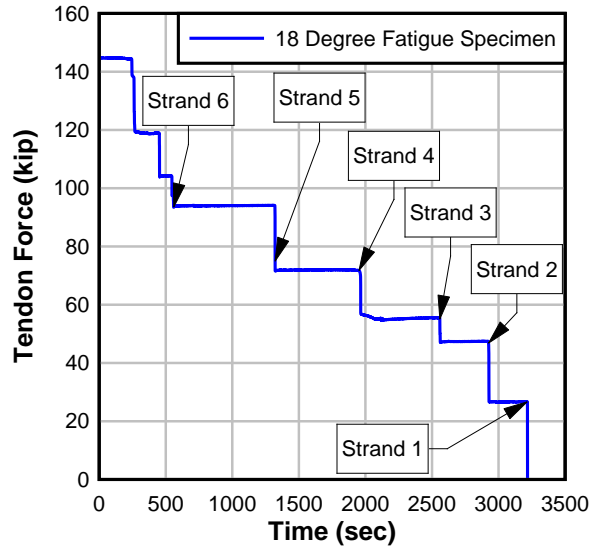


Figure 13-12 Tendon force during detensioning for F1



Figure 13-13 Dissection of F1 (a) detensioning and (b) tendon removal

Following tendon removal, specimen F1 was separated and inspected for damage. The deviator exit at the dead end was of interest due to spalling that occurred when the formwork was removed. No observable degradation of the specimen, however, was noted during the inspection. The concrete repair (Figure 13-14) was inspected and remained intact at the end of cyclic loading with signs of minor wear.



Figure 13-14 Concrete repair for specimen F1 at the end of cyclic loading

The mechanical hinge was lubricated at the start of the cyclic loading and only moderate wear was visually noted following the fatigue test indicating that the hinge had performed its intended purpose for this experiment by providing smooth, relatively friction-free rotation during the cyclic loading (Figure 13-15 and Figure 13-16).



Figure 13-15 Mechanical hinge post-dissection – dead end segment



Figure 13-16 Mechanical hinge post-dissection – live end segment

Following removal of the strand bundle, the HDPE pipe section that passed through the deviator was cut and removed. The section was cut into 2 in. sections that were inspected for internal damage caused by strands and external wear caused by the concrete. The pipe thickness at the deepest groove for each section was measured (Figure 13-17, Figure 13-18). The portion of duct close to the deviator dead-end lost approximately 40% of its original thickness, which was the most significant. The thickness loss at the opposite end, however, was minimal with a loss of approximately 12% of its original thickness. The duct appeared to have experienced a highly localized damage or “pinching” at the dead-end exit of the deviator.

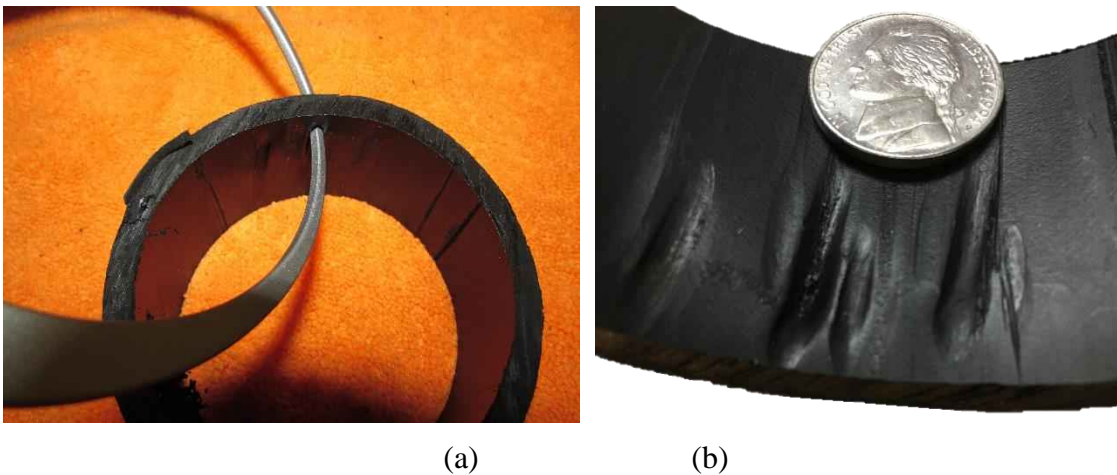


Figure 13-17 HDPE pipe section from F1 near south deviator exit (a) measurement of groove depth (b) pipe wear.

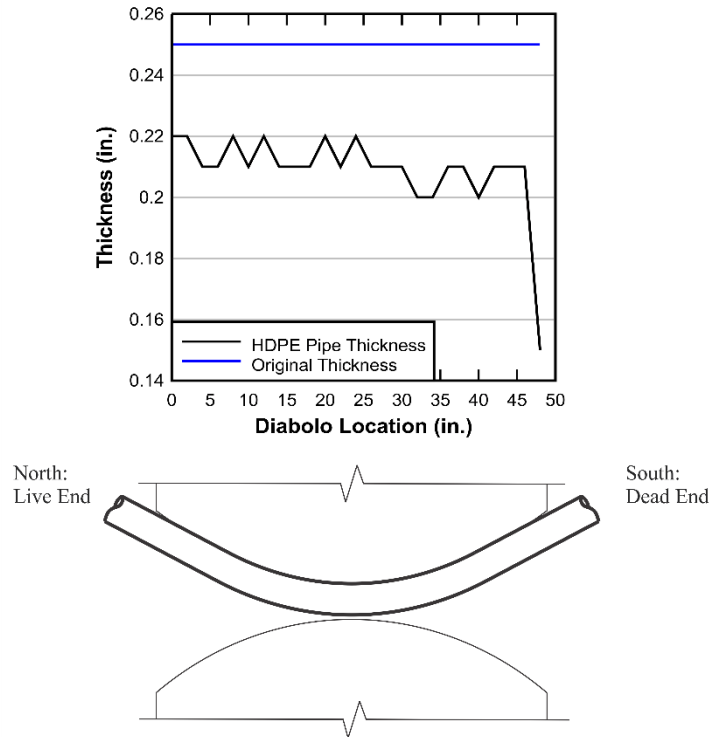


Figure 13-18 HDPE pipe thickness along length of deviator for F1

It is theorized that the pinching (Figure 13-19) was due to lack of clearance between concrete and duct at the exit point of the duct. This creates an abrupt tendon angle change leading to a stress concentration. The higher stress concentrations due to pinching led to significant duct wear, which was about three times deeper than the live end. This only occurred at the south end of the deviator for this specimen. It is not clear why the pinching did not occur at the opposite end of this deviator or on specimen F2. One possibility is that the deviator form insert was misaligned during construction; extra attention was placed on the construction of specimen F2 to ensure there would be no misalignment. This location was repaired after construction due to spalling that occurred as the diabolo form insert was being extracted, which could have contributed to the problem. Because the other deviator exit locations did not exhibit this behavior, it is concluded that the geometry selected for the diabolo was adequate. Nevertheless, providing additional flare curvature beyond that provided for this design would allow more tolerance for misalignment during construction. Furthermore, inspection of the deviator would be prudent prior to tendon installation to ensure that pinching does not occur.



(a)



(b)



(c)

Figure 13-19 HDPE pipe at deviator corner (a) live end (b) dead end (c) pinched duct at dead end

Wedges were inspected at the end of cyclic loading (Figure 13-20) and displayed typical hairline longitudinal cracks from the strand seating process. No signs of fatigue damage were found on the wedges.

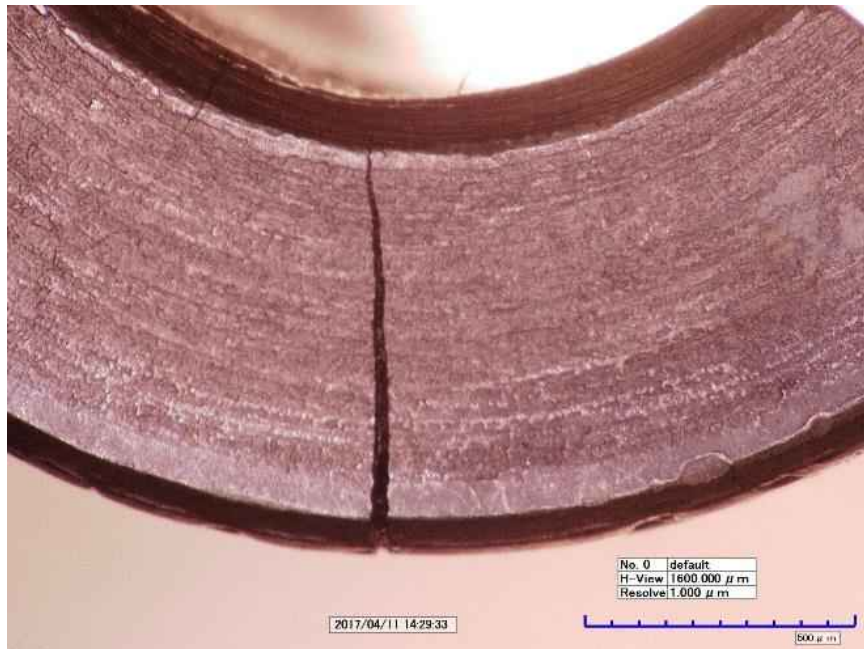


Figure 13-20 Wedge inspection post-cyclic loading for specimen F1

Impressions on the prestressing strands from wedge serrations were visually inspected under a 40× microscope. The strands had evenly spaced ductile impressions with no cracking at the corners, indicating successful wedge seating (Figure 13-21). Wedge impressions gradually lengthened from the front of the wedge and maintained a consistent width before tapering to a shorter length near the wide portion of the wedge (Figure 13-22).

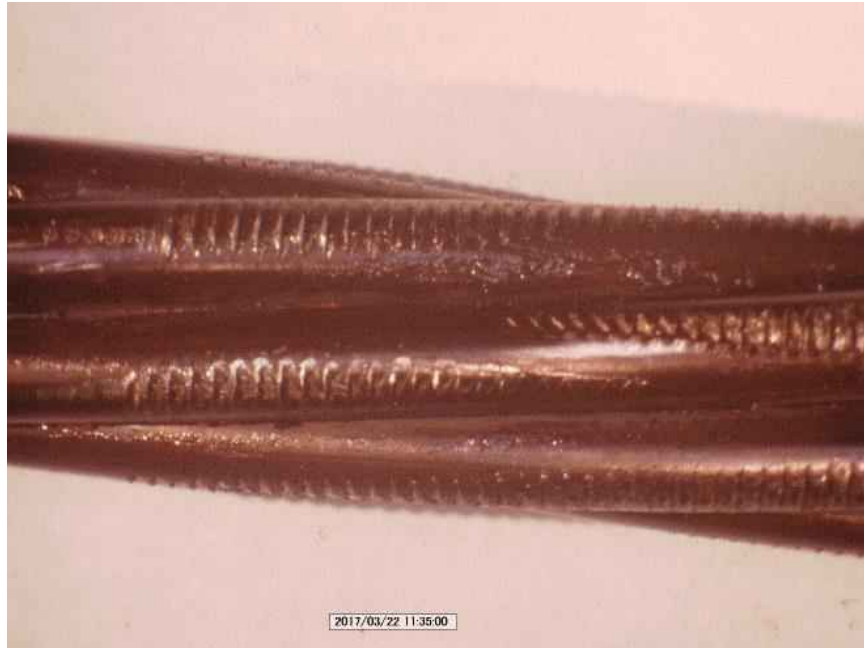
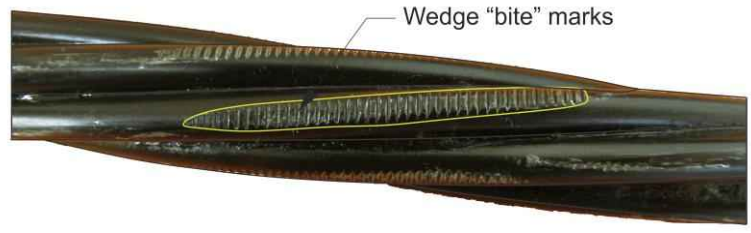
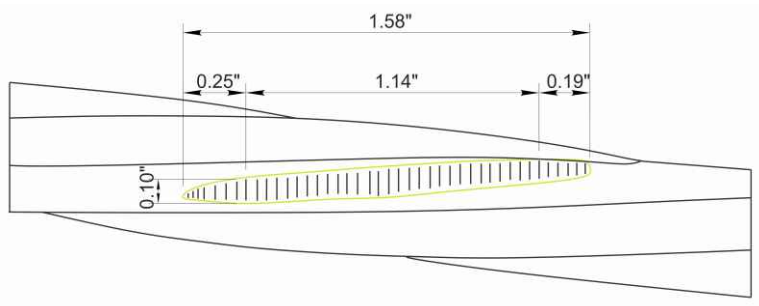


Figure 13-21 Wedge serration impressions on strands following cyclic loading



(a)



(b)

Figure 13-22 Wedge “bite” marks specimen F1 (a) image of marks (b) schematic of marks

13.4.2 Fatigue Specimen F2

F2 was detensioned in the same manner as F1. Tendon force readings were continuously taken and the results of the detensioning are shown in Figure 13-23. The tendon was completely removed once detensioning was completed (Figure 13-24).

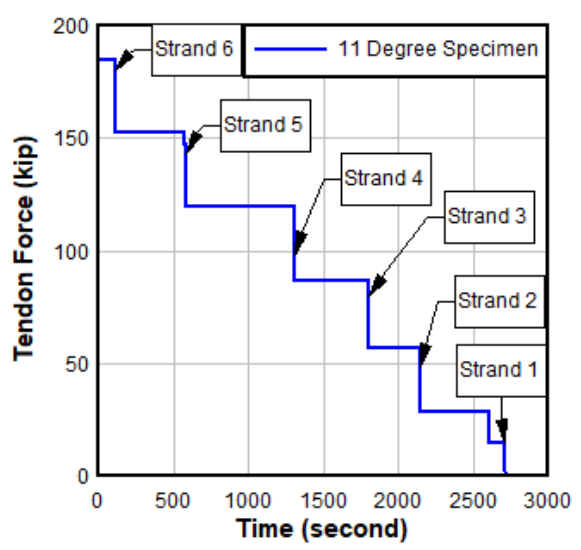


Figure 13-23 Tendon force during detensioning for F2



Figure 13-24 Tendon removal from F2

The HDPE pipe section located inside the deviator of F2 was removed for dissection and inspected for wear. The pipe was cut into 2-in. lengths and the thickness at the deepest groove for each piece was measured (Figure 13-25). The strands contacted the pipe 6 in. into the deviator from the live end side and contacted the pipe 4 in. in the deviator from the dead end side. The maximum thickness loss was 16% of the original pipe thickness, which occurred at approximately 16 in. from each end of the deviator and away from the midpoint. This is confirmed by visual observation of the duct at those two locations (Figure 13-26).

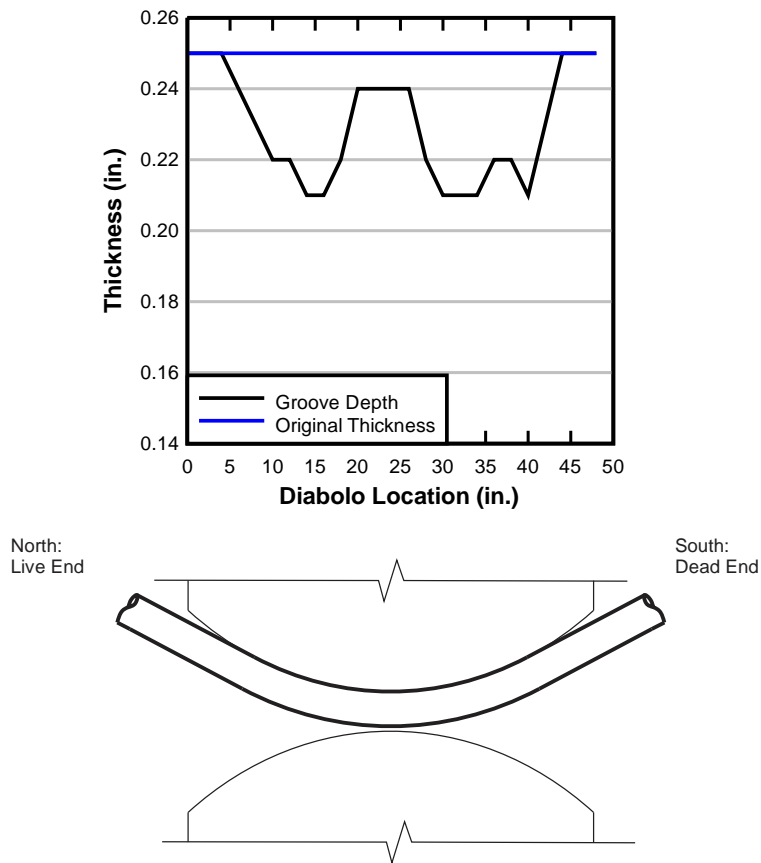


Figure 13-25 HDPE Pipe Thickness along length of deviator for F2

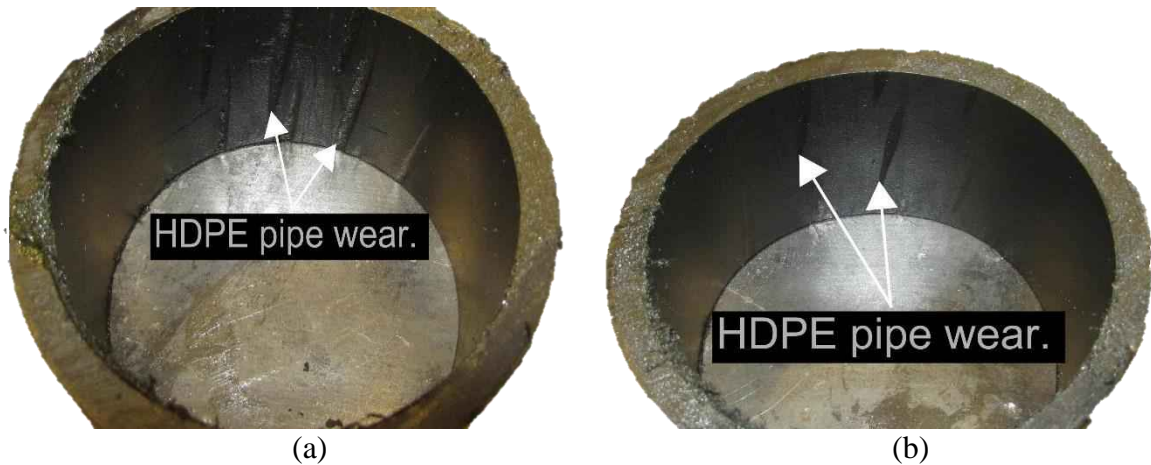


Figure 13-26 F2 HDPE damage at (a) point of maximum groove depth and (b) at midpoint of deviator

Strands and wedges were removed from the wedge plates similar to F1. Results similar to those noted in F1 were found. Impressions from wedge serrations appeared to be relatively uniform with no fatigue cracks apparent. Only the typical longitudinal fractures were noted in the wedges.

13.4.3 Strand Tensile Strength Tests

Obtaining a quantitative measure of fretting fatigue was done by performing tensile strength tests on portions of the strands from both specimens along with control strands for comparison. The samples were 6 ft in length and included the 4 ft deviator section (Figure 13-27) to ensure the likely region that fretting fatigue would occur was included in the tensile tests. Samples included the high stress region directly below the mechanical hinge and the low stress region at the opposite end of the deviator.

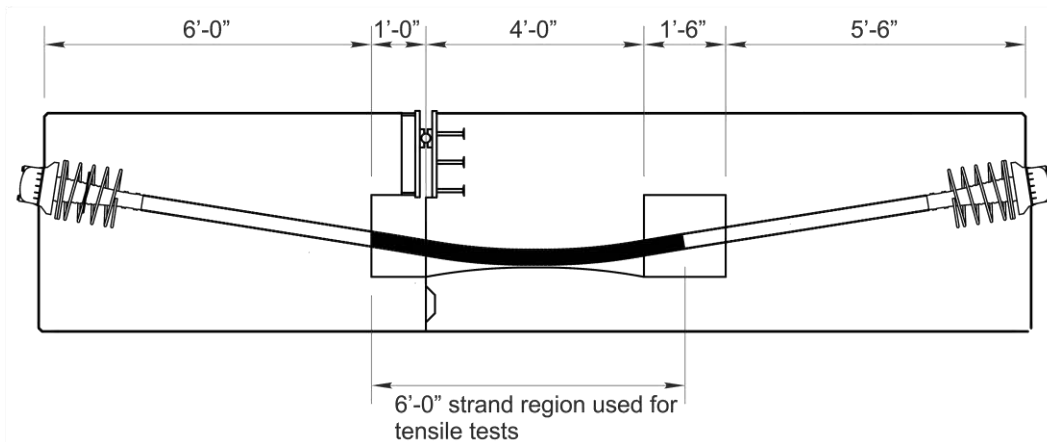


Figure 13-27 Strand sampling location for tensile tests

The strength tests were based on ASTM A416 minimum requirements for 0.6-in. Grade 270 low-relaxation seven-wire strands (Table 13-1) and results were also compared to the steel manufacturer certification values (Table 13-2).

Table 13-1 Minimum 0.6-in. strand requirements for ASTM A416

Strand Properties	
Diameter of Strand	0.6 in.
Nominal Area	0.217 in. ²
Minimum Breaking strength (MUTS)	58.60 kip
Yield Strength Requirement (\geq)	52.74 kip
Elongation (\geq)	3.50%

Table 13-2 Steel certification results from manufacturer

Strand Properties	
Diameter of Strand	0.6 in.
Actual Area	0.2191 in. ²
Ultimate Breaking Strength (MUTS)	62.72 kip
Yield Strength (1% Extension)	56.88 kip
Ultimate Elongation	5.47%

Test results are shown in (Table 13-3). The control results indicate that the prestressing strand used in the fatigue test initially met the strength and ductility requirements of ASTM A416. As shown in Figure 13-28, necking with a cup/cone fracture surface was observed in the individual wires, indicating a ductile failure mode.

Table 13-3 Summary of tensile test results for strands

Strand ID	Yield Strength		Breaking Strength		Elongation	Pass/Fail	Failure Mode
	kip	%MUTS	kip	%MUTS			
c-1	55.4	94.5	63.2	107.8	6.9%	Pass	Free Length, 1 wire break
c-2	54.4	92.8	62.8	107.2	7.2%	Pass	Free Length, 3 wire breaks
1-1	-	-	62.6	106.8	-	Pass	Grip, 3 wire breaks
1-2	-	-	62.8	107.2	-	Pass	Grip, 1 wire break
1-3	-	-	62.6	106.8	-	Pass	Grip, 1 wire break
1-4	-	-	62.4	106.5	-	Pass	Free Length, 7 wire breaks
1-5	-	-	62.4	106.5	-	Pass	Grip, 1 wire break
1-6	-	-	62.6	106.8	-	Pass	Grip, 7 wire breaks
2-1	-	-	62.8	107.2	-	Pass	Free Length, 2 wire breaks
2-2	-	-	52.0	88.7	-	Fail	Grip, 7 wire breaks
2-3	-	-	62.6	106.8	-	Pass	Free Length, 3 wire breaks
2-4	-	-	54.0	92.2	-	Fail	Grip
2-5	-	-	62.4	106.5	-	Pass	Free Length, 2 wire breaks
2-6	-	-	55.2	94.2	-	Fail	Grip, 3 wire breaks

MUTS = Minimum Ultimate Tensile Strength

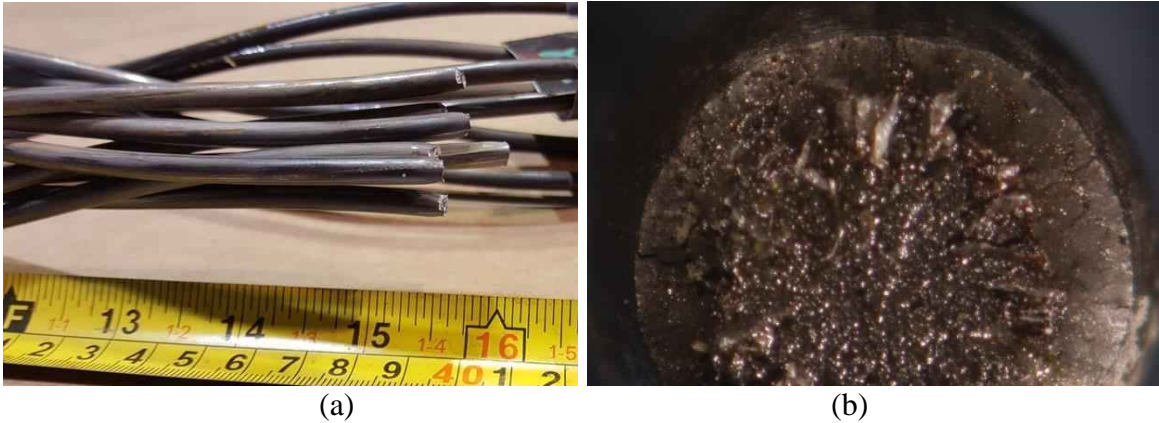


Figure 13-28 Fracture surfaces of control specimens (a) c-2 (b) magnified fracture surface

Strands from specimen F1 (18-degree tendon deviation angle) all experienced ductile failure modes (Figure 13-29) and satisfied ASTM A416 strength and ductility requirements. The average breaking strength was 62.6 kip, which was 106.5% of the minimum ultimate strength. Fretting fatigue is dependent on the slip amplitude; if the slip is too small or too large there will be no fretting fatigue. The larger tendon deviation angle of this specimen appears to have provided sufficient friction force between the deviator and tendon to prevent the strands from slipping at a magnitude that might generate fretting fatigue.



Figure 13-29 Specimen F1 strand ductile failures after tensile tests

Tests results on three of the six strands from specimen F2 (11-degree tendon deviation angle), however, did not satisfy the strength requirements of ASTM A416. These strands exhibited the classic fingernail-shaped brittle fracture surface (Figure 13-30). The fractures may have been generated by fretting based on signs of abrasion that were observed near the initiation point of the fracture. The location of the abrasion makes strand-to-strand contact the likely cause. It is thought that the smaller tendon-deviator force due to the lower tendon angle caused sufficient friction force reduction such that the strand slip led to fretting fatigue. Strands that experienced a brittle failure had a loss in ultimate tensile strength of 12% - 20%. Brittle failure of the strands occurred near the hinge location, which is where most of the strand elongation occurred during cycling (Figure 13-31).

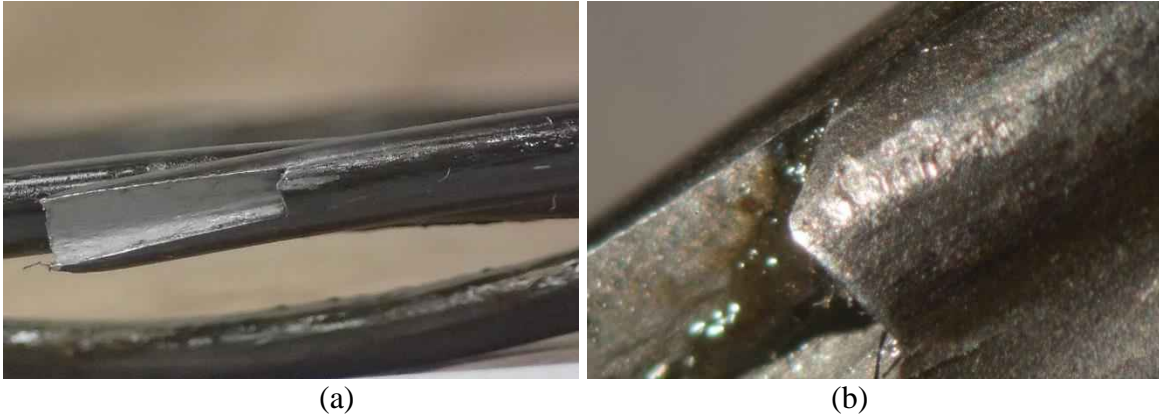


Figure 13-30 Specimen F2 strand brittle failure (a) fretting fatigue (b) close-up of fracture due to fretting

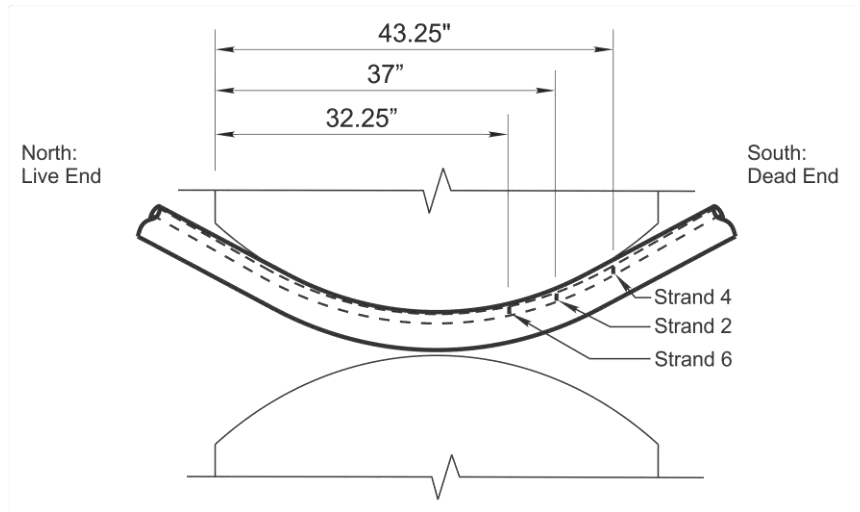


Figure 13-31 Specimen F2 strand fracture locations

13.4.4 Strand Slip

Under static load conditions, the post-tensioning tendon imposes a normal force on the deviator. If the tendon stress on one side of the deviator is increased, then the static frictional force between the deviator and tendon must be exceeded before stress is transferred to the opposite side of the deviator. In terms of deformation, strand slip occurs at the point when the frictional forces preventing the tendon movement is overcome by the stress difference across the deviator (Figure 13-34). Tendons with a larger prestressing force or tendons with larger deviation angles, or both, create a larger friction force, which requires a larger stress range to overcome and cause strand slip.

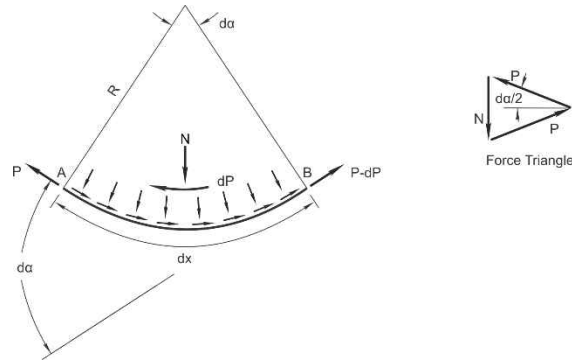


Figure 13-32 Forces on a short tendon segment at a deviator

The unit frictional force is a function of the friction coefficient and curvature as follows:

$$\frac{dP}{P} = \mu d\alpha \tag{Equation 34}$$

where

dP is the force difference in the tendon on opposite sides of the deviator

P is the prestress force

μ is the curvature friction coefficient

During cycling, the strain readings in the tendon on the opposite side of the hinge were very small (<0.3 ksi) for F1 (Figure 13-5) while they were substantial (3 ksi to 5 ksi) for F2 (Figure 13-9). Following the cyclic loading, the specimens were statically loaded; tendon strain readings from a portion of this loading are shown in Figure 13-33. The plots are focused on the point in the static loading where the slopes change significantly. The slope change for S3/S4 is due to the gap opening and the slope change in S1/S2 is due to the point at which the strands slip relative to the deviator. The difference in tendon force at the point of slip is equal to the force required to overcome the frictional force as illustrated on the plot. The plots were used to determine the tendon force and frictional force at the point of slip (Table 13-4).

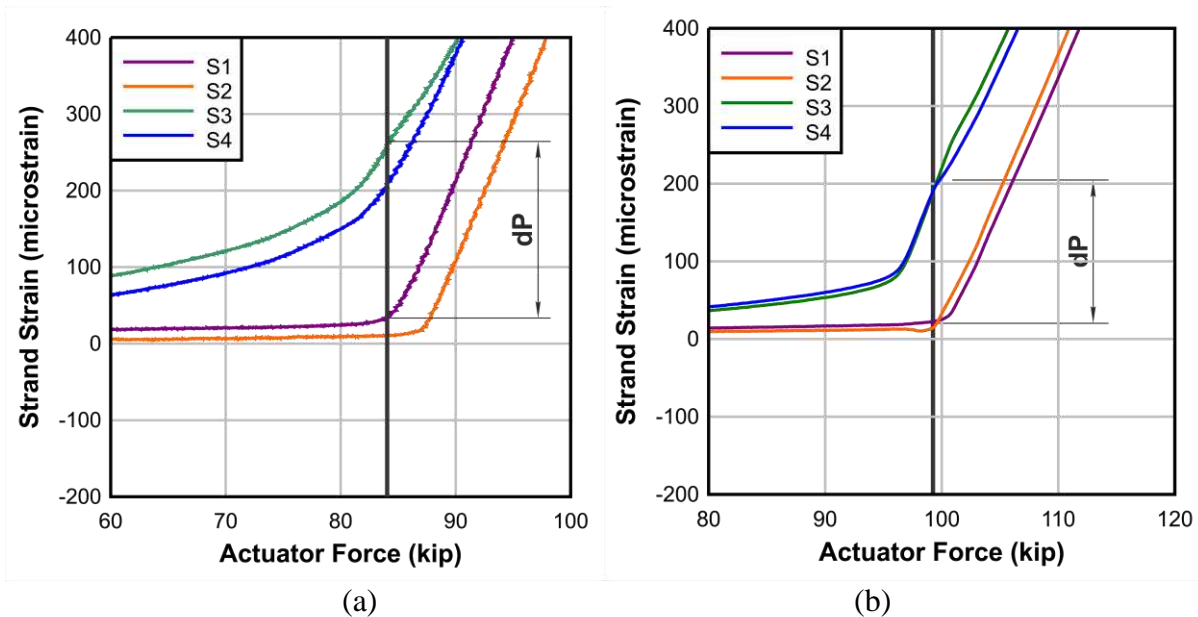


Figure 13-33 Stress difference when tendon slip occurs (a) Specimen F1 (b) Specimen F2

Table 13-4 Strand slip results for both specimens

Specimen	Angle change, $d\alpha$ (deg)	Slip stress (ksi)	Force difference, dP (kip)	Tendon force at slip, P (kip)
F1	18	5.823	7.58	161.97
F2	11	4.931	6.42	195.23

The amount of deformation required in the specimen to generate the target tendon stress range was quite large. This is demonstrated by the gap opening of approximately 0.1 in. that was measured during the load cycling. Given that post-tensioned bridges are typically designed to avoid cracking under service load conditions, the possibility of generating the kind of deformation associated with this fatigue test seems remote.

To investigate this notion, strand slip in a prototype segmental bridge with external tendons was analyzed for fatigue loading (Figure 13-34). The prototype modeled a 135-ft span single-cell segmental box girder. The cross-section is 35-ft wide by 7-ft deep and contains six external PT tendons with (27) 0.5 in. strands each. The deviation angles of the tendons are 8.5, 6.9 and 5 degrees. The model was formed with frame elements to simulate the box girder section and truss members to simulate the tendons. Rigid deviator elements were used to connect the tendons to the box girder using the prototype geometry; truss elements were rigidly fixed to the deviators. A single lane fatigue truck was positioned in a number of locations to maximize the difference in tendon force across several of the deviators. No other loads were considered in the analysis.

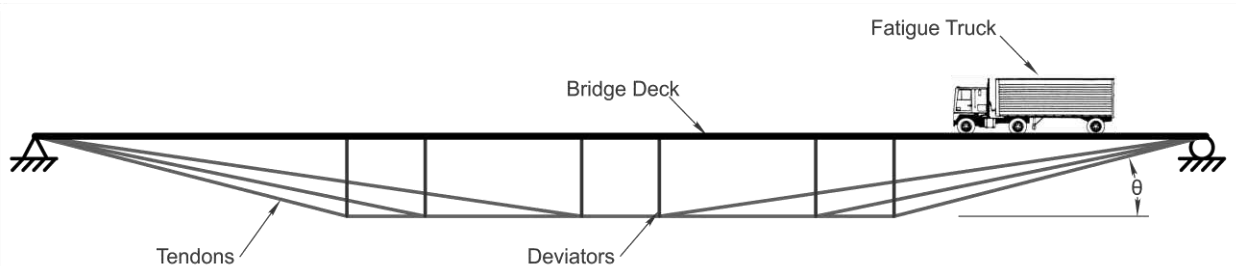


Figure 13-34 Structural bridge model for strand slip investigation

The results are plotted in Figure 13-35 for comparison with the results of the fatigue tests. For any given deviation angle, the linear regression line for the test data represents the static friction force, that, when exceeded, will result in tendon slip relative to the deviator.

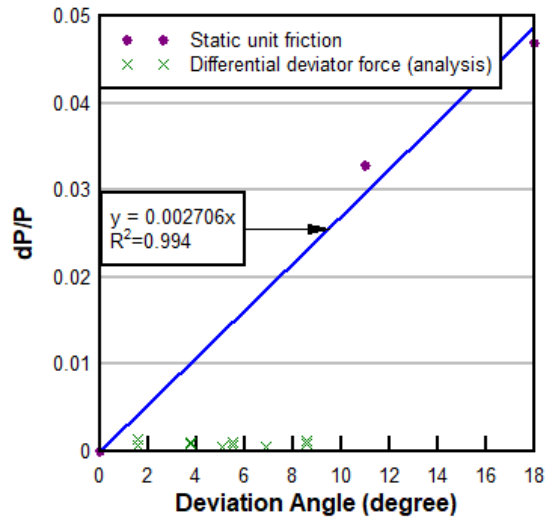


Figure 13-35 Unit tendon friction variation with deviation angle

Clearly the results from the analysis indicate that the differential forces that develop across a deviator is relatively small and is not likely to generate slip and the accompanying fretting that may occur as a result. The key assumption here, though, is that the section remains uncracked under fatigue truck loading. If cracking is allowed, then the differential will increase drastically and could result in slip and potential fretting.

14 Summary and Conclusions

This report covers Tasks 2, 3 and 4 of the “Replaceable Unbonded Tendons for Post-Tensioned Bridges” FDOT Project BDV31-977-15, which was comprised of static and fatigue load testing of full-scale structural specimens. Five 40-ft long I-girder beams – three beams with an internal parabolic 12-strand tendon and two beams with a pair of externally deviated 6-strand tendons – were post-tensioned, injected with filler material, and load tested. Two fatigue specimen were constructed and utilized to conduct a series of fatigue tests. This report covers the specimen design and construction, laboratory testing, and post-mortem inspection. Tendon replacement was also performed on one internal tendon specimen and is described herein.

Conclusions:

- The flexural strength of members with external unbonded tendons with flexible fillers was adequately predicted by AASHTO-LRFD (AASHTO 2014b) for unbonded tendons.
- The hinge length in mixed tendon specimens (with internal tendons), as estimated from inspection of the final cracking patterns, was found to be less than that assumed in the formulation of the unbonded tendon stress prediction equation given in AASHTO-LRFD (Section 5.7.3.1.2).
- Unbonded tendon stress at ultimate flexural strength is dependent on the effective prestress. A reasonable estimation of effective prestress is required to ensure an accurate prediction of ultimate flexural strength.
- Unbonded tendon stress at ultimate flexural strength is dependent on the global deformation patterns and geometry of the entire member.
- As in a fully unbonded case, components with mixed tendons (bonded and unbonded), the ductility and ultimate strength are governed by the rotational capacity of the hinge region.
- Ultimate flexural strength in specimen IWC and IWS were controlled by bonded strand rupture. This phenomenon limited the available increase in unbonded tendon stress for mixed tendons and the ultimate flexural strength.
- For single point loading, concentrated loads in mixed tendon members with low quantities of bonded steel, the observed hinge length was approximately d , the depth of the section, and did not match AASHTO-LRFD assumption ($2*Z_s$). It is likely that the hinge length will vary as the ratio of bonded and unbonded tendons vary.
- The simplified approach given in AASHTO-LRFD was insufficient to predict flexural strength for in one tested specimen with mixed bonded and unbonded reinforcement. Particular care should be taken with low quantities of bonded reinforcement.
- Up to 20% reduction in ultimate tensile strength of prestressing strands was noted in the fatigue specimen with a tendon deviation angle of 11 degrees. Brittle fracture patterns were noted that appear to have been induced by strand-to-strand fretting. The tensile strength of the prestressing strands in the fatigue specimen with the 18 degree deviation angle exceeded the minimum ultimate tensile strength requirement.
- Threshold friction curvature coefficients were determined for the deviators and were compared to an analysis of a prototype bridge. The analysis indicated that the differential force across the deviators were well below those required to cause slip in the fatigue specimens.

- Duct damage was noted at one of the deviator exit locations that was the result of the strands pinching the HDPE wall against the concrete. Because the other deviator exit locations did not exhibit this behavior, it is concluded that the geometry selected for the diabolo was adequate and that the damage may have been caused by diabolo misalignment. Providing additional flare curvature beyond that provided for this design would allow more tolerance for misalignment during construction. Furthermore, inspection of the deviator would be prudent prior to tendon installation to ensure that pinching does not occur.
- Strands were installed parallel in both fatigue specimens, which provides the ideal case that is practically unattainable in the field. Future work should examine the effect of twisted strand on the fatigue resistance of the tendons.

Based on the performed testing and the available literature, it is recommended that design of members with mixed bonded and unbonded reinforcement include a detailed analysis considering global deformation behavior and strain compatibility between the concrete section and the bonded reinforcement; in lieu of a detailed analysis, a modification to the simplified approach given in AASHTO-LRFD is warranted, based on testing conducted in this project.

As of the completion of this research, little code guidance is available to address the use of mixed tendons. The existing AASHTO-LRFD provisions considering mixed tendons were evaluated using the simplified approach. Comparison of AASHTO-LRFD provisions for members with mixed bonded and unbonded components versus experimentally and analytically determined ultimate strength and unbonded tendon stress reveals an overestimation by the code, leading to moderately unconservative predictions of ultimate strength and the unbonded tendon stress in one test specimen. Members with mixed reinforcement were found to exhibit behavior different from fully bonded and fully unbonded systems. Further investigation of the parameters influencing the ultimate strength of mixed tendon members is warranted, as is more expansive guidance within the structural codes.

References

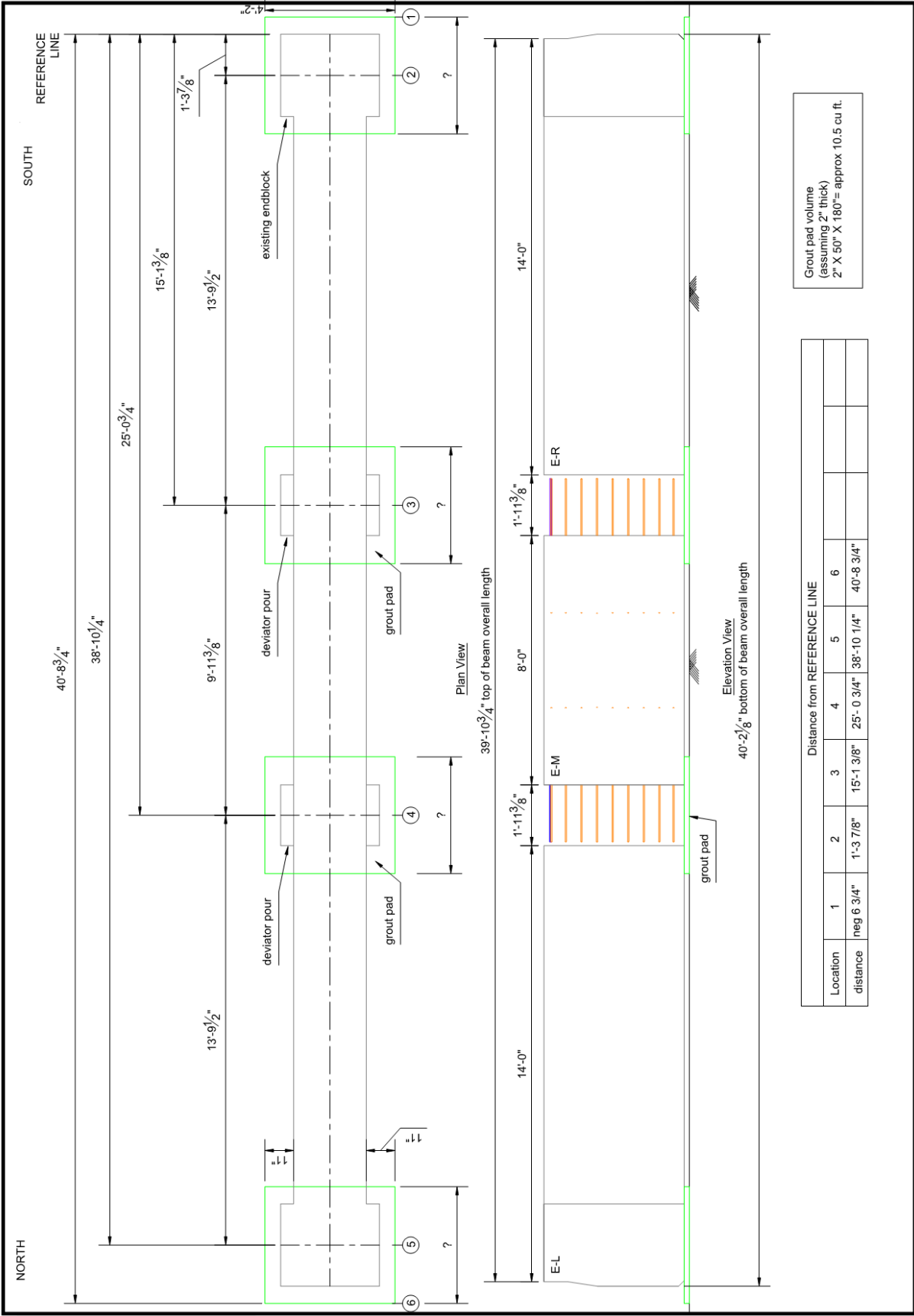
- AASHTO. (2014a). AASHTO-LRFD Bridge Construction Specifications (3rd edition with 2014 interim revisions). American Association of State Highway and Transportation Officials, Washington D.C.
- AASHTO. (2014b). AASHTO-LRFD Bridge Design Specifications (6th edition with 2014 interim revisions). American Association of State Highway and Transportation Officials, Washington D.C.
- ACI 318-14 (2014). Building Code Requirements for Structural Concrete (ACI318-14) and Commentary. American Concrete Institute, Farmington Hills, MI.
- ACI 358. (1986). "Analysis and Design of Reinforced Concrete Guideway Structures", ACI Journal, Sept.- Oct., pp. 862-866.
- Bill, R. C. (1981). "Fretting Wear of Iron, Nickel, and Titanium Under Varied Environmental Conditions." NASA TM-78972, National Aeronautics and Space Administration.
- Bill, R. C. (1982). "Review of Factors That Influence Fretting Wear," Materials Evaluation Under Fretting Conditions. ASTM STP 780. American Society for Testing and Materials. pp. 165-182.
- Brondum-Nielson, T. (1973). "Effect of Grouting on the Fatigue Strength of Post-Tensioned Concrete Beams," IABSE Final Report, Vol. 14, 1973.
- Burns, N.H. and Hemakom, R. (1985). "Test of Post-Tensioned Flat Plate with Banded Tendons." Journal of Structural Engineering, ASCE, V. 111, No. 9. pp.1899-1915.
- Cordes, H., and Lapp-Emden, H. (1984). "Untersuchung zur Dauerfestigkeit von Spanngliedern für die besonderen Bedingungen der teilweisen Vorspannung (Investigation of the Fatigue Strength of Tendons in Partially Prestressed Concrete Structures)," Report 18/84, Institut für Massivbau, Technical University Aachen, June 1984 (original in German; referred to information reported by Wollmann et al. 1988).
- Diab, J.G. (1988). "Fatigue Tests of Post-Tensioned Concrete Girders", Unpublished M.S. Thesis, The University of Texas at Austin, Dec. 1988.
- FDOT (Florida Department of Transportation) (1994). Channel 5 Bridge Construction Drawings, FDOT, Tallahassee, FL.
- FDOT. (Florida Department of Transportation (2002). "New Direction for Florida Post-Tensioned Bridges," FDOT, Tallahassee, FL.
- FDOT (Florida Department of Transportation) (2008). US19/US98 Bridge Construction Drawings, FDOT, Tallahassee, FL.

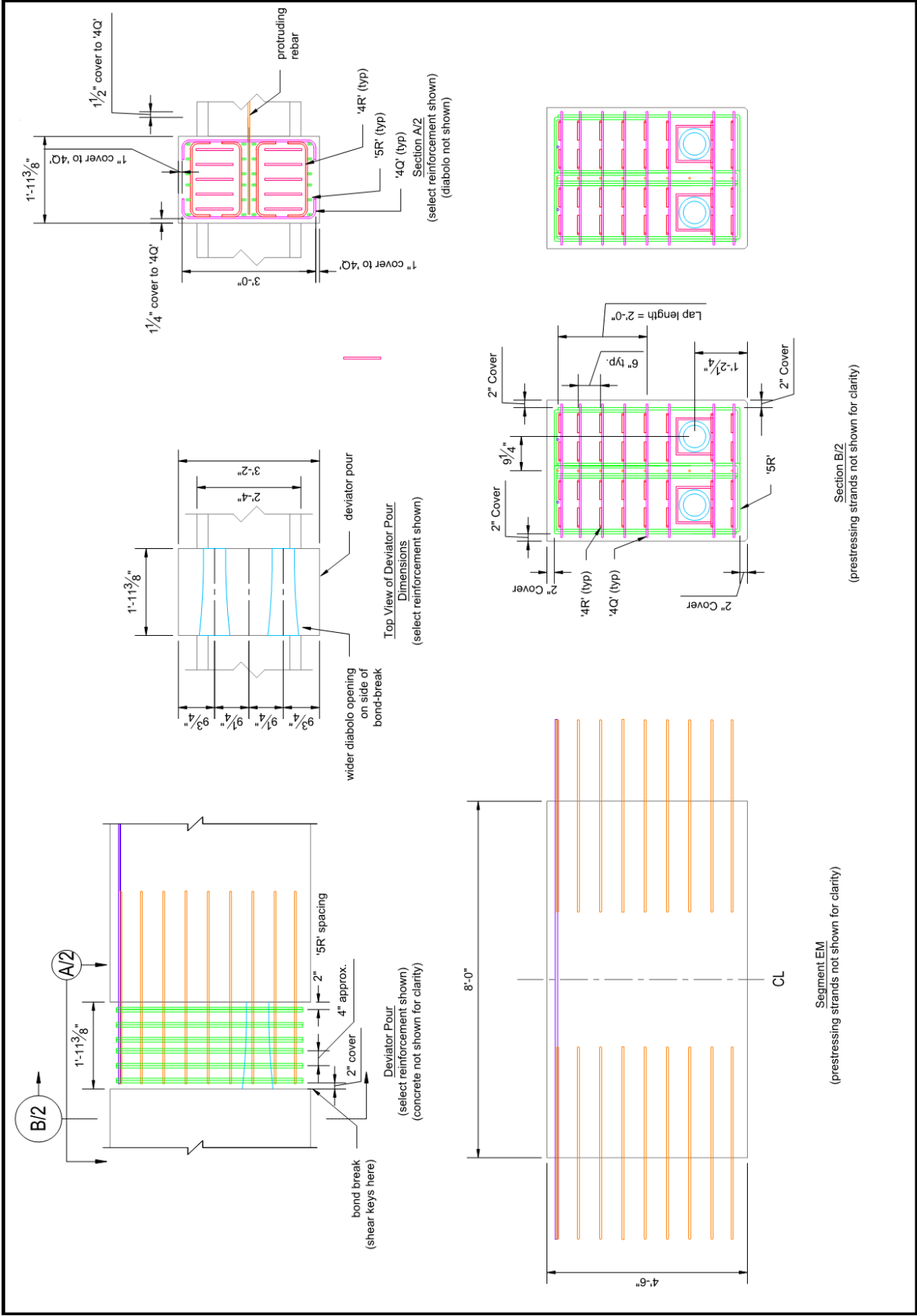
- FDOT (Florida Department of Transportation) (2014). FDOT Structures Design Bulletin 14-06. (2014). Issued April 30, 2014. FDOT, Tallahassee, FL.
- Gauvreau, D. P. (1992). "Load Tests of Concrete Girders Prestressed with Unbonded Tendons," Report No. 194, Institute of Structural Engineering ETH Zurich, Birkh ser Publishers, 239 pp.
- Georgiou, T.P. (1989). "A Study of Fretting Fatigue in Post-Tensioned Concrete Beams." Unpublished M.S. Thesis, The University of Texas at Austin, Aug. 1989.
- Gerber, L.L., and Burns, N.H. (1971). "Ultimate Strength Tests of Post-Tensioned Flat Plates." PCI Journal. 16(6). Nov-Dec 1971. 40-58.
- Hall, C.R. (1990). "Development of Test Apparatus for Examining the Fretting Fatigue in Post-tensioned, External Tendons in Box Girder Deviator Ducts." Unpublished M.S. Thesis, The University of Texas at Austin, Dec. 1990.
- Harajli, M. H. (2006). "On the Stress in Unbonded Tendons at Ultimate: Critical Assessment and Proposed Changes," *ACI Structural Journal*; Farmington Hills Vol. 103, No. 6, pp. 803-812.
- Harajli, M. H. (2012). "Tendon stress at ultimate in continuous unbonded post-tensioned members: Proposed modification of ACI 318, eq. (18-4) and (18-5)." *ACI Structural Journal*, 109(2), 183-192.
- Kasan, J., and Harries, K. A. (2011), "Redevelopment of Prestressing Force in Severed Prestressing Strands". ASCE Journal of Bridge Engineering.
- Kosut, G.M., Burns, N.H., and Winter, C.V. "Test of Four-Panel Post-Tensioned Flat Plate." ASCE Proceedings, ASCE, 111(9), Sept 1985. 1916-1929.
- MacGregor, R. J. G., Kreger, M. E., and Breen, J. E. (1989). "Strength and Ductility of a Three-span Externally Post-Tensioned Segmental Box Girder Bridge Model." Center for Transportation Research Report No. 365-3F, University of Texas at Austin, 323 pp.
- Mackie, K. R., Elie, A., El Zghayar, and Haber, B. Z. (2011). "External Post-tensioning Anchorage"
- Megally, S. H., Garg, M., Seibel, F., Dowell, R. K. (2002). "Seismic Performance of Precast Segmental Bridge Superstructures." Structural Systems Research Project, University of California, San Diego. Research Report No. SSRP-2001/24.
- Mietz, J., Burkert, A., and Eich, G. (2006). "Investigations on the Protection Effect of Filling Materials for Post-tensioning Systems under Construction Conditions."
- Mojtahedi, S., and Gamble, W. L. (1978), "Ultimate Steel Stresses in Unbonded Prestressed Concrete."

- Muller, H.H. (1986), "Fatigue Strength of Prestressing Tendons," *Betonwerk und Fertigteiltechnik*, December 1986, pp. 804- 808. (original in German; referred to information reported by Wollmann et al. 1988)
- Naaman, A. E., and Alkhairi, F. M. (1991a). "Stress at Ultimate in Unbonded Prestressing Tendons—Part I: Evaluation of the State-of-the- Art." *ACI Structural Journal*. V. 89, No. 5. Sept.-Oct. pp. 641-651.
- Naaman, A. E., and Alkhairi, F. M. (1991b). "Stress at Ultimate in Unbonded Prestressing Tendons—Part II: Proposed Methodology." *ACI Structural Journal*. V. 89, No. 6. Nov.-Dec. pp. 683-692.
- Naaman, A. E., Burns, N., French, C., Gamble, W. L., and Mattock, A. H. (2002). "Stresses in Unbonded Prestressing Tendons at Ultimate: Recommendation." *ACI Structural Journal*. V. 99, No. 4. Jul.-Aug. pp. 518-529.
- Oertle, J., Thurlimann, B., and Esslinger, V. (1987). "Versuche zur Reibermüdung einbetonierter Spannkabel (Fretting Fatigue Tests of Post-Tensioning Tendons)," Institut für Baustatik und Konstruktion, ETH Zurich (Swiss Federal Institute of Technology), Report 8101-2. (original in German; referred to information reported by Hall et al. 1990).
- Ozkul, O., Nassif, H., Tanchan, P., and Harajli, M. (2008). "Rational approach for predicting stress in beams with unbonded tendons." *ACI Structural Journal*, 105(3), 338-347.
- Paulson, C., Frank, K.H. and Breen, J. E. (1984). "A Fatigue Study of Prestressing Steel" Center for Transportation Research Report 300-1, University of Texas at Austin, 124 pp.
- PCI Industry Handbook Committee. (2010). *PCI Design Handbook: Precast and Prestressed Concrete*.
- Post-tensioning Institute (PTI) (2006). "Post-tensioning Manual 6th Edition." 59 pp.
- Pessiki, S., Kaczinski, M. and Wescott, H.H. (1996). "Evaluation of Effective Prestress Force in 28-Year-Old Prestressed Concrete Bridge Beams." *PCI Journal*, 78-89.
- Rigon, C. and Thürlimann, B. (1985). "Fatigue tests on post-tensioned concrete beams," Birkhäuser.
- Roberts-Wollmann, C. L., Kreger, M. E., Rogowsky, D. M., and Breen, J. E., (2005). "Stresses in External Tendons at Ultimate," *ACI Structural Journal*, V. 102, No. 2, Mar.-Apr.
- Ryals, K. K., Breen, J. E., and Kreger, M. K. (1992). "Fretting Fatigue in External Post Tensioned" University of Texas Dissertation.
- Tam, A. and Pannell, F.N. (1976). "Ultimate Moment Resistance of Unbonded Partially Prestressed Reinforced Concrete Beams," *Magazine of Concrete Research*, V. 28, No. 97. Dec. pp. 203-208.

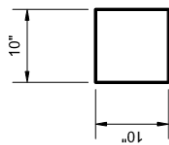
- Traute M. and Weiher H. (2011). "Improved Sustainability in Post-tensioning by Replaceable Internal Unbonded Tendons," Symposium Prague, Session 3-4, 2011, p 831-834.
- Virlogeux, M. (1983), "La Precontrainte Exterieur," Annales de l'Institut Technique du Bâtiment et des Travaux Publics, Dec. 1983.
- Waterhouse, R. B. (1982). "Occurrence of Fretting in Practice and Its Simulation in the Laboratory," Materials Evaluation Under Fretting Conditions, ASTM STP 780. American Society for Testing and Materials. pp. 3-16.
- Waterhouse, R.B. (1972). *Fretting Corrosion*. Pergamon Press, Hungary.
- Waterhouse, R.B. and Taylor, D. E. (1971). *Lubrication Engineering*, Vol. 27, No. 123.
- Wollman, G. P., Yates, D. L., Breen, J.E., and Kreger, M.E., (1988). "Fretting Fatigue in Post-tensioned Concrete." Center for Transportation Research Report, University of Texas at Austin, 167 pp.
- Wollman, G. P., Yates, D. L., Breen, J.E., and Kreger, M.E., (1996). "Fretting Fatigue in Post-tensioned Concrete Beams," *ACI Structural Journal*, V. #, No. #, Mar.-Apr.
- Yates, D. L. (1987) "A Study of Fretting Fatigue in Post-Tensioned Concrete Beams." Unpublished M.S. Thesis, The University of Texas at Austin, December 1987.

Appendix A—Assembly Drawings External I-Girder

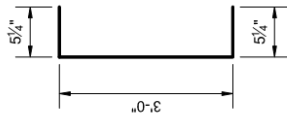




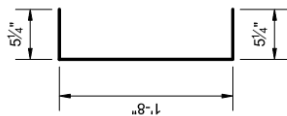
Bar Bending
 #3 Bars: bend
 around 1 1/2" dia. pin
 #4 Bars: bend
 around 2" dia. pin
 #5 Bars: bend
 around 2 1/2" dia. pin
 All dims are
 out-to-out



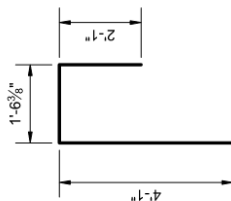
5Z



4Q



4R



5R

Bill of Material: Deviator (qty per pour block)

Piece	Size	Qty	Length	Notes
5R	#5	24	7'-8 7/8"	See above Min. Lap = 2'-0"
4R	#4	32	2'-6"	See above
4Q	#4	16	3'-11"	See above
4Z	#4	10	3'-5"	See above

Appendix B—Prestressing Strand and Post-Tensioning Hardware Information



MATERIAL CERTIFICATION OF COMPLIANCE

Sanderson, FL

UNIVERSITY OF FLORIDA
5007 NE 39TH AVENUE
TALLAHASSEE FL 32310

Bill of Lading: 00149134
Order Number: 412957
PO Number: 1400326714

Insteel Wire Products Company hereby certifies that the specimens taken from production lot(s) consisting of one or more of the following Lot/serial numbers were tested in accordance with and met the specification requirements of A 416 - 12a. The attached test report(s) represent the result of such test(s).

.600 (15.2mm) 7W 270 LR ASTM A416

Test Report Number: 10084756

Lot/Serial Numbers

1302464132615
1302464132616

Heat Number/Lot Number

25307

The products listed in this certification were manufactured and fabricated in the United States of America.

Insteel Wire Products Company hereby certifies that the prestressing strand described above meets or exceeds the minimum bonding requirements as currently accepted in the NASP (North American Strand Producers) pull-out test and the Moustaffa block pull-out test.

All Domestic Prestressing Strand was made from steel rod that was manufactured and processed completely in America. The rod was then manufactured into PC Strand in the United States at Insteel Wire Products Company plant in either Jacksonville, FL or Gallatin, TN. The material meets the "Buy America" requirements of 23 CFR 635.410.

The products listed in this certification were manufactured in the U.S.A. from wire rod which was manufactured in the U.S.A.

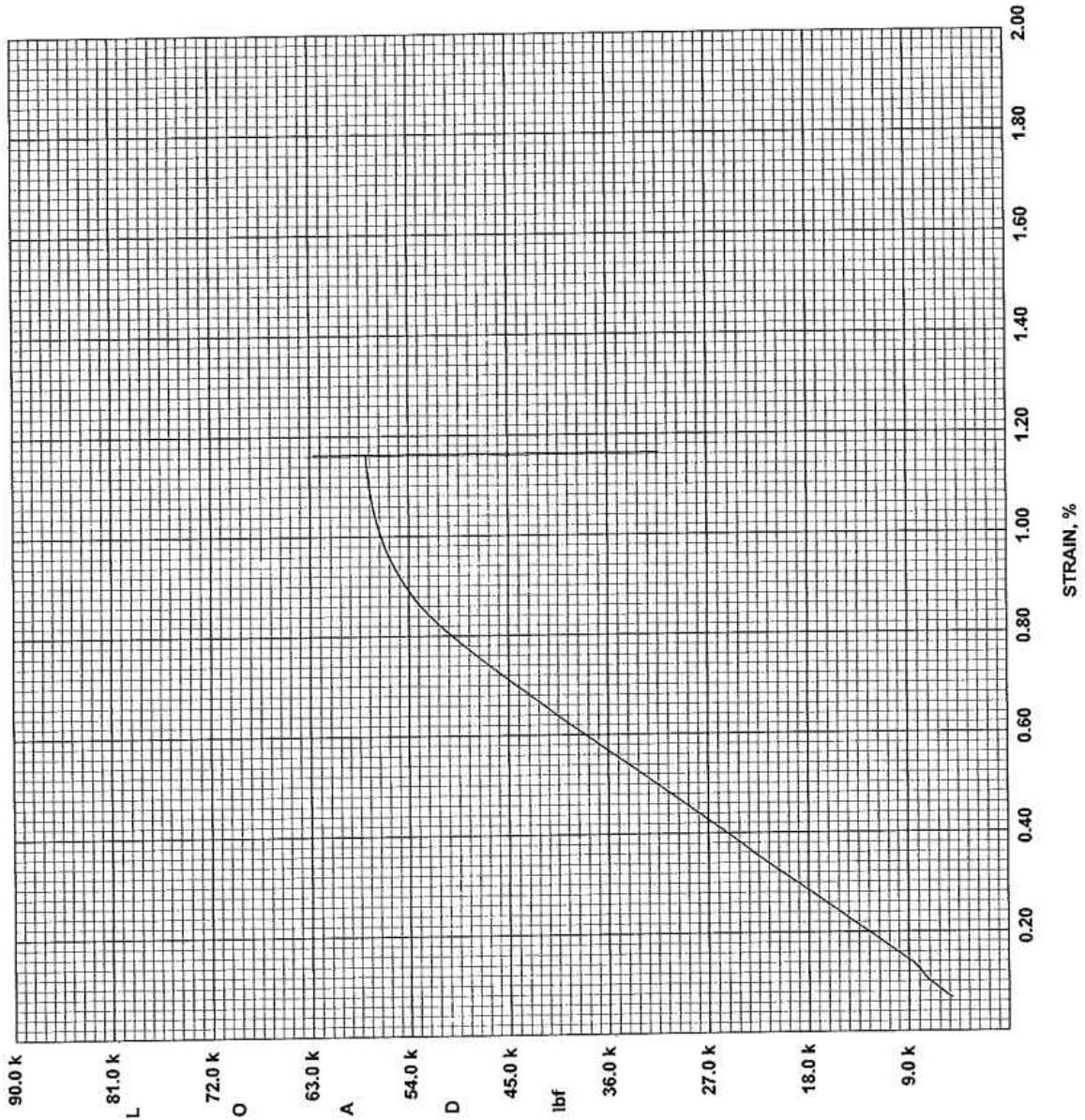
Quality Assurance Manager: Channing E. R. Hoover Jr.

Date: 16-MAY-2014

**Insteel Wire Products
Prestressed Concrete Strand**

.600" 270 7W LOW RELAXATION

Test Number: 10084756
 Tested By: CER
 Ultimate Breaking Strength, lbf: 62751
 Ultimate Breaking Strength, kN: 279
 Load @ 1% Extension, lbf: 56575
 Load @ 1% Extension, kN: 252
 Ultimate Elongation, %: 5.73
 Representative Area, in²: 0.217
 Representative Area, mm²: 140
 Actual Area, in²: 0.2187
 Actual Area, mm²: 141.1103
 Avg Modulus of Elasticity, Mpsi: 29.0
 Avg Modulus of Elasticity, MPa: 199947.6
 Reference:



May 16, 2014 8:39:32 AM
 SN: 206250-R2 V7.02.07



SUMIDEN WIRE PRODUCTS CORPORATION

Customer Service - PC Strand

East: Toll Free 866-491-5020 • 710 Marshall Stuart Dr., Dickson, TN 37055

West: Toll Free 866-246-3758 • 1412 El Pinal Dr., Stockton, CA 95205

SWPC

CERTIFICATE OF INSPECTION

Order Number: SIPC150016-1

Page No : 1 OF 1

B/L No: SIPC150031

Issue Date : 01/08/2015

Commodity: Steel Strand, Uncoated Seven Wire for Prestressed Concrete
Size & Grade: 6/10" x 270 KSI
Specification: ASTM A416 - Latest 6/10" - Low Relaxation
Customer Name: UNIVERSITY OF FLORIDA
Customer P.O.: DONATION
Destination: FLDEPTTRANS
State Job No:

Table with 8 columns: No, Pack #, Heat #, B.S., Elong., Y.P., Area, E-Modulus, CURVE#. It contains three rows of inspection data for different pack numbers.

We hereby certify that:

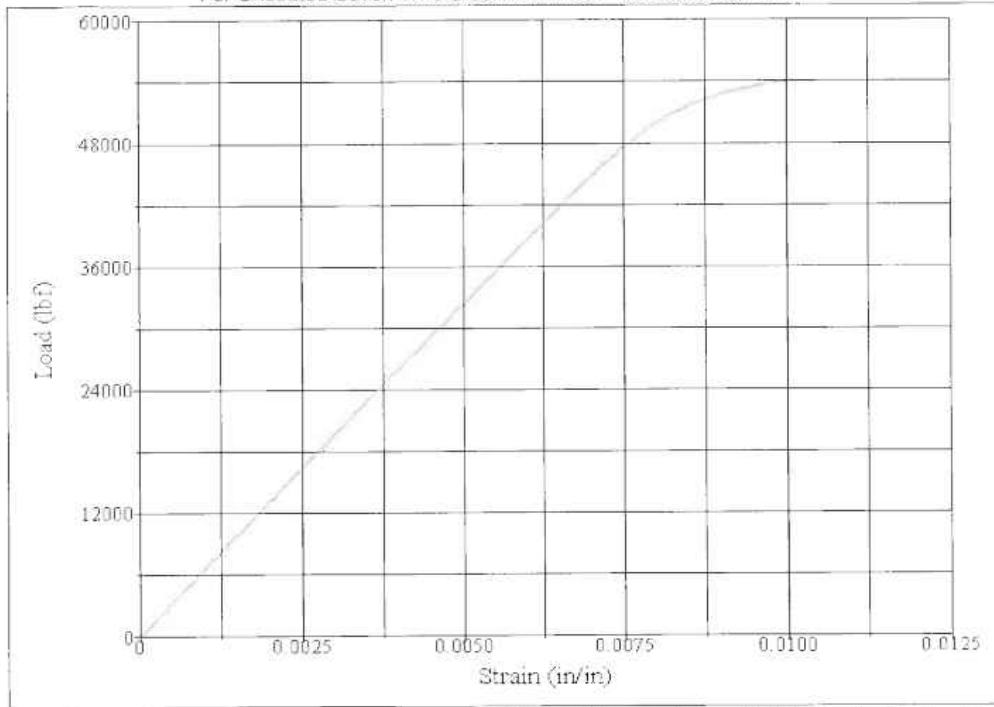
- * We have accurately carried out the inspection of COMMODITY and met the requirements in accordance with the applicable SPECIFICATION, both listed above.
* The raw material, and all manufacturing processes used in the production of the COMMODITY described above occurred in the USA, in compliance with the Buy America requirements of 23 CFR 635.410.
* The material described above will bond to concrete of a normal strength and consistency in conformance with the prediction equations for transfer and development length given in the ACI/AASHTO specifications.
* The individual below has the authority to make this certificate legally binding for SWPC.

Handwritten signature of an official from the Quality Assurance Section.

Quality Assurance Section

Load - Elongation Curve

For Uncoated Seven Wire Steel Strand for Prestressed Concrete



* Vertical Line is drawn at 1% Extension Under Load
* Tested to ASTM A1061 Standards

Curve Number D300002R
Size 0.6"
Grade 270K
Area 0.2186 in²
Modulus 28.6 Msi



Approval

Curve D300002R

Sumiden Wire Products Corporation - PC Strand Division - 710 Marshall Stuart Drive, Dickson, TN 37055 - Phone - (615) 446-3199

Replaceable Unbonded Tendons for Post-Tensioned Bridges

Part III Wire Break Detection

This report is one of a four-part compilation published under separate covers as follows:

Extended Summary

Part I Mockup for Flexible Filler Injection

Part II Structural Testing

Part III Wire Break Detection

Final Report

December 2017

Principal investigator:

H. R. Hamilton

Co-Principal investigator:

J. A. Rice

Research assistants:

A.B.M. Abdullah

Rahul Bhatia

Natassia Brenkus

Devon Skelton

Sponsor:

Florida Department of Transportation (FDOT)

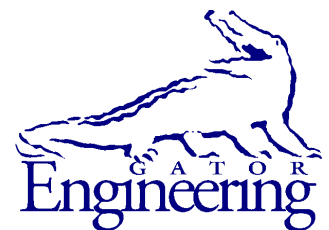
William Potter, P.E. – Project Manager

Rick W. Vallier, P.E. –Project Manager

Contract:

UF Project No. 000112216 & 000112218

FDOT Contract No. BDV31-977-15



University of Florida

Engineering School of Sustainable Infrastructure and Environment

Department of Civil and Coastal Engineering

University of Florida

P.O. Box 116580

Gainesville, Florida 32611

Disclaimer

The opinions, findings, and conclusions expressed in this publication are those of the authors and not necessarily those of the State of Florida Department of Transportation.

Units of Measurement Conversion

SI* (MODERN METRIC) CONVERSION FACTORS

APPROXIMATE CONVERSIONS TO SI UNITS

SYMBOL	WHEN YOU KNOW	MULTIPLY BY	TO FIND	SYMBOL
LENGTH				
in	inches	25.4	millimeters	mm
ft	feet	0.305	meters	m
yd	yards	0.914	meters	m
mi	miles	1.61	kilometers	km
AREA				
in²	square inches	645.2	square millimeters	mm ²
ft²	square feet	0.093	square meters	m ²
yd²	square yard	0.836	square meters	m ²
ac	acres	0.405	hectares	ha
mi²	square miles	2.59	square kilometers	km ²
VOLUME				
fl oz	fluid ounces	29.57	milliliters	mL
gal	gallons	3.785	liters	L
ft³	cubic feet	0.028	cubic meters	m ³
yd³	cubic yards	0.765	cubic meters	m ³
NOTE: volumes greater than 1000 L shall be shown in m ³				
MASS				
oz	ounces	28.35	grams	g
lb	pounds	0.454	kilograms	kg
T	short tons (2000 lb)	0.907	megagrams	Mg (or "t")
TEMPERATURE (exact degrees)				
°F	Fahrenheit	5(F-32)/9 or (F-32)/1.8	Celsius	°C
ILLUMINATION				
fc	foot-candles	10.76	lux	lx
fl	foot-Lamberts	3.426	candela/m ²	cd/m ²
FORCE and PRESSURE or STRESS				
kip	1000 pound force	4.45	kilonewtons	kN
lbf	pound force	4.45	newtons	N
lbf/in²	pound force per square	6.89	kilopascals	kPa

*SI is the symbol for the International System of Units. Appropriate rounding should be made to comply with Section 4 of ASTM E380.

SI* (MODERN METRIC) CONVERSION FACTORS
APPROXIMATE CONVERSIONS FROM SI UNITS

SYMBOL	WHEN YOU KNOW	MULTIPLY BY	TO FIND	SYMBOL
LENGTH				
mm	millimeters	0.039	inches	in
m	meters	3.28	feet	ft
m	meters	1.09	yards	yd
km	kilometers	0.621	miles	mi
AREA				
mm²	square millimeters	0.0016	square inches	in ²
m²	square meters	10.764	square feet	ft ²
m²	square meters	1.195	square yards	yd ²
ha	hectares	2.47	acres	ac
km²	square kilometers	0.386	square miles	mi ²
VOLUME				
mL	milliliters	0.034	fluid ounces	fl oz
L	liters	0.264	gallons	gal
m³	cubic meters	35.314	cubic feet	ft ³
m³	cubic meters	1.307	cubic yards	yd ³
MASS				
g	grams	0.035	ounces	oz
kg	kilograms	2.202	pounds	lb
Mg (or "t")	megagrams (or "metric ton")	1.103	short tons (2000 lb)	T
TEMPERATURE (exact degrees)				
°C	Celsius	1.8C+32	Fahrenheit	°F
ILLUMINATION				
lx	lux	0.0929	foot-candles	fc
cd/m²	candela/m ²	0.2919	foot-Lamberts	fl
FORCE and PRESSURE or STRESS				
kN	kilonewtons	0.225	1000 pound force	kip
N	newtons	0.225	pound force	lbf
kPa	kilopascals	0.145	pound force per square inch	lbf/in ²

*SI is the symbol for the International System of Units. Appropriate rounding should be made to comply with Section 4 of ASTM E380.

Table of Contents

Disclaimer	ii
Units of Measurement Conversion	iii
List of Figures	viii
List of Tables	xiii
1 Introduction.....	1
2 Research Approach.....	2
3 Literature Review.....	3
3.1 Structural Health Monitoring.....	3
3.2 Existing Tendon Monitoring Techniques	3
3.2.1 Visual Inspection.....	4
3.2.2 Screwdriver Penetration Test	4
3.2.3 Radiography	5
3.2.4 Global Dynamic Approach.....	5
3.2.5 Remnant Magnetism/Magnetic Flux Leakage	5
3.2.6 Magnetic Permeability	5
3.2.7 Magnetostrictive Sensing	6
3.2.8 Electrical Resistance Method	6
3.2.9 Time-domain Reflectometry	6
3.2.10 Impact-echo	6
3.2.11 Ultrasonic Impulse-echo.....	6
3.2.12 Electro-mechanical Impedance Method.....	7
3.2.13 Guided Wave Ultrasonic Technique	10
3.2.14 Acoustic Emission.....	14
3.2.15 Comparison of Existing Monitoring Approaches	19
3.3 Examples of Full-scale Implementation	20
3.3.1 Bois de Rosset Viaduct.....	21
3.3.2 Ponte Moesa	21
3.3.3 Huntingdon Railway Viaduct.....	21
3.3.4 Fred Hartman Bridge.....	22
3.4 Finite Element Modeling of Post-tensioning Strand and Anchorage	23
3.4.1 Classification of Contact Interactions	24
3.4.2 Selection of Contact Pair.....	24
3.4.3 Discretization of Contact Surfaces	24
3.4.4 Contact Forces.....	24
3.4.5 Kinematic Constraints	25
3.4.6 Strict Enforcement of Contact Constraints.....	26
3.4.7 Constraints Enforcement Methods	28
3.4.8 Numerical Methods	29
3.4.9 Loading Scheme	30
3.5 Investigations on cable mechanics.....	30
3.6 An Overview of Standard Strain Gages and Data Acquisition Systems	33
3.7 Summary.....	34
4 Proof-of-Concept Study.....	36
4.1 Calibration Test.....	37
4.1.1 Instrumentation and Setup.....	38

4.1.2	Experiment	41
4.1.3	Results	41
4.2	Finite Element Model Development.....	42
4.2.1	Mechanical Properties	42
4.2.2	FE Formulation.....	43
4.3	Wire Breakage Detection: General Framework.....	45
4.4	Parametric Study with E 6-19 Anchorage	49
4.5	Summary.....	55
5	Experimental Evaluation of Strain Distribution in Anchors.....	56
5.1	Test setup	56
5.2	Experiment.....	58
5.3	Results.....	60
5.3.1	Axial Strains	60
5.3.2	Circumferential and Radial Strains	62
5.4	Summary.....	63
6	Tendon Monitoring Algorithm	64
6.1	Tendon Monitoring Framework.....	65
6.2	Layer-based Broken Strand Identification Framework.....	66
6.2.1	Underlying Framework	66
6.2.2	Damage Parameters and Thresholds	67
6.2.3	Algorithm Development.....	68
6.2.4	Error Sensitivity Analysis	69
6.2.5	Effects of Differential Wedge Seating on the Proposed Model	72
6.3	Group-based Broken Strand Identification Framework.....	73
6.3.1	Underlying Framework	73
6.3.2	Algorithm Development.....	74
6.4	Selecting the Number of Sensors in Anchors	75
6.5	Summary.....	76
7	Analytical Characterization of Strand Response	78
7.1	Model Geometric and Material Properties.....	78
7.1.1	Geometric Features.....	78
7.1.2	Material Characterization	79
7.2	Model Development.....	80
7.2.1	Element Selection and Mesh Generation	80
7.2.2	Boundary Conditions and Loading.....	80
7.2.3	Interwire Friction.....	81
7.2.4	Model Verification	82
7.3	Sensitivity Analysis of FE Parameters.....	82
7.3.1	Time Variation of Applied Load	83
7.3.2	Loading Rate	84
7.3.3	Friction Model.....	85
7.3.4	Damping	86
7.4	Load Redistribution Among Wires.....	87
7.5	Wire break Simulation and Post-breakage Response	89
7.5.1	Wire break Simulation Procedure	90
7.5.2	Post-breakage Response	90

7.6	Summary	96
8	Experimental Evaluation of Tendon Behavior	97
8.1	Experimental Setup and Procedure	97
8.1.1	Test Specimen Design and Construction.....	97
8.1.2	Instrumentation.....	99
8.1.3	Test Procedures	99
8.2	Experimental Results and Discussion.....	100
8.2.1	Global Static Response at Anchors	100
8.2.2	Localized Static Response along the Wires	101
8.2.3	Global Dynamic Response at Anchors.....	102
8.3	Numerical Investigation.....	103
8.3.1	Characterization of Tensile Properties of Wire and Strand for FE model	103
8.3.2	Model Formulation.....	104
8.3.3	FEA Results.....	106
8.4	Summary.....	107
9	Full-scale Experiments.....	109
9.1	Internal Bonded Tendon	109
9.1.1	Test Specimen, Instrumentation, and Procedure	109
9.1.2	Experimental Results.....	111
9.2	Test with External Unbonded Tendon	115
9.2.1	Test Specimen, Instrumentation, and Procedure	115
9.2.2	Experimental Results.....	119
9.3	Test with Internal Unbonded Tendon	127
9.3.1	Test Specimen, Instrumentation, and Procedure	127
9.3.2	Experimental Results.....	128
9.3.3	Broken Strand Identification through Tendon Monitoring Algorithm.....	138
9.4	Summary.....	145
10	Summary and Conclusions	147
11	Future Research	148
11.1	Damage Parameters and Thresholds Adjustment	148
11.2	Durability Enhancement of Strain Sensors	148
11.3	Model Improvement.....	148
11.4	Sensor Arrangement Optimization	148
11.5	Investigation on Additional Damage Indicators	149
11.6	In-field Deployment.....	149
	References.....	150
	Appendix A—Electro-Mechanical Impedance Testing.....	158
	Appendix B—Detail Experimental Results: Internal Bonded Tendon.....	162
	Appendix C—Detail Experimental Results: External Unbonded Tendon	182
	Appendix D—Detail Experimental Results: Internal Unbonded Tendon	187
	Appendix E—Acoustic Monitoring Testing.....	220
	Appendix F—Automated Damage Detection.....	236

List of Figures

Figure 3-1 Interaction between PZT Patch and host structure.....	7
Figure 3-2 Resonant frequency shift in impedance signature due to damage	8
Figure 3-3 Geometry of a seven-wire strand	13
Figure 3-4 Acoustic emission testing.....	15
Figure 3-5 Kaiser Effect.....	16
Figure 3-6 Lamb waves	17
Figure 3-7 SoundPrint® acoustic monitoring system.....	18
Figure 3-8 Sensor locations and detected signals	18
Figure 3-9 FE model: (a) anchorage; (b) multi-strand tendon; (c) wire break; (d) birdcaging ...	23
Figure 3-10 Contact pair: (a) more refined surface as slave; (b) more refined surface as master	24
Figure 3-11 Resistive forces in a wedge-anchor head system	25
Figure 3-12 Contact constraints	25
Figure 3-13 Pressure-overclosure relationship	27
Figure 3-14 Coulomb friction model	28
Figure 3-15 Tangential direction behavior	28
Figure 3-16 Non-linearity of contact problem	30
Figure 4-1 Post-tensioning method: (a) bonded; (b) unbonded.....	37
Figure 4-2 Details of stressing frame: (a) plan; (b) end plate elevation; (c) two-part wedge.....	38
Figure 4-3 Strain gage placement on ECI 6-7 anchorage: (a) anchor head elevation; (b) plan...	40
Figure 4-4 Experimental setup.....	41
Figure 4-5 Characteristics of elastoplastic behavior of the anchorage components	42
Figure 4-6 Discretization and boundary conditions of FE model for calibration	43
Figure 4-7 Estimation of friction coefficient acting at the wedge-anchor head interface (μ_{w-h})..	44
Figure 4-8 Estimation of friction coefficient acting at the anchor head-plate interface (μ_{h-p}).....	45
Figure 4-9 Discretization and boundary conditions of VSL ECI 6-7 anchor head.....	45
Figure 4-10 Strain distribution: (a) before breakage; (b) after wire break	46
Figure 4-11 Comparison of axial strains in ECI 6-7 anchorage before and after wire breaks ...	48
Figure 4-12 Strain variations in ECI 6-7: (a) single wire break; (b) multiple wire breaks.....	49
Figure 4-13 VSL E 6-19 anchorage: (a) discretization; (b) boundary conditions	49
Figure 4-14 E 6-19 anchorage details: (a) top view; (b) section Y-Y	50
Figure 4-15 Comparison of axial strains in E 6-19 anchorage before and after wire breaks	52
Figure 4-16 Strain variations in E 6-19: (a) single wire break; (b) multiple wire breaks.....	53
Figure 4-17 Strain variation due to wire breakage at different strain measurement locations ...	54
Figure 5-1 Reaction fixture details and sensor layout	57
Figure 5-2 Tendon stressing and cutting apparatus	58
Figure 5-3 Experimental setup.....	59
Figure 5-4 Time history of measured strains by gage L	60
Figure 5-5 Axial strain variations due to wire breaks.....	61
Figure 5-6 Circumferential strain variations due to wire breaks	62
Figure 5-7 Radial strain variations due to wire breaks	63
Figure 6-1 Wire breakage identification flowchart.....	65
Figure 6-2 Monitoring locations and representative strain variations from FE analyses	66
Figure 6-3 Wire breakage identification flowchart.....	68
Figure 6-4 Error due to misalignment of strain gage.....	71
Figure 6-5 Transverse sensitivity of strain gage	71

Figure 6-6 Differential wedge seating	73
Figure 6-7 Wire breakage identification flowchart.....	74
Figure 6-8 Sensor arrangement in layer- and group-based approaches	76
Figure 7-1 Seven-wire prestressing strand.....	79
Figure 7-2 Mesh convergence study	80
Figure 7-3 Boundary conditions and loading.....	81
Figure 7-4 Stress-strain curves for strand	82
Figure 7-5 Time variation of applied loads.....	84
Figure 7-6 Kinetic energy history for linear and smooth load ramp.....	84
Figure 7-7 Convergence of developed force with slower loading rate	85
Figure 7-8 Exponential decay friction model	85
Figure 7-9 Occurrence of interwire slip.....	86
Figure 7-10 Effect of damping on linear load ramp: (a) developed force; (b) kinetic energy.....	87
Figure 7-11 Addition of damping to damp the oscillation originating from interwire slip	87
Figure 7-12 Comparison of load distribution among wires in a long- and short-strand.....	88
Figure 7-13 Load redistribution among wires with the onset of slip.....	89
Figure 7-14 Typical stressing profile and post-breakage response.....	90
Figure 7-15 Effect of friction coefficient on remaining prestressing force	92
Figure 7-16 Birdcage formation and broken wire separation	92
Figure 7-17 Birdcage formation and broken wire separation	93
Figure 7-18 Birdcage formation and broken wire separation	93
Figure 7-19 Frequency shift with successive wire breaks	94
Figure 7-20 Deviated multi-strand tendon.....	95
Figure 7-21 Comparison of prestressing force after wire breaks.....	95
Figure 8-1 Test configuration schematic	98
Figure 8-2 Experimental details: (a) strand bundle close-up; (b) wire cuts; (c) birdcaging	99
Figure 8-3 Stressing in Experiment 1: (a) load vs. elongation; (b) load vs. strain	100
Figure 8-4 Global static response: (a) load history during wire cuts in <i>Experiment 1</i> ; (b) comparison of prestress loss between Experiment 1 and <i>Experiment 2</i>	101
Figure 8-5 Measured surface strain on helical wires	101
Figure 8-6 Shift of natural frequencies with successive wire cuts.....	102
Figure 8-7 Tensile tests with single wire and FEA input.....	104
Figure 8-8 Tensile tests with strand and FEA output	105
Figure 8-9 FE model of strand: (a) unconfined; (b) fully confined	106
Figure 8-10 Change of prestress force after wire break in unconfined state: (a) FEA; (b) experiment.....	107
Figure 9-1 Internal tendon specimen with parabolically draped profile.....	110
Figure 9-2 Test specimen with internal bonded tendon.....	110
Figure 9-3 Strain sensor layout for internal tendon specimen	111
Figure 9-4 Post-tensioning: (a) load cell time history at dead end ‘A’; (b) anchor strain time history; (c) anchor strain vs. prestressing force; (d) final strain at the end of post-tensioning	112
Figure 9-5 Strain change in a gage with stressing of each strand.....	113
Figure 9-6 Beam loading: (a) load vs. displacement; (b) loading time history	114
Figure 9-7 Beam loading time history: (a) load cell at dead end ‘A’; (b) anchor strains	114
Figure 9-8 Live end ‘B’ anchor strain time history during detensioning	115

Figure 9-9 External tendon specimen with two-point harped profile	116
Figure 9-10 Test specimen with external unbonded tendons.....	116
Figure 9-11 Strain sensor layout for external unbonded specimen.....	117
Figure 9-12 Cutting the strands.....	118
Figure 9-13 Wedge movement after strand cuts	118
Figure 9-14 Acoustic monitoring.....	118
Figure 9-15 Post-tensioning time history at dead end load cell: (a) Tendon 1; (b) Tendon 2 ...	120
Figure 9-16 Post-tensioning time history for strain gages: (a) Tendon 1; (b) Tendon 2	120
Figure 9-17 Beam loading: (a) load vs. displacement; (d) loading time history	121
Figure 9-18 Time history of load cells during beam loading: (a) Tendon 1; (b) Tendon 2.....	122
Figure 9-19 Time history of strain gages during beam loading: (a) Tendon 1; (b) Tendon 2 ...	122
Figure 9-20 Time history of load cells during detensioning: (a) Tendon 1; (b) Tendon 2	123
Figure 9-21 Time history of strain gages during detensioning: (a) Tendon 1; (b) Tendon 2	123
Figure 9-22 Strain change with wire cuts in Tendon 1	124
Figure 9-23 Strain change with wire cuts in Tendon 2.....	125
Figure 9-24 Mean strain change per sensor after wire cuts (first strand cut)	126
Figure 9-25 Test setup for internal unbonded specimen: (a) live end; (b) dead end and access window for wire cuts; (c) anchor instrumentation; (d) tendon close-up after strand cuts ..	127
Figure 9-26 Wedge movements after strand cuts	128
Figure 9-27 Acoustic sensor placement on internal unbonded tendon specimen.....	128
Figure 9-28 Post-tensioning: (a) load cell time history; (b) anchor strain time history; (c) anchor strain vs. prestressing force; (d) final anchor strain at the end of post-tensioning	129
Figure 9-29 Strain change in a gage with stressing of each strand.....	130
Figure 9-30 Distance and strain change relationship: (a) linear fit; (b) quadratic fit; (c) exponential fit; (d) normalized exponential fit, strain change for unit (1 kip) applied prestressing force	131
Figure 9-31 Load vs. displacement.....	132
Figure 9-32 Beam loading: (a) load cell time history at dead end ‘A’; (b) anchor strain time history; (c) anchor instrumentation; (d) final strain at the end of load test.....	133
Figure 9-33 Strain change in anchors during beam loading: (a) loading time history; (d) axial strain and strain change.....	134
Figure 9-34 Detensioning time history	135
Figure 9-35 Wire break events detected by acoustic sensor and strain gage.....	135
Figure 9-36 Mean strain change per sensor for the first strand cut	136
Figure 9-37 Strain change after first strand cut	137
Figure 9-38 Strain change after second strand cut.....	138
Figure 9-39 Success rate of the proposed model (Section 6.3) identifying the broken strand ..	140
Figure 9-40 Performance of the algorithm with six sensors: (a) sensor layout; (b) strain change in near anchor ‘A’ for the first strand cut; (c) strain change in far anchor ‘B’ for the first strand cut; (d) success rate for all strand cuts	141
Figure 9-41 Performance of the algorithm with six sensors: (a) sensor layout; (b) strain change in near anchor ‘A’ for the first strand cut; (c) strain change in far anchor ‘B’ for the first strand cut; (d) success rate for all strand cuts	142
Figure 9-42 Performance of the algorithm with three sensors: (a) sensor layout; (b) strain change in near anchor ‘A’ for the first strand cut; (c) strain change in far anchor ‘B’ for the first strand cut; (d) success rate for all strand cuts	143

Figure 9-43 Performance of the algorithm with three sensors: (a) sensor layout; (b) strain change in near anchor ‘A’ for the first strand cut; (c) strain change in far anchor ‘B’ for the first strand cut; (d) success rate for all strand cuts	144
Figure 9-44 Performance of the algorithm with one broken sensor	145
Figure A-1 EMI test setup schematic.....	158
Figure A-2 EMI test setup schematic (with safety cover)	158
Figure A-3 EMI test setup.....	159
Figure A-4 PZT patches on end plate	159
Figure A-5 EMI test results.....	160
Figure A-6 Frequency shift vs force loss.....	161
Figure A-7 Peak impedance vs force loss.....	161
Figure B-8 Strain comparison between two anchors during stressing (gage A-F).....	162
Figure B-9 Strain comparison between two anchors during stressing (gage G-L).....	163
Figure B-10 Strain vs. prestressing force at two anchors during stressing (strain gage A-F) ...	164
Figure B-11 Strain vs. prestressing force at two anchors during stressing (strain gage G-L) ...	165
Figure B-12 Strain change in a gage with stressing of each strand (gage A-F, dead end)	166
Figure B-13 Strain change in a gage with stressing of each strand (gage G-L, dead end).....	167
Figure B-14 Strain change in a gage with stressing of each strand (gage A-F, live end).....	168
Figure B-15 Strain change in a gage with stressing of each strand (gage G-L, live end).....	169
Figure B-16 Strain-distance statistical fits (gage A and B, dead end)	170
Figure B-17 Strain-distance statistical fits (gage C and D, dead end)	171
Figure B-18 Strain-distance statistical fits (gage E and F, dead end).....	172
Figure B-19 Strain-distance statistical fits (gage G and H, dead end).....	173
Figure B-20 Strain-distance statistical fits (gage I and J, dead end).....	174
Figure B-21 Strain-distance statistical fits (gage K and L, dead end)	175
Figure B-22 Strain-distance statistical fits (gage A and B, live end).....	176
Figure B-23 Strain-distance statistical fits (gage C and D, live end).....	177
Figure B-24 Strain-distance statistical fits (gage E and F, live end)	178
Figure B-25 Strain-distance statistical fits (gage G and H, live end)	179
Figure B-26 Strain-distance statistical fits (gage I and J, live end)	180
Figure B-27 Strain-distance statistical fits (gage K and L, live end).....	181
Figure C-28 Strain change in anchor ‘A1’ (baseline strain updated after each strand cut)	182
Figure C-29 Strain change in anchor ‘B1’ (baseline strain updated after each strand cut)	183
Figure C-30 Strain change in anchor ‘A2’ (baseline strain updated after each strand cut)	184
Figure C-31 Strain change in anchor ‘B2’ (baseline strain updated after each strand cut)	185
Figure C-32 Frequency shift with wire cuts	186
Figure D-33 Strain comparison between two anchors during stressing (gage A-F).....	187
Figure D-34 Strain comparison between two anchors during stressing (gage G-L).....	188
Figure D-35 Strain vs. prestressing force at two anchors during stressing (strain gage A-F) ...	189
Figure D-36 Strain vs. prestressing force at two anchors during stressing (strain gage G-L) ...	190
Figure D-37 Strain change in a gage with stressing of each strand (gage A-F, dead end).....	191
Figure D-38 Strain change in a gage with stressing of each strand (gage G-L, dead end).....	192
Figure D-39 Strain change in a gage with stressing of each strand (gage A-F, live end).....	193
Figure D-40 Strain change in a gage with stressing of each strand (gage G-L, live end)	194
Figure D-41 Strain-distance statistical fits (gage A and B, dead end).....	195
Figure D-42 Strain-distance statistical fits (gage C and D, dead end).....	196

Figure D-43 Strain-distance statistical fits (gage E and F, dead end).....	197
Figure D-44 Strain-distance statistical fits (gage G and H, dead end).....	198
Figure D-45 Strain-distance statistical fits (gage I and J, dead end)	199
Figure D-46 Strain-distance statistical fits (gage K and L, dead end).....	200
Figure D-47 Strain-distance statistical fits (gage A and B, live end)	201
Figure D-48 Strain-distance statistical fits (gage C and D, live end)	202
Figure D-49 Strain-distance statistical fits (gage E and F, live end)	203
Figure D-50 Strain-distance statistical fits (gage G and H, live end)	204
Figure D-51 Strain-distance statistical fits (gage I and J, live end).....	205
Figure D-52 Strain-distance statistical fits (gage K and L, live end).....	206
Figure D-53 Strain change with wire cuts (dead end anchor ‘A’).....	207
Figure D-54 Strain change with wire cuts (live end anchor ‘B’).....	208
Figure D-55 Strain change relative to the original strain (dead end anchor ‘A’)	209
Figure D-56 Strain change relative to the original strain (live end anchor ‘B’)	210
Figure D-57 Strain change after the breakage of entire strand (dead end anchor ‘A’).....	211
Figure D-58 Strain change after the breakage of entire strand (dead end anchor ‘A’).....	212
Figure D-59 Strain change after the breakage of entire strand (live end anchor ‘B’)	213
Figure D-60 Strain change after the breakage of entire strand (live end anchor ‘B’)	214
Figure D-61 Relative strain change after the breakage of entire strand (dead end anchor ‘A’)	215
Figure D-62 Relative strain change after the breakage of entire strand (dead end anchor ‘A’)	216
Figure D-63 Relative strain change after the breakage of entire strand (live end anchor ‘B’)..	217
Figure D-64 Relative strain change after the breakage of entire strand (live end anchor ‘B’)..	218
Figure D-65 Frequency shift with wire cuts	219
Figure E-66 Acoustic sensor layout and event (wire cut) locations determined by acoustic system	220
Figure E-67 Acoustic signals (time vs. voltage) due to wire cuts (top left: channel A0; top right: channel A1; bottom left: channel A2; bottom right: channel A3 [inactive]).....	222
Figure E-68 Acoustic sensor layout and event (wire cut) locations determined by acoustic system	227
Figure E-69 Acoustic signals (time vs. voltage) due to wire cuts (top left: channel A0; top right: channel A1; bottom left: channel A2; bottom right: channel A3)	230
Figure F-70 Damage indices and visualization of tendon damage (Strand 1-Strand 3)	236
Figure F-71 Damage indices and visualization of tendon damage (Strand 4-Strand 6)	237
Figure F-72 Damage indices and visualization of tendon damage (Strand 7-Strand 9)	238
Figure F-73 Damage indices and visualization of tendon damage (Strand 10-Strand 12)	239
Figure F-74 Damage indices and visualization of tendon damage (Strand 13-Strand 15)	240
Figure F-75 Damage indices and visualization of tendon damage (Strand 16-Strand 18)	241
Figure F-76 Damage indices and visualization of tendon damage (Strand 19).....	242

List of Tables

Table 3-1. Comparison of existing monitoring approaches	20
Table 4-1 Experimentally measured strains	41
Table 4-2 Mechanical properties of the anchorage assembly	42
Table 4-3 Wire breakage cases	47
Table 4-4 Test matrix and results	51
Table 5-1 Test matrix and results	59
Table 6-1 Success rate of single wire break identification	72
Table 7-1 Geometric and material properties of a seven-wire prestressing strand	79
Table 7-2 Parameters for analyzing strand response during stressing	83
Table 7-3 Final load distribution among wires	88
Table 7-4 Wire breakage simulation matrix	89
Table 7-5 Prestress loss due to wire breaks	91
Table 7-6 Frequency drop with wire breaks	94
Table 8-1 Seven-wire prestressing strand: geometric and material parameters	98
Table 8-2 Change in modal properties with successive wire cuts	103
Table 8-3. Prestress loss after first wire break	107
Table 9-1 Distance and strain change relationship fit statistics (Coeff. of determination, R^2)..	113
Table 9-2 Distance and strain change relationship fit statistics (Coeff. of determination, R^2).	130
Table 9-3 Broken strand identification: End 'A' (Near end)	139
Table 9-4 Broken strand identification: End 'B' (Far end)	139
Table A-1 Impedance analysis results	160
Table E-2 Event (wire cut) detection and location by acoustic sensors	220
Table E-3 Event (wire cut) detection and location by acoustic sensors	227

1 Introduction

This is Part III of the research report covering the health-monitoring components of Tasks 2 and 3 of the FDOT Project BDV31-977-15 “Replaceable Unbonded Tendons for Post-Tensioned Bridges”. Several small scale test setups were constructed to evaluate the breaking behavior of single prestressing strands. Following testing of the full-scale specimens in Part II, wires were cut while monitoring to gather data to validate the wire break location algorithm. Finally, finite element analyses were conducted in support of the development of the algorithm.

Chapter 2 provides a brief overview of the approach taken in this portion of the research project. A summary of the literature on existing monitoring techniques and a background study on finite element (FE) modeling of prestressing strand and anchorage are given in Chapter 3. Chapter 4 presents a proof-of-concept study on a monitoring method to detect wire breakage in unbonded tendons based on relative strain variation (relative strain change among discrete monitoring points) in post-tensioning anchors. Experimental work and FEA are used to complete the study. Chapter 5 provides experimental validation of the proposed method by evaluating the sensitivity of strain distribution in anchors with wire breaks. After confirming the responsiveness of the end anchors to tendon damage, a wire breakage detection algorithm is presented in Chapter 6. Chapter 7 focuses on characterizing the stressing and breakage response of a prestressing strand through a parametrized FE model. The experimental evaluation of post-breakage response is described in Chapter 8. Chapter 9 describes the experimental investigations with full-size girders and assesses the proposed method’s effectiveness in breakage detection. Finally, Chapter 10 summarizes the research and provides recommendations followed by Chapter 11, which presents possible further research.

2 Research Approach

This part of the research project focused on developing a robust and cost-effective monitoring system for unbonded post-tensioning tendons. Although corrosion detection is considered a critical aspect of tendon monitoring, many of the monitoring approaches are insensitive to small defects or corrosion at an early stage, making them challenging to implement in a full-scale setting. By virtue of safety factors, the breakage of an individual wire in a multi-strand tendon system can serve as a warning and an early detection of the breakage can enable proactive maintenance. Thus, the primary objective of this work is to develop an efficient system for tendon damage detection with the ultimate goal of providing maintenance decision support. Specifically, the aim is to detect a breakage event and identify the broken strand at the earliest possible stage, as early as a single wire break.

In developing the monitoring system, this research considers: 1) a comprehensive investigation of existing monitoring approaches to determine their limitations, 2) the development of an efficient method particularly suitable for unbonded tendons, 3) the creation of detailed analytical models to investigate strand failure mechanisms and assess the feasibility of the proposed monitoring method, 4) validation experiments to confirm its effectiveness and practicality, 5) an extensive parametric study to achieve an optimized sensor arrangement, 6) the development of an efficient data processing algorithm to detect, locate, and quantify the tendon damage programmatically, 7) a sensitivity study with measurement errors to examine the robustness of the model, 8) the characterization of static and dynamic strand response to loading and wire breakage, 9) a behavioral investigation of wire breaks with various confinement conditions, 10) the investigation on stress recovery and load distribution among wires to determine the effectiveness of the method, and 11) full-scale laboratory experiments with both internal and external tendons to investigate the effectiveness of the proposed monitoring approach. Completion of these tasks have resulted in an efficient breakage detection framework that enables an automated tendon monitoring strategy suitable for in-field implementation.

3 Literature Review

This chapter first presents a literature review on the available monitoring methods. Examples of full-scale implementation of these methods and their limitations are listed. Selection of different finite element parameters required for a proper model of contact interactions at the anchorage is discussed. The FE parameters include discretization of contact surfaces, contact enforcement methods, numerical algorithms and loading schemes. A background study is then conducted on the mechanical behavior of wire strands and ropes. Finally, an overview of standard strain gages and data acquisition systems is provided.

3.1 Structural Health Monitoring

Structural health monitoring (SHM) is the process of the development and implementation of a strategy to detect, locate and quantify damage in engineered structures, where damage refers to the change introduced into the structure that adversely affects its functional behavior. The SHM process involves the integration of sensors, extraction of damage-sensitive features, analysis of the data and development of a statistical model to determine the current condition of the structure compared to its pristine state. Clearly, SHM has significant economic and life-safety implications and the information obtained from monitoring is generally used to prioritize maintenance.

Non-continuous periodic monitoring has been used for many years that often involves destructive testing by physically breaking into the system. The current trend is towards uninterrupted continuous non-destructive testing (NDT) with greater automation. Many monitoring techniques have been developed over the years, which may be broadly categorized as follows (Hellier 2003) –

- Visual testing
- Imaging techniques
- Vibration-based testing
- Magnetic particle testing
- Electrical resistance/impedance-based testing
- Penetrant testing
- Thermal infrared testing
- Wave propagation/reflection-based technique

3.2 Existing Tendon Monitoring Techniques

Various techniques have been sought for defect (or breakage) detection and monitoring of prestress levels in post-tensioning tendons. Some of these are:

- Visual inspection
- Screwdriver penetration test
- Radiography (Imaging technique)

- Global dynamic approach
 - Remnant Magnetism (RM)/Magnetic flux leakage (MFL)
 - Magnetic permeability
 - Magnetostrictive sensing
- } Magnetic methods
- Electrical resistance based method
 - Electro-mechanical impedance (EMI) technique
- } Electrical methods
- Time-domain reflectometry (TDR)
 - Impact-echo (IE) method
 - Ultrasonic pulse-echo technique
 - Guided wave ultrasonic technique (GWUT)
 - Acoustic emission (AE) technique
- } Wave propagation based approaches

Efforts to develop and implement these approaches have produced mixed results and levels of success. Each of these methods will be introduced briefly in the subsequent paragraphs while three of them (i.e., EMI, GWUT and AE) will be discussed in detail at the end of this section as they deemed to be more suitable for unbonded construction.

3.2.1 Visual Inspection

Periodic visual inspection, the most common tendon monitoring technique at present, uses visual observation to examine prestressing tendons without utilizing any specialized equipment. It is known to be the oldest form of SHM technique, which is applicable when the degradation is visible by itself or by physically breaking the tendon duct system. Although construction drawings help in locating the tendon profile, defects can occur anywhere along the length. Exposure of the tendon duct is commonly carried out by drilling holes at positions where defects are most likely to occur, such as near the high points; hence, locating the defect is a somewhat arbitrary process (Williams and Hulse 1995). In addition, the subjective assessment might potentially result in incorrect or inadequate condition evaluation. Drilling and coring to facilitate visual inspection is also limited by its destructive nature, which frequently leads to further complications; its localized scope; and by the fact that the tendons are often inaccessible.

3.2.2 Screwdriver Penetration Test

In this monitoring approach, the concrete cover is removed and a flat-head screwdriver is kept perpendicular to the exposed strand, while placing the screwdriver tip in the groove between two outer wires (Jimenez 2013; Harder and Webster 2001). The screwdriver is then struck with a standard hammer. Under the lack of tension in one or both of the two wires, the screwdriver penetrates, indicating the presence of breakage somewhere along the tendon length. This process

is repeated for the rest of the outer wires. This method is, however, subjective and may not identify tension deficiencies or wire breakages away from the inspection location.

3.2.3 Radiography

Imaging technology, especially radiography, has been successfully used in several applications for non-destructive evaluation (NDE) and defect detection (Pla-Rucki and Eberhard 1995). Its application in concrete structures, however, has been limited because the heterogeneous nature of concrete tends to scatter the X-rays. In addition to the requirements of expensive equipment and trained operators, difficulties with accessibility and radiation hazard pose challenges to its in-field application.

3.2.4 Global Dynamic Approach

A modal analysis-based approach examines changes in global vibration response to characterize structural damage by correlating shifts in resonant frequencies or changes in mode shapes to the level of deterioration. This technique has been successfully employed to measure cable load in stays as well as to detect damage in many other structures (Chang et al. 2003; Tabatabai et al. 1998; Salawu 1997; Doebling et al. 1996). Though this approach alone may not be sufficient to identify the damage location, it is still useful to confirm if damage has occurred so that further measures can be taken to determine its location. This method, however, is found sensitive only if the structure as a whole undergoes substantial damage; local structural degradation such as wire faults in post-tensioning tendons is often not reflected in the measured global dynamic characteristics because of low signal-to-noise ratio (SNR). In addition, the severity of damage necessary to result in a detectable change in modal parameters can limit this approach's ability to provide timely assessment of large structures such as prestressed concrete bridges.

3.2.5 Remnant Magnetism/Magnetic Flux Leakage

In remnant magnetism (RM) and magnetic flux leakage (MFL) methods, the magnetization of ferromagnetic tendons is performed with an electromagnet. A part of the total induced magnetization remains in the tendons (residual magnetization) even after removing the magnetizing field because of remanence phenomenon. In the vicinity of a defect, a localized discontinuity (leakage), as compared to the defect-free state, is introduced due to magnetic dipole redistribution identified by a magnetic detector (Scheel and Hillemeier 2003, 1997; Ghorbanpoor et al. 2000). These methods have been applied in condition assessment of post-tensioning tendons; however, the measured data poses a detection challenge as the magnetic field is often disturbed by other embedded steel elements, making signal interpretation difficult.

3.2.6 Magnetic Permeability

Wang et al. (2000) described another magnetic method based on magnetic permeability (the degree of magnetization that a material obtains in response to an applied magnetic field) of ferromagnetic substances to detect cable defects. This method, however, requires a bulky magnet to run along the tendon, causing difficulty with accessibility, and is not applicable for continuous structural health monitoring.

3.2.7 Magnetostrictive Sensing

In magnetostriction, electric current in transmitter coil induces a variation of magnetic field within the coil, which in turn produces a change of magnetization within the ferromagnetic test material (PT strand), causing a subsequent deformation (Joule's effect), and produces a stress wave. Inversely, the wave propagating in the ferromagnetic material modulates an existing magnetic field (Villari's effect), thereby exciting a voltage pulse in the receiver coil (Faraday's law) (Lanza di Scalea et al. 2003). Kwun and Bartels (1998) discussed magnetostrictive sensing and its application in condition monitoring of various engineering systems. Later, Lanza di Scalea et al. (2003) used magnetostrictive transducers to detect defects in strands. This technique requires access to a portion of the tendon away from the ends and like other magnetic methods this technique is also not suitable for continuous monitoring.

3.2.8 Electrical Resistance Method

The electrical resistance-based approach (Elsener 2008; Della Vedova and Elsener 2006) measures electrical impedance (total opposition to the flow of an alternating current (AC) that includes resistance, capacitance, and inductance) to detect faults in electrically isolated tendons (EIT). The steel strand, the duct, the reinforcing steel, and the surrounding concrete constitute the impedance measurement system. The presence of a defect introduces a parallel resistance into the system, which results in a reduction of the equivalent resistance measured between the strand and the reinforcing steel. Despite the advantage of simple electric connection at the anchors, establishing the baseline impedance may be a challenge in practical applications.

3.2.9 Time-domain Reflectometry

In time-domain reflectometry (TDR), an impulse of energy is initially introduced into the system and the nature of defect is then determined by analyzing the magnitude, duration and shape of the reflected waveform. This approach has been traditionally used to identify and locate discontinuities in electrical transmission lines and was successful for defect detection in suspension bridge cables and reinforcing steel (Liu et al. 2002, 1999). Although TDR seems promising, there is no documented success to date of detecting tendon breakage or prestress loss.

3.2.10 Impact-echo

The impact-echo (IE) method has been proven as an effective NDE technique where a short duration mechanical impact at a free surface of the structure generates low-frequency waves that propagate through the thickness and are subsequently reflected by internal flaws and external boundaries. Defects are characterized by early wave echoes (reflection from internal flaws) registered at the free surface. This technique was successful in detecting grout voids in tendon ducts of post-tensioned concrete slabs (Jaeger et al. 1996), but is found ineffective in detecting tendon defects (corrosion, wire breakage, or prestress loss).

3.2.11 Ultrasonic Impulse-echo

Ultrasonic testing (UT) impulse-echo method uses short duration ultrasonic pulse waves launched into materials to detect internal flaws. The wave is then reflected from an imperfection within the object and the defect is located from the arrival time of reflected wave. This approach mainly evaluates the ultrasonic wave propagating in thickness (least dimension) direction and is found suitable only for localized inspection.

3.2.12 Electro-mechanical Impedance Method

Overview. The electro-mechanical impedance (EMI) method correlates the variation of localized dynamic characteristic of a structural component (anchor block in post-tensioned construction), resulting from wire breakage or loss of prestress, to the observed change in EMI signature (measured electrical impedance in a coupled electro-mechanical system). A harmonic voltage is applied to a piezoceramic patch bonded to the structure to induce harmonic excitation into the structure, which in turn produces a modified electrical signal to reflect the modulation in dynamic parameters as a result of structural damage.

Liang et al. (1994) showed that the change in mechanical impedance (due to structural damage) of a host structure can be detected by monitoring the change in the EMI signature of a piezoelectric material, such as lead zirconate titanate (PZT), surface-bonded to the structure. As the PZT is bonded to the structure, an input voltage to the PZT induces a deformation into the structure (inverse piezoelectric effect) for displacement compatibility. Figure 3-1 shows an arbitrary deflected shape (dashed line) of host structure due to an imposed displacement from PZT; the true deflection of the host structure, however, will depend on the boundary conditions of the structure as well as the stress field around the PZT-structure interface.

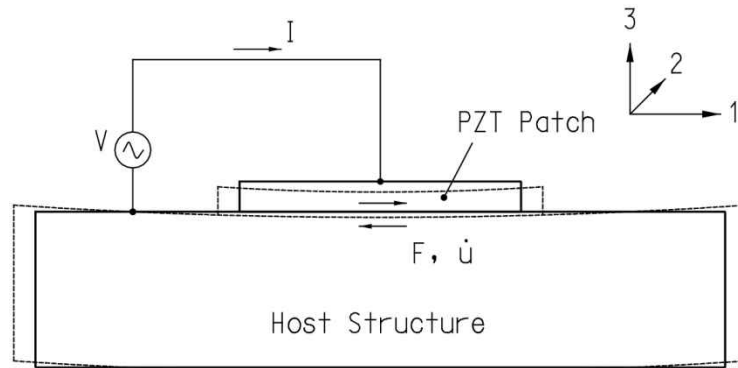


Figure 3-1 Interaction between PZT Patch and host structure

The idea is to apply harmonic voltage to the PZT to result in resonance response of the electro-mechanical system, which occurs when the PZT's mechanical impedance matches the structure's mechanical impedance, and continuously (or intermittently) monitor the vibration feedback. A change in structural condition modifies the vibration response, which in turn modulates the output current (direct piezoelectric effect) manifested by alteration of EMI signature. Thus, a key aspect of this active sensing technology is the use of PZT material as a collocated sensor and actuator (transducer) on the basis of energy transfer between the transducer and its host mechanical system. The electro-mechanical impedance is first recorded in a healthy condition and the measurement is then continued until the presence of damage is traced by changes in signal characteristics (such as statistical index or resonant frequency shift in impedance signature, shown in Figure 3-2) in a damaged condition. Thus the variation in electro-mechanical impedance over a range of frequencies is analogous to that of the frequency response functions (FRFs) of a structure (Park et al. 2003).

It is noteworthy that macro-fiber composite (MFC), a relatively new type of piezoceramic material, has also been used recently. MFC is known to have certain advantages over ordinary PZT, such as being more flexible and less affected by bonding defects (Kim et al. 2010).

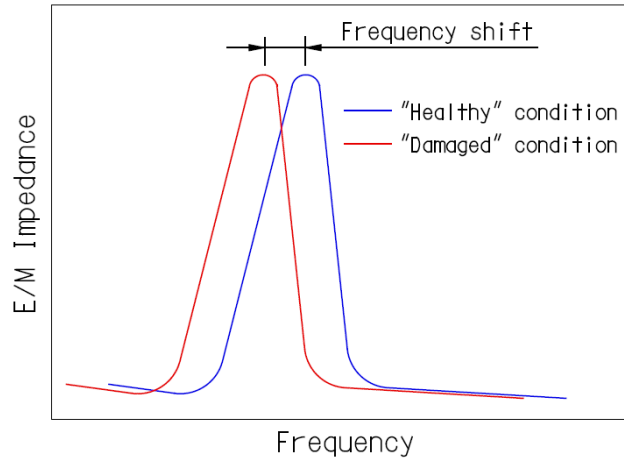


Figure 3-2 Resonant frequency shift in impedance signature due to damage

Theoretical Development. The groundwork for theoretical development of impedance measurement for structural health monitoring applications was laid by Liang et al. (1994); their work showed that the electro-mechanical impedance of PZT transducer is a combined function of mechanical impedance of PZT and that of the host structure:

$$\frac{V}{I} = Z^{em} = \frac{1}{i\bar{\omega}a \left[\hat{\epsilon}_{33}^T - \frac{1}{\frac{Z^p}{Z^s} + 1} (d_{3x})^2 \hat{Y}_{xx}^E \right]} \quad \text{Equation 1}$$

Where,

V = input voltage to the PZT

I = output current from the PZT

$\bar{\omega}$ = angular frequency of excitation voltage

Z^{em} = electro-mechanical impedance of the system

Z^p = mechanical impedance of bonded PZT

Z^s = mechanical impedance of host structure

d_{3x} = piezoelectric coupling constant

Subscript x = direction 1 or 2, subscript 3 = direction of polarity (Figure 3-1). The first subscript indicates the direction of the electric field associated with the voltage applied, or the change produced. The second subscript indicates the direction of the mechanical stress or strain.

Superscript T = Zero stress and E= Zero electric field.

wafer to them. It was found that the cracks modify the EMI spectrum compared to the pristine plates. Bhalla and Soh (2003) instrumented PZT patches to a two-story reinforced concrete portal frame. To simulate loadings from earthquake or underground explosions, the test frame was subjected to base motions that induced flexural and shear cracks into the frame. The instrumented PZT patches were found to provide meaningful information of the incipient damage by showing prominent shift in the conductance signature. Mascarenas et al. (2007) demonstrated the effectiveness of impedance method by detecting the loss of preload in a bolted joint. PZT patches were mounted on washers of the bolted joint in a moment-resisting frame made of aluminum. The bolted joint was progressively tightened and an impedance measurement was made at each level of tightening. The method identified “healthy” and “damaged” condition as characterized by the level of tightening.

A 6-m long T-beam with an ungrouted monostrand post-tensioning tendon was investigated by Kim et al. (2010) to detect tendon damage. A MFC patch was bonded to the surface of the anchor plate near the jacking area. Different levels of prestress force were applied to the test structure and the corresponding EMI signatures were recorded. The recorded results confirmed the tendon damage simulated by prestress-loss. In this test, the piezoelectric patch was bonded at a very stiff region, demanding a very high frequency excitation to obtain resonance response of the structure. To eliminate the need of high frequency excitation, Nguyen and Kim (2012) conducted a similar experiment on the laboratory-scale tendon-anchorage connection but introduced an additional thin plate equipped with flexible PZT patch sandwiched between the bearing plate and anchor block. The system was successful in detecting prestress-loss from the observed variation of the impedance signature.

Implementation Considerations. The EMI-based technique is deemed promising as it captures the change in local dynamic characteristics of tendon-anchorage connection and is less affected by global changes that may not necessarily be triggered by strand wire breakage. As indicated above, evidence of conducting laboratory experiments with monostrand tendons is found in literature. In addition, preliminary assessment of this method has been conducted as a part of this research through small-scale, single tendon tests using a specially designed test frame, details of which can be found in the literature. However, issues such as distributing the piezoceramic (PZT or MFC) patches on multi-strand tendon anchor block, costs associated with instrumentation (impedance analyzer or alternative circuits), weathering effects on patches, and bonding materials must be addressed for practical implementation consideration.

3.2.13 Guided Wave Ultrasonic Technique

Overview. The guided wave ultrasonic testing (GWUT) approach is an active sensing method in which an array of transducers is used to generate ultrasonic waves that propagate along the boundaries of the waveguide (tendon itself) and are then measured by ultrasonic sensors. This technique presents a wide spectrum of applicability for non-destructive evaluation and structural health monitoring in bounded media. At present, it is one of the most widely used NDE methods in industry to inspect various engineering structures, especially metallic pipelines. GWUT has been successfully implemented in pipeline inspection, defect detection in railroad tracks and has also shown promises in monitoring prestressing tendon by exploiting its waveguide geometry. In recent years, progress has been made to use this technique in detecting post-tensioning tendon faults; two approaches are common for tendon defect detection with GWUT – arrival time of propagated wave and inter-wire energy leakage (or cross talk) between the wires in a strand.

In open space (unbounded media), waves propagate spherically in all directions and lose power as they travel away from the center of disturbance. The presence of a boundary, however, while traveling along a cylindrical bar, plate or a medium with generic cross-section, guides the wave to propagate unidirectionally along the longitudinal axis, resulting in less energy loss and longer travel distance. With this behavior, guided waves are explained as the ultrasonic mechanical stress waves that propagate in one direction (along the length) of a structure while guided by and confined in its geometric boundaries (waveguides) due to reflection from the waveguide wall.

A transducer is used to induce ultrasonic harmonic stress waves in the structure. The longitudinal and shear components of bulk wave interact with boundaries of the waveguide, which, in general, is uniform in one direction (along the longitudinal axis). As waves are confined inside the waveguide due to multiple reflections back and forth between the walls, the propagation inside the waveguide can be described approximately as a zigzag between the boundary surfaces until a series of reflections and mode conversions occur to form wave packets (or wave envelope) from their superposition (Bartoli et al. 2011). A steady-state situation is then achieved from the constructive interference of incident and reflected waves and the wave packet propagates essentially along the longitudinal axis. After allowing the waves to travel through the structure, the propagated waves are read back by the same (or a separate) transducer and the arrival time and/or energy content of the captured waves are analyzed to identify a potential defect.

The available two detection approaches of GWUT are applied in tendon monitoring; one of them addresses that the end-to-end traveling time of stress wave through the strand is sensitive to prestress level, and the other accounts for the variation of inter-wire cross-talk (energy leakage due to the change in contact) as a function of stress level.

Theoretical Development. The evidence of studying guided waves dates back to the end of 19th century, when Pochhammer and Chree worked on mechanical wave equation for cylindrical elastic waveguides. Gazis and Zemanek extended the work of Pochhammer and Chree and conducted a thorough investigation on propagation phenomena. Afterwards, Rayleigh and others contributed in explaining various aspects of wave propagation in bounded media. Detail calculations and theories of guided waves in elastic isotropic media are well documented by Achenbach (1973) and others.

Chen and Wissawapaisal (2001) utilized the wave velocity equations and Pochhammer's frequency equation (Achenbach 1973) to explain the change in traveling time of stress wave as a function of uniaxial tensile stress. The center (core) wire of seven-wire strand was considered as a slender, isotropic, and elastic waveguide. The governing equation of wave motion in a circular waveguide with radius a is given as

$$\frac{2p}{a} (q^2 + k^2) J_1(pa) J_1(qa) - (q^2 - k^2)^2 J_0(pa) J_1(qa) - 4k^2 pq J_1(pa) J_0(qa) = 0 \quad \text{Equation 2}$$

Where

$$p^2 = \frac{\omega^2}{C_L^2} - k^2$$

$$q^2 = \frac{\omega^2}{C_T^2} - k^2$$

ω = angular frequency of propagating wave

k = wave number (spatial frequency of wave in radians per unit distance)

$J_0()$ and $J_1()$ = Bessel functions of the first kind of order 0 and 1, respectively.

It is noticed that the propagation frequency (ω) has multiple roots, implying different propagation modes.

The wave velocity equations are expressed as

$$\rho C_L^2 = \lambda + 2\mu + \left(\frac{\lambda + 2l + \frac{(\mu + \lambda)(4\lambda + 10\mu + 4m)}{\mu}}{3\lambda + 2\mu} \right) \sigma \quad \text{Equation 3}$$

$$\rho C_T^2 = \mu + \left(\frac{4\lambda + 4\mu + m + \frac{\lambda n}{4\mu}}{3\lambda + 2\mu} \right) \sigma \quad \text{Equation 4}$$

Where ρ = mass density of steel strand; λ and μ = Lamé's elastic constants; and l , m , and n = Murnaghan's third-order elastic constants. It is noted that both longitudinal and transverse wave velocity (C_L and C_T , respectively) are inversely proportional to the increase in tensile stress (σ).

The group velocity at which the overall shape of the wave amplitudes (the modulation or envelope of the wave) propagates through space is defined as

$$C_g = \frac{d\omega}{dk} \quad \text{Equation 5}$$

As observed from Equation 2 and Equation 5, wave motion in slender circular rod is dispersive, i.e., propagation velocity is a function of frequency. Thus the traveling time (t) of a wave to propagate distance z (length of the strand) at any particular frequency (ω) can be calculated as

$$t = \frac{z}{C_g(\omega)} \quad \text{Equation 6}$$

In developing energy leakage-based detection method for tendon monitoring, Bartoli et al. (2011) observed that depending on the load conditions, each helical (peripheral) wire in a strand can be in contact with the two adjacent wires, or the core, or with both core and adjacent wires. In the absence of axial load, the six helical wires and the core wire can be seen as independent waveguides, whereas under load, contact stresses force the wires to remain attached to each other and thus the whole strand is considered as a global waveguide.

A seven-wire strand was studied in which six helical wires were wrapped around a core wire as shown in Figure 3-3. The following assumptions were made:

- The helical waveguide has dispersion properties similar to those of the straight central core waveguide.
- Because of negligible difference in lengths, signals propagating in the core wire and in the helical wires are detected simultaneously.
- Axial force in the helical wire is assumed to be equal to axial force in core wire due to small lay angle.
- Bending and twisting stresses developed in helical and core wires are insignificant compared to axial stress and can be neglected.

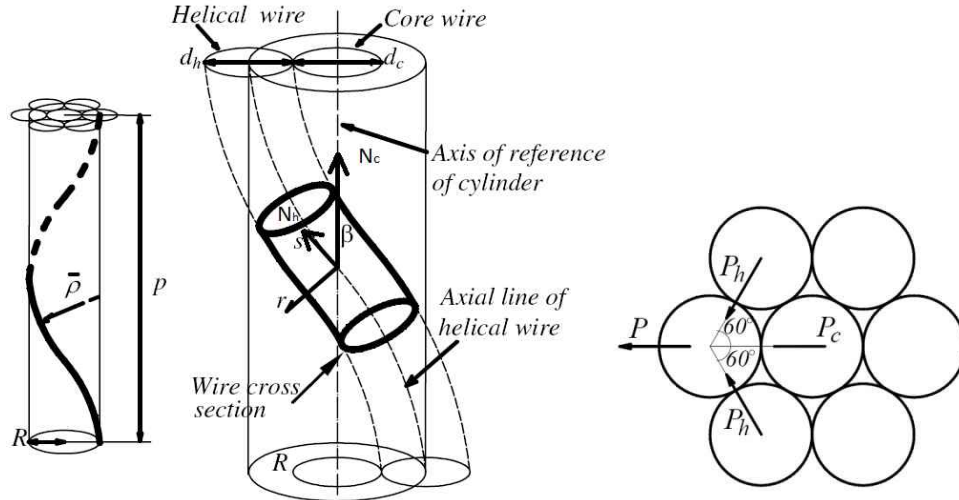


Figure 3-3 Geometry of a seven-wire strand

In Figure 3-3,

$$\beta = \text{lay angle of helical wire} = \tan^{-1} \left(\frac{2\pi R}{p} \right)$$

$$\bar{\rho} = \text{radius of curvature of the axis of helical wire} = R + \frac{1}{R} \left(\frac{p}{2\pi} \right)^2$$

$$s = \text{arc length of helical wire} = \frac{l}{p} \sqrt{p^2 + (2\pi R)^2}$$

R = radius of reference cylinder

p = pitch of helical wire

A = cross sectional area of wire

d_c = diameter of core wire

d_h = diameter of helical wire

l = length of undeformed strand

$$P = \text{resultant of contact forces per unit length} = P_h + P_c = \frac{N_h}{\bar{\rho}}$$

P_h = resultant of contact forces between adjacent helical wires

P_c = resultant force due to contact between helical and core wire

$$N_c = \text{axial force in core wire} = \frac{A_c N}{A_c + 6A_h \cos^3(\beta)}$$

$$N_h = \text{axial force in the helical wire} = \frac{A_h \cos^2(\beta) N}{A_c + 6A_h \cos^3(\beta)}$$

$$N = \text{axial tensile force applied to the strand} = N_c + 6N_h \cos(\beta)$$

A_c = cross-sectional area of center wire

A_h = cross-sectional area of helical wire.

The contact length between helical and core wire was estimated as

$$a = \sqrt{\frac{8P(1-\nu^2)}{\pi E} \frac{d_c d_h}{l(d_c + d_h)}}$$

Equation 7

Where, ν = Poisson's ratio and E = Young's modulus of steel strand.

Due to the contact between wires, a single wire of the strand leaks energy into the surrounding wires. From Equation 7, it is observed that contact length (a) is proportional to the square root of the resultant of contact forces (P). Consequently, a decreased contact between wires associated with prestress loss (due to defects) results in a reduced energy leakage and vice-versa.

Experimental Validation. To evaluate the prestress level in post-tensioning tendons, Chen and Wissawapaisal (2001) conducted an experiment with a ~15 ft long seven-wire strand located inside a hollow core space of a reinforced concrete beam. An acoustic emission transducer was placed at one end of the core wire to produce a short duration impulse (with the help of a pulse generator) and another AE transducer was mounted at the other end to register the wave motion. Both transducers were installed perpendicular to the wire's cross-section to generate and capture longitudinal wave. Tests were performed with different prestress levels and shifts of arrival times (time of flight) of the recorded waveforms were observed due to change in wire diameter and wave speeds as indicated in Equation 2 to Equation 7.

To generate and detect stress waves on a monostrand tendon, magnetostrictive transducers were used by Lanza di Scalea et al. (2003) exploiting the strand's waveguide geometry. Tests were performed with both wires with partial indentation and complete fracture. Substantial reduction of signal amplitude relative to the defect-free condition was observed due to the presence of an indentation (compared to the reduction of cross-sectional area of strand) from the recorded time-domain waveforms. The presence of fully fractured wire was confirmed by the complete disappearance of registered echo.

Bartoli et al. (2011) tested a ~3 ft long seven-wire single strand to monitor prestress loss based on inter-wire energy leakage. Ultrasonic waves were generated using a PZT actuator bonded on the external surface of a peripheral wire. The propagated wave was measured by a pair of AE sensors located at the end (perpendicular to the wire's cross-section) – one at peripheral wire and the other at core wire. It was observed that the inter-wire leakage (from peripheral to core) increases substantially with increasing load level as a result of the increasing inter-wire contact.

Implementation Considerations. The time of flight-based damage detection approach has the advantage that access is required only at the two ends of tendon for installing actuators and sensors. In addition, as transducers are placed on core wires, which are less likely to degrade before the surrounding peripheral wires, breakage detection of peripheral wires on the same strand or wires of other strands on the tendon might be possible due to redistribution of loads on individual wire. These advantages have made the guided wave technique a promising candidate for in situ application. Until now, however, reduced scale experiments have been conducted on prestressing tendons in a laboratory environment. Also, parameters such as temperature variation and signal attenuation at deviator and anchorage locations must be considered for on-site practical application.

3.2.14 Acoustic Emission

Overview. Acoustic emission (AE) is a passive method that relies on the sudden release of localized stress energy within a material (due to wire damage or breakage) to produce elastic stress waves, which are eventually captured by ultrasonic sensors as a measure of defect detection. In recent years, AE system has been installed on several bridges for long-term monitoring of prestressing tendon wires and stay cables.

When the material within a structure experiences abrupt dislocations at an atomic scale as a result of localized failure such as breakage, yielding, buckling, denting, debonding, etc., it triggers sudden release of strain energy in the form of elastic waves (mechanical wave that propagates through elastic medium in which a displacement proportional force acts on a previously deformed particle to restore its original position). AE refers to the micromechanical process of the generation of elastic waves due to the release of energy within the material (ndt-ed.org 2013). The energy is emitted as a short impulse and propagates through the material in the form of stress or sound waves with a wide frequency range. The propagated wave is registered by sensors, and the signal from the sensor is recorded by an AE system whenever it passes a preset threshold that is a predefined criterion to detect and locate active defects (Figure 3-4).

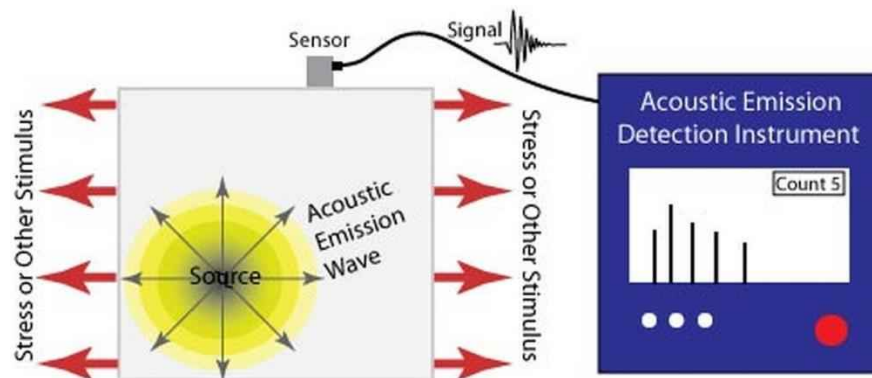


Figure 3-4 Acoustic emission testing

Acoustic emission testing (AET) has become a recognized NDT method in structural health monitoring and has various industrial and academic research applications, such as detecting active material flaws, leaks, corrosion, and the formation of cracks during the welding process. Unlike other active NDT methods (e.g., ultrasonic testing), AET is passive in the sense that it relies on the energy initiated within the structure internally rather than supplying external energy to the structure under examination. To reduce the inclusion of unwanted signals (background noise, which is commonly of low frequency), increase the detectability (as most energy release occurs at high frequency), and achieve high sensitivity of produced signal in response to damage, AET often involves capturing the signals in a high frequency range of 100-500 kHz (Hellier 2001).

In addition to flaw detection, AET can also be used to determine the location of the flaw or a breakage event by measuring signal arrival time, considering a constant velocity of acoustic wave in a particular material. Multiple acoustic sensors are placed at different locations to listen for the sounds of structural failure, and the signal arrival times at each sensor position are registered. Based on the recorded hits (the process of detecting an AE event) and their arrival times, the location of the occurrence is then determined from geometric triangulation (Fricker and Vogel 2007).

Theoretical Development. The AE process begins with sudden redistribution of stress inside a material, which causes atomic-scale deformations. These deformations release energy in the form of elastic waves, which propagate through the material as acoustic waves. Hellier (2001) indicates that the origination of AE method is attributed to J. Kaiser in the 1950s when he reported the effect of the absence of acoustic emission in materials under stress levels below

those previously applied on that material (Kaiser effect). Figure 3-5 shows this phenomenon in the load versus cumulative AE plot (ndt-ed.org, 2013). As the load (stress) on the structure is raised, acoustic emission events accumulate (segment AB), but when the load is lowered (BC) and reapplied (CB), AE events do not occur again until the load at point B (previous maximum load) is exceeded. Emission continues as the load is increased further (BD).

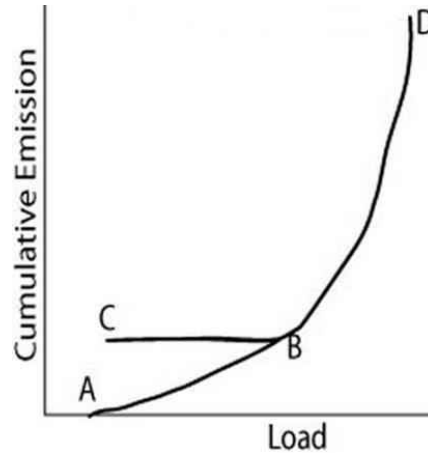


Figure 3-5 Kaiser Effect

The original waveform of released stresses at the AE source location is essentially pulse-like. The width and height of the pulse depend on the dynamics of the source and consequently, the amplitude and energy of the primitive pulse vary over a wide range. Waves radiate from the source in all directions but often have a strong directionality depending on the nature of the source (ndt-ed.org, 2013). As these primitive waves travel through a material, their form is changed considerably as they often undergo multiple changes due to attenuation, dispersion, diffraction, scattering, reflection from boundaries, interaction with reflected waves and so forth. Therefore, waves of different types propagate at different velocities and with different oscillation directions and frequencies while passing through a medium (Muravin 2009).

AE wave propagation is commonly interpreted as Lamb waves (elastic sine waves propagating in solid plates whose particle motion is bounded by the plate surface causing a wave-guide effect) and as shown in Figure 3-6, it often considers the lowest antisymmetric mode (flexural mode a_0) as it travels faster and usually produces higher amplitudes than the other family of Lamb waves (extensional/symmetric mode s_0). Other higher order modes of these two families of Lamb waves, though travel faster than the parent members, are relatively less important as their amplitudes tend to be low (Hellier 2001).

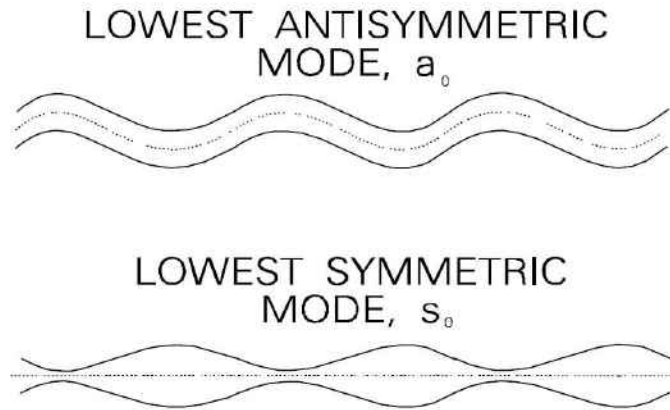


Figure 3-6 Lamb waves

The amplitude of AE wave attenuates as it travels through the structure. As explained by Hellier (2001), this is primarily due to geometric spreading (natural tendency of wave to spread throughout the volume of structure), scattering at boundaries (reflections and mode conversions when a wave meets a discontinuity), and energy absorption (conversion into heat energy). Geometric spreading is the biggest contributor to attenuation when the event source is located closely to the sensor, whereas scattering and absorption become more influential at a greater distance.

Experimental Validation. Cullington et al. (2001) conducted an extensive examination on the operation of a SoundPrint[®] acoustic monitoring system (Piezo-electric AE sensors, data acquisition and signal processing unit, shown in Figure 3-7) for breakage detection of wires in bonded post-tensioned bridges. An external wire break device (containing a stressed strand with anchorage plates) was attached to the concrete surface of a full-scale bridge to mimic a genuine wire breakage event. The anchorage plates were acoustically coupled to the concrete surface to ensure transmission of the acoustic event (generated by wire breakage) into the bridge and a real wire break event was simulated by inducing breakage into the external wire. A symmetric array of AE sensors, placed at approximately 2 m intervals, was installed on the concrete surface to capture the events. Open and blind trials, by inducing wire breakage through grinding and accelerated corrosion, respectively, were conducted in both laboratory conditions and in-service environments, and most of the wire breakage events were successfully identified and located by the AE monitoring system.

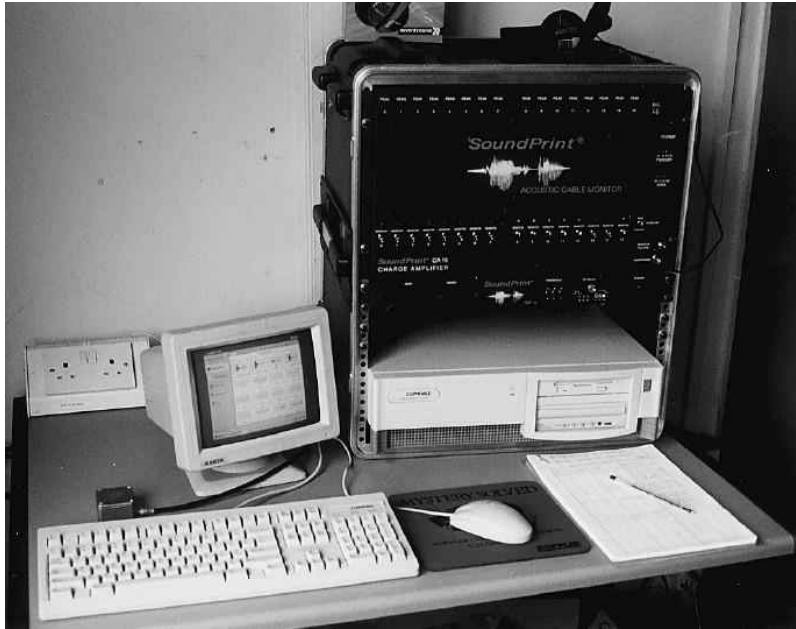


Figure 3-7 SoundPrint® acoustic monitoring system

To investigate the performance of continuous acoustic monitoring of a real-life post-tensioned bridge with bonded tendons, Fricker and Vogel (2007) installed AE sensors on a post-tensioned bridge under active deterioration and spontaneous wire breaks (Figure 3-8). In addition to uncontrolled wire breaks, factitious breakages were generated by employing electrolytic corrosion cells to create wire breaks without producing unwanted noise from cutting or grinding. The 60 m long x 6 m wide bridge was equipped with 16 AE sensors with an average sensor density of one sensor per 31 m² of bridge deck. The AE system was successful in detecting the artificially generated wire breaks in the grouted tendons along with several spontaneous wire breakage events.

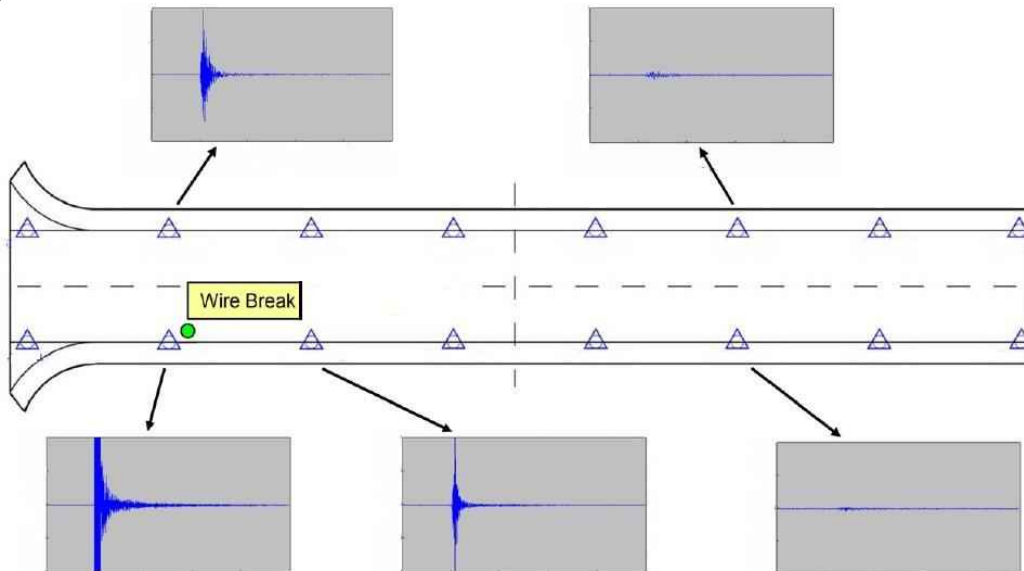


Figure 3-8 Sensor locations and detected signals

A comprehensive parametric study was conducted by Yuyama et al. (2007) to examine the applicability of AET in post-tensioned construction. Physical Acoustic Corporation's (PAC) 18-channel SPARTAN and 8-channel MISTRAS AE systems were employed for continuous monitoring. Besides two in-service bridges (T-beam and box-girder), studies were carried out in laboratory setting with beams post-tensioned by steel bar, strand and parallel wire cable with different grout conditions (unbonded, partially grouted and fully grouted). Greater reliability, in terms of detectability of wire breaks, was observed in case of bridge with T-beam than the one with box-girder due to simpler wave path. Larger signal amplitudes were produced by breakage of steel bars compared to wires in strand and cable. Because of specific beam configuration and sensor locations (combined effect of source-sensor distance and grouting condition, as lesser distance meaning lower signal attenuation, whereas grouting is likely to attenuate the amplitude), the success rate of wire breaks detection was found to be the highest in case of partially grouted condition (the source-sensor distance was more than fully grouted condition, but might have experienced lower signal attenuation due to partially grouted condition) followed by fully grouted (though the distance is the minimum in fully grouted, significant amplitude attenuation might have occurred) and unbonded conditions (the distance is the maximum).

Implementation Considerations. Acoustic emission has been tested in laboratory conditions and implemented in in-service post-tensioned bridges and stay cables to identify the onset of failure (Zejli et al. 2012; Salamone et al. 2012; Fricker and Vogel 2007; Yuyama et al. 2007; Cullington et al. 2001). In addition, the efficacy of acoustic monitoring in detecting wire failures has been examined as a part of this research and the results are reported in Appendix E. A major advantage is that the sensors are placed externally on the concrete surface, thus accessing the tendon or anchorage is not warranted. However, as the method relies on naturally generated acoustic events, continuous monitoring at high sample rates with appropriate filtering is required and the recorded data is further analyzed to classify the events, which is often conducted semi-automatically. The key parameter is to select the optimum number of sensors and their placement (sensor array) on the structure under examination. Determining the threshold amplitude as breakage indicator could also be challenging due to irregular non-fracture events, such as traffic noise and various impacts. In addition, other parameters, such as characteristics of acoustic waves (velocity and attenuation), event location, distribution of sensor arrays, and the number of sensors detecting the breakage, must be considered. Furthermore, many AE providers do not provide raw data but must act as ongoing consultants to analyze data and only report the breakage events.

3.2.15 Comparison of Existing Monitoring Approaches

The three approaches that are found more suitable for unbonded tendon monitoring are outlined in the following table.

Table 3-1. Comparison of existing monitoring approaches

Approach	Description	Advantages	Disadvantages
EMI	Correlates the variation of localized dynamic characteristic of anchorage, resulting from wire breakage, to the observed change in EMI signature.	<ul style="list-style-type: none"> • Less affected by non-breakage events. • Requires access only at anchorage locations. 	<ul style="list-style-type: none"> • Costly instrumentation (impedance analyzer) unless an alternative circuit is developed. • Unable to determine defect location.
GWUT	Transducers generate ultrasonic waves that propagate along the waveguide (tendon) and then measured by ultrasonic sensors.	<ul style="list-style-type: none"> • Continuous monitoring. • Less costly (compared to impedance analyzer). 	<ul style="list-style-type: none"> • Signal attenuation at deviator and anchorage locations. • Requires large number of sensors • May require access to portion of tendons.
AE	Naturally generated elastic wave (due to wire breakage) travels through tendon and registered by ultrasonic sensors.	<ul style="list-style-type: none"> • A few sensors are capable of detecting and localizing breakage. • Data is continuously collected but only recorded when thresholds are exceeded. • Sensors are installed externally to concrete surface. 	<ul style="list-style-type: none"> • Appropriate filtering is required to eliminate background noise. • Continuous monitoring at high sample rates. • Passive technique (cannot evaluate existing condition).

3.3 Examples of Full-scale Implementation

With the exception of some AE monitoring systems, most of the other aforementioned monitoring approaches are under development in laboratory facilities and the existing practice of in situ monitoring still primarily relies on visual inspection and several non-continuous monitoring tools, such as screwdriver penetration test, impact echo, radiography, endoscopy (imaging) and few more prohibitively expensive techniques for periodic inspection. Visual inspection commonly involves exposing tendon ducts and anchorages through stitch drilling, diamond coring and other invasive actions and thus requires utmost care to ensure that the intended inspection method does not cause further damage or lead to a more vulnerable

environment, for instance by inadvertently introducing water to a voided duct (Williams and Thompson 1997).

In recent years, however, long-term monitoring systems have been installed on several bridges for detecting breakage or defects of prestressing tendon wires and stay cables. The employed systems are predominantly based on the acoustic emission technique to evaluate its diagnostic performance in in situ conditions. Some representative full-scale applications are listed in the following paragraphs.

3.3.1 Bois de Rosset Viaduct

Bois de Rosset Viaduct, a box girder bridge located in Vaud, Switzerland, was instrumented as a part of long-term monitoring program. The 15-span, 617 m long, 2x13 m wide bridge was built in 1990 to cross a railway line at a height of 10 m. The bridge consists of twin superstructures and is longitudinally post-tensioned with four 12-strand external tendons. Each strand is individually greased and polyethylene-sheathed and is grouted inside a thick walled polyethylene duct. The tendons are arranged in pairs along each web and the tendon lengths range from 196 m to 216 m. The monostrand bundles are placed inside the steel troughs, routed over a maximum of five upper deviation saddles and ten lower saddles, and locked off at a multistrand anchor head with threads. The tendon anchorages are equipped with permanent VSL load cells installed at the threaded anchor head to aid in the assessment of long-term behavior of the bridge (Parsons Brinckerhoff 2012).

3.3.2 Ponte Moesa

The Ponte Moesa, one of the first prestressed concrete bridges in Switzerland, was built in 1952 in Grisons, Switzerland. The 2-span, 60 m long x 6 m wide bridge has hollow-core section with varying depth along the span (0.70 m deep at mid-span and 1.30 m at the pier.). The bridge is longitudinally prestressed with 63 bonded tendons, totaling 756 prestressing wires at mid-span and 1008 wires above the pier. The bridge was under active deterioration, as revealed during a routine inspection in 2001 when out of 25 inspected ducts 13 were found not grouted at all, nine were poorly grouted and only three were in a grouted condition; some of the wires were found completely corroded. As a consequence, an acoustic monitoring system, developed by SoundPrint[®], was installed on the bridge in 2004 (Fricker and Vogel 2007).

The monitoring system consists of 16 acoustic sensors attached in two rows on both sides of the bridge with maximum sensor spacing of 8.30 m in longitudinal and 6.50 m in transverse direction. To provide a good acoustic coupling, the sensors are attached to the concrete using polyester resin adhesive filler. Reference impacts, induced by a rebound hammer, were used to determine a suitable threshold for the signal detection. Data is continuously collected at a rate of 40,000 samples per second from each sensor and recorded whenever the predefined threshold is exceeded. The software then filters, stores, and transfers the data to the analysis center thru internet. After the installation of the monitoring system, several spontaneous wire breaks were recorded and localized on the upper side of the bridge near the pier, which were later substantiated by invasive inspection.

3.3.3 Huntingdon Railway Viaduct

Huntingdon Railway Viaduct, a six-span, 225 m long bridge, was constructed in Huntingdon, UK in 1975. Previous inspection indicated the presence of voids, water and chlorides in the tendon ducts and as a part of further investigation, SoundPrint[®] acoustic

monitoring system was installed on the bridge to monitor tendon wire break activity (Cullington et al. 2001). In total, 36 sensors, mostly concentrated on a cantilever segment of the bridge, were installed with a sensor spacing of 5 m. Cyanoacrylate adhesive was used to attach the sensors to the bridge soffit. Since the installation of the monitoring system in 1998, the system is running continuously on site with close to 100% up-time (Cullington et al. 2001). The bridge has not experienced any naturally-occurring wire break during monitoring; however, to test the performance of the monitoring system in noisy environments, external wire breaks have been artificially created and detected successfully in blind trials.

3.3.4 Fred Hartman Bridge

Fred Hartman Bridge, a cable-stayed bridge opened in 1995, is located near Houston, TX. The 2.6 miles long bridge includes twin 78-foot wide concrete decks, each supported on steel plate girders and has 192 stay cables fanning out from four diamond-shaped concrete towers. Soon after the bridge opened to traffic, users began noticing large amplitude stay-cable oscillations, particularly during rain and light winds. As a response, TxDOT initiated investigation into the serviceability and long-term durability of the stay-cable system and focused on fatigue of the steel strands in the stay-cable due to cyclic loading from the oscillations.

After performing a reliability study in laboratory environment, SoundPrint® acoustic monitoring system was set up on the bridge in 2002. A total of 576 sensors were installed, three to each stay-cable: one at the deck anchorage, one above the anchorage near deck level, and one at the tower anchorage with epoxy and strapping. After installation, a possible wire break was reported by Pure Technologies Ltd. (developer of SoundPrint® system); however, the occurrence of the wire break event could not be confirmed, as no evidence of loss of force or any structural problem associated with this wire break was found from initial investigation (Kowalik 2012).

3.4 Finite Element Modeling of Post-tensioning Strand and Anchorage

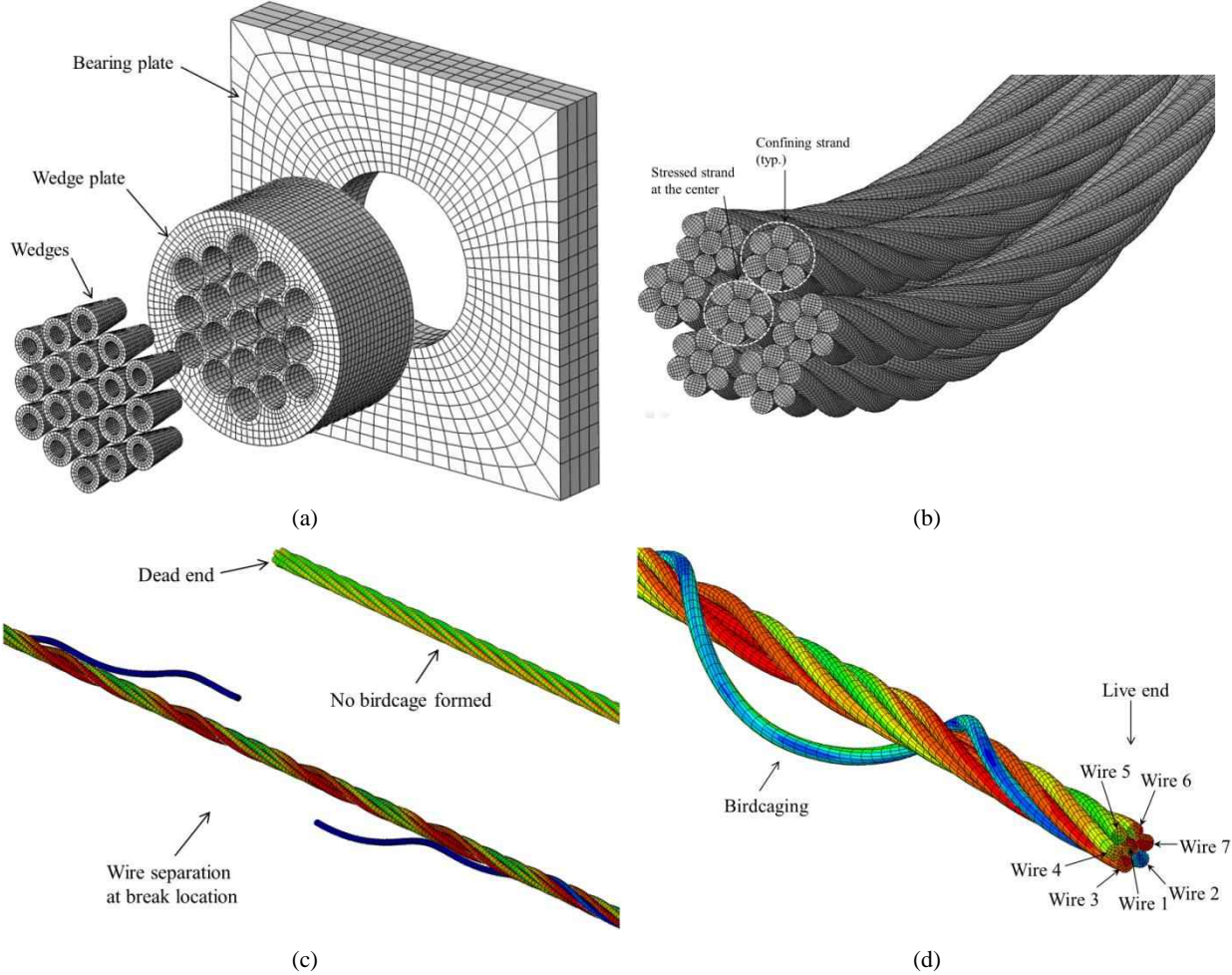


Figure 3-9 FE model: (a) anchorage; (b) multi-strand tendon; (c) wire break; (d) birdcaging

Experimental testing with a heavily loaded post-tensioning system is a costly and time-intensive endeavor. Finite element (FE) models of the strand and anchorage assembly (Figure 3-9) are therefore appropriate for system assessment and parametric analysis prior to conducting experiments. A properly calibrated model enables predicting the behavior of the anchorage under various wire break conditions and also helps to determine a proper experimental set-up. The interactions between adjacent wires in a strand as well as wedge-anchor head and anchor head-anchor plate interfaces in post-tensioning anchorage, however, give rise to frictional contact problems; hence the FE model requires a special treatment that accounts for the complex mechanical phenomena originating from contact non-linearities. Accordingly, a background study is necessary on contact mechanics that deals with the deformation of bodies (or a body) that touch (no gap or penetration) each other (or itself) at one or more points.

This section focuses on key aspects of contact problems, which are found essential to develop a representative model. The selection of appropriate contact parameters to generate the anchorage model is discussed. It is intended here to provide a general outline of contact parameters and the description tends to omit detail mathematical formulation that can be found elsewhere (Johnson 1987). In addition, more detailed information on the selection of contact

parameters in general can be found in Simulia Corporation (2012). The discussion in the following paragraphs focuses on defining the contact classification for post-tensioning anchorage interfaces, selecting the master/slave role in formulating the contact pair, discretizing the contact surfaces, contact enforcement method, numerical algorithm and loading scheme to solve the contact problem.

3.4.1 Classification of Contact Interactions

The contact classification for post-tensioning anchorage is a finite-sliding deformable-to-deformable two-body contact. This formulation allows relative movement of finite amplitude and provides a more realistic representation of the slide plane.

3.4.2 Selection of Contact Pair

In selecting master/slave role, the more refined surface is usually treated as slave as it tends to allow less penetration (Figure 3-10).

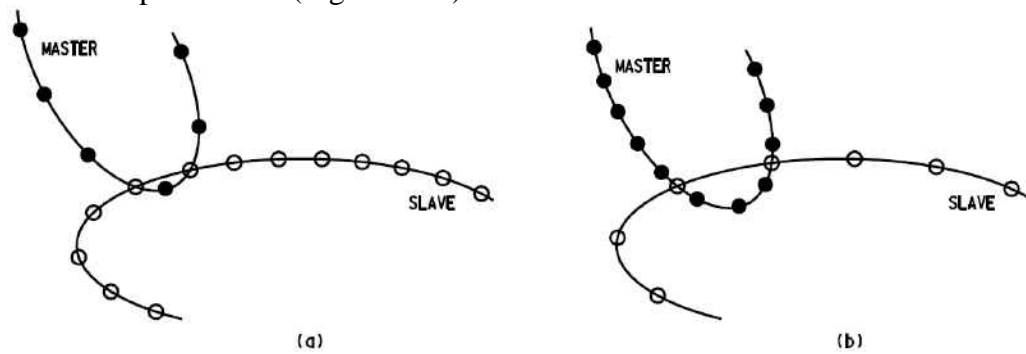


Figure 3-10 Contact pair: (a) more refined surface as slave; (b) more refined surface as master

The anchorage model in this research considers the wedge surface as slave and the anchor head as master in wedge-anchor head interface, whereas the anchor head acts as slave and anchor plate as master in the anchor head-anchor plate interface.

3.4.3 Discretization of Contact Surfaces

As node-to-node formulation often produces discontinuity in analysis results due to misalignment of the slave/master nodes in the deformed state (Zienkiewicz and Taylor 2005) and node-to-surface tends to produce incorrect local contact stresses, surface-to-surface discretization technique was used for both wedge-anchor head and anchor head-anchor plate interfaces of the anchorage model in this study.

In surface-to-surface (S-to-S) treatment, contact is enforced in an integral sense over a region surrounding the slave nodes and a facet on the slave body interacts with facets on the master body. S-to-S discretization reduces the likelihood of large localized penetrations of master nodes into slave surface and often improves the accuracy of contact stresses. In addition, this method reduces the sensitivity of results to master/slave roles and provides better convergence due to inherent smoothing.

3.4.4 Contact Forces

Bodies move freely prior to contact but soon generates resistive forces once contact is established. As illustrated by the wedge-anchor head interface shown in Figure 3-11, the resistive

force has two components: contact pressure (N) acting normal to the interface resisting penetration and frictional shear force (T) acting tangentially at the interface that resists sliding (Chacos 1993).

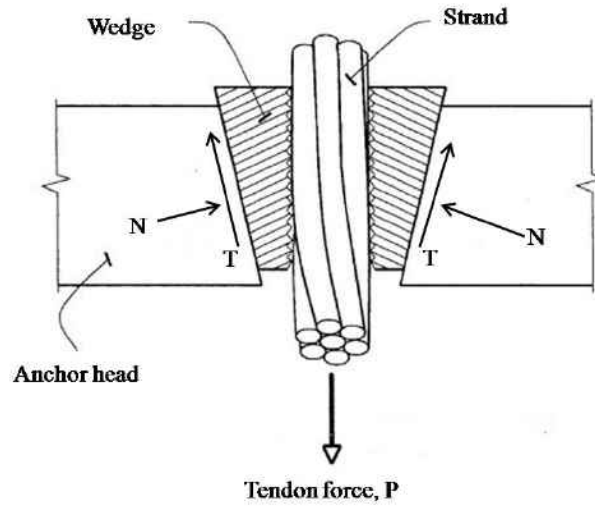


Figure 3-11 Resistive forces in a wedge-anchor head system

3.4.5 Kinematic Constraints

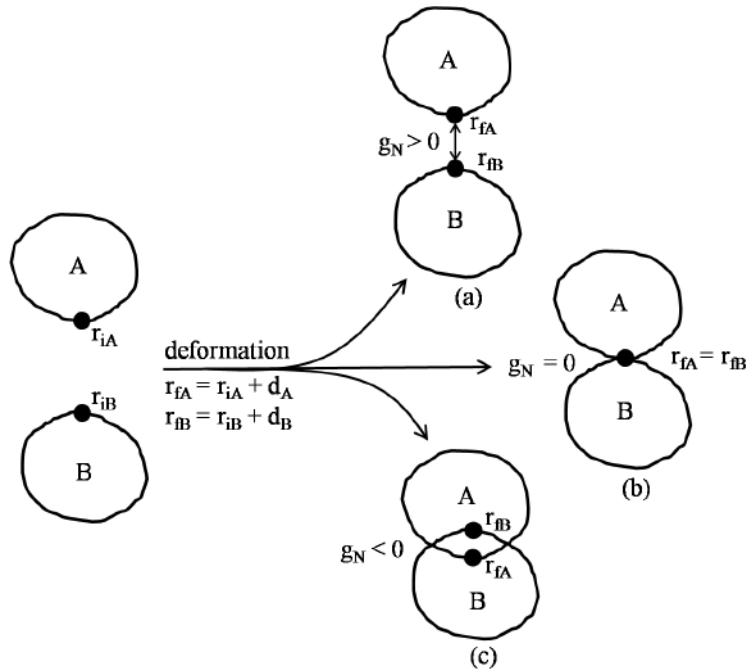


Figure 3-12 Contact constraints

Consider two bodies, A and B, presented in Figure 3-12, that undergoes deformation (Litewka 2010). The positions of arbitrary points before deformation are denoted by position vector r_{iA} and r_{iB} on surfaces of A and B, respectively. After the points undergo displacement d_A and d_B , the final positions become r_{fA} and r_{fB} , which can be expressed as

$$\begin{aligned} r_{jA} &= r_{iA} + d_A \\ r_{jB} &= r_{iB} + d_B \end{aligned} \quad \text{Equation 8}$$

In the process of deformation, the inter-penetration situation shown in Figure 3-12c may be theoretically possible but is not allowed in reality. Thus to exclude those unreal situations, constraints, called contact kinematic constraints, must be introduced. The constraints are formulated with a gap function, g_N , which provides the distance between the two points

$$g_N = r_{jA} - r_{jB} \quad \text{Equation 9}$$

And, the condition of impenetrability requires that the gap function remains non-negative

$$g_N \geq 0 \quad \text{Equation 10}$$

In a computational approach, a search procedure is performed to find the spots where the constraint (Equation 10) is not satisfied ($g_N < 0$). The search involves defining a gap function, g_N , for all possible nodal pairs between A and B and creating an active set by selecting only those not fulfilling the constraint. Subsequently, for the nodal pairs in the active set, the gap function is set to zero to enforce the constraint and all other nodal pairs are not considered at all. In this way, the inequality constraint (Equation 10) becomes an equality constraint as follows

$$g_N = 0 \quad \text{Equation 11}$$

3.4.6 Strict Enforcement of Contact Constraints

Normal Direction: Hard Pressure-Overclosure Model. Hard contact models assume zero pressure when there is no contact but considers any pressure possible when in contact to resist penetration (Figure 3-13). In this model, the contact pressure, p , between two interacting surfaces is a function of the overclosure (interpenetration of the surfaces), g_N , and can be described as follows:

$$\begin{aligned} p &= 0 \text{ for } g_N > 0 \text{ (open)} \\ g_N &= 0 \text{ for } p > 0 \text{ (closed)} \end{aligned}$$

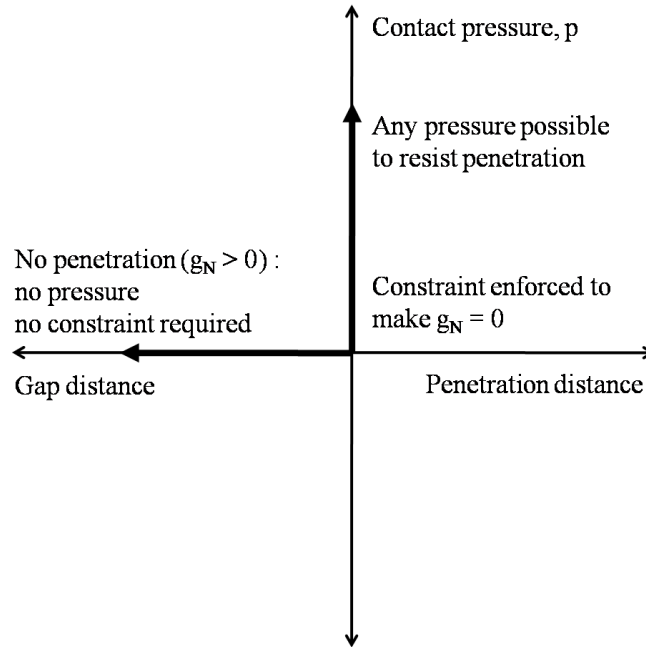


Figure 3-13 Pressure-overclosure relationship

Tangential Direction: Coulomb Friction Model. The Coulomb friction model considers that the interacting surfaces can carry shear stresses up to a certain magnitude (critical stress $\tau_{critical}$) when no slip occurs but cannot take any shear (provides no resistance) once the critical magnitude is exceeded (Figure 3-15). The model assumes that the critical shear stress, $\tau_{critical}$, is proportional to the contact pressure, p , and related to it through the coefficient of friction (μ) (Figure 3-14) as follows:

$$\tau_{critical} = \mu p$$

$$g_T^p = 0 \text{ for } \tau < \tau_{critical} \text{ (stick)}$$

$$g_T^p = \infty \text{ for } \tau > \tau_{critical} \text{ (slip)}$$

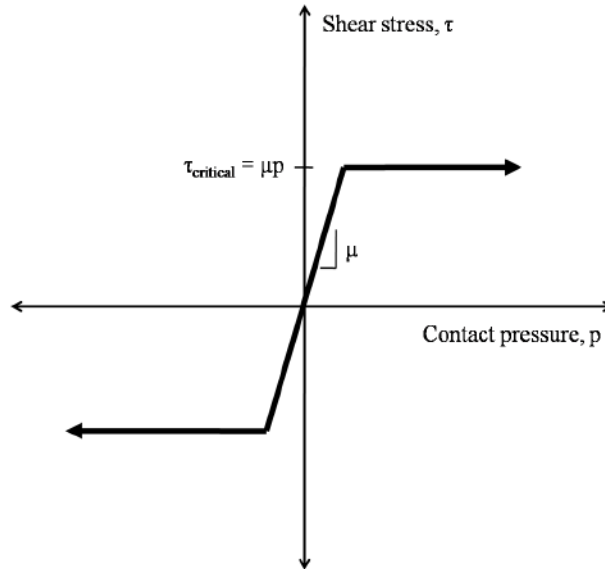


Figure 3-14 Coulomb friction model

A rough frictional surface is represented by an infinite coefficient of friction ($\mu = \infty$) meaning that sliding is prevented for any magnitude of shear stress, while a zero coefficient ($\mu = 0$) represents a frictionless condition meaning no shear stresses will develop and the contact surfaces are free to slide.

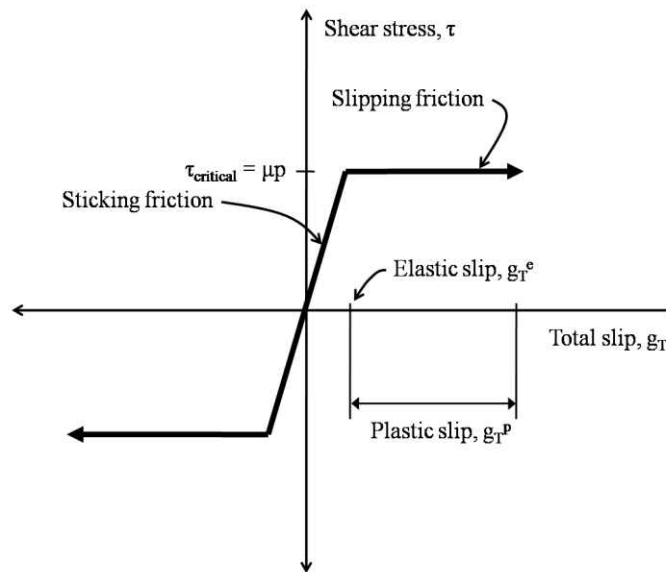


Figure 3-15 Tangential direction behavior

3.4.7 Constraints Enforcement Methods

The potential energy functional Π_p can be written as

$$\Pi_p = \frac{1}{2} \{D\}^T [K] \{D\} - \{D\}^T \{F\}$$

where $\{D\}$ = global degrees of freedom vector (translations and rotations)

$[K]$ = global stiffness matrix

$\{F\}$ = global load vector

From the principle of stationary/minimum potential energy and the requirement of non-penetrability condition, contact is a problem of functional minimization with equality constraints. Such a constrained optimization problem can be solved by several numerical methods; three of the common methods are: Lagrange Multiplier Method, Penalty Functions Method, and Augmented Lagrangian Method.

The Lagrange Multiplier Method ensures strict or direct enforcement of the contact constraints. However, Lagrange multipliers are additional unknowns to be solved after each iteration, which increase computational demands. Also, strict enforcement of constraints leads to some purely numerical issues, such as zero diagonal matrix in Newton solution process. The penalty method does not increase the number of unknowns but allows penetration within a preset tolerance and thus the exact fulfillment of the constraint condition (Equation 11) is compromised. Although a large value of penalty stiffness tends to result in small penetration, the stiffness cannot take arbitrarily large number because this leads to a numerical instability.

The Augmented Lagrangian method is a combination of Lagrange multipliers and the penalty method, where a compromise between multipliers and penalty functions is achieved by using an iterative update of the multiplier. In this approach, the multipliers do not enter the set of unknowns but their values are updated after each Newton iteration using a penalty parameter. This method eliminates the problem of additional unknowns and zero diagonals in Lagrange multipliers approach and minimizes the problem of convergence difficulty due to poor choice of penalty coefficient in penalty method. This approach, however, requires a complicated numerical algorithm and also does not strictly fulfill the constraint condition. Therefore, penalty method has been used in this work to evaluate frictional contact conditions both in the anchorage and strand models. This approach has also been successfully used to solve similar contact problems (Jiang et al. 2008; Bastien et al. 2007; Marceau et al. 2001).

3.4.8 Numerical Methods

Kinematic constraints (condition of no penetration or slip) must be enforced during contact whereas bodies move without any resistance prior to contact. Thus contact causes a slope discontinuity (kinks) in the load-displacement plot upon change in contact status (Figure 3-16), which makes the contact problem inherently non-linear.

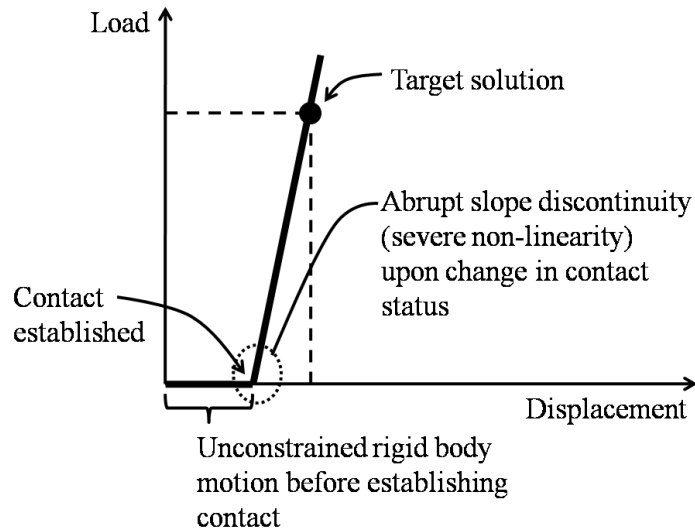


Figure 3-16 Non-linearity of contact problem

In general, a predictor-corrector approach is utilized to linearize the problem. The Newton-Raphson iterative method is commonly employed for linearization. In certain situations, the classical Newton-Raphson method is found expensive as it requires the stiffness matrix to be updated after each iteration. A modified Newton-Raphson iterative scheme is generally used to expedite the convergence, in which the stiffness matrix is not updated for each iteration but only updated after each load step.

In cases of severe non-linearity, such as contact problems, traditional methods, like classical or modified Newton-Raphson, alone may experience extreme convergence difficulty. In such situations, a continuation or path following approach, e.g., arc length method, is found suitable to achieve convergence, in which the solution converges along an arc (Bastien et al. 2007). However, the Newton-Raphson method with incremental load steps was adopted in this study.

3.4.9 Loading Scheme

Prior to establishing contact, force-controlled loading results in singular stiffness matrix. The consequence is that the stiffness matrix is not invertible to obtain displacement vector. Therefore, displacement-controlled loading is employed to avoid the singularity problem before contact. However, once contact is established, the stiffness matrix becomes non-singular for force-controlled loading; hence, the system of equation becomes stable. In this work, the displacement-controlled loading approach was used throughout the analysis.

3.5 Investigations on cable mechanics

Wire strands and ropes often find unique engineering applications because of their high tensile capacity coupled with workable bending flexibility. Accordingly, they are widely used in diverse engineering systems ranging from major transportation structures, such as bridges and aerial cableways, to various hoisting equipment like elevators and cranes. The mechanical behavior of steel cable, however, is complicated by its intricate geometric pattern. While being subjected to pretensioning or in-service loading, a complicated stress-state condition arises that

combines the effects of tension, torsion, flexure and shear along with multiple nonlinear phenomena such as interwire motion (the relative movement between wires), contact, friction, plasticity, and large deformation. Studies on cable mechanics, therefore, have received significant research attention for well over half a century. Presently, developing a better understanding of strand response to wire breaks is critical for the development of wire break detection techniques.

Several theoretical models have been proposed in the literature to explain the mechanical characteristics of wire strands and ropes, where strands consist of a layer of wires twisted around a center wire and ropes consist of strands twisted around a straight core. Costello and Phillips (1976) examined the sensitivity of strand stiffness to the change in helix angle as loading progresses, as well as investigated its dependency on initial helix angle and end conditions. This study, however, neglected the effect of friction and wire flattening to make the closed-form solution tractable. To obtain the static response of complex wire ropes with less computational effort, Velinsky et al. (1984) linearized the nonlinear equations of equilibrium. The reduction of effective modulus with addition of strands was demonstrated by analyzing a rope with an independent core. Later, Velinsky (1985) compared these results with nonlinear theory and found them identical in practical load ranges.

Utting and Jones (1987a, 1987b) conducted a series of experiments on seven-wire strands under tensile loads and proposed an analytical model that indicates insignificant effects of interwire friction and contact deformation on the overall strand response. Chaplin (1995), however, reported that these phenomena, along with other factors, affect the failure mechanisms of wire ropes. Raof and Kraincanic (1995) considered the effects of interwire friction in their theoretical model and obtained the upper and lower bounds of rope's effective stiffness that correspond to the no-slip and full-slip condition, respectively. Unlike the classical discrete modeling approach (Costello and Phillips 1976; Velinsky et al. 1984; Velinsky 1985) where each wire is treated as individual helical rod, Jolicoeur and Cardou (1996) presented an alternative approach in which each layer of wires is represented by an orthotropic hollow circular cylinder. This semi-continuous model was applied to several types of cable, concluding that this approach tends to produce more satisfactory results for cables with larger number of wires. Elata et al. (2004) considered the twisted wires in the outer layer of a rope and analyzed two extreme kinematic conditions: zero and infinite friction between adjacent wires. However, the flexural and torsional rigidity of wires were neglected.

In general, most of the aforementioned analytical models have made approximations and simplifying assumptions to obtain a closed-form solution. Although these models can be used to predict the global response of a cable, they are unable to provide a comprehensive description on many localized phenomena, such as yielding along contact lines, uneven bending of outer wires, stress redistribution among wires, etc. With the rapid advancement of computing technology, finite element (FE) methods have been developed over the past few decades to examine these characteristics in addition to other critical aspects of wire ropes, such as microstructural characterization during manufacturing process (Fontanari et al. 2005) and the mechanisms controlling their ductility (Phelippeau et al. 2006).

Chiang (1996) conducted a FE-based parametric study to show the individual and combined effects of different geometric, boundary and contact conditions on stress response of a strand. By utilizing the helical symmetry of geometry and loading, Jiang et al. (2000) developed a concise FE model of a seven-wire strand. The model was further extended (Jiang et al. 1999) to analyze a three-layered 19-wire strand by updating the constraint equations and boundary

conditions. Nawrocki and Labrosse (2000) considered different interwire motions, namely, sliding, rolling and pivoting, and showed that pivoting and sliding governs the axial and bending behavior, respectively. Contrasting the conventional assumption of contact occurrence only between the center and outer wires, Jiang et al. (2008) demonstrated that the contact also takes place between neighboring outer wires.

Erdönmez and Imrak (2009) analyzed the behavior of a curved strand and later considered a rope to examine the load distribution among wires (Imrak et al. 2010). Stanova et al. (2011a) derived parametric equations for geometric models of complex wire ropes and implemented them in a FE program (Stanova et al. 2011b). Zhou and Tian (2013) proposed a FE model for single-layered strand based on geometric compatibility and material elasticity theory. Nodal constraint relations between core and helical wires were obtained for axial tension and bending. However, the model did not account for the effect of interwire friction or sliding. Kmet et al. (2013) investigated a rope deviated over a saddle and observed non-uniform stress distribution among wires. Fontanari et al. (2015) studied the elasto-plastic response of a rope with a polymeric fiber core. A FE model of length equal to 1/16 of helical pitch was used to examine the load distribution among wires in the elastic regime as well as the redistribution of load with the evolution of plastic deformation.

To reduce the computational demand, many of the previously proposed models either make simplifying assumptions or only consider a small segment of rope geometry (partial length and/or partial cross section) for analyzing stressed strands. However, a relatively large model with high mesh resolution is needed to study various phenomena, such as the strand response after a wire breakage, so that the contact and frictional conditions may adequately develop. In addition, the representative lengths used in existing models are often too short to observe interwire pivoting (Labrosse et al. 2000) or stick/slip friction (Huang and Vinogradov 1996a; 1996b) and the effects of such phenomena on load redistribution among wires while stressing. The requirement of a sufficiently large model, combined with high material and boundary nonlinearities, make the use of an explicit analysis scheme a favorable candidate.

In analyzing complicated contact problems like wire strands and similar structures, explicit time integration has proven successful for its computational efficiency, robustness, and solution stability (i.e., lack of convergence difficulty) (Erdönmez and Imrak 2009; Stanova et al. 2011b; Kmet et al. 2013; Waisman 2010). However, simulating strand stressing in a quasi-static manner when using an explicit dynamic procedure requires special considerations such as proper selection of loading rate, time variation of applied load, and energy dissipation mechanisms other than frictional sliding, which become extremely critical in large models.

The detection range of wire breaks through the proposed approach is a function of recovery length, defined as the length measured from the break to the location where the broken wire regains its original share of the total axial load (Chien and Costello 1985; Gjelsvik 1991; Raouf 1991), which requires a detailed investigation on post-breakage tendon behavior. Apart from investigations on stressing behavior of strands and ropes, several analytical studies on wire breakage and recovery length are reported in the literature. The theory by Chien and Costello (1985) postulated that a fractured wire in a rope recovers its appropriate share of load in a relatively short length when subjected to large radial confining pressure. Gjelsvik (1991), and later Raouf and Huang (1992), analyzed the effects of hydrostatic forces, exerted by continuous wrapping and intermittent clamping bands, on the recovery length of parallel-wire strands in suspension bridge cables. The proposed models also demonstrated that the Poisson effect may significantly reduce recovery length as long as the cable is restrained against lateral expansion.

The center wire in a multilayered spiral strand was investigated by Raoof (1991), showing the recovery length to be a function of both axial tension and cable construction technique (Feyrer 2007; Costello 1990). Later, the theory was extended to cover various layers of the strand with relatively large number of wires (Raoof and Kraincanic 1998). Waisman et al. (2010) investigated the interwire load transfer with various clamping conditions and studied a parallel seven-wire strand with the center wire shorter than the outer wires to directly apply axial loads only to the outer wires. In addition to several previous attempts to experimentally measure the wire recovery length in multi-strand ropes (Chaplin and Tantrum 1985; Hankus 1981; Wiek 1977; Davidsson 1955), Noyan et al. (2010) recently used neutron diffraction to measure individual wire strain in a parallel-wire strand and observed strong correlation between load distribution among wires and radial clamping force.

MacDougall and Bartlett (2005, 2006) proposed analytical models for analyzing two different breakage configurations of a draped monostrand tendon. The first model considered two diametrically opposed broken outer wires at midspan. This symmetric arrangement of the broken wires around tendon cross section allowed a simplified analysis because all the unbroken wires experienced equal strain at any location along the tendon length. The model was then extended to the case of an asymmetric arrangement of broken wires, considering an unbonded seven-wire strand with a single broken outer wire. This modified model suggested that the axial strains in the two unbroken outer wires adjacent to the broken wire increase while the rest of the outer wires decrease at the cut location, primarily due to the tendency of the strand to deflect perpendicular to its axis toward the broken wire. Due to interwire friction, these strain differences were shown to diminish exponentially as the distance from the cut location increases, until the wires eventually restore their original strains at the end of the recovery length. In addition, laboratory experiments were conducted with broken outer wires to investigate wire strain distribution, affected length, and remaining prestress fraction of a draped tendon (MacDougall and Bartlett 2003). The wire cuts, however, were made before tensioning; therefore, neither the model nor the experiments captured dynamic effects associated with a wire break in a stressed strand.

3.6 An Overview of Standard Strain Gages and Data Acquisition Systems

Standard resistance strain gages have been used in the experimental investigation presented in this report. The primary advantage of strain gages is their low cost relative to other sensor options (e.g., fiber optic sensors) (Edwards 2000). Therefore, these metallic (copper-nickel or nickel-chrome alloy) foil (a grid of wire filament) gages are commonly used in measuring surface strains (Kyowa Electronic Instruments 2015). The sensor is bonded to the target surface by epoxy resin (often cyanoacrylates) and when the surface is strained, the electrical resistance of the foil wire changes in response to the change of its original length (and diameter). Usually, the ratio of relative change in electrical resistance to the mechanical strain (i.e., gage factor or strain factor, indicating the sensitivity of strain measurements) is around 2.0. For measuring the change of resistance, the gage is connected to an electric circuit (Wheatstone bridge with bridge resistances of 120Ω or 350Ω), which is attached to a data acquisition and processing unit (Omega Engineering 2015). In general, strain measurements are of resolution between $\pm 0.1 \mu\epsilon$ and $\pm 1.0 \mu\epsilon$, accuracy between $\pm 0.05\%$ and $\pm 0.1\%$ with measurement range over $\pm 30,000 \mu\epsilon$, and gage length or grid length (the length of the strain sensing part) ranging from 0.2 mm (0.008 in) to 100 mm (4 in) (Ramazani et al. 2013; Micro-Measurements 2015a, b). However, strain measurements can be affected by many environmental and installation variables

other than the applied strain, resulting from electrical noise (Micro-Measurements 2015c), temperature-induced apparent strain, gage factor variation with temperature (Micro-Measurements 2015d), errors due to misalignment of gages (Micro-Measurements 2015e), and errors due to transverse sensitivity (Micro-Measurements 2015f). Practically, the errors caused by many of these effects are quite small and can be minimized by using self-temperature-compensated gages and careful installation practices. The noise from external electrostatic and electromagnetic sources can also be reduced with appropriate cable shielding (e.g., conductive shields), efforts to minimize cable lengths, and attempts to achieve noise cancellation (Micro-Measurements 2015c).

3.7 Summary

In this chapter, an overview of the existing monitoring methods and the state of the art in strand behavioral study have been provided to find out the knowledge gap. In addition, critical modeling parameters for anchorage and strands have been discussed. Finally, a general overview of the standard strain gages has been given.

While several tendon monitoring approaches have been proposed in the literature, it was found that some of the existing techniques are not suitable to operate on a daily basis, some are susceptible to environmental noise, some face accessibility difficulties, some require modifications in the traditional construction detailing and quality control, and some are costly. Moreover, none of them attempted to identify the broken strand by monitoring the end anchors. Thus there is a need for a reliable and efficient monitoring solution for post-tensioning tendons.

Several theoretical studies are available in the literature on strand behavior. However, most of these analytical models have made approximations and simplifying assumptions to obtain closed-form solutions representing the complex mechanical behavior of a twisted strand, ignoring many localized effects, such as contact deformation and plasticity along contact line. In addition, several finite element-based numerical studies are also available in the literature. However, the representative lengths used in many of these models are too short to observe many critical phenomena like stick/slip frictional transition and its effects on stress redistribution among wires. Furthermore, no study is available on simulating wire breaks and investigating post-break response. Some experimental attempts have been also made to study stress recovery or strand behavior in general. To investigate the behavior of a broken strand, wire cuts were made in some of these experiments but were done before tensioning, thus these tests could not capture the change in strand's dynamic characteristics (e.g., shift of strand's natural frequencies) with wire breaks, which might be a potential damage indicator. In addition, no study is available investigating the anchor response to wire breaks in a waxed and deviated tendon condition.

In the literature, the post-tensioning anchorage and strand have been classified as finite-sliding deformable-to-deformable two-body contact. Surface-to-surface discretization with a more refined wedge surface has been treated as slave and the anchor head as master in wedge-anchor head interface whereas the anchor head acted as slave and anchor plate as master in the anchor head-anchor plate interface. To evaluate the frictional contact conditions, penalty method has been used for anchorage and strands. The Newton-Raphson method with incrementally applied displacement-controlled loading has been employed to linearize the problem. These parameters and modeling procedures have been used in preparing the anchor and strand models in the subsequent chapters.

After providing the background of the proposed monitoring approach in this chapter, the next chapter introduces the key concept of the method. A preliminary assessment of the concept

has also been conducted with experimentally calibrated finite element models of 7- and 19-strand anchors.

4 Proof-of-Concept Study

This chapter outlines a strain-based monitoring approach and a preliminary experimental assessment of this approach with an experimentally calibrated analytical model. This method uses the measurement of strain relief at anchors due to wire breaks. Because an unbonded tendon does not form a bond with the surrounding concrete over its length, the tendons are connected to the structure only at specific locations through deviators and anchorages. During tendon stressing, the entire prestressing force, minus the friction loss, is carried by the anchor head through contact with the prestressing strand wedges. Finite element analysis (FEA) has shown that these very large forces result in large strain gradients over the anchors. If a wire breaks in a bonded system, the grout transfers bond stresses locally around that break to the concrete (Figure 4-1). Consequently, if the wire break occurs away from the anchor head, no change in the stress state of the anchor head will occur. If a wire breaks in an unbonded system, however, the strain distribution in the anchorage undergoes significant changes. Whereas a uniform strain variation over the entire anchorage region is attributed to environmental or traffic loading, a wire breakage in an eccentrically located strand on the anchor head essentially results in non-uniform variations in strain magnitude. Thus, a careful selection and placement of a strain gage array on the anchor head can capture this uneven variation of measured strains in axial, circumferential, and radial directions.

A proof-of-concept structural health monitoring strategy is demonstrated using finite element simulation to compute relative strain variation in the anchorage as a result of wire breakage. A finite element model is first calibrated with experimental data from a small seven-strand anchor head (VSL ECI 6-7, VSL International, K oniz, Switzerland). The calibration test enables the tuning of the numerical model with kinematics and contact non-linearities. The calibrated model is then used to develop a general framework for the proposed technique for wire breakage detection. The model is subsequently extended to a more commonly used 19-strand anchor head (VSL E 6-19, VSL International) to conduct a parametric study on the observed strain variations from simulated wire breaks.

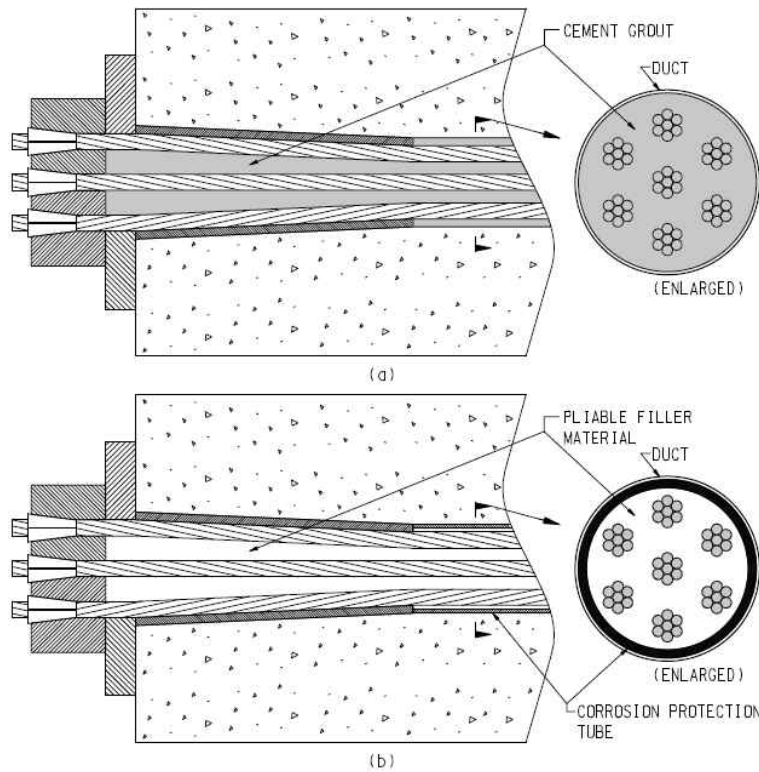


Figure 4-1 Post-tensioning method: (a) bonded; (b) unbonded

4.1 Calibration Test

To assess the proposed tendon monitoring method, an accurate finite element model is required. This section describes the experimental efforts undertaken to prepare a calibrated finite element model to represent the complex behavior of a multi-strand tendon anchor originating from frictional contact and large relative displacement at the interfaces. The contact parameters at the wedge-anchor head and anchor head-anchor plate interfaces, particularly the friction coefficient at the wedge-anchor head interface, can significantly influence the behavior of the mechanism and the resulting transfer of forces from the stressed tendons to the anchor head (Marceau et al. 2001). Estimating the appropriate friction coefficients at the interfaces is therefore necessary prior to performing accurate finite element simulation. A calibration test was performed to estimate the friction coefficients to be subsequently used in the finite element model. Because of limitations of the stressing equipment, a relatively small multi-strand anchor head (ECI 6-7) with a single center strand loaded to approximately 32 percent of its ultimate strength ($0.32 F_u$) was used.

4.1.1 Instrumentation and Setup

Stressing Frame

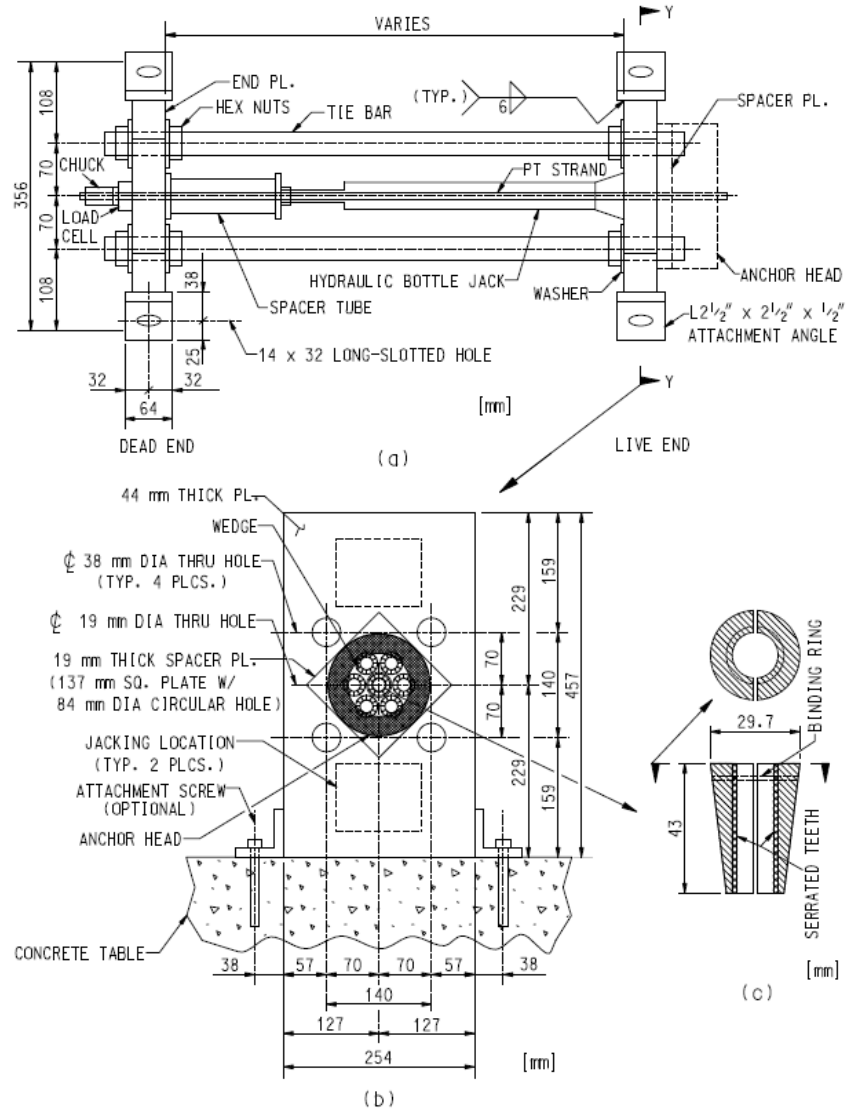


Figure 4-2 Details of stressing frame: (a) plan; (b) end plate elevation; (c) two-part wedge

A structural steel stressing frame (Figure 4-2) was designed to apply tension in the strand. The frame comprised two end plates with four threaded tie rods passing through symmetrically placed through holes. A strand, which passed through a hole located at the center of the plates, was gripped by a reusable chuck at the dead (or passive) end and a conical wedge on the anchor head at the live (or active) end. A spacer plate with a circular hole at its center was positioned between the end plate and the anchor head at the stressing end to ensure that the anchor head was in contact with the plate only at the annular area (Figure 4-3). The distance between the two end plates can be adjusted to accommodate specific test needs. In this test setup, the plates were placed approximately 0.6 m (2 ft) apart.

PT Strand and Anchorage Assembly

The tested strand specimen was approximately 1.2 m (4 ft) long, 15.2 mm (0.6 in) diameter Grade 270 low-relaxation seven-wire strand with a cross-sectional area of 140 mm² (0.217 in²). The ASTM A416 (ASTM 2006) strand has Young's modulus of approximately 195 GPa (28.5×10⁶ psi), minimum breaking strength of 260 kN (58,600 lb), minimum yield strength of 235 kN (52,740 lb) at 1% extension, minimum elongation of 3.5% at 0.6 m (24 in) gage and maximum relaxation of 3.5% after 1000 hours loaded to 80% UTS. The multi-strand anchorage consisted of an anchor head, an anchor plate, and a wedge (Figure 4-2). The anchor head was an iron casting with conical holes. Figure 4-3 is a detailed geometrical illustration of the seven-strand anchor head. In practice, the anchor head is set on an anchor plate that bears against the concrete surface. In this experiment, the concrete was replaced by the thick end plate while the spacer plate served as the anchor plate. The wedge (Figure 4-2) was a two-piece slotted cone that gripped the strand in its serrated teeth and seated in a conical hole in the anchor head, securing the strand in place. A binding ring around the wedge held the wedge pieces together.

Strain Gage Array and Data Acquisition System

To obtain a thorough description of the state of strain developed at the external surface of the anchor head under loading, a total of 16 strain gages were installed at different locations on the anchor head (Figure 4-3). Four strain gages were mounted on the face of the anchor head to capture radial strains (indicated by strain gage group R). Axial and circumferential strains were measured by 12 strain gages (six in each group) as labeled by group A and C, respectively. The data from this arrangement of strain gages were used for finite element model calibration as the friction coefficients at the interfaces were adjusted to match the experimental strains at multiple locations in axial, radial, and circumferential directions.

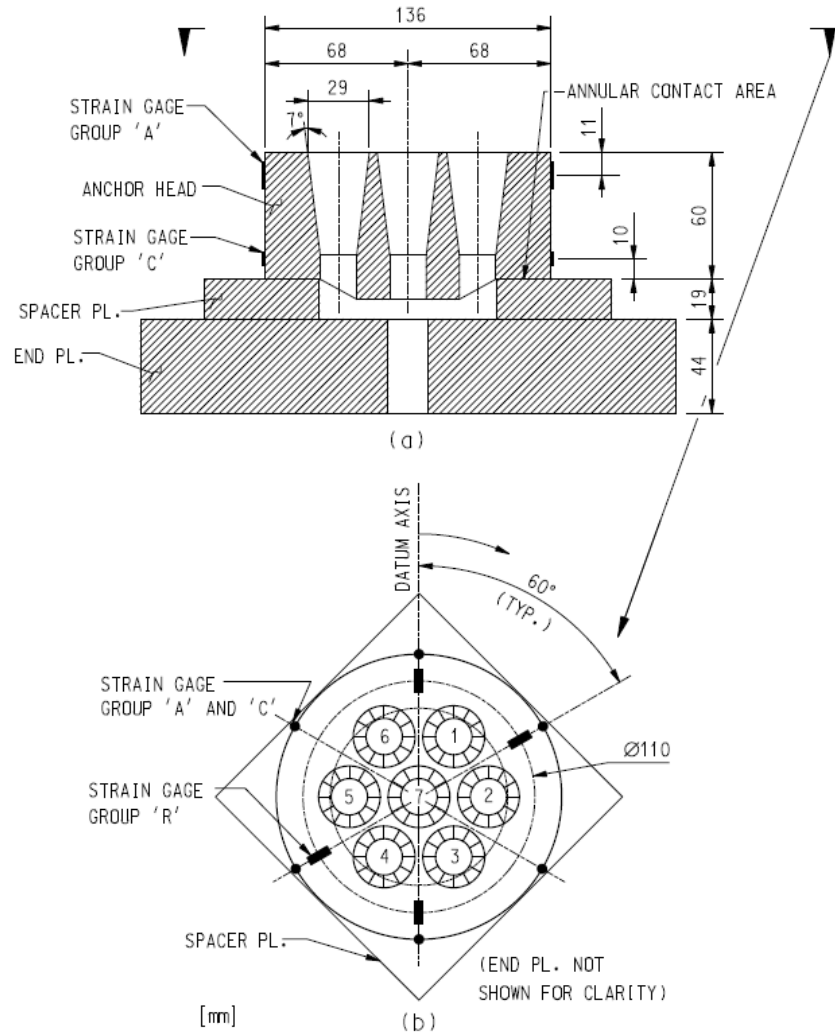


Figure 4-3 Strain gage placement on ECI 6-7 anchorage: (a) anchor head elevation; (b) plan

Strain gages were placed away from the interfaces to avoid any possible zone with localized uneven stress distribution caused by unequal slippage of the two parts of wedge or the effect of surface roughness on establishing mechanical contact. Foil strain gages (Vishay C2A-06-250LW-350; gage length of 6.35 mm) with pre-attached stranded instrument cable were used in this experiment. However, based on durability of gages in the operating temperature range along with other environmental factors, more investigations on gage selection are necessary for long-term in-field instrumentation.

The strain gages were connected with a quarter bridge configuration. The gage leads, soldered to shielded sensor cables, were attached to a National Instruments (NI) compact data acquisition (cDAQ) system. A terminal block for strain gages (NI 9236) was connected to the NI cDAQ-9178. To continuously monitor the applied load, a MD Totco 3100-30K load cell was configured with the NI cDAQ via an NI 9237 terminal and NI 9949 cDAQ module. LabVIEW 2012 was used for data acquisition and processing.

4.1.2 Experiment

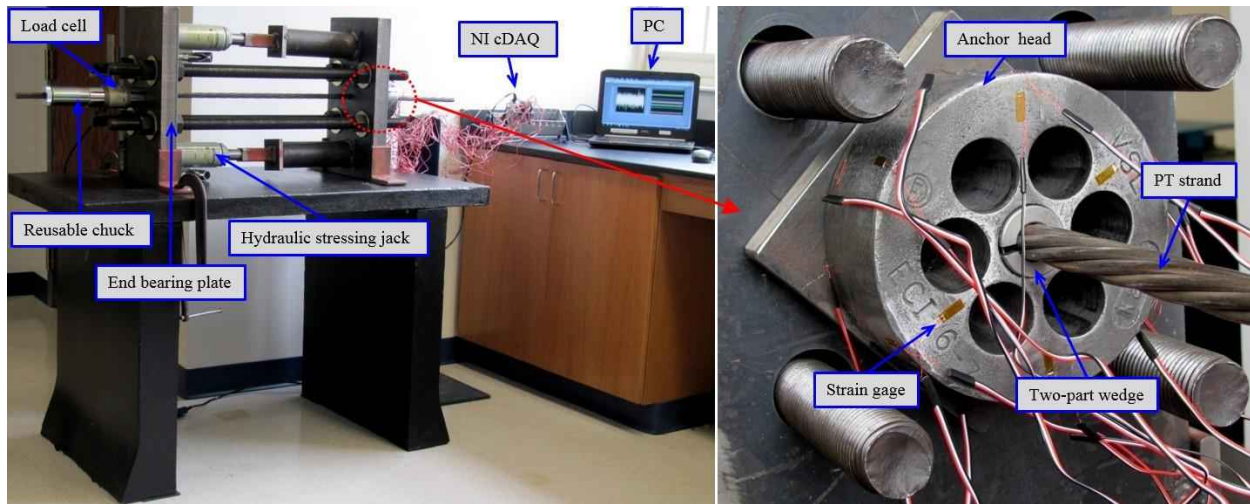


Figure 4-4 Experimental setup

The tendon was incrementally tensioned by hydraulic stressing jacks that react against the two end plates (Figure 4-4). When the tendon was stressed to the target level ($0.32 F_u$), as indicated by the load cell sandwiched between the chuck and the dead end plate, the hex nuts at the stressing end were adjusted to be in line with the new position of the live end plate. Consequently, the end plates bore against the hex nuts, and the strand was therefore wedged in position and maintained tension after the jacks were removed. After maintaining the target load for few minutes, the strand was gradually de-tensioned to zero load. The strain data during the entire loading and unloading period were recorded.

4.1.3 Results

As expected, near identical strain values (coefficient of variation less than 15%) were obtained from strain gages placed at symmetrical locations. This relatively minor strain dispersion between symmetric gages may be due to gage misalignment and unequal seating of wedge parts. The average measured strains of each group are summarized in Table 4-1. The listed values correspond to the loading of $0.32 F_u$, which was the highest load level achieved in this test. Widening of the anchor head due to seating of the wedge into the conical hole is demonstrated by a positive circumferential strain (indicating tension) and a negative radial strain (indicating compression), whereas the compressive loading is characterized by negative axial strains.

Table 4-1 Experimentally measured strains

Strain gage group	Direction of strain	Average $\mu\epsilon$
A	Axial	-25
C	Circumferential	+68
R	Radial	-70

4.2 Finite Element Model Development

A three-dimensional (3D) finite element model was prepared and calibrated with experimental results to estimate the friction coefficients at the wedge-anchor head (μ_{w-h}), anchor head-spacer plate and spacer plate-end plate interfaces; the coefficients of the latter two interfaces were considered similar and are jointly designated as μ_{h-p} .

4.2.1 Mechanical Properties

In accordance with the material data provided by the manufacturers, Table 4-2 lists the key mechanical properties of the anchorage mechanism used in numerical analysis. Due to the heat treated hard surface, a perfectly elastic behavior is considered for the wedge, while the mechanical behavior of the end plate, spacer plate, and anchor head is represented by an idealized bilinear elastoplastic stress-strain curve (Figure 4-5). Similar approximations were made in the literature to characterize the post-tensioning anchorage behavior (Bastien et al. 2007; Marceau et al. 2001).

Table 4-2 Mechanical properties of the anchorage assembly

Elastic		
Young's modulus (MPa)	= 200000	
Poisson's ratio	= 0.3	
Plastic		
	End plate/Spacer plate	Anchor head
Yield stress (MPa)	248	414
Ultimate strength (MPa)	414	689
Plastic strain (%)	25	15

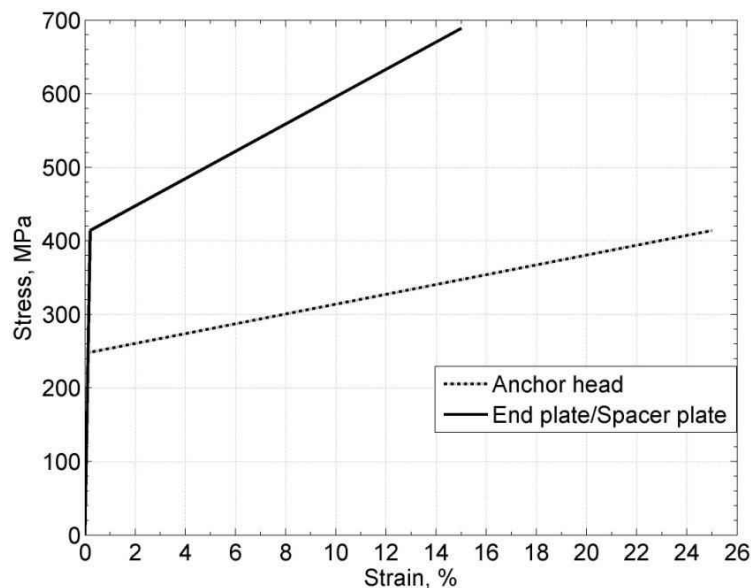


Figure 4-5 Characteristics of elastoplastic behavior of the anchorage components

4.2.2 FE Formulation

The FE model accounts for all the complex mechanical phenomena originating from heavy prestressing loads and contact non-linearities, such as plasticity, large relative displacement, and frictional interactions at the interfaces. Plasticity, however, did not develop because of the reduced load in the calibration model but occurred near the inner face of the anchor head when larger loads are applied in the wire breakage models discussed in the subsequent sections. Under load, the wedge and strand are considered to act monolithically (Bastien et al. 2007; Marceau et al. 2001) and thereby, the wedge-strand assembly was replaced by a single truncated conical component. The contact condition at the interfaces was treated with a penalty method using a Coulomb friction model and a master-slave approach was adopted for contact detection. The theoretical details of this approach as well as validation with experimental results for mono-strand anchorages can be found in Marceau et al. (2001). Later, Bastien et al. (1996, 2007) also used this model successfully in analyzing a multi-strand anchorage mechanism. This formulation was used in this study to evaluate the mechanical contact at the interfaces.

Discretization, Loading, and Boundary Conditions

The model was discretized with quadratic hexahedral and quadratic tetrahedral elements. A mesh convergence study was performed to confirm the adequacy of discretization. The compressive load was applied on the wedge with displacement-controlled method using variable incremental steps. Idealized pinned boundary conditions were enforced at four bolt locations as shown in Figure 4-6.

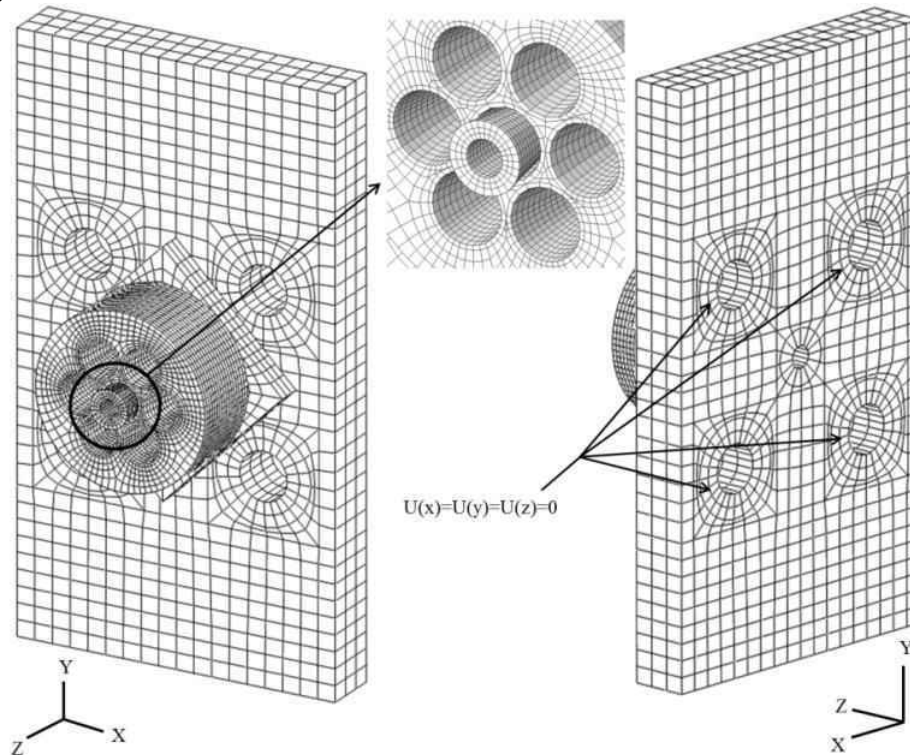


Figure 4-6 Discretization and boundary conditions of FE model for calibration

Estimation of Frictional Coefficients

In determining the frictional coefficient acting at the wedge-anchor head interface (μ_{w-h}), the value of μ_{w-h} was varied from 0 (rough surface) to 0.05 with an increment of 0.01 while keeping the coefficient at the other interface (anchor head-plate) unchanged. The coefficient μ_{w-h} has been taken 0.015 as the corresponding strains from FEA were found to be in the closest agreement with experimentally measured strains (Figure 4-7). The estimated friction coefficient closely matches the value obtained by Bastien et al. (1996). Figure 4-7 also confirms the success of the calibration step by showing that the three FE strain curves match the experimental measurements satisfactorily for a specific friction coefficient. The small value of μ_{w-h} was expected due the use of lubrication coupled with hardened surface of the wedge.

A similar procedure was adopted to estimate μ_{h-p} as 0.1. The value of μ_{h-p} was varied from 0.05 to 0.3 with an increment of 0.05 while setting the other coefficient (μ_{w-h}) constant to 0.015. As seen from Figure 4-8, the axial and radial strains were almost insensitive to an alteration of μ_{h-p} , the circumferential stain, however, were found marginally sensitive to μ_{h-p} because of the orientation and proximity of frictional surface with respect to strain measurement direction. Marceau et al. (2001) also observed this behavior. Thus, it is expected that the use of thick steel plate in this experiment in place of concrete does not significantly affect the global strain response.

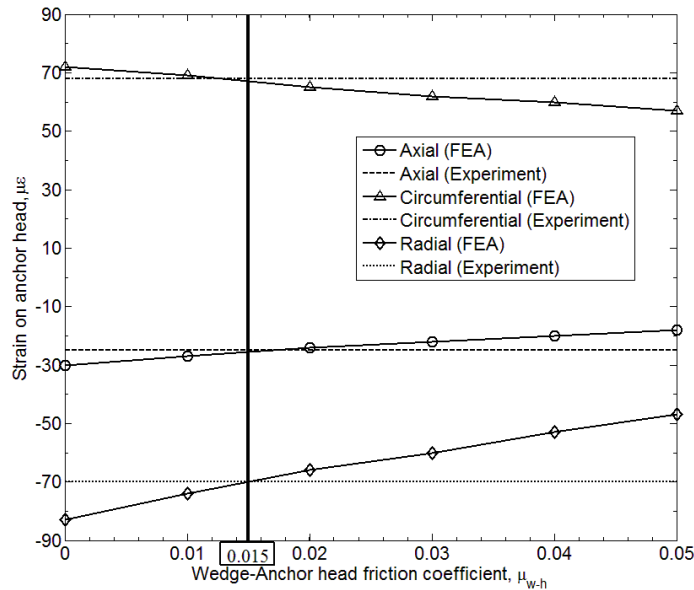


Figure 4-7 Estimation of friction coefficient acting at the wedge-anchor head interface (μ_{w-h})

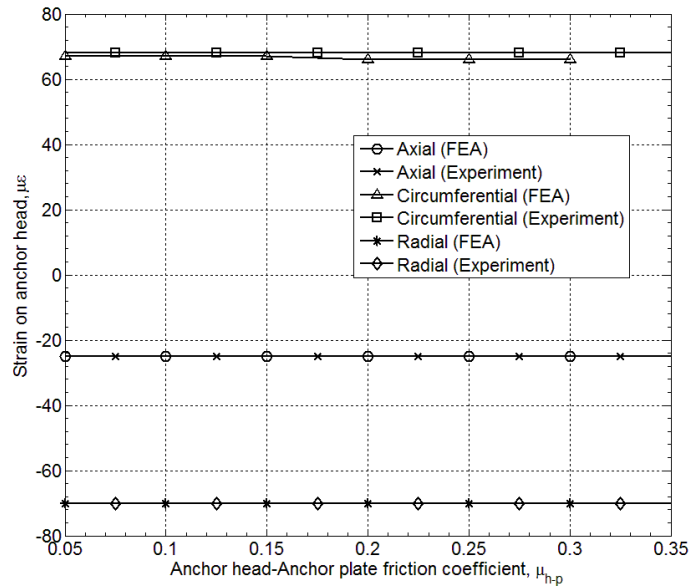


Figure 4-8 Estimation of friction coefficient acting at the anchor head-plate interface (μ_{h-p})

4.3 Wire Breakage Detection: General Framework

This section describes the proposed technique for wire breakage detection using FEA results from a seven-strand anchor head. The friction coefficients estimated in the preceding section are used in solving interface problems. Meshing techniques and other FE parameters used in calibration phase remain unchanged. Nevertheless, the end plate underneath the anchor plate (spacer plate) has been replaced by equivalent supports (Figure 4-9). Ideally, the boundary condition for anchor plate should be treated as elastic spring with the axial stiffness of the concrete girder, which is a function of the specified compressive strength of concrete and the length of the girder under consideration. In general, however, the spring stiffness is remarkably high; the support condition is therefore regarded as infinitely stiff pin.

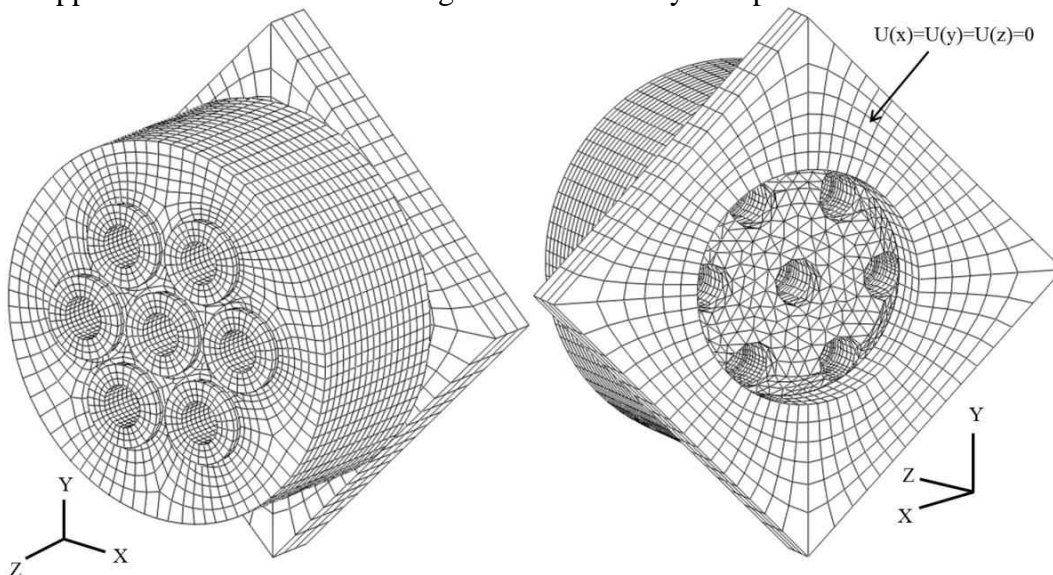


Figure 4-9 Discretization and boundary conditions of VSL ECI 6-7 anchor head

First, FEA is performed to simulate the pristine condition in which each strand of a fully populated ECI 6-7 anchorage is loaded to $0.80 F_u$, followed by reducing the loads to $0.63 F_u$ to account for all short- and long-term losses. Due to the heavy load, yielding started to appear in the anchor head but was concentrated at the inner face of the head and the strain monitoring points located at the outer face were not really affected. At this stage, the developed strain in the anchor head is calculated. The effect of a wire break is then simulated by withdrawal of the proportional fraction of loading from the corresponding strand. Consequently, the resulting strain field is updated depending on the number and location of wire breaks (Figure 4-10). The change in strain values from the original condition is calculated and compared with adjacent locations. The portion of anchor head near the broken strand experiences a significantly higher strain drop compared with distant locations and thereby, a distinct peak is observed in the strain variation plot. The magnitude of the observed peak indicates the extent of a potential damage. Although strain variation occurs in a complete 3D state, only the axial strain around the anchor head is registered and considered to correlate with wire breakage.

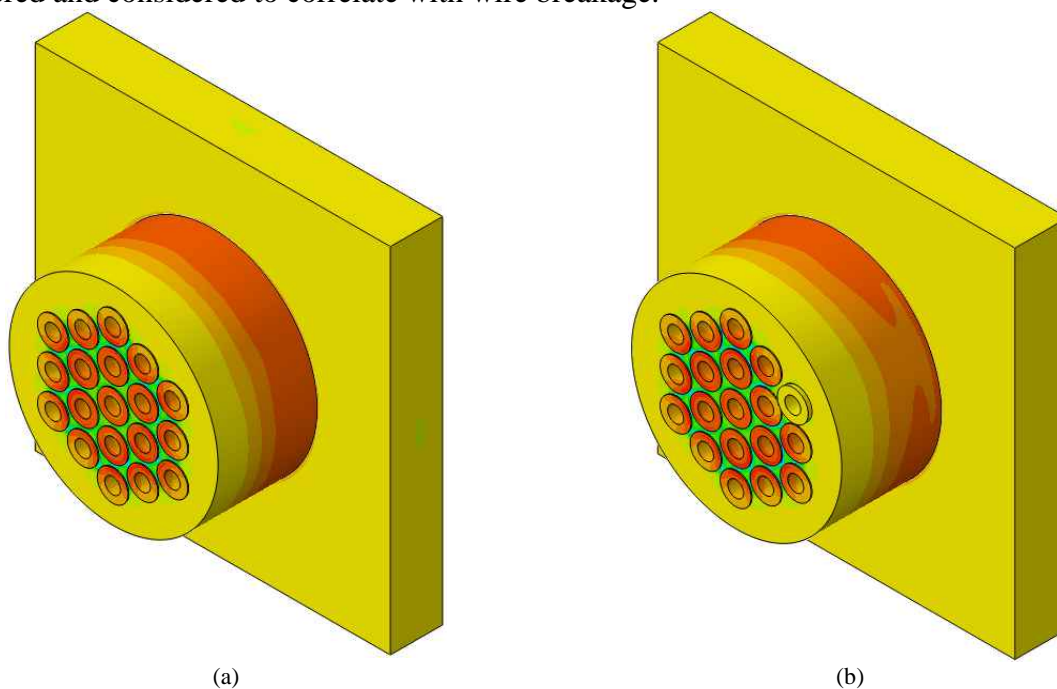


Figure 4-10 Strain distribution: (a) before breakage; (b) after wire break

It is noted that to obtain the effect of a wire breakage in FEA, the corresponding strand load is reduced by full proportion, e.g., $1/7$ -load reduction in case of one wire breakage in a seven-wire strand. In reality, the amount of load relief due to the wire break is expected to be somewhat less because of the presence of deviator points and also as a result of interwire contact forces (Bartoli et al. 2011; Salamone et al. 2011; Lanza di Scalea et al. 2003); thus, it would be a function of the stress recovery length depending on the breakage location along the tendon. It is deemed reasonable, however, to postulate that ignoring these load losses would not pose a considerable limit on the method's efficiency of wire breakage detection because the relative variation of strain magnitudes would still be evident. It is also noted that, for long-term in-field measurements, the baseline strains would need to be updated to account for time-dependent

losses, such as relaxation of steel. However, the amount of relaxation is expected to be minimal through the use of low-relaxation strands.

Table 4-3 Wire breakage cases

Case ID	Description	Broken wires (Figure 4-3)
A1	Wire breaks in symmetrically located strands	Two wires in strand 2 One wire in strand 5
A2	Different number of wire breaks in the same strand	One/two/three wires in strand 3
A3	Wire breaks in two dissimilar strands	One wire in strand 2 One wire in strand 4
A4	Wire break in the core strand	One wire in strand 7

Analyses have been performed for different numbers and combinations of wire breakage to verify the sensitivity of measured strain with various damage conditions (Table 4-3). In Case A1, factitious wire breaks are induced at two strands (2 and 5) located at similar places on the anchor head. Strand 2 contains two broken wires whereas strand 5 holds one. Figure 4-11a shows the strain change that occurs due to wire breakage in contrast to original ‘no breakage’ condition. It is obvious from the plot that the maximum variation in strain takes place at the vicinity of the broken strands 2 and 5. In addition, the magnitude of strain variation indicates a greater severity of damage in strand 2. These observations are confirmed by the strain variation plot (Figure 4-12b), where two distinct peaks can be identified at locations 90° and 270° from the datum axis (Figure 4-3), which are adjacent to strand 2 and 5, respectively. It is noted that, the angular asymmetry of unbroken state strain diagram in Figure 4-11 stems from the lack of symmetry of strand locations about the angular points.

Figure 4-11b demonstrates the degree of strain change in relation to the number of wire breaks at the same strand (Case A2). The largest strain drop occurs surrounding strand 3, whereas other places on the anchor head remains mostly unaffected. Again, a clear peak with an increasing magnitude of strain variation is observed in Figure 4-12 as the number of wire breaks increases. Furthermore, two wire breaks (one at each location) are introduced in Case A3 in two separate strands (2 and 4) located at dissimilar places on the anchor head. Figure 4-11c confirms the greatest strain variation around the broken strand locations indicating a damage, which is substantiated by pronounced peaks in Figure 4-12. In the case of wire breakage in center strand 7 (Case A4), the observed variation of strain all around the anchor head is almost to the same extent (Figure 4-11c). The breakage event, though challenging, may still be identified from the equal shift of strains between the pre-breakage and post-breakage measurements, as depicted in Figure 4-12a. These measurements would require a rigorous statistical model to filter out the effects of non-breakage events, such as temperature fluctuations and traffic loads. In addition, during construction, the center strand at one end of the girder may not remain center at the other end. Thus, the breakage will likely be captured by strain variation in one of the two monitored anchor heads.

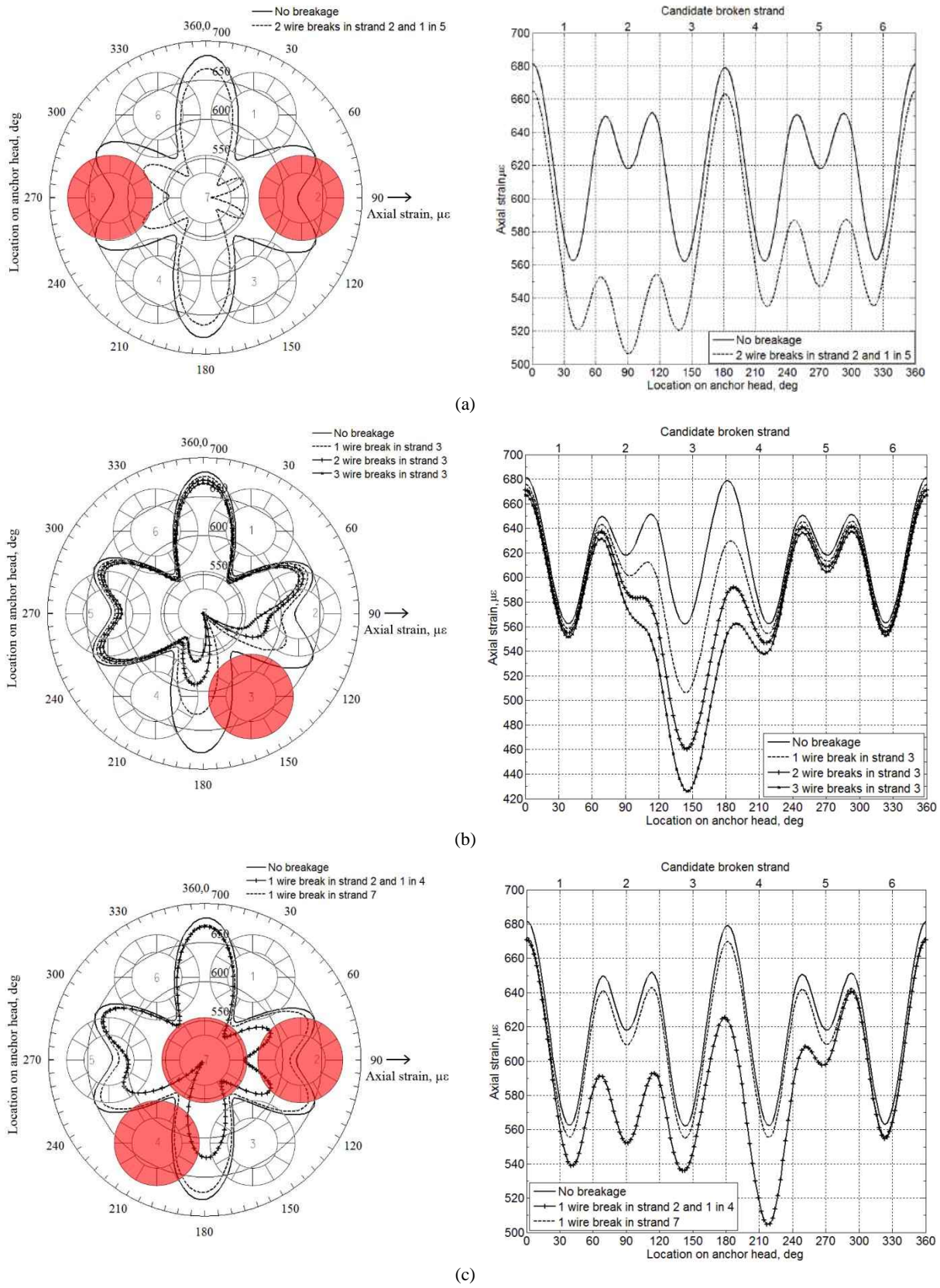


Figure 4-11 Comparison of axial strains in ECI 6-7 anchorage before and after wire breaks

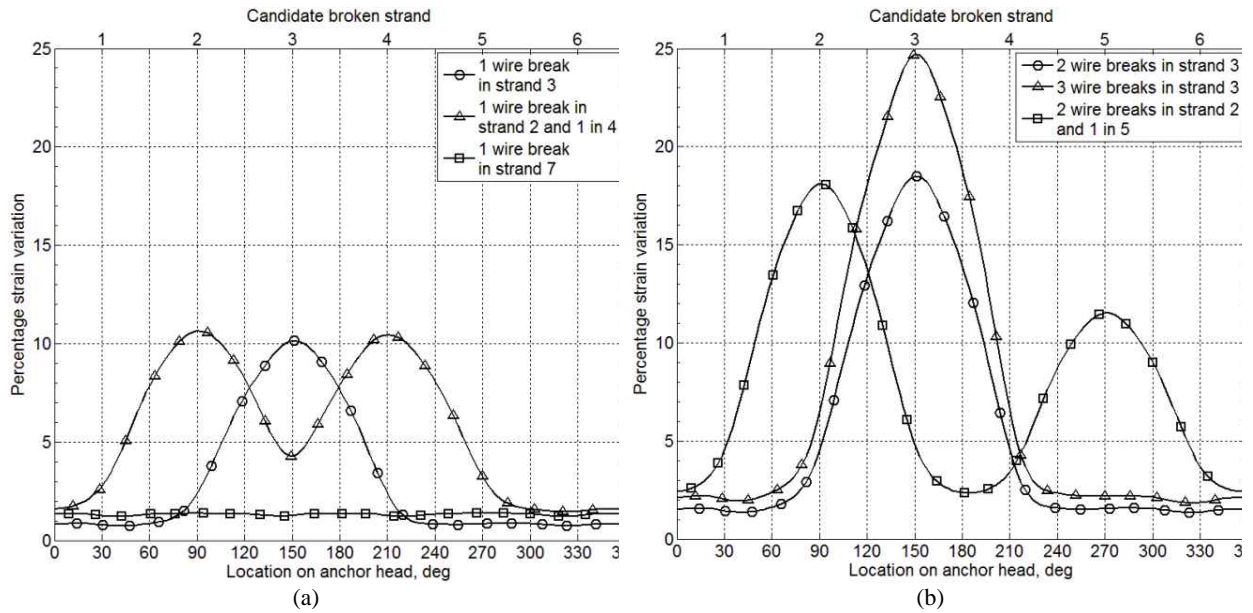


Figure 4-12 Strain variations in ECI 6-7: (a) single wire break; (b) multiple wire breaks

4.4 Parametric Study with E 6-19 Anchorage

A detailed numerical study using the proposed approach was conducted on a 19-strand anchorage assembly (Figure 4-14). A procedure similar to the one described in the previous section was adopted, while keeping the interface parameters, loading scheme, mesh control, and boundary conditions (Figure 4-13) unchanged.

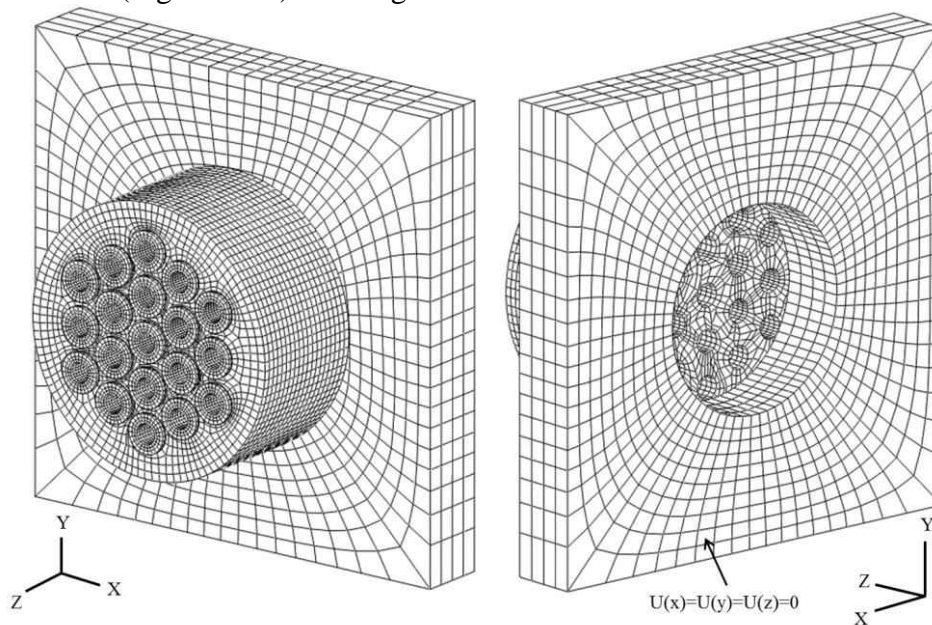


Figure 4-13 VSL E 6-19 anchorage: (a) discretization; (b) boundary conditions

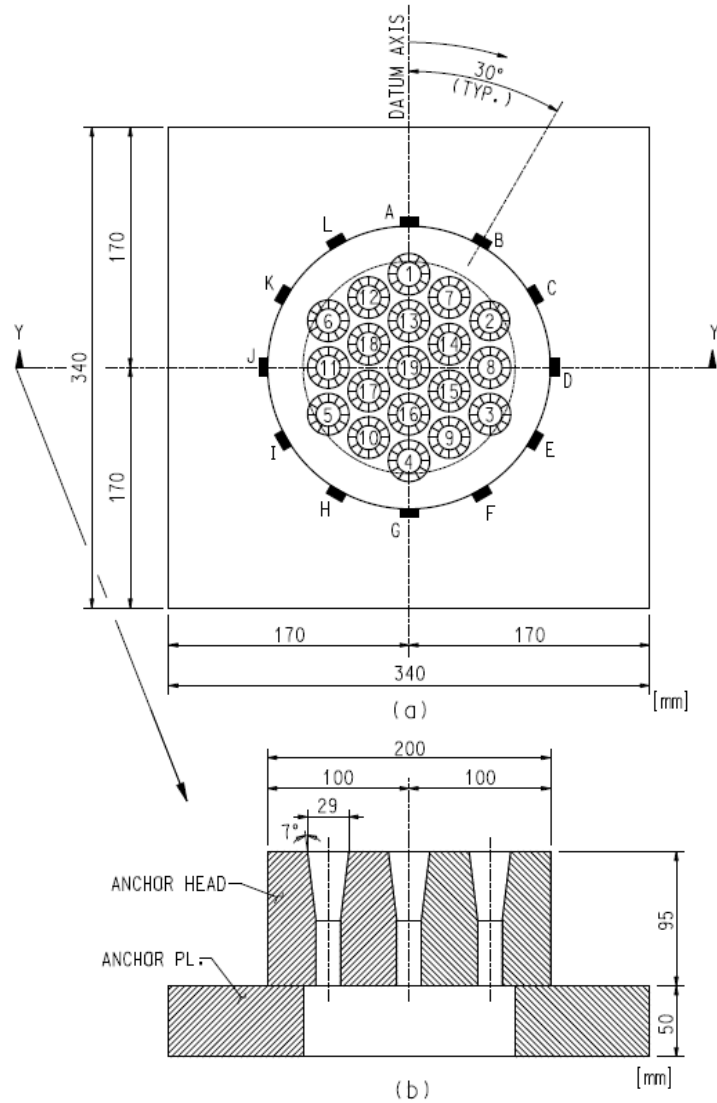


Figure 4-14 E 6-19 anchorage details: (a) top view; (b) section Y-Y

The objective of this extended model is to examine the detectability of wire breakage in a strand arrangement commonly used in industry. Moreover, the model is tested with a finite number of strain monitoring points to predict its performance in characterizing wire breakage in a more practical setting.

The FEAs have been conducted for a number of cases to cover a broad spectrum of damage scenarios. The damage cases are selected to examine the method's performance in detecting single and multiple wire breaks in strands wedged in different holes on the anchor head. Table 4-4 outlines the analysis results.

Table 4-4 Test matrix and results

Case ID	Description	Broken wire	Maximum strain variation		
			Absolute variation ($\mu\epsilon$)	% variation	Location (Figure 4-14)
B1	Different number of broken wires in the same strand	One wire in strand 10	53	4.5	H
		Two wires in strand 10	85	7.2	H
		Three wires in strand 10	108	9.0	H
B2	Wire breaks in two strands at different locations on the anchor head	One wire in strand 2	58	5.2	C
		One wire in strand 17	16	1.4	I
B3	Wire break in a distant strand from the anchor head perimeter	One wire in strand 16	18	1.6	G
B4	Wire break in adjacent strand from the anchor head perimeter	One wire in strand 5	57	5.1	I
B5	Wire break in the core strand	One wire in strand 19	8	0.7	-

In general, the peak strain variation occurs at the closest location from broken strand on the anchor head perimeter and the intensity of strain variation rises with the severity of damage. Figure 4-15 shows a sample plot of absolute strains before and after breakage. A continuous plot of strain variations all around the anchor head is shown in Figure 4-16 for different wire breakage conditions.

Figure 4-15a shows that the maximum strain variation occurs at a location 210° from the datum axis, which is the closest location on the anchor head from the affected strand 10. Additionally, the intensity of the variation rises with the increased severity of damage. The variation peaks and their difference in magnitude around the anchor head can be seen in Figure 4-16.

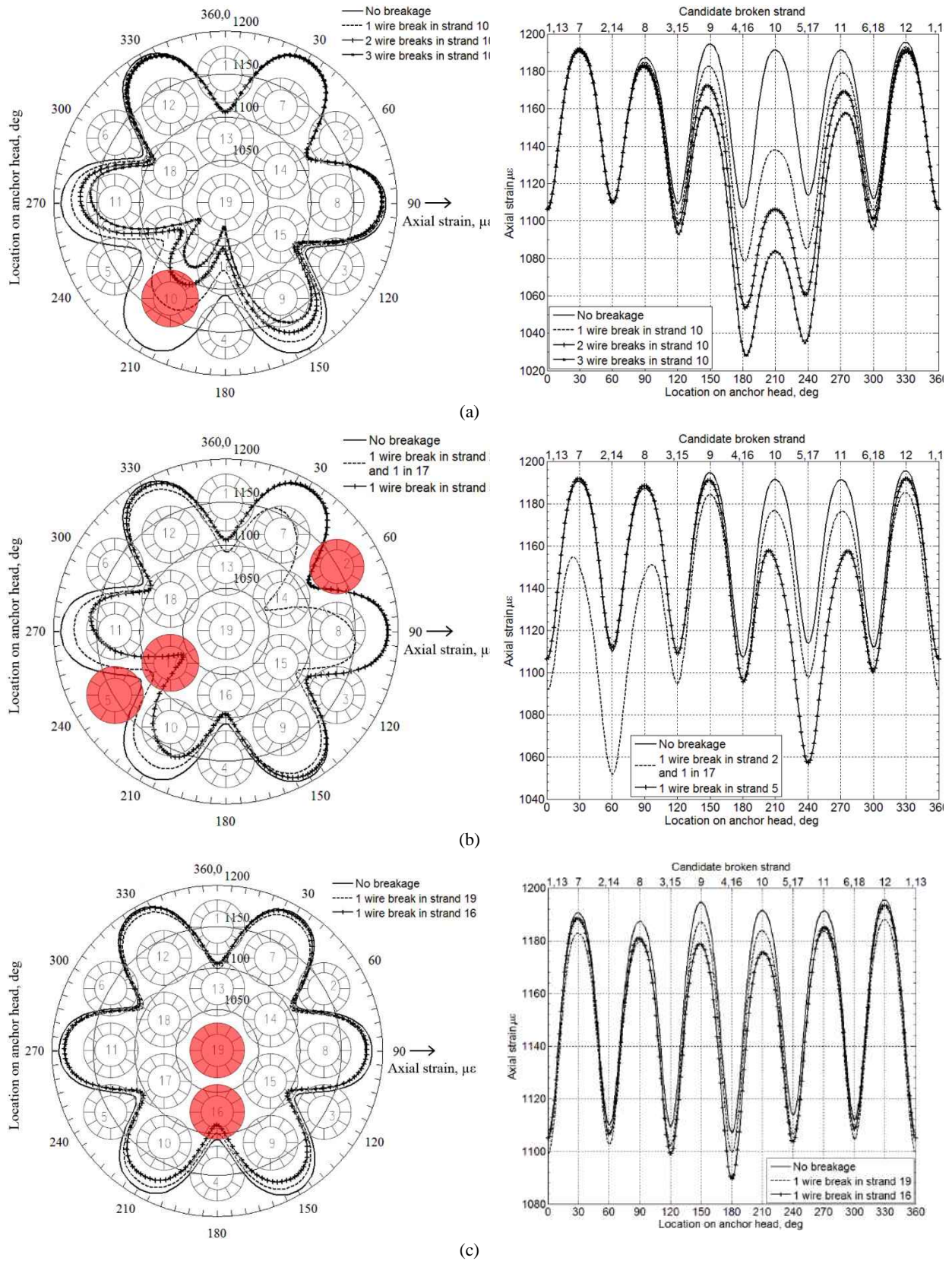


Figure 4-15 Comparison of axial strains in E 6-19 anchorage before and after wire breaks

The wire breakage events can also be successfully captured with limited monitoring points as shown in Figure 4-17, where consistent results accompanying sharp peak variation were noticed. For example, monitoring point H, which is the closest location from the broken strand 10 (Case B1), experiences the highest strain variation, followed by the adjacent points G and I, and it continues to decrease as the distance from the event location increases.

For Case B2, the variation of axial strain experienced by the anchor head due to wire breaks in strand 2 and 17 is shown in Figure 4-16b. As expected, a larger strain drop occurs for wire break in strand 2 because of its proximity to the strain measurement locations and therefore, a distinct peak at location C is evident in Figure 4-17. Even though the other breakage occurs in one of the inner strands (strand 17) located at a distance from the monitoring points, the breakage can still be detected from the observed peak at location I.

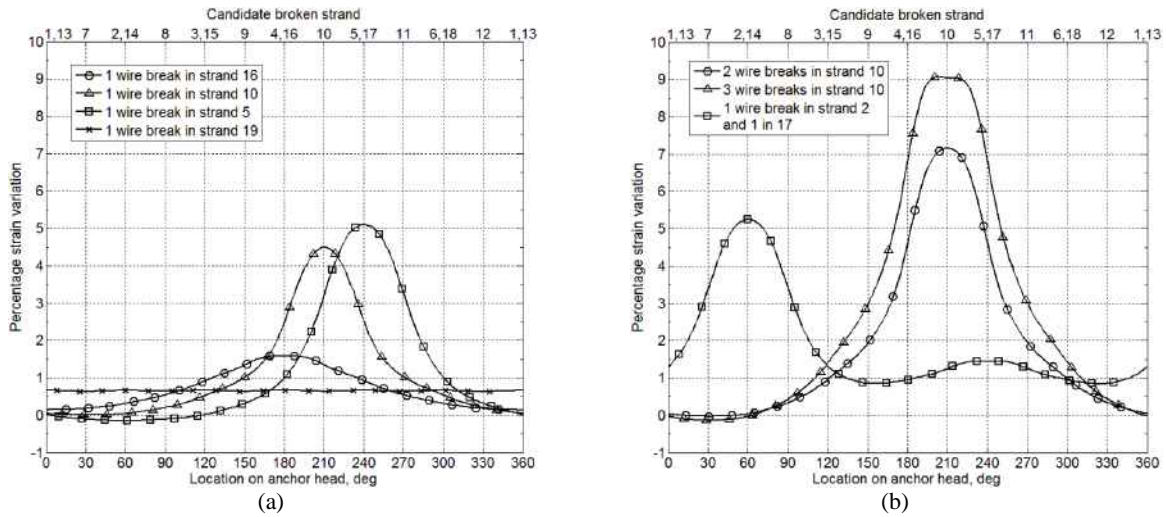
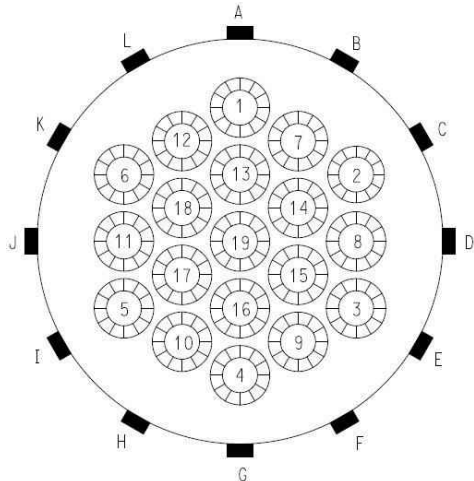


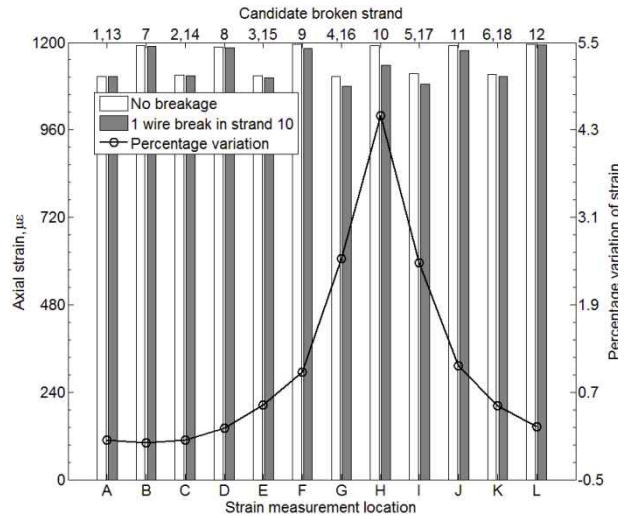
Figure 4-16 Strain variations in E 6-19: (a) single wire break; (b) multiple wire breaks

Similarly, a wire break in strand 16 (Case B3) yields a lower strain variation than strand 5 because of the greater distance from monitoring locations. The resulting strain drops by $18 \mu\epsilon$ (1.6%) in the case of strand 16 as compared with $57 \mu\epsilon$ (5.1%) for strand 5 (Case B4); both of the breakage events, however, can be detected by observing distinct peaks at locations G and I, respectively, which are the nearest locations to the corresponding strands.

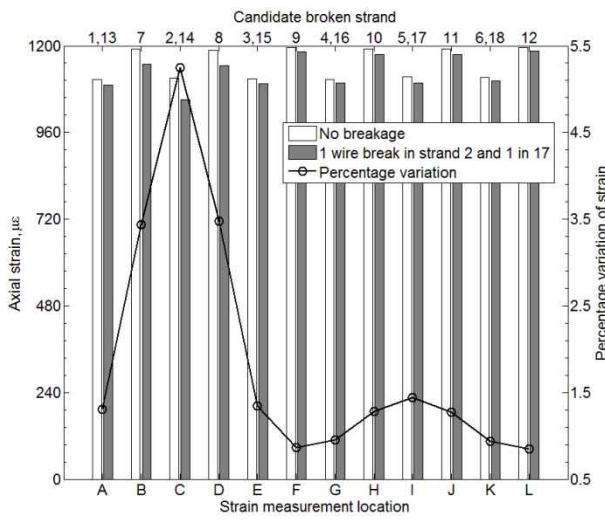


Strain measurement locations and strand ID

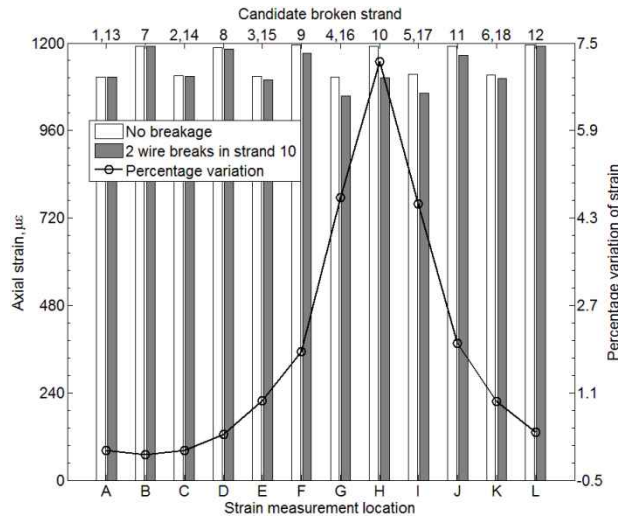
(a)



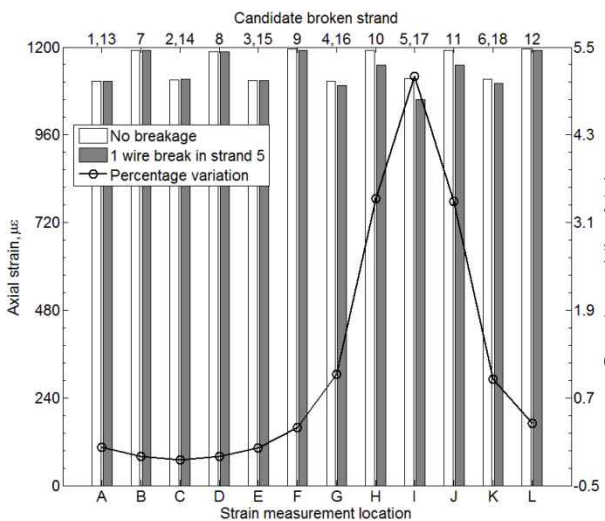
(b)



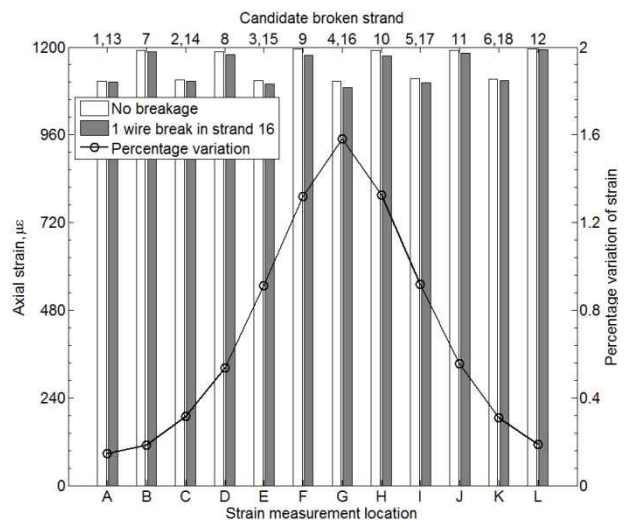
(c)



(d)



(e)



(f)

Figure 4-17 Strain variation due to wire breakage at different strain measurement locations

Finally, for wire breakage in the core strand 19 (Case B5), because all monitoring points on the anchor head are equidistant from the event location, all of them experience almost the same amount of strain variation and no definite peak is observed. However, an extensive statistical analysis may enable the equal shift of strains between the pre-breakage and post-breakage measurements (Figure 4-16a) to identify the breakage.

In a real monitoring environment with the presence of noise, capturing some of the small strain variations in one monitoring point is likely to be a challenge. Taking a holistic approach, however, by considering strain variations at all monitoring locations, yields a more detectable magnitude. For example, adding the strain variations at all monitoring locations for Case B3 produces $96 \mu\epsilon$. A more efficient algorithm to amplify the strain variation is to be sought in the future.

4.5 Summary

The analytical investigation reported in this chapter demonstrated the correlation between wire breaks and strain distribution in anchors. A self-contained stressing frame was designed and fabricated to conduct laboratory-scale experiments with monostrand/multistrand anchorage devices. To determine the friction coefficients at the wedge-anchor head and anchor head-anchor plate interfaces, a calibration test was performed with a seven-strand anchorage system. The estimated friction coefficients from the calibration experiment were subsequently used in defining the contact parameters in the finite element simulations. The intended strand breakage detection method was first outlined by FEA of the seven-strand anchorage used for calibration. Afterward, the detection method was extended to analyze a larger anchorage mechanism to investigate its effectiveness in a more complex setting.

As the numerical results illustrate, the proposed approach is promising for monitoring wire breakage in unbonded tendons. Although the intensity of strain variation decreases with a greater distance between event location and monitoring points, the breakage event is still evident from the relative strain variation among the monitoring points. Consistent results and distinct peaks in strain variation plots indicate the method's capability to detect and locate wire breakage with a limited number of strain monitoring locations. In addition, the magnitude of strain variation can be used to evaluate the severity of damage in terms of number of wire breaks.

The study presented in this chapter, however, only considers the variation of strains in the axial direction at the external surface of anchor head. The strain change in the radial and circumferential directions at other potential monitoring locations is evaluated in the next chapter through a laboratory experiment that also validates the analytical model.

5 Experimental Evaluation of Strain Distribution in Anchors

This chapter provides experimental validation of strain variation in the 19-strand anchor reported in the previous chapter. A detailed investigation on the change in strain distribution in anchor heads was conducted by generating wire breaks using a mechanical device. The experiment comprised multiple tests with fully populated, partially-stressed 19-strand anchor heads and evaluated the levels of strain variation with the number of wire breaks in different strands. The sensitivity of strain variation with wire breaks in circumferential and radial directions of anchor head in addition to the axial direction (parallel to the strand) were investigated.

Although it is likely that the outer strands will be more susceptible to corrosion and fretting fatigue in in-field conditions, wire breaks may potentially occur in any strand layer. The experimental program, therefore, included three sets of tests, where each set involved stressing and cutting each of the wires of the center and a non-center strand on different layers. The resulting strain in a 19-strand anchor head was continuously measured with a group of strain gages installed at different locations on the external surface of the anchor head (Figure 5-1). The state of strain at pristine condition was then compared with the strains after different numbers of wire breaks to calculate the corresponding strain variation.

5.1 Test setup

An approximately 1.5-m (5-ft) long steel reaction fixture (Figure 5-1) was used to react against the applied load in the strands. A stiffened anchor plate was placed at the stressing end of the fixture to bear an anchor head, whereas a load cell was positioned between the end bearing plate and the anchor plate at dead end. The strands were passed through a longitudinal conduit located at the center of the fixture and was anchored to the dead end anchorage. The other end of the strands was held by the grippers of a hydraulic jack for tensioning and was finally anchored to the stressing end anchorage. An opening near the stressing end allowed access to the strands for cutting.

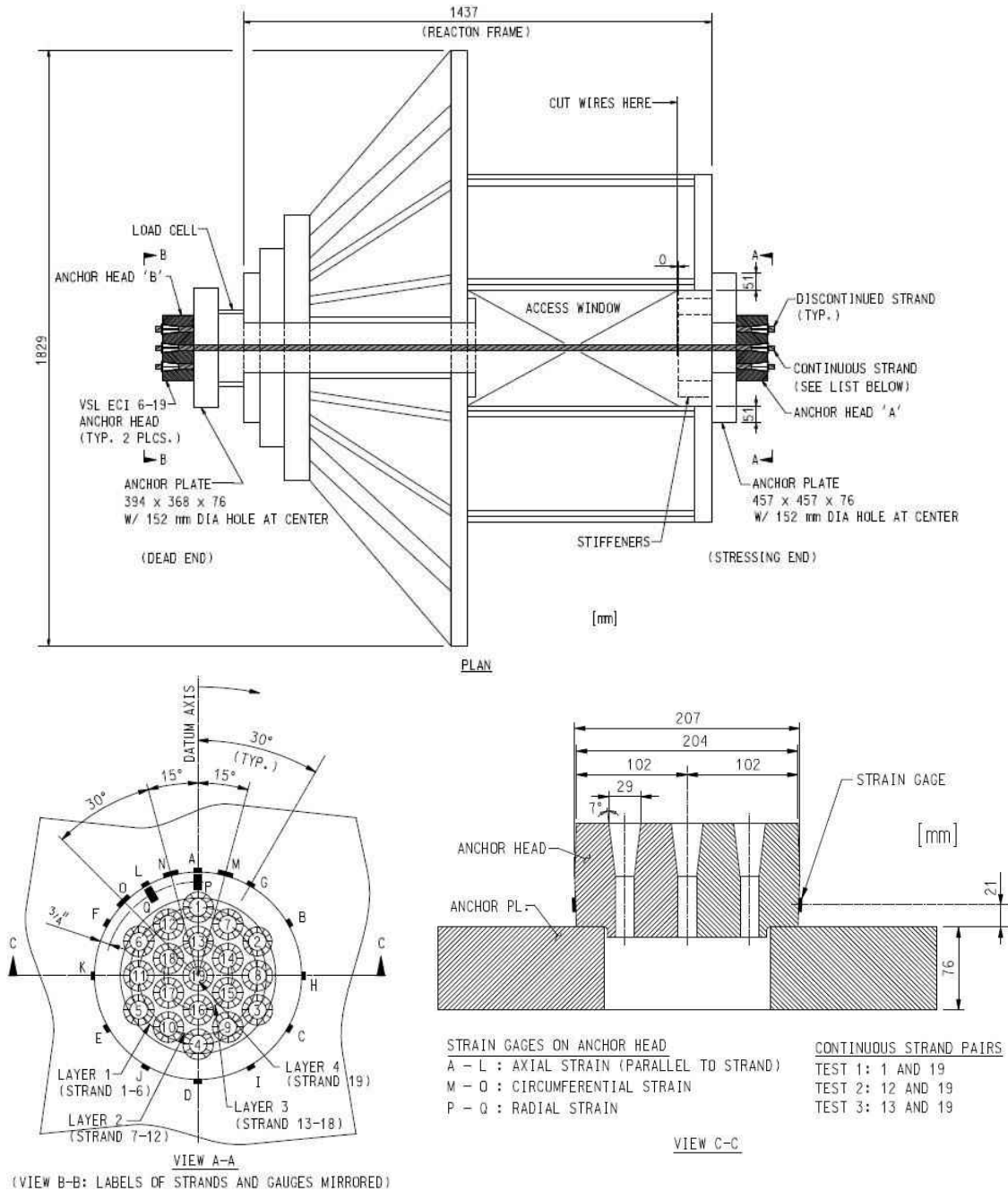


Figure 5-1 Reaction fixture details and sensor layout

15.2 mm (0.6 in) diameter Grade 270 strands, conforming to ASTM A416 (ASTM 2006), were used in this experiment. The low-relaxation seven-wire strands were approximately 2.75-m (9-ft) long with a cross sectional area of 140 mm² (0.217 in²). The post-tensioning anchorage comprised a 19-strand anchor head (VSL ECI 6-19, VSL International, Köniz, Switzerland) sitting on a 76 mm (3 in) thick anchor plate at each end. The wedge cavities in the anchor heads accommodated two-part wedges.

Seventeen foil strain gages (gage length of 5 mm) were installed on each of the two anchor heads (Figure 5-1); twelve (A-L) to measure axial strain, three (M-O) for circumferential

strain and two (P-Q) for radial strain. A donut load cell was placed at the dead end of the reaction fixture to monitor the total tendon force during the entire duration of stressing and cutting phase. In addition, six foil strain gages (gage length of 0.5 mm) were installed on wires to estimate the individual strand load during stressing.

The equipment used for stressing the tendon consisted of a mono-strand jack, a calibrated pressure gage and a hydraulic pump. To manually introduce wire breaks, the wires were mechanically cut with a Dremel[®] high-speed rotary tool. Relatively small diameter (31.75 mm), fiberglass-reinforced cutoff wheels were used to facilitate separate wire cuts. A Dremel[®] flexible shaft attached to a specially designed guiding rod with an adjustable clamp helped in cutting the stressed wires through the access window from a safe distance (Figure 5-2).

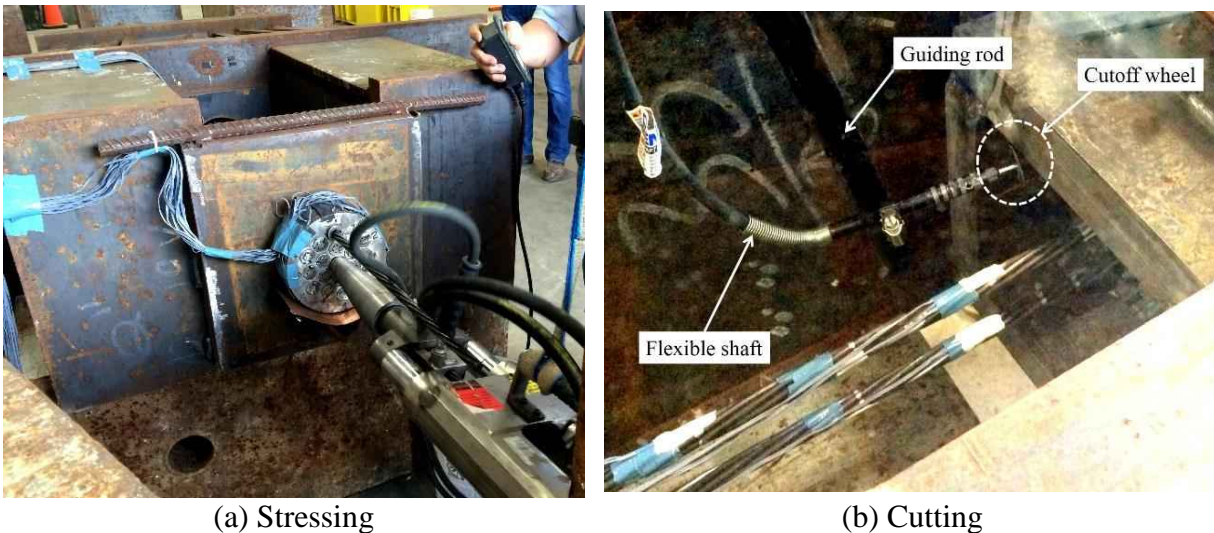


Figure 5-2 Tendon stressing and cutting apparatus

5.2 Experiment

In each of the three sets of test, two strands were stressed during the experiment (Figure 5-3). Table 5-1 lists the amount of tension applied to each of these strands. A larger load could not be achieved due to high seating loss in short tendons. Because of limitations of the reaction fixture, the remaining strands were not continued to the other end but the wedges on both of the anchor heads were pre-stressed by stressing the respective strands to approximately 74% of their ultimate strength ($0.74 F_u$). Although the anchor plates were under less-than-practical stress levels (as all the strands were not continued to the other end), the fully populated anchor heads with pre-stressed wedge provided a reasonable test condition to examine the state of strain.

Table 5-1 Test matrix and results

Test ID	Strand/Wedge label (Fig. 2)	Applied load	
		kN (kip)	% of F_u
1	Strand 1	101.0 (22.7)	39%
	Strand 19	131.7 (29.6)	51%
	Preseated wedge 2-18	193.0 (43.3)	74%
2	Strand 12	114.8 (25.8)	44%
	Strand 19	135.7 (30.5)	52%
	Preseated wedge 1-11, 13-18	193.0 (43.3)	74%
3	Strand 13	110.8 (24.9)	42%
	Strand 19	130.3 (29.3)	50%
	Preseated wedge 1-12, 14-18	193.0 (43.3)	74%

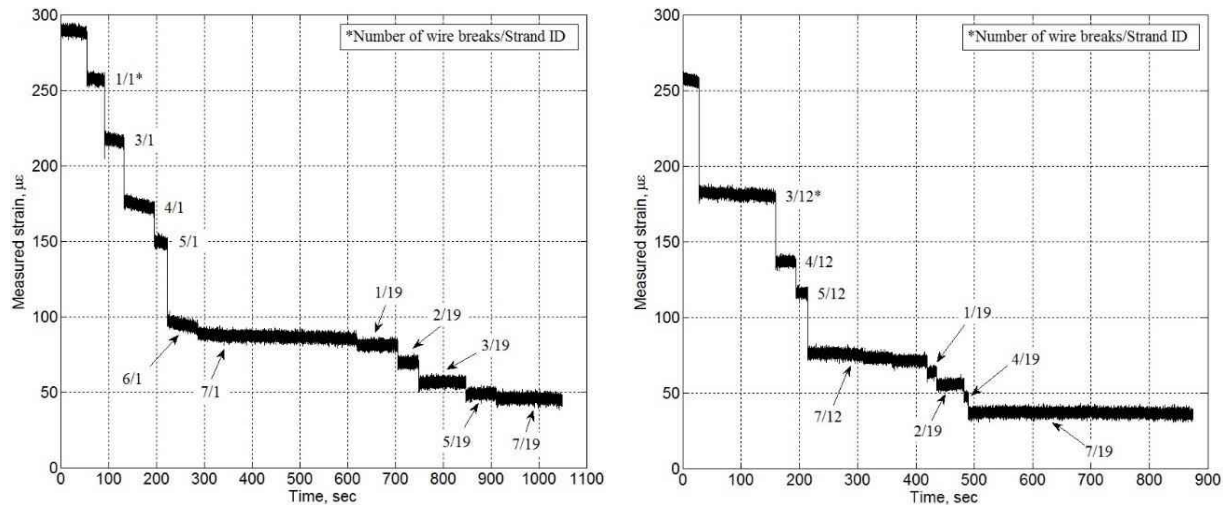


(a) Test frame

(b) Stressing end

Figure 5-3 Experimental setup

In Test 1, tension was gradually applied to the center strand (strand 19) with a mono-strand jack, followed by the non-center strand (strand 1). The effective loads in individual strands were measured by a pressure gage attached to the jack and foil strain gages installed on wires, along with the total tendon force reading from the load cell. After achieving the target stress level in each of the strands (Table 5-1), the wires of strand 1 were gradually cut until the complete breakage of the strand was achieved. After cutting all the wires in strand 1, the wires in strand 19 were cut. The resulting strains in both anchor heads were recorded during the entire duration of stressing and cutting phase with sampling frequency of 10 Hz and 100 Hz, respectively. Stressing and cutting of other strands in Test 2 and Test 3 were carried out by following a similar procedure.



(a) Test 1: wire breaks in strand 1 and 19

(b) Test 2: wire breaks in strand 12 and 19

Figure 5-4 Time history of measured strains by gage L

Figure 5-4 shows representative time histories of measured strains during cutting that illustrate the cutting procedure. For Test 1 where only the outermost strand 1 and the center strand 19 were stressed, strain change continued to occur even between two wire cuts (indicated by the strain slopes between cuts in Figure 5-4a). For example, the strain change between the 3rd and 4th wire cuts was around 16% of the total strain change for the 4th wire cut. Before cutting, the wedge plate was under highly localized stress (originating from uneven bearing of the wedge plate to the anchor plate) for a relatively long period of time (compared to the subsequent tests to prepare for wire cuts) while exposed to environmental temperature. This has possibly caused the wedge plate to creep, which resulted in the strain change between cuts. However, such phenomenon was not evident in other inner strand cuts because the bearing was more uniform and the anchor was under less severe localized stress.

5.3 Results

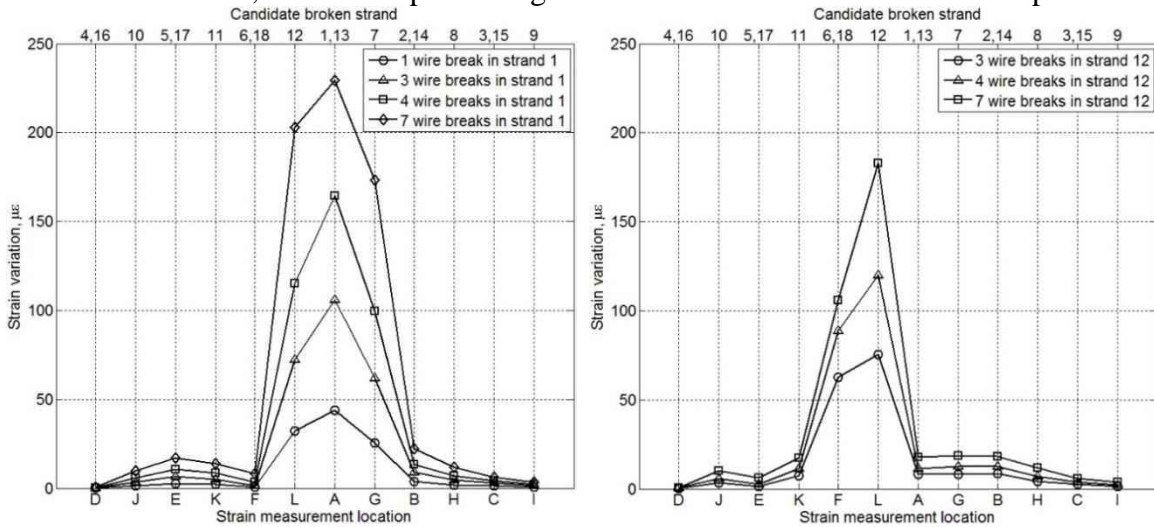
Under the loading and boundary conditions, the resulting strain in an anchor head is expected to develop primarily in three directions: axial (because of tension in strands), circumferential and radial (because of wedge seating in anchor head). The strain response in all these three directions was captured to assess the sensitivity of measured strains to wire breaks.

5.3.1 Axial Strains

Because of wire breaks in strand 1 on the outermost layer, the maximum axial strain drop was experienced by strain gage A (closest gage to the broken strand), followed by the adjacent gages, and the magnitude of strain drop increased with the number of wire breaks (Figure 5-5).

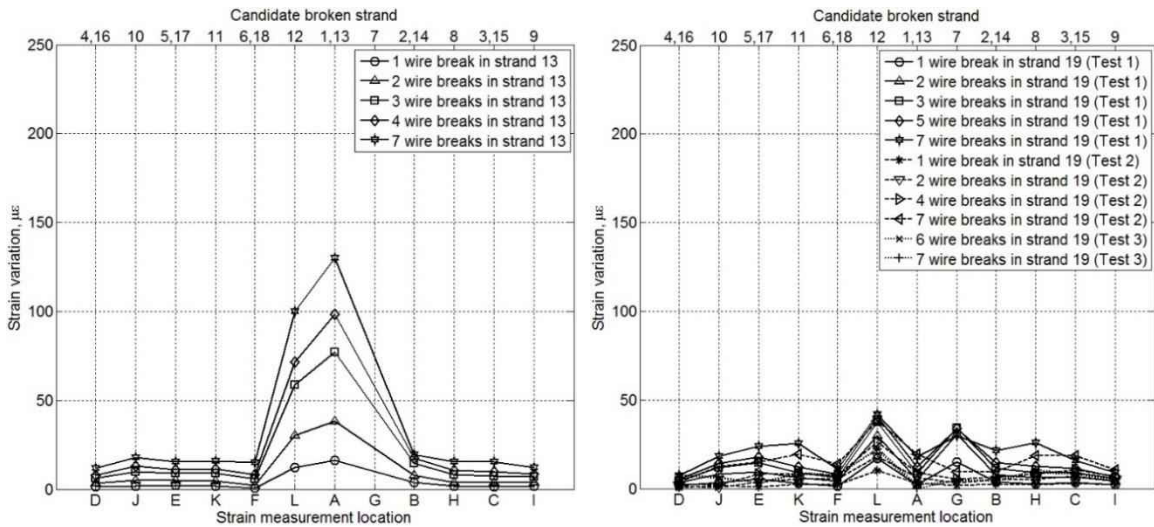
Similarly, in case of Test 2, where wire breaks occurred in strand 12 on layer 2, gage L (closest gage to strand 12) captured the highest strain drop and as expected, strain relief increased with each subsequent wire break. Observations in Test 1 and Test 2 held in Test 3, where wire breaks occurred in strand 13 on layer 3. Gage A, which was the closest gage to broken strand 13, recorded the greatest strain drop and the extent of strain drop increased

monotonically with the number of wire breaks. Additionally, larger strain drops occurred for wire breaks in outer layer strands compared to the inner layer, noting that all the three non-center strands (strand 1, 12 and 13) were almost equally stressed (ranging from 0.39 to 0.44 F_u). However, Figure 5-5(a)-(c) show unequal strain variation at two symmetric locations about the broken strand, which is likely due to unequal seating of wedge parts (designated as differential wedge seating) as is discussed later. In case of wire breaks in the center strand 19, the strain decreased at all monitoring points by a small amount; however, as all the gages were equidistant from the broken strand, no distinct peak/trough was observed in the strain variation plot.



(a) Wire breaks in strand 1 (*Test 1*)

(b) Wire breaks in strand 12 (*Test 2*)



(c) Wire breaks in strand 13 (*Test 3*)

(d) Wire breaks in the core strand (strand 19)

Figure 5-5 Axial strain variations due to wire breaks

5.3.2 Circumferential and Radial Strains

Circumferential strains, measured by gage M, N, and O (Figure 5-1), decreased consistently with wire breaks in both non-center (strand 1, 12 and 13) and center (strand 19) strands (Figure 5-6); however, the magnitude of the strain decreases were less than that of axial strains. Furthermore, radial strains, captured by gage P and Q, were the least sensitive among the three groups of strain measurement (Figure 5-7). Although relatively small, the strain variations were consistent with the number of wire breaks. Thus, both circumferential and radial strains were found less sensitive compared to axial strains. This is due to the fact that the tendon force transfers from anchor head to anchor plate mainly through bearing, which results in high axial compressive strain in anchor head. The tensile circumferential strains and compressive radial strains occur only due to the widening of anchor head resulting from seating of wedges into the conical hole through frictional contact.

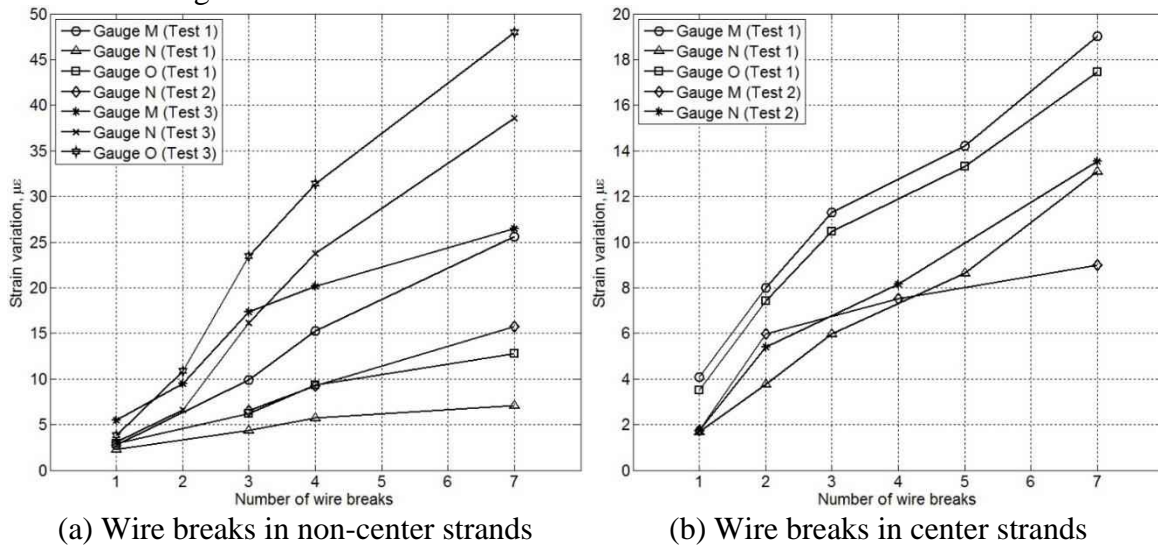


Figure 5-6 Circumferential strain variations due to wire breaks

It is noted that near identical strain variations were observed at most of the matching gages in the two anchor heads, except some anticipated discrepancies due to dissimilar support conditions of the two anchor plates. In this chapter, the measured strains in anchor head A have been reported. However, although preliminary protective measures were taken, a few gages debonded and/or disconnected during the testing; results from those non-functioning gages are not reported. This gage debonding issue highlights the importance of a rigorous investigation on durability of gages for long-term monitoring, such as exploring a more effective gage protector or examining the practicality of embedding the gages into the anchor head.

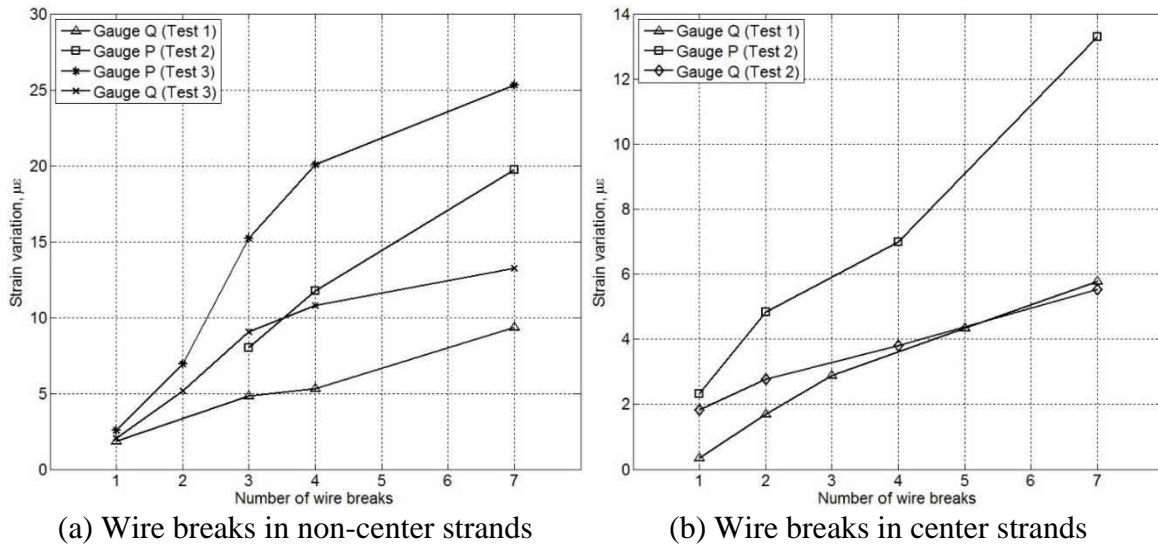


Figure 5-7 Radial strain variations due to wire breaks

5.4 Summary

The experimental results confirm the presence of strain variations due to wire breaks as well as the occurrence of the maximum axial strain drop at the closest monitoring location. As expected, the extent of strain drop consistently increased with the number of wire breaks and a larger strain decrease occurred due to breakage in an outer strand. In addition, axial strain has been found to be the most sensitive strain to wire breaks and radial strain to be the least.

Therefore, the experimental study shows evidence of the detectability of wire breaks from the measured strain variations in the anchor head. Following this experiment, a wire breakage detection algorithm has been presented in the next chapter that enables the adoption of an automated monitoring strategy.

6 Tendon Monitoring Algorithm

After confirming the sensitivity of strain distribution in the wedge plate to tendon damage in the previous chapter, this chapter presents a tendon monitoring framework suitable for autonomous damage detection, quantification, and broken strand identification. Building on the general monitoring framework, two broken strand identification models have been developed: one is based on strand layers (defined later in this chapter) and the other is based on strand groups. The layer-based model is designed for large wedge plates where fewer sensors can be used relative to the number of strands, while the group-based model is better suited for smaller wedge plates. The two models have been demonstrated with two wedge plate patterns commonly used in industry: 19- and 12-strand wedge plates. The layer-based model demonstrated on the 19-strand wedge plate is capable of detecting single or multiple wire breaks in the same strand; however, the more challenging single wire break condition has been considered for demonstration. FEA results of a fully-stressed 19-strand anchor head, obtained from Chapter 3, have been used to illustrate the algorithm. The robustness of the model has been preliminarily tested through a sensitivity analysis with pseudorandom measurement errors. In addition, as almost inevitably encountered during tendon stressing, the effects of differential wedge seating on the proposed model have been analyzed.

The group-based model has been developed considering additional practical conditions, such as the effects of subsequent strand breaks on anchor strain distribution. Therefore, this model, demonstrated on the 12-strand wedge plate, takes into account the contributions from several nearby gages from a strand instead of merely the nearest gage. The performance of this algorithm has been tested with experimental results reported in Chapter 8. It should be noted that neither of the methods presented in this chapter are limited in any way to the specific wedge plates used for their demonstration; each method may be extended for other strand numbers and configurations.

6.1 Tendon Monitoring Framework

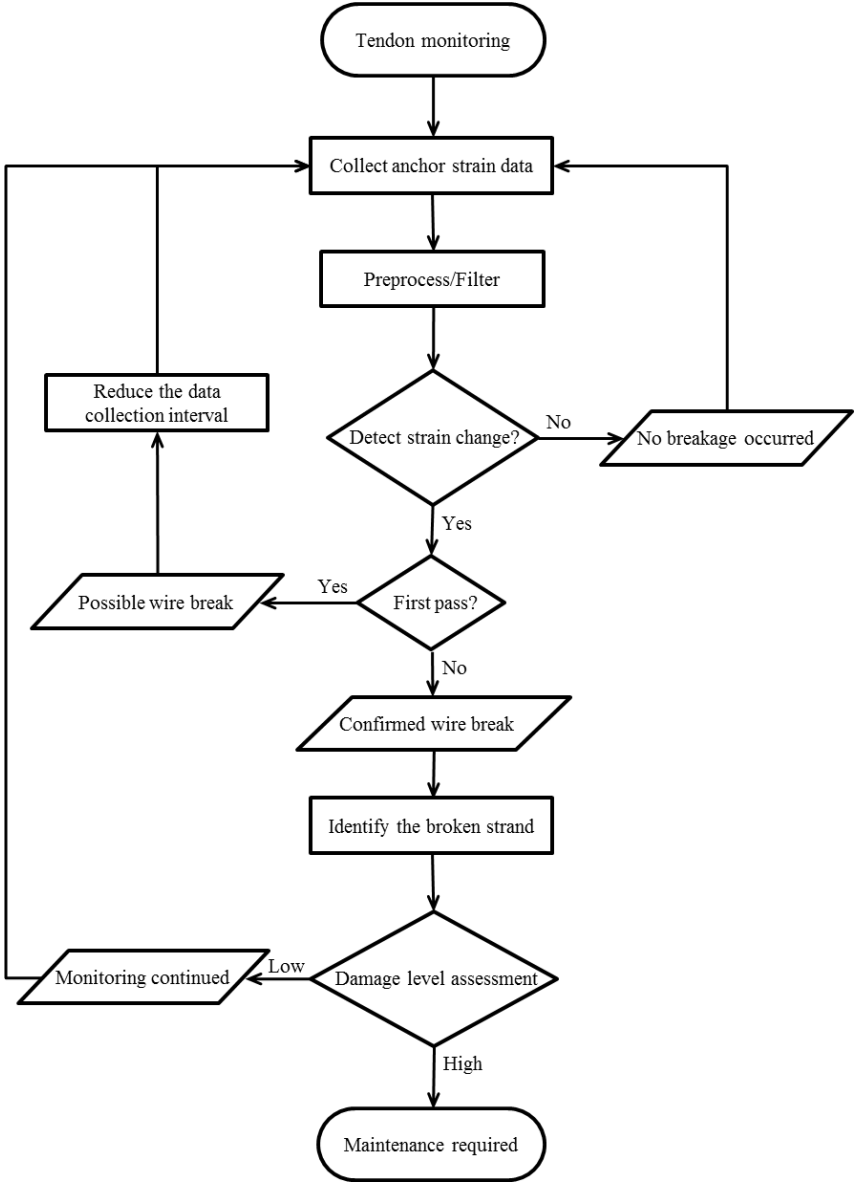


Figure 6-1 Wire breakage identification flowchart

Figure 6-1 shows a simple monitoring framework for the strain-based approach presented in this section. The purpose of the framework is to provide alerts when strand breakage is detected and identify the strand that has sustained the damage. The data collection and processing is expected to be fully automated, requiring very little user input. The framework assumes that at least one wedge plate for the strand(s) of interest is instrumented with a number of strain gages capturing axial strains on a predetermined schedule (e.g. daily or weekly), such as at night when traffic loads and temperature loads are expected to be at their lowest. The anchor strain data are collected for an amount of time adequate to capture mean strain levels each day. Then the captured data may be pre-processed to exclude the effects of live load, temperature differentials, and other non-breakage events. The preprocessed data are compared with the data

collected during the previous monitoring event to determine if any significant strain change has occurred, indicating a wire break. After detecting a break event, the next step is to identify the broken strands. Finally, an assessment of the damage level, relative to previous monitoring events, is carried out. The damage level assessment may then be used by the maintenance office to decide whether to continue monitoring the strains or to perform a maintenance operation.

6.2 Layer-based Broken Strand Identification Framework

6.2.1 Underlying Framework

One of the primary challenges in identifying the broken strand is that the strand pattern in the wedge plate results in a number of concentric strand layers as illustrated in Figure 6-2a, with the outer layer strands much closer to the monitoring points. As such, a wire break in an outer layer strand produces a sharper peak in strain variation plots compared to the inner layers, e.g., breakages in strand 1 and 12 result in a narrow peak, whereas breakage in strand 13 yields a wider plot (extended over a larger region) with smaller peak, and that core strand produces a mostly flat plot (Figure 6-2). These characteristics of strain plots represent a dissimilar strain variation among the monitoring points, which are used to calculate two damage-sensitive parameters: the peak percentage strain variation (p) and the peak relative percentage strain variation (r). These parameters are then checked against a group of preset thresholds (ϕ , γ , λ , ψ) to verify a breakage event and to select a pool of candidate strands by identifying the strand layer on which the broken wire lies. After selecting the candidate strands, strain variations at all the monitoring points are considered to identify the broken strand. As each strand is located at a different distance from the strain monitoring points, the calculated strain variations are normalized by the distances between the monitoring points and the strand. The maximum of these normalized strain variations, designated as the damage index (DI) in this paper, is calculated for each of the candidate strands and the maximum damage index (DI_{max}) determines the broken strand.

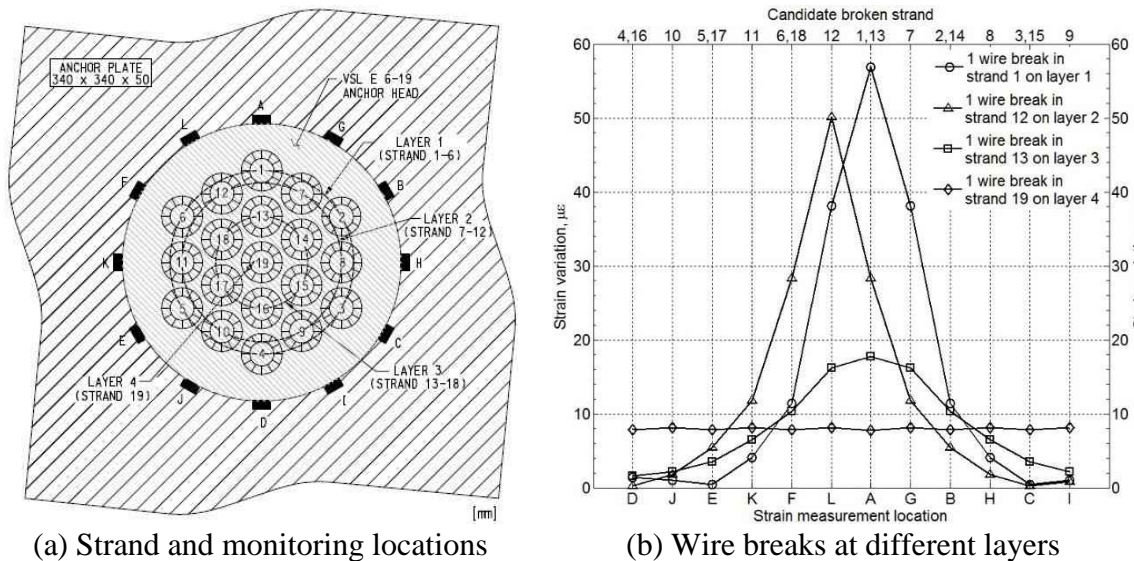


Figure 6-2 Monitoring locations and representative strain variations from FE analyses

6.2.2 Damage Parameters and Thresholds

The proposed model incorporates several key parameters and thresholds in developing the wire breakage detection algorithm. A list of these parameters and thresholds is provided as follows:

$(\varepsilon_i)_b$: Calculated strain at monitoring point i before the occurrence of wire breakage

$(\varepsilon_i)_a$: Calculated strain at monitoring point i after the occurrence of wire breakage

$\Delta\varepsilon_i$: Percentage strain variation at monitoring point i

p : Peak percentage strain variation

r : Peak relative percentage strain variation

ϕ : Threshold to assess the occurrence of wire break

γ : Upper bound of parameter r to identify the breakage occurred in layer 1

ψ : Lower bound of parameter p to identify the breakage occurred in layer 2

λ : Upper bound of parameter r to identify the breakage occurred in layer 3

DI_j : Damage index for strand j

d_{ij} : True distance between monitoring point i and strand j

DI_{\max} : Maximum damage index

The above parameters have been calculated in different steps of the algorithm using the following equations:

$$\Delta\varepsilon_i = \frac{(\varepsilon_i)_a - (\varepsilon_i)_b}{(\varepsilon_i)_b} \times 100 \quad \text{Equation 12}$$

$$p = \max(\Delta\varepsilon_i) \quad \text{Equation 13}$$

$$r = \max\left(\frac{\Delta\varepsilon_i}{\max(\Delta\varepsilon_i)}\right) \quad \text{Equation 14}$$

$$DI_j = \max\left(\frac{\Delta\varepsilon_i}{d_{ij}}\right) \quad \text{Equation 15}$$

$$DI_{\max} = \max(DI_j) \quad \text{Equation 16}$$

6.2.3 Algorithm Development

The various stages where different parameters and thresholds were introduced into the model are summarized in Figure 6-3 followed by a stepwise description of the algorithm.

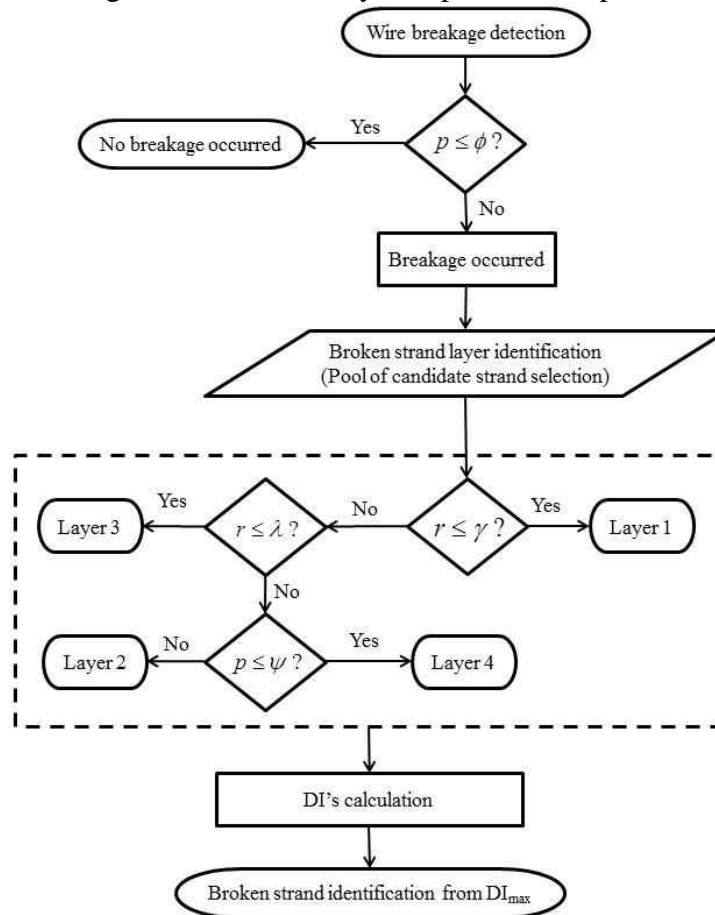


Figure 6-3 Wire breakage identification flowchart

Step 1: Wire break occurrence assessment

Peak percentage strain variation calculation

First, the peak percentage strain variation (p) among the six monitoring points 'A' to 'F' is calculated using Equation 12 and Equation 13. Because of the relative positions of the strands and monitoring points, it has been found that considering the strain variations at these six non-adjacent points, in place of 12, is more effective in establishing widely spaced thresholds to differentiate closely located strand layers, such as layer 1 and 2. After identifying the candidate strands, however, all the 12 monitoring points have been taken into account to calculate the damage indices.

Threshold check

The occurrence of a wire breakage event is then confirmed by checking the parameter p against the threshold ϕ as shown in Figure 6-3.

Step 2: Broken strand layer identification

Peak relative percentage strain variation calculation

If Step 1 indicates that a breakage has occurred, then the peak relative percentage strain variation (r) is calculated among the six monitoring points ‘A’ to ‘F’ using Equation 12 and Equation 14.

Threshold check

The parameter r is then compared to thresholds γ and λ to identify the broken strand layer. An additional threshold ψ has been found necessary for layers 2 and 4 to check against parameter p calculated in Step 1 (Figure 6-3).

Step 3: Broken strand detection

Damage index calculations

After identifying the broken strand layer in Step 2, a damage index, DI , is calculated for each of the strands on that layer from Equation 12 and Equation 15 considering all the 12 monitoring points (‘A’ to ‘L’).

Locating the breakage

Finally, the strand associated with the maximum of all the calculated damage indices (DI_{max}) is identified as the broken strand.

It is noted that, although the DI s indicate the relative likelihood of wire breakage in individual strands on the identified layer, there is no explicitly defined threshold for DI that a strand must exceed to be determined as broken. This is because the DI s are calculated only if a breakage is confirmed by satisfying the criterion that the peak percentage strain variation (p) exceeds the threshold ϕ in Step 1. Moreover, additional thresholds (γ , λ , ψ) are incorporated in Step 2 to identify the broken strand layer. Thus the DI s inherently entail several thresholds and the model, therefore, identifies the broken strand by picking the maximum damage index (DI_{max}) and disregards the rest of the DI s. However, the individual and/or relative magnitudes of the damage indices (DI s) may indicate wire breaks occurring in different strands. The calculated damage indices and identified broken strands of the 19-strand anchor model are included in Appendix F.

6.2.4 Error Sensitivity Analysis

A preliminary test with a pre-determined set of thresholds has been performed to evaluate the robustness of the model in the presence of random measurement errors. Some artificial errors were assigned to the original strain measurements and the detectability of wire breaks was then estimated through Monte Carlo simulation.

Determination of Thresholds

A parametric study was conducted on an E 6-19 wedge plate to investigate the strain distribution for all possible single wire breakage conditions. From this study, the thresholds defined previously were selected as follows:

$$\gamma = 0.4 ; \lambda = 0.7 ; \psi = 1.0 ; \phi = 0.5$$

It is noted that these thresholds have been used only to assess the performance of the model with limited measurement errors and may not be able to utilized universally. Individual thresholds will vary with the type of wedge plate and need to be adjusted to cope with in-field noise and measurement errors. This will require a long-term statistical data of in-field noise associated with the strain measurements and a realistic estimation of all the measurement uncertainties due to environmental and traffic loads, differential wedge seating and other non-

breakage events, to refine the thresholds and achieve a target detectability under the given field conditions.

Sensitivity Study of Measurement Errors

Systematic errors may occur in strain measurements due to fabrication faults in strain gages along with random errors due to gage misalignment (Figure 6-4), transverse sensitivity of gages (Figure 6-5) (Micro-Measurements 2015e), or differential temperature at monitoring locations. The notation shown in the figure are defined as:

$\varepsilon_1, \varepsilon_2$ = maximum and minimum principal strains, respectively.

$\varepsilon_a, \varepsilon_t$ = strains parallel to and perpendicular to the gauge axis, respectively.

ϕ = angle between the maximum principal strain axis 1-1 and the intended axis of strain measurements X-X.

β = angular mounting error (angle between the gauge axis after bonding X'-X' and the intended axis of strain measurements X-X).

K_t = transverse sensitivity coefficient.

ν_0 = the Poisson's ratio of the material on which the manufacturer's gage factor was measured.

In addition, differential wedge seating may cause somewhat irregular strain distribution (discussed in the following section). The sensitivity of the proposed model to these imperfections and unevenness has been tested with uniformly distributed pseudorandom errors.

Three sets of Monte Carlo simulations were conducted with a sample size of 1000; in Simulation I, errors ranging from -6.0 to +6.0 $\mu\varepsilon$ were randomly added to all the strain measurements. Tolerance limits for different strand layers were determined in Simulation II to achieve a target detectability of at least 80%. In Simulation III, higher errors (-10.0 to +10.0 $\mu\varepsilon$) were added to two randomly selected gages than the remainder of gages (error range: -2.0 to 2.0 $\mu\varepsilon$). As expected, the simulation results show fewer false negatives, hence higher detectability of wire breaks, in outer layer strands compared to the inner layers (Table 6-1). However, it is noted that the error levels were selected to test the model under certain measurement uncertainties; a more refined error sensitivity analysis with in-field measurements is necessary and the current model should be applied to experimental data with more realistic measurement errors.

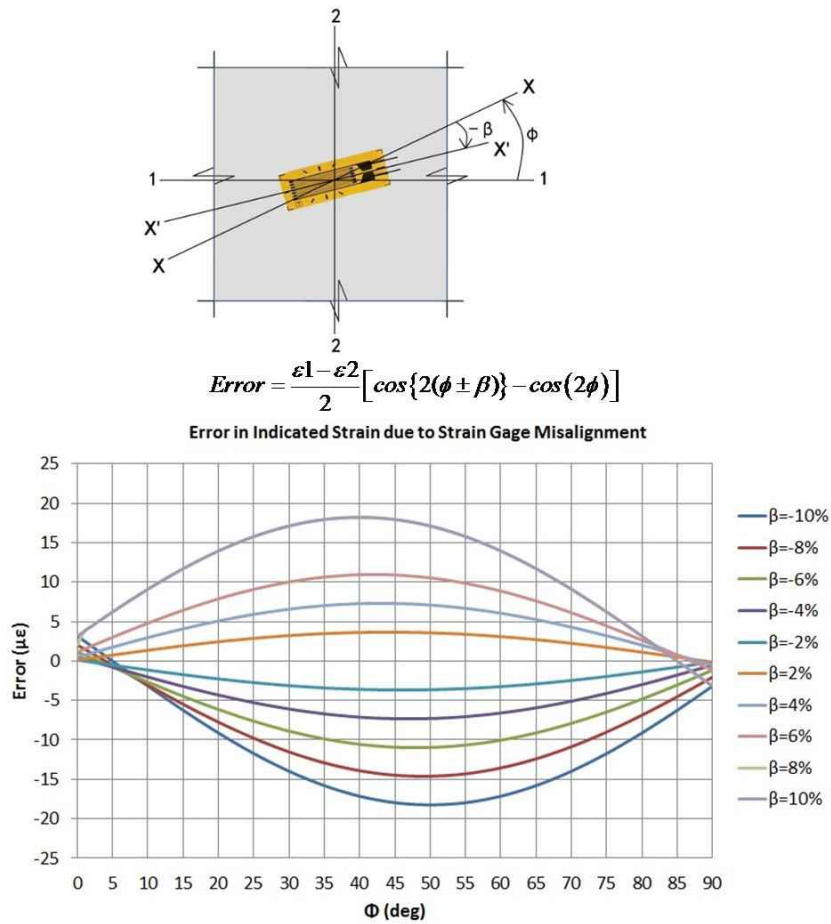


Figure 6-4 Error due to misalignment of strain gage

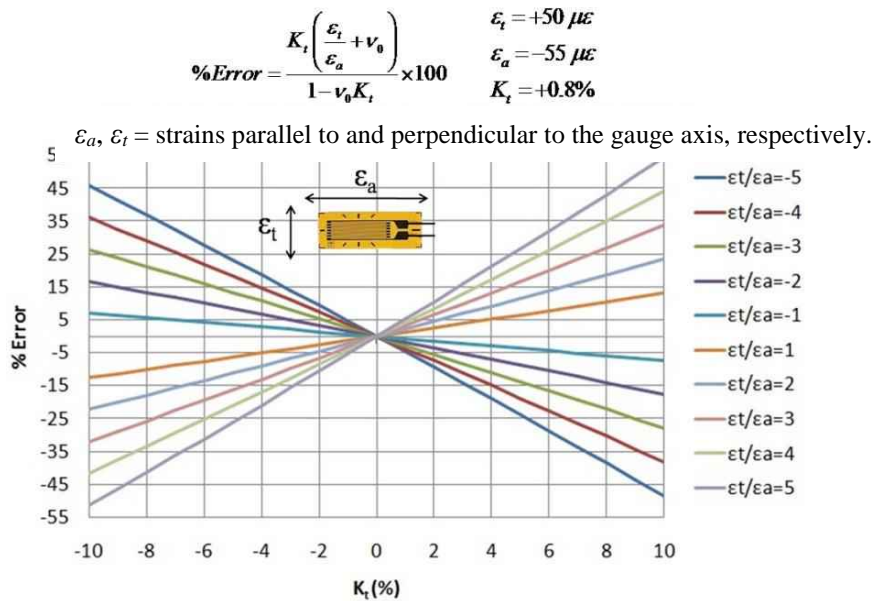


Figure 6-5 Transverse sensitivity of strain gage

Table 6-1 Success rate of single wire break identification

Broken strand ID	Strand layer	Simulation I		Simulation II		Simulation III	
		Error range, $\mu\epsilon$	Success rate of detection (95% CI*)	Error range, $\mu\epsilon$	Success rate of detection (95% CI)	Error range, $\mu\epsilon$	Success rate of detection (95% CI)
1	Layer 1	-6.0 to +6.0 (in all gages)	98-99	-9.5 to +9.5 (in all gages)	80-85	-10.0 to +10.0 (in two random gages) and -2.0 to +2.0 (in the rest of the gages)	96-98
2			98-99		81-85		97-99
3			98-99		82-87		97-99
4			97-99		81-85		97-99
5			98-99		81-86		96-98
6			98-99		81-86		97-99
7	Layer 2	-6.0 to +6.0 (in all gages)	84-88	-6.0 to +6.0 (in all gages)	84-88	-10.0 to +10.0 (in two random gages) and -2.0 to +2.0 (in the rest of the gages)	91-95
8			80-85		80-85		91-94
9			81-86		81-86		90-94
10			80-85		80-85		90-93
11			80-85		80-85		91-94
12			83-88		83-88		91-95
13	Layer 3	-6.0 to +6.0 (in all gages)	26-32	-1.5 to +1.5 (in all gages)	80-85	-10.0 to +10.0 (in two random gages) and -2.0 to +2.0 (in the rest of the gages)	46-52
14			36-42		84-88		54-60
15			25-30		83-88		47-50
16			33-39		81-86		50-56
17			31-37		84-88		49-56
18			32-39		83-87		57-63
19	Layer 4		12-16	-2.0 to +2.0 (in all gages)	85-89		58-64

*CI: Confidence interval

6.2.5 Effects of Differential Wedge Seating on the Proposed Model

Another potential source of nonuniformity in anchor strain distribution is the differential wedge seating. From the experiments, axial strain variations were clearly observed with wire breaks in case of non-center strands. For example, in Test 1 (Figure 5-5a), the closest gage to the broken strand 1 (gage A) captured higher strain variations relative to other gages. The plot, however, is not symmetric about point A; e.g., strain variations measured by two symmetrically placed gages L and G are not equal. A finite element analysis implies that this asymmetry may be attributed to differential wedge seating (unequal seating of the two wedge parts) along with other factors, such as gage misalignments. To investigate this, the FE model described earlier in Chapter 3 Section 4.2.2 with a single equivalent wedge component was modified. In this revised model, the two wedge parts were allowed to slide over one another assuming frictionless interactions at their interfaces. Figure 6-6b shows a comparison of strain variations between an ideal equal wedge seating and a differential wedge seating condition. In both cases, a single wire break was considered in strand 4 and the unequal wedge seating was conducted with 5% differential seating between the two wedge parts.

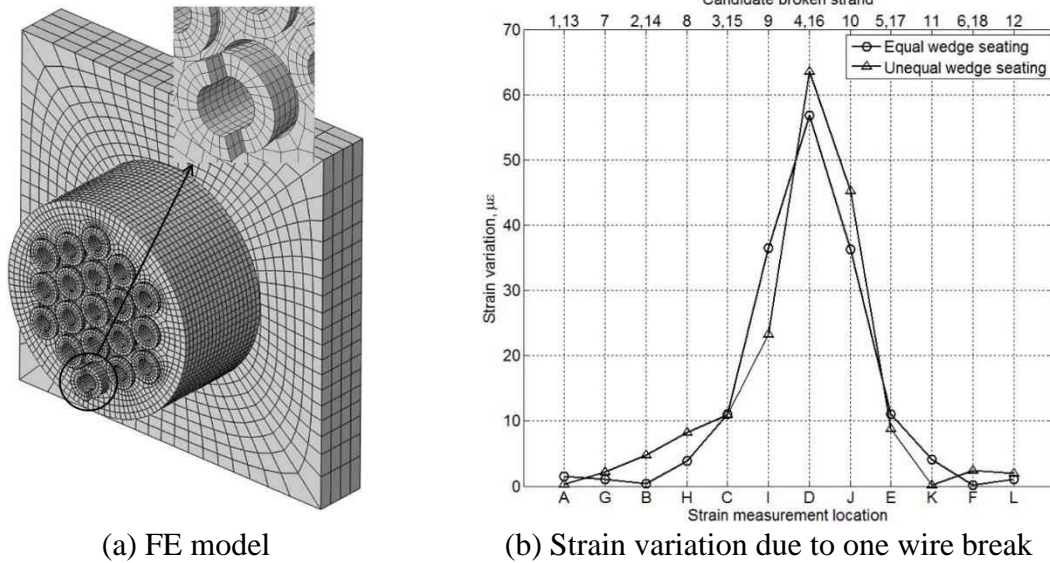


Figure 6-6 Differential wedge seating

Although the differential wedge seating for a single strand appears to create some uneven strain distribution, many of these individual effects are likely to mitigate each other when considering all the wedges in a fully populated anchor head. This combined effect of differential wedge seating has been regarded as one of the random measurement uncertainties in the previous section. A more practical assessment of this effect along with other measurement errors should be pursued in future experiments.

6.3 Group-based Broken Strand Identification Framework

6.3.1 Underlying Framework

The concept of identifying the broken strand is based on the fact that the portion of the wedge plate near the broken strand experiences higher strain relief compared to distant region. As shown earlier, the relative strain change in discrete strain monitoring points results in a distinct peak at the nearest monitoring point from the broken strand and the magnitude of the peak indicates the extent of a potential damage. The previous model only considered the first broken strand and uniform wedge seating, and the peak simply appeared at the closest point, which easily determined the broken strand. However, during in-field application, several factors, such as subsequent breakage in other strands, differential seating of wedge parts due to geometrical imperfections, uneven bearing of the wedge plate to the anchor plate or stressing mechanism may potentially change the overall strain distribution over the anchor and thus identifying the newly broken strand becomes more difficult. Thus, rather than considering only the nearest gage from a strand, taking into account the contributions from several nearby gages become necessary. Considering all these practical conditions, a simple framework has been developed for identifying the broken strand and is demonstrated on a standard 12-strand anchor head.

6.3.2 Algorithm Development

Based on the strand pattern the wedge plate has been divided into 6-60° slices and the strands within each slice constitute a strand group (Figure 6-7). Similarly for each strand the contributions of the 3 nearest gages have been taken that fall within a 60° slice. For example, for strand 1, gage L, A, and G; for strand 2, gage G, B, and H have been considered, and so on, thus the total count of strain monitoring points is also 12.

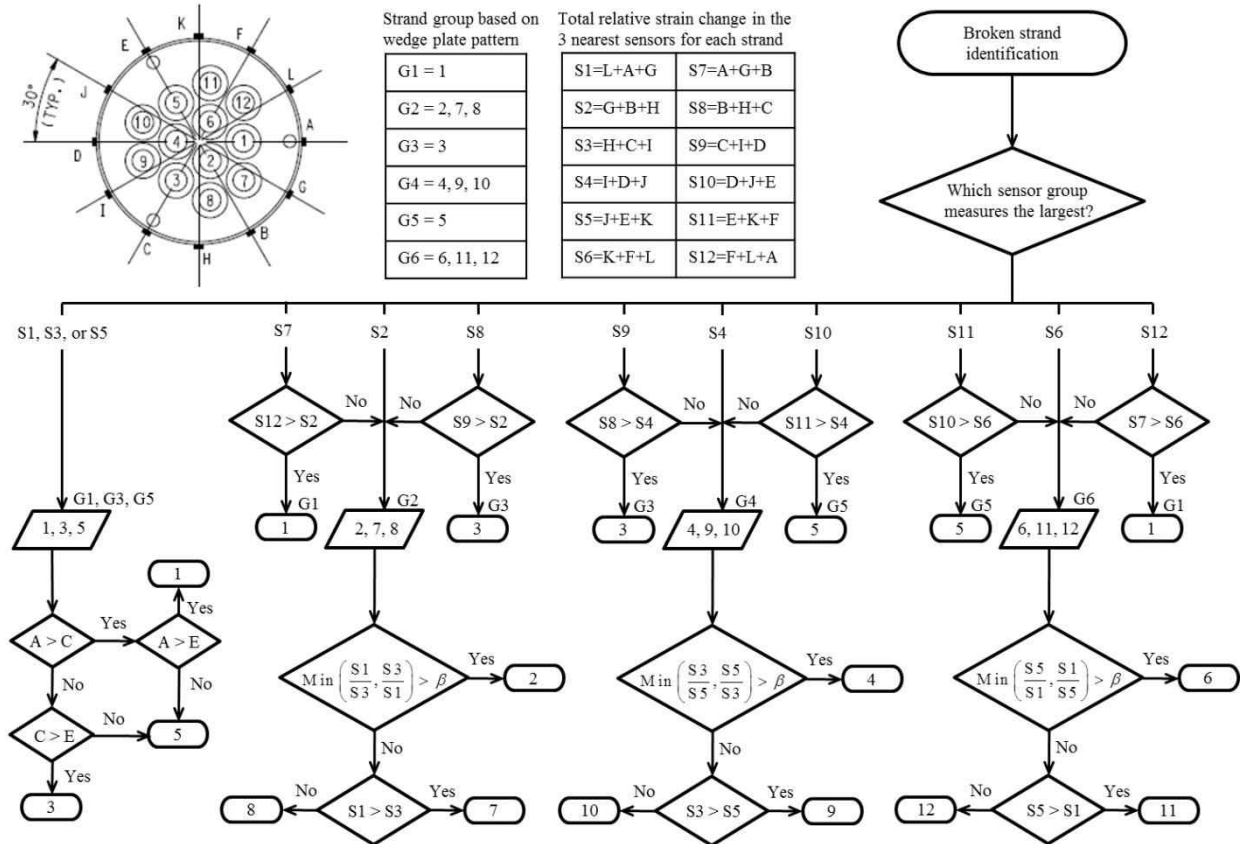


Figure 6-7 Wire breakage identification flowchart

First, the sensor group that measures the largest strain is identified. As illustrated in Figure 6-7, sensor group S2, S7, and S8 correspond to multi-strand group G2. Similarly, S4, S9, and S10 correspond to G4 and S6, S11, and S12 correspond to G6, and the rest correspond to the single strand groups G1, G3, and G5.

If sensor group S2, S7, or S8 measured the largest strain, the candidate broken strands fall in strand group G2 (Strand 2, 7 and 8). However, the boundary strands 1 and 3 must also be checked. If the largest sensor group is S7 or S8, sensor group S2 (G, B, H) must be compared with the adjacent groups S12 (F, L, A) or S9 (C, I, D) to confirm the broken strand falls in group G2.

In determining the exact strand within group G2 (2, 7, 8) sensor group S1, which is L, A, G and S3, which is H, C, I must be compared. If strand 2 is broken, then S1 and S3 are expected to be almost equal, because it's equidistant from these two sensor groups. Thus, the ratio between S1 and S3 is compared with a threshold β , which is close to unity. If S1 is greater than

the broken strand is 7, otherwise the broken strand is 8. Similar procedure is applicable for sensor group S4, S9, and S10 and group S6, S11, and S12.

In case the largest sensor group is found either S1, S3, or S5, which correspond to the single strand groups, then the broken strand is either 1, 3, or 5. To determine the exact strand among 1, 3, 5 the nearest gages alone must be compared to exclude the effects of already broken strands.

The effectiveness of this detection method based on strand groups is evaluated in Chapter 8, where experimental results are presented.

6.4 Selecting the Number of Sensors in Anchors

As described earlier, the strands in some wedge plates (e.g., 19-strand wedge plate) are arranged in several concentric layers based on their radial distance from the anchor's circumferential surface where the sensors are located. For example, in a 19-strand wedge plate (Figure 6-8a), strands 1-6 constitute layer 1, which is the closest from the surface, followed by strand 7-12 on layer 2, 13-18 on layer 3, and strand 19 at the center, which is the farthest from the surface. To minimize the strand-sensor distance, the sensors are placed on the radial lines connecting the anchor center and each individual strand. The strand pattern on such a wedge plate, however, results in fewer numbers of unique radial lines than the number of strands (only 12 unique radial lines for the 19 strands), because multiple strands of different layers fall on the same line. Some wedge plates (e.g., 12-strand wedge plate), on the other hand, do not possess such property of collinear radial lines and a unique radial line exists for each of the strands. Because the algorithms capture the peak strain change at the closest sensor from a broken strand, the proposed framework requires a minimum number of sensors equaling the number of unique radial lines. The performance of the model deteriorates if a sensor malfunctions or fewer sensors are used, as illustrated by an investigation with the experimental results reported in Chapter 8.

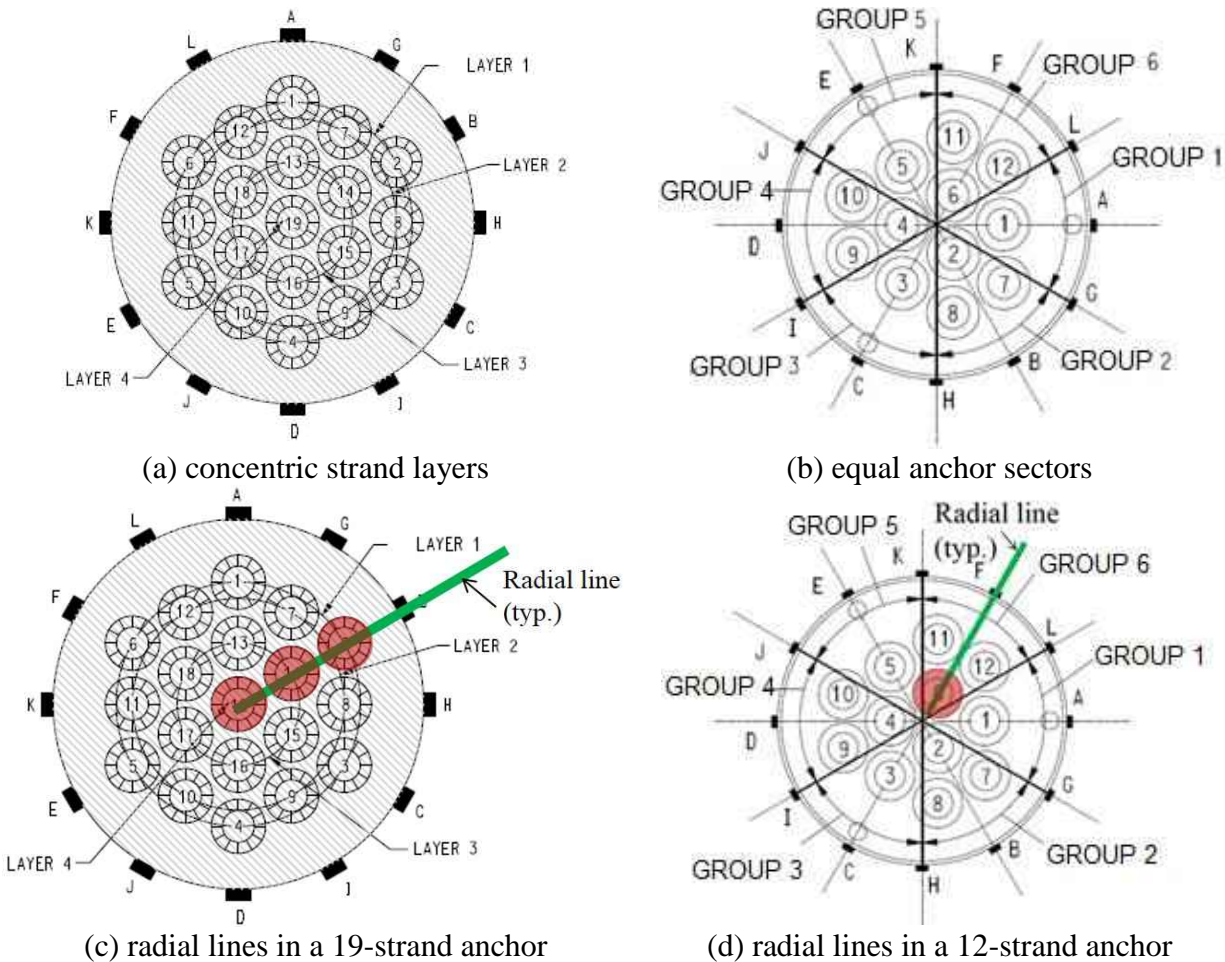


Figure 6-8 Sensor arrangement in layer- and group-based approaches

6.5 Summary

A promising monitoring framework is presented to detect a wire break and identify the broken strand in a multi-strand unbonded tendon. For identifying the broken strand, two methods have been proposed—a layer-based method and a group-based method—depending on the number of strands and complexity of wedge plate configuration. Strain variations for a broad spectrum of wire break conditions were obtained from FEA and the results were used in estimating the thresholds in the layer-based model. The susceptibility of the model to in-field conditions have been preliminarily tested with artificially generated random measurement errors. Different combinations of measurement uncertainties were incorporated into the model and detectability of wire breaks were estimated.

The layer-based model performed well with randomly selected measurement errors, showing higher detectability of breakage in outer strands. Relatively low detectability, however, was observed in cases of single wire breakage in inner layer strands because they resulted in small strain variations. Locating such breakages in in-field conditions with the presence of ambient noise is expected to be difficult; however, multiple wire breaks in the strand would increase the detectability.

The group-based model, designed for smaller wedge plates, considers the effects of multiple (subsequent) strand break conditions. This model has been applied to the results of a

full-scale experiment conducted on an internal unbonded tendon specimen reported later. Although these two monitoring algorithms have been demonstrated for specific wedge plate patterns, these models can be generalized for different anchor configurations.

The general detection framework presented in this chapter appears to be promising; however, the detection range of wire breaks along the tendon length is dependent on the post-breakage tendon behavior, which requires a detailed investigation on its stressing and breakage response. The next chapter deals with an extensive finite element analysis to characterize both static and dynamic behavior of the strands to determine their effects on breakage detectability and broken strand identification.

7 Analytical Characterization of Strand Response

The mechanical response of a wire strand is inherently complex because the helical wires undergo evolving stress and contact conditions as the strand is loaded. Further complications are added to the strand behavior if one or more of the wires break due to strand degradation over time. A detailed investigation on strand behavior is critically important for evaluating the effectiveness of the strain-based monitoring approach introduced in earlier chapters. This study also investigates the stress recovery away from a break (discussed in the next chapter), predicting the capacity of a broken strand, as well as provides additional damage indicators that might be useful in developing other monitoring approaches.

A finite element model is generally useful to study the global strand response, along with many localized phenomena that have strong influence on its performance, but are difficult to capture either experimentally or through closed-form analytical models. Investigations on certain behaviors, such as wire breaks, however, require a relatively large or even a full-scale model to adequately develop contact and frictional conditions. Moreover, such a sizeable model can account for any deviation points and may avoid edge effects. Consequently, several finite element parameters, such as the time variation of the applied load, loading rate, effects of damping and interwire friction, become critical for an accurate and efficient model.

This chapter first presents the use of a parametrized model to study strand behavior and evaluates the effects of these modelling parameters on strand response; load distribution and redistribution among the wires at the onset of interwire motion are also considered. These techniques are then used to simulate wire breakage in a prestressing strand, so that various aspects of post-breakage response can be examined. Numerical results show that a linear load ramp or stressing too quickly may lead to an inaccurate axial tension developed in the strand, whereas the inclusion of nominal mass-based damping has been found effective in achieving a quasi-static solution at a reasonable computational cost. In addition, the wire break simulation results indicate that breakage of an outer wire results in greater prestress loss than breakage of the center wire, which have important implications for the proposed non-destructive wire breakage detection method.

7.1 Model Geometric and Material Properties

7.1.1 Geometric Features

Although the construction of wire strands varies in different parameters, such as wire diameter, helix angle, number of wires, group pattern, lays, etc. (Costello 1990; Feyrer 2007), the basic geometry of all these strands consists of a straight wire surrounded by a layer of helical wires (Nawrocki and Labrosse 2000). The cable investigated in this chapter is a seven-wire strand (Figure 7-1), which is commonly used in prestressed concrete (PC) structures. The ASTM A416 Grade 270 strand (ASTM 2006) is made of six helical wires encasing the center wire. The helix angle and wire diameters have been chosen such that, in the undeformed configuration, each helical wire barely touches its two neighboring helical wires in addition to touching the straight center wire (Jiang et al. 2008). Details of the geometric and material data are listed in Table 7-1.

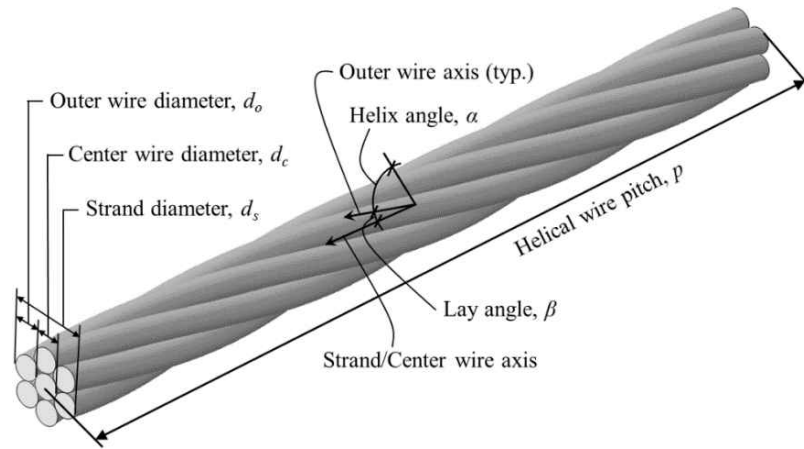


Figure 7-1 Seven-wire prestressing strand

Table 7-1 Geometric and material properties of a seven-wire prestressing strand

Geometry		Material	
Strand diameter, d_s	15.240 mm (0.6 in)	Young's modulus	198.5 GPa (28800 ksi)
Center wire diameter, d_c	5.150 mm (0.2028 in)	Poisson's ratio	0.3
Outer wire diameter, d_o	5.045 mm (0.1986 in)	Yield strain	0.0085
Helical wire pitch, p	190.5 mm (7.5 in)	Yield stress	1687.8 MPa (244.8 ksi)
Helix angle, α	80.46°	Rupture strain	0.07
Lay angle, β	9.54°	Rupture stress	1857.4 MPa (269.4 ksi)

7.1.2 Material Characterization

The material behavior has been characterized by an elastic-plastic model with isotropic hardening. Similar assumptions were made in earlier studies and were found reasonable for metallic materials (Fontanari et al. 2015). The stress-strain curve for seven-wire prestressing strand in the PCI Design Handbook (PCI 2010) has been considered. The effective strand modulus, however, is expected to be somewhat less than the individual wire material modulus because of the change in helix angle under load (Costello and Phillips 1976). Therefore, the input material modulus was adjusted following Costello's model (Costello 1990) so that the calculated strand modulus matches the target strand modulus in PCI (2010); the difference between wire and strand moduli was found to be approximately 4.5%. It is noted, however, that because of minor difference between center and outer wire diameters (Table 7-1), the size effect on tensile properties of individual wires (Fontanari et al. 2015) is expected to be insignificant and therefore has not been taken into account.

7.2 Model Development

7.2.1 Element Selection and Mesh Generation

The geometric volume was discretized with trilinear (8-node) hexahedral elements that use reduced integration and hourglass control, which have been successfully implemented in other studies involving steel cables (Chiang 1996; Jiang et al. 2008; Erdönmez and Imrak 2009; Stanova et al. 2011b; Kmet et al. 2013; Fontanari et al. 2015). A mesh convergence study was conducted using these elements with the aim of numerically simulating the effective strand modulus in PCI Design Handbook (PCI 2010). A 190.5 mm (7.5 in) strand length, which is equal to the length of one helical pitch, was considered for the mesh convergence study; other modeling parameters are described in the following section. As anticipated, a high-resolution mesh was required to effectively model the contact area between wires. Figure 7-2 shows that with mesh refinement, the moduli obtained from FE analyses using different mesh densities approaches the target modulus. Considering accuracy and computational cost, the characteristic radial and circumferential element dimensions were chosen to be 1/10 of wire diameter, d , and the longitudinal dimension to be 1/100 of helical pitch, p .

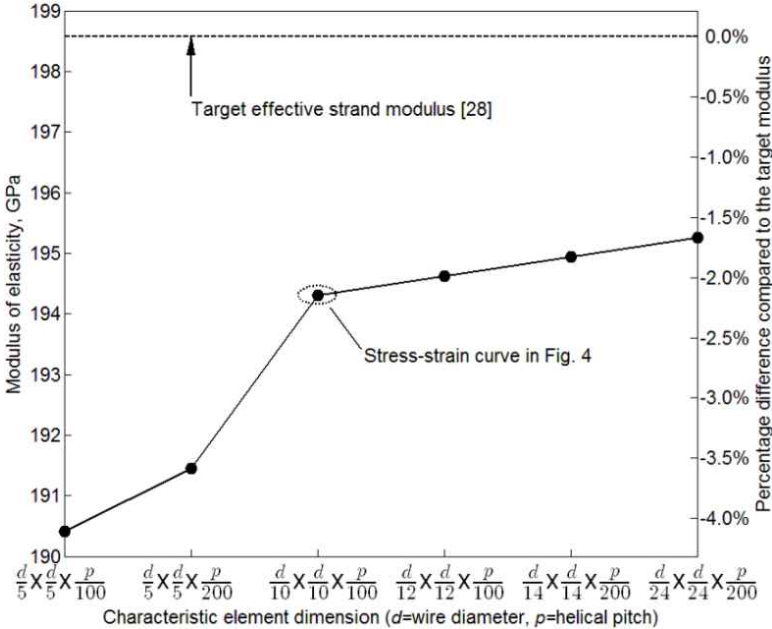


Figure 7-2 Mesh convergence study

7.2.2 Boundary Conditions and Loading

Translation along the strand’s longitudinal axis was restrained at one end (dead end) but permitted at the other end (live end) for applying displacement-controlled loading. Although the wedge grips only the outer wires, the applied load is transmitted to the center wire through friction under high normal pressure exerted by the wedging mechanism. This loading process was approximated by imposing a moving boundary along the strand axis on all wires at the live end. After fully stressing the strand, the axial translation was prohibited at both terminations to prepare the strand for simulating wire breaks. To prevent unwinding of helical wires, the ends must be constrained from axial rotation; this was achieved by restraining the circumferential motion. Furthermore, radial contraction (during stressing) and expansion (after breakage) of

wires due to Poisson effect were allowed at both ends. The details of imposed boundary and loading conditions are shown in Figure 7-3.

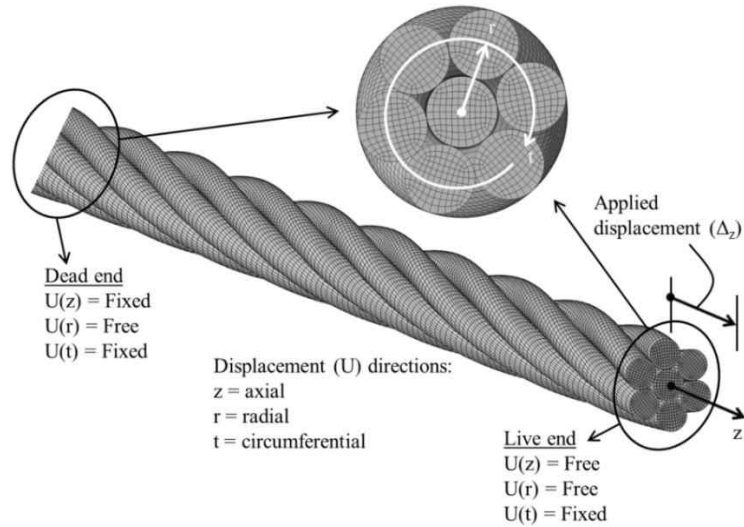


Figure 7-3 Boundary conditions and loading

7.2.3 Interwire Friction

The FE model must also address friction at the contact points between wires. Therefore, the model must account for all the complex mechanical phenomena originating from contact nonlinearities. The wire-to-wire contact interactions were considered as deformable-to-deformable contact pairs. Finite sliding formulation was used to account for possible large interwire motion after wire breaks as well as at the end of sticking phase while stressing. Surface-to-surface contact discretization was used as it reduces the likelihood of large localized penetrations of master nodes into slave surface and also reduces the sensitivity of results to master/slave roles (Simulia Corporation 2012). Penalty functions were used to enforce the impenetrability requirement. Although the exact fulfillment of the constraint condition is compromised, this approach does not increase the number of unknowns (hence computational demand) like other algorithms, such as Lagrange multiplier or augmented Lagrangian formulations, but has been shown to produce reasonably accurate solutions in other similar applications (Jiang et al. 2008). Friction was characterized by an isotropic Coulomb friction model.

7.2.4 Model Verification

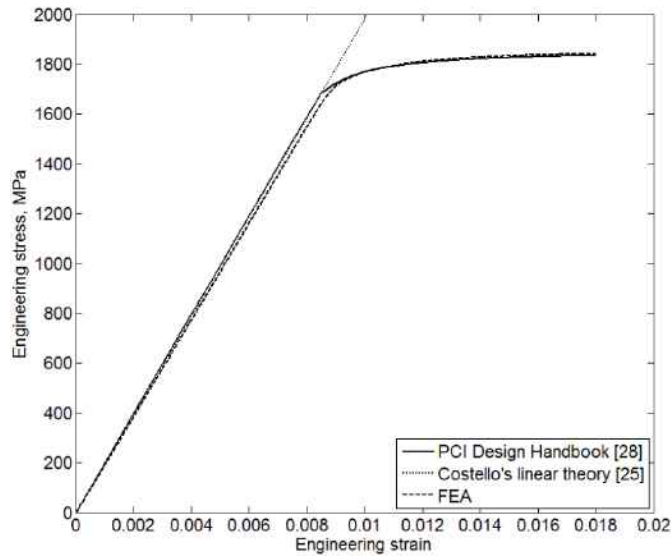


Figure 7-4 Stress-strain curves for strand

To verify the accuracy of the model, finite element analysis (FEA) results were compared with Costello's theory (Costello 1990), which is valid only up to the elastic limit. Therefore, to evaluate the analysis results beyond material yielding, the complete stress-strain curve obtained from FEA was also compared with the curve provided in PCI Design Handbook (PCI 2010). The minor mismatch between the analytical and FEA curve (difference in moduli less than 2.5%), as can be seen in Figure 7-4, is in part because of mesh resolution (Figure 7-2) and also due to the fact that contact deformation was neglected in Costello's model.

7.3 Sensitivity Analysis of FE Parameters

This section investigates the sensitivity of strand response to several FE parameters, namely, ramp profile or time variation of the applied load, loading rate, friction model, and damping. Appropriate parameters have been determined for an accurate and efficient model to be used in analyzing strand behavior as well as simulating wire breakages in the subsequent sections. The modeling parameters used in different studies are shown in Table 7-2.

Table 7-2 Parameters for analyzing strand response during stressing

Model ID	Section	Variable	Length (mm)	μ	Ramp profile	ζ	Ramp duration
S1	7.2.1	Mesh resolution	190.5	0.1	Smooth	10%	$10T_n$
S2	7.3.1	Ramp profile	190.5	0.1	-	0%	$10T_n$
S3	7.3.2	Loading rate	190.5	0.1	Smooth	10%	-
S4	7.3.3	Friction model	952.5	-	Smooth	10%	$10T_n$
S5	7.3.4	Damping	952.5	0.1	Smooth	-	$10T_n$
S6	7.4	-	952.5	0.1	Smooth	10%	$10T_n$
S7	7.4	-	190.5	0.1	Smooth	10%	$10T_n$

μ : Friction coefficient; ζ : Fraction of mass critical damping (damping ratio) corresponding to the fundamental longitudinal mode of vibration; T_n : natural period of the fundamental longitudinal mode of vibration

7.3.1 Time Variation of Applied Load

The time variation of prescribed displacement at the live end, which is the strand's total elongation, has a notable effect on strand response during simulation of prestressing. A linear displacement ramp with time (Figure 7-5a) produces an oscillatory response (Figure 7-5b) because of sudden application of velocity, which also causes the kinetic energy to fluctuate throughout the ramp duration (Figure 7-6). The time lag of response (t_l) observed in Figure 7-5b is the time required by the stress wave to traverse the strand length. A quasi-static response is obtained (Figure 7-5b), however, if the displacement is ramped up such that velocity is zero at the beginning, then increases smoothly until the middle of the step, followed by decreasing over the rest of the time and finally return to zero (Figure 7-5a) (Simulia Corporation 2012). Following the velocity profile, the kinetic energy history (Figure 7-6) varies smoothly over the loading process with a peak at the middle, confirming the consistency of the applied procedure. It is noted that the ramp speed was kept sufficiently slow during both linear and smooth load ramp to avoid any unwanted dynamic effect.

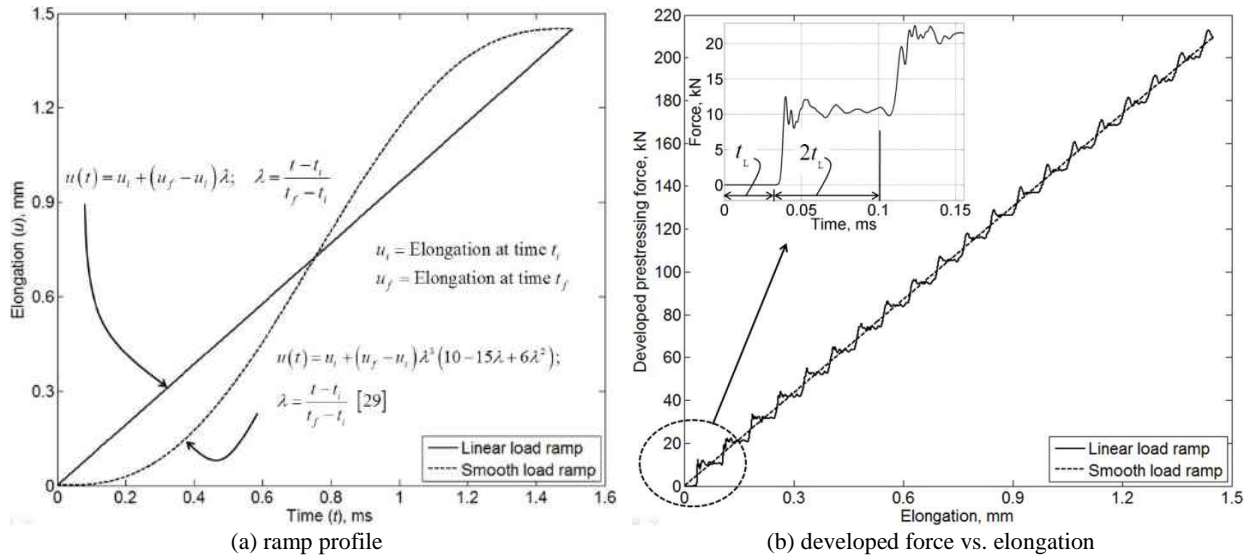


Figure 7-5 Time variation of applied loads

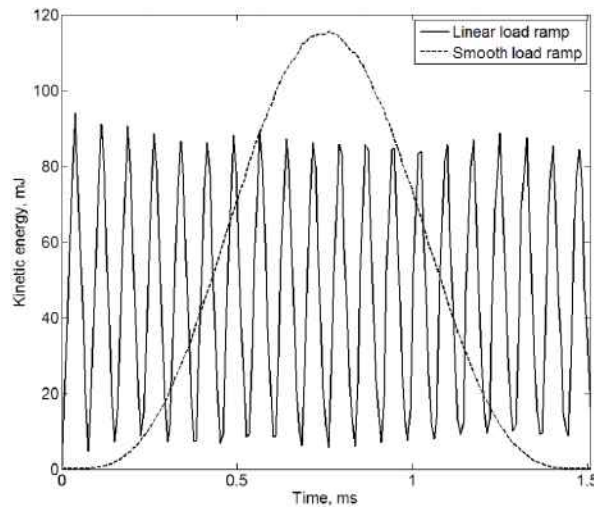


Figure 7-6 Kinetic energy history for linear and smooth load ramp

7.3.2 Loading Rate

In practice, the actual time taken to complete the stressing operation of a prestressing strand is relatively long (at least in the order of few seconds). Stressing a long strand in such a physical timescale, however, is often not feasible in FEA due to very small time increment (generally, in the order of nanoseconds in this type of analysis) caused by the extra fine mesh. Therefore, a parametric study has been conducted with various loading rates to obtain an economical solution while not being significantly affected by inertial effects. Analysis results show that a load ramp duration of at least three times the natural period of the fundamental longitudinal (axial) mode of vibration, T_n , is adequate for this particular analysis to achieve a static response (Figure 7-7). A higher loading rate results in non-uniform stress distribution along the strand, which indicates the inadequacy of the analysis. Moreover, the higher-than-static forces suggest the presence of dynamic effects.

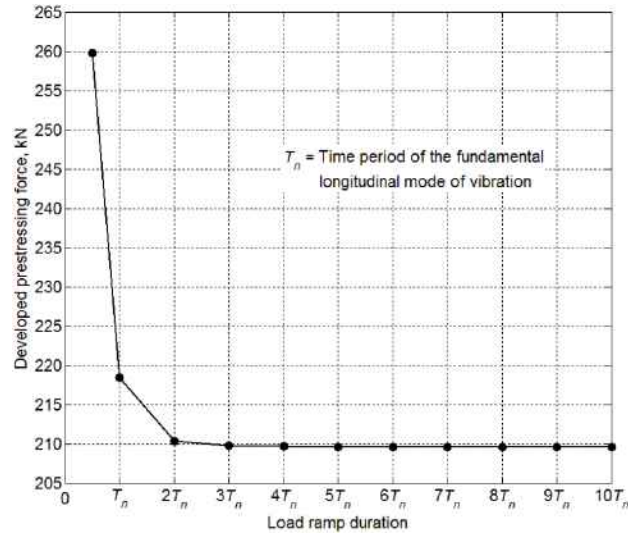


Figure 7-7 Convergence of developed force with slower loading rate

7.3.3 Friction Model

In literature, apart from theoretical models that consider either or both the two extreme cases of zero and infinite friction (Costello and Phillips 1976; Velinsky 1985; Raof and Kraincanic 1995; Jolicoeur and Cardou 1996; Elata et al. 2004), the interwire frictional effect has been predominantly modeled with a constant friction coefficient lying between 0.1 and 0.2 (Jiang et al. 2008; Imrak et al. 2010; Stanova et al. 2011b; Kmet et al. 2013; Fontanari et al. 2015). In this section, these two values are taken as lower and upper bounds of friction, respectively, and are defined as kinetic (μ_k) and static (μ_s) friction coefficients with an exponential decay model (Figure 7-8) (Simulia Corporation 2012).

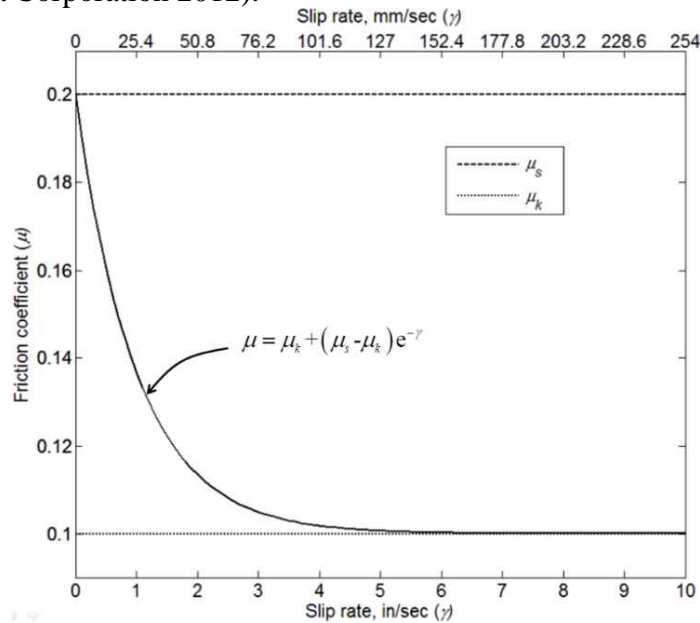


Figure 7-8 Exponential decay friction model

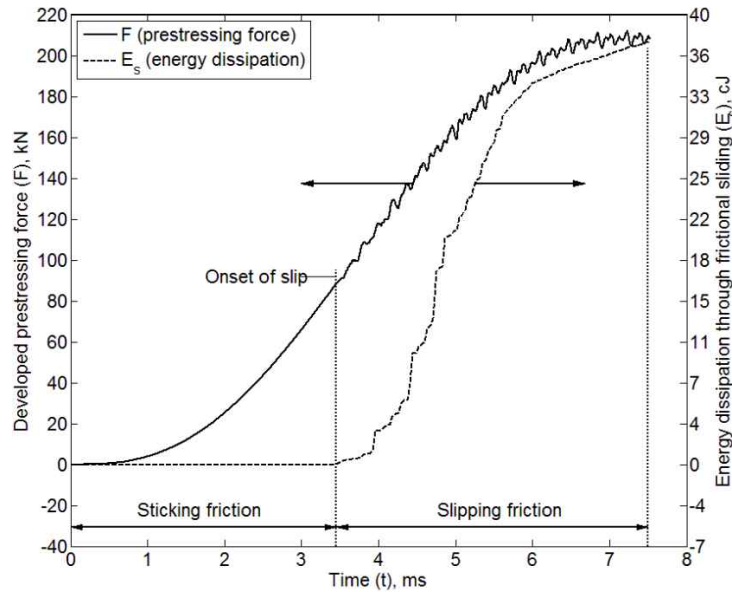


Figure 7-9 Occurrence of interwire slip

Figure 7-9 illustrates the transition from interwire sticking state to slipping as the loading progresses. The onset of interwire slip can be also confirmed by the sliding energy history. It is noteworthy that this stick/slip transition was not obvious in shorter strand models (S1, S2 or S3 in Table 7-2), which appears to be because of edge effects, but became evident in relatively long strand of length equal to five times the helical pitch (952.5 mm).

The final prestressing force, as well as the post-breakage response, however, are mostly governed by the slipping portion of frictional condition. Although minor shifting of the onset of slip is possible depending on the individual friction coefficients, it is not expected to significantly affect the global strand response because of lack of interwire motion (Costello 1990; Feyrer 2007) in the sticking phase. Therefore, a constant friction equal to the kinetic friction coefficient is used in the rest of the analyses for simplicity.

7.3.4 Damping

As observed in previous plots (Figure 7-5b, Figure 7-6, Figure 7-9), linear load ramp or stick/slip transition during stressing induces dynamic effects in the model, which resulted in an oscillatory response. Although the vibration energy was dissipated through frictional sliding, it required significant computation time for the oscillation to die out. This is because the sliding energy was relatively small (Labrosse et al. 2000). Therefore, an additional energy dissipation mechanism was introduced utilizing mass proportional damping to achieve a static response in a tractable timescale. The analysis results show that an addition of nominal damping (10% of the critical mass damping corresponding to the fundamental longitudinal mode of vibration) was effective in damping the oscillation (Figure 7-10, Figure 7-11).

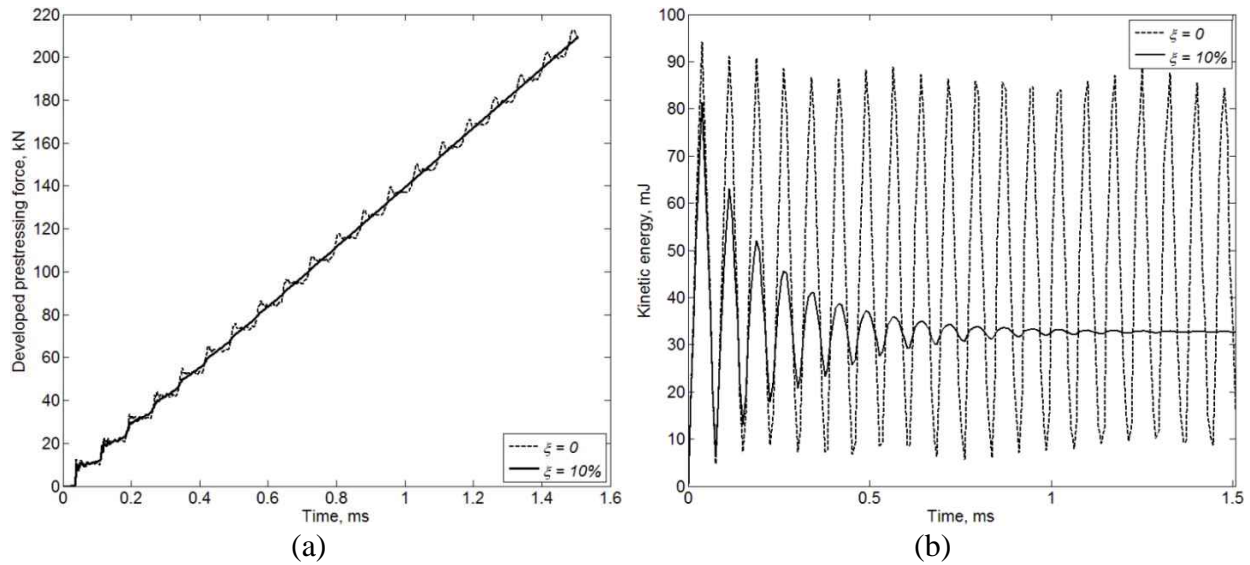


Figure 7-10 Effect of damping on linear load ramp: (a) developed force; (b) kinetic energy

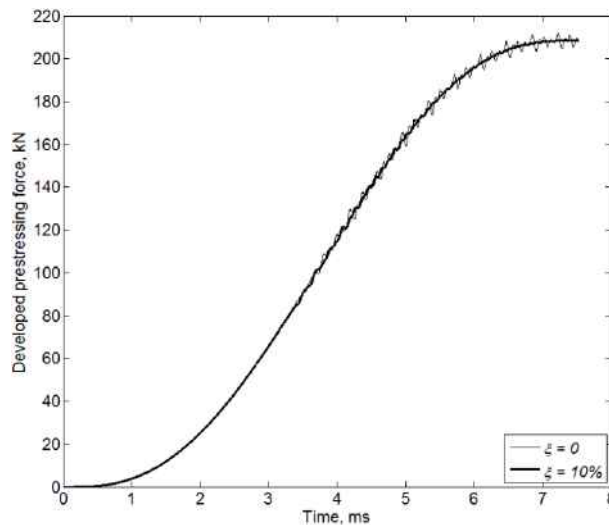


Figure 7-11 Addition of damping to damp the oscillation originating from interwire slip

7.4 Load Redistribution Among Wires

The center wire has greater axial stiffness than the outer wires because of its larger diameter (Table 7-1) as well as the frictional contact provided by the surrounding wires. In addition, when the strand is under uniaxial load, the center wire displaces along the strand axis, but the displacement of the outer wires along their own axes is reduced proportionally to the lay angle of the strand (Figure 7-1) (Fontanari et al. 2015). As a result, the center wire carries a larger share of axial force than the outer wires, provided that there is no significant interwire motion. Such a condition is observed in a relatively short strand model, i.e., model S7 in Figure 7-12, where the relative motion between the wires is restricted by edge effects.

The interwire motion, however, becomes more pronounced in a relatively long strand (model S6) when the wires experience a post-slip state of friction. As expected, the center wire initially carries a greater share of axial force as long as the material remains elastic and there is

no considerable relative motion (Figure 7-13). After the stick/slip transition occurs, a portion of the system energy is dissipated through frictional sliding. Because the center wire has more contact areas than the outer wires, the sliding energy dissipation associated with the center wire is higher than the outer wires. In addition, the onset of yielding along the contact helices primarily affects the center wire, which contributes further to redistribute the load to the outer wires (Fontanari et al. 2015). Thus, the initial load distribution is finally reversed and the outer wires carry a larger share (Table 7-3).

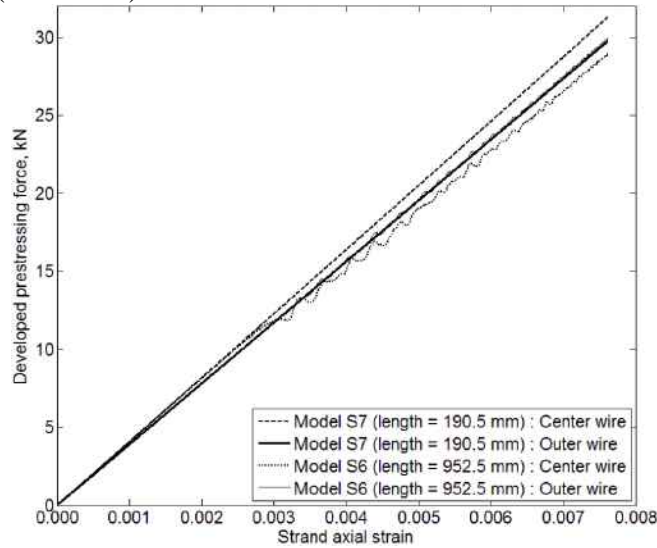


Figure 7-12 Comparison of load distribution among wires in a long- and short-strand

Table 7-3 Final load distribution among wires

Model ID (Table 7-2)	Total load	Center wire		Outer wire	
S7	209.5 kN	31.3 kN	14.94%	29.7 kN	14.18%
S6	209.0 kN	29.0 kN	13.90%	30.0 kN	14.35%

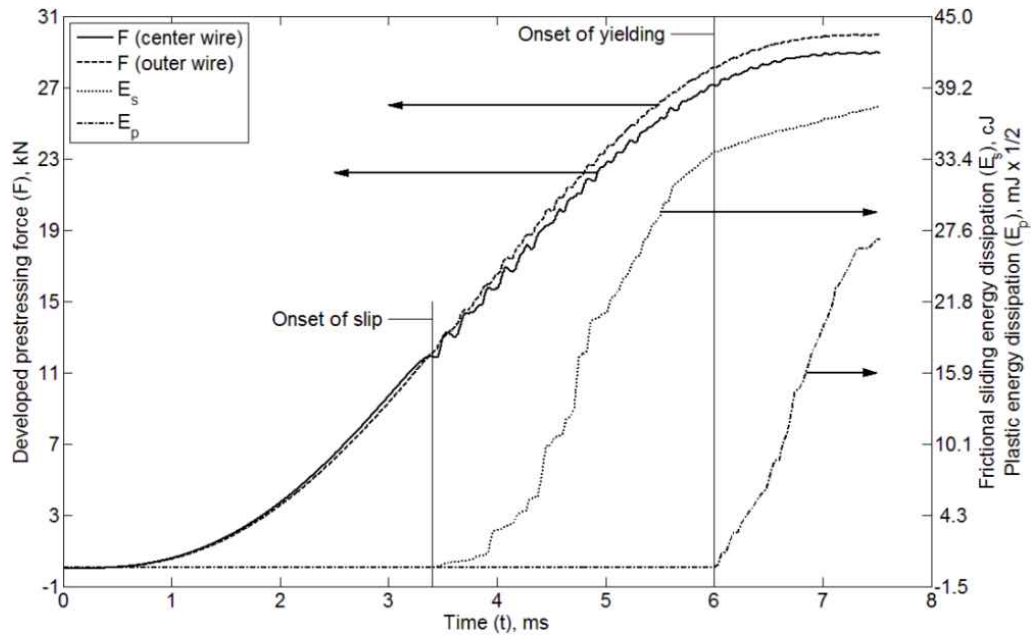


Figure 7-13 Load redistribution among wires with the onset of slip

7.5 Wire break Simulation and Post-breakage Response

This section covers simulations of a center wire break, an outer wire break, a wire break in a confined strand, and successive multiple wire breaks (Table 7-4). Such investigation has practical significance because it enables the analysis of the impact of wire breaks on structural performance and can inform the development of wire breakage detection methods. Of particular interest is the change in prestressing force that occurs when wires break.

Table 7-4 Wire breakage simulation matrix

Model ID	Section	Broken wire	Length (mm)	Break location from dead end (mm)	Confinement condition	Friction coefficient, μ
B1	0	Center	952.5	857.25	Bare	0.1
B2	0	Outer	952.5	857.25	Bare	0.1
B3	0	Outer	952.5	857.25	Confined	0.1
B4	0	Center	952.5	857.25	Bare	-Varies-
B5	0	Outer	3,352.8	3,048.0	Bare	-Varies-
B6	0	Outer	19,812.0	-Varies-	Bare	0.3
B7	0	Outer (multiple)	952.5	857.25	Bare	0.1

7.5.1 Wire break Simulation Procedure

The strand was first stressed to 80% of its ultimate strength ($0.80 F_u$), followed by ramping down to $0.60 F_u$ to include the prestress losses, such as elastic shortening, shrinkage, and creep of concrete, relaxation of steel, anchor set (Kelley 2000) that commonly occur in PC structures. The complete stressing history was necessary to account for the plasticity that forms in the contact areas between the wires when the strand experiences higher stresses.

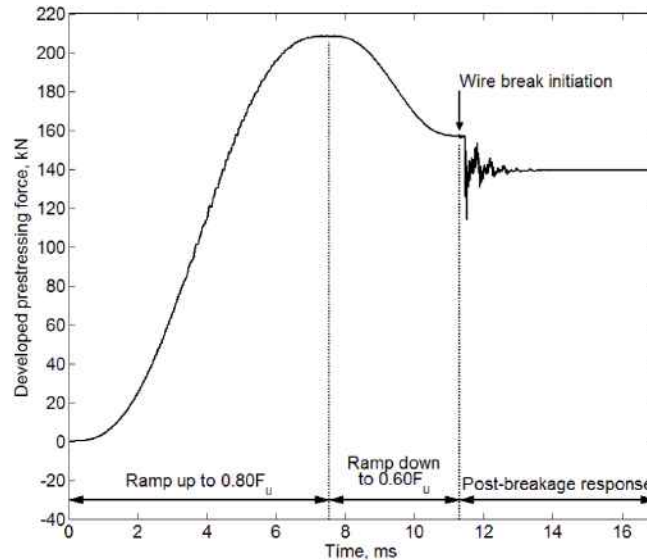


Figure 7-14 Typical stressing profile and post-breakage response

Once the pretensioning step was completed, the stiffness and strength of a target element group, located at a position where the break was intended, were artificially reduced to locally increase the effective strain within these elements. To introduce damage in this element group, a certain value of equivalent plastic strain, around 5.15% in this simulation, was set as damage initiation criterion. Once this criterion was reached, the material was progressively led to failure following a linear law for damage evolution with effective plastic displacement (Simulia Corporation 2012). The failure mechanism was then completed when the effective plastic displacement reached a predetermined ultimate value (6.15%) and finally, the fully degraded elements were deleted from the discretized geometry. It can be noted that the low-relaxation prestressing strand is typically stretched and annealed to reduce residual stresses induced by the cold-drawing process. Moreover, the generated wire break was not caused by strand rupture due to overstressing. Thus, the effect of residual stresses left by the manufacturing process is expected to be marginal on the overall strand response, and therefore has not been taken into account. Figure 7-14 shows a complete stressing profile with a typical post-breakage response.

7.5.2 Post-breakage Response

Center and Outer Wire breaks

An analysis was conducted to compare the load loss due to breakages in center and outer wires. The results show that breakage in an outer wire caused approximately 17.4% prestress loss in the strand, whereas breakage in the core wire resulted in only 6.6% loss (Table 7-5). This greater load loss due to an outer wire break was expected because the center and adjacent wires

partially lost their frictional contact area and radial pressure in addition to lose of the broken wire's share of the total force (Table 7-3). In addition, the smaller load loss in case of the core wire break is attributed to the fact that it was under much higher radial pressure than the outer wires, which resulted in greater frictional resistance.

Table 7-5 Prestress loss due to wire breaks

Model ID (Table 7-4)	Prestress loss
B1	6.6%
B2	17.4%
B3	15.3%

Outer Wire breaks in a Confined Strand

In practice, a mono-strand tendon is generally placed in a plastic sheath for corrosion protection. Similarly, in a multi-strand system, a bundle of strands is usually contained inside a duct. The plastic sheath in mono-strand tendons and the presence of duct and other strands in a multi-strand setting may potentially limit a wire's lateral movement after breakage. This situation has been simulated by modeling a cylindrical container around the strand with the cylinder barely touching the strand in an unloaded state. To minimize additional computational expense, the cylindrical geometry has been discretized with rigid elements. The interaction between the cylinder and the strand is considered frictionless and no confining pressure has been applied to the cylinder. As listed in Table 7-5, a wire break in confined condition contains greater prestressing force after breakage compared to the bare condition. This is because the broken wire is restricted from being separated from its neighboring wires in confined condition, which results in greater frictional resistance to prestress loss.

Center and Outer Wire breaks in a Strand with Various Friction Coefficients

Force loss due to wire breakage in an aged, partially corroded strand is expected to be different from that in a new, uncorroded strand. A parametric study was conducted on strands with various friction coefficients, in which a lower coefficient represented a newer strand, whereas a higher coefficient characterized a corroded strand. The study also helped examine the effect of lubrication on strand response in the presence of different filler materials used in post-tensioning ducts. Figure 7-15 shows the remaining prestressing force after an outer wire breakage in an approximately 3.4-m long strand (Table 7-4) with different friction coefficients. A similar study was performed with shorter strand length (952.5 mm) for core wire breaks. Force loss was significantly less due to breakage in core wire even with shorter length, which is because the core wire was under much higher radial pressure exerted by the helical wires. The results indicate that the total prestressing force may remain almost unaffected by a breakage in the core wire in an aging strand. Figure 7-15 illustrates the mild nonlinearity in the relationship between force loss and friction coefficient, for both center and outer wire breaks. This nonlinearity appears to be due to the effect of friction on the formation of birdcaging (illustrated in Figure 7-16) as well as the loss of contact between the broken wire and the rest of the strand around the break location.

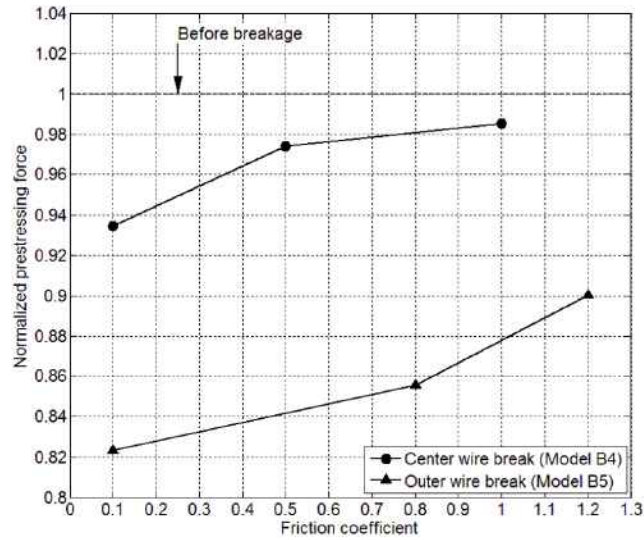


Figure 7-15 Effect of friction coefficient on remaining prestressing force

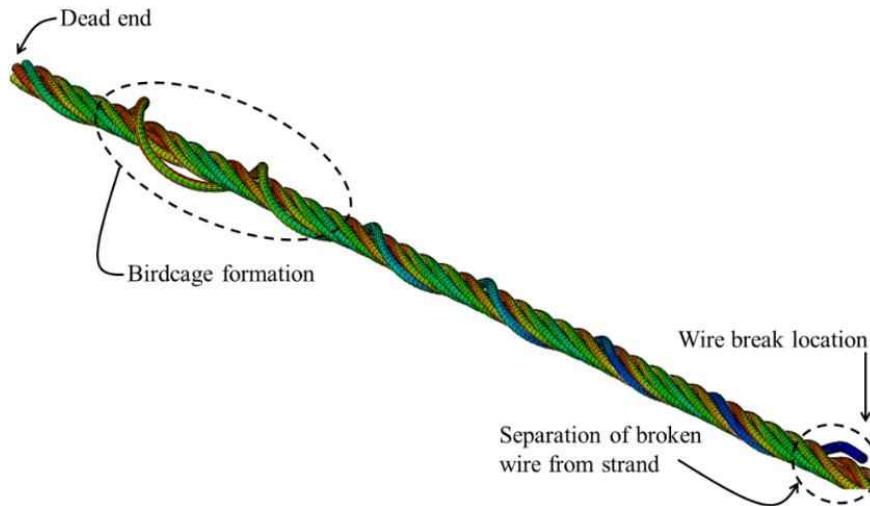


Figure 7-16 Birdcage formation and broken wire separation

Outer Wire breaks at Different Locations in a Long Strand

A parametric study was conducted where wire breaks were simulated at different locations along the length of a nearly 20-m long strand. A coarser mesh (1.27 mm x 1.27 mm x 5.08 mm) was used to keep the problem size tractable, and a relatively high friction coefficient ($\mu = 0.3$) was used to emphasize the effect of break location on prestress loss in a partially corroded strand.

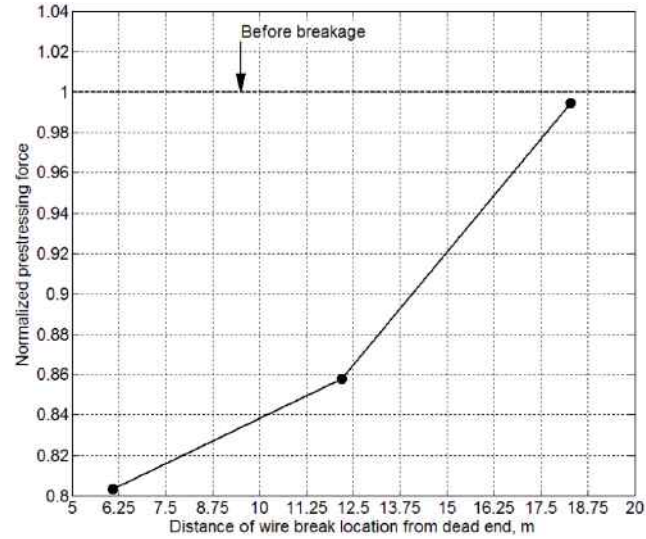


Figure 7-17 Birdcage formation and broken wire separation

As expected, Figure 7-17 shows that the prestressing force was less affected when the breakage occurred away from the dead end. It is noteworthy that parameters such as birdcage (the permanent appearance of a wire rope forced into compression) location and size, along with the length around the breakage location over which the broken wire remains completely separated from the strand, vary with the break length because the strain energy stored by wires changes along the length. As a result, the force loss was somewhat nonlinearly related to the break length due to complex interaction of multiple factors, such as, friction, birdcaging as well as the separation length around break location.

Successive Wire breaks

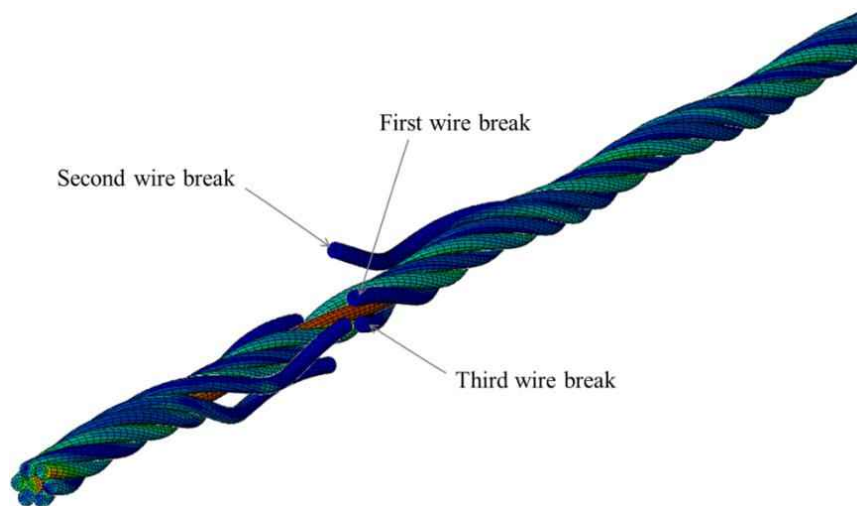


Figure 7-18 Birdcage formation and broken wire separation

After analyzing various wire break conditions and their effects on prestressing force in the earlier sections, this section investigates the dynamic post-breakage behavior of strand. Such investigation can be useful in developing new breakage detection methods that continuously

monitor the strand response at the end anchors to capture any change in strand dynamics. A multiple wire break condition (Figure 7-18) has been considered and natural frequencies of the contributing vibration modes were extracted from time history after each wire break. Figure 7-19 shows the magnitude spectra of the vibration response of the strand after the first and third wire break. The obtained frequencies (determined by peaks in the spectra) were compared (Table 7-6) with the frequency of unbroken strand estimated through an Eigen analysis as well as an analytical prediction (Meirovitch 1967). It is observed that the frequencies, as well as the respective magnitudes, decrease with successive wire breaks. This decrease is because the stiffness of the strand reduces with wire breaks due to cumulative loss of broken wire cross-sectional area along with reduction in confinement. In addition, the damping (estimated by half-power bandwidth) tends to increase with the number of wire breaks because of greater interactions among the broken wires.

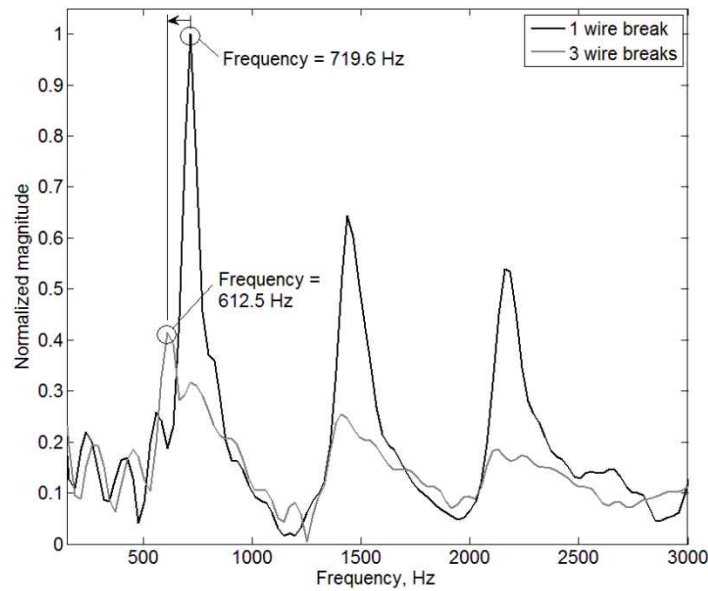


Figure 7-19 Frequency shift with successive wire breaks

Table 7-6 Frequency drop with wire breaks

Breakage condition	Frequency	
	Hz	Drop
Unbroken strand	754.1	-
First wire break	719.6	4.6%
Third wire break	612.5	18.8%

Wire breaks in a Deviated Multi-strand Tendon

In addition to analyzing the wire break response of a lone strand, a preliminary model has been created for a multi-strand tendon with deviators (Figure 7-20). The 40-ft long tendon was passed through two deviators, each located 15 ft-6 in. from the near end. The stressed strand was

surrounded by four additional strands for confinement. For computational efficiency, the deviators and the surrounding strands were defined as rigid elements; however the broken wire frictionally interacted with the confining strands and the deviators. As expected, a wire break in the deviated strand resulted in less prestress loss compared to a straight mono-strand of equal length (Figure 7-21).

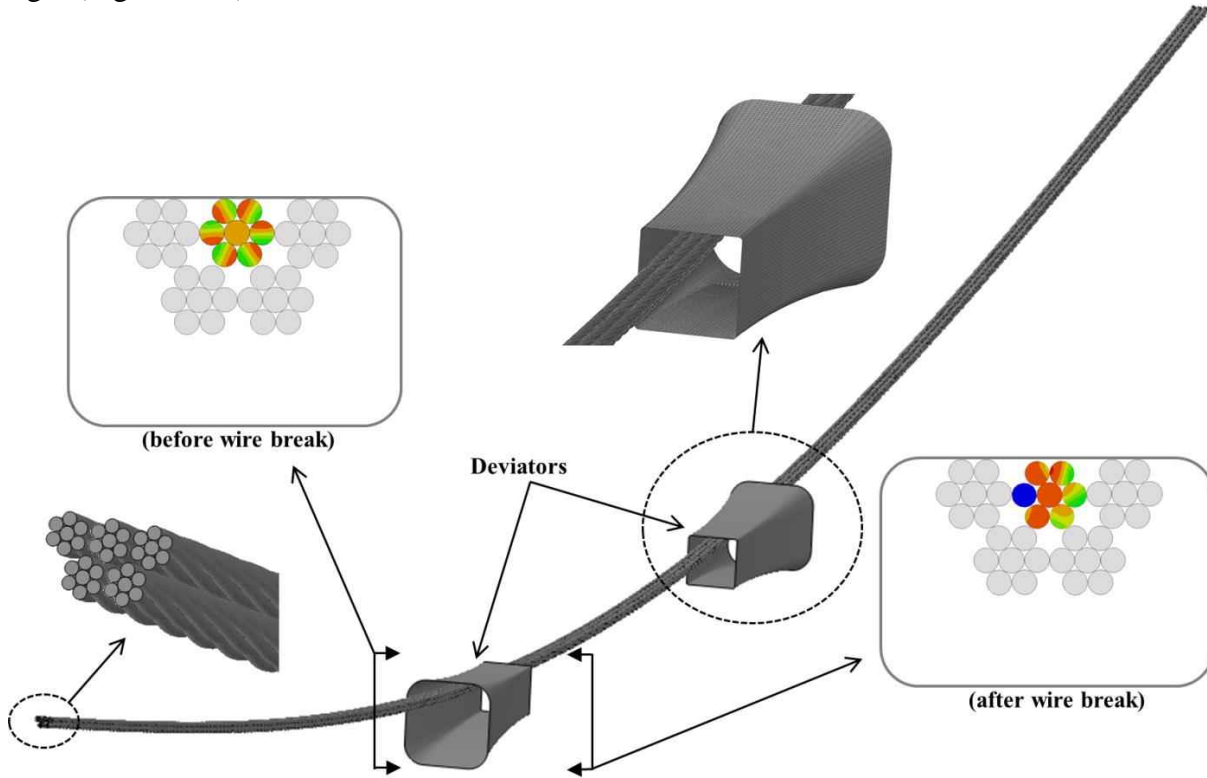


Figure 7-20 Deviated multi-strand tendon

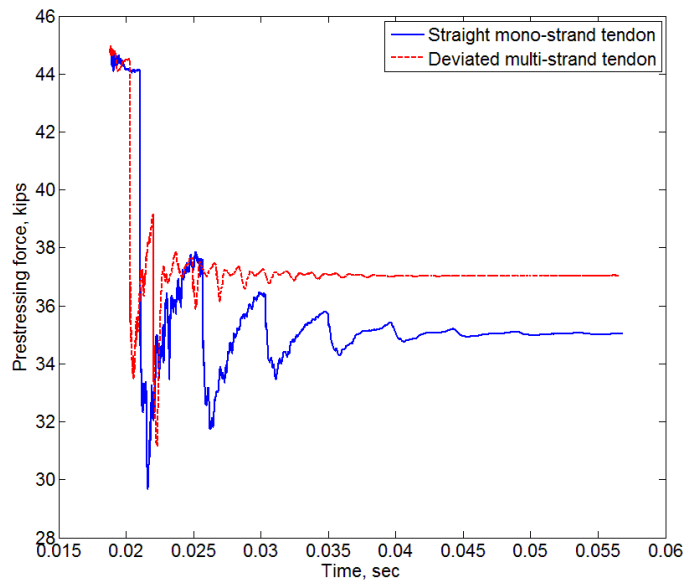


Figure 7-21 Comparison of prestressing force after wire breaks

7.6 Summary

An FE model of prestressing strand has been developed for a detailed analysis of its mechanical behavior. The analysis facilitates a comprehensive understanding of both static and dynamic response of the strand, and captures useful information on strand behavior for developing wire break detection methods. The model considers an accurate representation of material, geometric, and frictional conditions that enable the investigation of interwire motion during stressing as well as the strand response after a wire breakage. A sensitivity study of several FE parameters, such as load ramp profile, loading rate, friction model, and damping, has been conducted first to determine the appropriate parameters for an efficient model. After validating the analysis results with available analytical works in literature, the model was then used to conduct a detailed investigation on load distribution among wires, followed by various parametric studies on wire breaks.

The analysis results show that a linear load ramp profile or ramp duration less than three times the fundamental longitudinal period of the strand induces unwanted dynamic effects into the system. The presence of inertial effects was also observed due to stick/slip transition and the addition of nominal mass damping has been found effective in obtaining a static response. The model illustrates the influence of interwire motion on strand response, especially on the load distribution among wires. Though the center wire carries a larger share of total load than the outer wires before slippage, this distribution has been found to be reversed after the occurrence of stick/slip transition, when the outer wires begin to carry a larger share. Furthermore, the post-breakage response demonstrates that an outer wire break causes significantly higher force loss (17.4% loss) compared to the center wire (6.6% loss), while a confined strand loses less force due to a wire break than a bare strand. Mild nonlinearities have been observed in strand response with friction and break location. The analysis results also indicate correlation between successive wire breaks and change in dynamic characteristics; the strand's fundamental longitudinal natural frequency dropped by 18.8% after three wire breaks.

An experimental study is reported in the following chapter to evaluate the behavior of post-tensioning tendons subjected to successive wire breaks. The experimental findings are used to validate and extend the numerical models described in this chapter.

8 Experimental Evaluation of Tendon Behavior

Wire fractures in unbonded tendons are expected to induce global strand and anchor response through the progression of prestress loss from the break to the end anchors. Radial pressure, interwire friction, and lateral confinement, however, affect the magnitude of prestress loss carried to the anchors and have important implications on breakage detectability by tendon monitoring methods that rely on anchor response. This chapter investigates the effects of multiple wire breaks on prestress loss as well as dynamic post-breakage behavior of a loaded strand through experimental tests. To demonstrate the effects of confinement on stress recovery, large-scale experiments have been conducted with two confinement conditions—confined and unconfined, representing practical scenarios with mono- and multi-strand systems, respectively. An unconfined condition comprised a bare strand with no lateral confinement, while a confined condition consisted of a strand wrapped by a group of unstressed strands.

In addition, both these conditions have been simulated using a finite element (FE) model of the prestressing strand. Multiple tensile tests with single wires and composite strands were conducted to determine material properties for use in the FE model, and to perform a preliminary verification of the model with measured test data. The numerical results obtained from the model were then compared with the breakage experiment. The validated model considers the complex tendon response caused by wire breaks and is useful in various post-breakage behavioral investigations. The numerical study investigates the change in strand response with the level of confinement and also illustrates the change in strand's dynamic response with wire breaks. Both experimental and numerical results show significant prestress loss even at distant locations from wire breaks and confirm a correlation between wire breakage and modal properties, which can be a useful damage indicator.

8.1 Experimental Setup and Procedure

Two separate experiments, *Experiment 1* and *Experiment 2*, were conducted with unconfined and confined strands, respectively. Both the experiments involved stressing a seven-wire prestressing strand to a designated force, followed by cutting of individual wires at a preset location until complete breakage of the strand was induced. Strand elongation, prestress force, and surface strain of individual wires were measured during wire cutting to capture the behavior when each wire ruptured.

8.1.1 Test Specimen Design and Construction

Approximately 33.5 m (110 ft) of seven-wire prestressing strands were used (anchor-to-anchor length of 31.6 m or 103 ft - 7.5 in) in the experiments. Geometric and material properties of the cold-drawn, low-relaxation strands conformed with ASTM A416 (ASTM 2006). Average material parameters obtained from the tensile tests (reported later in this paper) are listed in Table 8-1 together with detailed geometric features of the tested strand.

Table 8-1 Seven-wire prestressing strand: geometric and material parameters

Geometry	Nominal strand diameter	Lay length	Strand cross-sectional area	Center wire diameter	Outer wire diameter
		15.2 mm (0.6 in)	218 mm (8.6 in)	142 mm ² (0.220 in ²)	5.3 mm (0.207 in)
Material	Grade	Modulus of elasticity	Yield strength (at 1% extension)	Breaking strength	Ultimate elongation
	1860 (270)	201 GPa (29,200 ksi)	251 kN (56.4 kip)	283 kN (63.6 kip)	6.8%

While a lone strand was used in Experiment 1, six additional strands were placed around the center strand in Experiment 2 to provide lateral confinement (Figure 8-1), in which the strand group was held together with rebar tie wires (Figure 8-2a). As a safeguard for accidental wire rupture, the strands were passed through a series of 6.1-m (20-ft) square hollow structural sections (HSS4×4×3/8) all along the tendon length in both experiments. Intermittent gaps between adjacent sections allowed access to the strand for strain gage and extensometer installation as well as for inducing wire cuts. The hollow sections were placed on wide flange beams (W10×30) and fastened with C-Clamps. At the terminations, the strand was anchored to reusable chucks that were held against bearing plates and were ultimately supported by reaction fixtures secured to the strong floor. The monostrand chuck included a cylindrical barrel with tapered hole to fit with a two-piece conical wedge having serrated interior face for gripping the strand (Sideris et al. 2014). A protective cover, made up of expanded metal and Plexiglas acrylic sheet, was placed around the intended wire break location to ensure safety during wire cuts.

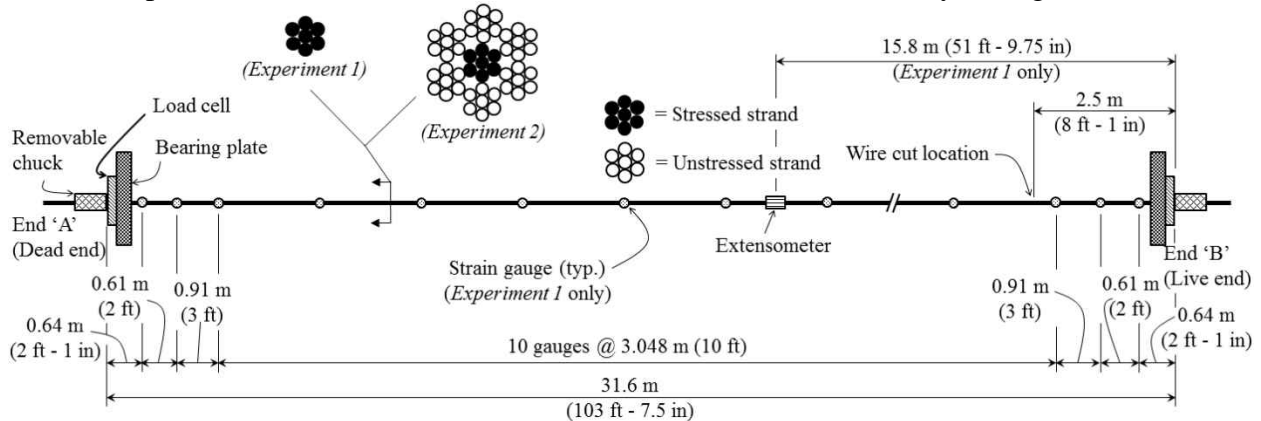


Figure 8-1 Test configuration schematic

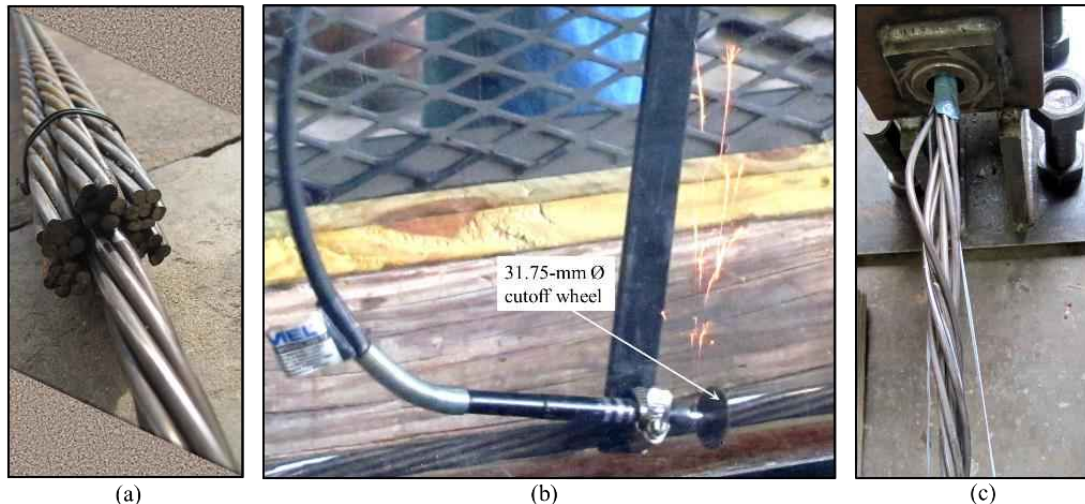


Figure 8-2 Experimental details: (a) strand bundle close-up; (b) wire cuts; (c) birdcaging

8.1.2 Instrumentation

A mono-strand jack, with a hydraulic pump and a calibrated pressure gage, was used to stress the strand. The stressed wires were mechanically cut with a fiberglass-reinforced cutoff wheel driven by a high-speed rotary tool (Figure 8-2b). The cutoff wheel was attached to the tip of a flexible shaft, which was fastened to a specially designed guiding rod with a screw clamp. The entire stressing and cutting history was recorded using hollow-core load cells positioned between the bearing plate and the multi-use anchor chuck at both ends. In light of the longitudinal natural frequency of the broken strand (~ 80 Hz) obtained from FEA (discussed later in this chapter) and Nyquist criterion, load cell data were collected at a sampling rate of 2 kHz during wire cuts to capture dynamic strand response. To measure surface strain along the individual wire axis, and interwire load transfer after wire cuts, fourteen foil strain gages of 0.5 mm gage length were installed on each of two adjacent outer wires in Experiment 1 (Figure 8-1). In addition, an extensometer of 152.4 mm (6 in) gage length was located at mid-length to monitor strand elongation during stressing. In Experiment 2, however, neither strain gages nor an extensometer could be installed due to interference with the confining strands around the stressed strand. Thus, only prestress force was recorded by load cells placed at the ends in this experiment.

8.1.3 Test Procedures

In Experiment 1, the strand was incrementally tensioned to the target stress level of approximately 74% of its tensile capacity ($0.74 F_u$), which is within the limits specified in the AASHTO LRFD Bridge Design Specifications (AASHTO, 2010, section 5.9). Readings from the extensometer, load cells, and strain gages were recorded. At the end of stressing, the extensometer was detached from the strand and the setup was prepared for wire cuts. One of the instrumented wires was cut first with the rotating cutoff wheel to investigate the load transfer between the broken and its adjacent unbroken wire. Wheel diameter of 31.75 mm (1.25 in) was used to ensure a single wire cut without damaging adjacent wires. The strand cutting process continued, wire-by-wire, until all the seven wires were broken. Prestress loss and change in surface strain (of individual wires) caused by breakage were recorded throughout the cutting

operation. A similar procedure was adopted in Experiment 2, where only the center strand was loaded to 0.74 Fu, keeping the rest of the surrounding strands unstressed.

8.2 Experimental Results and Discussion

Strand response to stressing and breakage was continuously monitored by a 31-channel data acquisition system over the entire test duration. Figure 8-3 shows the stressing response and compares the load-elongation and load-strain response obtained from Experiment 1 with PCI (2010). The observed deviation of the measured elongation at the beginning is possibly caused by resetting of the stressing jack due to its limited stroke; however, the response eventually became steady. This effect of jack reset on stressing response has also been reported in MacDougall and Bartlett (2003). Details of the breakage response, both static and dynamic, are described in the following paragraphs.

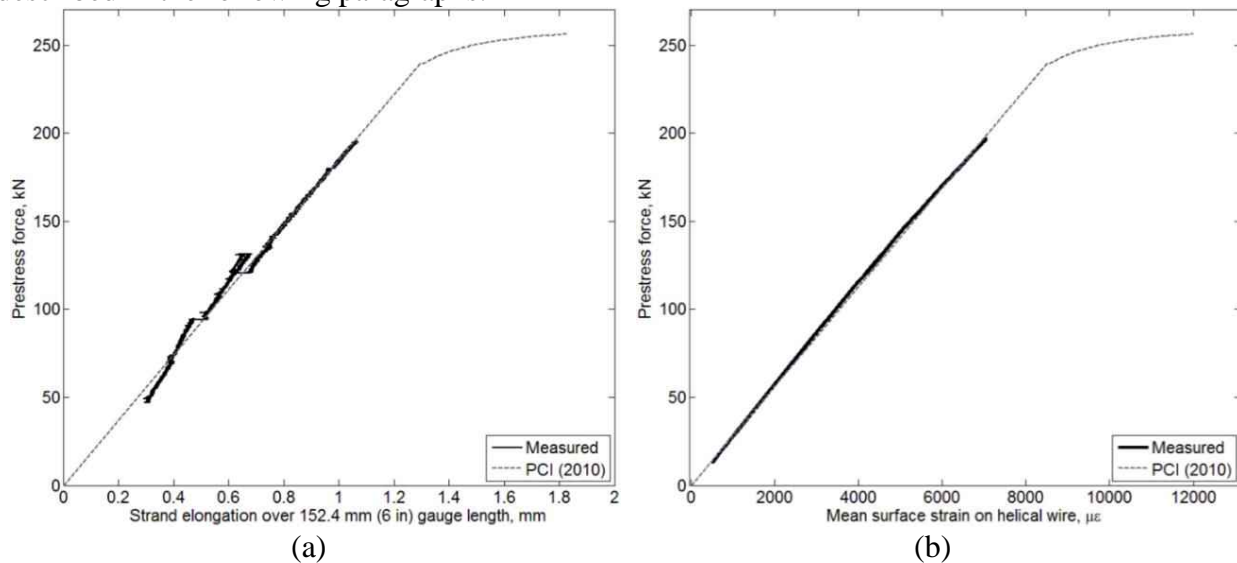


Figure 8-3 Stressing in Experiment 1: (a) load vs. elongation; (b) load vs. strain

8.2.1 Global Static Response at Anchors

A complete history of strand load during the cutting process, recorded by the load cell at the dead end (Figure 8-1), is shown in Figure 8-4a. After each wire was cut, a sudden decrease in force was observed at the measurement point located nearly 29 m (95 ft) away from the cut. Figure 8-4b illustrates the cumulative decrease in force due to successive wire cuts and compares the behavior of unconfined and confined strands used in Experiment 1 and Experiment 2, respectively. Cut wires in the unconfined strand lost contact with the remaining unbroken wires around the cut location and also near the termination where a ‘birdcage’ formed (Figure 8-2c). Cut wires in the confined strand, however, were prevented from separating by radial pressure exerted by the finger-tight reinforcing tie wires that enclosed the strand bundle. The increased interwire frictional resistance therefore caused the confined strand to recover more stress than did the unconfined strand.

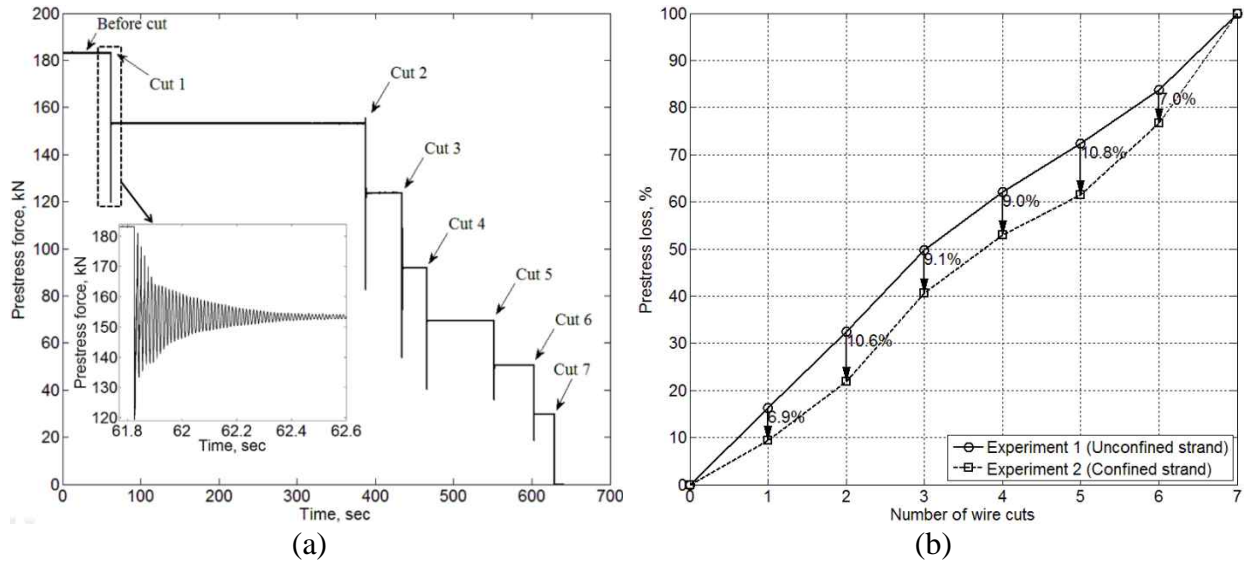


Figure 8-4 Global static response: (a) load history during wire cuts in *Experiment 1*; (b) comparison of prestress loss between *Experiment 1* and *Experiment 2*

8.2.2 Localized Static Response along the Wires

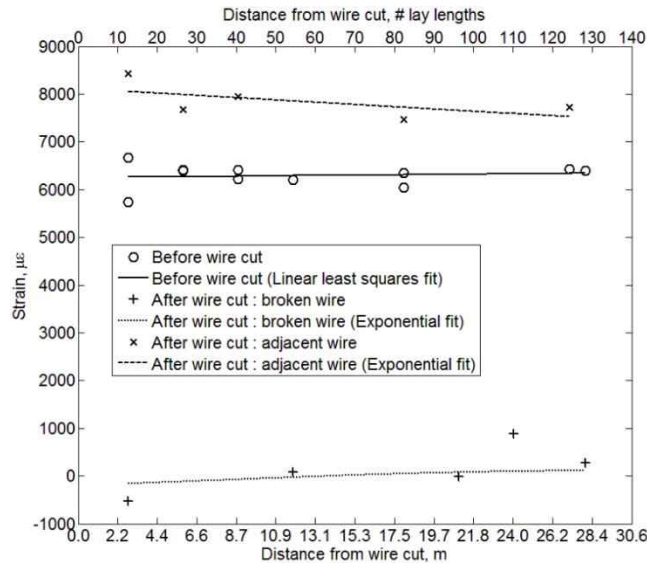


Figure 8-5 Measured surface strain on helical wires

Figure 8-5 shows strain variation along the axes of the broken and adjacent unbroken wires after the first wire cut in Experiment 1. The broken wire lost all pre-strain at the break location but tended to regain the strain with distance from the break due to frictional resistance. The strand achieved a new equilibrium state for balancing the lost contact force of broken wire, which resulted in a strain-increase in adjacent unbroken outer wires at the break. Again, interwire friction caused the increased strain to diminish with distance. MacDougall and Bartlett (2006,

2003) also observed similar response with exponential strain recovery in a draped strand (with pre-broken wires) under external concrete-tendon contact force. The wires in Experiment 1, however, could not regain their original strains over the tested strand length (~29 m) due to lack of radial pressure; therefore, the tested length is deemed too short to notice a clear exponential progression to full recovery. The results indicate significant recovery length in the absence of external contact pressure. In such cases, loss of prestress can extend all the way to the ends and thereby increases the breakage detection range (the tendon length from the end anchor over which a wire breakage can be detected) in unbonded tendons through monitoring the global anchor response.

8.2.3 Global Dynamic Response at Anchors

Changes in strand's dynamic response with successive wire cuts were examined by extracting natural frequencies from the captured time histories of oscillatory prestress force immediately after the cuts (Figure 8-4a). As Figure 8-6 depicts, fundamental longitudinal strand frequencies decreased with successive wire cuts. This was expected due to the reduction in strand axial stiffness that resulted from loss of effective cross-sectional area and confinement with each successive cut. Table 8-2 reports the frequency drops after each wire cut compared to the analytically estimated (Meirovitch 1967) natural frequency of the unbroken strand. Furthermore, spectral magnitudes and vibration energy (represented by the area under each spectrum) tended to decrease with successive cuts. The increasing degree of spread present in the successive spectra indicate that damping continued to increase with successive wire cuts, possibly due to greater interaction between the current and preceding broken wires.

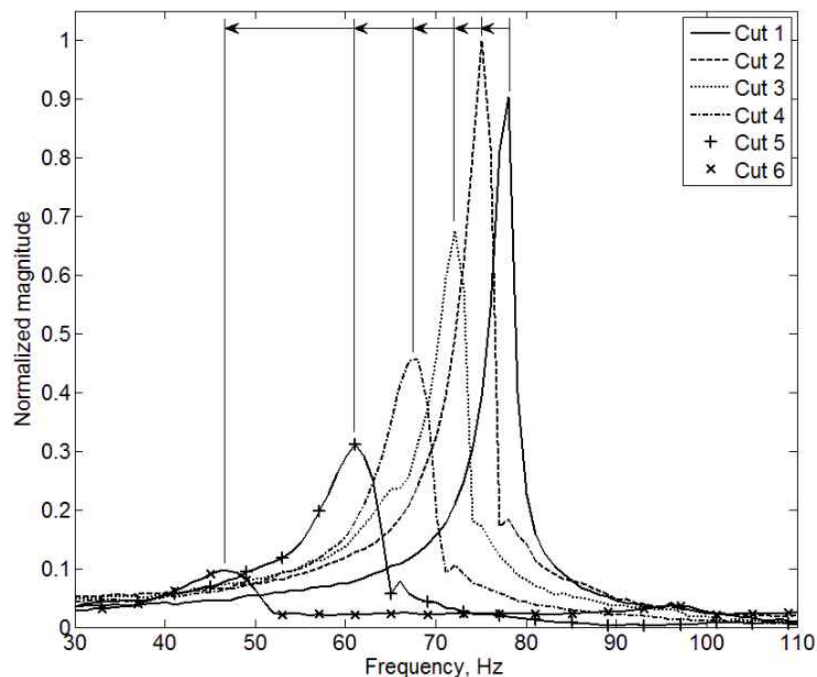


Figure 8-6 Shift of natural frequencies with successive wire cuts

Table 8-2 Change in modal properties with successive wire cuts

Wire cut status	Fundamental longitudinal natural frequency, Hz	Cumulative frequency drop	
		Hz	%
Before cut	80.1	-	-
1 wire cut	78.1	2.0	2.5
2 wire cuts	75.1	5.0	6.2
3 wire cuts	72.1	8.0	10.0
4 wire cuts	68.1	12.0	15.0
5 wire cuts	61.1	19.0	23.7
6 wire cuts	47.1	33.0	41.2

8.3 Numerical Investigation

A detailed finite element model of the prestressing strand was developed to characterize and numerically study dynamic wire breakage response. The complete elasto-plastic behavior of a single wire was determined through a series of tensile tests and then used as input data (material properties) to the FE model. A similar set of tensile tests were carried out on multi-wire strands to validate the FE model against the experimental stress-strain data. Wire breaks were simulated in the FE model and the response was compared to the experimental data reported in the previous section. In addition to characterizing wire breakage, the FE model provided useful insights into the effects that confinement has on strand response.

8.3.1 Characterization of Tensile Properties of Wire and Strand for FE model

The structural response of a single wire is expected to be different from that of a composite strand due to geometrical dissimilarities. Therefore, tests were conducted to determine their stress-strain properties to use in FE model. In general, each wire of different diameter in a strand should be tested as the diameter of each individual wire affects its mechanical properties due to the degree of cold drawing; a smaller diameter wire experiences a more intense cold drawing and therefore exhibits greater strength but lesser ductility (Fontanari et al. 2015). The difference between the center and outer wire diameters in a prestressing strand, however, is relatively small (0.2 mm or 0.008 in); therefore, only the center wire was tested to determine single wire characteristics (material properties). Three wire specimens having length of 1,270 mm (50 in) were prepared. The wire ends were anchored to specially designed grip inserts for the holding jaws of a material test frame equipped with a force transducer. Tests were conducted per ASTM A370 (ASTM 2006) using a universal testing machine (frame capacity of 3,500 kN or 800,000 lbf) with a crosshead speed of 5 mm/min (0.2 in/min) and 63.5 mm/min (2.5 in/min) in the pre- and post-yield regimes, respectively. Elongation up to the onset of yielding was measured with an extensometer that met the resolution and accuracy requirements of ASTM E83 Class B-1 (ASTM 2006) and had a gage length of 609.6 mm (24 in) and a travel of 25.4 mm (1 in). The extensometer was then removed and the strain data were calculated from the crosshead

movements while the loading was continued until rupture. Figure 8-7 shows the true stress-strain curves obtained from the three tests and their average representative curve used in the FE model.

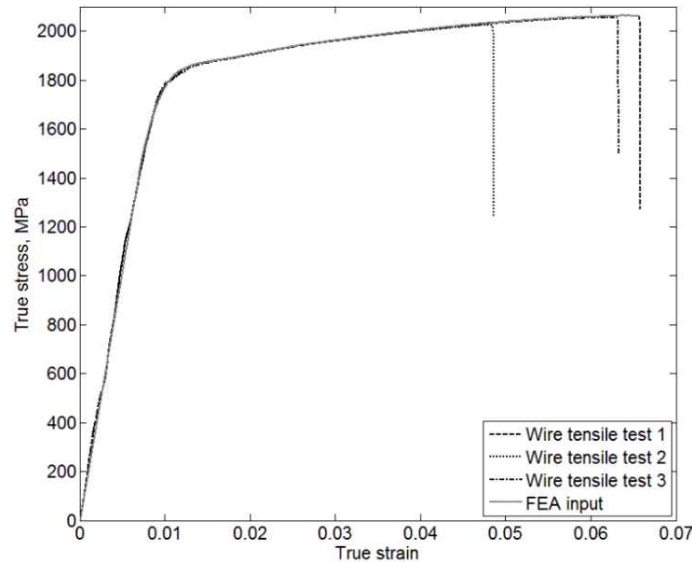


Figure 8-7 Tensile tests with single wire and FEA input

Similarly, three tests were conducted with 1.3-m (50-in.) long specimens to obtain the tensile properties of the multi-wire strand and compare them with corresponding finite element analysis (FEA) results. The first two specimens were progressively loaded to rupture, maintaining a crosshead speed of 17.7 mm/min (0.7 in/min) and 63.5 mm/min (2.5 in/min) respectively in the pre- and post-yield regimes. To achieve a more realistic representation of the in-service strand behavior, a procedure of pre-compacting and aligning the wires (Fontanari et al. 2015) was adopted for the third sample, which was subjected to six loading-unloading cycles (loading to nearly one half of the predicted rupture load followed by unloading) before loading to rupture. Differences in the elastic moduli obtained from the tensile samples were found to be insignificant (modulus of the third sample was approximately 0.6% greater than the first two). The complete stress-strain curves obtained from the tensile tests with strands are included in the subsequent section.

8.3.2 Model Formulation

The center wire and each helical outer wire in the strand FE model were discretized with eight-node brick elements having characteristic dimensions of 1.27 mm x 1.27 mm x 5.08 mm. Although a finer mesh reproduced the experimental results more accurately (Figure 8-8), stress results obtained from the selected mesh resolution were satisfactory, and maintained a good balance between solution accuracy and computational efficiency. The eight-node (trilinear) element has also been shown to produce reasonable results in other similar applications (Kmet et al. 2013; Jiang et al. 2008; Chiang 1996). The translational degree of freedom was restrained at one end of the strand model but freed at the other end to permit application of prestress force. In addition, nodes at both ends of the FE model were restrained against circumferential motion to avoid wire unwinding, while the radial motion was permitted so that Poisson contraction could occur. Surface-to-surface interaction between adjacent wires was defined using deformable-to-

deformable contact, governed by Coulomb’s law of friction. The friction coefficient of an uncorroded strand was assumed to be 0.16 (MacDougall and Bartlett 2006). The finite-sliding contact tracking algorithm (Dassault Systemes 2012) was used throughout the model. This contact algorithm, which is based on the penalty method, utilizes continuous re-calculation of contact area based on the updated (deformed) shapes of the contacting bodies. The maximum penetration violation between the interacting surfaces resulting from the weak fulfilment of the contact constraint (the non-penetrability condition) was minimal for the models analyzed (0.03% of strand diameter). To analyze the dynamic post-break strand response, an explicit dynamic time stepping algorithm was employed. Mass proportional damping (10% of the critical damping for the fundamental longitudinal mode) was used to achieve a reasonable solution time. Figure 8-8 shows numerical results from the FE model as compared to the experimentally obtained engineering stress-strain curves.

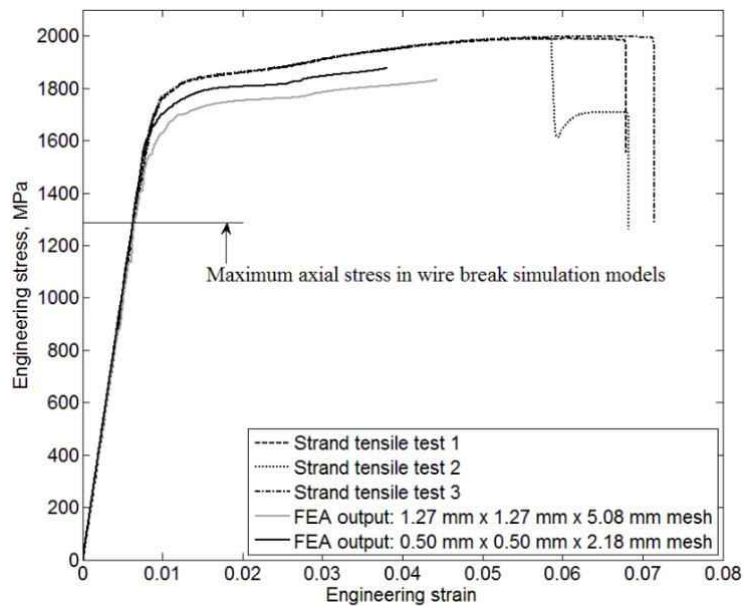


Figure 8-8 Tensile tests with strand and FEA output

In the FE model, wire breakage after completion of stressing was simulated by abruptly deleting a set of elements from the target wire at the intended break location. The model considered the same strand length, break location, geometrical parameters, and stress levels as in the experimental investigation. To investigate an upper bound of confinement, the strand was placed inside a frictionless cylinder (with no gap between the strand and cylinder wall before the strand was stressed), made up of discrete rigid shell elements (Figure 8-9). Clearly, the level of confinement imposed on the strand in the FE model was higher than that in the experiment.

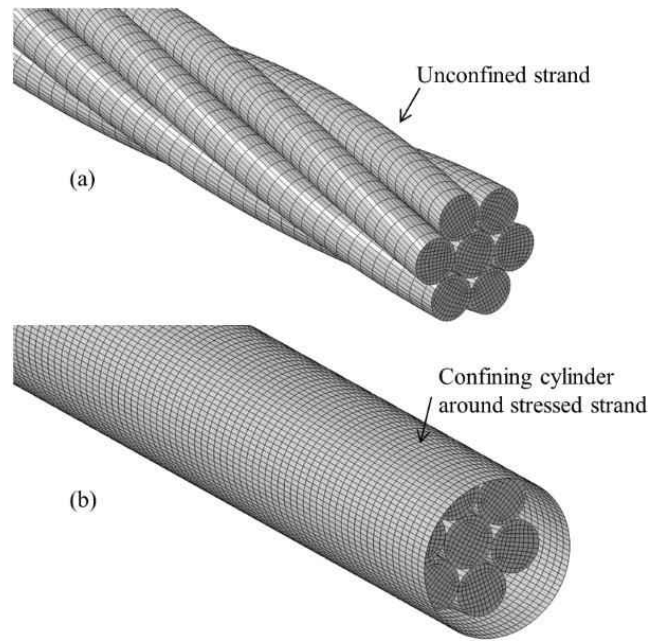


Figure 8-9 FE model of strand: (a) unconfined; (b) fully confined

8.3.3 FEA Results

Figure 8-10a shows the post-breakage dynamic response time history after a single wire break under the unconfined condition simulated using FEA. The extracted natural frequency (corresponding to the fundamental longitudinal mode of vibration) from the FEA (77.4 Hz) matches well with the experiment (78.1 Hz). The initial oscillatory response decays over time and eventually reaches a static equilibrium. The FEA prestress force decreases by 13.2% compared to 16.3% in Experiment 1. Potential reasons for this dissimilarity are: penetration tolerance between contacting surfaces for computational efficiency of the FEA, possible difference between interwire friction coefficients of the tested strand and the FE model, and the selection of mesh resolution in FEA. It is also noted that the FEA response reaches the static state faster than the experiment (Figure 8-10b) due to the addition of artificial damping to reduce the solution cost. The additional damping had negligible effect on the final response (around 1% difference compared to the model with no artificial damping added) as was observed from a study conducted on a shorter strand model (1.5 m or 5 ft).

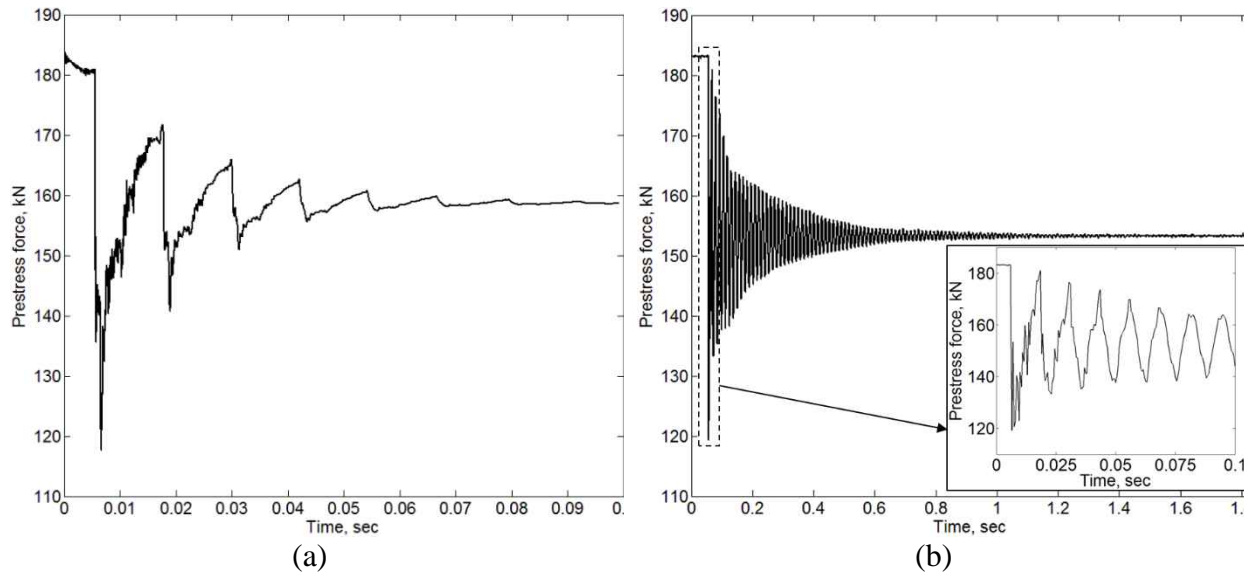


Figure 8-10 Change of prestress force after wire break in unconfined state: (a) FEA; (b) experiment

From the FE model with confined condition, prestress loss has been found to be significantly lower compared to the unconfined state, indicating substantial stress recovery with length (Table 8-3). In addition, the difference in prestress loss between the confined and unconfined conditions in FEA (10.5%) is higher than that in the experiments (6.9%). This is expected because of the difference in the level of confinement. In Experiment 2, the confinement was provided through a set of surrounding strands loosely held by finger-tightened rebar tie wires. Moreover, a portion of the strand at the ends could not be confined because of limited access around the anchors. Conversely, the strand model in FEA is confined throughout the length by containing the stressed strand inside a rigid cylindrical body, and thus a stiffer and complete confinement has been achieved.

Table 8-3. Prestress loss after first wire break

Confinement condition	Prestress loss			
	Experiment		FEA	
Unconfined	29.7 kN	16.3%	24.2 kN	13.2%
Confined with unstressed strands	16.2 kN	9.4%	-	-
Fully confined with rigid cylinder	-	-	4.9 kN	2.7%

8.4 Summary

Increasing interests in unbonded tendons and methods for monitoring their integrity underscores the importance of a detailed investigation on strand response to wire breakage. Whereas the studies available in the literature mostly deal with static response of prestressing strands or strands with pre-induced broken wires prior to stressing, this research addresses both

static and dynamic aspects of wire breaks under varying confinement conditions. An experimental study was conducted to assess the behavior of a stressed strand subjected to wire cuts. Load redistribution between the wires after wire cuts was examined by measuring the surface strain on helical wires along the strand length. The recorded load cell data was analyzed to extract the natural frequencies of the strand after each wire cut and to detect the changes in strand dynamics associated with a cut. A finite element model of the prestressing strand was first validated by experimental data and then used to study the strand response under confined and unconfined conditions.

Recovery length has been determined to be significantly long (more than 30 m, based on the maximum length tested in this research) under minimal external radial pressure and confinement, which is a typical condition for external tendons in box girder bridges within the segment between the end anchor and a deviator. The long recovery length indicates that wires broken far from the anchor can still be detected through changes in the anchor's strain distribution. The low stress recovery also allows the stress wave generated by the suddenly released strain energy to propagate to the anchors, suggesting potential detection methods based on changes in strand's dynamic response. Moreover, the measured strain distribution in broken and unbroken outer wires along the strand length are in agreement with the available literature. Change in dynamic properties has been identified through the decrease in strand's longitudinal natural frequency with successive wire breaks from both the experiments and FEA. In addition, the FE model successfully captured the expected change in prestress recovery and demonstrated that an increase in the level of confinement decreased the prestress loss at anchors.

9 Full-scale Experiments

The encouraging results obtained from the simplified laboratory experiments and analytical models described in earlier chapters motivated the full-scale experiments reported in this chapter. Although the tendon monitoring framework presented in this report is expected to be applicable only to unbonded post-tensioning systems, a bonded (grouted) tendon was tested first to confirm that the anchors are unresponsive to wire breaks. Tests were then conducted with both external and internal unbonded (waxed) I-girder specimens having deviated tendon profile. After post-tensioning, the beams were loaded under three-point bending (simply supported beam with concentrated load at the midspan) to investigate their ultimate capacity (presented in Part II) and then unloaded. Finally, the strands were detensioned (by individual wire cuts) and the changes in anchor strain distribution were captured. The broken strand identification model for a 12-strand wedge plate described in Chapter 5 has been applied to the experimental results. In addition, an acoustic sensing system was installed to independently monitor the breakage events in unbonded specimens.

9.1 Internal Bonded Tendon

9.1.1 Test Specimen, Instrumentation, and Procedure

An overall 40-ft long specimen (35-ft I-girder (FIB54) plus two 2 ft-6 in. end blocks to house the anchorage) with 8-in. deck was used in the experiment (Figure 9-1, Figure 9-2). Twelve 7-wire prestressing strands of 0.6-in. diameter were pushed inside a corrugated polypropylene duct with a parabolic drape profile. The tendon was anchored at the dead end 'A' and stressed with a mono-strand jack at the live end 'B'. A 600-kip load cell was placed between the girder and the wedge plate at the dead end to measure the prestressing force. The two wedge plates at the girder ends were instrumented with 12 strain gages of 5-mm (0.2-in.) gage length, which were placed along the radial lines (with some adjustments to obtain uniform sensor distribution and avoid instrumentation difficulties) described in Chapter 5; details of the sensor arrangement are shown in Figure 9-3. Each of the strands was first stressed to $0.20F_u$ (in the order listed in Figure 9-3) before loading to the target stress of $0.75F_u$ for pre-seating the wedges to ensure uniform bearing of the wedge plates against the anchor plates embedded into the girder. The anchor strain and load cell data were recorded at 2 Hz during the stressing operation. Grout was then injected into the duct and was allowed to set to create the bond between the tendon and concrete. Once the grout was set, the beam was loaded to its ultimate capacity (indicated by deck crushing), followed by complete unloading while the anchor strains and load cell data were captured at 10 Hz.

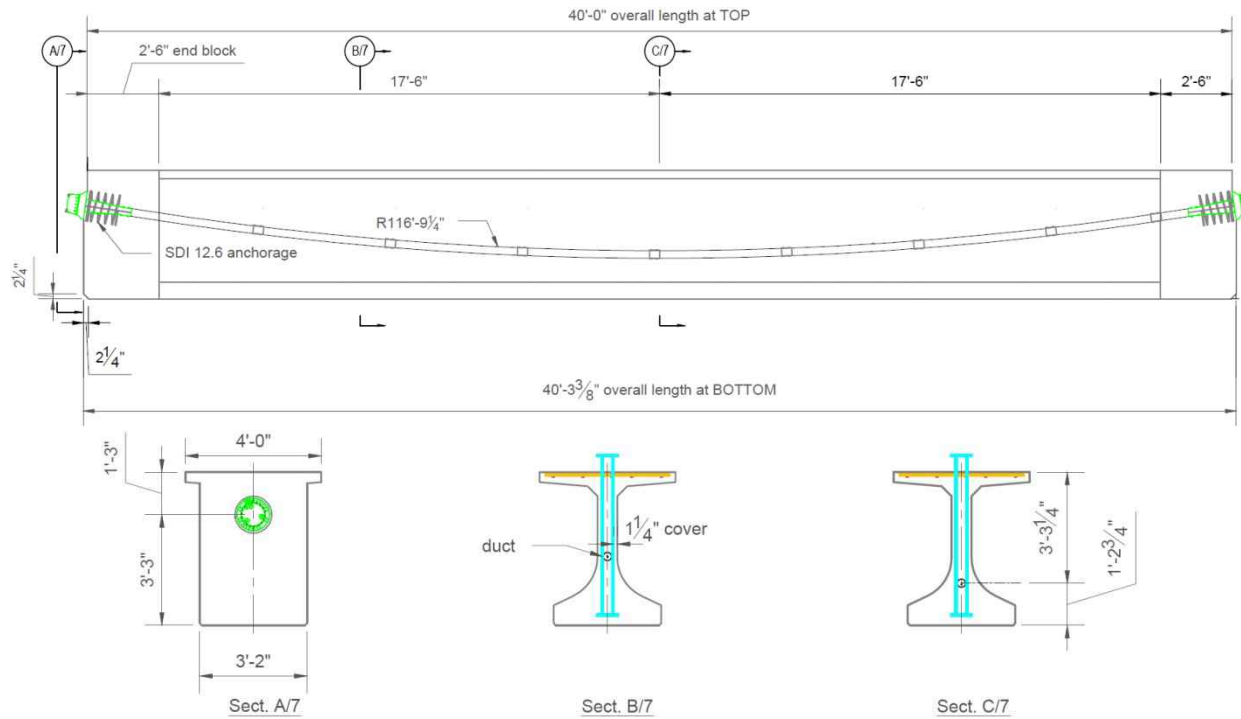


Figure 9-1 Internal tendon specimen with parabolically draped profile

After the beam was unloaded, the strands were detensioned by torching the wedges at the dead end anchor 'A' (unlike coring and cutting individual wires in the tests with unbonded specimens described later in this chapter). The strain gage and load cell data were recorded at 2 kHz throughout the detensioning operation.

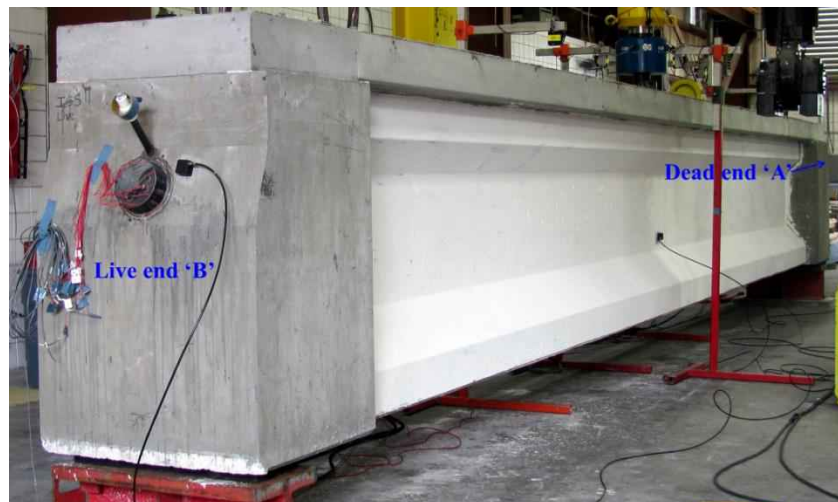


Figure 9-2 Test specimen with internal bonded tendon

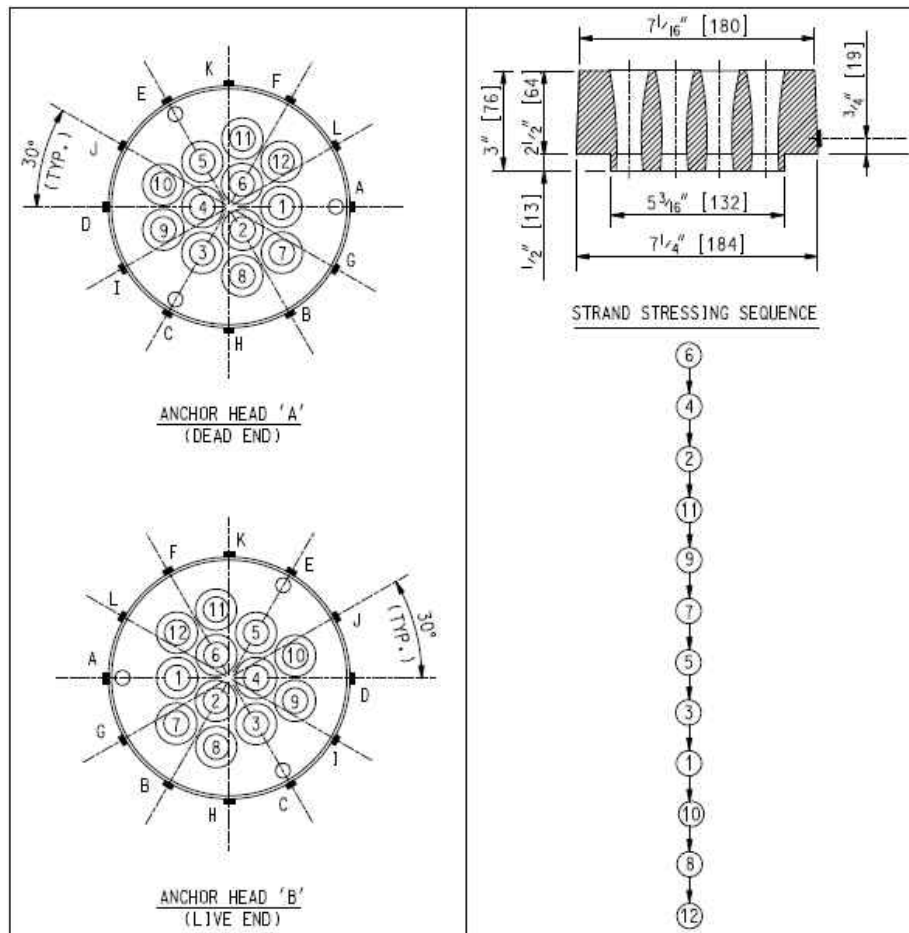


Figure 9-3 Strain sensor layout for internal tendon specimen

9.1.2 Experimental Results

Post-tensioning

Figure 9-4a shows the time history of prestressing force as the strands were stressed. The smaller abrupt force surges indicate the initial preloads ($0.20F_u$) of individual strands, followed by higher force surges representing the final loads ($0.75F_u$). The anchor strain time history in Figure 9-4b and the final strains at the end of post-tensioning in Figure 9-4d suggest that the dead end anchor was under greater strain than the live end anchor, because of the seating loss at the live end resulting from the stressing mechanism. Figure 9-4c demonstrates the captured strains by individual gages with stressing. Pairwise strain plots for each of the gages comparing the dead and live end anchors are given in Appendix B.

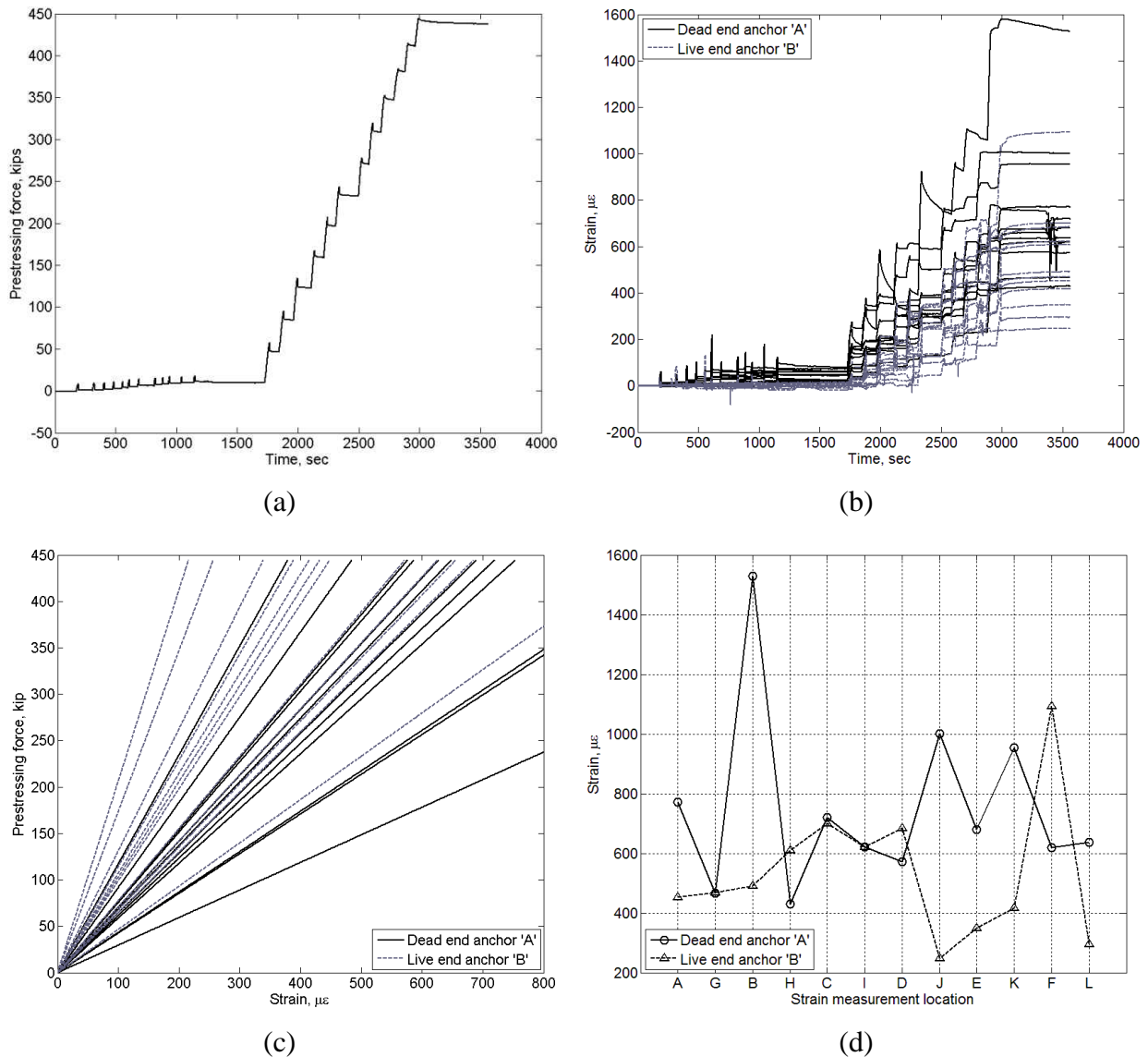
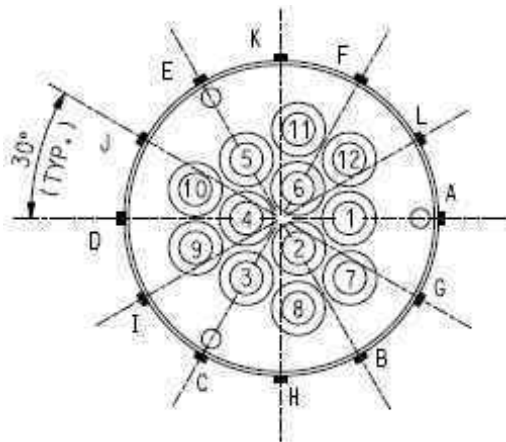
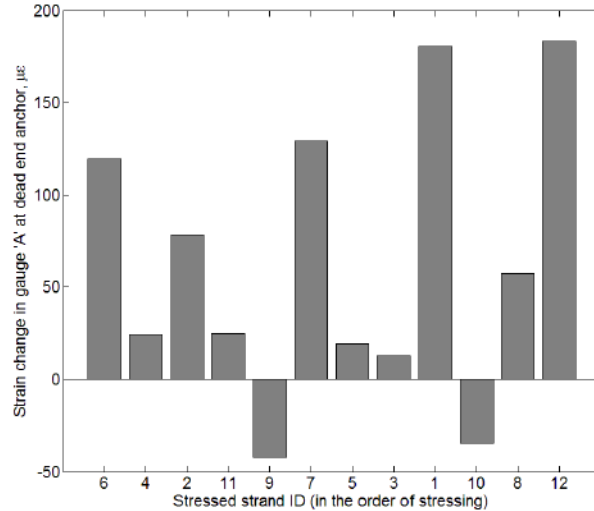


Figure 9-4 Post-tensioning: (a) load cell time history at dead end 'A'; (b) anchor strain time history; (c) anchor strain vs. prestressing force; (d) final strain at the end of post-tensioning

As the strands were stressed one-by-one, the strain in each of the gages changed according to their distance from the stressed strand. For example, gage 'A' at the dead end anchor experienced large strain increase while stressing its near strands 1, 7, and 12 (Figure 9-5). Similarly, stressing of the next closest strands 2 and 6 resulted in relatively high strain increase compared to the other remote strands, whereas stressing the diametrically opposite strands 9 and 10 caused strain relief. Thus, this stressing procedure in post-tensioning (before grouting) can be treated as a reversed process of strand cuts in unbonded tendons, where the largest strain drop is expected to occur at the nearest gage from the broken strand. The strain changes experienced by the rest of the gages at both dead and live end anchors are included in Appendix B.



(a) anchor instrumentation



(b) strain change in gage 'A' at dead end

Figure 9-5 Strain change in a gage with stressing of each strand

An attempt has been made to find a relationship between strain change at a monitoring point and its distance from the wedge through statistical analysis. Table 9-1 lists different statistical fits [linear (Lin), quadratic (Quad), and exponential (Exp)] for individual gages and indicates that the strain change is exponentially related to the distance between wedge and gage (Appendix B contains individual fit plots). These results have been combined later with other test results for obtaining a generalized strain-distance relationship.

Table 9-1 Distance and strain change relationship fit statistics (Coeff. of determination, R^2)

Gage	Dead end anchor			Live end anchor		
	Lin	Quad	Exp	Lin	Quad	Exp
A	0.9320	0.9432	0.9430	0.7884	0.8074	0.7884
B	0.8939	0.9285	0.9349	0.6294	0.7789	0.8042
C	0.8894	0.9258	0.9315	0.6987	0.8011	0.7992
D	0.7541	0.8600	0.8771	0.6991	0.7850	0.8004
E	0.9437	0.9608	0.9619	0.7212	0.7642	0.7684
F	0.7630	0.8414	0.8471	0.7061	0.7800	0.7981
G	0.9167	0.9377	0.9410	0.7728	0.9327	0.9344
H	0.5878	0.8377	0.9597	0.8440	0.8825	0.8842
I	0.8406	0.9293	0.9429	0.4822	0.4826	0.4825
J	0.8374	0.8818	0.8910	0.3928	0.8757	0.9371
K	0.9406	0.9520	0.9512	0.7837	0.7976	0.7959
L	0.7822	0.8823	0.9261	0.5231	0.8487	0.9493

Beam loading (three-point bending)

After the grout was injected and fully cured, the beam was subjected to a three-point bending test and underwent a loading-unloading cycle (Figure 9-6b) for pre-cracking the

specimen before loading to its ultimate capacity. The loading was then resumed past cracking until the ultimate capacity was reached, followed by complete removal of the applied load. As expected, the load cell and anchor strains were mostly unaffected by the loading due to the bonded construction. However, the strain change observed at some of the gages (Figure 9-7b) might have been caused by strand slippage during the loading process.

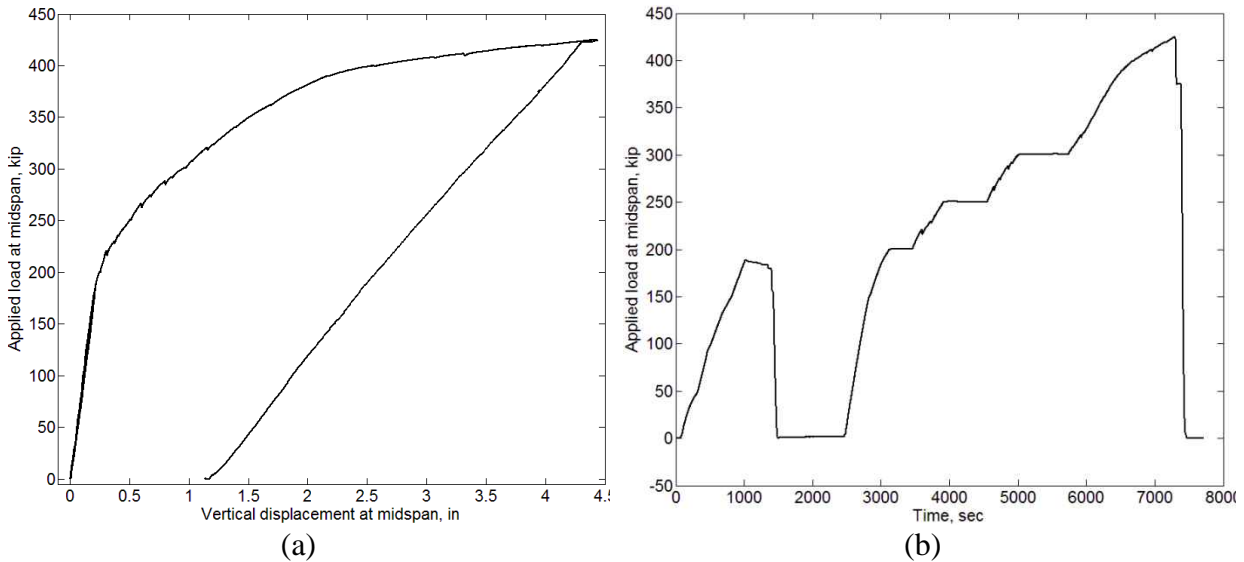


Figure 9-6 Beam loading: (a) load vs. displacement; (b) loading time history

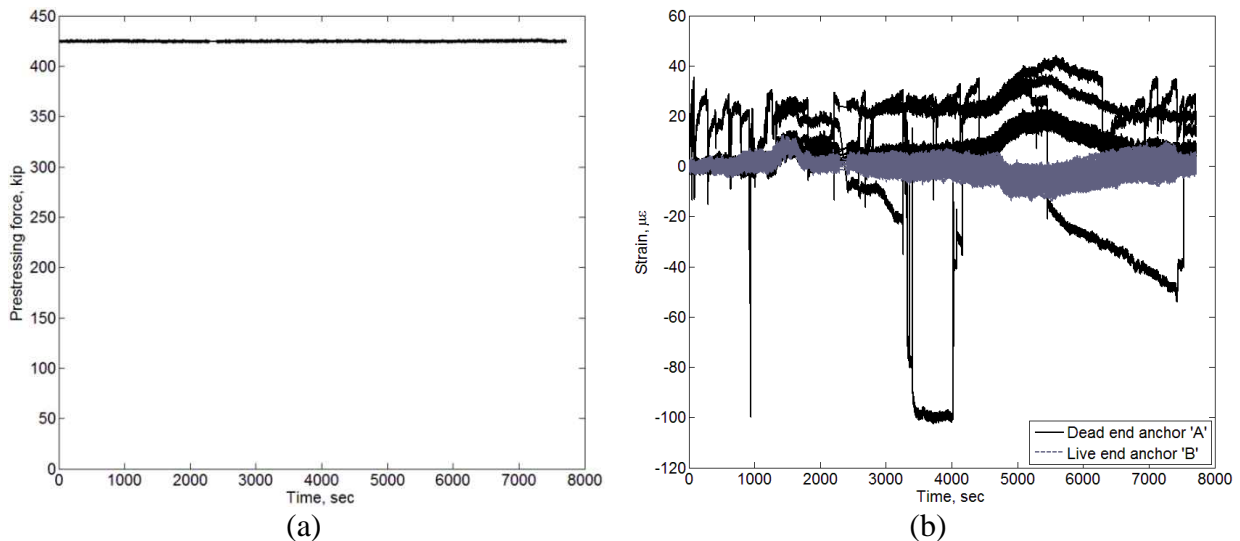


Figure 9-7 Beam loading time history: (a) load cell at dead end ‘A’; (b) anchor strains

Detensioning (wedge torching)

As expected, no strain change was observed during detensioning due to the bonded nature of the tendon (Figure 9-8).

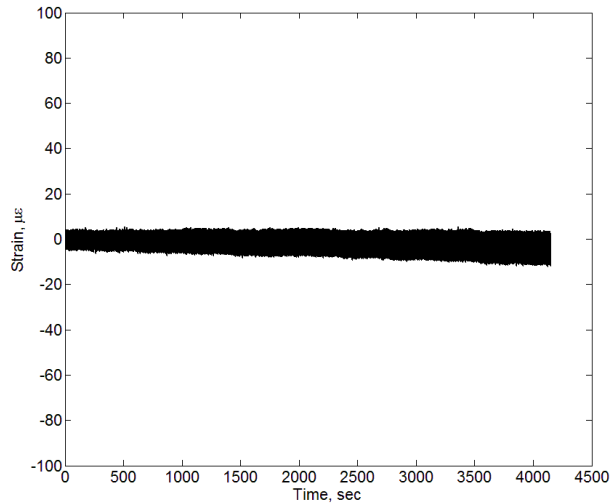


Figure 9-8 Live end ‘B’ anchor strain time history during detensioning

9.2 Test with External Unbonded Tendon

9.2.1 Test Specimen, Instrumentation, and Procedure

For the test with external unbonded specimen, a 40-ft long beam (one 7-ft and two 12-ft I-girder segments (FIB54), two 2-ft long intermediate blocks for deviators, and two 2 ft-6 in. end blocks to house the anchorage) with two tendons (designated as Tendon 1 and Tendon 2) was used (Figure 9-9, Figure 9-10). Each of the tendons comprised six seven-wire prestressing strands of 0.6-in. diameter placed inside smooth HDPE ducts with two-point harp profile. The two tendons were anchored at the dead end ‘A’ (designated as anchor ‘A1’, and ‘A2’) and stressed with a mono-strand jack at the live end ‘B’ (designated as anchor ‘B1’, and ‘B2’) with 600-kip load cells between the girder and wedge plates at the dead end. Like the bonded specimen, 12-strand wedge plates were used; however, only the six inner wedge holes were filled with strands (Figure 9-11) because of capacity limitation of the girder. Each of the four wedge plates was instrumented with six strain gages of 5-mm (0.2-in.) gage length; details of the sensor arrangement are shown in Figure 9-11. Similar to the bonded test, stressing of each of the strands was completed in two steps to ensure uniform bearing of the wedge plates and the anchor strain and load cell data were recorded at 2 Hz. The strands of the two tendons, however, were alternately stressed to avoid prestressing force imbalance. At the end of post-tensioning, wax was injected into the ducts and once the wax was set, the beam was loaded to its ultimate capacity (indicated by crushing of top flange). The beam was then unloaded and was prepared for detensioning. The anchor strains and load cell data were captured at 10 Hz during the loading/unloading process. It is noted that the strands were not damaged in anyway during the ultimate capacity test (explained later in this section), which would otherwise affect the detensioning step.

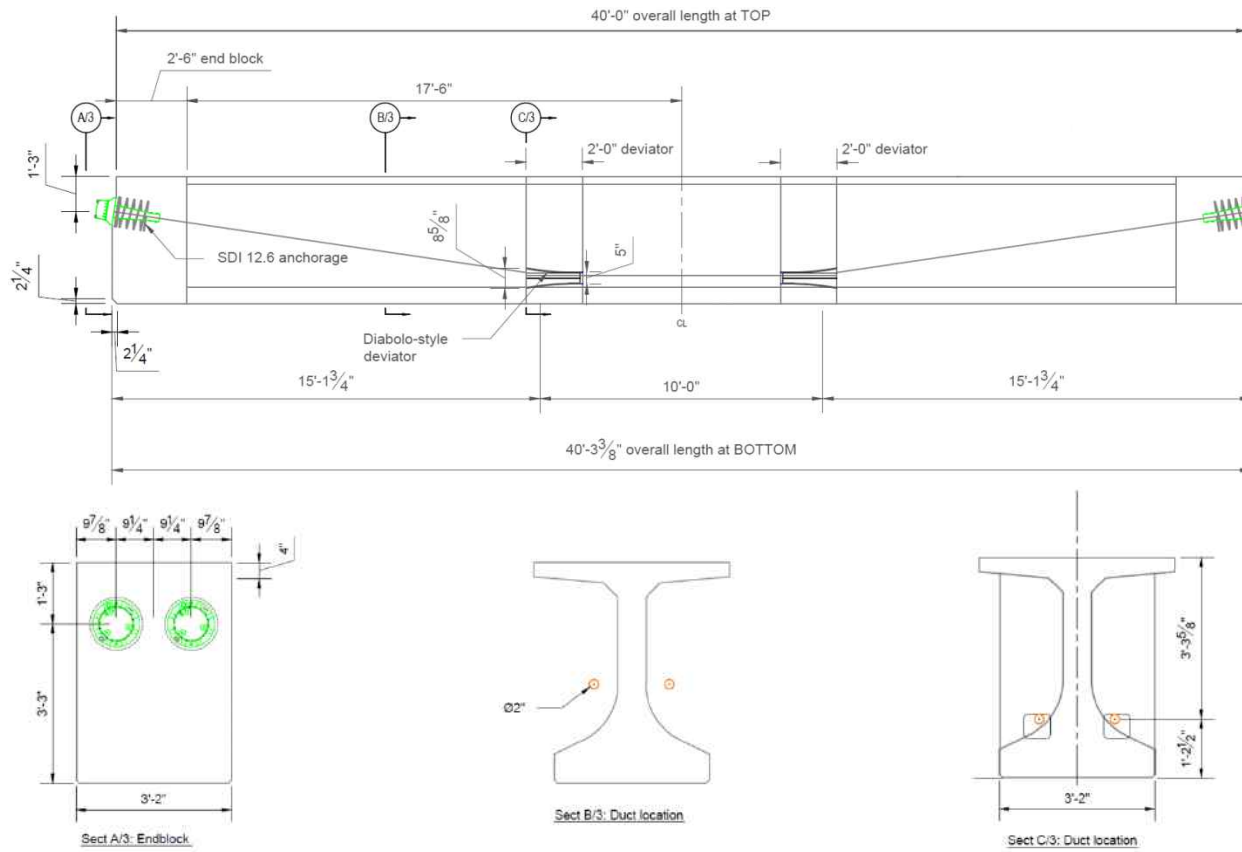


Figure 9-9 External tendon specimen with two-point harped profile

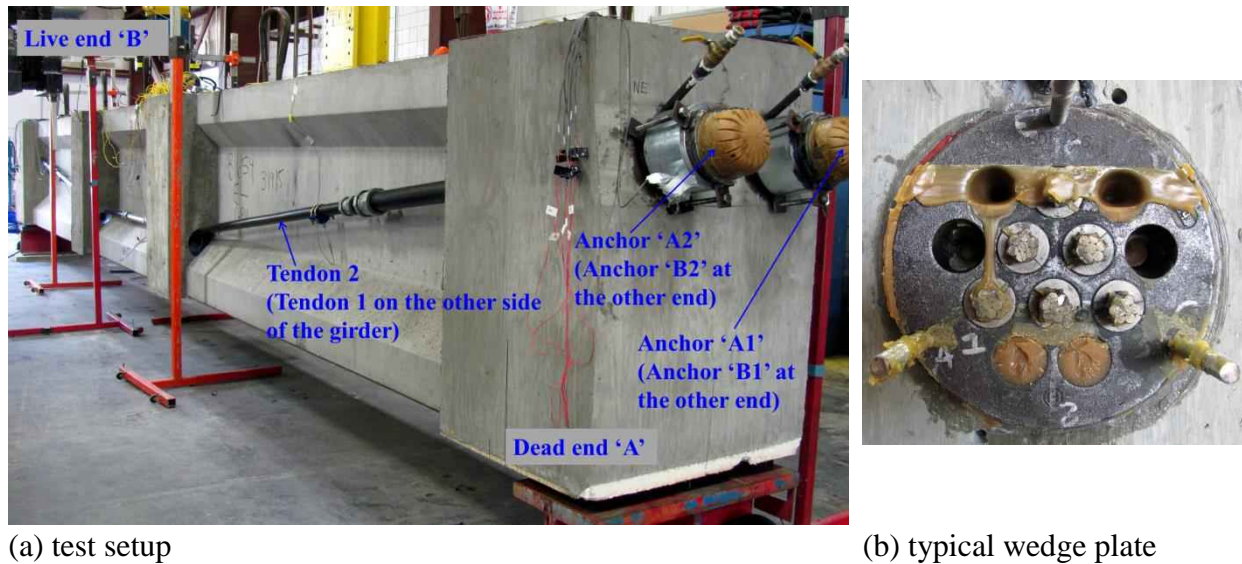


Figure 9-10 Test specimen with external unbonded tendons

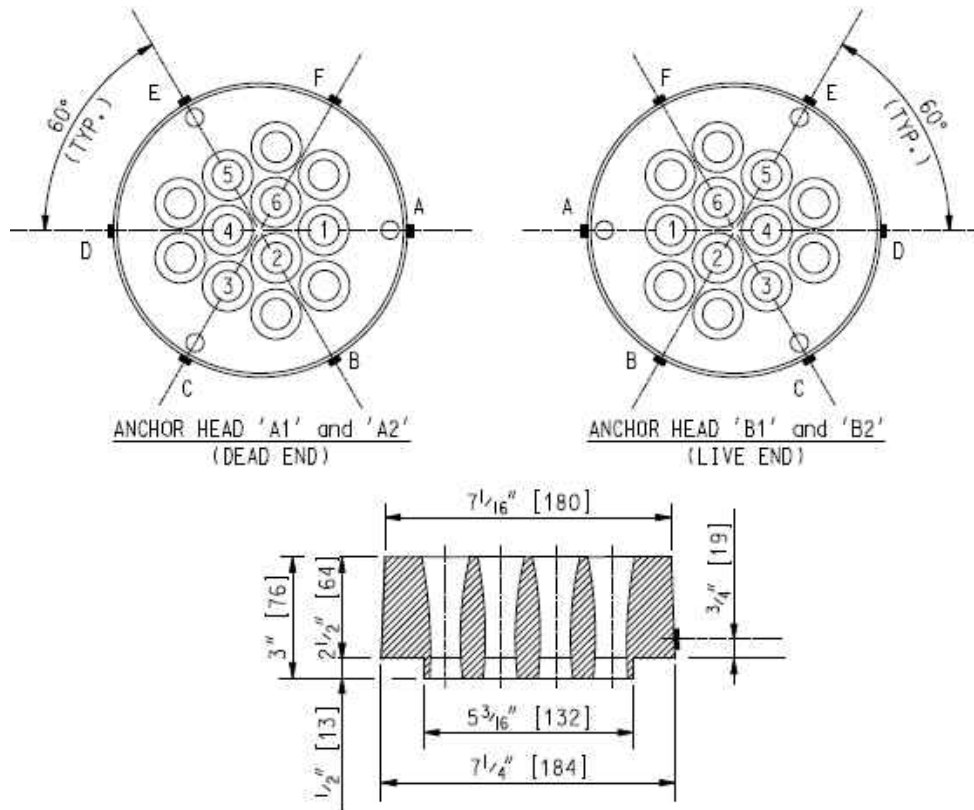


Figure 9-11 Strain sensor layout for external unbonded specimen

The tendon ducts were opened after unloading the beam to access the strands for making wire cuts (Figure 9-12a). The two tendons were cut at different locations to investigate the breakage detectability at different distances from the anchors: Tendon 1 was cut at about 36ft-4in away from anchor 'A1' (3ft-8in from anchor 'B1'), whereas Tendon 2 was cut at about 22ft-7in from anchor 'A2' (17ft-5in from anchor 'B2'). All 12 strands were cut wire-by-wire using a Dremel tool with rotating cutoff wheel of 31.75 mm (1.25 in) diameter. Again, the strands of the two tendons were alternately cut to avoid prestressing force imbalance. In case of some strand cuts, the wedges of the broken strands came out of the wedge plate immediately after the whole strand was severed (Figure 9-13), which confirmed the identification of the broken strand. The strain gage and load cell data were recorded at a higher sampling rate (2 kHz) during the cutting operation to capture the dynamic response of the broken strands (Appendix C) in addition to the static strain response of the anchors.



(a) exposing the duct to access the strands



(b) wire cuts with Dremel tool

Figure 9-12 Cutting the strands



(a) before strand cuts



(b) after strand cuts

Figure 9-13 Wedge movement after strand cuts



(a) acoustic sensor placement



(b) SoundPrint DAQ

Figure 9-14 Acoustic monitoring

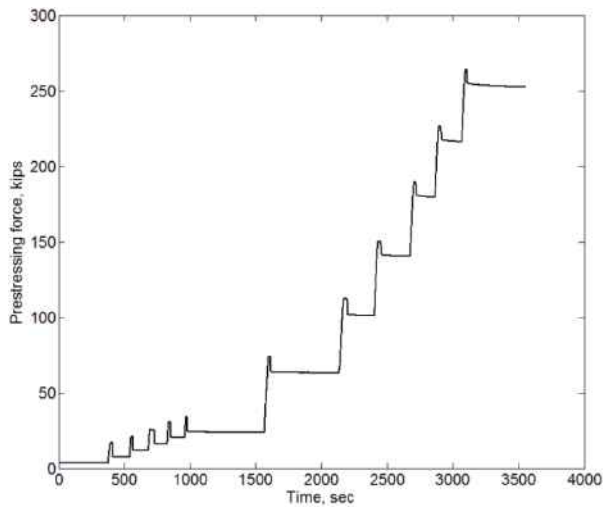
In addition to the anchor strain measurements, four acoustic sensors (piezoelectric accelerometers of frequency range up to 22 kHz) were mounted to the concrete surface with cyanoacrylate adhesive, one next to each of the wedge plates (Figure 9-14). Through coaxial cable, the sensors were connected to a calibrated acoustic monitoring DAQ (Pure Technologies' SoundPrint acoustic monitoring system), where the captured signals were preprocessed and filtered. The data were then transmitted using standard internet protocols to a remote data processing center for further processing, event classification (possible wire break/wire break/confirmed wire break), and reporting.

In general, the AE system performed well in detecting wire breaks both in external and internal unbonded tendons. The experimental results (discussed later in this chapter) demonstrate that the strain changes in anchors captured by strain gages occurred at the same time as when the breakage events were detected by the acoustic sensors. This confirmed that the strain changes in anchors were in line with the breakage events identified by AE sensors. In addition, the locations of the wire breaks along the tendon length were determined by AE system based on relative intensity of the AE signals captured by AE sensors positioned at different distances from the wire-cut locations. The AE-determined breakage locations are reported in Appendix E, which show that the AE system performed reasonably well in locating the wire-cuts in the laboratory experiment. The AE system successfully capturing wire breakage events in controlled laboratory conditions on relatively small bridge girders. Field tests should be conducted, however, on full-scale bridge elements to confirm its performance in practical conditions in the presence of environmental and traffic noise. Also, unlike the strain-based system, the AE sensors were unable to detect which particular strand was broken. More details of the acoustic sensor arrangement and experimental results may be found in Appendix E.

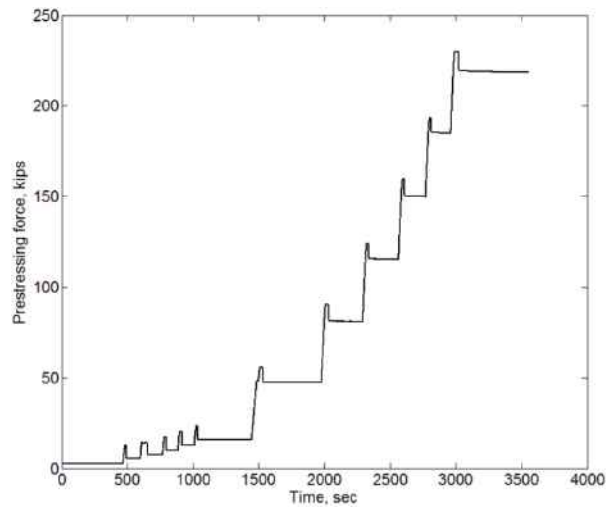
9.2.2 Experimental Results

Post-tensioning

The prestressing force and anchor strain time history of the two tendons during stressing are shown in Figure 9-15 and Figure 9-16, respectively. The plots confirm significant strain increase in wedge plates as the strands were stressed.

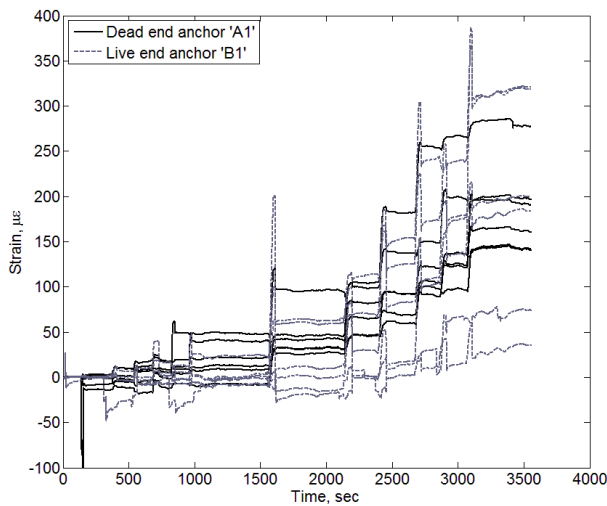


(a)

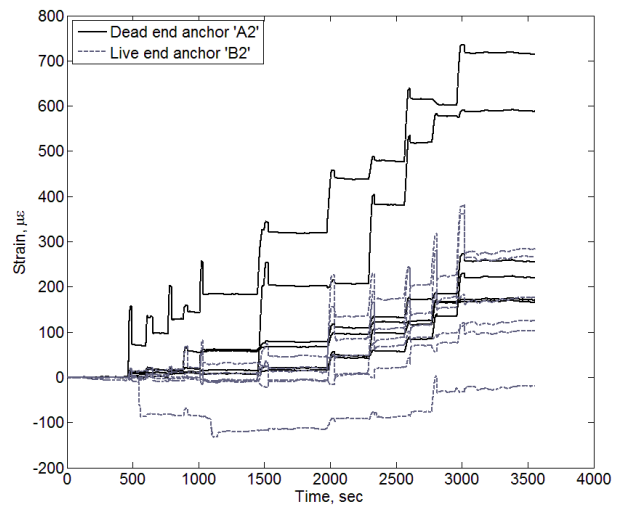


(b)

Figure 9-15 Post-tensioning time history at dead end load cell: (a) Tendon 1; (b) Tendon 2



(a)



(b)

Figure 9-16 Post-tensioning time history for strain gages: (a) Tendon 1; (b) Tendon 2

Beam loading (three-point bending)

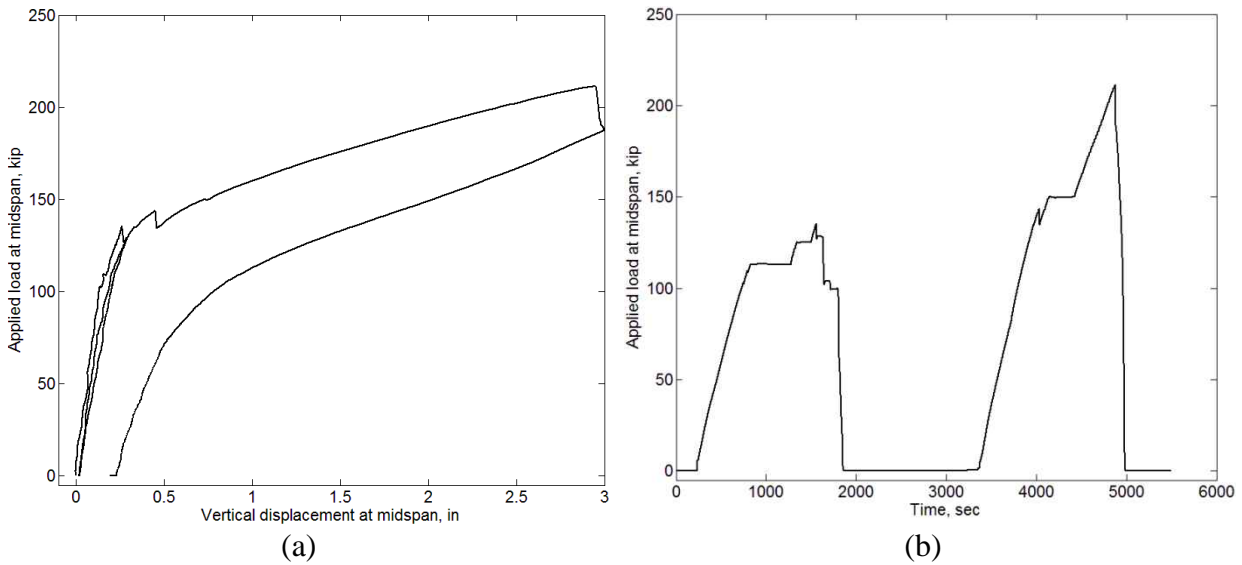


Figure 9-17 Beam loading: (a) load vs. displacement; (d) loading time history

Similar to the bonded specimen, the beam first underwent a loading-unloading cycle to pre-crack the specimen (Figure 9-17). The loading was then continued to the ultimate capacity and finally, the beam was completely unloaded. Unlike the bonded specimen, the load cell reading increased significantly when the beam was loaded, but went back nearly to the original prestressing force after the load was removed (Figure 9-18). This preservation of prestressing force indicated that the strands were not yielded even after the beam was loaded to its ultimate capacity. Thus, the detensioning step (described in the following section), in which wire cuts were made to investigate the strain change in anchors, was not affected by the beam loading. The increased anchor strains during the loading process, on the other hand, were not entirely relieved even after the complete removal of the beam load (Figure 9-19), which was possibly due to the Poisson's effect on the wedge plates originated from the wedge seating mechanism.

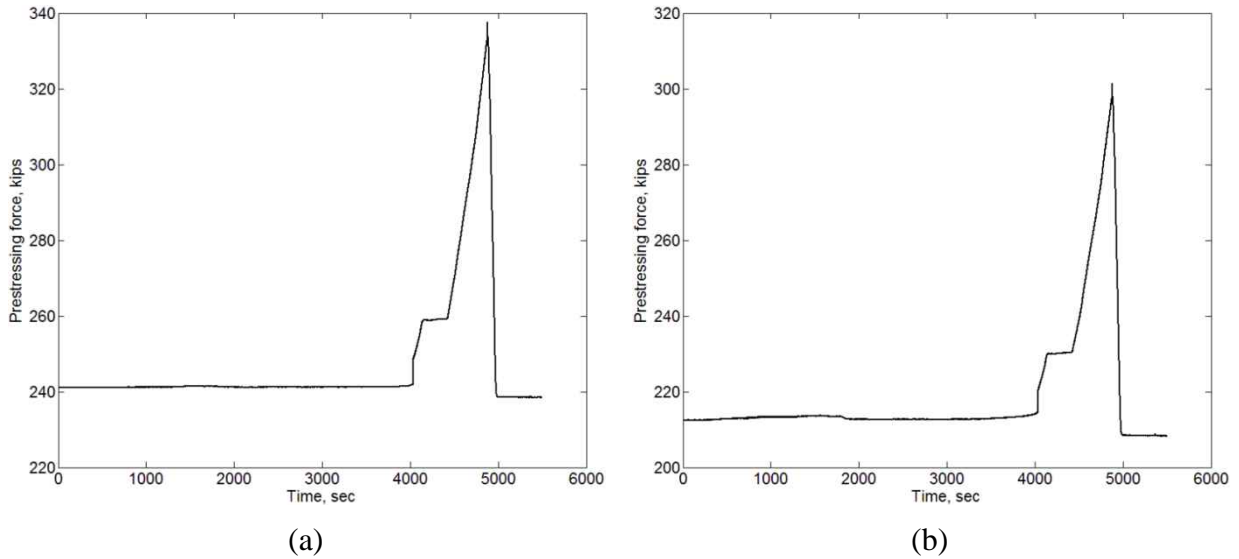


Figure 9-18 Time history of load cells during beam loading: (a) Tendon 1; (b) Tendon 2

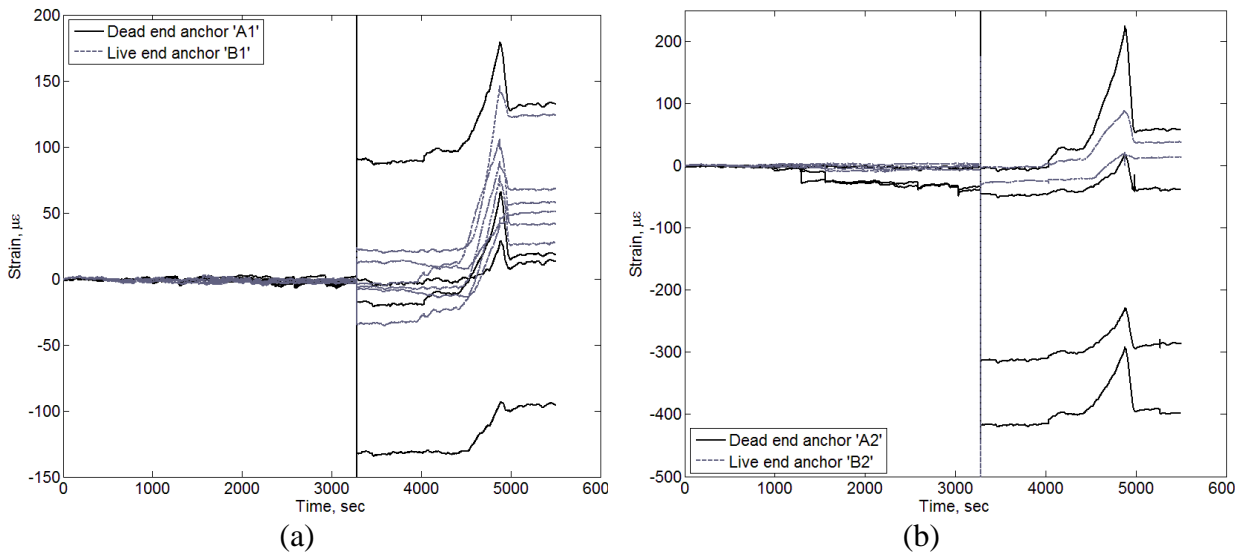
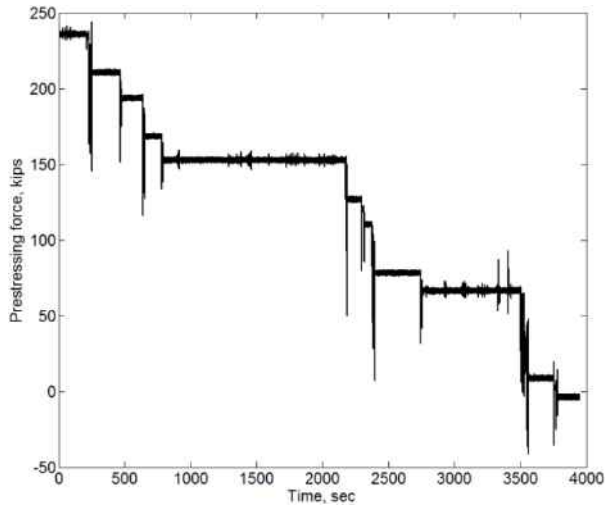


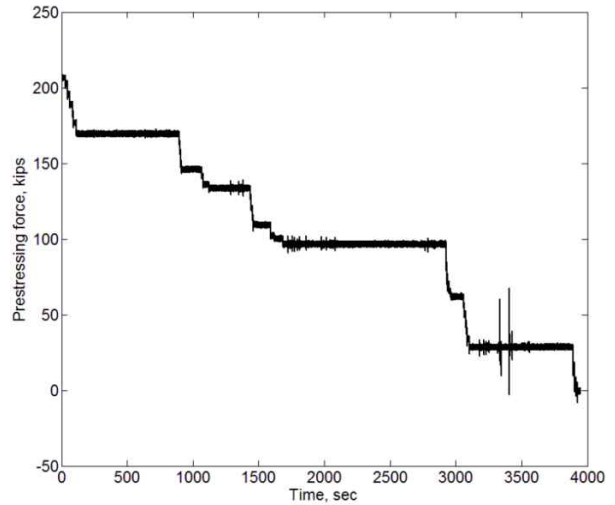
Figure 9-19 Time history of strain gages during beam loading: (a) Tendon 1; (b) Tendon 2

Detensioning (wire cutting)

The strands in the two tendons were alternately cut (wire-by-wire) after the beam load was removed. Figure 9-20 and Figure 9-21 show the time history of prestressing force and anchor strain, respectively, during the detensioning operation. Clearly, both the prestressing force and anchor strains significantly changed with wire cuts, indicating prestress loss at the ends.

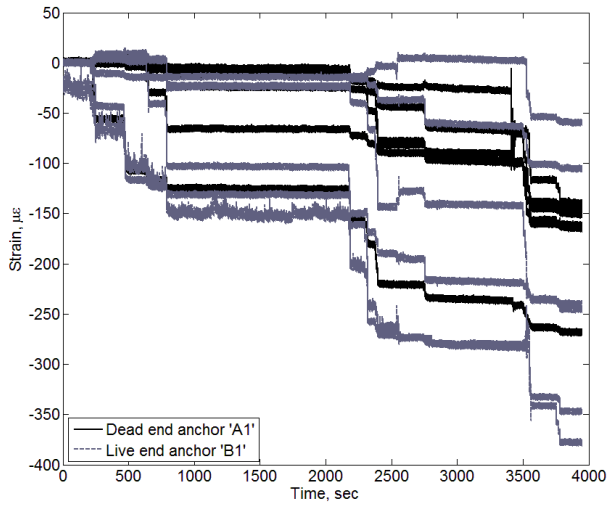


(a)

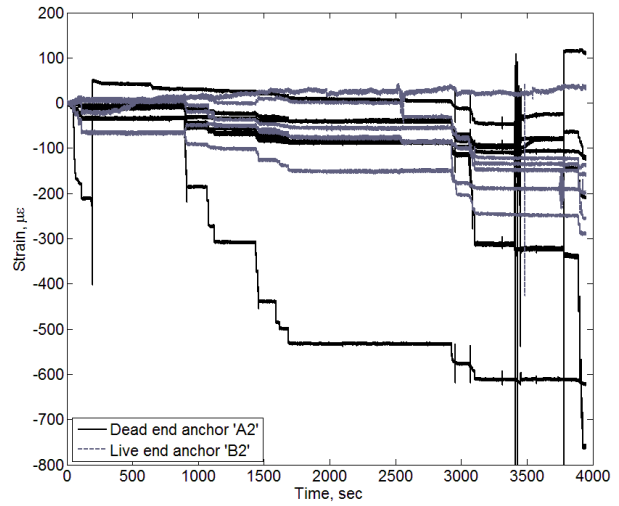


(b)

Figure 9-20 Time history of load cells during detensioning: (a) Tendon 1; (b) Tendon 2



(a)



(b)

Figure 9-21 Time history of strain gages during detensioning: (a) Tendon 1; (b) Tendon 2

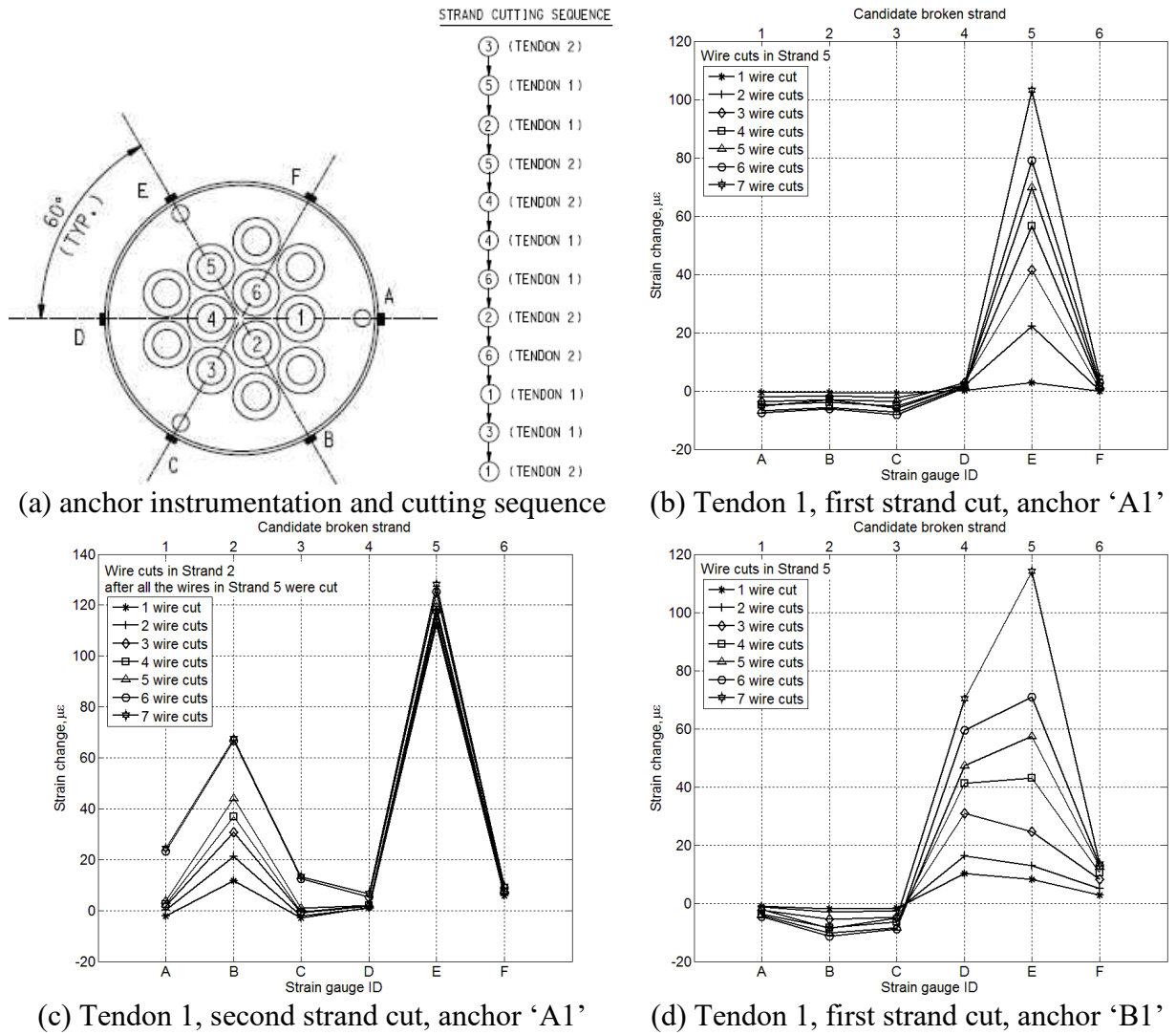
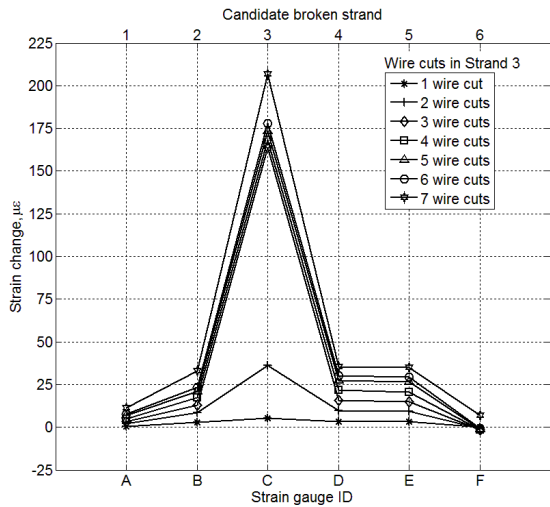
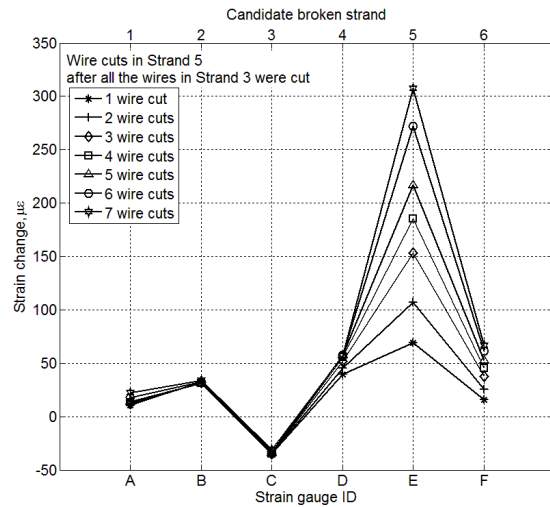


Figure 9-22 Strain change with wire cuts in Tendon 1

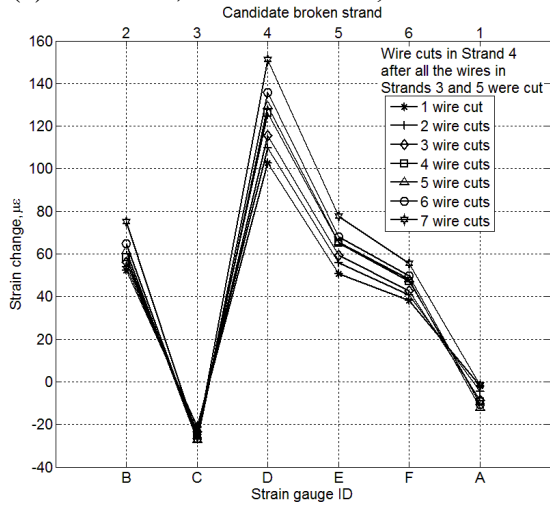
Sample strain change plots are shown in Figure 9-22 and Figure 9-23. As expected, for the first strand cut in Tendon 1 (Strand 5), the highest strain change was observed in gage E and the magnitude of strain change increased with the number of wire cuts (Figure 9-22b). Figure 9-22c shows the strain change when Strand 2 was cut after strand 5, where two peaks were observed, one for each of the broken strands. However, the peak strain at gage E (nearest to strand 5) did not change with wire cuts in Strand 2, but the peak strain at gage B (nearest to Strand 2) actively increased with wire cuts. Similarly, several other breakage conditions in Tendon 2 are illustrated in Figure 9-23.



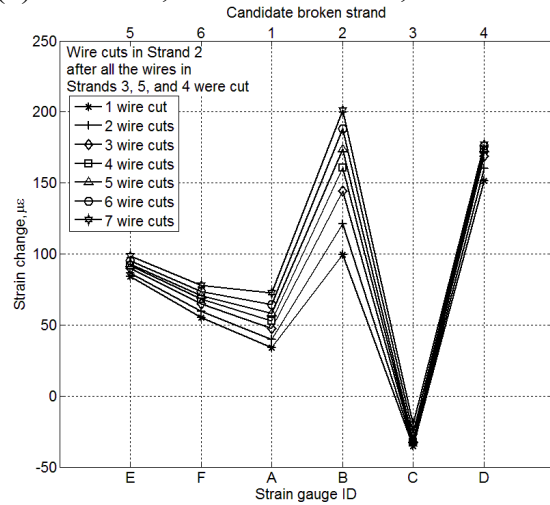
(a) Tendon 2, first strand cut, anchor 'A2'



(b) Tendon 2, second strand cut, anchor 'A2'



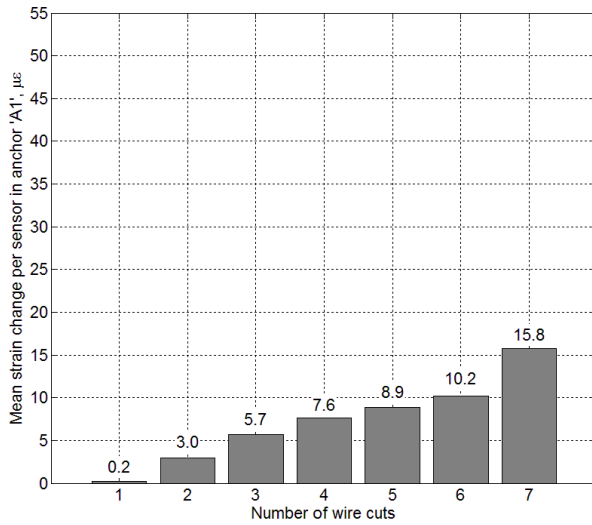
(c) Tendon 2, third strand cut, anchor 'B2'



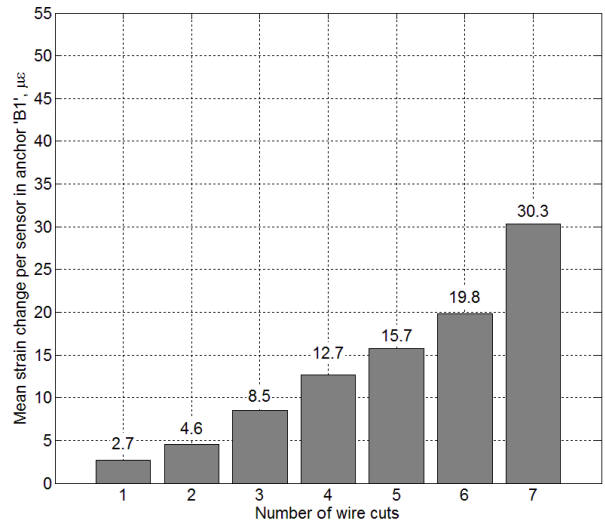
(d) Tendon 2, fourth strand cut, anchor 'B2'

Figure 9-23 Strain change with wire cuts in Tendon 2

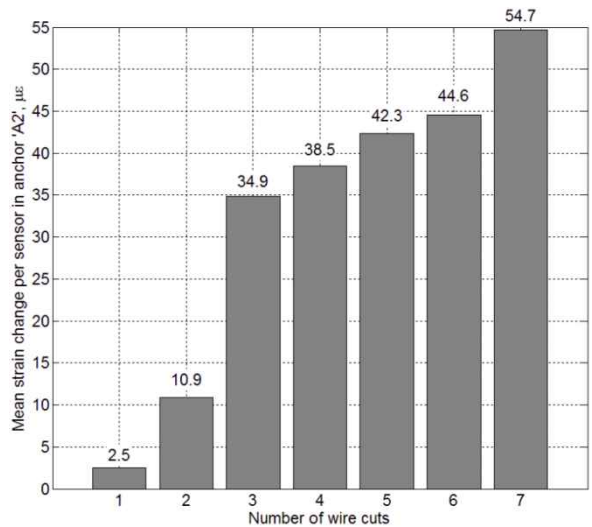
Figure 9-24 shows the magnitudes of mean strain change per sensor at the six strain gages in the four anchors. As expected, greater strain change occurred in the near anchor 'B1' than the far anchor 'A1' for Tendon 1. For Tendon 2, however, strain change in anchor 'A2' was larger than anchor 'B2' because anchor 'A2' was under larger initial strain at the beginning of detensioning due to post-tensioning and the beam loading process (Figure 9-16b, Figure 9-19b).



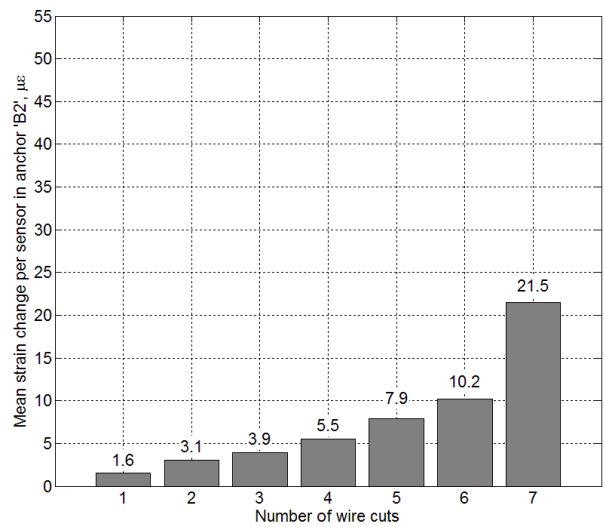
(a) wire cut distance from anchor: 36ft-4in



(b) wire cut distance from anchor: 3ft-8in



(c) wire cut distance from anchor: 22ft-7in



(d) wire cut distance from anchor: 17ft-5in

Figure 9-24 Mean strain change per sensor after wire cuts (first strand cut)

Although the anchor strain plots (Figure 9-23, Figure 9-24) confirmed significant strain change (compared to the magnitudes associated with loading/unloading of live loads discussed later), indicating the potential for the success of the monitoring algorithms proposed in Chapter 5, the algorithms have not been applied to these experimental results because the wedge plates were not fully populated. However, fully populated wedge plates were used in the test with internal unbonded tendon (reported in the following section) where the algorithm has been applied.

9.3 Test with Internal Unbonded Tendon

9.3.1 Test Specimen, Instrumentation, and Procedure

The experimental setup, including the dimensions of the test specimen, wedge plate pattern, tendon profile, strain sensor layout, stressing procedure, and data sampling rate, was the same as in the bonded specimen (Section 9.1.1, Figure 9-1, Figure 9-3). However, in lieu of grout, wax was injected into a smooth HDPE duct at the end of strand stressing. Similar to the first two tests, the beam was then loaded to its ultimate capacity (indicated by deck crushing), under three-point bending after the wax was set, followed by complete unloading. It is noted that the strands were not yielded during the ultimate capacity test (explained later in this section), thus not affecting the detensioning step where wire cuts were made to investigate the strain change in anchors.

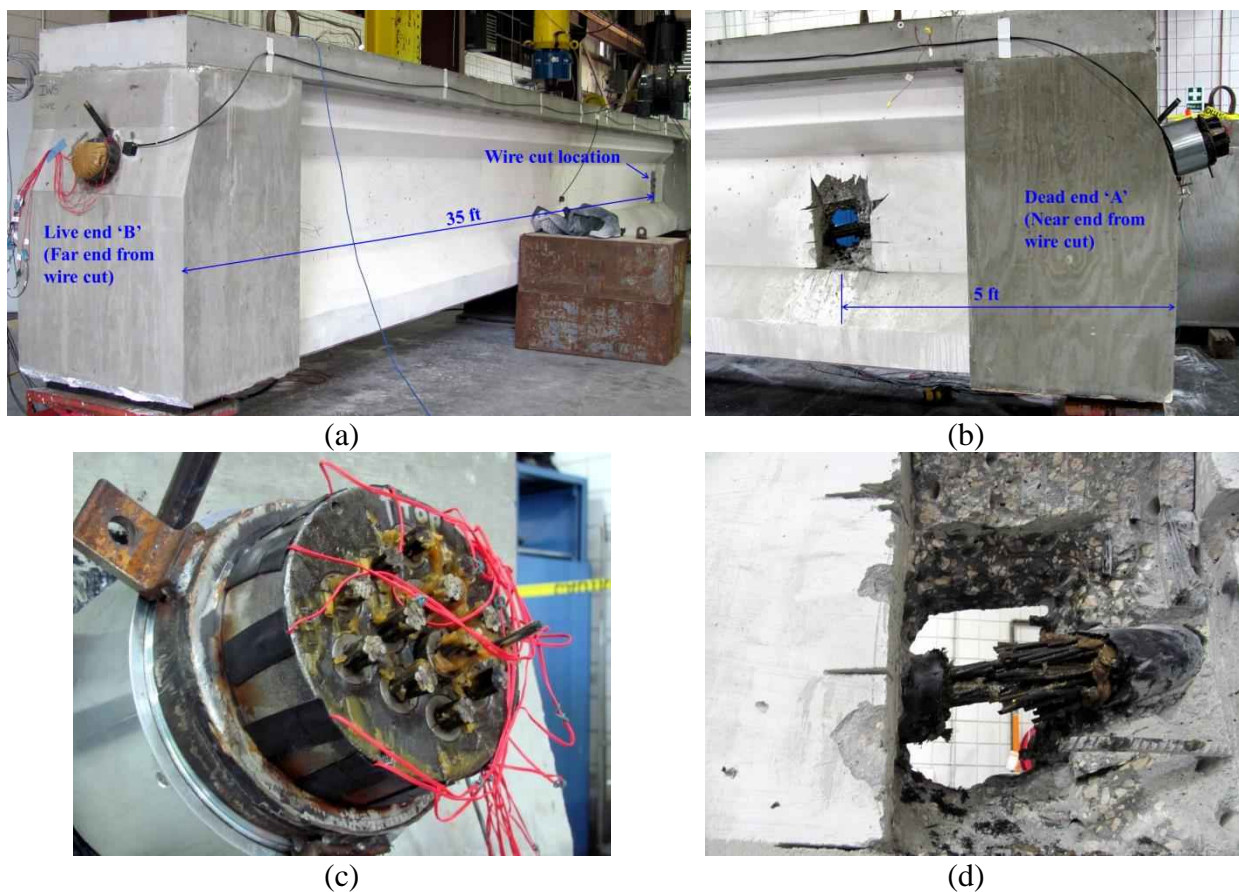


Figure 9-25 Test setup for internal unbonded specimen: (a) live end; (b) dead end and access window for wire cuts; (c) anchor instrumentation; (d) tendon close-up after strand cuts

As shown in Figure 9-25b, a core was drilled to expose the strands for making wire cuts following the loading/unloading tests. The cut location was intentionally chosen far from one anchor (35-ft) to investigate the effects of stress recovery on the anchor strain. The first six strand cuts were made wire-by-wire with a rotating cutoff wheel of 31.75 mm (1.25 in) diameter, while the rest of the strands were cut using a larger diameter wheel, not attempting to make individual wire cuts. After all the seven wires in a strand were cut, the wedge of the broken

strand came out of the wedge plate at the near end anchor 'A' (Figure 9-26). The wedges at the far end anchor 'B', however, were visually unaffected by the strand cuts. In addition to the 12 strain gages, the three acoustic sensors were installed next to the wedge plates and at the midspan (Figure 9-27) to capture the wire break events.

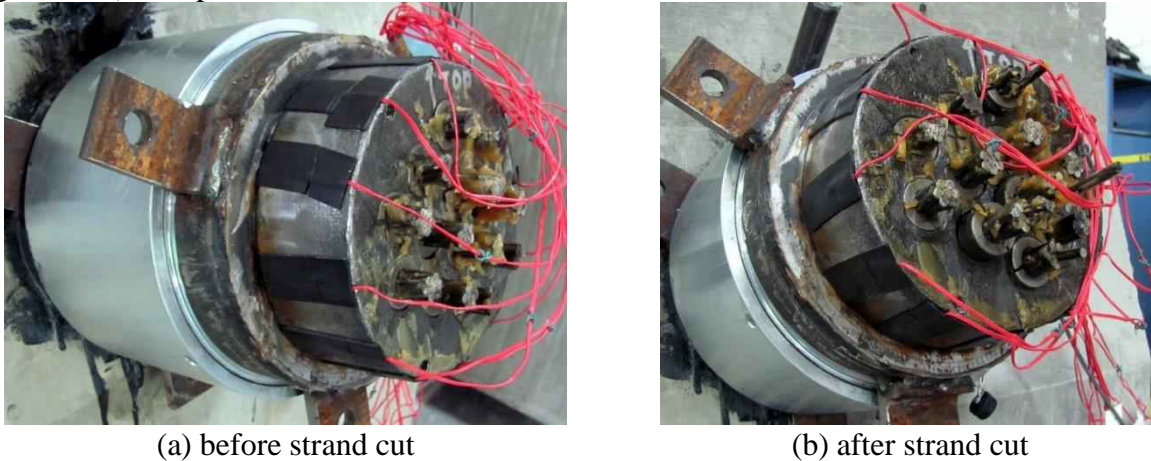


Figure 9-26 Wedge movements after strand cuts

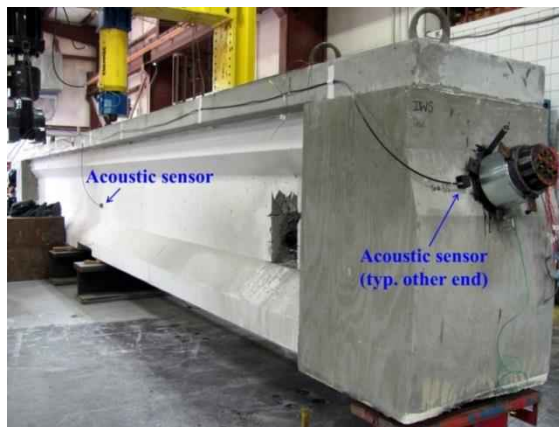
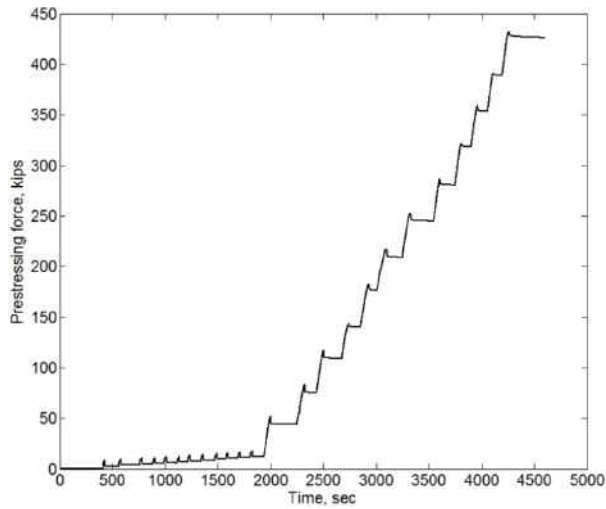


Figure 9-27 Acoustic sensor placement on internal unbonded tendon specimen

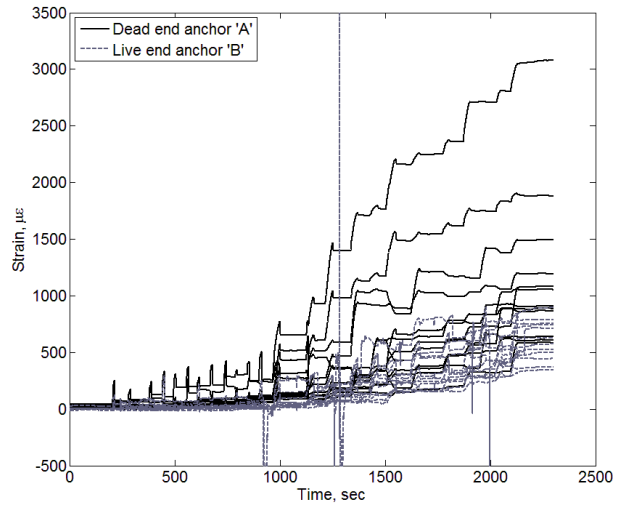
9.3.2 Experimental Results

Post-tensioning

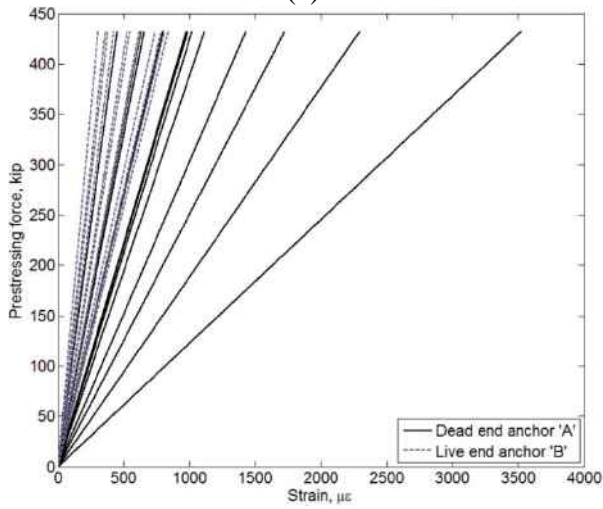
Figure 9-28a illustrates the stepwise strand stressing and Figure 9-28c shows the strain increase in anchors with stressing. Similar to the test with the bonded tendon, Figure 9-29 shows an example strain change plot, demonstrating that the strain change in a gage decreases with the distance from the stressed strand. The strain change plots for other gages are provided in Appendix D.



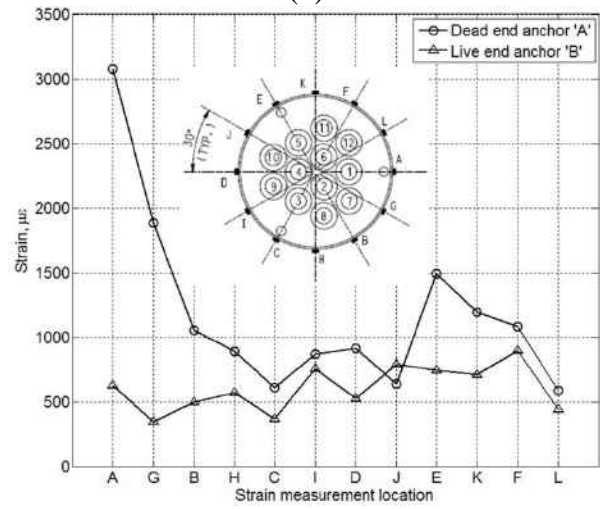
(a)



(b)

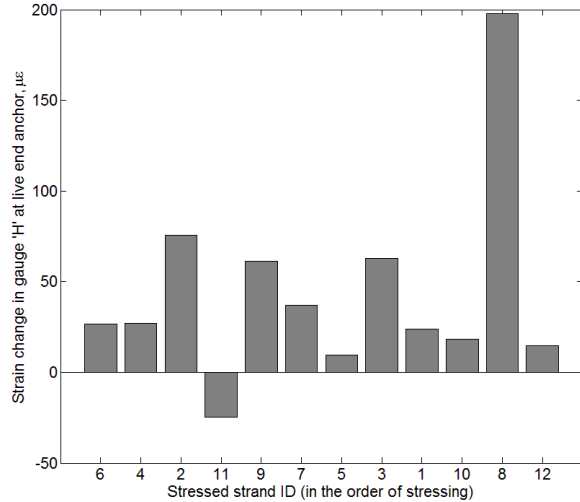
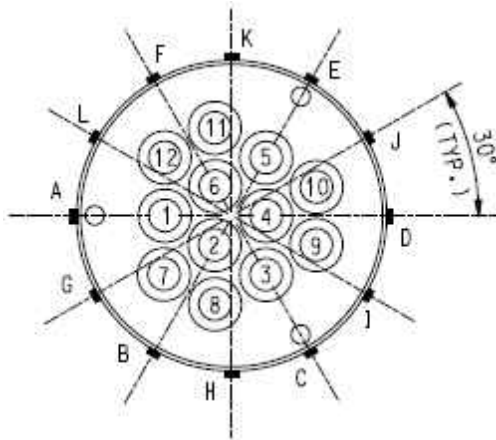


(c)



(d)

Figure 9-28 Post-tensioning: (a) load cell time history; (b) anchor strain time history; (c) anchor strain vs. prestressing force; (d) final anchor strain at the end of post-tensioning



(a) anchor instrumentation

(b) strain change in gauge 'H' at live end

Figure 9-29 Strain change in a gage with stressing of each strand

Similar to the bonded test results, statistical analysis was performed on strain change data for each of the gages to obtain a strain-distance relationship (Table 9-2, Appendix D).

Table 9-2 Distance and strain change relationship fit statistics (Coeff. of determination, R^2)

Gage	Dead end anchor			Live end anchor		
	Lin	Quad	Exp	Lin	Quad	Exp
A	0.5392	0.6195	0.5392	0.8908	0.8957	0.8956
B	0.3231	0.5797	0.5175	0.7230	0.8842	0.9239
C	0.4660	0.4875	0.5237	0.6541	0.7634	0.8352
D	0.7915	0.7987	0.7977	0.8138	0.9480	0.9534
E	0.8239	0.8272	0.8269	0.9020	0.9337	0.9381
F	0.6560	0.7966	0.8323	0.4412	0.5536	0.6074
G	0.2821	0.2929	0.2821	0.7109	0.8822	0.8742
H	0.7031	0.9065	0.9469	0.7023	0.8050	0.8766
I	0.7650	0.8079	0.8227	0.8377	0.8935	0.9039
J	0.2252	0.2268	0.2343	0.8789	0.8897	0.8911
K	0.5563	0.6728	0.7943	0.3969	0.7158	0.7045
L	0.5923	0.8871	0.9410	0.8493	0.9648	0.9733

The post-tensioning results from the internal bonded and unbonded tests have been combined in an attempt to find a generalized strain-displacement relationship, which can be used to predict the strain change at a monitoring location on wedge plate due to a wire break. Figure 9-30 shows the statistical fits obtained for the combined data. As the R^2 values indicate, better fits were achieved for individual gages (Table 9-1, Table 9-2) compared to the combined data

(Figure 9-30) because of the effects of previously stressed strands on the anchor strain distribution.

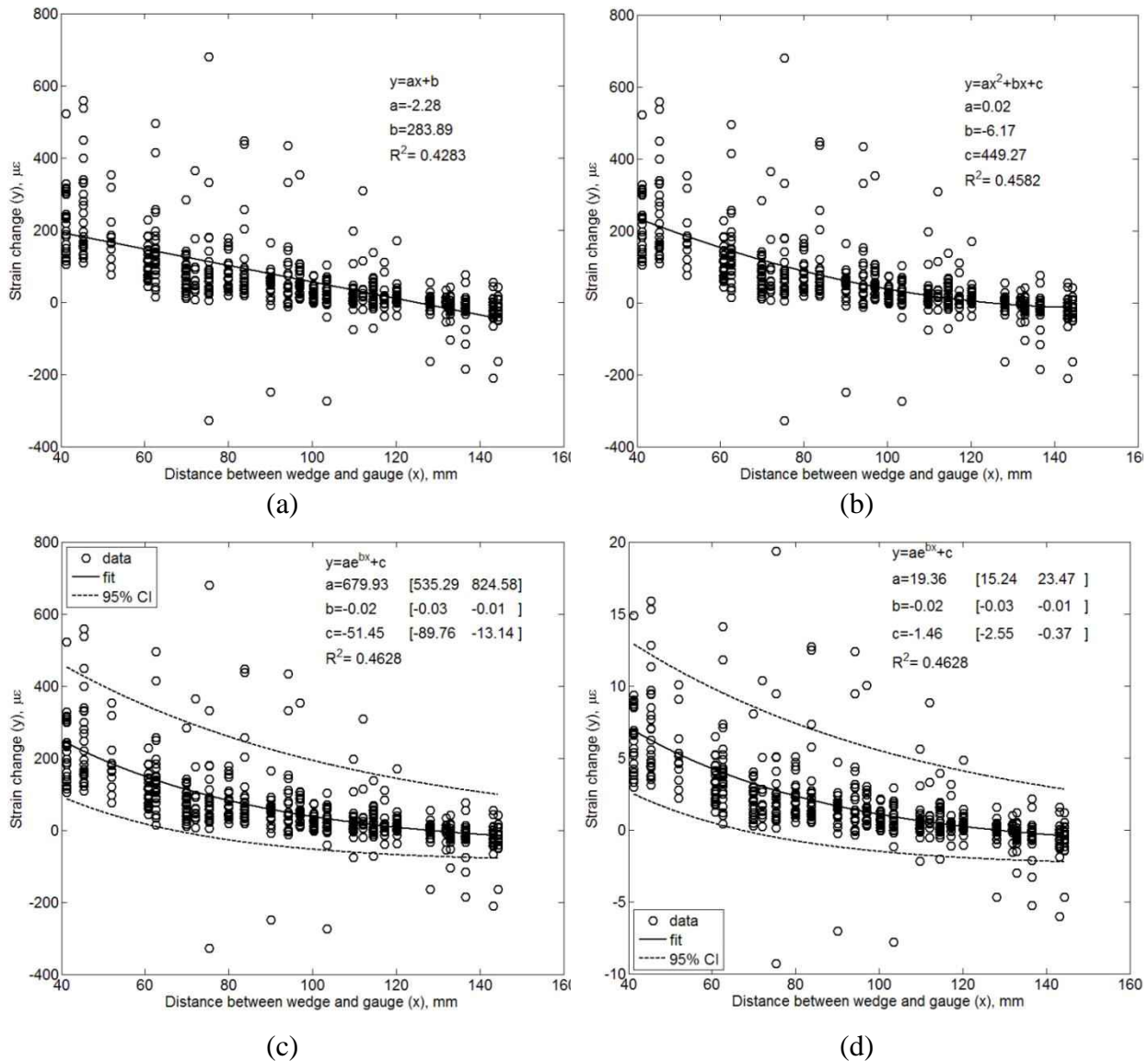


Figure 9-30 Distance and strain change relationship: (a) linear fit; (b) quadratic fit; (c) exponential fit; (d) normalized exponential fit, strain change for unit (1 kip) applied prestressing force

Beam loading (three-point bending)

Before loading to its ultimate capacity, the beam underwent two loading-unloading cycles for pre-cracking the specimen (Figure 9-31) and then loaded to the ultimate capacity, followed by complete unloading. As expected in an unbonded construction, the anchors experienced significantly increased prestressing force during the loading process. However, the original prestressing force was mostly preserved after withdrawal of the applied load (Figure 9-32a), indicating that the unbonded strands remained elastic, not affecting the detensioning step

described in the following section. It is noted, however, that wire rupture of some of the pre-tensioned bonded strands was observed during the loading operation. Similar to the external tendon specimen, the increased anchor strains were not entirely relieved even after unloading (Figure 9-32b, c), which was possibly due to the Poisson's effect on the wedge plates as described earlier.

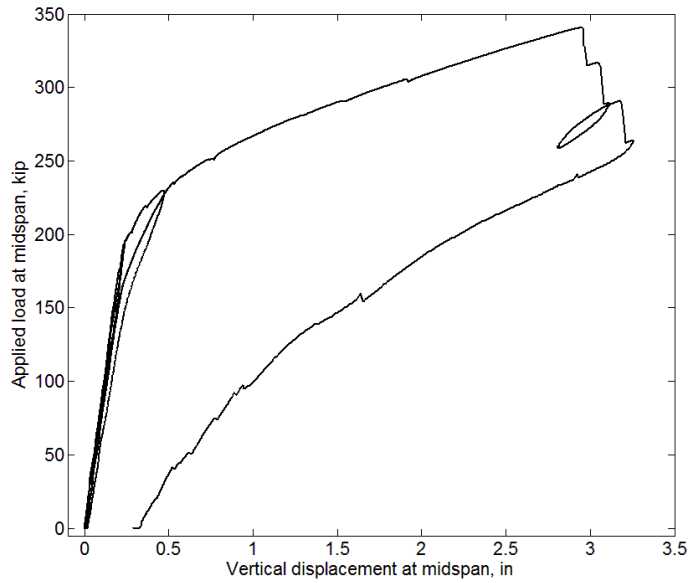


Figure 9-31 Load vs. displacement

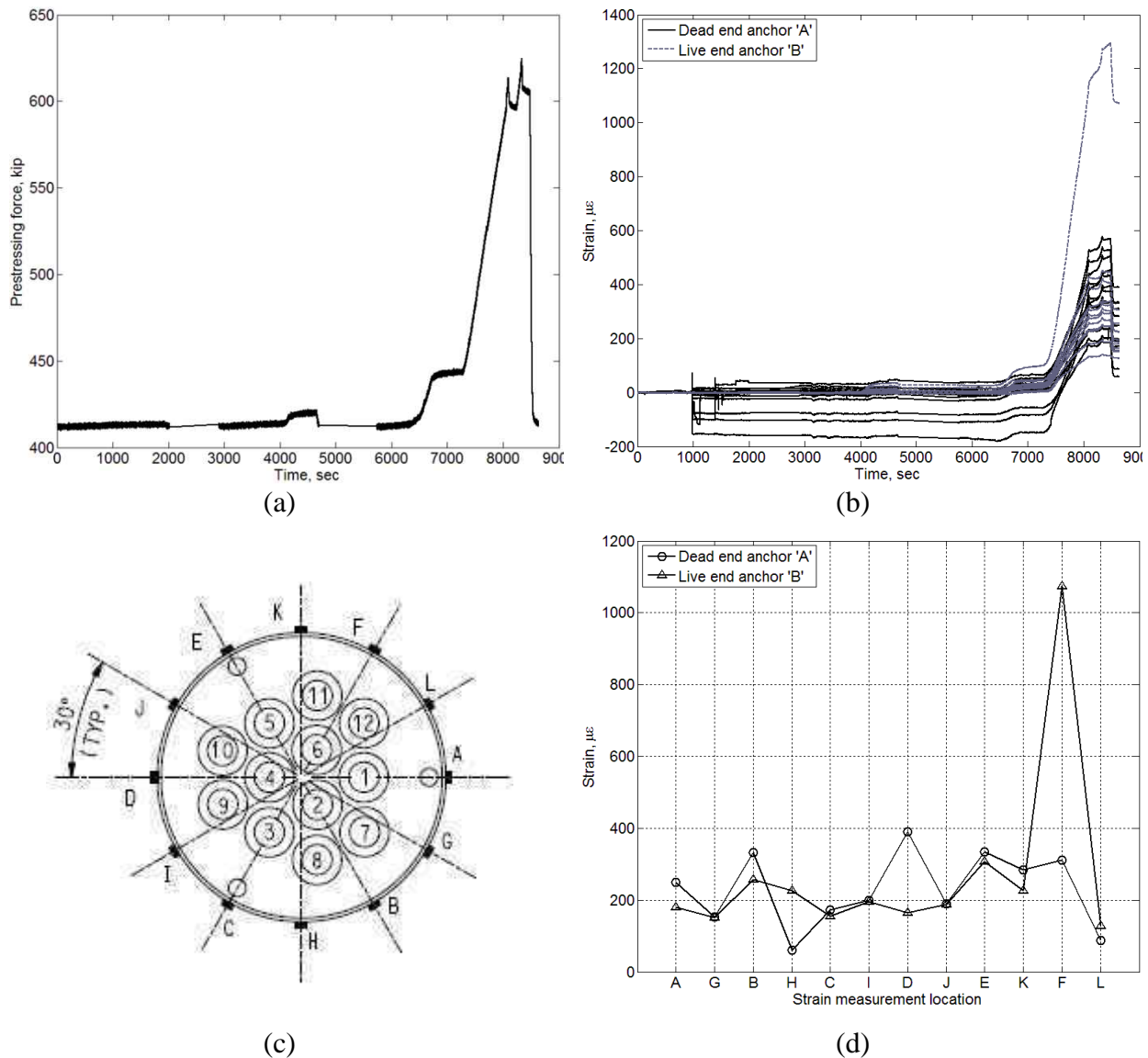


Figure 9-32 Beam loading: (a) load cell time history at dead end ‘A’; (b) anchor strain time history; (c) anchor instrumentation; (d) final strain at the end of load test

The proposed monitoring framework described in Chapter 5 uses the change of mean strain level (over the data collection period) between two consecutive monitoring events for detecting a breakage. Unless a wire break occurs, an anchor is expected to return to its original strain state after the live load disappears. However, several factors, such as interactions among the twisted strand bundle inside the tendon duct and wedge seating during loading, may cause the strain level to change to a certain extent even after the beam is unloaded and thus, may affect the breakage detectability (by signaling false positives). In an attempt to estimate the strain change due to these non-breakage reasons, the strain state at the anchors at the end of first two loading-unloading cycles (Figure 9-33) were considered and the mean strain change per sensor between these two cycles was found to be $2.4 \mu\epsilon$ (total strain change in the 12 sensors $28.5 \mu\epsilon$). In

addition, an estimation of strain change under service load condition was obtained by measuring the anchor strain at approximately 50% of the beam's ultimate capacity in the third cycle. The mean strain change per sensor for this loaded condition was $5.3 \mu\epsilon$ (total strain change in the 12 sensors $63.1 \mu\epsilon$). Figure 9-33a demonstrates the loading/unloading time history, where the three markers represent the selected data points at the end of the first two cycles and when the beam was loaded to 50% of its capacity in the final cycle. The corresponding strain values are plotted in Figure 9-33b with the magnitudes of strain change among them. These strain measurements have been considered as baselines to compare with the strain change after wire cuts (described in the following section) to conduct a preliminary assessment of the breakage detectability under the effects of live loads.

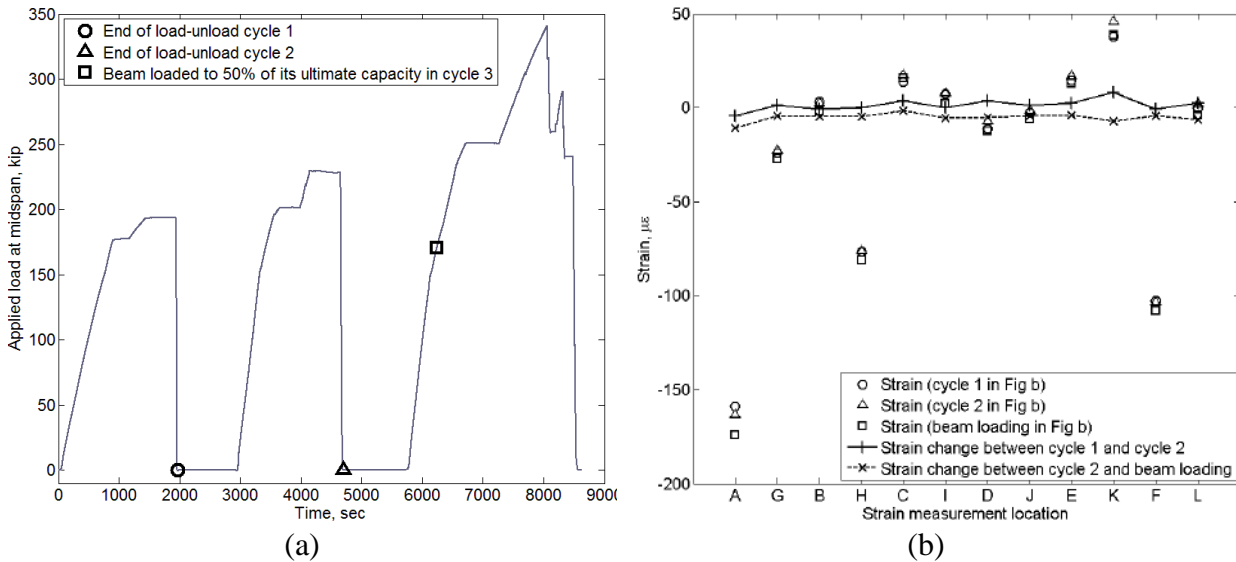


Figure 9-33 Strain change in anchors during beam loading: (a) loading time history; (d) axial strain and strain change

Detensioning (wire cutting)

After unloading the beam, wire cuts were made with a Dremel tool at a distance about 35ft from the live end anchor. The time history of prestressing force and anchor strain during the detensioning are shown in Figure 9-34. In addition to the prestress force and anchor strain, the wire cut events were also confirmed by the acoustic monitoring system. Figure 9-35 demonstrates that the strain changes in anchors are in line with the wire break events detected by the acoustic sensors.

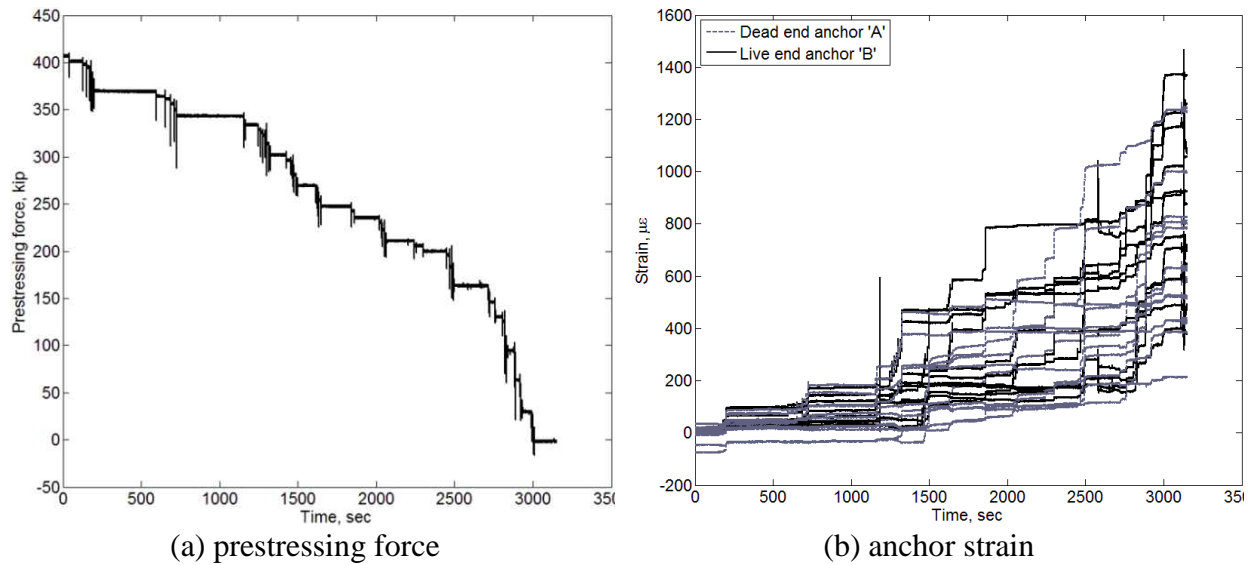


Figure 9-34 Detensioning time history

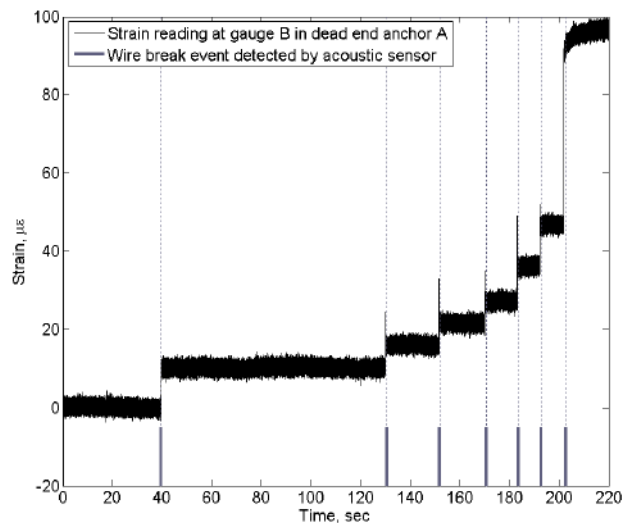
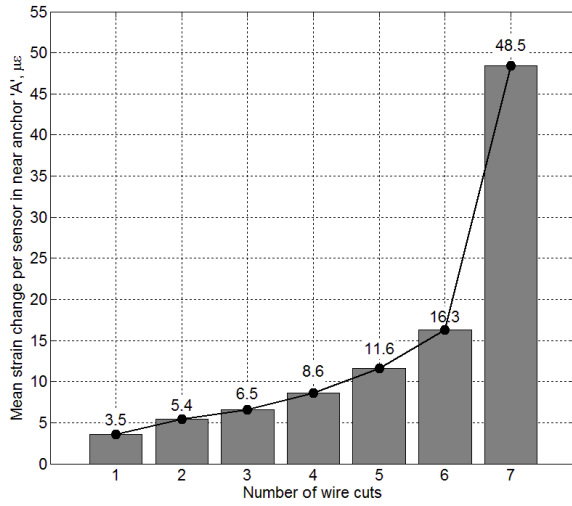


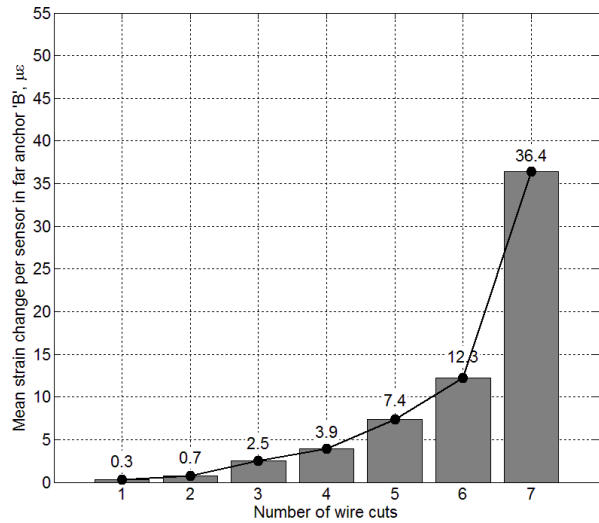
Figure 9-35 Wire break events detected by acoustic sensor and strain gage

Figure 9-36a shows the strain change observed in the near end anchor 'A'. The mean strain change per sensor after the first wire cut was around $3.5 \mu\epsilon$, which increased to over $10 \mu\epsilon$ after five wire cuts, and reached almost $50 \mu\epsilon$ (total strain change in 12 sensors nearly $600 \mu\epsilon$) after the breakage of the whole strand. Clearly, these levels of strain change were significant compared to the previously obtained magnitudes associated with loading/unloading of live loads (around $2.4 \mu\epsilon$ per sensor), indicating the detectability of these breakage events. In the far end anchor 'B', due to stress recovery of broken wires away from the break, the mean strain change per sensor after the first wire cut was only about $0.3 \mu\epsilon$, indicating that detecting such a breakage away from the anchor after just one wire break might be challenging under in-field conditions. However, the strain change increased with the number of wire breaks, which accumulated over $35 \mu\epsilon$ per sensor (total of over $400 \mu\epsilon$) after the entire strand was severed. As discussed earlier in Chapter 2, these magnitudes of strand change are within the measurement capabilities of

standard strain gages. In addition, it is noteworthy that significantly high strain change was observed when the whole strand was broken, which can be used to distinguish between wire-level breaks and the entire strand break.



(a) near anchor from the cuts (anchor A)



(b) far anchor from the cuts (anchor B)

Figure 9-36 Mean strain change per sensor for the first strand cut

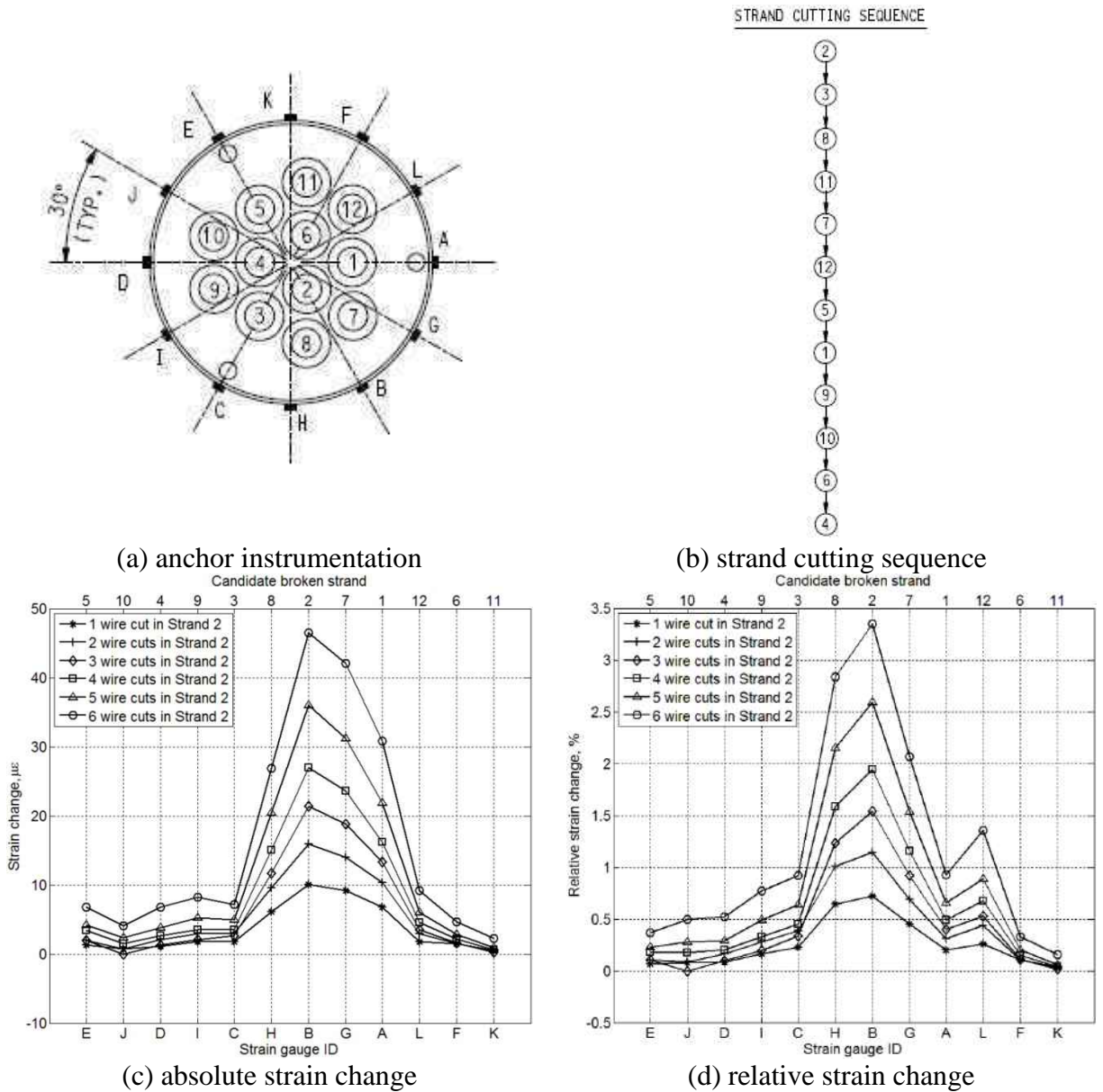


Figure 9-37 Strain change after first strand cut

Sample plots illustrating the strain change at different gages are shown in Figure 9-37 and Figure 9-38. Figure 9-37c and Figure 9-38a depict the absolute strain change from the unbroken state after the first and second strand cuts, respectively, whereas Figure 9-37d and Figure 9-38b show the strain change relative to the original state of strain at the beginning of detensioning. As shown in the figures, the first strand cut resulted in clear peaks at the nearest gage. However, the second strand cut produced peaks at other gage locations because the pre-existing condition (the effects of the earlier strand cuts) affected the strain distribution in anchors. Similar strain change plots of other wire cuts are given in Appendix D.

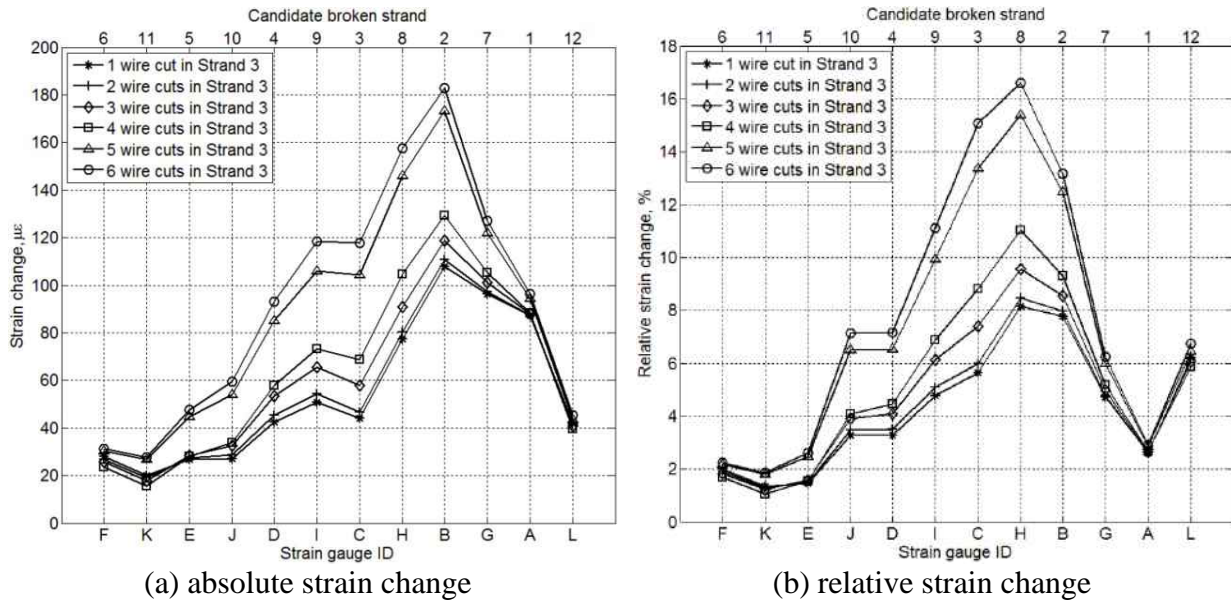


Figure 9-38 Strain change after second strand cut

9.3.3 Broken Strand Identification through Tendon Monitoring Algorithm

The group-based broken strand identification algorithm demonstrated with the 12-strand anchor developed in Chapter 5 has been applied to the experimental data from the internal unbonded test. The success of the model on the experimental data in identifying the broken strand is quantified in Table 9-3 and Table 9-4. As shown in the tables, the model is very successful in identifying the broken strand by monitoring the strain change in the near end anchor, which is 5ft away from the cut location. In case of far end anchor, located 35ft away from the cuts, the model is less successful than the near end, which was expected due to the stress recovery of the broken wire away from the break. In this case, the model fails to identify the exact strand in few early wire break cases but the overall performance of the model is quite satisfactory. Figure 9-39 is a graphical representation of the success rate of the model on the experimental data. Again, the plot shows that the model is very successful (almost 100%) even with just one wire break when the break is near the anchor, but requires several wire breaks to identify the broken strand when the damage occurs far from anchor. However, the success rate in general increases with the number of wire cuts and full strand failure is identified at least 92% of the time regardless of the distance from the break.

Table 9-3 Broken strand identification: End 'A' (Near end)

Broken strand (in the order of cut)	Wire cut 1	Wire cut 2	Wire cut 3	Wire cut 4	Wire cut 5	Wire cut 6	Wire cut 7
Strand 2	✓	✓	✗	✓	✓	✓	✓
Strand 3	✓	✓	✓	✓	✓	✓	✓
Strand 8	✓	✓	✓	✓	✓	✓	✓
Strand 11	✓	✓	✓	✓	✓	✓	✓
Strand 7	✓	✓	✓	✓	✓	✓	✓
Strand 12	✓	✓	✓	✓	✓	✓	✓
Strand 5	-	-	-	-	-	-	✓
Strand 1	-	-	-	-	-	-	✓
Strand 9	-	-	-	-	-	-	✓
Strand 10	-	-	-	-	-	-	✓
Strand 6	-	-	-	-	-	-	✓
Strand 4	-	-	-	-	-	-	✓

Table 9-4 Broken strand identification: End 'B' (Far end)

Broken strand (in the order of cut)	Wire cut 1	Wire cut 2	Wire cut 3	Wire cut 4	Wire cut 5	Wire cut 6	Wire cut 7
Strand 2	✗	✗	✗	✗	✗	✗	✓
Strand 3	✓	✓	✓	✓	✓	✓	✓
Strand 8	✗	✓	✓	✓	✓	✓	✓
Strand 11	✗	✗	✓	✓	✓	✓	✓
Strand 7	✗	✓	✓	✓	✗	✓	✓
Strand 12	✗	✗	✗	✗	✗	✗	✓
Strand 5	-	-	-	-	-	-	✓
Strand 1	-	-	-	-	-	-	✓
Strand 9	-	-	-	-	-	-	✓
Strand 10	-	-	-	-	-	-	✓
Strand 6	-	-	-	-	-	-	✗
Strand 4	-	-	-	-	-	-	✓

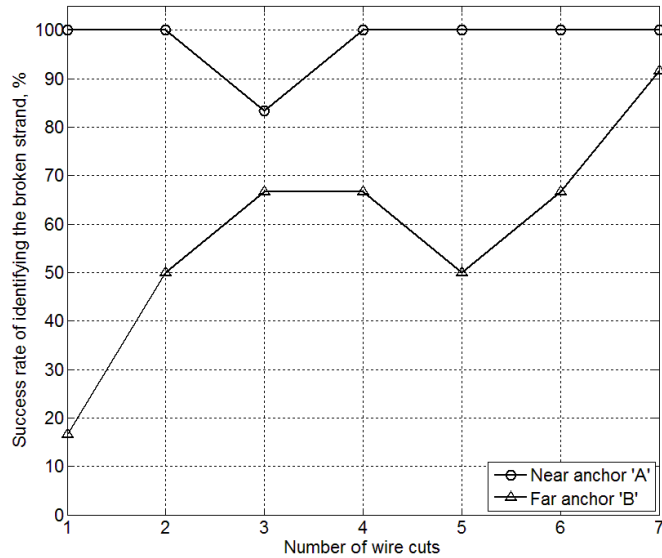


Figure 9-39 Success rate of the proposed model (Section 6.3) identifying the broken strand

The performance of the model has been also tested with reduced number of sensors: two configurations with six sensors and another two configurations with three sensors, in which strain gages were placed only on selected radial lines (the second and fourth adjacent radial lines, respectively). Figure 9-40a demonstrates a six-sensor layout for which the mean strain change per sensor at the near (anchor 'A') and far (anchor 'B') anchor are shown in Figure 9-40b and Figure 9-40c, respectively. As illustrated by these plots, significant strain change occurred even after one wire break near the anchor as well as after few wire breaks far from anchor, which indicates the detectability of these breakage events. However, as expected, the success rate of identifying the broken strand (Figure 9-40d) for this six-sensor arrangement decreases compared to that for the 12-sensor layout shown earlier in Figure 9-39. The success rate is nevertheless still quite high for multiple wire breaks occurring near the anchor. Similarly, another arrangement with six sensors and the performance of the monitoring algorithm with this configuration is illustrated in Figure 9-41. Two other configurations with three sensors have been considered (Figure 9-42 and Figure 9-43) and, as expected, lower success rates have been found compared to the six- and 12-sensor arrays.

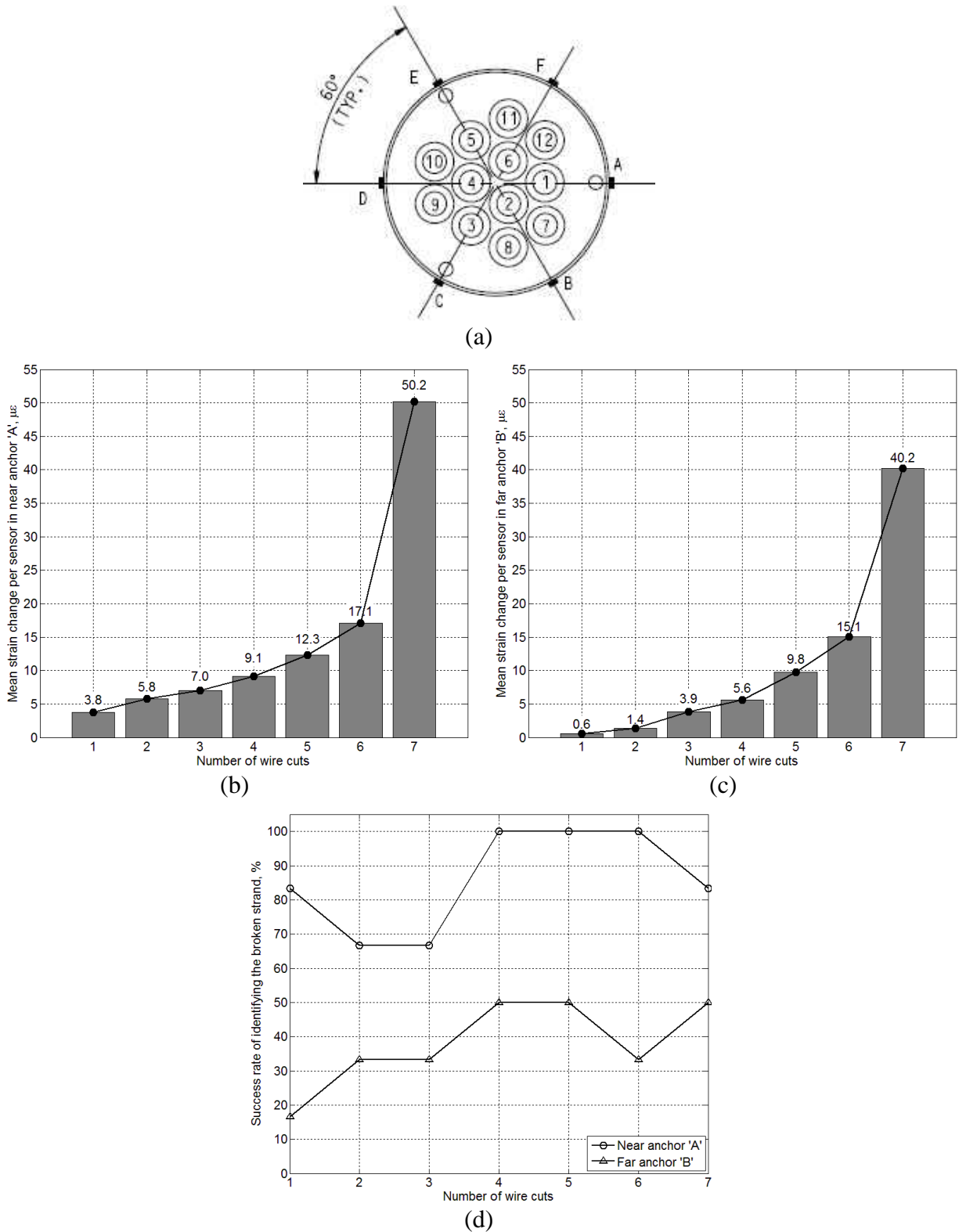
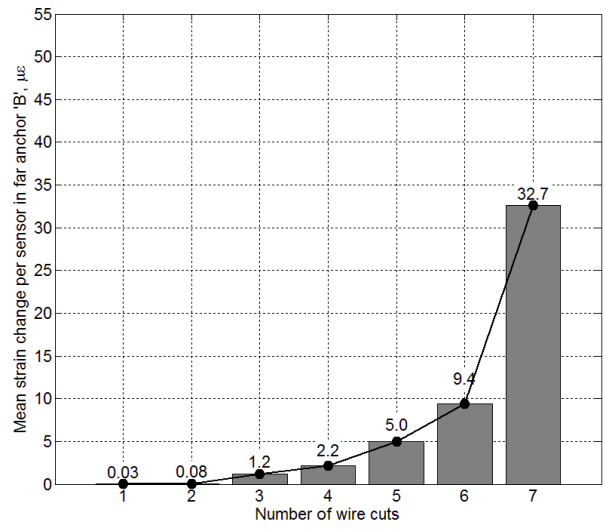
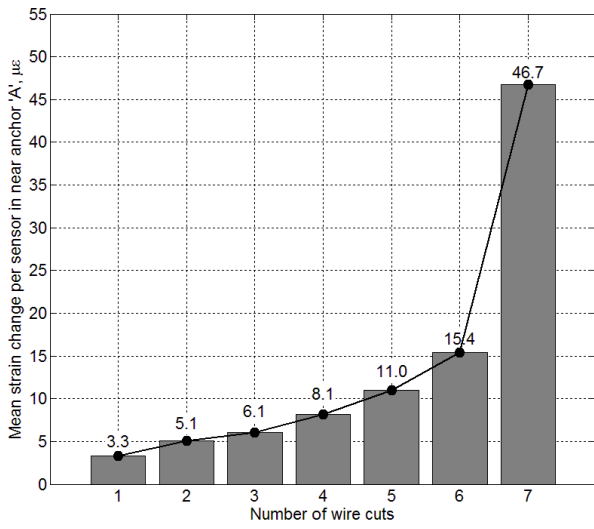
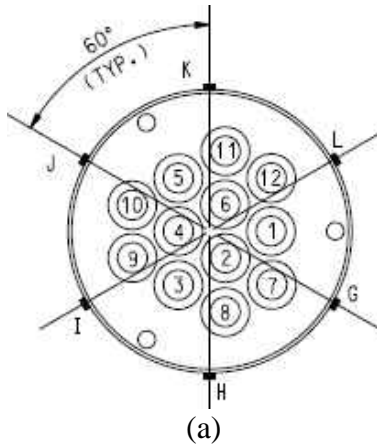
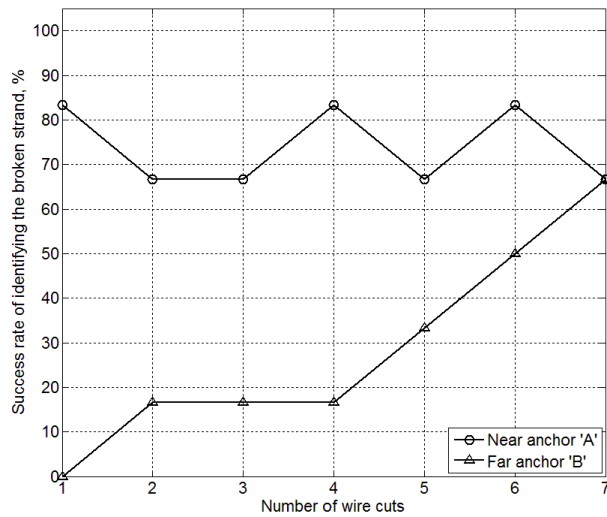


Figure 9-40 Performance of the algorithm with six sensors: (a) sensor layout; (b) strain change in near anchor 'A' for the first strand cut; (c) strain change in far anchor 'B' for the first strand cut; (d) success rate for all strand cuts



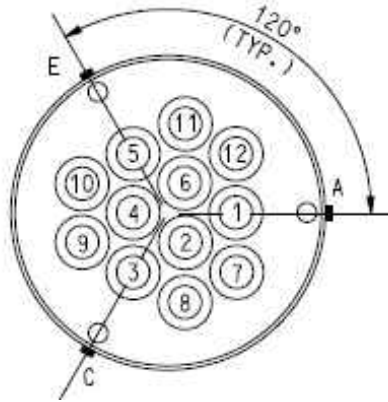
(b)

(c)

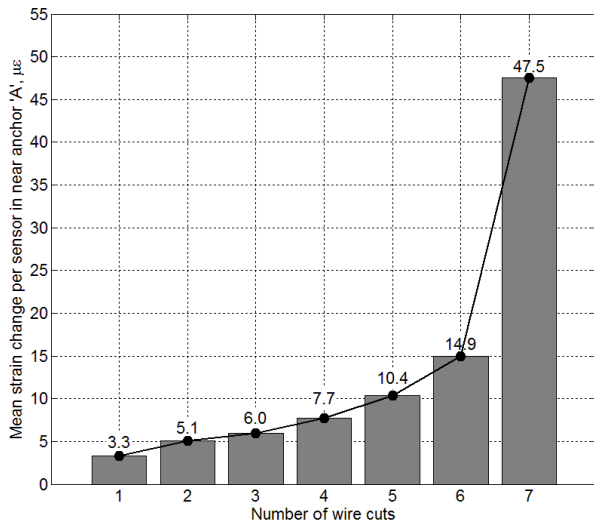


(d)

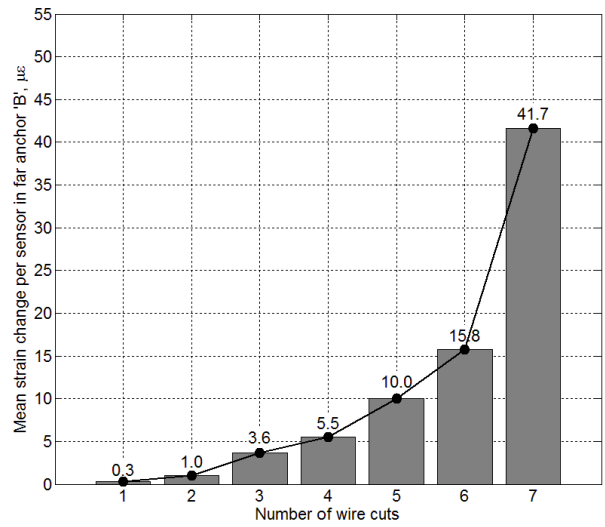
Figure 9-41 Performance of the algorithm with six sensors: (a) sensor layout; (b) strain change in near anchor 'A' for the first strand cut; (c) strain change in far anchor 'B' for the first strand cut; (d) success rate for all strand cuts



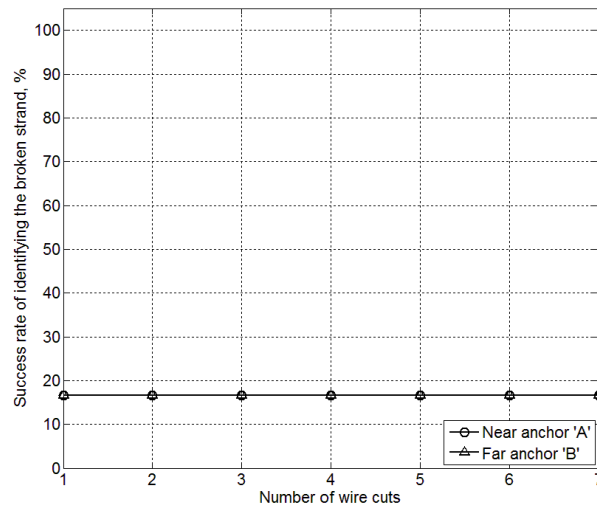
(a)



(b)



(c)



(d)

Figure 9-42 Performance of the algorithm with three sensors: (a) sensor layout; (b) strain change in near anchor 'A' for the first strand cut; (c) strain change in far anchor 'B' for the first strand cut; (d) success rate for all strand cuts

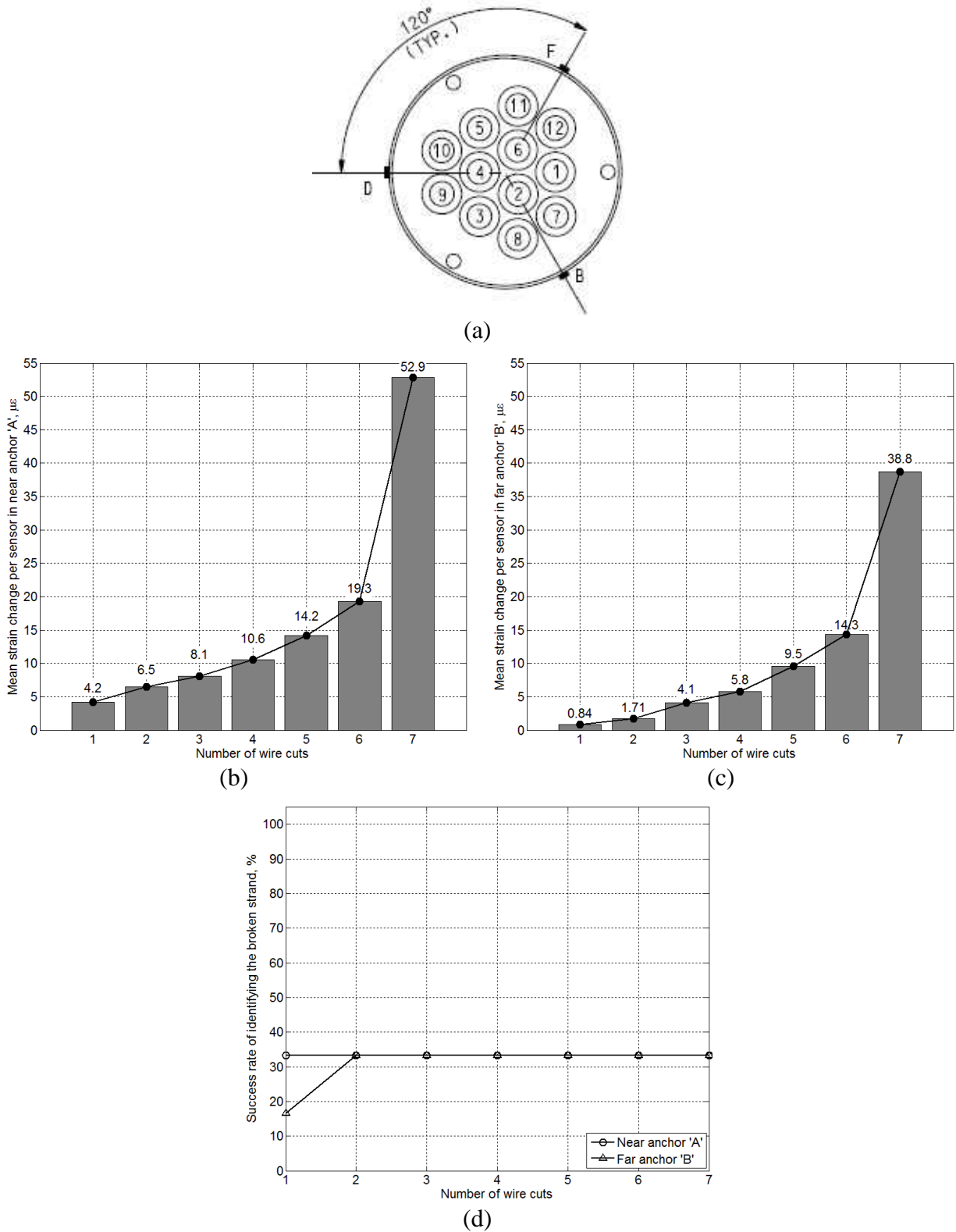


Figure 9-43 Performance of the algorithm with three sensors: (a) sensor layout; (b) strain change in near anchor 'A' for the first strand cut; (c) strain change in far anchor 'B' for the first strand cut; (d) success rate for all strand cuts

A scenario with a malfunctioning sensor (gauge 'C') has also been considered and its impact on the breakage detectability as well as broken strand identification has been analyzed. As expected, the algorithm failed to identify the broken strand 3 (the nearest strand from the lost gauge 'C'), reducing the overall success rate of broken strand identification (Figure 9-44d). However, the identification of other strands remained unaffected. In addition, although the mean strain change per sensor decreased (because the closest sensor to broken strand 3 was lost), the magnitudes of strain change were still significant ($5.3 \mu\epsilon$ per sensor for one wire cut) to detect the breakage events.

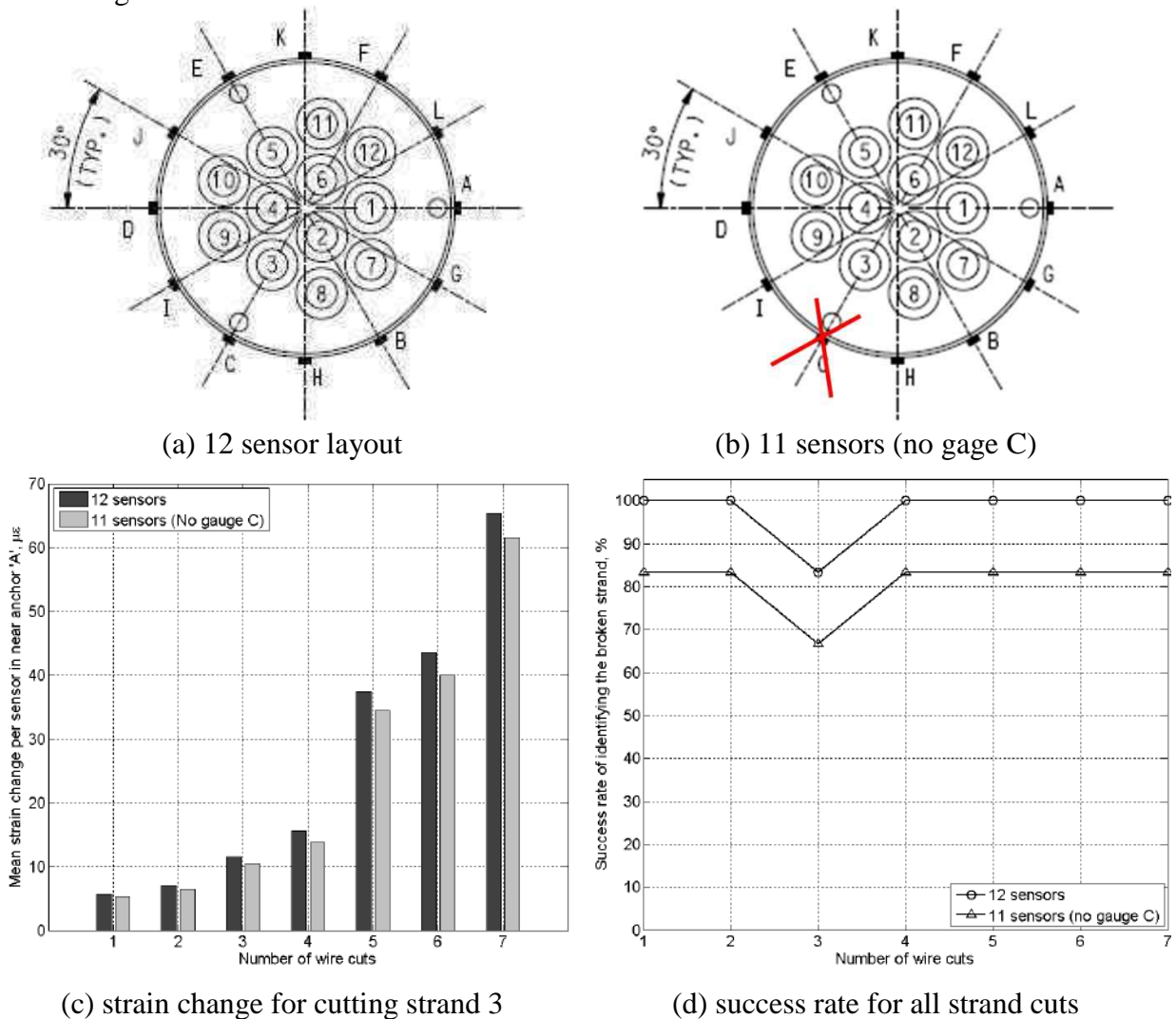


Figure 9-44 Performance of the algorithm with one broken sensor

9.4 Summary

Multiple laboratory experiments with full-size specimens have been conducted to investigate the detectability of wire breaks by monitoring the anchor strain. The experiments included both internal and external tendons with deviated tendon profile commonly practiced in post-tensioned bridge constructions. As expected, the test with bonded tendon showed no anchor response, while the tests with unbonded tendons exhibited significant strain change in anchors

after a breakage event. Strands were cut at different locations along the tendon length to examine the detectability of wire breaks occurring away from anchors. Although in some cases small strain changes were observed after the first wire cut away from the anchor, the strain change in general was quite significant for multiple wire cuts and even for one wire cut near the anchor. The performance of the broken strand identification algorithm has been tested with the experimental data and was found effective with a success rate over 90 % in all monitoring cases. In addition to the arrangement with minimum number of sensors required by the model, several layouts with fewer sensors have also been examined. Although the success rates of broken strand identification reduced because of using fewer-than-minimum sensors, most of the breakages were still detectable by the mean strain change per sensor.

10 Summary and Conclusions

Analytical and experimental investigations were performed to develop an algorithm that can be used to detect, locate, and quantify tendon damage by monitoring the strain distribution in the wedge plates of the anchors. Because unbonded tendons are connected to the structure only through deviators and end anchorages, the anchor heads are normally under high prestressing load. A wire break in the strand results in prestress loss and consequently, the strain distribution in the wedge plate varies from the unbroken state. This variation of strain field has been used to detect the wire breakage.

The algorithm was first investigated using a finite-element model calibrated with experimental data from a seven-strand anchor head. The model accounted for plasticity, large displacement, and other contact non-linearity. To account for the contact problem originating from the interactions of wedge-anchor head and anchor head-anchor plate interfaces, the FE model has been calibrated with friction coefficients of 0.015 and 0.1, respectively.

FE analysis results of a 19-strand wedge plate were used to demonstrate use of the algorithm. To locate the broken strand, damage indices were calculated for the candidate strands by considering the combined effect of the strain variations at monitoring points and their true distances from the respective wedge locations. The candidate strand group was selected by identifying the strand layer where the damage had occurred, and finally, the strand associated with the maximum index is identified as the broken strand. Monte Carlo simulations were used in a sensitivity study of measurement errors due to gage misalignment, transverse sensitivity of gages, fabrication fault, or differential temperature at monitoring locations on wedge plates to examine the robustness of the model. The proposed model allows an efficient data processing algorithm and the adoption of an automated monitoring package for breakage detection. In addition, it overcomes many of the challenges faced by the available approaches through the use of low-cost sensors and conventional data acquisition, minimal accessibility requirement, easy instrumentation, sensor installation, and replacement. The following specific conclusions are noted:

- The anchorage region near the broken strand is more affected by a wire break compared to other regions, which results in differential strain variation among the monitoring points (strain gage locations) around the wedge plate perimeter.
- Because of proximity to the monitoring points, a larger strain drop occurs for breakages on the outer layer strands in contrast to the inner layers.
- The magnitude of strain-change increases with the number of wire breaks, indicating the severity of damage.
- Axial strain in the wedge plate was found to be the most sensitive strain to wire breakage.
- In experimental work on the unraveling of a single wire from a strand, confined strands lost less force due to a wire break than a bare strand even under minimal radial pressure.
- Wire breaks in outer strands were found detectable in the presence of higher measurement errors compared to the inner strands.
- The AE system successfully captured wire breakage events in controlled laboratory conditions on relatively small bridge girders. Field tests should be conducted, however, on full-scale bridge elements to confirm its performance in practical conditions in the presence of environmental and traffic noise.

11 Future Research

11.1 *Damage Parameters and Thresholds Adjustment*

Although the damage detection model performed well with the proposed set of parameters and thresholds, additional investigation is necessary to assess the in-field measurement uncertainties. An estimation of noise along with differential temperature and wedge seating on a fully-loaded anchor head, and the effects of traffic and other environmental loads on the measured strains would be required to adjust the individual parameters and thresholds associated with the current model. Moreover, the given thresholds are applicable only for a specific anchor type (19-strand anchors); the possibility of achieving a generalized group of thresholds could be explored.

11.2 *Durability Enhancement of Strain Sensors*

Standard foil strain gages (or gages) have been used in the experiments conducted in this research. Considering the operating temperature range and other environmental factors, a detailed investigation on gage durability and protection is necessary for long-term in-field implementation. Alternative sensor options for monitoring the anchor strains could also be sought. A wireless smart sensing system with preinstalled sensor array and online data streaming capability could be a potential research direction for transforming the existing monitoring practices of unbonded PT bridges.

11.3 *Model Improvement*

The research presented herein primarily considers a straight strand with helical wires under an external load applied along the strand axis. Further investigation is required on simulating wire breaks in a deviated strand under a realistic radial pressure in addition to the axial tension. Wire breakage in a multi-strand tendon would be interesting as well to obtain a more practical representation of interaction of the broken wire with the surrounding strands and its effects on overall response and recovery length. Moreover, the anchorage and strand models have been analyzed separately; an effort to combine these models would more accurately simulate the effects of wire breaks on anchor strain distribution.

11.4 *Sensor Arrangement Optimization*

In this research, the minimum number and placement of strain gages on a wedge plate was devised based on the wedge plate pattern with the constraint of minimizing the wedge-sensor distance. Specifically, a sensor was placed on the circumferential surface of the wedge plate where its perimeter intersects the radial line connecting the center of a wedge and the wedge plate; whereas the axial location was chosen where the maximum strain was expected under prestressing force (from FE models of anchors). In addition, the breakage detectability has also been tested with fewer than the minimum recommended sensors. As expected, the study showed that detecting a break event requires fewer sensors than identifying the broken strand. Similarly, detecting the damage after an entire strand break requires fewer sensors than detecting a wire break. Further study is necessary on developing a selection array (sensor layout options), which would allow the maintenance office to select the appropriate layout based on the structural evaluation and redundancy of a given bridge.

11.5 Investigation on Additional Damage Indicators

The observation on frequency shifts with successive wire breaks in Chapter 6 and Chapter 7 appears to be promising for strand breakage detection; however, more investigation is necessary to determine its feasibility as a potential wire break detection criterion. This approach can be combined with the strain-based method, either using independent sensors or sharing the same sensor array, which would increase its reliability and more effectively filter out the effects of non-breakage events.

11.6 In-field Deployment

The analytical and experimental results show promise for the in situ practicality of this monitoring approach. However, proven full-scale implementations are required before this framework may be widely implemented. A rigorous statistical analysis should be developed and applied to filter out the effects of non-breakage events. Moreover, the reference strains will also require adjustments over time to account for time-dependent losses, such as relaxation of the steel strands. Furthermore, field verification tests are required to assess its functional performance, practical integration, long-term weathering effects, and other challenges associated with in situ implementation.

References

- AASHTO. (2010). "AASHTO LRFD Bridge Design Specifications." 5th Ed. Washington, DC.
- Achenbach, J. (2012). Wave propagation in elastic solids (Vol. 16). Elsevier.
- ACI. (1998). "Corrosion and repair of unbonded single strand tendons." *ACI 423.4R-98*, Farmington Hills, MI.
- ASTM. (2006). "Standard specification for steel strand, uncoated sevenwire for prestressed concrete." *A416*, West Conshohocken, PA.
- Bartoli, I., Salamone, S., Phillips, R., Lanza di Scalea, F., and Sikorsky, C. S. (2011). "Use of interwire ultrasonic leakage to quantify loss of prestress in multiwire tendons." *J. Eng. Mech.*, 10.1061/(ASCE)EM.1943-7889.0000227, 324–333.
- Bastien, J., Marceau, D., Fafard, M., and Chabert, A. (1996). "Experimental and numerical study of multi-strands wedge anchor heads." *Proc., Symp. on Post-Tensioned Concrete Structures*, Concrete Society, Slough, U.K., 695–704.
- Bastien, J., Marceau, D., Fafard, M., and Ganz, H. R. (2007). "Use of FEA for design of posttensioning anchor head." *J. Bridge Eng.*, 10.1061/(ASCE)1084-0702(2007)12:2(194), 194–204.
- Bhalla, S. and Kiong Soh, C. (2003). Structural impedance based damage diagnosis by piezo-transducers. *Earthquake Engineering & Structural Dynamics*, 32(12), 1897-1916.
- Chacos, G. P. (1993). Wedge forces on post-tensioning strand anchors. PTI–Post-Tensioned Institute: Technical Notes, (2).
- Chang, P. C., Flatau, A., and Liu, S. C. (2003). "Review paper: Health monitoring of civil infrastructure." *Struct. Health Monit.*, 2(3), 257–267.
- Chaplin, CR, and Tantrum, NRH (1985). "The influence of wire break distribution on strength." Organisation Internationale pour l'Etude de l'Endurance des Cables (OIPEEC), Round Table Conference, NEL Glasgow.
- Chaplin, C. R. (1995). "Failure mechanisms in wire ropes." *Engineering failure analysis*, 2(1), 45-57.
- Chen, H.-L. R., and Wissawapaisal, K. (2001). "Measurement of tensile forces in a seven-wire prestressing strand using stress waves." *J. Eng. Mech.*, 10.1061/(ASCE)0733-9399(2001)127:6(599), 599–606.
- Chiang, Y. J. (1996). "Characterizing simple-stranded wire cables under axial loading." *Finite elements in analysis and design*, 24(2), 49-66.

- Chien, C. H. and Costello, G. A. (1985). "Effective length of a fractured wire in wire rope." *Journal of engineering mechanics*, 111(7), 952-961.
- Costello, G. A. (1990). "Theory of wire rope." New York: Springer-Verlag.
- Costello, G. A. and Phillips, J. W. (1976). "Effective modulus of twisted wire cables." *Journal of the Engineering Mechanics Division*, 102(1), 171-181.
- Cullington, D. W., MacNeil, D., Paulson, P., and Elliott, J. (2001). "Continuous acoustic monitoring of grouted post-tensioned concrete bridges." *NDT Int.*, 34(5), 95–105.
- Simulia Corporation. (2012), "Abaqus 6.12 Documentation." Dassault Systemes.
- Davidsson, W. (1955). "Investigation and calculation of the remaining tensile strength in wire ropes with broken wires."
- Della Vedova, M., and Elsener, B. (2006). "Enhanced durability, quality control and monitoring of electrically isolated tendons." *Proc., 2nd Int. fib Congress*, Vol. 5, Naples, Italy.
- Doebling, S. W., Farrar, C. R., Prime, M. B., and Shevitz, D. W. (1996). "Damage identification and health monitoring of structural and mechanical systems from changes in their vibration characteristics: A literature review." *Rep. LA-13070-MS*, Los Alamos National Laboratory, Los Alamos, NM.
- Edwards, A. T. (2000). "Comparison of Strain Gage and Fiber Optic Sensors On A Sting Balance In A Supersonic Wind Tunnel." Masters Thesis, Virginia Polytechnic Institute and State University, Blacksburg, Virginia.
- Elata, D., Eshkenazy, R., and Weiss, M. P. (2004). "The mechanical behavior of a wire rope with an independent wire rope core." *International Journal of Solids and Structures*, 41(5), 1157-1172.
- Elsener, B. (2008). "Monitoring of electrically isolated post-tensioning tendons." *Tailor made concrete structures*, Chapter 42, J. C. Walraven and D. Stoelhorst, eds., Taylor & Francis, London, 231–236.
- Erdönmez, C. and Imrak, C. E. (2009). "Modeling and numerical analysis of the wire strand." *Journal of Naval Science and Engineering*, 5(1), 30-38.
- Feyrer, K. (2007). "Wire ropes." Berlin: Springer-Verlag Berlin Heidelberg.
- Fontanari, V., Benedetti, M., and Monelli, B. D. (2015). "Elasto-plastic behavior of a Warrington-Seale rope: Experimental analysis and finite element modeling." *Engineering Structures*, 82, 113-120.
- Fontanari, V., Bulf, U., and Benedetti, M. (2005). "Numerical analysis of the rolling process of shaped wires for locked steel ropes." *Journal of materials processing technology*, 170(1), 97-107.

- Fricker, S., and Vogel, T. (2007). "Site installation and testing of a continuous acoustic monitoring." *Construct. Build. Mater.*, 21(3), 501–510.
- Ghorbanpoor, A., Borchelt, R., Edwards, M., and Abdel Salam, E. (2000). "Magnetic-based NDE of prestressed and post-tensioned concrete members—The MFL system." *Rep. No. FHWA-RD-00-026*, U.S. DOT, Federal Highway Administration (FHWA), Washington, DC.
- Gjelsvik, A. (1991). "Development length for single wire in suspension bridge cable." *Journal of Structural Engineering*, 117(4), 1189-1200.
- Giurgiutiu, V. and Zagrai, A. N. (2000). Characterization of piezoelectric wafer active sensors. *Journal of Intelligent Material Systems and Structures*, 11(12), 959-976.
- Hankus, J. (1981) "Safety factor for hoisting rope weakened by fatigue cracks in wires. Organisation Internationale pour l'Etude de l'Endurance des Cables (OIPEEC), Round Table Conference, Krakow.
- Harder, J., and Webster, N. R. (2001). "Durability of post-tensioning tendons." *Proc., 1st. FIB Workshop*, Ghent, Belgium.
- Hellier, C.J. (2001), "Handbook of Nondestructive Evaluation", *McGraw-Hill*, DOI: 10.1036/007139947X.
- Huang, X. L. and Vinogradov, O. G. (1996a). "Extension of a cable in the presence of dry friction." *Structural Engineering and Mechanics*, 4(3), 313-329.
- Huang, X., and Vinogradov, O. G. (1996b). "Dry friction losses in axially loaded cables." *Structural Engineering and Mechanics*, 4(3), 330-344.
- Imrak, C. E., Erdönmez, C., Gumussuyu, I., and Maslak, I. (2010). "On the problem of wire rope model generation with axial loading." *Mathematical and Computational Applications*, 15(2), 259-268.
- Jaeger, B. J., Sansalone, M. J., and Poston, R. W. (1996). "Detecting voids in grouted ducts of post-tensioned concrete structures using the impact echo method." *ACI Struct. J.*, 93(4), 462–473.
- Jiang, W. G., Henshall, J. L., and Walton, J. M. (2000). "A concise finite element model for three-layered straight wire rope strand." *International Journal of Mechanical Sciences*, 42(1), 63-86.
- Jiang, W. G., Warby, M. K., and Henshall, J. L. (2008). "Statically indeterminate contacts in axially loaded wire strand." *European Journal of Mechanics-A/Solids*, 27(1), 69-78.
- Jiang, W. G., Yao, M. S., and Walton, J. M. (1999). "A concise finite element model for simple straight wire rope strand." *International Journal of Mechanical Sciences*, 41(2), 143-161.

- Jimenez, G. A. (2013). "Guide for Evaluation and Repair of Unbonded Post-Tensioned Concrete Structures." *Concrete repair bulletin*, PTI DC80.3-12/ICRI 320.6.
- Jolicoeur, C. and Cardou, A. (1996). "Semi-continuous mathematical model for bending of multilayered wire strands." *Journal of engineering Mechanics*, 122(7), 643-650.
- Johnson, K. L., (1987). *Contact mechanics*. Cambridge university press.
- Kelley, G. S., "Prestress Losses in Post-Tensioned Structures," PTI Technical Note #10, Sept. 2000, 6 pp.
- Kim, J.-T., Park, J.-H., Hong, D.-S., and Park, W.-S. (2010). "Hybrid health monitoring of prestressed concrete girder bridges by sequential vibration impedance approaches." *Eng. Struct.*, 32(1), 115–128.
- Kmet, S., Stanova, E., Fedorko, G., Fabian, M., and Brodniansky, J. (2013). "Experimental investigation and finite element analysis of a four-layered spiral strand bent over a curved support." *Engineering Structures*, 57, 475-483.
- Kowalik, A. (2012). "Acoustic Monitoring on the Fred Hartman Bridge.", Bridge Division, Texas Department of Transportation, Retrieved Sept. 7, 2012 from http://ftp.dot.state.tx.us/pub/txdot-info/library/pubs/bus/bridge/hartman_acoustic_monitoring.pdf
- Kwun, H., and Bartels, K. A. (1998). "Magnetostrictive sensor technology and its applications." *Ultrasonics*, 36(1–5), 171–178.
- Kyowa Electronic Instruments (2015). "Principle of Strain Gauges." <http://www.kyowa-ei.com/>.
- Labrosse, M., Nawrocki, A., and Conway, T. (2000). "Frictional dissipation in axially loaded simple straight strands." *Journal of Engineering Mechanics*, 126(6), 641-646.
- Lanza di Scalea, F., Rizzo, P., and Seible, F. (2003). "Stress measurement and defect detection in steel strands by guided stress waves." *J. Mater. Civ. Eng.*, 10.1061/(ASCE)0899-1561(2003)15:3(219), 219–227.
- Liang, C., Sun, F. P., and Rogers, C. A. (1994). "An impedance method for dynamic analysis of active material systems." *Journal of Vibration and Acoustics*, 116(1), 120-128.
- Litewka, P. (2010). *Finite element analysis of beam-to-beam contact* (Vol. 53). Springer Science & Business Media.
- Liu, W., Hunsperger, R. G., Folliard, K., Chajes, M. J., Barot, J., and Jhaveri, D. (1999). "Detection and characterization of corrosion of bridge cables by time domain reflectometry." *Proc., SPIE: Nondestructive Evaluation of Bridges and Highways III*, S. B. Chase, ed., Vol. 3,587, Society of Photo-Optical Instrumentation Engineers (SPIE), Bellingham, WA, 28–39.

- Liu, W., Hunsperger, R.G., Chajes, M. J., Folliard, K. J., and Kunz, E. (2002). "Corrosion detection of steel cables using time domain reflectometry." *J. Mater. Civ. Eng.*, 10.1061/(ASCE)0899-1561(2002)14:3(217), 217–223.
- MacDougall, C. and Bartlett, F. M. (2003). "Tests of unbonded seven-wire tendon with broken outer wires." *ACI Structural Journal*, 100(5).
- MacDougall, C. and Bartlett, F. M. (2005). "Mechanical model for unbonded seven-wire tendon with symmetric wire breaks." *Journal of Engineering Mechanics*, 131(12), 1239-1247.
- MacDougall, C. and Bartlett, F. M. (2006). "Mechanical model for unbonded seven-wire tendon with single broken wire." *Journal of engineering mechanics*, 132(12), 1345-1353.
- Marceau, D., Bastien, J., and Fafard, M. (2001). "Experimental and numerical studies of mono-strand anchorage." *Struct. Eng. Mech.*, 12(2), 119–134.
- Mascarenas, D. L., Todd, M. D., Park, G., and Farrar, C. R. (2007). Development of an impedance-based wireless sensor node for structural health monitoring. *Smart Materials and Structures*, 16(6), 2137.
- Meirovitch, L. (1967) "Analytical methods in vibrations." Macmillan Company London, 2.
- Micro-Measurements (2015a). "Strain Gage Selection: Criteria, Procedures, Recommendations." *Tech Note TN-505-4*.
- Micro-Measurements (2015b). "Strain Gage Instrumentation." *Document No. 11048*.
- Micro-Measurements (2015c). "Noise Control in Strain Gage Measurements." *Tech Note TN-501-2*.
- Micro-Measurements (2015d). "Strain Gage Thermal Output and Gage Factor Variation with Temperature." *Tech Note TN-504-1*.
- Micro-Measurements (2015e). "Errors Due to Misalignment of Strain Gages." *Tech Note TN-511*.
- Micro-Measurements (2015f). "Errors Due to Transverse Sensitivity in Strain Gages." *Tech Note TN-509*.
- Muravin, B. (2009), "Acoustic Emission Science and Technology", *Journal of Building and Infrastructure Engineering*, Israeli Association of Engineers and Architects (originally published in Hebrew).
- Nawrocki, A. and Labrosse, M. (2000). "A finite element model for simple straight wire rope strands." *Computers & Structures*, 77(4), 345-359.
- ndt-ed.org (2013), "https://www.ndt-ed.org/EducationResources/CommunityCollege/Other%20Methods/AE/AE_Intro.php"

- Nguyen, K.-D., and Kim, J.-T. (2012). "Smart PZT-interface for wireless impedance-based prestress-loss monitoring in tendon-anchorage connection." *Smart Struct. Syst.*, 9(6), 489–504.
- Noyan, I. C., Brügger, A., Betti, R., and Clausen, B. (2010). "Measurement of strain/load transfer in parallel seven-wire strands with neutron diffraction." *Experimental mechanics*, 50(2), 265-272.
- Omega Engineering (2015). "Introduction to Strain Gages." <http://www.omega.com/>.
- Park, G., Cudney, H.H. and Inman, D.J. (2001), "Feasibility of using impedance-based damage assessment for pipeline structures", *Earthq. Eng. Struct. D.*, 30(10), 1463-1474.
- Park, G., Sohn, H., Farrar, C. and Inman, D. (2003), "Overview of piezoelectric impedance-based health monitoring and path forward." *Shock Vib.*, 35(6), 451-463.
- Parsons Brinckerhoff (2012). "Un-bonded tendon system practices for bridges in Europe".
- Phelippeau, A., Pommier, S., Tsakalagos, T., Clavel, M., and Prioul, C. (2006). "Cold drawn steel wires—processing, residual stresses and ductility—part I: metallography and finite element analyses." *Fatigue & fracture of engineering materials & structures*, 29(3), 201-207.
- Pla-Rucki, G. F., and Eberhard, M. O. (1995). "Imaging of reinforced concrete: State-of-the-art review." *J. Infrastruct. Syst.*, 10.1061/(ASCE) 1076-0342(1995)1:2(134), 134–141.
- Ramazani, M. R., Noroozi, S., Sewell, P., Khandan, R., and Cripps, B. (2013). "Using artificial neural networks and strain gauges for the determination of static loads on a thin square fully-constrained composite marine panel subjected to a large central displacement." *Insight-Non-Destructive Testing and Condition Monitoring*, 55(8), 442-448.
- Raof, M. (1991). "Wire recovery length in a helical strand under axial-fatigue loading." *International journal of fatigue*, 13(2), 127-132.
- Raof, M. and Huang, Y. P. (1992). "Wire recovery length in suspension bridge cable." *Journal of Structural Engineering*, 118(12), 3255-3267.
- Raof, M. and Kraincanic, I. (1995). "Analysis of large diameter steel ropes." *Journal of engineering mechanics*, 121(6), 667-675.
- Raof, M. and Kraincanic, I. (1998). "Determination of wire recovery length in steel cables and its practical applications." *Computers & structures*, 68(5), 445-459.
- Salamone, S., Bartoli, I., Phillips, R., Nucera, C., and Lanza di Scalea, F. (2011). "Health monitoring of prestressing tendons in posttensioned concrete bridges." *Transportation Research Record 2220*, Transportation Research Board, Washington, DC, 21–27.

- Salamone, S., Veletzos, M. J., Lanza di Scalea, F., and Restrepo, J. I. (2012). "Detection of initial yield and onset of failure in bonded posttensioned concrete beams." *J. Bridge Eng.*, 10.1061/(ASCE)BE.1943-5592.0000311, 966–974.
- Salawu, O. S. (1997). "Detection of structural damage through changes in frequency: A review." *Eng. Struct.*, 19(9), 718–723.
- Scheel, H., and Hillemeier, B. (1997). "Capacity of the remanent magnetism method to detect fractures of steel in tendons embedded in prestressed concrete." *NDT and E Int.*, 30(4), 211–216.
- Scheel, H., and Hillemeier, B. (2003). "Location of prestressing steel fractures in concrete." *J. Mater. Civ. Eng.*, 10.1061/(ASCE)0899-1561(2003)15:3(228), 228–234.
- Sideris, P., Aref, A. J., and Filiatrault, A. (2014). "Effects of anchorage hardware on the cyclic tensile response of unbonded monostrands." *PCI Journal*, 59(3).
- Stanova, E., Fedorko, G., Fabian, M., and Kmet, S. (2011a). "Computer modelling of wire strands and ropes Part I: Theory and computer implementation." *Advances in engineering software*, 42(6), 305-315.
- Stanova, E., Fedorko, G., Fabian, M., and Kmet, S. (2011b). "Computer modelling of wire strands and ropes part II: Finite element-based applications." *Advances in Engineering Software*, 42(6), 322-331.
- Sun, F.P., Chaudhry, Z., Liang, C., and Rogers, C.A. (1995). "Truss Structure Integrity Identification Using PZT Sensor–Actuator." *Journal of Intelligent Material Systems and Structures*, Vol. 6, 134–139.
- Tabatabai, H., Mehrabi, A. B., and Yen, W. P. (1998). "Bridge stay cable condition assessment using vibration measurement techniques." *Proc., SPIE: Structural Materials Technology III: An NDT Conf.*, R. D. Medlock and D. C. Laffey, eds., Vol. 3,400, Society of Photo-Optical Instrumentation Engineers (SPIE), Bellingham, WA, 194–204.
- Utting, W. S. and Jones, N. (1987a). "The response of wire rope strands to axial tensile loads—Part I. Experimental results and theoretical predictions." *International journal of mechanical sciences*, 29(9), 605-619.
- Utting, W. S. and Jones, N. (1987b). "The response of wire rope strands to axial tensile loads—Part II. Comparison of experimental results and theoretical predictions." *International journal of mechanical sciences*, 29(9), 621-636.
- Velinsky, S. A. (1985). "General nonlinear theory for complex wire rope." *International journal of mechanical sciences*, 27(7), 497-507.
- Velinsky, S. A., Anderson, G. L., and Costello, G. A. (1984). "Wire rope with complex cross sections." *Journal of Engineering Mechanics*, 110(3), 380-391.

- Waisman, H., Montoya, A., Betti, R., and Noyan, I. C. (2010). "Load transfer and recovery length in parallel wires of suspension bridge cables." *Journal of Engineering Mechanics*, 137(4), 227-237.
- Wang, X.M., Ehlers, C., and Neitzel, M. (1997). "An Analytical Investigation of Static Models of Piezoelectric Patches Attached to Beams and Plates." *Smart Materials and Structures*, Vol. 6, 204–213.
- Wang, M. L., Chen, Z. L., Koontz, S. S., and Lloyd, G. M. (2000). "Magnetoelastic permeability measurement for stress monitoring in steel tendons and cables." *Proc., SPIE: Nondestructive Evaluation of Highways, Utilities, and Pipelines IV*, A. E. Aktan and S. R. Gosselin, eds., Vol. 3995, Society of Photo-Optical Instrumentation Engineers (SPIE), Bellingham, WA, 492–500.
- Wiek, L. (1977). "The influence of broken wires on wire rope strength and discarding." In *Organisation Internationale Pour l'Etude de l'Endurance des Cables (OIPEEC)*, Round Table Conf, Luxembourg (October 1977).
- Williams, H. T., and Hulse, M. E. (1995). "From theory to experience with inspection of post-tensioned bridges." *Proc., 6th Int. Conf. on Structural Faults and Repairs*, M. C. Forde, ed., Vol. 1, Engineering Techniques, San Jose, CA, 199–202.
- Williams, H.T., Thompson, K.A.(1997), "Practical considerations of inspecting post-tensioned bridges", proceedings of the seventh international conference on structural faults and repair, Edinburgh, UK, 8 July 1997. Vol 1: Extending the life of bridges.
- Yuyama, S., Yokoyama, K., Niitani, K., Ohtsu, M., and Uomoto, T. (2007). "Detection and evaluation of failures in high-strength tendon of prestressed concrete bridges by acoustic emission." *Construct. Build. Mater.*, 21(3), 491–500.
- Zienkiewicz, O. C. and Taylor, R. L. (2005). *The finite element method for solid and structural mechanics*. Butterworth-heinemann.
- Zejli, H., Gaillet, L., Laksimi, A., and Benmedakhene, S. (2012). "Detection of the presence of broken wires in cables by acoustic emission inspection." *J. Bridge Eng.*, 10.1061/(ASCE)BE.1943-5592.0000404, 921–927.
- Zhou, W. and Tian, H. Q. (2013). "A novel finite element model for single-layered wire strand." *Journal of Central South University*, 20, 1767-1771.

Appendix A—Electro-Mechanical Impedance Testing

A preliminary experiment (Figure A-1, Figure A-3) has been performed to examine the sensitivity of electro-mechanical impedance to wire breakage. In this test, wire breakage was simulated by reducing the force in the strand. PZT patches were bonded to the end plate near to the strand chuck with electrically conductive epoxy (Figure A-4).

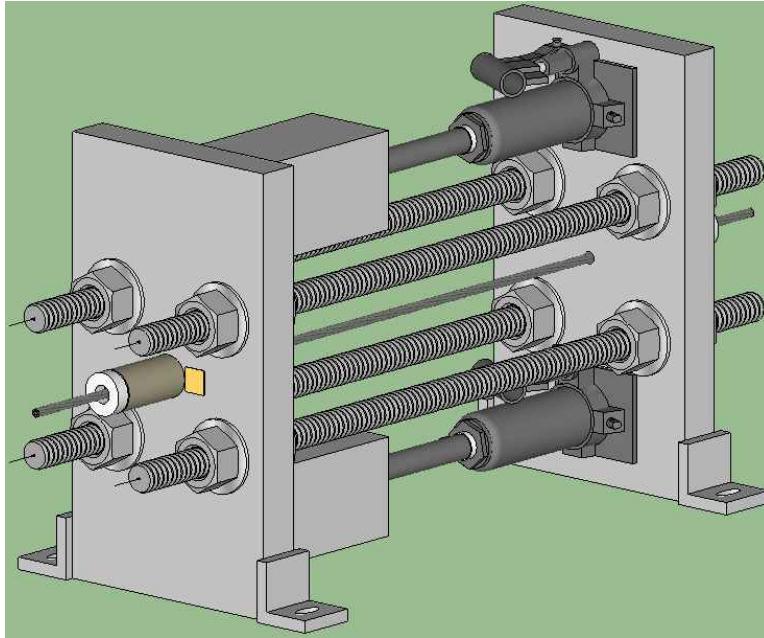


Figure A-1 EMI test setup schematic

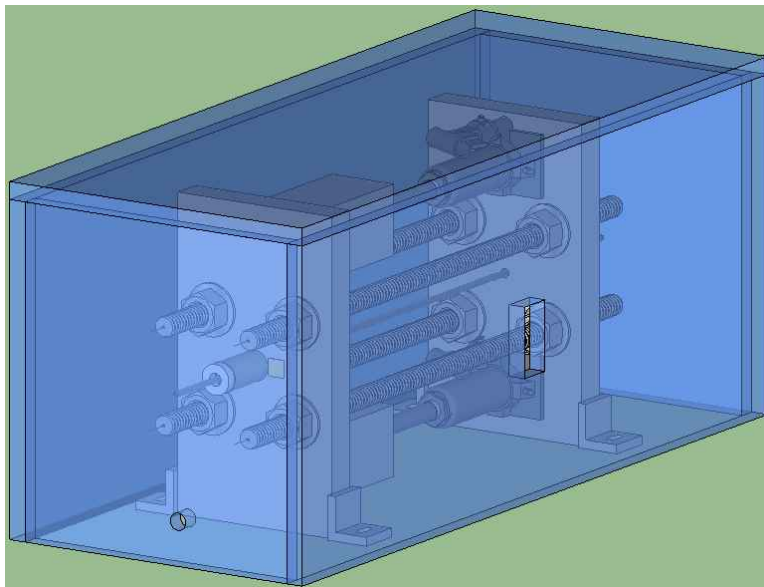


Figure A-2 EMI test setup schematic (with safety cover)

A harmonic voltage (oscillation level 25 mV) was applied to the PZT and the output impedance values (both real and imaginary part) were recorded for different strand force. The

force in the strand was adjusted by hydraulic jacks and the applied loads were measured by a load cell.

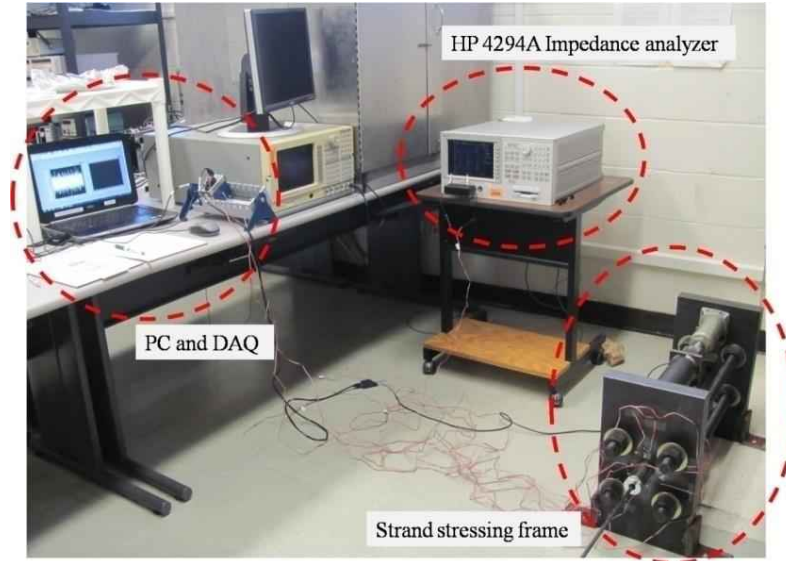


Figure A-3 EMI test setup

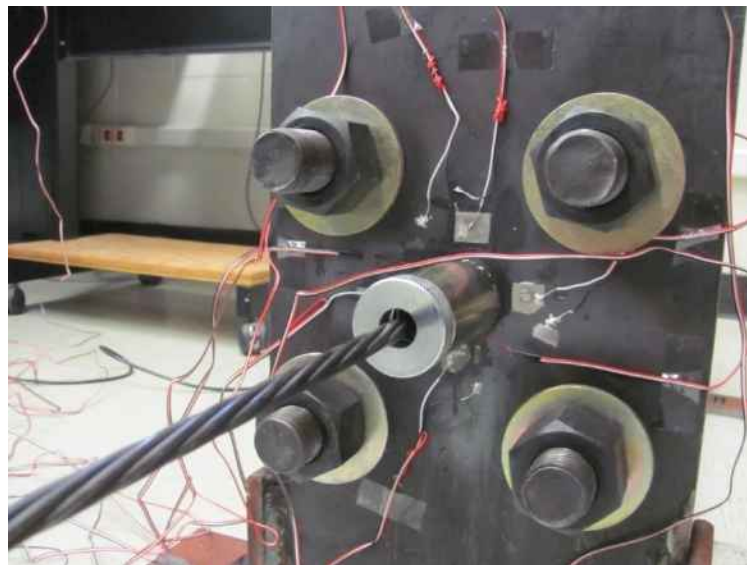


Figure A-4 PZT patches on end plate

As seen from Figure A-5, the resonances in impedance signature were observed at very high frequencies (in the order of MHz). This high frequency is due to the fact that the very low amplitude excitation induced in the thick end plate only excites localized modes of vibration. Also, the shifts of impedance signature become more evident in higher frequencies. These observations are consistent with the works available in literature (Kim et al. 2010, Part et al. 2006). Table A-1 lists the strand forces and corresponding shifts of resonant frequency and peak impedance observed at the highest resonant mode (frequency of ~80 MHz) recorded in this test.

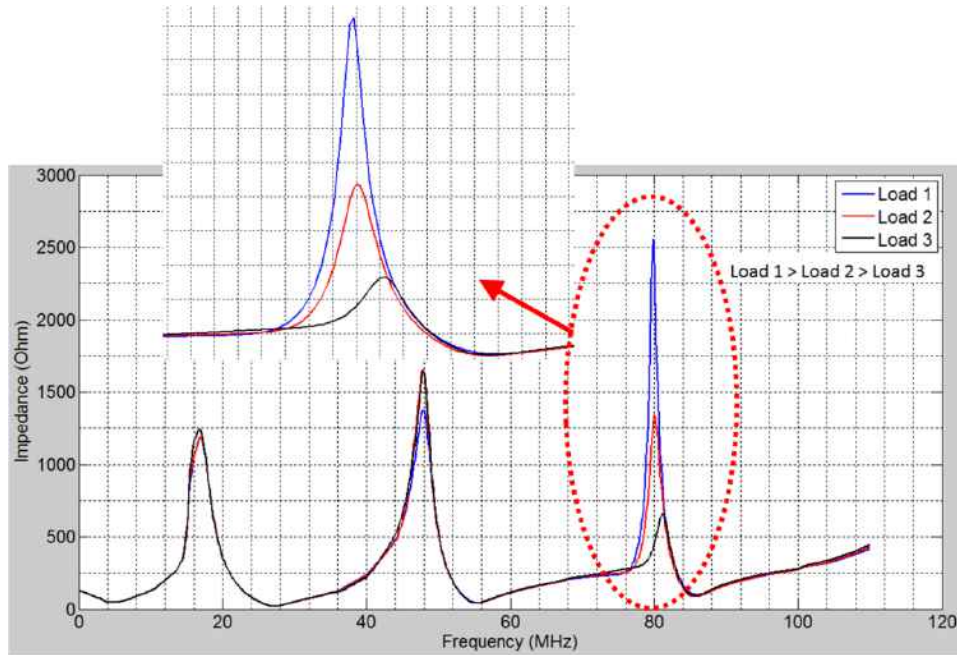


Figure A-5 EMI test results

Table A-1 Impedance analysis results

Case	Strand force		Resonant freq. (MHz)	Resonant freq. shift (MHz)	Peak impedance (Ohm)	Peak impedance shift (Ohm)
	P (lbf)	$\Delta P/P_0$ (%)				
Load 1	11570	0	79.89	0	2557	0
Load 2	9660	16.5	80.03	0.14	1342	-1215
Load 3	5770	50.1	81.13	1.24	660	-1897

Figure A-6 shows the relationship between strand force loss and shift of resonant frequency. From this relationship, the empirical equations (Equation 17) is obtained that can be used to confirm force loss due to wire breakage.

$$\frac{\Delta P}{P_0}(\%) = \frac{\Delta f_{res}}{0.023} \quad \text{Equation 17}$$

where P_0 denotes stands for the force corresponding to load 1, ΔP stands for the amount of force reduction in a subsequent measurement, $\Delta P/P_0$ is the relative loss of strand force and Δf_{res} is the associated resonant frequency shift.

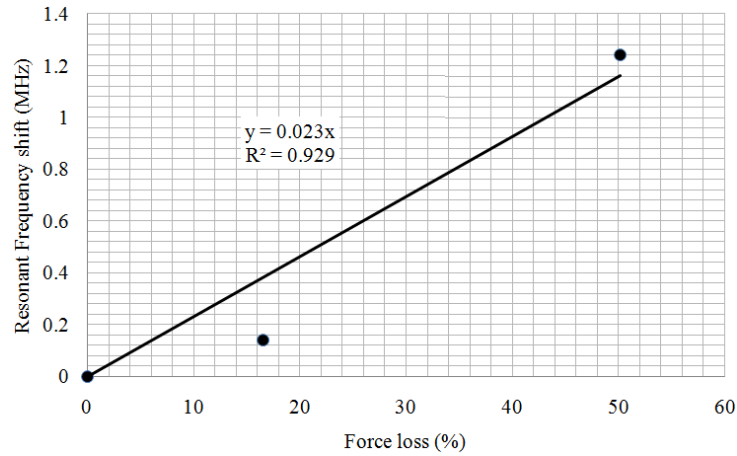


Figure A-6 Frequency shift vs force loss

Similarly, an empirical formula can be obtained based on the observed relationship between force loss and shift of peak impedance as follows –

$$\frac{\Delta P}{P_0}(\%) = -\frac{\Delta Z_{peak}}{41.33} \quad \text{Equation 18}$$

where ΔZ_{peak} represents the shift of peak impedance magnitude.

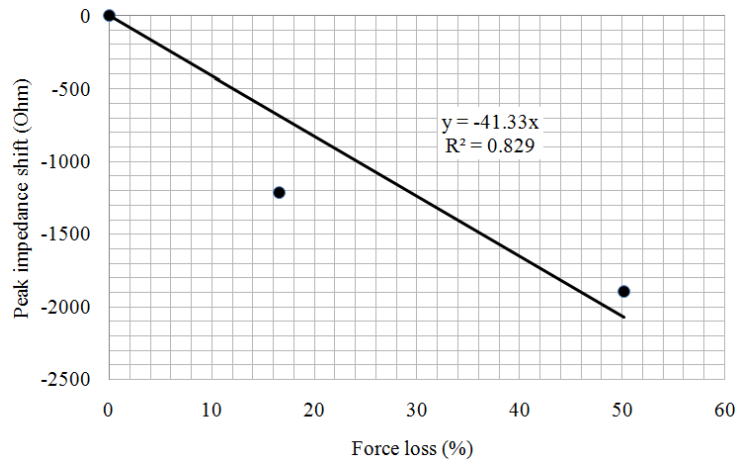


Figure A-7 Peak impedance vs force loss

It is noted that, more measurement points would be required to obtain more accurate trend lines, and thus a better estimation of frequency shift and peak impedance, than that projected from the three points (Figure A-6 and Figure A-7) in this study.

Appendix B—Detail Experimental Results: Internal Bonded Tendon

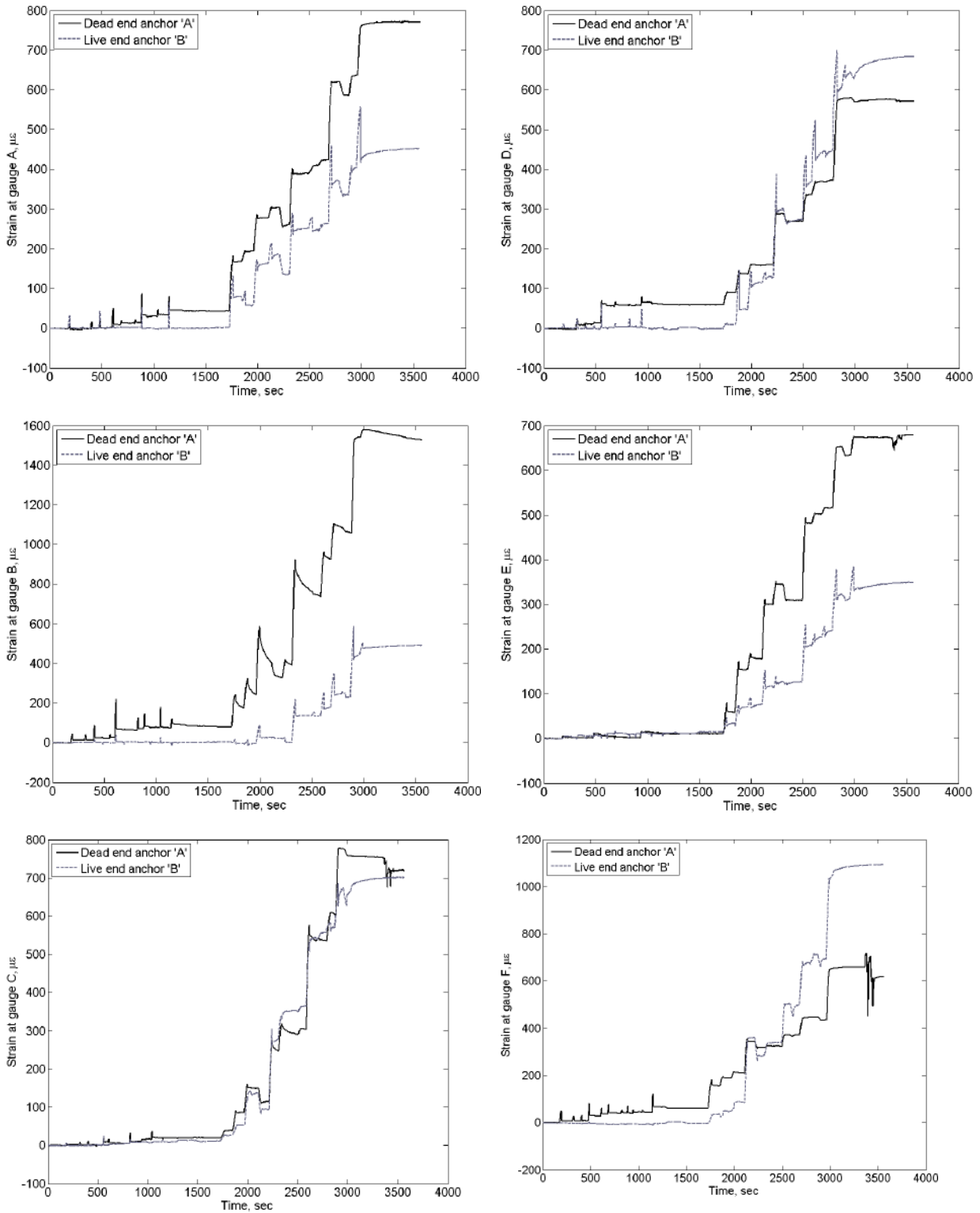


Figure B-8 Strain comparison between two anchors during stressing (gauge A-F)

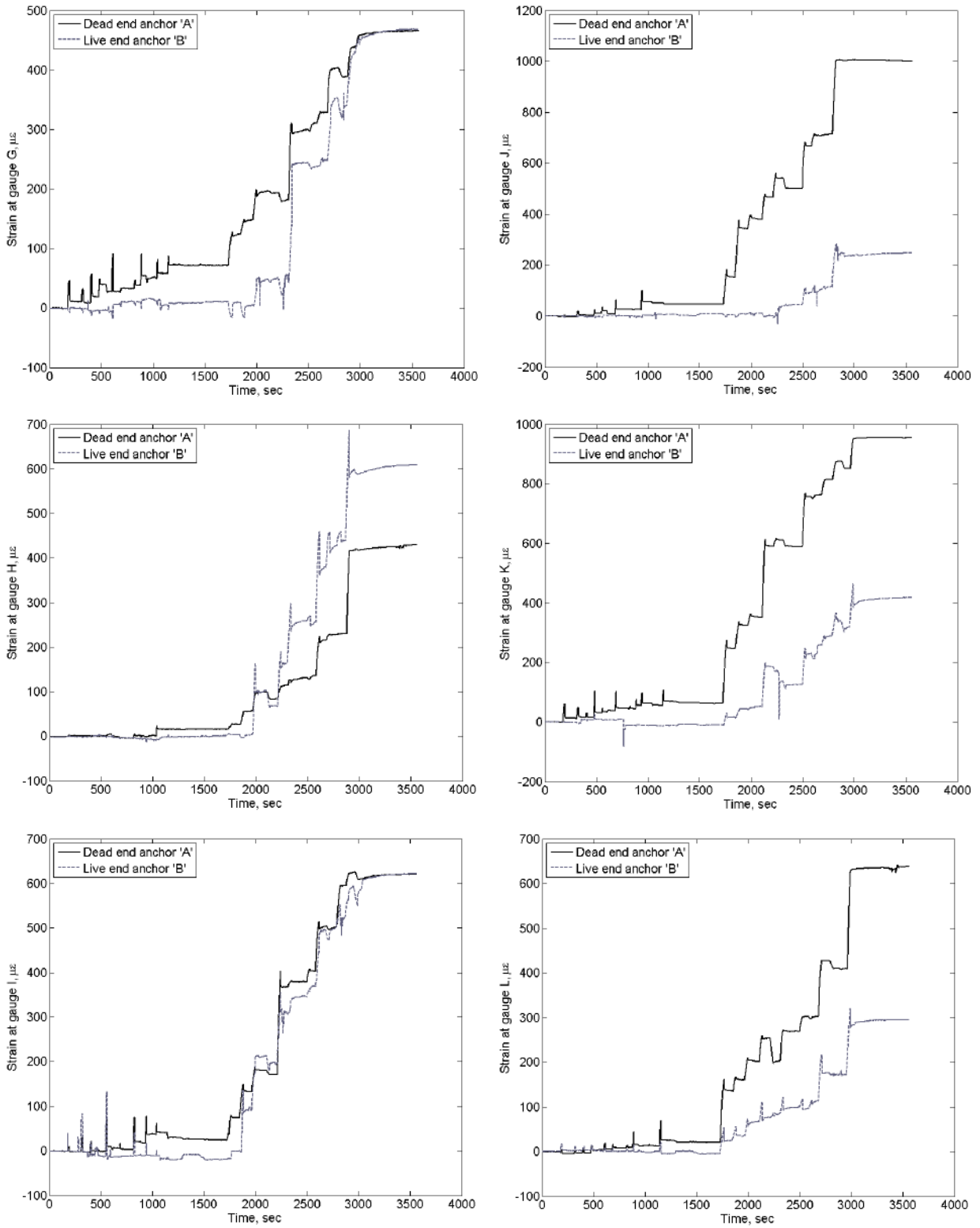


Figure B-9 Strain comparison between two anchors during stressing (gauge G-L)

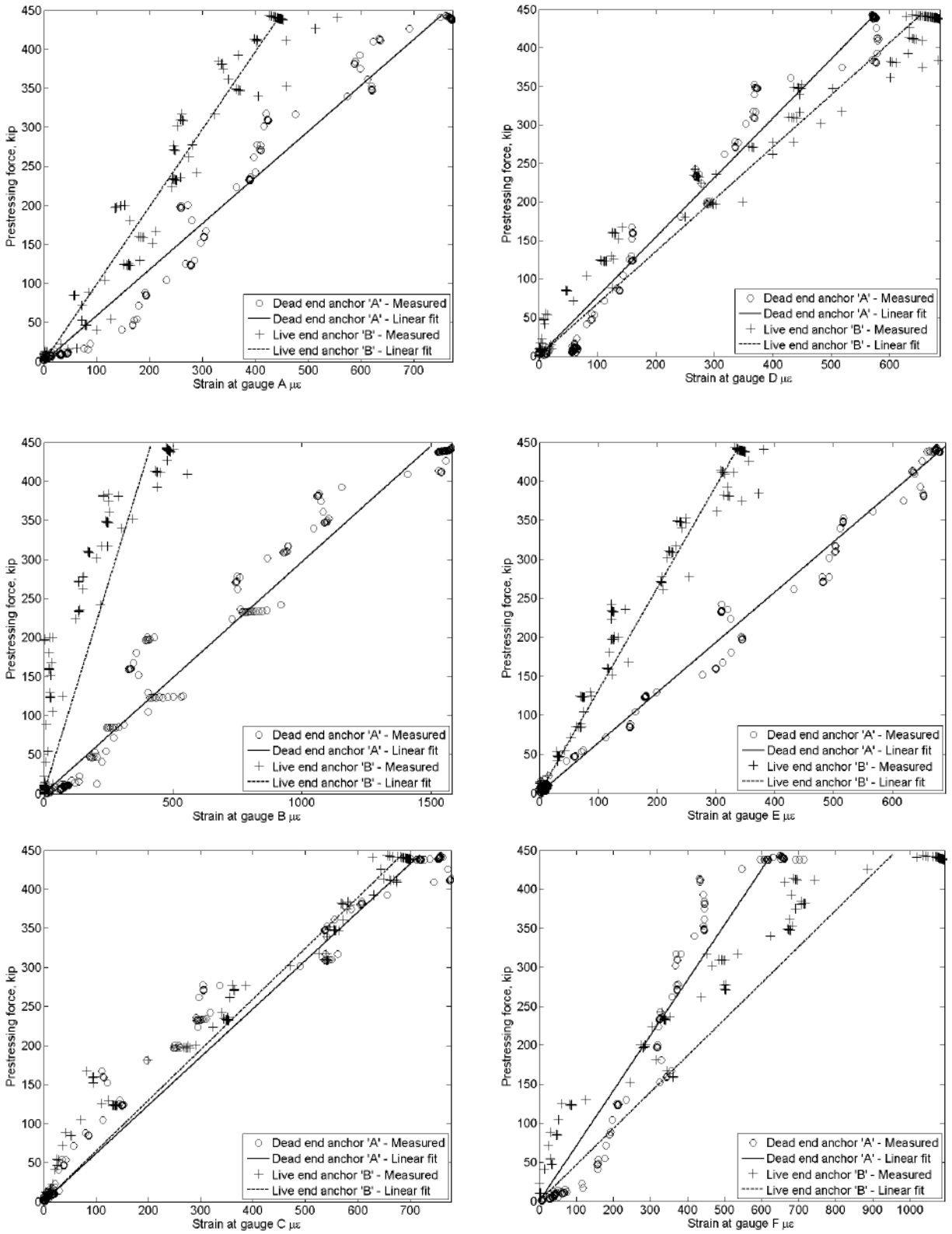


Figure B-10 Strain vs. prestressing force at two anchors during stressing (strain gage A-F)

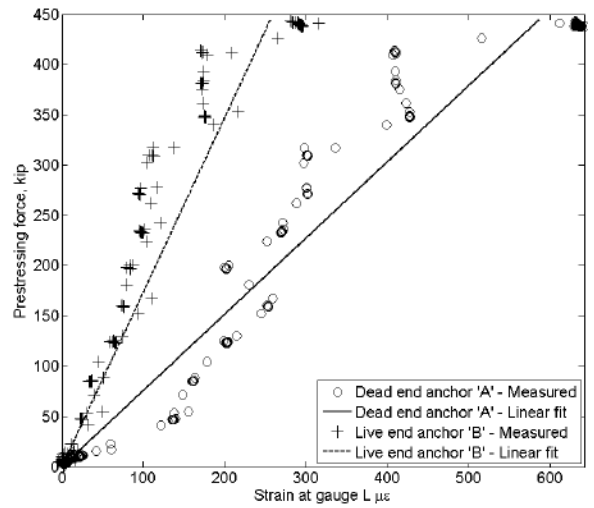
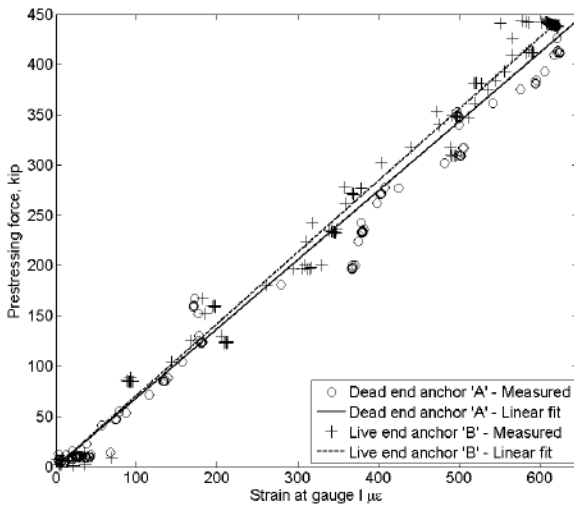
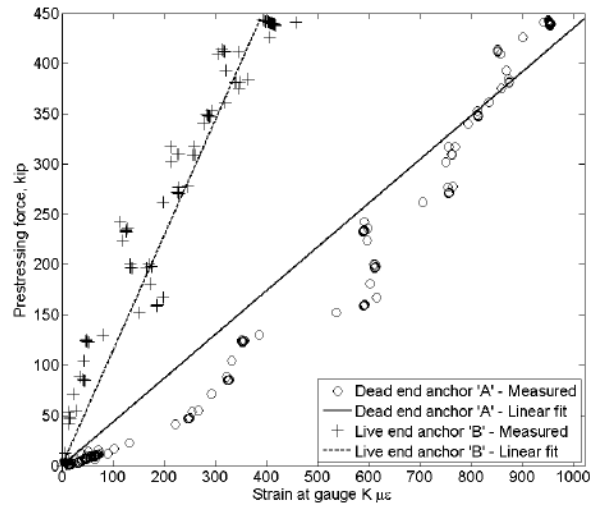
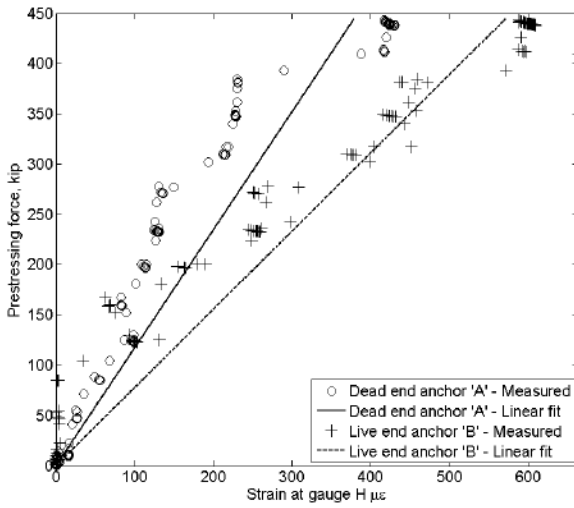
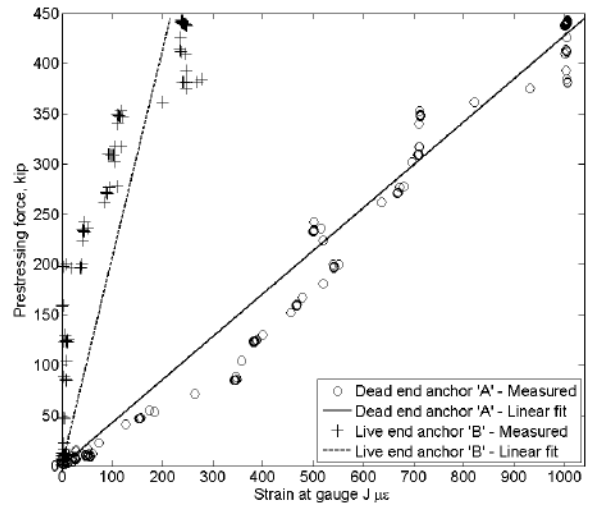
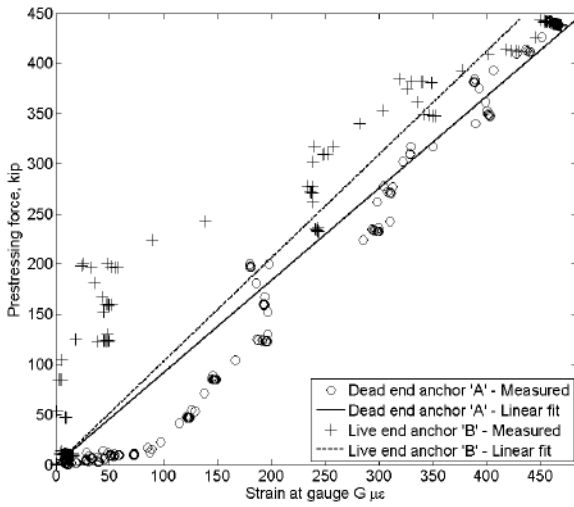


Figure B-11 Strain vs. prestressing force at two anchors during stressing (strain gage G-L)

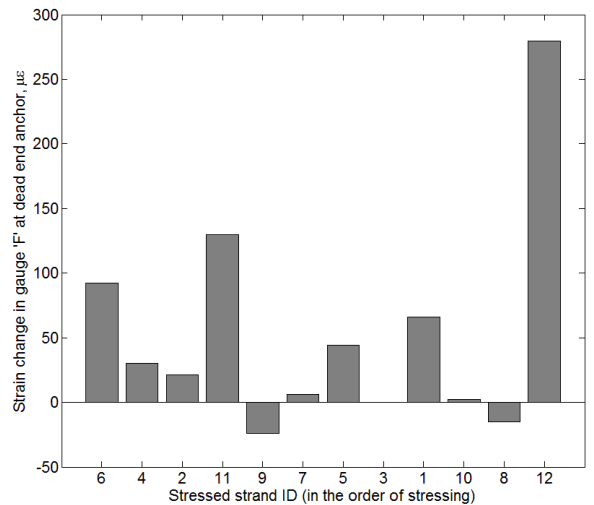
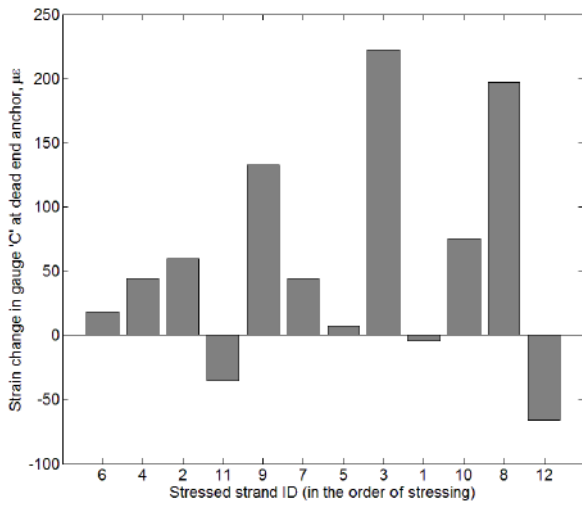
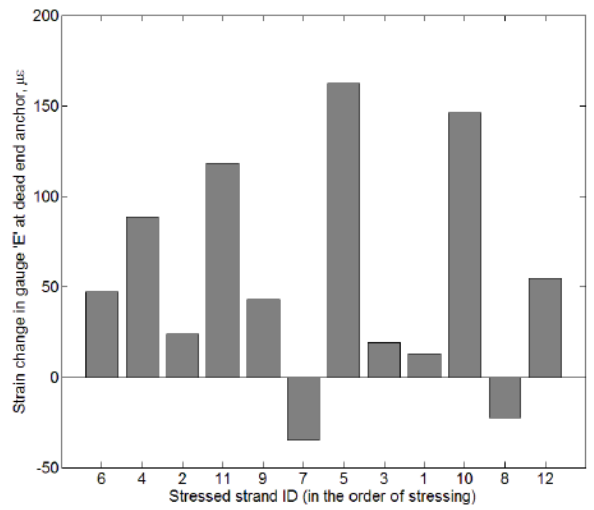
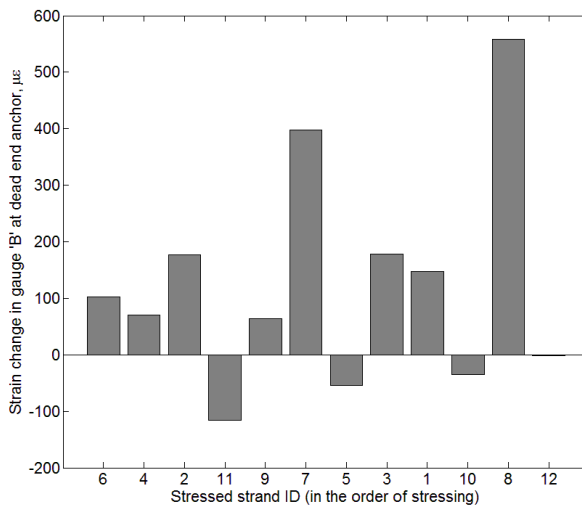
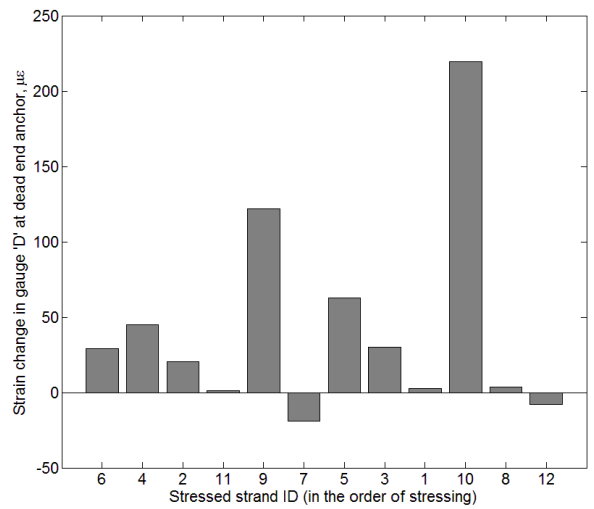
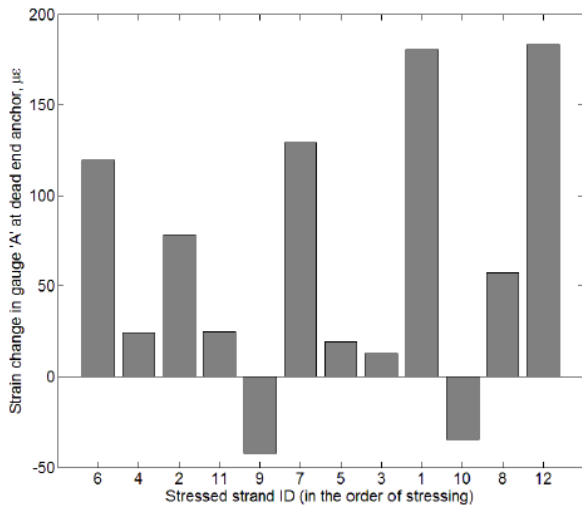


Figure B-12 Strain change in a gage with stressing of each strand (gage A-F, dead end)

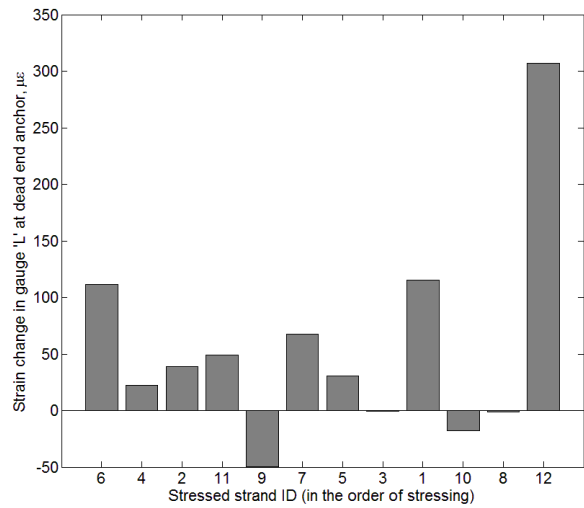
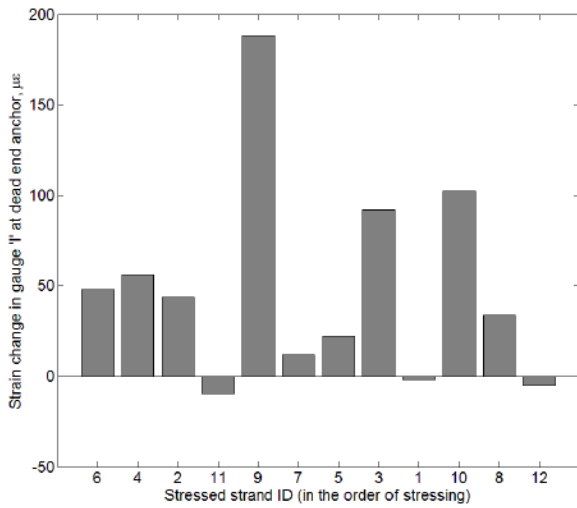
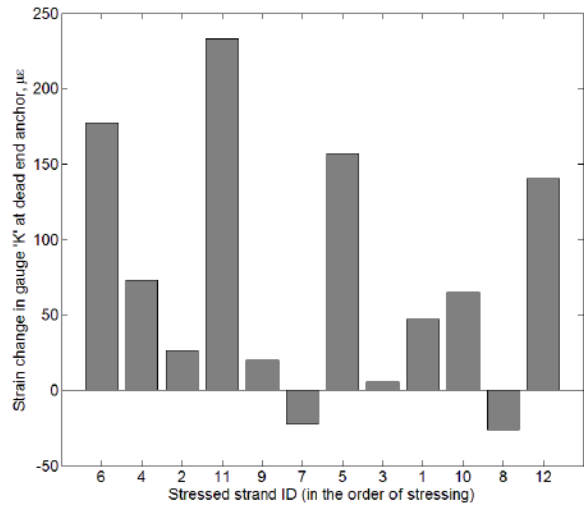
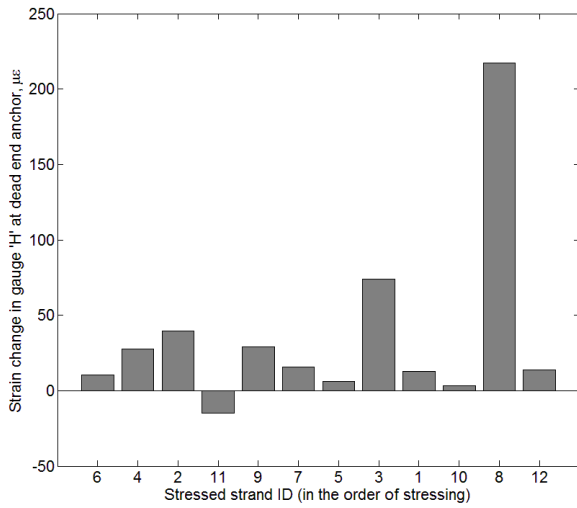
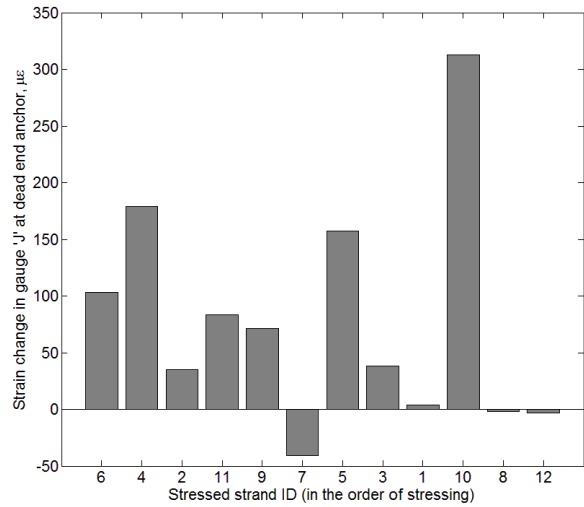
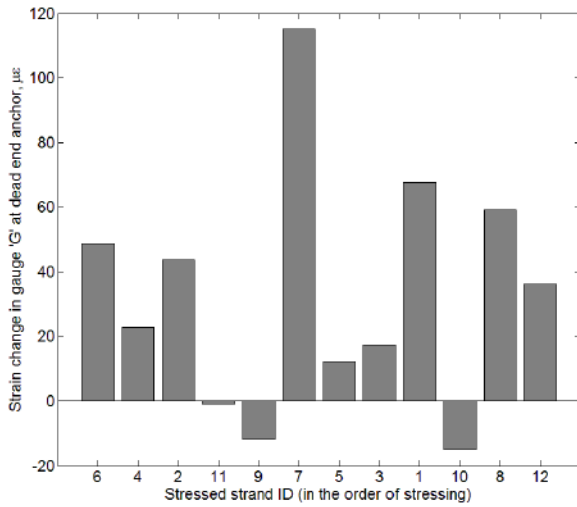


Figure B-13 Strain change in a gage with stressing of each strand (gage G-L, dead end)

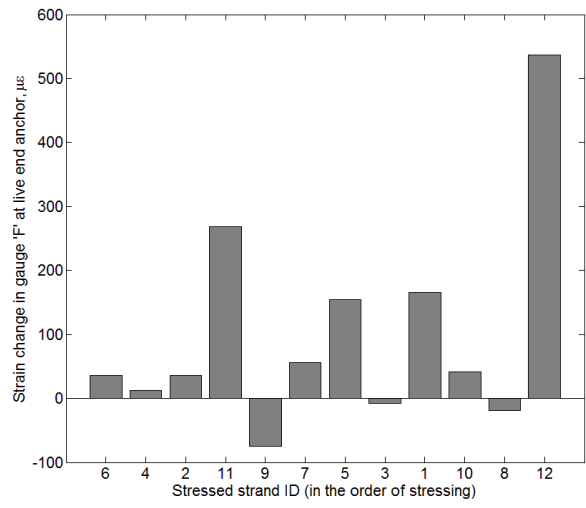
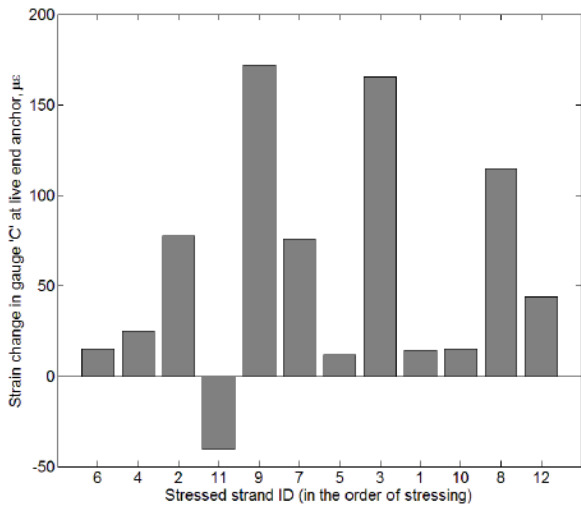
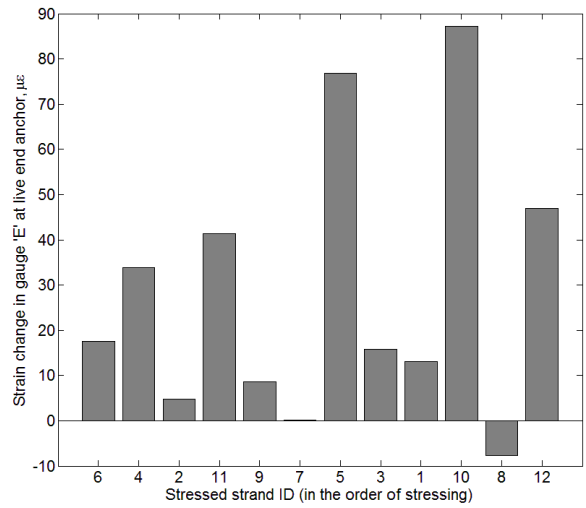
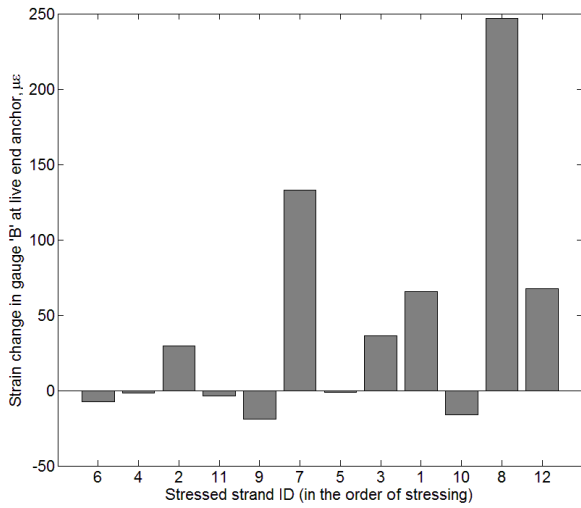
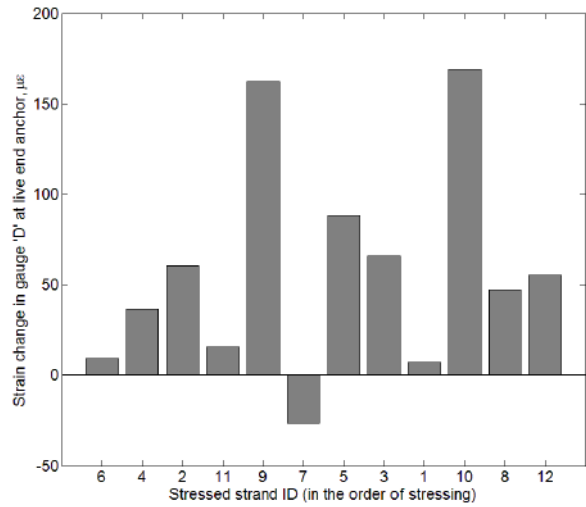
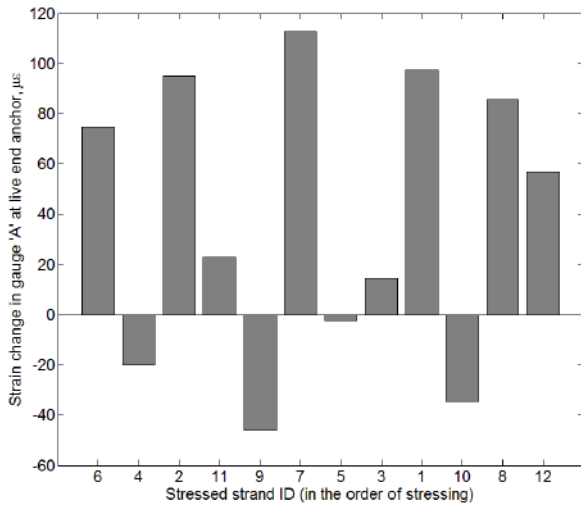


Figure B-14 Strain change in a gage with stressing of each strand (gage A-F, live end)

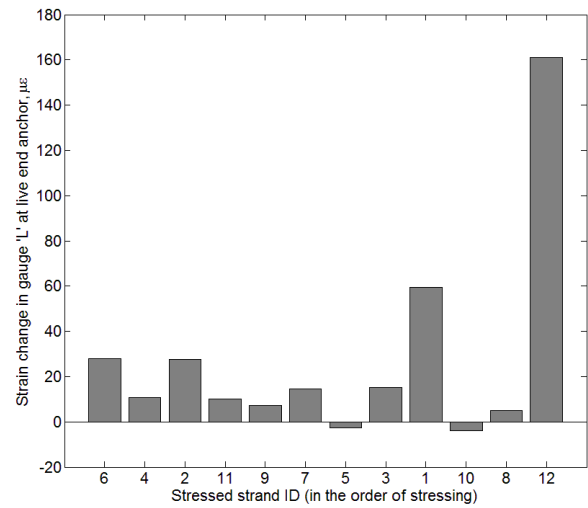
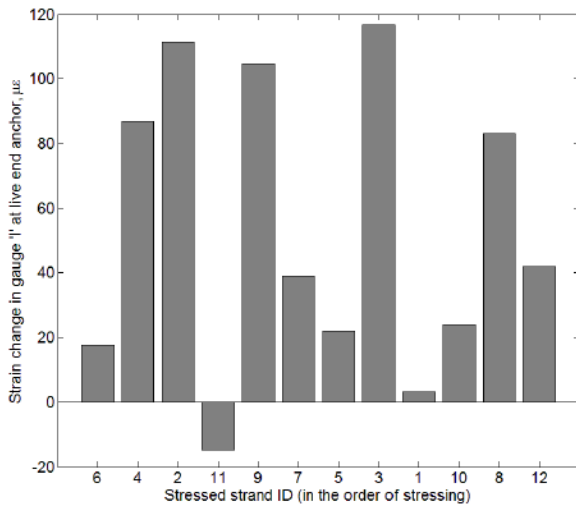
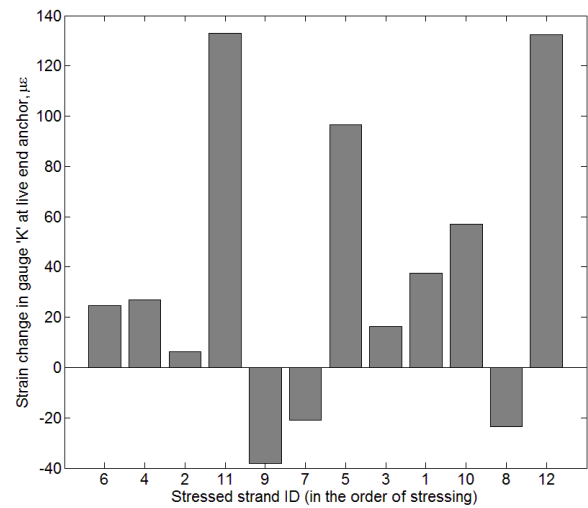
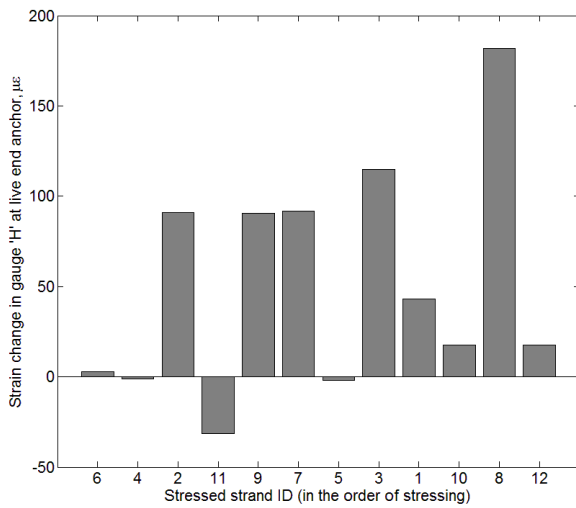
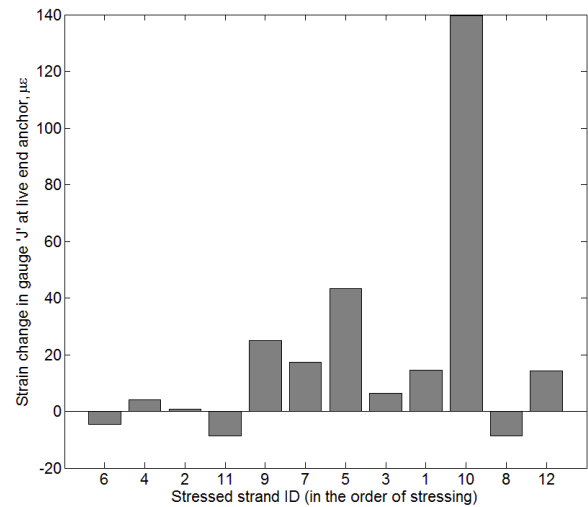
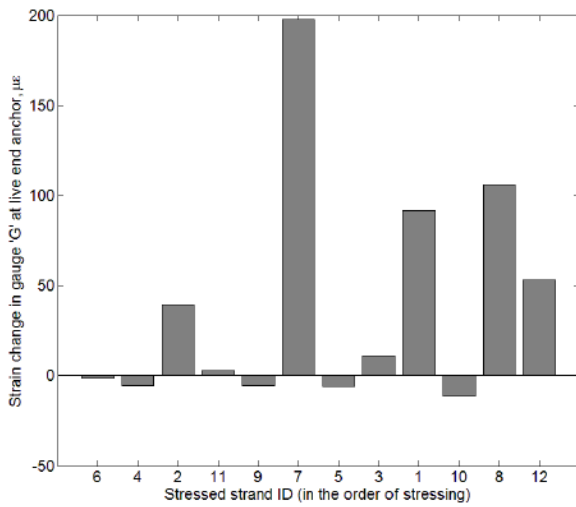


Figure B-15 Strain change in a gage with stressing of each strand (gage G-L, live end)

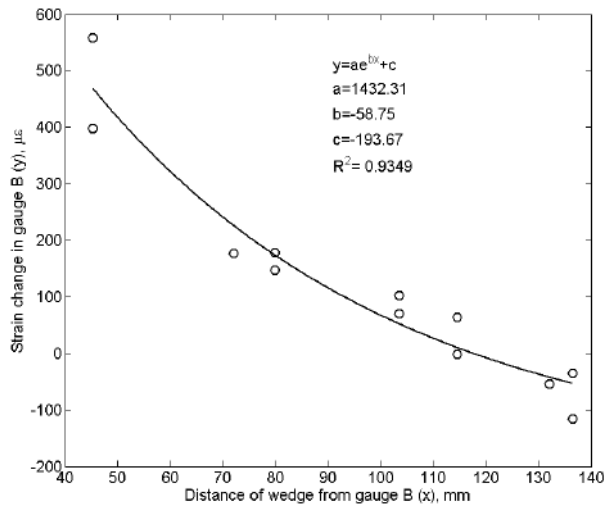
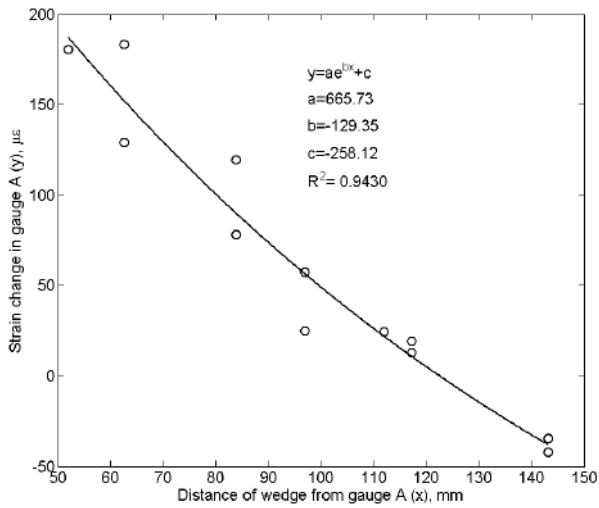
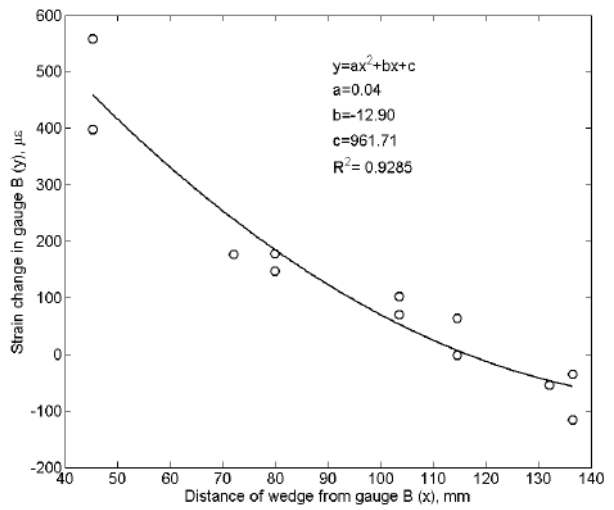
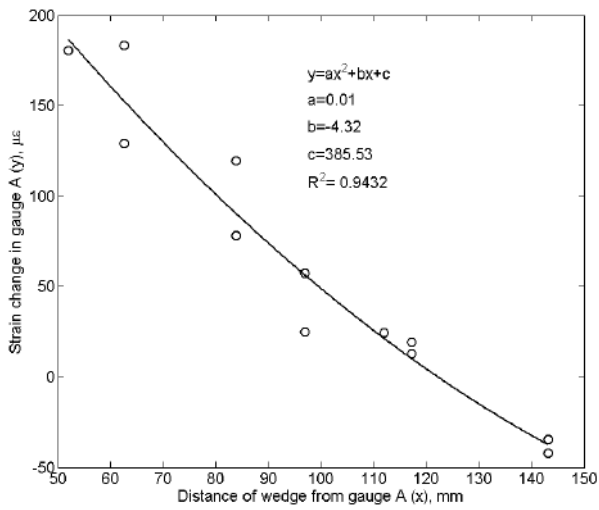
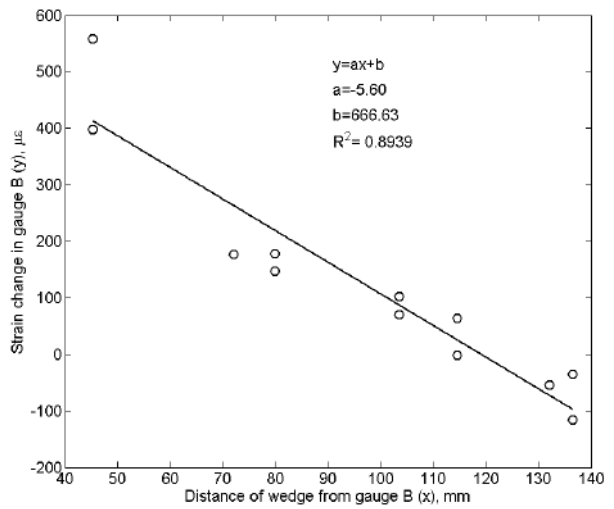
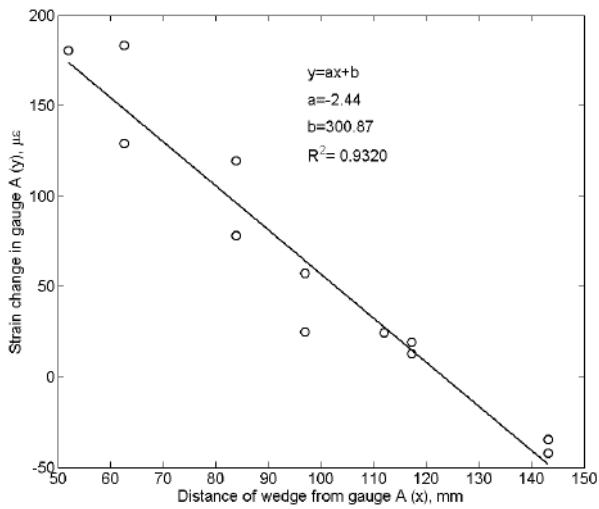


Figure B-16 Strain-distance statistical fits (gage A and B, dead end)

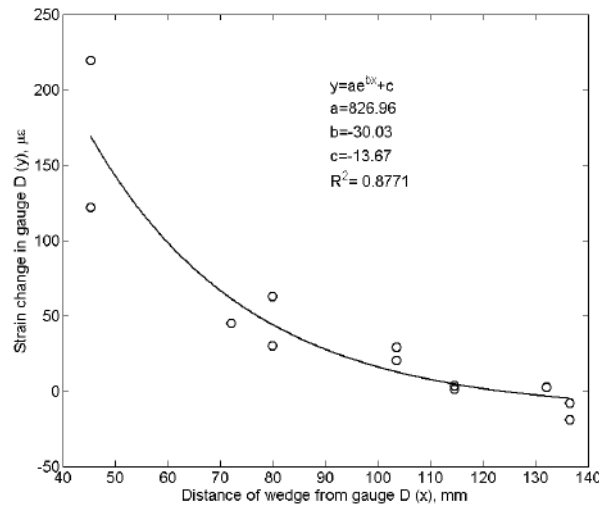
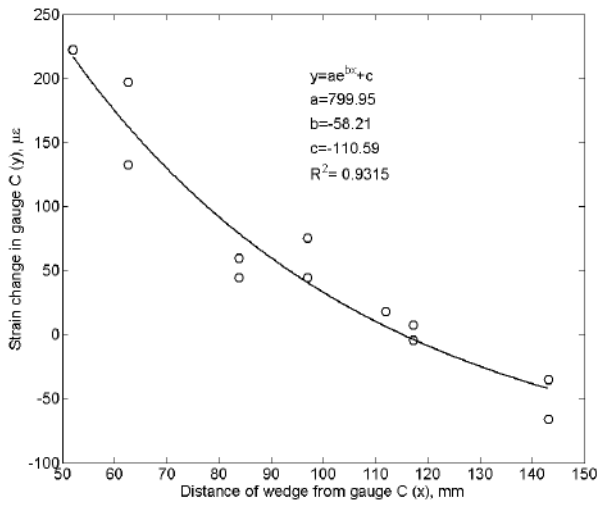
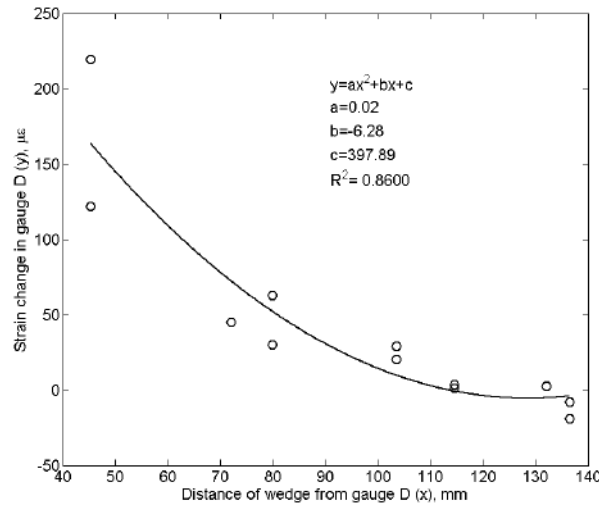
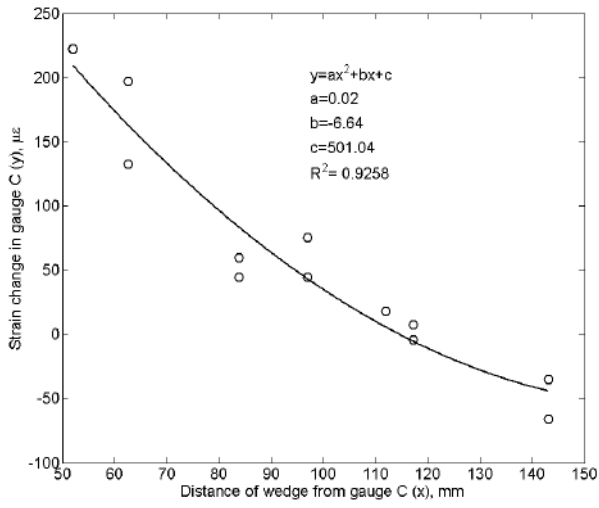
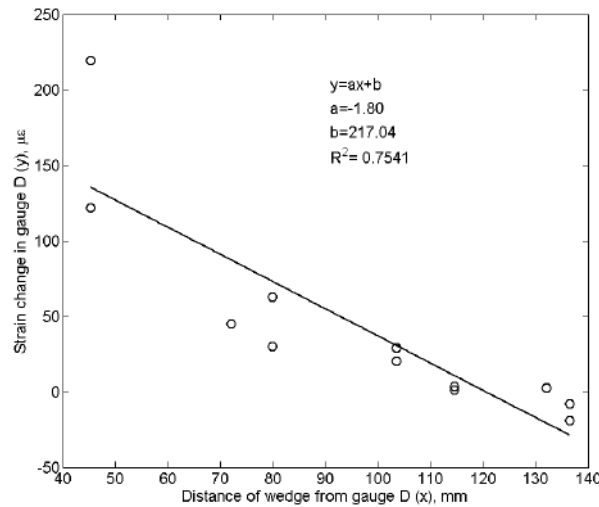
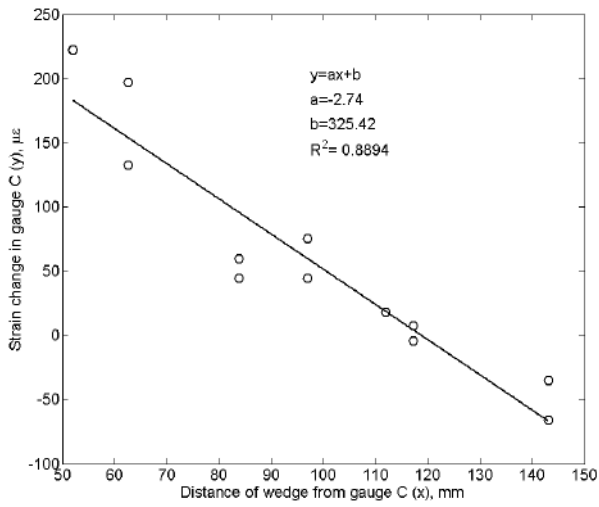


Figure B-17 Strain-distance statistical fits (gage C and D, dead end)

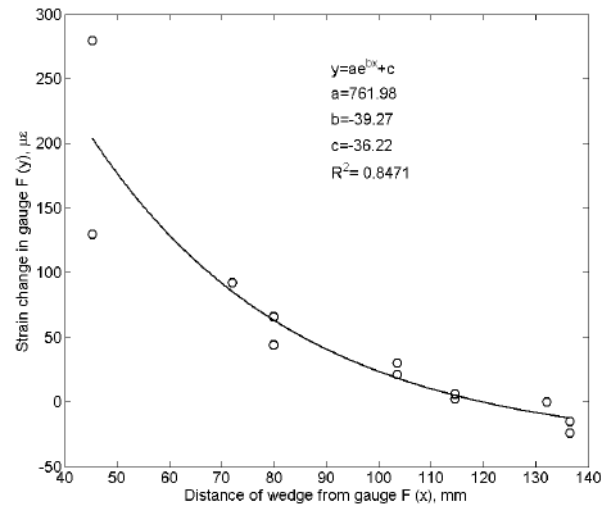
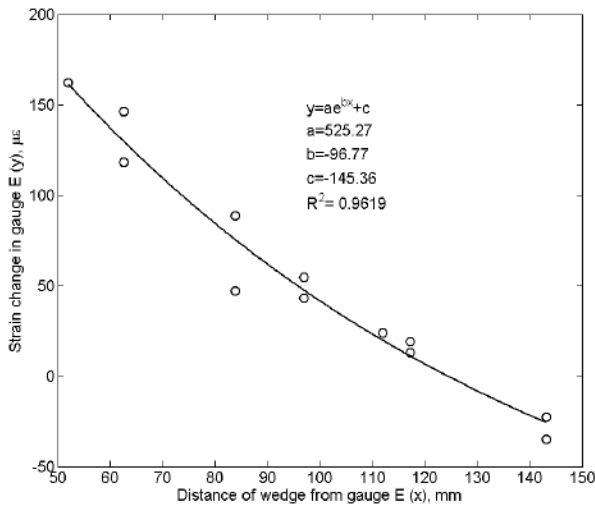
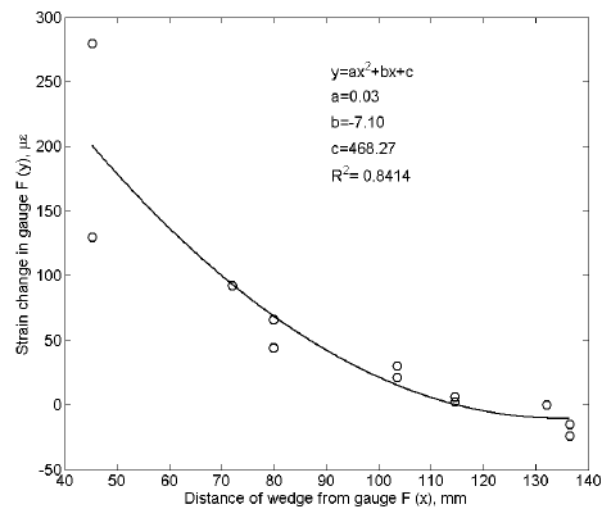
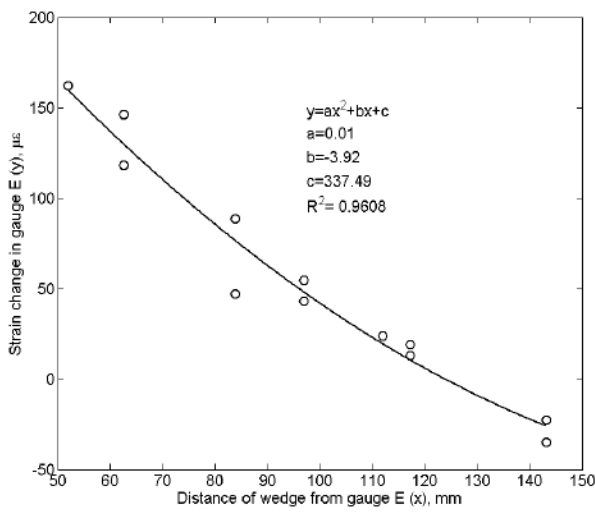
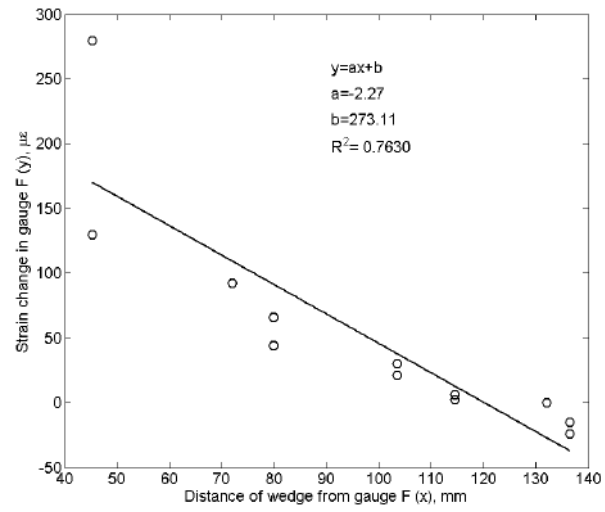
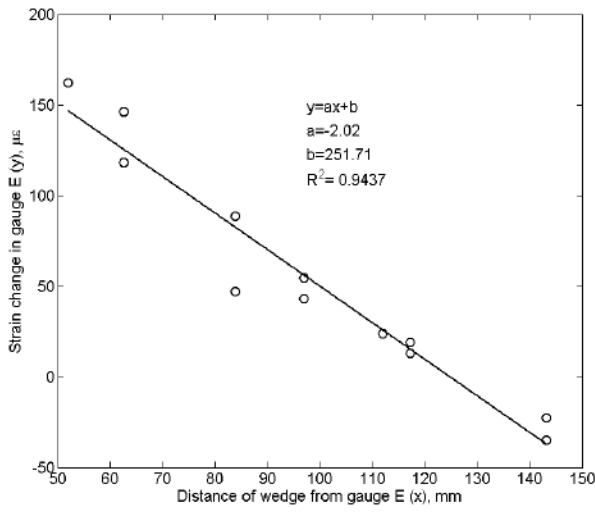


Figure B-18 Strain-distance statistical fits (gauge E and F, dead end)

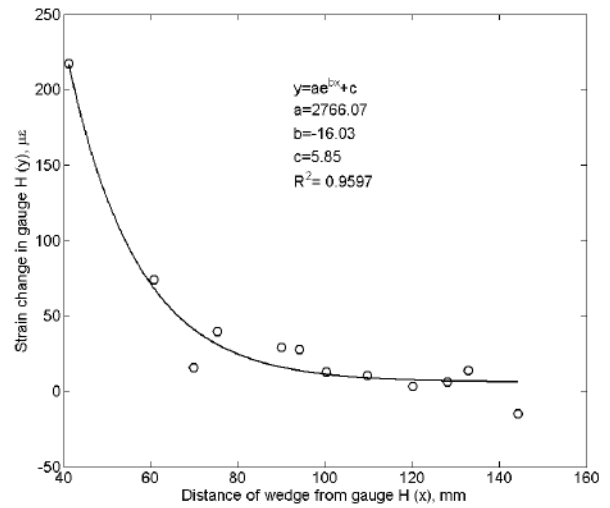
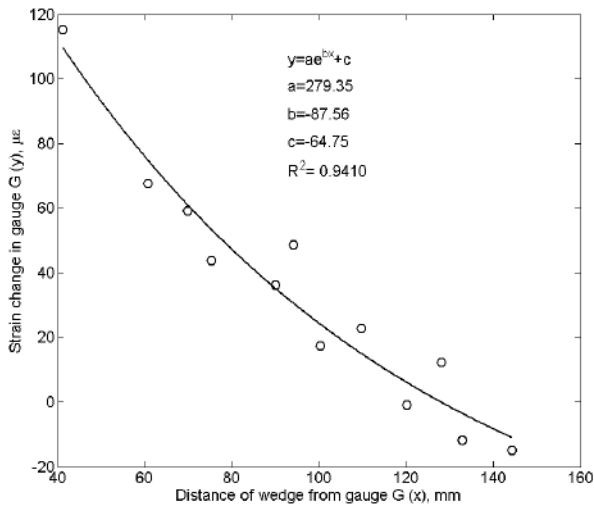
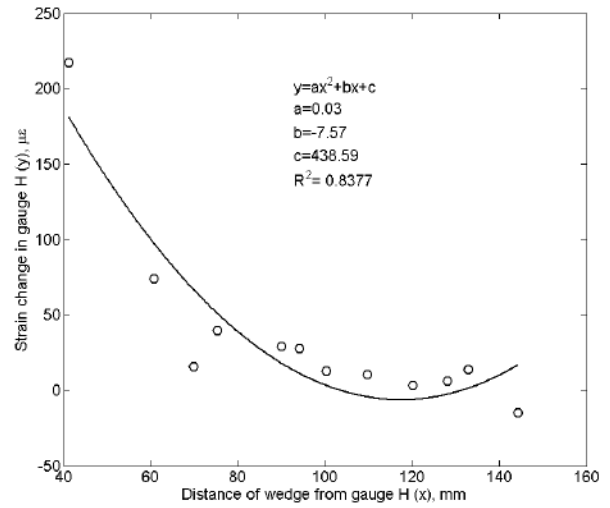
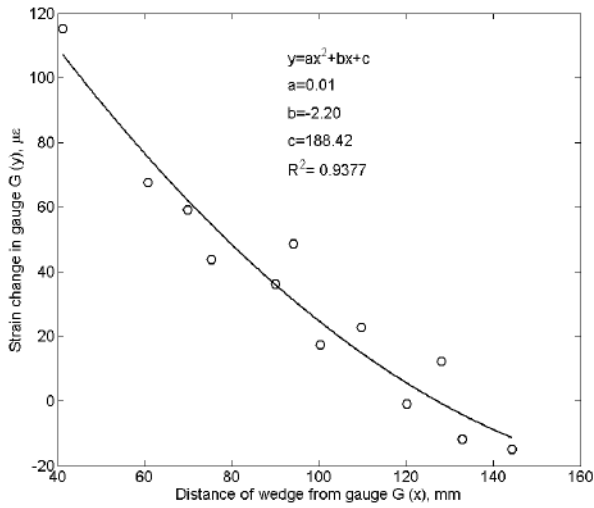
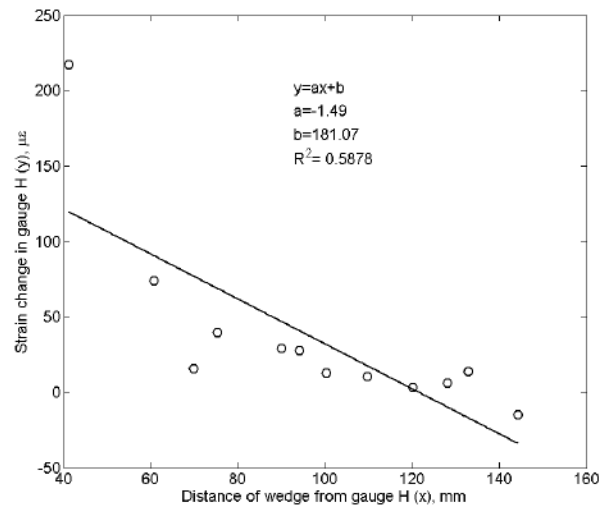
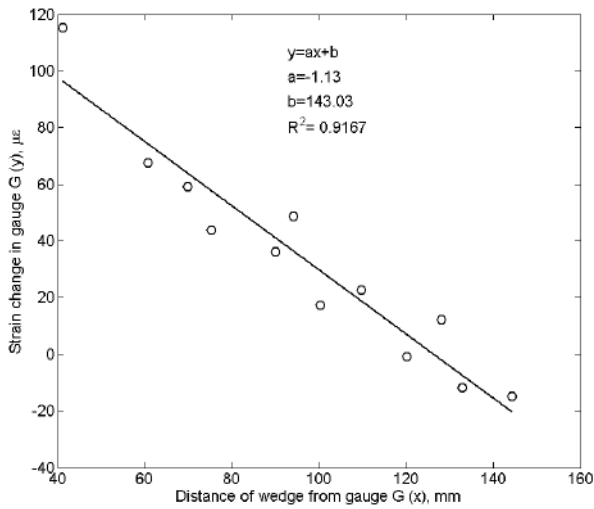


Figure B-19 Strain-distance statistical fits (gage G and H, dead end)

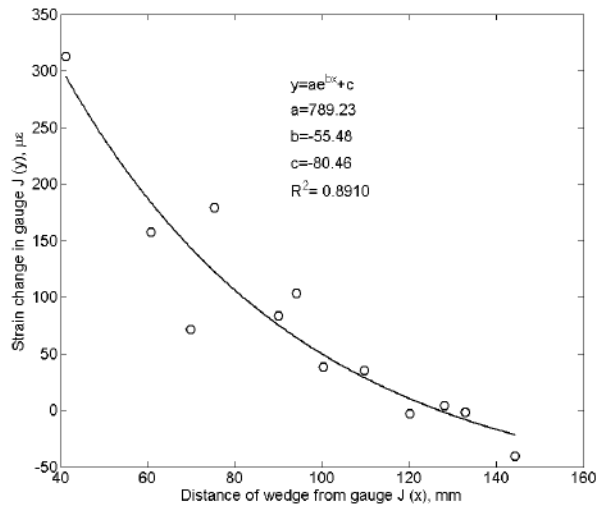
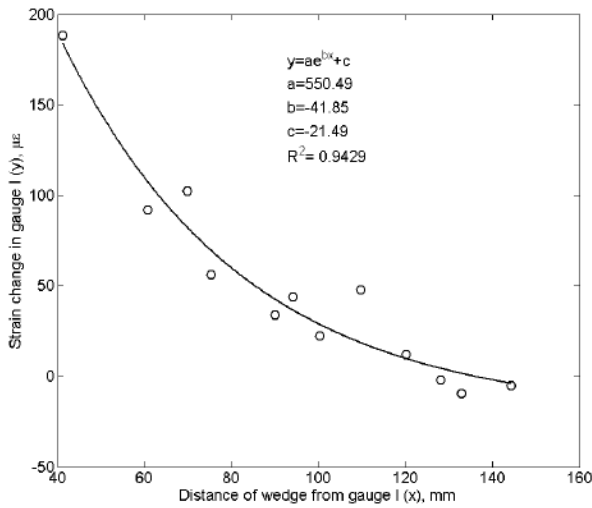
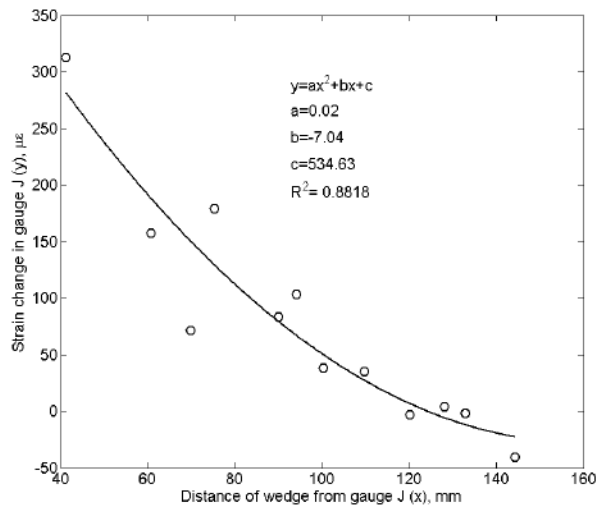
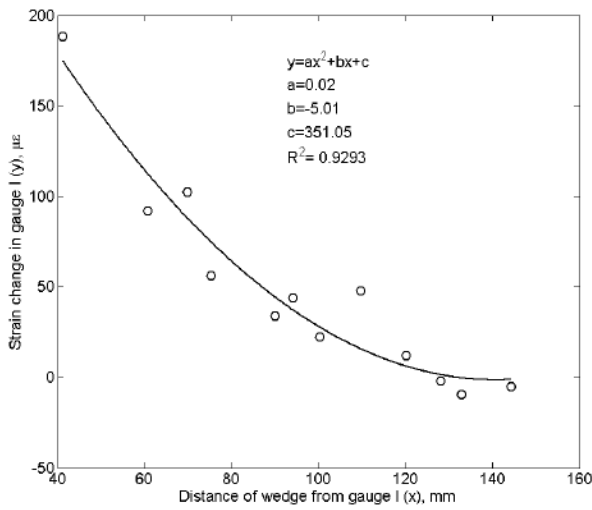
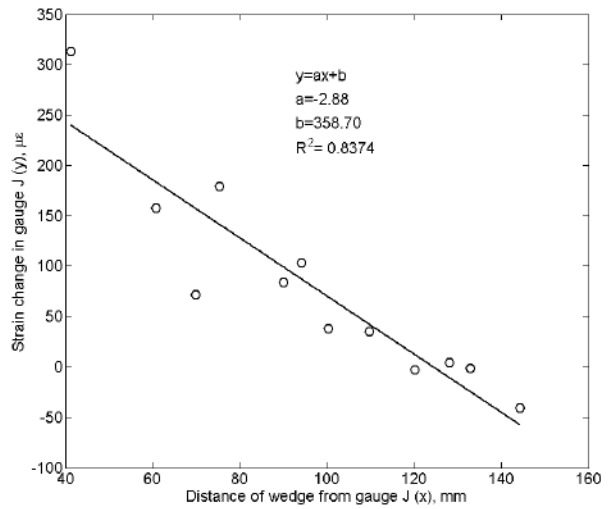
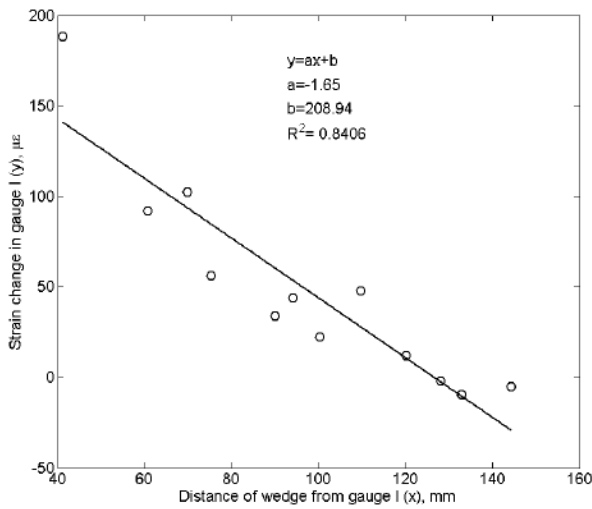


Figure B-20 Strain-distance statistical fits (gauge I and J, dead end)

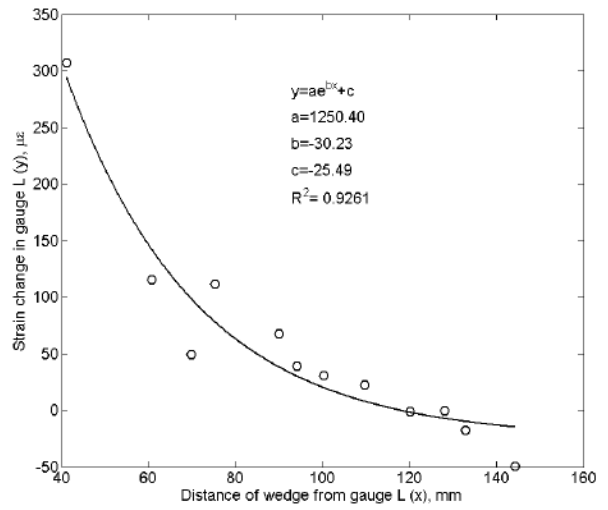
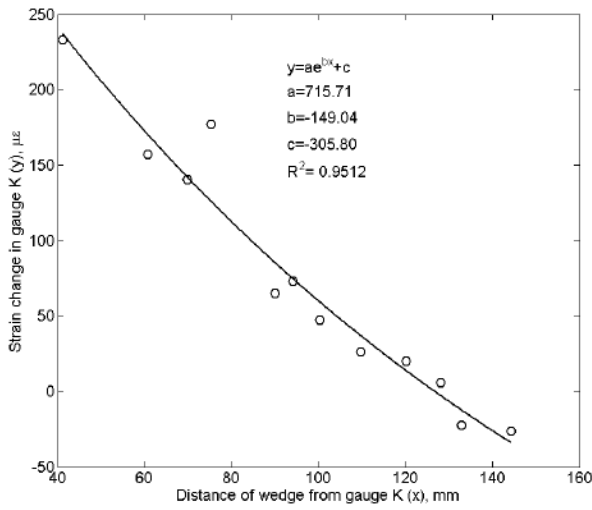
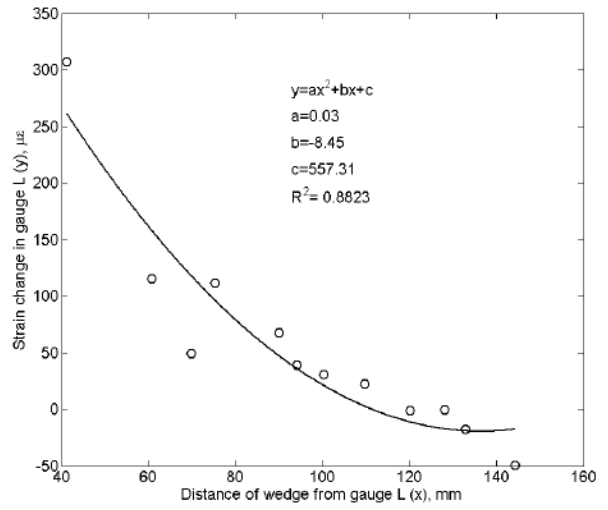
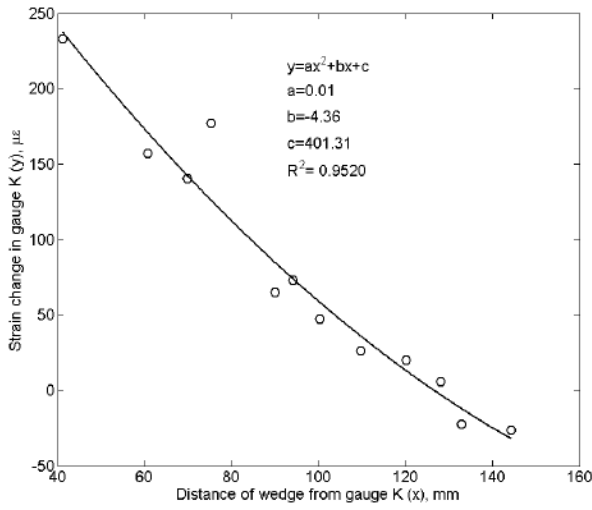
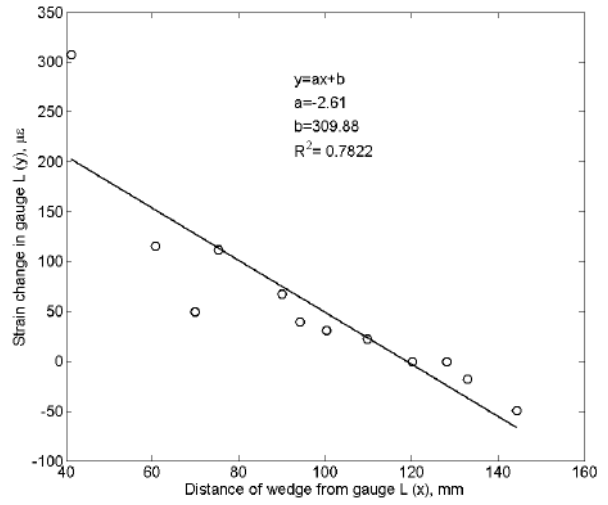
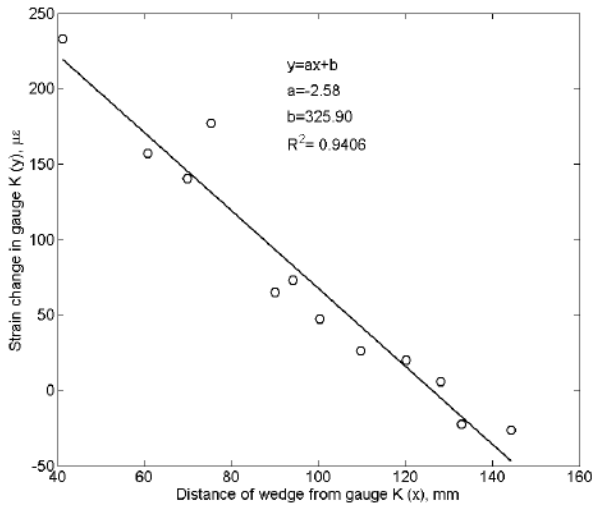


Figure B-21 Strain-distance statistical fits (gauge K and L, dead end)

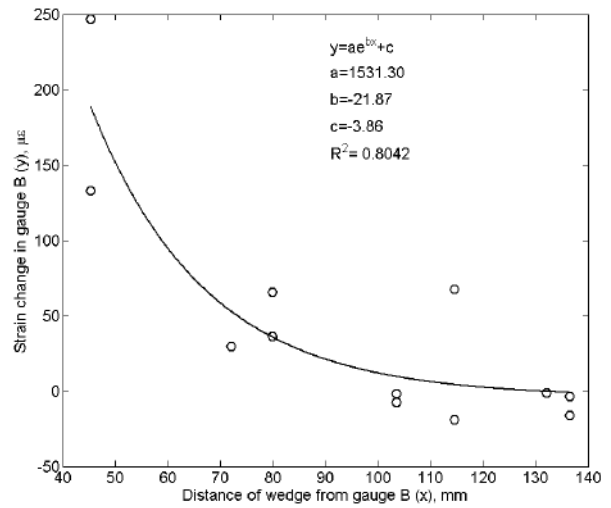
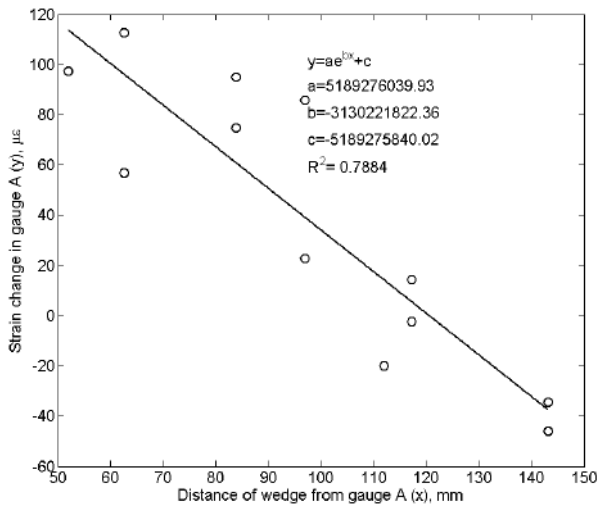
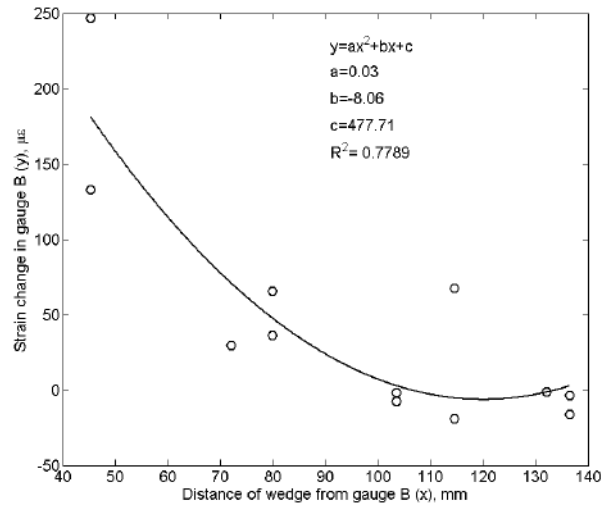
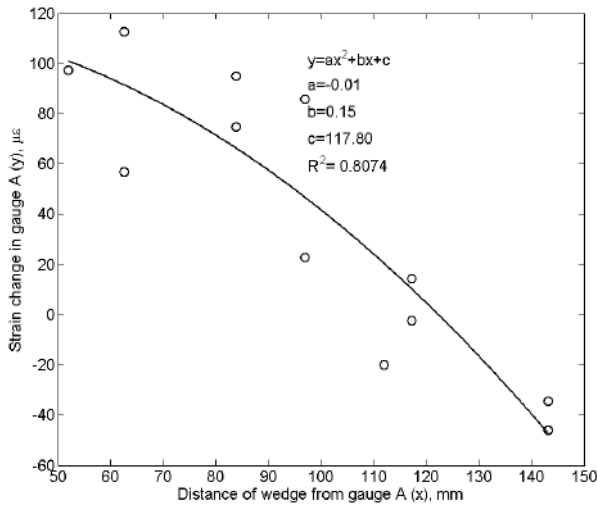
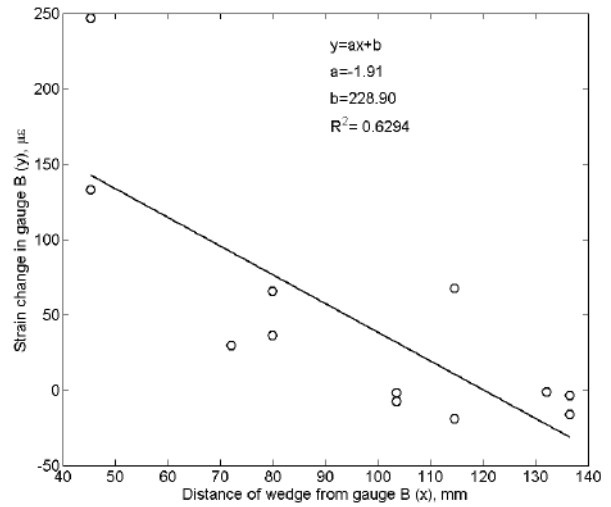
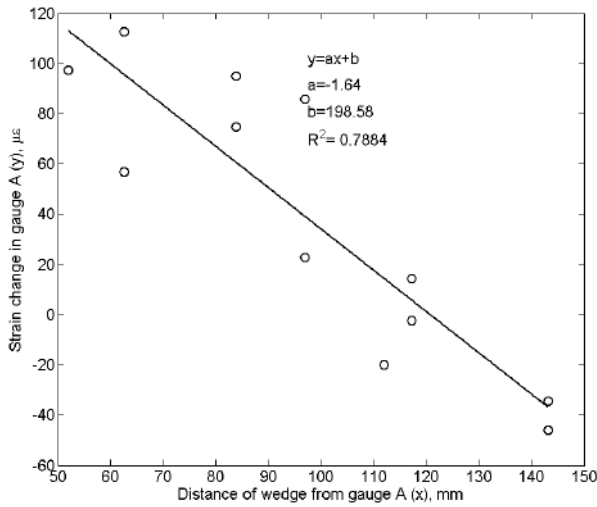


Figure B-22 Strain-distance statistical fits (gauge A and B, live end)

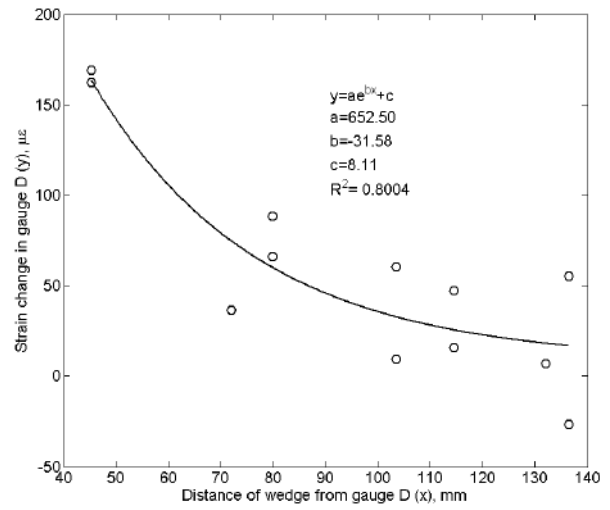
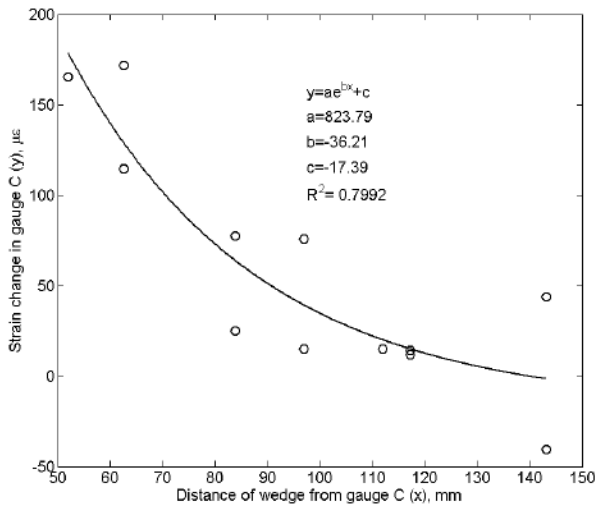
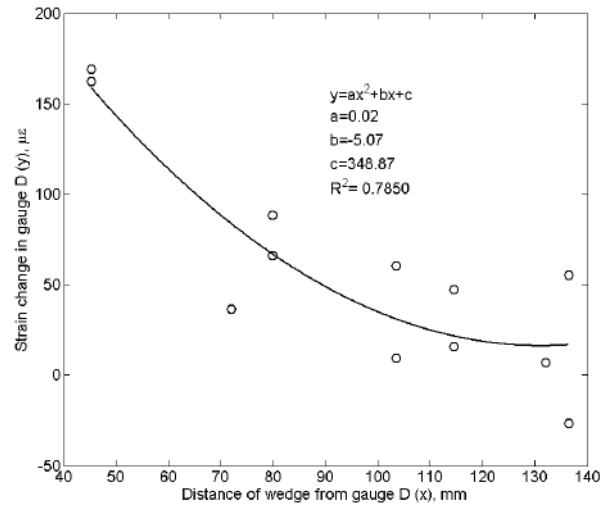
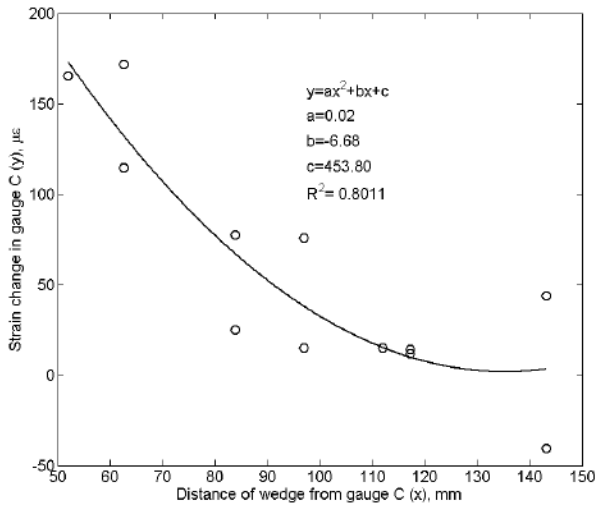
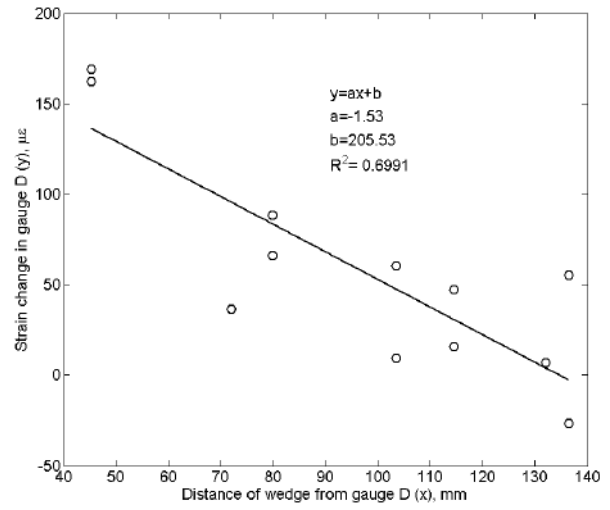
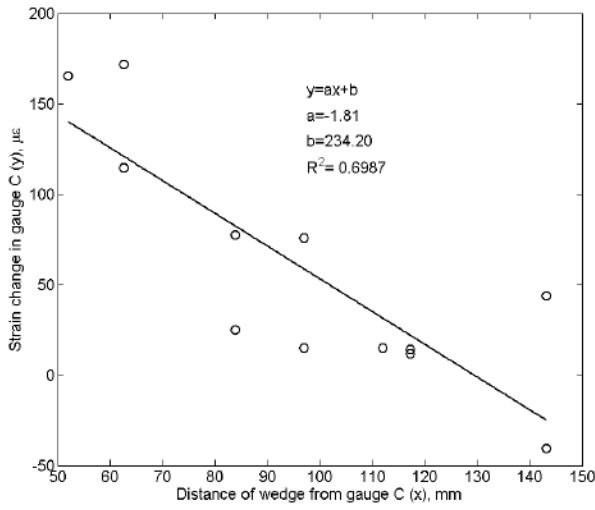


Figure B-23 Strain-distance statistical fits (gauge C and D, live end)

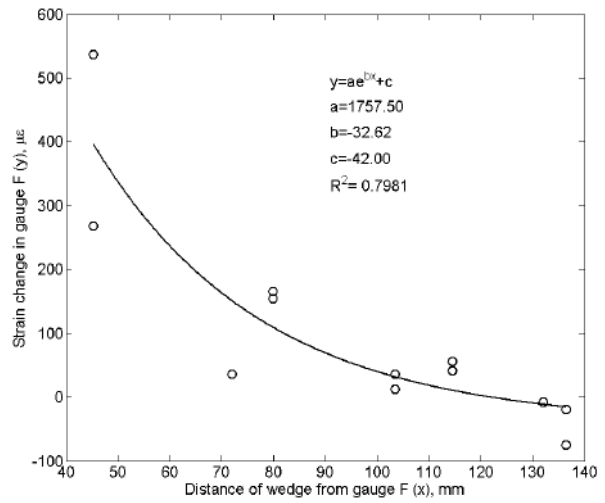
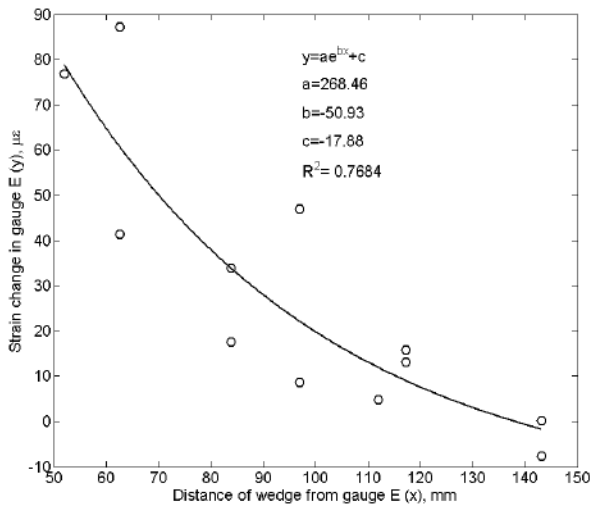
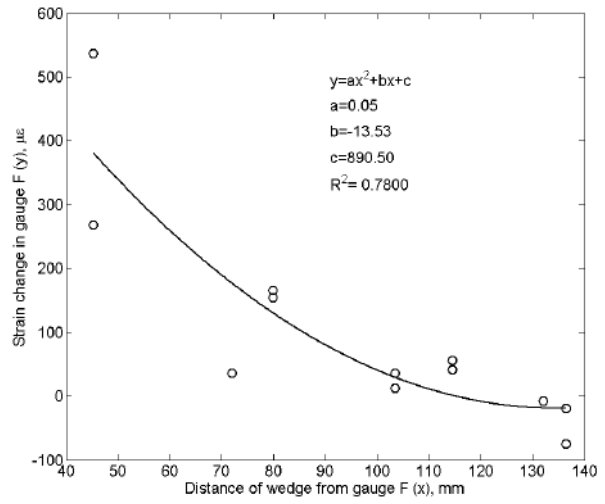
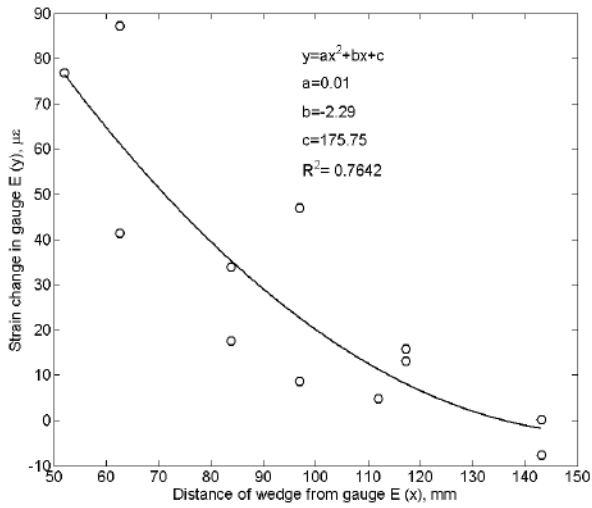
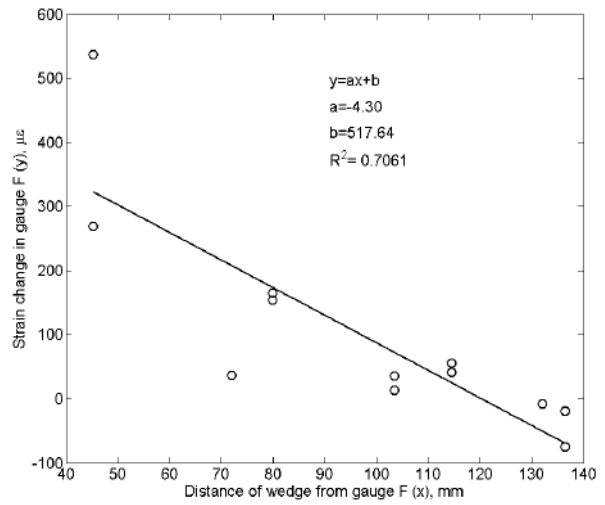
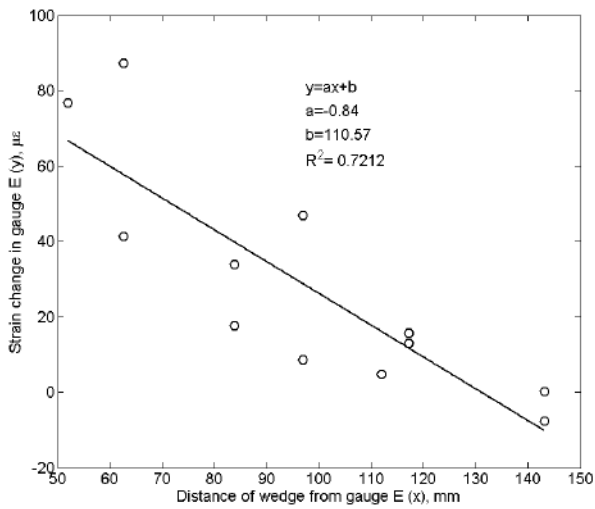


Figure B-24 Strain-distance statistical fits (gage E and F, live end)

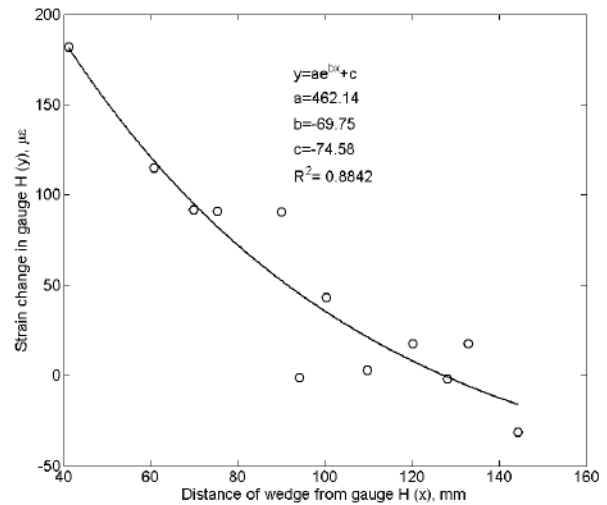
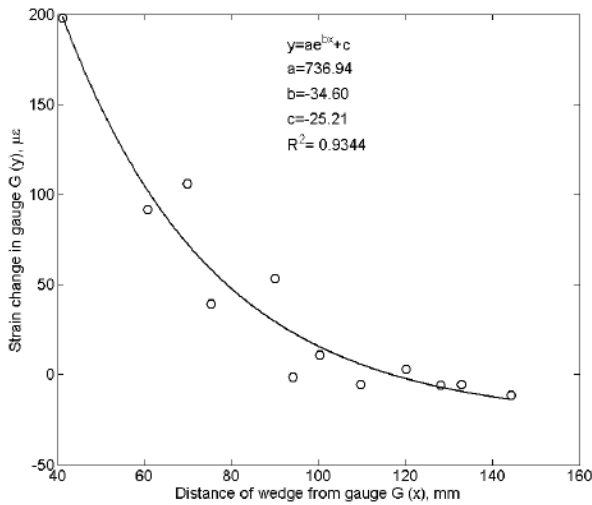
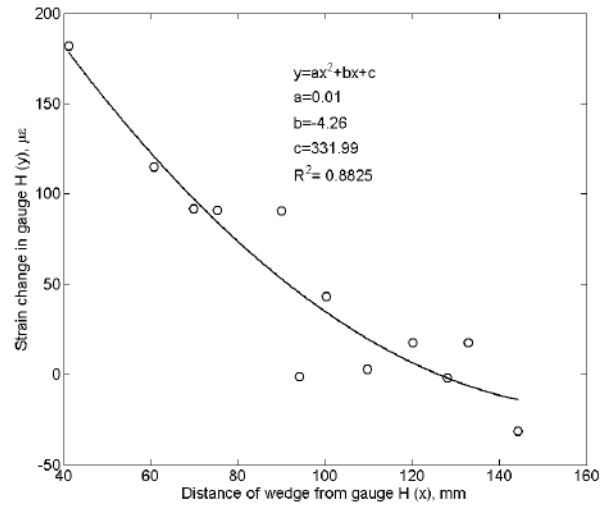
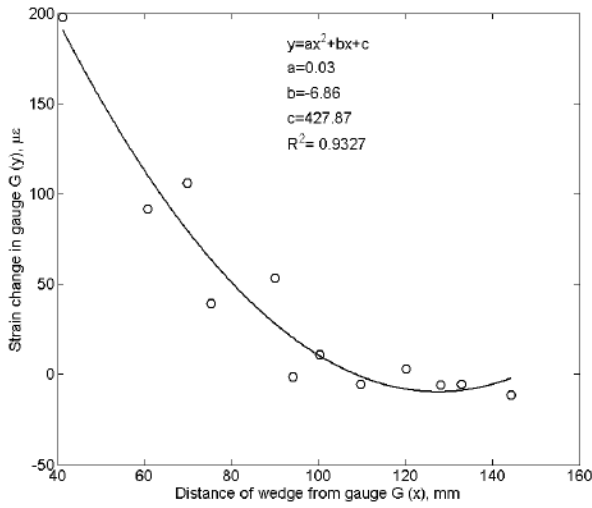
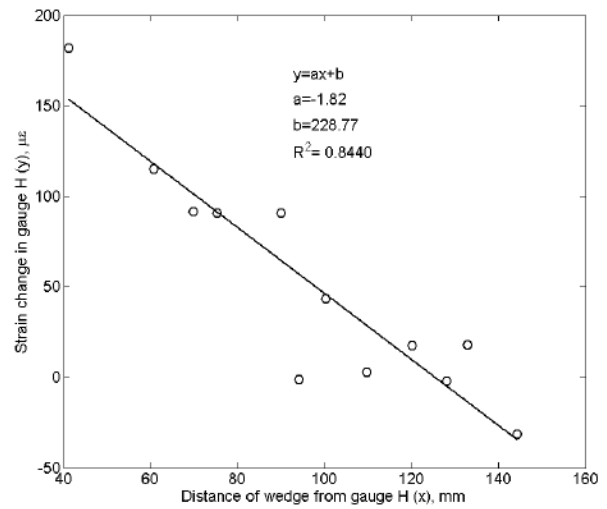
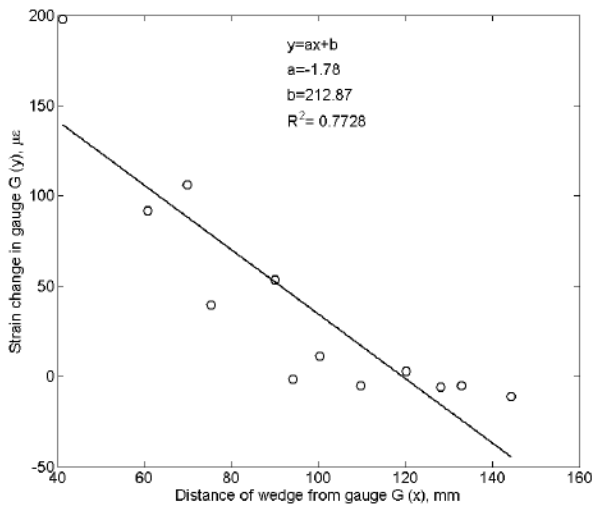


Figure B-25 Strain-distance statistical fits (gage G and H, live end)

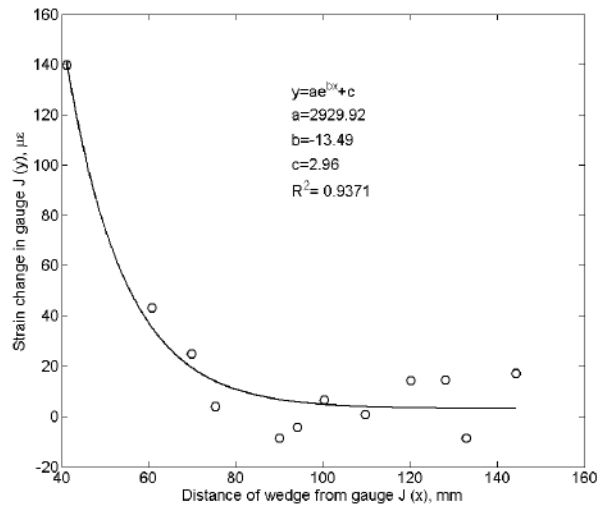
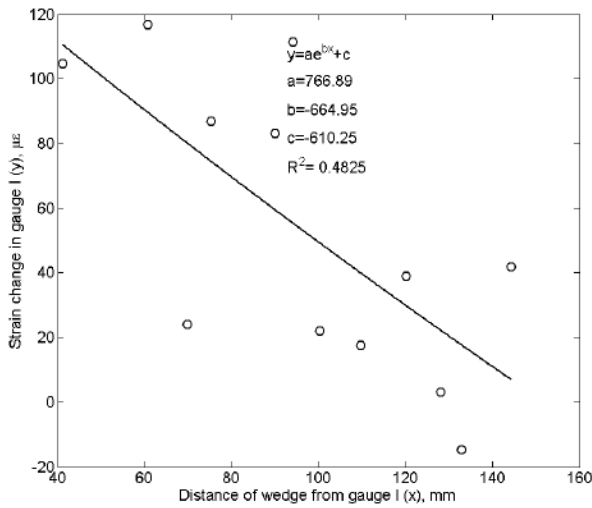
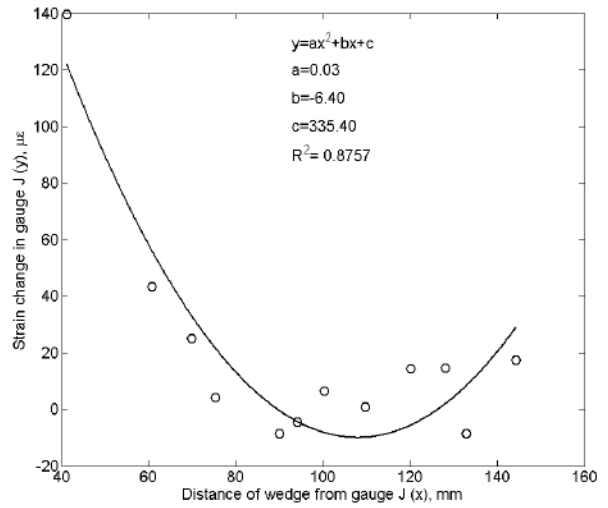
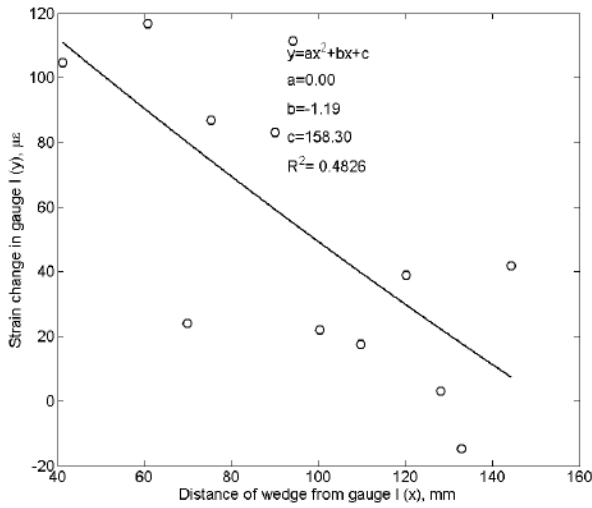
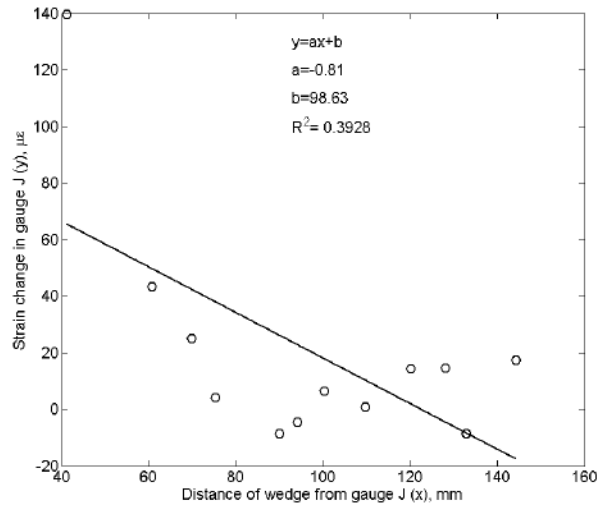
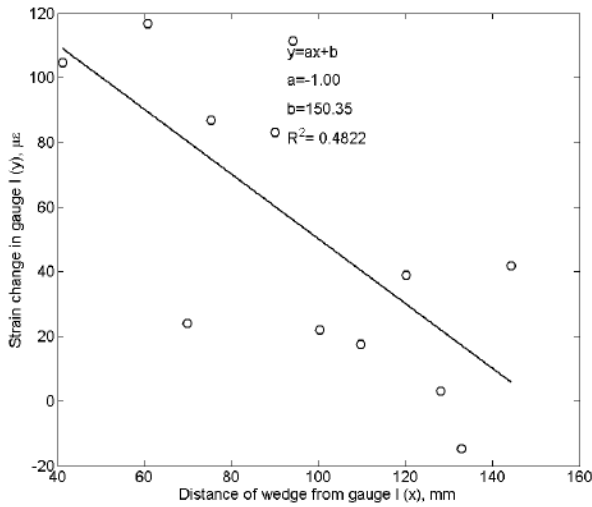


Figure B-26 Strain-distance statistical fits (gage I and J, live end)

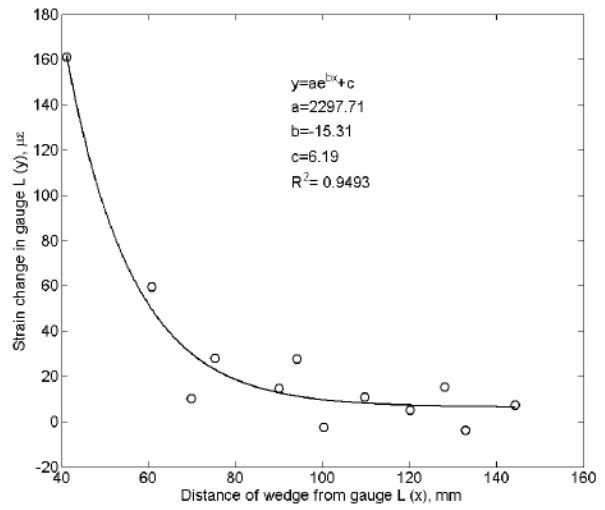
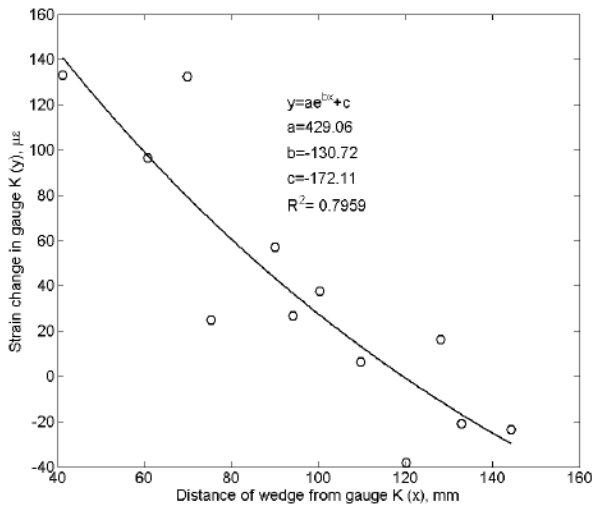
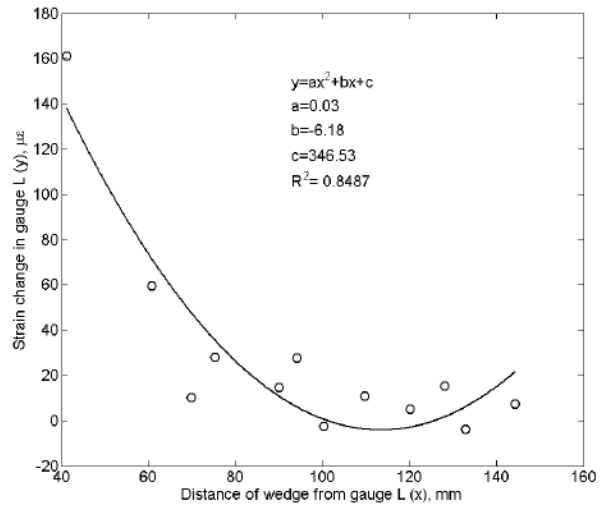
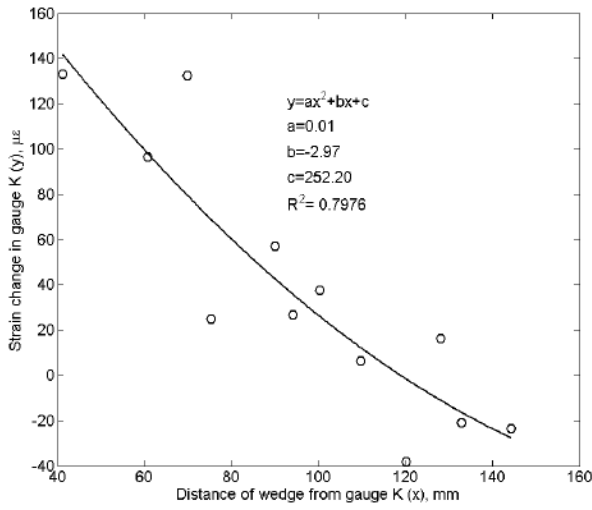
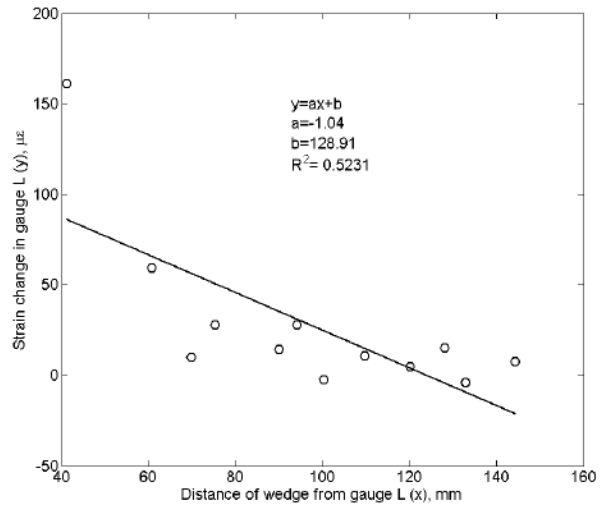
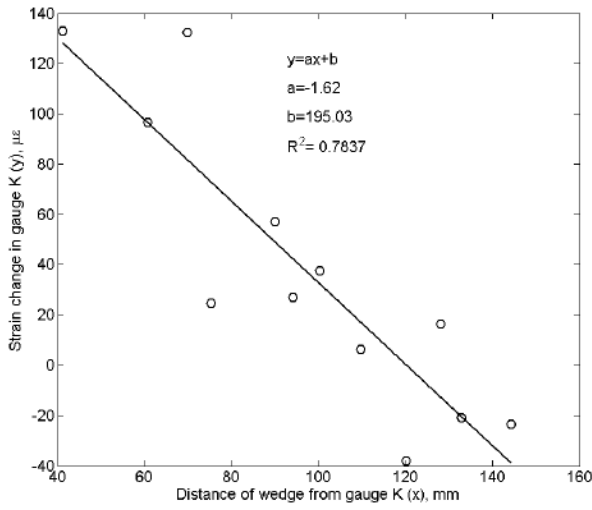


Figure B-27 Strain-distance statistical fits (gauge K and L, live end)

Appendix C—Detail Experimental Results: External Unbonded Tendon

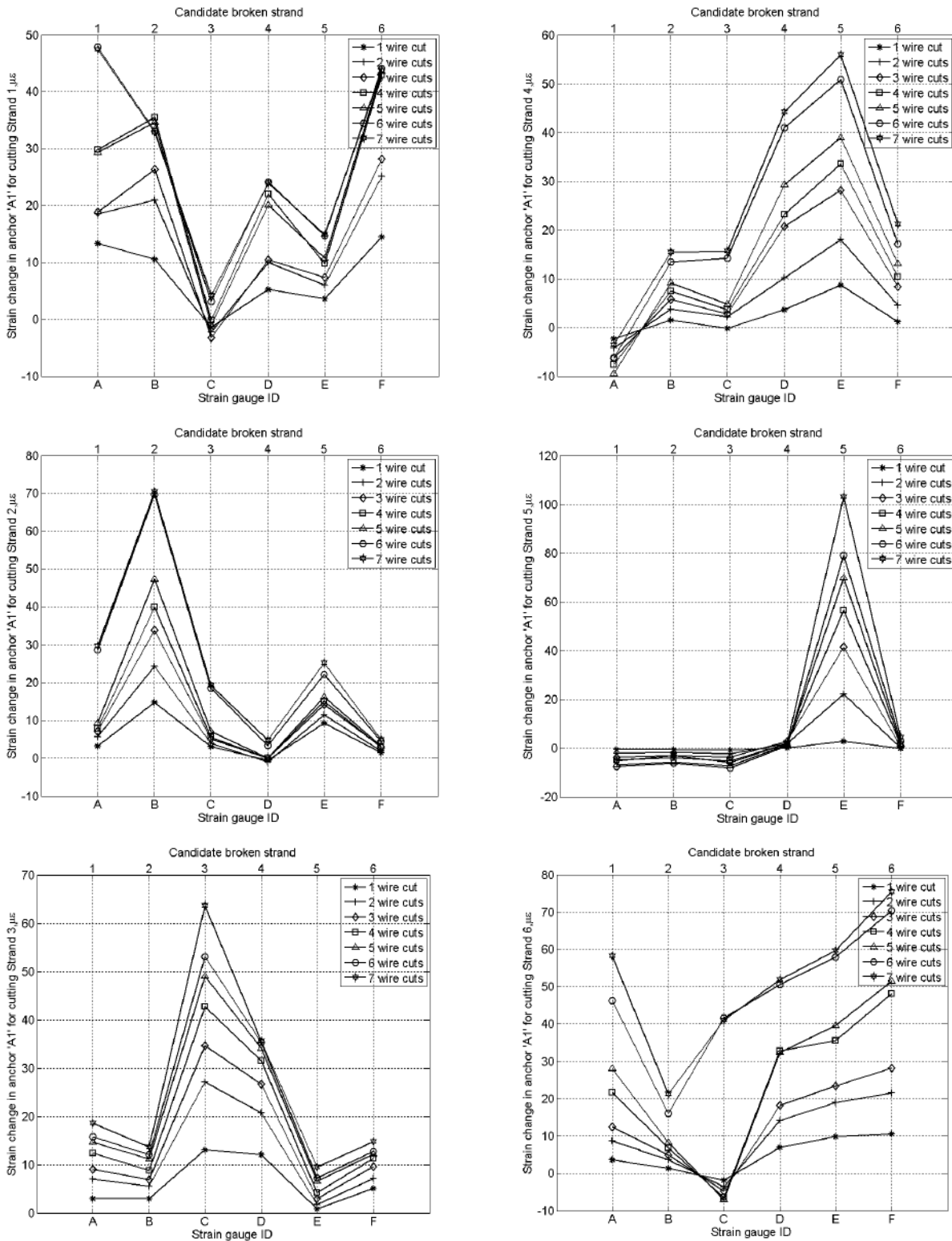


Figure C-28 Strain change in anchor 'A1' (baseline strain updated after each strand cut)

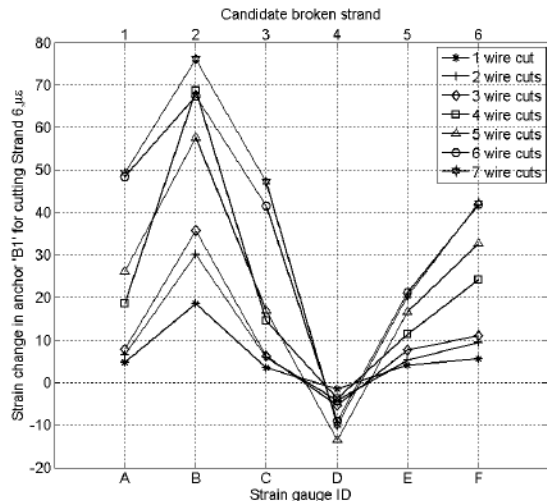
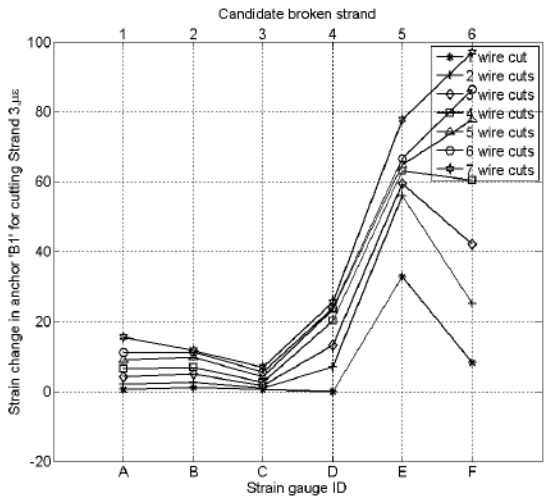
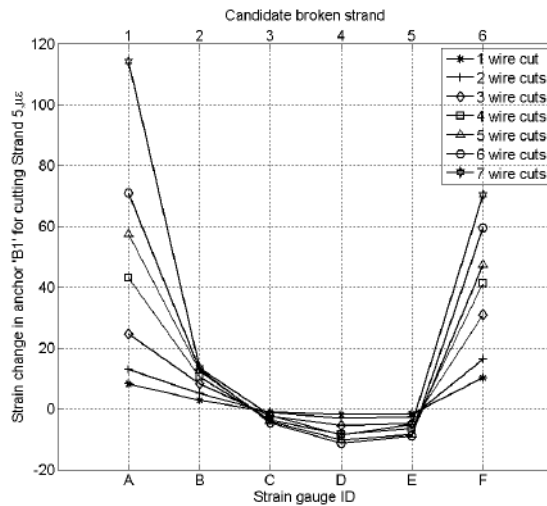
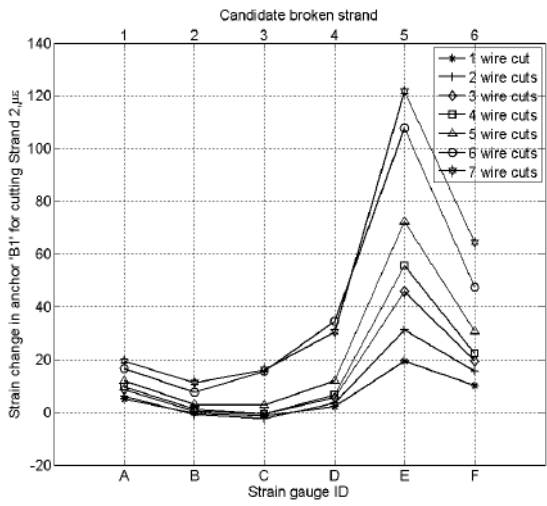
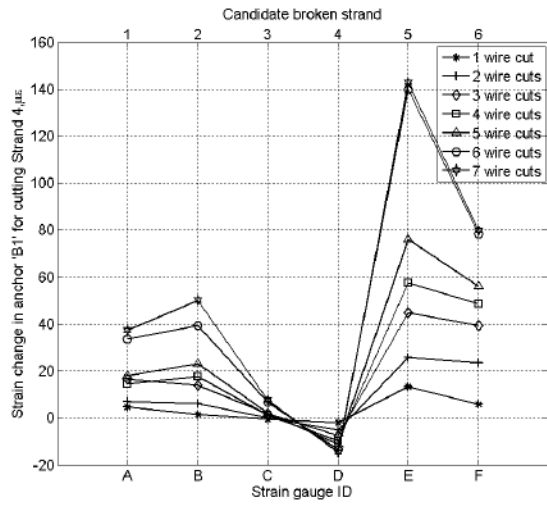
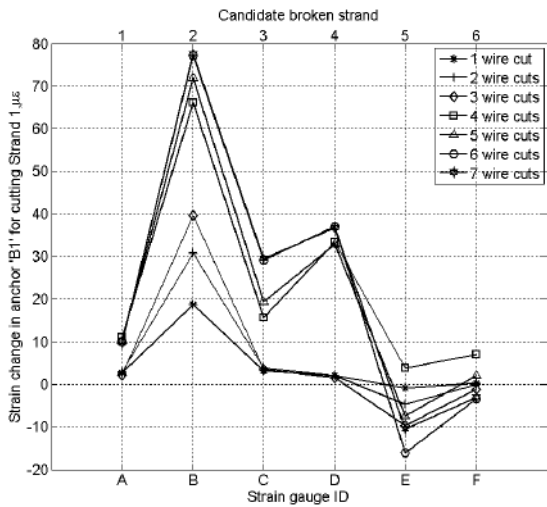


Figure C-29 Strain change in anchor 'B1' (baseline strain updated after each strand cut)

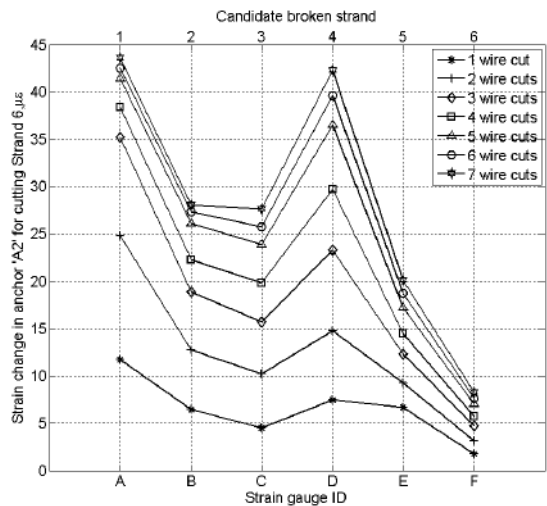
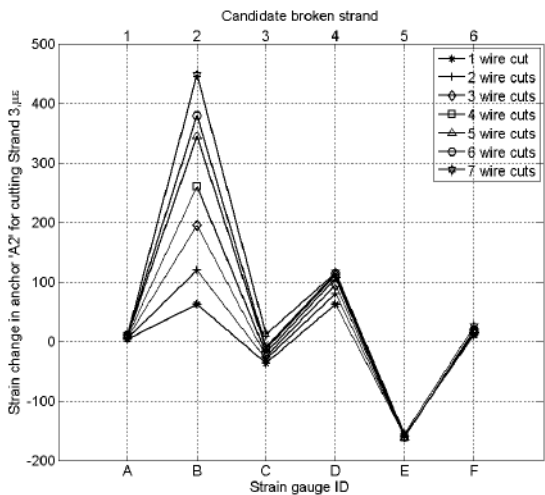
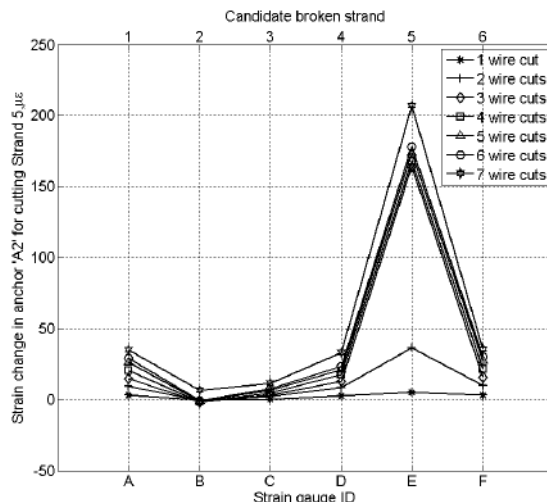
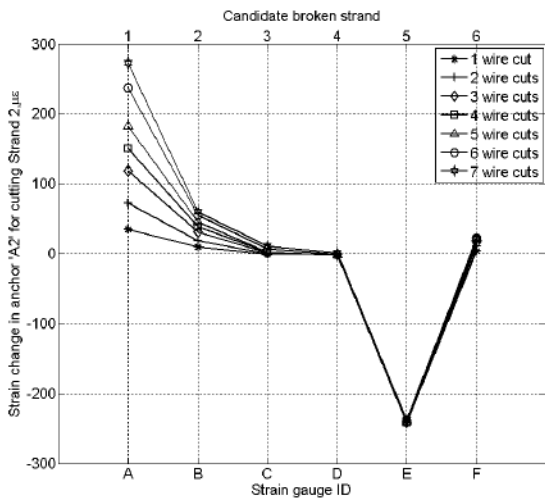
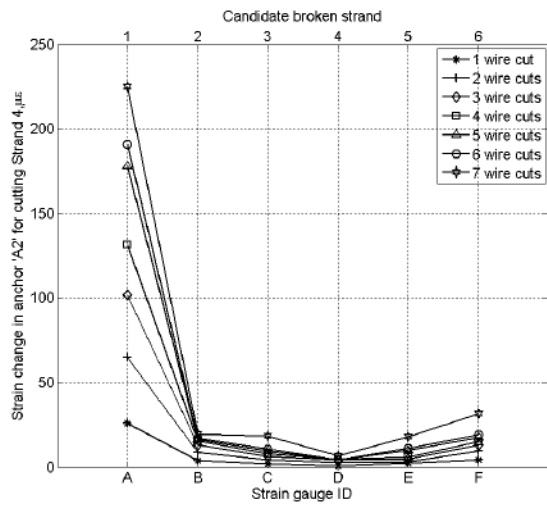
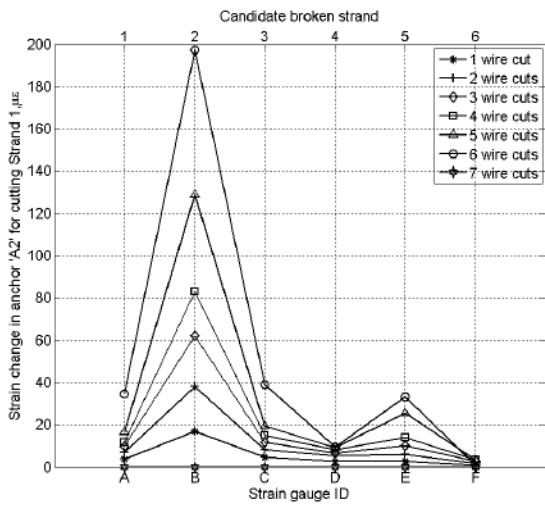


Figure C-30 Strain change in anchor 'A2' (baseline strain updated after each strand cut)

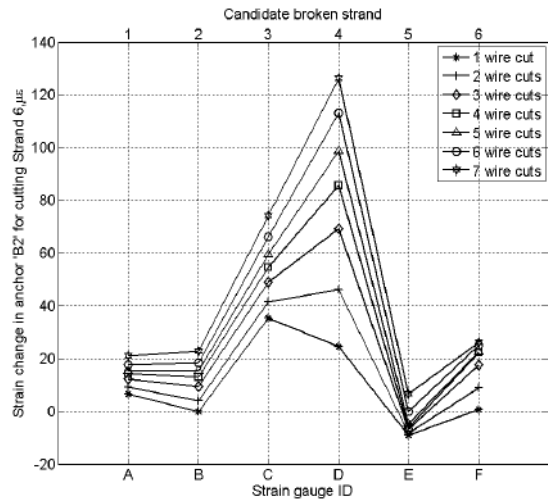
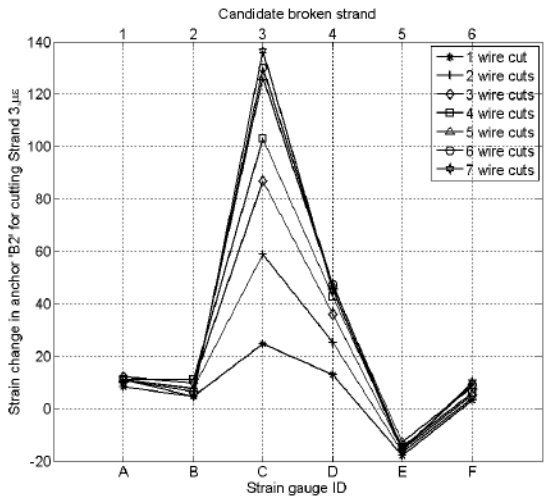
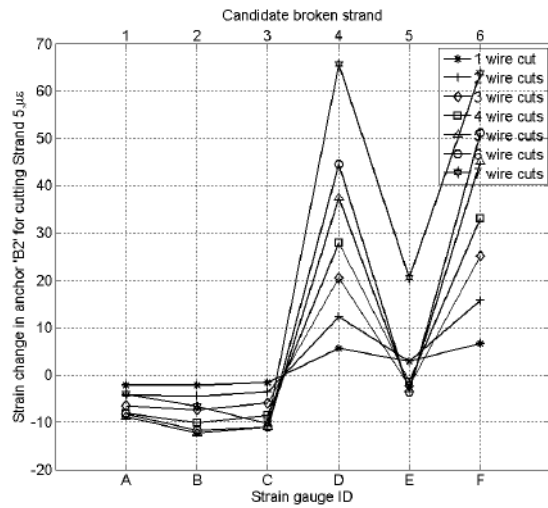
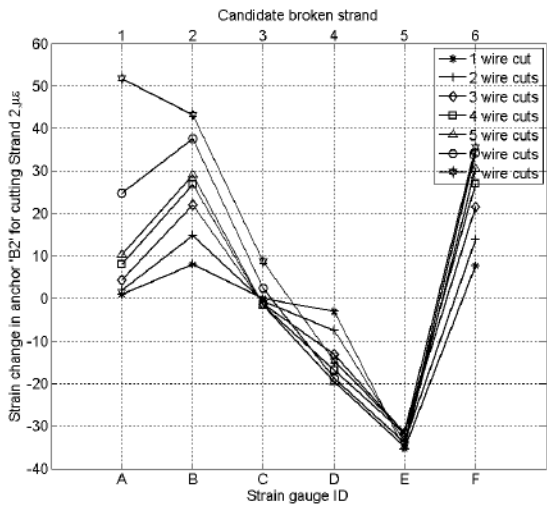
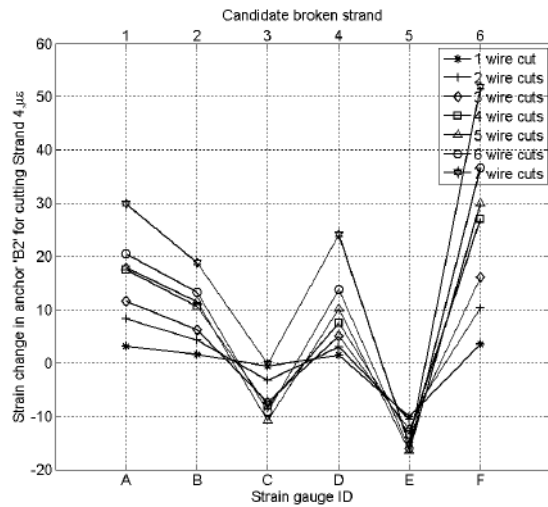
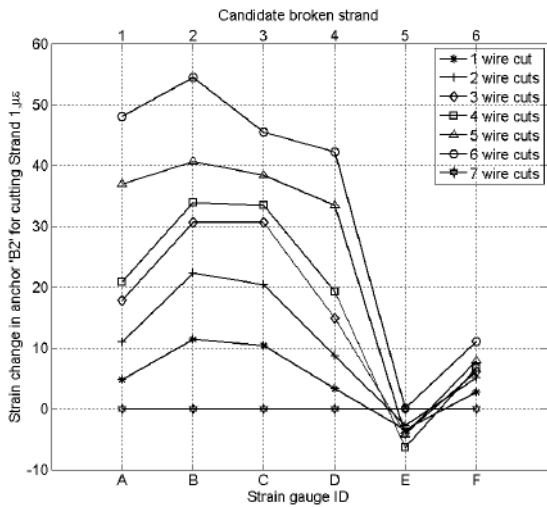


Figure C-31 Strain change in anchor 'B2' (baseline strain updated after each strand cut)

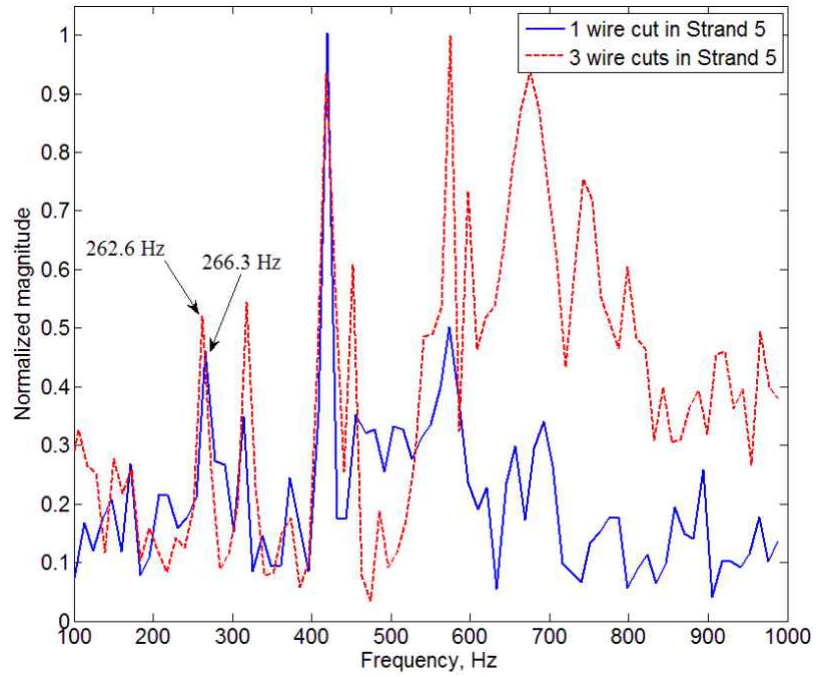


Figure C-32 Frequency shift with wire cuts

Appendix D—Detail Experimental Results: Internal Unbonded Tendon

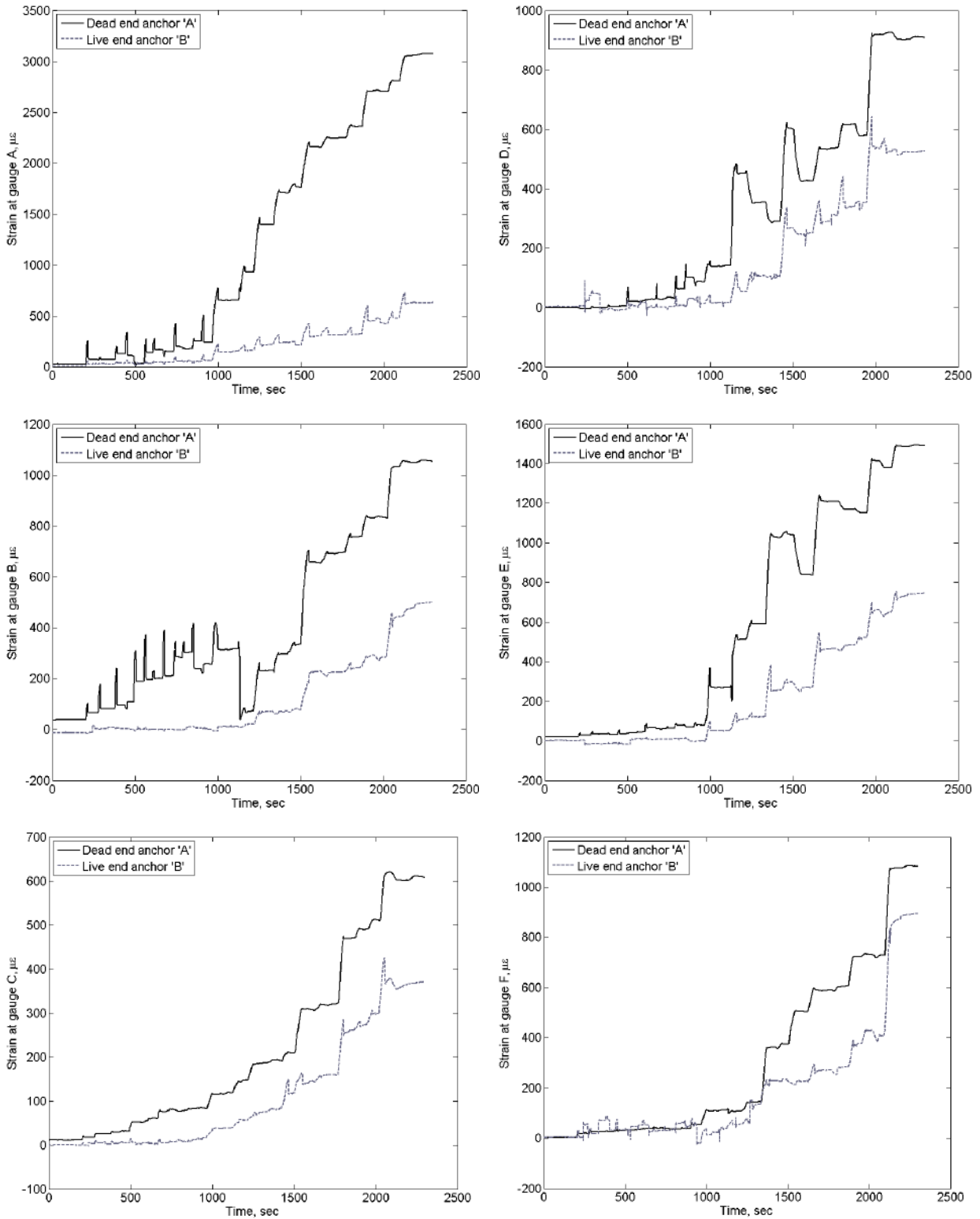


Figure D-33 Strain comparison between two anchors during stressing (gauge A-F)

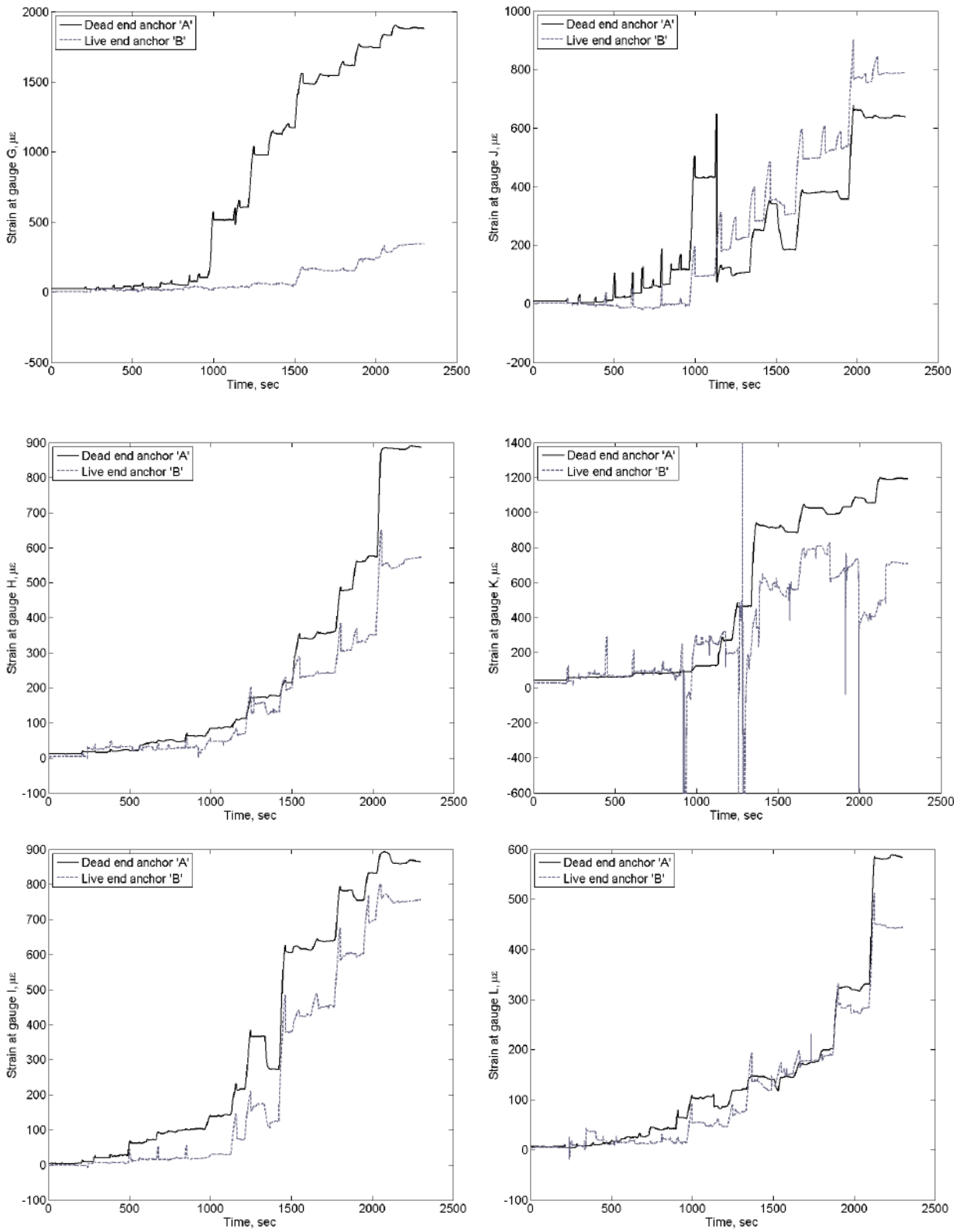


Figure D-34 Strain comparison between two anchors during stressing (gauge G-L)

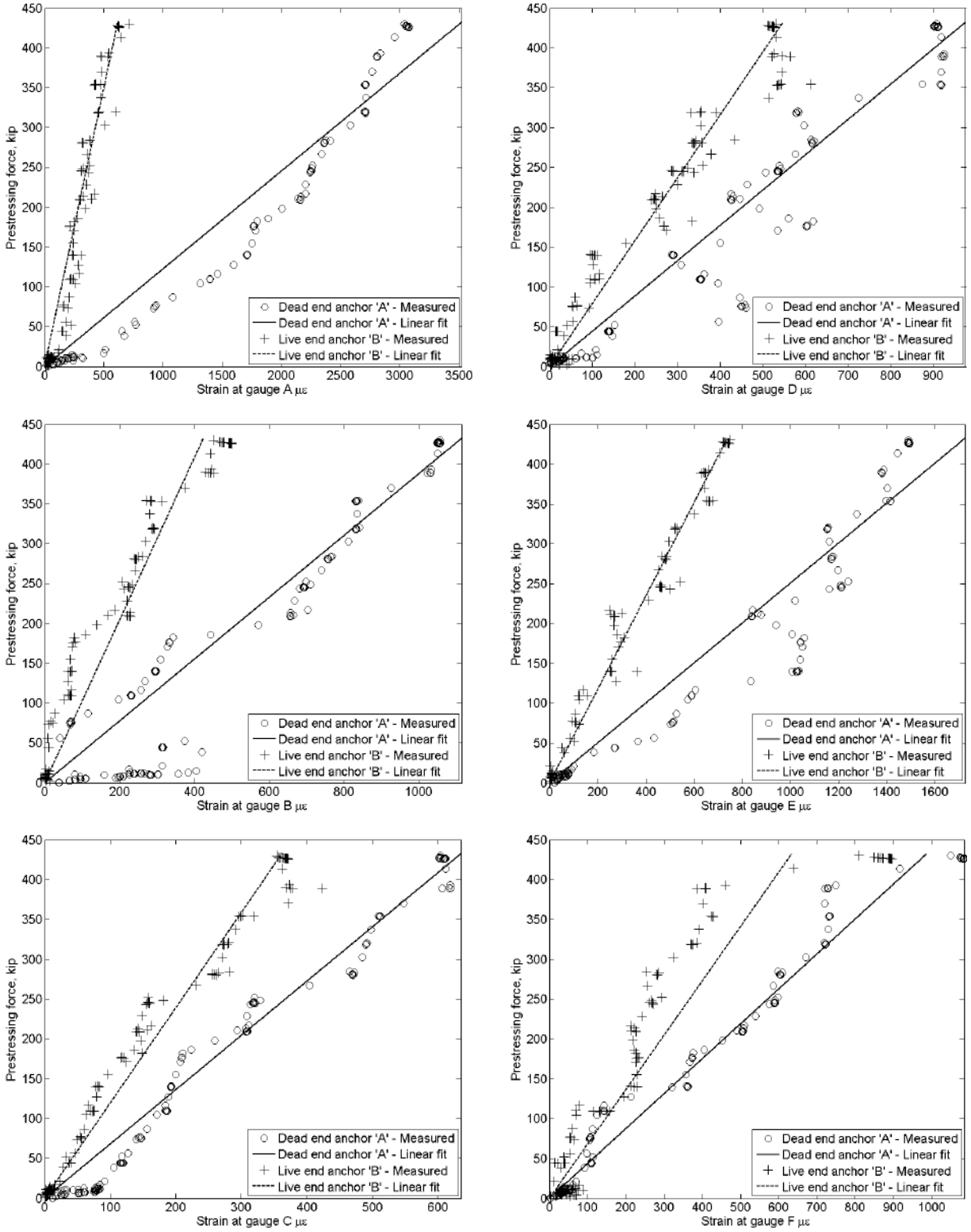


Figure D-35 Strain vs. prestressing force at two anchors during stressing (strain gage A-F)

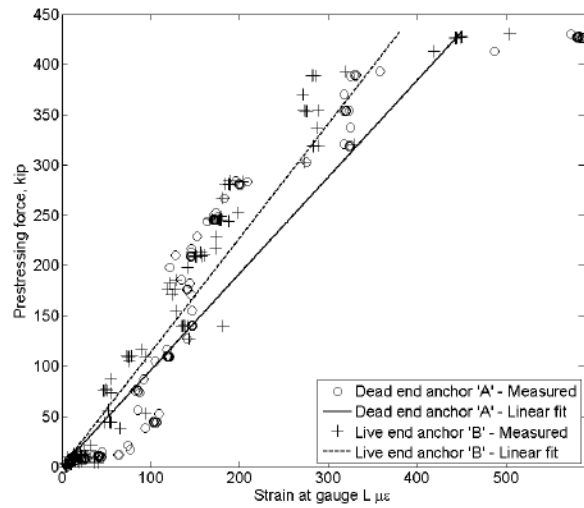
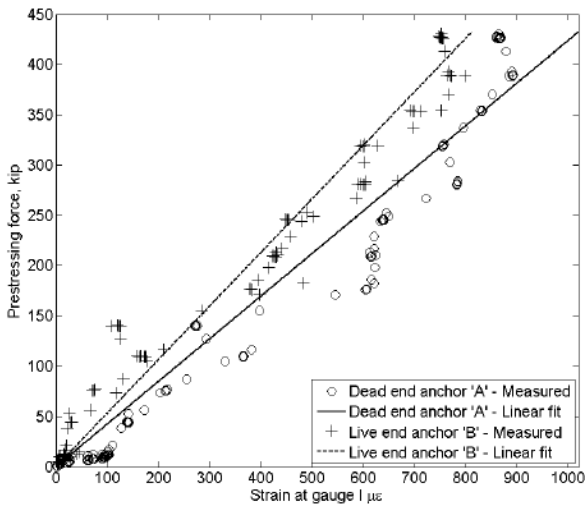
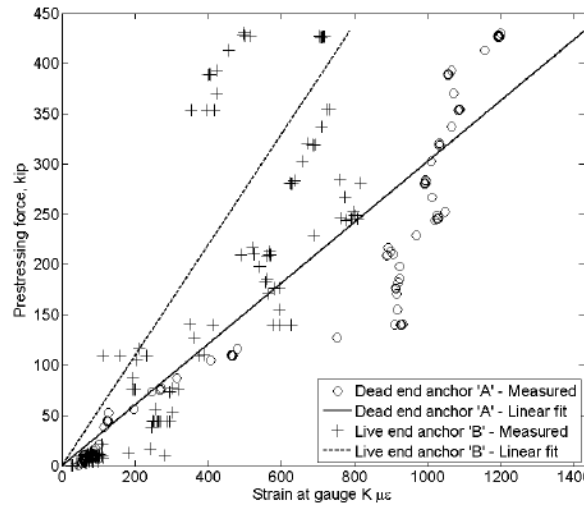
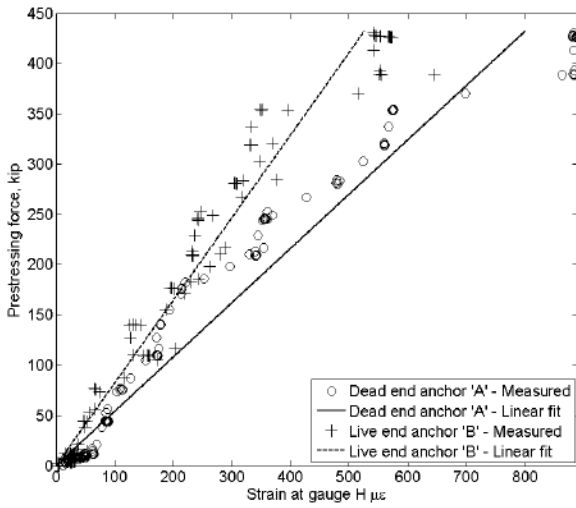
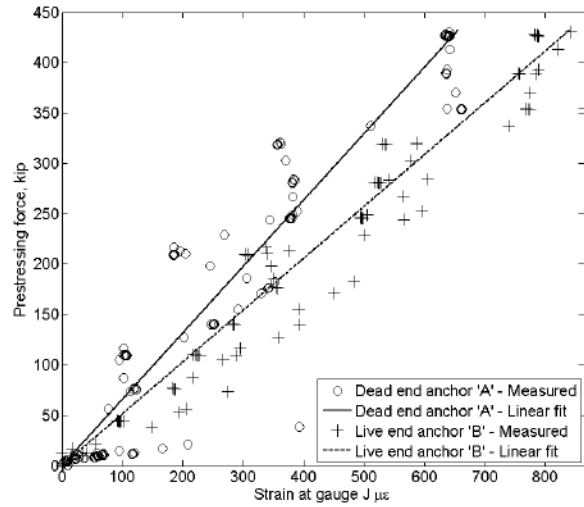
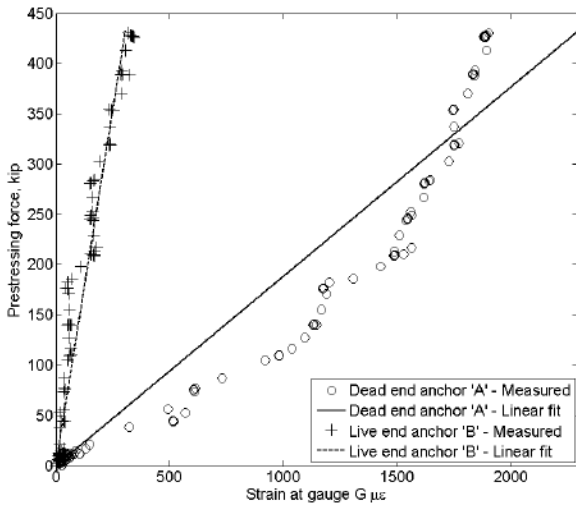


Figure D-36 Strain vs. prestressing force at two anchors during stressing (strain gauge G-L)

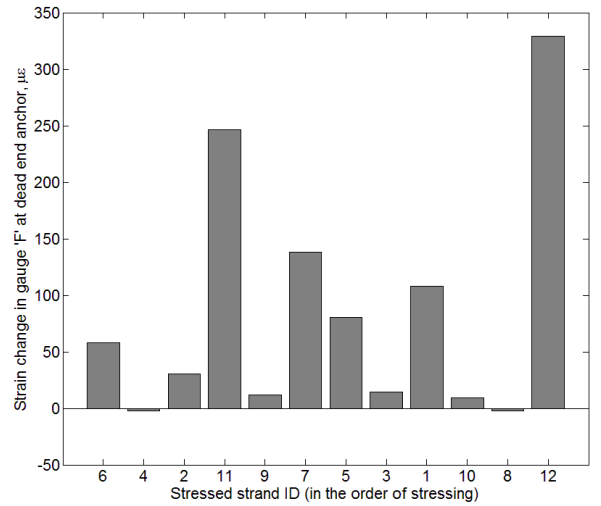
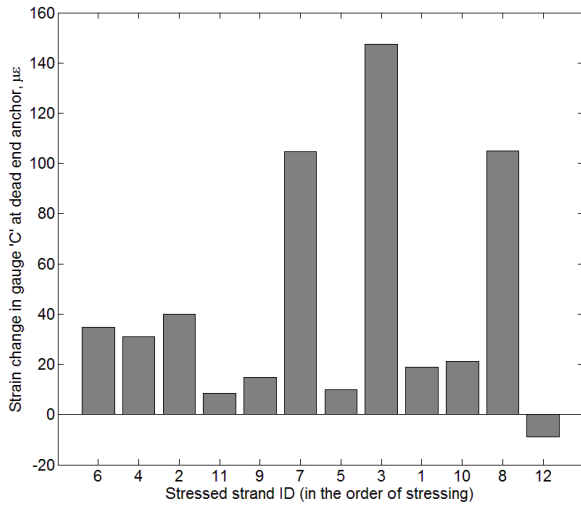
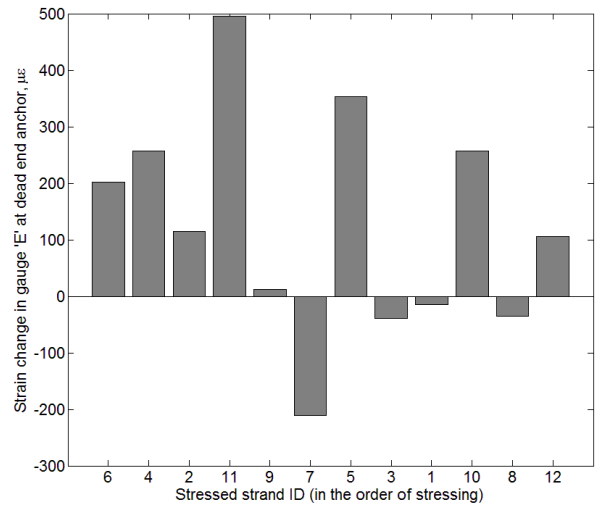
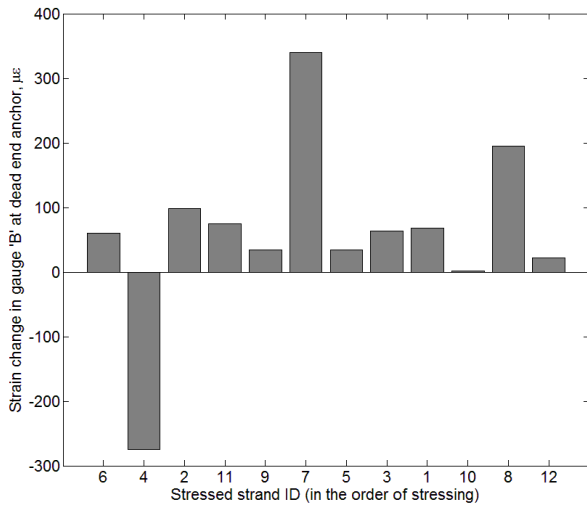
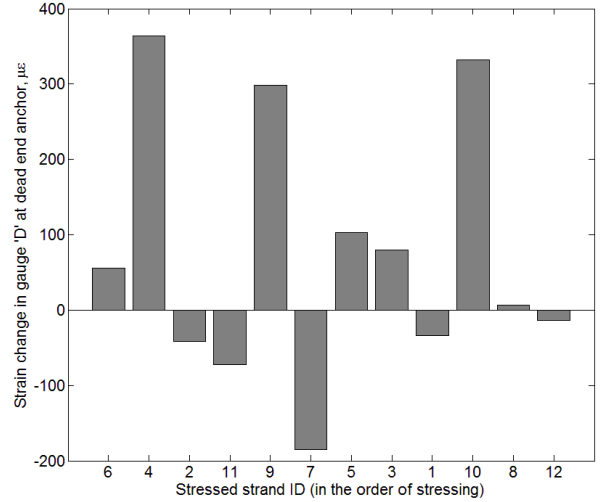
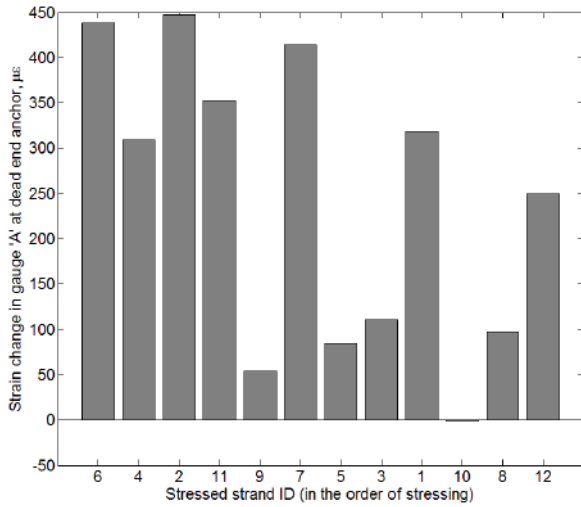


Figure D-37 Strain change in a gage with stressing of each strand (gage A-F, dead end)

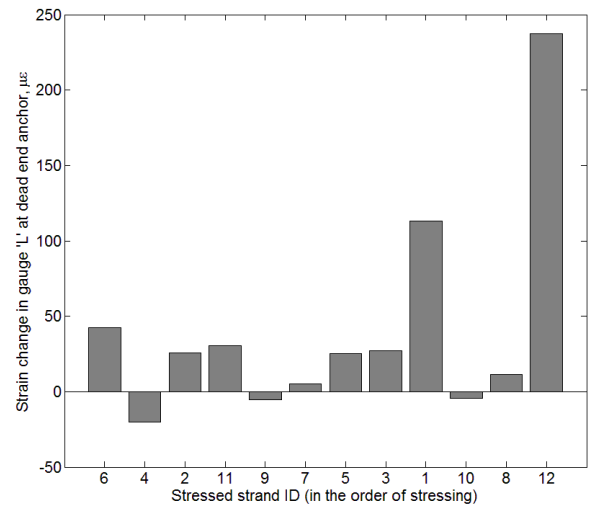
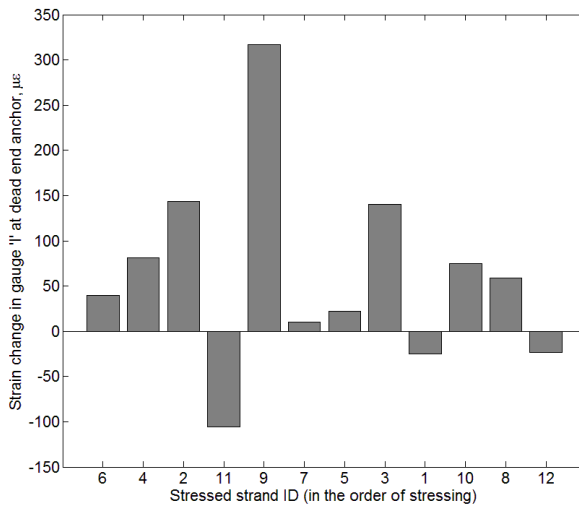
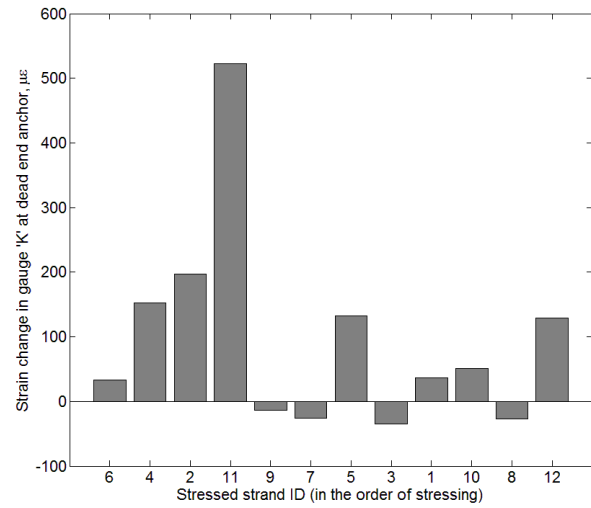
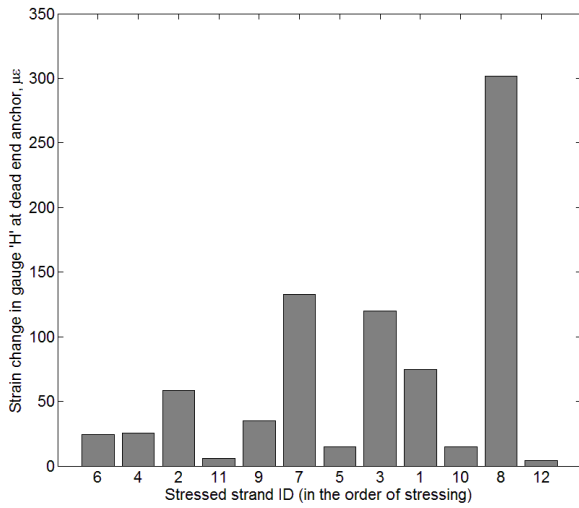
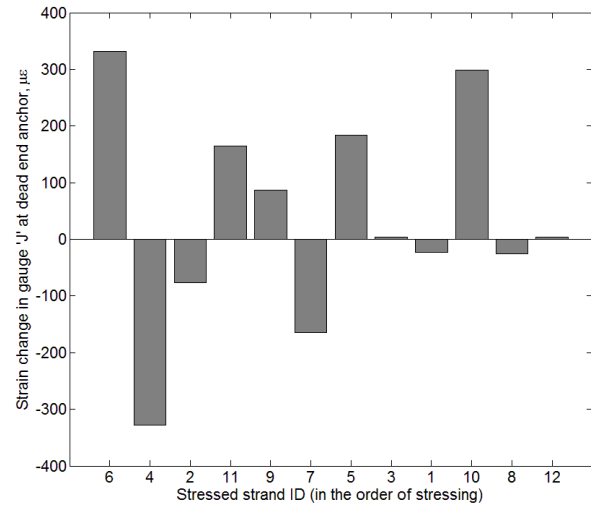
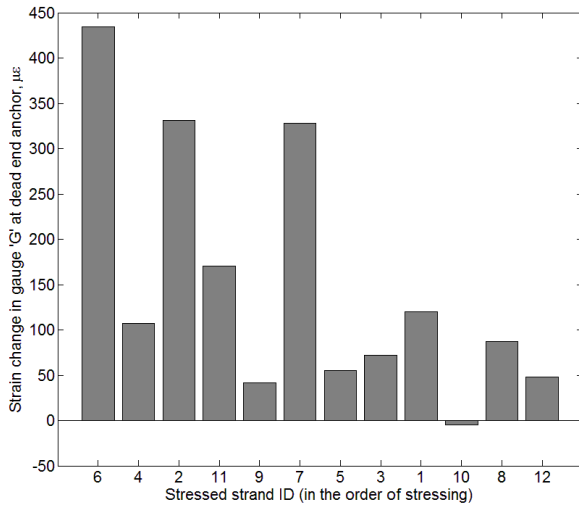


Figure D-38 Strain change in a gage with stressing of each strand (gage G-L, dead end)

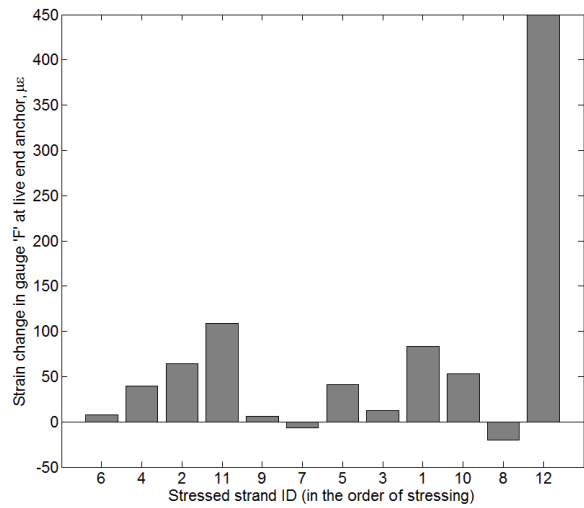
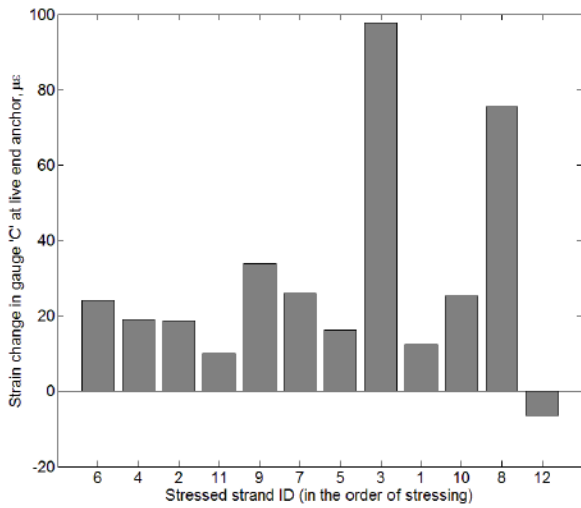
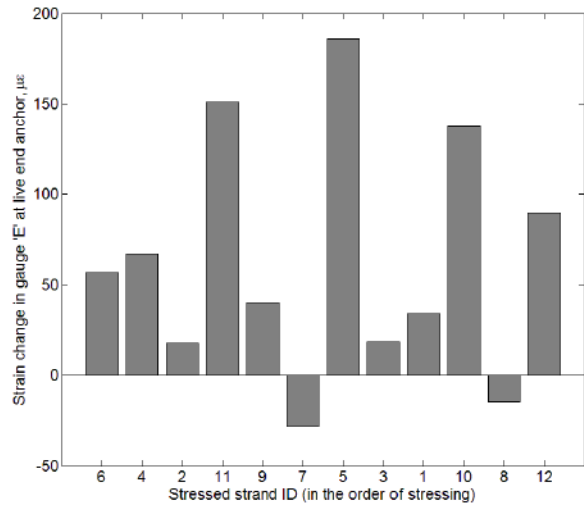
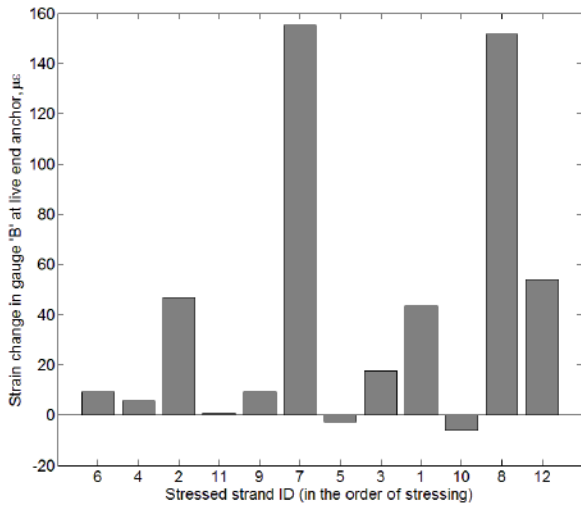
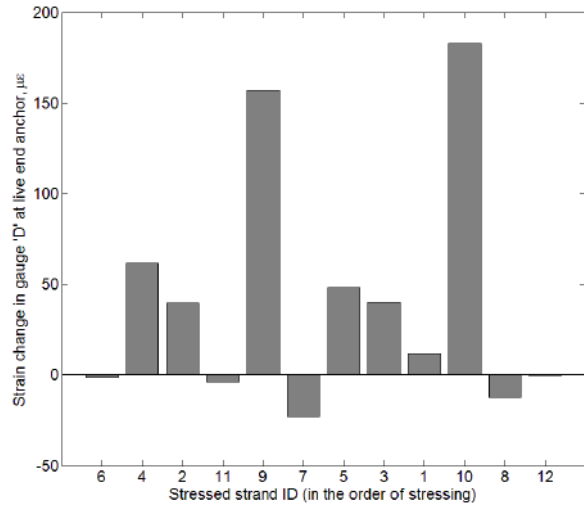
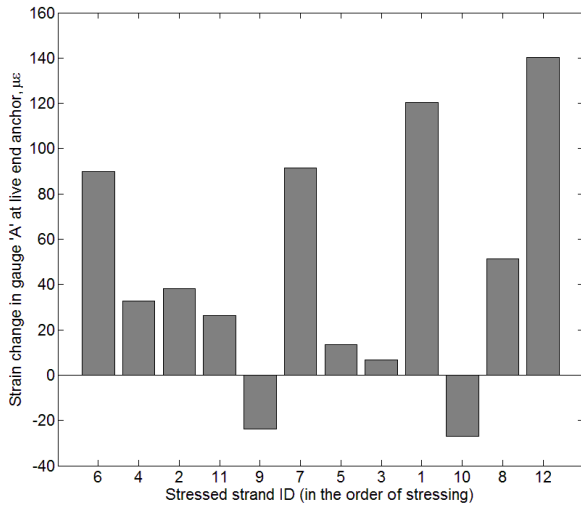


Figure D-39 Strain change in a gage with stressing of each strand (gage A-F, live end)

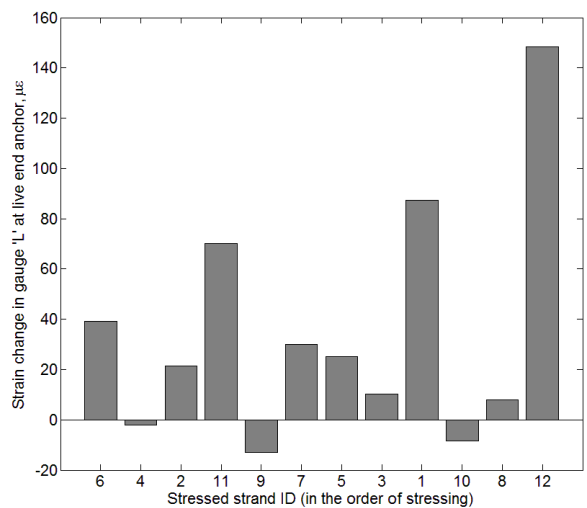
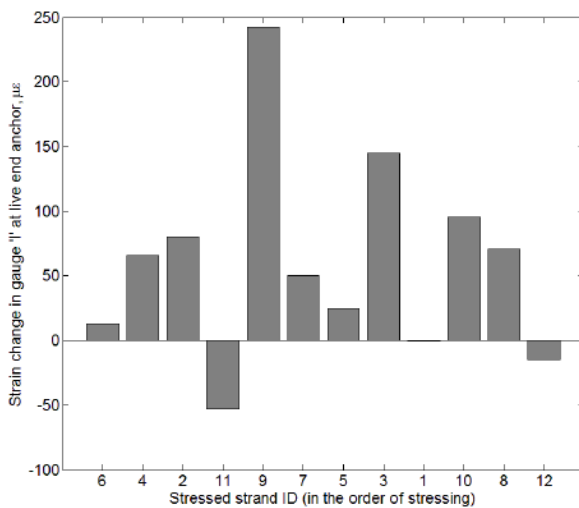
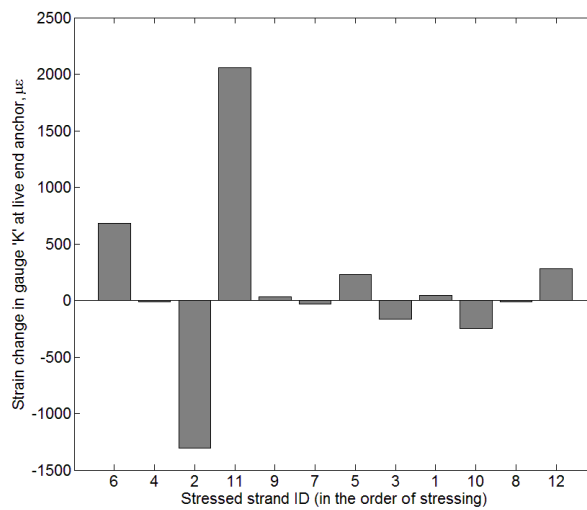
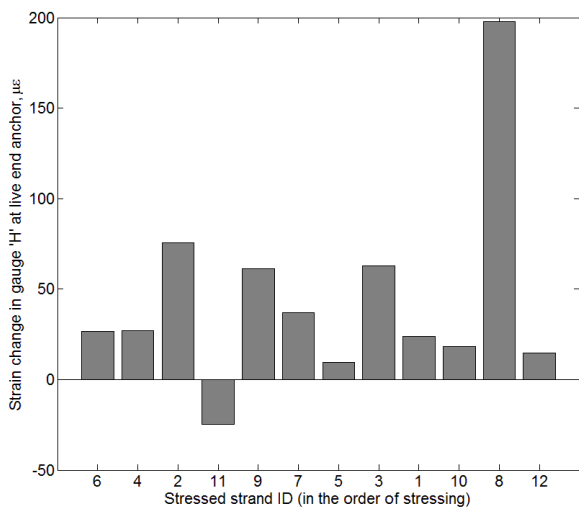
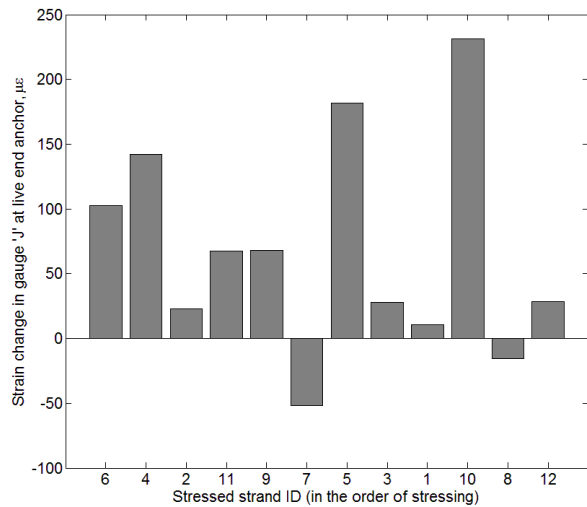
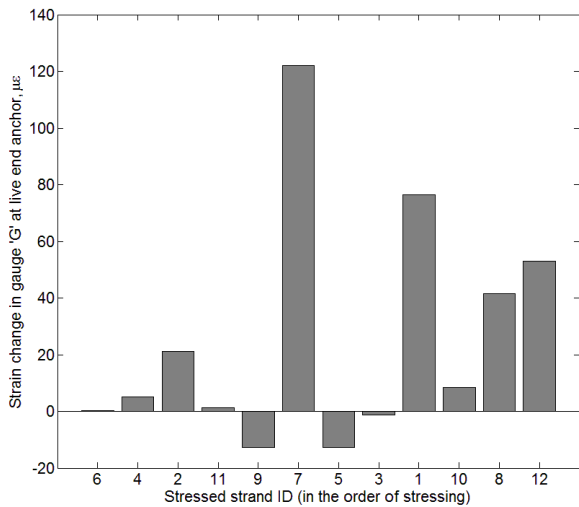


Figure D-40 Strain change in a gage with stressing of each strand (gage G-L, live end)

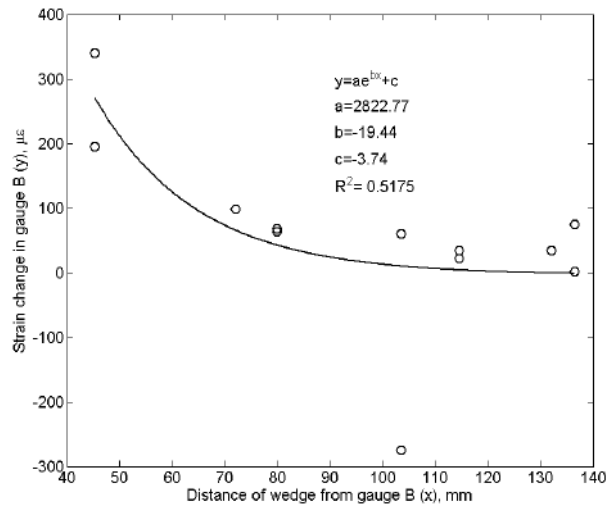
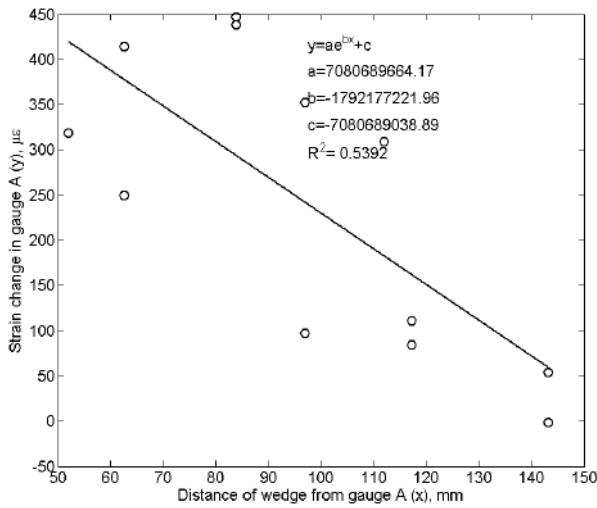
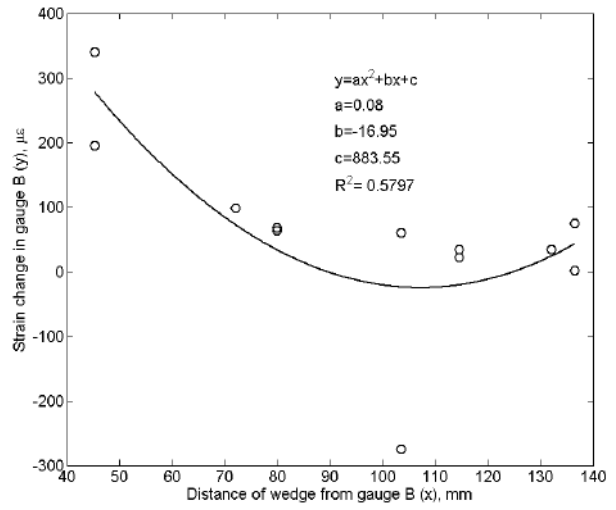
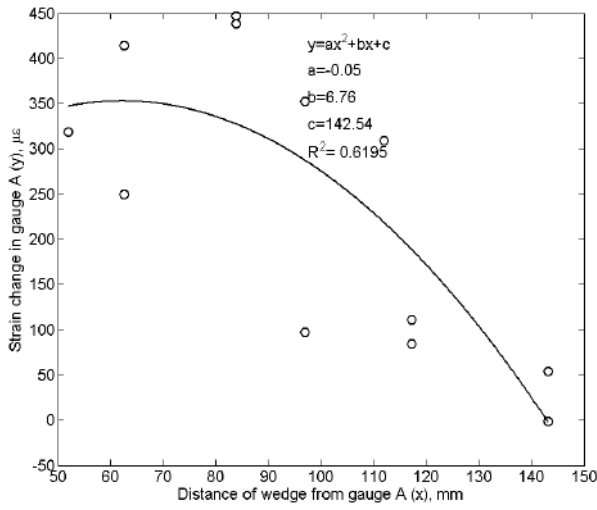
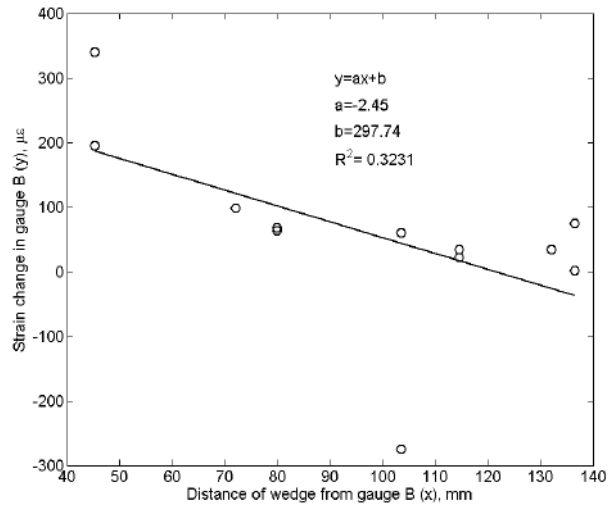
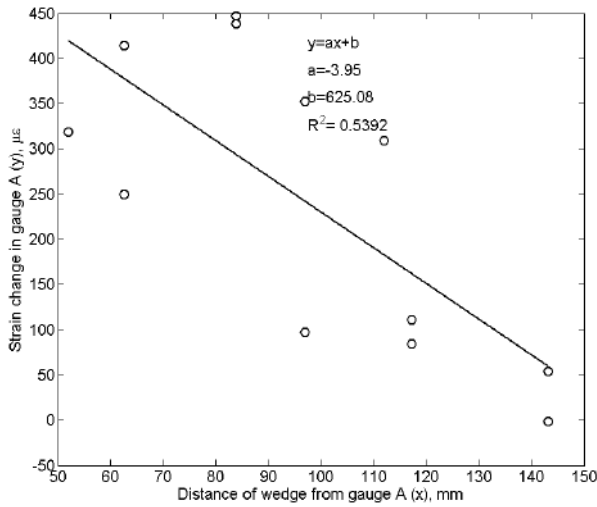


Figure D-41 Strain-distance statistical fits (gauge A and B, dead end)

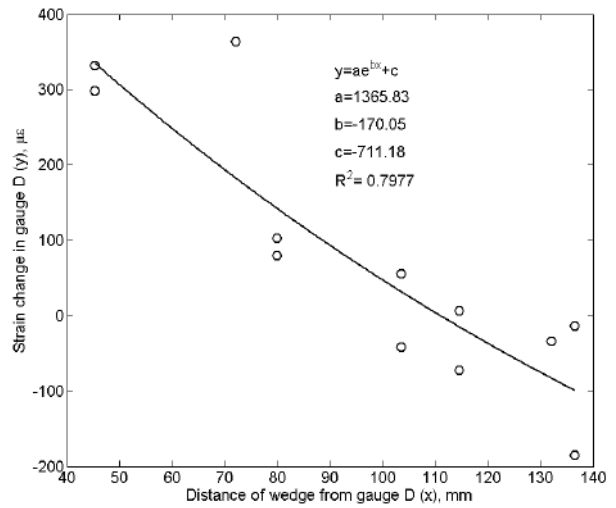
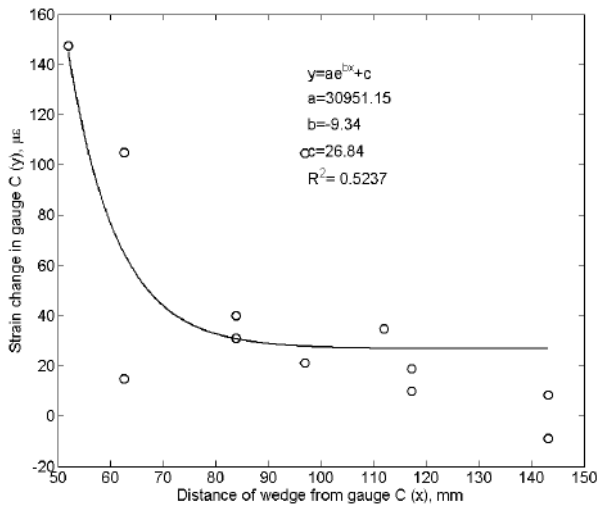
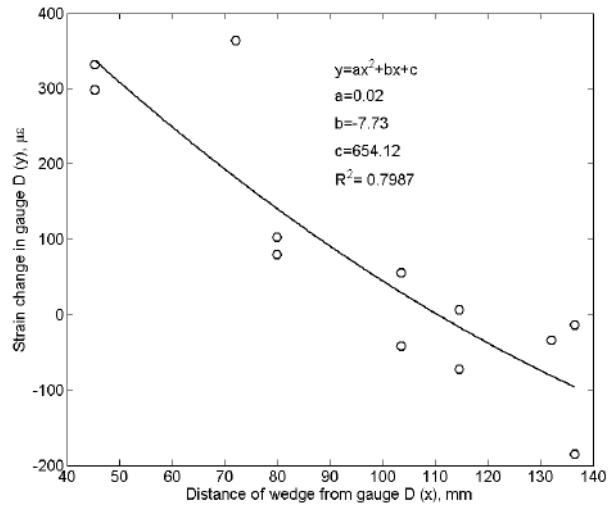
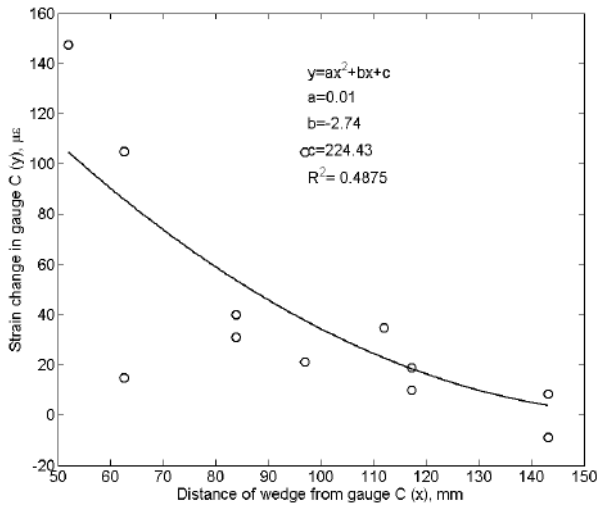
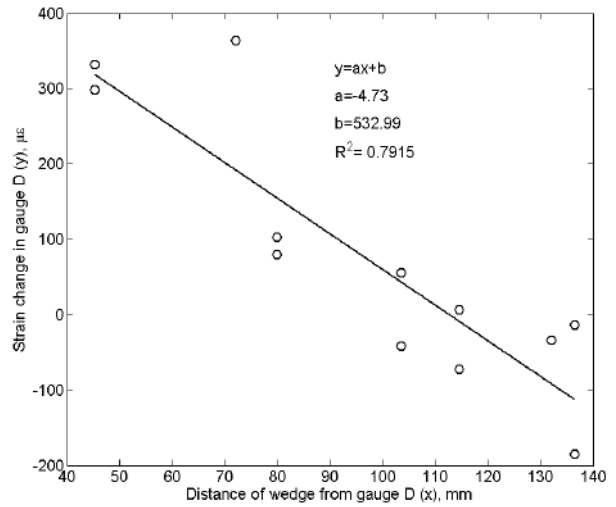
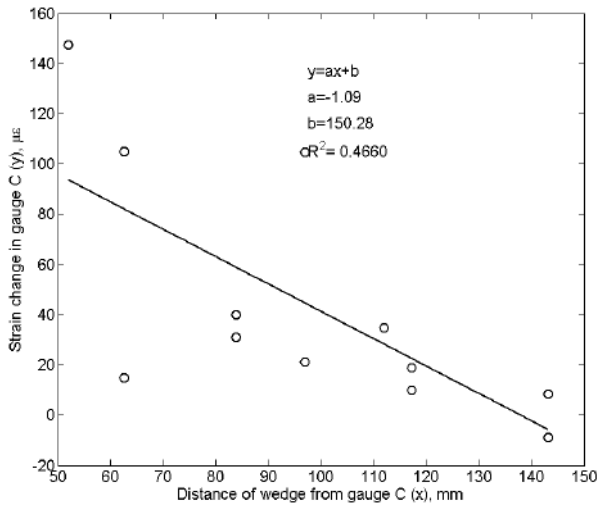


Figure D-42 Strain-distance statistical fits (gauge C and D, dead end)

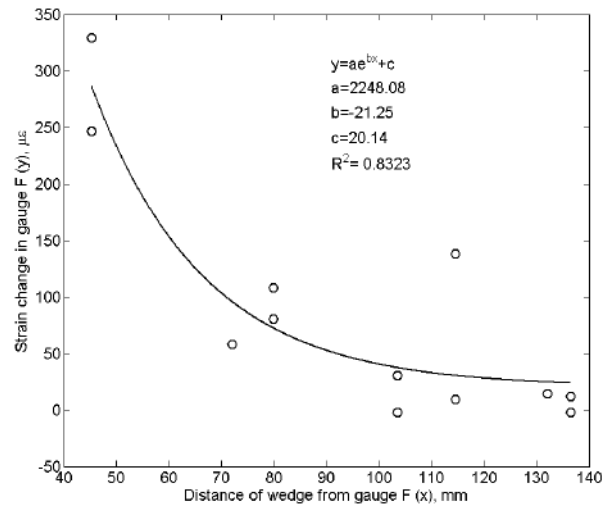
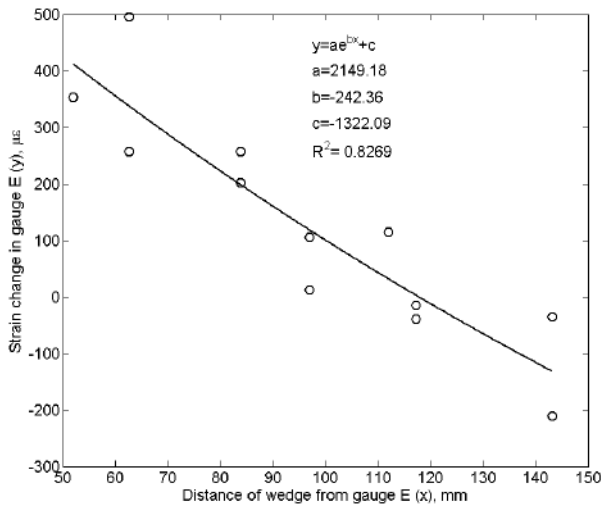
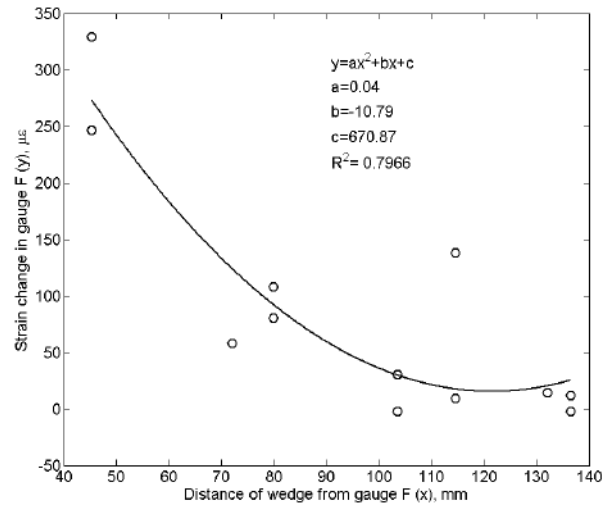
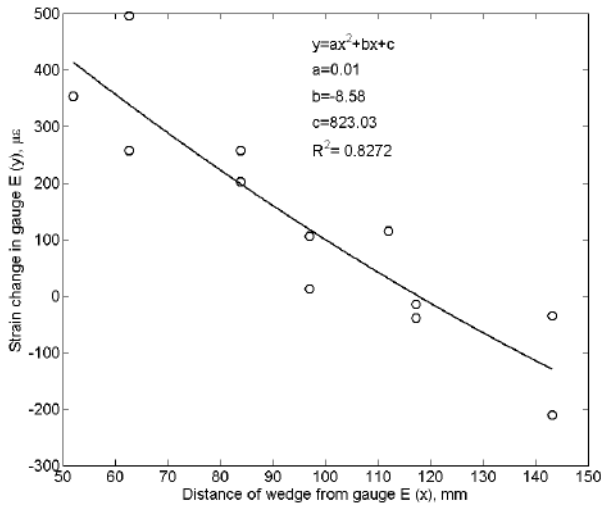
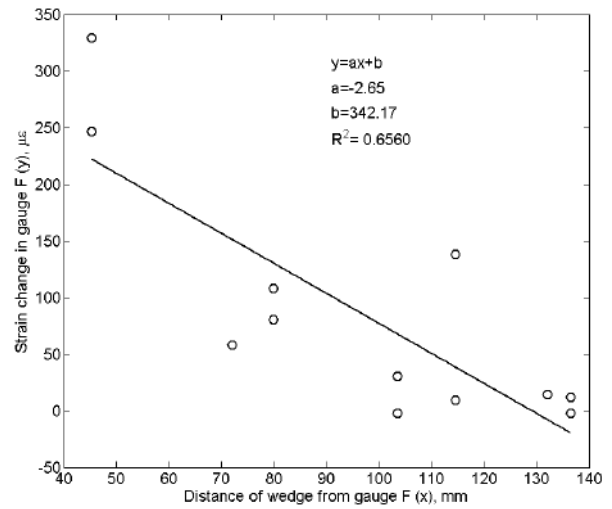
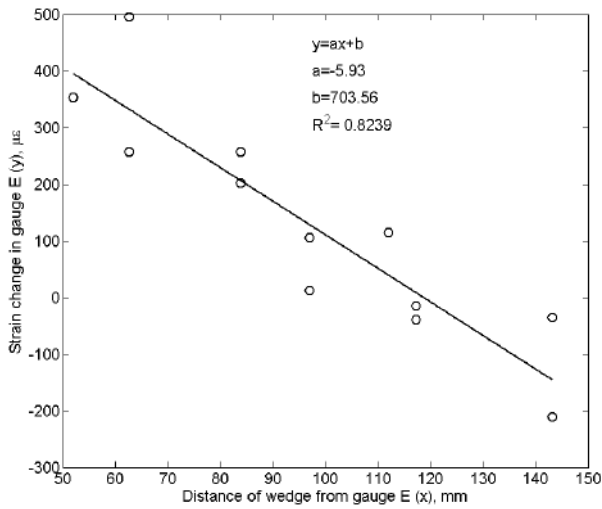


Figure D-43 Strain-distance statistical fits (gage E and F, dead end)

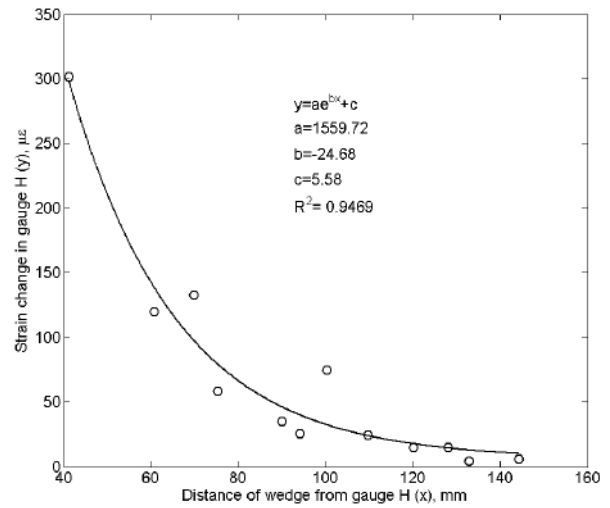
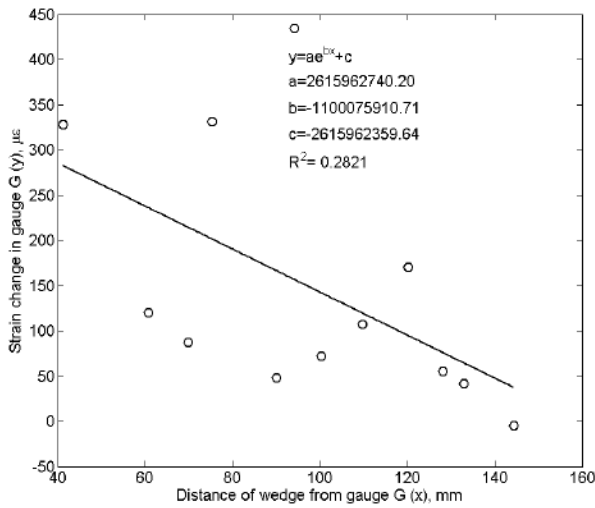
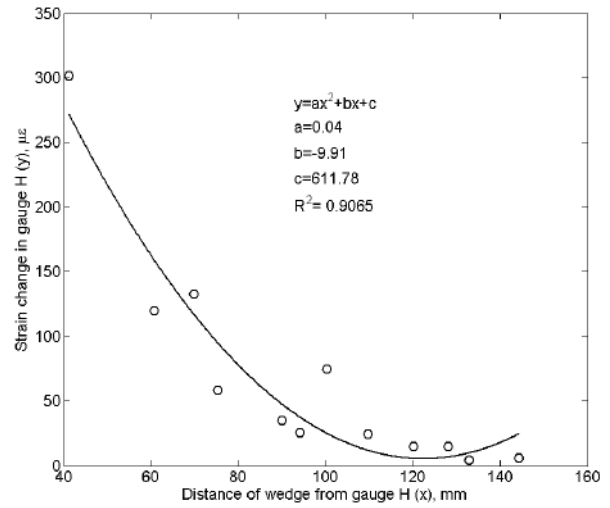
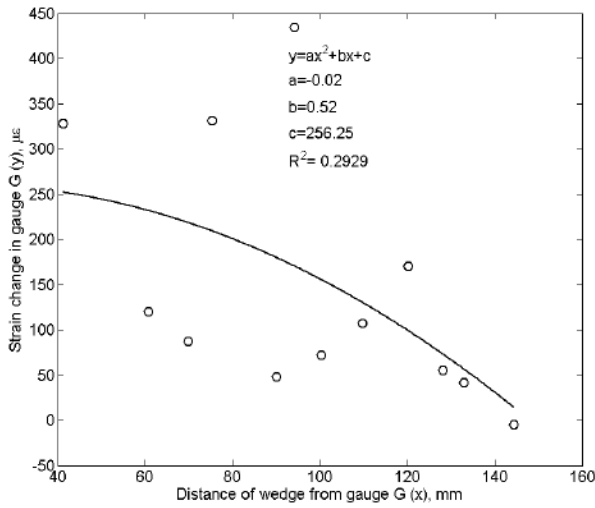
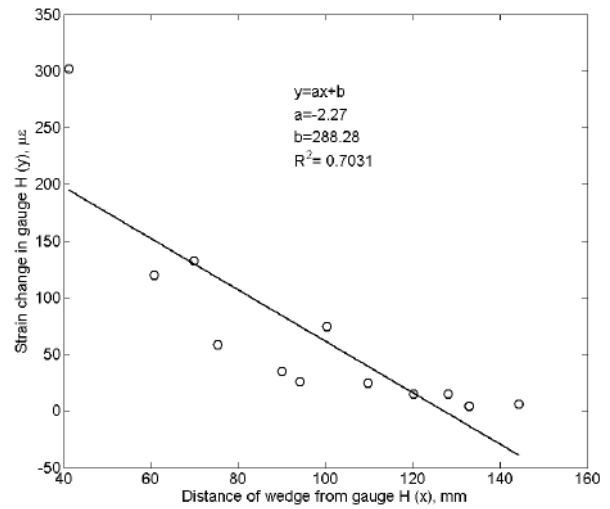
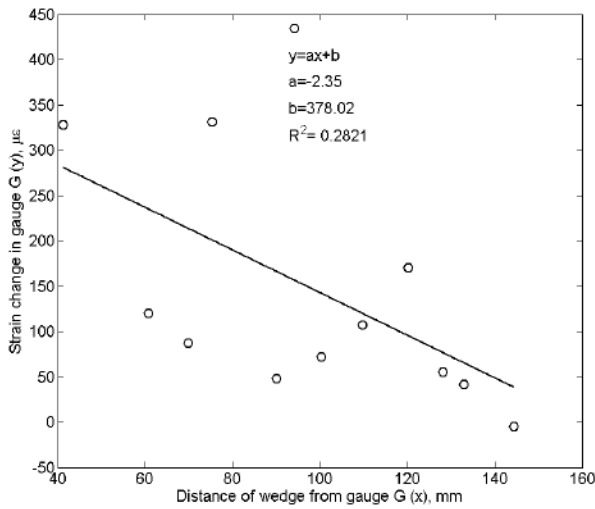


Figure D-44 Strain-distance statistical fits (gage G and H, dead end)

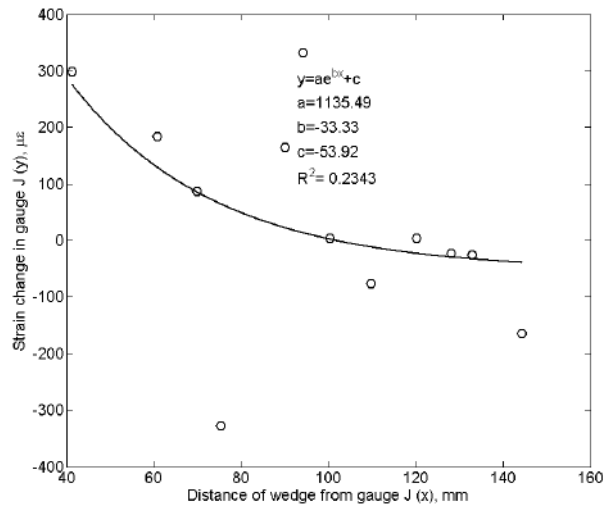
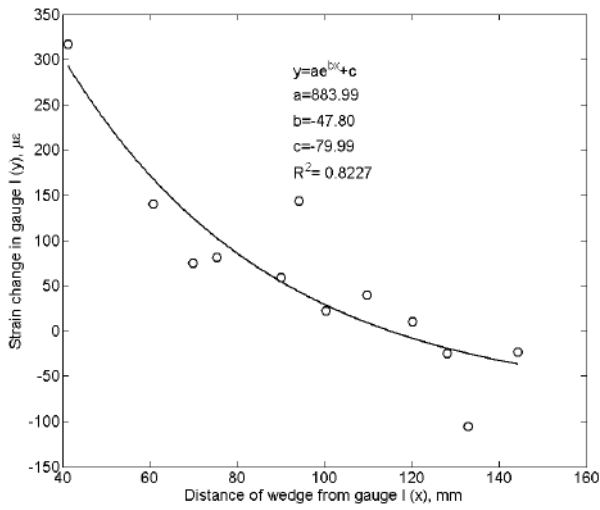
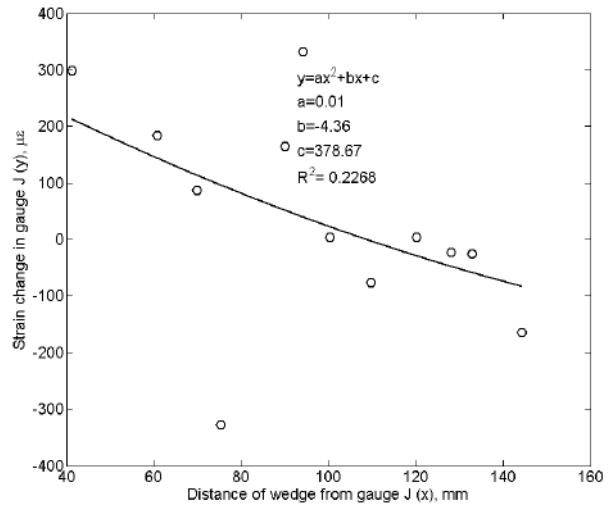
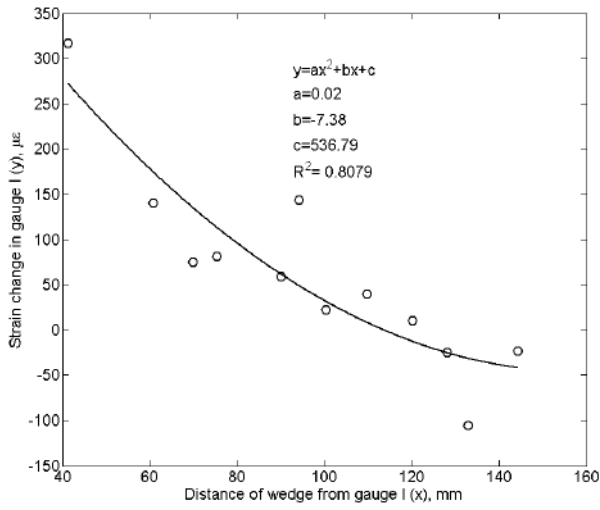
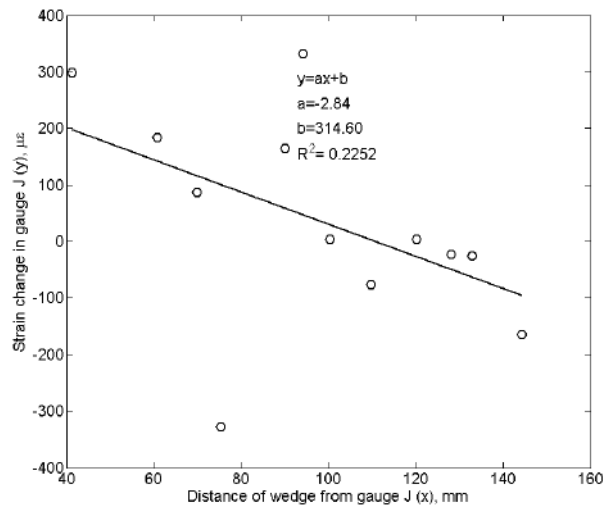
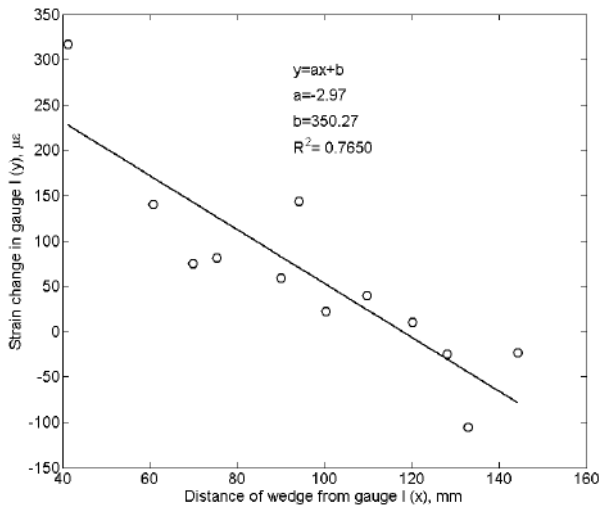


Figure D-45 Strain-distance statistical fits (gauge I and J, dead end)

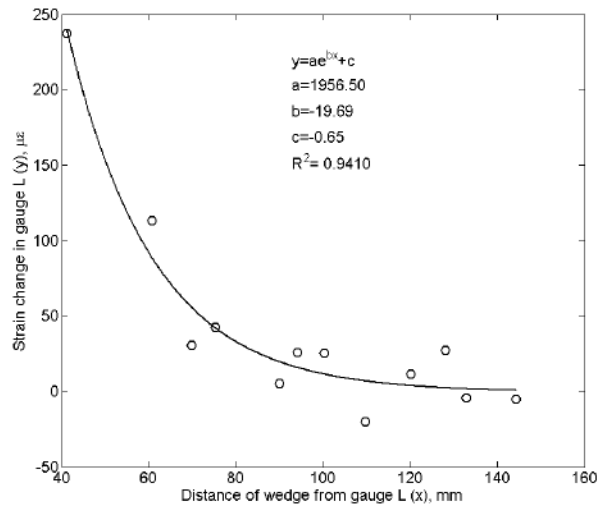
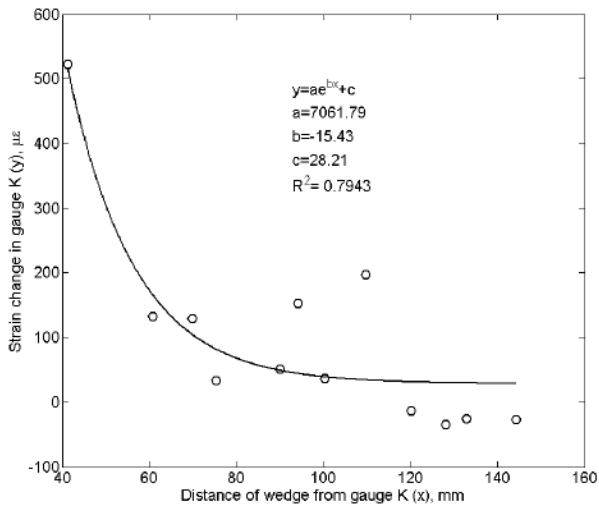
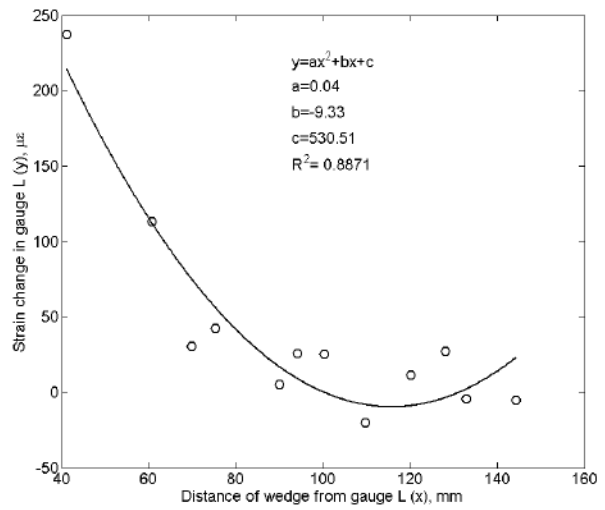
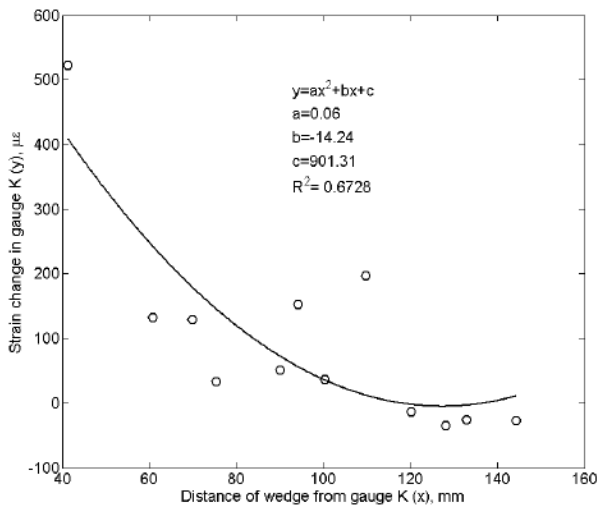
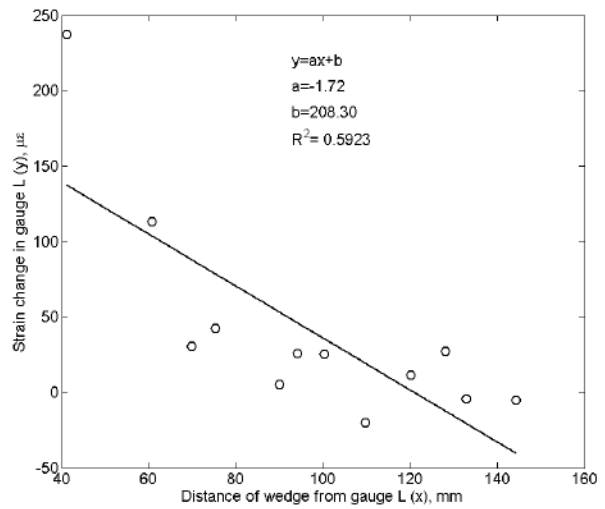
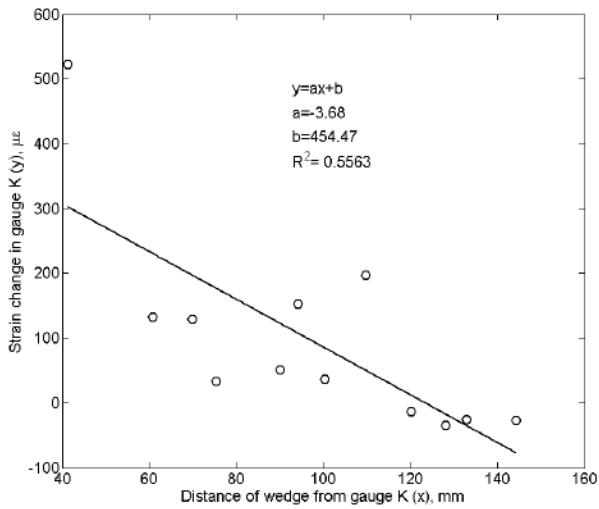


Figure D-46 Strain-distance statistical fits (gauge K and L, dead end)

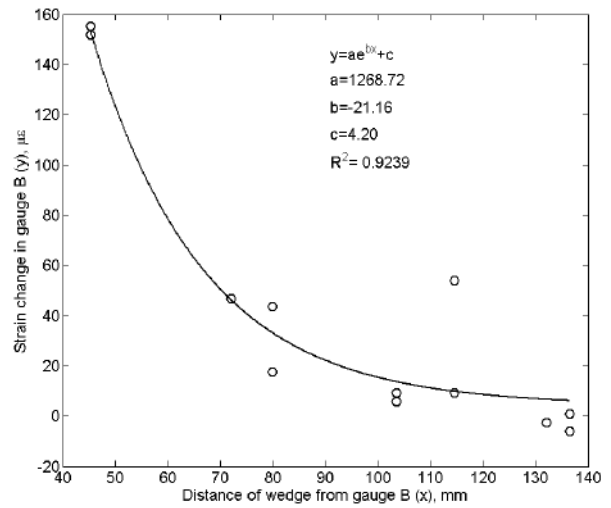
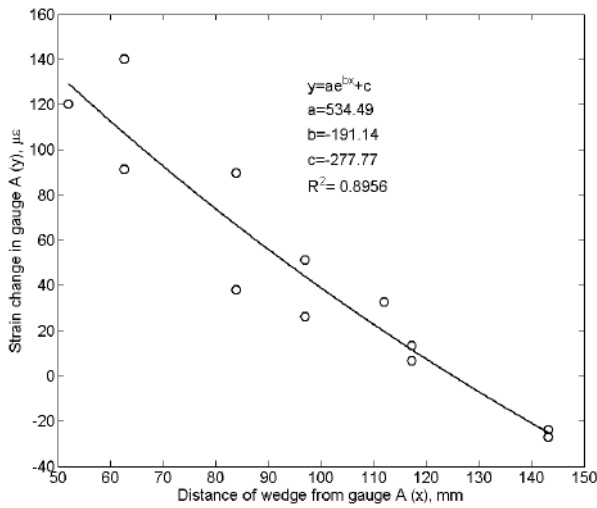
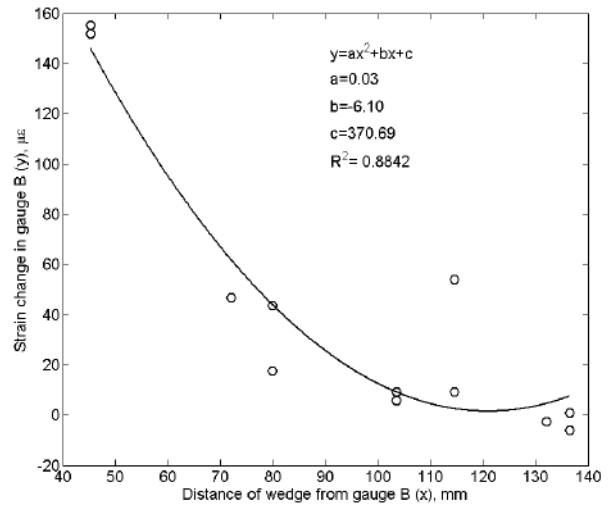
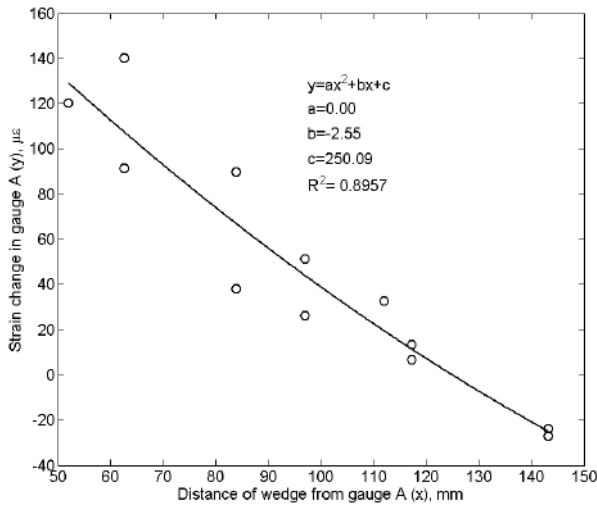
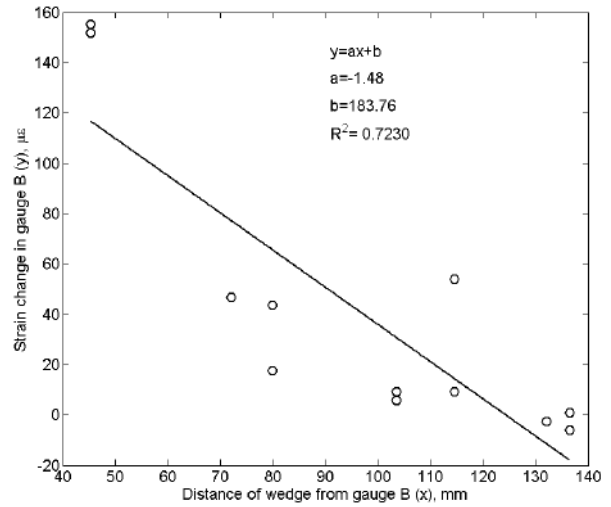
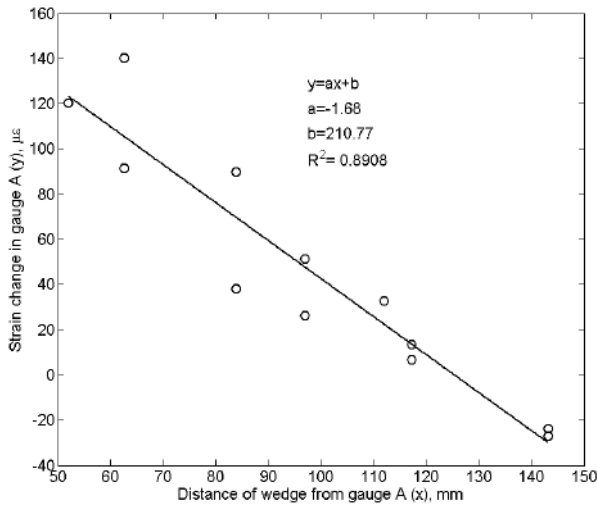


Figure D-47 Strain-distance statistical fits (gage A and B, live end)

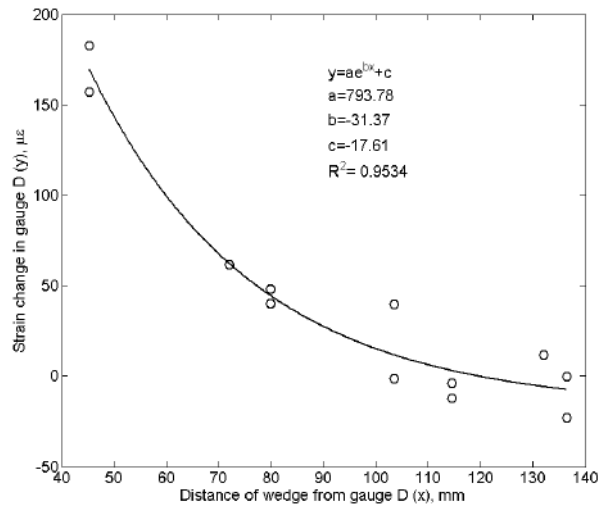
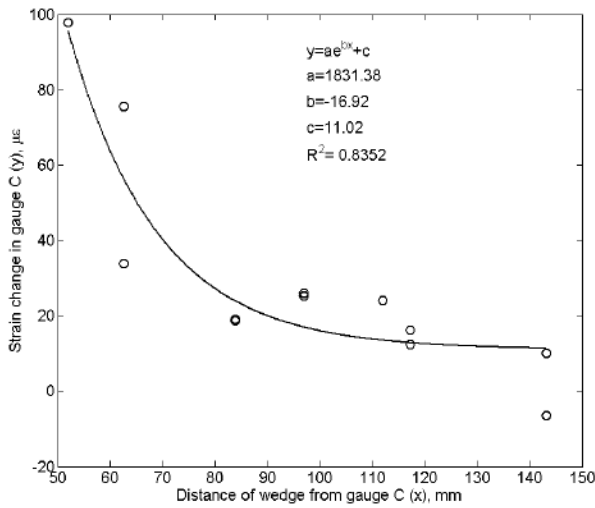
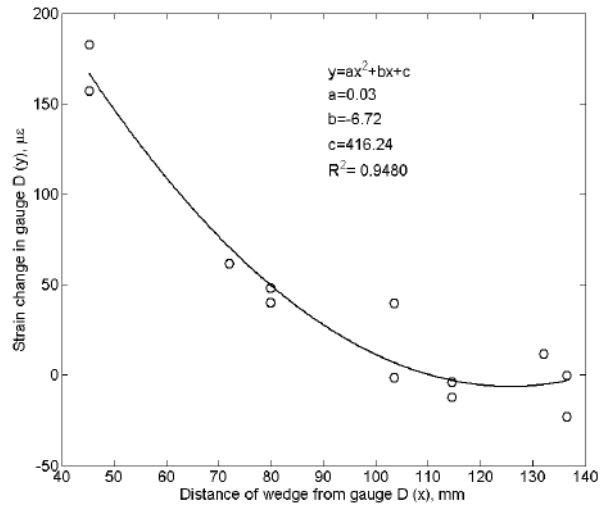
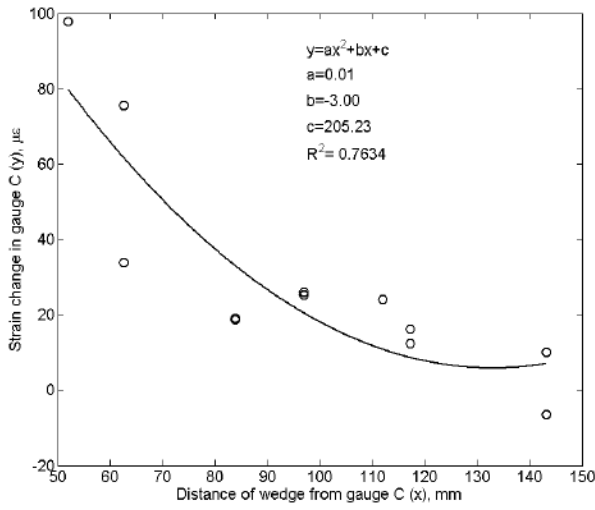
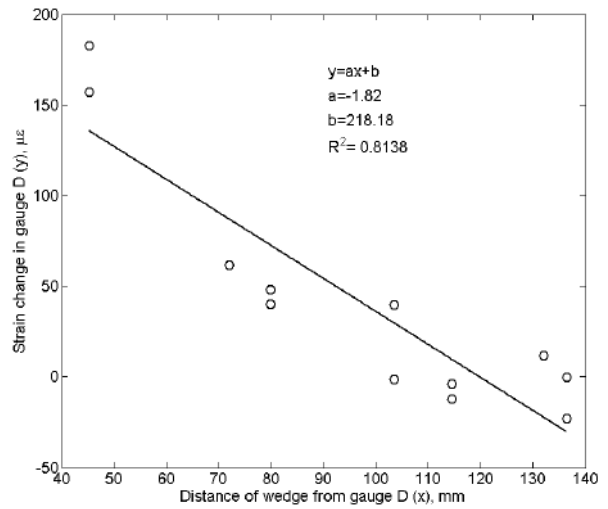
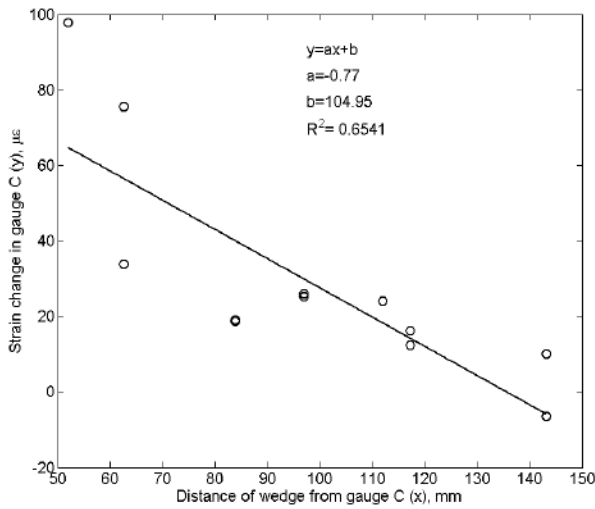


Figure D-48 Strain-distance statistical fits (gage C and D, live end)

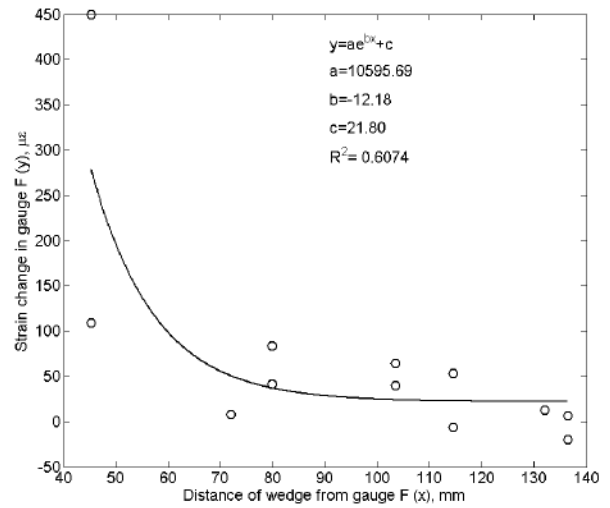
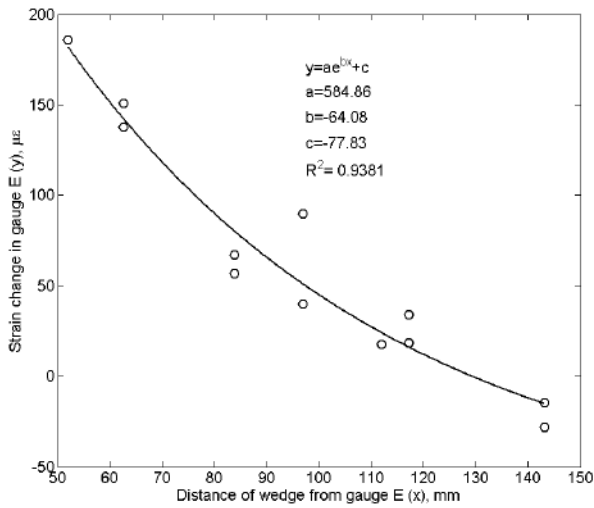
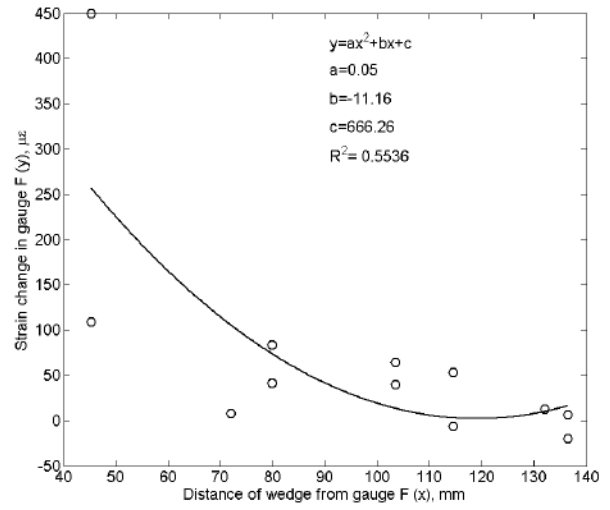
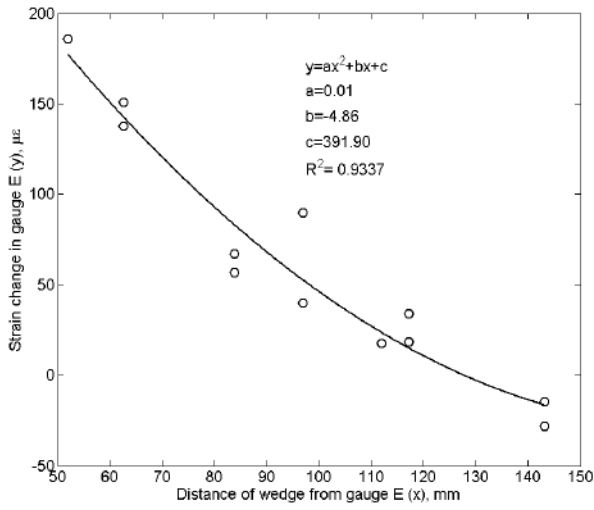
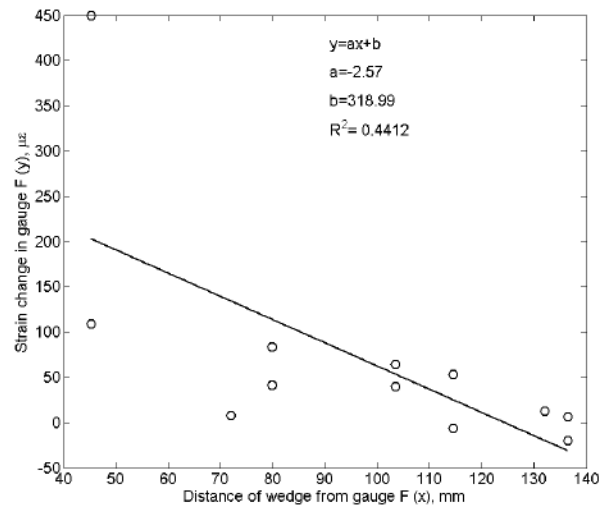
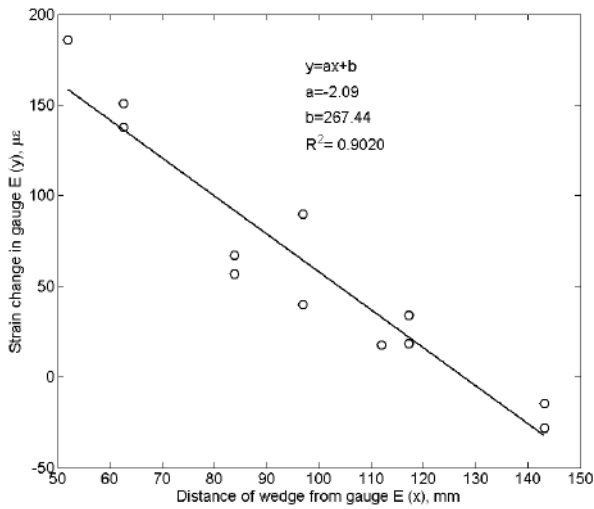


Figure D-49 Strain-distance statistical fits (gage E and F, live end)

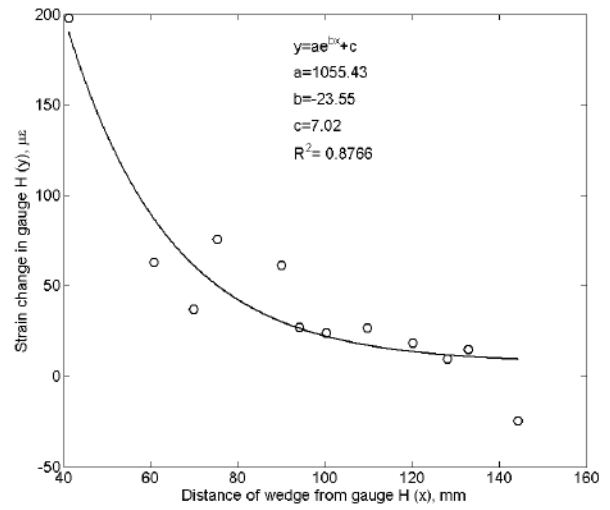
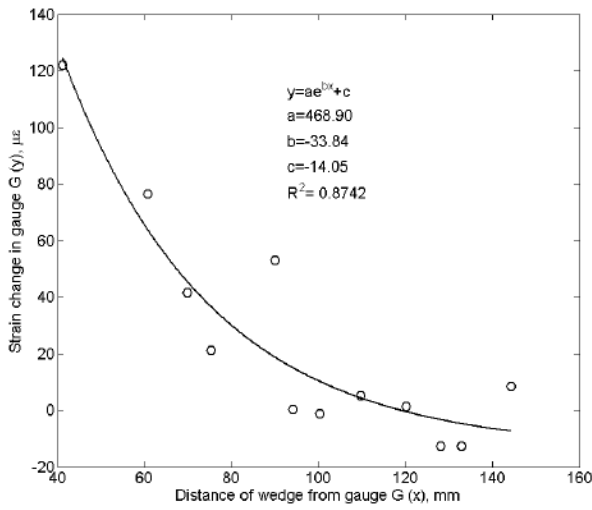
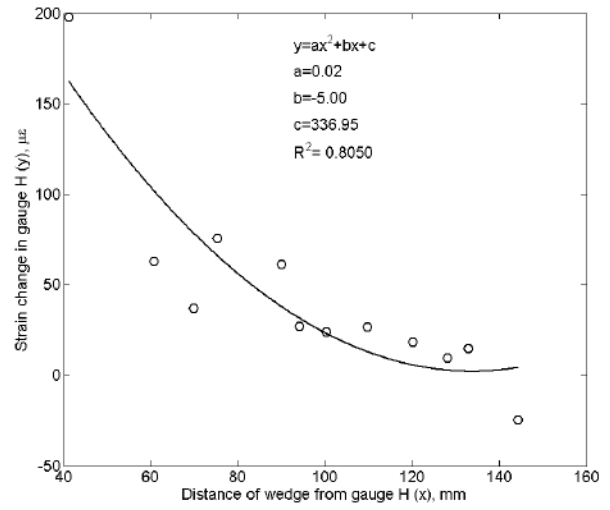
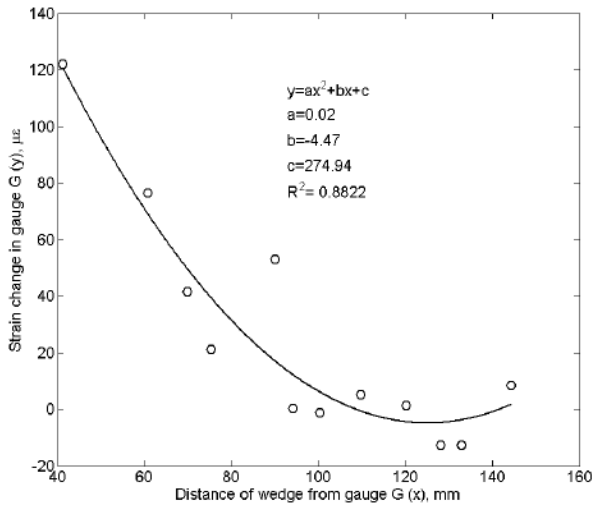
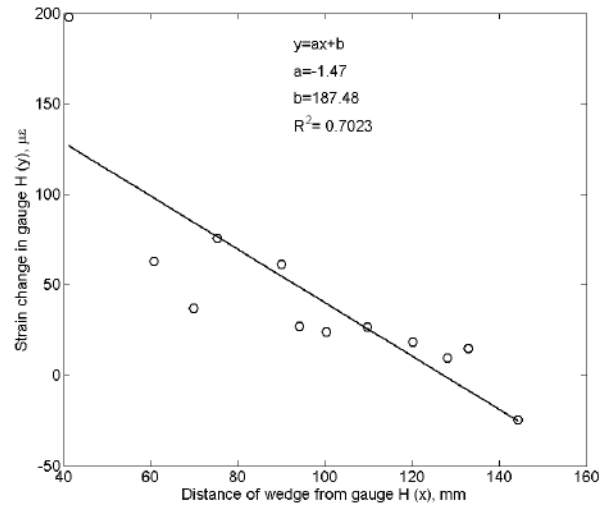
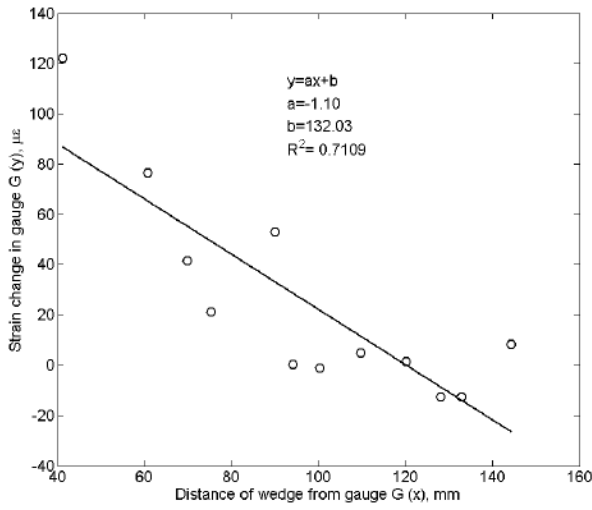


Figure D-50 Strain-distance statistical fits (gage G and H, live end)

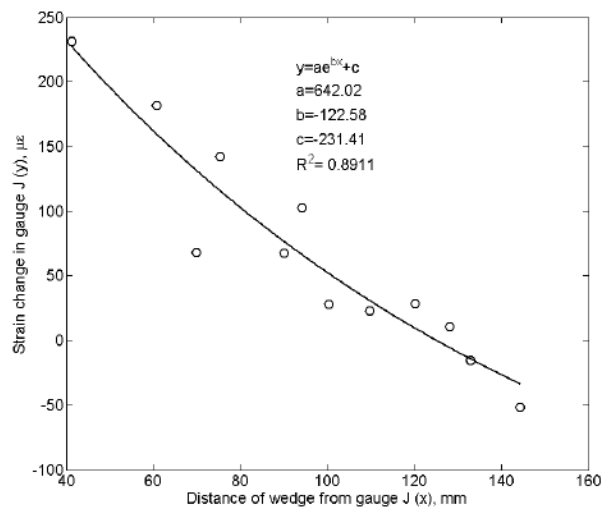
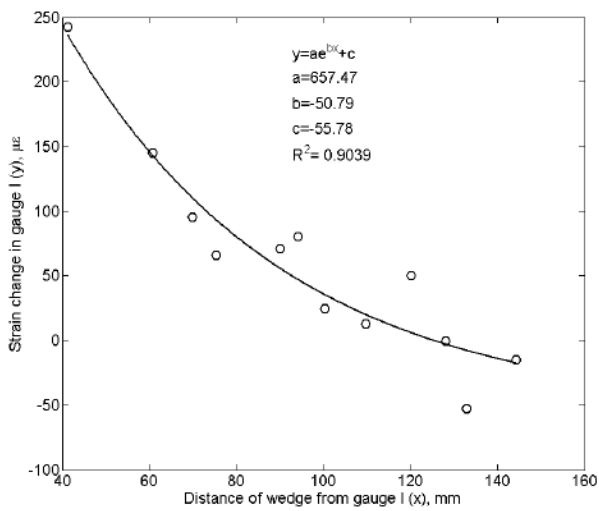
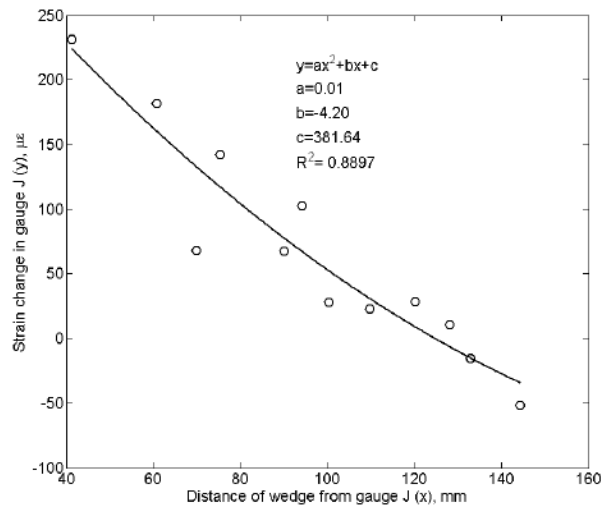
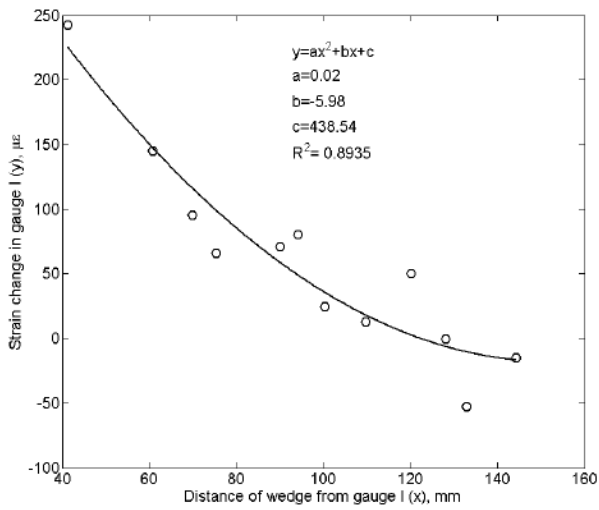
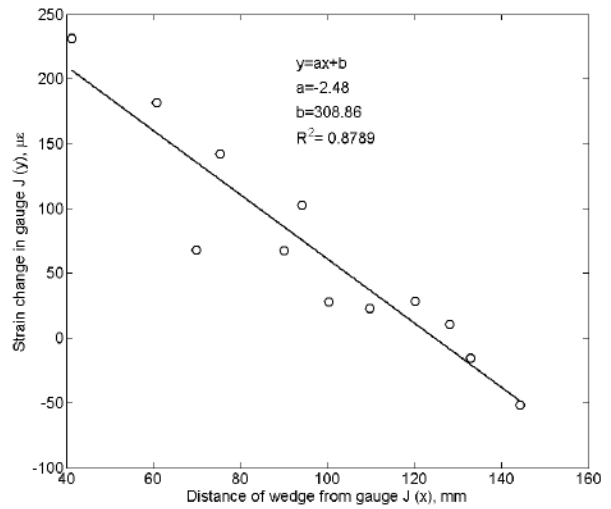
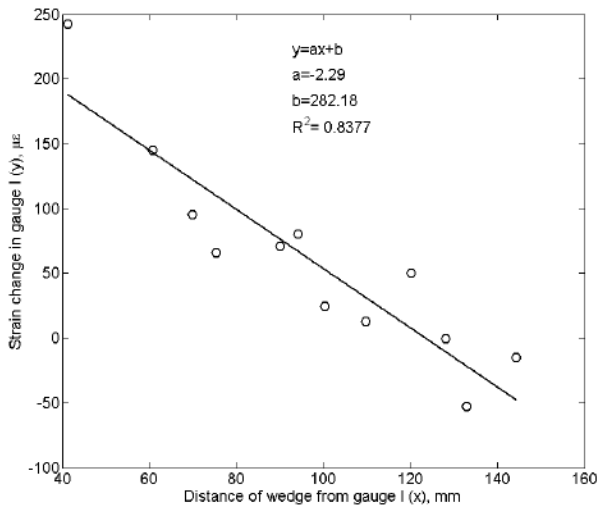


Figure D-51 Strain-distance statistical fits (gage I and J, live end)

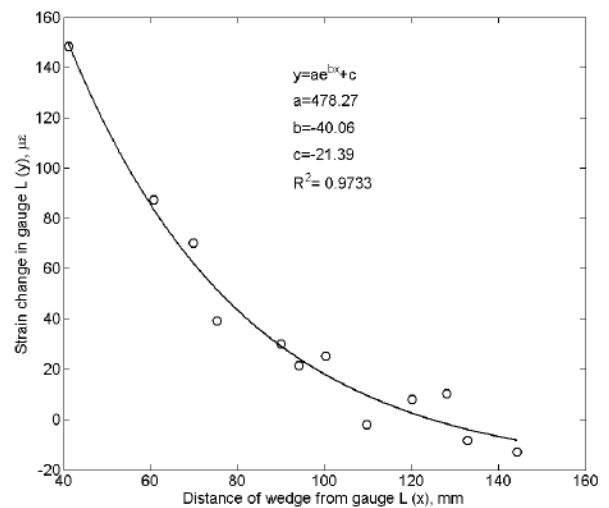
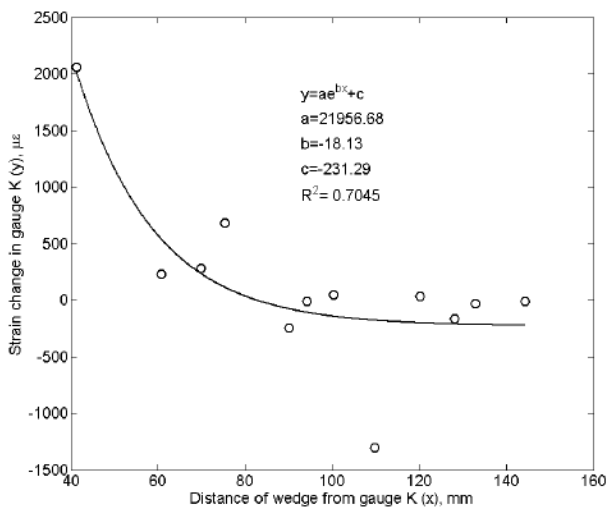
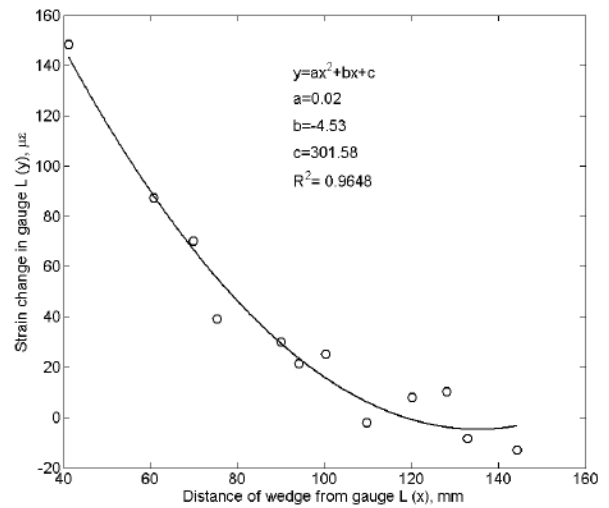
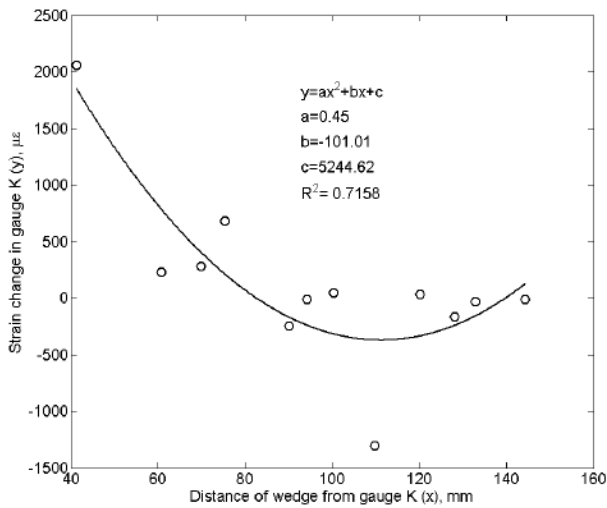
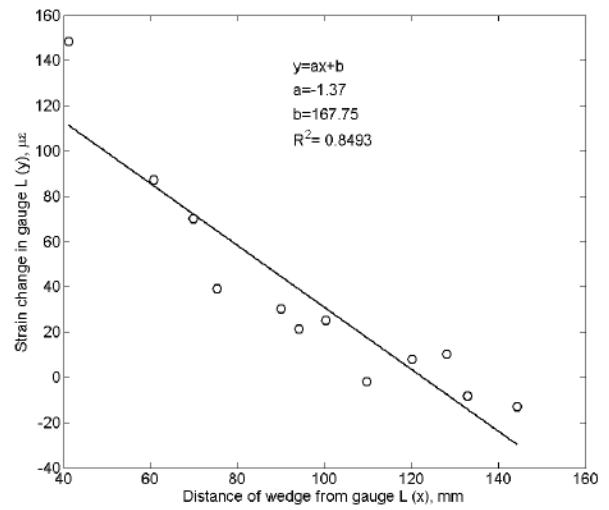
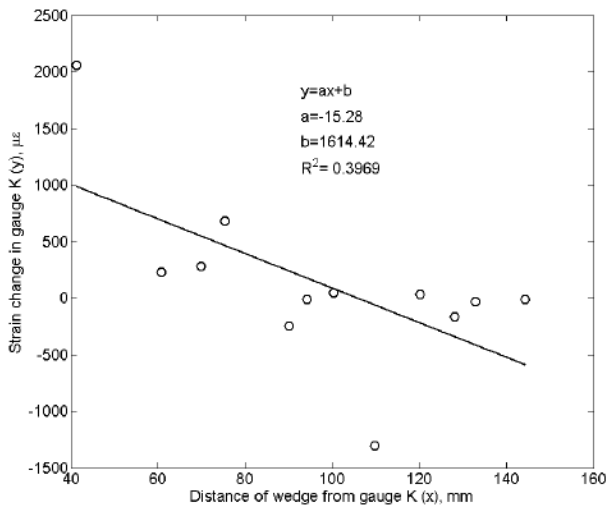


Figure D-52 Strain-distance statistical fits (gage K and L, live end)

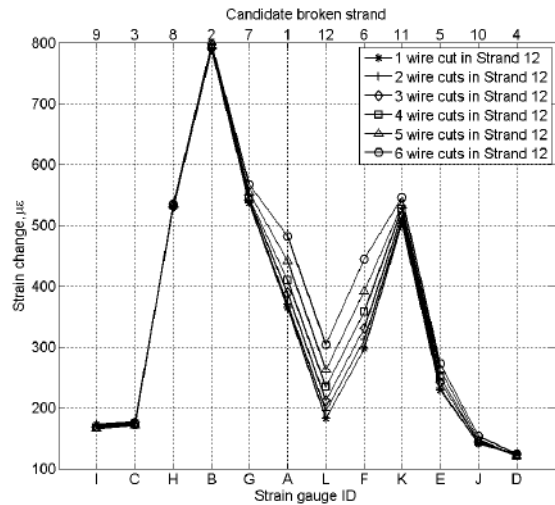
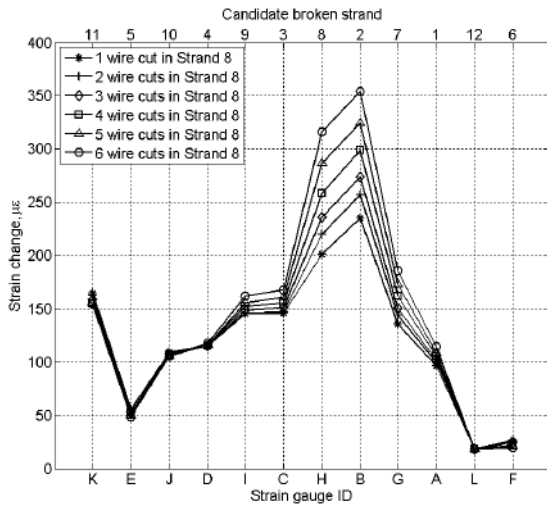
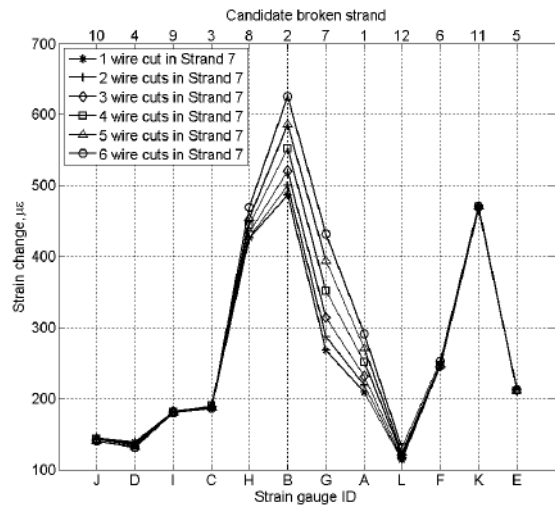
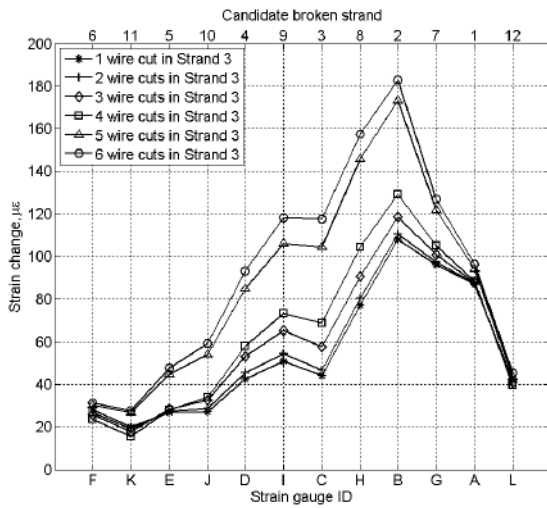
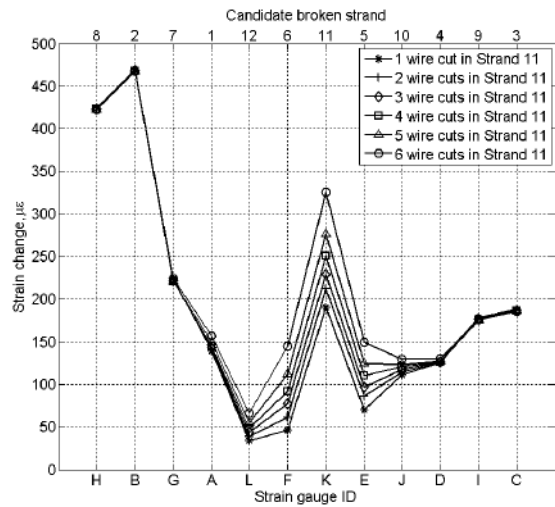
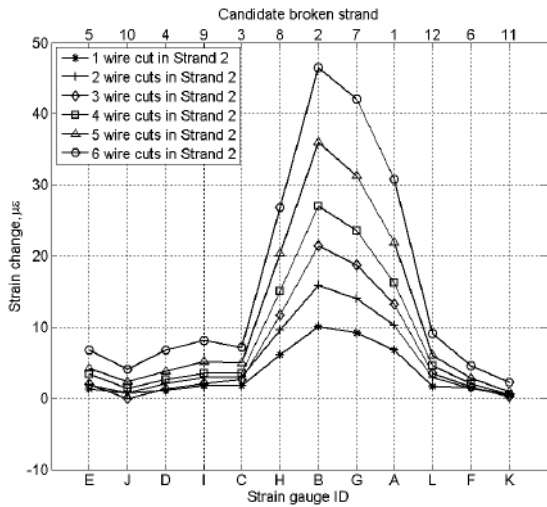


Figure D-53 Strain change with wire cuts (dead end anchor 'A')

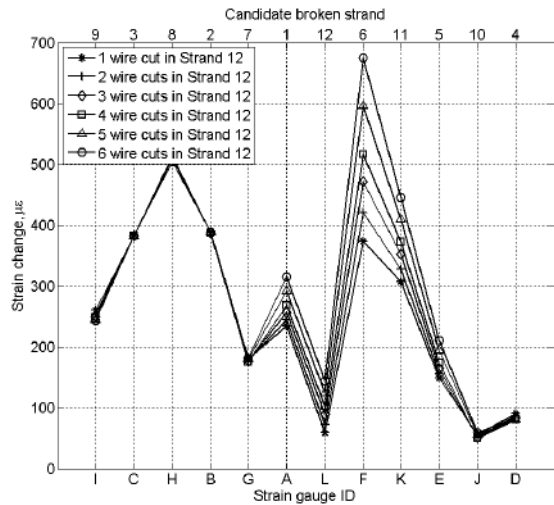
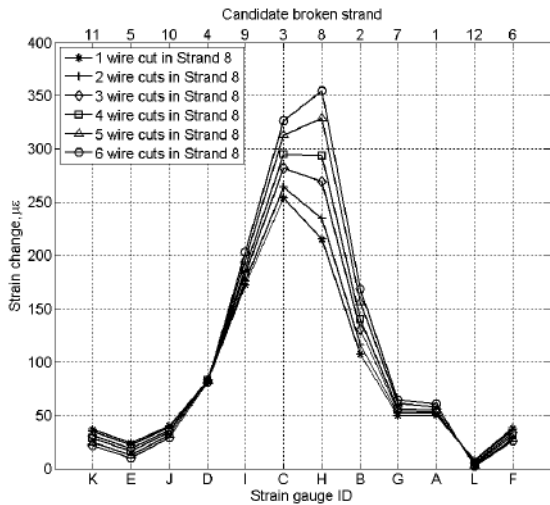
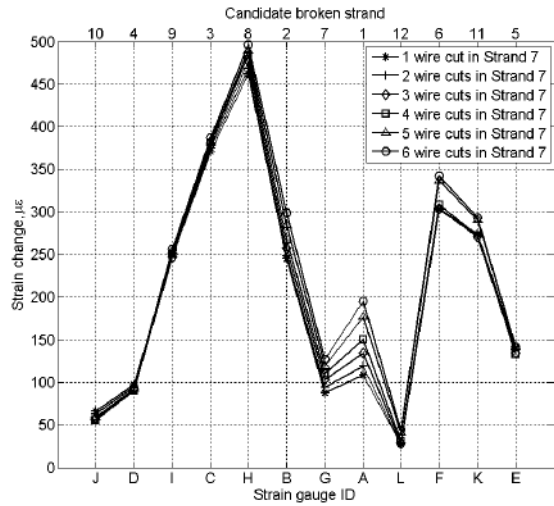
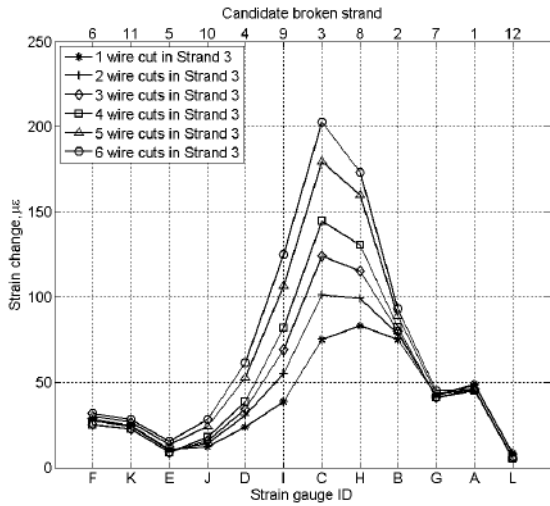
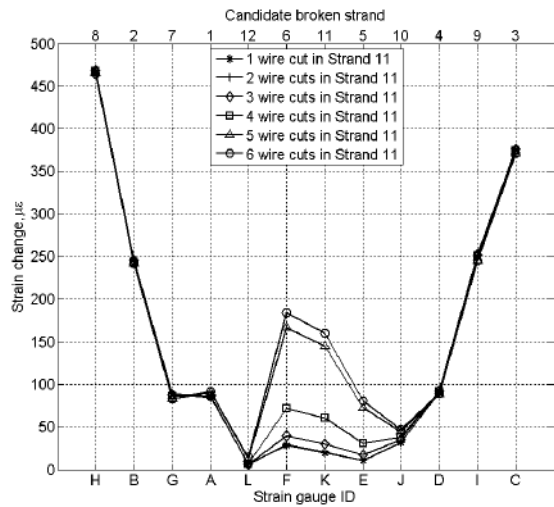
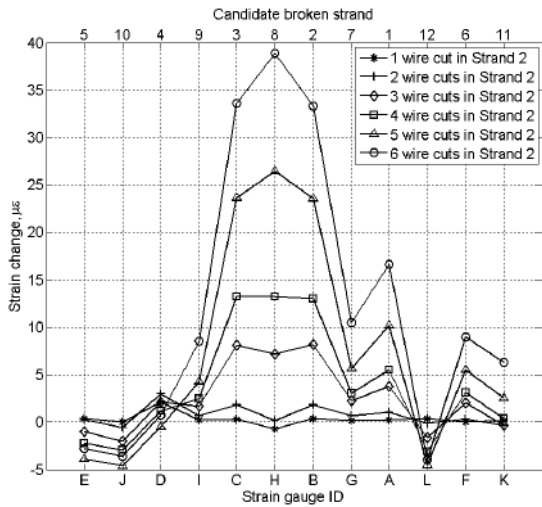


Figure D-54 Strain change with wire cuts (live end anchor 'B')

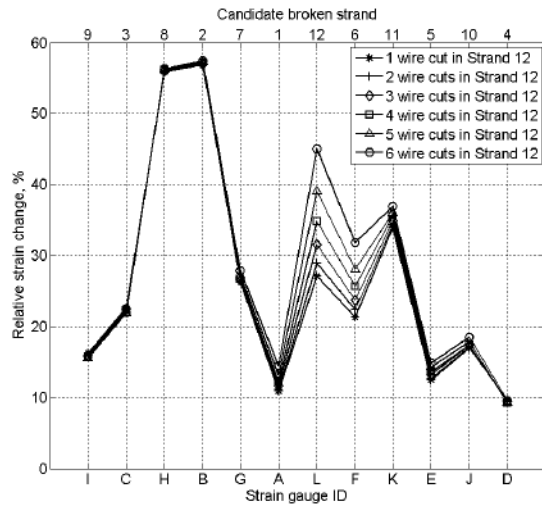
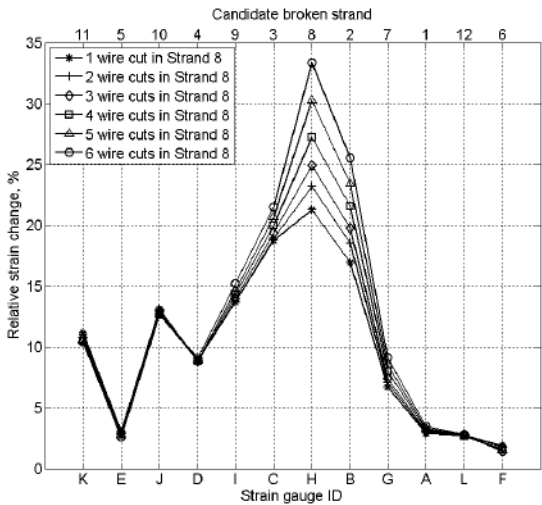
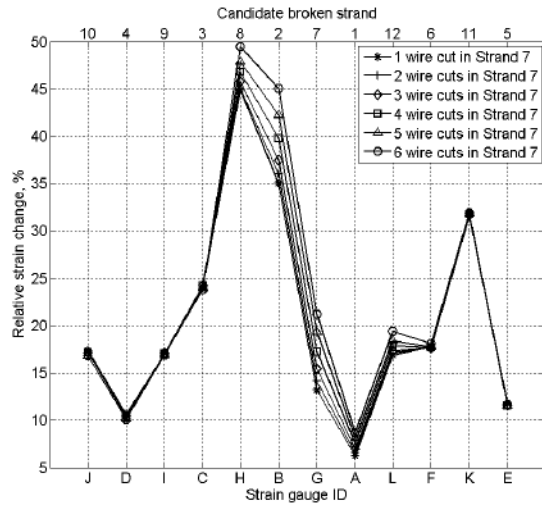
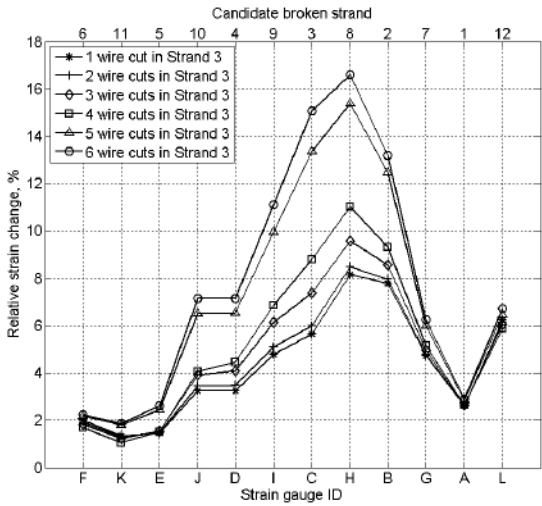
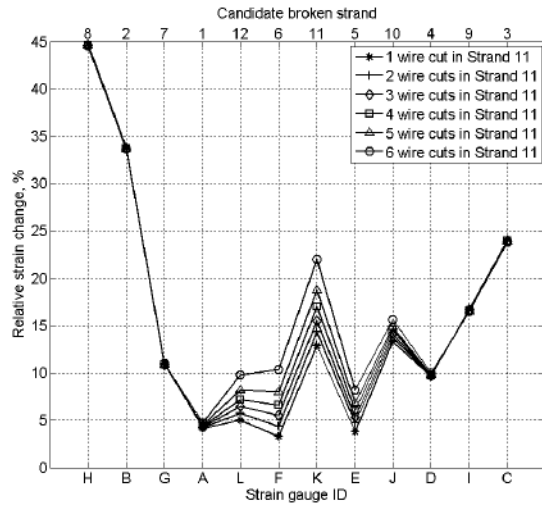
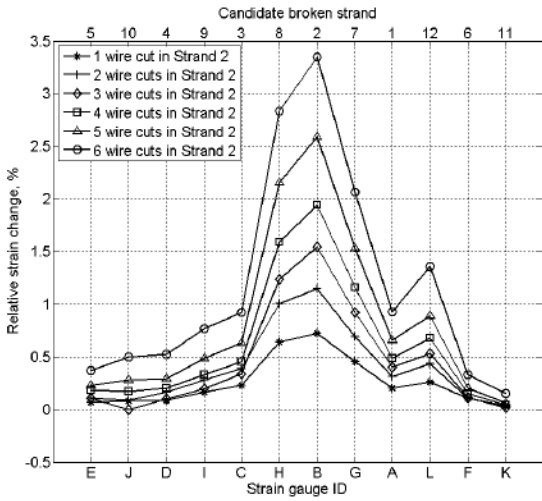


Figure D-55 Strain change relative to the original strain (dead end anchor 'A')

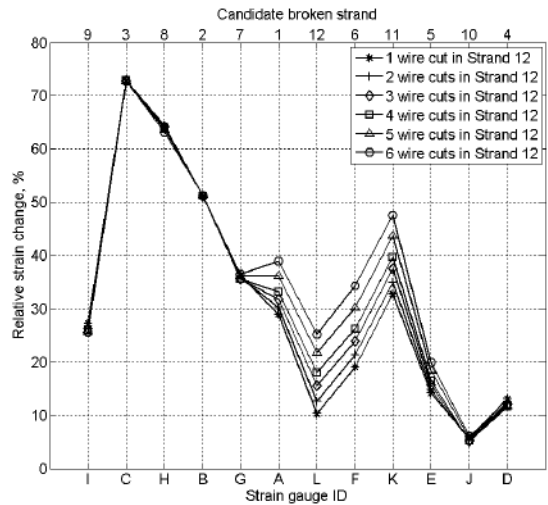
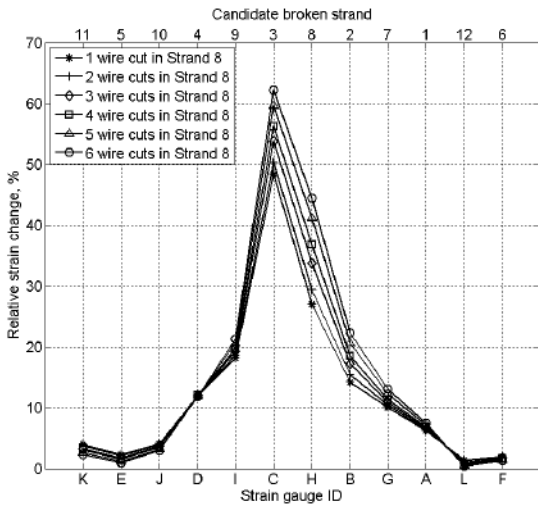
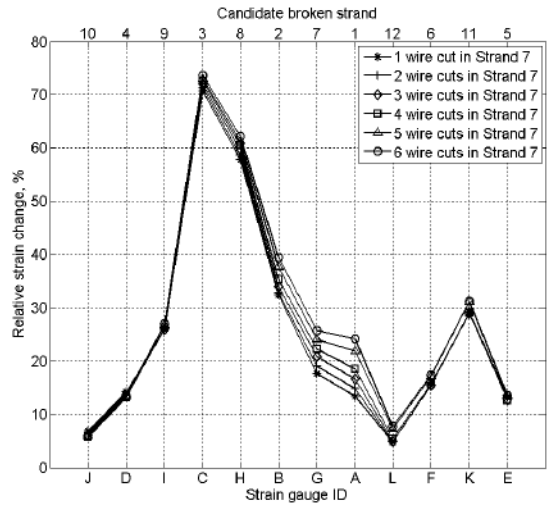
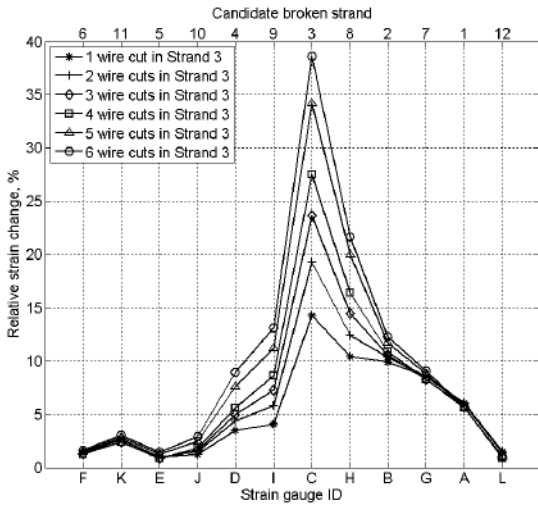
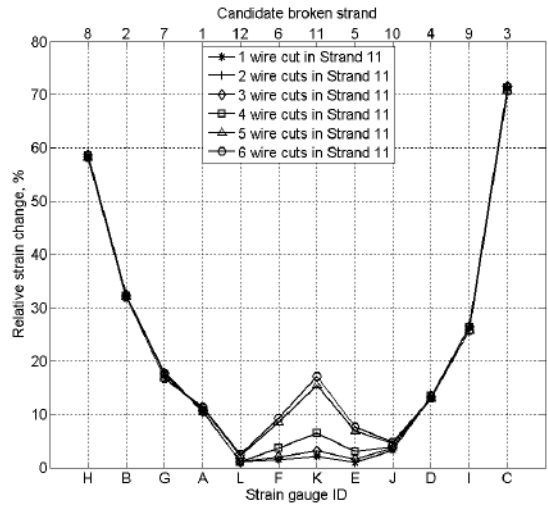
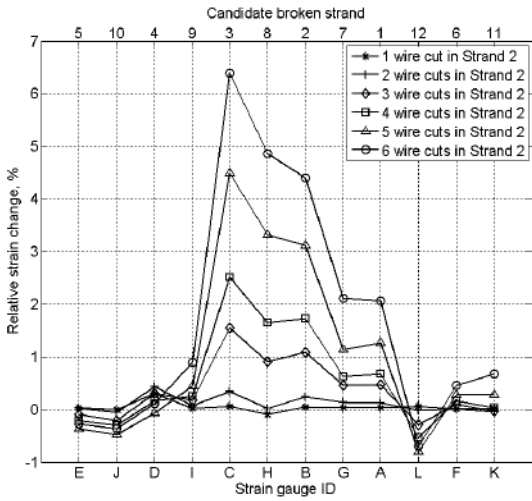


Figure D-56 Strain change relative to the original strain (live end anchor 'B')

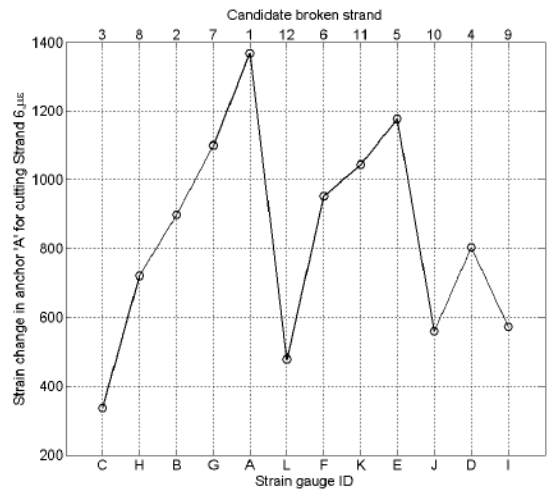
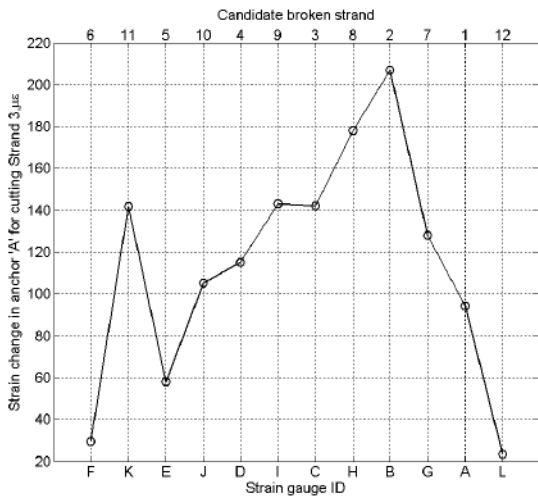
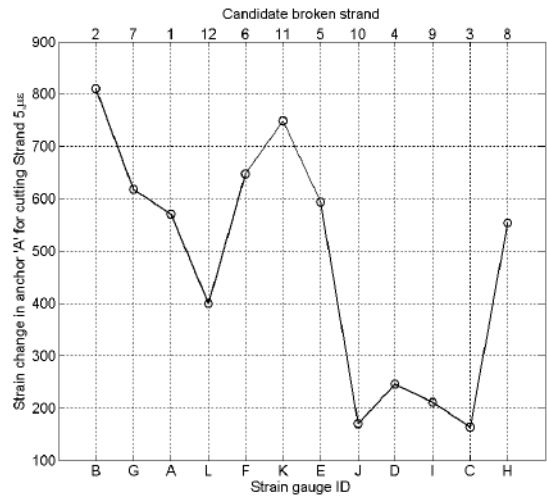
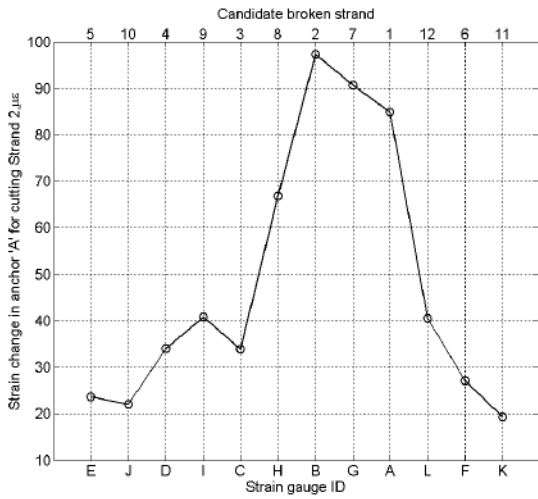
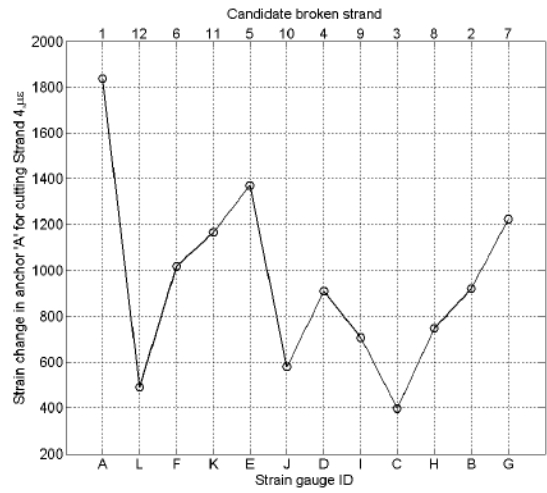
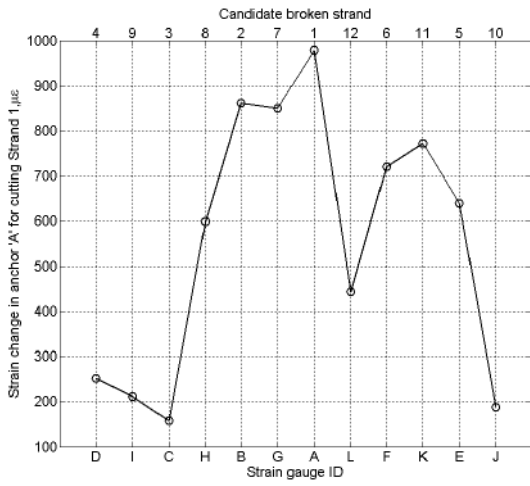


Figure D-57 Strain change after the breakage of entire strand (dead end anchor 'A')

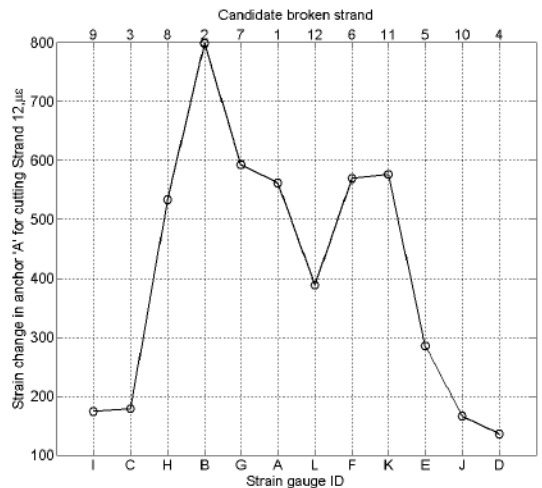
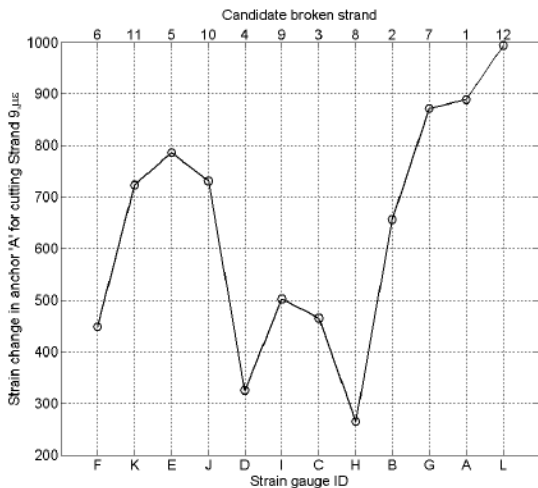
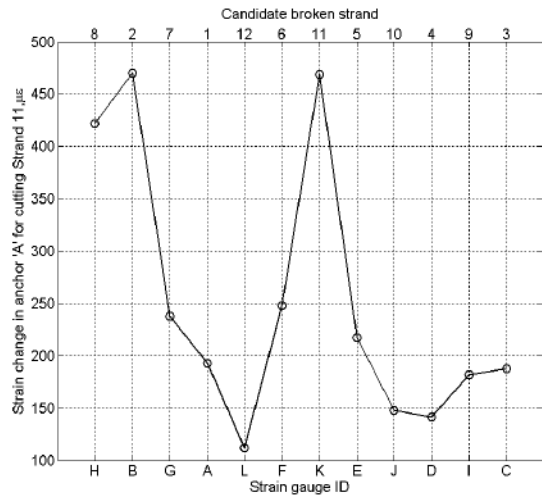
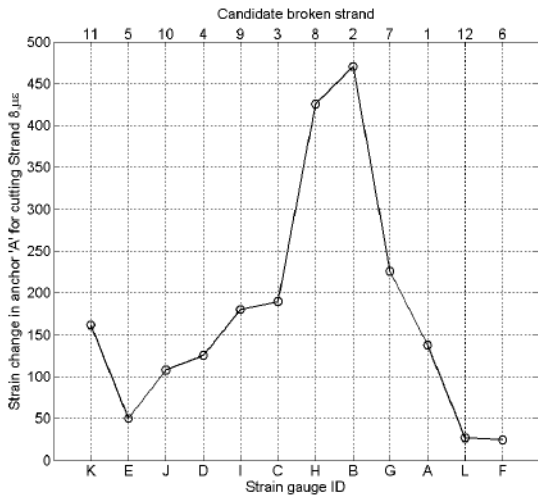
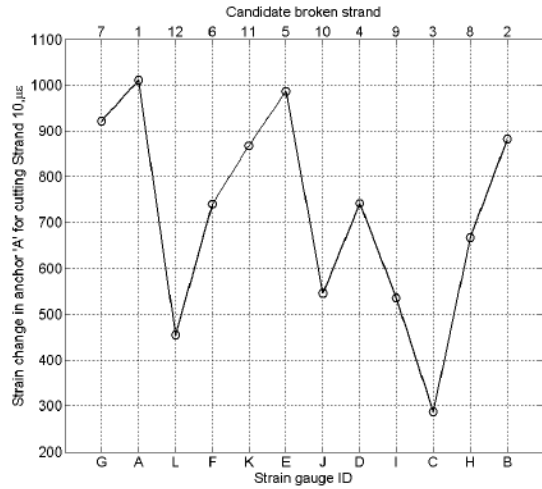
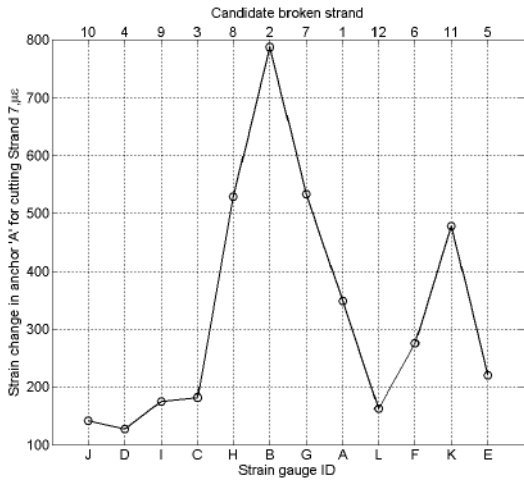


Figure D-58 Strain change after the breakage of entire strand (dead end anchor 'A')

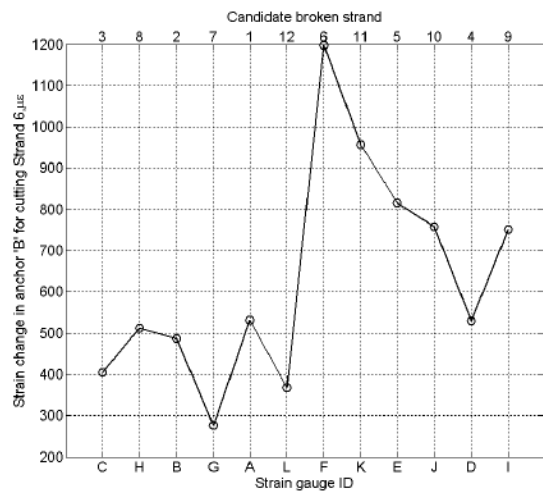
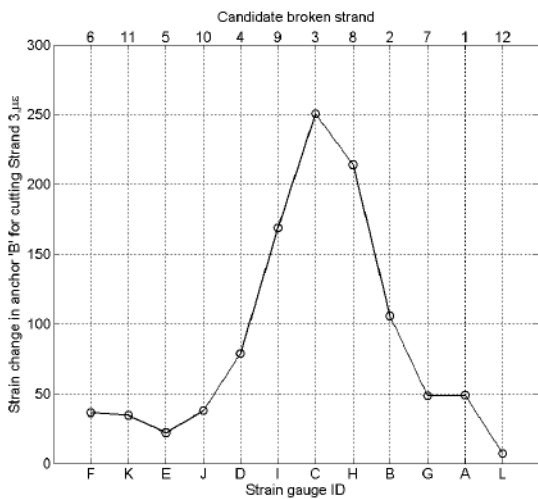
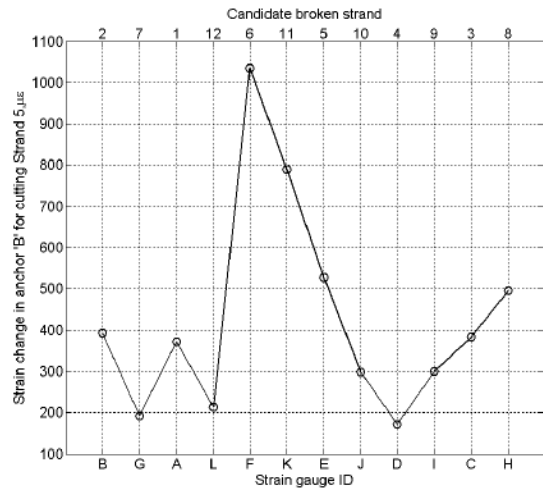
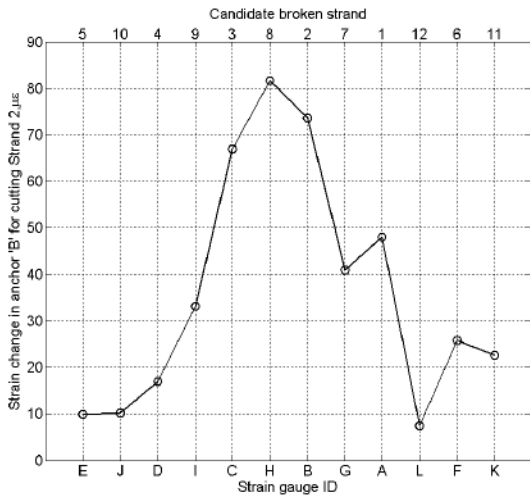
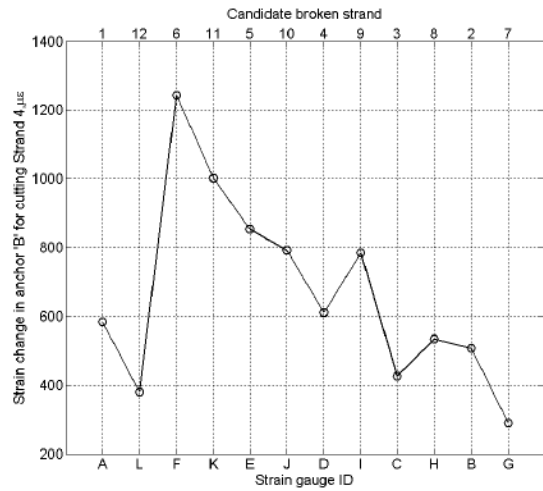
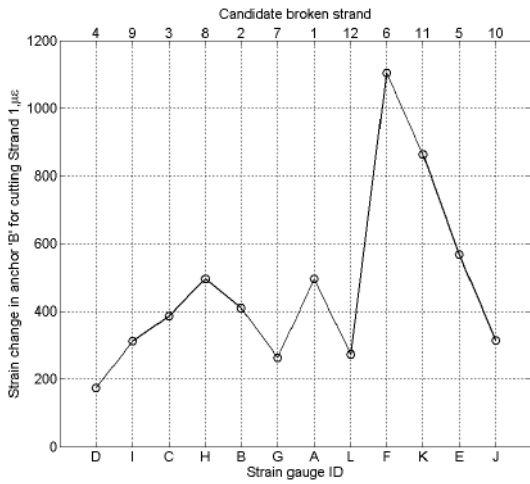


Figure D-59 Strain change after the breakage of entire strand (live end anchor 'B')

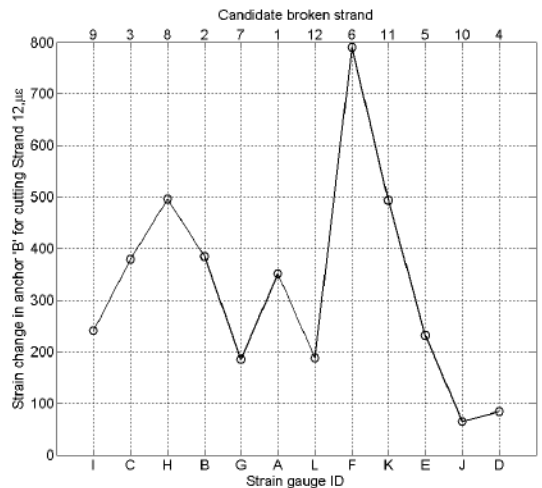
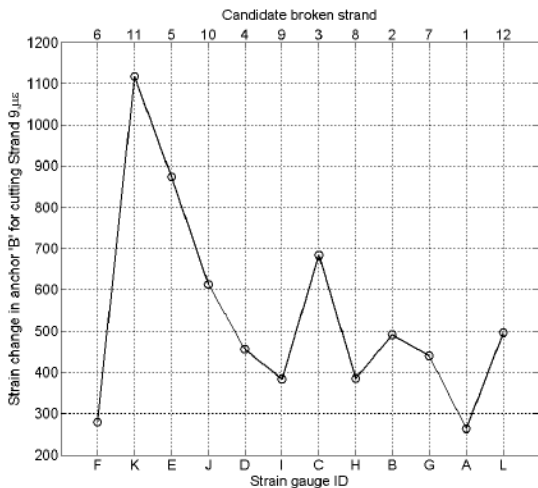
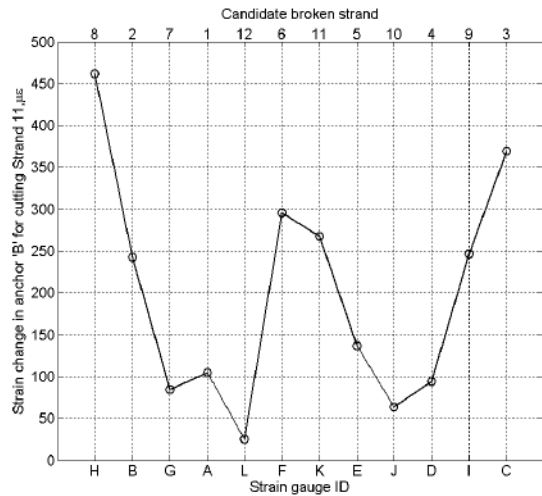
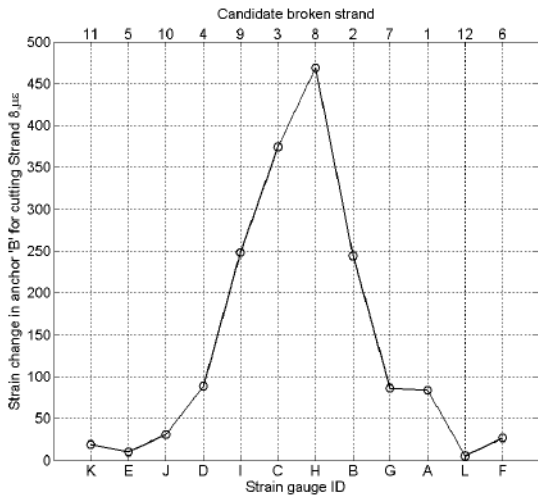
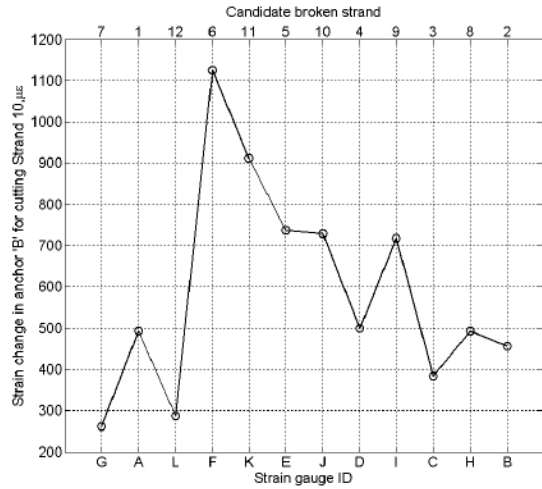
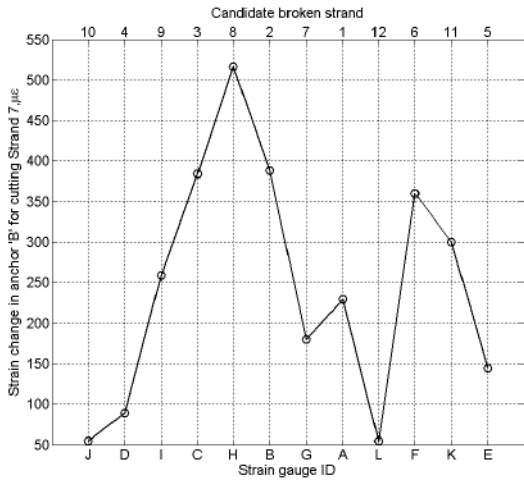


Figure D-60 Strain change after the breakage of entire strand (live end anchor 'B')

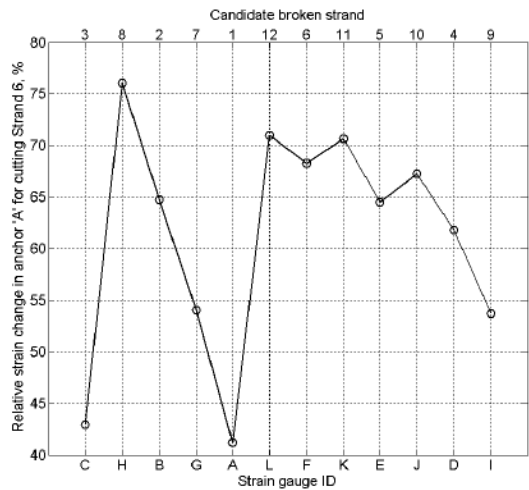
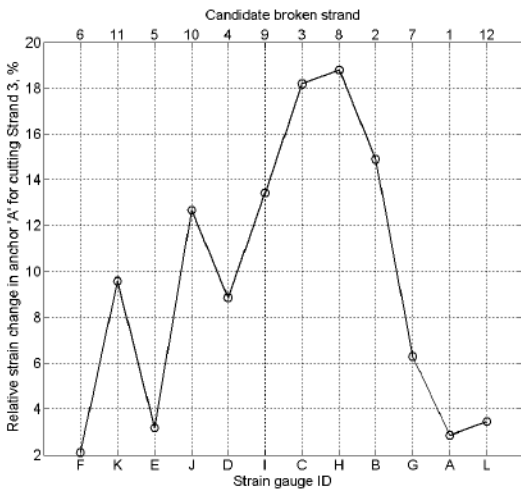
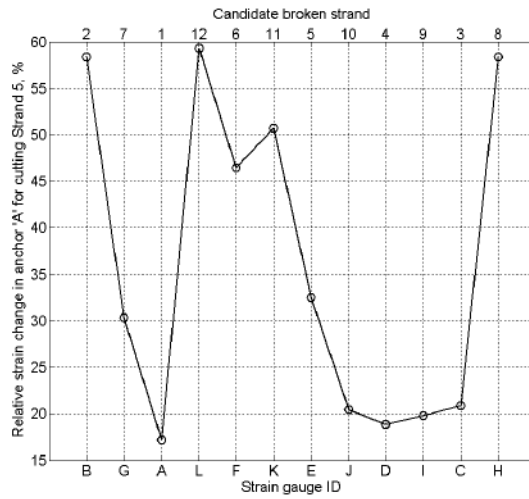
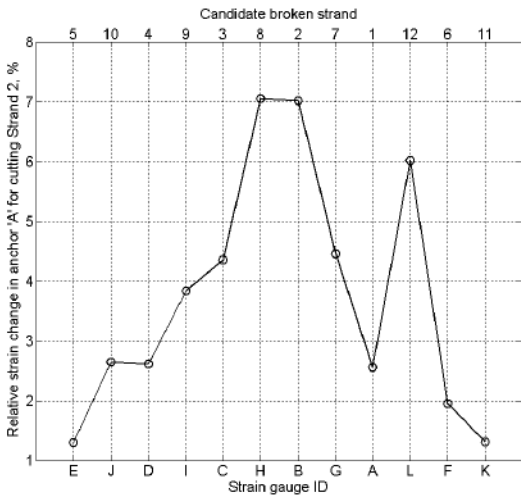
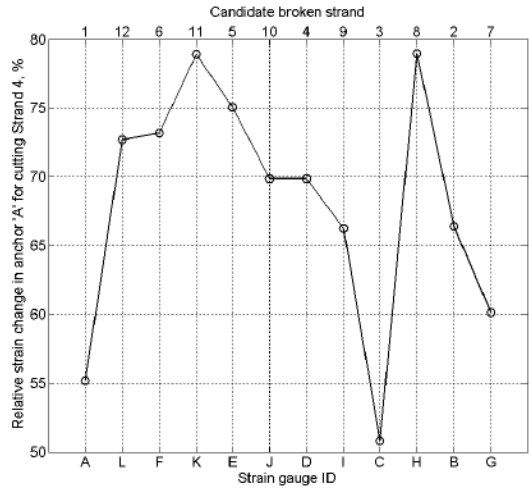
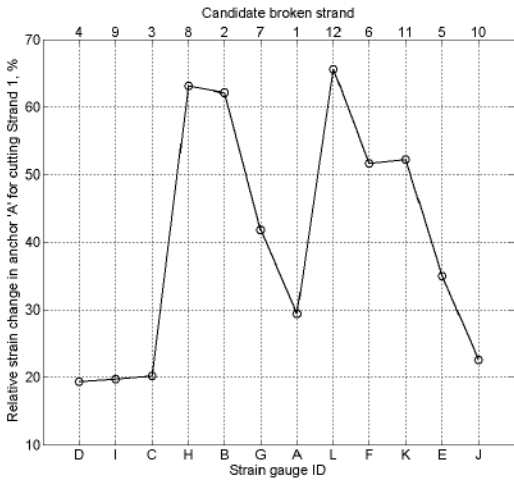


Figure D-61 Relative strain change after the breakage of entire strand (dead end anchor 'A')

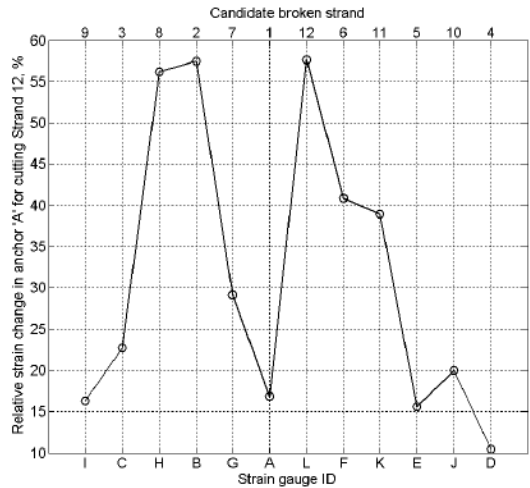
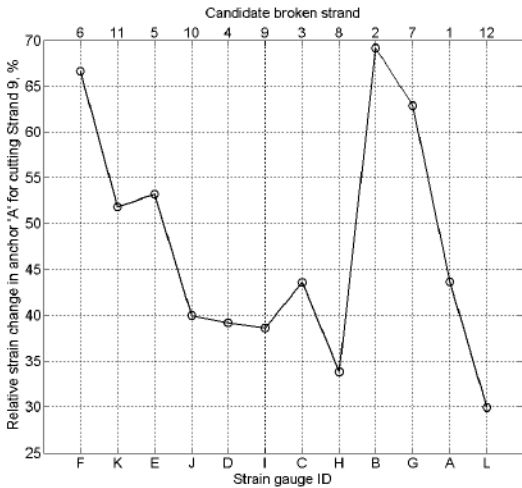
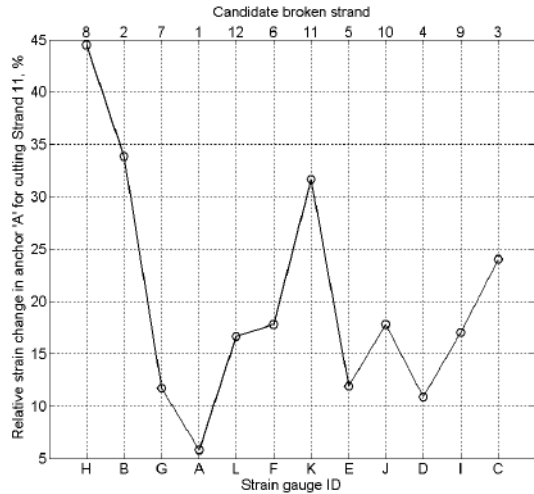
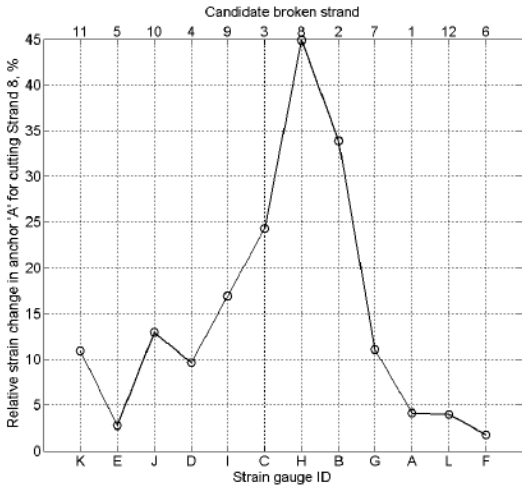
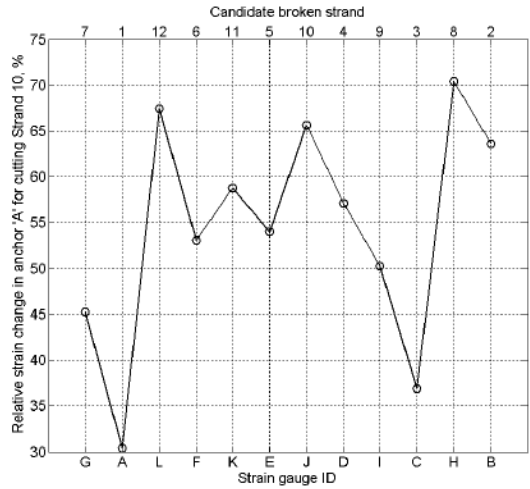
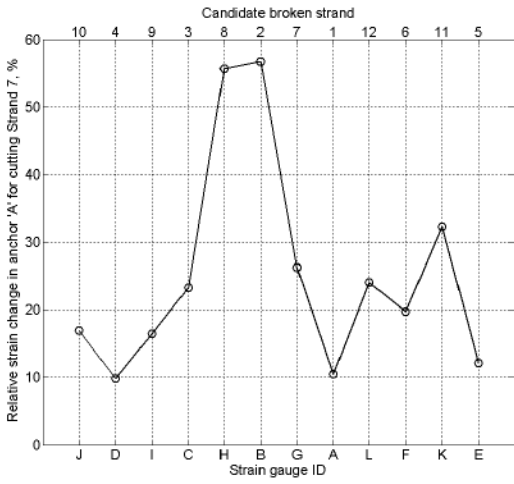


Figure D-62 Relative strain change after the breakage of entire strand (dead end anchor 'A')

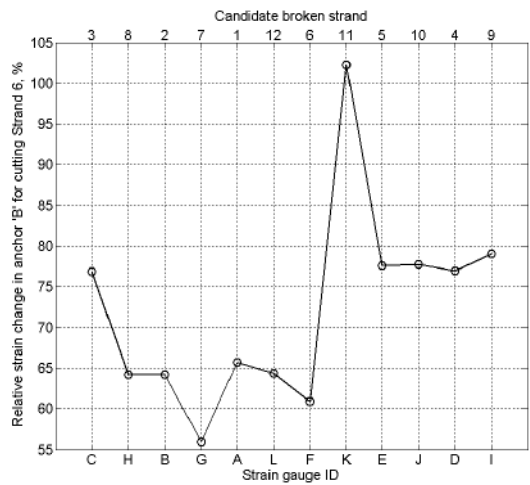
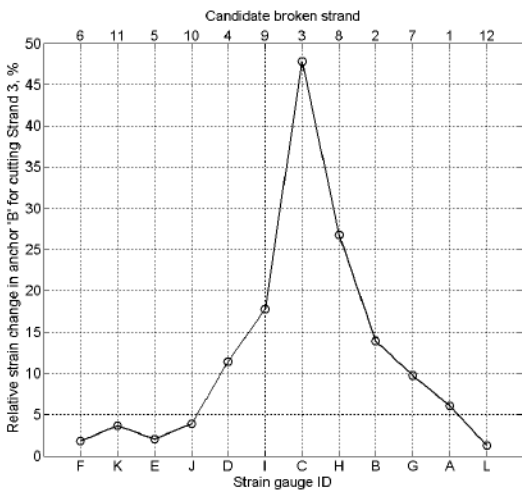
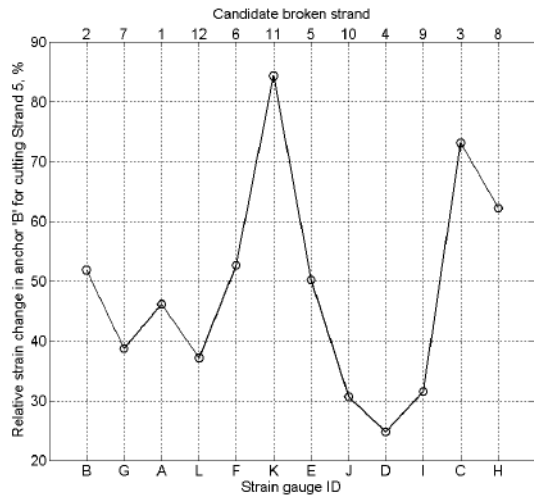
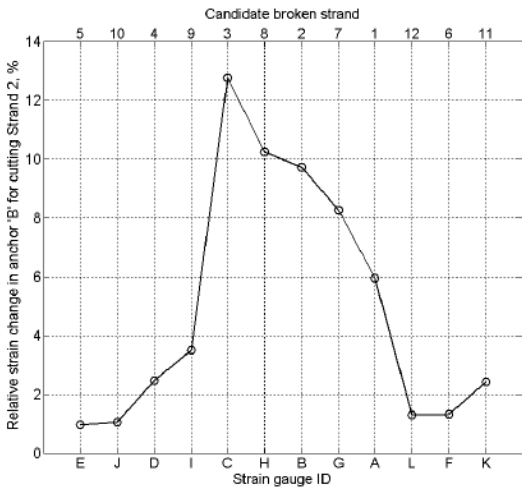
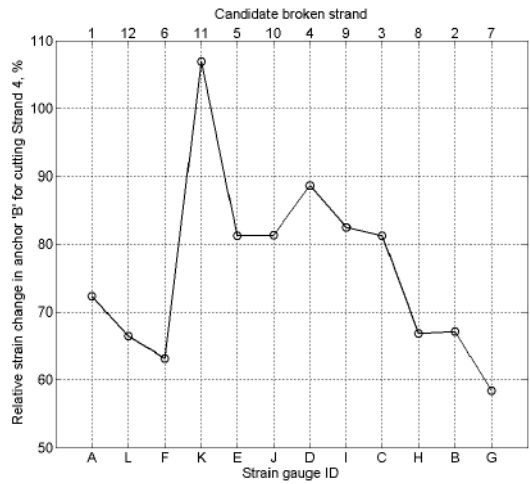
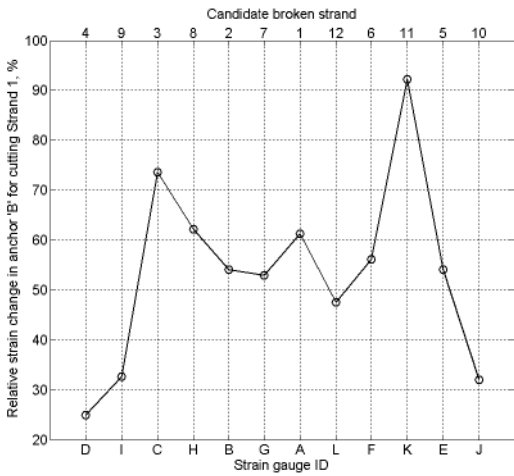


Figure D-63 Relative strain change after the breakage of entire strand (live end anchor 'B')

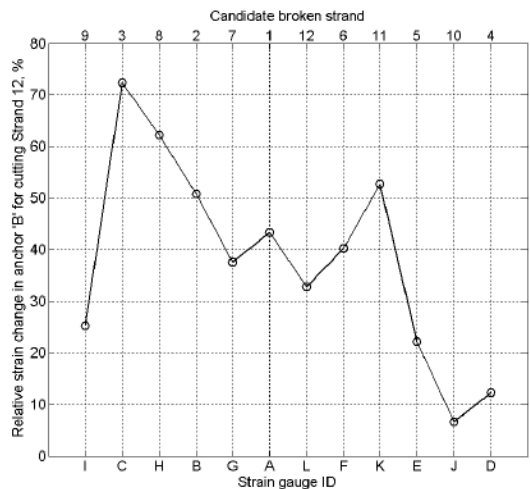
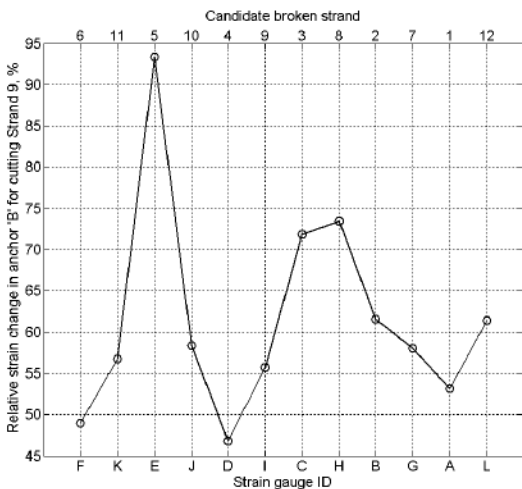
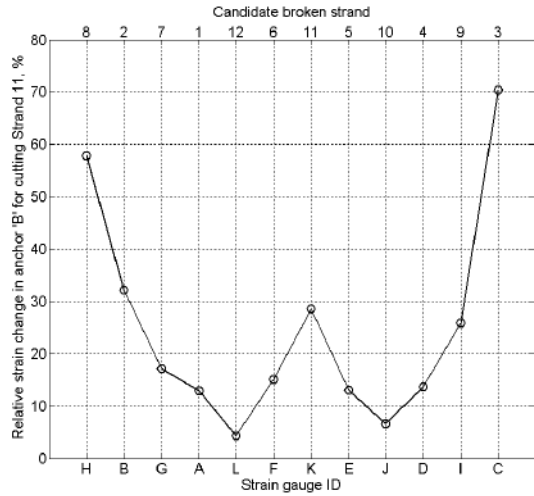
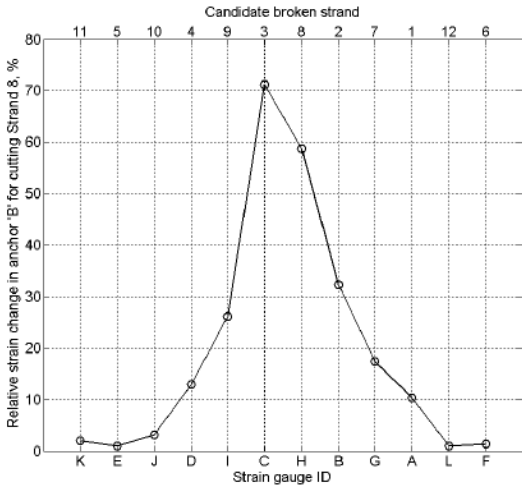
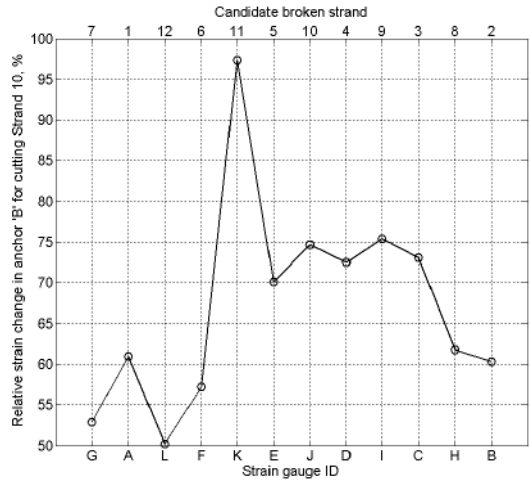
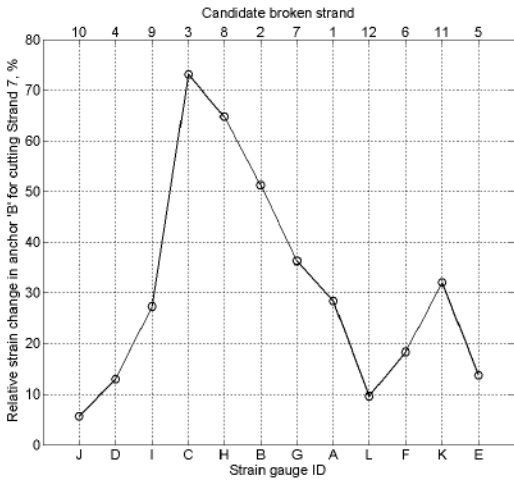


Figure D-64 Relative strain change after the breakage of entire strand (live end anchor 'B')

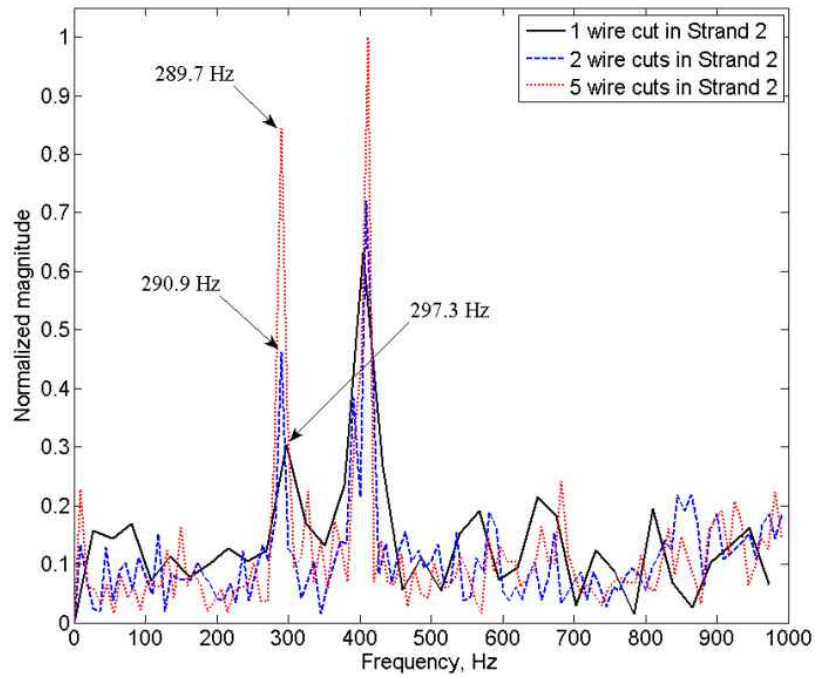


Figure D-65 Frequency shift with wire cuts

Appendix E—Acoustic Monitoring Testing

Internal Unbonded Specimen

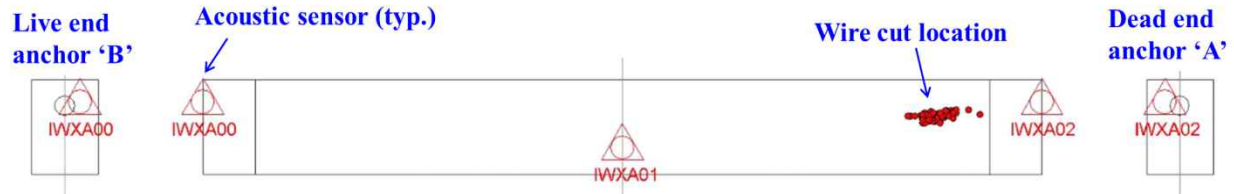


Figure E-66 Acoustic sensor layout and event (wire cut) locations determined by acoustic system

Table E-2 Event (wire cut) detection and location by acoustic sensors

Event ID	Time	Sensor ID (Event distance from sensor, m)	Event ID	Time	Sensor ID (Event distance from sensor, m)	Event ID	Time	Sensor ID (Event distance from sensor, m)
1	6/18/2015	IWXA02(1.25)	12	6/18/2015	IWXA02(1.73)	23	6/18/2015	IWXA02(1.43)
	5:29:28 PM	IWXA01(4.88)		5:40:53 PM	IWXA01(4.41)		5:53:03 PM	IWXA01(4.70)
	GMT	IWXA00(10.95)		GMT	IWXA00(10.48)		GMT	IWXA00(10.78)
2	6/18/2015	IWXA02(1.52)	13	6/18/2015	IWXA02(1.91)	24	6/18/2015	IWXA02(1.52)
	5:30:59 PM	IWXA01(4.62)		5:48:02 PM	IWXA01(4.22)		5:53:12 PM	IWXA01(4.61)
	GMT	IWXA00(10.69)		GMT	IWXA00(10.30)		GMT	IWXA00(10.69)
3	6/18/2015	IWXA02(1.52)	14	6/18/2015	IWXA02(1.96)	25	6/18/2015	IWXA02(1.61)
	5:31:20 PM	IWXA01(4.62)		5:48:13 PM	IWXA01(4.17)		5:53:17 PM	IWXA01(4.52)
	GMT	IWXA00(10.69)		GMT	IWXA00(10.25)		GMT	IWXA00(10.60)
4	6/18/2015	IWXA02(1.25)	15	6/18/2015	IWXA02(1.41)	26	6/18/2015	IWXA02(1.86)
	5:31:39 PM	IWXA01(4.88)		5:49:36 PM	IWXA01(4.72)		5:53:25 PM	IWXA01(4.27)
	GMT	IWXA00(10.95)		GMT	IWXA00(10.79)		GMT	IWXA00(10.35)
5	6/18/2015	IWXA02(1.33)	16	6/18/2015	IWXA02(1.07)	27	6/18/2015	IWXA02(1.61)
	5:31:52 PM	IWXA01(4.80)		5:49:53 PM	IWXA01(5.06)		5:53:37 PM	IWXA01(4.52)
	GMT	IWXA00(10.87)		GMT	IWXA00(11.13)		GMT	IWXA00(10.59)
6	6/18/2015	IWXA02(1.52)	17	6/18/2015	IWXA02(1.38)	28	6/18/2015	IWXA02(1.71)
	5:32:01 PM	IWXA01(4.62)		5:50:06 PM	IWXA01(4.75)		5:53:46 PM	IWXA01(4.42)
	GMT	IWXA00(10.69)		GMT	IWXA00(10.82)		GMT	IWXA00(10.49)
7	6/18/2015	IWXA02(1.77)	18	6/18/2015	IWXA02(1.28)	29	6/18/2015	IWXA02(1.71)
	5:32:11 PM	IWXA01(4.36)		5:50:21 PM	IWXA01(4.85)		5:55:43 PM	IWXA01(4.42)
	GMT	IWXA00(10.44)		GMT	IWXA00(10.92)		GMT	IWXA00(10.49)
8	6/18/2015	IWXA02(1.86)	19	6/18/2015	IWXA02(1.25)	30	6/18/2015	IWXA02(1.71)
	5:38:45 PM	IWXA01(4.27)		5:50:28 PM	IWXA01(4.88)		5:55:53 PM	IWXA01(4.42)
	GMT	IWXA00(10.35)		GMT	IWXA00(10.95)		GMT	IWXA00(10.50)
9	6/18/2015	IWXA02(1.94)	20	6/18/2015	IWXA02(1.50)	31	6/18/2015	IWXA02(1.65)
	5:39:42 PM	IWXA01(4.19)		5:50:43 PM	IWXA01(4.64)		5:55:59 PM	IWXA01(4.48)
	GMT	IWXA00(10.27)		GMT	IWXA00(10.72)		GMT	IWXA00(10.56)
10	6/18/2015	IWXA02(1.86)	21	6/18/2015	IWXA02(1.37)	32	6/18/2015	IWXA02(1.65)
	5:40:18 PM	IWXA01(4.27)		5:50:52 PM	IWXA01(4.77)		5:56:04 PM	IWXA01(4.48)
	GMT	IWXA00(10.35)		GMT	IWXA00(10.84)		GMT	IWXA00(10.56)
11	6/18/2015	IWXA02(1.86)	22	6/18/2015	IWXA02(1.53)	33	6/18/2015	IWXA02(1.74)
	5:40:40 PM	IWXA01(4.27)		5:52:37 PM	IWXA01(4.60)		5:56:18 PM	IWXA01(4.39)
	GMT	IWXA00(10.35)		GMT	IWXA00(10.68)		GMT	IWXA00(10.47)

Table E-2 cont'd.

Event ID	Time	Sensor ID (Event distance from sensor, m)	Event ID	Time	Sensor ID (Event distance from sensor, m)	Event ID	Time	Sensor ID (Event distance from sensor, m)
34	6/18/2015 5:59:32 PM GMT	IWXA02(1.62) IWXA01(4.51) IWXA00(10.59)	48	6/18/2015 6:10:25 PM GMT	IWXA02(1.50) IWXA01(4.64) IWXA00(10.72)	62	6/18/2015 6:16:59 PM GMT	IWXA02(1.46) IWXA01(4.67) IWXA00(10.74)
35	6/18/2015 5:59:49 PM GMT	IWXA02(1.57) IWXA01(4.57) IWXA00(10.66)	49	6/18/2015 6:14:06 PM GMT	IWXA02(1.46) IWXA01(4.67) IWXA00(10.75)	63	6/18/2015 6:17:28 PM GMT	IWXA02(1.59) IWXA01(4.55) IWXA00(10.62)
36	6/18/2015 6:02:28 PM GMT	IWXA02(1.65) IWXA01(4.48) IWXA00(10.57)	50	6/18/2015 6:14:08 PM GMT	IWXA02(1.66) IWXA01(4.48) IWXA00(10.56)	64	6/18/2015 6:17:32 PM GMT	IWXA02(0.92) IWXA01(5.22) IWXA00(11.29)
37	6/18/2015 6:02:41 PM GMT	IWXA02(1.60) IWXA01(4.54) IWXA00(10.62)	51	6/18/2015 6:14:11 PM GMT	IWXA02(1.58) IWXA01(4.55) IWXA00(10.63)	65	6/18/2015 6:17:41 PM GMT	IWXA02(1.62) IWXA01(4.51) IWXA00(10.58)
38	6/18/2015 6:02:50 PM GMT	IWXA02(1.37) IWXA01(4.76) IWXA00(10.84)	52	6/18/2015 6:14:12 PM GMT	IWXA02(1.49) IWXA01(4.65) IWXA00(10.72)	66	6/18/2015 6:17:44 PM GMT	IWXA02(1.47) IWXA01(4.67) IWXA00(10.74)
39	6/18/2015 6:03:02 PM GMT	IWXA02(1.31) IWXA01(4.82) IWXA00(10.90)	53	6/18/2015 6:14:46 PM GMT	IWXA02(1.49) IWXA01(4.65) IWXA00(10.72)	67	6/18/2015 6:17:47 PM GMT	IWXA02(1.51) IWXA01(4.63) IWXA00(10.72)
40	6/18/2015 6:03:14 PM GMT	IWXA02(1.75) IWXA01(4.38) IWXA00(10.47)	54	6/18/2015 6:14:50 PM GMT	IWXA02(1.53) IWXA01(4.60) IWXA00(10.68)	68	6/18/2015 6:18:39 PM GMT	IWXA02(1.62) IWXA01(4.51) IWXA00(10.58)
41	6/18/2015 6:06:10 PM GMT	IWXA02(1.54) IWXA01(4.60) IWXA00(10.68)	55	6/18/2015 6:14:52 PM GMT	IWXA02(1.73) IWXA01(4.41) IWXA00(10.48)	69	6/18/2015 6:18:45 PM GMT	IWXA02(1.41) IWXA01(4.72) IWXA00(10.79)
42	6/18/2015 6:07:08 PM GMT	IWXA02(1.54) IWXA01(4.60) IWXA00(10.68)	56	6/18/2015 6:15:38 PM GMT	IWXA02(1.43) IWXA01(4.70) IWXA00(10.78)	70	6/18/2015 6:18:46 PM GMT	IWXA02(1.49) IWXA01(4.65) IWXA00(10.72)
43	6/18/2015 6:09:41 PM GMT	IWXA02(1.73) IWXA01(4.41) IWXA00(10.50)	57	6/18/2015 6:15:48 PM GMT	IWXA02(1.67) IWXA01(4.46) IWXA00(10.53)	71	6/18/2015 6:18:48 PM GMT	IWXA02(1.25) IWXA01(4.88) IWXA00(10.95)
44	6/18/2015 6:09:58 PM GMT	IWXA02(1.59) IWXA01(4.54) IWXA00(10.62)	58	6/18/2015 6:15:49 PM GMT	IWXA02(1.53) IWXA01(4.61) IWXA00(10.68)	72	6/18/2015 6:18:53 PM GMT	IWXA02(1.30) IWXA01(4.83) IWXA00(10.90)
45	6/18/2015 6:10:13 PM GMT	IWXA02(1.45) IWXA01(4.68) IWXA00(10.75)	59	6/18/2015 6:15:58 PM GMT	IWXA02(1.53) IWXA01(4.60) IWXA00(10.68)	73	6/18/2015 6:18:57 PM GMT	IWXA02(1.58) IWXA01(4.55) IWXA00(10.62)
46	6/18/2015 6:10:21 PM GMT	IWXA02(1.64) IWXA01(4.49) IWXA00(10.56)	60	6/18/2015 6:16:12 PM GMT	IWXA02(1.75) IWXA01(4.39) IWXA00(10.47)			
47	6/18/2015 6:10:23 PM GMT	IWXA02(1.52) IWXA01(4.62) IWXA00(10.69)	61	6/18/2015 6:16:53 PM GMT	IWXA02(1.74) IWXA01(4.40) IWXA00(10.47)			

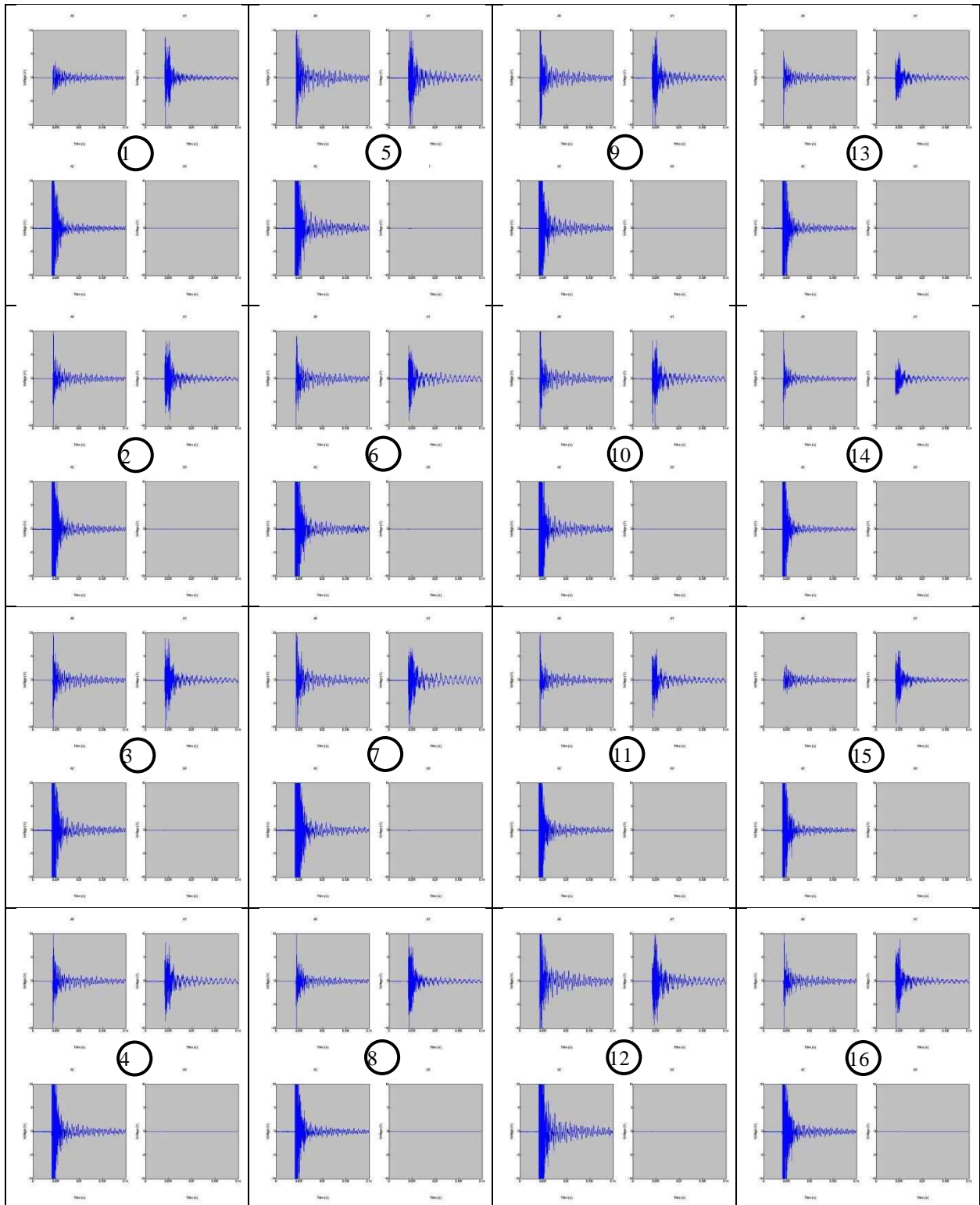


Figure E-67 Acoustic signals (time vs. voltage) due to wire cuts (top left: channel A0; top right: channel A1; bottom left: channel A2; bottom right: channel A3 [inactive])

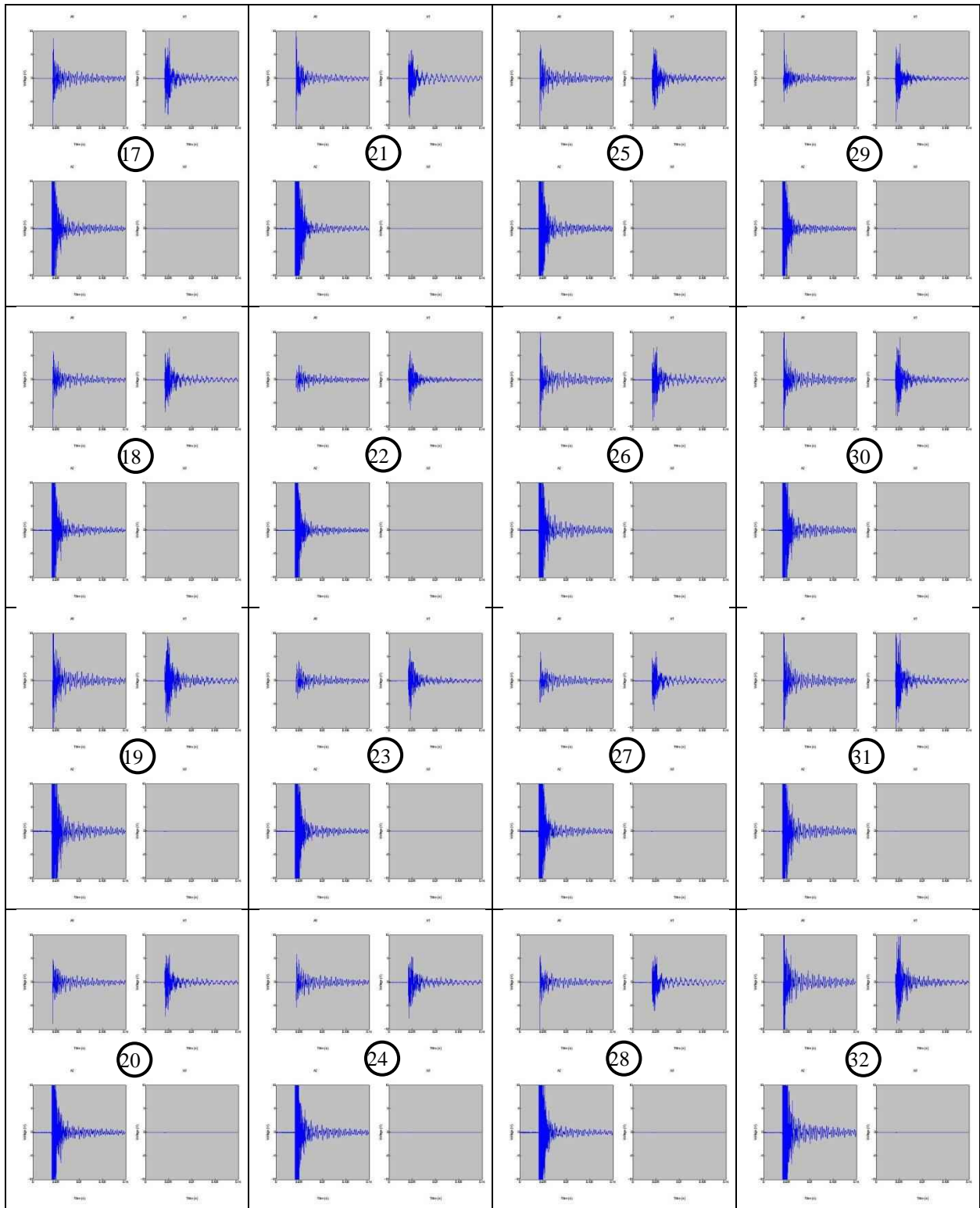


Figure E-67 (cont'd.) Acoustic signals (time vs. voltage) due to wire cuts (top left: channel A0; top right: channel A1; bottom left: channel A2; bottom right: channel A3 [inactive])

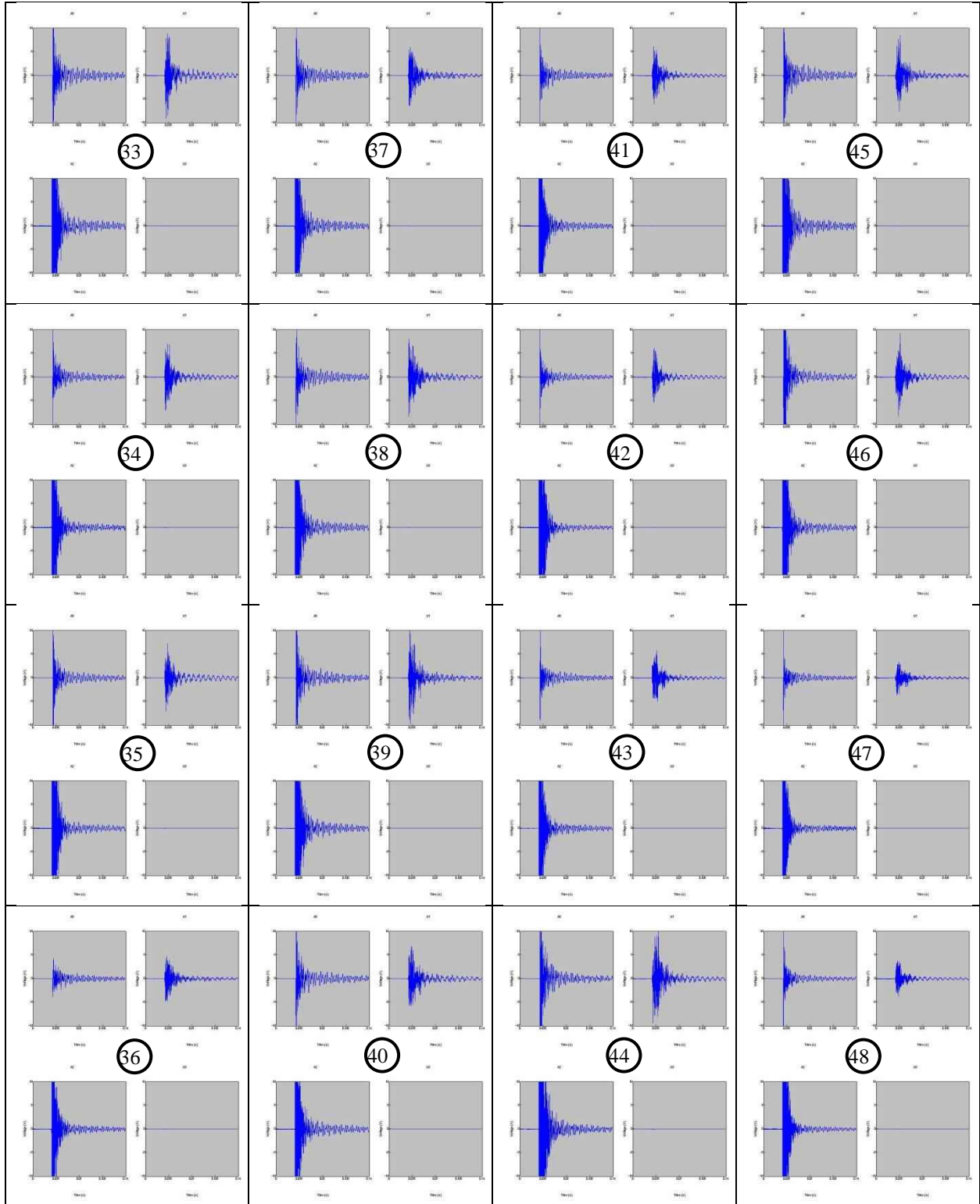


Figure E-67 (cont'd.) Acoustic signals (time vs. voltage) due to wire cuts (top left: channel A0; top right: channel A1; bottom left: channel A2; bottom right: channel A3 [inactive])

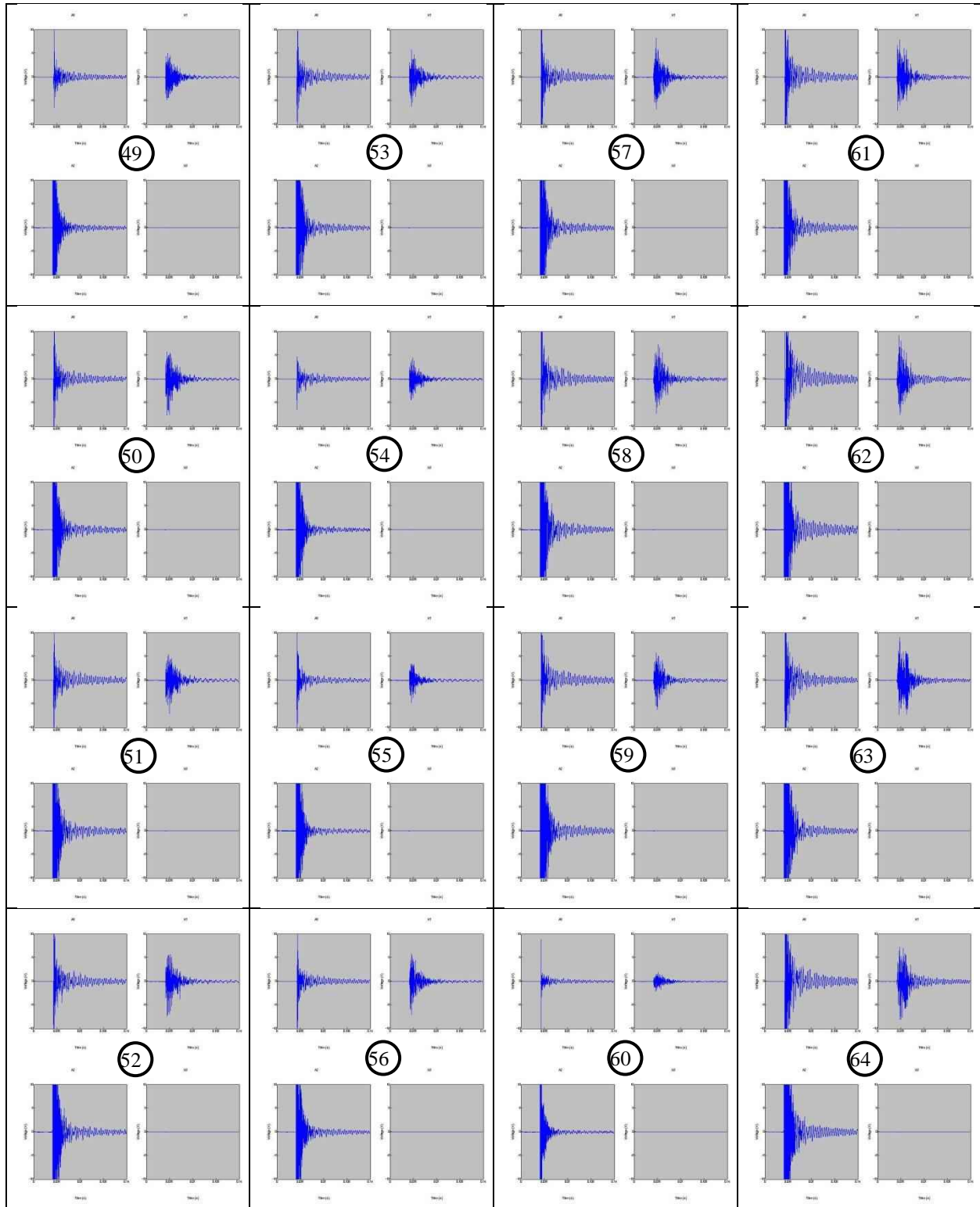


Figure E-67 (cont'd.) Acoustic signals (time vs. voltage) due to wire cuts (top left: channel A0; top right: channel A1; bottom left: channel A2; bottom right: channel A3 [inactive])

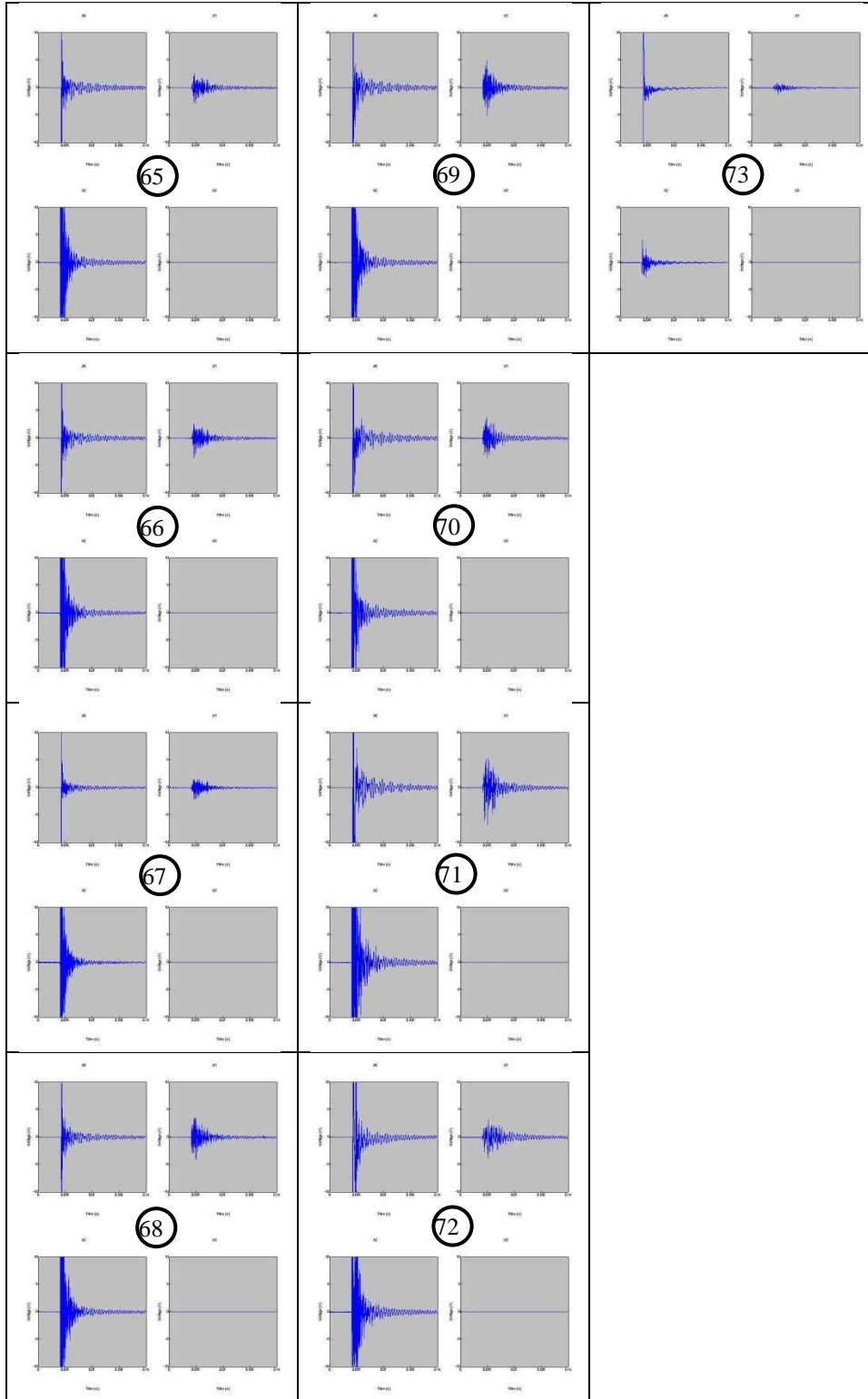


Figure E-67 (cont'd.) Acoustic signals (time vs. voltage) due to wire cuts (top left: channel A0; top right: channel A1; bottom left: channel A2; bottom right: channel A3 [inactive])

External Unbonded Specimen

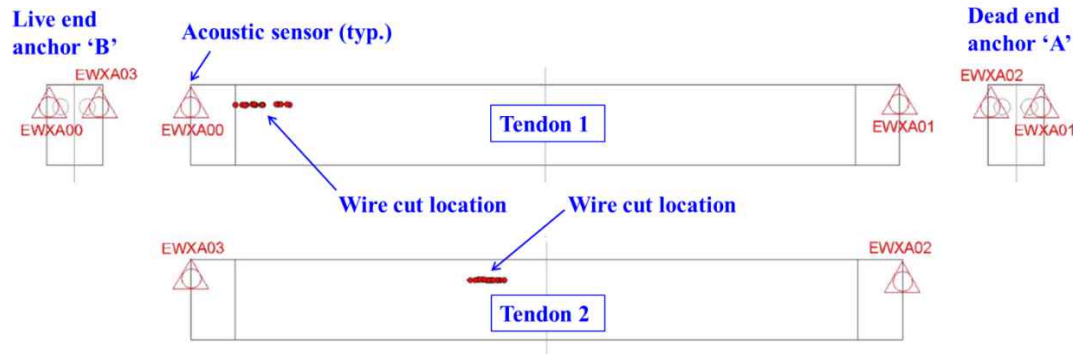


Figure E-68 Acoustic sensor layout and event (wire cut) locations determined by acoustic system

Table E-3 Event (wire cut) detection and location by acoustic sensors

Event ID	Time	Sensor ID (Event distance from sensor, m)	Event ID	Time	Sensor ID (Event distance from sensor, m)	Event ID	Time	Sensor ID (Event distance from sensor, m)
1	7/29/2015 3:15:58 PM GMT	EWXA03(5.16)	11	7/29/2015 3:19:39 PM GMT	EWXA00(1.47)	21	7/29/2015 3:30:26 PM GMT	EWXA03(5.12)
		EWXA01(5.93)			EWXA02(3.29)			EWXA01(5.90)
		EWXA02(7.03)			EWXA01(10.72)			EWXA02(7.07)
2	7/29/2015 3:16:17 PM GMT	EWXA03(5.36)	12	7/29/2015 3:23:17 PM GMT	EWXA00(1.10)	22	7/29/2015 3:30:33 PM GMT	EWXA03(5.12)
		EWXA01(6.11)			EWXA02(3.13)			EWXA01(5.90)
		EWXA02(6.83)			EWXA01(11.09)			EWXA02(7.07)
3	7/29/2015 3:16:35 PM GMT	EWXA03(5.29)	13	7/29/2015 3:23:23 PM GMT	EWXA00(1.06)	23	7/29/2015 3:30:38 PM GMT	EWXA03(5.12)
		EWXA01(6.05)			EWXA02(3.13)			EWXA01(5.90)
		EWXA02(6.90)			EWXA01(11.13)			EWXA02(7.07)
4	7/29/2015 3:16:55 PM GMT	EWXA03(5.16)	14	7/29/2015 3:23:28 PM GMT	EWXA00(1.06)	24	7/29/2015 3:30:42 PM GMT	EWXA03(5.12)
		EWXA01(5.93)			EWXA02(3.13)			EWXA01(5.90)
		EWXA02(7.03)			EWXA01(11.13)			EWXA02(7.07)
5	7/29/2015 3:17:01 PM GMT	EWXA03(5.16)	15	7/29/2015 3:26:05 PM GMT	EWXA00(0.96)	25	7/29/2015 3:33:18 PM GMT	EWXA03(5.16)
		EWXA01(5.93)			EWXA02(3.09)			EWXA01(5.93)
		EWXA02(7.03)			EWXA01(11.23)			EWXA02(7.03)
6	7/29/2015 3:17:21 PM GMT	EWXA03(5.25)	16	7/29/2015 3:26:19 PM GMT	EWXA00(1.66)	26	7/29/2015 3:33:29 PM GMT	EWXA03(5.18)
		EWXA01(6.01)			EWXA02(3.38)			EWXA01(5.95)
		EWXA02(6.94)			EWXA01(10.53)			EWXA02(7.01)
7	7/29/2015 3:17:25 PM GMT	EWXA03(5.16)	17	7/29/2015 3:26:24 PM GMT	EWXA00(1.71)	27	7/29/2015 3:34:12 PM GMT	EWXA03(5.16)
		EWXA01(5.93)			EWXA02(3.40)			EWXA01(5.93)
		EWXA02(7.03)			EWXA01(10.48)			EWXA02(7.03)
8	7/29/2015 3:19:00 PM GMT	EWXA00(1.12)	18	7/29/2015 3:28:29 PM GMT	EWXA00(1.47)	28	7/29/2015 3:39:26 PM GMT	EWXA03(5.01)
		EWXA02(3.14)			EWXA02(3.29)			EWXA01(5.80)
		EWXA01(11.07)			EWXA01(10.72)			EWXA02(7.18)
9	7/29/2015 3:19:19 PM GMT	EWXA00(1.71)	19	7/29/2015 3:28:40 PM GMT	EWXA00(1.71)	29	7/29/2015 3:39:32 PM GMT	EWXA03(4.99)
		EWXA02(3.40)			EWXA02(3.40)			EWXA01(5.78)
		EWXA01(10.48)			EWXA01(10.48)			EWXA02(7.20)
10	7/29/2015 3:19:33 PM GMT	EWXA00(1.47)	20	7/29/2015 3:28:44 PM GMT	EWXA00(1.22)	30	7/29/2015 3:39:46 PM GMT	EWXA03(5.01)
		EWXA02(3.29)			EWXA02(3.18)			EWXA01(5.80)
		EWXA01(10.72)			EWXA01(10.97)			EWXA02(7.18)

Table E-3 Event (wire cut) detection and location by acoustic sensors

Event ID	Time	Sensor ID (Event distance from sensor, m)	Event ID	Time	Sensor ID (Event distance from sensor, m)	Event ID	Time	Sensor ID (Event distance from sensor, m)
31	7/29/2015 3:39:52 PM GMT	EWXA03(4.99) EWXA01(5.78) EWXA02(7.20)	47	7/29/2015 4:01:16 PM GMT	EWXA00(1.25) EWXA02(3.19) EWXA01(10.94)	63	7/29/2015 4:13:56 PM GMT	EWXA00(1.56) EWXA02(3.33) EWXA01(10.63)
32	7/29/2015 3:42:04 PM GMT	EWXA03(5.18) EWXA01(5.95) EWXA02(7.01)	48	7/29/2015 4:01:27 PM GMT	EWXA00(1.25) EWXA02(3.19) EWXA01(10.94)	64	7/29/2015 4:14:08 PM GMT	EWXA00(1.56) EWXA02(3.33) EWXA01(10.63)
33	7/29/2015 3:42:28 PM GMT	EWXA03(5.23) EWXA01(5.99) EWXA02(6.96)	49	7/29/2015 4:04:17 PM GMT	EWXA03(5.18) EWXA01(5.95) EWXA02(7.01)	65	7/29/2015 4:14:14 PM GMT	EWXA00(1.51) EWXA02(3.31) EWXA01(10.68)
34	7/29/2015 3:43:35 PM GMT	EWXA03(5.01) EWXA01(5.80) EWXA02(7.18)	50	7/29/2015 4:04:19 PM GMT	EWXA03(5.01) EWXA01(5.80) EWXA02(7.18)	66	7/29/2015 4:14:16 PM GMT	EWXA00(1.56) EWXA02(3.33) EWXA01(10.63)
35	7/29/2015 3:51:48 PM GMT	EWXA00(0.94) EWXA02(3.07) EWXA01(11.25)	51	7/29/2015 4:04:24 PM GMT	EWXA03(4.91) EWXA01(5.71) EWXA02(7.28)	67	7/29/2015 4:14:23 PM GMT	EWXA00(1.66) EWXA02(3.38) EWXA01(10.53)
36	7/29/2015 3:51:52 PM GMT	EWXA00(1.25) EWXA02(3.19) EWXA01(10.94)	52	7/29/2015 4:04:27 PM GMT	EWXA03(5.18) EWXA01(5.95) EWXA02(7.01)	68	7/29/2015 4:14:28 PM GMT	EWXA00(1.47) EWXA02(3.29) EWXA01(10.72)
37	7/29/2015 3:51:56 PM GMT	EWXA00(1.25) EWXA02(3.19) EWXA01(10.94)	53	7/29/2015 4:04:41 PM GMT	EWXA03(5.18) EWXA01(5.95) EWXA02(7.01)	69	7/29/2015 4:14:39 PM GMT	EWXA00(1.56) EWXA02(3.33) EWXA01(10.63)
38	7/29/2015 3:52:00 PM GMT	EWXA00(1.25) EWXA02(3.19) EWXA01(10.94)	54	7/29/2015 4:04:48 PM GMT	EWXA03(5.18) EWXA01(5.95) EWXA02(7.01)	70	7/29/2015 4:14:42 PM GMT	EWXA00(1.66) EWXA02(3.38) EWXA01(10.53)
39	7/29/2015 3:53:50 PM GMT	EWXA00(0.89) EWXA02(3.06) EWXA01(11.30)	55	7/29/2015 4:04:54 PM GMT	EWXA03(5.18) EWXA01(5.95) EWXA02(7.01)	71	7/29/2015 4:14:47 PM GMT	EWXA00(1.56) EWXA02(3.33) EWXA01(10.63)
40	7/29/2015 3:54:03 PM GMT	EWXA00(1.25) EWXA02(3.19) EWXA01(10.94)	56	7/29/2015 4:06:29 PM GMT	EWXA03(5.13) EWXA01(5.91) EWXA02(7.06)	72	7/29/2015 4:14:49 PM GMT	EWXA00(1.56) EWXA02(3.33) EWXA01(10.63)
41	7/29/2015 3:54:08 PM GMT	EWXA00(1.25) EWXA02(3.19) EWXA01(10.94)	57	7/29/2015 4:06:36 PM GMT	EWXA03(5.01) EWXA01(5.80) EWXA02(7.18)	73	7/29/2015 4:18:07 PM GMT	EWXA00(1.06) EWXA02(3.13) EWXA01(11.13)
42	7/29/2015 3:55:04 PM GMT	EWXA00(0.77) EWXA02(3.03) EWXA01(11.42)	58	7/29/2015 4:06:45 PM GMT	EWXA03(5.06) EWXA01(5.84) EWXA02(7.13)	74	7/29/2015 4:18:23 PM GMT	EWXA00(1.09) EWXA02(3.14) EWXA01(11.10)
43	7/29/2015 3:55:09 PM GMT	EWXA00(1.25) EWXA02(3.19) EWXA01(10.94)	59	7/29/2015 4:06:53 PM GMT	EWXA03(5.12) EWXA01(5.90) EWXA02(7.07)	75	7/29/2015 4:18:31 PM GMT	EWXA00(0.94) EWXA02(3.07) EWXA01(11.25)
44	7/29/2015 3:55:15 PM GMT	EWXA00(1.25) EWXA02(3.19) EWXA01(10.94)	60	7/29/2015 4:06:58 PM GMT	EWXA03(5.18) EWXA01(5.95) EWXA02(7.01)	76	7/29/2015 4:20:20 PM GMT	EWXA03(5.00) EWXA01(5.79) EWXA02(7.19)
45	7/29/2015 3:55:22 PM GMT	EWXA00(0.94) EWXA02(3.07) EWXA01(11.25)	61	7/29/2015 4:07:12 PM GMT	EWXA03(5.08) EWXA01(5.86) EWXA02(7.11)	77	7/29/2015 4:20:25 PM GMT	EWXA03(5.18) EWXA01(5.95) EWXA02(7.01)
46	7/29/2015 3:55:25 PM GMT	EWXA00(1.25) EWXA02(3.19) EWXA01(10.94)	62	7/29/2015 4:13:52 PM GMT	EWXA00(1.23) EWXA02(3.18) EWXA01(10.96)	78	7/29/2015 4:20:31 PM GMT	EWXA03(4.95) EWXA01(5.75) EWXA02(7.24)

Table E-3 Event (wire cut) detection and location by acoustic sensors

Event ID	Time	Sensor ID (Event distance from sensor, m)
79	7/29/2015	EWXA03(5.01)
	4:20:36 PM	EWXA01(5.80)
	GMT	EWXA02(7.18)
80	7/29/2015	EWXA03(5.01)
	4:20:43 PM	EWXA01(5.80)
	GMT	EWXA02(7.18)
81	7/29/2015	EWXA03(4.86)
	4:20:52 PM	EWXA01(5.67)
	GMT	EWXA02(7.33)
82	7/29/2015	EWXA03(4.78)
	4:20:56 PM	EWXA01(5.61)
	GMT	EWXA02(7.41)

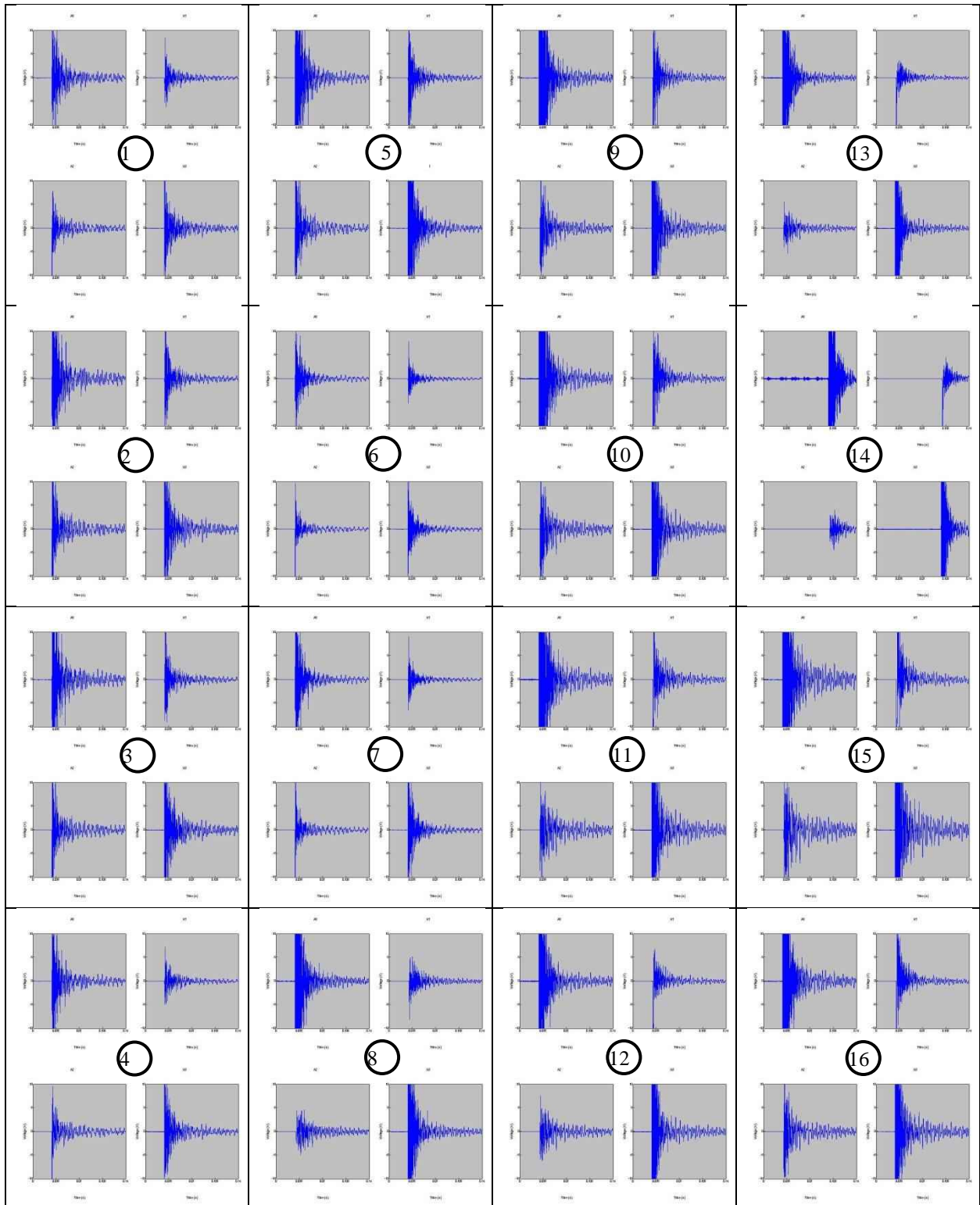


Figure E-69 Acoustic signals (time vs. voltage) due to wire cuts (top left: channel A0; top right: channel A1; bottom left: channel A2; bottom right: channel A3)

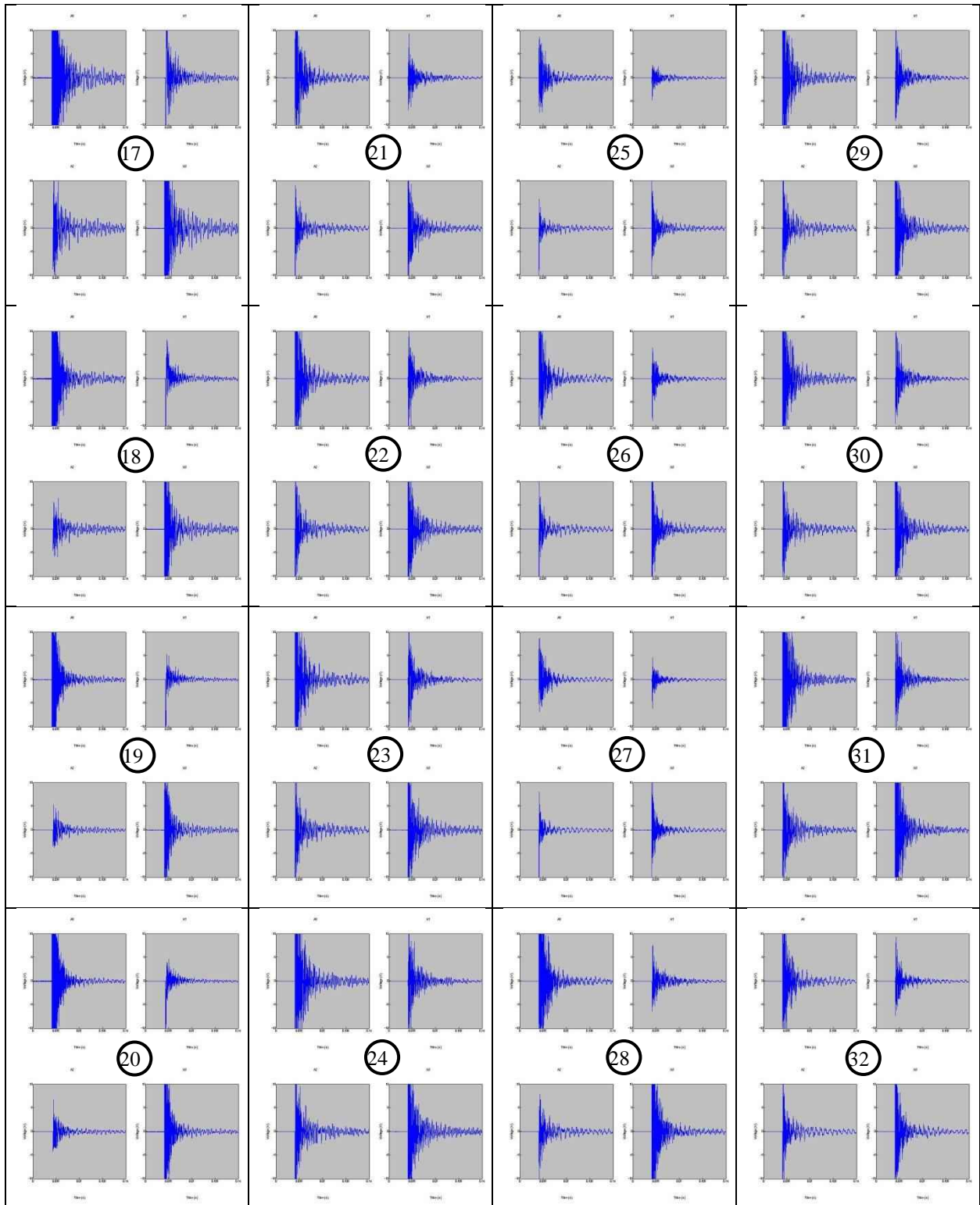


Figure E-69 (cont'd.) Acoustic signals (time vs. voltage) due to wire cuts (top left: channel A0; top right: channel A1; bottom left: channel A2; bottom right: channel A3)

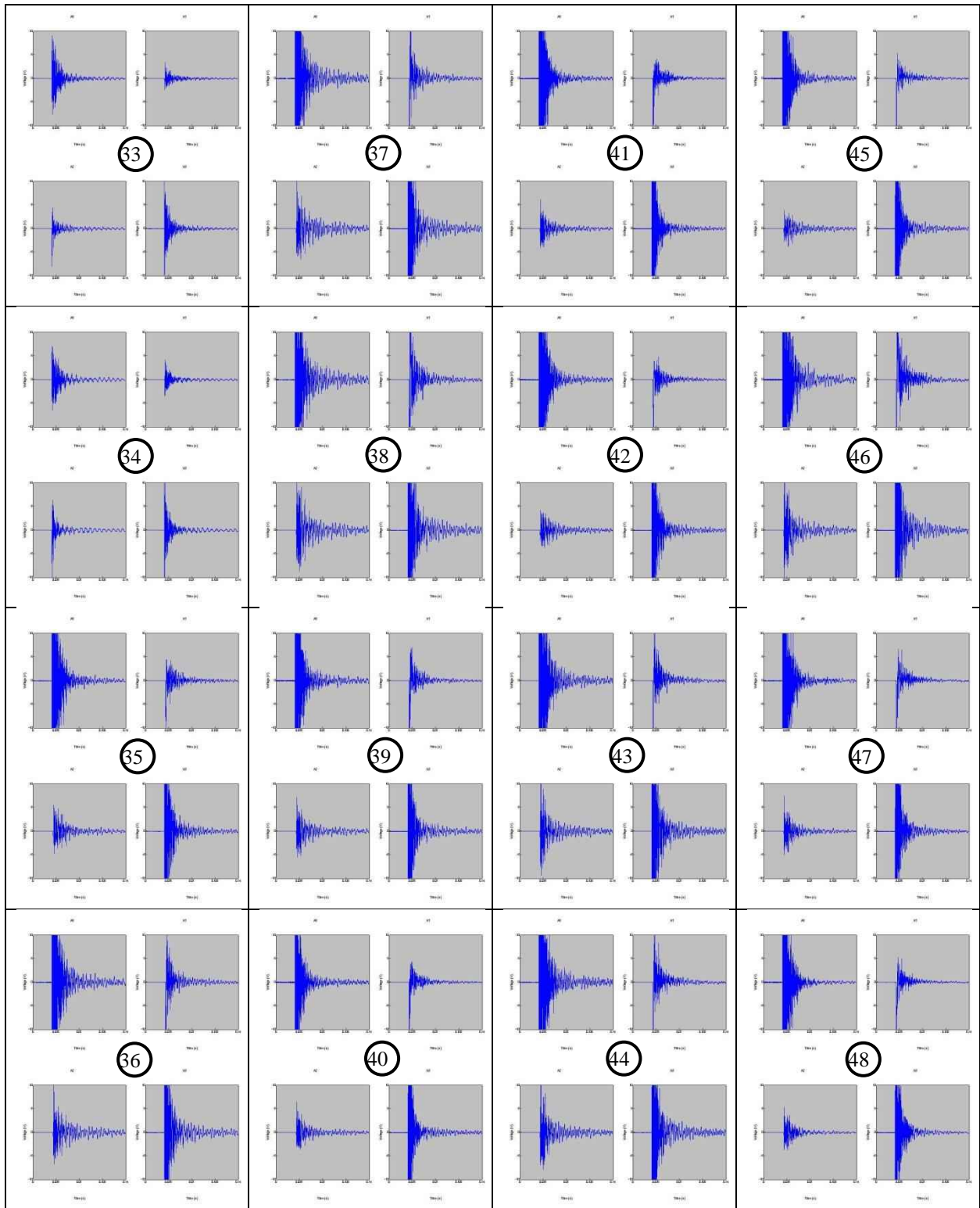


Figure E-69 (cont'd.) Acoustic signals (time vs. voltage) due to wire cuts (top left: channel A0; top right: channel A1; bottom left: channel A2; bottom right: channel A3)

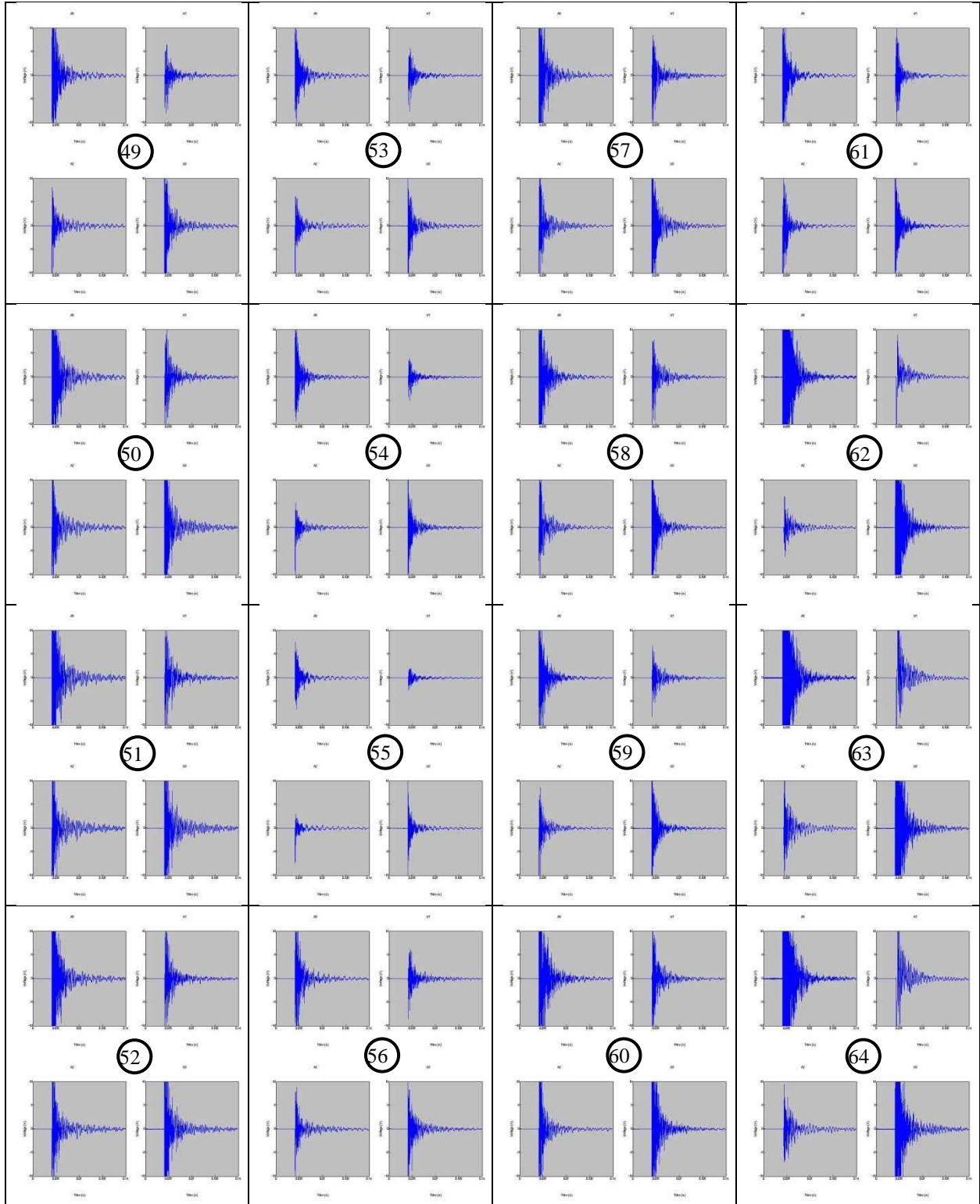


Figure E-69 (cont'd.) Acoustic signals (time vs. voltage) due to wire cuts (top left: channel A0; top right: channel A1; bottom left: channel A2; bottom right: channel A3)

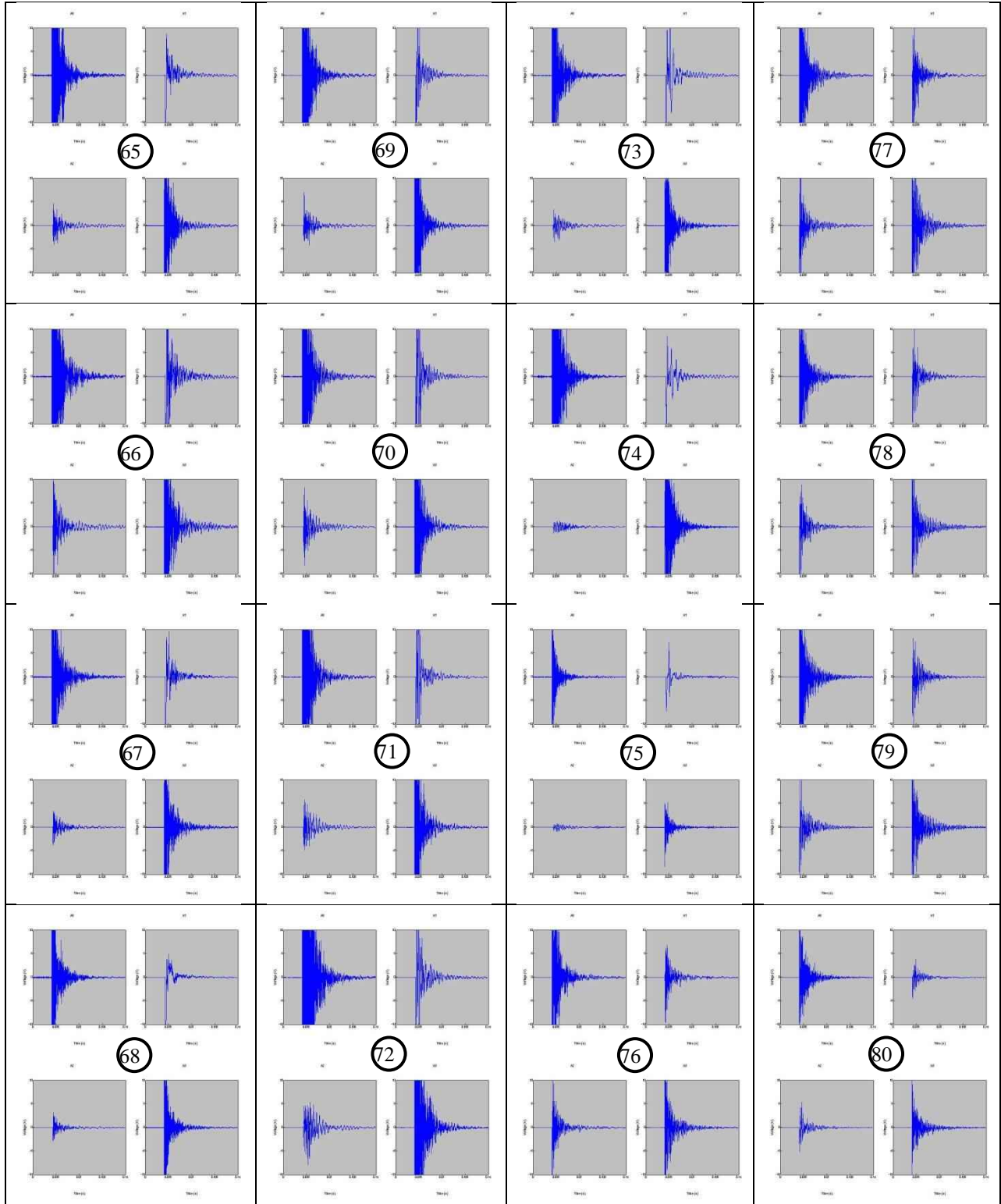


Figure E-69 (cont'd.) Acoustic signals (time vs. voltage) due to wire cuts (top left: channel A0; top right: channel A1; bottom left: channel A2; bottom right: channel A3)

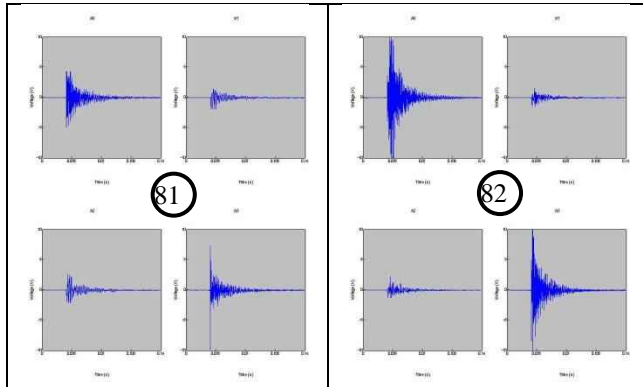


Figure E-69 (cont'd.) Acoustic signals (time vs. voltage) due to wire cuts (top left: channel A0; top right: channel A1; bottom left: channel A2; bottom right: channel A3)

Appendix F—Automated Damage Detection

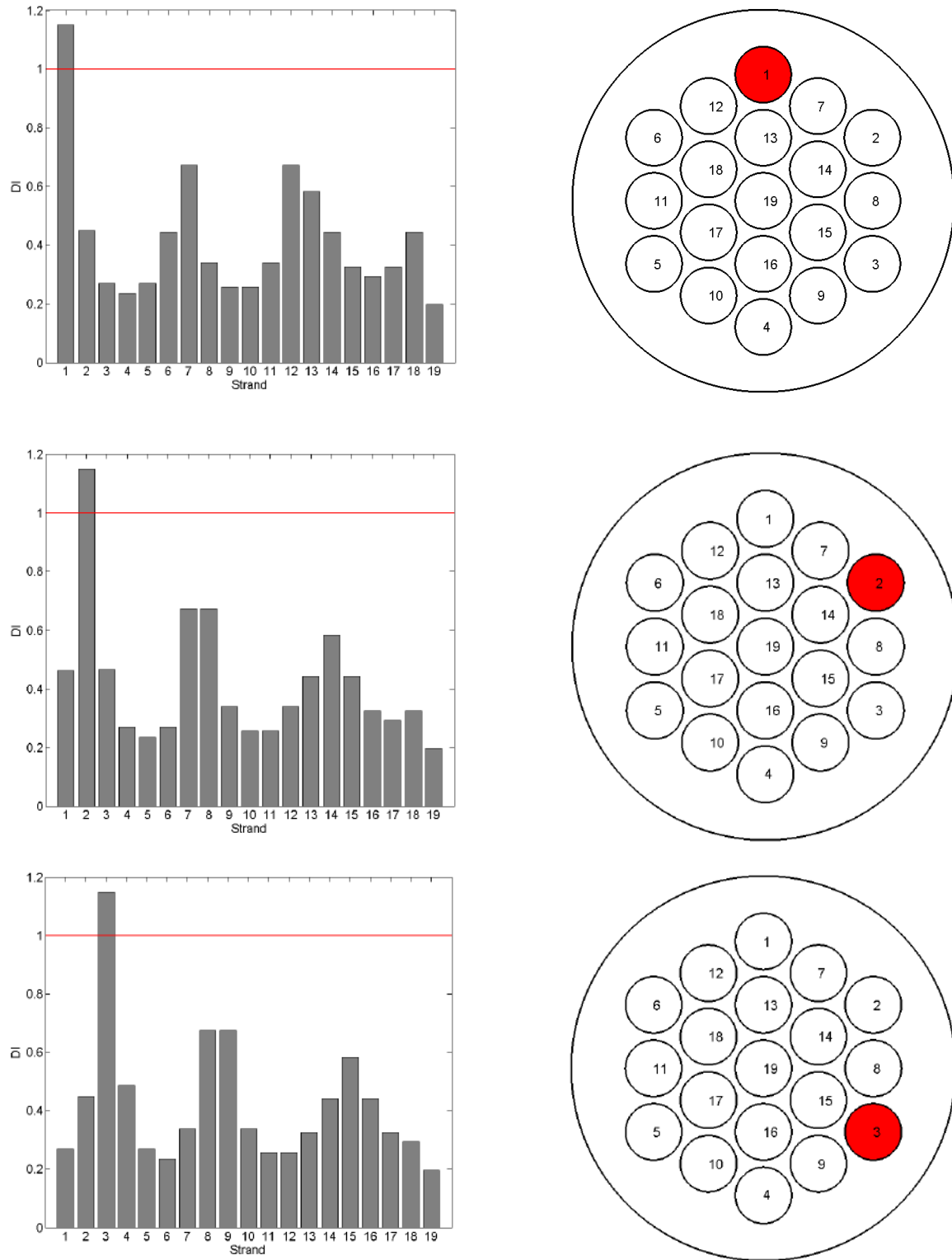


Figure F-70 Damage indices and visualization of tendon damage (Strand 1-Strand 3)

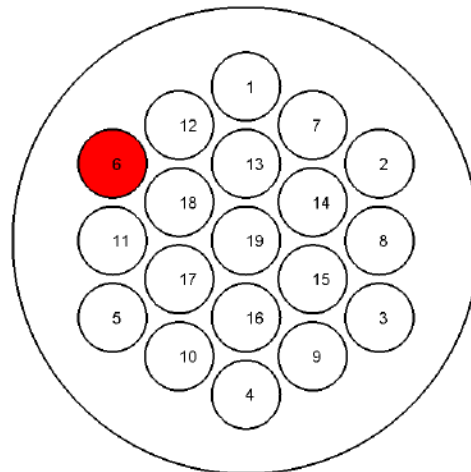
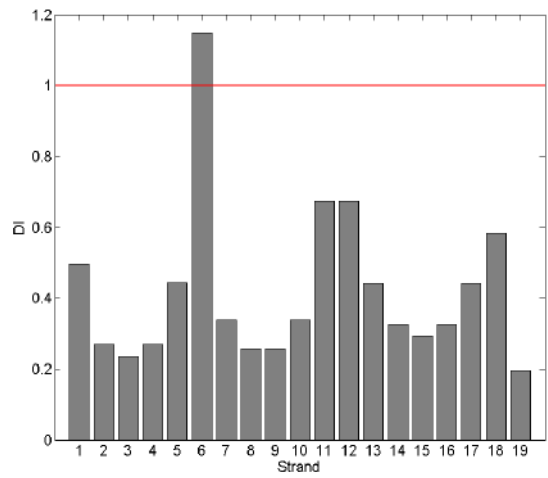
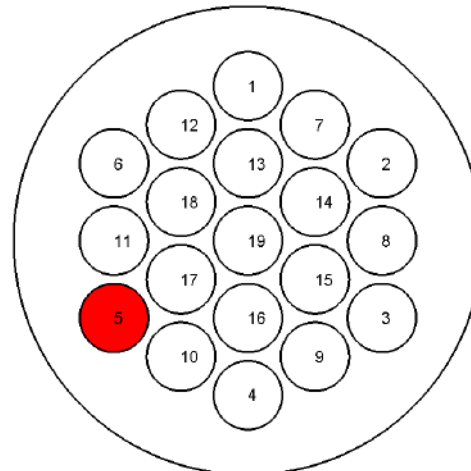
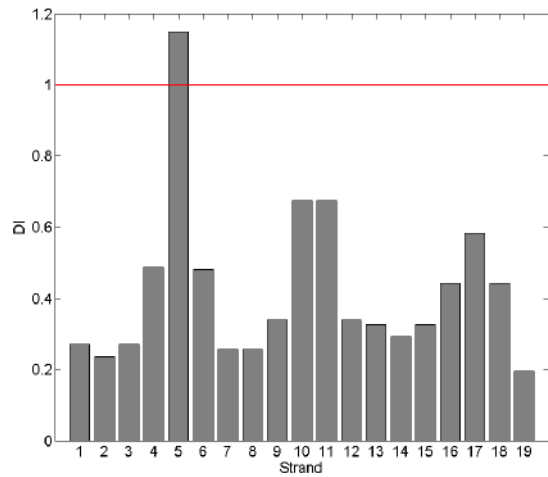
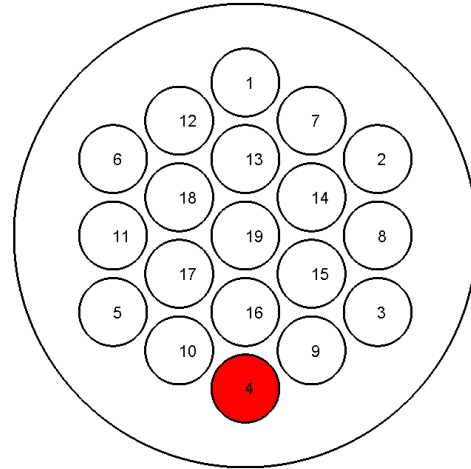
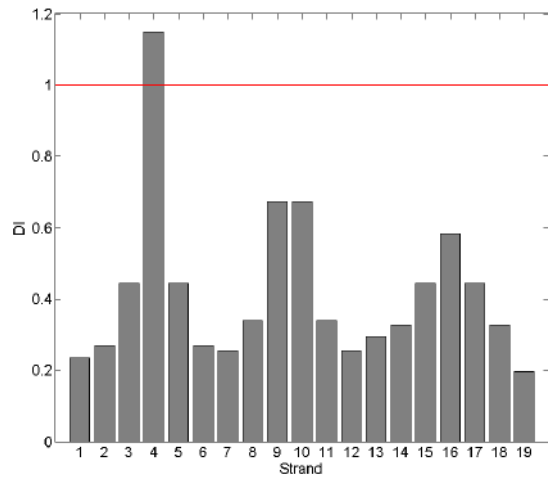


Figure F-71 Damage indices and visualization of tendon damage (Strand 4-Strand 6)

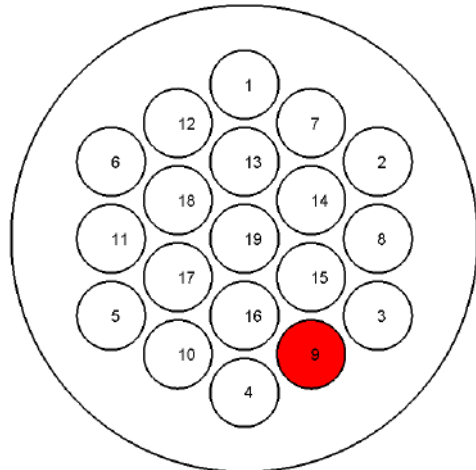
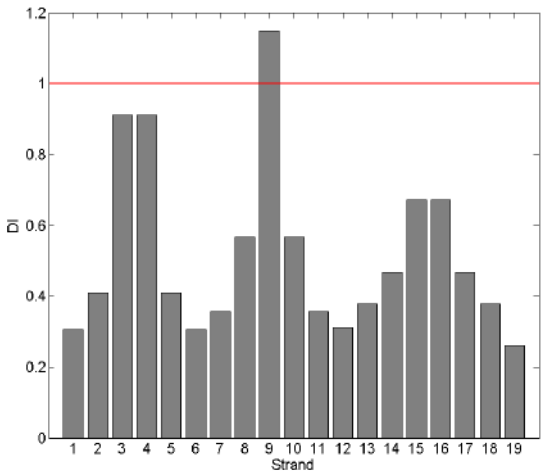
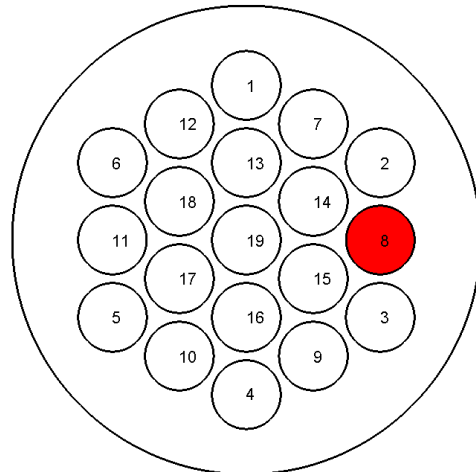
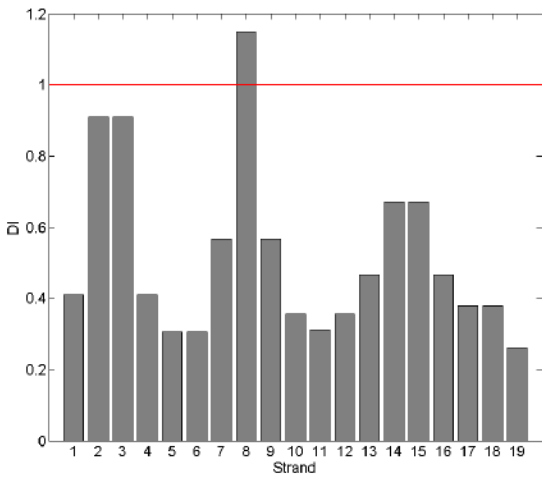
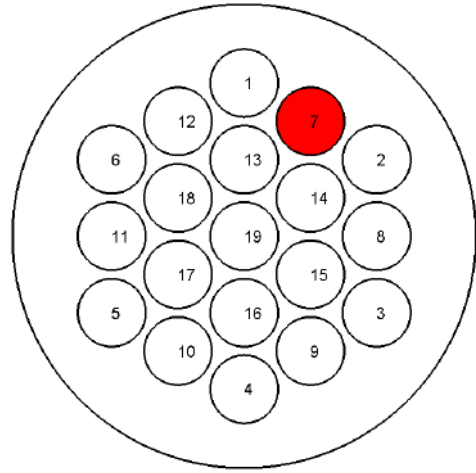
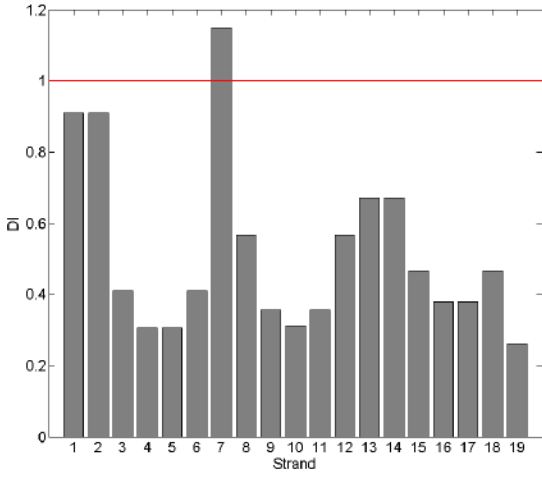


Figure F-72 Damage indices and visualization of tendon damage (Strand 7-Strand 9)

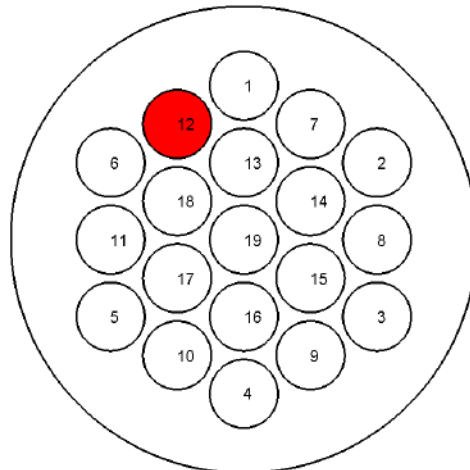
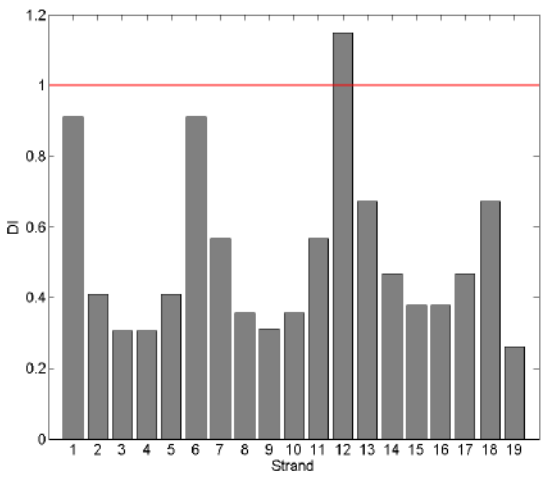
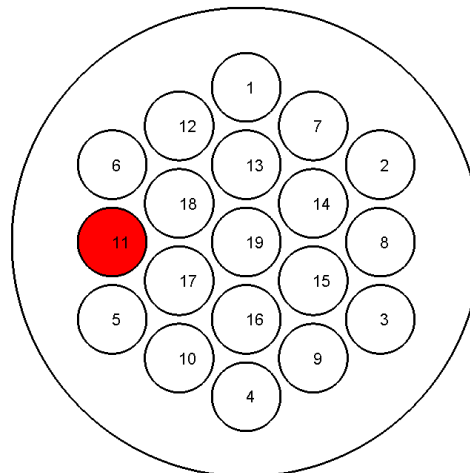
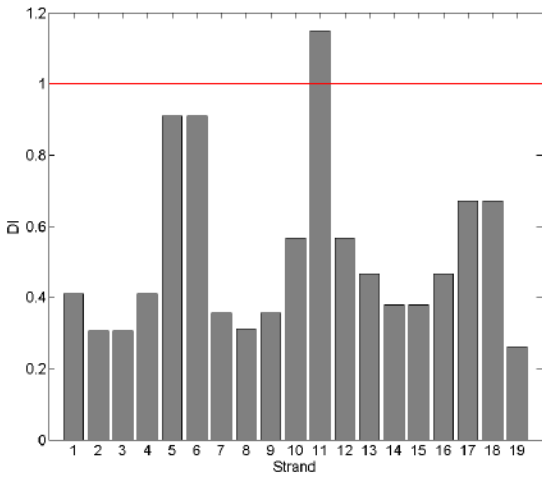
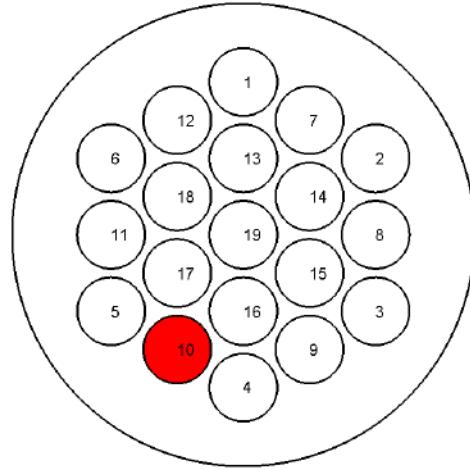
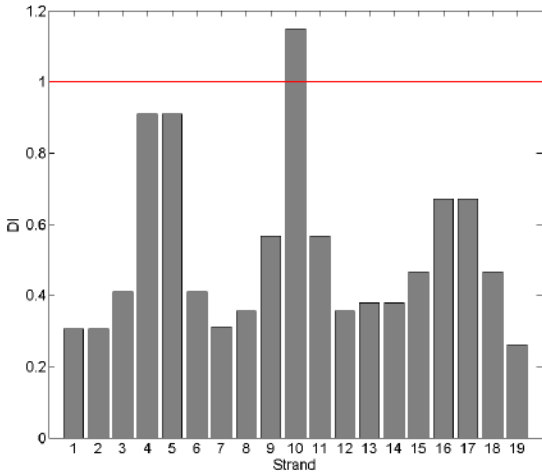


Figure F-73 Damage indices and visualization of tendon damage (Strand 10-Strand 12)

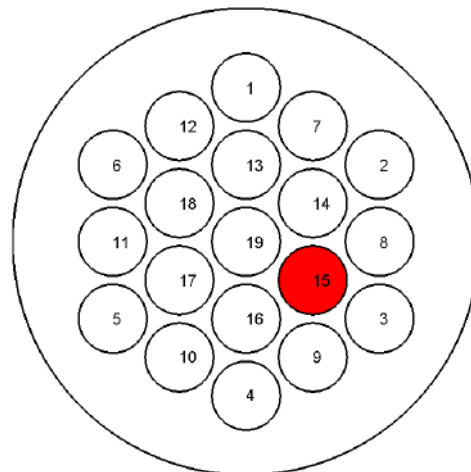
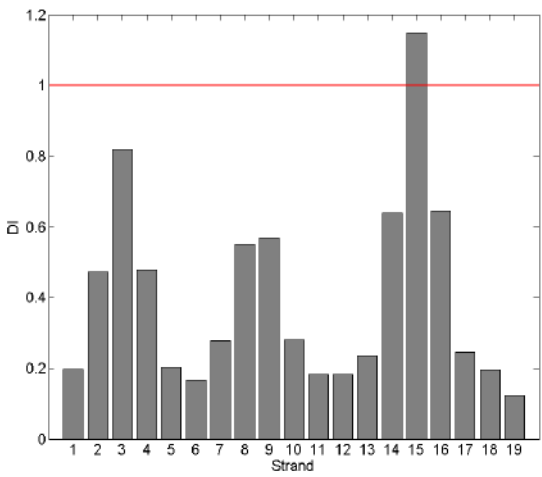
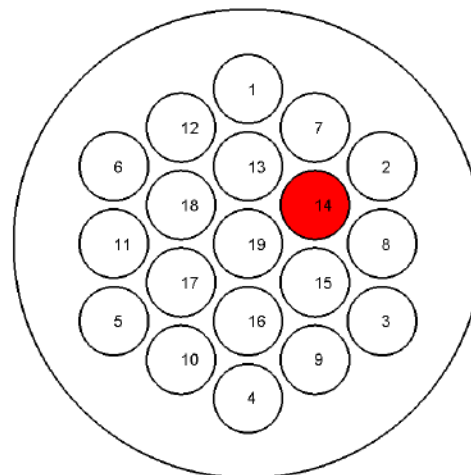
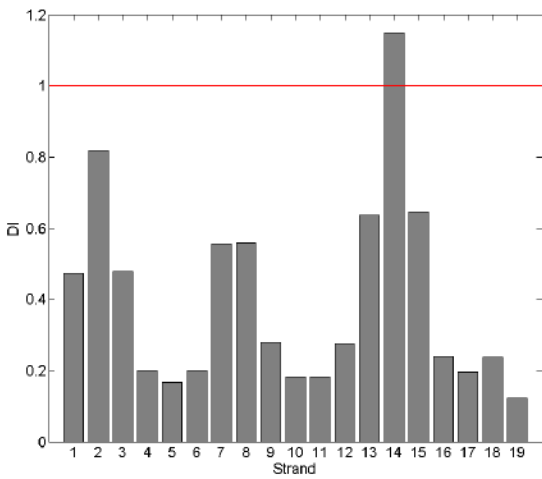
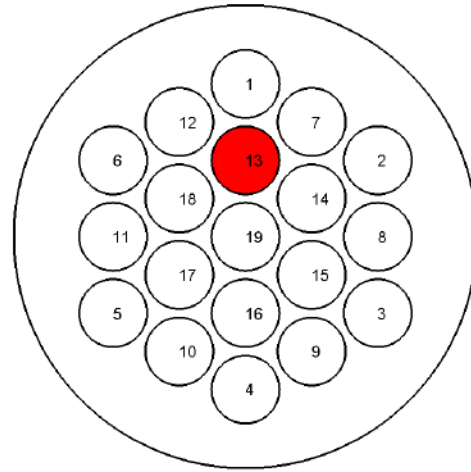
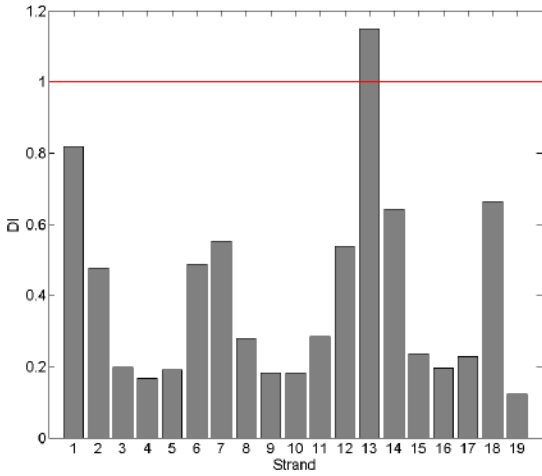


Figure F-74 Damage indices and visualization of tendon damage (Strand 13-Strand 15)

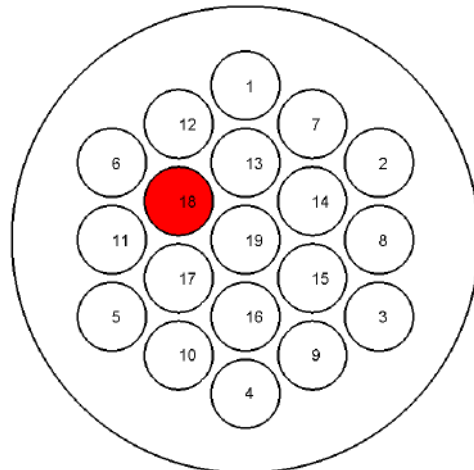
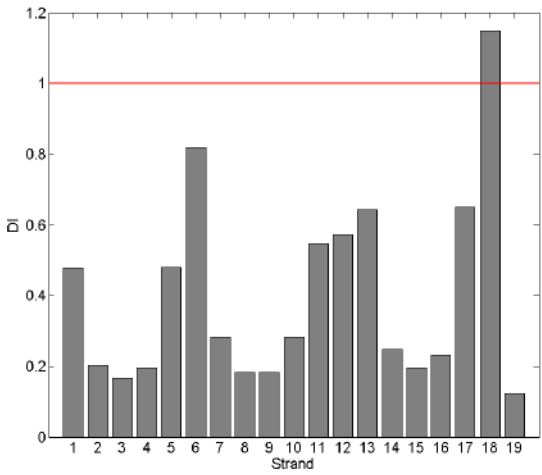
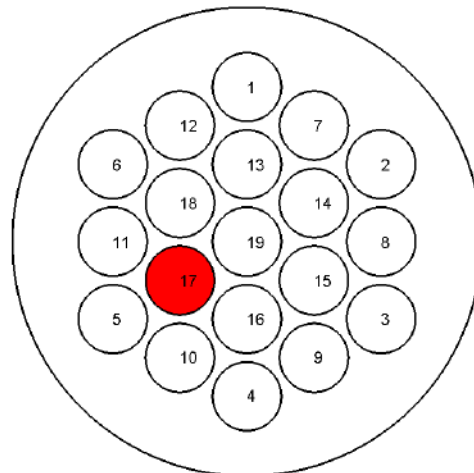
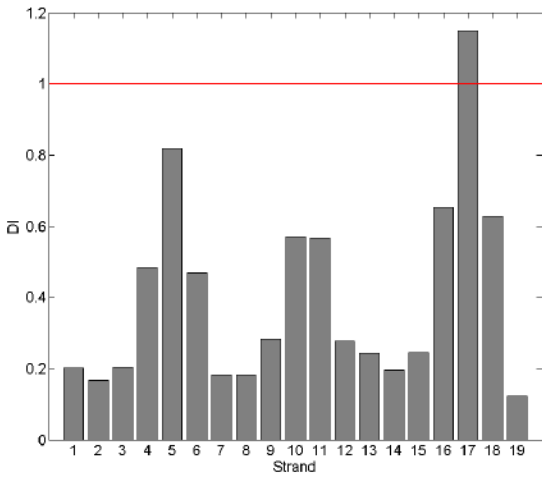
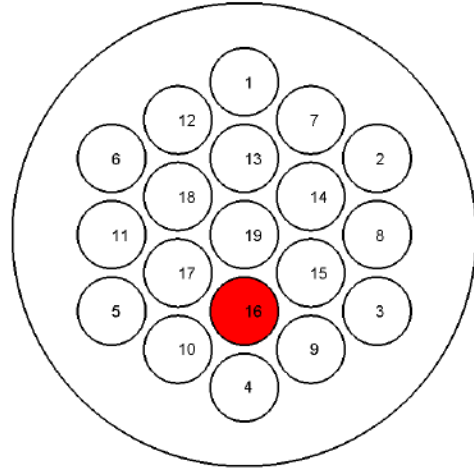
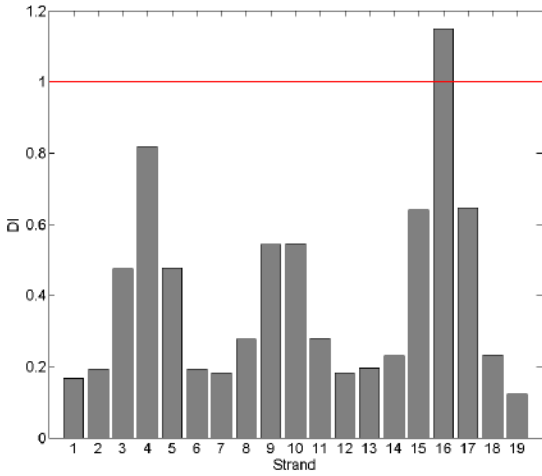


Figure F-75 Damage indices and visualization of tendon damage (Strand 16-Strand 18)

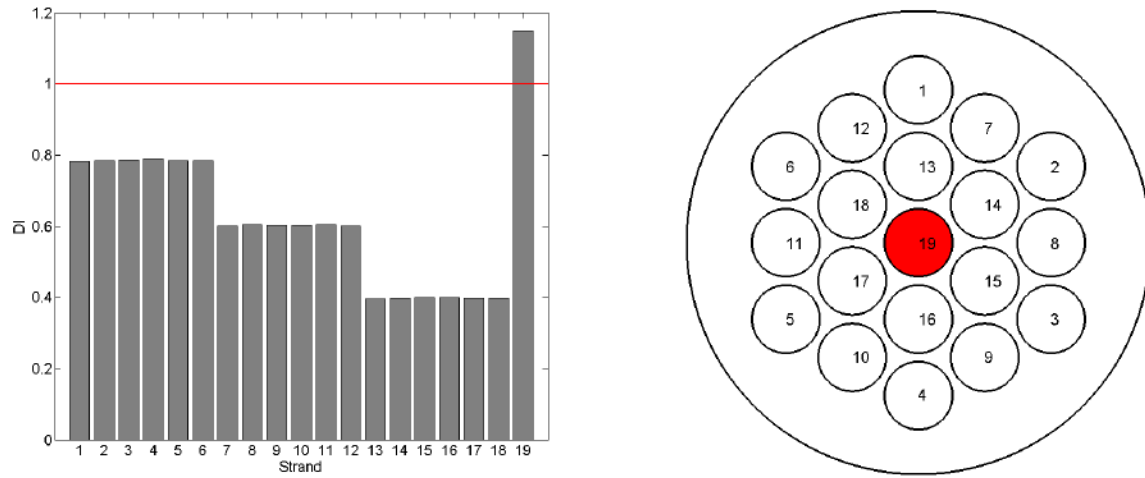


Figure F-76 Damage indices and visualization of tendon damage (Strand 19)